AD-A040 144 ADVISORY GROUP FOR AEROSPACE RESEARCH AND DEVELOPMENT--ETC F/G 17/9
NEW DEVICES, TECHNIQUES AND SYSTEMS IN RADAR.(U)
FEB 77

UNCLASSIFIED AGARD-CP-197 NL

1 OF 7
AD
AD040144

AGARD

ADVISORY GROUP FOR AEROSPACE RESEARCH & DEVELOPMENT

7 RUE ANCELLE · 92200 NEUILLY SUR SEINE FRANCE

AGARD CONFERENCE PROCEEDINGS No. 197

on

New Devices, Techniques and Systems in Radar

NORTH ATLANTIC TREATY ORGANIZATION

DISTRIBUTION AND AVAILABILITY ON BACK COVER

(14) AGARD-CP-197

NORTH ATLANTIC TREATY ORGANIZATION

ADVISORY GROUP FOR AEROSPACE RESEARCH AND DEVELOPMENT

(ORGANISATION DU TRAITE DE L'ATLANTIQUE NORD)

(9) AGARD Conference Proceedings, No.197

(6) NEW DEVICES, TECHNIQUES AND SYSTEMS IN RADAR.

(11) Feb 77

(12) 614p.

400 043

88.

(21) NATO furnished.

Papers presented at the Avionics Panel Symposium, ~~held in~~ The Hague, Netherlands, 14–17 Jun[redacted]76.

THE MISSION OF AGARD

The mission of AGARD is to bring together the leading personalities of the NATO nations in the fields of science and technology relating to aerospace for the following purposes:

- Exchanging of scientific and technical information;
- Continuously stimulating advances in the aerospace sciences relevant to strengthening the common defence posture;
- Improving the co-operation among member nations in aerospace research and development;
- Providing scientific and technical advice and assistance to the North Atlantic Military Committee in the field of aerospace research and development;
- Rendering scientific and technical assistance, as requested, to other NATO bodies and to member nations in connection with research and development problems in the aerospace field;
- Providing assistance to member nations for the purpose of increasing their scientific and technical potential;
- Recommending effective ways for the member nations to use their research and development capabilities for the common benefit of the NATO community.

The highest authority within AGARD is the National Delegates Board consisting of officially appointed senior representatives from each member nation. The mission of AGARD is carried out through the Panels which are composed of experts appointed by the National Delegates, the Consultant and Exchange Program and the Aerospace Applications Studies Program. The results of AGARD work are reported to the member nations and the NATO Authorities through the AGARD series of publications of which this is one.

Participation in AGARD activities is by invitation only and is normally limited to citizens of the NATO nations.

Published February 1977

ISBN 92-835-0185-3

Printed by Technical Editing and Reproduction Ltd
Harford House, 7–9 Charlotte St, London, W1P 1HD

PROGRAM AND MEETING OFFICIALS

PROGRAM CHAIRMAN:

Mr C.W.Cooper
Head, Airborne Radar Group
R.S.R.E.
St Andrews Road
Malvern, Worcs WR14 3PS
UK

PROGRAM COMMITTEE

Mr Y.Brault
Division Equipements Avioniques
& Spatiaux
178 Bld Gabriel Peri
92240 Malakoff
France

Dr K.G.Corless
R.S.R.E.
St Andrews Road
Malvern, Worcs WR14 3PS
UK

Mr J.Freedman
Assistant Director
MIT Lincoln Laboratory
Lexington MA. 02173
USA

Mr A.J.Kampstra
S.T.C.
P.O. Box 174,
The Hague
Netherlands

Prof. G.Ravelli
Scuola di Ingegneria Aerospaziale
Via Eudossiana, 16
00184 Roma
Italy

Dr Ing. M.Vogel
DFVLR
8031 Oberpfaffenhofen
Post Wessling/obb
Germany

AVIONICS PANEL

CHAIRMAN: Mr J.N.Bloom, C.R.C., Ottawa, Canada
DEPUTY CHAIRMAN: Ir. H.A.Timmers, NLR, Amsterdam, Netherlands

AVIONICS PANEL EXECUTIVE

Cdr D.G.Carruthers, USN
AGARD

PREFACE

Progress in the development of radar systems stems from a number of contributory factors. For example, the availability of new devices offers greater reliability, lower cost and reduced space/weight demands. Another contributory factor is the application of new techniques such as digital methods of signal processing and data handling. Some advances are made possible by a better understanding of fundamentals, while the need for operation in a complex radar environment, including countermeasures, is an increasingly significant influence on system design. The capability of radar may be extended by exploiting little-used parts of the electro-magnetic spectrum and from time to time radically new system concepts emerge.

In May 1970, an AGARD Symposium entitled "Advanced Radar Systems" was held in Istanbul, Turkey. The object of the 1976 Symposium was to bring together scientists and engineers concerned with all aspects of modern radar research and development in order to review progress in the intervening years and to discern the major influences on radar system design.

In planning the 1976 Symposium the Programme Committee decided not to emphasise antenna and display techniques as these topics were covered by AGARD Symposia in 1972 and 1975 respectively.

The programme was arranged in five sessions covering:

Devices and Modules,
Radar Techniques,
Target, clutter and propagation,
Simulation and detection theory,
New systems and concepts.

The papers in the Proceedings are grouped in the same way.

Session 1 opens with a review (Paper 1) of the state of development of solid-state amplifiers and oscillators, which have now been developed to the point where they are meeting the transmitter requirements of low-power radars. Papers 2 and 3 describe inexpensive low-noise amplifiers which offer the system designer a wider choice of performance level in relation to cost. Papers 4 and 5 emphasise the continuing development of high power amplifiers such as TWTs and klystrons, which clearly remain dominant in their field. Significant developments of high-power PIN-diode phase-shifters are described in Paper 6 while Paper 7 describes some novel ideas in reviewing a wide range of millimetre-wave components. Paper 8 surveys the use of surface-acoustic wave devices in radar systems and emphasises the variety of capabilities which these components now offer. Paper 9 effectively complements this treatment of SAW technology by describing a particularly interesting form of surface-wave analog-memory correlator and by presenting some of the design techniques used in advanced forms of these devices. The Session closes with two papers on new developments in doppler filtering – Paper 10 is concerned with serial analog memories in MTI while Paper 11 discusses the design of a real-time Fast Fourier Transform processor, and is an illustration of the impact of digital techniques on complex signal-processing. Although not covered specifically, this Session revealed the importance of high performance analog-digital converters and the potential of combining CCDs with SAW devices in order to extend the use of the latter to lower frequencies.

Session 2 covers a wide range of radar techniques and opens with a presentation (Paper 12) of the value and capability of digital techniques in signal manipulation prior to display, including scan-conversion. Another important application of digital techniques is that of clutter cancellation and MTI in surveillance radars and this is emphasised in Papers 13 and 14, while Paper 18 describes valuable improvements to design methods for digital MTI cancellers used with staggered-prf radars. Paper 15 reports encouraging progress on the well-known problem of tracking air targets at low elevation angles. Radar imaging is dealt with in Papers 16 and 17 which present methods based upon doppler processing. Papers 19, 20 and 21 deal with plot extraction and tracking, where the influence of rapidly developing computer technology is manifest and the use of adaptive techniques is a clearly apparent trend. In maritime radars the problem of false alarm control is particularly acute and the effectiveness of 'non-parametric' threshold setting is well illustrated in Paper 22. The technique of sidelobe suppression is finding application in ground-based surveillance radars for clutter and interference rejection. Its potentialities and limitations have been thoroughly studied and are reviewed in Paper 23. The two papers which conclude this Session relate to secondary radar. Some interesting experimental results on the application of phase-comparison monopulse to improve azimuth measurements are presented in Paper 24 while Paper 25 quantifies the severity of interference problems in a dense environment.

Session 3 deals with targets, clutter and propagation. Relatively few abstracts were submitted and only two papers could be presented. The first of these, Paper 26, should be of value to designers of satellite radars as it presents some interesting results from a satellite-borne radar over North America, Brazil and the oceans. Paper 27 deals comprehensively with a sea-clutter model for the North Atlantic and with target characteristics. It is a highly significant contribution towards the ultimate aim of a unified clutter model.

Session 4 covers simulation and detection theory, there being two papers on each topic. Papers 29 and 32 deal with simulation; the first emphasising radar environment simulation while the second is concerned with tracking a scintillating,

glinting target in multipath conditions. Both papers are valuable in highlighting the significance and power of simulation techniques in system design. Papers 30 and 31 deal with detection theory. The first analyses the possibility of employing adaptive polarisation to discriminate target from background, while the second describes improved methods of calculating the detection probability of fluctuating signals.

The Proceedings conclude with Session 5 in which new systems and concepts are reviewed in eight wide-ranging papers. Paper 33 opens the Session with an impressive illustration of the extension of coherent radar techniques to the infra-red part of the spectrum, drawing attention to the differences which arise in system design concepts. Paper 34 deals comprehensively with the potentialities of laser radar. At the shorter wave-lengths propagation characteristics are particularly important and this gave rise to some discussion at the Symposium. The point is emphasised in Paper 35, on a millimetre-wave tracking radar. Phased array radars are gradually becoming more numerous and Paper 36 exemplifies system and performance aspects of a phased-array radar with automatic phase adjustment. An unusual application of radar is described in Paper 37, which is concerned with radar images of objects in space. Paper 38 deals with a monopulse array antenna with independent elevation beam-scanning. Airfield ground-movement monitoring is an unusual aspect of secondary radar and Paper 39 describes experimental work which has demonstrated its feasibility. Paper 41 concludes the Session with an indication of the way in which a number of modern techniques, including a microprocessor and liquid-crystal display are combined in an all solid-state radar for wind measurement.

The papers and subsequent discussions clearly indicate the ways in which the capability of radar is being extended and draw attention to a number of significant trends. In the field of radar components and sub-systems, steady progress can be observed on a wide front with some microwave elements displaying novel and ingenious design concepts. These developments offer considerable benefits in the performance and reliability of radar systems. Digital technology is having a major impact on signal processing. However analog signal processing techniques, based on surface-acoustic wave and charge-coupled devices, are also advancing impressively. It seems clear that digital and analog techniques will continue to be complementary in the field of signal processing. In data handling and displays, the powerful influence of digital technology and computers has been augmented by the arrival of the microprocessor. Rapid advances in digital technology are motivated by strong commercial incentives and radar is deriving great benefit from this, particularly in military applications. In the understanding of target and clutter characteristics and in the improvement of detection theory, progress is steady rather than dramatic. In these areas, refinements rather than radically new concepts are to be expected. The extent to which radar systems and their environment can now be simulated by computer techniques offers a powerful method of evaluating and optimising system design, with consequent savings in time and cost of development. This is seen as an expanding field of activity. There is continuing interest and progress in phased-array techniques and the number of applications is increasing, particularly when electronic scanning is combined with mechanical scanning. However the cost of full electronic scanning for 3D radars is still preventing its widespread application. While impressive technical developments are facilitating the exploitation of the higher frequencies of the radar spectrum, the limits of system performance are being dictated largely by atmospheric propagation characteristics. After several decades of intensive development of radar systems it is noteworthy that advances in many specialised areas are enabling a high rate of overall progress to be maintained.

The lively verbal exchanges at the Symposium supplemented by subsequent written contributions, have provided much discussion material. Consequently the record of the discussion period has been inserted in the Proceedings immediately after the relevant Paper. Discussion has been recorded in the languages used at the time, so that the specialist reader may have direct access to the original statements.

C.W.COOPER, Program Chaiman
K.G.CORLESS, Editor

CONTENTS

Reference

SESSION 5 – NEW SYSTEMS AND CONCEPTS

SOLID STATE MICROWAVE AMPLIFIERS AND LOCKED OSCILLATORS

FOR COHERENT RADAR TRANSMITTERS

I.W. Mackintosh, P.W. Braddock, M. Dixon, R. Genner and R.J. Royds
Royal Radar Establishment
Malvern, Worcestershire
United Kingdom

SUMMARY

This paper gives an account of work directed at providing a range of solid-state components for various types of coherent radar transmitter. The emphasis is on transmitter operation in the region 8 to 10 GHz, and the components considered are IMPATT diode amplifiers, and TRAPATT diode and LSA diode oscillators. These components may be considered for use as driver stages to tube output stages or as transmitters in all solid-state radars. The paper examines the potential role and present status of each of these devices and describes their performance in terms of parameters relevant to radar transmitter operation.

Results are presented on IMPATT amplifiers with up to 6W CW power output and up to 20W peak power output over 4 μs pulses, TRAPATT oscillators capable of 10W peak power output over 5 μs pulses with high efficiency, and LSA oscillators with 100W peak power output over 250 ns pulses.

1. INTRODUCTION

The point has been reached where designers of radar systems, as a matter of course, need to examine solid-state solutions for components in their transmitters. This is particularly the case with radars for which all-solid-state transmitters, and hence all-solid-state systems are now possible. It will be seen, from results presented in this paper, that all-solid-state solutions are possible in the band 8 to 10 GHz for CW output powers and mean output powers of the order of watts. A more exact estimate of the power available is dependent upon the choice of device which in turn is dependent upon choice of waveform, pulse length and duty cycle. This is discussed in more detail below.

The standard advantages claimed for solid-state microwave components are those of small size, low weight, low cost, high reliability and compatibility with microwave integrated circuit technology. Low voltage operation and absence of heaters are additional advantages. Small size and low weight solid-state transmitters are being realized by the engineering of components using diodes mounted in miniature coaxial cavities, followed by the development of integrated transmitters using microstrip. Low cost is expected to result from for example the adoption of thick film on alumina technology. High reliability is being actively pursued by device manufacturers paying attention to device contact metallization giving enhanced median-time-to-failure performance.

2. PEAK POWER AND MEAN POWER

It is important to distinguish between best laboratory performance and the performance of developed components. A developed component is one which not only meets requirements with respect to power and efficiency (primary parameters) but also with respect to specifications in regard of so-called secondary parameters such as bandwidth, phase linearity with frequency, rise time, etc. The component will also be required to work over a temperature range and may be subject to other environmental conditions.

The power output of a developed component is less than the best laboratory device performance on account of a number of factors. The material, structure and heat sinking of the best laboratory device will not be consistently reproduced in the developed devices. The requirement to work over a temperature range coupled with a specification on a minimum value of median-time-to-failure means that a ceiling is placed on device temperature, and this will limit the output power. With pulsed devices, the simultaneous specification of pulse length and duty cycle will reduce the peak power available - this is particularly evident with the LSA device. Additionally, the more exacting are the secondary parameter specifications, the greater is the reduction in developed performance.

Table 1 lists IMPATT, TRAPATT and LSA devices used in the programme, together with their origin and oscillator performance. The data in the table refers to the performance of developed devices except where otherwise indicated.

TABLE 1

OSCILLATOR PERFORMANCE ~9.5 GHz

DEVICE	STRUCTURE	FIRM	POWER OUTPUT W	EFFICIENCY %	
GaAs IMPATT	SD UNIFORM DOPING	PLESSEY(1)	1.5	12	CW
GaAs IMPATT	READ	STL(1)	3 2	15 24	} CW(2) 9 GHz
Si IMPATT	SD UNIFORM DOPING	MICROWAVE ASSOCIATES	1	5	CW
Si IMPATT	DD	HEWLETT PACKARD	3	10	CW
Si IMPATT	DD	HEWLETT PACKARD	10	10	PULSED 25% DUTY 5 μs PULSE
Si TRAPATT		PLESSEY(1)	12	35	8.5 GHz PULSED(3)
GaAs LSA		STL(1)	100	10	PULSED 250 ns 0.2% DUTY

(1) Devices supplied under CVD contract

(2) Device research result

(3) Device research result, Purcell et al, 1975.

SD = single drift, DD = double drift.

Figure 1 shows the peak power performance plotted against duty cycle, including CW data along the 100% ordinate. Figure 2 shows the data recast as mean power versus duty cycle. For comparison, data on a commercially available pulsed Gunn diode working at 1% duty cycle is also shown. The efficiency shown for the GaAs LSA is for an overall efficiency of a complete transmitter module. The efficiency shown for the TRAPATT is a projected developed efficiency.

The classification of device performance on the basis of duty cycle allows the identification of the roles of the devices in regard of the type of transmitted waveform.

The simplest scheme is to use a pulse, without additional in-pulse modulation, of a duration appropriate to the desired range resolution. LSA devices are attractive in this respect in that they provide high peak powers over short pulses (up to about 0.5 μs). Mean powers for developed transmitter modules are up to about 300 mW. However, it is clear that in its present form the LSA device is of lower mean power and lower efficiency than the best of its competitors.

Higher mean power is obtainable from higher duty cycle devices TRAPATTs and double drift IMPATTs (10 to 25% duty cycle), coupled, in the case of TRAPATT devices, with high efficiency. Good range resolution will be possible with long pulse (>5 μs) operation and pulse compression. However this will be at the expense of an increase in minimum range, which may be unacceptable. This problem may be circumvented by use of a shorter pulse with reduced mean power for short range, but with added system and operational complexity.

CW operation gives good power performance and can take advantage of high efficiency IMPATTs. The problems associated with thermal transients are avoided and the need for a pulse modulator is eliminated. Dual antennas, however, are probably always required at transmitter power levels of a few watts, and, if linear FM is used, control of the linearity of the modulation can prove to be difficult.

An alternative to CW operation is interrupted CW (~50% duty cycle) in order to avoid the dual antenna problem; a reduction in efficiency compared to CW operation will result if the transmitter is allowed to consume power continuously.

All four types of waveform need to be considered by the system designer, and there is no general a priori reason to eliminate any of them. In the authors' opinion, bearing in mind efficiency and mean power performance, and also the use of surface acoustic wave pulse compression filters, the advantage presently lies with long pulse operation of IMPATT and TRAPATT devices.

3. COHERENT TRANSMITTERS

A feature of a coherent radar system is the generation of a signal at a low power level and which carries a reference phase embedded in the modulation on the signal, and to add power to this signal in the transmitter. With solid-state devices, this power addition may be achieved with either a stable amplifier or with a locked oscillator. IMPATTs and TRAPATTs may be operated in either configuration, and LSA devices may be used as locked oscillators.

Data on the bandwidth performance of IMPATT amplifiers is given in the next section - it will be seen that bandwidths up to 3 GHz are possible (with dynamic ranges up to 6 dB) LSA locked oscillators have bandwidths of about 200 MHz with gains of about 8 dB. TRAPATT locked oscillators have bandwidths of about 100 MHz at 10 dB gain, and TRAPATT amplifiers have bandwidths of up to ~500 MHz.

With simple pulsed oscillator transmitters, a significant transmitter parameter is the in-pulse chirp, ie. the change in frequency during the pulse due to a change in device temperature or bias with time. With the pulsed amplifier or locked oscillator changes in device temperature or bias result in a change in output phase with respect to the input phase. Control of this variation is important with their use in pulse compression systems, in coherent radars with I and Q receiver output channels and in transmitting arrays of solid-state components. Arrays may be considered as a means of combining the outputs of a number of devices, as in phased arrays, or in transmitting arrays with array signal processing in which the array is used to tailor the transmit antenna polar diagram.

Due to the sensitivity of the free-running frequency to temperature and bias, phase stability could be a serious problem for the LSA locked oscillator. Results presented later in the paper will show that good phase stability may be achieved in developed LSA transmitters by compensation for temperature changes and using stable bias pulses.

TABLE 2

Single Stage single diode IMPATT amplifiers

Device	Frequency GHz	Power Output W	Bandwidth (-1 dB) MHz	Efficiency %	Gain, (saturation) dB	Gain, small signal dB
Silicon SD	10.0	0.6	420	5	6	>16
Silicon DD	9.0	3.4	900	12	6	11
GaAs SD	10.0	1.3	520	12	6	>16
GaAs READ	7.8	2.8	140	21	6	>16
Silicon DD (PULSED) 4 μs, 2% duty	9.6	12	1,500	10	6.5	>16

SD = single drift

DD = double drift

4. IMPATT AMPLIFIERS

Table 2 summarizes the performance obtained with single stage, single tuned, single diode coaxial amplifiers using diodes whose origin is specified in Table 1. It can be seen that the largest bandwidths are obtainable with silicon double drift devices, see Figure 3, followed by GaAs single drift CW devices. At a gain of 4 dB, GaAs single drift devices have a bandwidth capability of 3 GHz. With the Read device, the limited range in both bias and output power over which high efficiency may be achieved results in a small instantaneous bandwidth at the saturated output level.

In order to increase the output powers further, it is necessary to consider combining devices. There are a number of ways of combining. At the device level, it is possible to incorporate a number of mesas in the same package; this is the case for the CW silicon double drift devices appearing in Tables 1 and 2; it is not the case for the GaAs single drift devices above. The next stage is to combine packaged devices in the same oscillator or amplifier cavity. A technique for achieving this has been described by Rucker (Rucker, C.T., 1969). This technique gives good combining efficiency and wide bandwidth and results are presented below on amplifiers constructed using this technique. Finally, further power addition may be obtained by combining cavities using 3-dB couplers or Wilkinson power combiners.

The Rucker combining technique places diodes each end of a coaxial cavity. Power is extracted at the centre of the cavity by a capacitance coupled probe. In order to suppress an unwanted mode, in which the diodes oscillate in antiphase, a resistance is placed at the cavity centre which impedes the current

flow associated with the unwanted mode. Two diodes may be combined readily with this technique, and four diodes may be combined with diode selection and careful circuit adjustment.

Table 3 gives the performance of multidiode single stage IMPATT amplifiers. With the exception of the silicon pulsed double drift result, which used a 3 dB coupler, the results refer to Rucker combining. Figure 4 shows a photograph of the amplifier stage which combines four single drift silicon IMPATTs. Figure 5 shows the response of a 2.6W CW amplifier which combines two GaAs single drift IMPATTs.

Table 4 gives the performance of a multi-stage silicon single drift IMPATT amplifier which combines two diodes in the penultimate stage and four diodes in the final stage. Two final stages have been combined to give an output power of 13W CW. A schematic of the amplifier chain is shown in Figure 6. This multi-stage amplifier minus its final stage (ie. a 2W CW amplifier) has been used in conjunction with a p-i-n diode switch as the transmitter in an airborne pulse compression radar. The pulse length was 5 μs and the pulse repetition frequency was 16 KHz. The linear in-pulse FM was 25 MHz; the phase linearity and the amplitude ripple with frequency of the amplifier did not degrade the range resolution of the radar. A range performance of 4 nautical miles was demonstrated in airborne trials.

TABLE 3

Single stage multiple diode IMPATT amplifiers

Device	Number combined	Frequency GHz	Power Output W	Bandwidth (-1 dB) MHz	Efficiency %	Gain (saturation) dB	Gain, small signal dB
Silicon SD	2	9.5	2.75	420	5	6	>16
	4	9.5	6.5	300	5	6	>16
Silicon DD	2	10.7	7.0	450	12	6	>16
GaAs SD	2	8.9	2.6	700	12	6	>16
Silicon DD (PULSED) 4 μs, 2% duty	2	9.6	17	3,300	8	6.5	10

TABLE 4

4-Stage IMPATT Amplifier

MICROWAVE PERFORMANCE

f_o	9.6 GHz
P_{out}(Sat.)	6.3 W
Gain(Sat.)	28 dB
Gain(S.sig.)	49 dB
BW(-1dB)	200 MHz
Phase Linearity	$\pm 3^o$ over 30 MHz band
Amplitude Ripple	<0.2 dB over 30 MHz band
Group Delay	12 nS
AM/PM (Sat.)	18^o/dB
-1 dB Gain Comp.	-8 dB down on Saturation
Efficiency	4.5 %

ELECTRICAL REQUIREMENTS

Voltage	100 V
Current	1.4 A (Constand Current)

The volume and weight of IMPATT amplifiers may be reduced by using microstrip construction. The amplifier equalization circuit, bias network and circulator may all be placed on the same substrate. Table 5 gives data on examples of silicon single drift single stage thick-film microstrip IMPATT amplifiers. The gain figures do not include losses in the circulator and bias network. With a completely integrated amplifier, bias network and circulator projected losses are 1 dB per stage. These figures apply to an integrated construction on alumina substrates with ferrite discs inserted in the alumina to form the circulators. Insertion losses of circulators on all ferrite substrates have been measured to be 0.4 dB per pass. Figure 7 shows a photograph of thick film microstrip components for IMPATT amplifiers.

TABLE 5

Examples of CW thick-film microstrip IMPATT amplifiers at 9.3 GHz ML70405 diode.

Input Power mW	Output Power mW	Gain dB
83	275	5.2
125	410	5.2
170	500	4.7
210	580	4.4
250	645	4.1

5. TRAPATT OSCILLATORS AND AMPLIFIERS

The attraction of the TRAPATT diode is the high conversion efficiency achievable with the oscillator at frequencies up to about 10 GHz. Best efficiencies exceed 50% up to about 1.5 GHz, and efficiencies of 30% or more have been achieved with good reproducibility at around 9 GHz (Purcell et al, 1975). Peak powers at 9 GHz exceed 10W; mean output powers of 1W and pulse lengths of greater than 5 μs have been demonstrated (Purcell and Oxley, 1976). The mean power may be exploited using pulse compression with surface acoustic wave compression filters. The use of solid-state devices in a pulse compression system in the band of interest with a pulse length of 5 μs has already been demonstrated as described in the section on IMPATT amplifiers.

It is clear that for a pulse compression system, using linear FM for example, that the TRAPATT diode needs to be incorporated in at least the final stage of an amplifier chain. Best reported efficiencies for 8 to 10 GHz TRAPPATT amplifiers are up to 17% (Cox et al, 1974) in coaxial circuits and 10% in microstrip (Ho and Curtice, 1974). With both the oscillator and the amplifier a major drawback to the full exploitation of the best laboratory 8-10 GHz results in developed components is the lack of proven circuit design techniques. This contrasts with the situation with IMPATT circuits. It is clear therefore that techniques are to be established which allow the systematic design of TRAPATT amplifier responses.

Circuit aspects may be divided into those associated with (a) the diode package and its microwave mount (b) the external oscillator or amplifier circuit. In the case of the diode mount, it is essential that the package and diode mount have a high cut-off frequency (Mackintosh and Royds, 1973) in order to allow passage of the components in the diode's waveforms up to at least the third harmonic. Cut-off frequencies for diodes in AV162 packages mounted in 3.5 mm coaxial airline are around 32 GHz and the best laboratory 9 GHz performance is obtained under these conditions. However, the external circuit used for maximum efficiency contains a number of position-adjustable low characteristic impedance sections which are adjusted for optimum performance. Simpler oscillator circuits have so far achieved efficiencies of 17% at 9 GHz, and an example of the construction of such an oscillator is shown in Figure 8, and a photograph in Figure 9.

6. LSA TRANSMITTERS

In this section we report on the performance of GaAs LSA transmitter modules* which consisted of a circulator-coupled Gunn diode locked oscillator first stage, followed by a circulator-coupled LSA locked oscillator output stage, Figure 10. The LSA diode is mounted in a double-sided heat sink in a pseudo-lumped circuit, and is operated in the relaxation oscillation mode (Mun, J., et al, 1973).

The centre frequency of operation is 9.3 GHz and the output peak power in the band centre is 95W. The bandwidth is 200 MHz. The transmitter module included the pulse bias modulators for the Gunn diode and the LSA diode. The module's dimensions were 120 mm x 120 mm x 18 mm.

The module was capable of being driven at a repetition frequency of 8 KHz. In the experiments reported here it was driven at 4 KHz. With this particular module, the input pulse used was of 0.5 μs duration (2W peak power), the Gunn diode stage was biased with a 0.5 μs pulse and the LSA diode was biased with a 250 ns pulse. The output from the Gunn diode stage was 10W.

The variation of peak power with temperature and frequency offset from 9.3 GHz is shown in Figure 11, and the variation in insertion phase is shown in Figure 12.

*supplied by STL Harlow under a CVD contract.

The module incorporated compensation for shifts in the LSA free-running frequency with temperature via thermistor control of the bias voltage pulse applied to the LSA diode. The rate of change of frequency with temperature was 30 MHz/^{o}C, and the rate of change of frequency with bias was 28 MHz/V. The change in frequency resulting from a change in temperature from 27^{o}C to 50^{o}C would have been 690 MHz, and with temperature compensation this was reduced to 125 MHz. This particular frequency offset was sufficient to compensate phase changes with temperature external to the LSA locked oscillator, resulting in an extremely low variation of insertion phase with temperature. Repeated measurements (made in order to eliminate the effects of module thermal time constants of about 5 mins) at the band centre showed that the curves (of Figure 12) did not deviate by more than 20^{o} from coincidence.

Of particular concern is the phase stability of LSA locked oscillators, as previously mentioned. Measurements were made of the in-pulse phase variation at the output of the module as a function of time during the pulse. This was achieved by pulse modulating the output from a klystron with p-i-n switch, amplifying with a TWT amplifier whose output was used to drive the LSA module. The output from the module and a reference using a sample of the klystron output were fed to a polar phase discriminator, which provided in-phase and quadrature outputs. These were sampled with the gate of a boxcar integration system. In the results presented below, the gate duration was 100 ns. Knowledge of the in-phase and quadrature variations allow the calculation of the variation of the phase of the module output during the pulse.

Examples are shown in Figure 13 for an earlier version of the module for both the Gunn and LSA stages, showing how the measured output phase variation (13(d)) agrees with the sum of the individual variations. A single parameter measure of the phase stability is the rms phase deviation during the pulse. Figure 14 shows the variation of the in-pulse rms phase deviation as a function of temperature and frequency offset, measured at the same time as the power and insertion phase data shown above. It can be seen than rms phase deviations of less than 10^{o} can be obtained over a bandwidth of 170 MHz from 0^{o}C to 50^{o}C for a boxcar gate of 100 ns.

7. REFERENCES

Cox, N.W., Rucker, C.T., Hill, G.N., and Gsteiger, K.E., 1974, "X-band TRAPATT amplifier", IEEE Trans. Microwave Theory and Techniques, pp. 1325-1328.

Ho, P.T., and Curtice, W.R., 1974, "A microstrip TRAPATT amplifier for X-band operation", Proc. IEEE, pp. 1029-30.

Mackintosh, I.W., and Royds, R.J., 1973, "Characteristic parameters of TRAPATT diodes", European Microwave Conference, Brussels, Paper A.8.3.

Mun, J., Wasse, M.P., Cooke, R.E., and Heeks, J.S., 1973, "LSA operation in pseudo-lumped circuits", Proceeding Fourth Biennial Cornell Electrical Engineering Conference, Ithaca, New York.

Purcell, J.J., Weatherhead, M.R., Gordon, S.M.R., Oxley, C.H. and Wickens, P.R., 1975, "High efficiency TRAPATT operation in X-band", Electronics Letters, 29 May, pp. 236-238.

Purcell, J.J. and Oxley, C.H., 1976, "High efficiency X-band TRAPATT oscillators", IEE Colloquium on Solid State Transmitters for Radar, London.

Rucker, C.T., 1969, "A multiple-diode high average-power avalanche diode oscillator", IEEE Trans. Microwave Theory and Techniques, pp. 1156-1158.

This paper has been contributed by permission of the Director RRE.

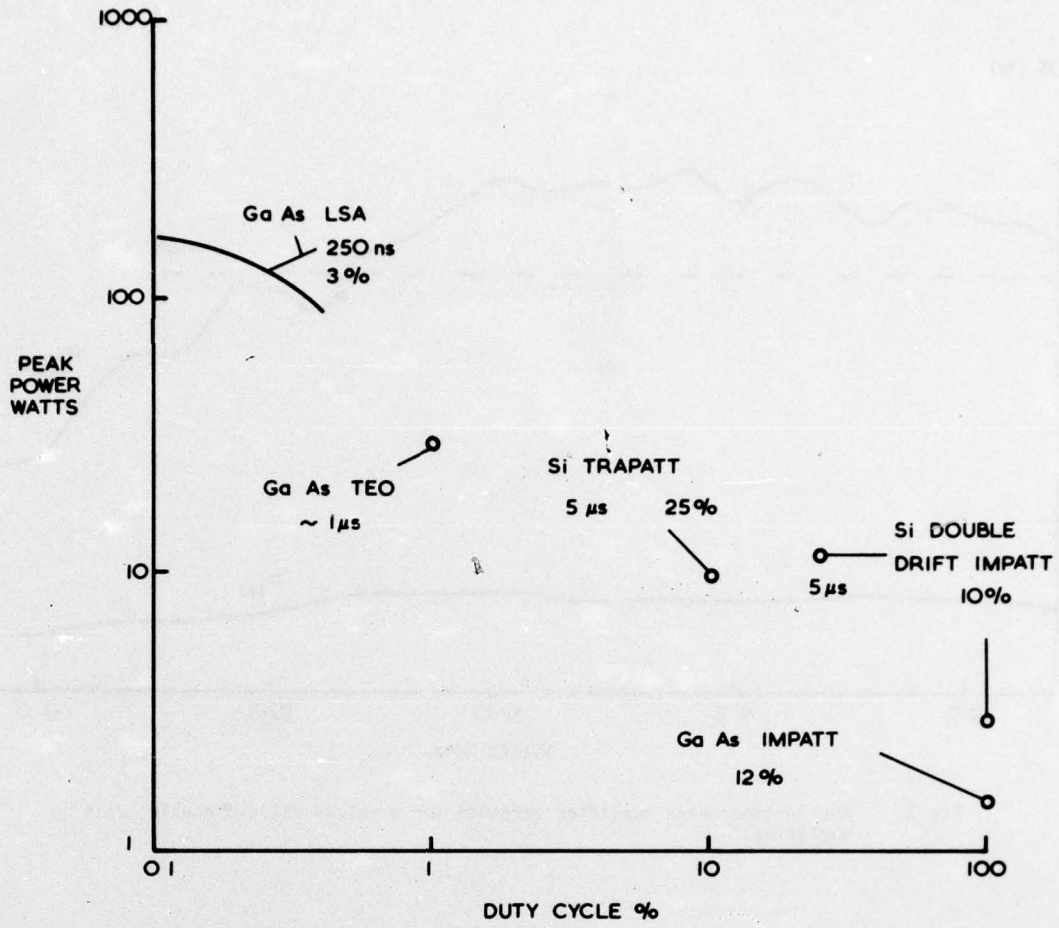

Fig 1. Peak output power of developed microwave solid state devices for the 8 to 10 GHz band.

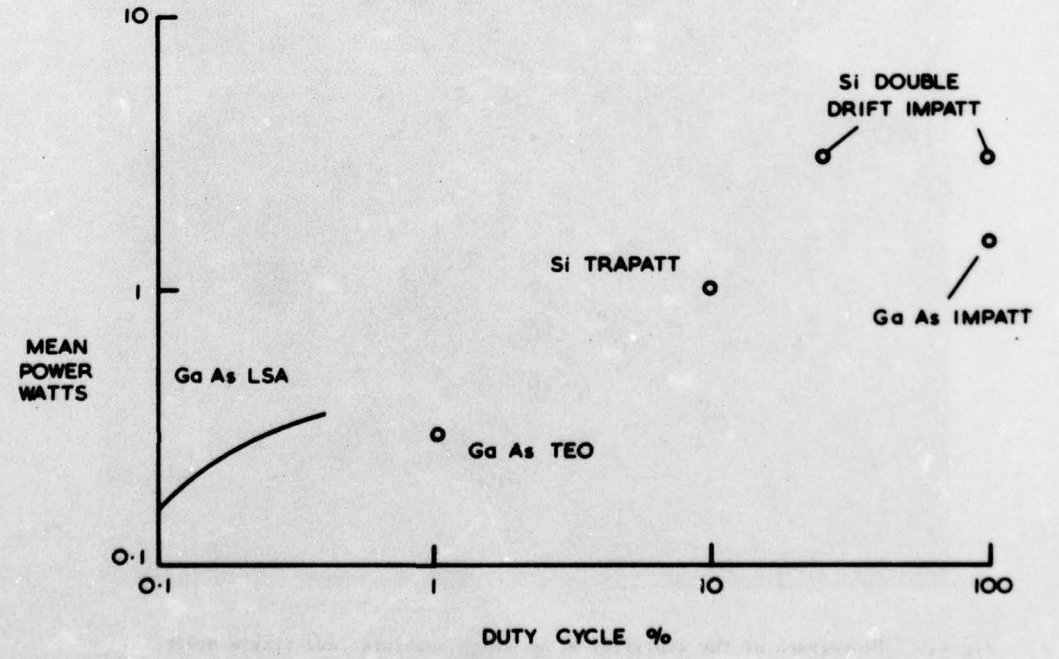

Fig 2. Mean output power of developed microwave solid state devices for the 8 to 10 GHz band.

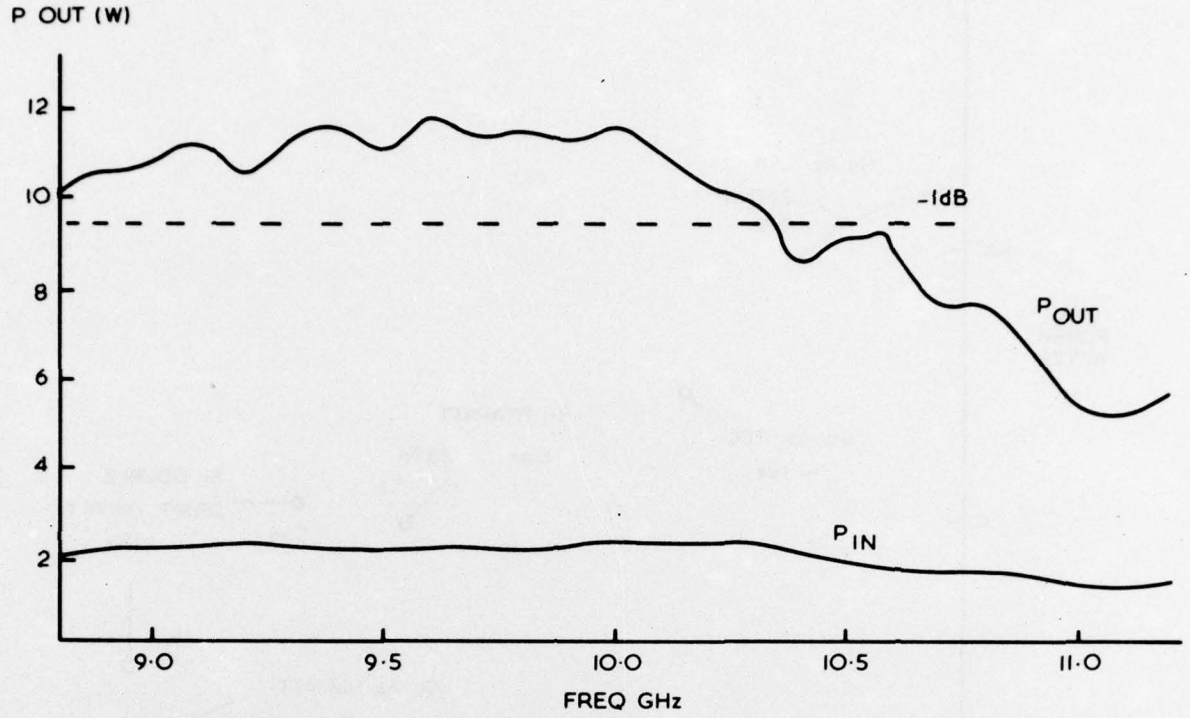

Fig 3. The instantaneous amplifier response for a pulsed silicon double drift amplifier.

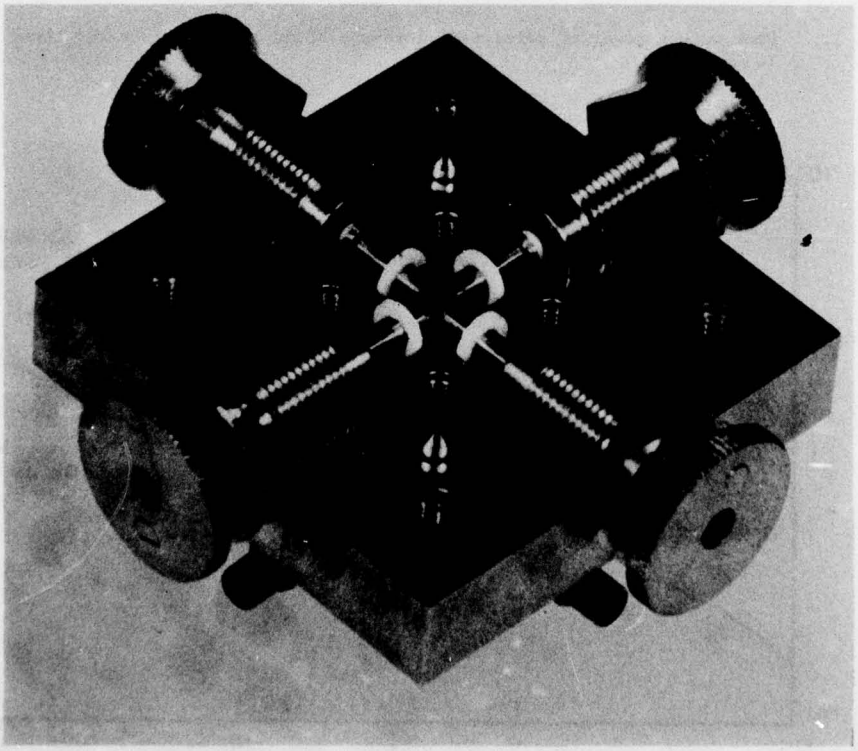

Fig 4. Photograph of the amplifier stage which combines four single drift silicon IMPATT diodes.

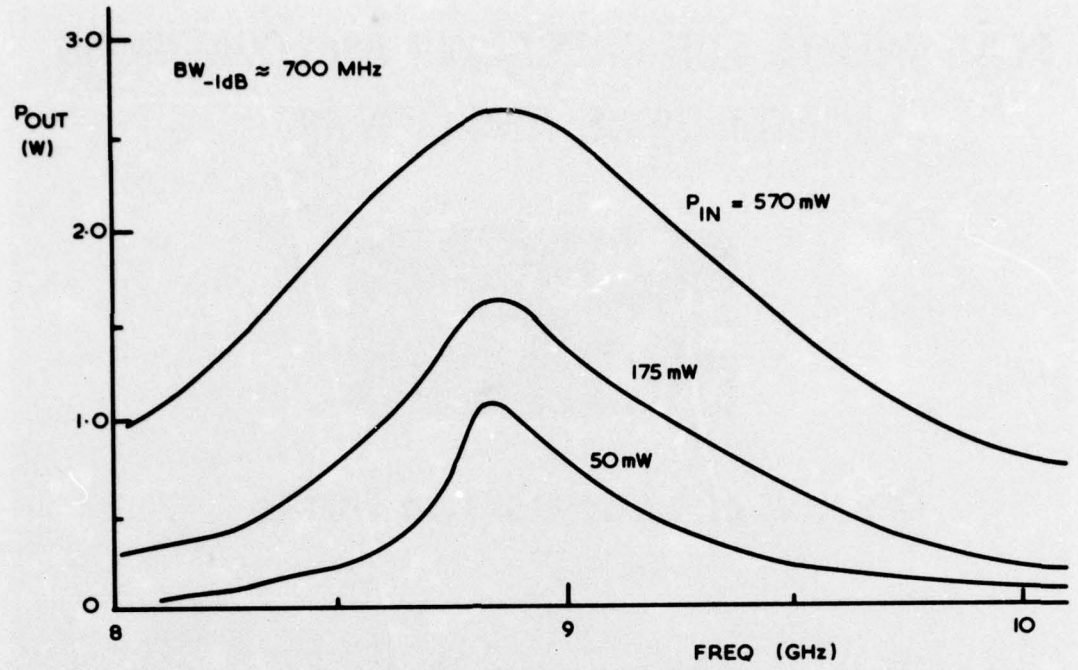

Fig 5. The instantaneous amplifier response of 2.6W CW amplifier which combines two GaAs single drift IMPATTs.

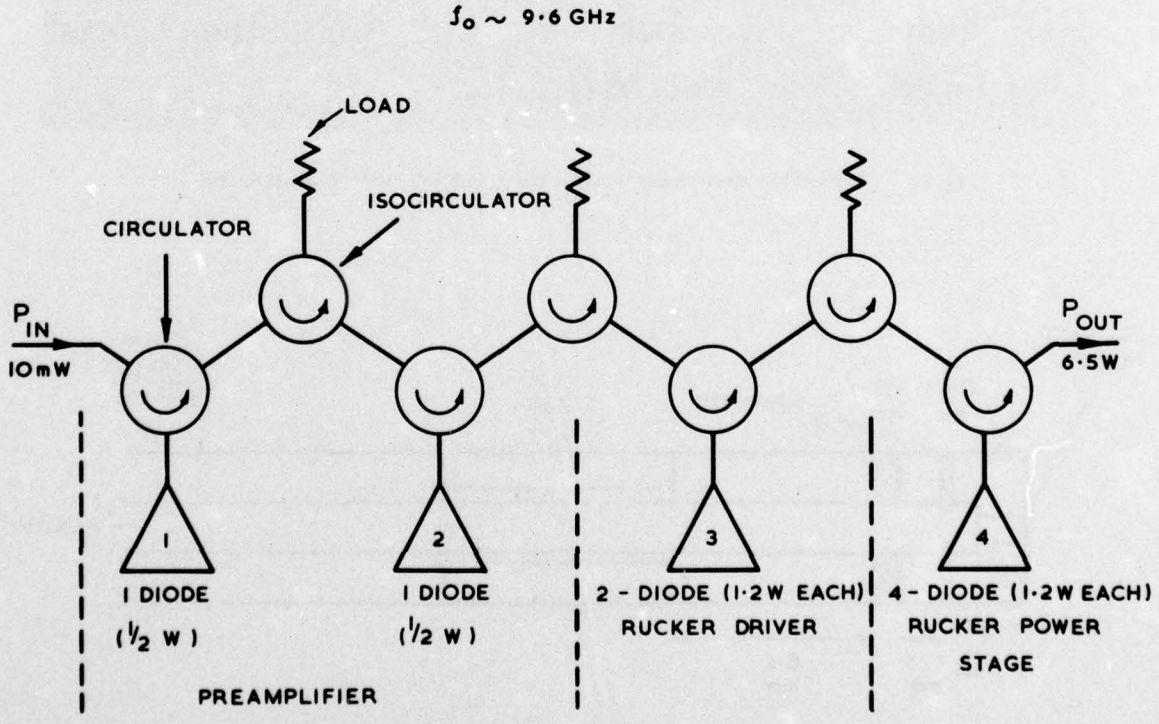

Fig 6. A schematic of the 6W CW multi-stage amplifier.

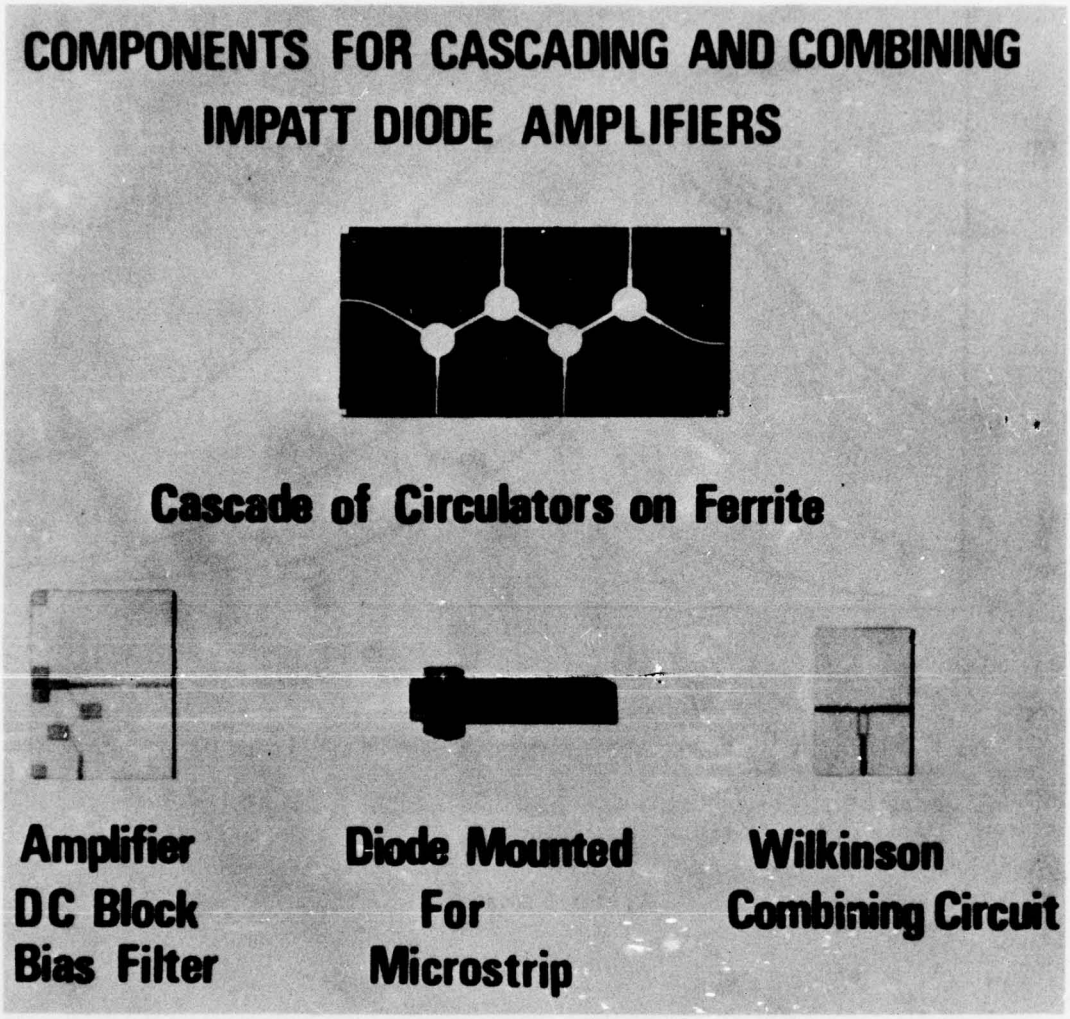

Fig 7. Thick-film microstrip components for 9 GHz IMPATT amplifiers.

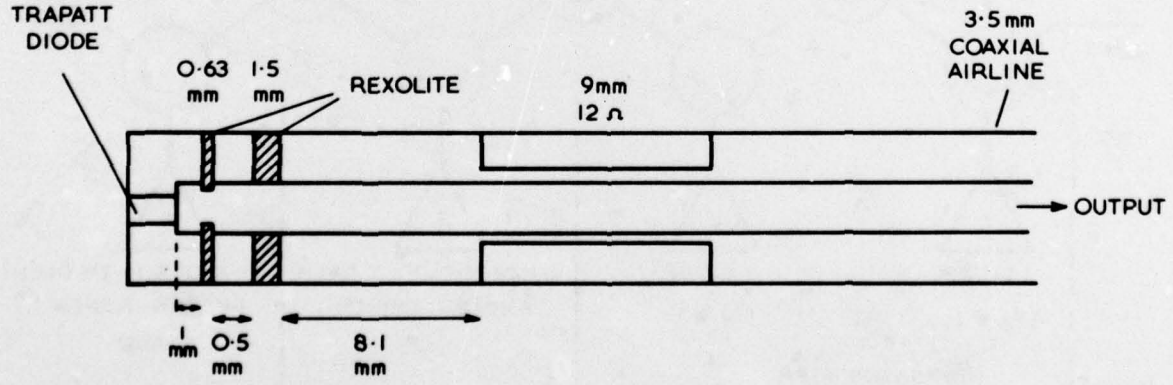

Fig 8. The coaxial cavity of a 9 GHz TRAPATT oscillator containing dielectric loading at approximately a quarter-wavelength from the diode, and a quarter wavelength sleeve at approximately a half-wavelength from the diode.

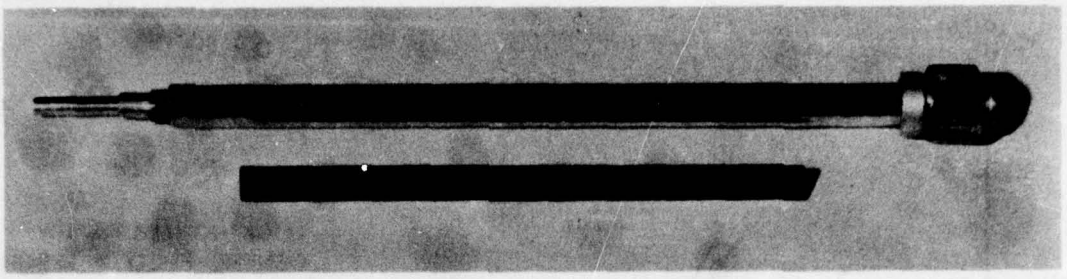

Fig 9. Photograph of a 9 GHz TRAPATT oscillator.

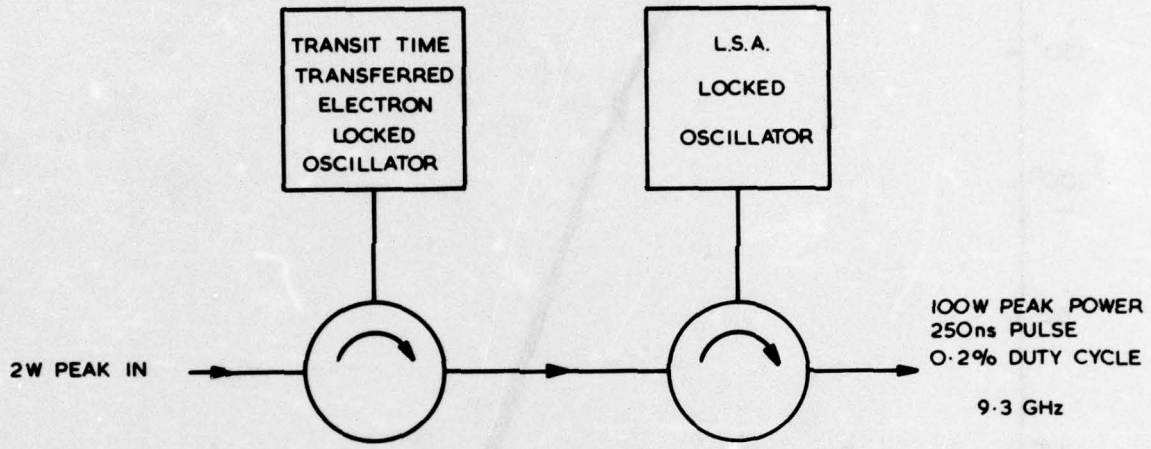

Fig 10. The configuration of the LSA transmitter module.

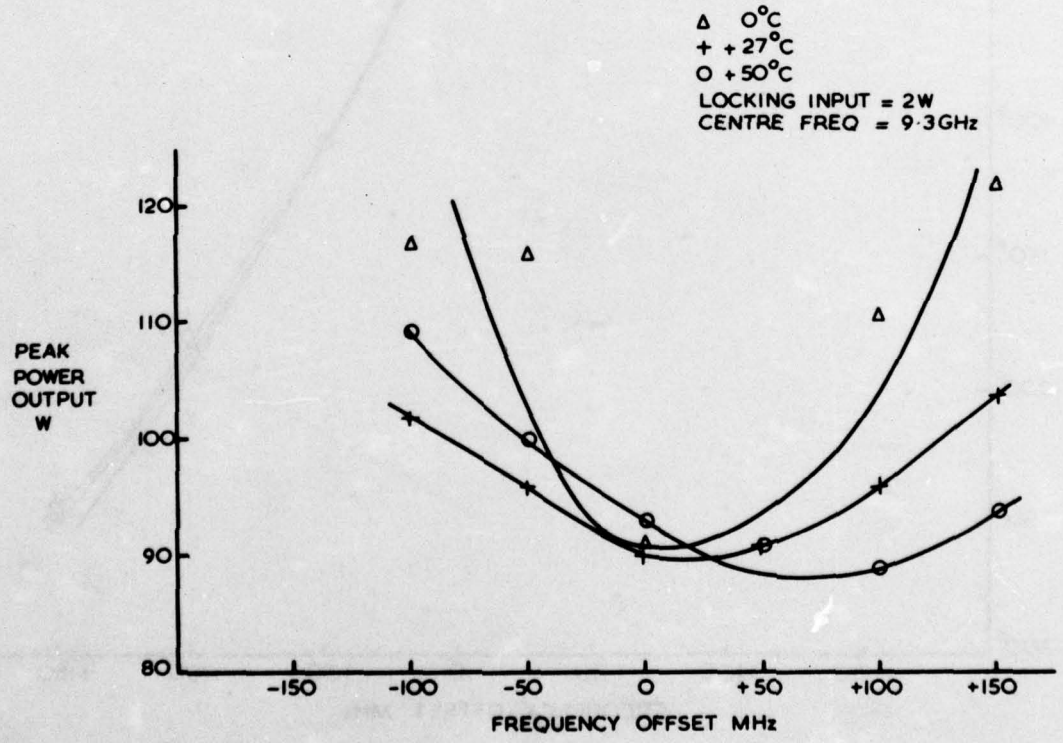

Fig 11. The variation of peak power output with frequency offset at 0°C, 27°C and 50°C for the LSA transmitter module.

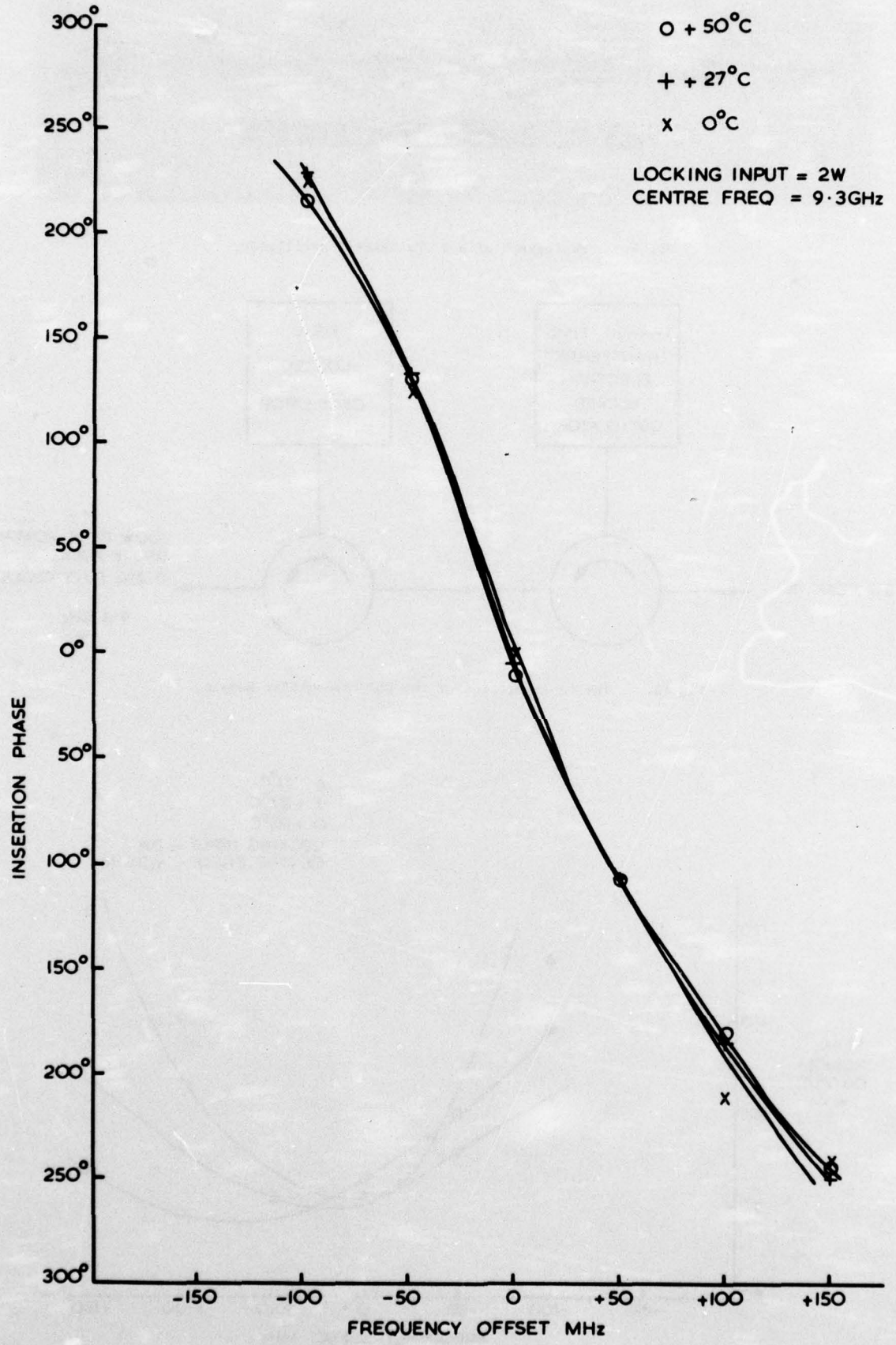

Fig 12. The variation of insertion phase with frequency offset for the LSA transmitter module.

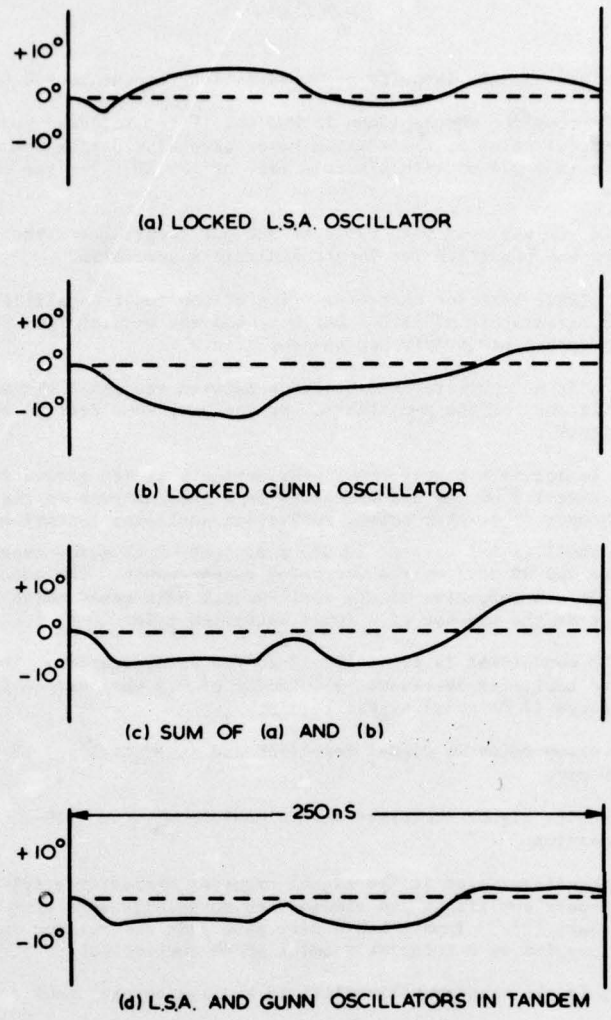

Fig 13. Measured in-pulse phase variations for locked Gunn and LSA oscillators, singly and in tandem.

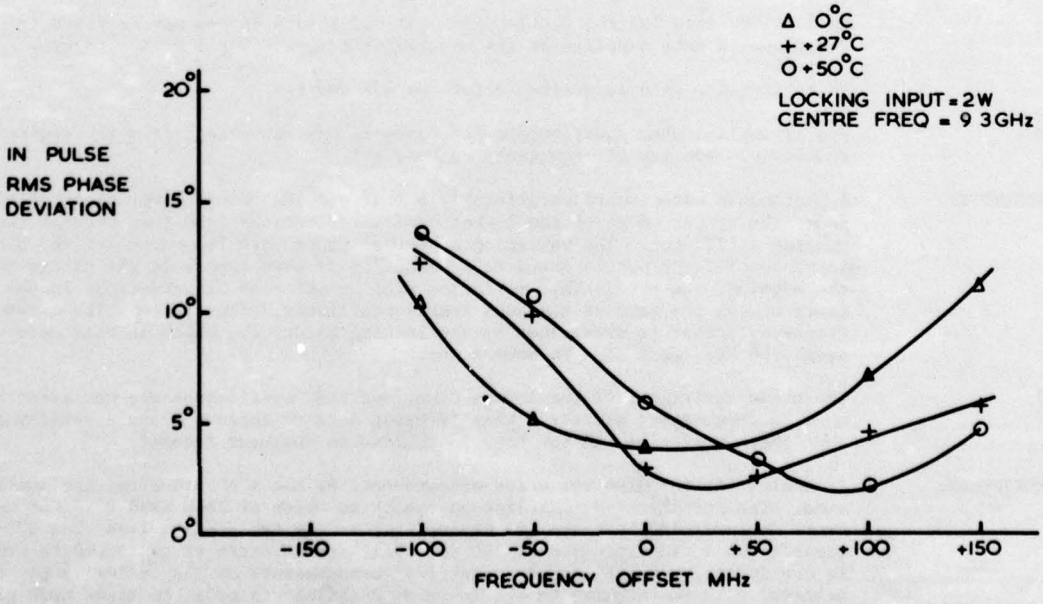

Fig 14. The measured in-pulse rms phase deviation for the LSA transmitter module as a function of frequency offset at 0°C, 27°C and 50°C.

DISCUSSION

C HAMILTON: How large is the in-pulse power variation for the locked Gunn and LSA oscillators?

I W MACKINTOSH: For a complete module (Gunn locked oscillator followed by an LSA locked oscillator) a typical value of the maximum power excursion during the centre 125 nS of a 250 nS pulse is $\pm$ 0.4 dB with a sample gate of 100 nS. The rms power deviation is much less.

G ROSENBERG: Could you say over what range of ambient temperatures the quoted figures of output power and bandwidth for Impatt amplifiers are valid?

I W MACKINTOSH: The signal transfer characteristics of the Impatt amplifiers all refer to a heat sink temperature of 23°C. Our work has not yet involved the measurement of the temperature sensitivity of the amplifiers.

G A VAN DER SPEK: There is a considerable difference between the small-signal and saturated-gain conditions for the amplifiers. Do you have some data on the linearity of these devices?

I W MACKINTOSH: The Impatt is a highly non-linear device over its active frequency range ($\triangleq$ octave). The severity of the non-linearity is a maximum near to the small-signal cut-off frequency (f_a). For normal reflection amplifier operation at a frequency $\triangleq \sqrt{2}f_a$ and small-signal gain of 20 dB, a typical -1 dB gain-compression point would be -8 to -10 dB down on the saturated output power. The saturated gain would be $\triangleq$ 7 dB. A reduction of the small-signal gain would raise the -1 dB compression point at the expense of a lower saturated gain.

AM/PM conversion is typically 10-20°/dB at saturation. The bandwidth of a single tuned amplifier increases by a factor of $\triangleq$ 5 when driven from small (20 dB gain) to large (7 dB gain) signal levels.

The group delay is signal dependent and is typically 1 nS/50 MHz for a single tuned response.

The noise figure increases with signal level from $\triangleq$ 30-35 dB up to $\triangleq$ 55 dB at saturation.

The nonlinearities in the signal transfer characteristics of single and double-drift Si Impatt amplifiers are similar and marginally less than their GaAs equivalents. The GaAs 'Read' Impatt has a very soft gain compression characteristic but is accompanied by a relatively small AM/PM coefficient ($\triangleq$ 5°/dB).

A J R WESTBROEK: What is the average reliability of the components used?

I W MACKINTOSH: The single-drift GaAs Impatt device was required to have a median-time-to-failure of greater than 5000 hours when delivering 1.5 W CW of output power and mounted on a heat sink with a maximum temperature of 50°C. This corresponded to a device temperature of about 270°C. The specification was met.

Reliability data for the double-drift silicon Impatt diodes may be found by reference to data supplied by the manufacturer (see Table 1 in the paper).

No reliability data is available for the LSA devices.

K MILNE: Fig 11 implies that power output increases if one works away from the centre frequency. How far off-frequency can one go?

I W MACKINTOSH: A phenomenon with locked oscillators is that of 'quenching'. On injection of power the output power of the locked oscillator becomes less than that of the free-running oscillator. The variation of output power with frequency for the LSA locked oscillator module shows that quenching is more severe in the centre than at the edges of the band. This variation will be affected by variations in the output power across the band of the Gunn locked-oscillator driver stage. The maximum frequency offset is determined by the locking bandwidth, which in this case was about 200 MHz (band edge to band edge).

H LUEG: The phase variations of the locked Gunn, and LSA, oscillators are too great to be used in phase-array systems. What is being done to improve phase stability and what phase variations do you hope to achieve in the near future?

I W MACKINTOSH: In making the in-pulse variation measurements we had a phased-array application in mind. The specification required an rms phase error of less than 5°. Our measurements demonstrated that the LSA transmitter module can achieve less than 10° rms error (with a sampling gate of 100 nS) over a temperature range from 0 to 50°C. It is our intention to relate the results of measurements on the radiation patterns achieved with two modules to the in-pulse stability in order to state more precisely what specification is required and how well it has been achieved.

A CHEAP LOW NOISE (2.5 dB) X-BAND AMPLIFIER

R.E. Pearson
Mullard Research Laboratories
Redhill, Surrey, England.

SUMMARY

Low noise amplifiers have for some years been production items in the form of paramps, but their complexity and cost has severely restricted their range of application. This paper discusses how thin film techniques have been applied to the design of a room temperature X-band amplifier to produce a unit which combines simplicity and low cost with the following performance:

Frequency	:	Low X-band
Gain	:	15 dB
Bandwidth (3dB)	:	100 MHz
Noise figure	:	2.5 dB max.

The unit is, with the exception of the Ka band Gunn pump, constructed completely by thin film techniques; complete with temperature stabilisation circuitry it measures 60 mm x 60 mm x 20 mm and can weigh as little as 200 grams. Computer modelling indicates the design can be scaled over a frequency range of at least 3-10 GHz without significantly modifying the configuration. Bandwidths up to 500 MHz and noise figures as low as 1.9 dB have been achieved.

The performance of the amplifier has not been significantly compromised and the result is a unit comparable in cost and simplicity of operation with an X-band GaAs MESFET amplifier but having a lower noise figure. It is considered that such a unit will extend the potential application of paramps and make them available for a wide range of system designs.

1. INTRODUCTION

Low noise parametric amplifiers have been in production for many years but their complexity and cost has severely restricted their range of application. This paper discusses how thin film techniques have been applied to the design of a room temperature X-band amplifier to produce a unit with a maximum noise figure of 2.5 dB that promises in production to be cost competitive with FET amplifiers. The design was established a year ago and a 7.5 GHz amplifier is now in the final stages of development; noise figures as low as 1.9 dB have been achieved at this frequency. A computer model of the circuit has been used successfully to predict the performance of the amplifier. This model indicates that the design can be scaled over the frequency range from 3-10 GHz.

2. EVOLUTION OF THE CONCEPT

Paramp design has progressed through a number of distinct phases. Initially their performance was unstable. The pump oscillator was a klystron driven by a high voltage power supply of poor stability. The paramp consequently earned a reputation of having an unreliable performance. Significant improvements were eventually obtained by applying precision engineering with inevitable high cost. Pump sources were closely temperature stabilised to about $\pm$ 1°C and often the klystron was replaced by a transistor oscillator and frequency multiplier chain (AITCHISON, et al, 1968). The pump power output was servo controlled to ensure long term stability and the noise figure of the paramp was usually reduced by cooling with a closed cycle cryogenic machine to 20°K. Using these techniques reliable broad band (500 MHz) paramps with noise temperatures of less than 50°K were constructed. Improvements in the quality of varactor diodes and the evolution of high frequency fundamental solid state oscillators has enabled this performance to be maintained in a solid state sub-assembly operating close to ambient temperature. The concept of the paramp being a complex and costly system remained and to achieve state of the art performance a certain degree of costly engineering is still necessary, thus limiting production to relatively small numbers. Their state of art performance however now exceeds the requirements of many systems but cost precludes their use. The question arises as to whether a significant cost reduction would result by slightly relaxing the specification.

A consideration of various systems indicated that a noise figure of between 2.2 - 2.5 dB would be attractive for the lower half of X-band compared to a state of the art performance without Peltier cooling of the varactor and circulator of between 1.2 - 1.8 dB. This performance relaxation permits a significant number of design changes. Firstly, the diode quality is considerably reduced thereby increasing the device yield. Secondly the pump frequency may be almost halved; the reduction in pump frequency eases the design of the paramp circuit which can be fabricated in microstrip with which excellent repeatability is achieved at low cost. Finally a microstrip circulator can replace the commonly used stripline circulator.

3. BASIC PARAMP DESIGN

An idealised parametric amplifier circuit is shown in Figure 1. The time varying capacitance(C(t)) is coupled to a circuit which provides the appropriately overcoupled source resistance (R_g) and resonating reactance (X_s) at the signal frequency. It is also coupled to a reactance (X_i) which provides a

conjugate reactance at an appropriate idling frequency. For optimum performance the practical circuit should be simple, stray reactance should be minimised and signal, idling and pump energies should be confined to appropriate regions of the circuit (F_s, F_i) (AITCHISON, et al. 1967). Referring to Figure 1 the basic expression for the noise temperature of a non-degenerate paramp (T_{amp}) at a physical temperature T_d operating at greater than 15 dB gain is given by:

$$T_{amp} = T_d \left[\frac{1}{P} + \frac{f_s}{f_i} \left(1 + \frac{1}{P}\right) \right] \quad (1)$$

where f_s and f_i are the signal and idler frequencies respectively. The quality factor required from the varactor diode in a paramp may be defined by:

$$(\gamma f_c)^2 = f_s f_i \, (1 + p) \quad (2)$$

where γ capacitance variation coefficient and f_c is the cut off frequency of the varactor. The overcoupling ratio p is the vswr of the unpumped signal circuit at the resonant frequency. A readily achievable figure of merit (γf_c) for a varactor in a microstrip paramp, without the need for selection is 40 GHz. This is an effective figure of merit since microstrip losses must be added to the loss of the diode. The noise temperature T_{amp} of an 8 GHz paramp is plotted as a function of idler frequency for a diode with γf_c = 40 GHz in Figure 2. It can be seen that there is little advantage to be gained by increasing the idler frequency above 27 GHz corresponding to a pump frequency of 34-37 GHz for lower X-band.

3.1 The microstrip amplifier circuit

As indicated earlier the paramp signal circuit consists of an impedance transformer and an inductance to resonate the varactor, which is also resonated at the idler frequency by a second reactance. In a microstrip circuit it is essential to reduce dimensions in order to minimise loss. Consequently a single quarter wave transformer was chosen to present the required source resistance to the diode. The signal circuit resonating element consists of an inductive length of high impedance line (Figure 3). To minimise cost a novel packaging technique has been developed in which the paramp circuit and the diode mount are equivalent to a conventional diode package. The diode chip is bonded and alloyed to a post on a copper block (6 x 3 mm) which supports the paramp circuit. The diode is wire bonded to the circuit and etched to form the signal resonance in a similar way to diodes that are mesa etched in the package to a specific capacitance. Mounting the chip in this way minimises parasitic reactance and enables a simple idler circuit to be achieved. The idler circuit elements of diode capacitance and bond wire inductance are made series resonant with an open circuited stub and a microstrip band stop filter is included in the signal tuning inductance to confine the idler energy to the vicinity of the diode. The idler resonant frequency may be adjusted by laser trimming of the length of the idler stub while the paramp is operating (Figure 4). The paramp circuits are produced on a 50 x 50 x 0.5 mm alumina substrate; 66 units are fabricated simultaneously and subsequently separated using a diamond cutter.

3.2 The pump source

A paramp requires a stable high Q pump oscillator. Although avalanche oscillators offer higher power and better efficiency than Gunn oscillators their noise characteristics demand the inclusion of a filter in the oscillator output to reject the F.M. components of oscillator noise. The Gunn device does not require such a filter and is thus the obvious pump source for a low cost paramp. The basic noise and stability properties of the device are modified by the loaded Q factor of the resonant circuit of the oscillator. Furthermore, with care in the design of the paramp pump circuit, pump oscillators with a loaded Q factor in excess of 200 avoid the need for a pump isolator. Q-values as high as this are extremely difficult to achieve in microstrip circuits because of the inherent loss. (Microstrip has an unloaded Q factor of approximately 200 at 30 GHz). A high Q dielectric resonator could provide the appropriate Q factor, but frequency setting is difficult. On the other hand waveguide circuits with unloaded Q factors in excess of 1000 at 30 GHz readily achieve the desired loaded Q factor values. In this context a further advantage of the Gunn is its ability to generate power at near optimum efficiency into a wide range of loaded impedances (approaching 10 to 1). This enables the use of a simple post-coupled waveguide cavity to define the oscillator frequency and avoids the mechanical complexity and associated high cost of the alternative iris coupled configuration. The cavity can be mechanically tuned over a 500 MHz bandwidth in Ka band (26 to 40 GHz) by a dielectric screw inserted in the cavity. The pump power is coupled directly to the varactor diode. The paramp circuit is mounted in a box section which is designed to be cut off at all frequencies below 46 GHz which includes the upper sideband frequency (ROBINSON, G.H., 1971). The diode is situated in the broad face of the Ka band waveguide and is coupled to the guide by a simple transformer system (Figure 5). This system is broadband and efficient; it operates over Ka band with pump power requirements as low as 6 mW. It has the advantage that the high pass characteristic of the waveguide avoids any loading of the signal circuit by the pump feed circuit. Coupling direct from the waveguide to the diode obviates the need for a waveguide to microstrip transition which demands tight mechanical tolerances for consistent operation at mid Ka band. The pump power level that is incident on the diode and hence the amplifier gain is preset during assembly by a simple card attenuator in the pump feed waveguide. Fine adjustment of the gain is achieved by setting the voltage of the Gunn supply.

3.3 The circulator

The paramp is a reflection type amplifier and uses a circulator to separate the input from the output signal. The loss of the input transit of the circulator contributes directly to the noise figure of the amplifier. Stripline circulators offer a loss of less than 0.1 dB per transit, but such circulators are considerably more expensive than a microstrip design. Microstrip designs also demonstrate excellent reproducibility, require negligible adjustment on assembly and readily integrate with the microstrip paramp circuit. A microstrip design is therefore used in this amplifier. Low cost is achieved with an all ferrite substrate and losses are reduced by using a substrate thickness of 1 mm and screening the circuit. (NEWTON, et al, 1975).

Input vswr of the amplifier should be less than 1.4 to provide a flat gain and a linear phase response across the operating frequency range when operating in a system. This implies a net isolation of about 15 dB which corresponds to a circulator isolation of 30 dB at 15 dB gain. In radar systems the amplifier may be effectively short circuited during the transmit period but the net isolation of 15 dB also ensures a gain change of less than 3 dB during this period.

The adverse effects of output mismatches on the gain frequency response are overcome by including an isolator in the output circuit of the amplifier. This isolator consists of a circulator with one port terminated in a matched load. It is constructed on the same substrate as the input isolator effectively forming a four-port circulator. This configuration also permits two parametric amplifiers to be cascaded together to achieve high gain. Thus a four-port circulator with at least 30 dB isolation and minimum loss on the input port is required. The performance achieved over a 500 MHz bandwidth at X-band for the microstrip circulator design is:

Isolation	: 30 dB minimum	)
Insertion loss	: 0.25 dB maximum	) per transit

The overall noise temperature for the paramp (T_{sys}) including circulator is given by:

$$T_{(sys)} = (\alpha - 1)\, T_o + \alpha T_{amp} \qquad (3)$$

where α is the loss of the circulator at temperature T_o. Referring to Figure 2, and using (1) in (3) T_{amp} = 164K, thus T_{sys} = 193K or 2.2 dB.

3.4 The integrated parametric amplifier assembly

The complete paramp assembly (Fig.6 & 7) is constructed from three separate units milled under numerical control. The main unit supports the circulator substrate the lower magnets associated with the circulator, and the lower half of the pump waveguide with the resistive card attenuator used for pre-setting the gain. The upper block completes the pump waveguide and retains the upper pair of circulator magnets. The remaining block forms the oscillator body. The complete unit measures 60 mm x 60 mm x 20 mm and weighs 200 grams. Also contained in the unit is a proportional temperature controller to maintain gain stability over an ambient temperature range of -20°C to 55°C. This requires 30 watts maximum power and for transportable systems it is unsatisfactory; an alternative system has been developed to reduce the total power requirements to that of the Gunn oscillator alone. The heat from the Gunn oscillator is dissipated by natural convection from the finned top plate (Figure 8). The unit is held away from its mounting by thermally insulating spacers. The input and output connections are 3 mm coaxial line.

4. THE AMPLIFIER PERFORMANCE

The performance of a particular version of the amplifier is summarised below.

Frequency	:	Low X-band
Gain	:	15 dB
Bandwidth (3 dB)	:	125 MHz
Noise figure	:	2.5 dB max. 2.2 dB typical
Input vswr	:	1.4 max.
Short term gain stability	:	$\pm$0.2 dB
Long term gain stability	:	$\pm$1 dB
1 dB gain compression	:	-20 dBm (at the output)
Operating temperature range	:	-20 to 55°C
Maximum safe spike leakage	:	2×10^{-7}; joules per pulse
Power supply requirements	:	5V 1.5 amp (Gunn oscillator) 30 watts heater

5. EXTENDED PERFORMANCE

A computer model of the circuit has been used to predict successfully the general performance of the amplifier which indicates that the design can be realised over a frequency range of at least 3-10 GHz without significantly modifying the configuration. Methods of extending the bandwidth of parametric amplifiers (HUMPHREYS, 1964, AITCHISON,C.S. WILLIAMS,J.C., 1969) are well established and a bandwidth of 500 MHz has already been achieved in a version of the above amplifier at 7.5 GHz. By selecting higher quality diodes noise figures as low as 1.9 dB have been measured.

6. CONCLUSIONS

The article has described a paramp which as a result of employing thin film techniques and a simple pump oscillator design is low cost. At the same time the performance has not been significantly compromised and the result is a unit comparable in cost and simplicity of operation with an X-band GaAs MESFET amplifier

but achieving lower noise. It is considered that such a unit extends the potential application of paramps and makes these available for a wide range of system designs.

7. ACKNOWLEDGMENT

The considerable contribution to the work by R.Davies and the design of the pump oscillator by I.D. Higgins is gratefully acknowledged.

This work has been carried out with the support of Procurement Executive, Ministry of Defence.

8. REFERENCES

AITCHISON, et al, 1967. 'A simple diode parametric amplifier design for use at S C and X-band', IEEE Trans. MTT. Vol. MTT-15, No.1. Jan. 1967.

AITCHISON, et al, 1968, 'A stable, 100 mW Ka band solid state source', Proceedings of MOGA 68, Hamburg, Paper 17.8.

AITCHISON, C.S., WILLIAMS, J.C., 1969. 'Active reactance compensation of parametric amplifiers', Electronics Letters, Vol. 5. No. 7.

HUMPHREYS, 1964. 'Characteristics of broadband parametric amplifiers using filter networks'. Proc. IEE, Vol. III, No.2. February 1964. pp264-275.

NEWTON, et al, 1975. 'The design and realisation of MIC subassemblies on ferrite substrates', IEEE Trans. Magnetics, Vol. MAG-11, No.5. pp 1270-1272.

ROBINSON, G.H., 1971. 'Resonant frequency calculation for microstrip cavities', IEEE Trans. MTT Vol.MTT-19, No. 7.

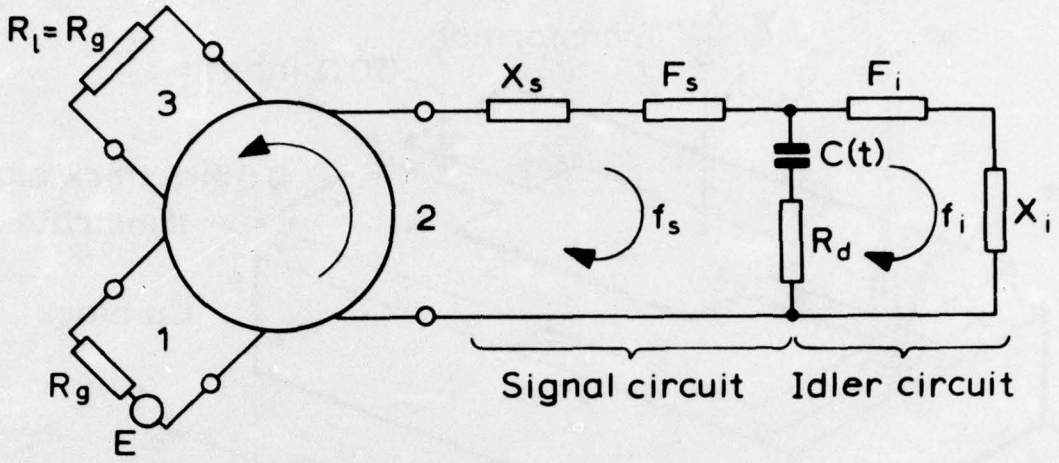

Figure 1. An idealized paramp circuit.

The idler and signal circuits are coupled by the varactor diode, which is driven by a pump signal to make it behave as a time varying capacitance C(t). (The pump circuit is not shown). Loss in the diode is represented by the spreading resistance R_d. The reactance X_s resonates the signal circuit at the frequency f_s, and reactance X_i resonates the idler circuit at frequency f_i. Bandpass filters F_s and F_i confine the currents to the appropriate circuits. Parametric amplification is achieved where $f_s + f_i = f_p$, where f_p is the pump frequency.

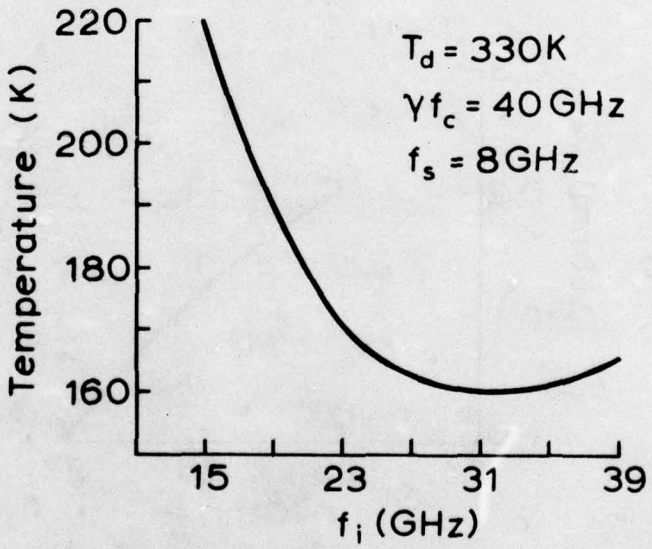

Figure 2. The calculated noise temperature of the amplifier (T_{amp}) (Equations 1 & 2) as a function of idler frequency (f_i).

The noise contribution of the circulator is excluded.

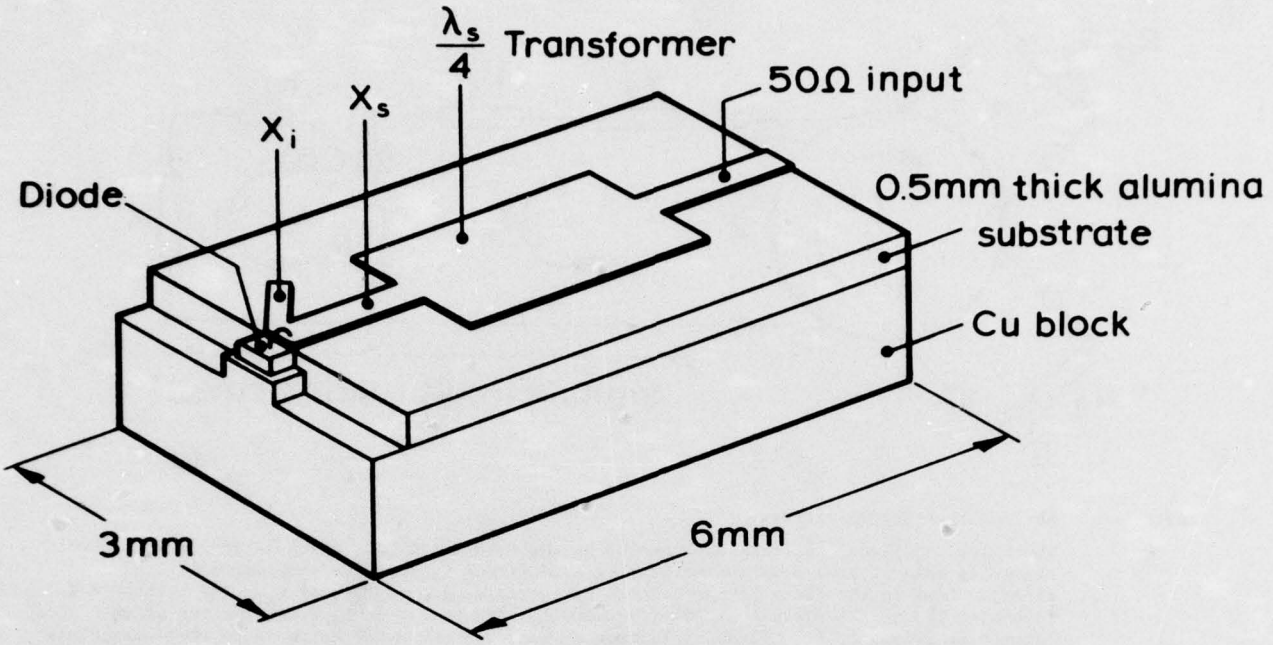

Figure 3. The diode and paramp circuit 'package'.
The package is assembled and tested before inserting into the integrated unit.

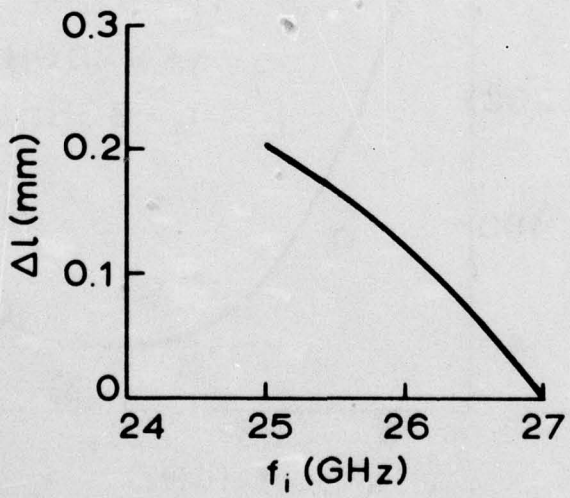

Figure 4. Idler frequency (f_i) is plotted as a function of the change in length ($\Delta\ell$) of the idler stub.
The idler stub may be laser trimmed while the paramp is operating.

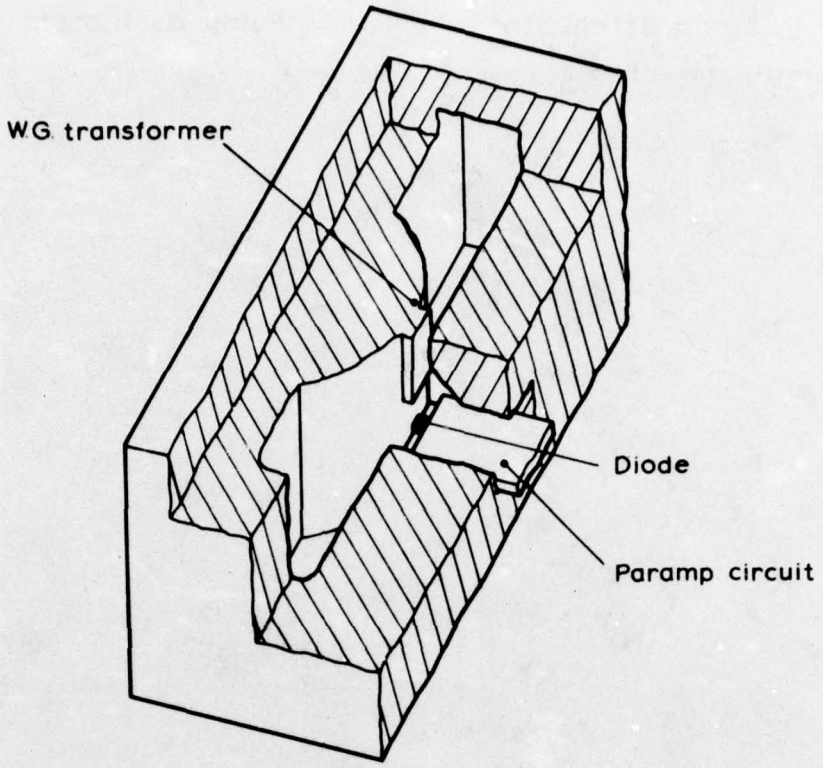

Figure 5. The sketch shows the waveguide (W.G.) to diode transformer. The diode protrudes through a slot in the broad face of the waveguide.

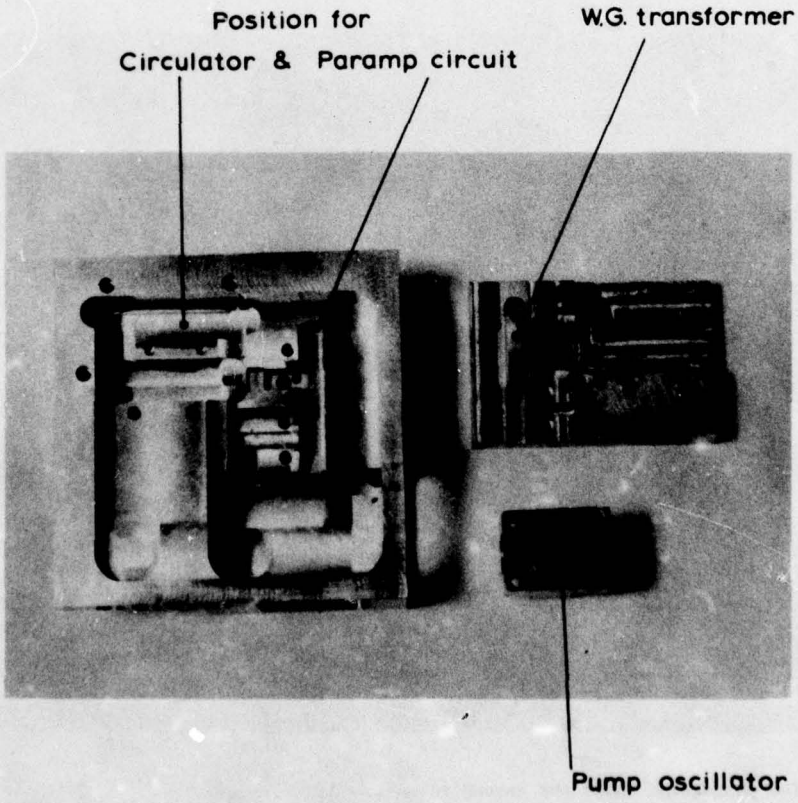

Figure 6. The photograph shows the three milled components. The components are milled from aluminium by numerical control.

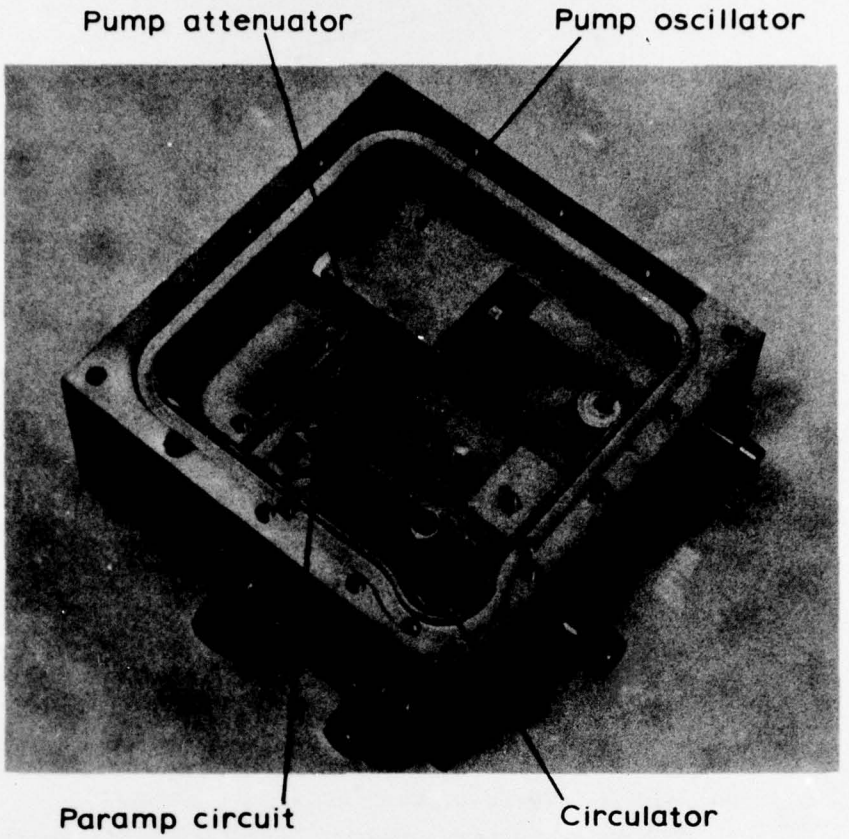

Figure 7. The photograph shows the assembled unit with the top removed.

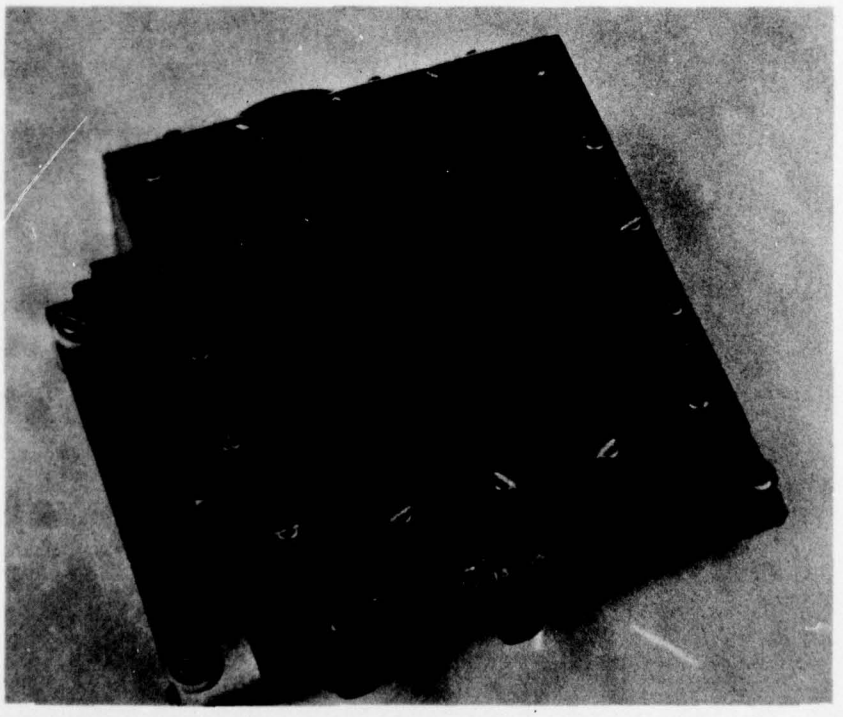

Figure 8. The photograph shows the assembled unit.

The third coaxial port, normally terminated by a matched load, can be used for monitoring diode current.

DISCUSSION

J S YU: One of your slides shows (NF) x (PRICE) as low as 2 dB. On another you show NF = 2 dB. Does it imply that the price is one British Pound?

R E PEARSON: The slide mentioned plotted the product of

NF (dB) x PRICE (£1000's)

The conventional paramp and FET amplifier achieve a similar product in excess of 3. The MIC paramp is shown as having a product between 1.5 and 2.5 which indicates a potential cost advantage. Thus, a mean product of 2 and a 2 dB NF suggest a price of £1000.

J BRACE: What would the noise figure be over a bandwidth of 500 MHz at an f_o of 10 GHz?

R E PEARSON: I mentioned during the lecture that at present an achieved diode quality factor of γf_c = 40 GHz was chosen to avoid diode selection. I also mentioned that diodes with γf_c > 100 GHz were available and for 10 GHz operation the amplifier performance could be maintained by selecting diodes with $\gamma f_c \geq 60$ GHz and pumping at 42 GHz.

Increasing the bandwidth to 500 MHz does not significantly degrade the noise figure.

The amplifier noise figure would be maintained at a typical figure of 2.3 dB at a maximum ambient of 50°C.

B T NEALE: Is there a problem with microphony?

R E PEARSON: The big advantage of microstrip compared to conventional coaxial construction, apart from its low cost, is its freedom from variable contacts. Tests on the pump oscillator have indicated that it is also not susceptible to vibration.

The system is more robust and less sensitive to vibration than conventional paramps.

C B WILLIAMS: What are the implications of increasing the operating temperature range from -54°C to +70°C?

R E PEARSON: The MIC paramp module is temperature stabilised 10°C above the highest ambient, that is 80°C in this case. To maintain this temperature over the range to -54°C would approximately double the present power consumption to nearly 100 watts. Although the Gunn diode is suitable for a pin temperature up to 90°C continuous operation at 80°C would degrade its MTBF. The noise figure would increase by not more than 0.1 dB.

AMPLIFICATEUR BAS BRUIT A TRANSISTORS

F.E.T. au GaAs

P. Baudet, M. Parisot, R. Veilex

Laboratoires d'Electronique et de Physique appliquée
3, avenue Descartes - 94450 Limeil-Brévannes

France

RESUME

Grâce à une méthode originale d'autoalignement de la grille d'un transistor à effet de champ à l'Arséniure de Gallium, nous avons pu obtenir un produit de haute performance et ne présentant pas de dérive. Ces transistors nous ont permis de réaliser un amplificateur avec un facteur de bruit inférieur à 6 db et un gain de 30 db à $\pm$ 1 db sur 750 MHz.

La conception et la réalisation de cet amplificateur sont décrites.

Nous indiquons les dernières performances et les progrès en cours pour les transistors et les circuits. Les perspectives à court terme sont un facteur de bruit de 5 db sur une bande de 1 GHz ou plus, ces performances étant maintenues jusqu'à 80°C.

1. INTRODUCTION

Il est aujourd'hui admis que les transistors à effet de champ au GaAs sont appelés à remplacer la plupart des amplificateurs hyperfréquences bas bruit jusqu'à 14 GHz ou plus.

Pour évaluer les difficultés à résoudre suivant le type d'application, nous avons entrepris la réalisation de divers prototypes.

Nous présentons aujourd'hui une étude d'amplificateur destiné à répondre à un besoin militaire. Nous décrirons :

- la réalisation du composant,
- la caractérisation électrique,
- la conception et la réalisation de l'amplificateur,
- les résultats.

En conclusion, nous indiquerons les perspectives pour les prochaines années.

2. REALISATION DU COMPOSANT

2.1. Matériau (HOLLAN L., 1974)

La qualité d'un transistor dépend en tout premier lieu de la qualité du matériau de départ. Pour un transistor faible bruit, on dépose successivement, sur un substrat de haute résistivité ($10^8 \Omega$.cm), dans un même réacteur, une couche de haute résistivité de quelques µm d'épaisseur et une couche active de 0,2 µm d'épaisseur, et de dopage $n=10^{17}$ at.cm^{-3}. Si nécessaire, l'épaisseur de la couche active peut être ajustée par décapage chimique ou électrochimique. La couche "tampon" est aujourd'hui faite sans dopage, la couche active est faite par dopage au soufre.

2.2. Technologie

La technologie mise en oeuvre est plus puissante que les technologies classiques de photolithographie et moins onéreuse que le masquage à l'aide de faisceau d'électrons. (MOHR Th. O., 1970), (DOERBEEK F.H., 1970), (DRIVER M.C., 1971), (MIDDELHOEK S., 1970),(DEAN R.H., 1975). Elle nous a permis aujourd'hui d'obtenir des grilles de longueur 0,7 µm parfaitement centrées dans un espace drain-source de 2,5 µm, en utilisant la sous-gravure toujours associée à une gravure chimique conventionnelle.

Les étapes de la fabrication sont les suivantes : (BAUDET P.- 1976)

1 - Décapage localisé de la couche n pour définir les zones actives des transistors (photo 1).

2 - Evaporation d'aluminium sur toute la plaquette dans un bâti ultra-vide après nettoyage de la surface du matériau (figure 1a).

3 - Par photogravure classique, ouverture des contacts source et drain dans l'aluminium, la gravure est poursuivie jusqu'à l'obtention de la longueur de grille recherchée (figure 1b).

4 - Evaporation d'or/germanium sur toute la plaquette, l'effet d'ombre de la laque assurant un autoalignement parfait des contacts par rapport à la grille (figure 1c). La laque et l'or/germanium superflus sont éliminés par dissolution de la laque.(figure 1d)

5 - Une dernière gravure de l'aluminium définit le plot de contact de la grille (photo 2).

6 - Un recuit à 450°C sous hydrogène assure la qualité des contacts.

On constate donc qu'il n'y a pas, dans cette technologie, d'alignements successifs très précis ; un seul masque doit être de haute qualité, le nombre est limité à trois et trois masques suffisent.

2.3. Résultats

Cette simplicité conduit, en laboratoire, à des rendements de 80 % sur une bonne plaquette. De plus, les premières expériences de durée de vie nous font penser que nous n'aurons pas les problèmes de fiabilité rencontrés avec les autres technologies. Ceci est compréhensible, car ici la grille est déposée dès le début des opérations, sur un matériau parfaitement propre, alors que dans les autres technologies autoalignées, il faut, avant le dépôt de la grille, nettoyer la surface du semiconducteur au fond d'un sillon très étroit.

Nous avons mis quelques transistors en durée ; nous n'observons pas de dégradation après 2000 h. D'autre part, nous n'observons pas de dérive à court terme du gain des transistors, la variation dans les première minutes reste inférieure à 0,1 db pour un amplificateur de 9 db, nous avons vérifié cette stabilité sur plus de 10 h. Les fréquences de coupure observées pour une grille de longueur 0,7 µm dans 2,5 µm sont de 50 GHz (figure 2).

Le facteur de bruit est inférieur à 4 db à 10 GHz avec un gain associé de 7 db. Les tensions de coude varient entre 0,9 et 1,5 volt suivant la plaquette d'origine des transistors (photo 3). Les résultats présentés correspondent à des transistors de 200 µm de largeur de grille.

3. CARACTERISATION (BINET M., 1976)

Ces transistors sont destinés à la réalisation d'amplificateurs bas bruit et il importe donc de connaître les paramètres de bruit et les paramètres S à faible signal.

Pour les mesures, les transistors nus sont soudés directement sur un substrat d'alumine de 4 x 6 x 0,635 mm sur lequel se trouvent des lignes coplanaires de 50 ohms (photo 4).

Les paramètres S sont mesurés à l'aide d'un analyseur de réseau HP. L'appareil est calibré avec des éléments "étalons" standard APC 7 ; des éléments de référence ont été réalisés dans la même structure coplanaire.

Le comportement en bruit du transistor peut être prédit par les quatre paramètres bien connus NF_{MIN}, R_N, G_o, B_o. Le facteur de bruit d'un quadripole connecté à une admittance de source Y_s à une fréquence donnée peut s'écrire (IRE Standards, 1960), (EISENBERG J.A., 1973) :

$$NF = NF_{MIN} + \frac{R_N}{G_s} (Y - Y_o)^2$$

où $Y_o = G_o + j\, B_o$ est l'admittance inconnue qui, présentée à l'entrée du quadripole conduit au facteur de bruit minimum NF_{MIN}, et R_N la résistance de bruit équivalente.

Les mesures sont faites à l'aide d'un mesureur de bruit automatique AIL et de l'analyseur de réseau. Cet analyseur est en fait incorporé à un banc automatique de test qui nous permettra de faire ces mesures en fonction de la fréquence, de la polarisation, de la température et de l'amplitude du signal. Le miniordinateur du banc automatique permet de traiter les mesures. Pour les paramètres de bruit, onze mesures sont faites pour différents réglages du circuit à fréquence et polarisation données. Un programme d'analyse statistique permet de minimiser les erreurs de mesures.

A titre d'exemple, les paramètres de bruit d'un transistor provenant d'une bonne plaquette sont présentés sur la figure 3.

Un autre programme de calcul permet de tracer automatiquement les cercles de bruit constant dans le plan d'entrée du quadripole. Les figures 4a et 4b représentent les cercles de gain constant et les cercles de bruit constant pour deux fréquences différentes. Comme on peut le voir, les cercles de plus bas bruit ne sont pas très éloignés pour des fréquences différentes. L'optimisation d'un amplificateur large bande sera donc d'abord un problème d'optimisation en fonction du gain.

4. CONCEPTION ET REALISATION DE L'AMPLIFICATEUR

4.1. Spécification

Nous nous étions donné comme objectif la réalisation de l'amplificateur suivant :

F : 8,8 à 9,8 GHz
G : 30 db ± 1 db
NF : $<$ 6 db
puissance de sortie à saturation $>$ 10 dbm

4.2. Réalisation

Une première étape est la réalisation d'un amplificateur à un étage avec entrée et sortie 50 ohms. L'entrée et la sortie étant adaptées de façon à obtenir le meilleur facteur de mérite pour les premiers étages et le plus grand gain pour les étages de sortie, les adaptations permettant de compenser la variation du gain du transistor avec la fréquence.

Nous avons essayé tout d'abord une technologie microstrip. Les transistors de la même série que ceux qui ont été caractérisés sont soudés sur un rail de cuivre de 0,4 mm de largeur, séparant en deux parties égales un support de cuivre doré de 1 pouce x 1 pouce. Les circuits d'entrée et de sortie sont réalisés par des conducteurs en or sur deux plaquettes d'alumine de 1/2 pouce et d'épaisseur 0,635 mm. Ces conducteurs sont obtenus par gravure d'une couche de 5 µm d'or préalablement déposée (photo 5).

[Cette technologie est très simple mais chère ; nous avons également utilisé une autre technologie qui consiste à graver une couche mince qui est ensuite rechargée. On peut encore réduire le coût en utilisant des couches épaisses obtenues par sérigraphie de pâtes à l'or. Nos premières mesures de lignes faites par cette technologie nous laissent penser que celle-ci pourra être utilisée jusqu'en bande X.]

Un tel montage permet de caractériser les circuits à l'analyseur de réseau avant la soudure des connexions du transistor. Le circuit d'alimentation gravé sur le même substrat comprend un filtre passe bas et des composants discrets : condensateur de découplage et résistance VDR de protection sur la grille. (photo 6)

Les modules élémentaires ainsi réalisés peuvent être cascadés par l'intermédiaire de prises miniatures, mais les circuits ont été conçus pour être associés après mesure, dans un boîtier unique.

4.3. Conception (VIDALLON C., 1976)

Il est toujours souhaitable d'avoir le minimum d'éléments d'adaptation. Le circuit simple qui nous a donné de bonnes performances consiste en une ligne à haute impédance suivie d'un transformateur quart d'onde basse impédance. Cette structure permet également une connexion aisée du circuit de polarisation à un bord du transformateur basse impédance. Les performances obtenues avec ce type de circuit ne sont pas très satisfaisantes pour les amplificateurs large bande. Des calculs d'optimisation à l'aide de programmes mis au point en collaboration avec l'Université de Toulouse (Acline + Optim)nous ayant montré que pour réaliser des amplificateurs large bande il fallait utiliser des éléments localisés, nous avons entrepris des essais en utilisant comme self un fil tendu entre le transistor et la ligne microstrip. Les résultats sont bons et nous cherchons actuellement une solution plus satisfaisante du point de vue technologique et permettant de résister à un environnement sévère.

Les performances mesurées étant aujourd'hui proches des performances calculées, nous étudions l'adaptation entre les différents étages, sans repasser par une impédance de 50 ohms.

5. RESULTATS

5.1. Modules élémentaires

Ces modules ont été réalisés avec les transistors décrits ci-dessus pour une fréquence de 9,3 GHz.

	G (db)	NF (db)	T °C
bande étroite	11	3,5	- 150
	9	5	25
	8,5	5,5	85
bande 1 GHz	5	4,4	20
	9		20

étage de sortie : le même type de transistor peut délivrer une puissance supérieure à 20 mW (figure 5). On peut associer plusieurs transistors pour atteindre 100 mW (photo 7).

Amplificateur large bande : par adaptation avec des éléments localisés, on peut réaliser des amplificateurs très large bande, par exemple 8 à 12 GHz (figure 6). Ceci montre clairement qu'il faut, soit monter les transistors sans boîtier, soit prévoir une préadaptation dans le boîtier.

5.2. Amplificateur grand gain

L'objectif étant de réaliser un gain supérieur à 30 db, une première maquette a été réalisée avec cinq modules en technologie microstrip. Comme indiqué plus haut, les cinq modules peuvent être montés dans un boîtier unique de dimensions 10 x 3 x 0,5 cm. Il apparaît que si les performances de bruit et de gain sont tenues, le gain n'est pas constant dans la bande. Une amélioration importante peut déjà être obtenue en remplaçant certains modules par des amplificateurs à constantes localisées. Sur la figure 7, un seul module est à constantes localisées.

5.3. Conclusions

Les performances ne sont tenues que sur 750 MHz, car nous n'avons modifié qu'un étage ; en modifiant deux ou trois étages, nous obtiendrons une courbe de gain respectant la spécification.

La détérioration du bruit à 85°C étant de 0,5 db, le bruit restera inférieur à 6,2 db dans toute la bande. La variation du gain avec la température peut aisément être corrigée par un circuit de compensation sur l'alimentation des deux derniers étages. Avec les performances des transistors annoncées par nos compétiteurs ou obtenus récemment dans notre laboratoire (NF = 3 db à 10 GHz), on peut gagner 1 db sur le facteur de bruit et réduire le nombre d'étages à quatre.

6. PERSPECTIVES

6.1. Amplificateur bas bruit

Des progrès importants sont encore possibles pour le matériau, spécialement au niveau de l'interface entre le substrat et la couche active, progrès qui se traduiront par des améliorations notables de performances.

En dehors des techniques classiques d'épitaxie vapeur ou liquide, trois voies sont actuellement explorées :

- épitaxie vapeur basse température : (630°C)
  nous avons obtenu à ce jour :

	NF (db)	Ga (db)	G_{max} (db)	F GHz
sans couche tampon	4	6	10	10
avec couche tampon	3	5	10	10

- épitaxie par jets moléculaires

  Nous avons obtenu sans couche tampon un facteur de bruit de 4 db et un gain associé de 6 db.

- implantation ionique

nous n'avons pas encore de transistors faits par cette technique, mais les couches obtenues sont de bonne qualité.

Au niveau de la technologie, il reste encore à améliorer la qualité des contacts et à rendre reproductibles et économiques les transistors à grille de longueur 0,5 µm. Le problème le plus important pour l'utilisateur paraît être la présentation des transistors ; il faut trouver une technique permettant la manipulation, la mesure et le montage des transistors aussi simplement qu'avec un boîtier, mais avec des éléments parasites plus faibles, le montage des transistors sur film souple permettra peut être de remplir ces exigences.

Au niveau des performances, dès aujourd'hui on voit annoncer des bruits de 2,5 db à 10 GHz pour des longueurs de grille de 0,5 µm. On ne verra sans doute pas beaucoup mieux, au moins à température ambiante. Avec ce facteur de bruit et des gains associés de 7 ou 8 db, on pourra réaliser des amplificateurs bande étroite et grand gain avec un facteur de bruit de 3,5 db. Dès que l'on veut réaliser un amplificateur à large bande, il faut compter sur une détérioration de 1 à 1,5 db, soit un facteur de bruit inférieur à 5 db.

6.2. Amplificateur de puissance

Les pessimistes prévoient une puissance de 1 W en bande X, en fait cette performance a déjà été obtenue en laboratoire. Les optimistes disent 5 W en bande X ; je crois que dans ce domaine il faut toujours croire les optimistes. Il faut souligner que la fiabilité de ces éléments de puissance n'est pas encore garantie ; il faut donc attendre avant de les mettre dans des équipements opérationnels, mais il n'y a cependant aucune raison pour que les dispositifs réalisés sur GaAs aient une fiabilité inférieure à ceux réalisés sur silicium. Un des grands avantages du transistor à effet de champ provient du coefficient de température positif qui assure automatiquement une répartition convenable du courant dans les différents doigts du transistor.

6.3. Circuits Intégrés (photo 9)

Un autre domaine très prometteur est la logique rapide sur GaAs. Nous avons nous-mêmes réalisés des portes et des circuits simples avec des temps de propagation de 0,1 ns ; on peut espérer un produit consommation/temps de propagation de 2 pj pour des portes internes. Des circuits intégrés comportant près de 100 éléments ont déjà été réalisés (LIECHTI, 1976). On peut aussi imaginer des mémoires de 4 kilobits qui consommeraient quelques mW, tout en ayant un temps d'accès de 20 ou 25 ns. Allons plus loin dans les perspectives : nous avons entamé un programme d'évaluation d'un récepteur intégré pour télédiffusion à 12 GHz.

6.4. Conclusion

Les transistors à effet de champ au GaAs ouvrent des perspectives prometteuses, non seulement pour les amplificateurs bas bruit, bande large ou étroite, mais aussi pour les amplificateurs de puissance et les circuits logiques rapides. Dès maintenant, les concepteurs de matériels doivent envisager l'utilisation de tels composants qui seront offerts très prochainement sur le marché avec des performances, des prix et une fiabilité convenables.

REFERENCES

BAUDET P., BINET M., BOCCON-GIBOD D., 1976, "Submicrometer self aligned GaAs MESFET", IEEE-MTT, and "Submicrometer self aligned GaAs MESFET", San Diego, Ca.

BINET M., KRAMER B., PARISOT M., 1976, "Characterization and Applications of GaAs MESFETS", Microwave Systems News.

DEAN R.H., MATANESE R.J., 1975, IEE Trans. on Elec. Dev.

DOERBEEK F.H., 1970, 3rd Int. Symp. on GaAs and Related Compounds, Aachen.

DRIVER M.C., KIM H.B., BARRETT D.L., 1971, Proc. of the IEEE.

EISENBERG J.A., 1973, Proc. Fourth Biennal Cornell Electrical Engineering Conf.

HOLLAN L., 1974, Vth Int. Conf. on GaAs and Related Compounds, Deauville.

IRE Standards, 1959, "Method of measuring noise in linear twoports.

LIECHTI, 1976, "High speed GaAs MIS", Philadelphie.

MIDDELHOEK S., 1970, IBM J. Res. Dev.

MOHR Th. O., 1970, IBM R. Res. Dev.

VIDALLON C., BENSASSON M., 1976, "Un pas vers un traitement complet d'un problème de C.A.O., Onde Electrique.

Photo 1 - forme du mésa sous la métallisation de grille.

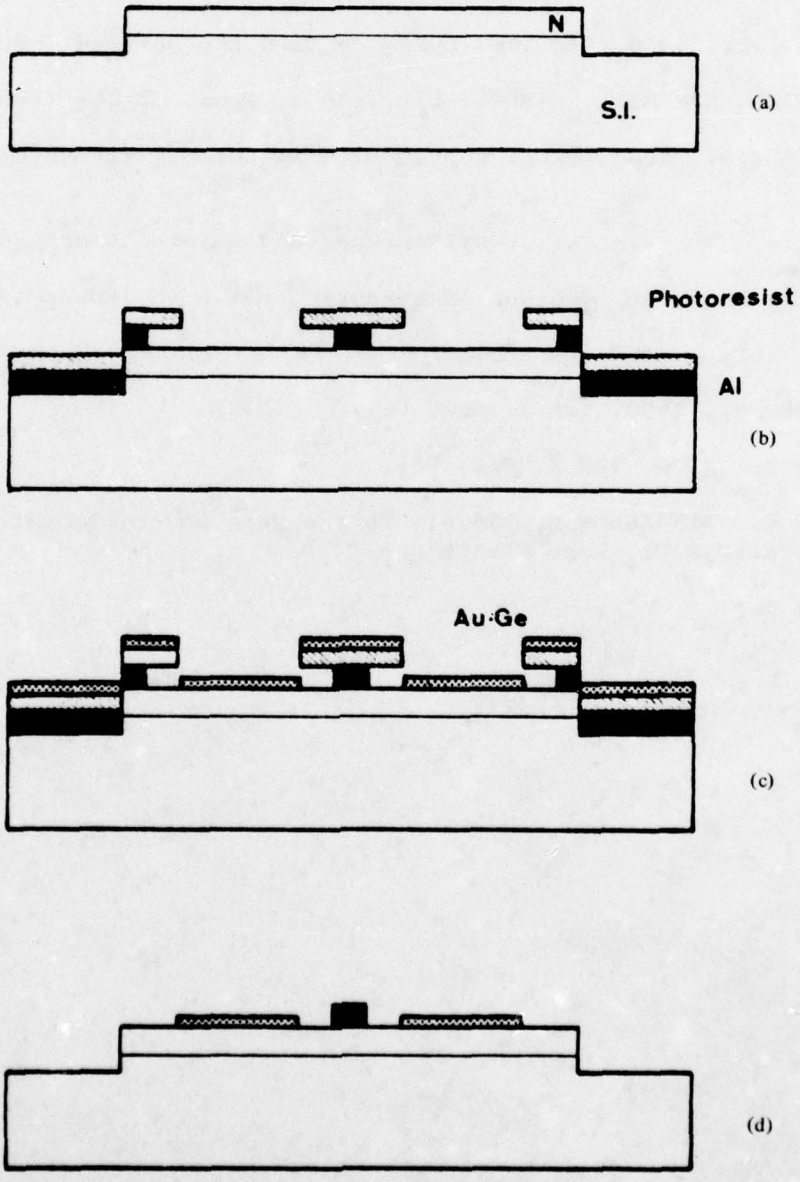

Figure 1 a, b, c, d, - étapes successives de la technologie.

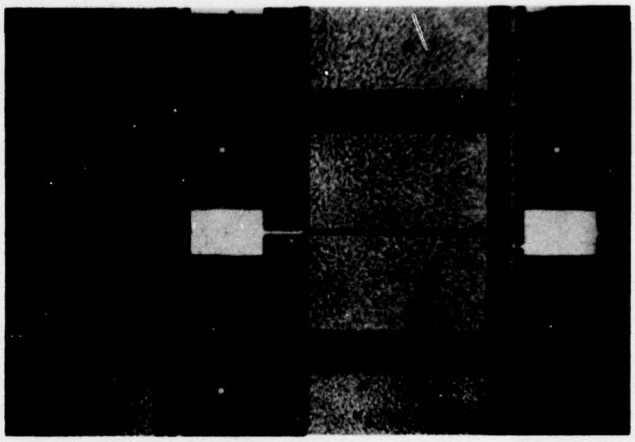

Photo 2 - plaque de transistors avant découpe.

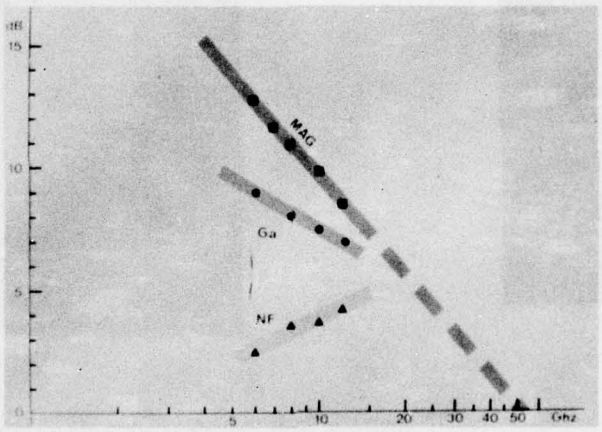

Figure 2 - gain maximum possible (MAG). Facteur de bruit (NF) et gain associé à ce facteur de bruit (Ga) en fonction de la fréquence.

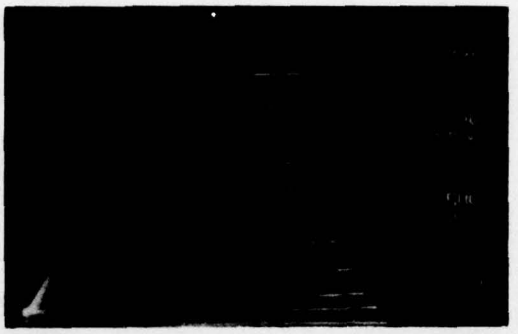

Photo 3 - réseau de courbes I_D en fonction de V_{DS} ; avec V_{GS} comme paramètre.

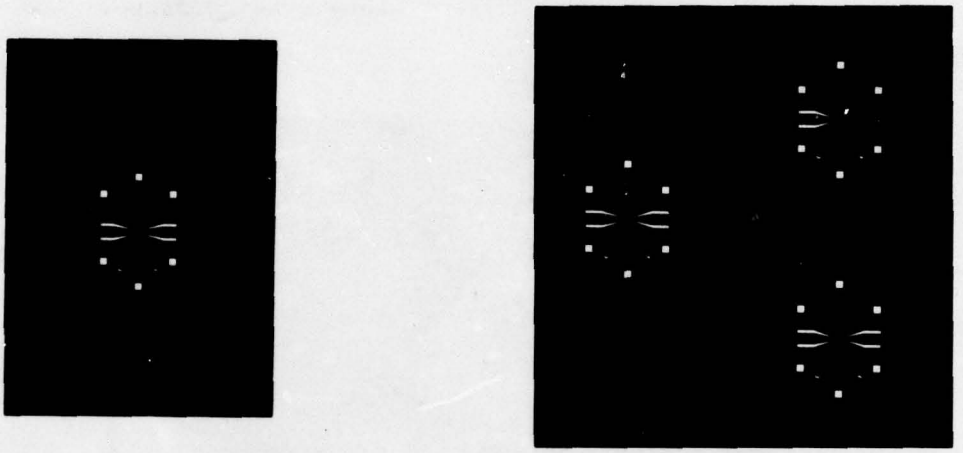

Photo 4 - circuit pour test des transistors et éléments de référence.

F	NF_{min} (db)	R_N (ohms)	G_o (mn hos)	B_o (mn hos)
6.0	2.5	90.0	4.50	- 15.10
9.3	3.3	94.0	16.50	- 18.18
12.0	3.7	93.0	38.60	- 23.05

Figure 3 - paramètres de bruit d'un transistor.

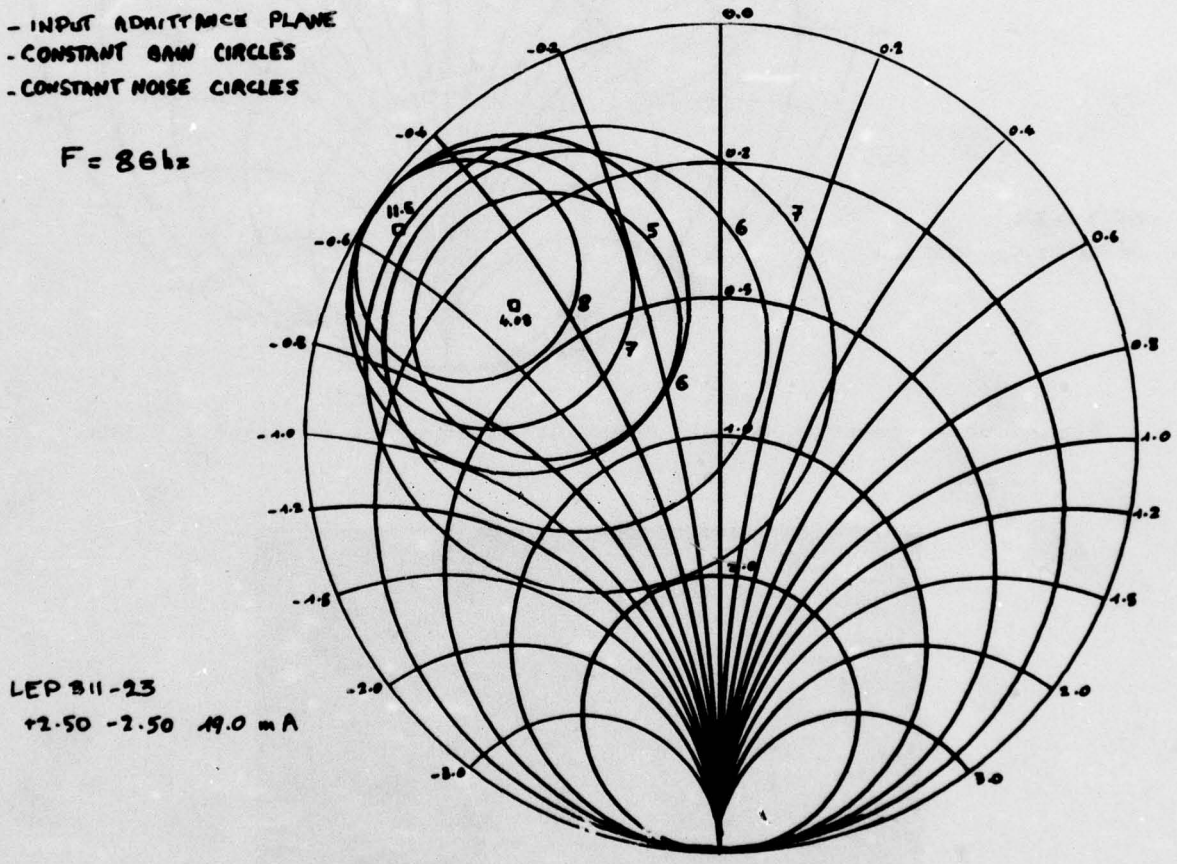

Figure 4a - cercles de gain constant et de bruit constant à 8 GHz.

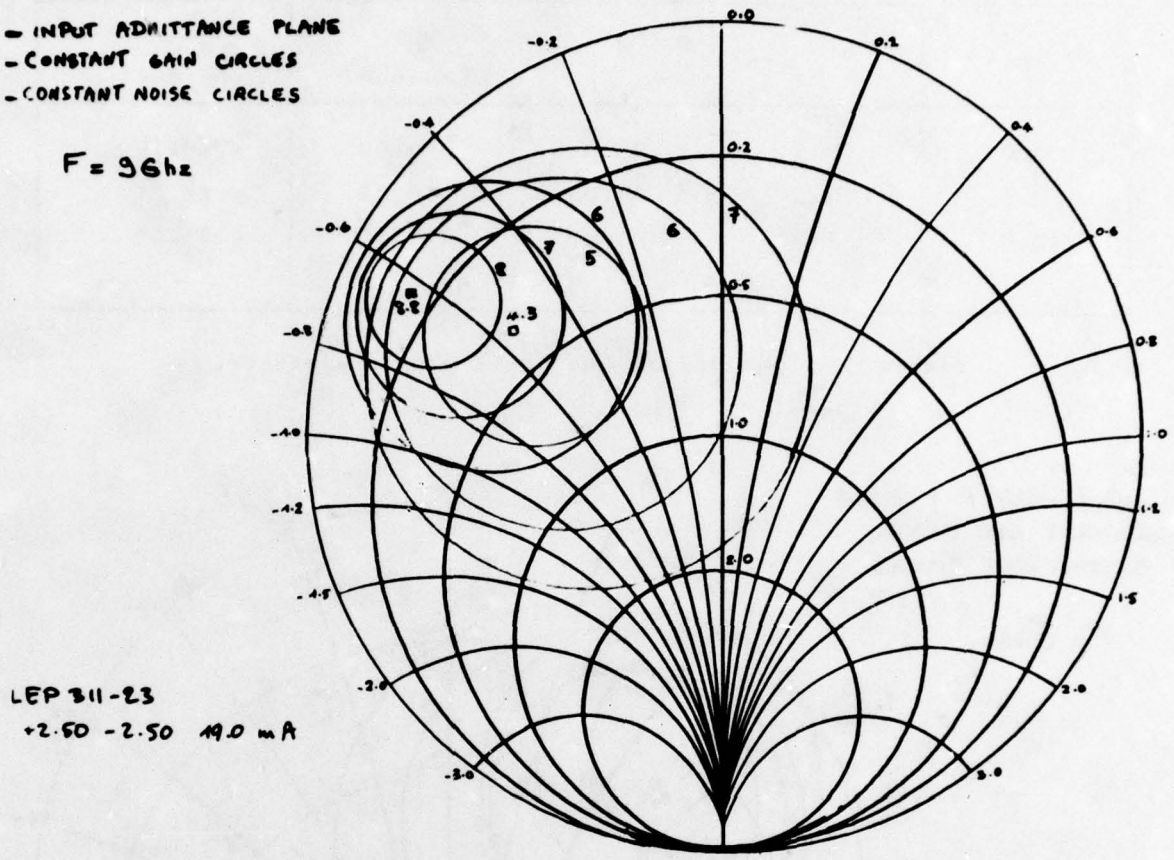

Figure 4b - cercles de gain constant et de bruit constant à 9 GHz.

Photo 5 - circuits d'adaptation et d'alimentation.

Photo 6 - vue d'un module élémentaire.

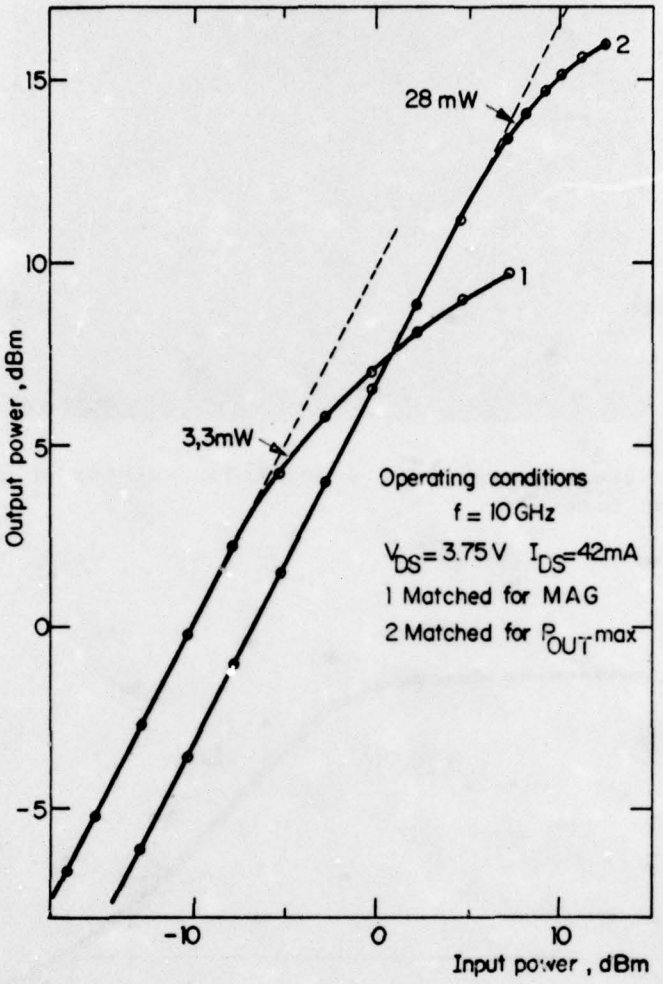

Figure 5 - puissance de sortie en fonction de la puissance d'entrée.

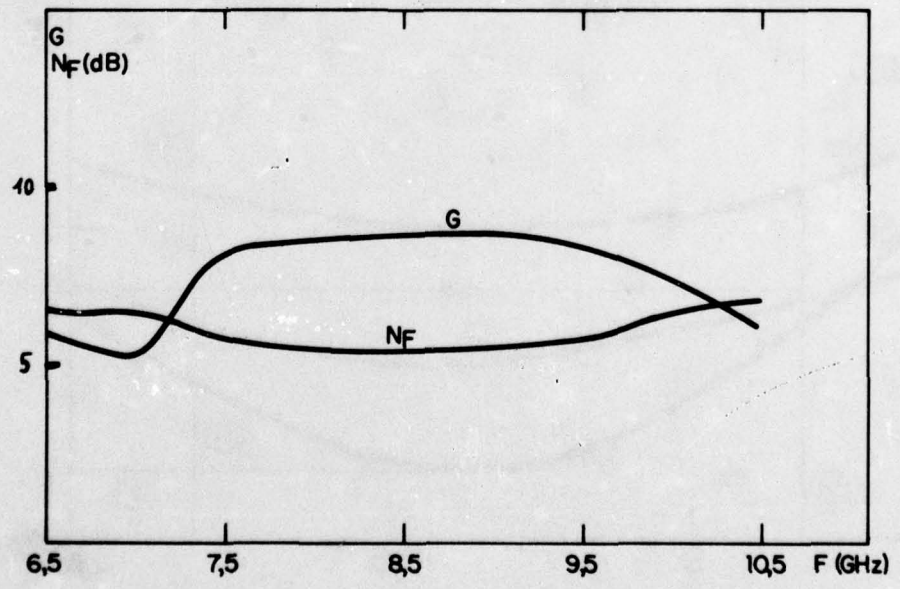

Figure 6 - gain en fonction de la fréquence avec adaptation à constantes localisées.

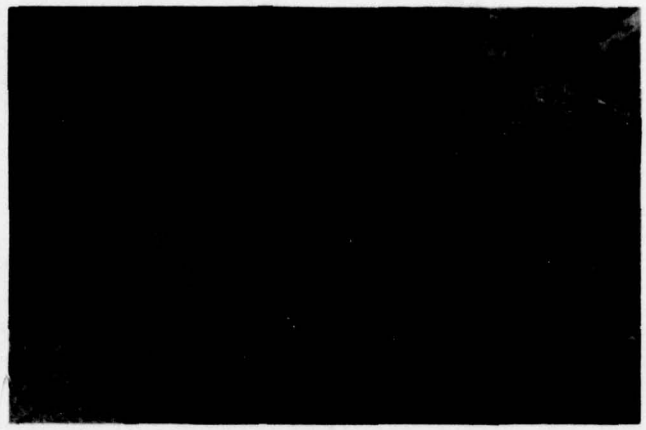

Photo 7 - plusieurs transistors peuvent être montés en parallèle sur le même circuit.

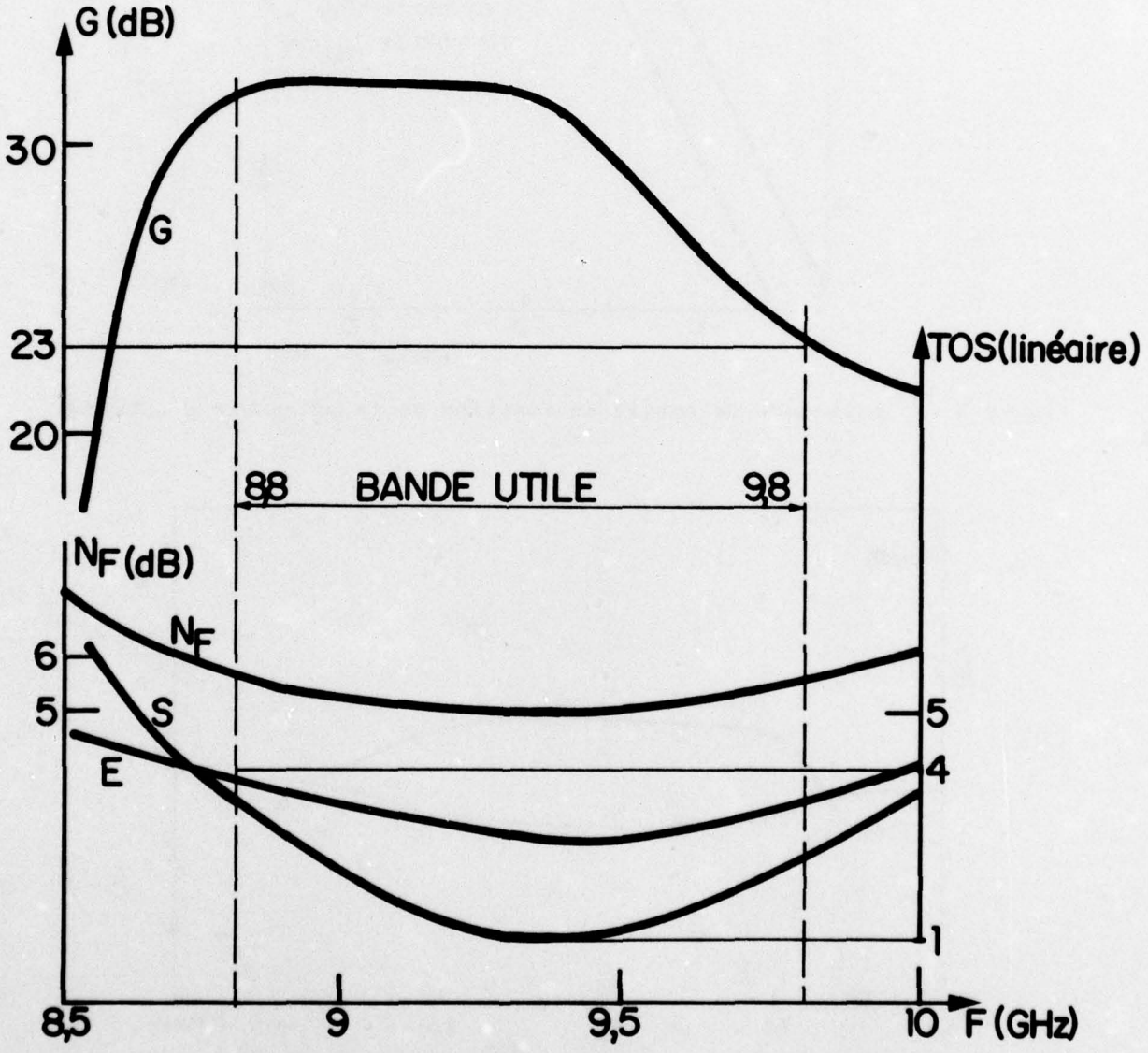

Figure 7 - gain et bruit en fonction de la fréquence pour un amplificateur de 5 modules dont l'un à constantes localisées.

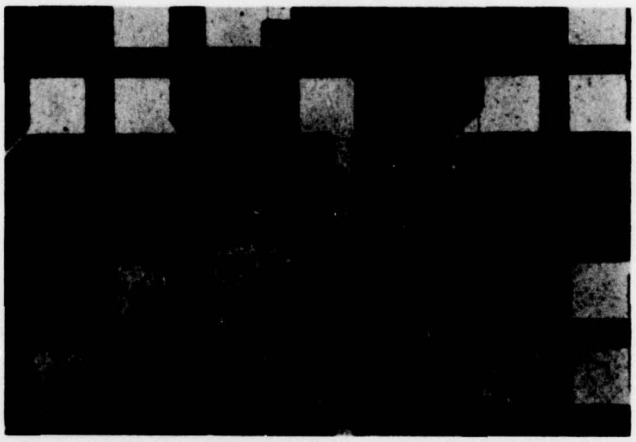

Photo 9 - porte logique - temps de propagation $\simeq$ 0,1 nanoseconde.

DISCUSSION

I W MACKINTOSH: Are you required to meet a specification on burn-out resistance? Have you made any measurements?

R VEILEX: Nous avons entrepris des expériences sur ce sujet mais nous n'avons pas encore de résultats.

Je veux simplement remarquer que la grille du transistor peut supporter plusieurs volts en continu et elle est protégée contre les sustensions des alimentations par des éléments VDR à réponse relativement lente, on peut donc supposer que cette grille supportera des impulsions relativement longues et de puissance moyenne.

NEW ADVANCES IN RELIABILITY AND EFFICIENCY IN LIGHTWEIGHT TWTs

Robert Berry and Armand Staprans
Varian Associates
611 Hansen Way
Palo Alto, California 94303
U.S.A.

SUMMARY

The most commonly used microwave power amplifier in recently developed airborne radars is the coupled-cavity traveling wave tube. This tube is favored because of its large bandwidth, high peak and average power capability, high gain and good signal purity. A number of recent developments have been concerned with improvement of the special characteristics important for airborne use such as reliability, efficiency, small size and weight, and simplicity of power supplies. This paper reviews recent developments and describes the various trade-offs for these areas.

I. INTRODUCTION

Modern airborne radars, with their demand for coherence, low spectral noise and multiple functions, combined with the wide bandwidths required for ECCM, have placed strenuous requirements on the transmitter output tube. When these are coupled with the need for minimum size and weight along with higher efficiency, reliability has often been compromised. Devices capable of providing the rf performance are available; and in recent years, the emphasis has been on improving the efficiency and reliability of these devices.

Linear beam tubes are generally preferred for new airborne radars because of the requirements for coherence and spectral purity, as well as the ease of modulation which has become possible with the advent of the non-intercepting control grid. Where bandwidths of 5% or more are required, the choice of linear beam tubes is limited to the traveling wave tube. The most commonly used, when more than a few kilowatts of peak power or more than a few hundred watts of average power are required, is the coupled-cavity TWT. As the rf circuits are all metal and can be directly cooled, the coupled-cavity TWT has a distinct advantage in average power capability when compared to the more conventional helix TWT which requires dielectric supports for the rf circuit. This paper will concern itself primarily with coupled-cavity TWTs; however, many of the advances mentioned are also applicable to helix or helix-derived TWTs.

Advances in efficiency and reliability as well as the tradeoffs in tube performance, which determine the eventual design configuration, will be discussed. Such features as peak power output versus beam voltage, frequency and focusing, as well as average power output versus size and weight, are given in the figures.

II. TWT ELEMENTS AND APPLICATIONS

A. TWT ELEMENTS

All linear beam tubes consist of an electron gun and focusing structure used to generate a long cylindrical beam of electrons, an rf structure which provides gain and power output by interaction with the beam, and a collector where the unused beam energy is converted to heat (Staprans, A., et al, 1973). This is shown schematically in Figure 1. Linear beam tubes differ one from another principally in the characteristics of the interaction circuit.

The electron gun contains a cathode, normally thermionic, which provides the electrons as a result of indirect heating. The electrons are formed into a cylindrical beam and directed into the rf interaction circuit by properly designed focusing electrodes and voltage between the cathode and anode, the latter normally at the entrance to the rf interaction circuit. Figure 2 shows the relative size and physical relationship of these elements.

As mentioned earlier, there are two basic types of rf interaction circuits used in traveling wave tubes. One is the familiar helix and derivations thereof, such as the ring loop and ring bar circuit, all of which are made of metal (usually molybdenum or tungsten), and supported on dielectric rods inside a cylindrical body. The other is the coupled-cavity circuit which consists of an array of tuned cavities that are coupled to each other, generally through a slot in their common wall. A hole is provided at the center of the cavity end walls through which the electron beam passes. Figure 3 shows a schematic drawing of the types of circuits. The signal to be amplified is introduced through an rf window and transducer at the gun end of the circuit, and the amplified rf is taken out through a similar device at the collector end of the circuit.

The electron beam, after transiting the circuit, then impinges on a bucket-shaped element known as a collector. The collector is connected to the positive side of the power supply, and completes the electrical circuit. The average electron velocity is reduced by an amount related to the increase in rf energy; in fact, this reduction in average electron velocity, resulting from the interaction of the traveling wave on the circuit and the electron beam, accounts for the energy transferred to the rf wave which is extracted at the output. The collector must convert the energy of the beam

to heat; and as there are periods of no rf output, the collector is generally designed to handle the maximum beam power.

B. TWT APPLICATIONS

The role commonly accorded the TWT in modern radars is that of the final output amplifier in the transmitter. This function has varying requirements; depending upon the type and the modes of operation assigned, it may include high duty cycle, high prf operation; or high peak power, low duty cycle operation. Where pulse compression is used, stringent phase linearity requirements apply. Some TWTs are operated cw for missile illumination, and the helix type of TWT is used frequently in active seekers for missiles.

Where high peak or average power is required, the choice is for a coupled-cavity TWT. These devices have been delivered for experimental aircraft radars at peak power levels as high as 200 kW and at average powers in excess of 5 kW. When driven by a stable oscillator, the TWT provides pulse-to-pulse coherence, as well as spectral purity, which is amplitude and phase noise free 100 dB down from the carrier. These features, along with its wide dynamic power output range and its broad bandwidth, have made the coupled-cavity TWT an even more logical choice for sophisticated airborne radars. Where multiple modes of operation are required, a single tube may fulfill the requirements for search, map, terrain following, navigation and air-to-air combat. Coupled-cavity TWTs are presently employed as the final amplifier on the MRCA, F-14, F-15, and F-16 radars and will probably be used in the F-18. In addition, they are used in many other more specialized airborne radars and in fixed, transportable, and shipboard radars.

III. RELIABILITY

A. FAILURE MODES

It is desirable that the tube operate without changes in essential characteristics, be insensitive to limited changes in system characteristics, and be easily protected in case of gross malfunctions in the system. Any discussion of reliability must begin with a description of the failure modes. In the case of a TWT, they are similar to that of any other linear beam tube, since the basic elements of the tube are little different. The failure modes for high power TWTs can be listed as follows:

Relevant Failure Modes

1. Loss of cathode emission due to cathode depletion
2. Heater failures
3. Grid shorts
4. Vacuum leaks due to thermal cycling
5. Ceramic seal leakage causing excessive high voltage arcing
6. Changes in beam characteristics caused by changes in spacings of gun elements
7. Emission from the shadow grid resulting in high values of control grid current

Nonrelevant Failure Modes

1. Mechanical damage due to improper handling
2. Melting of internal tube elements
3. Window breakage
4. Coolant channel clogging or coolant path leakage

Though all failures are of concern to the system, the nonrelevant modes are not within the control of the tube builder and require teamwork between the systems designer and the tube designer to minimize their occurence. It should also be noted that one failure mode may trigger additional failure mechanisms. For example, a broken window will cause loss of vacuum and heater burnout if the heater is operated for any length of time after the window failure occurs. Likewise, a grid short could conceivably cause melting of the circuit. In some cases, the initial cause of failure is not easily determined, making identification of the failure mode difficult.

B. THE ELECTRON GUN

The development of the non-intercepting gridded electron gun has made possible pulse repetition rates of 300 KHz and more, along with multiple prf's, in a lightweight high power transmitter. This gridded gun, though a boon to high power airborne radar designers, has complicated the tube builder's task, and has provided reliability inversely proportional to the radar performance. From a review of relevant failure modes above, we see that six of the seven modes are specifically identified as electron gun failures; while the seventh, vacuum leaks, is more general in nature.

Loss of emission and heater failure are not limited to gridded electron guns, but their occurrence can be related to the need for incorporation of a non-intercepting grid in the gun design, while grid shorts, beam characteristics changes, and grid emission are directly related to the gridded gun design.

C. NON-INTERCEPTING GRIDDED GUNS

In a conventional non-intercepting or shadow gridded gun, two identical grids are placed in perfect register on the beam axis, very near the cathode surface (Miram, G. V., 1970). This is shown schematically in Figure 4. The

grid closest to the cathode, called the shadow grid, is at cathode potential, and diverts the electrons around the second or control grid. Without this shadow grid, the control grid would intercept 10% to 20% of the beam current; in a high power tube, this would cause the grid to melt. The primary problem in building guns of this type is to design the elements and their supports so that they will not only be in the right position when the cathode is at operating temperature (about 1100°C), but so that they do not interfere mechanically during the temperature excursion from ambient temperature to operating temperature. At the same time the grids, though positioned only about a tenth of a millimeter from the cathode, must be thermally isolated and shielded so that they do not reach cathode temperature and also emit. This latter is the reason that the shadow grid is not normally placed on the cathode surface. Since the best focusing is achieved with the shadow grid on the cathode surface, the attempt has been to get it as close to the cathode as possible while maintaining the grid below the temperature at which it emits. The result has been shadow grid spacings of about 0.1 mm which must be controlled in design, assembly, and operation to within 0.01 mm. If the shadow grid moves outside these limits, then the beam focusing changes. This can cause increased interception on the control grid resulting in emission from or melting of that element and/or misfocusing of the beam, causing high body current and system shutoff. Likewise, if the movement of the shadow grid is sufficiently large, it can short the control grid electrically to the cathode, or touch the cathode and be heated to a temperature at which it emits. In the first case, the tube will operate continuously at zero grid bias which, in addition to causing radar failure, may also destroy the tube. If the shadow grid emits, this current will go to the control grid and, in all probability, destroy it. Maintaining the tight spacing of the shadow grid reliably is difficult in normal operation; for tubes which must operate reliably under the shock, vibration, and thermal environment of high performance aircraft, this element can become a major failure mechanism.

D. THE UNIGRID™

A new system for producing non-intercepting gridded guns has recently been developed which will eliminate the failure modes caused by movement or misplacement of the shadow grid. In this design, developed at Varian, the shadow grid is placed directly on the cathode surface thereby eliminating the requirement for close spacing just off the surface (Lien, E. L. and Miram, G. V., 1974). This, of course, means that the grid must be capable of operating at cathode temperature without emitting. Operation of this type has been achieved by coating the shadow grid with a material which is non-emitting at cathode temperature, and sufficiently passive that it does not migrate onto the cathode surface and inhibit emission from the desirable areas. This grid is bonded to the cathode and becomes an integral part of the cathode itself, thus leaving only one grid, the control grid, supported separately. Varian has applied the name UNIGRID to this unique system which provides a more laminar beam, as shown in Figure 5, and a more reliable gridded electron gun. An additional benefit is that of economy. As the critical spacing for this grid is eliminated the assembly is simplified, which results in reduced labor costs and improved yields. At the present time, over 100 tubes have been built and shipped with this type of gridded gun and there have been no failures involving the grid. Likewise, a life test being run at Varian on a VTX-5783 containing a UNIGRID reports 3,000 heater hours and 1,000 beam hours with no degradation in performance.

IV. EFFICIENCY

A. BASIC EFFICIENCY OF TWTs

The efficiency of the final amplifier is usually of great interest to radar transmitter and system designers, as this is the single biggest power consumer in the system. Often as much as 50% of the total system power is provided to the output tube which, if only 10% efficient, means that only 5% of the total system power is converted to rf energy.

The TWT relies upon continuous interaction between the electron beam and a wave of rf energy traveling on the circuit for amplification, and is quite sensitive to the beam velocity. In designing the tube, the beam voltage and cavity period are typically adjusted to give a flat gain characteristic with frequency. This adjustment, however, does not necessarily give the best power transfer to the circuit at the tube output, and results in efficiencies on the order of the 10% mentioned above. Further adjustments are normally made to increase the efficiency by improved velocity resynchronization in the last few cavities at the output. This can be done by reducing the period of these cavities to increase the energy exchange, or the beam voltage can be increased near the tube output. By tapering the output circuit, as reducing the cavity period is called, efficiencies of 15% to 25% have been achieved; the value depending upon the power output, bandwidth, and frequency. Further increases in efficiency have been achieved on experimental tubes by voltage jumps, which entails isolating the output section electrically and putting voltage on that section to increase the electron beam velocity into synchronism with the rf wave in the output section. Notable increases in efficiency have been made (on the order of 5% to 15%) by this method; however, the problems of high voltage isolation in the output section involving mechanical strength, compromised circuit characteristics, additional vacuum seals, and insulator leakage have made this technique unattractive for operational systems when other methods such as improved tapers and collector depression can achieve the same results.

B. DEPRESSED COLLECTOR OPERATION

The basic or beam efficiency is given as

$$\frac{P_{out}}{P_{in}} = \eta \qquad (1)$$

where: $P_{in} = E_b$ (beam voltage) x i_k (cathode current) and P_{out} = rf power output (at saturation).

Typically, 15% to 20% beam efficiency is obtained from the power supply arrangement shown in Figure 6. If the collector is isolated from the rf circuit, it can be operated at a reduced voltage without affecting the rf properties of the TWT. This requires a separate power supply to maintain the cathode to anode voltage; however, the efficiency can be enhanced by a power supply arrangement such as that shown in Figure 7. In this case, the efficiency becomes

$$\frac{P_{out}}{P_{in}} = \eta \qquad (2)$$

where: $P_{in} = (E_k \times I_{circuit}) + (E_{collector} \times I_{collector})$

E_k = cathode to anode voltage

$I_{circuit}$ = beam current intercepted on the anode and circuit

$E_{collector}$ = collector voltage

$I_{collector}$ = beam current reaching the collector

Since the beam current transmission (i.e., that proportion of the beam current reaching the collector) is typically 90%, it can be seen that operating the collector at a reduced voltage reduces the total input power. For instance, for equation (1), if the cathode voltage is 20 kV and the beam current is 3 amperes, then

$$P_{in} = 20 \times 3 = 60 \text{ kW}$$

whereas in equation (2) with 90% transmission and a collector voltage equal to 1/2 E_k or 10 kV, then

$$P_{in} = (20 \times 0.3) + (10 \times 2.7) = 33 \text{ kW}.$$

These values are typical for 10 to 12 kilowatts power output, depending upon the bandwidth required. It can be seen that a collector operating below the circuit potential can enhance the efficiency substantially.

As might be expected, there is a limit to the level below the circuit to which the collector voltage can be depressed. Because extracting energy from the beam during the rf interaction slows down the beam, it essentially lowers the average potential of the electrons; and as the collector voltage is reduced, an increasing number of electrons are unable to enter the collector. Therefore, at some point, the electrons returned to the circuit become excessive from either a thermal or an efficiency viewpoint and limit the amount of collector voltage depression. For a single-stage depressed collector, this normally occurs at a voltage between 50% and 70% of the cathode to anode voltage. Or, to state it differently, at a depression voltage of 30% to 50%. The amount of depression that can be achieved is inversely proportional to the basic efficiency of the TWT, and for single-stage collectors, the overall efficiency of the tube is limited to about 35%.

Figure 8 shows the rate of increase of circuit current with collector depression and also the efficiency versus collector voltage for a single-stage collector. By incorporating two stages of collector depression, the first stage is operated at a voltage 25% to 30% below the circuit so as to return a minimum of electrons to the circuit while a second stage is operated at lower voltage, 60% to 65% below the circuit, to catch the faster electrons at a voltage only 35% to 40% above the cathode voltage. As is shown in Figure 9, this can yield a beam efficiency in excess of 40% without excessive circuit interception. The data shown were taken on a 50 kW, X-band TWT developed at Varian for airborne applications. Further analytical work using computer programmed models indicate that three-stage collectors can yield efficiencies of 50%. As many as 12 collector stages have been demonstrated experimentally and proposed for high average power applications in outer space with theoretical efficiencies as high as 72%. However, the complexity and expense of construction and operation makes them impractical for the present application. Two-stage collector depression is probably the practical limit, except for the most stringent efficiency requirements such as, for example, may be experienced in outer space.

V. SIZE AND WEIGHT

A. CIRCUIT DESIGN

Because of the limitations on both size and weight which have been dictated by high performance aircraft, a great deal of effort has been put into packaging traveling wave tubes. The size of the electron gun is generally directly proportional to the peak power output, as this determines the peak operating voltage and current. The collector size is determined by the average power output, as this reflects the amount of beam energy to be converted to heat. The circuit size and weight is determined by several more complex factors. Cavity diameter and cross-section are directly proportional to wave length, being approximately 1/2 λ in diameter. Gain determines the number of cavities required, and the gain per cavity is inversely proportional to bandwidth. Peak and average power output influence the circuit size in that higher peak powers, with their attendant higher voltages, require longer rf periods and longer circuits; however, this effect can be small compared to the effect of average power.

As described earlier, the beam is formed into a column by the electron gun and anode. It is launched into the circuit and must then retain its cylindrical shape as it passes through the circuit in order to interact efficiently with

the rf wave. This requires some external field, usually magnetic, to maintain the focusing. This magnetic field can be supplied by a permanent magnet focusing structure or an electromagnet; the choice, which has a profound effect on the weight, is dependent upon the average rf power output requirements.

All high-gain TWTs require some circuit rf loading to prevent oscillation at the band edge frequencies. This can be done through resonant loss tuned to the band edge frequencies, or by selective distributed loss on the circuit. Where resonant loss buttons are used, as shown in Figure 10, the outer diameter of the tube body is enlarged. This increases the size and weight of the tube and requires a larger, heavier magnet structure as well. The application of distributed loss, also shown in Figure 10, has been developed and refined at Varian with the aid of an elaborate mathematical model. This model is programmed on the computer, and provides the necessary parameters for design and construction of the circuit for a given rf performance.

The use of distributed loss provides the minimum circuit diameter and the maximum gain per cavity, thereby reducing the size and weight of the circuit to a minimum. In addition, the attendant magnet focusing structure is reduced in size and weight.

B. THE FOCUSING MAGNET

In terms of size and weight, the beam-focusing structure of the TWT can comprise a relatively small part of the tube, or can triple its size and weight. One method of focusing the beam is by means of an electromagnet, usually called a solenoid. Because of its superior focusing qualities, the solenoid is used where the high average beam power demands very low body current. The required magnetic field can be supplied by some combination of the product of N (turns) and I (current). However, N also means size and weight, while I requires some external power, which degrades the efficiency. The size/weight and power required for a given field vary inversely, and there is always a tradeoff between those features. However, the NI requirement for a given field is also proportional to the area in which the field must be maintained and the size/weight and power of the magnet are proportional to length (gain). Therefore, bringing the magnet as close to the beam as possible reduces the NI required by the square of the radius. The virtues of the distributed loss circuit loading now become apparent, as the smaller circuit size reduces both the size and weight of the solenoid and also the power requirement.

Two techniques have been employed to reduce the size and power requirements of the solenoid. The first is to wind strips of aluminum foil directly on the tube body, or circuit, so that the inner diameter of the solenoid will not be limited by the aperture required to clear the electron gun for tube insertion and removal. By this means, tubes producing 5 kW average at X-band have been delivered with 50 dB gain in packages weighing less than 25 kilograms. The alternate approach is to reduce the cathode diameter. With the application of high voltage experience, and the shielding of standoff insulators, this technique has provided a TWT with an average power capability of 10 kW and a peak power of over 50 kW within a weight limitation of 33 kilograms.

C. PPM FOCUSING

The most attractive focusing method is PPM (periodic permanent magnet) focusing. This involves a series of magnetic field reversals along the beam axis supplied by an array of relatively small permanent magnets, which provide a light weight focusing system requiring no power. It has long been applied to low power tubes and, with the advent of new magnet materials, the average power level which can be focused by this method is increasing. Since this form of focusing relies upon a series of magnetic lenses, the beam tends to scallop and to exceed the focusing forces as the rf fields increase at the output end of the tube. The result is increased circuit interception. This is thermally compounded by the requirement for iron cavity walls to bring the magnetic flux into the beam. These iron walls, or polepieces as they are called because of their magnetic function, have only about one tenth the thermal conductivity of the copper normally used in the cavity walls and, therefore, also limit the average power handling capability of the tube.

A solution to increasing the average beam power which can be focused is to improve magnet materials so that they have higher energy products and produce high strength fields. This will provide better beam transmission and reduce the thermal load on the circuit. During the last few years, a great deal of work has been done with rare earth magnets, particularly samarium cobalt (SmCo). This material produces focusing fields at least two times that of conventional magnet materials such as Alnico. This material, now available from several sources, has resulted in PPM-focused coupled-cavity TWTs such as the VTX-5784 with 1 kilowatt average power output in X-band and helix TWTs with 500 watts cw power output at 10 GHz. Because of its high energy product, a small amount of SmCo can produce an adequate focusing field. An example of the attendant reduction in weight may be seen by comparing both types of focusing in the VTX-5680, a 50 kilowatt peak, 100 watt average, coupled-cavity TWT. This tube, when focused with Alnico 5 magnets, weighs 5.3 kilograms; the same tube focused with SmCo magnets weighs only 3.85 kilograms. Other examples of the light weights achievable with SmCo PPM focusing are shown in Table I.

In addition to the higher powers focused and the lighter weight achieved, SmCo can improve reliability. Most magnetic materials lose some of their charge when the mmf is shorted, as might occur when magnetic material, such as tools, are accidently placed against the magnets. SmCo returns to its former strength as soon as the perturbing material is removed, and thus provides protection against one of the common failure mechanisms of permanent-magnet-focused tubes.

D. THE POWER BOOSTER

A recent breakthrough in coupled cavity TWT development has been the demonstration of a low gain, high power TWT. Devices of this sort in the past have required the same rf stabilization (resonant or distributed loss) required

of high gain TWTs. The device recently demonstrated at Varian has no added loss, and is virtually transparent with only about 0.3 dB total loss from input to output. The tube demonstrated was a cw TWT with 10 kW of power output in the range from 7.9 to 8.4 GHz.

The tube is essentially a single-section TWT and is, consequently, short compared to a 50 dB gain tube. The virtue here is that the tube can be permanent-magnet-focused like a klystron, at much higher average power than a standard gain TWT; and because it has no circuit loss, is capable of efficiencies on the order of 40% with a single-stage depressed collector. The tube can be gridded and is expected to have noise, phase, and amplitude characteristics comparable to any high gain TWT. Its importance is in its ability to be a transparent booster of output power (7 dB gain has been demonstrated and 10 dB is predicted) which consumes no power except when the increased output is needed. Figure 11 shows data on an experimental model which demonstrate over 25% efficiency without collector depression and over 35% with single-stage collector depression.

IV. TRADEOFFS IN TUBE CHARACTERISTICS FOR TRANSMITTER DESIGN

The selection of peak power, average power, and bandwidth is largely determined by radar performance requirements. These primary tube characteristics, however, determine the operating voltage, the size and weight of the tube, efficiency and cooling requirements, and thereby influence the entire transmitter size and configuration. Furthermore, the selection of gain for the tube not only influences the driver requirement, but also affects tube size and weight. The following discussion summarizes the effect of primary tube performance specifications upon those factors which will most directly influence the transmitter configuration.

Since most airborne radars operate at X-band, this frequency range is chosen for this discussion. An overview of the various coupled-cavity TWT configuration possibilities is given in Table I. This table is limited to some typical X-band coupled-cavity TWTs at 50 kW peak power, which are specifically designed for airborne applications. Curves in Figures 12 to 16 will further limit the tradeoff discussion to gridded tubes with single-stage depressed collectors, which is the most commonly used tube configuration.

Figure 12 illustrates the consequences of peak output power. The most rapidly varying parameter is the cathode voltage required to generate the electron beam. Some latitude, however, is available through the choice of gun perveance. This parameter, which typically is about 1.25×10^{-6} for the middle of the peak power range (10 to 50 kilowatts), is variable within limits. Tube length and weight are less rapidly varying characteristics. These are shown for an average power, not exceeding about 500 watts, in order to illustrate the effects of peak power only.

Average power output does not influence cathode voltage or tube length. It does, however, determine the choice of tube cooling design and the method of beam focusing. Figure 13 shows the resulting effect upon tube weight. Above about the one kilowatt level, tube weight approximately doubles because of the focusing solenoid required to provide better beam transmission for the higher power beams. The focusing solenoid, in addition, requires its own input power, and thereby reduces the overall efficiency by one-fourth to one-half.

The effect of tube bandwidth is only moderate upon efficiency and tube physical characteristics for the usual radar bandwidth requirement of less than 10%. As shown in Figure 14, however, these effects become considerable for extremely broad-band TWTs, such as might be used for ECM applications.

The only parameters significantly affected by choice of tube gain are length and weight, as shown in Figure 15. Tube length increases much less than linearly with gain in dB because a significant portion of the tube (gun and collector) is not affected. Most tubes operate in the neighborhood of 50 dB gain in order to provide sufficient gain to minimize the driver size without too closely approaching the stability limit.

The effect of the choice of the operating frequency band is shown in Figure 16. Since tube dimensions must relate to the wavelength of operation, the variations in length and weight are easily understood. Because of dissipation densities, the average power-handling capability of the tubes varies accordingly. The power curve shown does not represent fundamental limitations, but rather shows the current state-of-the-art for PPM focused light-weight tubes. It is apparent from these data why X-band is so often the choice to provide sufficient radar power, together with a reasonably small, lightweight tube package.

V. CONCLUSION

The intent has been to point out the recent advances in the state of the TWT art which contribute to increased reliability and efficiency as well as reduced size and weight. The improvements in gridded gun construction, such as UNIGRID, will increase tube reliability as well as reduce the cost. Use of improved analytical techniques to increase interaction efficiencies and multiple-stage collector depression will provide higher efficiency in system operation. Improved magnet materials, such as SmCo, will contribute to size and weight reduction, and reduce prime power requirements. The booster TWT is another contribution which affords focusing advantages while also offering the flexibility of operating efficiently at more than one power output level. These advances will contribute to improved overall system performance in future airborne radars.

REFERENCES

Lien, E. L. and Miram, G. V., 1974, "Nonintercepting Gridded Guns," IEDM Technical Digest.

Miram, G. V., 1970, "A New Approach in the Design of Nonintercepting Gridded Guns for Pulsed, High-Power Microwave Tubes," MOGA Conference.

Staprans, A., McCune, E. W., and Ruetz, J. A., March 1973, "High Power Linear Beam Tubes," Proc. of the IEEE, vol. 61, No. 3.

TABLE I

Comparison of some 50 kW, X-band, coupled-cavity TWTs with 5% to 10% bandwidth and approximately 50 dB gain.

TYPE NO.	DUTY	MODULATION	COLLECTOR	BEAM EFFICIENCY (%)	FOCUSING	COOLING	LENGTH (cm)	WEIGHT (kg)
VTX-5680	0.002	Cathode	Undepr.	20	PPM	Conduction	41	3.9
VTX-5783	0.01	Grid	Undepr.	18.5	PPM	Forced Air	48	6.4
VTX-5784	0.02	Grid	1-Stage Depr.	30	PPM	Coolanol	50	6.4
VTX-5782A	0.10	Grid	1-Stage Depr.	33	Solenoid	Coolanol	63	27
VTX-5782B	0.10	Grid	2-Stage Depr.	40	Solenoid	Coolanol	63	27

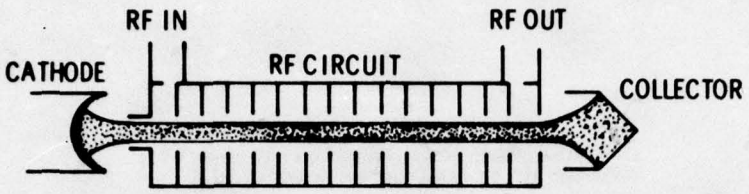

Fig.1 Traveling wave tube schematic diagram

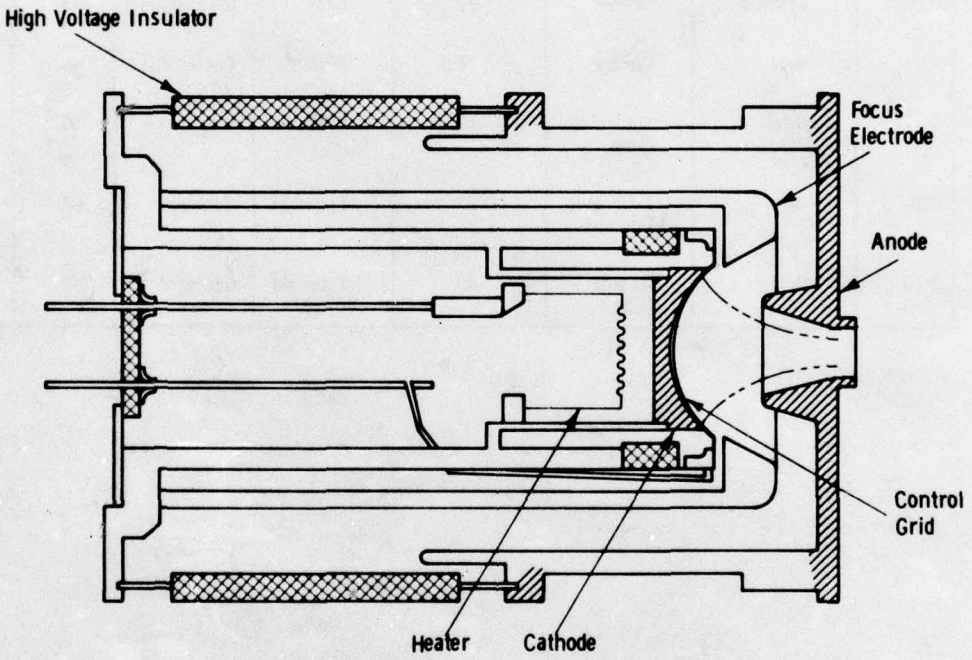

Fig.2 TWT electron gun

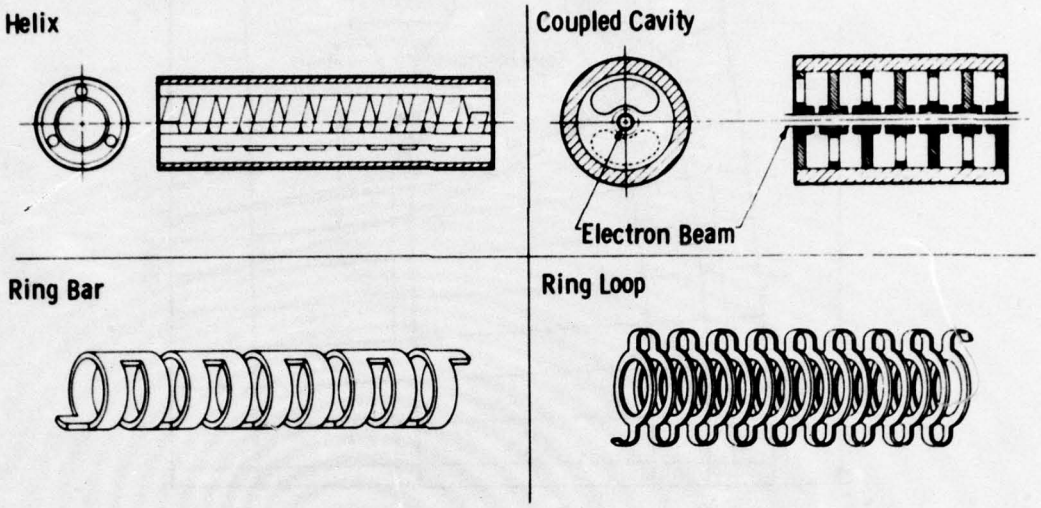

Fig.3 TWT rf circuits

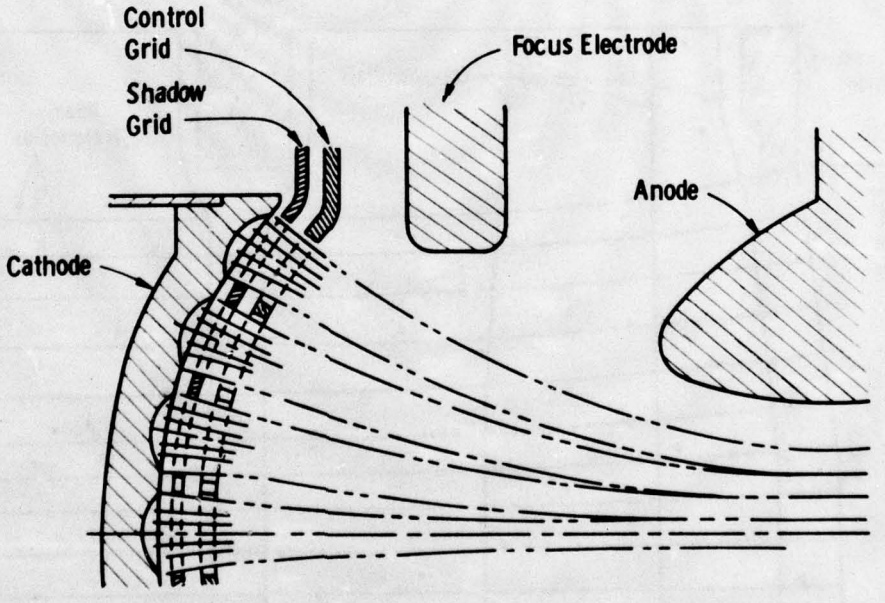

Fig.4 Conventional nonintercepting gridded electron gun

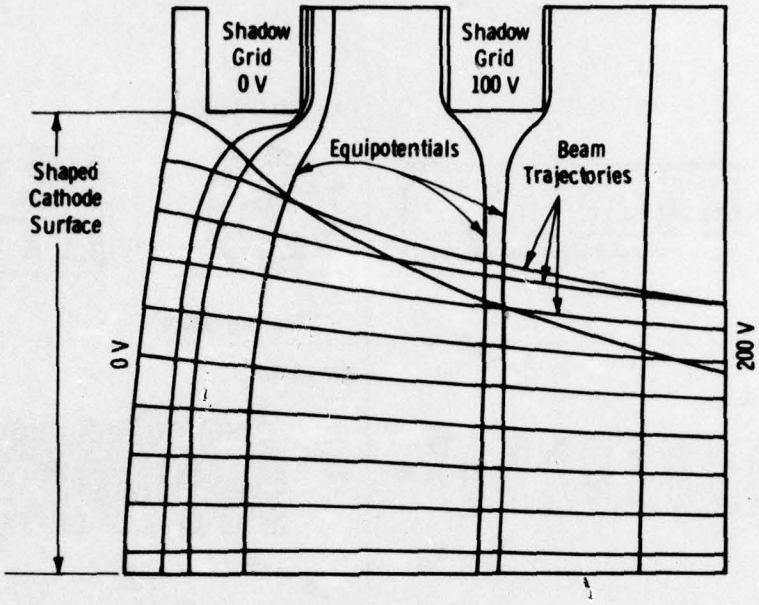

Fig.5A Electron trajectories for a conventional gridded gun (single cell shown)

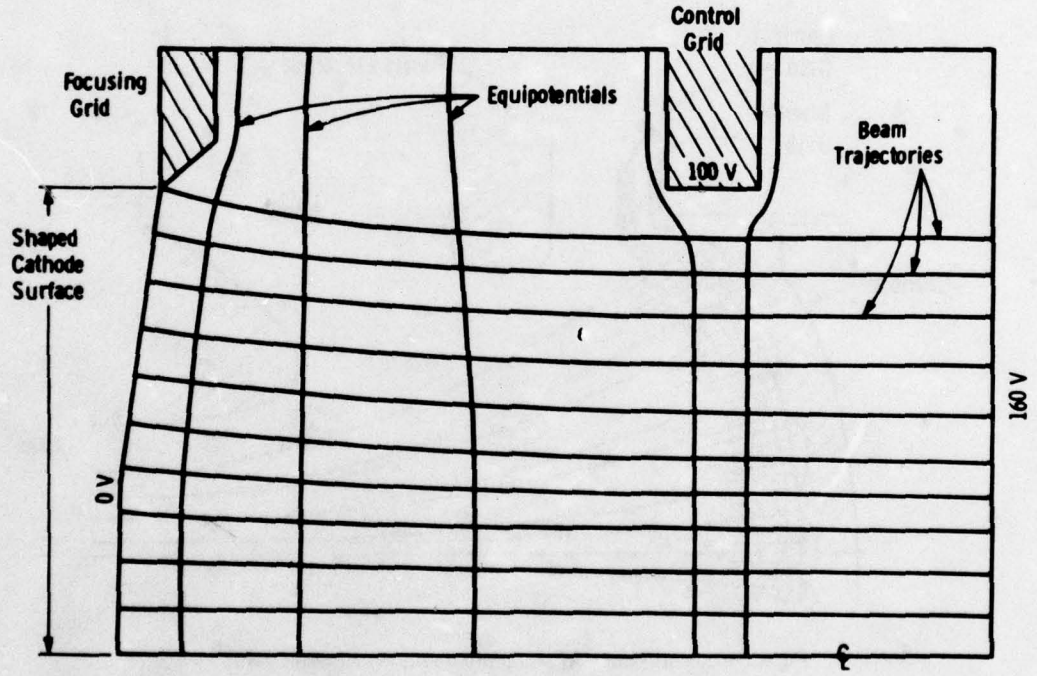

Fig.5B Electron trajectories for a Unigrid™ gun (single cell shown)

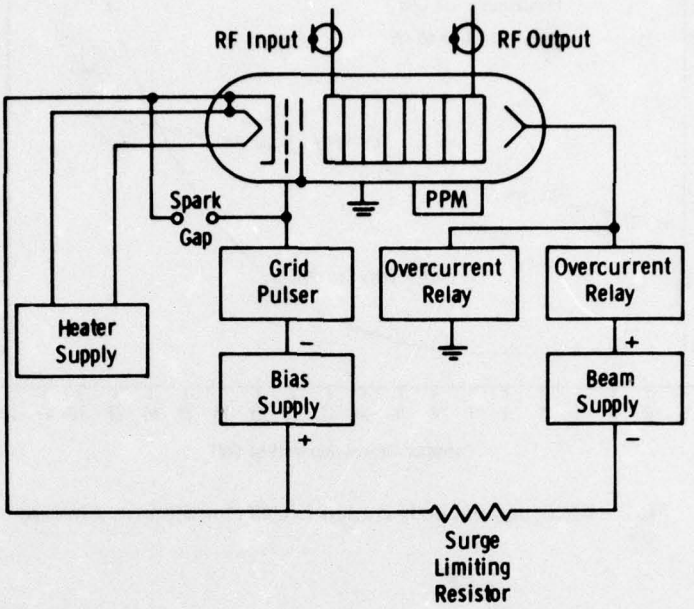

Fig.6 TWT power supply schematic (without collector depression)

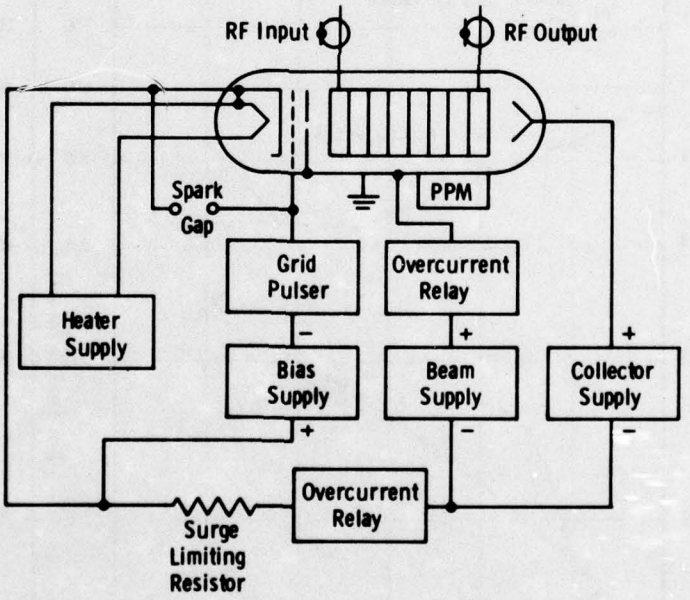

Fig.7 TWT power supply schematic (with collector depression)

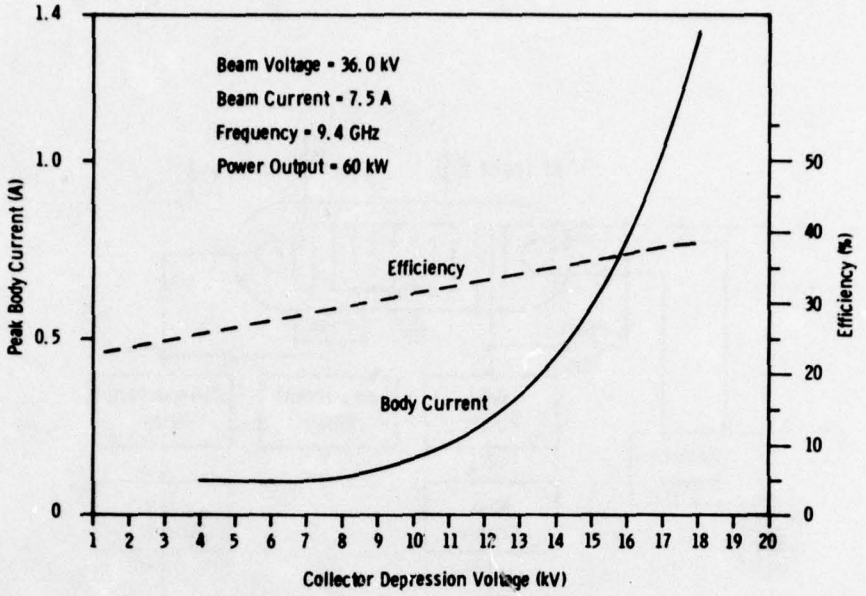

Fig.8 Efficiency and body current vs collector depression voltage

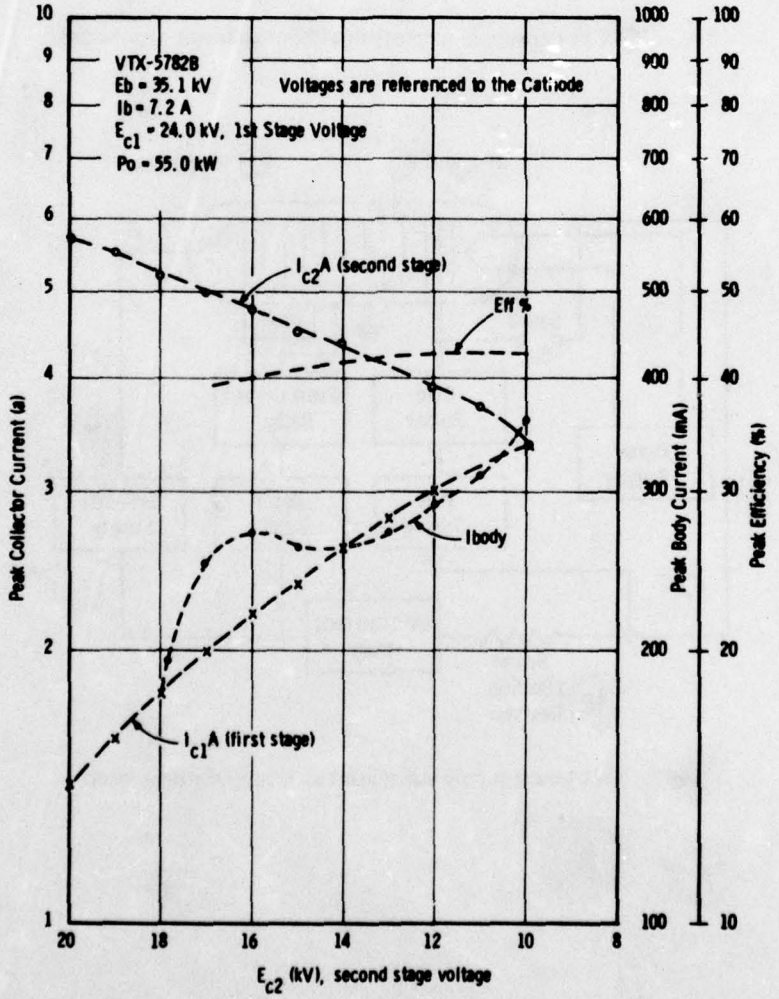

Fig.9 Two-stage collector operation

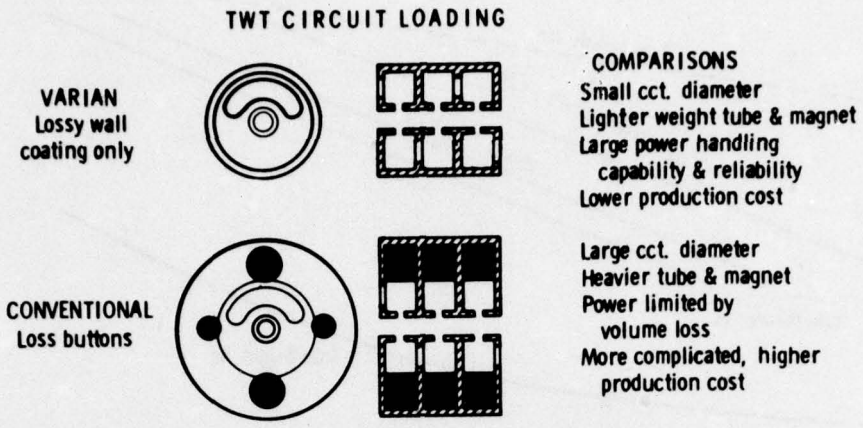

Fig.10 TWT circuit loading

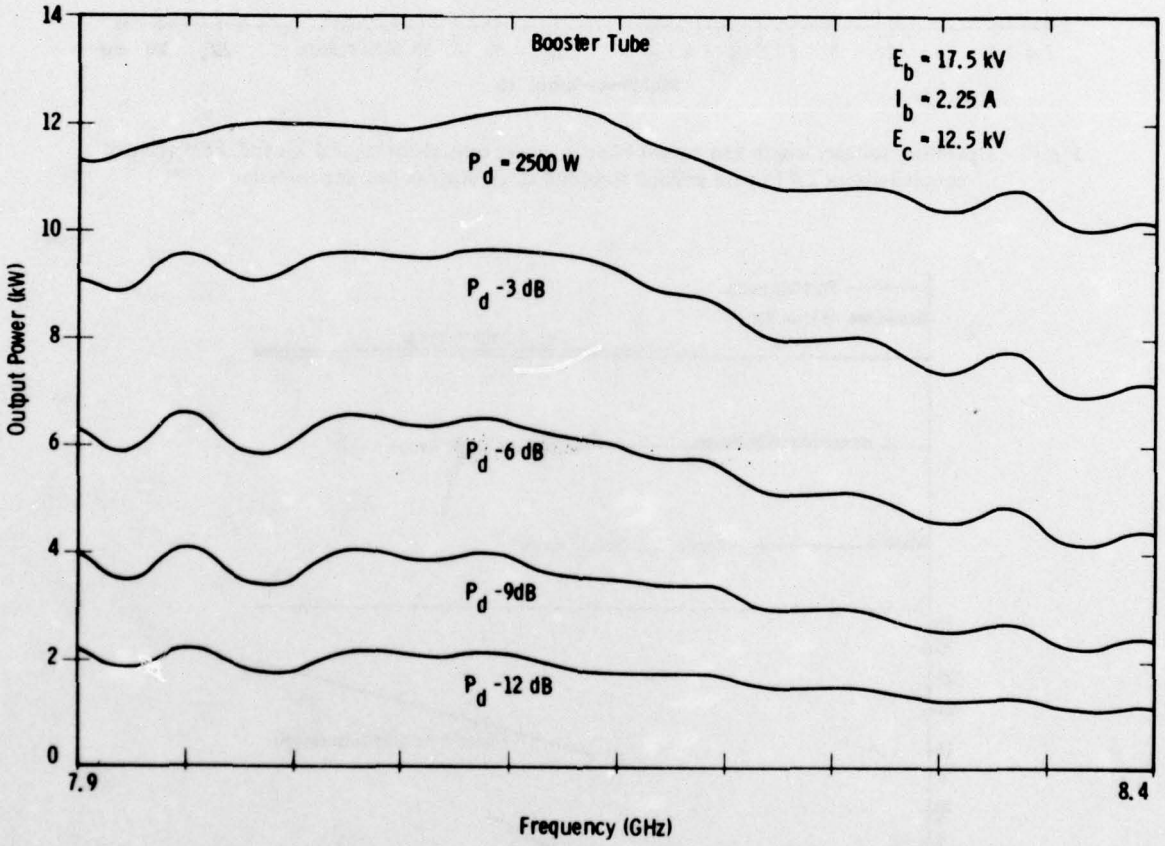

Fig.11 Booster TWT performance

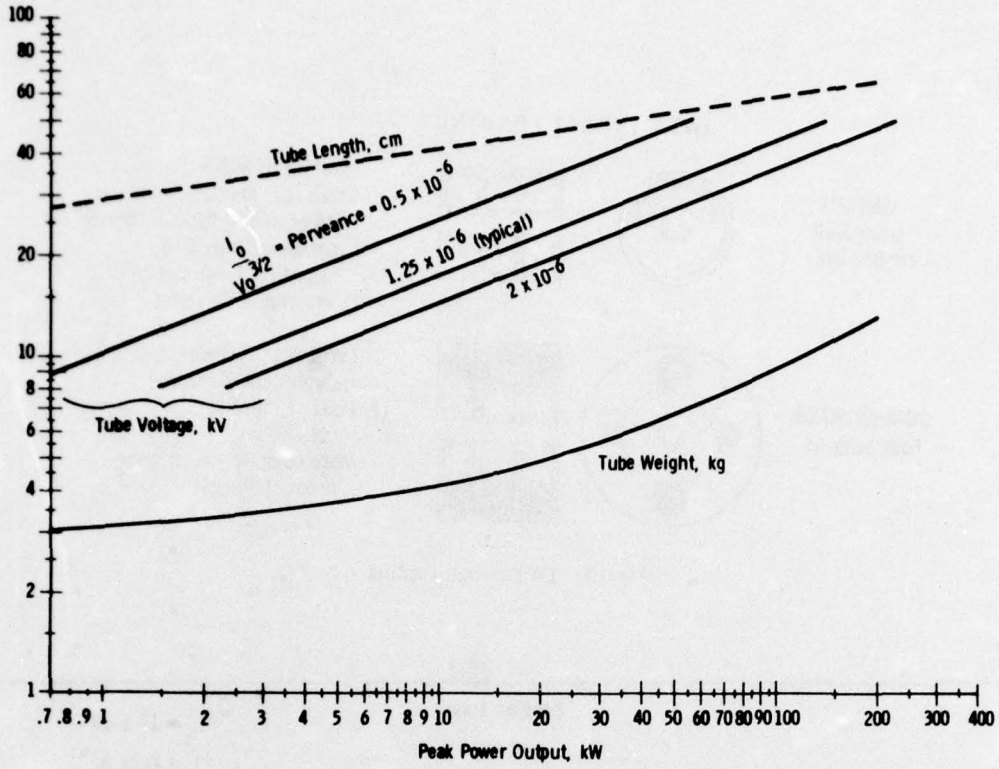

Fig. 12 Operating voltage, length and weight vs peak power output for typical X-band, PPM-focused coupled-cavity TWTs with gridded guns and single-stage collector depression

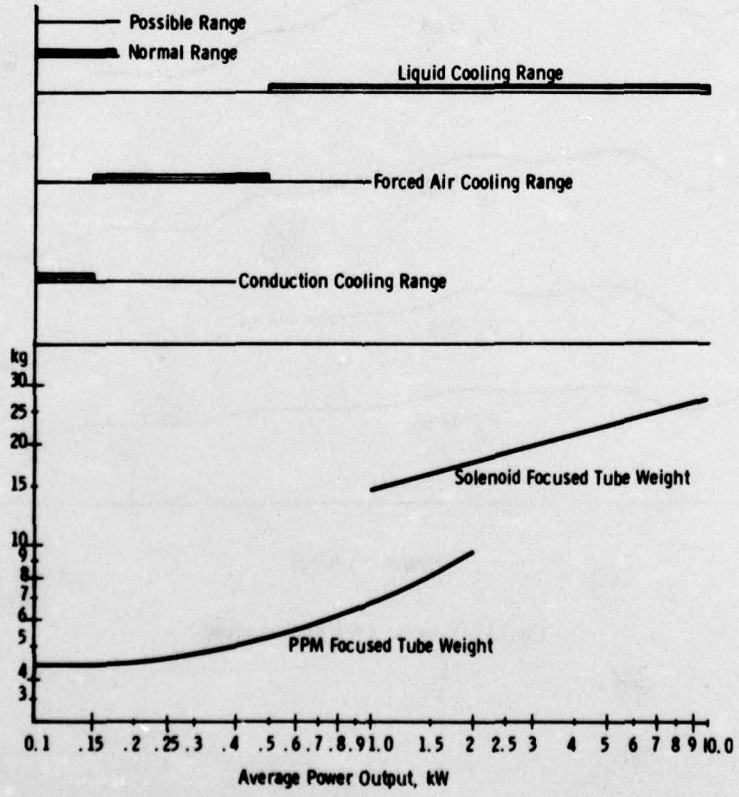

Fig. 13 Typical tube weight and cooling media vs average power for X-band, coupled-cavity TWTs with gridded guns and single-stage collector depression

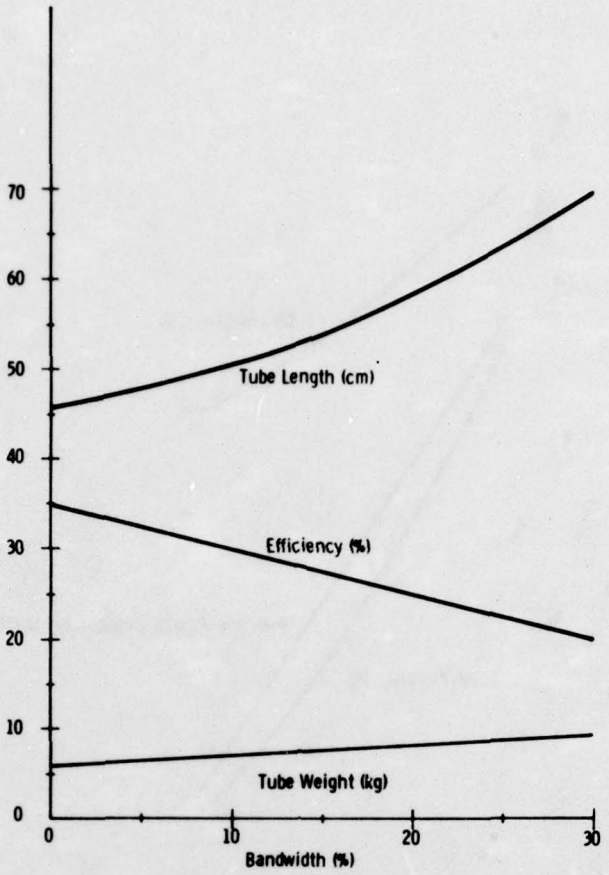

Fig.14 Efficiency, length and weight vs bandwidth for typical 50 kW, X-band PPM-focused coupled-cavity TWTs with gridded guns and single-stage collector depression

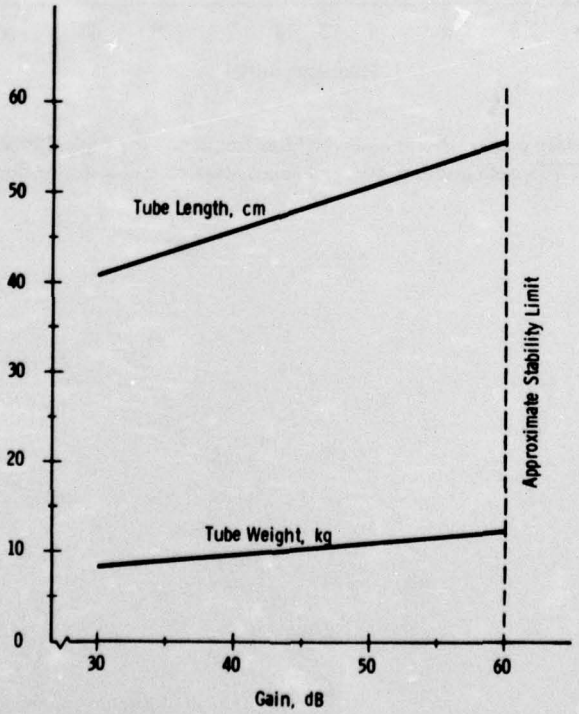

Fig.15 Length and weight vs gain for typical 50 kW, X-band, PPM focused coupled-cavity TWTs with gridded guns and single-stage collector depression (bandwidth 5 to 10 percent)

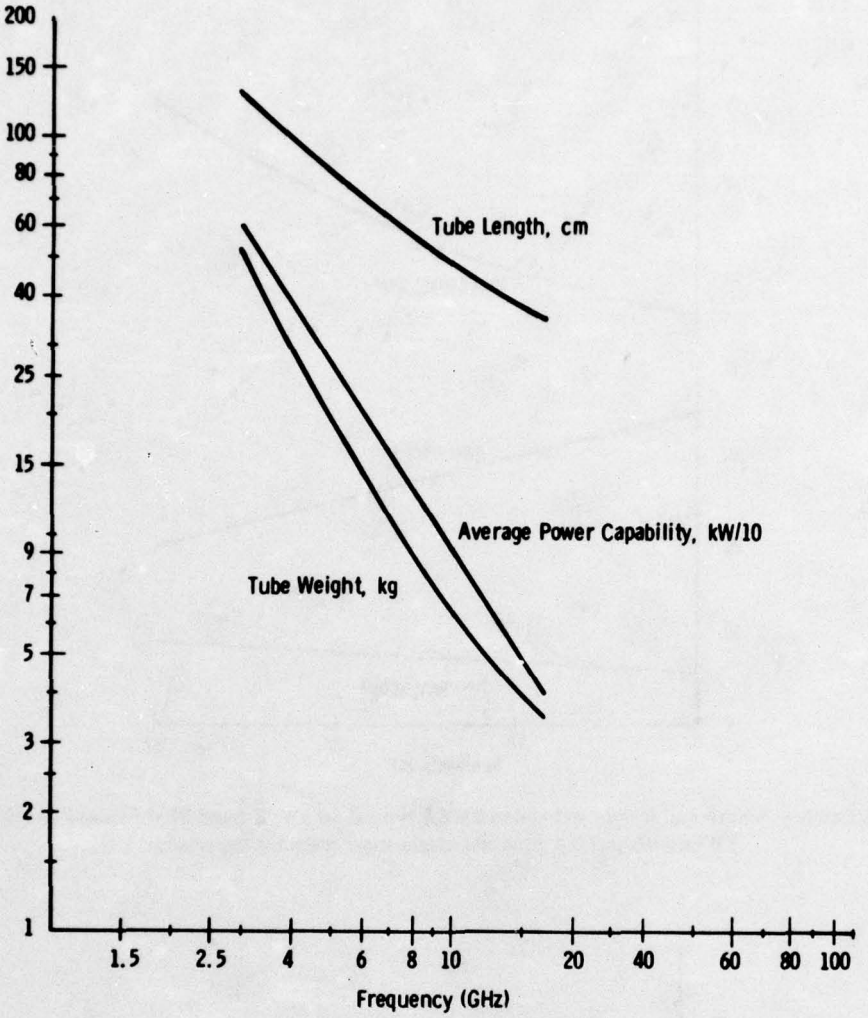

Fig.16 Approximate average power, length and weight vs frequency for typical PPM-focused, coupled cavity TWTs with gridded guns and single-stage collector depression

DISCUSSION

P BRADSELL: Does the 10 dB booster TWT have sufficiently low internal noise for it to be connected between the duplexer and antenna of a radar system so that it is transparent to the radar signals?

R BERRY: The booster noise will be within 10 dB of the thermal noise level when the booster tube is gated off.

E STERN: Do you have any data on reliability and life for the booster and TWT's?

R BERRY: We have no life data for the booster but it should be the same as any other linear beam tube. Most of the life data on coupled cavity TWT's is from operation in satellite communications ground stations where greater than 25,000 hours MTBF has been achieved. For airborne systems there are no results which exclude non-relevant failures.

Y BRAULT: In Fig 16 it seems to me that the upper frequency is limited to a value between 15 and 20 GHz. Is there a physical limitation?

R BERRY: No; until now these tubes have been designed for existing radar frequencies.

BROAD BAND MEGAWATT KLYSTRON AMPLIFIER

Utilising an overlapping-mode-extended interaction output section

D.Perring, G.Phillips and M.J.Smith
EMI-Varian Limited
Hayes, Middlesex
England.

SUMMARY

A description of theory, design and performance of an overlapping mode extended interaction output section for an S-band one megawatt pulsed klystron amplifier. The device is shown to have a broader bandwidth performance than the double tuned output version and a simpler construction than a hybrid tube. The theoretical design predictions are compared with the practical results.

1. INTRODUCTION

This paper describes the initial work on a high power klystron amplifier having an overlapping mode extended interaction output section.

A two cavity extended interaction resonator has two resonant modes, both of which provide impedance to the beam. It was first reported by Chodorow and Wessel-Berg (1961) and followed up by Preist and Leidigh (1963, 1964), Lien and Robinson (1965) and by Sun and Dalman (1968).

All these experimenters set the parameters of the output so that the beam interacted with just one of the resonant modes. The other resonant mode was tuned out of the band. Their argument was that the gain/bandwidth product of a klystron amplifier is determined basically by the ratio

$$\frac{\text{Characteristic impedance of cavity}}{\text{Characteristic impedance of beam}}$$

Now the characteristic impedance of a cavity is proportional to the ratio of its shunt resistance $\left(R_{sh}\right)$ to its quality factor (Q), where

$$\frac{R_{sh}}{Q} = \frac{(\text{r.f. gap voltage})^2}{\text{energy stored in cavity}}$$

Both the r.f. gap voltage and the energy stored in the cavity are proportional in turn to the number of cavities.

Hence $\frac{R_{sh}}{Q}$ is proportional to the number of cavities in the extended interaction section.

The experimenters showed that this increase in $\frac{R_{sh}}{Q}$ was not realisable in practice, although there was an improvement on a single gap cavity. The output tended to be unstable under typical operating conditions when the number of cavities exceeded three or four, and even with a two cavity output section the unused mode tended to be unstable.

The overlapping mode case was studied theoretically by Lien and Robinson (1967). They showed that when compared with the bandwidths of other types of resonators at a given maximum impedance level the two gap overlapping mode extended interaction resonator had a 1.0 dB bandwidth advantage of four to one over a conventional single gap cavity and approximately three to one over a two gap, single mode, extended interaction resonator. However, they did not produce a practical output.

It is believed that this is the first time that an output using both resonant modes overlapping has been used in a practical device.

The tube has a nominal operating voltage of 75 kV and a microperveance of 2.0. It has a high mu gridded gun with the following nominal grid characteristics: cut-off bias 1.0 kV, drive voltage 2.0 kV both relative to the cathode potential.

2. DESCRIPTION

Fig.1 shows a schematic diagram of an extended interaction output. It consists basically of two simple klystron cavities side by side, electrically coupled to each other by a slot cut in the adjoining wall and by the electron beam which passes through both cavity gaps. The power is coupled out of the second cavity to an output waveguide via an inductive iris.

The circuit has two modes of resonance; at one resonant frequency the voltages at the two cavity gaps are in phase - this is known as the zero or two pi-mode; at the lower resonant frequency the voltages at the gaps are in antiphase, this is known as the pi-mode. When the cavity parameters are

chosen so that the response of both modes overlap in the middle of the band, the output is known as an overlapping mode extended interaction output.

The output can be analysed by means of a straightforward, inductively coupled equivalent circuit. All the parameters of this circuit can be calculated from standard cold test measurements. The size of the slot in the adjoining wall determines, to the first order, the bandwidth of the response. The loading introduced by the output waveguide determines, to the first order, the flatness of the response. Unlike a double tuned output, the frequency response is not symmetrical if the two cavities are tuned to the same frequency. This is due to the additional coupling between cavities by the electron beam. At practical values of the pitch, which is the physical distance between the two cavity gaps, the phase change along the beam between the gaps favours the pi-mode. This means that the response is enhanced at the low frequency end of the band. The first cavity is tuned to a higher frequency than the second cavity to counteract this effect.

If the pitch is too large the output will, in theory, oscillate at the two pi-mode frequency. The stability of the output has been investigated in a number of ways, all of which agree.

The value of the beam loading conductance is a measure of the cavity's stability. If its value is negative and greater in amplitude than the conductance of the cavity with its load, the cavity will oscillate in a manner known as 'monotron oscillation'. Lien and Robinson (1965) derived an expression for the beam conductance in terms of the output pitch and various standard beam parameters, for the case where the voltages across the two gaps are of equal amplitude and either in perfect phase or anti-phase i.e.

$$V_2 = V_1 e^{j2\pi}$$

or

$$V_2 = V_1 e^{j\pi}$$

This assumption does not hold for the overlapping mode output, where the amplitudes and phases vary considerably across the band. The beam conductance can be shown to be given for the general case of

$$V_2 = R.\, V_1 e^{j\theta}$$

by

$$G_{el} = \frac{G_o}{8} \frac{\beta_e}{\beta_q} \left[M^2 \left(\beta_e - \beta_q \right) - M^2 \left(\beta_e + \beta_q \right) \right]$$

where the coupling coefficient, M(x), is given by

$$M(x) = M_g \cdot \frac{1}{2} \left[e^{-j(x)\frac{p}{2}} + R\, e^{j\theta}\ e^{j(x)\frac{p}{2}} \right]$$

where M_g is the single gap coupling coefficient

p is the output pitch

G_o is the beam conductance

β_e is the electron beam propagation constant

β_q is the reduced plasma propagation constant.

However, for an initial understanding of stability it is useful to plot the electronic conductance for a pure pi- and pure two pi- mode, as shown in Fig.2. This shows that for practical values of pitch, i.e. about 30 mm, any instability will occur around the two pi mode frequency. It also shows that an output will be maximally unstable with a pitch of about 37.5 mm, and maximally stable with a pitch of about 22.5 mm.

The above method is valuable for showing instability within the band, but it does not prove the absence of instability outside the band. To do this the output circuit was analysed using Nyquist's theorem which states that when the complex values of the open circuit gain of a system are plotted on real and imaginary axes, the system is stable if the locus of the points does not contain the point $1 + j0$.

The Nyquist plot for various values of pitch (Fig.3 a, b and c) shows that, outside the band, the gain falls off to such an extent that instability is very unlikely.

It can be seen that these plots agree very well with Fig.2. The shape of the plot is such that the output has the greatest probability of being unstable when the pitch is about 37.5 mm. The instability is in the two pi-mode. The pi-mode is obviously very stable. The greatest stability corresponds to a pitch of about 22.5 mm.

This approach has the advantage that it allows the effects of, say, reduction of beam voltage on stability to be visualised. As the beam voltage is reduced, the beam is slowed down, causing the phase difference between gaps to increase and the plot is rotated clockwise.

The bandwidth of any output circuit is limited by the circuit's ability to present adequate impedance to the electron beam over the band. The potential efficiency bandwidths of different output

circuits are, therefore, best compared by contrasting their impedance bandwidths.

Fig.4 shows a plot of the theoretical impedance bandwidths for a single resonant cavity, a double tuned output, and an extended interaction output. The plots show a bandwidth for an extended interaction output of about 12%, compared with 6% for a double tuned output, and 3% for a single cavity output.

The overall level of the impedance has to be chosen carefully in the same way the gap impedance in the output cavity needs to be set in a standard klystron. Too high an impedance will result in premature saturation due to the voltage across the output gap becoming large enough to stop and possibly reverse the flow of the electron beam. Too low an impedance will simply result in a low output power and saturation will occur due to lack of driving current as the drive current becomes of the same order as the beam current. In practice the output impedance should lie between 1.0 and 1.4 times the d.c. beam impedance. The impedance characteristic of an extended interaction output can be varied easily over a wide range of values, by simply adjusting output parameters such as, say, cavity frequency.

3. PRACTICAL RESULTS

The complete tube has two sections, a buncher section and an output section. To date, work has been concentrated mainly on the output section on the assumption that when the relationship between theory and practice has been established for the output section a matching buncher section can be designed. The saturated output power from a tube fitted with an extended interaction output section is shown in Fig.5. The peak output power is 1.4 MW (42% efficiency) and the bandwidth over which the output power is greater than 1.0 MW (30% efficiency) is 245 MHz (8.3%). The theoretical impedance shown is the equivalent impedance required by a single gap output to deliver the same output power.

The impedance at the top end of the band is too large causing premature saturation. In the middle of the band the impedance is slightly less than optimum; saturation is due to lack of drive current, while at the low end of the band the impedance is about optimum.

The saturated output power (Fig.6) was obtained using a broader band extended interaction output. The buncher section was unable to saturate the output below fo-85 MHz due to physical limitations but a prediction of the output power has been made by assuming it would be the same as shown in Fig.5 for equivalent values of the theoretical impedance. This output section has a bandwidth of 400 MHz (14%) over which the output power is greater than 0.75 MW (24% efficiency). Obviously the mid-band impedance is too low so the output power is very much drive current limited. If the perveance of the tube was increased from 2.0×10^{-6} $AV^{-1.5}$ to 2.5×10^{-6} $AV^{-1.5}$, the beam current would increase from 4lA to 5lA. The minimum output power would then increase by the square of the current difference from 0.75 MW (24% efficiency) to 1.16 MW (30% efficiency).

This potential (14%) bandwidth at greater than 30% efficiency, clearly, puts the overlapping mode extended interaction output klystron amplifier in the same league as the broadest band power travelling wave tubes produced.

4. CONCLUSION

This paper has shown that the overlapping mode extended interaction output section is a stable, practical output with efficiency and bandwidth capabilities comparable with any other type of output section. The construction is simple and its impedance characteristics can be easily tailored by simple adjustments to the output parameters.

5. ACKNOWLEDGEMENTS

The authors wish to thank the Directors of EMI-Varian Limited and the Ministry of Defence (Procurement Executive) for permission to publish this paper.

6. REFERENCES

Chodorow, M. and Wessel-Berg, T., (1961), 'A high-efficiency klystron with distributed interaction', IRE Trans., ED8. 44.

Lien, E. and Robinson, D., (1965)., 'Study and investigation leading to the design of broadband high power klystron amplifiers', Technical report ECOM-01362-1.

Lien, E. and Robinson, D., (1967), 'Study and investigation leading to the design of broadband high power klystron amplifiers', Technical report ECOM-02157-1.

Preist, D.H. and Leidigh, W.J., (1963), 'Experiments with high power CW klystrons using extended interaction catchers', IEEE Trans, ED10. 201.

Preist, D.H. and Leidigh, W.J., (1964), 'A two cavity extended interaction klystron yielding 65 per cent efficiency, IEEE Trans., ED11. 369.

Sun, C. and Dalman, G.C. (1968), 'Large signal behaviour of distributed klystrons, IEEE Trans. ED15, 60.

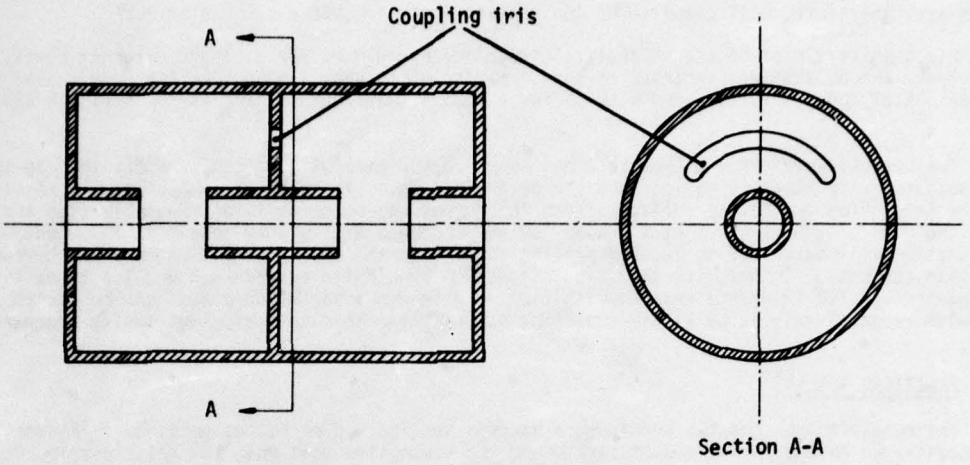

Fig.1 A double gap, output cavity

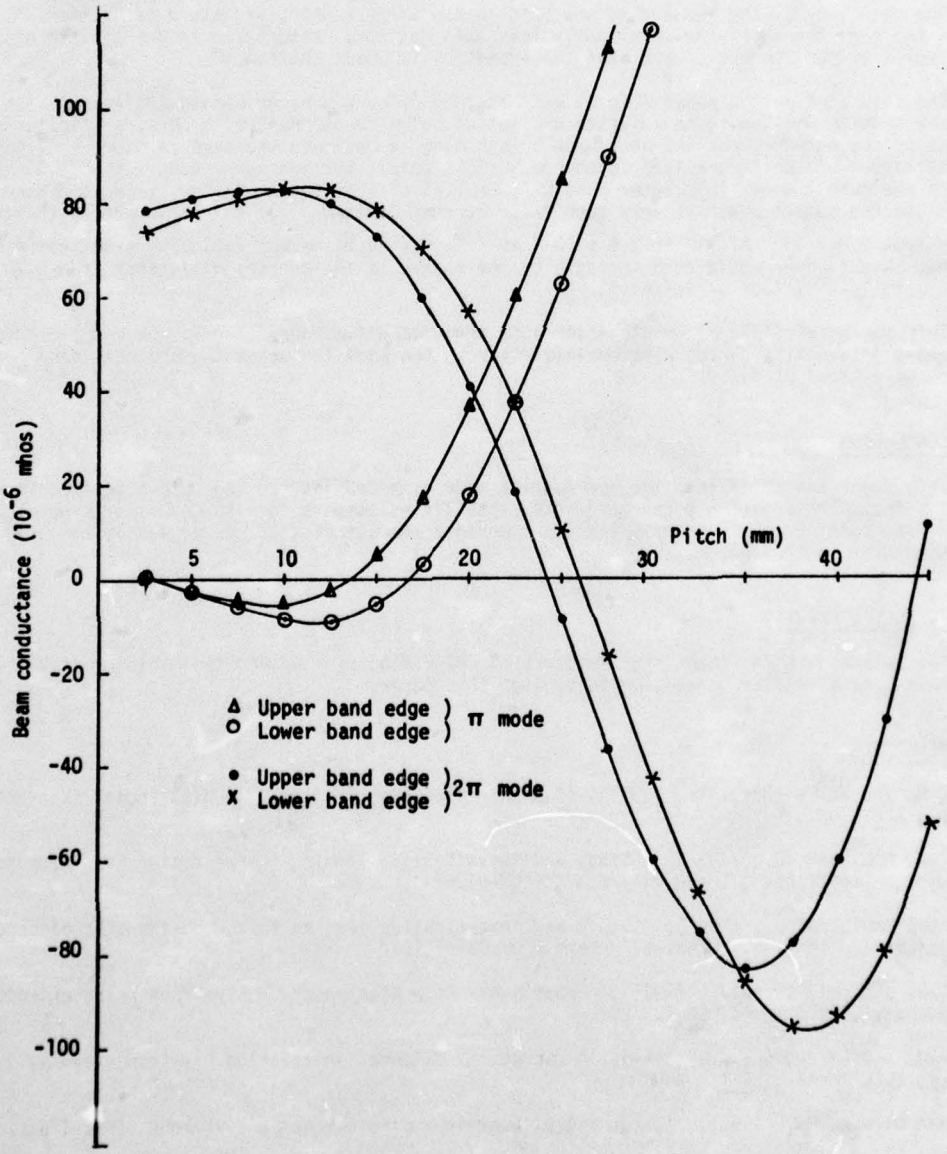

Fig.2 Beam conductance

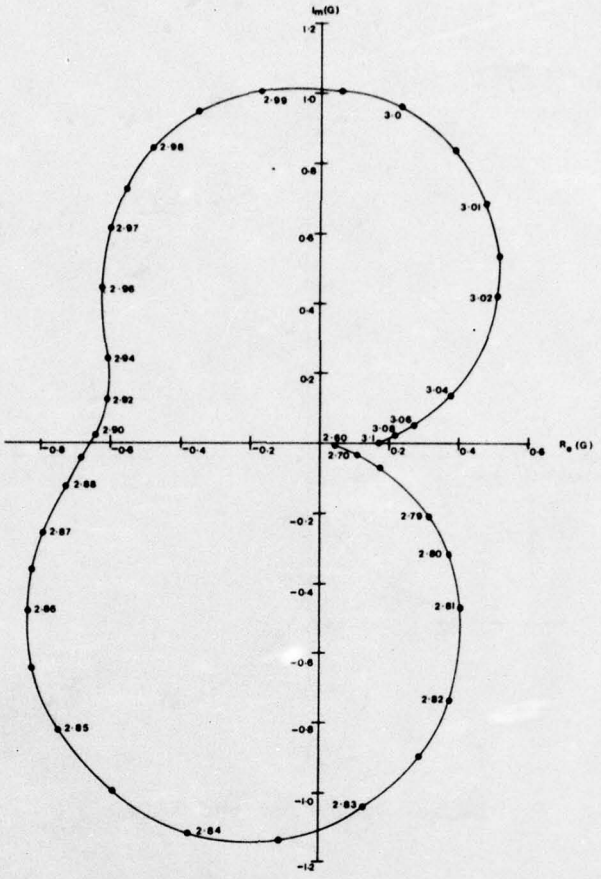

Fig.3(a) Nyquist plot: pitch 22.5 mm

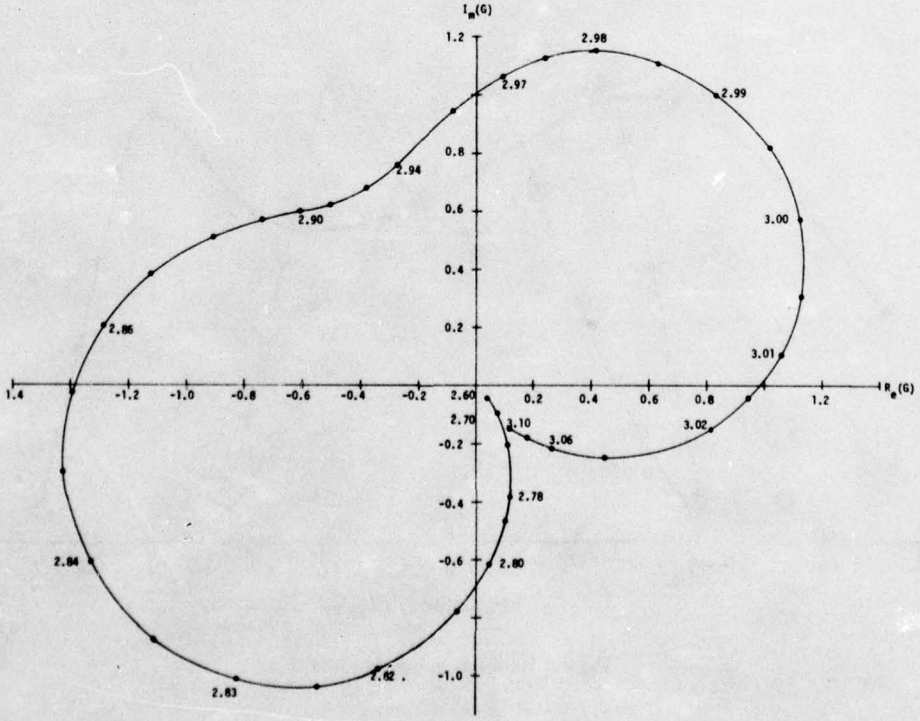

Fig.3(b) Nyquist plot: pitch 30.0 mm

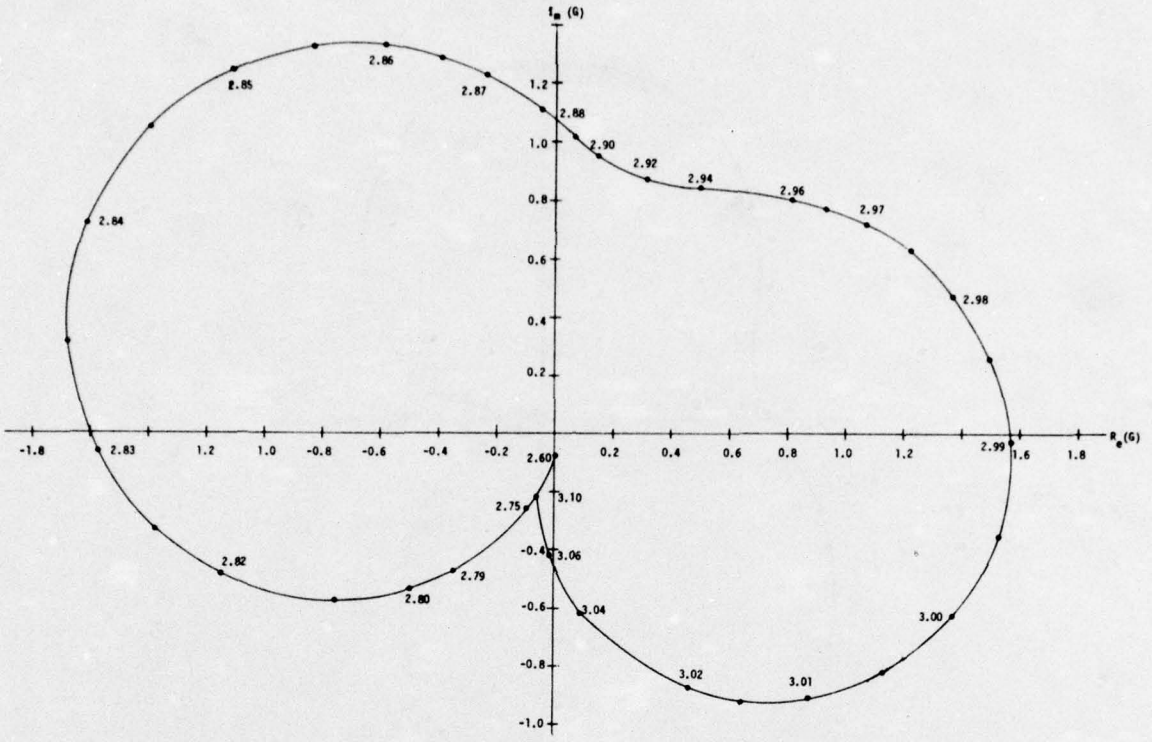

Fig.3(c) Nyquist plot: pitch 37.5 mm

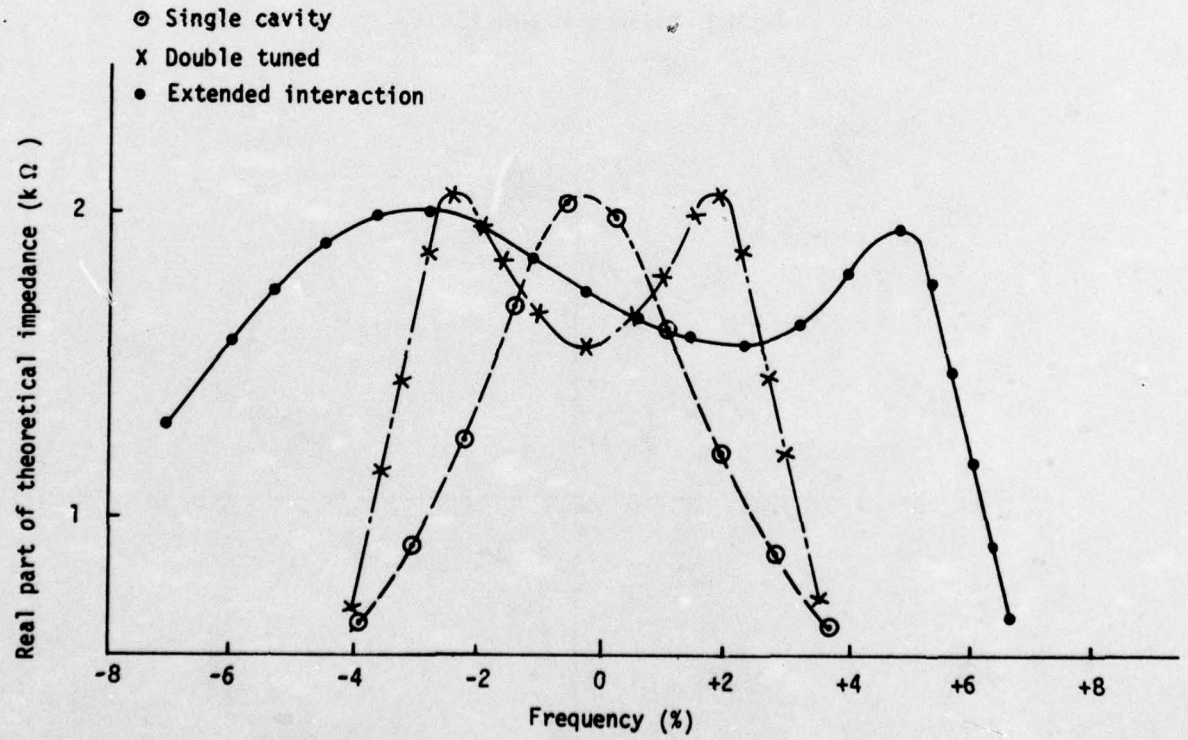

Fig.4 Impedance bandwidths

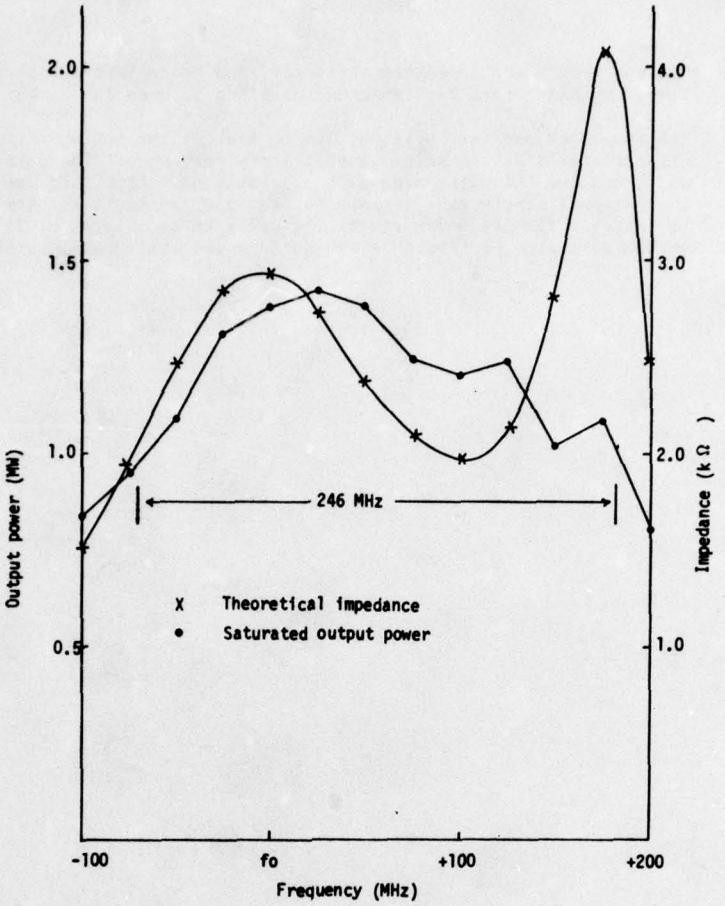

Fig.5 Saturated output power

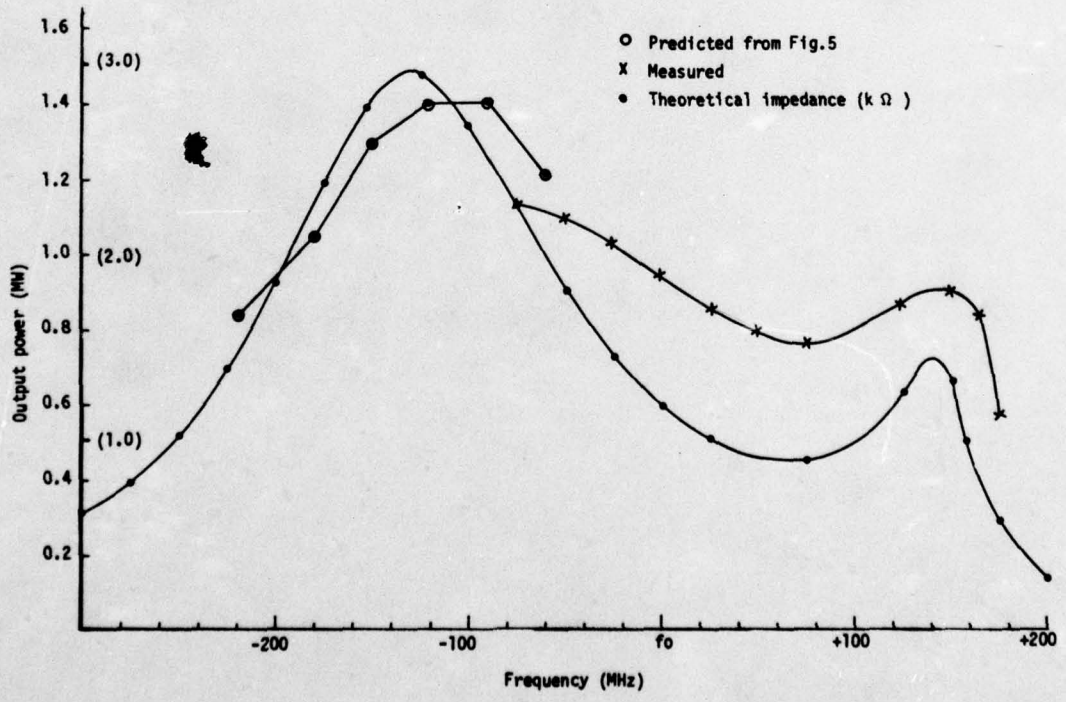

Fig.6 Saturated output power

DISCUSSION

A J DUNLOP: Can you reduce the impedance variation, and hence increase the broadband power level, by using more sophisticated coupling between the cavities?

M J SMITH: The impedance can vary by about 1.5 to 1 about the optimum (for maximum efficiency) without affecting the value of efficiency very much. The circuit described enables us to achieve this impedance over a greater bandwidth than can be obtained with conventional single gap circuits without sacrificing stability. It may be possible to increase the bandwidth further by using three coupled cavities but we have not yet investigated whether this can be done and still retain stability.

A HIGH POWER PIN DIODE PHASE SHIFTER IN X-BAND WAVEGUIDE

C.H. Hamilton
AEG-TELEFUNKEN
Elisabethenstraße 3
7900 Ulm
Germany

SUMMARY

A new type of polarization phase shifter is described which has been developed for a habour radar. It employs the inherent reactance of the PIN diode in a loaded-line type structure to produce the desired phase shift. Low impedance ridged waveguide and large volume diodes are used resulting in a design capable of considerably higher power handling capacity than has so far been reported for diode phase shifters in X-Band. At the same time the advantages of fast switching and low temperature sensitivity compared with presently available ferrite phase shifters have been retained.

Approximate design equations are given and the limitations of the circuit are discussed. In the experimental section measurements made on several phase shifters with power handling capacities of at least 70kW at 9GHz are presented. A bifurcation technique is described which may be used to raise this power level to at least 140kW, whilst calculations indicate that levels of up to 400kW are feasible.

1. INTRODUCTION

Recent investigations have shown that a two-frequency, two-polarization diversity radar can improve the signal-to-clutter ratio for seaborne targets by up to 3dB.[1] A diversity system of this type has been incorporated into a 9GHz coastal radar designed to control traffic on the Jade bay in northern Germany. In this radar the transmitter power is split into two channels and fed to an array of 220 radiators containing two orthogonal launchers. Horizontal, vertical or circular polarization may be selected by appropriately varying the phase relation between the two channels with an electronically controlled phase shifter. In order to prevent the phase shifter insertion loss from causing an amplitude imbalance, the 180^{o} shift required is produced by a combination of two variable 90^{o} bits and a fixed 90^{o} section, (see fig. 1). Since each channel transmits about 30kW, a ferrite phase shifter would normally be required; however, in order to avoid problems with temperature stability and switching speed associated with ferrite devices, a diode phase shifter was chosen. In this paper the problems encountered during the development of this device are discussed.

2. CIRCUIT DISCUSSION

2.1 Basic concept

Due to the high peak power requirement a waveguide circuit based on the loaded line model shown in fig. 2 was selected.[2] For a loss-free circuit the parameters R_o, Z_o and X are related to the mid-band phase shift 2ϕ by

$$X = R_o \cot(\phi)$$
$$Z_o = R_o \cos(\phi) \qquad (1)$$

At low frequencies the change between the two reactances $+jX$ and $-jX$ is produced by short- or open-circuiting an eighth wave long transmission line of impedance X with a PIN diode; however in X-Band the parasitic reactance of the diode is so low that this is no longer possible. In this work the change was produced by adding a series reactance jX_s to the PIN diode impedance in the "on" and "off" states where X_s is given by

$$X_s = -\frac{(X_{on} + X_{off})}{2} \qquad (2)$$

resulting in a switched impedance of

$$\pm j \frac{(X_{on} - X_{off})}{2} \qquad (3)$$

For large PIN diodes with breakdown voltages in the 1500V range, this impedance is of the order 18-50 ohms in X-Band; thus from equ.(1) a transmission line impedance R_o of the same level or lower is required to produce a phase shift of 90^o or less between the two states. These low levels are conviencently produced in waveguide using a ridged structure[4]. Initially a single 90^o bit was constructed, but because of problems with bandwidth and VSWR, the design was extended to 2, 3 and 4 bit versions.

2.2 PIN diode circuit

The equivalent circuit used for the PIN diode is shown in fig. 3a) where C_p is the package capacitance, L_p the package inductance and C_j the junction capacitance. R_j is the junction resistance and R_s the residual resistance in the two states $R_j \to 0$ and $R_j \to \infty$. The reactance variation in X-Band for a diode with the measured parameters C_j = 0.6pF, C_p = 0.23pF and L_p = 0.81nH is shown in fig. 3b). The diode parameters were established using an insertion loss method[3]. For a loss-free diode (i.e. $R_s \to 0$) the series impedance required to equalize the diode reactance is

$$X_s = -0.5 \left\{ \frac{\omega L_p}{(1-\omega^2 L_p C_p)} + \frac{\omega L_p - \frac{1}{\omega C_j}}{(1+\frac{C_p}{C_j} - \omega^2 L_p C_p)} \right\} \qquad (4)$$

resulting in a switched reactance of

$$X_d = \frac{\pm 1}{2\omega C_j (1-\omega^2 L_p C_p)(1+\frac{C_p}{C_j} - \omega^2 L_p C_p)} \qquad (5)$$

Here, as will be the case for most high power diodes in X-Band, X_s is negative, indicating a capacitative series reactance is required. This reactance may be introduced by a short transmission line as in fig. 4a) of impedance Z_o and electrical length θ^o where

$$X_s = Z_o \tan(\theta) \qquad (6)$$

Having found the value of X_d the main line impedance is then selected to obtain the desired phase shift using equ.(1). This approach has the advantage that the diodes are in direct thermal contact with a large heat sink, but it has the drawback that every bit must be the same size, as determined by the main line impedance. An alternative method of equalization is shown in fig. 4b) which is more versatile, but has the disadvantage that an additional thermal resistance is introduced between the diode and the ridge. If the diode impedance in the "on" and "off" states is jX_{on} and jX_{off} respectively, then the equalized impedance at the ridge will be

$$X_{in(on)} = -X_{in(off)} = Z_o \frac{(X_{on} + Z_o \tan(\theta))}{(Z_o - X_{on}\tan(\theta))} = -Z_o \frac{(X_{off} + Z_o \tan(\theta))}{(Z_o - X_{off}\tan(\theta))} \qquad (7)$$

Rearranging to express Z_o in terms of θ:

$$Z_o^2 + \frac{Z_o (X_{on} + X_{off})(1-\tan^2(\theta))}{2\tan(\theta)} - X_{on} X_{off} = 0 \qquad (8)$$

This equation may be used to determine the line parameters required for a particular switched impedance; taking the diode in fig. (3) as a specific example, the following table results:

θ^o	$Z_o(\Omega)$	$X_{in(on)}$, $X_{in(off)}$ $(j\Omega)$
10	6.33	53.32
15	9.79	55.53
20	13.66	58.96
25	18.13	64.05
30	23.46	71.49
35	30.00	83.39
40	38.17	98.50

As can be seen this form of equalization is well suited to producing the relatively high impedance levels required by small bits, and is thus complementary to the first method.

2.3 Insertion loss

The three main sources of insertion loss are line loss, reflection loss and diode loss. In general the diodes will contribute the major part of the loss if the waveguide transformers are well designed.

An expression for the mid-band insertion loss may be obtained in terms of the phase shift 2ϕ and the equalized Q factor (X_d/R'_s) where R'_s is the effective series resistance in the two bias states. For $R'^2_s << R_o$ the insertion loss of a single bit is given by

$$\alpha \approx 20 \log \left(1 + \frac{\tan(\phi)}{Q}\right) dB \qquad (9)$$

This result indicates that a cascade of small bits in a low loss line has a lower insertion loss than a single large bit. Since the power handling capacity may be increased by increasing the number of bits, this means the insertion loss is nominally independent of the power handling capacity.

2.4 Bandwidth

The bandwidth of a loaded line phase shifter for a given insertion loss or reflection coefficient is restricted by two factors; the deviation of the electrical separation of the diodes from the ideal $\lambda/4$, and the deviation of the shunt reactances from the centre frequency value. Other restrictions, such as the guide bandwidth, are unimportant by comparison. In most practical applications involving bandwidths of a few per cent the restriction caused by the line length variation is much smaller than that due to the shunting reactances; consequently the problem of increasing bandwidth resolves into one of minimizing this dependence. This in turn is a problem of choosing the best equalization method, since there is no way of reducing the variation of the diode reactance itself. The optimum method of equalization is with a lumped element, but in practice a transmission line equivalent must be used. For mechanical reasons a line $> \lambda/2$ is required, thus introducing an additional bandwidth restriction. The actual bandwidth available depends on the diodes and the size of the largest bit. For a single bit with a total phase shift under 45^o the centre line impedance can be made equal to the main line impedance R_o without a significant increase in the insertion loss. In this case the reflection loss is given in terms of R_o/X_d by

$$\alpha = 10 \log \left(1 + \frac{1}{4} \cdot \left(\frac{R_o}{X}\right)^4\right) dB \qquad (10)$$

Due to the 4th. power function, the loss increases rapidly as $X \rightarrow R_o$. For example, if the diode reactance in fig. 3b) is connected in series with a line 136^o long and of impedance 70 ohm and used in a 45^o bit, the following loss and phase shift results:-

f (GHz)	j(ohm)		dB		degrees
	X_{on}	X_{off}	α_{on}	α_{off}	$\Delta\phi^o$
8.8	28.9	-57.1	0.20	0.01	56
8.9	37.3	-51.9	0.07	0.01	49
9.0	45.7	-46.9	0.03	0.02	46
9.1	54.4	-42.0	0.01	0.04	44
9.2	62.2	-37.2	0.00	0.08	46

Note that the resistive loss is not included; this may be estimated from equ.(9), and will generally increase the above loss as the Q factor falls toward the band edges.

2.5 Power handling capacity

There are two separate limitations on the power handling capacity set by the average power and the peak power levels. In the first case the maximum average power P_o may be written in terms of the diode dissipation P_d as follows:

$$P_o = \frac{P_d Q}{\tan(\phi)} \qquad (11)$$

Where 2ϕ is the phase shift and Q the equalized diode Q factor at mid band. P_d is a diode parameter if a good heat sink is provided, and is about 10W for large PIN diodes. Thus a 22^o bit would be able to handle an average power of up to 1kW for a diode Q factor of 20.

Peak power handling is limited by the reverse bias junction breakdown voltage V_B for short pulse lengths. The input power P_o corresponding to a voltage V_B across the junction is given by

$$P_o \leq \left| V_B^2 \omega C_j \frac{(1-\omega^2 L_p C_p + \frac{C_p}{C_j})}{4\tan(\phi)\cdot(1-\omega^2 L_p C_p)} \right| \qquad (12)$$

As can be seen the package resonance $\omega^2 = \frac{1}{L_p C_p}$ has the effect of increasing the peak power handling. This effect was clearly observed during the experimental work, although it should be noted that it cannot be used to obtain an arbitary increase in power handling due to bandwidth problems and the risk of voltage breakdown inside the diode package[3].

3. PHYSICAL CONSTRUCTION

The construction of a single two diode bit is shown in fig. 5. It consists of a section of ridged waveguide matched to the main line by Tchebyschev transformers. A ridge-to-guide width ratio of s/a=0,85 was chosen since this results in a minimum impedance level for a given guide height. The dimensions of the ridge and transformers were calculated from published data on ridged waveguide[4]. Although this data is approximate in nature, it was found possible to construct transformers down to about 13 ohms with an insertion loss under 0.2dB and a VSWR less than 1.1:1 over a 12% band around 9GHz. The lower limit on the line impedance is set by the possibility of voltage breakdown between the ridge and the guide wall. Fig. (6) indicates the maximum power handling capacity for ridged guide in X-Band assuming air breakdown voltages of 3 and 1.5kV/mm and an s/a ratio of 0.85. This indicates that a power level of 60-100kW can be transmitted when allowing for a safety factor of 2 in the air breakdown. In the construction of fig. (5) the diodes are mounted directly in the ridge and the reactance equalized with a section of 70 ohm line electrically short circuited with a three section bias filter. Fig. (7) shows a photograph of an eight diode 90^o shifter. In this device the diode reactance was equalized with short mounting posts, and decoupled with filter sections as before. In both cases a 20 ohm guide was used and matched to the main line with a three section transformer. Matching screws mounted over the centre step allowed the VSWR to be reduced to better than 1.3:1 over the band 8.4-9.6GHz.

4. EXPERIMENTAL RESULTS

In this work 90° phase shifters were constructed to cover the band 8.8 - 9.2GHz with a peak power of 30kW and a mean power of 70W. Initially a single 90° bit was constructed with Unitrode UM7020 diodes and tested up to 50kW peak with a 0.2μs pulse at 1 kHz PRF. A reverse bias current of 5μA per diode was measured at this power level. This result compares well with the calculated power handling capacity of 54kW peak. The development of this device was not pursued as the useable bandwidth was too small, and additional phase shifters using 4, 6 and 8 diodes were constructed. Fig. 8 shows the insertion loss, phase shift and reflection coefficient for the six diode version.
The phase shifter shown in fig. 6 used 1600V Unitrode UM7016 diodes having $C_j \approx 1pF$, $L \approx 0.3nH$ and $C_R = 0$ (this latter value is a result of the bonded glass construction used by Unitrode). From the previous discussion a peak power handling capacity of about 160kW would be expected. A power test was carried out with a 0.2 μs pulse, 1kHz PRF generator up to 70kW without any measurable change in reflection coefficient or insertion loss. A similar 8 diode phase shifter was constructed in C-Band at 5.5GHz. In this case the power handling capacity was calculated to be about 99kW, (lower than X-Band due to the higher line impedance required to produce the same phase shift). Fig. 9 shows the variation of insertion loss as the power was increased. As can be seen there is evidence of limiting above 65kW, a rather lower level than calculated. This discrepancy is probably due to the diodes being more closely coupled in the "off" state than in the "on" state, since the equalization transformers were experimentally trimmed to give approximately equal insertion loss in the two states. Since the diode Q factor is highest in the "off" state, this will be used to produce a larger part of the total phase shift than the "on" state - thus reducing the peak power handling. For the same reason the power handling varies with frequency.

5. POWER HANDLING LIMITATIONS

As mentioned previously, the absolute power handling capacity is limited by the smallest bit size and by flash-over in the guide for a given diode. When this limit has been reached, a further 3dB increase may be obtained by bifurcating the guide and using two shifters, as shown in the diagram in fig. 10. Experimental measurements have shown that this system adds negligibly to the insertion loss.

6. CONCLUSIONS

A low loss waveguide phase shifter using standard high power PIN diodes has been described which is capable of handling peak powers of at least 70kW. By reducing the bit size below 22°, and using the bifurcation technique, a peak power handling level of about 400kW is at least theoretically possible.

References

[1] Speckter H.E; Nov. 1974 — "Meßtechnische Untersuchungen von Verfahren zur Verbesserung des Signal/Clutter-Abstandes bei Radarzielen im Seegang" DGON-Symposium, München

[2] White J.F; 1965 — "High power PIN controlled microwave transmission phase shifters" IEEE Trans. MTT-13, pp.233-242

[3] Hamilton C.H; 1975 — "An insertion loss method to determine PIN diode parameters" NTZ 28, H.8, pp. 284-286

...eers Technical and Buyers Guide, Dedham Massachusetts: ...ve Inc. 1968 pp. 35-38

[5] Hamilton C.H.; — "Forward Bias flash-over effects in high power PIN diodes" (to be published in NTZ, May 1976)

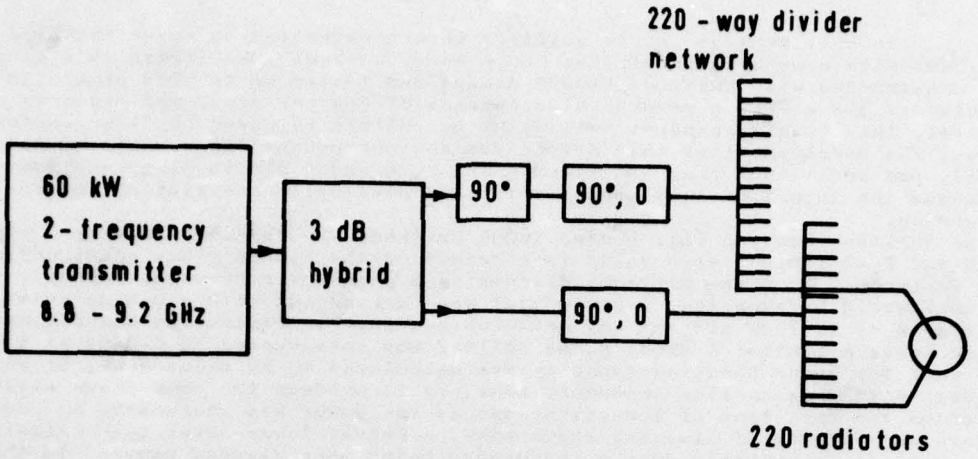

Polarization control circuit

fig. 1

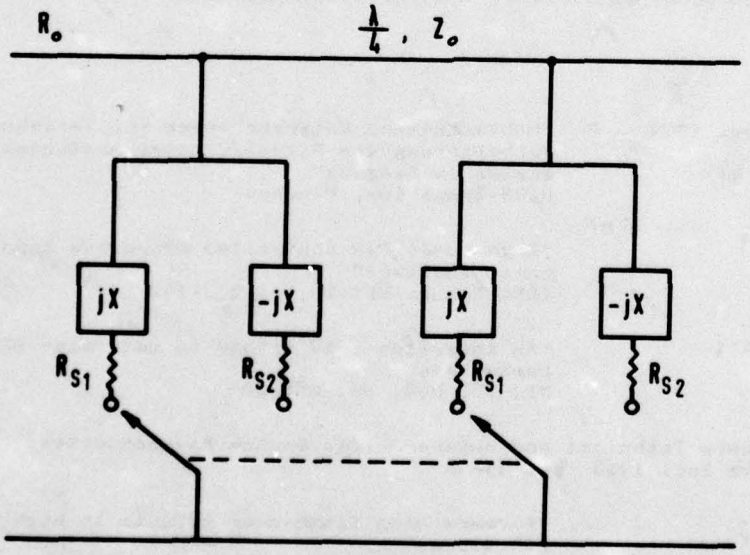

Loaded line prototype

fig. 2

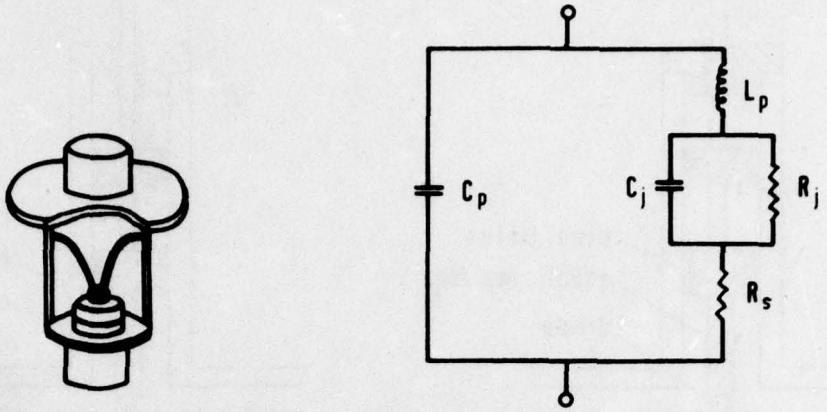

PIN Diode equivalent circuit

fig. 3a

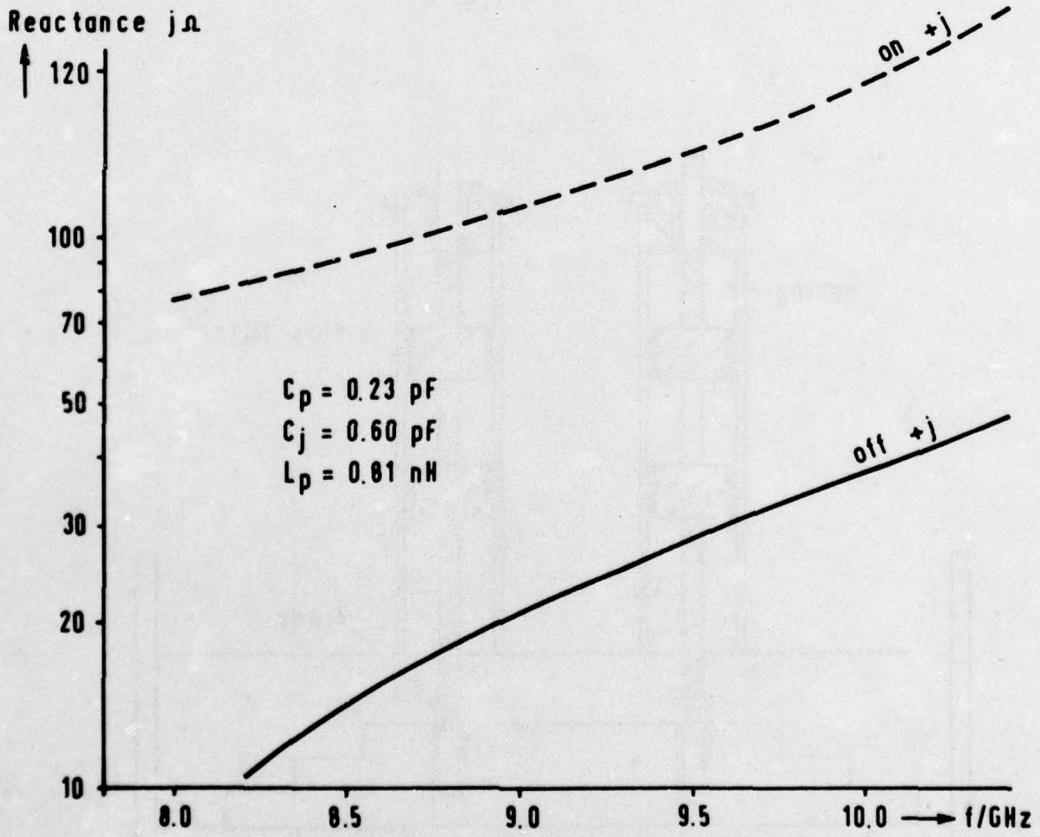

Reactance variation for CSF DH 499 - 02

fig. 3b

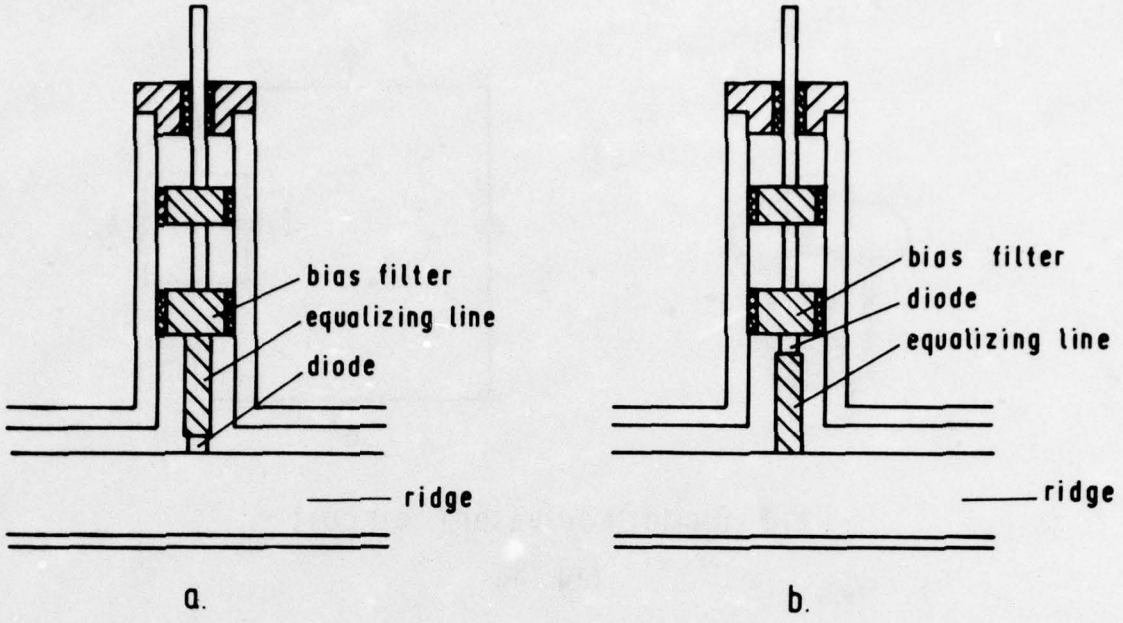

Diode reactance equalization

fig. 4

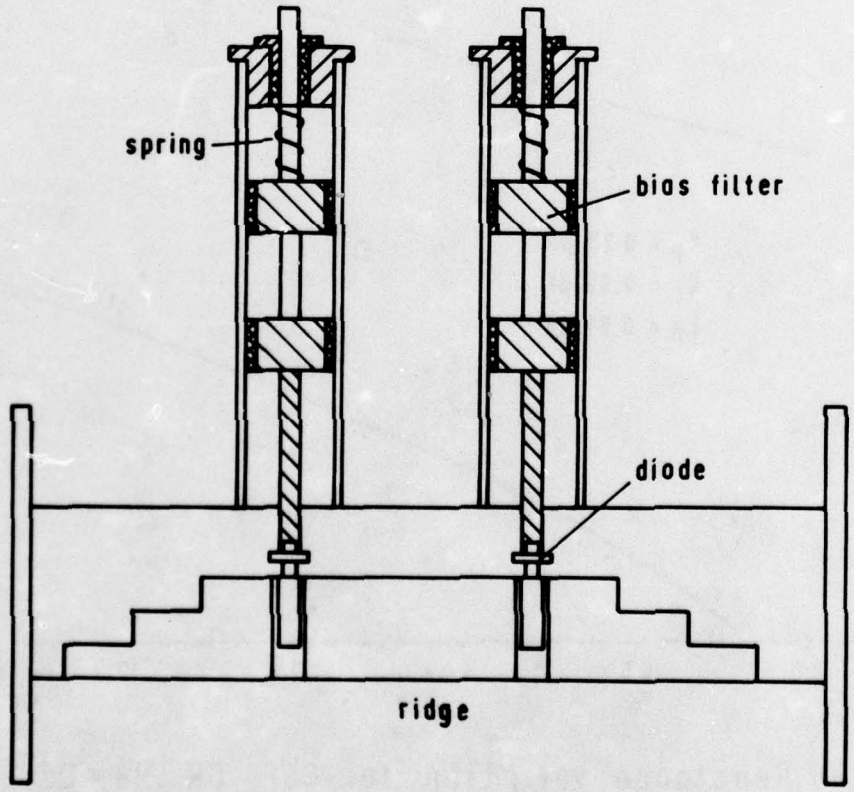

Construction of basic phase shifter bit

fig. 5

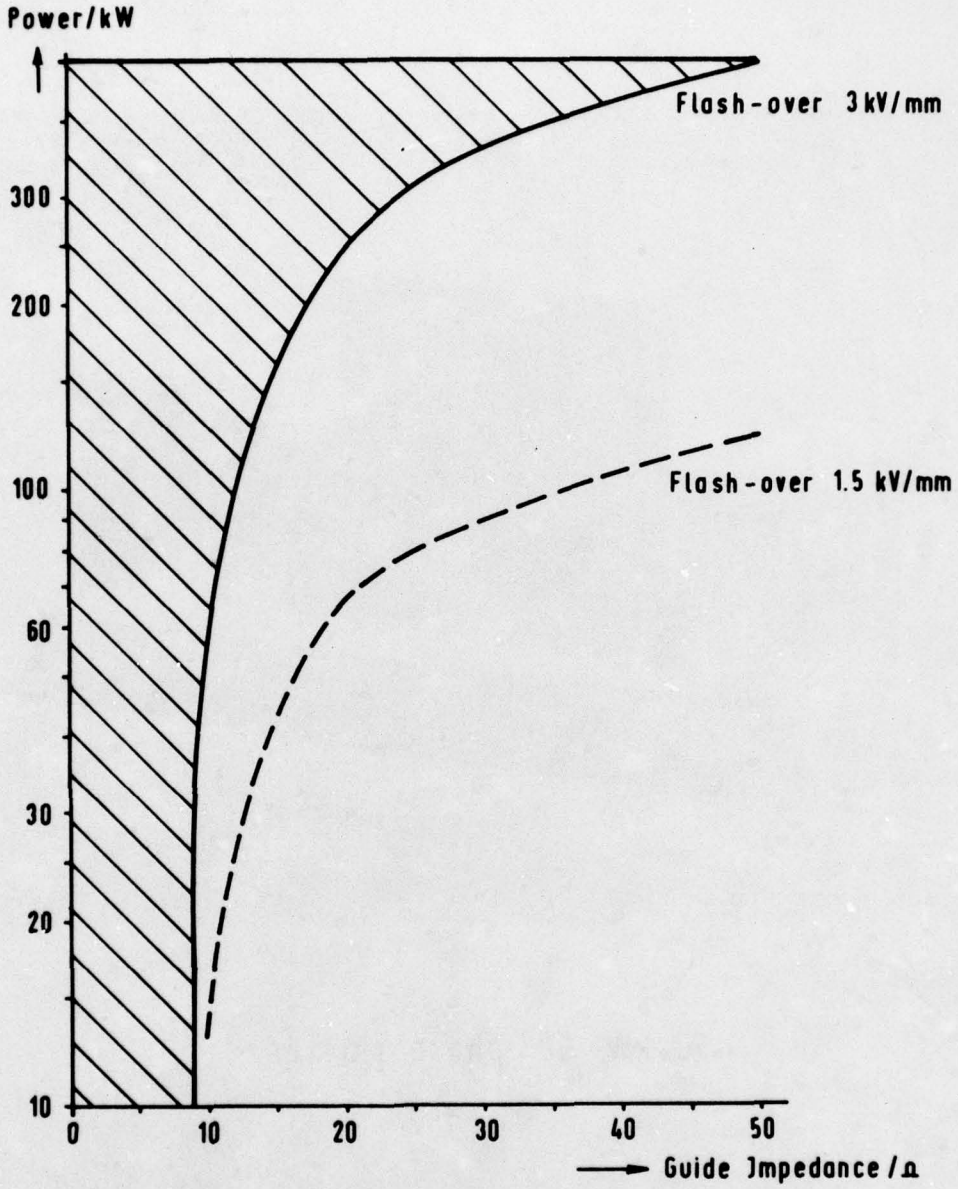

Flash-over limits in X-Band ridged waveguide
for $s/a = 0.85$

fig. 6

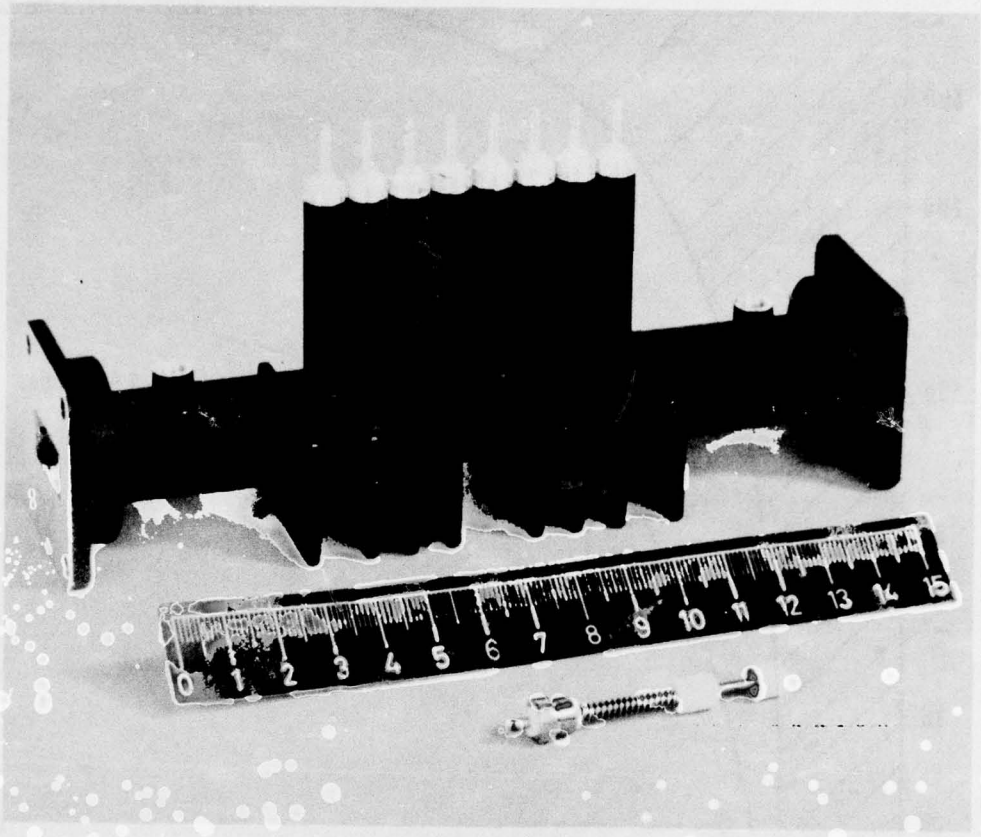

70 kW, 90° phase shifter

fig. 7

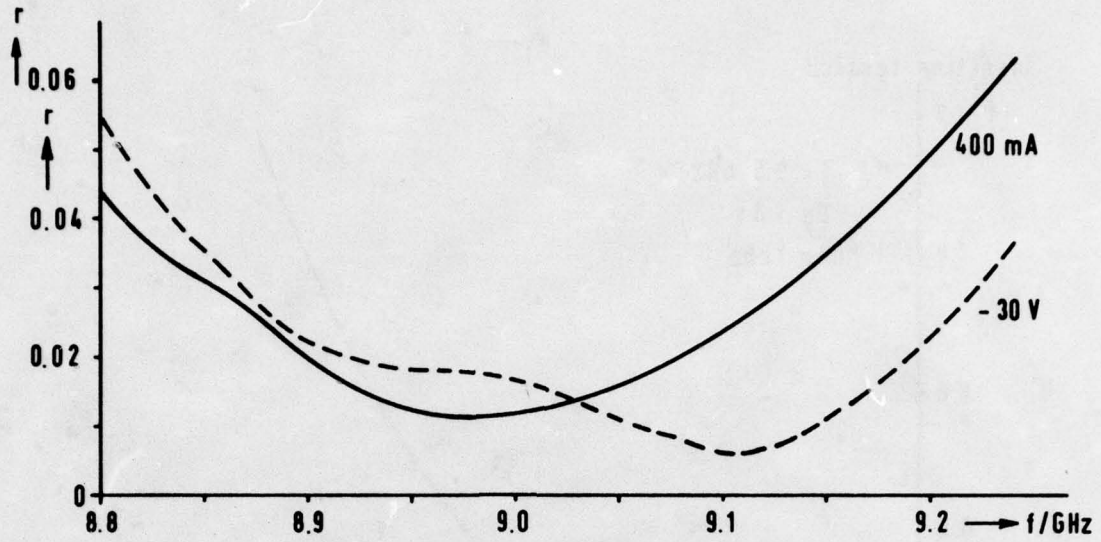

Reflection coefficient

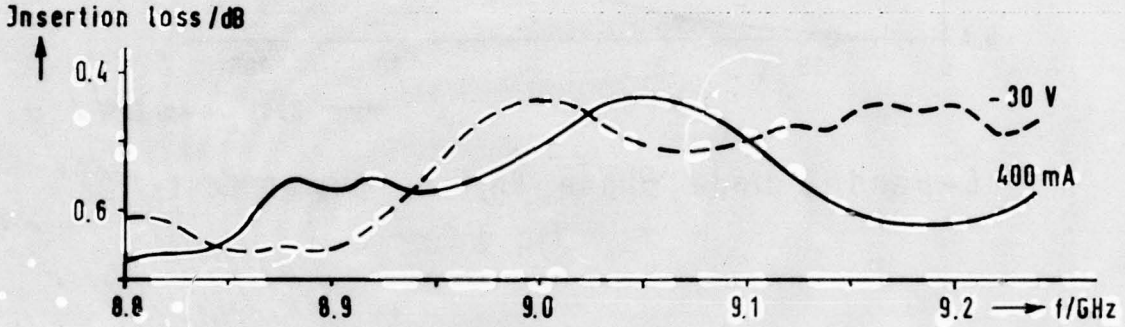

Insertion loss

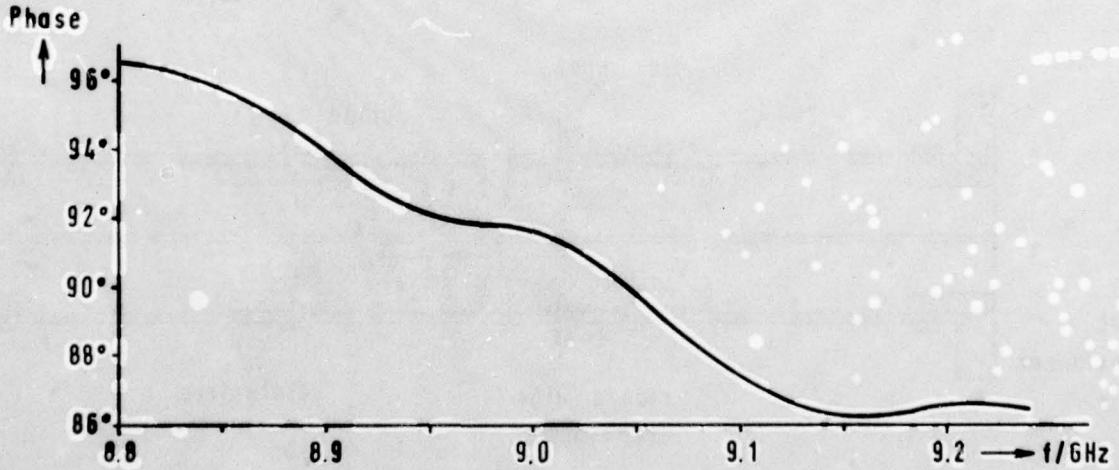

Phase shift

6 diode Phase shifter

fig. 8

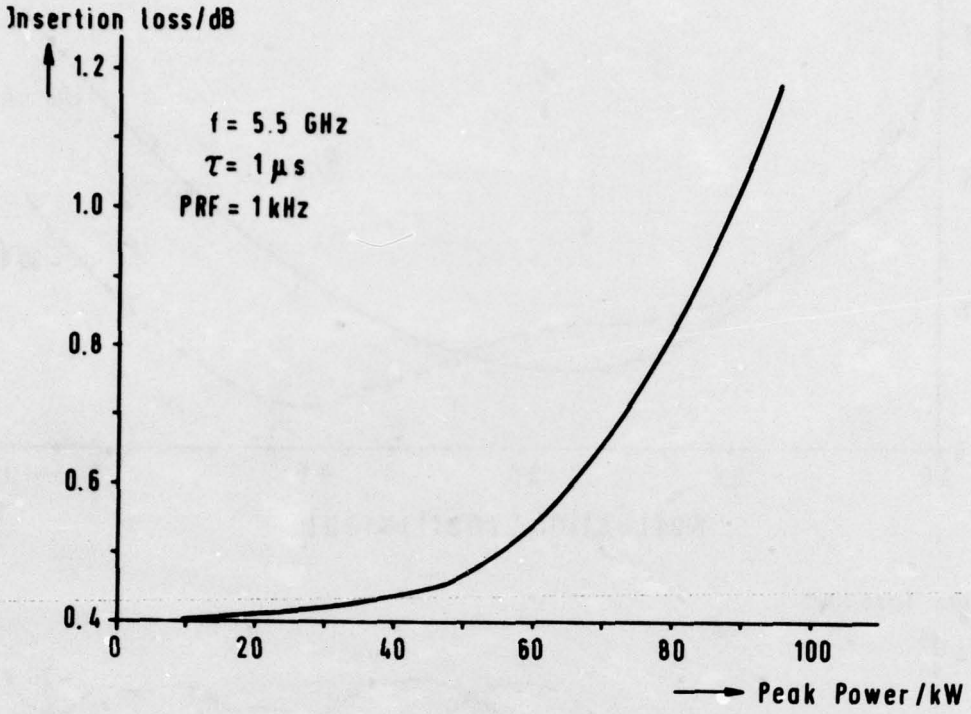

C-Band 8 diode phase shifter power test

fig. 9

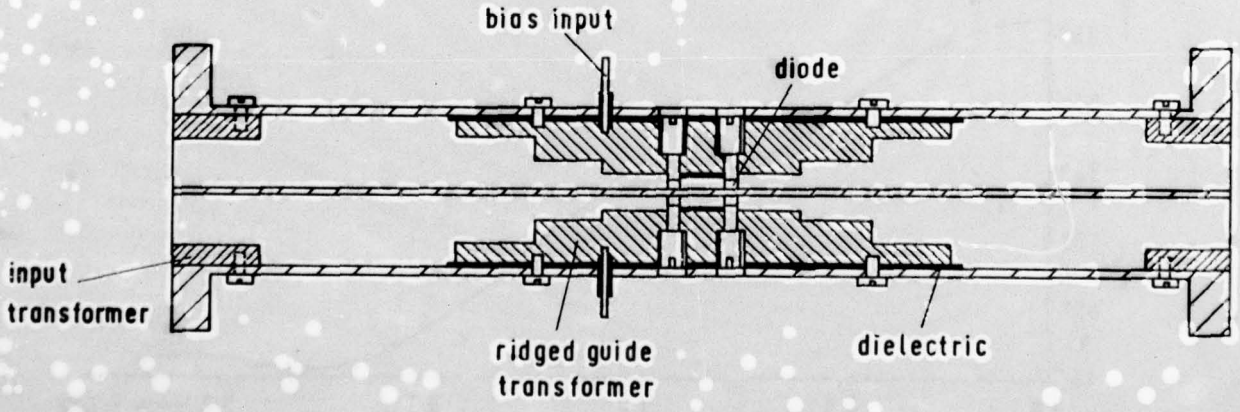

Bifurcation technique

fig. 10

DISCUSSION

Y BRAULT: In your conclusions you mention a future possibility of 400 KW peak power. What will be the associated bandwidth?

C HAMILTON: At that power 14% can be expected.

P BRADSELL: What is the switching time of this type of phase shifter?

C HAMILTON: Between 0.1 and 2 μS, depending on the diode carrier lifetime.

NOUVEAUX SOUS ENSEMBLES HYPERFREQUENCE EMISSION - RECEPTION POUR RADARS AUX ONDES MILLIMETRIQUES

B. CHIRON
J.R. MAHIEU
M. FACHE
S.A. LIGNES TELEGRAPHIQUES ET TELEPHONIQUES
Département Hyperfréquence
B.P. N° 5
78702 - CONFLANS SAINTE HONORINE
France

RESUME

Le développement des équipements aux longueurs d'onde millimétriques dépend en particulier de l'obtention de composants et dispositifs de caractéristiques satisfaisantes, de conception simple et reproductible, et corrélativement d'un coût raisonnable. L'objet de cet exposé est de décrire quelques nouveaux composants et dispositifs qui peuvent répondre aux critères généraux énoncés ci-dessus.

On montrera que les technologies microélectronique largement utilisées aux longueurs d'onde centimétriques et qui permettent la suppression des éléments de raccordements, la diminution des réglages, la réduction des encombrements et souvent des prix, dans le cas des grandes séries en particulier, et une meilleure reproductivité, sont largement extrapolables aux longueurs d'onde millimétriques.

Un nouveau résonateur, du type diélectrique, dont la stabilité en température est voisine de celle de l'Invar ($10^{-6}/°C$), sera présenté. De nouveaux composants non réciproques à ferrite, du type à jonction et mode "de bord", en onde millimétrique, dont les caractéristiques de largeur de bande sont très améliorées, seront décrits.

Dans le domaine des composants actifs, l'intérêt respectif des matériaux semiconducteurs de base dont le Si, l'AsGa et l'InP pour la réalisation de diodes en particulier sera discuté.

Des transposeurs de réception, d'émission, ainsi que des duplexeurs état solide originaux seront présentés. Ces sous-ensembles fonctionnels sont les éléments essentiels constitutifs des équipements millimétriques, dont les Radars.

I - INTRODUCTION

Depuis quelque temps, l'utilisation des ondes millimétriques a suscité un regain d'intérêt pour de nombreuses applications civiles et militaires. Dans ce dernier domaine, des études de radiomètre et de radar destinés à la surveillance des champs de bataille, à l'altimetrie, à l'anti-collision aérienne, au guidage terminal des avions et missiles Air-Sol, à la poursuite d'hélicoptère par la mesure de l'effet doppler des pales, etc..., sont effectuées dans de nombreux laboratoires.

Cependant, ces nouveaux équipements en ondes millimétriques ne pourront vraiment se développer que si, non seulement leur faisabilité d'emploi est démontrée, mais à condition également que leur coût soit raisonnable, et que le travail restant à effectuer concernant les composants en général, et la simplification technique de ceux-ci en particulier, soit poursuivi.

Le but de l'exposé est de décrire quelques nouveaux dispositifs ou sous-ensembles susceptibles d'être employés dans des futurs systèmes en ondes millimétriques.

II - CONSTITUTION GENERALE DES SOUS ENSEMBLES

Quels que soient les systèmes, et par suite, les types d'équipement à réaliser, ceux-ci sont obligatoirement constitués par des sous-ensembles fonctionnels (émission, réception, duplexage, etc...) comprenant eux-mêmes des composants dont l'association entre eux sous forme de dispositifs dépend de l'application envisagée et des caractéristiques générales recherchées.

La mise au point d'un sous-ensemble portera donc à la fois sur une étude particulière de composants élémentaires et complexes, et sur la mise en oeuvre de ceux-ci.

La figure 1 montre dans le cas général de sous-ensembles réception, émission et duplexage en ondes millimétriques, les divers points techniques qui seront examinés ci-après.

III - COMPOSANTS ELEMENTAIRES EN ONDES MILLIMETRIQUES

3.1.- Lignes microbandes en ondes millimétriques

Dans le but de réduire au maximum les dimensions, de supprimer les raccordements par bride et fiche, de diminuer les coûts, la faisabilité de réaliser plusieurs circuits en ondes millimétriques sur un même substrat microélectronique a été recherchée. Dans certains cas également, la possibilité d'associer des substrats céramiques et des substrats gyromagnétiques a été démontrée.

La figure 2 donne les types de substrats choisis et succinctement la technologie de réalisation employée.

La figure 3 donne les dimensions et caractéristiques essentielles des lignes microbande que nous utilisons, ainsi que celles des transitions de guide rectangulaire TE_{01} à ligne microbande quasi TEM.

3.2.- Résonateurs diélectriques

Les précisions mécaniques requises pour les structures de filtres en guide d'onde rectangulaire ou circulaire ainsi que les difficultés de mise au point et de réglage nous ont incités à rechercher une solution plus simple, utilisable en technologie microélectronique, et corrélativement moins encombrante.

Ce nouveau composant de base du type résonnant, qui a été étudié, est fondé sur l'emploi de matériaux diélectriques dont le volume, la permittivité et la tangente de pertes diélectriques déterminent les caractéristiques électriques essentielles du résonateur. Ce type de résonateur est maintenant connu, mais son emploi aux longueurs d'onde millimétriques d'une part, avec une stabilité en température satisfaisante d'autre part, n'avait pas encore été envisagé.

Les résonateurs que nous décrivons sont constitués par une association coaxiale ou superposée de plusieurs matériaux diélectriques (en général deux) dont les coefficients de température sont de signe opposé.

La figure 4 donne les caractéristiques électriques aux ondes millimétriques de quelques matériaux diélectriques qui ont été particulièrement étudiés à L.T.T. pour leur emploi dans des résonateurs (les valeurs des caractéristiques du TiO_2 sont données à titre de comparaison).

La figure 5 donne un exemple de réalisation de deux résonateurs vers 40 GHz et de leur montage sur un substrat microélectronique. On voit que les variations de la fréquence de résonance en fonction de la température sont inférieures à 2 ppm. Une réalisation plus récente utilisant les matériaux L.T.T. 6721 et 9101 a permis d'obtenir une variation de la fréquence en fonction de la température très voisine et même inférieure à la variation de fréquence correspondante des cavités résonnantes en matériau Invar.

3.3.- Circulateurs et isolateurs

Ces dispositifs non réciproques sont désormais devenus indispensables dans tous les équipements hyperfréquence. Dans le domaine des ondes millimétriques, nos principales préoccupations concernaient l'élargissement de la bande passante des circulateurs en technologie guide d'onde rectangulaire et la faisabilité de réaliser des circulateurs à jonction en technologie microélectronique, ainsi que des isolateurs et circulateurs à mode "de bord".

3.3.1.- Circulateurs à guide d'onde rectangulaire à large bande

L'étude de l'élargissement de la bande passante des circulateurs à guide d'onde rectangulaire a porté essentiellement sur un choix dimensionnel et reproductible de la structure. L'emploi de matériaux gyromagnétiques sélectionnés préalablement du point de vue des caractéristiques statiques et hyperfréquence (4 πMs, ε, u , tg δ, ΔH), ainsi que les précautions prises au montage des divers éléments constitutifs des circulateurs, ont permis en particulier de réaliser des circulateurs à hautes performances sans aucun réglage ni ajustement extérieur après montage.

Les caractéristiques électriques d'un circulateur qui vient d'être industrialisé à L.T.T. sont données ci-dessous à titre d'exemple :

Bande passante	:	34,5 à 45,5 GHz (bande passante = 11 GHz)
Affaiblissement d'insertion par porte	:	< 0,5 dB

Découplage entre portes adjacentes	:	> 20 dB
Taux d'ondes stationnaires	:	< 1,20
Gamme de température	:	- 40 à + 70°C
Dimensions hors tout	:	36 x 36 x 40 mm

Ces circulateurs ne comportant pas de réglage externe par vis ou transformateur par exemple, se prêtent particulièrement bien à une intégration, comme il est montré sur la photo de la figure 6.

3.3.2.- Circulateurs à jonction en technologie microélectronique

Dans ces circulateurs, les transformateurs d'adaptation de la jonction proprement dite sont réalisés directement sur le substrat ferrite. Les caractéristiques du dispositif réalisé sont relativement modestes, comparativement aux circulateurs en technologie guide d'onde.

Il a cependant été possible d'obtenir des affaiblissements inférieurs à 1 dB pour un découplage supérieur à 20 dB dans une bande passante de 32 à 40 GHz.

La dimension hors fiches et hors aimant du circulateur est par contre particulièrement faible : 0,2 x 5 x 5 mm.

3.3.3.- Isolateurs et circulateurs à modes "de bord"

L'emploi des ondes électromagnétiques "de bord" (edge mode) a probablement été une des plus grandes découvertes de ces dernières années dans le domaine des dispositifs non réciproques gyromagnétiques. La Société L.T.T. qui a pris une grande part dans ces recherches, a pu développer jusqu'à des fréquences de l'ordre de 18 GHz des isolateurs couvrant une bande passante atteignant 2,5 octaves et même plus.

Il nous a donc semblé particulièrement intéressant d'étudier la faisabilité de ces nouveaux composants aux longueurs d'onde millimétriques. La figure 7 montre à la fois la structure simplifiée d'un isolateur réalisé et les caractéristiques obtenues à ce jour. Les résultats qui sont présentés proviennent d'études très récentes et seront certainement très améliorées d'ici peu.

La photo de la figure 8 montre un exemple de circulateur multi-portes (8) à modes "de bord" réalisé à la fréquence de 35 GHz; ce dispositif est en cours d'étude. La largeur de bande à 1 dB de perte d'insertion, qui est de l'ordre de 300 MHz, est encore trop faible, mais ce circulateur s'avère dès maintenant, par sa simplicité et probablement son prix, d'un très grand intérêt, par exemple, en association avec des filtres, pour la réalisation de dispositifs multiplexage et démultiplexage de canaux séparés de transmission.

3.3.4.- Isolateurs et circulateurs miniatures à paramètres localisés

La figure 9 montre un circulateur de très faible encombrement dont la jonction est réalisée par des paramètres localisés, self - capacité. Les progrès enregistrés dans la technologie microélectronique hybride ont permis de réaliser des circulateurs et isolateurs fonctionnant dans diverses bandes de fréquences comprises entre 10 et 2000 MHz. Ces nouveaux composants sont facilement intégrables, et leur utilisation est actuellement prévue en grande quantité dans les divers sous-ensembles à fréquence intermédiaire.

3.4.- Composants actifs

Les composants actifs utilisés dans les équipements en ondes millimétriques ne diffèrent pas sensiblement de ceux employés à de plus grandes longueurs d'ondes. Les diodes Schottky, PIN, Impatt, Gunn, Varactor paramétriques par exemple, sont un élément essentiel de nombreux dispositifs. Nous n'examinerons donc rapidement dans le tableau de la figure 10 que quelques points techniques particuliers et orientations nouvelles relatifs à ces composants actifs.

3.5.- Mélangeur de réception

Les dispositifs qui ont été étudiés à L.T.T. permettent la transposition du signal en onde millimétrique en un signal à fréquence intermédiaire qui peut être aussi élevée que 5 GHz. Dans le cas d'une fréquence intermédiaire supérieure à 1 GHz, la préamplification à cette fréquence était soit du type transistor bipolaire ou FET, soit du type paramétrique.

Les mélangeurs du type symétrique et dissymétrique sont réalisés en technologie microélectronique. L'élimination de la fréquence image dans des mélangeurs a pu être effectuée d'une manière simple et efficace en utilisant des résonateurs diélectriques identiques à ceux décrits plus avant, et placés au voisinage de la diode Schottky mélangeuse. La figure 11 montre les caractéristiques d'un mélangeur réalisé à la fréquence de 43,6 GHz. On voit qu'une réjection de la fréquence image supérieure à 30 dB a entraîné une diminution de la perte de conversion de 1,3 dB.

La photo de la figure 12 montre le mélangeur de réception correspondant avec le résonateur diélectrique incorporé.

L'oscillateur local nécessaire utilise une diode Gunn montée en guide rectangulaire capable de délivrer une puissance de 20 mW. Le système de stabilisation entièrement passif basé sur l'utilisation de matériaux à coefficient de dilatation approprié en fonction de la température permet d'atteindre une stabilité de l'ordre de 10^{-6}/°C dans une gamme de température de - 40 à + 70°C.

3.6.- Mélangeur d'émission

Dans certaines applications, le traitement ou la régénération du signal à fréquence intermédiaire à la sortie du mélangeur de réception est indispensable. Cette opération effectuée, il est nécessaire de transposer à nouveau le signal à fréquence intermédiaire en un signal aux longueurs d'onde millimétriques. Les mélangeurs d'émission utilisés à cet effet à L.T.T. sont constitués par une association de circulateurs, filtre, et monture à varactor, comme il est montré sur la figure 13. Un tel montage améliore notablement les caractéristiques des mélangeurs d'émission classiques du point de vue de la bande passante et de la conversion amplitude/phase; cependant, leur perte de conversion est légèrement plus élevée. Une solution intermédiaire utilisant à nouveau un résonateur diélectrique, suppresseur de bandes latérales inférieures, à proximité du varactor, a permis de diminuer la perte de conversion d'environ 1 dB dans une partie réduite de la bande passante, comme il est aussi montré sur la figure 13.

3.7.- Amplificateurs état solide

Ces sous-ensembles sont appelés à de grandes utilisations dans les systèmes radar pour augmenter à l'émission par exemple la puissance de sortie d'un oscillateur état solide bas niveau, mais présentant une grande stabilité en fonction de la fréquence. Leur emploi est également prévu en association avec les mélangeurs d'émission décrits précédemment; dans cette dernière application, on recherche le meilleur compromis entre la puissance délivrée, la puissance dissipée, le prix et surtout dans le domaine des ondes millimétriques qui nous intéressent, la fiabilité.

Les réalisations que nous avons effectuées ont visé essentiellement l'élargissement de la bande passante lié à une grande stabilité. Les circulateurs à très grande largeur de bande décrits plus avant ont été d'une aide précieuse dans ce travail.

Un amplificateur à un seul étage centré autour de 40 GHz a été réalisé et présente dans une bande passante de 3 GHz un gain de 6 - 0,5 dB pour un niveau de sortie de 100 mW à 1 dB de compression.

3.8.- Duplexeurs

Ces dispositifs permettent dans un radar de séparer le signal émis du signal reçu. Nous avons développé à cet effet un duplexeur gyromagnétique basé sur l'utilisation du déphasage non réciproque dans les ferrites. Un tel dispositif est constitué par une association en cascade d'une jonction hybride 3 dB, d'une cellule de déphasage non réciproque et d'un coupleur 3 dB.

Un duplexeur de ce type a été réalisé à 35 GHz, il est capable de fonctionner à une puissance crête de 70 kW, une puissance moyenne de 50 W, pour un affaiblissement d'insertion inférieur à 0,5 dB et un découplage supérieur à 25 dB dans une largeur de bande de 200 MHz.

Un deuxième duplexeur fonctionnant à 70 GHz capable de supporter une puissance crête de 10 kW et une puissance moyenne de 10 W a été aussi réalisé. Il présente une perte d'insertion de 0,5 dB pour un découplage minimum de 28 dB dans une bande passante de 500 MHz.

Le découplage de ces duplexeurs entre les portes émetteur et récepteur de 25 dB minimum est insuffisant, et il est nécessaire de protéger le récepteur, et, par exemple, les diodes Schottky mélangeuses, par un dispositif du type limiteur.

Un premier dispositif semi-passif semi- actif constitué par un limiteur gyromagnétique à ferrite associé avec un limiteur de "pic" à varactor est en cours d'étude. Un deuxième limiteur, entièrement passif, utilisant un échantillon de silicium en volume dopé à l'antimoine, placé dans un guide d'onde rectangulaire, a également fait l'objet dans nos laboratoires d'importants travaux, particulièrement en bande X. Le principe de fonctionnement de ce limiteur est basé sur la décroissance de la conductivité et de la mobilité des porteurs quand le champ hyperfréquence augmente.

La figure 14 montre une courbe de limitation d'un tel limiteur en bande X, l'affaiblissement du dispositif est inférieur à 1 dB pour des puissances incidentes ne dépassant pas 0,3 kW crête; cet affaiblissement atteint 12 dB pour une puissance de 10 kW crête. L'effet de limitation de ce nouveau dispositif est à la fois absorbant et réfléchissant, et il semble d'après les nouveaux résultats obtenus dans nos laboratoires particulièrement attractif au-dessus de 30 GHz.

IV - CONCLUSION

Il a pu être montré dans cet exposé qu'il était possible de réaliser dans le domaine des ondes millimétriques des composants et dispositifs dont les caractéristiques électriques sont dans l'ensemble au moins égales à celles de leurs homologues utilisées aux longueurs d'ondes centimétriques. On a pu vérifier par ailleurs que la technologie microélectronique était applicable aux ondes millimétriques sans précautions particulières. De même, la possibilité de réaliser des composants simples, performants et bon marché, a été démontrée.

Ainsi, bien que l'ensemble des problèmes liés aux sous-ensembles hyperfréquence millimétriques n'ait pu être traité d'une manière exhaustive, les résultats présentés devraient contribuer à vaincre les hésitations que l'on rencontre encore chez certains utilisateurs potentiels des équipements en ondes millimétriques.

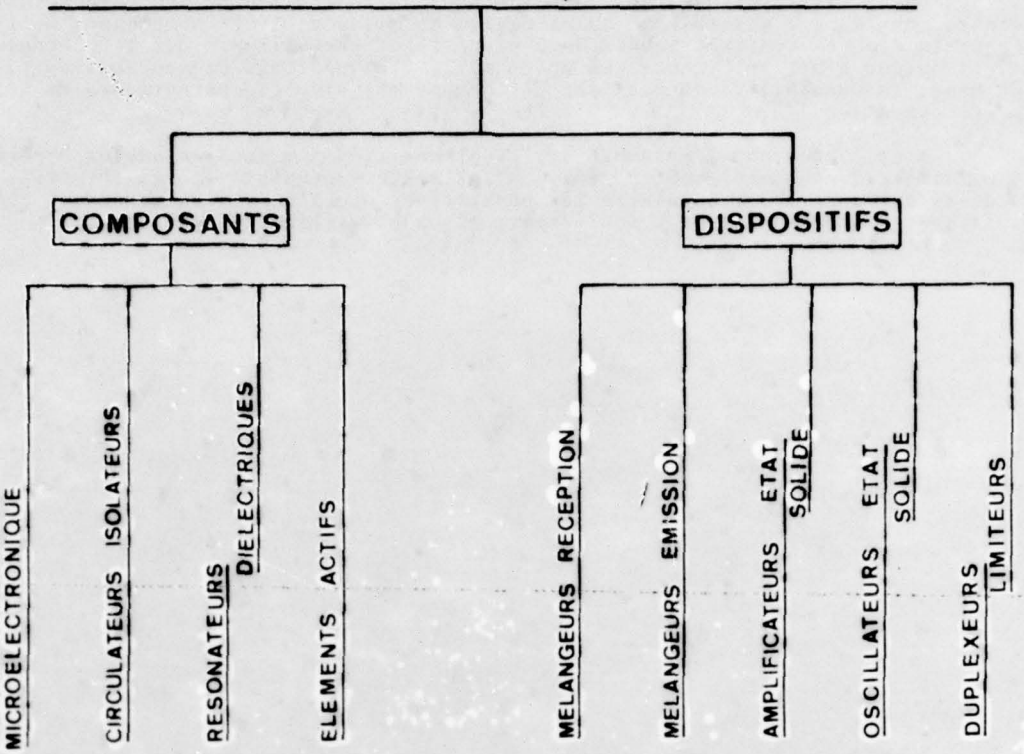

Figure 1 - Sous-ensembles : réception, émission, duplexage

SUBSTRATS	TECHNOLOGIE
DIELECTRIQUE: QUARTZ $\varepsilon r = 3,8$ Ep. = 0,30 mm pour F < 50 GHz Ep. = 0,15 mm pour F > 50 GHz	Préparation Chimique Métallisation : C_r - Ag
GYROMAGNETIQUE: FERRITE DE Ni $4\pi MS > 5000$ Gauss $\Delta H < 150$ Oe Ep. = 0,10 mm pour F < 50 GHz	Nettoyage Chimique Métallisation: P_t - A_u

Figure 2 - Substrats microélectronique

Transition

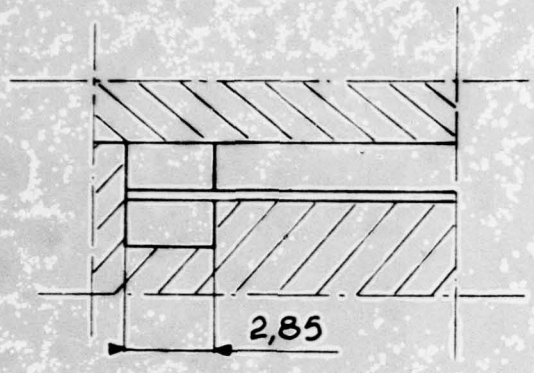

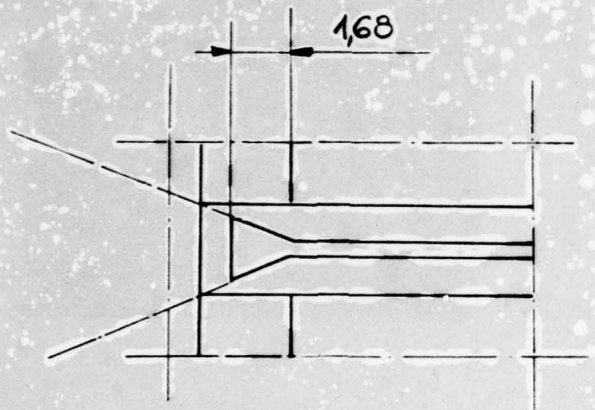

TOS < 1,20 jusqu'à F = 50 GHz

Affaiblissement < 0,1 dB

Lignes

Quartz

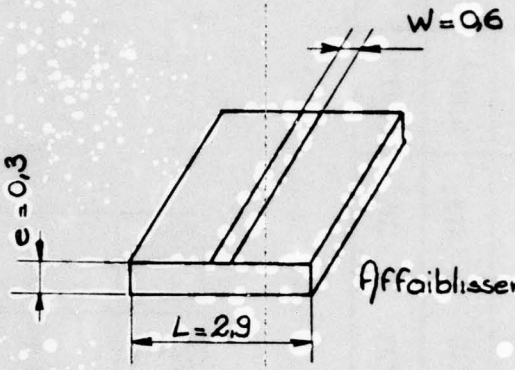

Affaiblissement < 0,25 dB/cm à 40 GHz

Ferrite

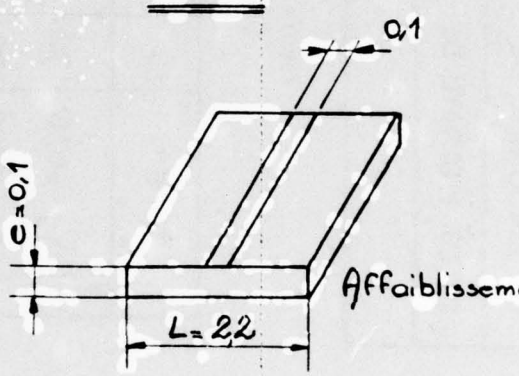

Affaiblissement < 0,4 dB/cm à 35 GHz

Figure 3 - Lignes microbandes

MATERIAUX	TYPE LTT	ε_r	$tg\,\delta$	$\frac{1}{\varepsilon}\cdot\frac{\Delta\varepsilon}{\Delta\theta}$
RUTILE ($Ti\,O_2$)	9100	99	5.10^{-4}	-890 p.p. m/c°
SOLUTION SOLIDE RUTILE, TITANATE DE Mg	9201	67	4.10^{-4}	-700 p.p. m/c°
TETRATITANATE DE Ba	9101	36	4.10^{-4}	-40 p.p.m/c°
SOLUTIONS SOLIDES	6717	32	3.10^{-4}	+100 p.p.m/c°
DE ZIRCONATE DE Sr	6718	33	4.10^{-4}	+65 p.p. m/c°
ET DE TITANATE DE Sr	6719	33	5.10^{-4}	+32 p.p.m/c°
d°	6721	35	8.10^{-4}	-38 p.p.m/c°

Figure 4 - Matériaux diélectriques

TYPE	ε_r	D mm	H mm	F_o GHz	$\frac{1}{F}\frac{\Delta F}{\Delta\theta}$ p.p.m/c°
6717	32	1,4	0,8	40,14	+2
9100	99	0,51	0,8		
6717	32	1,5	0,7	36,04	+1,5
9100	99	1,5	0,15		

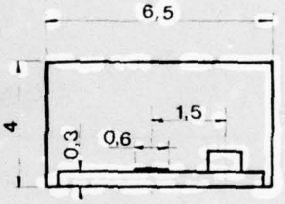

. Cotes en mm .

Figure 5 - Résonateurs compensés

Figure 6 - Circulateur 5 portes à jonction

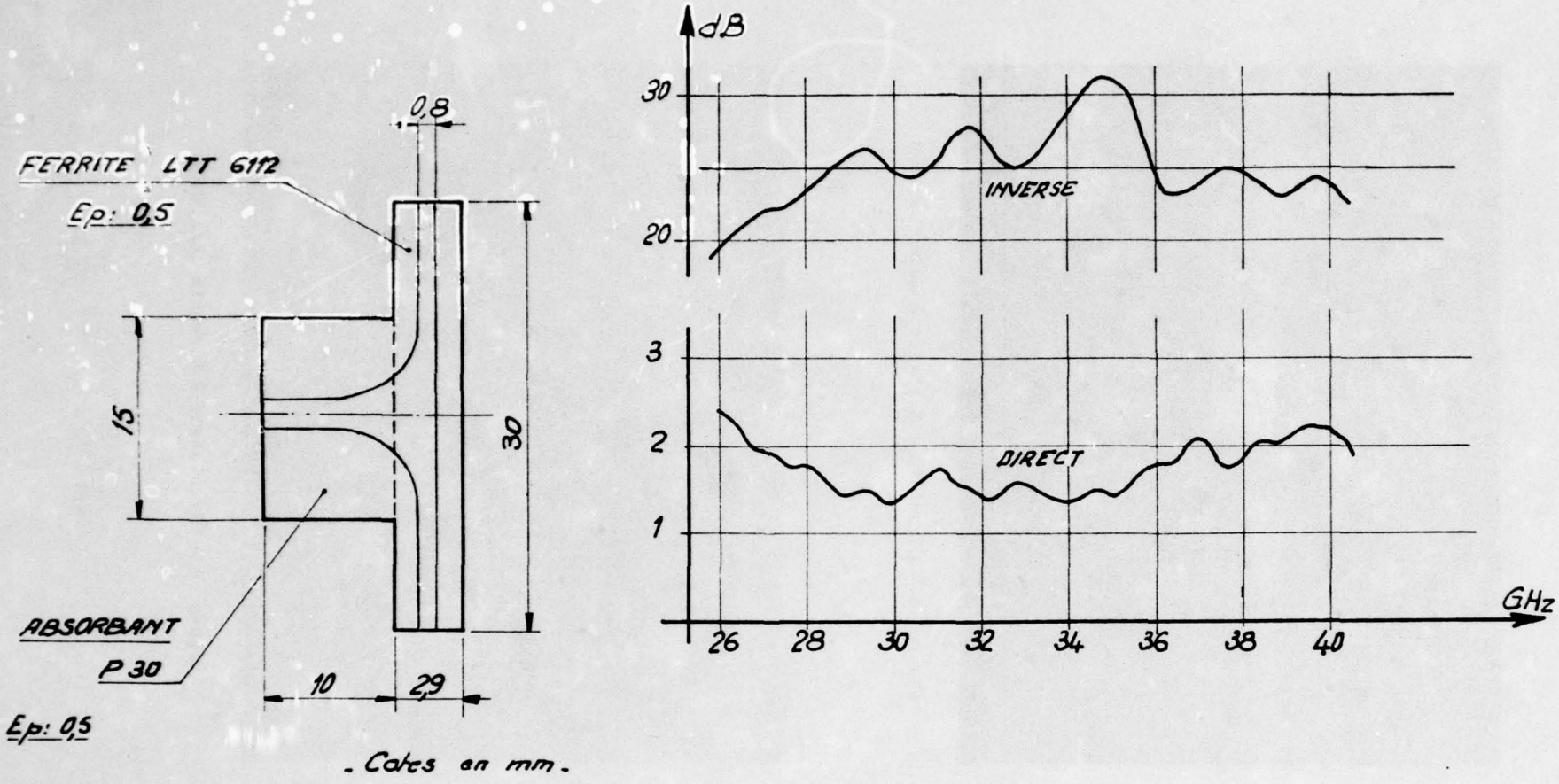

Figure 7 - Isolateur Osel

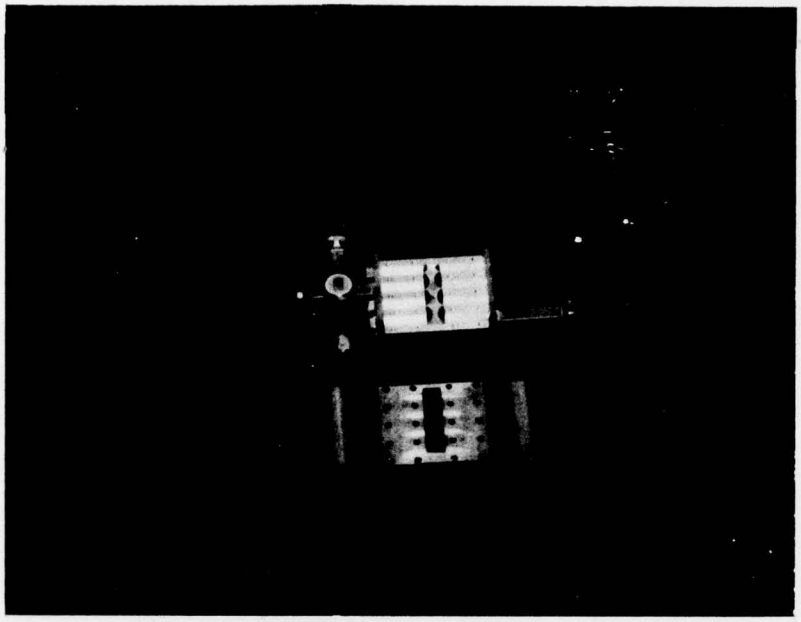

Figure 8 - Circulateur 8 portes à mode "de bord"

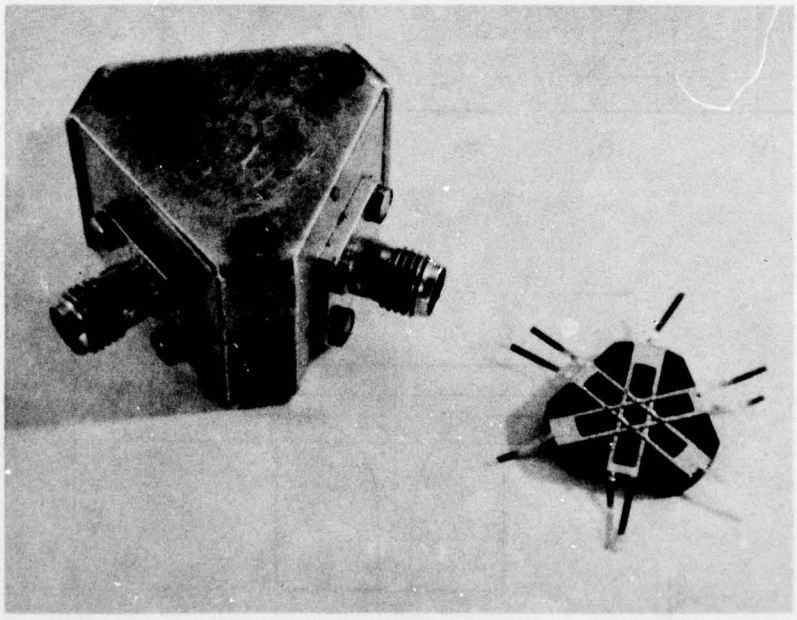

Figure 9 - Circulateur à éléments localisés

AD-A040 144 ADVISORY GROUP FOR AEROSPACE RESEARCH AND DEVELOPMENT--ETC F/G 17/9
NEW DEVICES, TECHNIQUES AND SYSTEMS IN RADAR.(U)
FEB 77

UNCLASSIFIED AGARD-CP-197 NL

2 OF 7
AD
AD040144

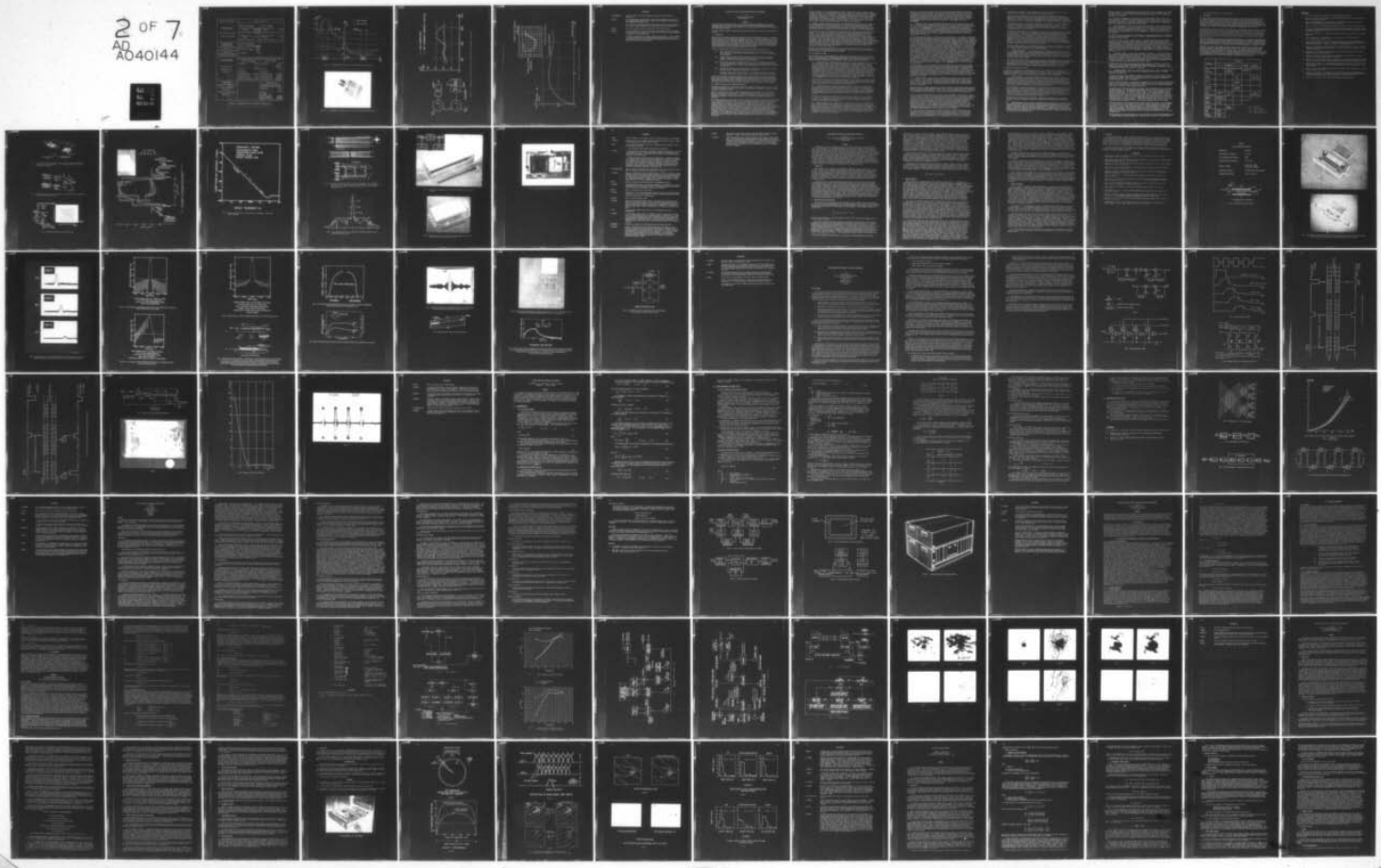

Type de composant	Caractéristiques	
DIODE SCHOTTKY Utilisation en transposeur de fréquence	Matériau Silicium Fréquence utilisation < 50 GHz Pertes de conversion < 5 dB Fréquence utilisation = 70 GHz Pertes de conversion = 7 dB	Matériau AsGa Fréquence utilisation < 50 GHz Pertes de conversion < 5 dB Fréquence utilisation = 70 GHz Pertes de conversion < 5,5 dB
DIODE SCHOTTKY en commutatrice Utilisation en modulateur de phase Utilisation en modulateur d'amplitude Déphaseur pour antennes à balayage électronique	Matériau Silicium Temps de commutation < 100ps Variation de $R_{série}$ $\frac{2500}{7\ \Omega}$ $I_{commande}$: 10mA	
DIODE AVALANCHE Utilisation en amplification Impatt CW	Caractéristiques obtenues Matériau Silicium Fréquence : 50 GHz ρ : 5 % P_{sortie} : 20 dBm 2 étages Gain par étage: 6 dB Bande passante: 2 GHz Facteur de bruit : 28 dB	Caractéristiques espérées Matériau AsGa Fréquence : 50 GHz ρ : 13 % P_{sortie} : 23 dBm 2 étages Gain par étage: 7 dB Bande passante: 3 GHz Facteur de bruit : 20 dB
DIODE GUNN Utilisation en amplification CW à transfert d'électron (transferred electron amplifiers)		Matériau InP Caractéristiques espérées avec diodes laboratoires Fréquence : 50 GHz ρ : 7 % P_{sortie} : 20 dBm 2 étages Gain par étage: 7 dB Bande passante : 5 GHz Facteur de bruit: 10 dB

Figure 10 - Composants actifs en ondes millimétriques

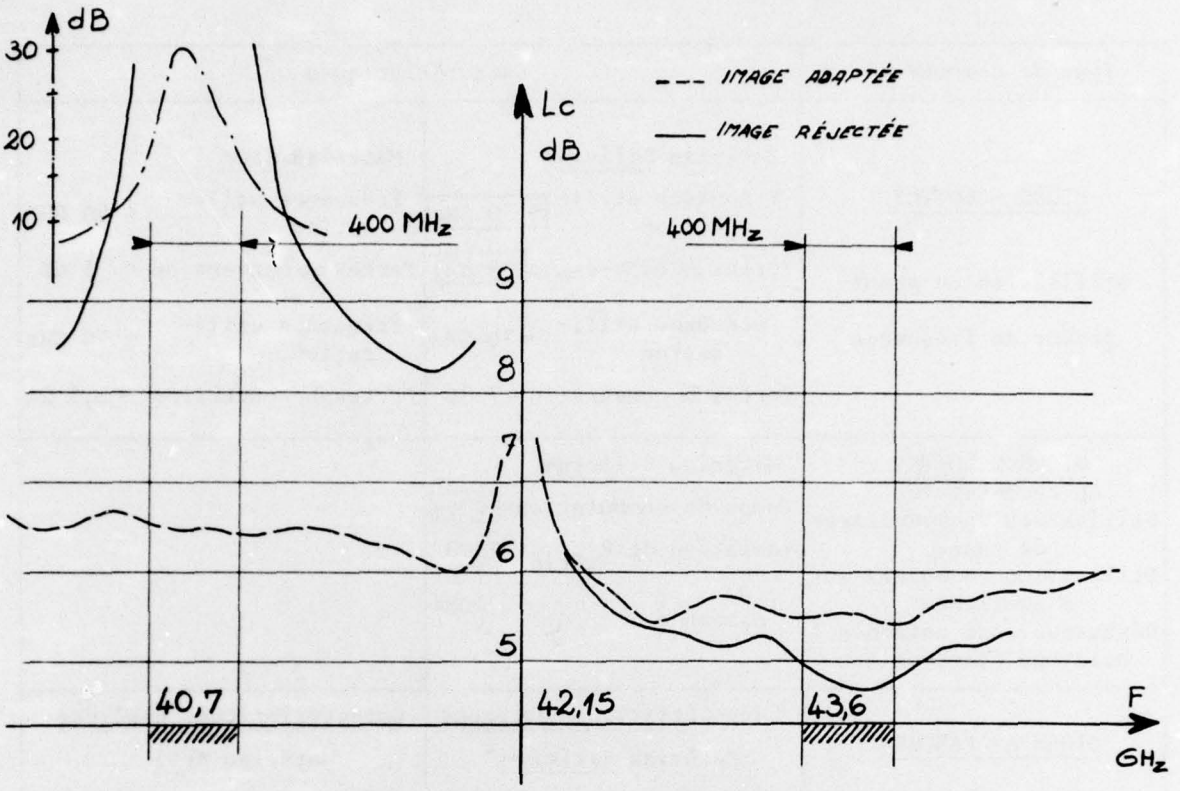

Figure 11 - Mélangeur de réception (caractéristiques électriques)

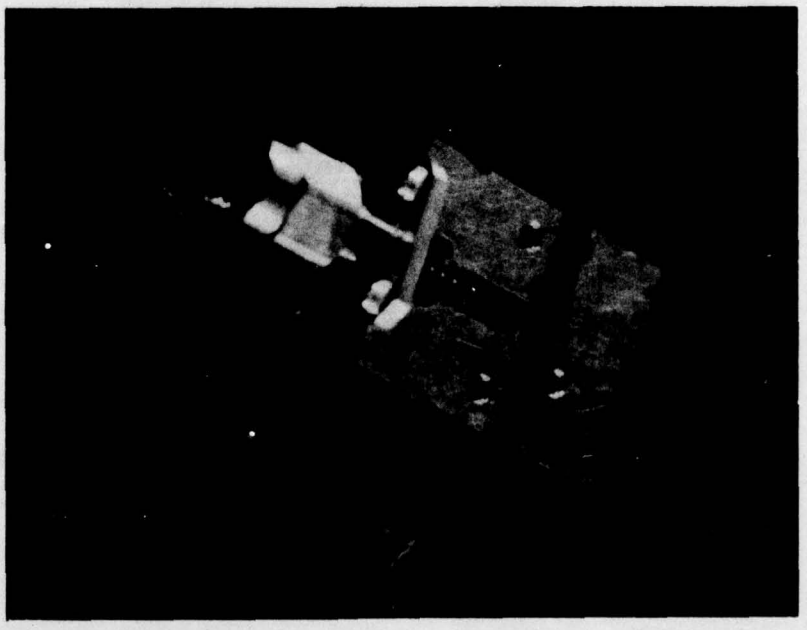

Figure 12 - Mélangeur de réception utilisant un résonateur diélectrique

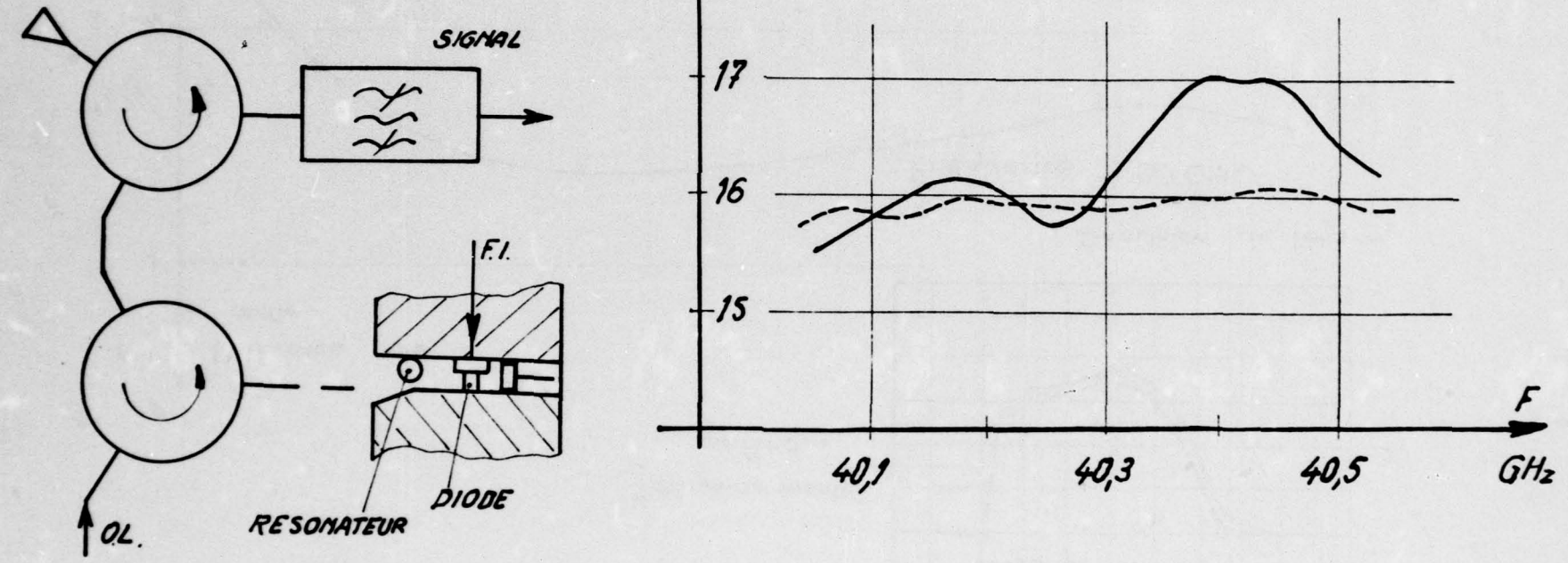

Figure 13 - Elimination de la bande latérale inférieure dans un mélangeur d'émission

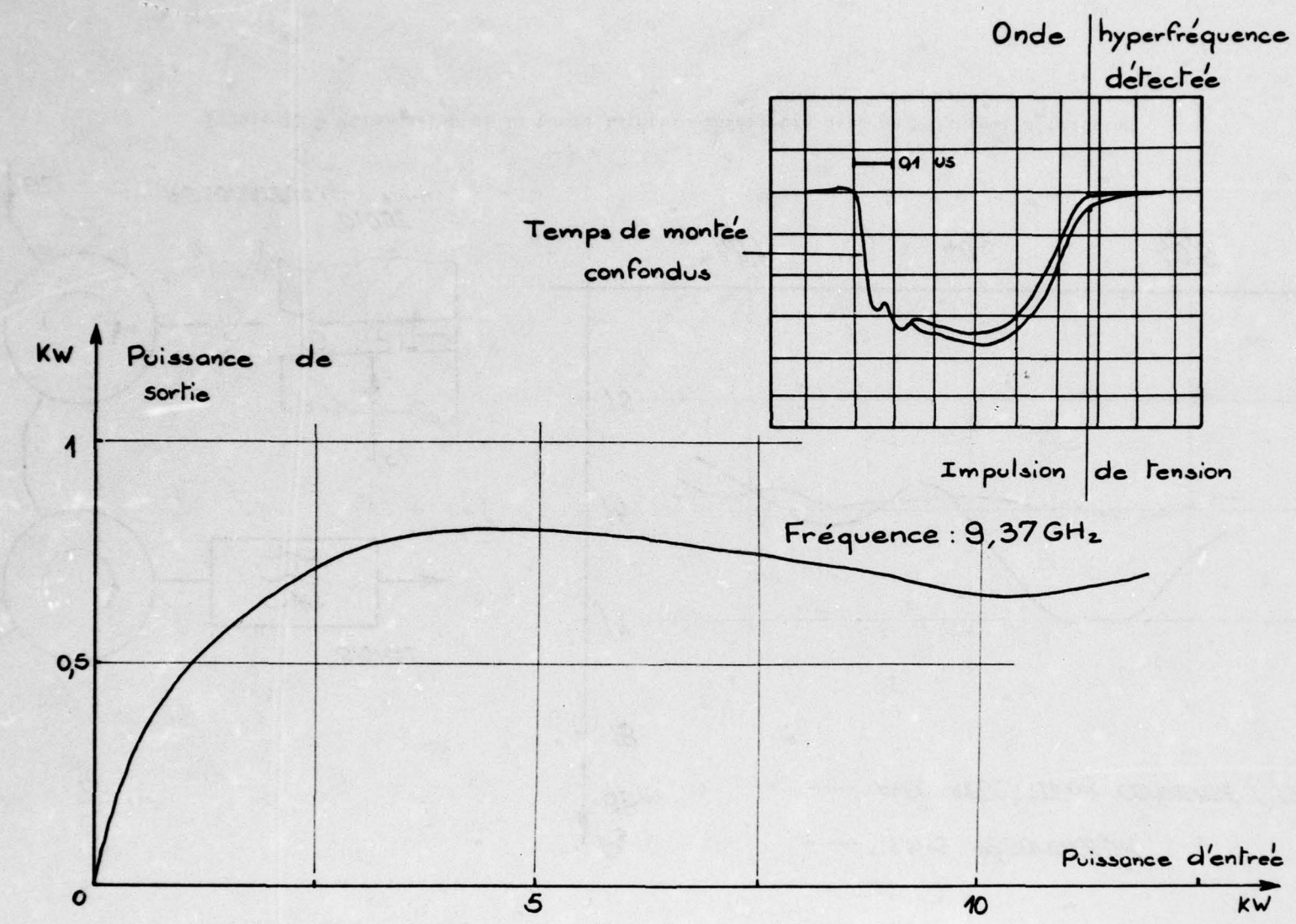

Figure 14 - Limiteur à silicium en volume

DISCUSSION

I W MACKINTOSH: Could you please clarify the performance that has been obtained with InP amplifiers?

B CHIRON: Les caractéristiques d'amplificateurs que nous avons données sont celles que l'on peut raisonnablement espérer obtenir, compte tenu de précédents résultats acquis à des fréquences autour de 40 GHz.

Les diodes InP, dont dépendent essentiellement les performances des amplificateurs, font l'objet d'études d'amélioration en collaboration avec des universitaires.

E STERN: What is the insertion loss and recovery time of the Si bulk limiter?

B CHIRON: La perte d'insertion du limiteur à silicium de volume présenté, à titre d'exemple de faisabilité, est de 4 dB a 9,375 GHz, mais cette valeur sera fortement diminuée aux lingueurs d'onde millimétriques.

Le temps de recouvrement de ce type de limiteur est très faible. A titre d'exemple, il n'a été constaté aucune modification sensible du temps de descente avant et après limitation dans le cas d'un signal d'hyperfréquence pulsé de 60 ns de temps de montée et 100 ns de temps de descente.

A SURVEY OF THE USE OF SURFACE WAVE DEVICES IN RADAR SYSTEMS

by

J D Maines and E G S Paige
RRE, Malvern, U.K.

SUMMARY

During the past decade surface acoustic wave devices have emerged as important signal processing components which are particularly well suited to radar. Devices have been developed which meet demanding specifications and, for some equipments, are having a significant impact on both performance and system design philosophy.

This paper reviews the range of components which have been developed and identifies their applications in radar.

1. INTRODUCTION

Surface acoustic wave devices find direct application where it is necessary to store I.F. signals for times up to a few hundred microseconds and perform filtering operations with bandwidths up to a few hundreds megahirtz. It is because these parameters are well suited to many modern radar requirements that much of the effort in the upsurge of interest, which began in the late sixties, has been directed towards radar applications. As we shall see, there have been several significant achievements, most notable among them being the establishment of the use of SAW dispersive delay lines as the method for waveform generation and matched filtering in pulse compression systems. This method is both widely accepted and generally used in appropriate military and civil systems.

There are several general features which relate to SAW devices which make them attractive.

(i) They are planar structures which rely on a technology similar to but simpler than that employed in the fabrication of integrated circuits; e.g. the use of conventional photolithography.

(ii) The SAW device performance is almost exclusively controlled through the transducer design. Sophistication is built into the mask used in delineating the transducer structure. The mask ensures repeatability of performance.

(iii) The slow velocity of the acoustic wave relative to that of electromagnetic waves leads to a spatial compression of a signal. This, together with the large transduction bandwidth and low attenuation means that small surface wave devices can store large quantities of information.

(iv) Because this information is on the surface it is accessible for processing, for example, by tapping-off and recombining different parts of the signal.

(v) The surface acoustic wave is a stable wave; it is virtually unaffected by electrical and magnetic fields and, on some materials, is very insensitive to temperature change.

Surface waves have been the subject of several reviews, one which emphasises the basic phenomena(1) and one which discusses devices and component(2) provide material and references which conveniently expand this review. Here, in section II some basic information relating to surface waves and commonly used structures is presented. Then, in section III, a range of SAW devices are introduced. Their application to radar is discussed in section IV. Finally, section V presents concluding comments.

II. SOME BASIC INFORMATION AND COMMON SAW STRUCTURES.

The essential components of a surface-wave device in an electronic circuit are shown in Fig. 1. They comprise a substrate material with an optically polished surface and transducers for conversion between electrical and acoustical signals.

Except for specialist devices, none of which have passed beyond the research stage, the substrate material is piezoelectric, usually quartz or lithium niobate. When a voltage is applied to the transducer, alternately directed electric fields are set up resulting in a periodic stress in the piezo-electric crystal. This field-induced stress is the surface wave launching mechanism of the transducer.

The simplest transducer is the periodic structure shown in Fig. 1, normally formed photolithographically in an aluminium film about 1000 A thick. It has a conversion efficiency which peaks at a frequency of v/λ_o, where v is the velocity of the surface acoustic wave, typically 3×10^5 cm/s, and λ_o is the periodic length of the transducer. Size of substrate, convenience of fabrication and acoustic attenuation effectively limit operating frequencies to between 10 MHz and 1.5 GHz. Acoustically, the periodic transducer has a fractional bandwidth of N^{-1} where N is the number of finger pairs. Electrically, the transducer looks like a capacity shunted by a (radiation) resistance, which may be made 50Ω by choice of finger length. If the transducer is inductively tuned and impedance matched then a conversion efficiency close to 100 percent may be achieved for fractional bandwidths below $2K/\sqrt{\pi}$. (K [quartz] = 0.041, K [Niobate] = 0.21) The 100 per cent conversion efficiency is not fully exploited because of the bidirectional of typical transducer structure. There is also the usual possibility of trading conversion efficiency for bandwidth, octave bandwidth being possible with suitably designed transducers.

In many devices the role of the transducer is not only to convert from electric to acoustic energy but also to filter it. The impulse response of a single transducer is directly related to its geometry; the relative finger positions determine the phase and the source strength associated with the fingers determines the amplitude of the response. (A frequently used method of varying the source strength is by variation of finger overlap. It is usually confined to one transducer). Thus to first order of approximation, the frequency response of a structure such as shown in Fig. 1 is the product of the Fourier transform of the impulse response of each transducer. Fig. 2 illustrates the relationship between impulse response and transducer geometry for finger overlap weighting.

It is possible to design surface wave devices to meet tight and demanding specifications. However to do this successfully it is necessary to incorporate in the design corrections for, or methods of avoiding several problems, e.g. interaction with the external circuit, multiple reflections in a transducer, diffraction, refraction and bulk wave generation. The ways of overcoming these problems are now known and are incorporated in the designs precedures and software of the leading suppliers.

In the structure of Fig. 1, the surface wave is launched and detected without any intermediate interference. Various possibilities exist for redirecting and in some cases processing the signal in transit. One of these is the multistrip coupler and the range of components derived from it (2). The coupler finds important applications in improving the performance of devices made on lithium niobate. Another type of structure is the reflecting array structure (RAST). The basic RAST consists of a periodic set of reflectors. They may be set normal to the incident beam or inclined at some other angle. Though the intensity reflected from each reflector is usually low (-40 dB), constructive interference from a large number ($\sim$100) leads to good reflectivity ($\sim$98 percent) over a narrow bandwidth centred on $V/2p$ where p is the periodic length in the array. Typical reflectors are metal strips, dielectric strips or grooves. A weighted response can be realised by variation of effective length of the strips or depth of the grooves. The primary use of the RAST to date is in resonators and in dispersive delay lines (see Section III 5).

We conclude this section by pointing out that there are numerous other SAW structures ranging from waveguides, prisms and lenses to amplifiers and convolvers. These are in the research phase and will only be referred to if appropriate in the next section.

III. SAW DEVICES FOR RADAR.

Surface wave devices have found application in radar systems because they are well fitted to perform many of the functions required in modern signal processing. Their parameters are admirably suited to the usual IF processing function of delaying and filtering but, in addition, they can be used to form stable oscillators for COHO and STALO applications. The key SAW devices are reviewed below.

1) FIXED DELAY LINES. Delay times of interest lie in the range from nanoseconds for proximity fuze applications to milliseconds for delay line cancellers. Both are difficult to achieve; reported delay times fall in the 100 ns to 1 ms range with 1 - 50 μs being readily accessible without resorting to folded paths. They are typified by insertion loss in the range 3-30 dB, fractional bandwidths of 1-50% and spurious response -50dB. Applications include time ordering of multipulse radars, analogue MTI processing in high PRF radars, examination of a signal followed by corrective processing, and test target simulation. Considerable effort has been focussed on extending the delay to longer times with acceptable bandwidths for use as pre-whitening filters. These filters reduce the dynamic range requirement of subsequent Doppler processors. There are a number of techniques which hold out hope of competitive solutions. For example a delay line having a temperature coefficient of a few parts per million per degree centigrade, 220 μsec delay and -57dB spurious level has been built at University College London. (3)

SAW delay-lines can easily be tapped. The primary limit of tapped delay-lines is the density of taps. It is set by the density of electrical connections and the electrical interface. A 50 μm spacing is a typical limit (20 nsec separation) although smaller separations can be achieved by using parallel delay lines and distributing the taps conveniently.

2) VARIABLE DELAY LINES. Variable delay may be achieved discretely or continuously (2). Discrete variable delay has been obtained by switching between taps of a typical delay line. Continuously variable delay can be achieved using dispersive delay lines (See section III.5) making use of a VCO andthe ability of the delay line to delay an imput by an amount proportional to its frequency. In a single unit performance is limited by available dispersive delay lines to delays of $\sim$50 μseconds and bandwidths less than about 50 MHz. Some results are shown in Figure 3.

Surface-wave devices have recently been reported in which it is possible to store a replica of the signal for a variable time before recall. The information is stored in a semiconductor adjacent to the piezo-electric delay line. A number of techniques have been used and will be discussed at this conference by E. Stern. (4)

3) BAND-PASS FILTERS. The frequency filter has been one of the main foci of attention for those working on surface waves primarily due to its potential application as a TV filter. The detailed design procedure is now sufficiently well understood that precisely defined amplitude and phase specification can be met simultaneously in a single filter - see figure 4. Excellent filter results are achievable, with out-of-band response 70 dB down, insertion loss controlled to a fraction of a dB, and phase error held to a few degrees. Filters are being produced at a rate of thousands per week and several firms offer purpose-design filter capability. They are now accepted for missile and space applications.

SAW filters are attractive for modern radar since they are small enough for hybrid intergration, are stable and require no adjustments. In conjunction with wide-band IF amplifiers they offer an exchangeable filter capability which could meet a wide variety of radar applications. They are usually lossy-typically about 20 dB - and although this figure can be reduced using specialised techniques it is unlikely to become sufficiently low to allow the use of filters at the front end of the IF where S/N is seriously affected by loss. However, where radar performance is limited by interference rather than noise the precise pass-band of a compact SAW filter will be advantageous.

4) OSCILLATORS. The conventional SAW oscillator consists of a quartz delay line with output fed back to input through an amplifier with sufficient gain to exceed the delay-line insertion loss. (5). A comb of frequencies satisfy the condition that the phase shift round theloop is $2\pi N$, with N an integer. In the single mode oscillator, all butone of the possible modes are suppressed by choice of transducer and delay time. The advantageous features of the SAW oscillator have been widely stated; operation up to low gigahertz frequencies without multipliers, freedom from satellite modes, rugged, good short term stability, and easily frequency modulated are chief among them. The single mode oscillator is now accepted for application in military equipment and is actively being assessed for civil use.

One of the most important aspects of the oscillator is its stability. It is convenient to subdivide this into long term ($\sim$1 year), medium term ($\sim$1 h) and short term ($\ll$1 s). The Marconi Co. (Gt Baddow) have produced oscillators with the lowest ageing rate to date. An ageing rate of close to 1 part per million per month has been observed (6) which is comparable to a moderately good bulk quartz crystal and an order of magnitude worse than a good one. Since the origins of ageing have not yet been identified, possible improvements are difficult to predict. However, there are many applications in radar, where the ageing is relatively unimportant. In contrast, the short term stability can be a critical design parameter. It is particularly important in Doppler radars since it determines the spectral purity. Fig. 5 shows a plot of the single sideband FM noise spectral density as a function of off-set from centre frequency of a 396 MHz oscillator with a path length of 2500λ. A Q of 4×10^3 is realised. Though opimised in certain respects for low noise levels, an improvement of more than 10 dB could be anticipated because of the high (20 dB) insertion loss of the delay line. Nevertheless, the results shown in Fig. 5 compare favourably with those obtained at a similar frequency with bulk-wave oscillators and a multiplier chain. Clearly the compact SAW device has a practical advantage over the bulk wave device with multiplier chain in the VHF range. The short term stability performance of this oscillator has encouraged the development of devices for COHO and STALO applications. An attractive feature is the simplicity with which the oscillator is frequency modulated over a range of 1% of its centre frequency. The FM capability is particularly relevant to requirements which require pulling of the COHO (to take out aircraft motion for example). Other requirements demand a wider FM capability (frequency agile local oscillators for example); here the multimode version of the SAW oscillator find applications.

In the multimode oscillator the conditions that the phase shift round the loop shall equal $2\pi N$, can be satisfied by a range of N values. Each value of N (N^{th} mode) gives a particular frequency. In these oscillators it is possible to change from one frequency to another in a controlled way while maintaining similar stability to that of the fixed single mode device. One approach is to use wide band transducers so that any one of the comb of frequencies can be excited. A mode can be selectively excited to generate a particular frequency by injecting the approximate frequency component and switching on the amplifier (7). This technique now offers the possibility of switching quickly (few microseconds) across hundreds of MHz of bandwidth in an oscillator which is highly stable in the short term.

5) MATCHED FILTERS. A major part of the surface-wave effort has been directed at producing matched filters, i.e. filters which optimize the output peak-signal/mean noise (power) ratio. In this respect a signal s(t) will be optimally processed by a filter having an impulse response which is the time reverse of s(t). The flexibility in design of SAW transducers permits precise control of their impulse response. They are consequently considered for both signal generation (of s(t)) and reception.

Matched filters have widespread application in signal processing but typical surface-wave parameters make them suitable for pulse compression radars. They are used for both generation and reception of the frequency-modulated waveforms used in these radars. Linear frequency modulation is the commonest form of encoding in this application. It is characterised by pulse duration T and bandwidth B.

A "conventional" surface-wave structure for linear frequency modulation is shown in Fig. 6. (Both here and elsewhere, we shall refer to these as dispersive delay lines). In the receiver, a weighting filter is required in addition to the matched filter to suppress the time sidelobes adjacent to the correlation peak. In the surface-wave implementation this is usually built into the dispersive delay line as additional weighting. A great deal of detailed basic knowledge of generation, propagation and reception of surface waves is now incorporated into the design procedure of dispersive delay lines - see for example the discussion by Paige (8) and by Bristol (9). The success of the technique is well established and experimental performance is close to "ideal". Maximum sidelobe levels as low as -40dB with respect to the mainlobe are now produced using routine and automatic design procedures. (See Fig. 7.) At least three companies in the U.K., Marconi (Gt. Baddow), MESL (Edinburgh) and Plessey (Caswell) have such facilities.

The ideal behavior can be achieved for time-bandwidth products of several hundred, within the constraints of $B \lesssim 100$ MHz and $T \lesssim 60\ \mu S$, using the conventional structure. The time-bandwidth product is an important parameter; it is the pulse compression ratio, or the processing gain against white noise. The performance of SAW devices meets the requirements of the majority of radar systems as presently conceived and it is worth stressing that the structure is simple,

reproducible, and reliable. We feel these and other attractive features will ensure that the SAW device remains competitive for several generations of radar systems.

There are some specialised radars which require time-bandwidth products which exceed a few hundred and in recent years there has been some emphasis on reflecting array compressors (RAC). These have been shown to be very effective in meeting this need, providing compressors with time-bandwidth up to 10,000. They are based on reflecting-array structures introduced in Section II and are illustrated in Fig. 6. Considerable development of these simple structures has occurred (10).

Low time-bandwidth product compressors have presented special problems. However the flexibility of design of the SAW device has allowed the bandpass characteristic to be shaped so that the effect of large ripples in the spectrum of the transmitted pulse can be minimised. At IF, compressed pulses have been produced with sidelobes more than 35 dB down on the main pulse for a time-bandwidth product as low as 8 (11).

Waveforms other than linear FM can be designed with equal ease. For example, Barker coded devices are in production for radar systems. Particularly significant are the nonlinear FM waveforms that are being designed to overcome the mismatch loss which occurs when linear FM filters are amplitude weighted to reduce sidelobes. The spectrum of the transmitted waveform is "shaped" by deviating the phase of the signal from the quadratic variation of linear FM. The receiving transducer can be a matched filter for the modified waveform. The spectral shaping can be optimised to achieve low sidelobes and acceptable Doppler sensitivity with very low mismatch loss, e.g. 0.05 dB (12). This type of device will be widely accepted in future pulse compression systems. It can now be designed economically and accurately for the first time. The performance of a phase weighted generator and receiver is shown in Fig. 7.

It would be highly desirable to have transmitters and receivers capable of generating and receiving any waveform. There are a variety of SAW techniques being studied with this in mind but we shall not discuss them here as they are still in the research phase.

6) FOURIER TRANSFORMERS. Fourier transformation is an important signal processing function, its most extensive systems use being in spectrum analysis. The development of the fast Fourier transform (FFT) algorithm permits digital computers to perform Fourier transforms and this method of signal analysis is particularly relevent to Doppler radar systems. However, the requirement for real-time Fourier transformers has led to an interest in the alternative methods of transforming offered by SAW devices (and CCD's).

The Fourier transformation method now being investigated using SAW techniques is the chirp transformation. As illustrated in Fig. 8 the basic operation consists of multiplying the input signal s(t) by a linearly frequency-modulated waveform (chirp C_1) followed by convolution of the product with a filter whose impulse response is also a chirp (C_2), having a frequency-time relation of the opposite slope to C_1. The technique is easily implemented with surface wave components.

IV. EXAMPLES OF SAW DEVICES IN RADAR.

As shown in the preceeding section, numerous SAW devices are now developed to an advanced stage. In this section we give examples of the key role they play in a variety of radar systems including pulse compression, miniature radars, Doppler processors and air traffic control. We also include some examples related to electronic warfare since these subjects are of interest to the radar engineer.

1) PULSE COMPRESSION. The impact of surface-wave devices on pulse compression systems is considerable as we have indicated in Section III.5. They are now used to generate both the coded signal for transmission and to compress the return pulse from the target. The waveforms used in such systems can be optimally chosen since, for the first time in practical systems, the vital signal processing components can be flexibly designed, accurately made and economically produced. High and low time-bandwidth product, as well as the non-linear FM pulse compression components are good examples of SAW devices which are now influencing systems design.

A further important consideration brought about by the availability of these devices relates to the type of transmitter to be used in the system. For example, a low peak-power transmitter may not be able to meet range and resolution specifications unless its mean power can be increased and correlation techniques used. A suitable solid-state transmitter, such as a transistor oscillator has a longer life than a tube so that its use in conjunction with SAW correlators will contribute directly to increasing the mean-time-between-failures of equipments. Some important applications of SAW devices critically depend on this type of assessment.

The compatibility of SAW devices with integrated circuits aids the manufacture of relatively miniature sub-systems; examples of coherent and incoherent pulse compression units are given in Fig. 9.

2) MINIATURE RADARS. There are several developments which are significant for miniature radars. Fully coherent IF pulse compression units can now be produced without excessive cost, size and power consumption penalties. They offer new signal processing opportunities for low and medium range radars. For MTI applications the low-noise characteristics of a compact SAW oscillator/multiplier RF source should provide powerful competition against more conventional approaches. Spread-spectrum techniques are also a possibility and the use of SAW correlators should be particularly relevant for systems with relatively few range cells.

Man-borne radars have already benefited from the use of SAW delay lines. An example is the improvement that accrues in a clutter reference radar system by using a simple surface-wave tapped delay line [13]. Further advances in this area are more likely when the potential of SAW beamforming networks is fully realised.

It is interesting to speculate what the impact of the new technologies will be in the next few years; combinations of SAW/CCD and digital techniques will surely create a wealth of new, miniature, but sophisticated systems. The use of these techniques should be particularly valid where power dissipation, size, and cost are important. Miniature radar is an example; similar arguments should apply to lightweight communication systems and radar fuzes

3) DOPPLER PROCESSING. Surface wave devices are not well suited to Doppler processing since their typical bandwidths are too wide for the resolution requirements of normal radars. Exceptions include high velocity, missile-borne radars where it could be advantageous to use compact surface-wave devices with their low sensitivity to alien environments. Their use in optical "radars" is also under active investigation; in this case the bandwidths of SAW filters are ideally suited to the requirement.

The most likely area for exploitation of surface waves in standard Doppler radars is in conjunction with charge coupled devices (CCD). There are a number of such hybrid approaches, one of which has been reported by Roberts [14].

The basic requirement is to find a method capable of performing simultaneous range and Doppler processing for a pulsed Doppler radar in a compact, cheap unit. The proposed solution uses CCD techniques, firstly to store and then to speed up (by rapid clocking) the video radar signal. The increased bandwidth of the Doppler signals which results is analysed using the SAW Fourier transform technique described in section III.6). Typically the output will be time compressed by a factor of 1000 and consequently will allow 1000 range cells to be examined in real time with a Doppler resolution of about 50Hz. This technique could have a major impact on the design of pulsed Doppler radars. It is worth noting that it is equivalent to having a FFT analyser working in real time on each range cell.

4) AIR TRAFFIC CONTROL. The ATC market is potentially very great. It is basically concerned with communications, surveillance, and navigation. Each area has received the attention of SAW engineers, but successful application is slow due to the principle normally adopted that any change must be minor and compatible with existing systems. This fact means looking for retrofit applications such as filters and oscillators which show economic advantages rather than requiring major changes in philosophy. The recent acceptance of biphase coding for future ATC transponders though, is almost certain to require SAW device to demodulate the signal.

The SAW device shown in Fig. 10 was developed at RRE and produced at GEC (Wembley, UK) for this purpose. It is now incorporated in airborne SSR transponders which are in the process of undergoing MOD/COSSOR flight trials. The current view is that the SAW demodulator represents the most cost-effective solution for the extraction of DPSK data.

5) ELECTRONIC WARFARE. There are a number of activities related to radar processing for which SAW device development is important. Some of the more important ones relating to electronic warfare are discussed here.

A variety of devices are being developed to improve the performance of systems against electronic counter measures (ECM). Improvement in performance is achieved by using such techniques as pulse compression, frequency agility, array signal processing and spectrum spreading. Surface wave devices are applicable to each of these areas.

SAW delay lines have proved to be capable of storing signals for times of a few hundred microseconds. They should have application in large bandwidth, confusion jammers. Against unsophisticated radars, gating of the output can be used to achieve range deception. However, where faithful reproduction of the signal is necessary other techniques are required.

The use of complex signal waveforms makes it necessary to adopt techniques which do not distort the retransmitted signal. In this respect wide-band tapped delay lines are being assessed for range-gate pull-off applications. Programmable devices have been developed in which apparent range is varied by connecting each tap in turn to the output [15]. A more complex programmable system has been reported which uses both fixed and switchable tapped delays to achieve discretely variable timing of the output in steps of 40 ns up to 40 μs [16]. Instantaneous bandwidth is 200 MHz and switching speed 15 ns. Techniques for producing continuously variable delay using dispersive delay lines (Section III.2) may also be applied. Combined with switchable fixed delay lines they offer a powerful technique of target simulation. Target simulation can of course be used either for the disruptive measure discussed above or as an aid in system development and automatic testing.

Surface-wave devices are also being considered for use in set-on noise jammers. They are unlikely to be used directly at radar frequencies but responsive jamming techniques are being investigated which make use of surface wave devices operating at IF. One reported technique utilises a SAW filter bank. In this, a fixed frequency microwave oscillator down-converts the incoming signal which is then detected in the filter bank, followed by repetitive impulsing of the individual filter used to identify the signals with subsequent up conversion and retransmission. In an extension of this technique the same filter could be converted into an oscillator using a suitable feedback circuit.

ECM developments are at an early stage but it is already clear that the cost/size advantages of some of these new signal processing components will cause some basic rethinking. Considerable payoff

could occur in relation to expendable jammers.

V. CONCLUSIONS.

The radar application of SAW devices which we have discussed in this review are presented in Table 1. At a glance it is possible to see the range of application in radar. Partially obscured is the importance of dispersive delay lines; they not only have direct application in pulse compression but are, as we have seen, vital to the performance of spectrum analysers and variable delay lines. Our emphasis has been on devices which have at least reached the stage of use in experimental radar systems. Thus, many of the current surface wave research activities have been neglected. Activities which look promising include resonator structures [10], programmable filters [12] and memory correlators .

As analogue signal processors, surface wave devices should be compared with charge coupled devices (CCD) which in their basic form are analogue shift registers, but more generally can perform a wide range of signal processing operations. For processing fixed IF signals the wide bandwidth and dynamic range of the passive SAW devices give them clear-cut advantages. For very narrow bandwidth requirements such as the determination of Doppler frequency shifts we have seen how the two technologies can be married (Section IV). Of course charge coupled devices are being considered on their own merits as Doppler signal processors.

Competition with SAW devices comes also from digital circuitry but this is weakened by power consumption, cost, and the problems of achieving large dynamic range A/D converters operating over large bandwidths. Despite the inevitable advance of digital circuitry we foresee SAW devices having a continuing part to play when fixed waveforms have to be processed, when stable frequencies have to be generated and where the simplicity of the attributes of the SAW device are particularly striking (e.g. spectrum analysers).

Returning to the current achievements with SAW devices, we should recognise that the impact of SAW devices only becomes of major significance when their existance begins to influence system design. There are numerous cases where this is already happening. For example, passive generation and nonlinear chirp in pulse compression, very compact coherent pulse compression subsystems, clutter reference filters and sophistication of fuzes. As systems engineers become more familiar with the properties and potentialities of SAW devices we can anticipate an extension of this list to include, for example, spread spectrum techniques in radar and development of sophisticated ECM techniques.

Radar Applications	SAW DEVICE				
	Delay Line	Frequency Filters	Oscillators	Matched Filters	Fourier Transformers
Pulse Compression		Frequency Weighting		Dispersive D.L.	
Pulsed Doppler	M.T.I.		Coho Stalo		SAW + CCD Spec.Analyser
FM - CW			Scanning L.O.		
Frequency Agility			Multimode Oscillator		
Signal Identification	Dispersive D.L.	Filter Bank			SAW Spec.Analyser
Repeater Jammer	Recirculation Tapped D.L.				
Target Simulator	Variable D.L.				
Array Sig. Processor		Blass Array			
Radar Fuze	Tapped D.L.				
Clutter Reference	Tapped D.L.				

DL = Delay-line

LO = Local Oscillator

CCD = Charge coupled device

REFERENCES

1. White, R.M., "Surface elastic waves", Proc IEEE, 1970, 58, pp 1238-1276.

2. Maines, J D. and Paige, E.G.S., "Surface acoustic wave components, devices and applications", IEE, Rev. 1973, 120, pp 1078-1110.

3. Mason, I.M., Papadofrangakis, E. and Chambers, J. "Acoustic surface wave disc long delay lines". Special IEEE Sonics and Utrasonics Issue, May 1976.

4. Stern, E., "Analog memory correlators for Radar Signal Processing", Paper 9 this conference.

5. Lewis, M. F., "The design, performance and limitation of SAW oscillators", in Proc. Int. Seminar on Component Performance and Systems Applications of SAW Devices (Aviemore, Scotland) pp 63-72, 1973, IEE Publication 109.

6. Gratze, S.C. and Barton, R.K., "SAW oscillators long term stability", Electron Eng., pp 49-51, March 1975.

7. Bale, R.A., Maines, J.D. and Palmer, K.A., "Frequency hopping using SAW oscillators", Proc. Ultrasonic Symp., paper P-2 1975.

8. Paige, E.G.S., "Dispersive filters: Their design and application to pulse compression and temporal transformation", Proc. Int. Seminar on Component Performance and System Applications of SAW Devices (Aviemore, Scotland), pp 167-180, 1973, IEE Publication 109.

9. Bristol, T.W. "Analysis and Design of Surface Acoustic Wave Transducers" Proc. Int. Seminar on Component Performance and Systems Applications of SAW Devices (Aviemore, Scotland) pp 115-129, 173, IEE Publication 109.

10. Williamson, R.C., "Properties and applications of reflective array devices", Special IEEE Sonics and Ultrasonics Issue, May 1976.

11. Judd, G.W., "Technique for realising low time sidelobes in small compression ratio chirp waveforms", Proc. IEEE Ultrasonics Symp., p 479, 1973.

12. Newton, C.O., "Signal processing aspects of nonlinear chirp radar signal waveforms for surface wave pulse compression filters", Proc, Signal Processing Conf., (Lausanne, Switzerland), 1975.

13. Brown, M.A.C.S., Hannis, W.J., Skinner, J.M. and Turton, D.K., "The use of a SAW delay line to provide pseudo-coherence in a clutter reference pulse Doppler radar", Electron. Lett., vol 9, pp 17-19, 1972.

14. Roberts, J.B.G., "Radar Doppler processing using CCD and SAW devices", Electron. Lett., vol.11, No. 22, pp 525-526, Oct. 1975.

15. Gandolfo, D.A., Grasse, C.L. and O'Clock, Jr., G.D., "Surface acoustic wave components in electronic warfare", Proc. Int. Seminars on Components, Performance and Systems Applications of SAW Devices (Aviemore, Scotland), pp 231-242, 1973. IEE Publication 109.

16. Hurley, G.W. "Microwave variable time delay", Electronic Warfare, June 1973.

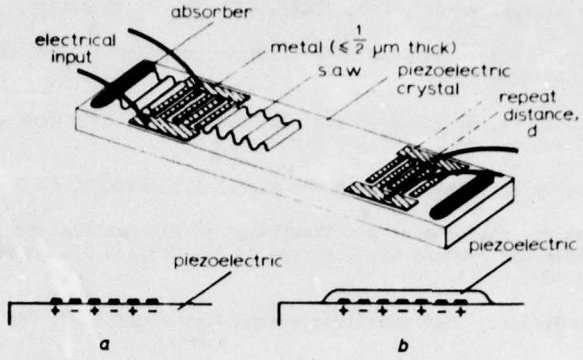

Fig 1 A simple surface-wave delay-line. Inset shows the transducer cross-section. (a) For piezoelectric substrates. (b) For piezoelectric layer on a non-piezoelectric substrate.

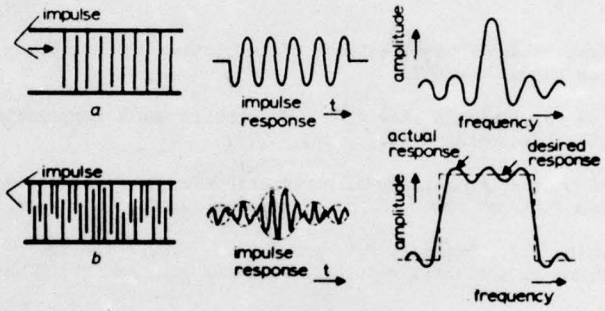

Fig 2 Impulse response and frequency response. (a) Unweighted periodic transducer. (b) Sinc X weighted structure.

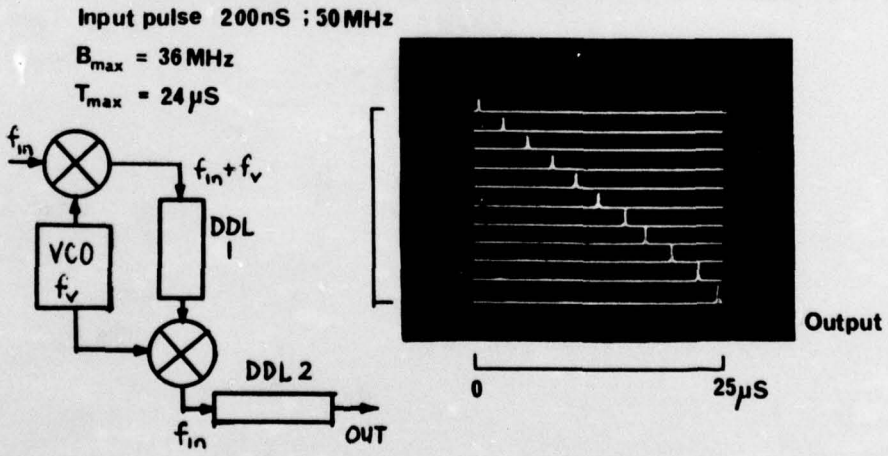

Fig 3 Performance of SAW variable delay-line unit.

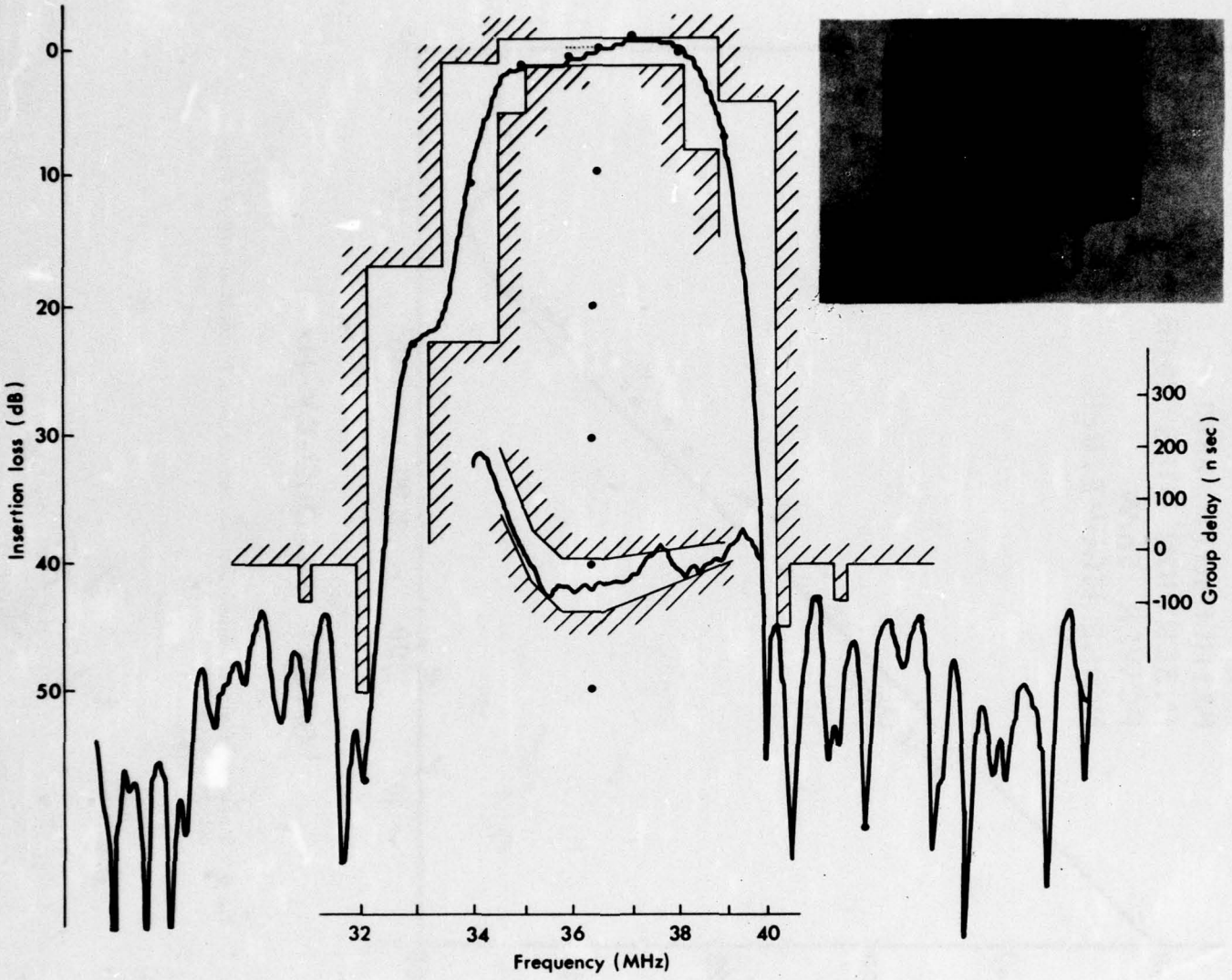

Fig 4 The performance of a Surface wave TV filter in comparison with its specification. The inset shows an encapsulated device.

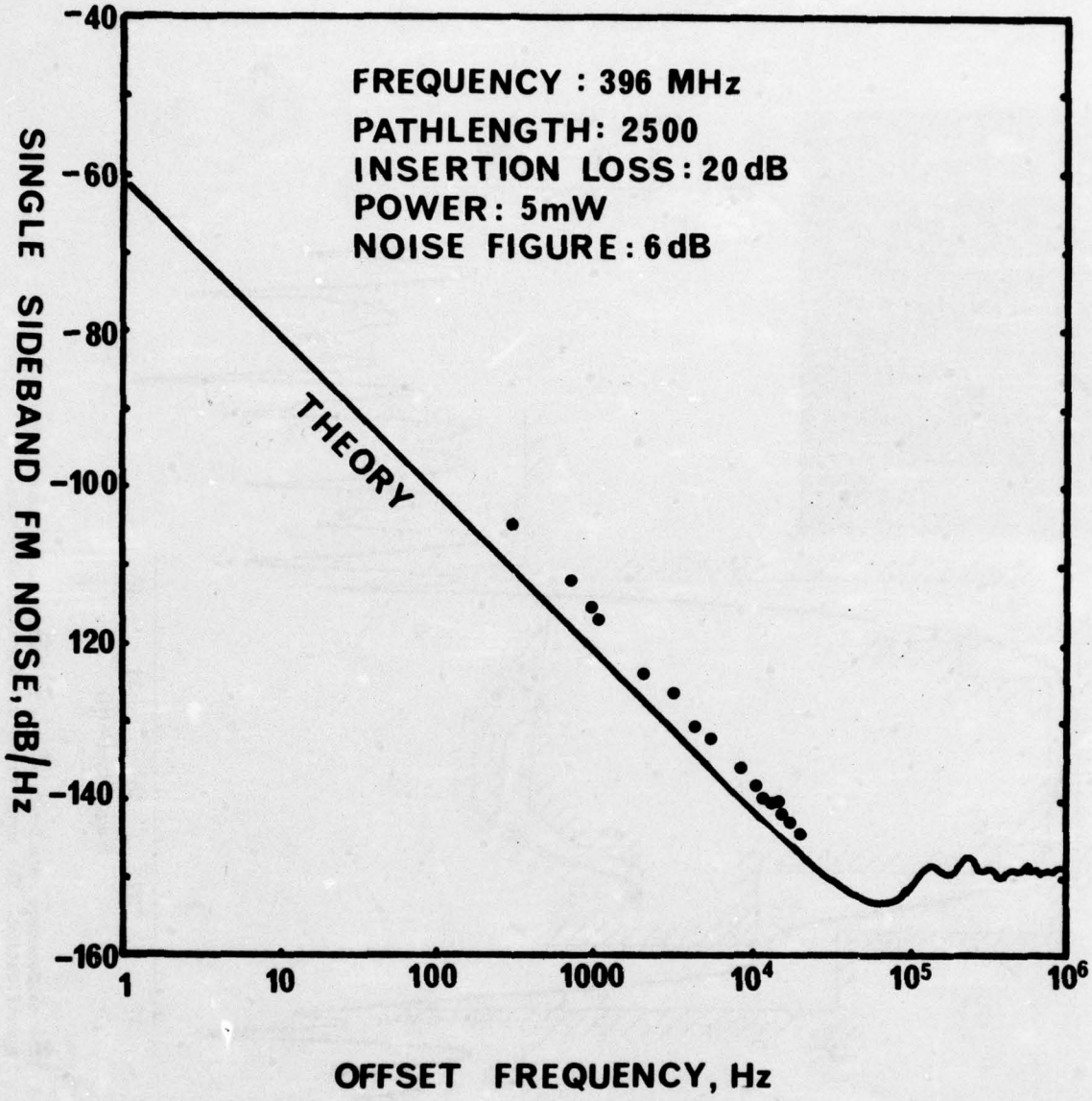

Fig 5 Single sideband FM noise spectral density as a function of offset from centre frequency.

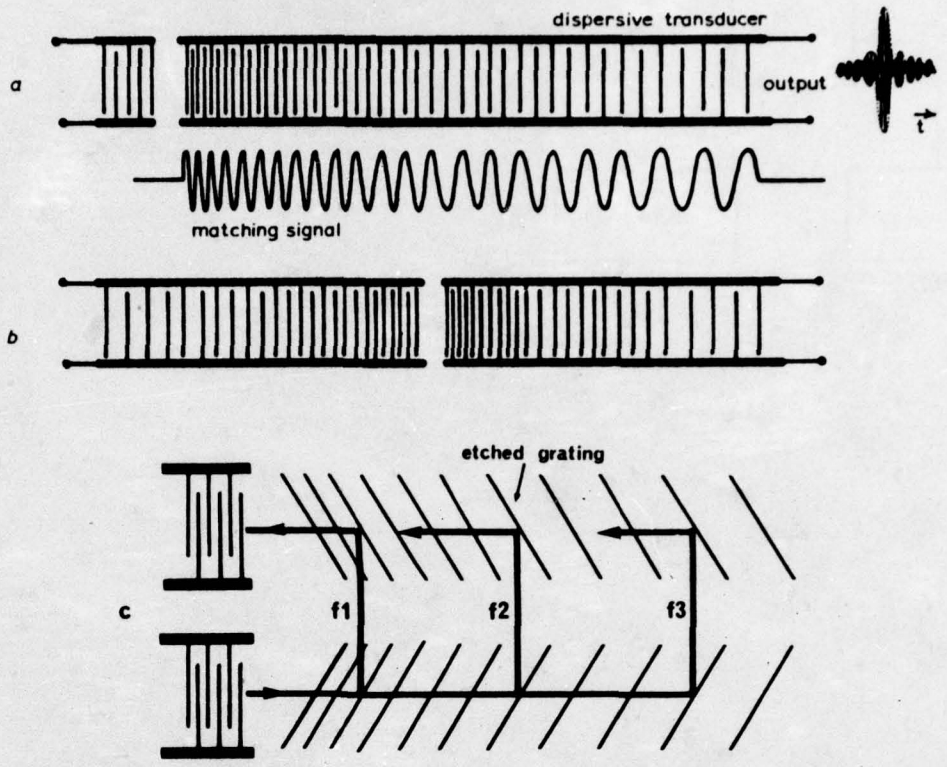

Fig 6 Three basic forms of matched filter for chirp signals. (a) A dispersive delay line with dispersion designed into one transducer. (b) A dispersive delay line with dispersion in both transducers. (c) A reflective array compressor (RAC).

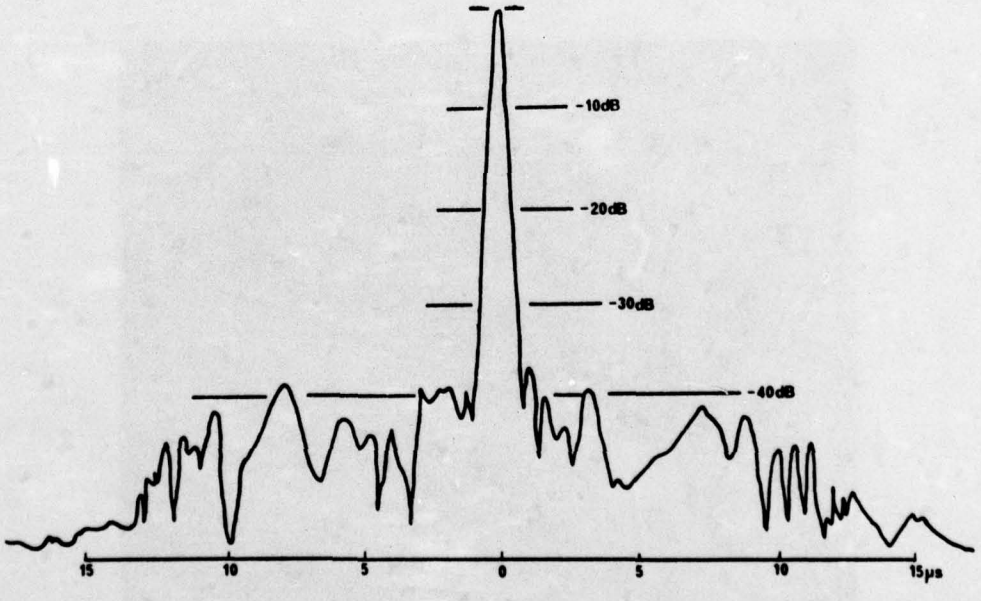

Fig 7 The sidelobes achieved using a SAW pulse compressor weighted by using a nonlinear FM phase profile.

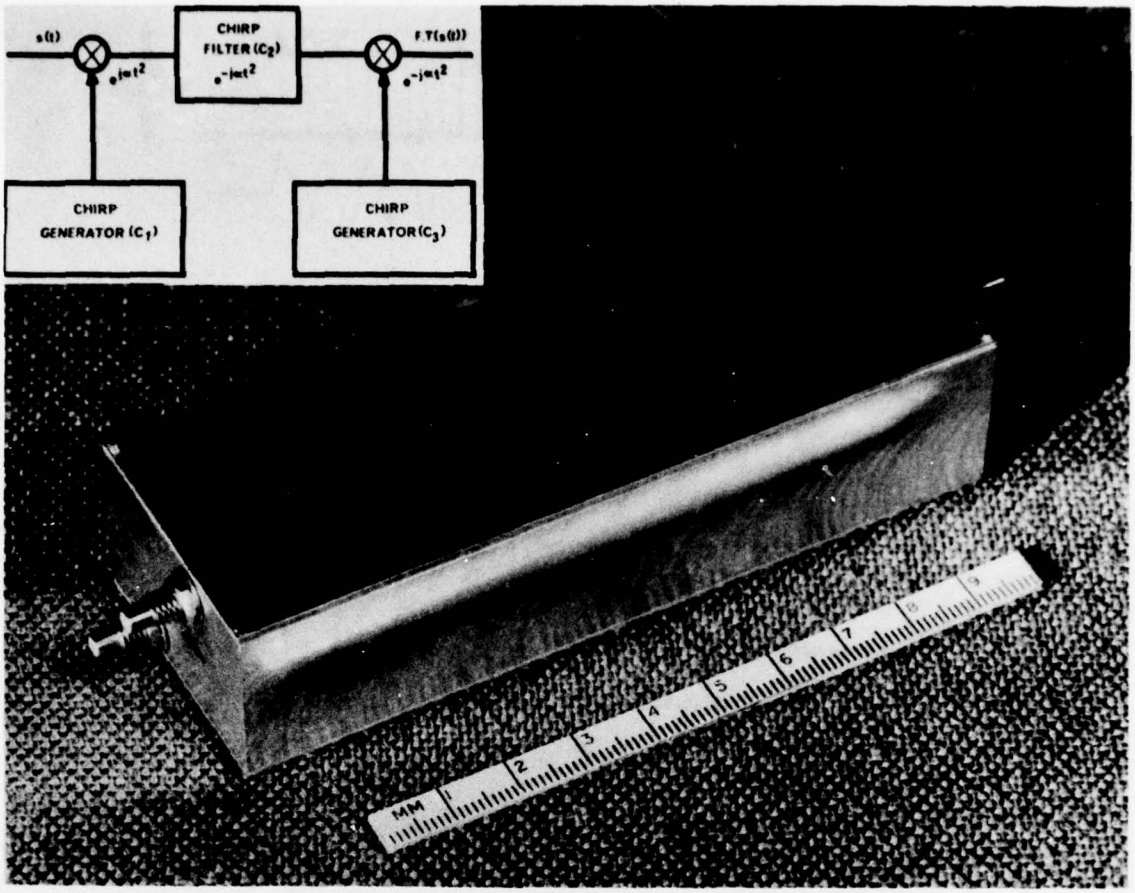

Fig 8 Surface-wave implementation of a Fourier transformer using the chirp transform.

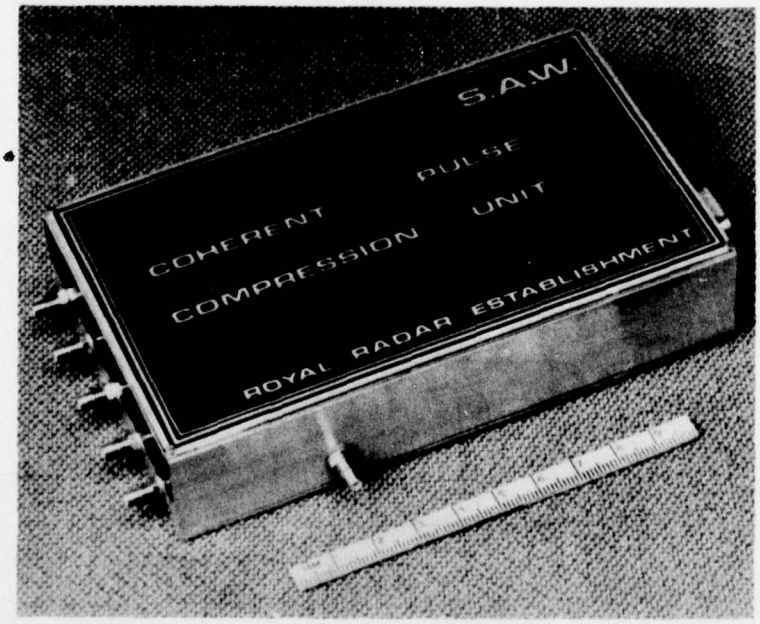

Fig 9 Complete IF unit for a coherent radar. The subsystem contains the waveform generator and IF receiver circuits.

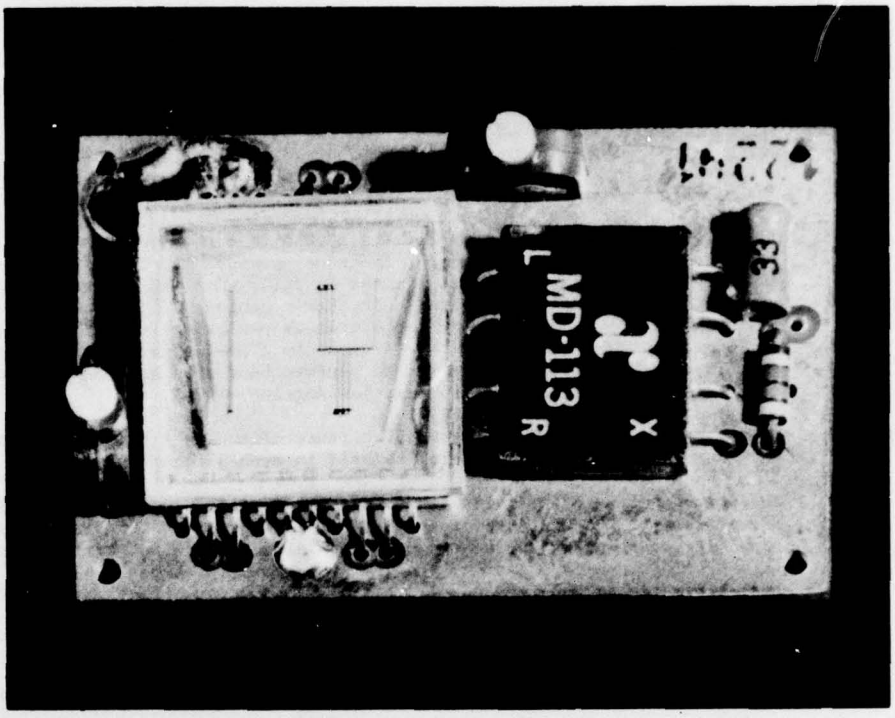

Fig 10 A prototype DDSK demodulator for application to SSR.

DISCUSSION

P NERI: Could you comment on the problems of multiple reflections between the transducers?

J D MAINES: Normally that part of the signal involved in multiple reflections is small. There is not enough time now to discuss this in detail.

G GRAF: 1 The delay in a SAW device is given by the spacing of the transducers. How are variable delay lines made?

2 Is it possible to make variable filters with this technique?

J D MAINES: 1 SAW delay lines usually have a fixed delay: discretely variable delay is possible using tapped delay lines. Continuously variable delay lines use combinations of dispersive delay lines and voltage-controlled oscillators. A particular scheme is described in the written paper.

2 Variable filters can be made using a related technique. A Fourier transformer (as already described) permits the frequency components of a signal to be displayed as a function of time. If this process is followed by an inverse Fourier transform, (equally easily implemented using SAW techniques) the signal is restored to its original form. Between the two processes manipulation of the signal can be performed to effect filtering, for example by time-gating, particular Fourier components can be stopped or selected to perform band stop or band pass functions. (See PROC IEEE Ultrasonic Symposium, Los Angeles, 1975).

B C KAYSERILIOGLU: What can be done to eliminate the RF capture effect in a pulse compression receiver? How can a non-linear gain control be used in such a receiver?

J D MAINES: The pulse compression filters I have discussed will do nothing to eliminate capture effects due to non-linear processes which precede them. Capture occurs where target responses overlap, and preventing overlap is the only effective means of reducing it. Overlap is a more serious problem in pulse compression because of the relatively long transmitted pulse. I suggest that the only practical method of eliminating capture is to use large dynamic range receivers.

R CARRE: Quel est le nombre de points definis dans la transformée de Fourier?

J D MAINES: The time-bandwidth product of the Fourier transformer I described was 250 so that it corresponds to a 250 point Fourier transform. This does not represent a limit and several thousand point transforms are in principle possible.

G GRAF: What is the dynamic range of SAW devices?

J D MAINES: SAW delay lines have a very large dynamic range, particularly on quartz (100 dB has been quoted). It is less for $LiNbO_3$ but, even so, the associated electronics are always the limiting factor in dynamic range.

R K MOORE: What is a typical insertion loss?

J D MAINES: Insertion loss varies with type of device. Using specialist techniques losses as low as 0.5 dB have been achieved in narrow band filters, while some dispersive delay lines give losses as high as 50 dB. 10 dB is an approximate figure for non-dispersive delay lines and 30 dB for dispersers. Fortunately, in IF processing loss in the SAW device is rarely a limiting factor in setting the S/N ratio of the receiver.

J S YU: Would you please comment on when and how a -70 dB sidelobe level could be accomplished?

J D MAINES: A -70 dB maximum sidelobe level is an extremely difficult proposition; it implies control of phase and amplitude to very small fractions of degrees and dB's. There is no motivation for achieving this level of performance in practical dispersers since the required weighting factor would produce a prohibitive broadening of the compressed pulse. In band-pass filters, out-of-band frequency responses as low as -70 dB have been achieved indicating a very high degree of control over spurious responses.

M TABOURIER: Problèmes de microphonie de dérivé thermique dans les dispositifs SAW?

J D MAINES: I have no direct experience with SAW devices operating in conditions of high vibration. However I can say that SAW oscillators and pulse compression filters have not exhibited any significant problems in this respect. Thermal effects can be minimised on quartz by correct choice of orientation. ST cut quartz exhibits a zero coefficient of temperature near room temperature. The temperature coefficient is approximately 3 ppm/°C over the range typically specified for military applications. $LiNbO_3$ is inferior in this respect, its temperature coefficient is about 80 ppm/°C.

B CHIRON: Quand on excite une onde de surface on excite également une onde(s) de volume parasite(s). Comment faites-vous pour éliminer l'onde de volume?

J D MAINES: Some volume waves are easily reduced by making the back surface of the substrate rough. This technique does not remove bulk waves which propagate close to the surface and such waves are usually eliminated by suitable choice of crystalographic orientation for the piezoelectric substrate or by the use of a device called a multistrip coupler in strongly piezoelectric materials. For most SAW devices, bulk acoustic waves should not now be a problem when the device is designed by a specialist laboratory.

ANALOG MEMORY CORRELATORS FOR RADAR SIGNAL PROCESSING*

Ernest Stern
Lincoln Laboratory, Massachusetts Institute of Technology
Lexington, Massachusetts 02173
United States

SUMMARY

Acoustoelectric convolvers, memory correlators and coherent integrators are being developed at M.I.T. Lincoln Laboratory for spread-spectrum communication and radar systems. Performance details of each of these devices is given, and their potential utility for radars is assessed. For example, memory-correlators have been realized which perform the functions of storing a reference waveform for a time-interval as long as 50 msec, and of cross-correlating subsequent signals with the stored reference. In a radar, a sample of the transmitted pulse could be stored in the device, and radar echoes from targets would subsequently correlate with a sample of the actual transmitted signal. This is in contrast to conventional radar receivers, where radar echoes cross-correlate with a predetermined matched filter, which may or may not be matched to the actual transmitted signal. Radar systems are periodically aligned, to bring the transmitted waveform characteristics as close as possible to the characteristics of the matched filter. By using a memory correlator in place of a matched filter it seems reasonable to expect a substantial reduction in time spent to re-align the system. Also the memory correlator can be used to process any waveform which lies within the time-bandwidth constraints of the device, whereas a separate matched filter is required for each waveform in conventional radars.

1. INTRODUCTION

Modern radars transmit frequency or phase-modulated waveforms to resolve targets in range and velocity. Usually a fixed matched filter is employed to obtain the maximum possible signal-to-noise ratio in the receiver, and a waveform generator-matched filter pair is employed for each waveform in the radar. The optimum waveform for a particular radar function depends on a host of parameters, including radar power, antenna gain, target cross-section, density of targets, range, the presence of interfering and jamming signals, clutter, etc. Thus a large number of waveforms would be desirable to provide for a large variety of situations. However, it is relatively expensive to implement a given waveform, and the radar designer with a limited budget specifies no more than several waveforms in conventional radars.

Considerable effort has been expended during the past decade to develop a more flexible signal processing device which is capable of processing many waveforms. The current flowering of digital signal processing technology is a result of this effort, and digital signal processors have been built that can handle a large variety of waveforms having moderate bandwidths and time-bandwidth products of several hundred. These devices rapidly increase in size and complexity for signals with a bandwidth in excess of several tens of MHz, or with a time bandwidth product larger than 1000. An alternative technology which exploits surface acoustic wave interactions with semiconductors is being explored which may provide similar signal processing flexibility at lower cost, power consumption and size. One approach is to use an analog Fourier transform technique called Chirp-Z. Dr. E.G.S. Paige, in a paper in this Proceedings, gives a detailed description of this technique. Other approaches utilizing non-linear acoustic and acoustoelectric interactions are also being explored for the purpose of providing either the convolution or correlation of two waveforms. This paper describes several devices currently under development at Lincoln Laboratory which perform this function.

2. SURFACE ACOUSTIC WAVE CONVOLVERS

The convolver has been investigated widely in Norway[1], France[2], England[3], and the United States[4]. Many different physical configurations have been proposed and studied. All of these devices provide for the propagation of one waveform through another, for the nonlinear interaction between the two waveforms at every point of overlap, and for summing these non-linear products. This provides the signal processing function

$$\int_0^L f_1(\omega t - \beta x) \cdot f_2(\omega t + \beta x)\,dx \quad .$$

Except for time compression of the output signal by a factor of two, the output corresponds exactly to the convolution of f_1 with f_2.

We at Lincoln Laboratory elected to develop an acoustoelectric convolver with a Lithium Niobate ($LiNbO_3$) surface wave delay line and an adjacent block of silicon (Si) as shown in Fig. 1. $LiNbO_3$ is a piezoelectric, and acoustic waves propagating along its surface typically have electric fields of several hundred volts/cm associated with the wave. A block of n-type Si is held a small fraction of an acoustic wavelength away from the surface of the $LiNbO_3$. The Si surface is ordinarily depleted of carriers, as shown in the figure. The piezoelectric field distorts the carrier distribution as shown schematically in the figure, and the impedance of incremental transverse segments of the structure are proportional to this field intensity. A reference waveform is entered from the left and a signal is entered from the right of the structure. Where these signals overlap a current is generated which is

* This work is sponsored by the Department of the Army and the Advanced Research Projects Agency.

proportional to the product of the local fields. These incremental currents are summed at the output electrode and the signal at the output terminal corresponds to the convolution of the reference with the signal. Typically the silicon must be held 2000 $\pm$ 100 Å away from the $LiNbO_3$ for optimum performance. This is done with a pseudorandom distribution of small spacer posts on the surface of the $LiNbO_3$. These posts are small in diameter compared to an acoustic wavelength and are separated by several hundred wavelengths to minimize the scattering of acoustic energy. The Si is held against the posts with a compliant RTV gel. A photograph of the open device is in Fig. 2a, which shows the Si strip on the transparent gel, and the $LiNbO_3$ delay line with aluminum ground electrodes and transducer. The Si is placed against the $LiNbO_3$, where it acts as the center conductor of a microstrip line. A picture of the partially assembled finished convolver, in Fig. 2b, shows the back of the silicon holder. The silicon strip has electrodes at each end and in the middle. The end electrodes are terminated with the characteristic impedance of the microstrip line inside the slots at the ends of the internal block. The central electrode is connected through a transformer to the output terminal. Impedance matching networks are visible at the two input terminals to the convolver.

The matched filter function in a radar is the correlation of a reference with the signal, which is equivalent to convolving the signal with the time-reverse of the reference. This can be done readily for phase coded waveforms by entering the reference signal into a first in, last out, random access memory. A typical correlation impulse is shown in Fig. 3 for a 1000-bit segment of a continuously changing, very long pseudorandom code with a bandwidth of 100 MHz, and a time duration of 10 μs. The smeared-out time sidelobes in this instance are due to the code, not the device. The performance characteristics of the device are summarized in Table 1.

Real-time signal processing requires several convolvers operated in tandem in order to provide for continuing presence of a time-reversed reference signal for returning radar echos. In order to avoid this difficulty, workers at Lincoln Laboratory searched for a means to provide a stationary reference waveform, and to correlate subsequent signals with the stationary stored reference. We call this process memory-correlation[5]. Such a device should perform the true mathematical function of correlation

$$\int_0^L f_1(kx) \cdot f_2(\omega t + kx)\, dx \quad .$$

3. MEMORY CORRELATOR

Memory correlators are currently under study at several laboratories[6,7,8]. We simulated on a computer the function of a memory correlator in order to evaluate the potential usefulness of the concept for processing typical radar waveforms. Figure 4a shows the cross-correlation of a doppler-shifted linear frequency-modulated waveform with an ideal amplitude-weighted reference. Note that range ambiguities occur 37 dB below the main signals. Figure 4b shows the cross-correlation of a badly distorted waveform (900° cubic, 300° quartic phase error) with an ideal reference. Here the main lobe is broadened, and many range ambiguities are obtained well above the -37 dB level. Figure 4c shows the cross correlation of a doppler-shifted distorted signal with a reference which corresponds to the initial distorted transmitted waveform. Notice in this instance the main pulse-width is not increased, and the range ambiguities have been reduced to a negligible number. Thus, the ability to commit to memory the actual linear-frequency modulated waveform and subsequently correlate radar echoes with this stored reference is likely to yield a signal processing system which is forgiving of phase distortions in the waveform generator and radar system. However, memory-correlators cannot compensate effectively for amplitude errors, and care must be taken to maintain the appropriate amplitude characteristics in the system.

The current most successful memory-correlator configuration is shown in Fig. 5. It is similar to the acoustoelectric convolver, except that the Si interface is covered with a two-dimensional array of Schottky diodes. The diodes are on 10 ohm-cm n-type Si. The equivalent circuit for the diodes is and electronically variable resistor in parallel with a variable capacitor. In the forward-bias state, the RC time constant of the circuit is about one ns, and in the reverse bias state, it can be as large as 0.1 sec at 25°C. A reference waveform is entered on the lithium niobate as shown in Fig. 5a. When the waveform is in position, the Schottky diodes are forward biased momentarily, currents flow in response to the combined bias and piezoelectric fields, and image-charges are retained in the diode contacts in response to the piezoelectric field of the surface wave. Figure 5b shows this retained charge distorting the underlying carrier distribution and locally affecting the impedance of the Si. A subsequent signal interacts nonlinearly with the Si to produce the true correlation of the signal with the stored image. Unlike the convolver of Fig. 1, the output signal is not time-compressed, because the reference waveform is stationary rather than moving. Since it is possible to enter the signal from the same port as the reference, it is not necessary to time-reverse the reference.

Prototype devices have been built and demonstrated, and some results obtained with the device are shown in Fig. 6, where a CW pulse signal is entered into storage, and a continuous sequence of identical read-out signals are applied. Since the read-out signals are identical, the variation in the output signal is directly proportional to the strength of the stored image. The output is shown as a function of writing impulse duration, and storage time. Notice that the full image is entered into storage in about a ns, and that the decay-time of a stored image is about 100 ms in this particular diode array. Most of this decay is due to leakage currents at the periphery of the Schottky diodes, and orders of magnitude greater storage time could be available by lowering the temperature of the diodes, and by minimizing these leakage effects. These measurements were made with a diode array on 12.5 μm centers. The output signal is found to be independent of signal frequency up to 100 MHz, at which point only 2 1/2 diodes per wavelength are available. Further increases in frequency cause a decline in output signal, due to insufficient storage elements per wavelength. A typical acoustic transducer has a fractional bandwidth of 30% and is 100 wavelengths wide. Consequently each signal sample is stored in approximately two thousand diodes, and since the diodes are not electrically interconnected, a random distribution of defective diodes has a negligible effect in the performance of the device. We are

currently working on a device with a bandwidth capacity of 100 MHz with a carrier frequency of 300 MHz. The diode arrays for this device are on 4 μm centers. A preliminary result with such an array, without the overlay metallization, was obtained, and is shown in Fig. 7. The insertion loss and the correlation output as a function of frequency is shown in the figure. Notice that the correlation output closely tracks the insertion loss of the delay line. Thus the bandwidth appears to be limited primarily by the delay line, and not by the Schottky diodes. Also notice that a bandwidth of approximately 30 MHz is available in this device at an output signal level of -40 dBm, for input signals of 15 dBm. A dynamic range of 45 dB is available with a post-amplifier having an output noise level of -96 dBm. A linear frequency-modulated waveform was entered into memory, and a subsequent identical signal was correlated with it. The output signal is shown in Fig. 8 with time sidelobes 13 dB below the main pulse. The nulls between sidelobes are distorted, partly as a result of the exponential amplitude-weighting of the stored image and of the subsequent signal, which is caused by the acoustoelectric loss in the device. It is possible to compensate for this effect by adjusting the gap spacing or by varying Schottky diode density.

Generally it is desirable to include some form of amplitude-weighting in a matched filter to minimize range ambiguities. Perhaps an accurate electronically-variable attenuator could be used to weight the reference signal with a Hamming function, or some other appropriate function. This attenuator would be placed in the reference waveform circuit, where its operation would be synchronized with the reference signal.

The output signal amplitude is proportional to the ratio of the signal length with respect to the memory correlator length. Thus cross-correlating a 0.1 μs pulse with its reference in a 10 μs-long device would produce an output signal of about -80 dBm, which would be 40 dB below the maximum available output. If radar pulses are to be accomodated with different time durations, then it would be desirable to use an extended phase-coded transducer on the correlator, as shown in Fig. 9. For example, if a transducer pattern 3 μs long is used, then the output signal due to a very short pulse could be no more than 10 dB below the maximum output signal in a 10 μs-long memory-correlator. This is because both the reference waveform and the subsequent signal would be time-expanded to at least 3 μs.

These concepts and results suggest that it should be possible to build a memory correlator having a bandwidth of 100 MHz, a time duration of 10 μs, a dynamic range of 50 dB and a storage time in excess of 10 ms. Such a device could accommodate all waveforms which lie within these values. Such a device would be forgiving of phase errors in linear frequency-modulated waveforms, and relatively inaccurate and inexpensive electronically variable analog waveform generators could be used. Since the memory-correlator is self-compensating for phase-variations in the transmitted waveform, a transversal equalizer might not be necessary in the radar set, and system down-time due to re-tuning the transversal equalizer might be avoidable.

4. COHERENT INTEGRATOR

There are radar waveforms which exceed these parameters. In particular, a sequence of phase-coherent radar pulses, often called a burst waveform, have coherence-time durations extending to the ms range. The subpulses in such waveforms are typically no larger than 20 μs long, and the subpulse is phase or frequency-modulated to improve range resolution. Such waveforms are used to resolve nearby radar targets by detecting differences in velocity due to doppler shifts. A modified version of the memory correlator has been demonstrated which could be used to provide this velocity resolution. The device is called a coherent integrator, and it is shown schematically in Fig. 10. It is identical to the memory correlator except that the Schottky diodes are overlayed with polycrystalline Si. The effect of this overlay is to connect a series-RC circuit across each diode with a time constant of approximately 1 μs, as shown in the figure. A signal stored in the Schottky diode array contacts diffuses into the polysilicon. The initial charge in the polysilicon is retained despite the subsequent application of a short impulse because of the relatively long time-constant of the polysilicon. If the second and successive signals are exactly registered with each other, then the stored charge in the polysilicon increases with the number of overlays.

A succession of 3 μs CW pulses were overlayed in a coherent integrator prototype, and the results are shown in Fig. 11. In this experiment a signal is entered every 8 ms, and an identical readout signal is entered shortly thereafter, as indicated in the figure. The output signals are plotted as a function of time. Notice that the stored signal exponentially approaches a saturation value in about 80 ms. This saturation effect is due to the storage time-constant of the back-biased Schottky diodes.

This device could be used to process burst waveforms. Suppose there are n subpulses in a burst waveform which is transmitted by a radar. Then the received signal would be connected in parallel to m identical coherent integrators as shown in Fig. 12. All coherent integrators are simultaneously impulsed to store the first pulse returned from all targets in the designated range window. Each coherent integrator is impulsed n-1 times more in an attempt to overlay the remaining pulses. However, the timing of the write impulses to each coherent integrator is modified slightly to correspond to the anticipated time compression anticipated in each velocity channel. Thus only echoes from targets with a particular velocity are overlayed in any one device. A reference waveform is subsequently propagated through all coherent integrators, and the output signals from any one device correspond to all targets of a particular velocity in the range window. The combined outputs from m coherent integrators resolve all targets in range and velocity that occur within the range window.

Such devices might eventually become available for processing burst waveform echoes from targets inside a 5 km range window. The burst could have sub-pulse bandwidths up to 100 MHz, and coherence times of 10 ms.

5. CONCLUSION

In summary, acoustoelectric convolvers have been reduced to practice with time-bandwidth products of 1000 and bandwidths of 100 MHz. Memory correlators with similar capacities show promise of being capable of processing a multitude of waveforms, and are expected to be insensitive to phase distortions in a radar. Coherent integrators have been demonstrated which may ultimately be capable of processing a large number of burst waveforms with many different subpulse and inter-pulse parameters, but with a limited range window of about five miles. The modulation of the subpulses in a particular burst waveform must be identical, but the time-delay among subpulses could be varied to minimize doppler and range ambiguity.

All these components are relatively small and are likely to require a relatively small amount of peripheral electronic equipment. With components such as these it may become possible to use sophisticated waveforms in relatively inexpensive radars.

REFERENCES

1. Svaasand, L.O., "Interaction Between Elastic Surface Waves in Piezoelectric Materials", Appl. Phys. Letters, Vol. 15, p. 300, 1969.

2. Defranould, P. and C. Maerfeld, "Acoustic Convolver Using Multistrip Beam Compressor", 1974 Ultrasonic Symposium Proceedings (IEEE: New York, 1974) p. 224.

3. Morgan, D.P. et al, "Programmable Correlation Using Parametric Interactions in Acoustic Surface Waves", Electron. Lett., Vol. 8, p. 40, 1972.

   Morgan, D. P. and J.M. Hannah, "Correlation of Long Sequences by a Surface Acoustic Wave Convolver", Electron. Lett., Vol. 11, p. 193, 1975.

4. Wang, W. C. and P. Das, "Surface Wave Convolver via Space Charge Nonlinearity", 1972 Ultrasonic Symposium Proceedings (IEEE: New York, 1972) p. 316.

   Otto, O. W. and N.J. Moll, "A Lithium Niobate Silicon Surface Wave Convolutor", Electron. Lett., Vol. 8, p. 600, 1972.

   Smith, J. M., et al, "Surface Acoustoelectric Convolvers", 1973 Ultrasonic Symposium Proceedings, (IEEE: New York, 1973) p. 142.

   Kino, G. S., et al, "Signal Processing by Parametric Interactions in Delay Line Devices", IEEE Trans. Sonics and Ultrasonics, Vol. SU20, p. 162, 1973.

5. Stern, E. and R. C. Williamson, "A New Signal Processing Concept", Electron. Lett., Vol. 10, p. 58, 1974.

6. Ingebrigtsen, K. A. et al, "A Schottky Diode Acoustic Memory and Correlator", Appl. Phys. Lett., Vol. 27, p. 170, 1975.

7. Shiren, N. S. and R. L. Melcher, "Acoustically Induced Charge Transfer and Storage in Piezoelectric Semiconductor", 1974 Ultrasonics Symposium Proceedings (IEEE: New York, 1974) p. 572.

8. Maerfeld, C. et al, "Acoustic Storage and Processing Devices Using P-N Diodes", Appl. Phys. Lett., Vol. 27, p. 577, 1975.

9. Ingebrigtsen, K. A. and E. Stern, "Coherent Integration and Correlation in a Modified Acousto-electric Memory Correlator", Appl. Phys. Lett., Vol. 27, p. 170, 1975.

TABLE 1

Convolver Performance Summary

Bandwidth	100 MHz
Convolution Interval	10 μsec
Time-Bandwidth Product	1000
Convolution Uniformity	± 1/2 dB
Dynamic Range	50 dB (+14 dBm reference input)
Spurious Signals	>40 dB down from output
Temperature Range	-25°C to +50°C

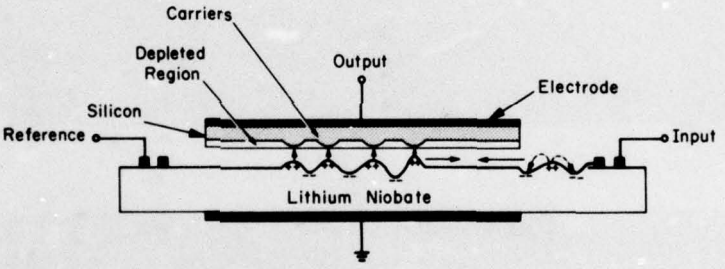

ACOUSTOELECTRIC CONVOLVER

Fig. 1 Acoustoelectric convolver schematic

(a)

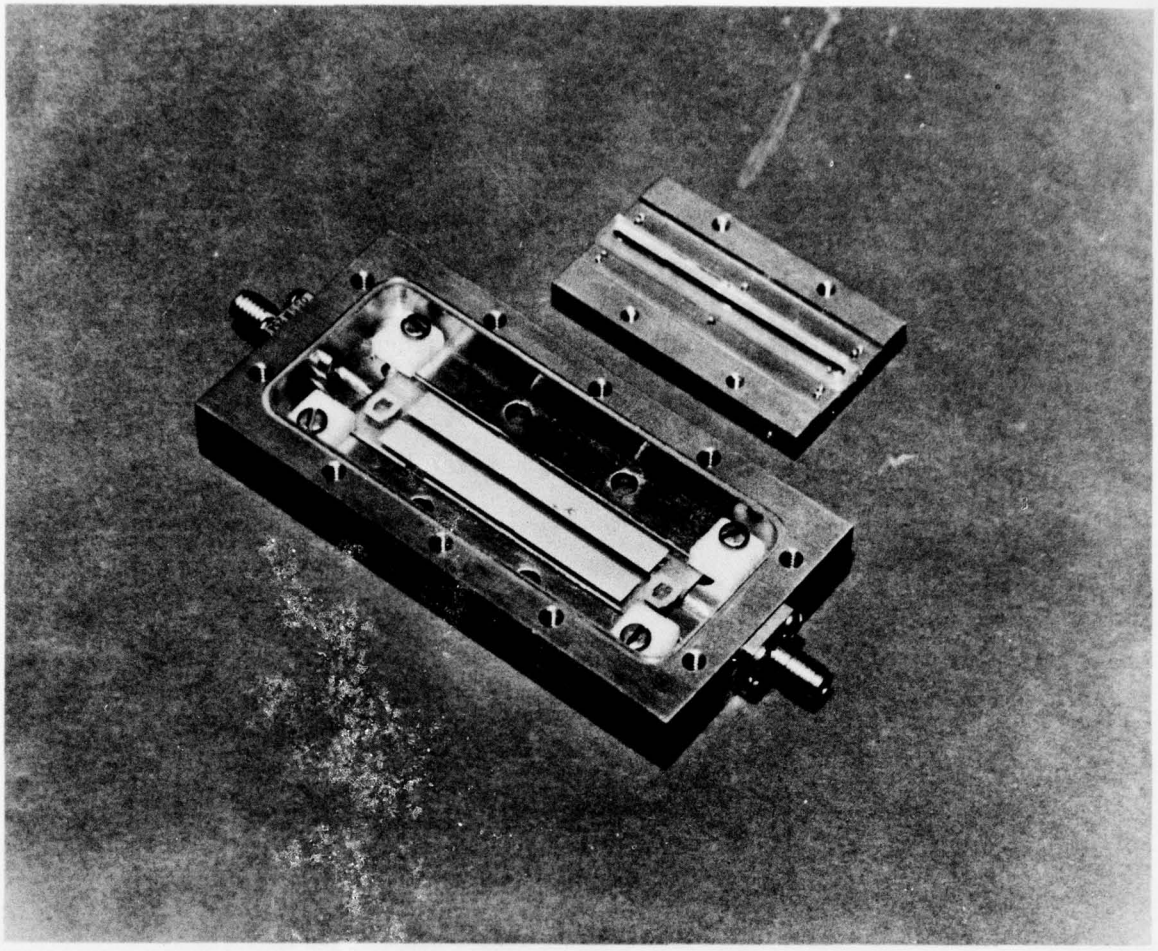

(b)

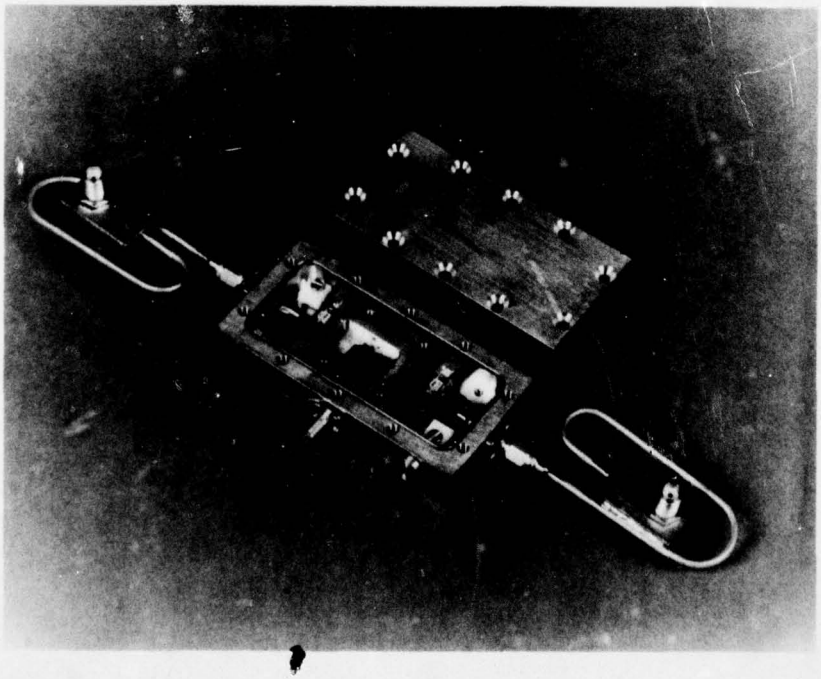

Fig. 2 Disassembled convolver showing lithium niobate and silicon elements. The silicon is on RTV gel, and the lithium niobate delay line has metallic ground planes and transducers on its surface

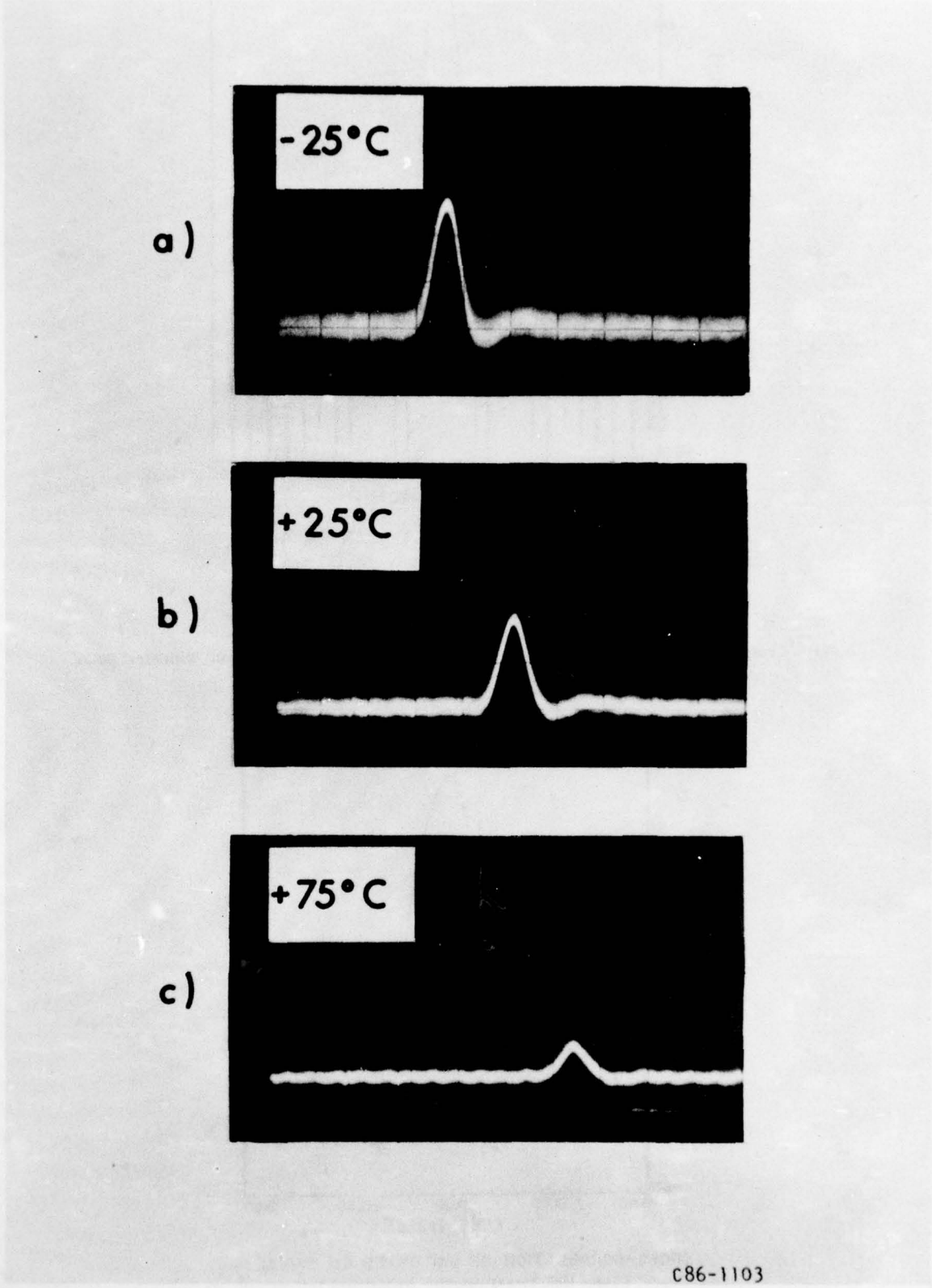

Fig.3 Correlation impulse of a 10-μs long pseudorandom code with 500 code elements. The code changes continuously and the average time-sidelobe level is 23 dB below the main pulse

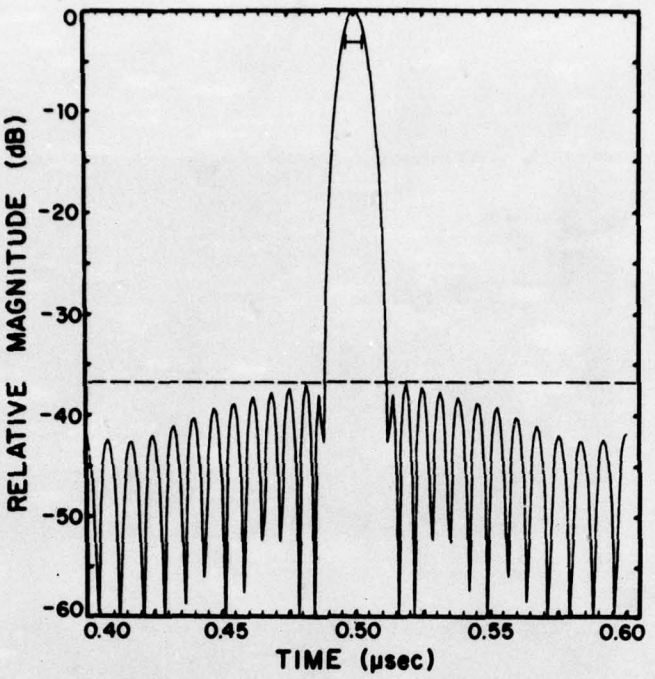

Fig.4(a) Cross correlation of linear FM signal (TW-150, target velocity 18000 mph) with ideal pulse compressor having 40-dB Taylor weighting

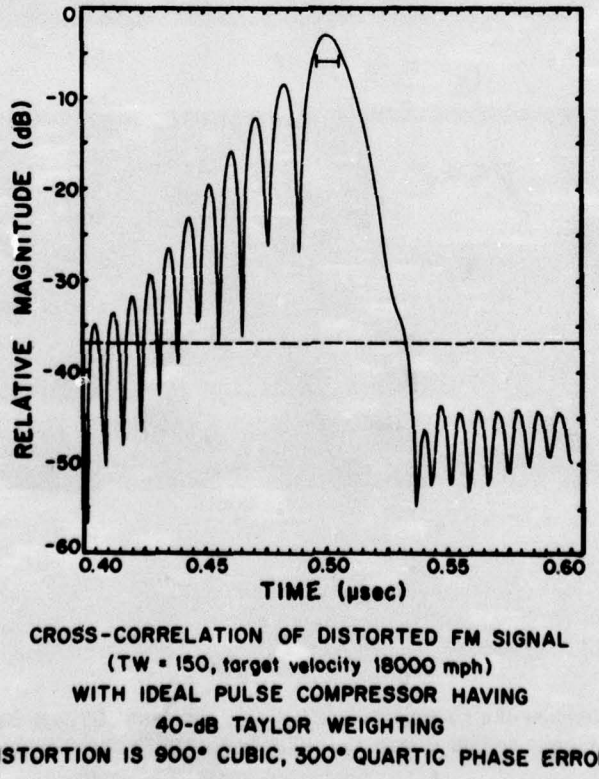

Fig.4(b) Cross correlation of distorted FM signal having 900-deg cubic, 300-deg quartic phase error with ideal pulse compressor

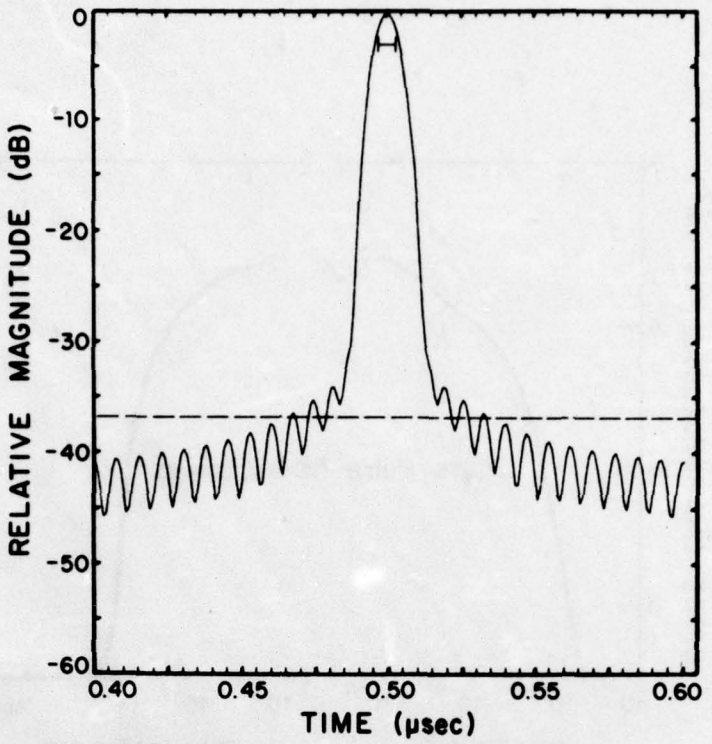

CROSS-CORRELATION OF DISTORTED FM SIGNAL
(TW = 150, target velocity is 18000 mph)
WITH DISTORTED REFERENCE WAVEFORM
HAVING 40-dB TAYLOR WEIGHTING
DISTORTION IS 900° CUBIC, AND 300° QUARTIC
PHASE ERROR

Fig.4(c) Autocorrelation of distorted FM signal having 900-deg cubic, 300-deg quartic phase error

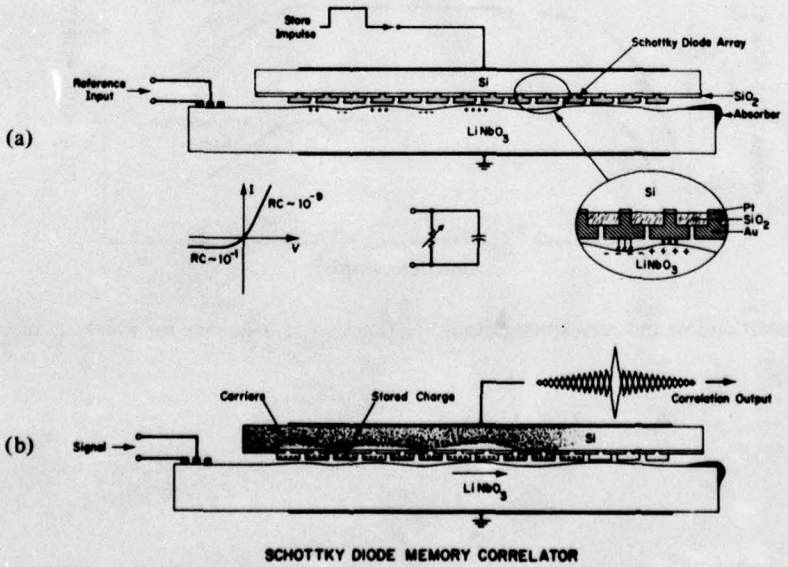

SCHOTTKY DIODE MEMORY CORRELATOR

Fig.5 Schottky diode memory correlator: (a) forward and reverse biased Schottky diodes have a time constant of 10^{-9} and 10^{-1} sec. Equivalent circuit is shown. When an acoustic signal is in position the diodes are forward biased momentarily and an instantaneous current flows in response to the piezoelectric field. (b) The retained charge on the Schottky diode contact distorts the carrier distribution in the bulk silicon. Subsequent signals cross-correlate with this carrier distribution

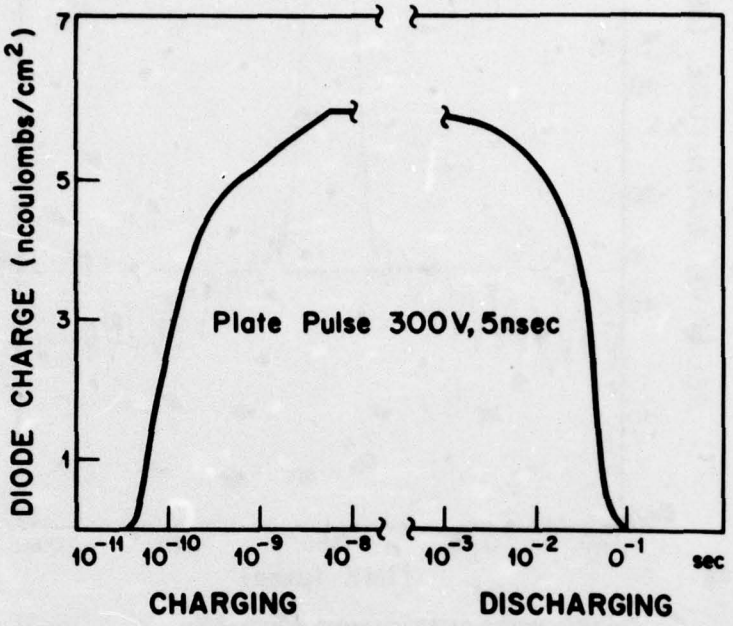

Fig.6 The charging and discharging characteristics of memory correlator. Note that the charging time constant is about one ns and the storage time is 0.1 sec

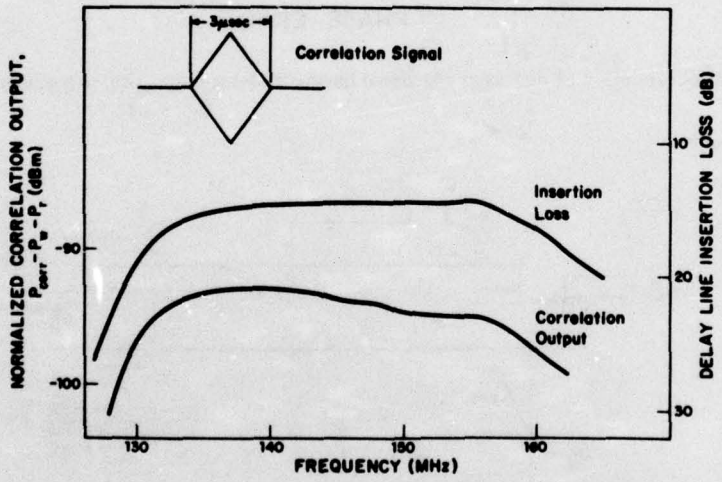

Fig.7 Delay line insertion loss and correlation output as a function of frequency for wideband memory correlator

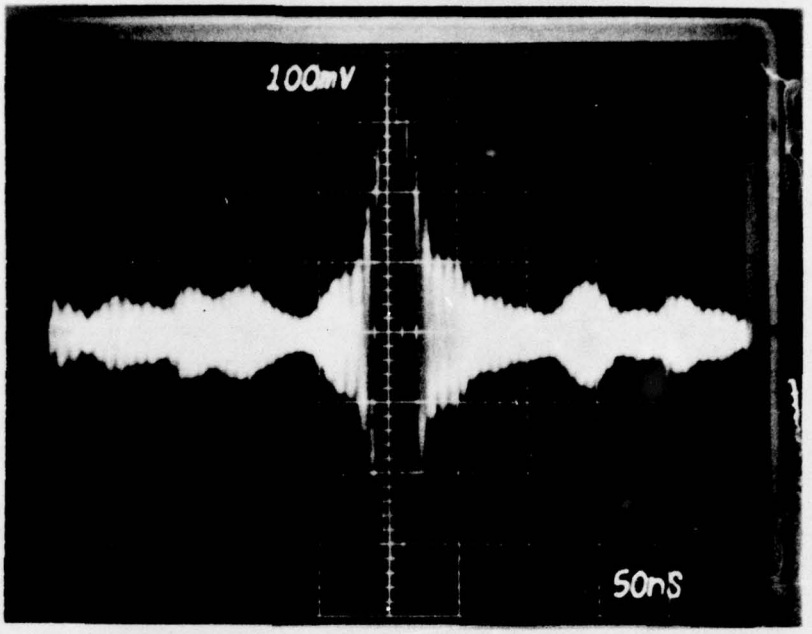

Fig.8 Correlation of a linear frequency-modulated impulse im memory correlator. The impuse bandwidth is 30 MHz with a duration time of 1.5 μs

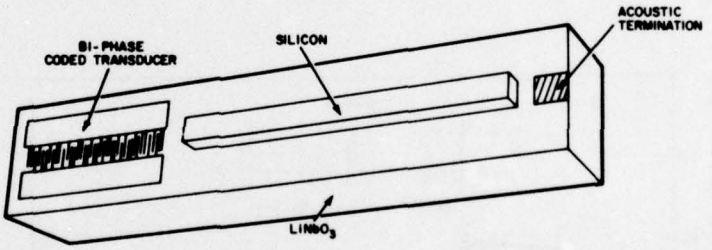

Fig.9 Memory correlator with extended input transducer

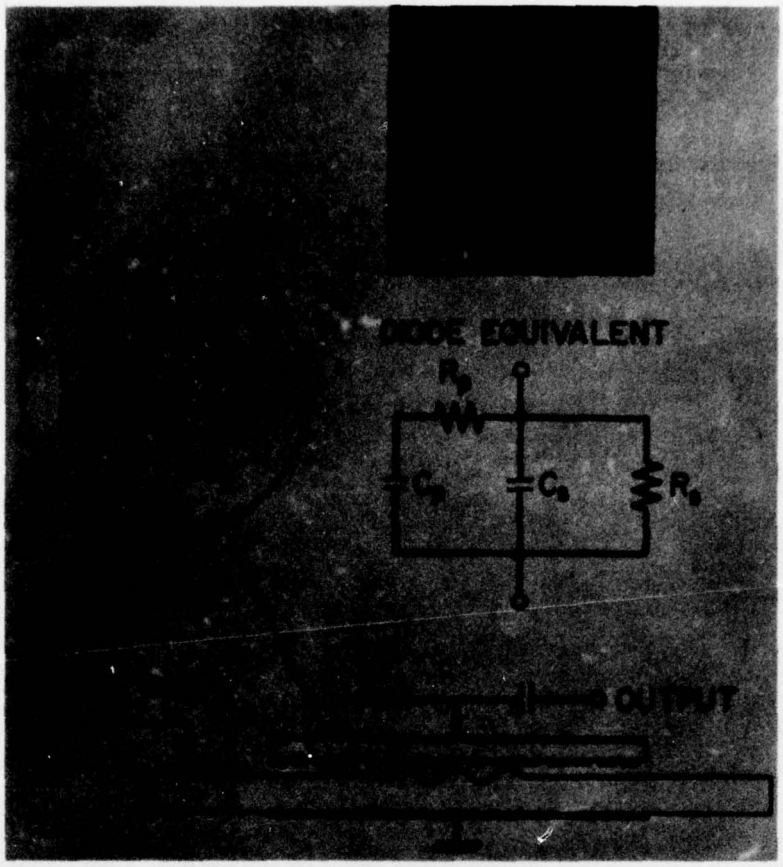

Fig.10 Schematic of coherent integrator. The time constant $R_pC_p = 10^{-6}$ sec. The constant R_sC_s of forward and reverse-biased Schottky diodes is 10^{-9} and 10^{-1} sec, respectively

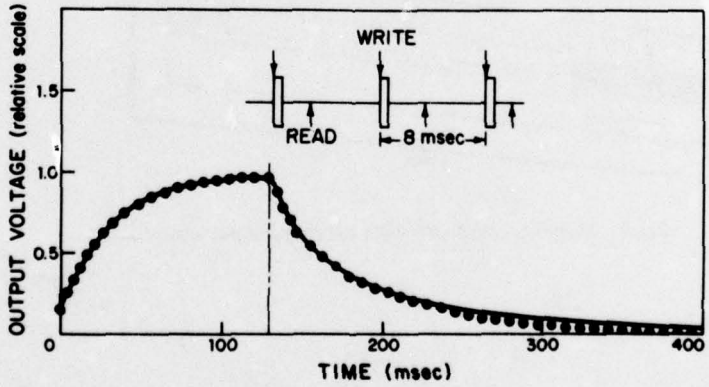

INTEGRATION GAIN AND DECAY

Fig.11 Output voltage of coherent integrator with respect to time. Pulses are entered into storage as indicated, and a read impulse is entered shortly thereafter. The output signal shows the cross-correlation of the read impulse with the accumulated stored sum. At 120 ms the writing is discontinued and the decay of the sorted sum is observed

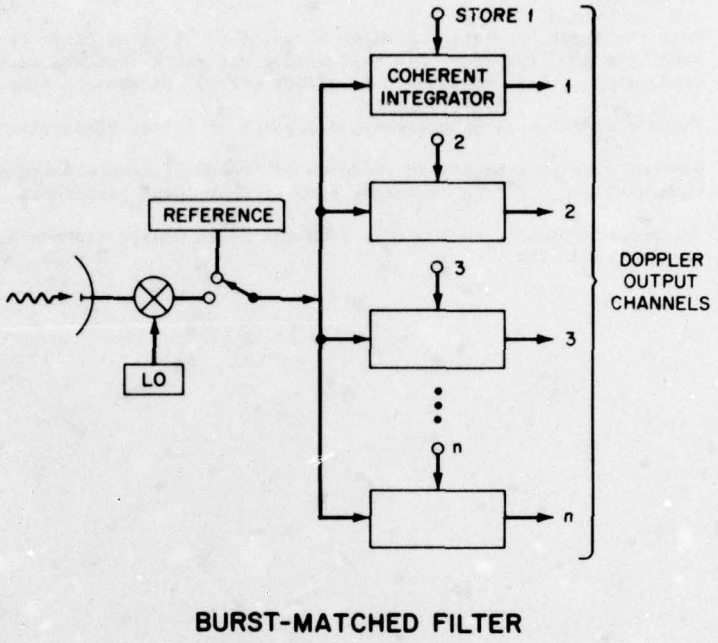

Fig. 12 Schematic of burst waveform processor with coherent integrators. The processor has n doppler resolution outputs

DISCUSSION

M J WITHERS: Could you comment on the possibility of making dispersive delay lines with a long dispersive time by cascading several lines?

E STERN: Cascading lines usually causes bandwidth compression and introduces phase error. Bandwidth compression can be anticipated and incorporated in the design, and phase error can be measured and subsequently corrected. We are building a device of two cascaded expander-compressors and anticipate good performance for a dispersion of 300 μS.

A J DUNLOP: Does the phase correction have to be added to an array after construction and metallisation, and does this represent a departure from the usual SAW device processing cycle? How does this affect overall processing time and device cost?

E STERN: Phase correction is unnecessary in devices of modest processing capacity.

Devices with time-bandwidth products in excess of several hundred require some compensation. It is a necessary step if near-ideal performance is desired.

The compensation is done with a computer-aided design procedure and increases the cost by about 25%.

MTI-FILTERS USING SERIAL ANALOGUE MEMORIES

by

Dr W.Kothmann
Siemens AG, Zentral-Laboratorium für
Nachrichtentecknik,
Lab. 747
8000 München 70
Postfach 70 00 77
Germany

MTI FILTERS

One of the many results of the great technological progress in the field of semiconductors in the last decade has been the development of MTI filters for the suppression of permanent echoes in pulse-doppler radar sets with considerably improved performance. The development objective has been greater flexibility and stability, higher processing speed, lower volume and smaller production costs. It is particularly since the appearance of large-scale integrated MOS shift registers and complete TTL arithmetic units that it has been possible to develop low-cost MTI filters which are satisfactory in operation. The following points favoured their development.

1. Simple adaptation of the filter characteristics to the special operating parameters of a radar set (e.g. minimum velocity of indicated target, variation of the pulse repetition frequency to avoid blind speeds etc.).
2. High stability of all characteristics with regard to environmental stresses and ageing phenomena.
3. Simple simulation procedure on a large computer, and as a result the possibility of optimizing all important operating parameters before hardware development. Furthermore, all the specification data necessary for the production of test records are obtained almost as a byproduct.
4. The use of components with standardized cases. This makes possible the development of a low-cost filter building-block system with simple test procedures for the individual modules (modular system).

Much effort has therefore been devoted in recent years to clarifying characteristics of these filters which have not previously been investigated, and to avoiding their weaknesses or at least reducing the effect of them. Efforts were concentrated in three principal directions:

(a) Improvements based on theoretical considerations. An attempt was made to extend the attainable dynamic range of the filters for a given signal resolution by suitable modification of the transfer function, by splitting into subsystems and by suitably combining the subsystems with each other.

(b) Improvements in the subsystems themselves as a result of optimization processes. By limiting the costly arithmetic units to the absolutely necessary, an endeavour was made to arrive at solutions with the minimum number of components, with low dissipations and maximum circuit transparency.

(c) Improvements in component technology. By using recently developed technologies, attempts have been made to obtain solutions requiring less space and less power with simultaneously increased filter operating speed.

In this context it has been possible to increase the speed of A/D converters, which represent the weakest link in a digital MTI filter, and favourable solutions have been found for the design of multipliers in the filter sections. As an example, (Fig.1), see Paper 1, I would like to show you a circuit design for a digital MTI filter with Chebyschev approximation response, which has been optimized with regard to dynamic range for permanent echoes and moving targets. It employs a signal resolution of 11 bits + sign. The filter coefficients have been reduced to a maximum of two simple powers of two, so that simple adders could be used instead of costly multiplers. The resulting deviation in magnitude of the transfer function from the nominal is not more than 0.5 dB. Operation of the A/D converter is based on the principle of step-by-step approximation with a conversion time of about 3 μs. It is the principal factor determining the maximum operating speed of the MTI Filter.

There are no doubt radar applications for which a moderate dynamic range is adequate, but for which a greater range resolution is required. This would require even higher conversion and computing speeds and could well be very difficult to realize.

A way out of this situation is available if the signals are retained in their original analogue form and electric charge storage devices are employed as storage elements. The following advantages result for the design.

1. The A/D converter is eliminated.
2. Simple resistive voltage dividers can be used instead of multipliers.
3. Adders take the form of small operational amplifiers.

The first analogue storage elements with low operating speed available on the market were the bucket-brigade devices. They consist of a chain of discrete sample-and-hold circuits, as shown in Figure 2. Each stage alternately stores signal values for half a clock period, i.e. two sample-and-hold circuits per delay stage are necessary.

Unfortunately the signal values are incompletely transferred from stage to stage, i.e. the input amplitude appears in an attenuated form after passing through the complete bucket chain and signal residues remain in the preceding stages – see Figure 3. This leads to target echo residue trailing behind the true target echo and results in range smearing on the indicator. The number of range intervals affected by range smearing increases with increasing shift-pulse frequency, i.e. as the range resolution of the radar set is increased. In addition, interference voltage components of the shift pulses considerably limit the dynamic range of the complete filter. Although the effect of the ambient temperature on the signal amplitude in the range intervals is relatively low in the individual stages, this effect is cumulative and not negligible at the end of the chain. It results in a filter with very temperature-dependent characteristics.

CCD's represent a further development of the analogue shift register. In principle they are similar to BBD's. In CCD's electric charges with magnitudes corresponding to the input signal amplitudes are transmitted beneath the surface of a semiconductor crystal in step with suitably chosen timing pulses and converted back into a signal voltage at the output. The characteristics of these devices have been continuously improved in recent years and their use in MTI filters has been investigated many times. The RETICON Co. of Mountain View, California has been offering low-cost serial analogue memories (SAM's) for about 1 1/2 years now.

Their mode of operation is as follows: Two independent shift registers activate a series of switches – see Figure 4. One register and its associated multiplexer sequentially time sample the analogue input signal, and store each sample on an individual capacitive storage element. This register is referred to as the read-in register since it reads the input signal into the memory. The second register (referred to as the read-out register) and its associated multiplexer are used to sequentially interrogate the memory elements, thus reconstructing an analogue output signal which is identical to the input signal, but with a new time base.

The two shift registers are driven by digital clocks which may be independent from each other and determine the read-in read-out sample rates. So the SAM may be operated as an analogue delay line by clocking both registers at the same rate, but delaying the initiation of read-out with respect to read-in.

This device is thus very flexible, any desired shift register length can be obtained by suitable clocking of the read-in and read-out processes. The maximum shift-pulse frequency is quoted as 12 MHz, i.e. a maximum range resolution of 12.5 m is theoretically possible in a radar set. A dynamic range of at least 50 dB is quoted for the device SAM 64. Using this device we have developed and tested a first laboratory model of an MTI filter. The results obtained indicate that the attainable dynamic range of the complete filter is smaller than anticipated. The reason for this is indicated below.

The signals in the individual storage locations of this device cannot be read out and read in again simultaneously. Thus when all available storage cells are used it is necessary to run the two processes sequentially, i.e. first read out and then read in again. The 64 storage locations in this device can thus accept signals from only 63 range intervals – see Figure 5.

This also means that signals from a particular range interval must be read into different storage locations in each receive period. The next illustration shows, as an example, how a signal is read in to storage location 1 during the first receive period while simultaneously storage location 2 is read out. After 63 range intervals, i.e. in the same range gate of the next receive period, the signal occurs in storage location 64. Storage location 1 is read out, in the following receive period storage location 63 is read in, storage location 64 read out, and so on. Since residual voltages of varying magnitudes occur at the switching transistors of the individual stages, the echo from a range interval is subjected to a different offset voltage in each receive period, which manifests itself as a periodic interference voltage limiting the filter dynamic range.

The conditions can be improved if the register is modified as shown in Figure 6.

1. An additional delay amounting to one range interval is provided by means of discrete sample-and-hold circuits at the outputs of the shift registers. The result of this is that a definite fixed storage location in the SAM 64 device can be assigned to each range interval after every 64 range intervals, and the offset voltage for each individual range interval remains constant.

2. A filter section after the manner of a delay-line canceller or a double-delay-line canceller is provided as the last filter stage and used to suppress the constant interference signals, so that only the residual offset voltage from this stage remains.

An MTI filter for 128 range intervals based on these principles has the circuit design shown in Figure 7. It consists of the series connection of a delay-line canceller and a double-recursive stage, in which the available shift registers are used twice, combined with a double-delay-line canceller. Strong permanent echoes are so attenuated in the first stage that they do not overdrive the double-recursive stage, which exhibits strong resonance in the vicinity of the filter cutoff frequency. The filter coefficients are set with the aid of potentiometers and are derived from a design based on a bilinear Z transformation for a filter with Chebyschev approximation.

Figure 8 shows the mechanical design of the filter using a Europa PC board with dimensions 100 x 160 mm. The associated transfer function in the range from zero to half the sampling frequency is shown in Figure 9 together with the theoretical curve. In the temperature range from $-40°C$ to $+85°C$ the curve does not deviate by more than ± 0.5 dB from that measured at 25°C. The signal at the filter output in 16 consecutive range intervals is shown in the next illustration in order to demonstrate the low crosstalk – see Figure 10. Simulated moving target signals were injected into every fourth range interval only. A crosstalk attenuation of about 35 dB was measured. The manufacturer quotes an upper clock frequency limit of 12 MHz for the SAM 64. However, the filter that we have built cannot operate so quickly, since some of the operational amplifiers employed cannot satisfactorily process signals at such a clock frequency.

I would like to conclude with a comparison. If one wished to produce the same filter using digital devices, one would preferably use filter components from a building block system for reasons of reduced development costs, simplified production and in-service testing.

It would probably have to consist of two or three modules of 100 x 160 mm Europa board size, together with at least one further module for the A/D converter. The complete MTI filter with comparable characteristics would thus consist of three or four modules. The necessary electric power would be in the ratio 3.5 : 1 and material costs about in the ratio 4 : 1.

The MTI filter that has been described represents a contribution in the search for smaller and more economic solutions and can be seen as an alternative to solutions using BBD's and CCD's. If it becomes possible in future to develop storage elements with even greater dynamic ranges and operational amplifiers with even higher cutoff frequencies accompanied by adequate gain, and if these devices also have sufficient temperature stability, there will be no barrier to the return to analogue signal processing in MTI filters.

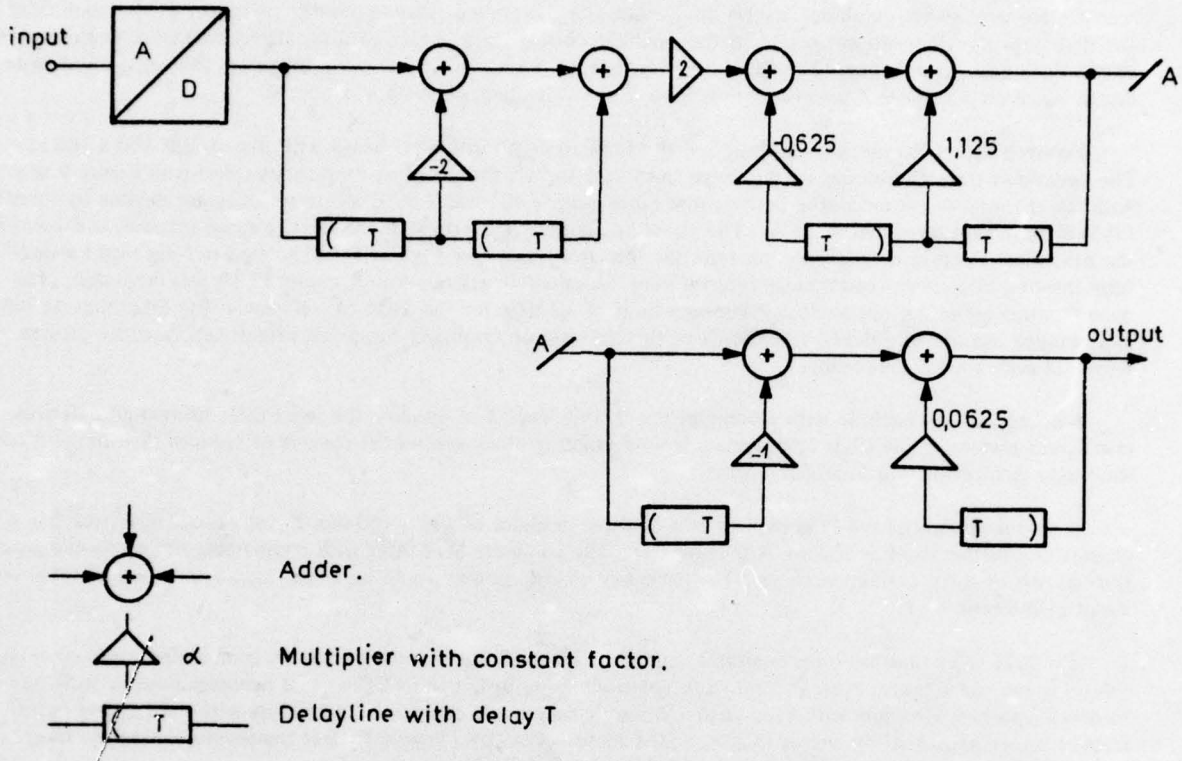

Figure 1

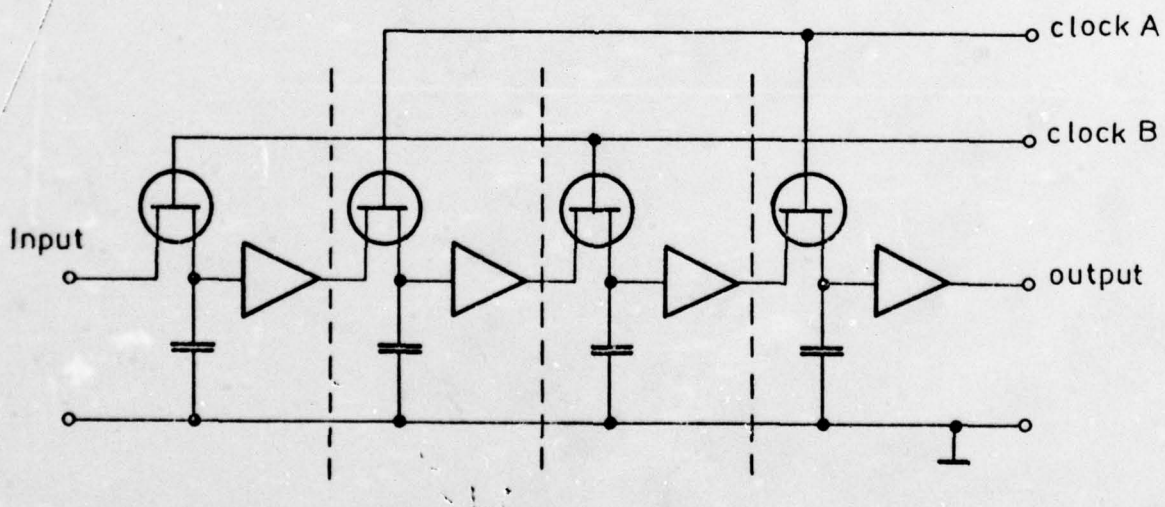

Fig.2 Bucket-brigade-device (BBD)

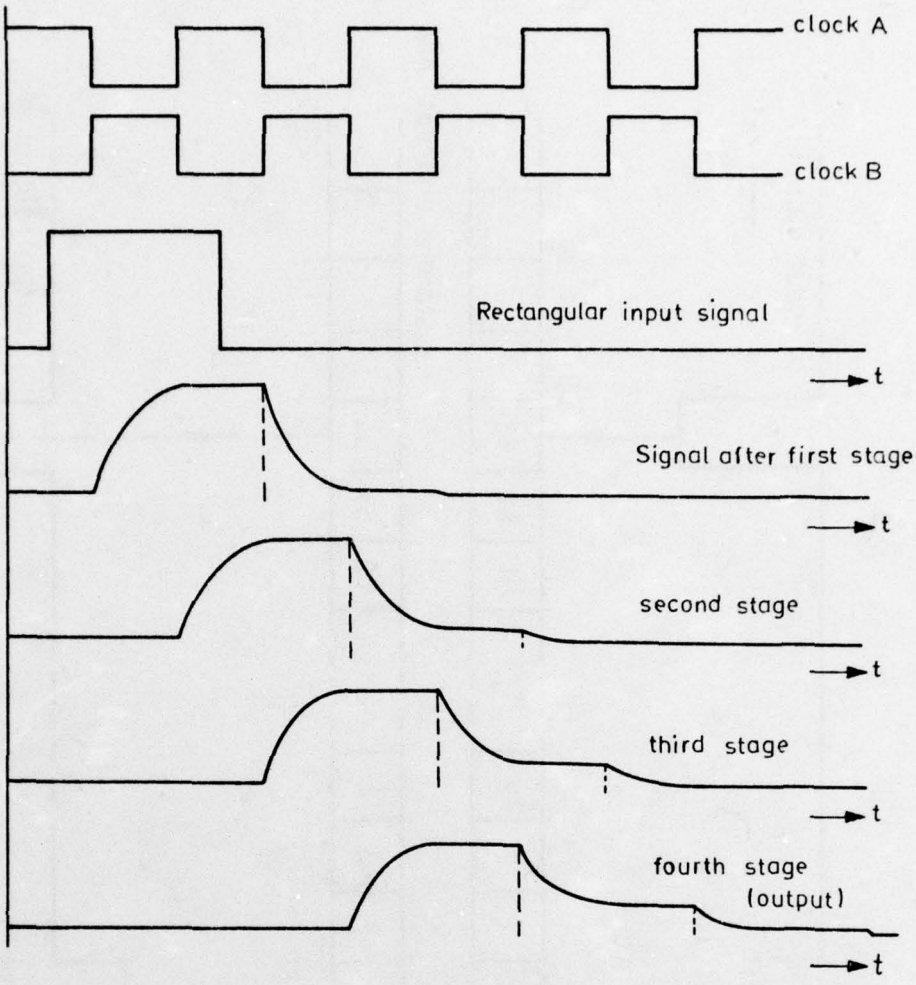

Fig.3 Signal waveforms in a BBD

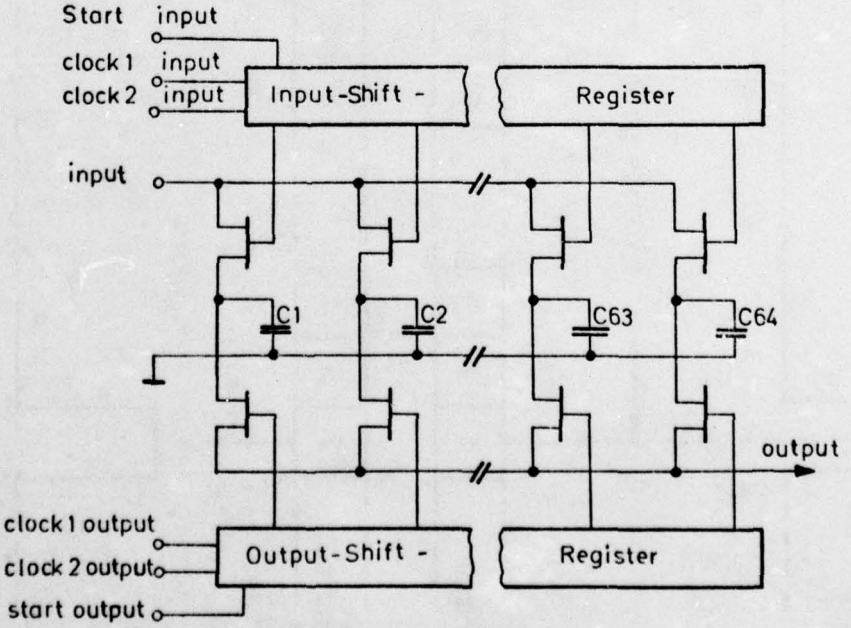

Fig.4 Principle of the serial – analogue memory SAM 64

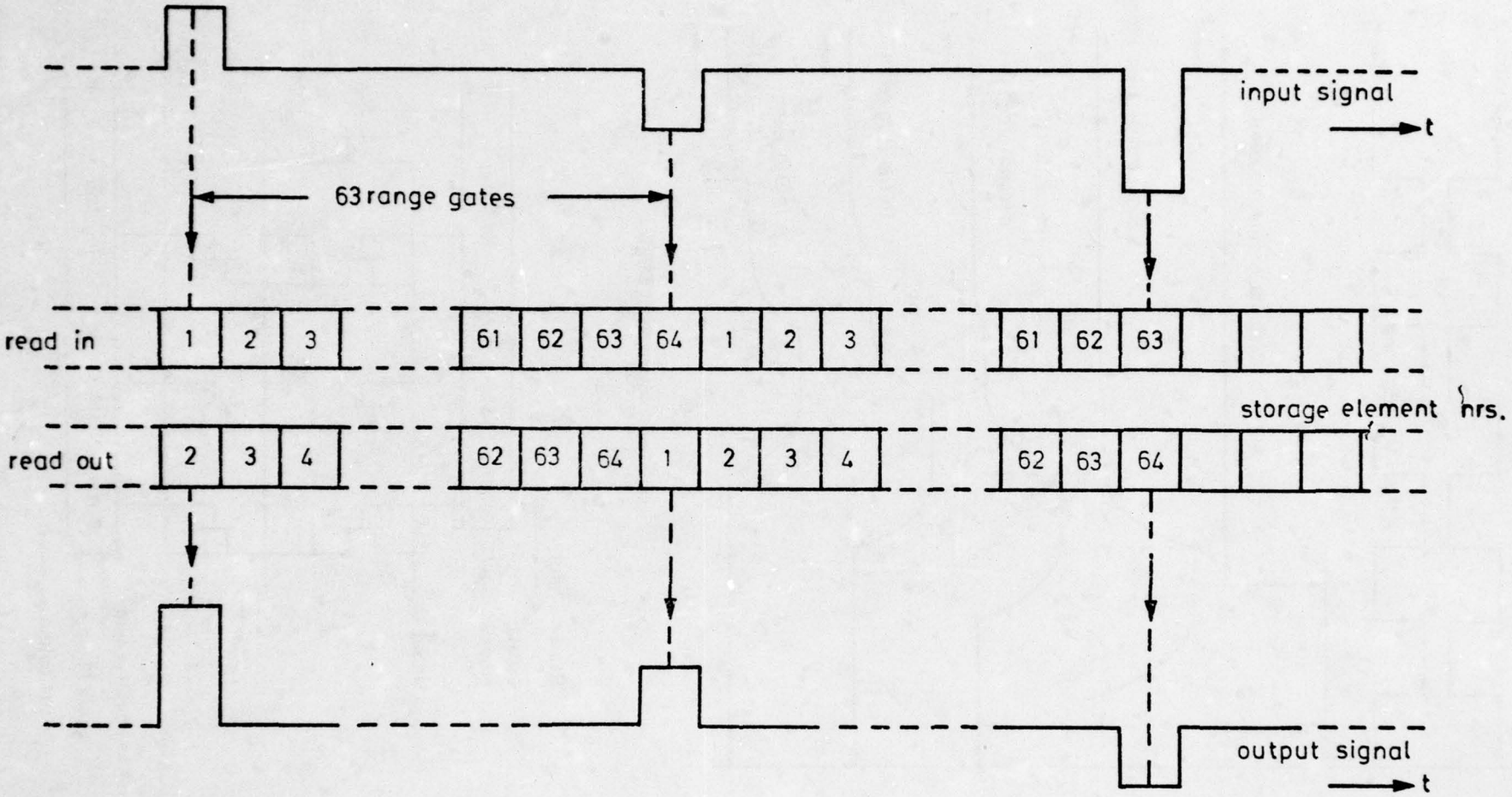

Fig.5 Processing scheme of SAM 64 (unmodified)

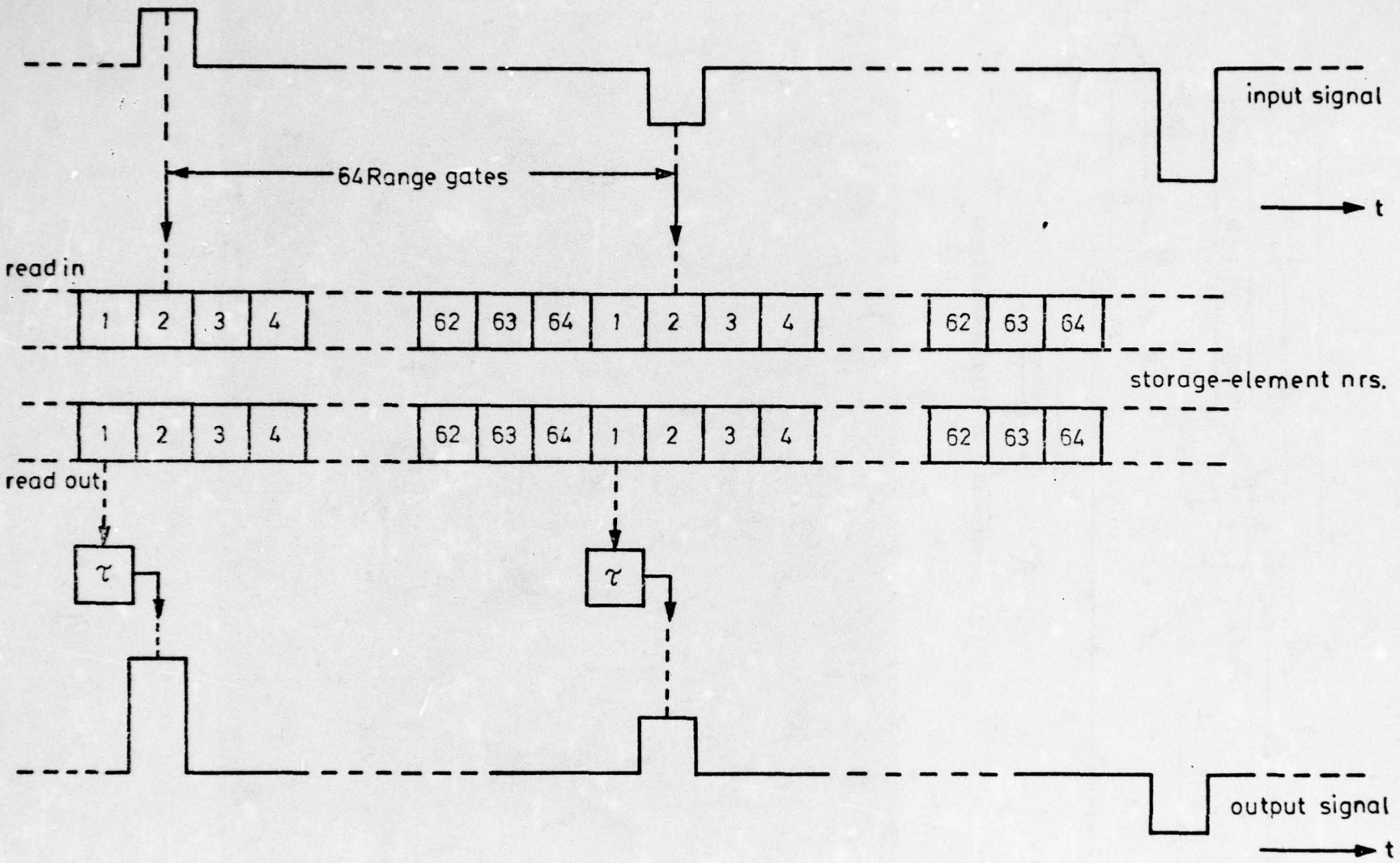

Fig.6 Processing scheme of SAM 64 with additional sample-and-hold-circuit

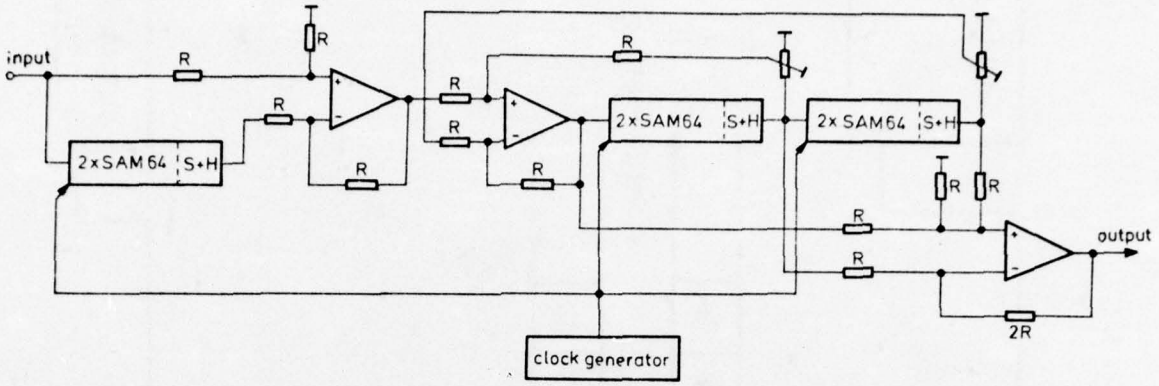

Fig.7 Actual circuit of the MTI filter with SAM 64

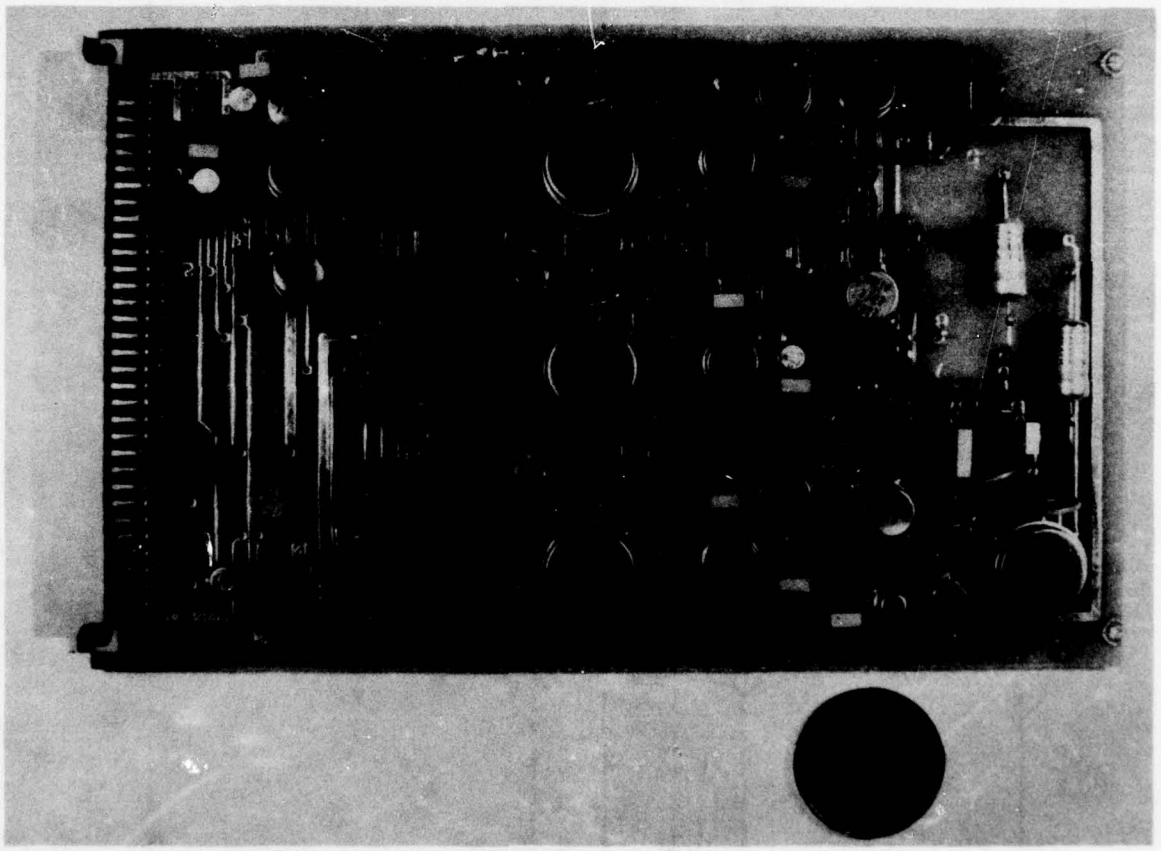

Figure 8

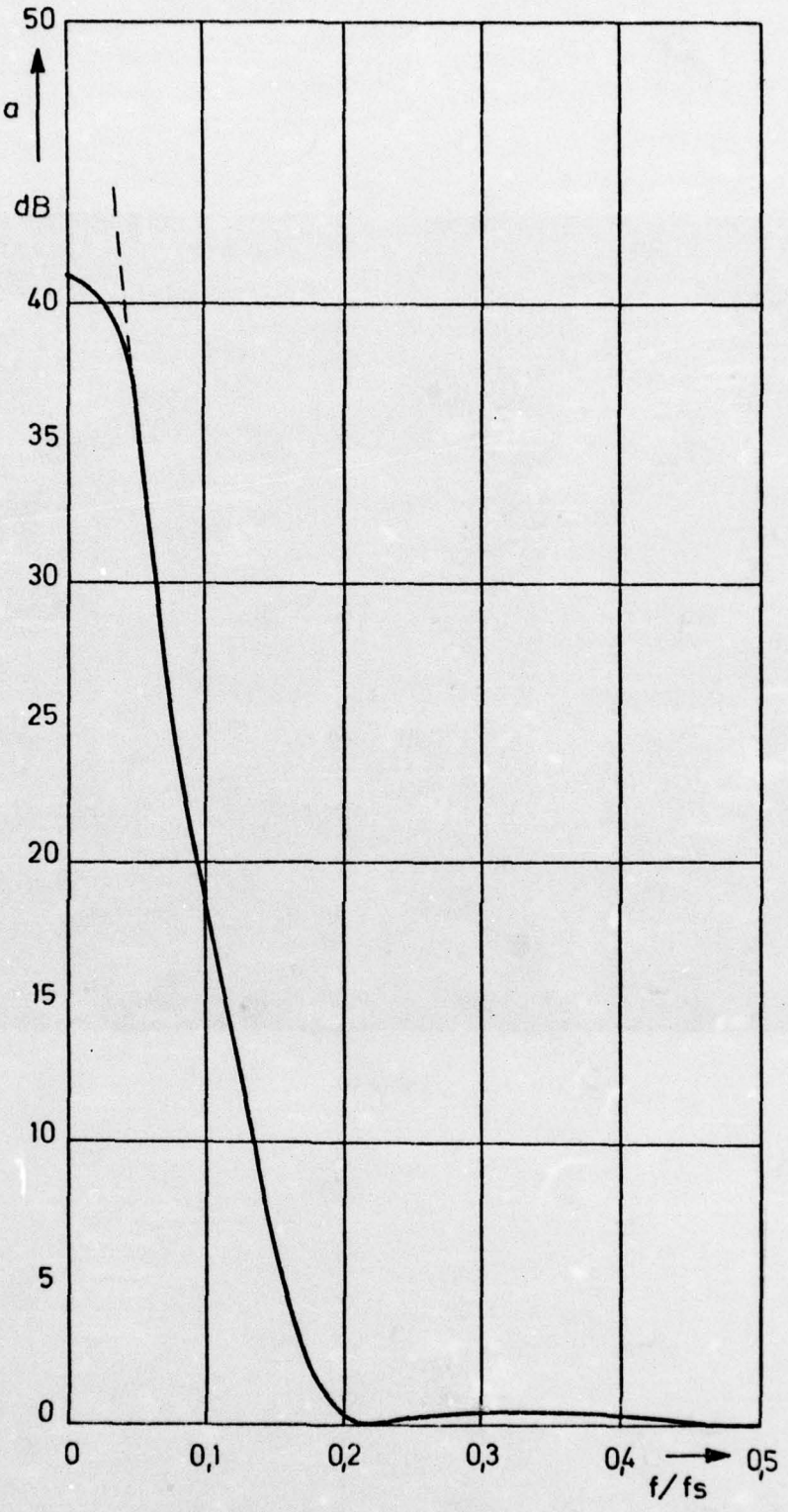

Fig.9 Frequency response of the MTI filter

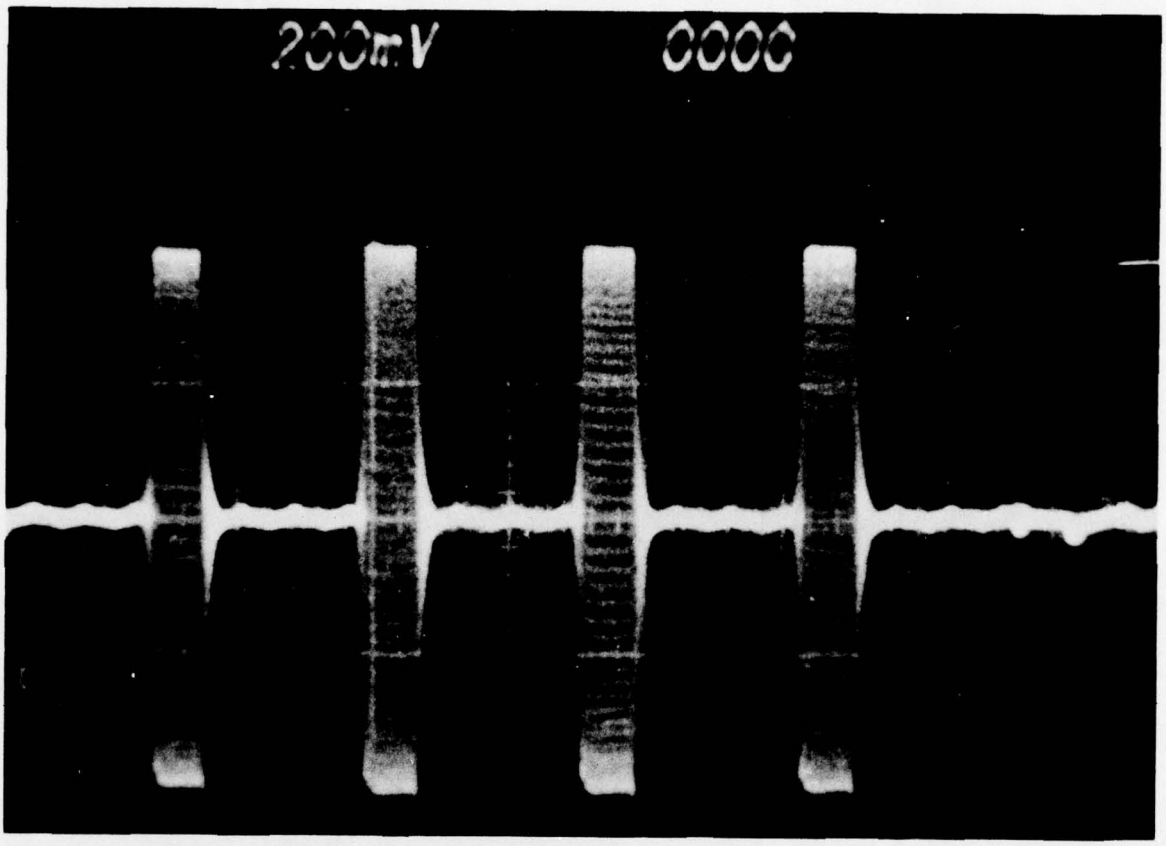

Figure 10

DISCUSSION

E STERN: What is the storage time in a BBD element?

W KOTHMANN: I cannot recall the exact values but, typically, these could be several micro-seconds delay time per cell. For exact values I recommend that you consult the data sheets from, for example, ITT, Philips etc. The total storage time is the delay time per cell multiplied by the number of cells in the particular element.

P BRADSELL: How could these filters be extended to cover more than 64 range cells, (for example by cascading storage elements) and would this result in any degradation of performance?

W KOTHMANN: Certainly it cannot be recommended to simply cascade the SAM 64 devices because the disturbing effects of each individual element would be added up. Better results are obtained if the signals to be delayed are interchangeably distributed on the several elements, ie signal from range element no. 1 is fed into SAM element No. 1, signal from range element No. 2 is fed into SAM element No. 2, signal from range element No. 3 is fed into SAM element No. 1 etc.

B C KAYSERILIOGLU: Could you quote a figure for sub-clutter visibility for your filter?

W KOTHMANN: An exact value of SCV cannot be given yet, but 35 to 40 dB is estimated. The SCV depends not only on the filter performance but also on the transmitter and local oscillator performances, etc.

" A REAL-TIME FFT PROCESSOR FOR RADAR "

A. Costanzi, S. Dicuonzo, G. Galati, P. Neri
SELENIA , Rome, Italy

SUMMARY

The paper is divided in sections. In the first one, the general features of FFT (Fast Fourier Transform) algorithm are briefly exposed, and the behaviour of an FFT processor in data filtering is summarized. The second section is dedicated to the problems connected to FFT processing in pulse-Doppler radars. The third sections shows how the architectural choices result from the system considerations exposed in section two. Besides, the FFT processor's prototype and its testing procedures are briefly described.

1. INTRODUCTION

1.1 The FFT algorithm

The Fourier Transform algorithm is very useful in processing of signals corrupted by white or colored noise, which is a common problem in electrical communications and radar field. When digital signal processing is used, the DFT algorithm [1] allows to transform a sequence of signal samples into a sequence of an equal number of samples that, under proper sampling conditions, are the samples of the signal spectrum. Therefore the DFT operator is the digital equivalent of the Fourier Transform.

Let $\{x_k\}$ be a sequence of N samples, equally spaced by T seconds; its DFT is, by definition, the sequence $\{X_l\}$ of N transform samples:

$$X_l = \sum_{0}^{N-1} x_k W_N^{-kl} \qquad l = 0, 1, \ldots, N-1 \tag{1}$$

where

$$W_N = \exp\left\{ j \frac{2\pi}{N} \right\} \tag{2}$$

The transform samples, $\{X_l\}$, are spaced in frequency by 1/NT Hz.

The FFT (Fast Fourier Transform), [1], [2], is a fast algorithm that represents the most convenient way to implement the DFT operator.

The computation of an N-samples DFT by means of the FFT requires a number of (complex) products equal to:

$$P(N) = \frac{N}{2} \log_2 N \tag{3}$$

instead of N^2 i.e. the number resulting from the DFT definition, expression (1). That is the first basic property of FFT.

The second basic property of this algorithm is the possibility of its implementation with a number of memory cells equal to N ("in place") without need for other memory capability to store the intermediate results [1], [2].

No other special features of FFT will be described here, nor its different flow graphs will be shown, with the exception of the DIF (Decimation In Frequency) graph for N=16, which is the case of the implementation described here. The graph is shown in figure 1.

1.2 Behaviour of a DFT processor

A DFT processor has the main characteristic of processing finite blocks of data, according to expression (1).

This feature makes it different from FIR or IIR digital filters, like MTI cancellers or radar pulse integrators, whose output is independent of the time of arrival of the signal.

The block diagram of a DFT (or a FFT) processor is shown in figure 2.
The input is assumed to be a sampled signal, as in pulse radar applications:

$$\{y(t-kT)\} = \{y_k\} \qquad k = 0, 1, \ldots, \infty \tag{3}$$

The time windows generates a block of N samples:

$$\{r_k\} = \{y_k\} \,, \quad k = 0, 1, \ldots, N-1 \tag{4}$$

The weighting consists in multiplying this sequence of N samples by a weight sequence:

$$\{q_k\} \qquad k = 0, 1, \ldots, N-1 \tag{5}$$

obtaining the $\{x_k\}$ sequence:

$$\{x_k\} = \{r_k\, q_k\} \,, \quad k = 0, 1, \ldots, N-1 \tag{6}$$

Finally, the DFT operator acts according to relationship (1), generating the output sequence:

$$\{X_l\} \,, \quad l = 0, 1, \ldots, N-1 \tag{7}$$

The complete analysis of this processor, including also the effects of the sampling of the originary signal $y(t)$, has been done by E. Teodori [3].
The main result, for this work's purpose, is the relationship between the transform sequence $\{X_l\}$ and the spectrum of the non-sampled signal, $Y(f)$. This relationship is:

$$X_l = \int_{-\infty}^{\infty} Y(f) \cdot Q(f_l - f)\, df \tag{8}$$

where

$$f_l = l\,\Delta f = \frac{l}{NT} \qquad , l = 0, 1, \ldots, N-1 \tag{9}$$

The function $Q(f)$ is the Fourier Transform of the weighting sequence $\{q_k\}$:

$$Q(f) = \mathcal{F}\left[\sum_{k=0}^{N-1} q_k\, \delta(t - kT)\right] \tag{10}$$

that is:

$$Q(f) = \sum_{k=0}^{N-1} q_k \exp(-j\, 2\pi\, kT f) \tag{11}$$

Expressions (8) and (11) allow the performance evaluation of a DFT processor. The FFT can be used to compute, with the required accuracy, the function $Q(f)$.
In the simple, but very important case, in which the input signal is a single sine wave:

$$Y(f) = \delta(f - f^*) \tag{12}$$

expression (8) reduces to:

$$X_l = Q(f_l - f^*) \qquad , l = 0, 1, \ldots, N-1 \tag{13}$$

that is, the output sequence is the sampling of the Fourier Transform of the weighting sequence.

2. FFT PROCESSING IN RADAR FIELD

2.1 Use of FFT in pulse-Doppler radars

The FFT algorithm has two main utilizations in radar systems.

The first one is the pulse compression, in which it is necessary to compute the correlation between the received signal and a replica of the transmitted signal, or another adeguate waveform.

The second one is the radar pulse integration, that can be done coherentely by means of a bank of Doppler filters; if the transmitted pulses are equally spaced, FFT provides a very efficient way to implement this bank of filters. The problems connected with FFT use are similar in both cases; to see more in detail those problems, the case of the pulse integration in a pulse-Doppler radar will be considered.

A pulse-Doppler radar provides the value of the target's radial speed without ambiguites, for all the speeds of interest. Such radars are characterized by a costant and high p.r.f. (pulse repetition frequency) and a large value of the number of pulses in the beamwidth, with respect to Doppler-ambiguous radars.

The FFT technique allows to implement at a high rate the DFT of the received pulses belonging to the same range-bin, and contiguous in azimuth. That is equivalent to a comb filter covering the whole range of Doppler frequencies.

The main advantages of such a processing are:

a) An improvement in signal-to-interference ratio for wide-band interferences. The Doppler filtering, which is an inherent characteristic of the system, allows that only the disturbance that falls in the Doppler filter matched with the target speed, can affect the signal.

b) An improvement of the signal-to-noise ratio due to coherent integration, that replaces the non-coherent integration commonly used in non-Doppler radar systems.

A pulse-Doppler receiver can be briefly described as follows.

The video signal, coherently detected, is sampled and digitally converted. Then, it is filtered by an MTI canceller, which reduces the clutter power. The samples are then grouped in blocks of length N (N = number of Doppler channels = = number of integrated pulses) and modulated by a weighting window.

The FFT processing is done on these blocks; the N outputs go to a bank of detectors and then to a CFAR system, whose output is sent to a synthetical indication generator, giving the targets coordinates indication.

A functional block diagram of this processing is shown in figure 3. The FFT processor of figure 3 is perfectly equivalent to the DFT processor of figure 2 from the functional point of view.

2.2 Design of FFT processor

The design of the FFT processor (figure 3) requires some basic choices. The mathematical tools necessary to do that have been developed in sect. 1.

From the point of view of the radar modeling, the important division between mechanical scanning and electronical scanning must be done.

In the first case, the received pulses are modulated by the antenna azimuthal pattern; therefore, the input sequence to the FFT processor (relationship (3)) can be written as:

$$\{y_k\} = \{n_k + g_k s_k\} \qquad (14)$$

where

- n_k = noise samples
- s_k = unmodulated signal samples
- g_k = $G(k\dot{\theta}T - \theta_0)$
- = two-way (voltage) antenna gain
- $G(\theta)$ = target azimuth for K = 0, measured with respect to antenna boresight
- $\dot{\theta}$ = antenna angular speed.

In the second case the expression is:

$$\{\gamma_K\} = \{n_K + q_0 \delta_K\} \qquad , K = 0, 1, \ldots, N-1 \qquad (15)$$

where

$q_0 = G(\theta_0)$
θ_0 = target azimuth, measured with respect to antenna boresight, during the considered "look".
N = number of pulses per look

As a matter of fact, the electronic scanning introduces a time window, which is functionally coincident with the one of FFT processor (figure 3). That reduces the amount of problems connected with FFT implementation with respect to the more critical case of mechanical scanning. Only the latter will be examined in this paper.

As the azimuth of the target is not known a priori, there is a random staggering between the sequence $\{\gamma_K\}$ of received signal samples and the time window. That give rise to an integration loss, whose magnitude depends on the window width and on the weighting law. Only the case of a window length equal to the 3 dB antenna beamwidth will be exposed here; as for as weighting is concerned, four laws have been taken into account, namely:

a) rectangular : $q_K = 1$

b) gaussian (matched with antenna shape) : $q_K = \exp\{-2.776\,\beta_K\}$

c) hamming : $q_K = \cos^2\gamma_K + 0.08(1 - \cos^2\gamma_K)$

d) $\cos^2$: $q_K = \cos^2\gamma_K$

where:

$$\beta_K = \frac{(K+0.5)}{N} - \frac{1}{2} \qquad \gamma_K = \pi\beta_K$$

and the range of variability for K is from 0 to N-1.

The effect of window staggering is specially interesting and has been evaluated separately. The loss in signal-to-noise ratio at the FFT output, L_S, due to the staggering, has been evaluated versus the ratio, D, between the staggering and the window length. The worst case is D = 0.5, because for greater values of D another window (the adiacent one) gives the main contribution to detection. The results are plotted in figure 4.

It results that for $D < 0.25$ the loss are small, ranging from 0.8 to 1.2 dB. Therefore, a system able to keep the maximum relative staggering in the range -0.25 +0.25 should nearly eliminate this kind of loss.

Such a system has two time windows, each followed by a weighting and by a DFT; the windows are half-length staggered (i.e., N/2 pulses).

The performance of such a processor have been evaluated and compared with a single-window processor.

The evaluation criterion is the loss in SNR with respect to a perfect IF integrator, i.e. an integrator whose signal-to-noise gain is:

$$G = 10 \lg_{10} N$$

where N is the number of integrated pulses. One must remember that such a criterion includes also the beamshape losses, which are common to all radar integrators and, for N equal to the number of pulses in 3-dB antenna pattern, is of the order of 1.6 dB.

The SNR loss is given in table 1, for three different weighting laws (b= gaussian, c= hamming, d= $\cos^2$) and for single and double-window processors. The value of false alarm probability is 10^{-6} and the one of detection probability is 80%.

The exam of Table 1 shows that the use of two windows reduces the SNR losses at a value practically equal to the sum of the beamshape loss (1.6 dB) and the loss due to the weighting.

The weighting loss is very small, not greater than 0.9 dB for the three examined weighting laws.

LOSS (dB)
with three different weightings

	B	C	D
single window	3.1	4.5	4.85
double window	1.8	2.35	2.45

TABLE 1

Another important feature of FFT processing is clutter spillover, i.e. the presence of clutter power on Doppler bands different from the clutter band. This effect is due to time windowing of the input signal, and can be evaluated by means of the analytical tools shown in sect. 1.

The weighting is necessary to reduce the clutter spillover. It is possible to evaluate in an analytic way the clutter power in different Doppler bands both for narrow-band (i.e. ground) and wide-band (i.e. rain) clutter.

In this paper, the case of fixed clutter, whose spectral spread is due only to antenna motion, will be dealt with. In this case the clutter spectrum 2 ms spread, σ_c' , normalized to the pulse repetition frequency, prf, depends on the number of pulses in 3-dB beamwidth, N_B, according to the relationship:

$$\sigma_c' = \frac{\sigma_c}{prf} = \frac{0.264}{N_B} \tag{16}$$

The window length is assumed equal to 3-dB beamwidth; therefore $N = N_B$.

It is convenient to define a "FFT Processor Improvement Factor", FIF_K , as the ratio between the output clutter power of the Doppler filter and the input clutter power, both powers being normalized to the noise power, the formula is

$$FIF_K = \frac{(C_K/N_K)}{(C_{iN}/N_{iN})} \tag{17}$$

This parameter has been computed for various values of N and different weightings; in Table 2 there are the values relative to $N = N_B = 32$, hamming and $\cos^2$ weights.

The independent variable in Table 2 is the central frequency of the filter normalized to pulse-repetition frequency.

fk/prf	FIF_K (dB) with: hamming weighting	$\cos^2$ weighting
$\frac{1}{16}$	14	11
$\frac{1}{8}$	31	36
$\frac{1}{4}$	34	52
$\frac{1}{2}$	37	58

TABLE 2

The choice of such an independent variable allows to extrapolate the data in Table 2 to different values of N; in fact, these FIF values do not change very much with N. In the case of Gaussian (matched) weighting, the FIF values are lower, and range from 11 to 27 dB.

As a global result, it is possible to claim that the clutter attenuation that can be obtained with an FFT processor is not sufficiently high for all Doppler filters; therefore, an MTI filter in cascade with such a processor may be required (see figure 3).

An advantage of such a configuration is the reduction of the dynamic range at the processor input; that allows an implementation with a small number of bits, allowing a simpler hardware.

The basic problem, when a FFT processor is inserted in a radar system, is to cope with the flow of data in real-time.

Keeping in mind this aim, we briefly examine the most important FFT hardware processors.

1) Serial processor

The serial processor, is the simplest hardware realization. It has only one arithmetic unit sequentially performing allthe FFT elementary operations (butterfly). The kind of elementary operation is: $A \pm WB$, where A and B are data and W is a weight. The number of these elementary operations is $(N/2) \times \lg_2 N$ as we can see from the FFT flow graph (figure 1). This FFT processor has been considered too slow to cope with the flow of data in real-time.

2) Array-iterative processor

This processor has N/2 arithmetic units performing at the same time, N/2 butterflies. In a N-sample FFT we need to perform $\lg_2 N$ steps, with N/2 elementary operations in each step. A very complex hardware implementation is foreseen for the array-iterative processor, particularly due to the control circuitry.

3) Array processor

This processor has $(N/2) \lg_2 N$ elementary units. Its structure comes from the array-iterative processor multiplying a single processor $\lg_2 N$ times. Array processor can perform a continuous flow of data bunched in N sample blocks at the right speed to cope with the radar data flow. Like the array-iterative processor the array processor structure is too complex and onerous, as it needs to many elementary units.

4) Pipeline processor

The basic idea of this processor comes from an assembly-line. It has been estimated that the required speed would be attained with a rather simple hardware implementation, particularly for the control circuitry.

As two FFT's have to be performed, we have chosen a two channel pipeline structure, that allows the processing of pulse Doppler radar signals.

The pipeline processor diagram with two channels for two independent 16 point FFT, is shown in figure 5. The processor has $\lg_2 N$ cascade arithmetic units connected by multiplexers. A continuous flow of data bunched in N sample blocks runs over each channel. Between the blocks of the two channels than is an N/2 sample shift.

In our hardware realization, we have 16 bits for each complex channel. There are 7 bits plus sign, both for real and imaginary part of the input data. The same is for the output channels.

The weight values used in our processor are 16 and their compact expression is:

$$W = \pm e^{-j\frac{k\pi}{8}} \qquad k = 0, 1, \ldots, 7$$

not considering the sign, the different values of the real and imaginary part of these weights are only 5:

1, 0.92388, 0.70711, 0.38268, 0

The weights 1 and 0 do not require multiplications. For the remaining three weights, we have used programmable-read-only-memories (PROM) to perform the multiplications. Our two channel pipeline processor has 8 digital PCB's (Printed circuit Boards), excluding interfaces.

Because of the full-time use of the arithmetic units and memories, sampling periods shorter than 0.5 usec are attainable. A correct use of this processor

requires an N/2 sample shift between the blocks on the two indipendent input channels. In our processor, a connection of the two input channels through an N/2 delay line allows to perform on FFT with shifted and overlapped blocks, as required in radar processing.

The prime features of this processor are, as follows:

1) the arithmetic units and memories work full time (without dead times);

2) the data flow at the input channels is continuous at a work period shorter than 0.5 μsec;

3) the processing is performed on two channels thus allowing a half-length overlapping of data block with no hardware addition.

3. PIPELINE PROCESSOR TESTS

We have successfully tested our special-purpose processor with a minicomputer GP-16 Selenia at the input and a display at the output. An appropriate interface has been used between the minicomputer and the FFT processor. Control clock was sent from the minicomputer to the FFT processor, through the interface, allowing different processing speeds. The purpose was both to check the circuitry and to make functional tests.

During first test set numerical data with well known spectra were coming from the minicomputer. We have moreover processed signal plus noise data to simulate a real radar system.

In our simulations a gaussian antenna pattern and three weighting window types (a) hamming, b) gaussian, c) $\cos^2$) have been used. We have finally simulated block shifts up to N/2 samples to compute processing losses.

Such functional tests have shown a good agreement with theorethical results.

REFERENCES

[1] Rabiner, R.L. and Gold, B. (1975) "Digital Signal Processing", Prentice Hall

[2] Bergland, G.D. (1969) "A guided tour of the Fast Fourier Transform" IEEE Spectrum, July 1969

[3] Teodori, E. (1973) "Signal Analysis with FFT" Selenia Technical Revue, Vol.1, No.3, 1973

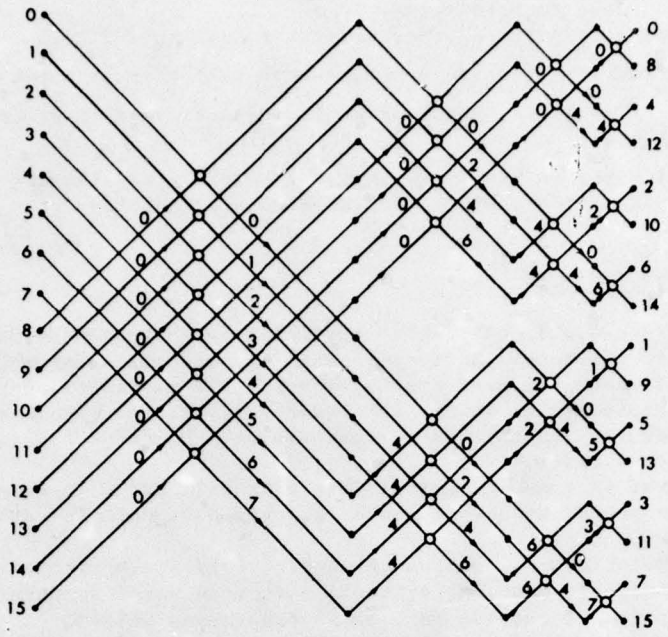

Fig.1 FFT graph with N = 16 (DIF technique)

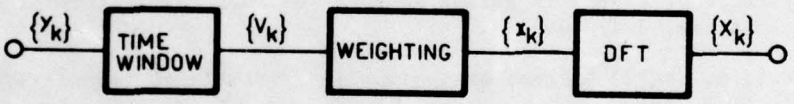

Fig.2 Block diagram of a DFT processor

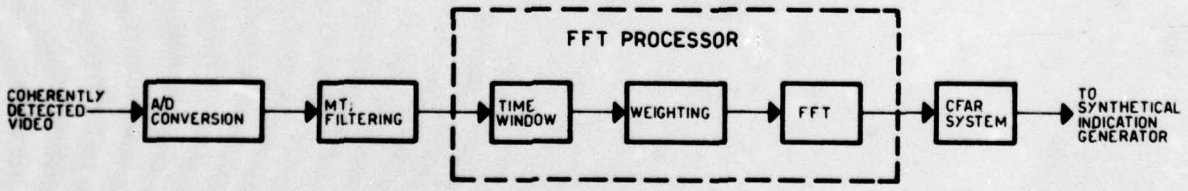

Fig.3 Functional diagram of a pulse-Doppler FFT receiver

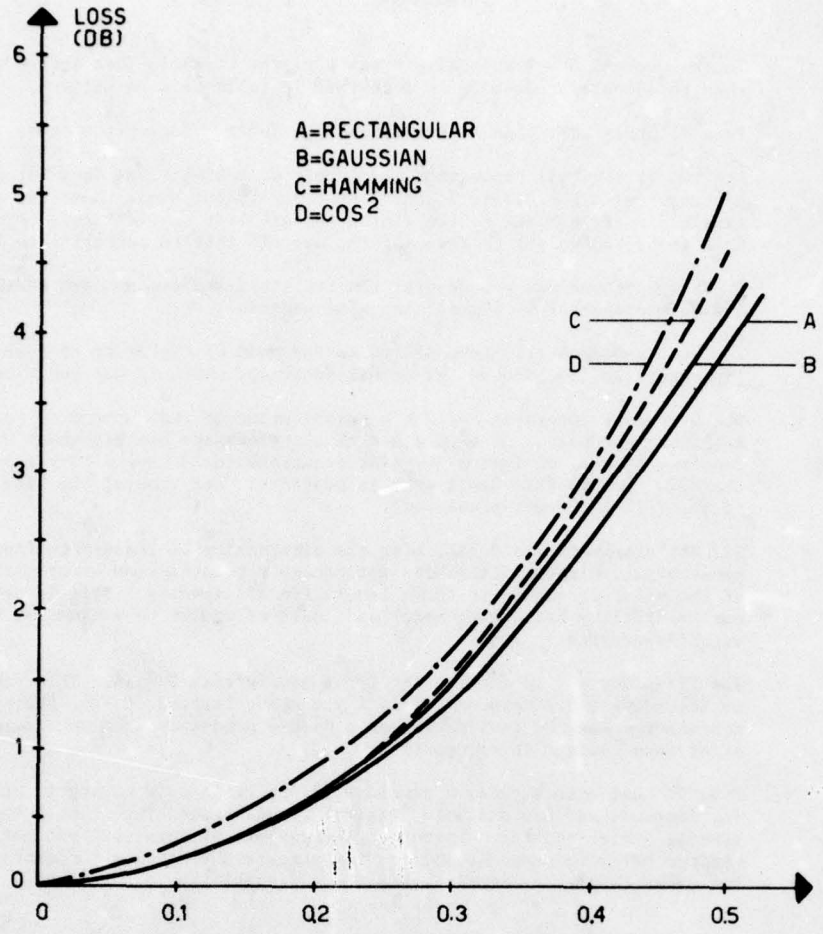

Fig.4 Integration loss of an FFT processor due to the normalized window staggering

$$D\left(D = \frac{\text{staggering}}{\text{window width}}\right)$$

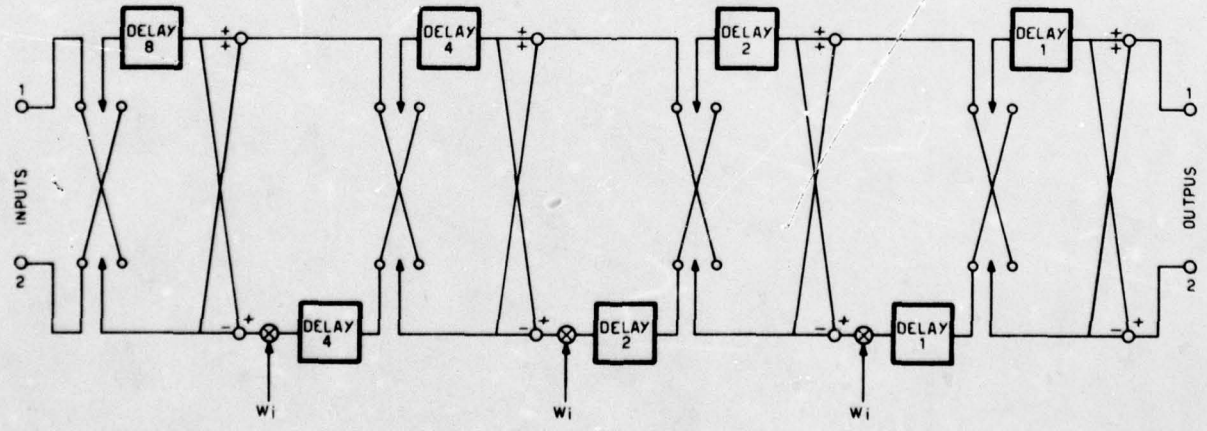

Fig.5 Structure of pipeline FFT processor for half-length staggered blocks

DISCUSSION

D F HAMMERS: In the overall SNR-loss analysis was a filter straddle-loss factor included, ie when the doppler frequency is such that it falls between filters?

G GALATI: Yes, slightly less than 1 dB was added to Table 1 for this effect.

K MILNE: Are two (staggered) processors absolutely essential? The loss for a single processor with D = 0.5 is 3½ to 4½ dB (Fig 4), but since there are two independent samples (corresponding to the window on each side of the beam) one would expect this to be equivalent to reducing the overall loss to perhaps 1 to 2 dB.

G GALATI: 1 We do not use two processors; the two staggered windows are easily obtained with a single processor by a small hardware addition.

2 The two-window structure allows an SNR gain of the order of 2 dB but, more important, is its improved azimuthal accuracy, which is not described in the paper.

P BRADSELL: The processor described has 8-bit quantisation of the input data in real and imaginary channels. At each stage of the processor the bit-count will tend to increase by one, so that a 16-point transform could have a 12-bit output in each channel. How is this dealt with in practice? Are some of the bits discarded or is the full bit-count preserved?

G GALATI: All the arithmetic is 8-bit, with the elimination of least-significant bits when necessary. This simplification introduces a quantisation error with an rms value of the order of the first three levels (in 127 levels). This is not a problem in our feasibility breadboard model and could of course be avoided by retaining all significant bits.

E FLAD: The FFT processor is implemented for a sample size N = 16. This could be achieved by cascading two stages of a base-4 processor instead of four stages of a base-2 processor. Was the realisation of a base-4 processor ever considered that might offer some savings in hardware?

G GALATI: I agree that with a radix-4 pipeline FFT there is some saving in multipliers (see for instance Rabiner and Gold 'Digital Signal Processing', p613) but radix-2 FFT permits easier control. Moreover, the purpose of this work was not to design an optimum hardware structure but to investigate the optimum functional structures for radar doppler processing, and their feasibility.

DIGITAL PROCESSING TECHNIQUES AND EQUIPMENT

A REVIEW

P.V. COATES
E.O.P.S. DEPT.
EMI Electronics Ltd.
Victoria Rd.
Feltham
Middlesex
England

SUMMARY

Advances in semi-conductor technology are continually opening new areas of application for digital systems. One of these areas is in the processing of video information derived from radar and other sensors prior to its display.

It is possible to modify both the data format and the visual image and to insert synthetic information, either externally or internally generated, by the use of digital techniques. This can enable an operator to obtain more useful information in a shorter time than would have been possible by displaying the image directly from the sensor output.

Some of these techniques are described together with simple block diagrams of various equipments which can perform this processing. A versatile digital equipment is described which uses a microprocessor to enable the single machine to be used to perform a wide variety of algorithms on the video outputs from many different sensors, in real time, by means of simple software modifications.

INTRODUCTION

It is generally the case that the output from a radar or other sensor system will be portrayed on a display for visual interpretation by an operator. This paper describes digital processing methods which can be applied to the detected signal prior to display. The advances in this area have been considerable over the last few years mainly due to the availability of complex digital integrated circuits. I.C. manufacturers are continually placing new, improved devices on the market, a trend which must result in continuing advances in this field.

The techniques to be described can be broadly divided into two types.

The first type concerns the manipulation of the data rate and/or format of the video signal. This is commonly known as Scan Conversion. The object of this form of processing is to convert the video signal into a uniform standard for display.

This can prove to be a useful tool to combat the increasing problem of restrictions in the amount of space available to house the electronics normally associated with modern detection and display equipment. The signals from a wide range of sensors (Radar, I.R., LLTV etc.) can be accepted, sampled and digitised in their respective scan formats and then converted, by means of a digital buffer store, into a single uniform display standard, which, after conversion back to analogue form, removes the requirement for several separate dedicated display equipments.

The second type of processing involves the adaptation of past, present and sometimes predicted data to modify the presentation of the video image, enabling an observer to extract the maximum amount of useful information in the minimum time for a particular operational requirement.

Within this category fall many well known techniques such as integration, MTI, track history and the overlay of synthetic information. The majority of these facilities can be produced, in their familiar form, by the use of digital techniques. However, a more important consideration is that of the many new possibilities now offered for the presentation of data. These arise from the ability to store, in a readily accessible manner, past information, together with the increase in arithmetic processing power afforded by the digital representation of the data.

SCAN CONVERSION

Digital scan conversion has been given a considerable boost in recent years by improvements in semiconductor memories, in particular the introduction of the N-channel MOS Random Access Memory. N-channel devices offer a higher speed to power ratio than P-channel devices and since the majority of semi-conductor manufacturers are concentrating on developing high capacity N-channel RAMs they are likely to be cheaper than any of their digital equivalents. 4k bits of store in one dual-in-line package is common and sample quantities of 16k devices are now available. Using the 16k device it is possible, with little serious attempt at miniaturisation, to construct a one megabit semi-conductor store with associated addressing control on one single 20 cm by 20 cm printed circuit card.

A typical scan converter arrangement is shown in figure 1. In this example the input video signal is first sampled at a high frequency sufficiently above the Nyquist rate to avoid aliasing effects. Then each sample is converted into a digital word. The digital quantization does not affect the picture provided that sufficient bits are used in each digital word. Extensive subjective tests have shown that, for a studio quality display of approximately 40 dB signal to noise ratio, 8 bits are required if quantization effects are to be rendered totally invisible. However, the majority of applications do not require studio quality images. 6 bits per word give a very acceptable picture which is normally sufficient for imaging applications unless a camera of exceptionally high signal to noise ratio is used. In radar applications one bit, giving two tone pictures, is often sufficient and rarely are more than 4 bits or 16 contrast levels required, the latter being ample for high resolution ground mapping modes.

The heart of the scan converter is the buffer store. In this example, this consists of an array of semi-conductor RAMs. These devices allow immediate access to an individual address location which makes them ideally suited to this application. The input and output data rates are likely to be quite high (up to 20 MHz for some applications) and the cycle time of the elements comprising the buffer store will not be sufficiently short to allow direct access to individual RAMs at these rates. It is therefore necessary to sub-divide the store into several parallel paths each running at a much lower rate. Input and output data multiplexers allow the overall throughput to be maintained. The store addresses, to which the input data is routed and from which the output data is obtained, are multiplexed into the main store in a similar way via small buffer stores. The RAMs used have a non-destructive read which allows asynchronous operation between input and output video. For instance, a slow line scan input which may take some seconds to build up a complete picture in the store, can be continually read out at TV rates since each stored picture point can be accessed many times with no loss of data until new information from the next input field overwrites it. The final process in the scan converter is to convert the stream of digital words back into analogue form and insert any sync. pulses required by the display format.

A radar display has a large number of target parameters to present in a two dimensional image and this has resulted in a wide variety of display formats being devised over the years; many of these require the data to be displayed in polar form. This generates a requirement for a special-to-type circular deflection display tube which cannot be used to display any other video format. The RAM organised scan converter is especially suited to the conversion of data from polar form to the cartesian raster form of most conventional displays. In its simplest form it is only necessary to interpose a polar to cartesian conversion in the store address circuitry which could be a specially programmed semi-conductor Read Only Memory.

The use of digital techniques is not the only method of scan conversion. The main alternatives are double and single ended storage tubes and charge coupled devices (CCDs).

Storage tubes are considered to be cheaper, smaller and to consume less power than digital equivalents. However, advances in large scale integration and a continuing reduction in the cost/bit of digital storage is tending to change this situation. Storage tubes are generally delicate, difficult to ruggedise and often require careful screening from stray fields. This can limit their use in a military environment.

There have been significant advances, of late, in CCD memory products and they are believed to have the potential for the lowest cost/bit of any read/write semi-conductor memory device by a factor of four. The size of the storage element can be made very small giving a high packing density and leading to high yields. The basic CCD, however, is a serial rather than random access organised device which can give rise to prolonged access times for individual bits of data and make it unsuitable for use in converters dealing with discontinuous scan formats. The internal charge transfer within the device is not 100% efficient and a large number of transfers can reduce the internal noise margin. It can also be adversely affected by elevated temperatures. Manufacturers are attempting to overcome these barriers and it may soon be possible to develop special-to-type CCDs organised for specific scan converter applications. It is, however, unlikely that CCDs will be able to compete with digital processing techniques for applications involving complex data manipulation, at least in the near future.

DIGITAL PROCESSING

For some applications scan conversion clearly has many advantages over dedicated display systems, but the most promising use of digital techniques is not just for scan conversion but also for image processing.

Improvements or modifications to a radar or other sensor system can be costly, especially to an already developed production item, and the improvement in performance obtained may not always justify the time and cost involved. If, however, one regards the transfer of information from display to observer as one of the fundamental tasks of the equipment, then a significant improvement in system performance may well result from a modification to the form of the displayed image. This would not necessarily require any more information from the sensor but would be concerned with presenting the existing information in a more efficient way. It is also the case that continuing improvements in sensor technology give rise to an increase in both the quality and the quantity of information that is required to be displayed. In order that the overall system does not become limited by its inability to transfer this information to the operator it is necessary to improve display techniques. It is in these areas that the digital processing of video information has much to offer.

Consider the simple block diagram of a digital processor shown in figure 2. This is basically similar to the scan converter previously described except for the addition of the digital arithmetic units which accept the streams of digital words and perform some specific arithmetic process on them. Variations in the type of arithmetic algorithm performed gives rise to the various processing functions.

Arithmetic unit A (figure 2) enables non recursive, linear phase processing algorithms to be implemented providing such facilities as aperture correction and edge contrast enhancement; whilst the arithmetic unit B provides the recursive processing path necessary for the implementation of such algorithms as will perform long term signal averaging.

This arrangement together with the store access flexibility afforded by the use of the random access memory enables a wide range of useful processing to be performed.

PICTURE FREEZE

One of the most obvious and simple processing facilities is that of freezing a picture on the display. This can be achieved merely by ceasing to write new information into the store. The non destructive read capability of the storage devices enables the last frame captured to be continually repeated, with no degradation, almost indefinitely. In a dynamically changing scene an observer can use this facility to examine an object of interest, held stationary on the screen, for as long as he requires.

RECURSIVE PROCESSING

More complex forms of processing can be implemented using the arithmetic unit paths in figure 2, as described above. Using the recursive feedback path it is possible to perform signal averaging or integration. A portion of each individual stored picture element is added to the corresponding incoming element appropriate to that point in the scene before being written back into the store. The stored data accumulated is composed of contributions from a number of consecutive input fields. This results in a restriction of the allowable rate of change of the picture and a consequential suppression of spurious signals and random noise.

This technique can be employed when polar to cartesian scan conversion is used. By varying the integration factor over the scan, use can be made of the overlaying of information which occurs towards the centre of the plot to provide an increase in the signal to noise ratio.

If there are a number of moving targets on the display then by recirculating data through the store it is possible to provide track history. This can be of aid to assessing the relative motion of moving targets. The lie of a track associated with a radar return indicates the direction of travel and the length of the track provides an indication of relative speed.

If the radar platform is itself subject to motion, as for instance in an airborne application, then recursive processing involving a number of input frames is not directly possible. In this case, some form of motion stabilisation is required before performing the processing. Stabilisation, or adjustments to the position of the data obtained from the store, is relatively simple with RAM organisation. If the store address is arranged in terms of X and Y positional components, then it is not difficult to add in the appropriate offset factors which, in the case of the airborne application, would be obtained from the aircraft speed and heading. In a similar way it is possible, in the handling of polar scan data, to introduce offsets in terms of R and θ to perform the same task.

MOVING PLATFORM PRESENTATION

If the radar set is itself in continuous motion, as in the airborne case, then the interpretation of the display in the presence of this relative movement is made more difficult for the observer. However, the wide variety of display modes afforded by the flexibility of the digital store can help to combat this problem although the display variations possible are to some extent limited by the input data format.

Consider, for example, a line scan system such as Sideways Looking Airborne Radar (SLAR). In this case the picture is built up on a line by line basis as the aircraft moves over the terrain and the data could be presented as a "rolling map" giving the operator the same view as he would get looking directly out of the bottom of the aircraft. This form of presentation does, however, result in a continually moving scene in which it is difficult to examine a particular object closely. By slightly increasing the capacity of the buffer store the operator can be given the facility of a momentary picture freeze. Whilst the scene remains stationary on the display the extra store capacity will accommodate the current incoming information. When the store is full, the freeze can be released and an increase in the picture roll rate implemented until the display "catches up" with the current scene and the extra storage space is again empty ready for another freeze. The duration of the freeze mode is, of course, dependent upon the extra buffer store capacity and the rate of picture roll, although the operator could be given the option to continue the freeze mode and accept the attendent loss of current incoming video. Alternatively, it is possible to provide an updated stationary display. This is a presentation in which a picture is frozen on the display and the new information is either overwritten line by line as it arrives from the sensor such that a boundary between new and old frames moves up the display, or new information is overwritten frame by frame such that complete stationary pictures of the terrain are presented one following the other. This latter form of display does, however, require twice the storage capacity since it is necessary to store the next frame whilst the current frame is being displayed. These forms of stationary display can present problems when it is necessary to interpret an object which encompasses the top of one picture and the bottom of the next. One method of overcoming this problem is to provide a frame overlap in which a portion of the top of one field is repeated at the bottom giving a measure of continuity at the boundary.

MOVING TARGET INDICATION

There are many ways of both drawing an observer's attention to a moving target and obtaining and displaying information about that target. The following are a few examples of this type of processing, some of which have been implemented in military digital equipment.

Utilising arithmetic unit A (figure 2), the current incoming video information can be compared digitally with the equivalent stored image at each individual point in the scene. This enables past and present images to be compared and, assuming that compensation can be applied to correct for any motion of the sensor platform, differences from one field to the next will represent moving targets of possible interest. These can be highlighted on the display and also be arranged to trigger an audible warning, as an aid to reducing the operator work load. To reduce false alarm rate in the presence of noise, both spatial and level filters can be readily implemented.

If the video output format is made compatible with standard TV, then it is possible to provide a relatively inexpensive multi-colour display using a standard colour tube monitor. If a harsh environment is envisaged, the trinitron form of colour tube tends to be more rugged than the shadow mask. With a multi-colour display, moving targets and track histories can be presented in colours different from the stationary "background" scene.

If a variety of spatial filters are employed on the MTI information, then it is possible to extract the relative velocities of the moving objects. These could be presented in different colours as an aid to target identification or, since the distance moved by the target and the time between input scans is known, the relative velocity can be calculated using digital arithmetic and the resultant figure portrayed as an alpha numeric overlay at the relevant position on the display.

A form of MTI display can also be generated by means of a recursive high pass digital filter. This is implemented using the arithmetic unit B (figure 2). With this form of digital filter, acting on the rate of change of scene content, stationary objects correspond to d.c. signals and are suppressed by the filter action whilst differences from frame to frame correspond to a.c. signals and are enhanced. Information on the relative velocity of the moving object is conveyed in the brightness of the image.

IMAGE CORRELATION

One of the processes afforded by the digital representation of image data is that of computing the correlation between two images. If two digitised pictures are compared, element by element, with each other, it is possible to derive a measure of their similarity. This measure will obviously be a maximum if they are identical.

This technique has a wide range of applications. For instance, in an air to ground radar it is possible to obtain details of the aircraft's velocity and track. By correlating past stored images with current input images one can find the best "match". The X and Y positional difference between past and present and the known time between scans can be used to derive the required information.

Correlation of picture elements can be used in applications such as map matching to aid navigation. In this case, stored navigational information is compared with current radar information and when the two match the present position can be computed.

Image correlation finds many other areas of application such as target recognition, auto lock follow and clutter rejection.

MATCHING DISPLAY TO SENSOR

If it is required to use a single, fixed video standard display to present the data from a wide variety of sensors, then it is necessary to be able to match the video information from the various sensors to the resolution capabilities of the display.

For example, it may be required to display the output of a line scan sensor (e.g. a SLAR) which has, say, 400 lines of information in the 4:3 aspect ratio of standard TV and this information has to be displayed on the 585 active lines of a 625 line monitor. Using processing techniques there are at least two possibilities. 400 of the available 585 active lines on the display can be used directly and, to preserve the aspect ratio, the data along the line can be compressed by increasing the rate of the store read clock. This format is shown in figure 3. It may, however, be felt that this is not a very efficient way of utilising the available display area, in which case it could be arranged that the required 585 lines be generated from the 400 available lines thus using the full area of the display. The form of interpolation used to derive the display lines can range from a simple repetition of the closest available input lines to a complex algorithm involving weighted contributions over a wide aperture for each display point. (DREWERY J.O. 1973, BBC 1966). Whilst it is clearly not possible to add information that was not present in the original sensor output, this technique can be used to enable the most efficient use to be made of the display when confronted with a wide variety of input data formats.

The display interpolation concept can be extended to provide a zoom facility where the displayed image is magnified about a selected point. In this case as the field zooms in, a reducing number of sensor elements have still to generate the requisite number of lines on the display. There is an obvious limit to the extent to which the image can be sensibly magnified, based on the resolution of the sensor.

If the sensor system is of a higher resolution than the display, then reverse interpolation algorithms, allowing the generation of one display line from a group of sensor lines, can be employed in order that the full field of view can be displayed on the monitor. In this instance each displayed picture element will contain a portion of its surrounding elements and the display will be limiting the system resolution. If the picture is then zoomed in about a selected point, the full sensor resolution can be displayed over a reduced field of view.

APERTURE CORRECTION

In imaging applications aperture effects result in a progressive attenuation of high component frequencies. It is possible to apply some degree of compensation to aperture degraded signals by means of a non recursive, and hence linear phase, high frequency boost digital filter. The realisation of this filter is relatively straightforward utilising the arithmetic unit A (figure 2). The algorithm operates on a block of adjacent picture points. These are normally obtained by means of accurate delay lines in the video signal path. However, the digital solution presents less problems since there is no difficulty in extracting a block of adjacent picture points from the buffer store.

The resultant aperture corrected display is one in which contrast edges and fine contrast detail are enhanced at the expense of a slightly degraded signal to noise ratio.

OVERLAY OF SYNTHETIC INFORMATION

In order to ease the problem of display interpretation, it is useful to be able to overlay synthetic data. This information may be the results of computations carried out on the radar return (i.e. target velocities or identification signals) or separately generated information such as range markers. In either case it is necessary to be able to superimpose this information onto the existing video signal.

The addition of any complex overlay information, such as a terrain map, is easier to implement in a digital storage system since it can be written into the store, when required, at selected locations and is then automatically read out with the stored video data, retaining its correct positional relationship. The usual problems associated with the synchronisation of two separately generated analogue video waveforms are not encountered.

In the case of continually changing overlay information, where it may not be convenient to allow the normal update of the stored data to erase the overlay, a separate storage plane can be implemented. The read out of data from this plane is addressed in parallel with the main store, but it can be written and erased separately, thus providing a very flexible system for overlaying information.

COMPUTER ORGANISED PROCESSING EQUIPMENT

Space, weight,and power restrictions on electronic equipment have led to a trend in which an increasing number of operational functions are incorporated in a single unit. Hence it is necessary that the single equipment be based on a very flexible design concept. In general, an equipment designed to perform a wide variety of tasks can be large, involved and difficult to service if designed on the principle of a hardwired interconnection of dedicated logic functions. A more attractive solution is to take advantage of the recent developments in micro-processors. The micro-processor is a natural development of the semiconductor manufacturers present ability to fabricate digital integrated circuits of high internal complexity and it can provide the basis for small, fast micro-programmable computer organised systems whose speed can match that of the N-channel MOS memory.

A flexible micro-processor controlled digital system has been designed to process video information from a wide variety of sensors (figure 5). The basic system concept is depicted in figure 4. The central hardwired element is a fast arithmetic unit capable of accepting and distributing data on several lines and also of performing digital computation on this data, all under the control of the micro-processor. Selection, by software programme, of the appropriate data paths enables both recursive and non recursive processing to be performed in the same arithmetic unit. The micro programme also supplies the information to the buffer store address generator to enable the various input data formats to be loaded correctly.

The following facilities were incorporated in the design of this equipment:

Standards Conversion

Most forms of scanning format can be converted to standard flicker free TV compatible video.

Asynchronous Operation

The incoming signals and output video can vary in both phase and frequency, thus allowing the equipment to be used as a buffer for imaging and display systems utilising different master sync. frequencies.

Moving Target Indication

Moving targets on the display may be amplitude or colour highlighted depending on the CRT used, with or without a background overlay of the normal scene. An audible or visual alarm system with discriminatory properties can be integrated with the MTI display.

Noise Reduction

The signal to noise ratio of the image can be improved by up to 24 dB with no degradation in system resolution.

Interpolation

Lines can be added to the output resulting in a more acceptable display should the input imaging system have only a limited number of lines.

Electronic Zoom

The magnification of the picture on the display may be altered by up to 10:1 whilst still maintaining the same number of lines on the display.

Auto Lock Follow

The system can be programmed to provide an auto lock follow facility to track a target of interest within the picture and to provide information for a stabilisation or tracking loop.

Aperture Correction

The definition of the displayed information can be improved by edge enhancement in both the vertical and horizontal planes.

Frozen Frame

A picture on the display may be frozen without degradation for as long as required.

Contrast Enhancement

The incoming video amplitude can be automatically adjusted such that the overall maximum and minimum signal levels encompass the complete grey tone range. This facility can be programmed to operate over a selected patch of the displayed scene.

Mini-Computer Interface

The processor can be coupled to a mini-computer in a master-slave arrangement for more complex picture point processing. The results of the computation can be held in a second buffer store, the contents of which can be continuously displayed on a standard TV monitor to provide a real time display of processing such as:

Convolution/deconvolution

Pattern Recognition

Removal of Blur Due to Movement

In view of the specialised nature of these processors, self checking hardware can be included to enable rapid fault location. This, coupled with plug-in-unit construction, enables down time to be minimised.

CONCLUSIONS

Emphasis has been placed on the importance of the form of the displayed image in terms of information transfer to the observer and attention has been drawn to the ways in which digital processing of the video information can increase the efficiency of the display/observer link.

This paper has deliberately not detailed any one specific type of processing. Rather it has attempted to draw attention to the many possibilities in this field afforded by the recent and anticipated advances in integrated circuit technology. The availability of memory devices with higher density, coupled with the improved system concepts made possible by micro-processor technology will, in turn, lead to significant advances in the processing of video information over the next few years.

REFERENCES

1. J.O. Drewery, J.R. Chew, G.M. LeCouteur, 1973, "Interpolation in Digital Line Store Standards Conversion: A Theoretical Study", BBC Engineering.

2. BBC, 1966, "The Choice of Interpolation Apertures for Line Store Standards Converters", BBC Research Department Report No. T-177.

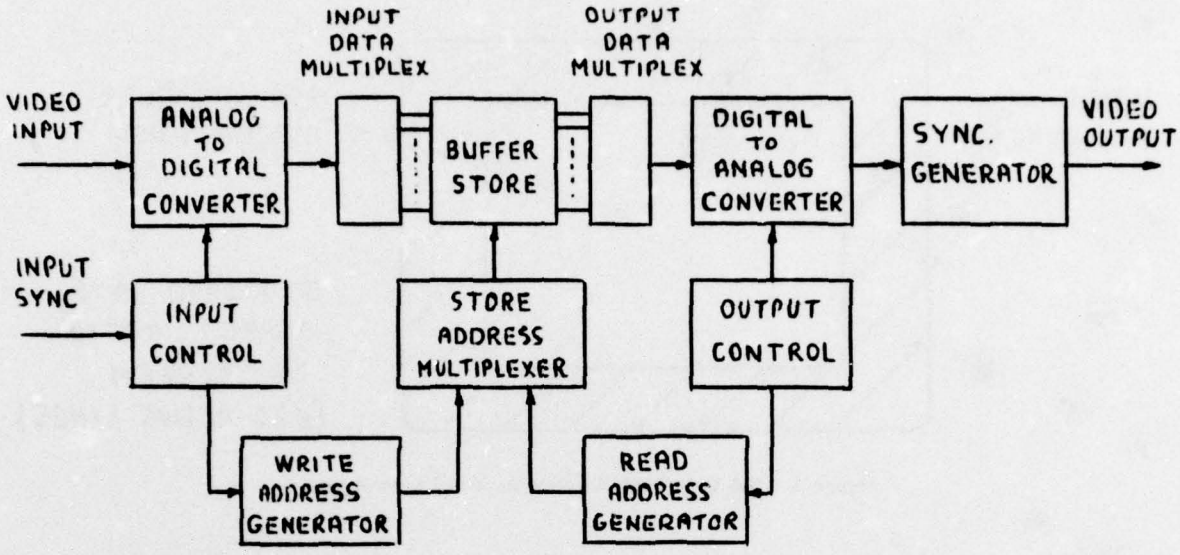

Figure 1. A Typical Digital Scan Converter Arrangement

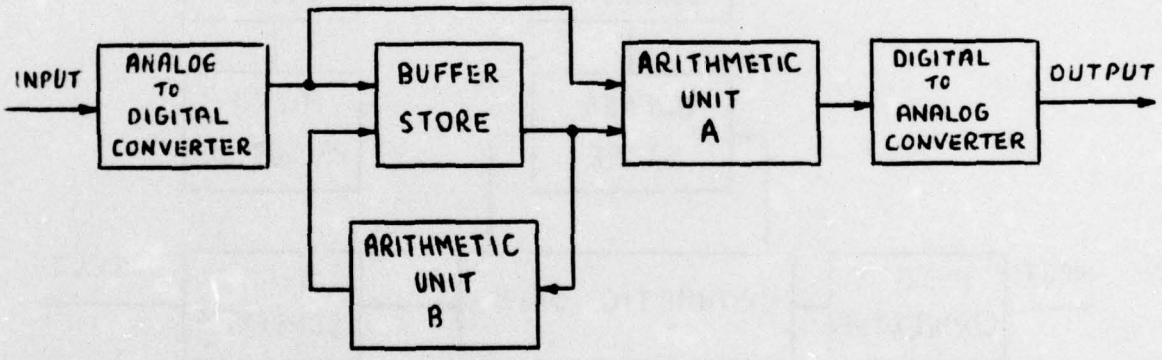

Figure 2. Digital Processor Block Diagram

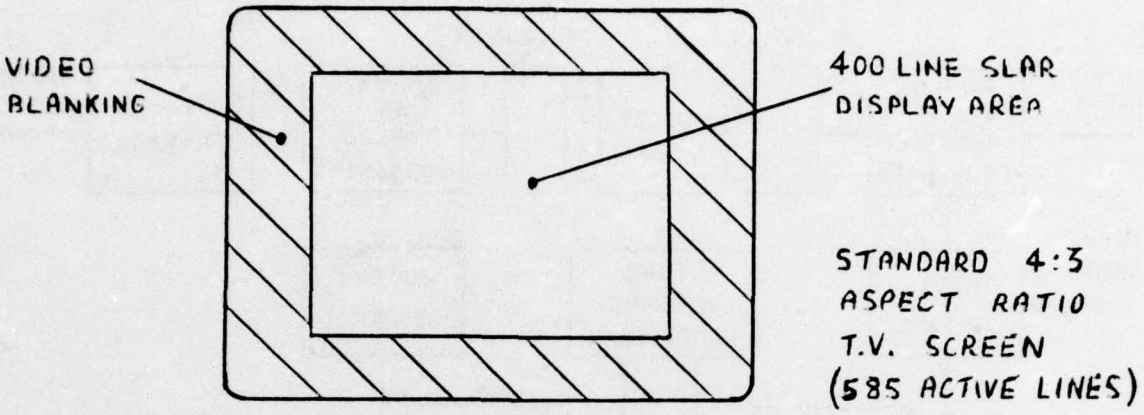

Figure 3. 400 Line SLAR Display On A 625 Line Monitor

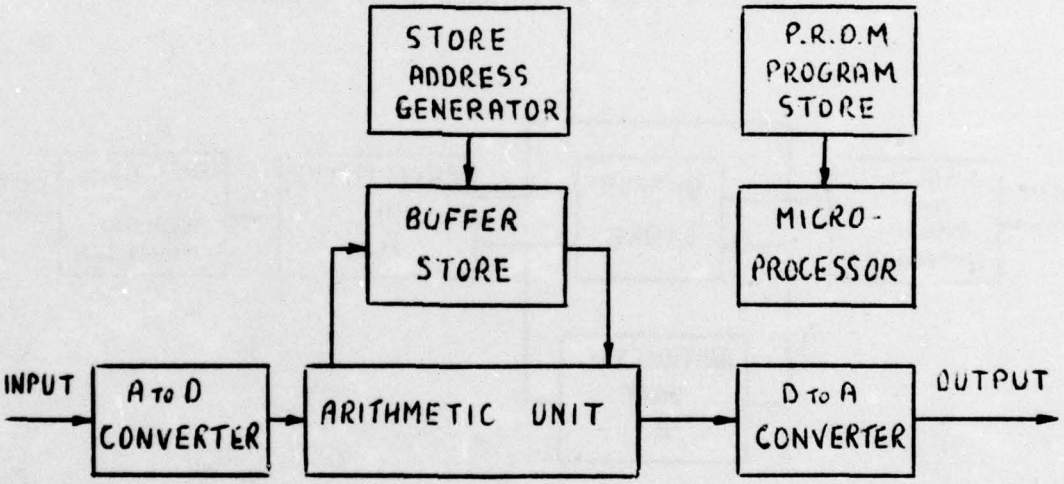

Figure 4. Micro-processor Controlled System

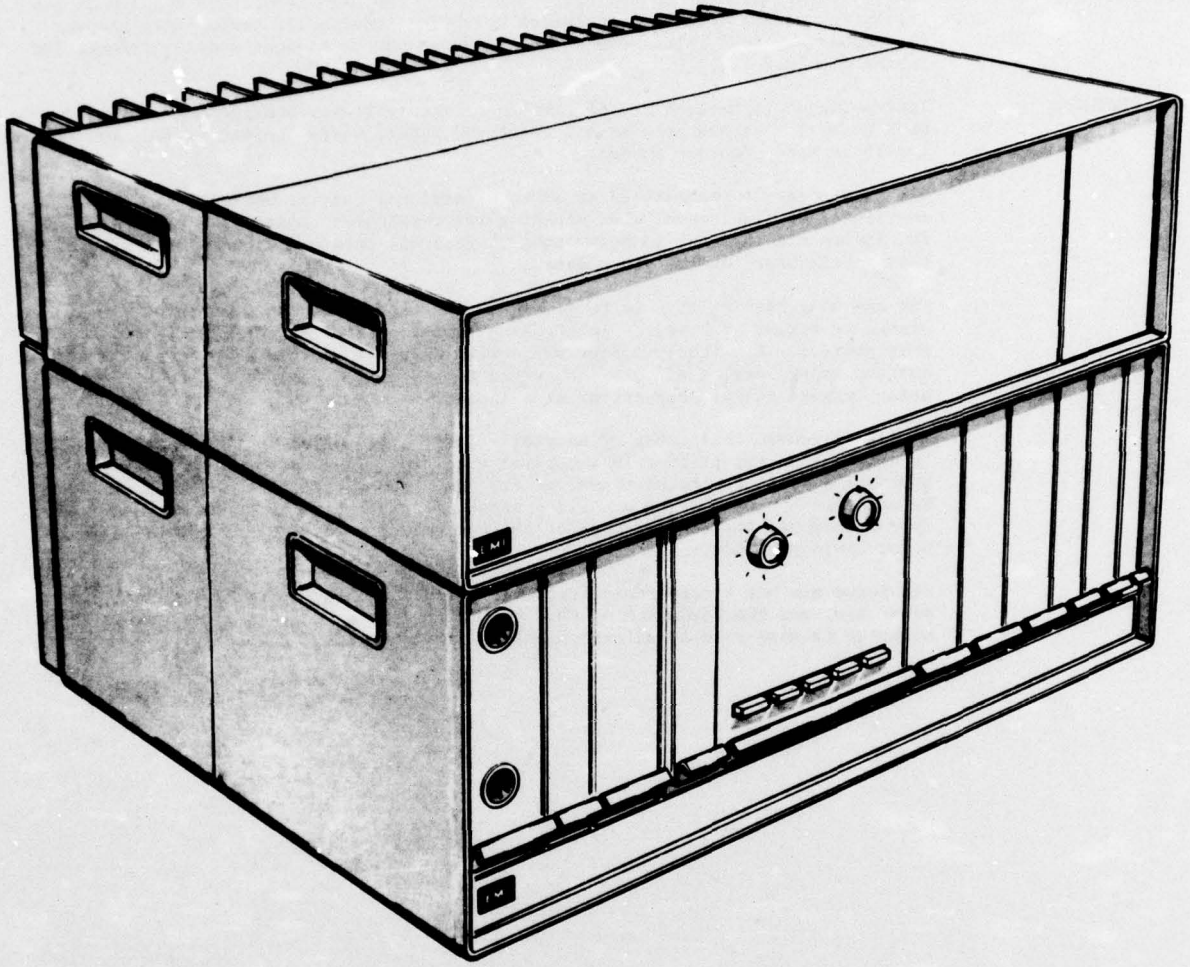

Figure 5. A Computer Organised Processing Equipment

DISCUSSION

D R BOLLARD: Does the requirement for sequential readout indicate that the large store package size may in fact inhibit power-down operation and the consequent reduction in power consumption?

P V COATES: Each case must be considered on its merits.

M VOGEL: Can you please comment on the optimum match of the high resolution display to low resolution sensor data (interpolation weighting functions), taking into account the emphasis placed by the human visual system on the highest spatial frequencies in the display?

P V COATES: Interpolation techniques are of particular interest when considering a display such as that obtained from an air-to-ground radar, where the requirement may be for 16 or more contrast shades.

If the display is represented as a two-dimensional matrix, where each element comprises one pixel then, when matching low resolution sensor data to a high resolution display, one is attempting to generate intermediate elements within this matrix based on the given data.

One way of achieving this is to generate a surface of facets by forming flat planes at triads of pixels. Interpolated points are obtained by projections on to this surface. A slightly better subjective result is obtained by forming a curved surface using, say, a sin x/x law, since this does not degrade contrast edges and point targets to the same extent as a linear law.

Having increased the number of display pixels, a reduction in the apparent 'sharpness' of the picture is sometimes obtained. This can be countered by applying a boost to the high spatial frequency components in the scene. This can be achieved by correlating a small aperture matrix (which can correspond to the two-dimensional impulse response of the system) with the picture matrix on a point-by-point basis.

The human eye has a non-linear amplitude response, often approximated by a $^{1}/_{3}$ power law, and the inclusion of this within the processing can often enable an observer to more readily extract scene detail from within a displayed picture.

DESIGN AND FIELD TESTING OF A DIGITAL AREA MTI-PLOT EXTRACTOR

J. Dekker
SHAPE TECHNICAL CENTRE
P.O. Box 174 - The Hague
Netherlands

SUMMARY

This paper describes a non-supervised, non-parametric learning algorithm which, incorporated in an automatic radar data extraction system, has the ability to maintain a given constant false alarm rate (CFAR) in an, a priori unknown and changing, clutter and interference environment. The actual performance of a thus implemented extraction system is demonstrated by the results of operational field tests and by a series of long-term extracted plot histories of recorded video signals from a variety of radar stations in Europe.

1. INTRODUCTION

As is well known (Skolnik), Area MTI is a processing method which divides a radar's area of surveillance into small cells or resolution elements. The principle of operation is that of a single threshold amplitude discrimination for each cell, i.e. the system rejects input signals having amplitudes less than a stored reference value. The requirement that the system should have a given constant false alarm rate (CFAR) while maintaining a maximum of target detection sensitivity, leads to the statement that this stored reference level should be a replica of a given p-percent value of whatever probability density function (pdf) is representative for the underlying background or clutter signals. Thus the problem of area MTI can be reduced to a control problem of estimating or restoring a given p-percent value of any underlying pdf of each resolution cell. A solution to this control problem and its incorporation in an actual automatic radar data extraction system will be discussed.

2. ESTIMATING A P-PERCENT VALUE OF A PROBABILITY DENSITY FUNCTION

2.1 A learning oriented approach

The approach to the solution of an estimation problem like this, depends on the amount of a priori information which is available about the pdf, such as functional form, parameters and, in the dynamic case, their time relationship. The usual, analytical approach is to assume that this a priori information is more or less completely available. Although this assumption has very often to be made just for the sake of an analytical treatment of the problem, the question may be posed whether it is always justified by existing knowledge about the real world phenomena. In the case of video signals received from a particular radar cell, it must be reckognized that the assumption of having a priori information available is not realistic. For example, consider a medium-distance radar cell located over a sea area illuminated by a land-based radar. The signals observed in such a cell may, depending on temporary conditions, be classified either as system noise, or originate from sea surface reflections, ground echoes received through the back- and sidelobes, weather clutter, or stationary platforms and ships, angles, interference or any combination of these. Even if the functional forms of the pdf of all these signal classes were known, which is not the case, it is impossible to predict the moments of occurrence. Hence, the level of uncertainty is very high and not small, as suggested by the assumption of sufficient a priori information in an analytical solution. The foregoing example and underlying considerations are, in a general way, valid for each radar cell within MTI range. Thus the only realistic modelling of a radar cell environment would be by means of a pdf with a priori unknown functional form, which may change in an unknown way at unknown moments. Now, if all forms and parameters change very often or even continuously, such a model would describe a chaotic situation, and there would be little hope of obtaining useful information from it. If, however, two consecutive changes of the same factor are separated by a sufficient time interval, non-parametric adaptive or learning algorithms can be applied. As pointed out by Tsypkin
"Adaptation and learning are characterized by a sequential gathering of information and the usage of current information to eliminate the uncertainty created by insufficient a priori information".
The application of learning algorithms appears to be very profitable, because it would eliminate the need for input signal analysis, which is often difficult and sometimes even impossible. Even if the analysis is feasible, the concept of "learning" instead of prior analysis may be attractive. There is of course a penalty to be paid. During the learning time needed to eliminate the uncertainty, the process output is undefined and can not be used effectively. Furthermore, the learning time is directly proportional to the uncertainty - the greater the uncertainty the longer the learning time. The model previously described assumes very limited a priori information (in fact, a degree of uncertainty is created at the instant of each of the pdf changes). The learning method selected for use in the model must therefore not only guarantee accurate convergence to the p% value after each change, but must also guarantee that this convergence is as fast as possible.

2.2 A learning algorithm

2.2.1 The basic algorithm

As a first step towards a suitable learning method one considers the flow diagram of Fig. 1. The value of the current level (LEV) is compared with the current input value (INPUT). If the latter is greater, a hit is declared and the current level is increased by a small amount (DELTA). This increment reduces slightly the probability of another hit in the same resolution cell at the next observation. If the current input is less, a miss is declared and a random number (uniformly distributed between 1 and N) is compared with a constant value (C). When equality occurs (which happens, on the average, once out of N miss declarations), the current level is decreased by the same small amount (DELTA). This decrement slightly reduces the probability of another miss in the cell at the next observation. If p (hit) is the probability of a hit declaration, the probability of one out of N miss declarations can be given as $N^{-1}\{1-p(hit)\}$. The mechanism strives for a stable balance, which is reached if both actions (increment and decrement) are equi-probable. Then

$$p(hit) = N^{-1}\{1-p(hit)\}$$

or

$$p(hit) = (N+1)^{-1},$$

which is the estimation of the $(N+1)^{-1}.100\%$ value of input pdf. Although, due to the hard-limited negative feedback, the balance is fundamentally stable and is always restored, the current level (LEV) fluctuates between two values, at which the deviation from the equi-probability becomes sufficiently great to affect the feedback. This effect depends on the steepness of the cumulative pdf of the input around the p% value, with respect to the value of (DELTA) by which the level (LEV) is updated. Since the functional form of the input pdf is assumed to be unknown (e.g. it could be a wide-spread Gaussian-, but may be a Dirac-function as well) and thus no optimal value of (DELTA) can be derived, this quantity should be selected as small as possible, i.e. corresponding to the least significant digit of the digitally converted signal. This reduces the fluctuations and thus increases accuracy as much as possible, although probably not always in the most efficient way. This deficiency becomes apparent if a change in one of the parameters of the input pdf necessitates a considerable modification of the current level (LEV). Since only one step (DELTA) can be taken at a time, the total time involved in the modification (the learning time) may become excessive and is not in correspondence with the requirement that the convergence to the p% level should be as fast as possible. However, a bigger value of (DELTA) violates the requirement of maximum accuracy. Any rigid compromise between learning speed and accuracy can never be completely satisfactory, and hence an adaptive value of (DELTA) must be considered - in other words, an acceleration of the convergence to the p% level is necessary. With reference to the algorithm of Fig. 1, acceleration becomes necessary if the deviation from equi-probability of increment and decrement exceeds preset limits. A convenient method for detecting this is the introduction of an asymmetric binary integrator, which integrates only if the ratio of the two input probabilities exceeds the inherent asymmetry. The contents of the integrator can, directly or via a transfer function, be used to modify the value of (DELTA). The asymmetrical binary integrator (ABI) operates on the observed states (S) of a binary input, i.e. an input state which is either true or false. If S_k denotes the state of the binary input at the kth observation, the output of the ABI is

$$Y_k = \sum_{i=1}^{k} X_i$$

where, if $Y_{k-1} \leq 0$,

$$X = \begin{cases} +A, & S_k = \text{true}; \; A > 1 \\ -1, & S_k = \text{false} \end{cases}$$

or, if $Y_{k-1} > 0$,

$$X = \begin{cases} +1, & S_k = \text{true} \\ -A, & S_k = \text{false}; \; |A| > 1 \end{cases}$$

The inclusion of $Y_{k-1} = 0$ in one of the two asymmetry modes is arbitrary and should, for unbiased operation, be randomized, i.e., it should occur with probability 0.5. The selected asymmetry mode can be given as the ratio of the selected increment and decrement, i.e. as A or as A^{-1}.

2.2.2 The modified algorithm

The introduction of the ABI in the basic algorithm is shown in Fig. 2. The asymmetrical binary integrator (ABI) is a signed integer. If (ABI) is positive, the selected asymmetry is A^{-1}. Hence the contents of (ABI) are decreased unless the increment probability is equal to or greater than A times the decrement probability. This is the case if

$$p(hit) \geq A.N^{-1}\{1-p(hit)\}$$

or

$$p(hit) \geq (A^{-1}.N+1)^{-1}$$

which is the condition for positive acceleration. If (ABI) is negative, the selected asymmetry is A. Hence, the contents of (ABI) are increased unless the decrement probability is equal to or greater than A times the increment probability. This is the case if

$$N^{-1}\{1-p(hit)\} \geq A.p(hit)$$

or

$$p(hit) \leq (A.N+1)^{-1}$$

which is the condition for negative acceleration. The contents of (ABI) thus fluctuate closely around zero as long as

$$(A^{-1}.N+1) > p(hit) > (A.N+1)^{-1}$$

which is normally the case if the input is stationary in a statistical sense. A temporary clustering of hit- or miss-declarations increases these fluctuations, but this should not be identified as a non-stationarity. To identify a non-stationary condition, a discrimination threshold (B) is applied. The contents of (ABI) must exceed the threshold (B) before action is taken to modify the value of (DELTA). The modified value of (DELTA) is used only with the same polarity as (ABI). This measure introduces a hysteresis in the feedback loop, suppressing a possible tendency for self-oscillation. Also, it seems likely that, whatever information is gained from tracking one gradient, can not be applied to track another gradient of opposite polarity. The contents of (ABI) may be used to indicate the "quality" of the generated level (LEV). If (ABI) is high, e.g., greater than threshold (B), the process is in a "learning" status and (LEV) can not be used effectively. If (ABI) is small, the status is "learned" and the quality of (LEV) may be considered high.

3. THE ACTUAL PERFORMANCE

3.1 General

It seems rather pointless to assess by means of a mathematical analysis or simulation the behaviour of a system of which the design objective is to operate on input data having completely unknown statistical properties on which no assumptions are made. In other words, the design environment is not a fictitious mathematical model, suited for analytical treatment, but rather a non-specified entity, which can assume any form and property and thus can exactly match the actual environment within the limits of the quantization of signal dynamic range and resolution cell dimensions. Hence, the resolution should be as high as economically and technically feasible. This conclusion is consonant with what may be called a general design rule for any self-learning device, i.e. there should be sufficient redundancy to create the possibility of adaptation to any conceivable situation. The costs of implementation of this rule, together with the deficiency of the necessary learning time is the price one has to pay for adopting this non-analytical approach. Because there is, it seems, no other alternative to justify this principle than by indicating its actual performance, several area MTI prototypes, utilizing this approach have been designed and built at STC during the past four years.

3.2 The first prototype

This prototype, implemented with the basic algorithm, was subjected to a series of operational field tests at a number of landbased and coastal, S- and L-band manually operated radar stations in Europe. The unit was installed and operationally integrated in these sites by making the area MTI output available as an optional video source to the PPI operators. During a three-months, day and night, test period per site, photographs were taken of the PPI-displays of linear- and MTI-video and the site-personnel commented on the operational value of the area MTI-video option. These reports were, in general, very favourable. To bypass the subjective element and to obtain some numerical results, two trained PPI operators were asked to track and record the blip-to-scan ratio of targets of opportunity in a range interval of 10 to 55 n mi. This area contained strong ground clutter and intermittent weather clutter in several directions. The exercise was performed over 5000 scans (i.e. about 15 hours total tracking time). The results have been compiled for L-band in Fig. 3 and for S-band in Fig. 4. The overall conclusion at the termination of the tests was that this kind of MTI-processing is entirely feasible and offers excellent performance in the case the clutter signals are stationary, or nearly stationary, in a statistical sense. This holds for ground- and sea-clutter, but also reflections from rain-, snow-, and chaff clouds under conditions of low wind speed. However, some deficiencies became also apparent such as:

(i) Vulnerability of the system to clutter levels being highly non-stationary in space and time (wind-driven scatterers, anomalous propagation), due to the long learning time of the implemented basic algorithm. This results locally in a too high or too low FAR.

(ii) Vulnerability of the system to wilful or accidental interference, due to integration of interference-power into the clutter map. This leads to a prolonged loss of target visibility.

(iii) Fluctuation of detection probability of a slow moving target during its transient from one resolution cell to the next.

(iv) Range dependency of minimum tangential target velocity threshold due to the increase of lateral dimension of the resolution cells with range.

To cope with these and some other minor problems a second prototype, implemented with the modified algorithm, was designed and built.

3.3 The second prototype

A block diagram of this new system, called PEACE (for Plot Extractor and Adaptive Clutter Eliminator), is given in Fig. 5. This shows the data flow to and from the storage devices, i.e. a head per track magnetic disc store (128 tracks, total capacity 6.4 MBits) and three autonomous core store modules (4 K words of 18 bits each), and the subsystems: Cluttermap Processor, Fast Noise Register and Data Extractor. A more detailed diagram of these subsystems is given in resp. Fig. 6, Fig. 7, and Fig. 8. Some salient design points and a summary of system specifications are described in Appendix A. To demonstrate the actual performance of this second prototype a different technique has been applied. It is believed that one of the most demanding and informative tests on the actual performance of any radar extractor is a long term integration of plots extracted from a-selective live radar data, i.e. recording the history of extracted plots over a randomly selected interval of more than 100 antenna-revolutions. The length of such a history-record allows an assessment of the quality and consistency of tracks formed by valid plots of targets of opportunity and also indicates the spatial distribution and densities of false plots. It suppresses also the inadvertent tendency of the experimentalist to be selective in producing evidence.

The trials were carried out by playing back three existing videotape recordings chosen from STC-stock. These tapes were previously recorded for other applications at three different sites. This method not only meets the requirement of aselectivity but also enables the trials to be run again without the area MTI function, to assess the insertion loss of this function. The method also demonstrates the versatility of the system in its ability to operate on radar signals with completely different characteristics.

The results of each trial are presented in two sets of two pictures. The first set shows the plot output of a single scan with and without the area MTI function operative. The second set shows the plot output integrated over a number of scans, also with and without the area MTI function. The integration time differs for each trial and is so chosen that in each case about 2500 plots are recorded on the picture with the area MTI function on. Range rings intervals are always 10 n mi.

TRIAL 1 (see Fig. 9)

The main characteristic of this trial is the presence of fast-moving weather clutter. The velocity is estimated at 48 knots. Although the elimination of clutter plots is good, a decrease of the probability of detection, due to the insertion loss, is noticeable. This can be partly explained by the rather low power of the site, enhancing the effects of a given insertion loss. Also, in this kind of clutter environment, the lack of a negative acceleration in the map function causes a reduction of the detection volume. Integration time: 125 scans.

TRIAL 2 (see Fig. 10)

The situation is comparable to that in Trial 1. However, the radar system is a more powerful one and so the effect of the insertion loss on detection probability is negligible. Due to the dense air traffic (about 50 targets per scan), the integration time was limited to 60 scans.

TRIAL 3 (see Fig. 11)

The environment is characterized by heavy ground clutter. A feature to note is a chaff exercise, visible at 80 n mi, 8 o'clock. Most plots extracted in this area are from the chaff-sowing aircraft, while only a few residual chaff plots were integrated. The visible radial signals are caused by playback errors of the video recorder and should be disregarded. Integration time: 160 scans.

4. CONCLUSIONS

The first prototype of the digital area MTI has matured to a full-grown extraction system with a integral MTI-function. The system is suited as a cost-effective retrofit[*] to existing 2D- and 3D-radars, whose parameters do not permit successful application of a coherent Doppler-MTI technique. The robust operation of the system, i.e. its resistance against transients and other unpredictable background events, insures a high degree of reliability and stability, as demonstrated by actual field trials. Some criticism may also be in place here. The applied MTI-technique, a single threshold amplitude discrimination has practically no subclutter visibility. Because no use is made of any a priori information which may be available, redundancy costs and speed limitations are substantial. However, these disadvantages have to be weighted against the "nervousness" and probability of malfunctioning, due to differences between assumed and true signal properties, which is experienced with a more sensitive and deterministic moving target detection process. Another point of possible criticism is that the non-analytical approach to the area MTI problem might have been adopted merely as a justification for the application of a special technique. This possibility does not invalidate, however, the evidence showing that non-analytical tasks can be performed very well by automatic control systems. Although, admittedly, the term "very well" cannot be defined easily in a quantitative sense.

APPENDIX A

TECHNICAL DESCRIPTION OF "PEACE"

(PLOT EXTRACTOR AND ADAPTIVE CLUTTER-ELIMINATOR)

A.1 General

The purpose of the work was to design an automatic radar data extraction system which, by using the raw video from an acquisition radar as input, could detect the presence of moving targets, extract the positional data from these targets, and present the information in suitable message format to a tracking computer, i.e. a Ferranti 1600B. Maximum use was to made of the ideas evolved in Chapter 2 and of the experience gained with the first prototype area MTI. The new system, called "PEACE" is in certain respects similar to the first prototype area MTI, but for convenience a complete description is given, with the emphasis on modifications and additions.

The system is designed around a magnetic disc store (128 tracks, total capacity 6.4 Mbits) in conjunction with three autonomous core store modules (4 K words of 18 bits each). The data flow to and from these storage devices is shown in Fig. 5. Module A is under the control of the extractor. At each radar trigger the complete block of all 2048 32-bit cells is transferred. Controlled by a range counter, each cell is sequentially read, processed in the extractor, and written back. Modules B and C function alternatively as an input/output buffer for the disc and as a working storage for the clutter map processor. The exchange of functions occurs at the end of each sector of 2.8^{o} in the antenna azimuth position. The contents of the module that has the function of input/output buffer are then transferred to the $(N-1)^{th}$ track of the disc, N being the number of current 2.8^{o} sector. Immediately after this operation the contents of the $(N+1)^{th}$ track of the disc are transferred to the same (now emptied) core store module. This two-way transfer needs, in the worst case, 2.25 disc revolutions, i.e. 39 ms. Thus the maximum antenna rotation rate allowed for is 12 revolutions per minute. The module that has the function of working storage contains the data of the N^{th} sector and is under the control of the clutter map processor. This data is subdivided into 16 "sweep blocks" of 392 eight-bit cells. At each radar trigger, one "sweep-block" transfer is effected, the block concerned being defined by the current azimuth position information. Controlled by a range counter, each cell of the appointed "sweep block" is sequentially read, presented for output, modified by the map processor, and written back.

A.2 Clutter map processor

A block diagram of the clutter map processor is given in Fig. 6. Cell (R,A,i) denotes the 8-bit clutter map data corresponding to the physical area defined by the range (R) and the azimuth (A) during the current scan number (i). This data is subdivided into a 5-bit amplitude part AMPL(R,A,i), a 2-bit acceleration part ACC(R,A,i), and a 1-bit part to record the plot history. The sweep number is a randomly-generated number, which is uniformly distributed between 1 and N. The actual mechanism is a serial counter, which counts the radar sweeps and is reset each N^{th} count. Random fluctuations and asynchronization of antenna movement and radar sweeps give, in most applications, a reasonable approximation of a uniform distribution

[*] Total component costs of the unit is approximately DG 50,000.

of the contents of the N-counter, when sampled on a scan-to-scan basis. In some applications, however, the use of a more sophisticated random-number generator must be considered. It is desirable that the map updating is performed only once per antenna revolution. For this reason a mechanism is introduced which assigns a label "valid" to the first radar sweep after a new "sweep block" is appointed (see Section A.1). Any following sweep before the next "sweep block" is appointed is labelled "not valid". During these sweeps the contents of the map cells are frozen. The clutter map processor executes the recurrence equations:

$$AMPL(R,A,i) = AMPL(R,A,i-1) + \Delta_s$$

$$ACC(R,A,i) = ACC(R,A,i-1) + \Delta_t,$$

where Δ_s and Δ_t assume values assigned by the following processes:

If there is a hit and ACC(R,A,i-1) < 2, then $\Delta_s = +2$
or, if there is a hit and ACC(R,A,i-1) = 2, then $\Delta_s = +4$
or, if there is a hit and ACC(A,R,i-1) = 3, then $\Delta_s = +8$
or, if there is a miss and sweep number= N, then $\Delta_s = -1$
or, if there is a miss and sweep number≠ N, then $\Delta_s = 0$
or, if there is a not-valid sweep , then $\Delta_s = 0$

If there is a hit , then $\Delta_t = +1$
or, if there is a miss and sweep number= N, then $\Delta_t = -1$
or, if there is a miss and sweep number≠ N, then $\Delta_t = 0$
or, if there is a not-valid sweep , then $\Delta_t = 0$

The design false alarm rate (FAR) of the cells is

$$100(2N+1)^{-1}\%,$$

where the parameter N is set by manual switches in the range of 1 to 256, in unit steps. Only a positive acceleration action is implemented. The condition for acceleration is

$$FAR \geq 100(N+1)^{-1}\%,$$

and the action is effected if

$$ACC(R,A,i-1) \geq 2.$$

The quality of the current and adjacent map levels is considered to poor if

$$ACC(R,A,i-1) = 3$$

and consequently this condition is applied to control the integration of possible hits into the moving window of the extractor.

A.3 Fast noise register (FNR)

Assuming the presence of noise-like or pulsed, non-synchronized interference, the objective of this mechanism is twofold - first to reduce considerably the amount of interference power integrated into the clutter map and secondly, to present resistance against the increased FAR, while maintaining at least some target sensitivity. Under normal conditions, the mechanism operates on thermal noise and generates the quantizing level controlling the FAR of noise cells outside the clutter map range. A block diagram of the FNR is given in Fig. 7. The sampling of interference or noise is performed each range interval within a distant range region, e.g. 40 times over the outermost 10 n mi of the radar sweeps. A deterministic count of the miss declarations is made to indicate the M^{th} misses. A gated clock, derived from the hits and the M^{th} misses, is used to update the register. If EAMPL(t) denotes the 12-bit amplitude contents and AECC(t) denotes the 8-bit acceleration contents of the FNR after the occurrence of gated clock pulse t, the following equations are executed:

$$DELTA = \max\{|EACC(t-1)| - B, +1\}$$

$$EACC(t) = EACC(t-1) + \Delta_u$$

$$EAMPL(t) = EAMPL(t-1) + \Delta_v,$$

where B is a constant, set by manual switches and

Δ_u and Δ_v assume values assigned by the following processes:

If there is a hit and EACC(t-1) is positive, then $\Delta_u = +1$, $\Delta_v = +DELTA$

or if there is a miss and EACC(t-1) is positive, then $\Delta_u = -2$, $\Delta_v = -1$

or, if there is a hit and EACC(t-1) is negative, then $\Delta_u = +2$, $\Delta_v = +1$

or, if there is a miss and EACC(t-1) is negative, then $\begin{cases}\Delta_u = -1 \\ \Delta_v = -\text{DELTA}\end{cases}$

The design FAR of the noise cells is

$$100(M+1)^{-1}\%,$$

where M is set by manual switches in the range of 1 to 256, in unit steps. The selected value of M should preferably be two times the selected value of N (see Section A.2). The FAR of the noise cells is then equal to the FAR of the map cells. As shown in Fig. 6, the quantizing level actually used is the higher of the values in the FNR and the current map cell. If the FNR is selected instead of a particular map cell, the feedback loop to that map cell is interrupted and consequently it behaves like an asymmetrical binary integrator. If the FAR defined by M is in correspondence with the asymmetry defined by N, the contents of the map cell remain basically unchanged. By choosing M slightly different from 2N, the user may opt for a slow addition of interference power into the map cell or a slow decrease in its original contents. The condition for positive acceleration is

$$\text{FAR} \geq 100(0.5M+1)^{-1}\%,$$

and for negative acceleration

$$\text{FAR} \leq 100(2M+1)^{-1}\%,$$

The threshold B is set by manual switches in the range of 1 to 256, in unit steps.

A.4 Data extraction process

The extractor is of the binary moving-window type. For each range bin, a 32-bit slot is available. This slot is subdivided into three parts: a moving window (MW) with a maximum capacity of 18 bits, a 12-bit azimuth storage (AZ), and a 2-bit status indicator (SI). The extractor process is shown in Fig. 8. When SI(R,k) = 1 (where k is the current radar sweep and R is the current range bin), the process searches for a "target begin" condition. The contents of MW(R,k) are compared with a threshold, T_{begin}.

If $\text{MW}(R,k) \geq T_{begin}$

then $\text{AZ}(R,k+1) = \text{current azimuth}$

and $\text{SI}(R,k+1) = \text{SI}(R,k) + 1$

When SI(R,k) = 2, the process searches for a "target end" condition. To prevent range splitting of the evolving target,

$$\text{MW}(R+1,k) = 0$$

and

$$\text{SI}(R+1,k) = 1$$

The contents of MW(R,k) are compared with a threshold T_{end}.

If $\text{MW}(R,k) \leq T_{end}$

then $\text{AZ}(R,k+1) = 0.5\ \{\text{current azimuth} + \text{AZ}(R,k)\}$

and $\text{SI}(R,k+1) = \text{SI}(R,k) + 1$

When SI(R,k) = 3, the process waits for a data transfer, via an output buffer register, to the tracking computer. If the output register is ready to accept data, it is loaded with a message composed of AZ(R,k) and the contents of a range counter. This message is subsequently transmitted to the tracking computer, controlled by the latter's interrupt system. The process is always concluded by the updating of the moving window. If QNT is the binary quantized amplitude of the video, i.e. QNT=1 for a hit and 0 for a miss, then

$$\text{MW}(R,k+1) = \text{MW}(R,k) - \text{QNT}(R,k-L) + \text{QNT}(R,k),$$

where L is the length of the moving window. The parameters T_{begin}, T_{end}, and L are set by manual switches: T_{begin} and T_{end} in the range of 1 to 16 and L in the range of 3 to 18.

A.5 Summary of system specifications

(A) Map cells

No. of cells	: 800,000
Range resolution	: 0.25 n mi and 0.5 n mi adjustable
Azimuth resolution	: 0.176^{o} or 0.352^{o}, range-dependent
Amplitude	: 5 bits (2^5)
Acceleration	: 2 bits (2^2)
Plot history	: 1 bit
Increment	: 2, 4, or 8 adaptive
Decrement	: 1
Decremental rate	: 1 to 256 selectable

(B) Fast noise cell

Sampling	: 40 intervals at distant range
Amplitude	: 12 bits (2^{12})
Acceleration	: 8 bits (2^{8})
Increment	: 1 to 256 adaptive
Decrement	: 1 to 256 adaptive
Decremental rate	: 1 to 256 selectable

(C) Slow noise cell

Sampling	: once in 1 to 256 sweeps
Amplitude	: 12 bits (2^{12})
Increment	: 1
Decrement	: 1
Decremental rate	: 1 to 256 selectable

(D) Extractor cell

Range resolution	: 0.25 n mi and 0.5 n mi adjustable
Word length	: 32 bits
Azimuth data	: 12 bits
Status indicator	: 2 bits
Moving window	: 3 to 18 selectable
Target-start criterion	: 1 to 16 selectable } and range
Target-end criterion	: 1 to 16 selectable } dependent

(E)

Maximum MTI range	: 98 n mi } range resolution
Maximum extractor range	: 512 n mi } 0.25 n mi
Starting range	: 0 n mi

(F) Radar signals

Antenna positional data	: ACP, 4096 increments TTL voltage or current drive
North alignment	: TTl voltage or current drive
Maximum antenna speed	: 12 rpm
Video input	: logarithmic or linear/logarithmic maximum 5 V p/p; impedance 75 Ohm
PPI output signals	: max. 5 V, 75 Ohm
Radar trigger input	: positive; 5 V (min) to 100 V (max)

(G) Plot message output : interface compatible with CIE channel of Ferranti 1600B computer

(H) Main input power : 220 V $\pm$ 10%, 50 Hz single phase; 1 kVA (ruuning); 3 kVA (starting).

REFERENCES

Skolnik, M., "Radar Handbook", pp. 17-54/55.

Tsypkin, Y.Z., "Adaptation and learning in automatic systems", Academic Press, N.Y.

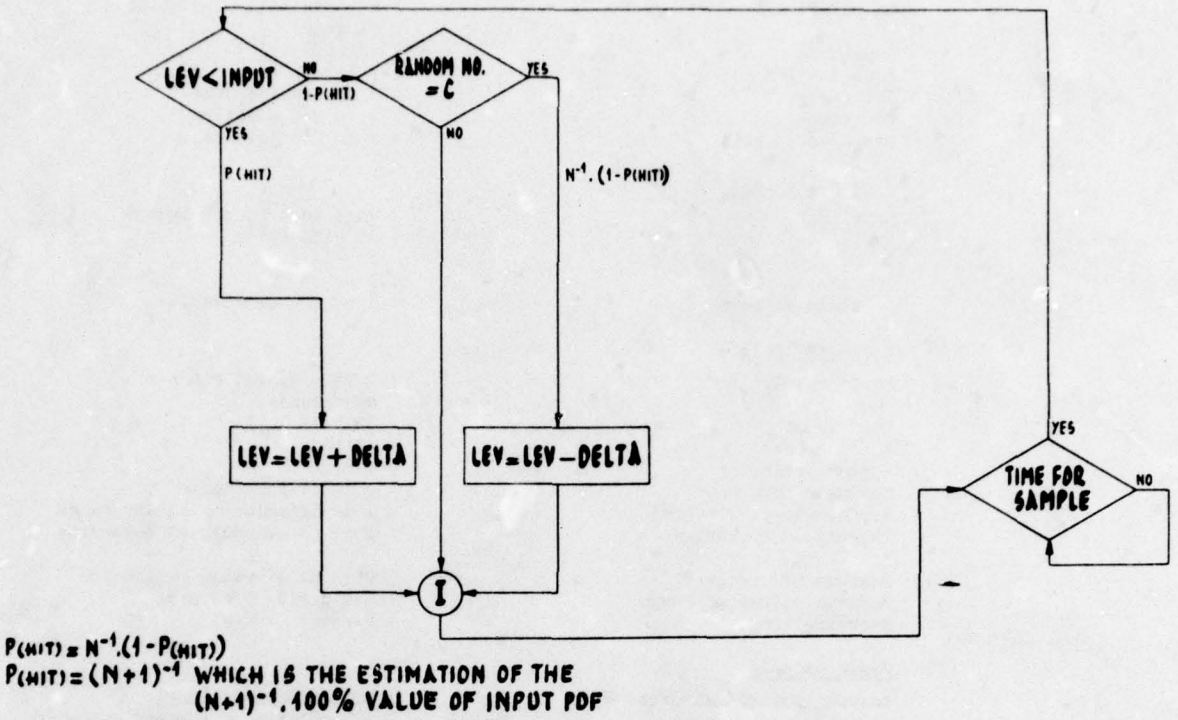

Fig. 1 Basic Algorithm

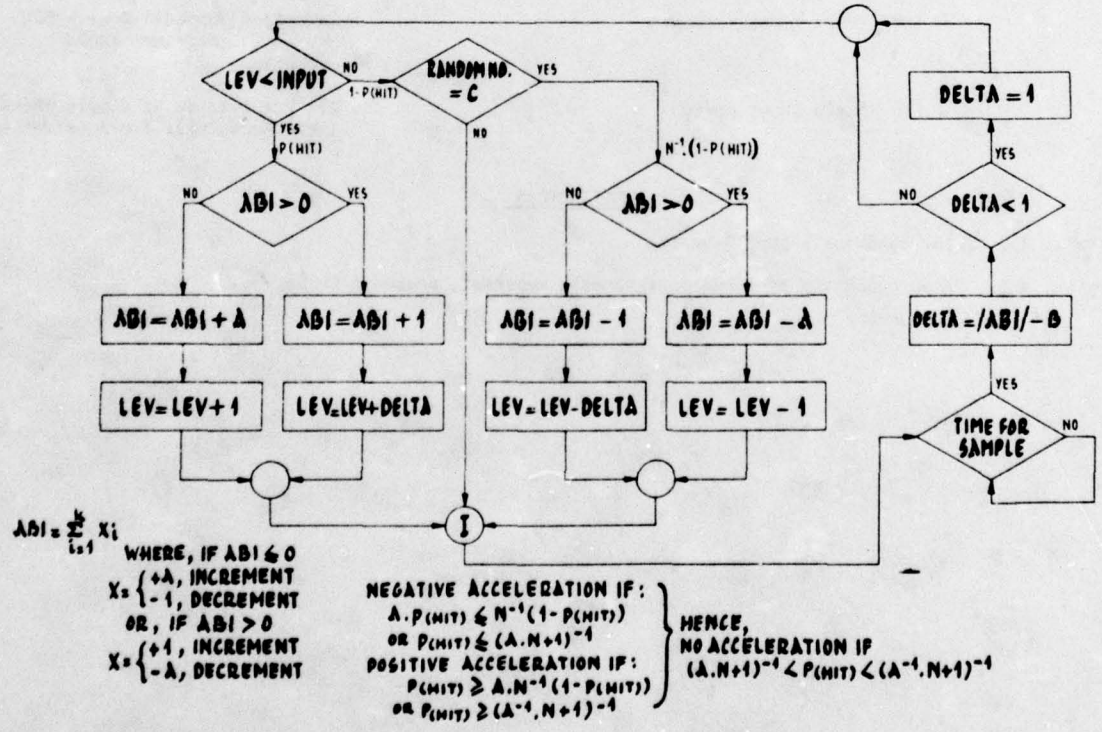

Fig. 2 Modified Algorithm

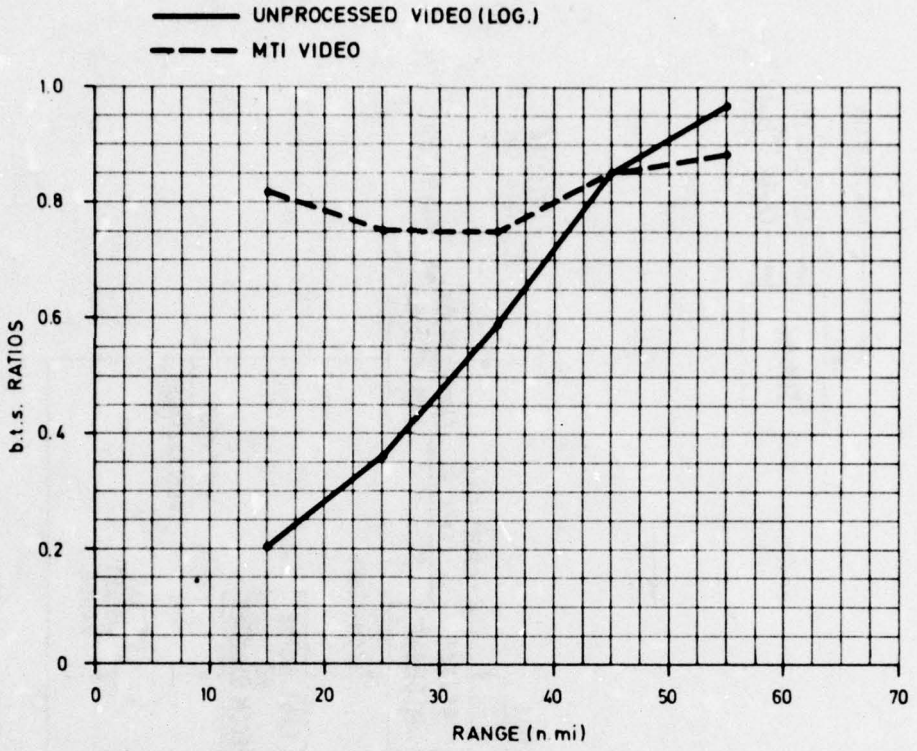

Fig. 3 Blip-to-scan ratio improvement obtained by means of digital area MTI (L-band radar)

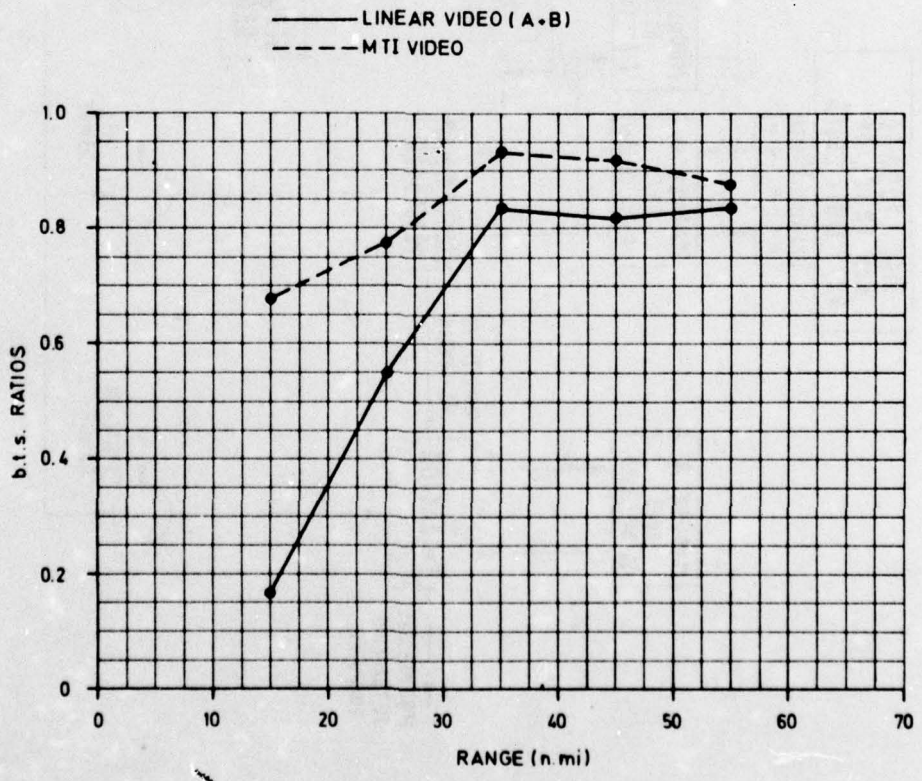

Fig. 4 Blip-to-scan ratio improvement obtained by means of digital area MTI (S-band radar)

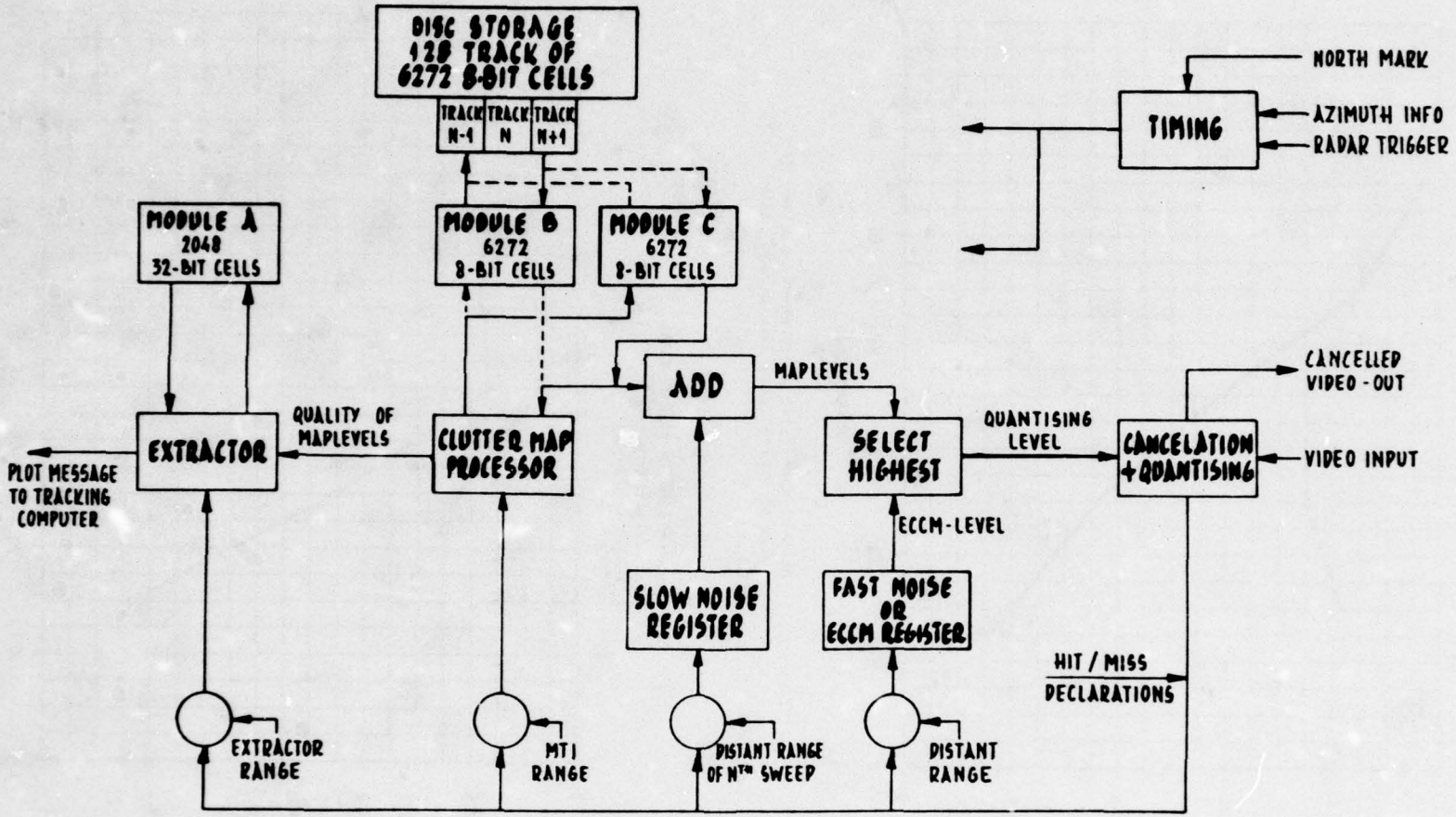

Fig. 5 "PEACE" (Plot extractor adaptive clutter eliminator)

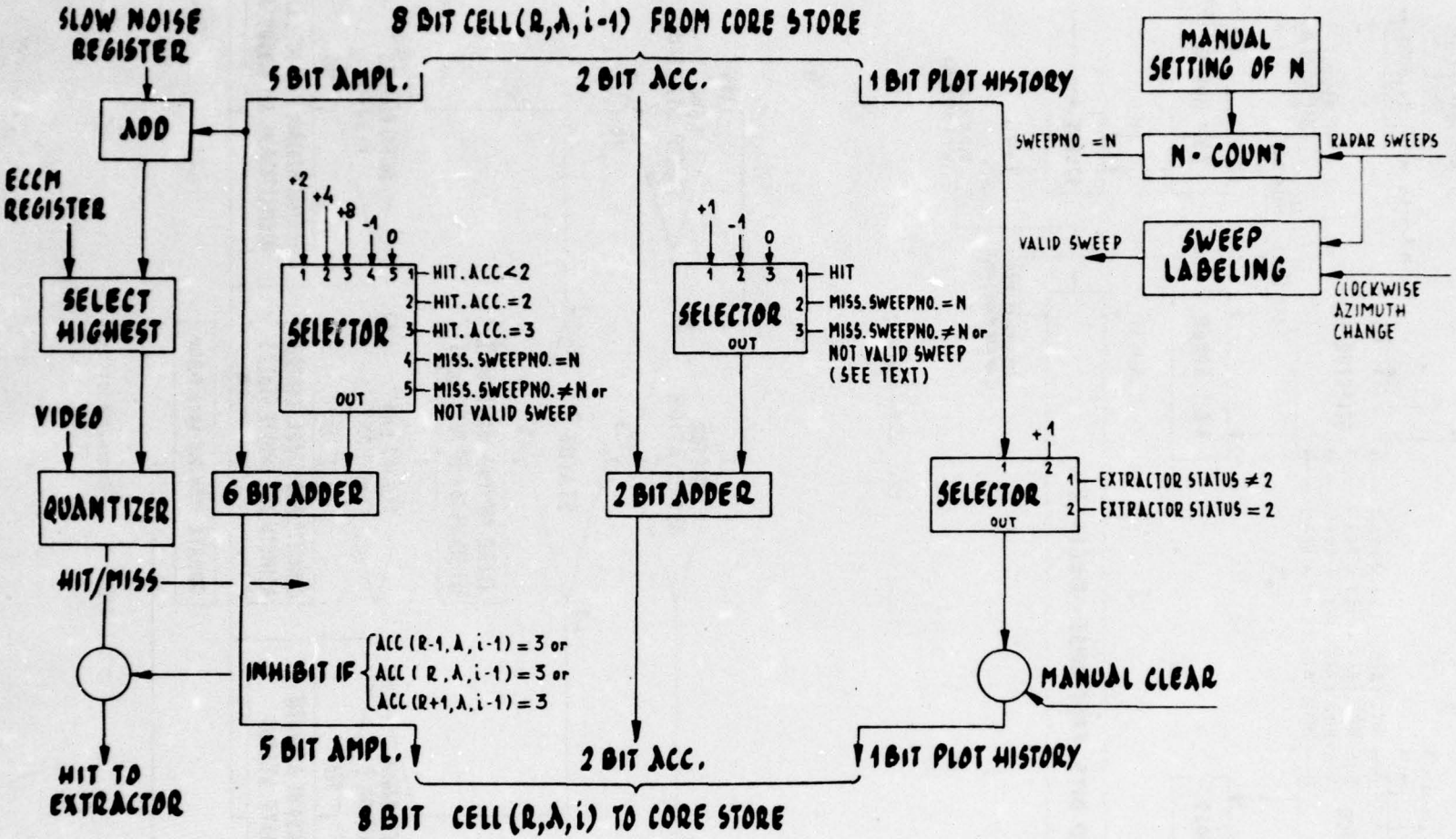

Fig. 6 Clutter map processor

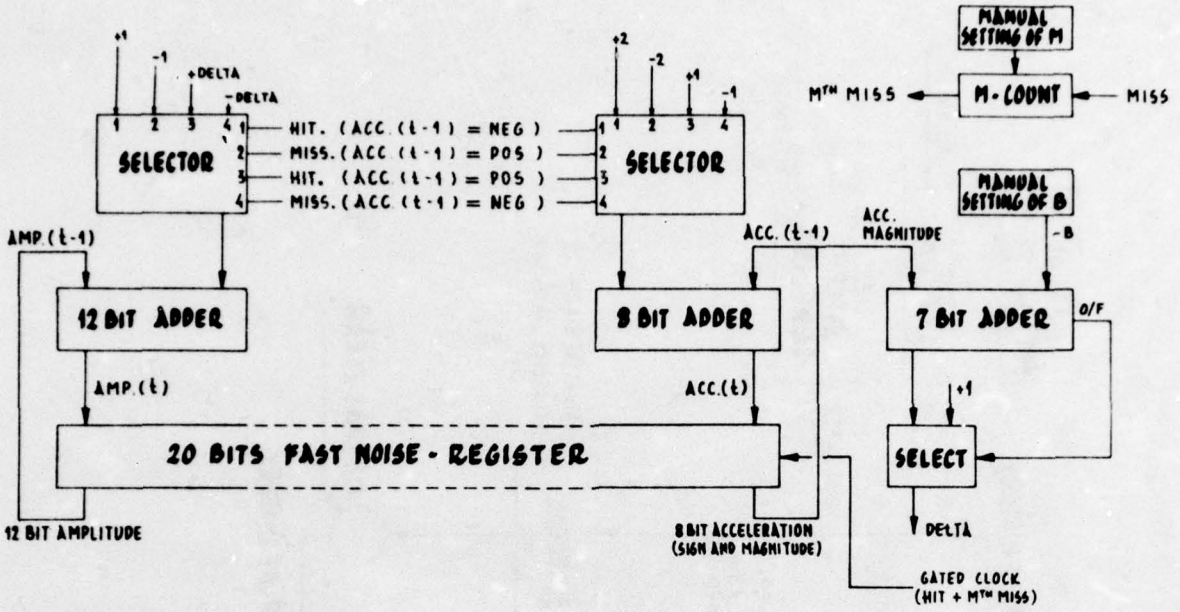

Fig. 7 Fast noise register

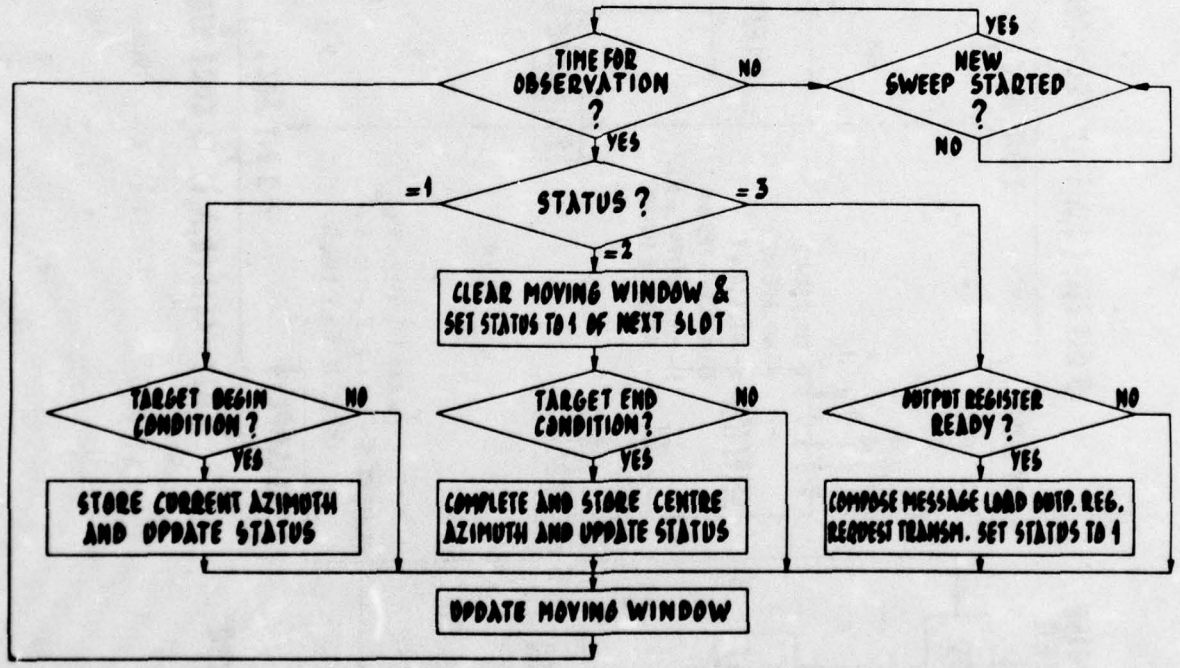

Fig. 8 Extractor process

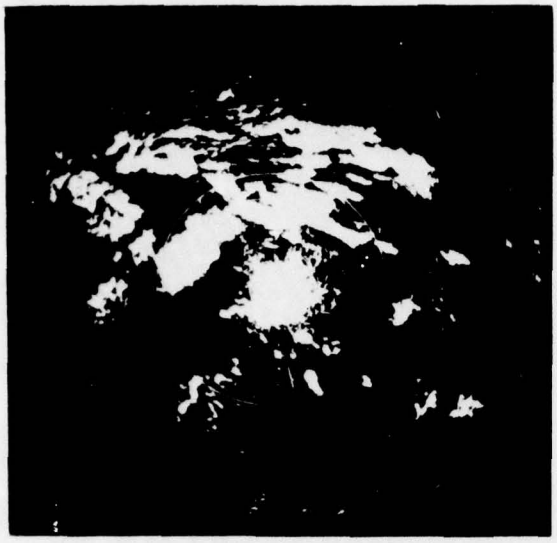

Area MTI
off

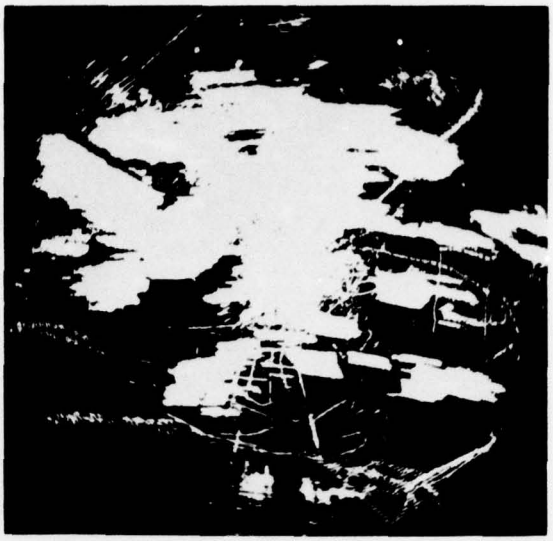

Area MTI
off

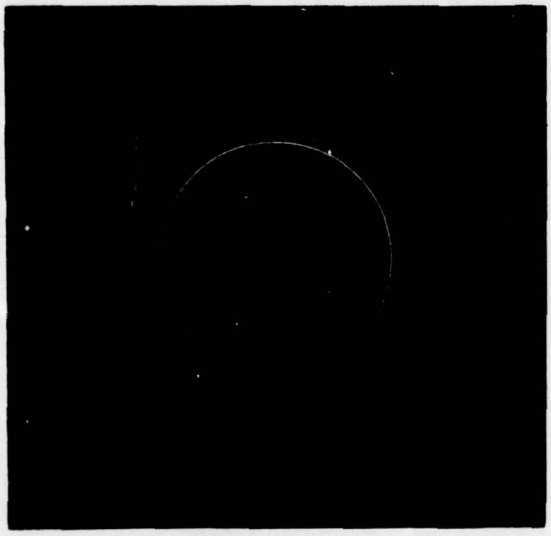

Area MTI
on

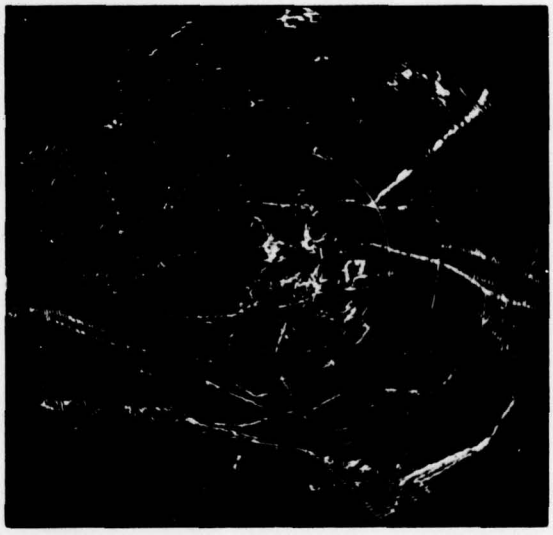

Area MTI
on

Fig. 9A Trial 1 - single scan

9B Trial 1 - 125 scans

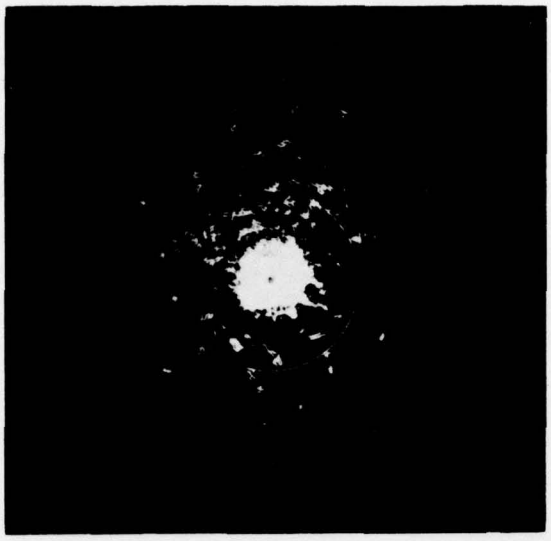

Area MTI
off

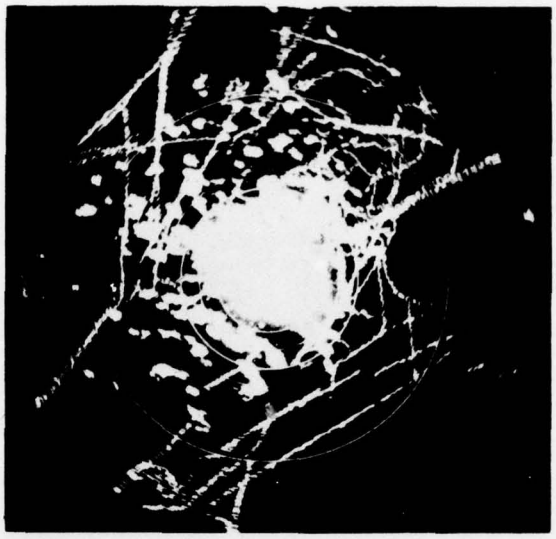

Area MTI
off

Area MTI
on

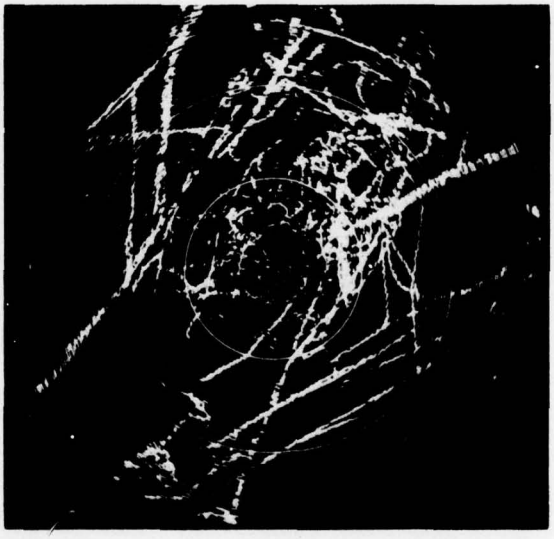

Area MTI
on

Fig. 10A Trial 2 - single scan

10B Trial 2 - 60 scans

Area MTI
off

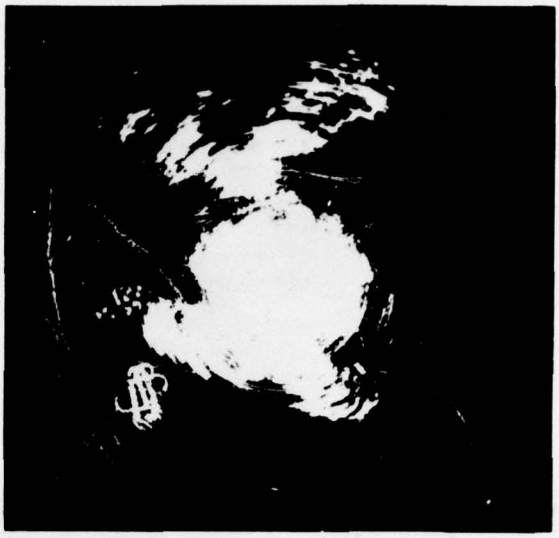

Area MTI
off

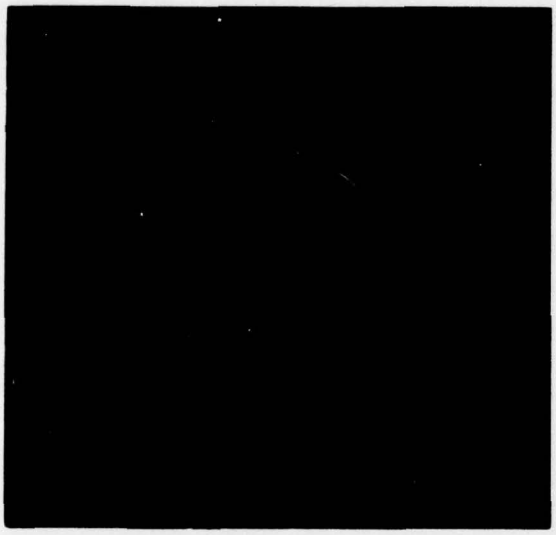

Area MTI
on

Area MTI
on

Fig. 11A Trial 3 - single scan

Fig.11B Trial 3 - 160 scans

DISCUSSION

E FLAD: What kind of storage technology is used for the clutter map?

J DEKKER: A rotary magnetic drum.

P BRADSELL: In your experience, is it advisable to use any pre-processing (eg log/pulse-length discriminator, coherent MTI) in front of the Area MTI system?

J DEKKER: The best performance is achieved if raw video is used as input (ie log or preferably lin/log).

R CARRE: Avez vous pu évaluer l'efficacite de votre MTI vis à vis des anges?

J DEKKER: If the speed of the angels is less than the minimum velocity-threshold defined by system parameters, the angel signals will be cancelled.

MOVING TARGET DETECTOR, AN IMPROVED SIGNAL PROCESSOR*

C. E. Muehe
Massachusetts Institute of Technology
LINCOLN LABORATORY
Lexington, Massachusetts 02173

SUMMARY

A three-year program directed toward radar improvements in an automated, air traffic control environment has successfully produced a practical radar signal processor which overcomes clutter effects and provides automatic acquisition and tracking of all aircraft within the radar antenna's field of view.

The new digital processor, called the Moving Target Detector (MTD) has been carefully evaluated, both theoretically and experimentally on an S-band Airport Surveillance Radar. The MTD radar exhibits 50-dB improvement factor in ground clutter, a subweather visibility better than 12 dB and complete elimination of second-time-around echoes. A ground clutter map gives the radar super- and intra-clutter visibility even on tangential aircraft (zero radial velocity).

The MTD completely masters false alarms giving no significant increase even in heavy precipitation and ground clutter. Mastery of the ground clutter problem allows detection of low flying aircraft and gives much greater freedom in siting the radar. The output is suitable for digital transmission over narrowband (telephone) lines.

1. INTRODUCTION

Over the past decade the Federal Aviation Administration (FAA) has been in the process of automating the Air Traffic Control (ATC) system in the United States. The initial objectives of automation were to aid the air traffic controller, relieving some of his workload, and to maintain safety in the ATC environment in the face of increasing numbers of aircraft. More recently a further goal of automation has been to regulate the flow of aircraft so as to avoid take-off and landing delays, thus making for a more efficient and economical flow of traffic. This latter goal is of particular importance to the air transport industry.

Automation is achieved by using computers. One of the prerequisites for automation is the inclusion of accurate, timely position reports of all aircraft in the ATC service volume into the computer's memory bank. In early 1972, at the start of the development work described herein, the FAA was in the process of automating 62 terminal areas with the ARTS-III (Automated Radar Terminal System). In this automated system, the beacon (ATCRBS) system output reported digitally to the computer in a reliable manner, but the primary radar output was not adequate for digitization. Rather, it was displayed on the PPI scope in raw, analog form. Attempts at providing digital radar data were unsuccessful. It was at this point that Lincoln Laboratory undertook a program whose goal was radar improvements sufficient to provide quality digital reports so that aircraft anywhere within the service volume of the primary radar could be automatically put into track and that a track so initiated would be continuous until the aircraft left the radar's service volume.

Initial studies showed that this lack of success with radar tracking was due to either an excess of false alarms from various forms of clutter (ground, rain, bird returns) or due to a lack of detectability of aircraft flying in the clutter areas or due to a lack of aircraft detection caused by circuits used for clutter elimination (e.g. tangential drop outs). Analysis shows that in a noise environment a probability of detection of 0.8 or higher per scan and a false alarm rate less than 10^{-5} will produce good tracking of aircraft. However, due to the requirement to follow manuevering aircraft, the tracker must have a fast transient response so that aircraft are typically dropped from track when not detected on three successive scans. The detection and false alarm requirements quoted above assume that detection dropouts are uncorrelated from scan to scan. When an aircraft enters a clutter region this requirement is not met. Detection is missed on a few scans and the aircraft track is dropped.

2. APPROACH TO PROBLEM

Our initial approach to this problem was threefold:

(1) To examine the nature of the aircraft and clutter radar returns so as to establish the required clutter rejection capability.

(2) To examine and analyze existing approaches being used to provide digitized radar output.

(3) To examine all techniques which appeared to provide better aircraft detection in clutter and to choose a compatible set which could be used to solve the primary radar tracking problem.

Reference 1 (Muehe, C.E., 1974) discusses in detail many of the conclusions reached by the initial studies. In this section we will only summarize these findings and add a few more observations before proceeding with a description of the digital signal processor which finally evolved.

The initial studies showed that the MTI improvement factor in ground clutter for a typical Airport Surveillance Radar environment should be about 50 dB instead of the 20 to 30 dB experienced in most ground-based surveillance radars. At the 50-dB level, reduced detection will occur only in very small isolated ground

*The work reported was prepared for the Federal Aviation Administration under Interagency Agreement DOT-FA-72-WAI-242 by Lincoln Laboratory, a center for research operated by Massachusetts Institute of Technology under Air Force Contract F19628-76-C-0002.

clutter regions. In addition, blind speeds must be eliminated especially those at zero radial velocity. A small aircraft flying by at longer ranges will typically go undetected on five to ten scans as it passes through the tangential point. It is regularly dropped from track when conventional MTI circuits are employed. When flying in the rain, small aircraft sometimes go undetected due to the radar's lack of any subweather visibility. Studies show that approximately 15 db of additional subweather visibility is required to see small aircraft in heavy rain.

In many areas, the so called second-time-around effect occurs. Reflections from the ground occur due to illumination of the ground by the second-to-last pulse transmitted. It is easy to see that circuits designed to eliminate close-in clutter will not also eliminate second-time-around clutter unless a constant PRF is employed and unless the transmitter is coherent from pulse to pulse so that a fixed phase relation exists between the returns from the last pulse and the second-to-last pulse.

Radar returns from bird flocks (angels) are also a problem. Fortunately, angels can be discriminated against by the size of their radar returns. Further discrimination using scan-to-scan correlation is usually also required to completely overcome the angel problem.

Not only must solutions be found to solve the detection and false alarm problems associated with each of the phenomena discussed above, but the solutions chosen must be compatible with each other. For instance, the constant PRF requirements to eliminate second-time-around clutter are not compatible with the usual staggered PRF used to eliminate blind speeds when conventional MTI cancellers are employed.

Practically all previous attempts to provide ground-based surveillance radars with automated detection capability have resorted to the so called "sliding-window detector". Each range increment of the radar video is first quantized to a single bit (0 or 1) using a first threshold. The number of hits (1's) are then counted in an azimuth window whose width is approximately equal to the number of pulses in an antenna beamwidth. A second threshold (the leading edge threshold) is set equal to a certain fraction of the samples in the azimuth sliding window. As the antenna beam passes the target the count in the sliding window eventually falls below a third threshold, the trailing edge threshold. The true azimuth position of the target is estimated from the positions of the leading and trailing edge threshold crossings.

There are several shortcomings to the sliding-window approach. Firstly, the sliding window simply performs the detection function. It cannot improve video signals (MTI, normal, log-FTC, etc.) which may already have passed through filtering and non-linear processes.

Secondly, the sliding-window detector incorporates a form of non-coherent integration, the sum of 1's in the sliding window. If the video contains clutter which is partially correlated from pulse to pulse (e.g. rain returns) a much higher false alarm rate will occur unless the leading edge threshold is raised corresponding to the degree of correlation of the clutter residue (Nathanson, F.E., 1969; Reid, W.S., et. al, 1975). If the leading edge threshold is raised however, the sensitivity suffers.

Thirdly, the azimuth accuracy of the sliding-window detector is poorer than other interpolation schemes used in track-while-scan radars. The leading and trailing edge positions are determined at a time when the target is well down on the sides of the azimuth main beam antenna pattern. At these times the signal-to-noise ratio is low (just adequate for detection) and azimuth determination is inaccurate.

With the rejection of the sliding-window detector as not being the suitable solution to solve the radar automation problem, the investigation turned to a host of other so called radar fixes which were being proposed or actually included in radars in 1972 to help solve the radar clutter problem. Table I is a partial list of the fixes considered.

TABLE I - RADAR FIXES TO IMPROVE PERFORMANCE

High-Low Beam Antennas

Scanning-Pencil-Beam Antennas

3- or 4-Pulse MTI Cancellers Following Limiters

Log-FTC-Antilog CFAR

Limiting Plus Non-Coherent Integration for Interference

CPACS, Coded-Pulse Anti-Clutter System

Clutter Reference MTI

Manual Range-Azimuth Gating (RAG) of MTI/Normal, High/Low Beam, Receiver Gain, STC, ETC

Analysis showed that while all of the fixes listed in Table I improved the situation in certain areas, all of them taken together would not improve an ASR to the point where it could automatically acquire and track aircraft everywhere within the radar's coverage volume.

Raising the antenna beam or using pencil beams for instance reduces ground clutter for higher flying aircraft, but provides no signal-to-clutter improvement on the low flying aircraft. Signal limiting prior to MTI causes clutter spectral spreading and a severe degradation in subclutter visibility. Some circuits used to control false alarms such as log-FTC-antilog, CPACS (pulse compression following 2-bit quantization), and limiting followed by non-coherent integration are simply normalizers or fast acting automatic gain control which help provide super-clutter visibility but do not provide any subclutter visibility. They merely turn down the gain so that false alarms do not occur but, at the same time, cause a loss of aircraft detectability.

Clutter referenced MTI is used sometimes to detect targets in moving rain. Signals from nearby range cells are amplified and limited for use as local oscillator signals to center the rain return in the notch of the MTI filter. This scheme falls apart when two sources of clutter are present (ground and rain) and does not provide for the varying width of the rain clutter spectrum.

Since each of the above fixes will only work over limited regions of the service volume, it is then suggested that some kind of gating will help solve the problem. The suggestion is to use different fixes in different parts of the service volume as seems appropriate. The use of range-azimuth gating admits that the fixes are only partial solutions to the clutter problem.

3. DESCRIPTION OF THE MTD

The solution to the problems involved in automating the ASR have been solved by the application of modern digital processing techniques. Figure 1 is a photograph of the resulting processor, called the Moving Target Detector (MTD). The signal to be processed is taken at IF from the output of the IF preamplifier and fed through a special linear, wide-dynamic-range amplifier to the quadrature video detectors. These are mounted in a chassis near the bottom of the rack (Figure 1). The two quadrature video detector outputs are converted to 10-bit digital numbers by the analog-to-digital converters shown and, hence, into the digital processor which occupies the rack space just below the converters. The MTD contains an 8000-word input memory and about 900 integrated circuits. A disc memory is used as a fine-grained ground clutter map. All the parts in the entire rack cost approximately $25,000.

The MTD achieves its superior performance principally through the fine resolution linear filtering and adaptive thresholding techniques. As Figure 2 depicts, on each scan of the antenna the entire coverage area is broken into 1/16 nmi by 3/4 degree range-azimuth cells, approximately 370,000 in all. In each 3/4 degree azimuth interval, called a Coherent Processing Interval (CPI), ten pulses are transmitted at a constant PRF. The ten complex digital samples collected in each range-azimuth cell are processed to form eight doppler filters which span the PRF interval. The radar output is thus divided into 2,900,000 range-azimuth-doppler cells. Each is adaptively thresholded as explained below.

4. GROUND-CLUTTER FILTERS AND THRESHOLDING

The filters depicted in Figure 2 are not simple filters, but rather they have been tailored for best rejection of ground clutter (Muehe, C.E., 1974) using linear, wide-dynamic-range processing. It is possible to achieve MTI improvement factors well in excess of those achieved in present-day ASR's. The comparison is depicted in Figure 3. Here the upper curve is the envelope of the MTI improvement factor when using the optimum filters employed in the MTD, and the lower curve is the corresponding curve for the usual 3-pulse canceller employed in an ASR following a limiting IF amplifier. Notice that approximately 25 dB greater improvement factor is achieved and a much narrower notch is experienced at zero velocity and the blind speeds.

Virtually all of the ground clutter returns appear in filter zero (see Figure 2) with a little bit spilling over into filters 1 and 7. *Because ground clutter is so spotty in nature* (i.e. varies widely in value from spot to spot on the ground) great difficulty is experienced in calculating appropriate threshold values for detection. To solve this problem, a digital ground clutter map is implemented with one word for each range-azimuth cell, 370,000 words in all. These are stored on the magnetic disc memory.

The map value is built up in a recursive manner by adding 1/8 of the output of the zero velocity filter on each scan to 7/8 of the value stored in the map. Thus, as rain moves into the area or as propagation conditions change, the clutter map value changes accordingly. The value stored in the map is multiplied by an appropriate constant to set the threshold for the zero velocity filter. Since the clutter signals appear at the output of the 1 and 7 filters, much attenuated, the clutter map value is also used to set one of two thresholds in these filters. The other is a mean-level threshold as described below.

5. WEATHER CLUTTER AND MEAN-LEVEL THRESHOLDING

Unlike ground clutter which has a constant spectral width centered at zero velocity, precipitation returns have a spectral shape which varies in width as well as average velocity (Muehe, C.E., 1974). Its shape is set by the wind field occupied by the rain. Wind velocity variations with altitude set its spectral width and the average wind velocity with respect to the radar sets the mean doppler.

If the set of eight doppler filters which were optimized to reject ground clutter are weighted properly, they will have moderately low side lobes (15 to 25 dB) and thus produce good discrimination between aircraft and rain at different velocities.

This is depicted in Figure 4. A typical rain spectrum is shown on the bottom line and the very narrow spectrum of an aircraft to the right. The PRF of the radar is changed about 20% on successive CPI's (groups of ten pulses). The aircraft's spectrum folds over (aliases) differently on each PRF so that it appears in filters 5 and 6 on PRF-1, but in filters 6 and 7 on PRF-2. In the example depicted in Figure 4, the aircraft will compete with the rain for detection on PRF-2, but it appears in one filter without any rain return (filter 5) in PRF-1. Thus, using two PRF's, the target appears in at least one filter free of rain over the whole velocity region from -600 to +600 knots except for the small region (approximately 30 knots wide) when the target's radial velocity is exactly that of the rain. Rain clutter rejection outside this small 30-knot interval is limited only by the side lobe level of the doppler filters.

The MTD is thus said to have subweather visibility. It can see aircraft whose cross section is many dB's below the radar cross section of the weather return. This feature was not previously available in ASR's and accounts for the MTD's excellent tracking ability of aircraft in rain.

The other nice feature of the filter bank approach is the facility with which proper thresholds can be established taking into consideration the presence of the rain. Again, referring to Figure 2 for each filter number, the detection threshold is established by summing the detected output in 16 range cells; eight on either side of the cell of interest. Thus, each filter output (except filter zero) is averaged over one mile

in range to establish the statistical mean level of the rain clutter or noise in each velocity increment. The mean levels are then multiplied by an appropriate constant to establish the desired false alarm level. If the signal in a particular filter exceeds this threshold, a target declaration is made and a digital hit report is generated.

The hit report contains the azimuth, range and amplitude of the target return as well as the filter number and PRF employed. As the antenna scans by a typical large aircraft as many as 20 hit reports may be generated in different filters, on several CPI's and in two range gates. These digital hit reports are passed on to a post-processor where all the reports which appear to come from a single aircraft are grouped together (correlated). An interpolation process is then used to find the best azimuth, range, amplitude and radial velocity of the aircraft. After the correlation-interpolation process and further sector thresholding based on target amplitude and doppler to reduce the angel count, the target reports are delivered to the tracker. The tracker further eliminates false hit reports which do not form tracks. Finally, the tracker output is displayed on the scope for use by the air traffic controller.

6. FLIGHT EVALUATION RESULTS

The MTD was connected to an ASR class of radar at the FAA's experimental facility (NAFEC) in Atlantic City, New Jersey, and extensive flight testing was used to evaluate its operational performance. It was compared to an ASR-7 which incorporated a digital, 3-pulse canceller and to an ASR-7 equipped with a modern sliding-window digitizer (Reid, W.S., et. al, 1975).

The two radars to be compared were diplexed onto a common antenna so that they were looking at the same aircraft and clutter environment at exactly the same time. The transmitter power and receiver sensitivity were adjusted so that the round trip sensitivity of the two against noise were identical to within 1 dB. What follows represents a small sampling of the rather extensive test results.

The MTD has been tested on radars with both klystron and magnetron transmitters with equally good results. The klystron radar was a greatly modified AN/FPS-18 radar. The magnetron radars used for testing were the ASR-5 and ASR-7 each equipped with a solid-state crystal-controlled stalo. Because they are not coherent from pulse to pulse, the magnetron radars will not reject second-time-around clutter returns.

7. GROUND CLUTTER TESTS

Figure 5 shows some results when tracking a controlled aircraft over ground clutter. The ground clutter was 30-45 dB above noise. The controlled aircraft (Piper Cherokee) was beacon equipped and flew in a race course pattern 1,000 ft above Atlantic City, New Jersey. Another radar-only (non-beacon-equipped) aircraft flew through the same area. Forty scans (3½ minutes) of tracker output data are depicted in Figure 5. Notice the clean, smooth tracks for the MTD and the blip-scan ratio of virtually 100%. Notice also that the beacon was missed for four scans as the controlled aircraft was in a turn with its beacon antenna shielded.

For the sliding-window detector many radar detections were missed. Track swapping occurred and several false tracks were formed.

8. PERFORMANCE IN RAIN

Figure 6 compares the detection performance in rain of the MTD and the MTI/sliding-window detector. Here the input to the tracker is depicted for 40 scans of the radar. Neither aircraft carried a beacon. This figure shows the general background of false alarms adjusted to about 40 per scan for both radars. Notice the even, continuous output of the MTD and the coarse output of the sliding-window detector with many missed detections. Rain covered most of the area but was particularly heavy in the spots missed by the sliding-window detector.

9. INTERFERENCE ELIMINATOR

Early in the tests at NAFEC difficulty was experienced due to pulse interference from a nearby radar only 15 MHz separated in frequency. A special circuit was then incorporated into the MTD to suppress pulse interference. Figure 7 shows the results.

This figure shows the raw output of the MTD (before correlation-interpolation and tracking). On the left we see the spiral interference. Counting the spots we find almost every pulse from the interfering radar caused a false alarm. The numbers on the face of the photograph are the filter numbers in which detections occurred (see Figure 2).

The blanker used to solve this problem merely added up the magnitudes of the ten pulse returns in a range gate and compared the magnitude of each pulse with the average magnitude of the ten. If one is about 12 dB larger than the average, the blanker censors that range-azimuth cell not allowing any detections. The photograph on the right shows the result. Pulse interference was completely eliminated.

10. POSITION ACCURACY

Approximately 100 tracks were analyzed to establish and compare range and azimuth accuracies. Only long tracks with over 90% blip-scan ratio were employed. A high-order polynomial curve (typically fifth order) was fitted separately to the azimuth vs. scan number curve and the range vs. scan number curve of each track. The standard deviation of the departure of the measured quantity (range or azimuth) from the fitted curve was determined. The resulting histograms of the standard deviations are shown in Figures 8 and 9. The MTD results were close to the beacon results. The azimuth accuracy for the MTD is typically about 1/10 beamwidth and substantially better than that for the sliding-window detector.

11. CONCLUSIONS

The MTD offers a new class of capability for ground-based air surveillance radars. Tests show that a radar equipped with MTD can track aircraft everywhere within the surveillance volume of the antenna. It permits tracking to be automatically initiated and the tracks are continuous despite ground and weather clutter and birds (angels). The radar now can be sited more freely overcoming most ground clutter limitations.

Further, the false alarm rate is so low that after a small amount of processing, the entire radar's output can be reliably transmitted over a narrow bandwidth telephone line. The MTD has no tuners or adjustments of any kind. It is an economical solution to the radar automation problem.

ACKNOWLEDGEMENTS

These developments have been sponsored by the FAA (ARD-200). In particular, Mr. Kenneth Coonley and Mr. Dan Hopson provided direction and guidance.

The MTD was developed in Lincoln Laboratory's Group 43 with contributions by many members. The major participants were Lincoln Cartledge, William Drury, Melvin Labitt and Robert O'Donnell. Herbert Weiss and Paul Drouilhet supervised the work and provided many helpful suggestions.

Testing and evaluation of the MTD was carried out principally by FAA personnel at NAFEC. Principal contributors were Ronald Bassford and William Goodchild. William Herget provided supervision and guidance.

This manuscript was prepared by Linda Wesley.

REFERENCES

(1) C. E. Muehe, et. al, June 1974, "New Techniques Applied to Air-Traffic-Control Radars," Proc. of IEEE, Volume 62, Number 6, pages 716-723.

(2) F. E. Nathanson, 1969, RADAR DESIGN PRINCIPLES, McGraw-Hill Book Co., pages 83-92.

(3) W. S. Reid, M. R. Saltsman, L. E. Vogel, 1974, "Technique for Clutter False Alarm Control in Automated Radar Detection Systems," IEEE 1975 International Radar Conference Record, pages 294-299.

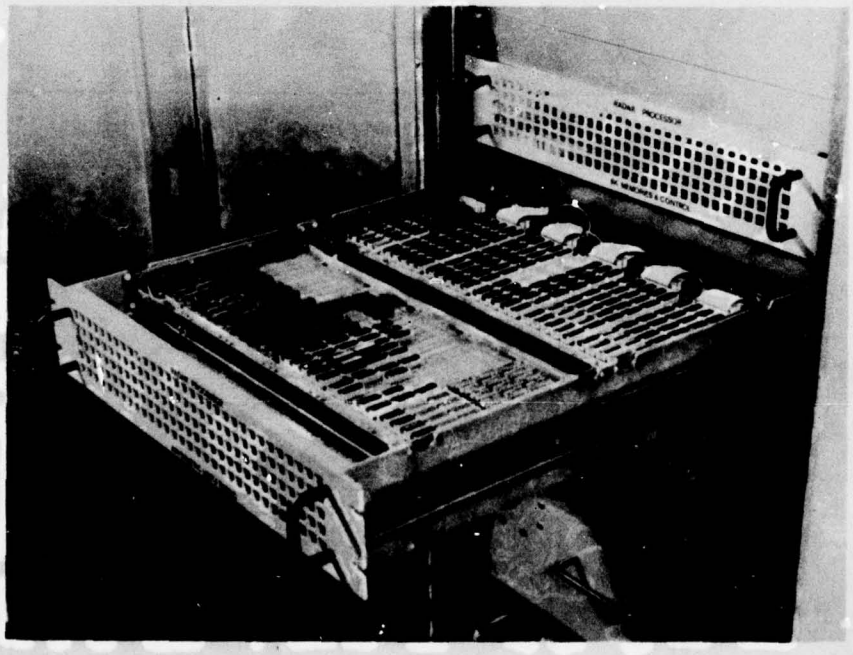

PHOTOGRAPH OF THE MTD

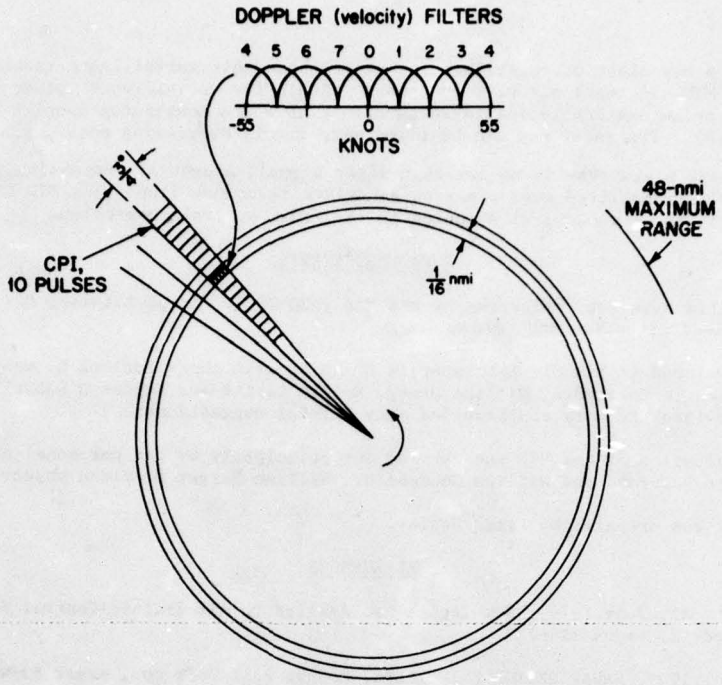

MTD RESOLUTION
2,900,000 RANGE – AZIMUTH – DOPPLER CELLS
EACH ADAPTIVELY THRESHOLDED

FIGURE 2

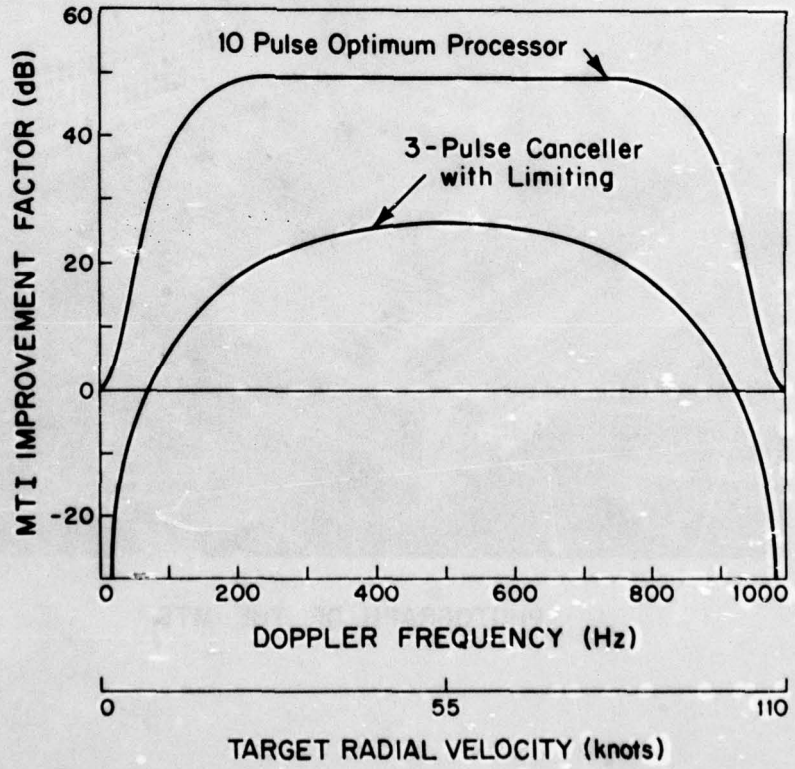

VELOCITY PERFORMANCE

FIGURE 3

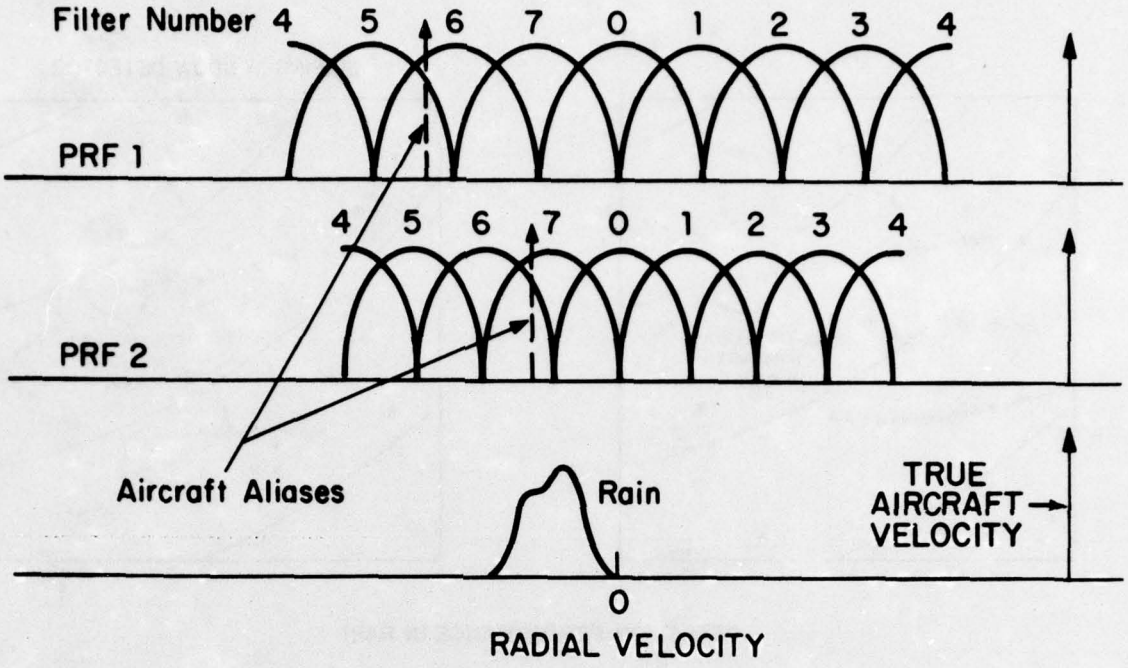

DETECTION IN RAIN USING TWO PRF'S

FIGURE 4

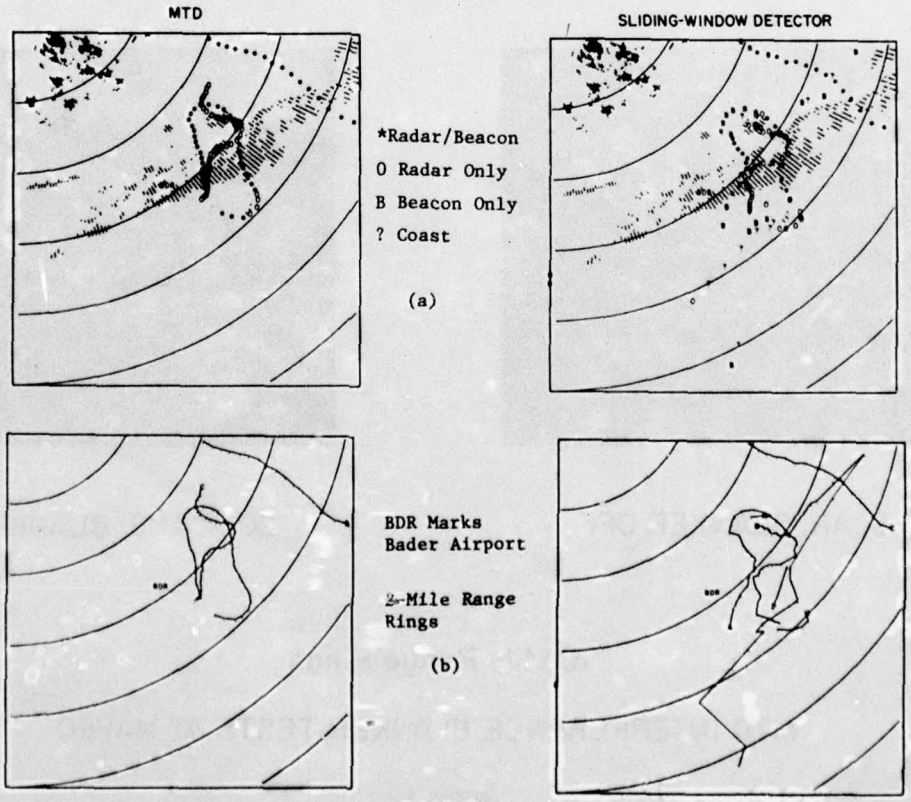

FIGURE 5

Detection and Tracking Tests in Ground Clutter
(a) with ground clutter superimposed and (b) aircraft tracks alone

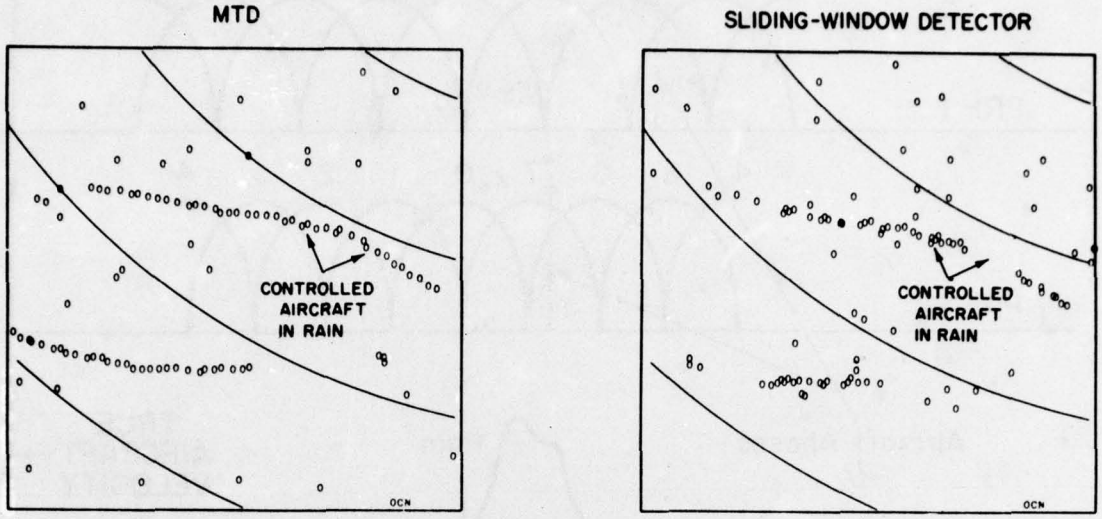

DETECTION PERFORMANCE IN RAIN

FIGURE 6

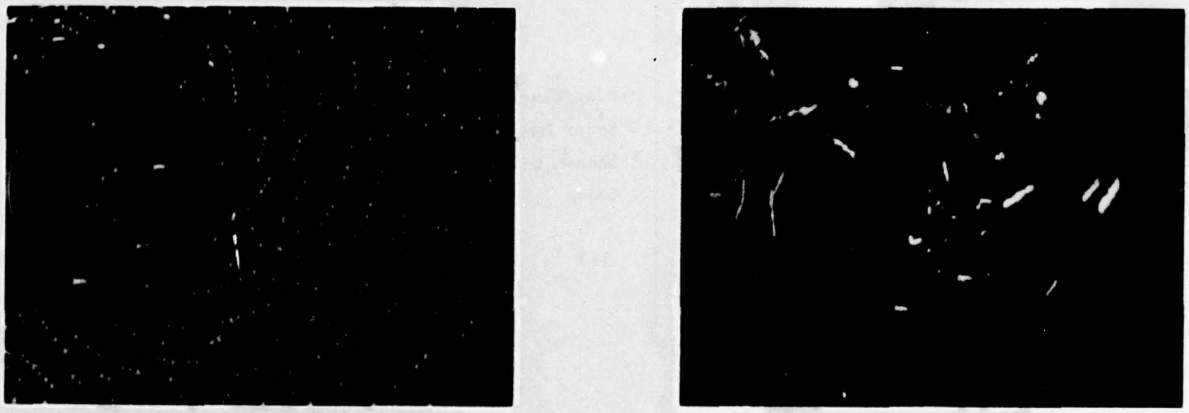

1 SCAN, BLANKER OFF

20 SCANS, BLANKER ON

10 Mile Range Rings

MTD INTERFERENCE BLANKER TESTS AT NAFEC

FIGURE 7

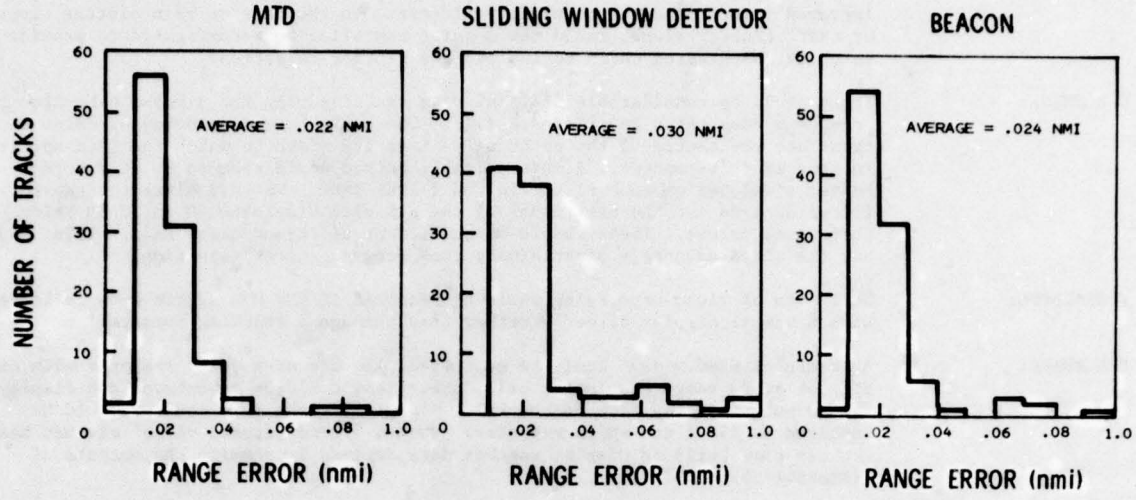

100 TRACKS

RANGE ACCURACY OF MTD, SLIDING-WINDOW DETECTOR AND BEACON REPORTS

FIGURE 8

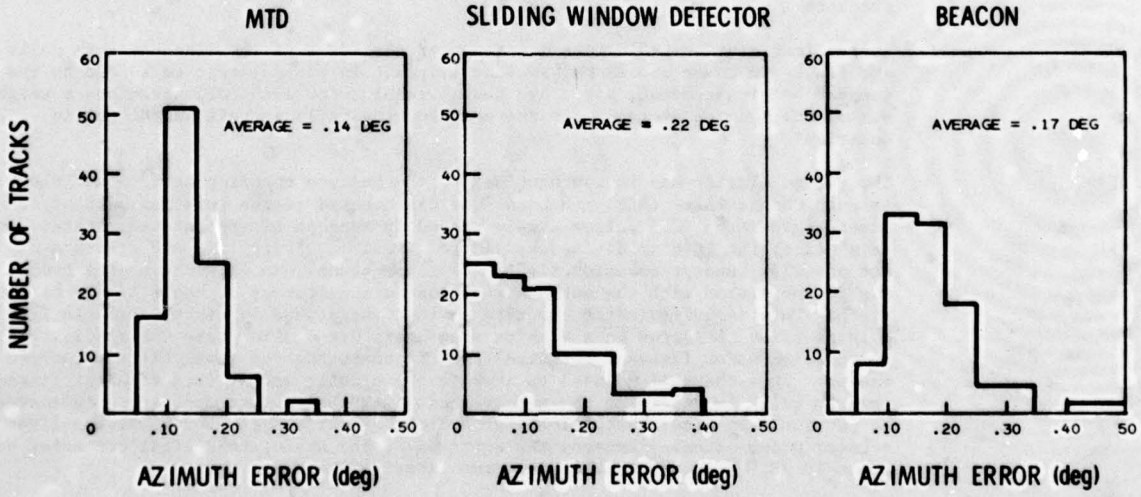

100 TRACKS

AZIMUTH ACCURACY OF MTD, SLIDING-WINDOW DETECTOR AND BEACON REPORTS

FIGURE 9

DISCUSSION

K MILNE: I assume that the 3-pulse canceller preceding the 8-point FFT is needed to give improved rejection of zero-velocity clutter. In the case of rain clutter alone, or chaff clutter alone, could the 3-pulse canceller be reconfigured to provide a velocity-compensated notch to improve the clutter rejection?

C E MUEHE: There would be considerable difficulty in reconfiguring the 3-pulse canceller to provide a deep notch to eliminate rain. One would have to provide circuits to translate the centre of the notch as well as its width to match the rain spectrum in some adaptive manner. A more suitable method would seem to be to provide better sidelobes on each filter in the filter bank. We have already prepared filter designs for the next model of the MTD with sidelobes 40 to 50 dB below their peak values. These should be sufficient to reject heavy rain. This solution has the added advantage of retaining good ground clutter rejection.

P BRADSELL: What form of video processing would be required if the MTD system were to interface with a visual display directly rather than through a tracking computer?

C E MUEHE: A 'reconstituted video' could be generated. By use of a shift register with one bit for every range resolution cell, detections could be remembered and displayed for 10 pulses on the face of the PPI. A digital range gate counter would be required to clock the shift register. Such a 'reconstituted video' circuit has already been built to display weather data derived by summing the outputs of filters 1 through 7.

M J WITHERS: Could you say how many scans of the radar antenna are required in order to build up the clutter map information in the disc store?

C E MUEHE: The disc store clutter map is refreshed by adding 1/8 of the output of the zero velocity filter to 7/8 of the value in the clutter map on each scan of the radar so that it requires 8 to 12 scans (about 40 seconds) to build up the clutter map to represent the average value of the ground clutter in any particular range-azimuth cell. This value of 1/8 was chosen on the basis of the velocity with which storm cells move through an area since the storm usually contains some zero velocity (tangential) cells.

G A VAN DER SPEK: Does the tracking process make use of the doppler information of the target returns?

C E MUEHE: At the present time the tracker does not employ the doppler information. A fairly simple α-β tracker is employed. Doppler information may be quite useful in sorting out targets with crossing tracks, a traditionally difficult task using simpler trackers.

R VOLES: Large fixed clutter reflectors located near the edges of the range-azimuth cells are likely to cause occasional spurious signals in the adjacent cells due to the inexact bearing readout, etc. Are the thresholds for each cell therefore a weighted sum of the running averages for the neighbouring cells as well as the one in question?

C E MUEHE: The ground clutter map is synchronised to the antenna rotation as follows: the Azimuth Change Pulse (ACP) generator rigidly mounted to the rotating part of the antenna generates 4096 pulses evenly spaced in azimuth as the antenna rotates one revolution; the 4096 is divided by 240 to give 17+. Every 17th ACP starts a new set of CPI's (except occasionally 18 ACP's are used). In this manner the ground map is registered with the antenna rotation to an accuracy of about 1/10th beam-width. This is sufficiently accurate so that variations in signal strength from a large fixed reflector on a scan to scan basis are smaller than the statistical fluctuation model (assumed Rayleigh) used in computing the appropriate threshold values. Thus there is no need to average the clutter values from adjacent range-azimuth cells to determine the zero velocity threshold. Our experience indicates no particularly persistent false alarms from large fixed clutter until the fixed clutter point actually exceeds the extremes of the analog-to-digital convertor by about 10 dB. This, of course, is a non-linear effect.

LOW ANGLE TRACKING TECHNIQUE

KENNETH C. STIEFVATER
Rome Air Development Center
Griffiss Air Force Base, New York 13441

SUMMARY

A new Low-Angle Tracking (LAT) radar technique is described which uses array antenna technology. The process enables the radar to track targets in elevation in the low-angle region between one beam width and the horizon. The technique uses the array facility to form two beams and a two-channel receiver system which forms the ratio of the signals from each beam. By design, this ratio is proportional to target elevation angle. The antenna patterns are designed to suppress the multipath signal energy, but residual image signal energy entering the receiver is processed with the target signal without degradation of system performance.

This technique was implemented and tested on an overwater range using an aircraft as the test target to gather data and evaluate system performance under varying reflective surface conditions. The system operated at 5.5 MHz and used a 12-foot array aperture. Tracking data was collected between elevation angles of 5 to 20 milliradians with 1/10 beamwidth accuracy. A description of the flight test is given and a summary of the experimental data is presented.

1. INTRODUCTION

One of the fundamental limitations of angle-tracking radars is the inability to track in elevation when the target is within a beam width of the horizon. This limitation is a result of the target image energy entering the antenna main and near side lobes, and is usually referred to as the multipath or low-E problem. Simply stated, this is a special case of multiple targets within the angular resolution of the system.

RADC has developed a technique for tracking targets at fractional beam width elevation angles. This system uses array antenna techniques to form two beam patterns (A and B). When a target is within the low-angle region two return signals are obtained (one from each antenna pattern) and are compared in an IF receiver processor to form the energy ratio (B/A). The patterns have the unique quality of having the same B/A ratio for target positions at equal angle positions above or below the reflecting surface.

The concept has been studied in detail by computer simulation under NSSC contract No. N00024-69-C-1295 to evaluate how well the system would work in a real-world environment. It was recognized that noise and sea surface conditions were the most important limitations of the system operating as an overwater tracking radar and that equipment tolerances would constitute a relatively minor limitation on achievable performance for rough seas but can be a limiting factor when the sea is smooth.

Based upon these theoretical results, and upon the practical consideration of implementing a basic experiment, a system was designed and constructed which operates in the 5.4 to 5.7 GHz frequency band. The objective of the experimental equipment was to demonstrate the basic technique and not to measure the quantitative absolute accuracy. Data gathering instrumentation was simplified for economic reasons. Therefore, the resulting data cannot be interpreted as representative of the systems limitations or potential capability. A more optimally designed system could be constructed that would result in higher angular resolution, over wider angular coverage (including increased performance below 1/4 beam width).

A four-horn array was used to form a 12-foot aperture with a nominal 1-degree beam width. The four antenna output signals were combined in a IF beam-forming system to generate the A and B patterns. An A-frame antenna mount was built to hold the linear array antenna, and the beam forming and receiving circuitry was fabricated to mount on standard relay-racks suitable for mounting in a small trailer. To simplify the experimental radar hardware, the normal radar transmitter and duplexer equipment was eliminated from the ground equipment and a CW beacon transmitter was constructed suitable for mounting in an aircraft. This CW approach permits the use of narrowband radar receivers and keeps the target beacon power at a reasonable level.

The receive-only radar was set up at the Eatons Neck Coast Guard Station overlooking Long Island Sound. The beacon-carrying aircraft flew constant-altitude flight profiles which covered the low-angle region from below 1/4 beam width up to several beam widths. The measured angle output data was taken on a pen recorder along with a signal-to-noise ratio (SNR) indication showing when the return SNR was below 20 dB. The results were taken over a 3-month period (January, February, and March 1973) with sea surface conditions varying from flat and calm to rough with 3 to 4 ft wave heights.

The receiver was arranged so that either low-angle or conventional monopulse signal processing could be performed. Data was recorded for both processes for comparison. Results indicate that no accurate elevation angle tracking of the target can be performed with monopulse processing under any of the observed sea conditions. However, the low-angle tracking (LAT) processor provided tracking information indicating target elevation angle within 1/10 beam width accuracy, under all sea surface conditions observed, down to 1/4 beam width of the horizon.

This effort was conducted for the Rome Air Development Center (RADC) by Airborne Instruments

Laboratory (AIL) a division of Cutler Hammer under Air Force contract AF30602-72-C-0357.

2. THEORY OF OPERATION

A. THEORETICAL PATTERN FORMATION

The antenna is capable of receiving simultaneously with two different antenna patterns. Denoting these patterns as $F_a(u)$ and $F_b(u)$, it is required that their ratio be subject to the symmetry condition:

$$\frac{F_b(u)}{F_a(u)} = \frac{F_b(-u)}{F_a(-u)} = R(u)$$

where

$u = \frac{\pi D}{\lambda} \sin E$

D = vertical aperture width
E = elevation angle above the horizon

Alternatively, the symmetry condition can be expressed as:

$$\frac{F_a(-u)}{F_a(u)} = \frac{F_b(-u)}{F_b(u)} = C(u)$$

The principle of operation is based on the fact that if the surface is smooth, the reflected ray is a mirror image of the direct ray and its angle of arrival is governed by Snell's Law. Assuming that the target is at great range and that the surface is flat, the elevation angle of the reflected ray will then be just the negative of that for the direct ray. (This relation is not exact for finite target range and a curved earth's surface.) If the effects of thermal noise are ignored for the moment, then the total signal received on the A-pattern may be expressed as:

$$E_a = S\left[F_a(u) + \rho_S\, \epsilon^{i\psi}\, F_a(-u)\right]$$

where

S = signal strength parameter
ρ_S = surface reflection coefficient
ψ = relative phase of the reflected ray including path difference effects

In a similar manner, for the voltage received on the B-pattern,

$$E_b = S\left[F_b(u) + \rho_S\, \epsilon^{i\psi}\, F_b(-u)\right]$$

The ratio of these two voltages is then:

$$\frac{E_b}{E_a} = \frac{S\left[F_b(u) + \rho_S\, \epsilon^{i\psi}\, F_b(-u)\right]}{S\left[F_a(u) + \rho_S\, \epsilon^{i\psi}\, F_a(-u)\right]}$$

$$= \frac{F_b(u)\left[1 + \rho_S\, \epsilon^{i\psi}\, F_b(-u)/F_b(u)\right]}{F_a(u)\left[1 + \rho_S\, \epsilon^{i\psi}\, F_a(-u)/F_a(u)\right]}$$

Assuming the symmetry condition is met, then:

$$\frac{E_b}{E_a} = \frac{F_b(u)\left[1 + \rho_S\, \epsilon^{\psi}\, C(u)\right]}{F_a(u)\left[1 + \rho_X\, \epsilon^{i\psi}\, C(u)\right]} = \frac{F_b(u)}{F_a(u)}$$

Note that this result is independent of the reflection. That is, the pattern ratio can be estimated by measuring the voltage ratio and from this the elevation angle can be deduced.

In a separate document, a synthesis procedure has been outlined that provides pattern pairs suitable for use with a LAT system and also provides patterns suitable for normal high-angle monopulse. Figure 1 shows several low-angle pairs produced by this method. In each case, the A pattern has the same shape but the peak of the A-beam is oriented at varying distances above the horizon. The upward tilt of the A-beam, which is called the squint, has the desirable effect of discriminating against the image ray. This discrimination is useful in discriminating against errors due to surface roughness. What is probably more important, however, is that it also limits the cancellation effects when the direct and reflected signals arrive with a 180-degree phase difference. This will become more apparent later.

The gains plotted in Figure 1 are normalized relative to the gain of a uniformly illuminated aperture

of the same dimensions. The gains as expressed in dB are, therefore, always negative. In each case, the pattern ratio function is of the parabolic form:

$$R(u) = F_b(u)/F_a(u) = Ku^2$$

Figure 2 is an expanded plot for the case of a 90-degree squint. Also shown in the lower portion of the graph are curves of R(u) and C(u). Note that R(u) = R(-u) and the C(u) <1 for positive values of u.

Although these patterns were derived in a semiempirical manner and cannot be said to be optimum, their characteristics appear to be quite creditable considering the constraints involved.

B. EXPERIMENTAL SYSTEM CONCEPT

Based upon these theoretical results, a system was designed suitable for use at the Eatons Neck radar site. The system beam forming network is shown in Figure 3. The beam forming is performed at IF for simplicity of hardware and maximum adjustment flexibility. Analysis of the design demonstrated that antenna patterns would be developed with the desirable squint characteristics and that limited steering of the axis of symmetry could be included (either manually or electronically controlled) making the experimental radar more applicable to the situation where the antenna is relatively high and the target range relatively short.

The design based upon the use of a linear array consisting of four large horns. The pattern generated can be expressed analytically in the following forms:

$$F_a = \cos(\phi - \phi_a) \cos^2 (\phi - \phi_s) \sin (\phi - \phi_h)/(\phi - \phi_h)$$

$$F_b = \cos(\phi - \phi_a) \sin^2 (\phi - \phi_s) \sin (\phi - \phi_h)/(\phi - \phi_h)$$

where ϕ_a, ϕ_s, and ϕ_h are the parameters which control the pattern shape, and ϕ is defined as 1/2 the phase progression from horn to horn. Therefore, ϕ is related to the elevation angle by the expression:

$$\phi = \frac{\pi}{\lambda} d \sin E = \frac{\pi}{\lambda} \frac{D}{4} \sin E$$

where D is the total aperture dimension and d is the center to center horn spacing.

The values of ϕ_a and ϕ_h were based upon the site geometry and chosen to produce desirable pattern shapes. ϕ_h is the value of phase corresponding to the angle between the horizon and the broadside axis of the array and is expressed as:

$$\phi_h = \frac{\pi}{\lambda} \frac{D}{4} \sin E_h$$

where E_h is the mechanical angle that the entire array is tilted upward. ϕ_a represents an upward tilt or squint of the patterns above the horizon and is controlled by electrical steering.

ϕ_s is the value corresponding to the symmetry axis or the axis about which the pattern ratio is symmetrical. When the target is at infinite range, this axis should be horizontal. On the other hand, when the target is at finite range and the antenna is elevated, the symmetry axis should be depressed below the horizontal. To a very accurate approximation, the correct depression angle for a flat earth can be written as:

$$E_s = - \sin^{-1} (h/R)$$

where h is the height of the radar and R is the range to the target. For a fixed radar height, ϕ_s is a function of target range:

$$\phi = - \frac{\pi d}{\lambda} \frac{h}{R} = - \frac{\pi D}{\lambda} \frac{h}{R}$$

Figure 4 shows the pattern pair that results when ϕ_s = 0 degree, ϕ_a = 30 degrees, and ϕ_h = 60 degrees. No attempt was made to determine the optimum values for ϕ_a and ϕ_h. It will be noted however that the patterns are quite creditable. The A-pattern does have a substantial side lobe about four beam widths above the horizon and another about four beam widths below the horizon. These would have been suppressed if ϕ_h had been set to zero. Within two beam widths of the horizon, however, both patterns seem quite well controlled. The pattern ratio is plotted in the lower portion of the figure. Since the ratio varies from zero to infinity, we have used an arc tan scale to show the ratio on a finite sheet of paper.

Figures 5 and 6 are similar plots showing the situation where ϕ_a and ϕ_h are held constant, and increasing depression angle is obtained by varying ϕ_s only. This is the way we can adapt the patterns for close in targets as seen from a high location. Figure 5 shows the case where ϕ_s = 10 degrees. For a total aperture of 60 wavelengths, this corresponds to a depression angle of about 3.7 mils. This value is about right for a radar height of 100 ft and a target range of 4.5 miles. In Figure 6, ϕ_s has been doubled to 20 degrees which is about right for a target range of 2.25 miles as seen from a radar height of 100 ft.

Figure 3 is a block diagram which shows the beam-forming network used to produce the designed patterns. As shown, the fixed values of ϕ_h and ϕ_s are placed in the appropriate locations behind the array. The phase-shifted horn signals are added in pairs as shown, and the range-dependent variable ϕ_s is controlled with phase shifters located between the first and second set of combinined in a hybrid tee to produce the A and B signals.

3. HARDWARE DESCRIPTION

For this discussion, the receiver is divided into four major sections (Figure 7):

RF head assembly
Beam-forming network
Arc tan processor
Monopulse-forming network and automatic frequency control (AFC)

A C-band RF source was used as the target beacon and will be described separately.

A. RF HEAD ASSEMBLY

This assembly consists of the antenna, four mixer/preamplifiers, a local oscillator and four-way power divider as shown in Figure 8. Heater pads at 110 V are used to stabilize the temperature of the preamplifiers. A proportional-type controller used to regulate the heater is housed in a compartment of the antenna structure.

1. Antenna

The antenna (Figure 9) consists of our individual horns mounted together to form a vertical array. The array is vertically polarized and operates in the band from 5450 to 5650 MHz. Proper system operation also requires that each horn maintain its vertical plane radiation pattern such that the array illumination is constant in amplitude and phase across the total vertical aperture. To accomplish this requirement, with a horn of reasonable depth, a hybrid design approach was utilized. In the H-plane (azimuthal plane) the horn width tapers from just above cutoff dimension at its rear end to a 12-inch aperture width. In the E-plane (vertical plane), the horn height remains constant (at 36 inches) from the aperture to the horn throat. Thus, the rear end of the horn throat is a waveguide of narrow width and large height.

A vertical array of 32 dipoles is used to uniformly excite the horn throat. The dipoles are etched on a thin sheet of copper-clad Teflon-fiber glass. This sheet also contains a complete corporate-type RF distribution network which feeds the dipoles. The portion of the sheet containing the dipoles is located within the horn; the portion containing the distribution network extends behind the horn (1/2 ft) as the center conductor of a strip-line structure. The sheet is sandwiched between two foam supports and two metallic ground planes.

Individual horn patterns were taken in both the horizontal and vertical planes as shown in Figures 10 and 11.

The electrical parameters of the antenna array are as follows:

Azimuth beam width (nominal) = 12 degrees
Elevation beam width (nominal) = 4 degrees
Individual horn gain = 26 dB

The antenna was mounted on a A-frame structure supported by guy wires.

The antenna was tilted upward (E_h = 1.14 degrees) as designed. The RF head electronics, mixer/preamplifier, local oscillator, etc. were mounted directly on the antenna structure.

2. Mixer Preamplifier and Local Oscillator Assembly

The local oscillator is a C-band, mechanically tuned cavity unit capable of being electrically tuned over a range of 20 MHz. This electronic tuning feature is used in the closed loop AFC mode and a manual tuning mode. The oscillator output is isolated and then feeds a four-way power divider. The output of the power divider feeds the local oscillator inputs of the four mixer/preamplifiers via four phase-matched semirigid coax lines. The four mixer/preamplifiers are phase and gain matched. The four RF inputs from the antenna horn assemblies are phase-matched semirigid coax. The IF outputs of the mixer/preamplifiers are fed to the beam-forming network via four phase-matched equal length coax cables.

B. BEAM FORMING NETWORK

The beam-forming network consists of a number of phase shifters, summers, dividers, pads, and special phase cut cables as shown in Figure 12. The four IF input signals (phase and amplitude matched) are fed from the RF head assembly to the four input phase shifters, A1 through A4.

To satisfy the mathematical expressions previously discussed, the phase shifts are adjusted as shown; A4 as reference, A3 at 60 degrees, A2 at 120 degrees, and A1 at 180 degrees.

The outputs of the phase shifters are combined to form three signals at the outputs of summers A6, A8, and A10. Referring to the output of A10 (designated as reference cable), the cable at the output of A8 is cut to lag the reference cable by 60 degrees. In the same manner the cable at the output of A6 is cut to lag the reference cable by 120 degrees. The reference cable signal and the -120 degree cable signal are combined in summer A25 and amplified in A26. This signal is the F2 signal. The -60 degree cable

directly feeds amplifier A27. This output is the F1 signal. The two amplifiers, A26 and A27, are phase and amplitude tracked and thus, preserve the relationships of the F1 to F2 signals. The hybrid outputs are the A-signal, which is the sum of F1 and F2, and the B-signal, which is the difference of F1 and F2. This satisfies the conditions of $\emptyset_s = 0$. When a $\emptyset_s$ other than 0 is required, an adjustment of the reference cable, and the -120 degree cable can modify the $\emptyset_s$ to any required angle.

In a practical system, for maximum system accuracy, the axis of symmetry pointing (controlled by $\emptyset_s$) should always be directed at the earth's surface directly below the target. This could be accomplished by electronic phase control of $\emptyset_s$ as a function of range. For the purpose of this equipment, however, a compromise midrange value of $\emptyset_s$ was used.

C. ARC TAN PROCESSOR

Figure 13 shows the components of the arc tan processor.

The system operation requires that the amplitude ratio of B/A be converted to two signals whose phase relationship varies directly with this ratio. This is accomplished in quadrature hybrid A31. These two outputs, designated as A-JB and B-JA are amplified and limited in phase tracked amplifiers A32 and A33. The outputs of these two amplifiers are fed to phase detector A34. A 90-degree phase shift cable is inserted in the A-JB signal to set the proper demodulating angle of the phase detector.

The output of the phase detector is fed to a narrowband dc amplifier A35 with its output designated as the arc tan output of the processor. The ratio of the amplitudes of the A and B patterns is conveniently measured in the standard arc tan type of processor.

D. MONOPULSE-FORMING NETWORK AND AFC

Figure 14 shows the monopulse-forming network and AFC circuitry. Two signals, tapped off from the beam-forming network in dividers A21 and A22 are fed to the input of a hybrid tee, A38. The outputs of this hybrid form the monopulse patterns, that is, Σ and Δ, and are linearly amplified in A39 and A40. A portion of the Σ signal is tapped off in a 10-dB directional coupler, A41 and fed to the AFC circuitry. The two nomopulse outputs, Σ and Δ, are then processed in the arc tan processor in the same manner as the LAT signals. During the experiment this was accomplished by changing coax patch cables on the front panel of the processor. The off-boresight monopulse data was recorded in the same manner as the LAT information.

The signal used for the AFC function is tapped from the main Σ signal and amplified by linear amplifier A36 and then fed to a limiter-discriminator A44. The detected dc output of the discriminator is processed by an active integrator, A45, and amplified by dc amplifier A46. The output of this amplifier is the electrical tuning voltage required to tune the RF local oscillator. A swing of 0 to +15 V will slew the local oscillator frequency approximately 20 MHz. A front panel switch allows for manual or closed loop AFC operation. Two zero-center panel meters are used to assist the operator in the acquisition of the CW target source. One meter, connected directly to the output of the discriminator, displays the relative frequency deviations above or below the 60-MHz center frequency of the IF amplifiers. A second meter, used during closed loop operation, displays integrated output voltage deviations above and below 0V. A front panel 10-turn potentiometer allows the operator to manually slew the local oscillator frequency during the manual search mode. Observation of the discriminator output meter enables the operator to properly tune the local oscillator frequency prior to closing the AFC loop. After the loop is closed any long-term drifts, either of the C-band CW source or the receiver RF local oscillator are sensed and corrected by the loop. Slow drifting can be observed on the integrator output meter as a deviation from zero and can be corrected or followed up by manually adjusting the 10-turn potentiometer.

E. C-BAND CW SOURCE

The LAT experiment was conducted with receive-only equipment so an RF target source was required. A CW cavity-tuned oscillator was used and located along with the ranging instrumentation package in the aircraft. The oscillator was powered by small storage batteries and voltage stabilized by a regulator to minimize oscillator drift. Drifting, due to ambient temperature changes was minimized by the addition of external thermostatically controlled heater pads. The unit was mounted on a 1/8-inch aluminum plate and suspended at the four corners by shock cards to eliminate any mechanical modulation of the oscillator due to aircraft vibrations. The output power of the oscillator is nominally +23 dBm. The output was routed, via a 2-foot length of coax cable, to a vertically polarized omnidirectional antenna located on the lower portion of the fuselage. The oscillator frequency was set for 5.540 GHz.

4. EXPERIMENTAL PROGRAM

A. GENERAL

The flight test site was located at the Eaton's Neck Coast Guard Station overlooking the Long Island Sound. The antenna was located on a bluff, 21 ft above sea level. A trailer, to house the processor, peripheral instrumentation equipment, was located 50 ft behind the antenna. The antenna was orientated in a north-easterly direction, thus allowing a minimum of 12 miles of overwater testing range. Figure 15 shows the range.

A flight consisted of one outbound and one inbound run on a predetermined heading to keep the target aircraft within the 12 degrees azimuth beam width of the antenna. Each flight was flown at a constant altitude of 100, 250, or 500 ft. For comparison purposes, both LAT and off-boresight monopulse data was recorded.

B. AIRCRAFT INSTRUMENTATION

Two different aircraft were used during the test period. During the first 50 hours of flying, a

AD-A040 144 ADVISORY GROUP FOR AEROSPACE RESEARCH AND DEVELOPMENT--ETC F/G 17/9
NEW DEVICES, TECHNIQUES AND SYSTEMS IN RADAR.(U)
FEB 77

UNCLASSIFIED AGARD-CP-197 NL

3 OF 7
AD
AD040144

Citabria float plane was used. During the next 50 hours, a Cessna 150 float plane was used. Each aircraft was instrumented in an identical manner to ensure consistent results.

The aircraft was equipped with a C-band CW source emitting approximately 200-mW RF power f eding a vertically polarized omnidirectional antenna located beneath the fuselage.

In addition to the C-band CW beacon, a X-band pulsed transponder and associated antenna was installed, to be used in conjunction with a ground-based ranging system. Constant communication was maintained between the aircraft and the ground test site via VHF radio on an assigned frequency of 123.5 MHz. Constant altitude was maintained using the aircraft's altimeter as a reference. This altimeter was a standard aircraft barometric type and was a source of accuracy error.

C. GROUND TEST SITE

The ground test site consisted of the LAT receiving antenna, a trailer to house the LAT processor, recording, ranging and peripheral equipment, and a portable engine driven ac generator to supply test site power.

Processor output data, consisting of arc tan output voltage and received signal level indication, was recorded on a Brush Mark II analog recorder. Range marks in 5 or 10 μs intervals were recorded on a third channel.

Recorded data, therefore, consisted of:

A continuous analog recording of either a LAT or monopulse voltage which was representative of the aircraft's elevation angular position.

Tick marks every 5 or 10 μs indicating the aircraft's range.

Continuous recording of the IF limiter output signal level to indicate signal fades. (SNR less than 20 dB.)

This recorded angle data was later compared to a theoretical plot to determine actual versus calculated aircraft position. Figure 16 is a complete instrumentation diagram, Figure 17 is a sample of the strip chart recording.

The ranging system consisted of a ground-based X-band transmitter, X-band transponder located in the aircraft, and a ground-based X-band receiver. The time interval between transmitted and received pulses was measured and read out on a time interval counter. This information was recorded on the analog recorder as range marks.

D. SYSTEM ADAPTATION FOR RADAR SITE GEOMETRY

One of the experimental conditions set by the physical location of the radar site was the height of the aperture above the reflecting surface. Normally, the measured radar elevation angle is that angle between the ray to the target and a ray-line extending from the antenna center parallel to the earth's surface (flat earth considered for short ranges). Because the antenna was located 27 feet above the mean water surface, neither the reflecting surface or the ray-line parallel to the surface represented the correct angle measurement reference. The correct reference line was that imaginary line extending from the center of the aperture to a point on the reflecting surface directly below the target (again assuming flat earth geometry for the short ranges being considered). This line then bisects the angle between the target ray and the target image ray.

In the design phase of this program, provision was made in the beam-forming network to adjust this axis of symmetry reference line based upon the antenna height above the water and some selected range position. Conceptually, in an operational configuration, the pointing of this axis of symmetry would be a dynamic processor-controlled function coupled with the radar range tracker. However, for this experimental program, a fixed midrange position was selected and the beam forming network adjusted accordingly. (The phase adjustment of ϕ_s in the processor controls the symmetry axis.) A series of computer calculations were performed to determine the elevation angle errors that would result for target range positions other than the design point. The results are shown in Figure 18.

The surveyed height of 27 feet was used with constant target heights of 100, 250, 500, and 1000 feet. With the symmetry axis set at -0.8 milliradian, the error in setting the symmetry axis is bounded by $\pm$ 0.5 mrad for target ranges in excess of 4 nmi.

The consequences of an error in setting the symmetry axis are discussed in W.D. White's "Noise and Tolerance Errors in the AIL Low-Angle Tracking System," AIL Technical Note LAT-2, July 1971. In summary of that discussion, the pointing error results in a measurement error which averages to approximately the pointing error. However, the instantaneous measurement error varies with image phase and reflection intensity over limits of from 0.9 to 2 times the pointing error for moderate reflection and from 0.7 to 10 times the pointing error for strong reflections.

Thus the test results should be more accurate (as far as the pointing error is concerned) in the 6 to 9 nmi region. At shorter ranges, undulation of the measured target elevation about the true value is expected to occur as the target opens or closes range. The amplitude of these undulations should be related directly to the magnitude of the pointing error and inversely to the sea state.

As pointed out previously, this error can be removed by varying the symmetry axis continuously with target range.

Once the geometrical pointing angle of 0.8 milliradian had been chosen, the electrical phase angle, ϕ_s, was calculated (ϕ_s = 5 degrees) and the appropriate phase adjustment set into the beam forming network. After this final phase control was set, the entire system, the antenna, beam forming network, and arc tangent processor circuits were tested on the AIL antenna range. The antenna was placed on a pedestal and rotated through several degrees in the elevation plane and the total system response was recorded. The output voltage is plotted as a function of antenna angle relative to the broadside of the array. The angular measurements were made with a theodolite physically mounted to a fixture on the antenna and sighting was made to a far-field source antenna. The resulting system characteristic curve is shown in Figure 19. The key reference points on the angle coordinates are the array broadside position and the axis of symmetry position. The system monopulse boresight is also shown.

It should also be recognized that the arc tangent processor produces ambiguous reading beyond 1.4 standard beam widths of the symmetry axis limiting the angular coverage of this experimental model. This limit is not the limit of the technique, but rather the limit of the type of processor used. The arc tangent processor also is affected by phase detector sensitivity loss as the elevation angle of the target approaches the axis of symmetry. This effect can also be eliminated by using a different signal processing method.

In addition to the LAT system characteristic, a monopulse characteristic was measured to determine the off-boresight angle versus output voltage characteristic, at $\pm$ 1/2 beam width about the boresight. The difference pattern was formed between the upper and lower array element, and the resultant characteristic was approximately a straight line. The output voltage from the system processor was $\pm$ 1.5 volts for target elevation angle positions of $\pm$ 1/2 beam width off monopulse boresite.

5. DATA REDUCTION

After the radar equipment was installed at the site and the aircraft instrumented with the beacon units, flight testing proceeded. Three constant altitude flight profiles were used: 500, 250, and 100 feet. Sea surface roughness was recorded for each flight as an external variable which could affect the recorded data.

The main system configuration was aligned to observe the performance of the LAT technique; in addition, for comparative purposes, a fix-antenna monopulse configuration was implemented to collect nominal representative data showing the multipath effect on standard monopulse performance at low angles.

Each flight data record was coded with a flight number indicating the date, the flight number for the day, and the direction (in-bound or out-bound) of the aircraft. In addition, the system configuration was noted at LAT or monopulse. All results were collected on a multichannel pen recorder, with target range position information taken from the X-band range-only equipment previously described. The total test program extended over a 3-month period from January through March 1973. The total aircraft flight time was 100 hours, but due to various initial test instrumentation problems, the total data collection was accumulated over approximately 65 flight hours.

Figure 17 shows pen recordings made for a typical LAT and monopulse run. The second channel on the recordings is a signal-to-noise indication. A threshold circuit was set to indicate when the SNR ratio was below 20 dB. Signals with less than 20-dB SNR were declared invalid indicators of the basic technique capability since the experiment was conducted with a minimum strength target beacon.

The data runs were converted from pen-recorder form to tabular form by reading the recorded voltage plot at 5 μs increments for each flight.

The LAT flights which produced little or no data due to signal fades below 20-dB SNR were not included in the tabulation. This tabulated LAT data was then put on punch-tape (Appendix II for punch-tape data) and fed to a time-shared computer.

The computer was programmed to convert the voltage readings to angles based on the system input angle versus output voltage characteristic.

Statistical data reduction was then performed on the angle data. First the flights were divided into six groups based on target altitude and calm or rough sea state conditions. Table I shows the six groups and the number of flights included in each group.

The LAT data, or file, for each group was compiled so that the average value of angle over all flights in the group was computed for range positions in 5 μs range increments. The computer also calculated the $\pm$ 1 σ value for the data population at each range position. The results of these calculations are plotted in relation to the theoretical target position for each group in Figures 20, 21, 22, 23, 24 and 25. The computations have all been adjusted to indicate elevation angle as measured from the antenna relative to a plane parallel to the earth's surface (flat earth).

Because of the random and nonrepeatable nature of the monopulse results, no attempt was made to average this data. Instead, a typical representative flight result was plotted for each of the six groups that the LAT data was divided into. The data is shown relative to the theoretical monopulse off-boresight characteristic in Figure 26, 27 and 28.

In addition to the discrete range distribution calculations for the LAT data, the rms values for each of the six groups were calculated and are presented in Table II. The rms error at each of the range positions was found by using the following expression:

$$\text{rms error} = \sqrt{(\bar{\theta} - \theta_{true})^2 + \sigma^2}$$

where

$\bar{\theta}$ = average measured elevation angle for all flights in a group

θ_{true} = theoretical elevation based on geometry

σ^2 = variance of the elevation measurements over all flights in a group.

These rms errors were averaged for each group separately, over slat ranges corresponding to elevation angles of 1.4 standard beam width (24.3 mrad) or less to produce the entries in the body of Table II.

Averaging over the target heights results in a 1.41 mrad and 1.79 mrad rms errors for calm and rough (wave height generally greater than 2 feet) seas, respectively. Finally the average of these two values, 1.6 mrad, is taken as representative of the overall low angle tracking performance (one-tenth beam width) over all flights performed for this experiment.

6. CONCLUSIONS

The results of the low angle tracking experiments demonstrate the ability of the system to consistently measure target elevation angle in the region from one-quarter beam width to 1.4 beam widths of the horizon with an rms accuracy of one-tenth beam width.

The experimental equipment built to demonstrate the B/A technique feasibility was optimized for targets at 7 miles range. However, the system performed consistently and accurately at other ranges within the expected error limits. Equipment limitations prevented data collection beyond 1.4 standard beam widths above the horizon. Site geometry and equipment sensitivity prevented accurate data collection at angles below one-quarter beam width. These equipment limitations can be eliminated by optimizing equipment designs and addressing accurate system performance rather than feasibility demonstration.

7. REFERENCE

Synthesis of Radiation Patterns for Low Angle Tracking, AIL Technical Note LAT-1 April 1971

W.D. White and S.W. Gery, Final Report on Low-Angle Study, AIL Report 4251-TR 1 prepared for Naval Ship Systems Command. Contract Number N0024-69-C-1295, AIL a division of Cutler Hammer Deer Park, New York 11729

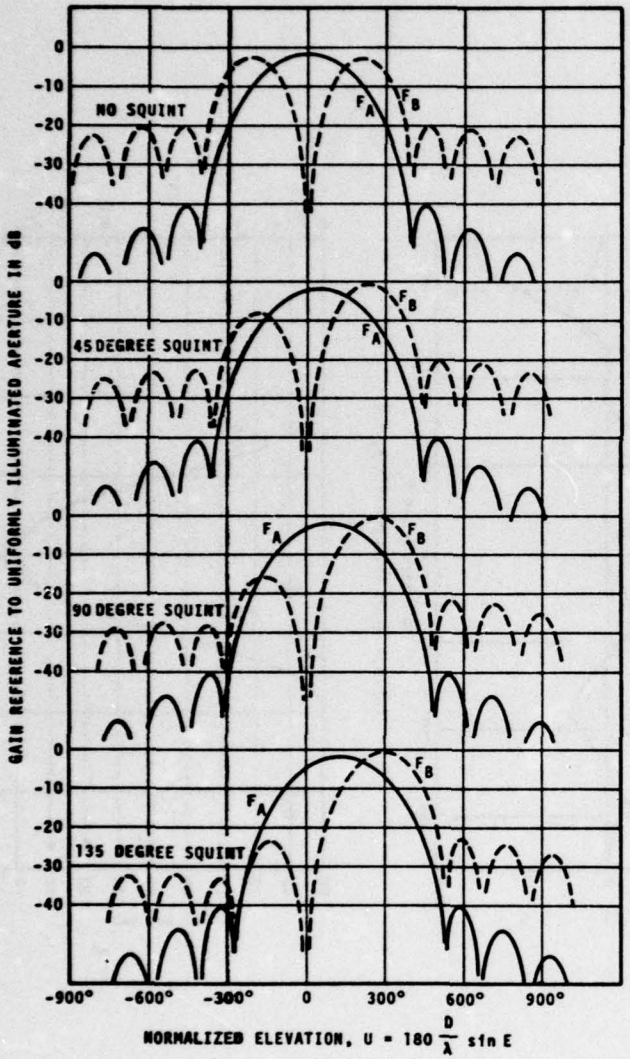

Figure 1 Low-Angle Tracking Patterns

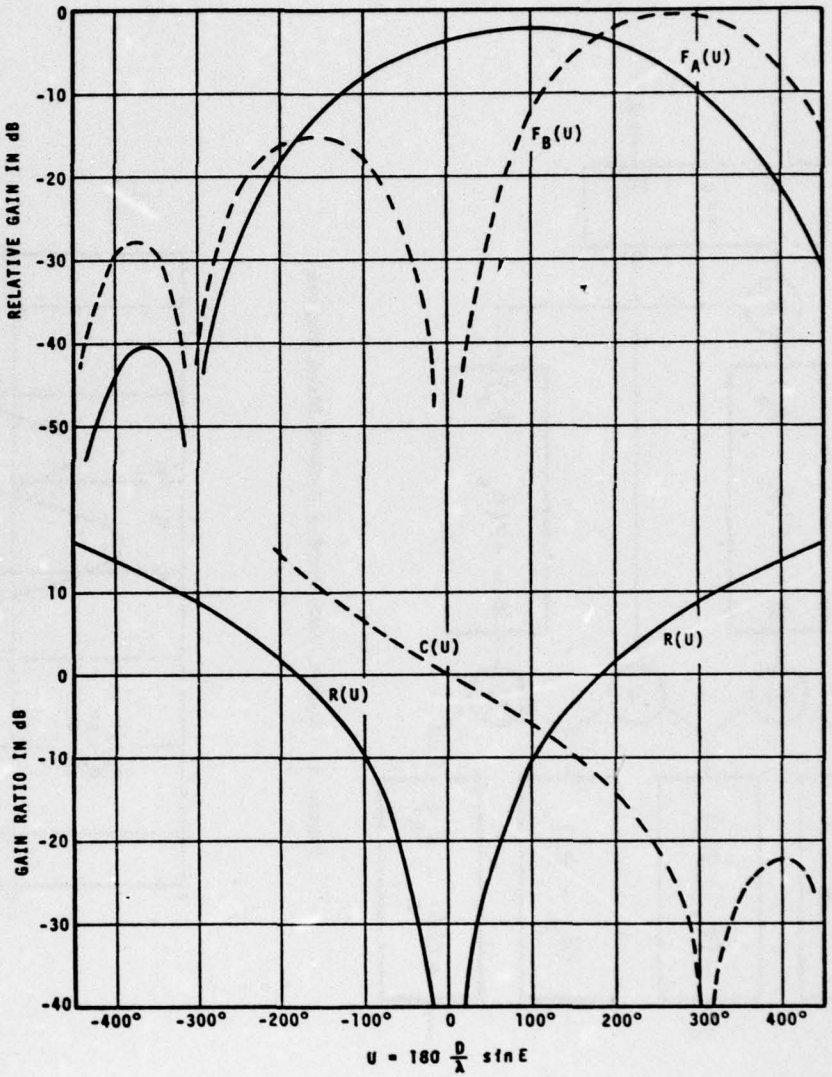

Figure 2 Expanded Antenna Patterns

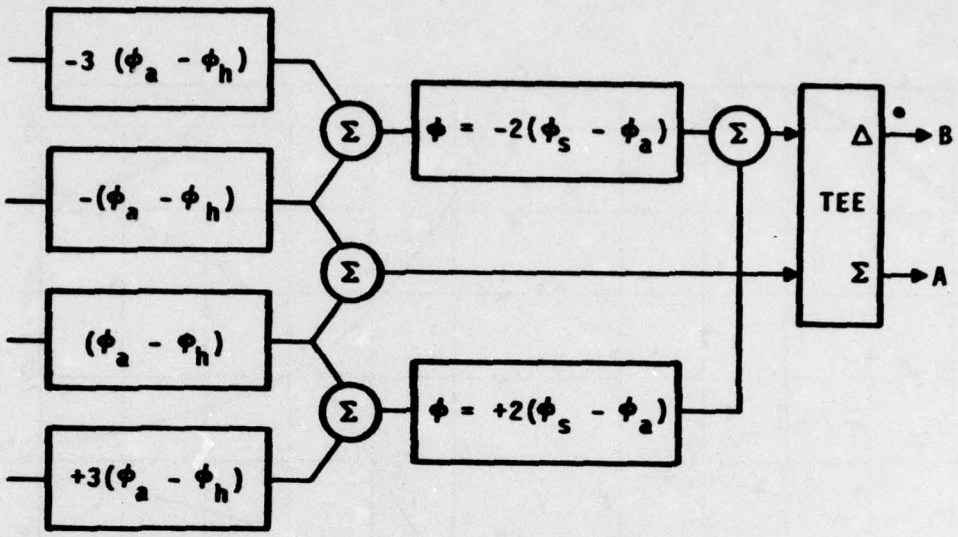

Figure 3 System Beam Forming Network Block Diagram

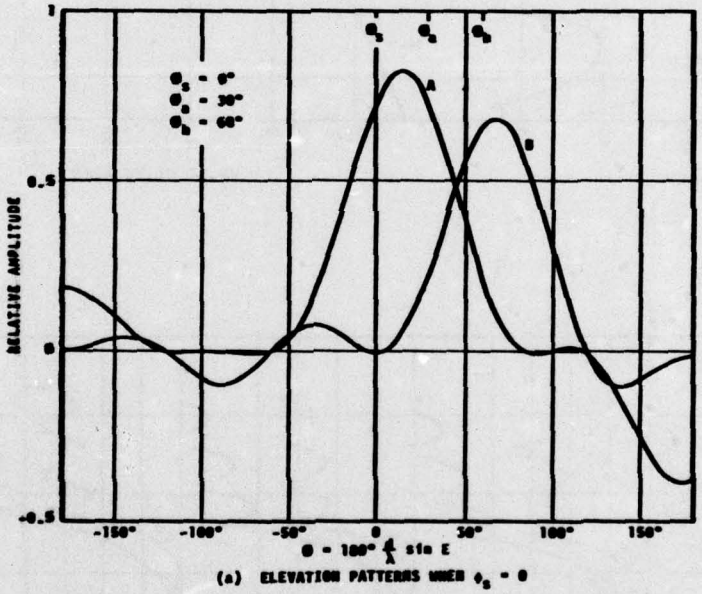

(a) ELEVATION PATTERNS WHEN ϕ_s = 0

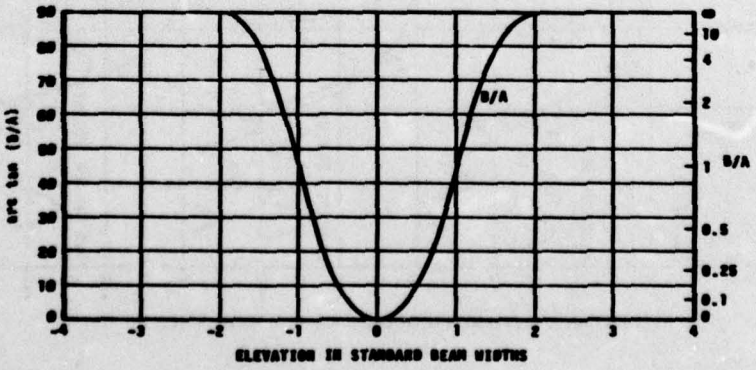

(b) B/A PATTERN RATIO

Figure 4 Theoretical Patterns, β_s = 0 degree

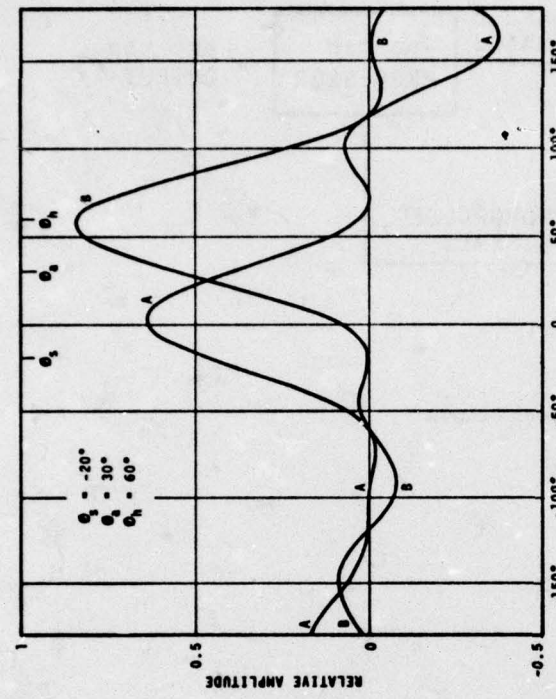

(a) ELEVATION PATTERNS WHEN ϕ_s = -20°

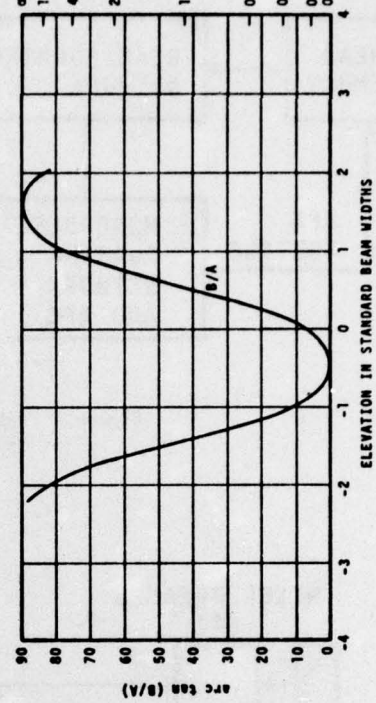

(b) B/A PATTERN RATIO

Figure 6 Theoretical Patterns, ϕ_s = -20 degrees

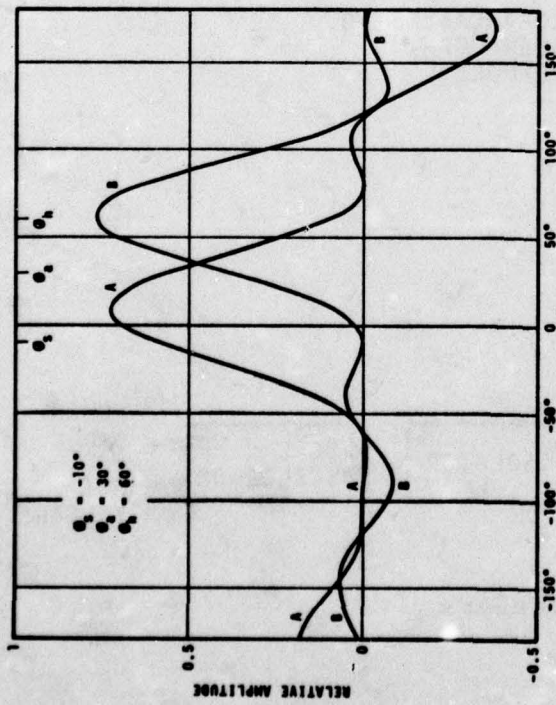

(a) ELEVATION PATTERNS WHEN ϕ_s = -10°

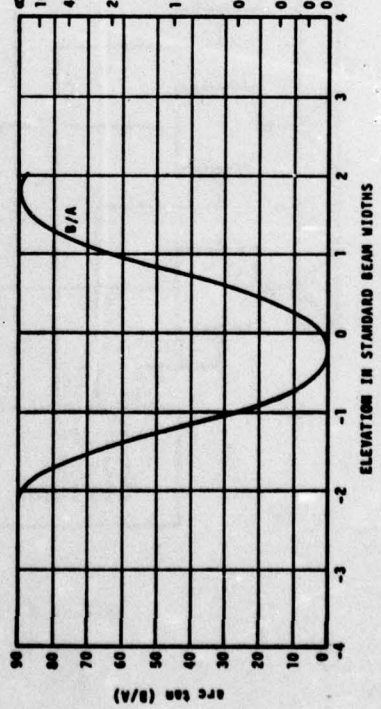

(b) B/A PATTERN RATIO

Figure 5 Theoretical Patterns, ϕ_s = -10 degrees

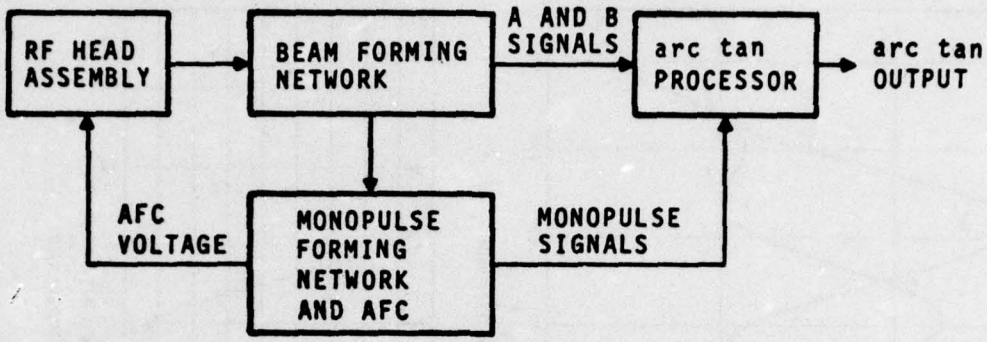

Figure 7 System Block Diagram

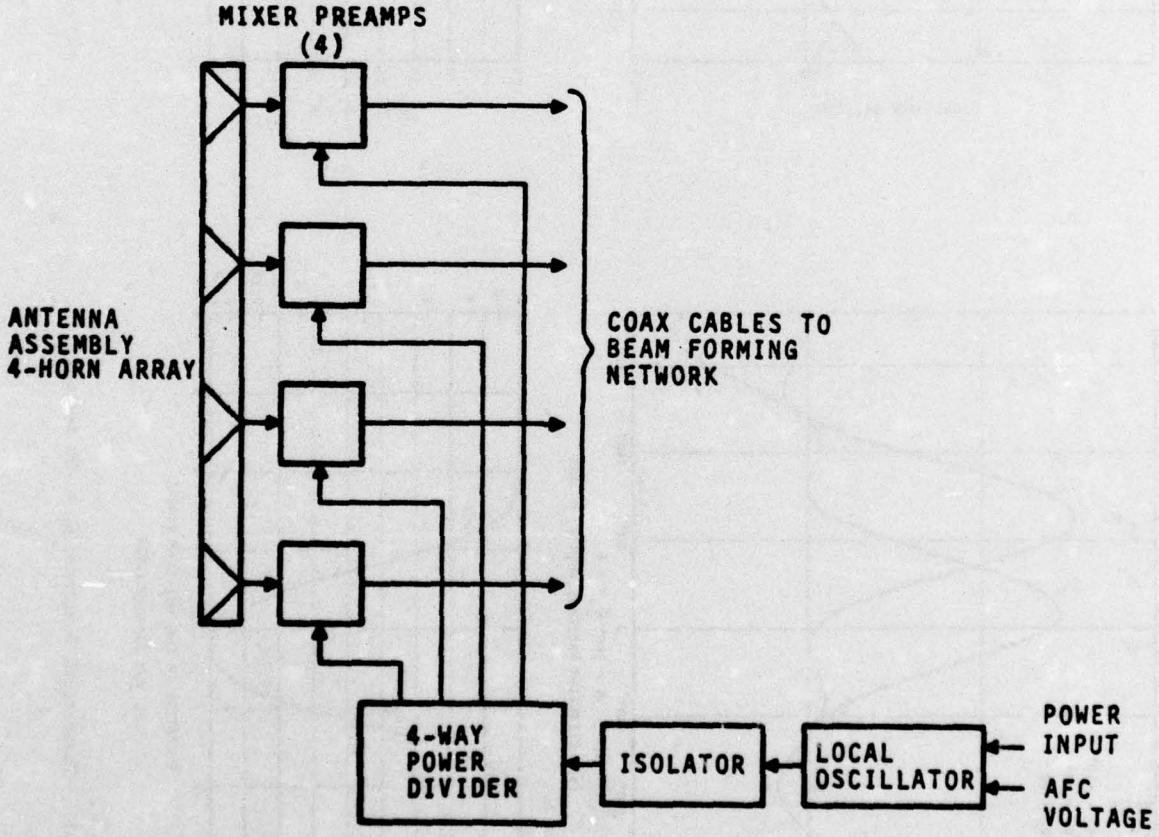

Figure 8 RF Head Assembly

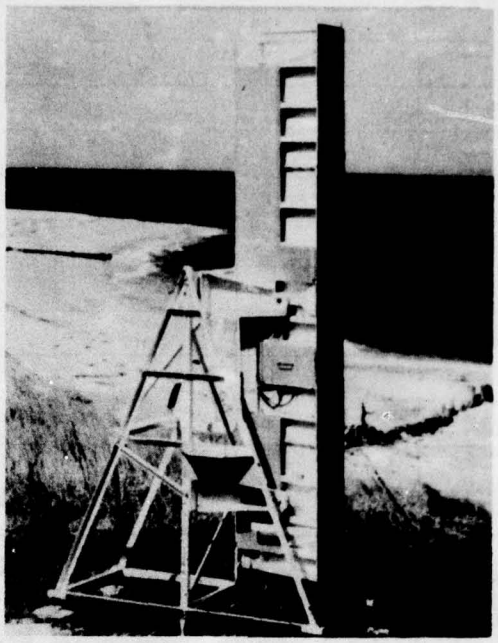

Figure 9 Low-Angle Antenna

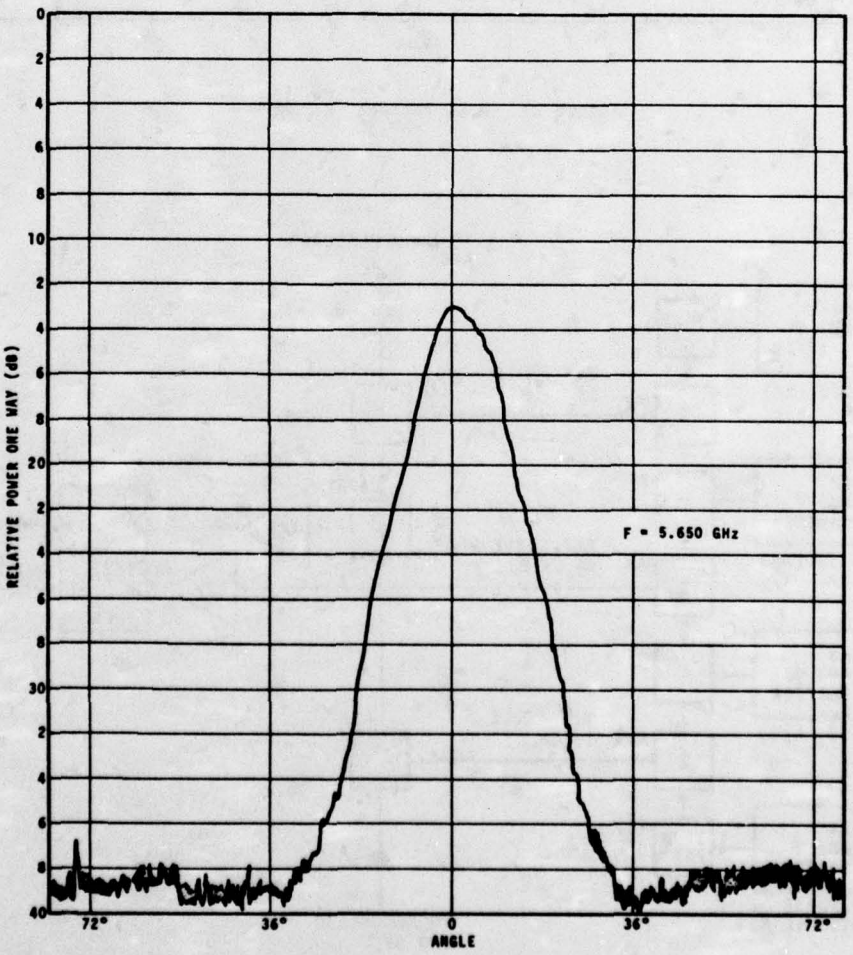

Figure 10 Horn Pattern, H-Plane

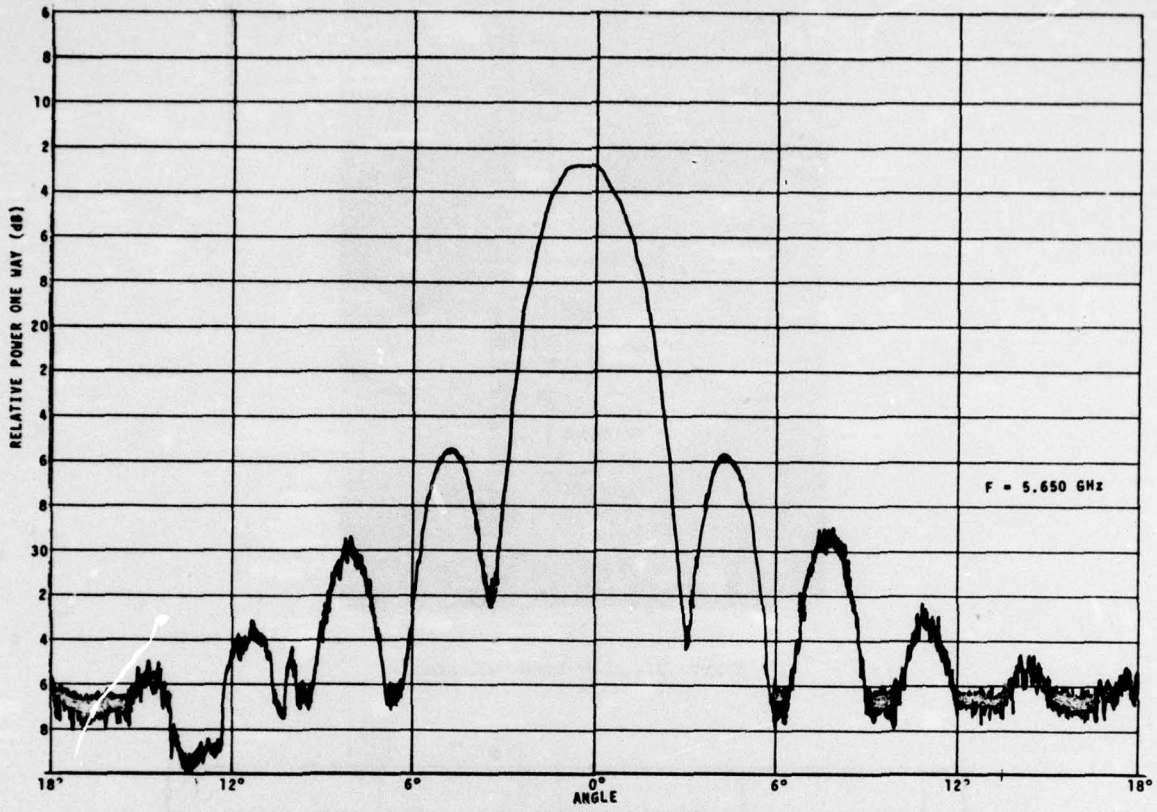

Figure 11 Horn Pattern, E-Plane

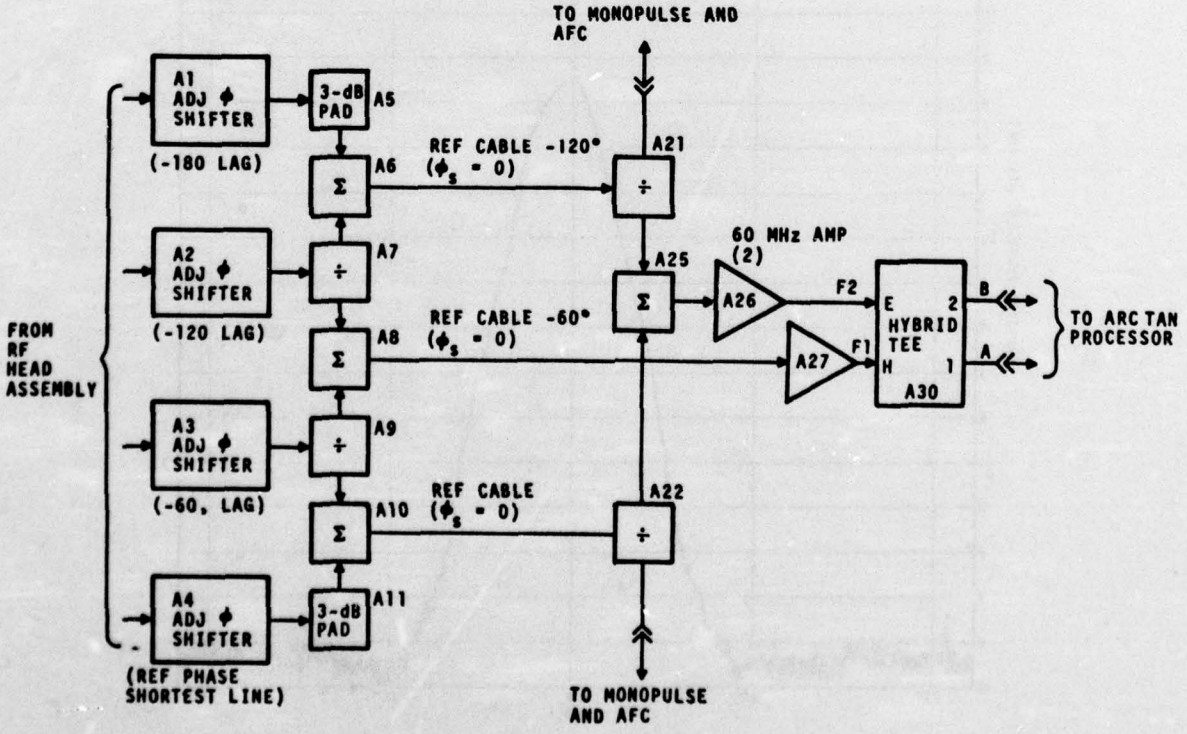

Figure 12 Beam-Forming Network

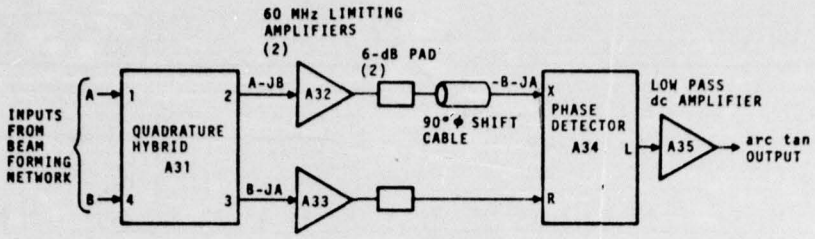

Figure 13 Arc Tan Processor

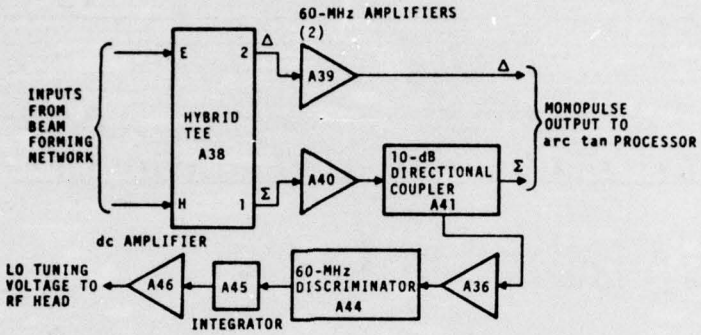

Figure 14 Monopulse Forming and AFC

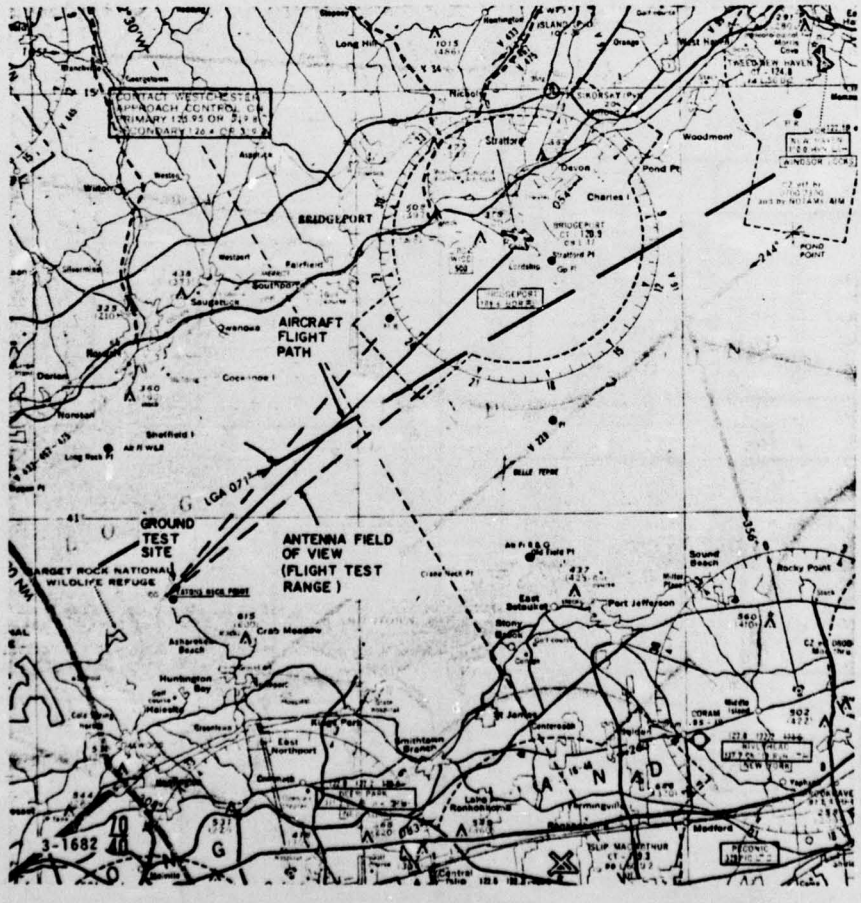

Figure 15 Map of Long Island Sound

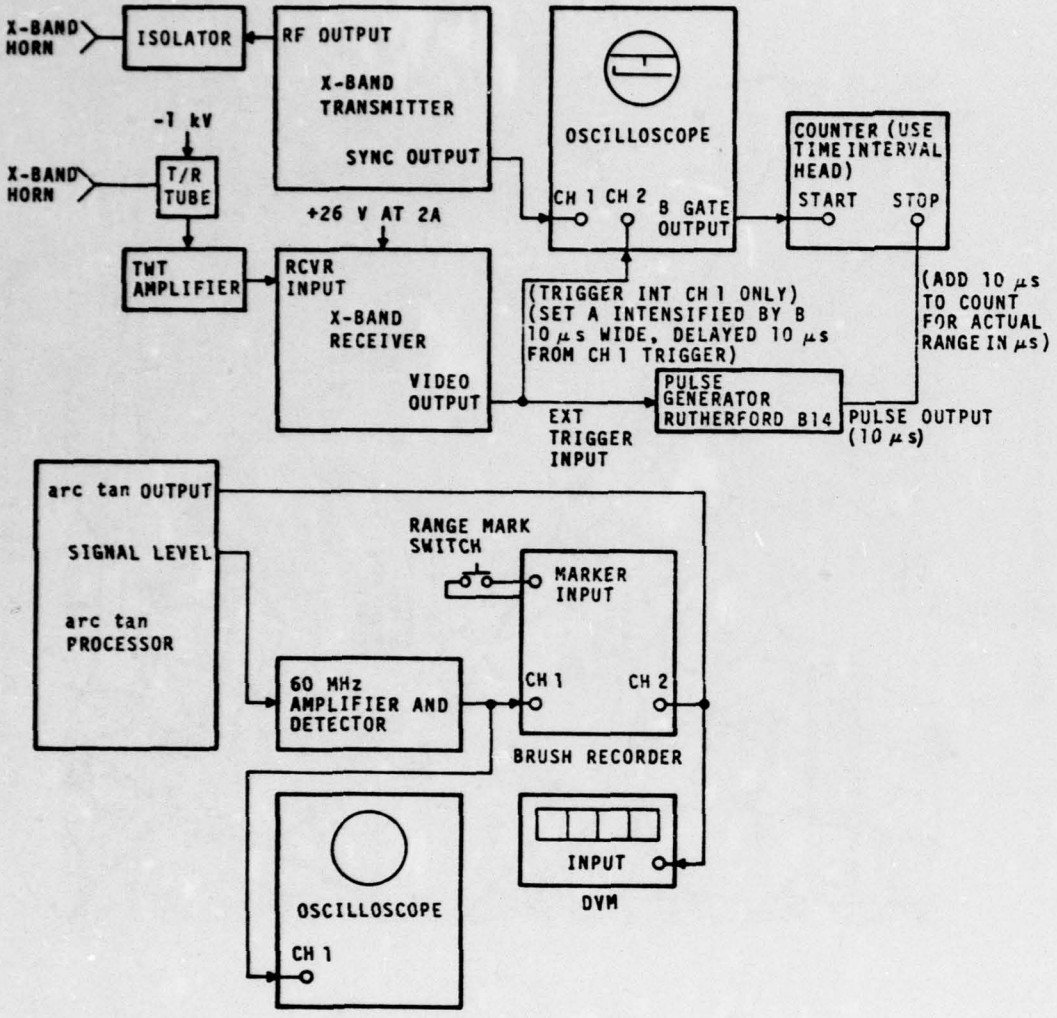

Figure 16 Instrumentation Diagram

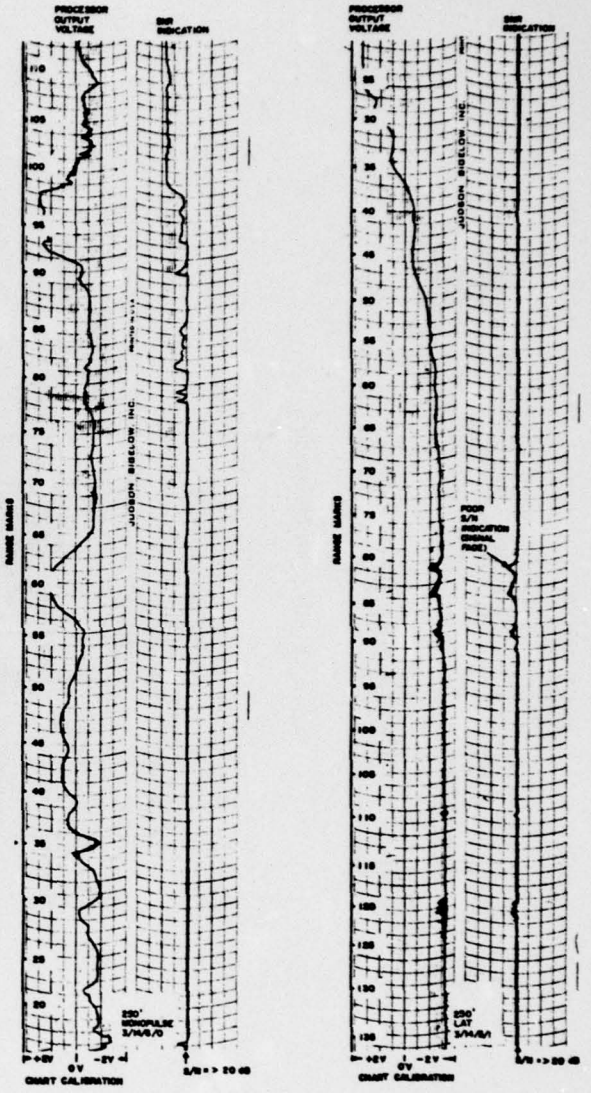

Figure 17 Strip Chart Recording

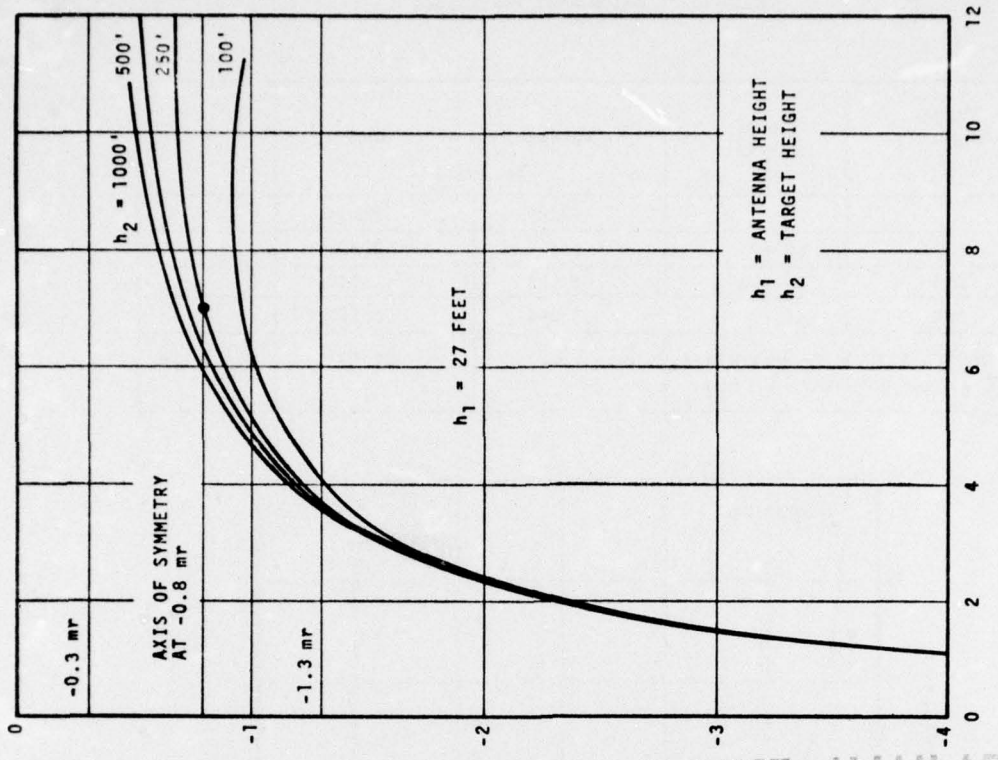

Figure 18 Angle Error Versus Range for E_s = 0.8 mrad

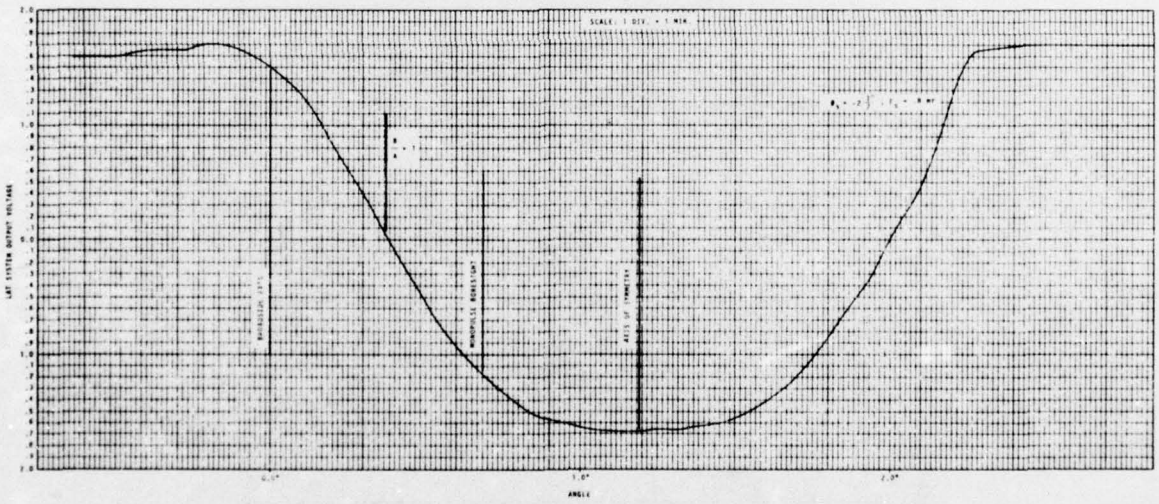

Figure 19 Voltage Versus Angle Characteristic Curve

Table I Flight Grouping

Group	Altitude (in feet)	Sea state (nominal)	Number of flights
1	100	calm	13
2	100	rough	37
3	250	calm	45
4	250	rough	43
5	500	calm	10
6	500	rough	10

Table II. Calculated rms Values

Target height, h_t (feet)	Range interval (μs)	$\bar{\rho}$ = average rms error (mrad) Sea state		
		Calm	Rough	
100	10-60	1.558	2.829	
250	20-140	1.702	1.342	
500	45-140	0.964	1.197	
TOTAL AVERAGE, rms Error C = calm R = rough T = total		$\tilde{\bar{\rho}}_C = 1.41$	$\tilde{\bar{\rho}}_R = 1.79$	$\tilde{\bar{\rho}}_T = 1.6$

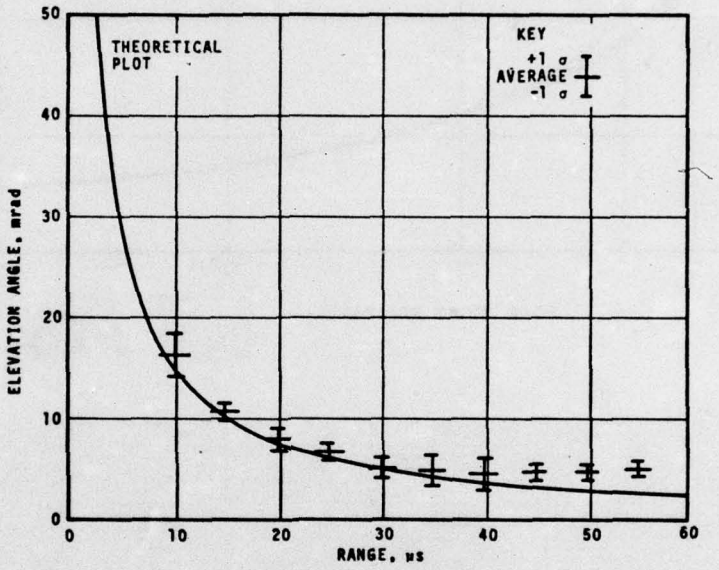

Figure 20 LAT Experimental Results, Altitude = 100 Feet, Sea Surface Calm

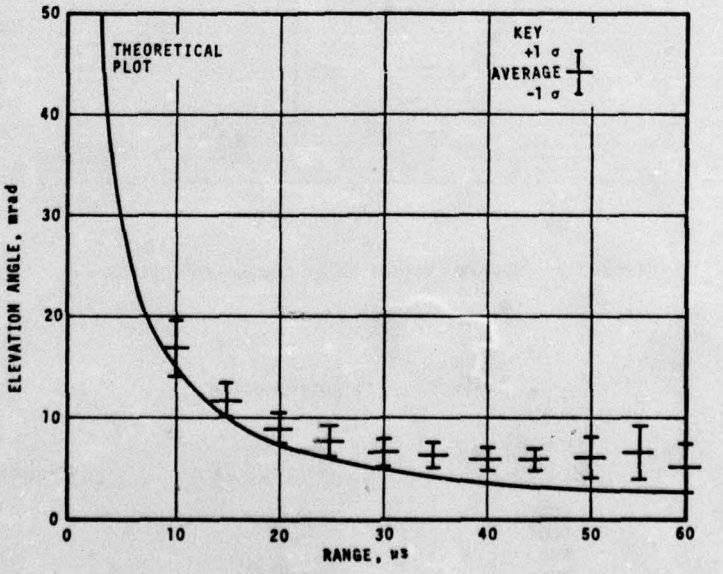

Figure 21 LAT Experimental Results, Altitude = 100 feet, Sea Surface Rough

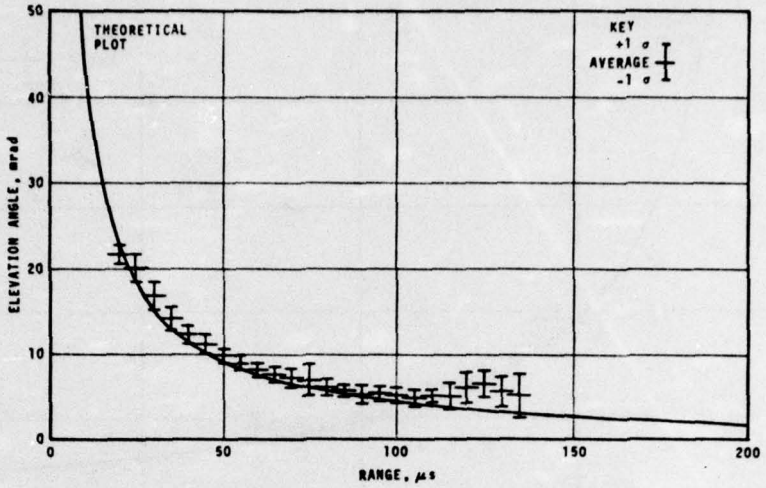

Figure 22 LAT Experimental Results, Altitude = 250 Feet, Sea Surface Calm

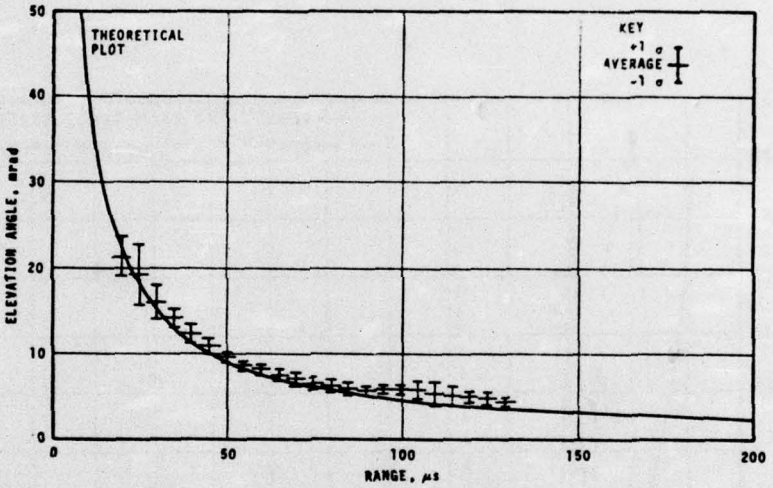

Figure 23 LAT Experimental Results, Altitude = 250 Feet, Sea Surface Rough

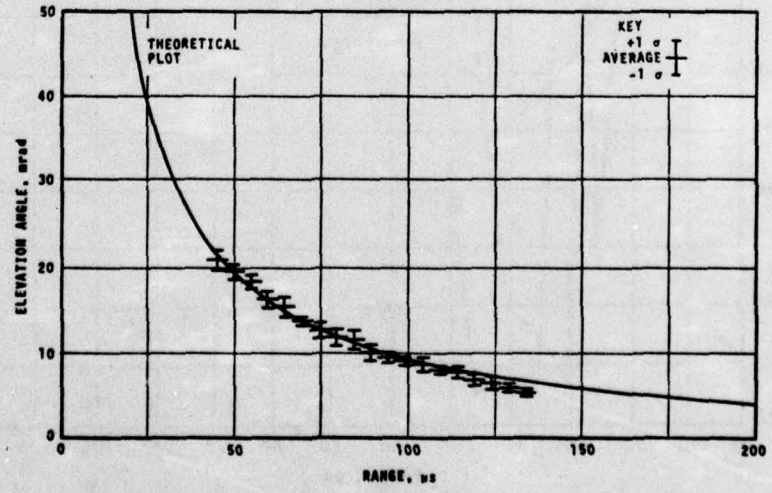

Figure 24 LAT Experimental Results, Altitude = 500 Feet, Sea Surface Calm

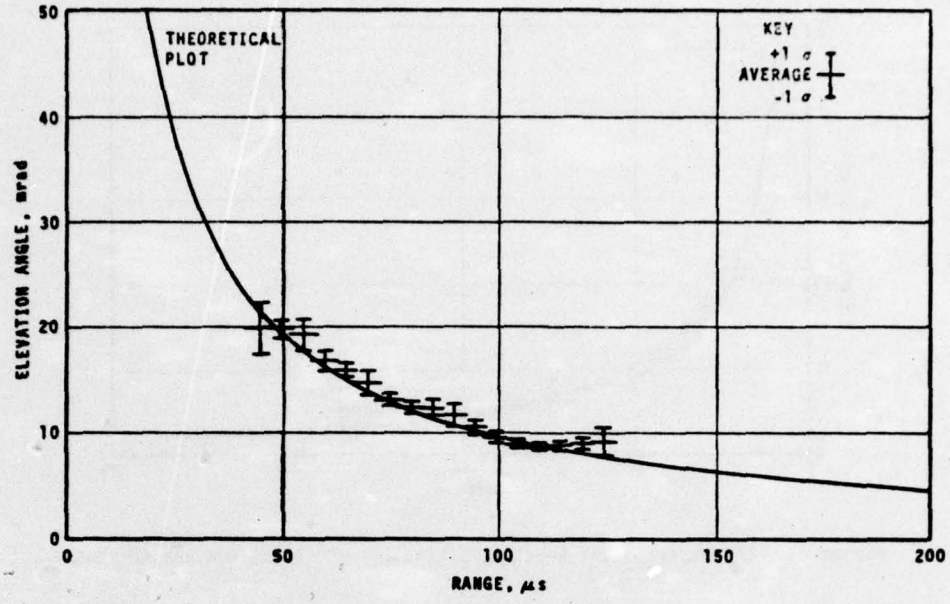

Figure 25 LAT Experimental Results, Altitude = 500 Feet, Sea Surface Rough

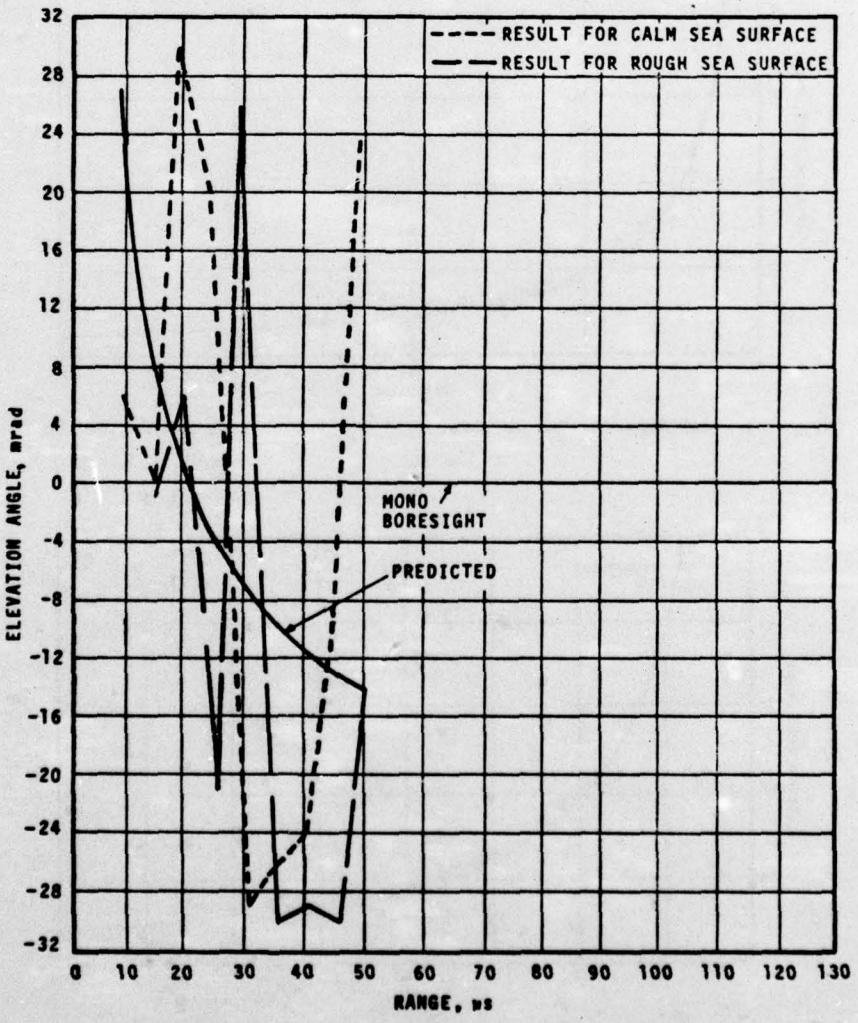

Figure 26 Typical Monopulse Performance, Altitude 100 Feet

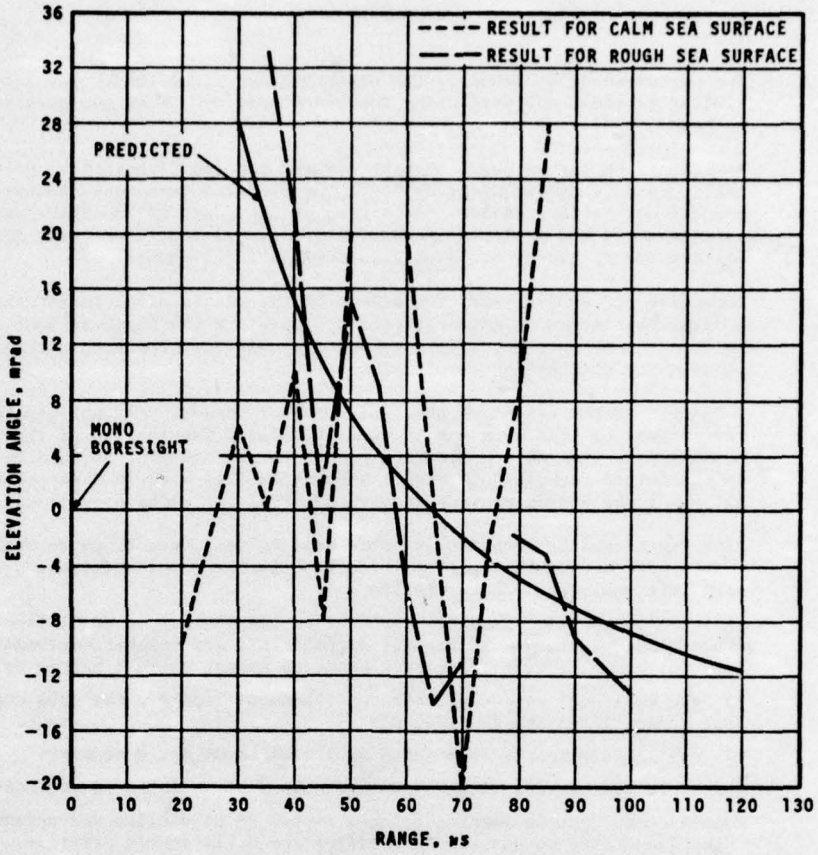

Figure 27 Typical Monopulse Performance, Altitude 250 Feet

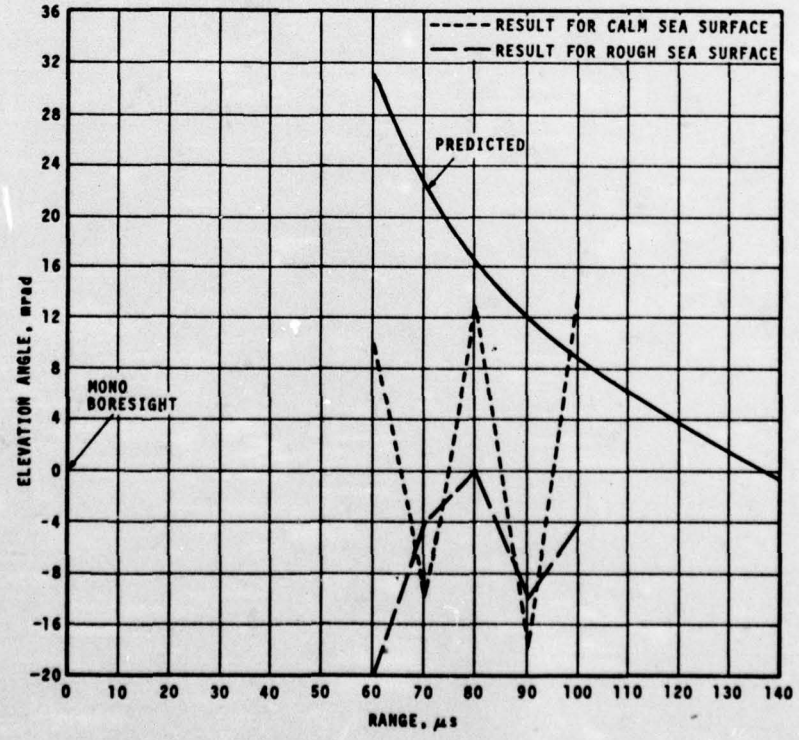

Figure 28 Typical Monopulse Performance, Altitude 500 Feet

DISCUSSION

P NERI: The performances achieved by the presented technique, which seems complex, are similar to those achieved using frequency agility. Have you compared the two methods?

K C STIEFVATER: No comparison per se has been made between the two techniques. However, from published data on frequency agility, the B over A technique achieved at least as good if not better results. As stated in the paper our accuracy was limited by site geometry and equipment sensitivity. If all conditions were optimised I believe the results would show considerable improvement.

G GALATI: According to our analysis, the effect of the finite dimension of the target on the nodding phenomenon is not negligible. Therefore the tests of your system should be done, in my opinion, with a common transmitting-receiving aerial. Are you planning to do that?

K C STIEFVATER: I agree that the effect of the finite target dimension is not negligible, however, the purpose of this work was to prove the basic feasibility of the technique, not to determine the maximum accuracy possible. We are not, at this time, planning to do any future work in this area. When additional work is undertaken it should by all means use a transmitting-receiving aerial as you have indicated.

M H CARPENTIER: Pour répondre à la question de notre ami Italien, nous avons en France conduit depuis 1968 un nombre significatif d'expériences sur l'utilisation d'un diagramme pair trés analogue. Il en résulte

a) que la précision angulaire obtenue est de l'ordre de un dixième de l'écart cible-image pourvu que le rapport signal/bruit soit significativement supèrieur à 20 dB, ce qui est le cas généralement au moment ou on a besoin de précision.

b) que ceci, qui est compatible du traitement Doppler, est trés supérieur à ce que peut donner l'agilité de fréquence.

c) que la question de complexité de l'equipement est à séparer:

- pour le traitement, il est complexe mais peut se faire en digital.
- pour ce qui est de l'antenne, cela dépend si on utilise une antenne spéciale supplémentaire ou une simple modification de la source primaire.

K C STIEFVATER: Thank you for your contribution.

RADAR CROSS SECTION ANALYSIS AND TARGET IMAGING FROM THE DOPPLER INFORMATION IN THE RADAR ECHO

G. GRAF

Institut für Flugfunk und Mikrowellen
Deutsche Forschungs- und Versuchsanstalt für Luft- und Raumfahrt e.V.
Oberpfaffenhofen, Bundesrepublik Deutschland

SUMMARY

The Doppler frequency spectrum of the radar echo from a rotating target with high resolution yields the distribution of the scattering centers in a cross range direction. The relation between Doppler spectra and the location of the scattering centers on a target is discussed and the optimum aspect angle window (integration time) that yields optimum resolution in the spectrum is given. Some experimental results show, that Doppler frequency analysis is a useful tool in the analysis of the scattering properties of complicated targets.

If in addition the phase of the spectra is used, a highly resolved image of the target can be constructed from instantaneous spectra corresponding to different aspect angles. In ideal cases resolution is 0.2 wavelengths. The principle of target imaging from Doppler spectra is given together with experimental results.

1. INTRODUCTION

In many cases of radar cross section investigations it is not sufficient to know only the radar cross section of a target. In problems of glint analysis, comouflage problems or in the synthesis of radar cross sections for example it is necessary to have knowledge about the location and the magnitude of the scattering centers on the target.

With short pulse radars or with frequency modulated radars it is possible to have high range resolution so that scattering centers with different distance from the radar can be resolved. Cross range resolution with these systems is only possible with a resolution corresponding to the beamwidth of the antenna.

The evaluation of the Doppler frequency spectrum of the radar return from a rotating target in contrast yields cross range resolution of a few wavelengths being independent of the distance between radar and target. Doppler frequency analysis thus is a comperatively simple means for getting high cross range resolution which is necessary for the analysis of the scattering properties of targets.

2. THE DOPPLER FREQUENCY SPECTRUM OF ROTATING TARGETS

In order to see the connection between the location of the scattering centers on a target and the Doppler frequency spectrum of its radar echo let us look at a target which is rotating round an axis with constant angular velocity $\dot{\alpha}$ and which is illuminated by a CW-radar. The axis of rotation for simplicity is assumed to be perpendicular to the line of sight. We furthermore assume for a moment, that the scattering centers on the target are fixed on it and that their radar cross section varies only slowly with aspect angle.

Each of these scattering centers because of the rotation of the whole target rotates round the common axis. During this rotation each scattering center moves towards the radar and back again, producing an instantaneous Doppler shift corresponding to its velocity in the direction of observation. For a single scattering center (Fig. 1) this velocity is

$$v(t) = \dot{\alpha} \cdot r \cdot \sin\alpha(t) \tag{1}$$

where r is the distance of the scattering center from the axis of rotation, $\alpha(t)$ is the instantaneous angular position and $\dot{\alpha}$ is the angular velocity which we assumed to be constant. Thus, the instantaneous Doppler shift of the echo from this scattering center is

$$f_d(t) = \frac{2\, v(t)}{\lambda} = \frac{2\, \dot{\alpha}\, r \sin\alpha(t)}{\lambda} \tag{2}$$

where λ is the wavelength of the radar.

The instantaneous Doppler shift of the radar echo from a single scattering center thus with a factor of $2\dot{\alpha}/\lambda$ is proportional to $r \sin\alpha(t)$. $r \sin\alpha(t)$ however is the component in the cross range direction of the distance of the scattering center from the axis of rotation (Fig. 1). The instantaneous Doppler shift thus is proportional to the instantaneous distance of the scattering center from the axis of rotation in a projection of the target into the direction towards the radar. This is valid for each scattering center, so that the radar echo from a target with several scattering centers yields a Doppler frequency spectrum, each line of which is given by (2) with radii $r = r_i$ and angles $\alpha(t) = \alpha_i(t)$ for the i-th scattering center. In Fig. 2 this situation is sketched for a target with several scattering centers. As the Doppler shifts are proportional to the distance of the respective scattering center in a cross range direction, the scaling factors can be chosen so, that the Doppler lines can be looked at as the projections of the scattering centers into the direction towards the radar. In a more detailed analysis (GRAF, 1972 and 1975) it was shown, that the intensities of the Doppler lines are proportional to the radar cross sections σ_i of the corresponding scattering centers, so that in principle from the instantaneous Doppler spectrum the location in the cross range direction and the individual radar cross sections of the scattering centers can be found.

In an experiment of course, the situation becomes much more complicated. First of all it is not possible to measure a spectrum of instantaneous Doppler frequencies with high resolution. If we use a short time

window Δt for the frequency analysis, because of the diffraction effects at the window, we obtain a Doppler line of the well known shape $\sin 2\pi f\Delta t / 2\pi f\Delta t$ which is the wider the smaller Δt and thus the better our approximation of "instantaneous". If, on the other hand, we use a long time window, the diffraction effects are reduced, now however we have no longer "instantaneous" Doppler frequencies, in contrast, the instantaneous Doppler frequency varies in the time window, so that the result is a wide and complicated spectrum.

In the following we shall look at such a spectrum, though it may be structured, as a widened Doppler line. It is obvious, that between the two extremes mentioned, there must be an optimum time window, that yields minimum line width in the Doppler spectrum. From an approximation, in which the resulting line width is put equal to the sum of the widths of the diffraction effect and the variation of the instantaneous Doppler frequency in the time window follows, that the optimum time window is a function of the location on the target of the scattering center to be resolved, of the aspect angle of the target in the center of the time window and on the weighting function to be used in the time window (GRAF, 1976). The analysis further shows, that the critical parameter is not the time window but the aspect angle window, which for constant angular velocity $\dot{\alpha}$ of the target however makes no difference.

As a result of such an approximation Fig. 3, for a Taylor weighting function with 40 dB side lobe level in its Fourier transform (HANSEN, 1966), shows a plot of lines of constant optimum aspect angle windows $\Delta\alpha$ in the r,α-plane of Fig. 1. For use of this plot the target is put on this plane with a given orientation (aspect angle) relative to the radar, the axis of rotation being perpendicular to the plane and piercing it at $r = 0$. If now the scattering centers are projected parallel to the axis of rotation onto this r,α-plane, the line crossing the projection of each scattering center gives the aspect angle window for optimum resolution of this scattering center for the given (medium) aspect angle of the target. Fig. 3 shows, that the lines of constant optimum aspect angle window in a wide range are straight lines, perpendicular to the direction of observation. This means, that a given aspect angle window gives best resolution for all scattering centers with equal distance before or behind the axis of rotation, seen from the radar. The choice of the aspect angle window thus results in a sort of focussing at the corresponding planes before and behind the axis of rotation.

2.1. Experimental Results

Fig. 4 shows a block diagram of an experimental setup, we use for the measurement and on-line-evaluation of Doppler spectra of various targets for radar cross section analysis.

The transmitter is a stabilized continuous wave source, which for long ranges is followed by a power amplifier. The antennas are horn antennas or excentric parabolas depending on the target to be investigated. The transmitter illuminates the target, which is rotating with constant angular velocity $\dot{\alpha}$ round an axis. The axis of rotation in general is not perpendicular to the direction of observation as assumed above. This however only changes the above scaling factor in the spectrum by a factor of $1/\sin\beta$ where β is the angle between the direction of observation and the axis of rotation.

In the receiver the radar echo from the target is coherently downconverted to any bias frequency between zero and 0.1 MHz. This bias frequency is used to shift the whole frequency spectrum, so that all negative Doppler frequencies appear in the positive frequency region so that foldover of the negative frequencies is avoided.

The frequency spectrum of the receiver output is analyzed by a spectrum analyzer and displayed on a scope. A television camera in front of the scope feeds the image of the spectrum into a TV-image mixing unit. The other input of this unit is fed by an optical image of the target, taken by a second TV-camera. At the output of the TV-image mixing unit, the image of the spectrum and the optical image of the target appear one upon the other and are displayed simultaneously on a screen, the Doppler lines appearing directly under the corresponding scattering centers on the target when the appropriate scaling factors for the spectrum and the optical image respectively have been chosen. The system thus, during the rotation of the target, on the TV-screen continuously shows the image of the target together with the location of the scattering centers on it, indicated by the Doppler lines.

The scaling factor for the spectrum according to the above (Equ. 2) only depends on the wavelength of the radar and the angular velocity of the target. Here however, when we compare the spectrum with the optical image of the target, we also have to take into account the scaling factor of the image.

Due to the integration time the spectrum is delayed compared to the signal input and compared to the optical image. As we have to superpose the spectrum with the optical image corresponding to the center of the integration interval or aspect angle window respectively, we have to delay the optical image by a time interval corresponding to half the integration time. This can be done by a time delay chain between the TV camera and the TV mixing unit or, more simply by a displacement of the camera from the radar into a position that yields an optical image the radar "saw" half the integration time earlier.

Figs. 5 and 6 show two examples. These images were taken from the TV-screen behind the TV mixing unit during the measurement of the scattering center distribution on a model of a VX-101 vertical take off aircraft. The wavelength for these measurements was 3 centimeters, the overall length of the model was 55 and its wingspan 23 wavelengths. The airplane for these measurements was lying on a styrofoam column, which was rotating round a vertical axis. Fig. 5 shows a broadside view of the aircraft. This is a view where we have only few discrete scattering centers. The Doppler frequency spectrum shows a broad Doppler "line" along the body of the aircraft corresponding to a long scattering center on the body. The intensity of the spectrum goes down to the right corresponding to the fact that the curvature of the body at the front end is thus, that there is no longer specular reflection into the direction of observation and due to the fact that the radius of the body decreases. The small maximum before the nose of the aircraft corresponds to the reflection from a pin of approximately 5 cm length at the nose of the aircraft, which cannot be seen on the optical image. The minima in the spectrum at the front ends and the rear ends of the engines (which are located at the very ends of the wings), are caused by phase differences between the reflections from the

engines and the body.

In Fig. 6 there are a few dominant scattering centers. At the left, the specular reflection from the nose of the aircraft gives a Doppler line of high intensity, in the center the reflections from the front ends of the engines are clearly visible.

The Doppler line corresponding to the right engine in this image is superposed by the Doppler line of the corner between the wing of the aircraft and the body. This can be seen, when Fig. 6 is compared with images for aspect angles some what closer to the nose of the aircraft (not shown here). The Doppler line at the right of Fig. 6 corresponds to the scattering from the tail of the VX-101. The scattering center here is located at the corner between the body and the altitude rudder and at the front edge of the altitude rudder.

The aspect angle window used for Figs. 5 and 6 was 0.6 radians.

3. IMAGING WITH DOPPLER SPECTRA

From the preceding sections we known, that except for a scaling factor the Doppler spectra of the radar echo can be looked at as "projections" of the scattering centers into the direction of observation. If now these "projections" for several aspect angles round the axis of rotation are known, it is possible to reconstruct an image of the scattering centers from the spectra. In order to do this we have to perform reserve projections from the spectra into the direction towards the target, which for the reconstruction is replaced by an image plane. According to their respective direction of observation we put all spectra round the image plane and project the Doppler lines into this plane where, by a computer, we add the intensities of all lines. The images resulting from this procedure show the distribution of the scattering centers, seen in the direction of the axis of rotation.

In Fig. 7 the projection procedure is sketched and Fig. 8 gives the experimental result for an ideal target which consisted of three cylinders, positioned in various distances parallel to the axis of rotation. Because of their symmetry only the axes of the cylinders, seen in the direction of the axis of rotation, are imaged. The location of the axis of rotation in Fig. 8 is indicated by a cross.

The distances of the three cylinders from the axis of rotation were 0.6, 2.1 and 6.3 wavelengths respectively. The locations of the axes of the cylinders in this image are clearly visible by the maxima of intensity. Resolution is in the order of one wavelength. Fig. 8 was made by producing in the image plane a computer plot of 150 x 150 small stars, the magnitude of which was proportional to the intensity of the image. This plot then was reduced in size and inverted photographically in order to get bright spots in the image at the places of high intensity.

For the image of Fig. 8 only the intensity in the Doppler spectra was used. If, instead of a simple spectral analysis of the signal, we use a complex Fourier transform, we are able to make use of the phases of the spectra and thus increase resolution in the image considerably.

In a detailed analysis (GRAF, 1972 and 1975) of the radar return from a rotating target and its Fourier transform, it can be shown, that the phase of a Doppler line corresponding to a given scattering center is proportional to the component in the range direction of the distance of this scattering center from the axis of rotation, the proportionality factors and constants being equal for all aspect angles. It therefore is possible to change the phase in the spectra along the path of projection into the image plane in such a way that the spectral lines from all aspect angles, corresponding to the same scattering center at the location of this scattering center in the image plane have the same phase. The phase change per unit length in the direction of projection for this procedure is the same for all spectra and all spectral lines. So if we perform the reconstruction with the complex spectra, at the location of the scattering centers we have an addition of the amplitudes of the spectral lines, all with the same phase, whereas in the environment of the scattering center the phases are not constant for different aspect angles, so that there in general we have an addition of intensities only.

The use of the phases in the spectra thus gives much sharper maxima at the location of the scattering centers. For a total aspect angle range of 360 degrees e.g. the intensity distribution in the image plane at the location of a point scatterer is given by a Bessel function of zero'th order, the first zeros of which have a distance of 0.2 wavelengths from the maximum, so that resolution now is 0.2 wavelengths. In contrast to the direct Doppler analysis described above, where there existed an optimum aspect angle window, here the approximation of the Bessel function becomes the better, the smaller the individual aspect angle ranges are chosen, in which the Fourier transforms are made. That is, the results are the better the more spectra out of the total aspect angle range are used.

Fig. 9 shows an image of the three scattering centers of Fig. 8, now with higher resolution, due to the use of the phases. This image was made with Doppler spectra out of 32 individual aspect angle windows, into which the total aspect angle of 360 degrees was subdivided. Due to the coarse raster of image points, compared to the width of the maximum of the Bessel function, the shape of the Bessel function cannot be seen in this image. The scattering centers in the experiment were located so, that in the image they coincided with a raster point. This was necessary to avoid very narrow spacing of the raster and thus to shorten computer time.

If the total aspect angle range is less than 360 degrees, the image points of the scattering centers become ellipses with their long axes in the direction of the center of the aspect angle range, the axes becoming the longer, the smaller the total aspect angle range (GRAF 1975, 1972). For a total aspect angle range of 90 degrees for example the length of the axes is approximately 0.25 and 0.9 wavelengths.

If complex targets are imaged, most of the scattering centers are not visible over the entire aspect angle range of 360 degrees, so that resolution for the individual scattering centers depends on their angle of visibility. As on such targets in general there are a lot of scattering centers, the image quality is

further deteriorated due to the superposition of the sidelobes of the images of the scattering centers and due to their motion on the target. The image quality for complex targets, the dimensions of which are only a few wavelengths, therefore is not very good. For large targets however better image quality can be expected.

4. CONCLUSION

While ameliorations are necessary in the details of the imaging process of radar targets with a simple continuous wave radar, the direct evaluation of Doppler spectra of the radar echo from rotating targets already is a comparatively simple and useful tool for the analysis of the scattering behaviour of complicated targets.

5. REFERENCES

GRAF, G., 1972, "Analyse des Dopplerfrequenzspektrums rotierender Körper".
Deutsche Luft- und Raumfahrt, FB 72-46.

GRAF, G., 1975, "On the Evaluation of Doppler Spectra for Radar Cross Section Analysis and Target Recognition".
Proceedings of the NATO Advanced Study Institute on "Atmospheric Effects on Radar Target Identification and Imaging", Sept. 22 - Okt. 3, 1975 at Goslar, FRG.

GRAF, G., 1976, "On the Optimization of the Aspect Angle Windows for the Doppler Analysis of the Radar Return of Rotating Targets".
IEEE, AP-24, Nr. 3, May 1976.

HANSEN, R.C., 1966, "Microwave Scanning Antennas".
Vol. I, Academic Press.

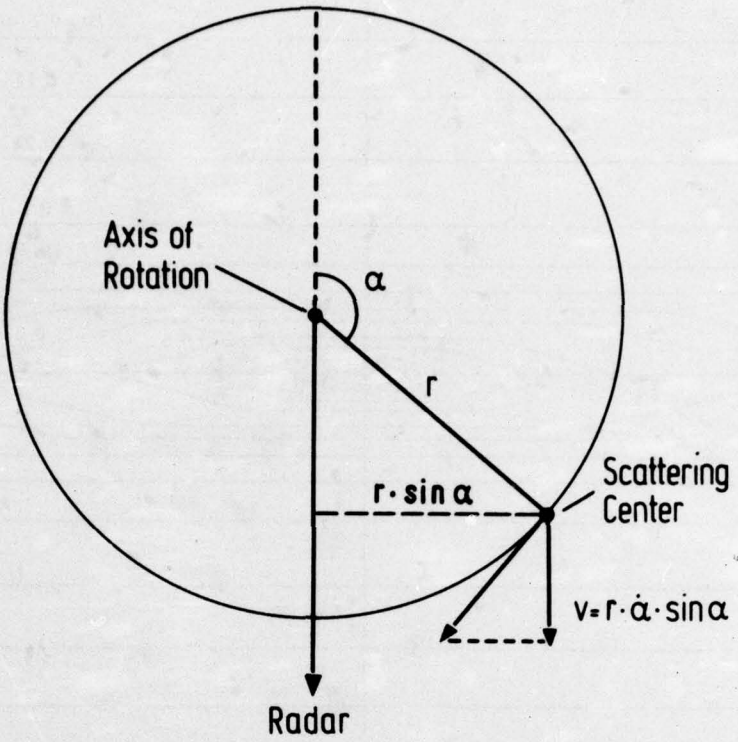

Fig. 1: Geometry of a single scattering center rotating round an axis.

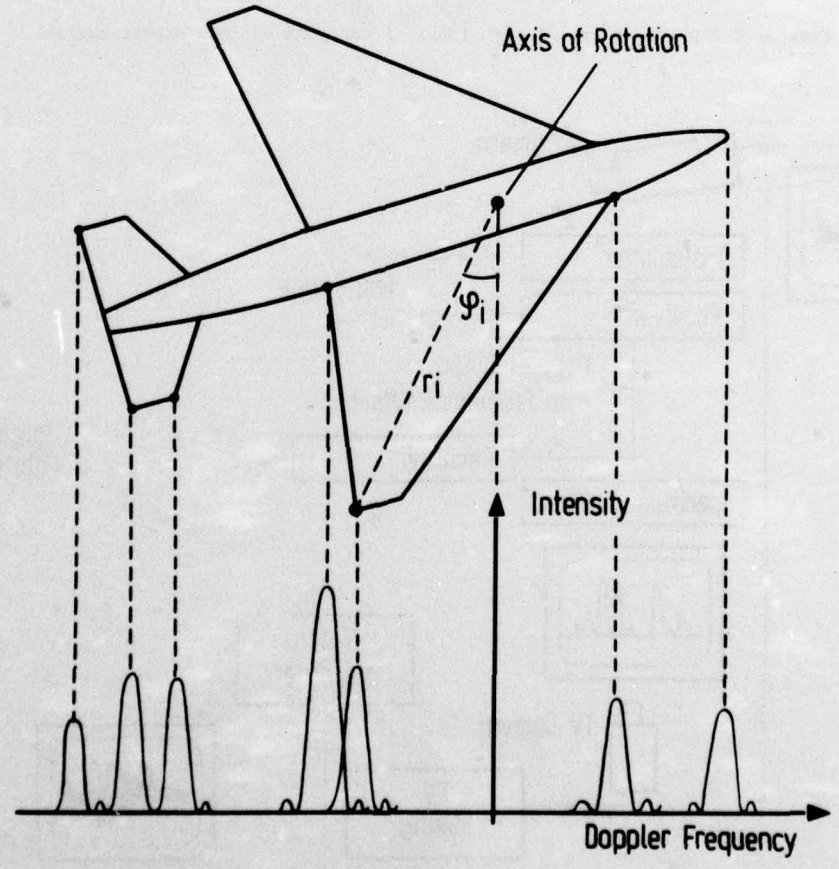

Fig. 2: The relationship between scattering centers on a rotating target and Doppler frequency spectrum.

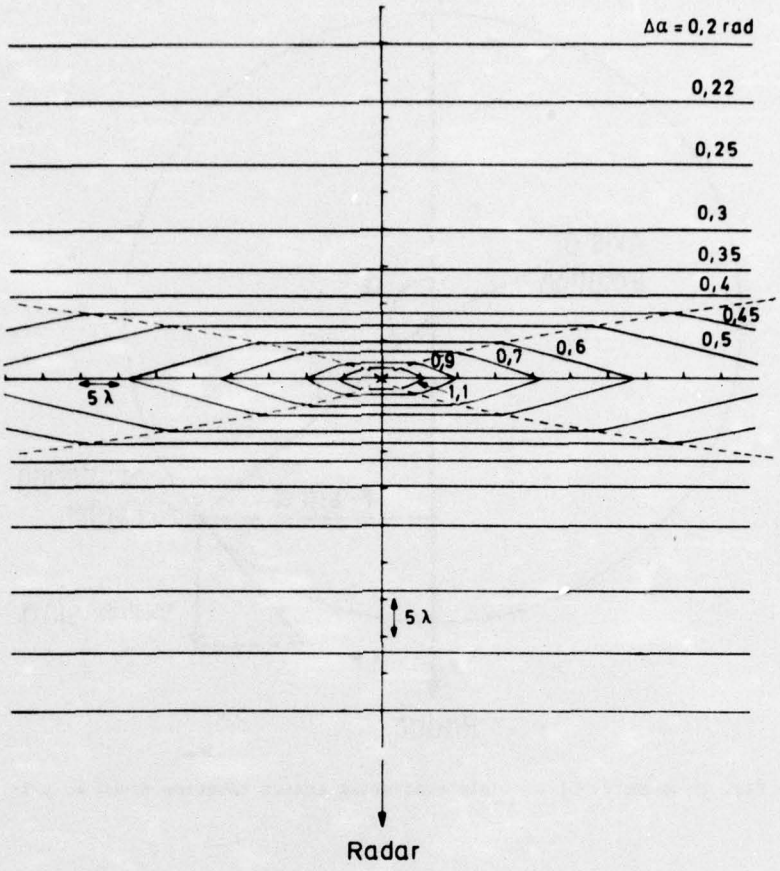

Fig. 3: r-α-plane of Fig. 1 with lines of constant optimum aspect angles.

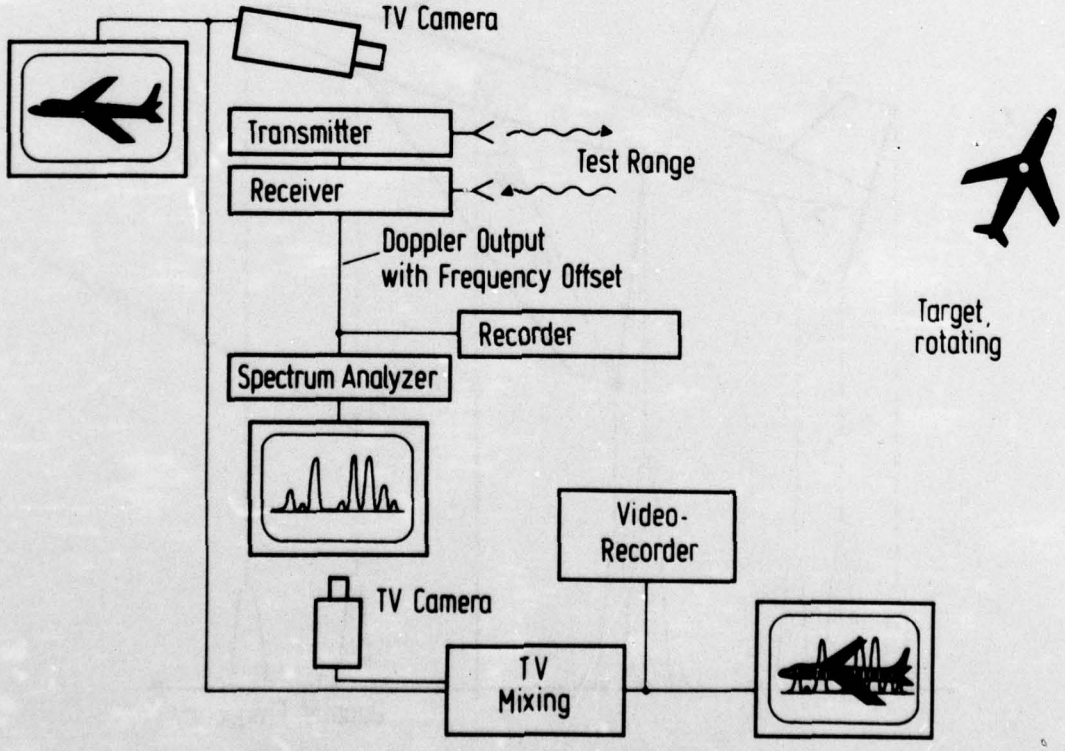

Fig. 4: Block diagram of a radar for on-line evaluation of Doppler spectra.

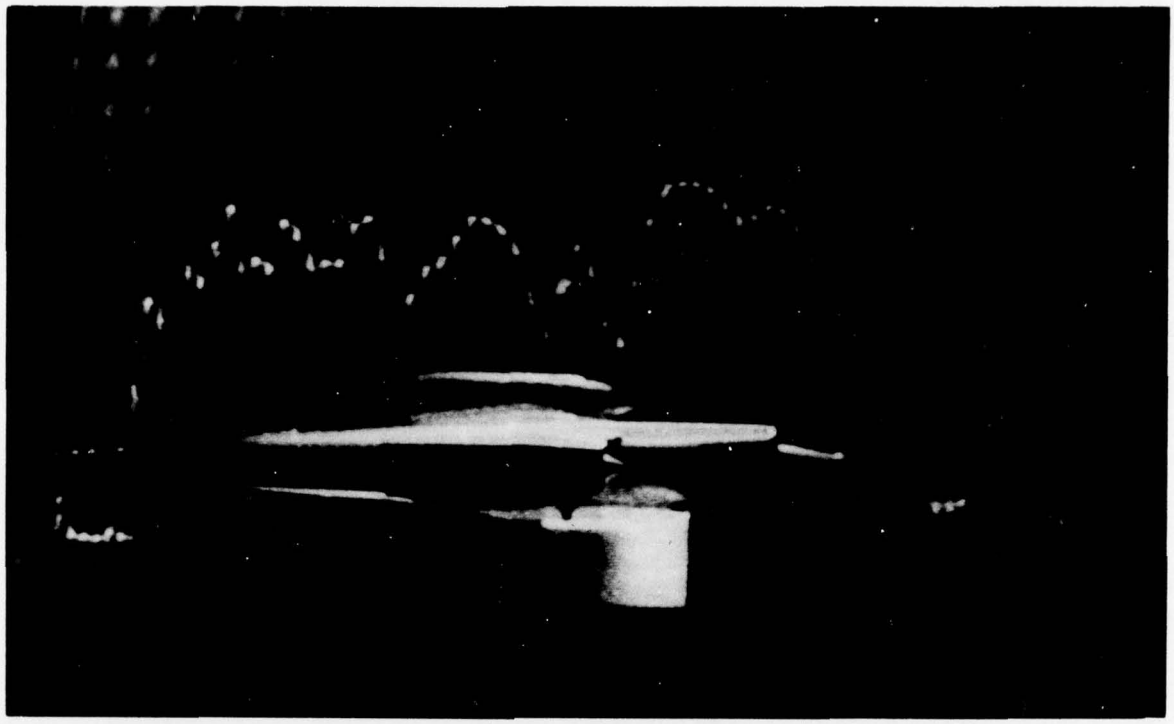

Fig. 5: Model of VX-101 with corresponding Doppler spectrum (side view).

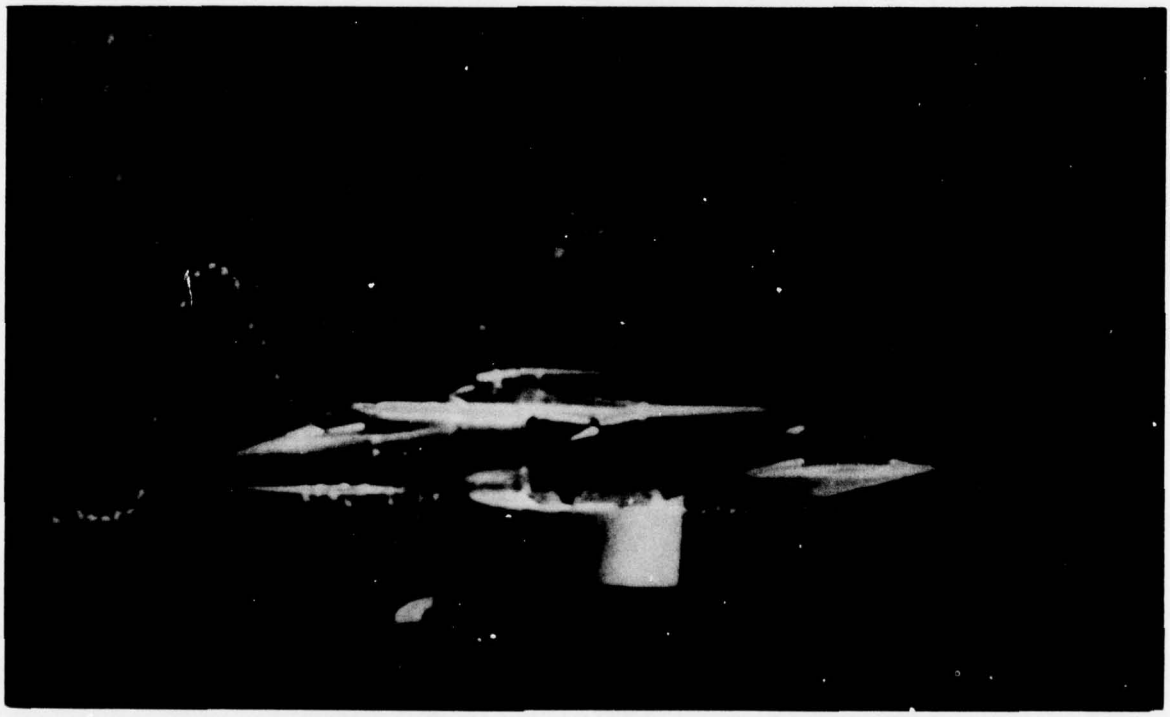

Fig. 6: Model of VX-101 with corresponding Doppler spectrum.

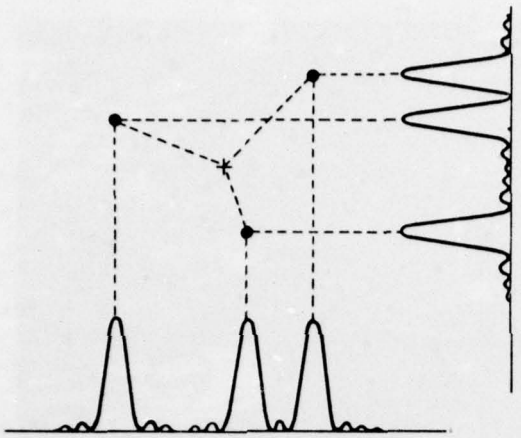

Fig. 7: Sketch of the "projection" process for target imaging from Doppler spectra.

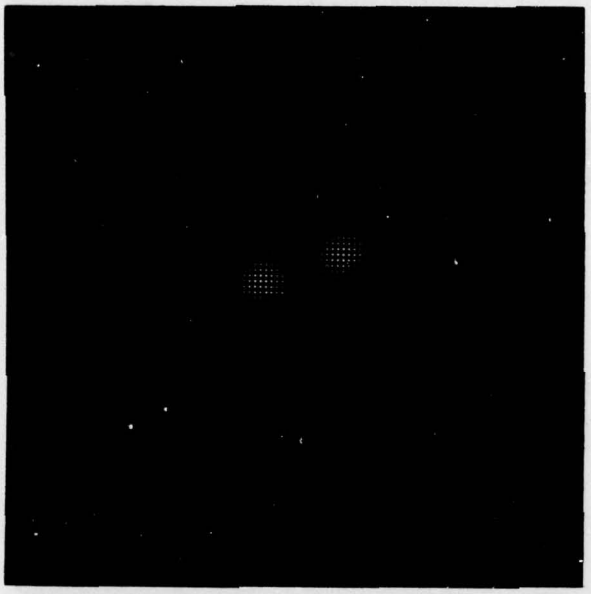

Fig. 8: Microwave image of three cylinders made from Doppler spectra (amplitude only).

Fig. 9: Microwave image of three cylinders made from complex Doppler spectra.

DISCUSSION

R VOLES: I should just like to make a couple of remarks.

Firstly, I always think that it is instructive to consider the doppler cross-range analysis as a generalisation of the synthetic-aperture principle. When the model rotation is large, the substantially parabolic phase-weighting normally used in aperture synthesis has to be properly instrumented as a sinusoidal phase weighting, the phase and amplitude of this phase function being determined by the polar coordinates of the scatterer in question with respect to the centre of rotation. This is effectively the form of the analysis used to derive the last figure in the paper, and it removes the constraints imposed by a limited azimuth window.

Secondly, I should like to comment on the usual situation met in practice when the scatterers are not omni-directional. Doppler analysis of such a scatterer leads to a position-error ellipse having a long major axis parallel to the range direction at the aspect angle when it was seen by the radar. Examination at the other aspect angles will do nothing to reduce the size of this error ellipse. Consequently, for real targets, a high spatial resolution can be guaranteed only by using a radar having a high resolution in range as well as doppler.

G GRAF: The only difference between data evaluation in synthetic aperture systems and in doppler analysis is that the correlation process is replaced by a simple Fourier transform, and the use of the Fourier transform introduces the limitations in aspect angle windows. The uncertainty ellipse mentioned cannot be avoided in the data evaluation according to the principle described unless range resolution is used. This however must not necessarily be a fundamental limitation, maybe that with another form of data evaluation the ellipses can be reduced in size.

H SITTROP: You have described a method by which the location and magnitude of the individual scattering centres of a complicated target can be identified. It should therefore be possible to compute the radar cross section of a complicated target, and indeed to do this in a multi-path environment (such as the sea) taking into account the rms specular reflection coefficient of the sea.

G GRAF: The energy content of each doppler line is proportional to the radar cross-section of the corresponding scattering centre. So, by evaluating the energy content of the doppler lines and by comparing it with the energy in a doppler line measured with a calibration sphere, the radar cross sections of the individual scattering centres on a target can be measured - if wanted as a function of aspect angle. These values can then, of course, be compared with values one would expect theoretically. At the moment however I have no quantitative values for such a comparison.

J SNIEDER: Can the technique described for measuring an aircraft also be applied to measure ships? If so, how can the water surface be simulated?

G GRAF: Yes, the technique is applicable to all types of target. For smooth water the surface could be simulated by a metal plate; rough seas could possibly be simulated by an aluminium foil or in a water tank. As the speed of rotation of the target can be very slow, in some cases it might even be possible to measure full scale targets in the sea.

RADAR A FAISCEAU LATERAL UTILISANT UNE ANTENNE SYNTHETIQUE

J.Genuist
Thomson-CSF
Malakoff, France

RESUME

Le radar à faisceau latéral, à antenne synthétique, permet d'obtenir une image de très grande résolution des terrains survolés par un avion.

La résolution en distance radar, suivant la direction perpendiculaire à la route de l'avion, est obtenue avec une émission-réception à impulsions très fines, réalisée avec la technique de compression d'impulsion.

La résolution longitudinale, suivant la route de l'avion est obtenue par traitement du signal Doppler.

Deux catégories de traitement ont été expérimentées :

- Traitement par simple filtrage qui conduit à une résolution théorique de la forme :

$$\sqrt{\frac{\lambda\, d_o}{2}}$$

λ : Longueur d'onde

d_o : Distance de la cible.

et à la notion d'antenne synthétique non-focalisée.

- Traitement par corrélation qui conduit à une résolution théorique de la forme : $\frac{L}{2}$

L : Dimension de l'aérien.

et à la notion d'antenne synthétique focalisée.

Différents résultats expérimentaux sont présentés pour chacun des procédés en analysant les avantages et inconvénients.

1 - INTRODUCTION

Le radar aéroporté à faisceau latéral à antenne synthétique permet d'obtenir, par tous temps, une carte de définition suffisante pour identifier les détails topographiques naturels ou artificiels de la région survolée, et pour faire apparaître, entre deux vols successifs, les modifications éventuelles de la configuration de la zône surveillée.

La résolution transversale, suivant la distance radar perpendiculaire à la route avion, dépend du spectre émis.

La résolution longitudinale, suivant la route avion, obtenue par traitement du signal Doppler est bien meilleure que la résolution naturelle due au faisceau de l'antenne, définie par :

$$\frac{\lambda}{L} d_o$$

λ : Longueur d'onde

L : Dimension de l'aérien

d_o : Distance de la cible

Différents traitements du signal peuvent être envisagés que l'on peut classer en deux catégories :

- Traitements par filtrage simple du signal qui conduit à une résolution

$$\sqrt{\frac{\lambda\, d_o}{2}}$$

et à la notion d'antenne synthétique non focalisée,

- Traitement par filtre adapté ou par corrélation qui conduit à une résolution

$$\frac{L}{2}$$

indépendante de la distance et à la notion d'antenne synthétique focalisée. La planche 1 donne, pour une dimension d'antenne, les résolutions théoriques comparées pour quelques exemples de distance.

THOMSON-CSF a expérimenté différents types de traitement, mais seuls les résultats obtenus avec le traitement par filtres électriques ou par corrélation optique retiendront notre attention au cours de cette conférence.

Les cartes radar ne figurent pas dans les planches de ce document, elles seront projetées en cours de conférence.

2 - RAPPEL DE LA GEOMETRIE DU SYSTEME

La représentation de la géométrie du radar à faisceau latéral est donnée planche 2. Le faisceau d'antenne est orienté perpendiculairement à la route avion. Pendant la traversée du faisceau, la distance avion-cible varie et passe par un minimum d_o quand la cible est vue par le travers de l'avion.

A cette variation de distance est liée une variation de phase, mise en évidence par l'utilisation d'un radar cohérent qui conserve la référence de la phase de l'onde émise.

En prenant comme origine, l'instant où l'avion passe par le travers de la cible, on peut écrire :

$$d = d_o + \frac{V^2 t^2}{2 d_o}$$

car le déplacement de l'avion est lié à sa vitesse par la relation $X = Vt$.

La phase du signal réfléchi comparée à la phase du signal émis, conservée en mémoire, s'écrit :

$$\phi = \frac{4\pi d}{\lambda} = \frac{4\pi}{\lambda} d_o + \frac{2\pi}{\lambda d_o} V^2 t^2 = \phi_o + kt^2$$

A la variation quadratique de la phase est liée une variation linéaire de la fréquence Doppler définie par la relation :

$$f_d = \frac{1}{2\pi} \frac{d\phi}{dt} = Kt$$

La détection synchrone met en évidence un signal radar de la forme :

$$S_R(t) = S \cos \phi = S \cos (\phi_o + kt^2)$$

La durée de ce signal est limitée au temps de traversée de la cible dans le faisceau :

$$T_o = \frac{2\theta_o d_o}{V}$$

avec $2\theta_o$: ouverture angulaire du faisceau d'antenne.

Les équations précédentes définissent le signal radar d'une cible ponctuelle, en supposant que le système global (radar et traitement) est linéaire, on peut par superposition appliquer les résultats à une cible réelle complexe.

3 - TRAITEMENT PAR FILTRAGE PASSE BAS

Principe

Avec ce type de traitement, seule est conservée la partie du signal contenant les fréquences Doppler très basses (planche 3). Dans ces conditions, la cible n'est visualisée qu'un court instant quand elle se présente par le travers de l'avion.

L'affinage obtenu est limité à une valeur telle que l'enveloppe du signal se réduit à un spectre dont la largeur égale celle du filtre passe bas.

La valeur optimum de la constante de temps du filtre qui donne le meilleur contraste du signal après traitement est égale à :

$$\sqrt{\frac{\lambda d_o}{2\pi V}}$$

Par rapport à la résolution naturelle $\frac{\lambda}{L} d_o$ due à l'ouverture du faisceau d'antenne, le taux d'affinage du traitement par filtre passe bas est :

$$\sqrt{\frac{2\lambda d_o}{L^2}}$$

La largeur de l'écho affiné étant : $\sqrt{\frac{\lambda d_o}{2}}$

Synoptique (Planche 4)

Le radar utilise un émetteur à magnétron dont la durée d'impulsion conduit à une

résolution transversale homogène avec la résolution longitudinale.

La phase du signal émis est mise en mémoire dans un oscillateur cohérent FI, synchronisé par l'impulsion magnétron après transposition en FI.

Après détection cohérente, les signaux reçus sont inscrits dans un banc de filtres permettant de traiter autant de signaux S_R (t) qu'il y a de quanta de distance à obtenir pour la résolution transversale recherchée dans le domaine de terrain à visualiser.

A chaque récurrence radar, un commutateur adresse, successivement dans le temps, les signaux vers le filtre correspondant au quantum de distance à traiter.

Après filtrage, un commutateur de lecture permet d'envoyer la "vidéo affinée" vers un système de représentation constitué d'un indicateur et d'un système photographique associé.

Résultats

Présentation de quelques cartes radar.

4 - TRAITEMENT PAR CORRELATION OPTIQUE

Principe

Le signal S_R (t) est inscrit en transparence sur un film. On a pris soin de superposer à S_R (t) une composante moyenne S_o telle que l'on puisse inscrire S_R (t) avec son signe (planche 5).

Cette inscription obtenue au moyen d'un tube cathodique devant lequel se déplace un film à vitesse constante transforme la fonction temporelle S_R (t) en fonction spatiale S_R (X) avec X = Vt (au facteur d'échelle près).

Plaçons ce film sur le chemin optique d'une onde plane (Planche 6).

Si $E_o \cos \omega t$ est le champ incident tombant sur le film, le champ transmis aura une répartition suivant X telle que :

$$S(X) = \frac{E_o}{2}\left[1 + \cos\left[k_1 X^2 + \phi_o\right]\right] \cos \omega t$$

ω : est la pulsation de la lumière incidente $\left[\omega = 2\pi f_L = \frac{2\pi c}{\lambda_L}\right]$

k_1 est égal à :

$$\frac{2\pi}{\lambda d_o}$$

La fonction S (X) est équivalente à trois ondes :

- Une onde plane α : $\frac{E_o}{2} \cos \omega t$
- Une onde sphérique convergente, de centre 02, β : $\frac{E_o}{4} \cos\left[\omega t + k_1 X^2 + \phi_o\right]$

- Une onde sphérique divergente, de centre 01, γ : $\frac{E_o}{4} \cos \left[\omega t - k_1 X^2 - \phi_o\right]$

Le facteur d'échelle μ étant connu, on trouve alors pour 00_1 et 00_2 la valeur commune :

$$F = 00_1 = 00_2 = \mu^2 \frac{\lambda}{\lambda_L} \frac{d_o}{2}$$

La décomposition optique ainsi obtenue est liée à l'axe de symétrie de la fonction S_R (X) inscrite, donc à la position du film le long de X.
Une fente très fine F fixe, placée en 02, recevra un flux lumineux important.

Un film de sortie placé derrière cette fente inscrira un signal comprimé quand l'axe de symétrie de la fonction passera par la fente F.

Pour obtenir une représentation conforme des échos enregistrés, il suffit de faire défiler le film de sortie en synchronisme avec le film sur lequel la fonction S_R (X) est inscrite.

Ce signal comprimé a une dimension égale à la dimension de l'antenne portée par l'avion au facteur d'échelle μ près.

La fonction ainsi obtenue est la fonction de corrélation de S_R (X) [planche 7] .

Pour obtenir une bonne dynamique, il faut éliminer la composante divergente parasite (onde γ). Ceci est réalisé en ajoutant une porteuse au signal Doppler enregistré.
Comme on le montre planche 8, cette porteuse confère au système en effet prismatique et permet ainsi de recueillir la composante utile (onde β) derrière une fente disposée en dehors des faisceaux des ondes parasites.

Tous les résultats précédents peuvent se retrouver en utilisant les phénomènes de diffraction qui font appel aux transformations de FOURIER.

Synoptique (planche 9)

Pour obtenir une résolution transversale homogène à la résolution longitudinale, le radar utilise une émission-réception d'impulsion très fine avec la technique de compression d'impulsions.

Après détection cohérente, les signaux Doppler sont envoyés à un système d'enregistrement photographique comprenant :

- un indicateur, équipé d'un tube cathodique flying-spot, modulé en lumière et balayé suivant une seule dimension : en distance radar,
- un objectif,
- une caméra qui fait défiler un film dans le plan image de la face avant de l'indicateur, perpendiculairement à la trace et à une vitesse proportionnelle à celle de l'avion.

La qualité du traitement par corrélation nécessite que la loi Doppler des signaux enregistrés soit aussi proche que possible de la loi de référence cos $(\phi_o + kt^2)$.

Cette loi idéale est obtenue en considérant que l'avion porteur, décrit une trajectoire rectiligne horizontale d'un mouvement uniforme.

Tout écart par rapport à cette trajectoire idéale, introduit sur les signaux reçus des variations de phase parasites qui doivent être compensées en réception. Ceci est réalisé en effectuant, sur l'onde de référence du détecteur cohérent, des corrections de phase proportionnelles aux écarts de l'avion par rapport à la trajectoire idéale.

Le film des informations Doppler, enregistré en vol, est développé au sol, puis analysé dans le corrélateur optique.

Le film de sortie du corrélateur donne la carte radar exploitable.

Des photographies des différents éléments du radar sont présentées au cours de la conférence.

Résultats

Présentation de quelques cartes radar.

CONCLUSION

Les expérimentations effectuées avec l'affinage par filtre ou par corrélation ont permis de s'approcher des limites théoriques des résolutions.

D'autres types de traitement ont également été essayés mais présentent des inconvénients divers, tels que l'affinage par spot et le filtre adapté associé à une mise en mémoire des informations Doppler sur un tube à mémoire.

Grâce aux progrès technologiques, d'autres orientations sont désormais possibles, comme la corrélation électronique numérique qui permet l'obtention des cartes radar en vol, pratiquement en temps réel.

Nous terminons en remerciant le Service Technique des Télécommunications de l'Air qui a financé ces différentes études et autorisé cette présentation de résultats.

Nous remercions également le Centre d'Essais en Vol de Brétigny qui a réalisé l'expérimentation de nos matériels.

LARGEUR THEORIQUE DES ECHOS EN ROUTE AVION

DISTANCE RADAR d_o	SANS TRAITEMENT $\frac{\lambda}{L} d_o$	AVEC TRAITEMENT	
		FILTRAGE $\sqrt{\frac{\lambda d_o}{2}}$	CORRELATION $\frac{L}{2}$
1 km	35 m	4 m	0,5 m
5 km	175 m	9 m	0,5 m
10 km	350 m	13 m	0,5 m

L = Longueur antenne = 1 mètre

λ = Longueur d'onde = 3,3 cm

PLANCHE 1

EFFET DOPPLER

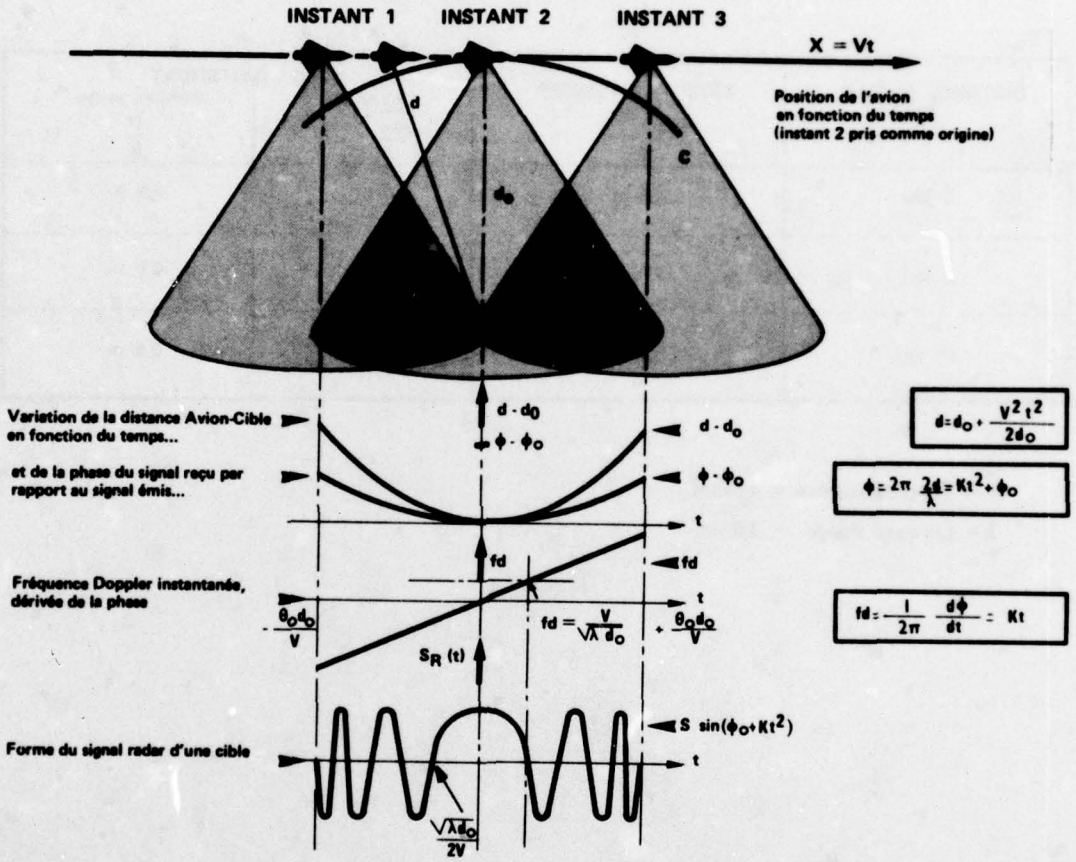

PLANCHE 2

AFFINAGE PAR FILTRE

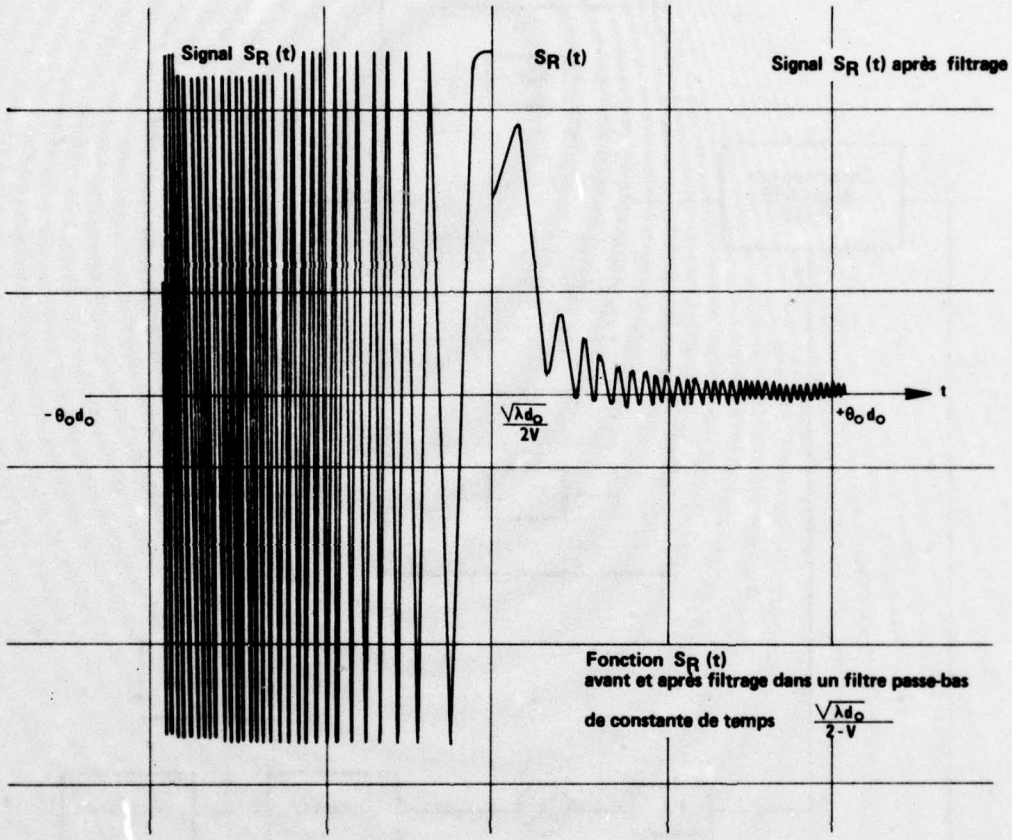

PLANCHE 3

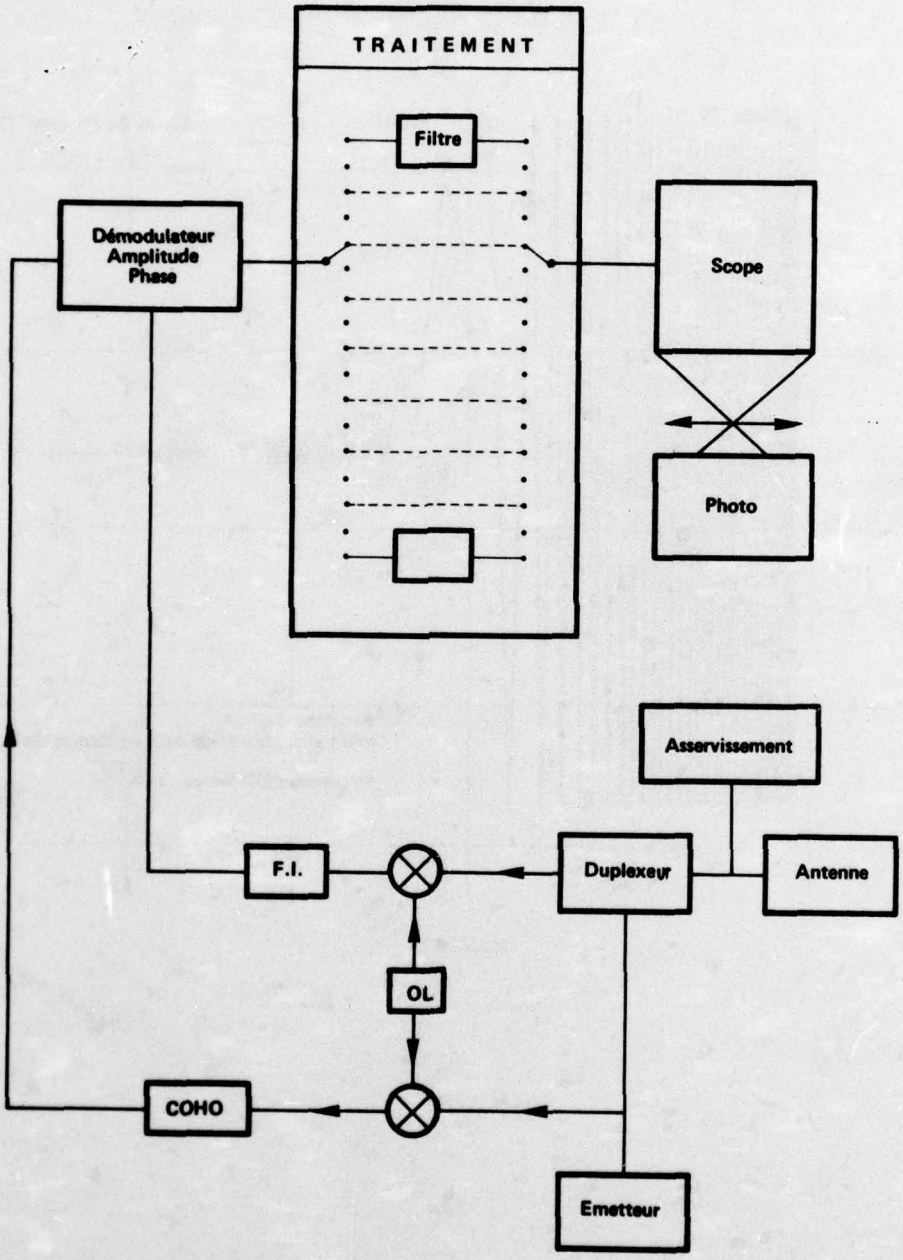
TRAITEMENT
Filtre
Démodulateur
Amplitude
Phase
Scope
Photo
Asservissement
F.I.
Duplexeur
Antenne
OL
COHO
Emetteur

PLANCHE 4

INFORMATION BRUTE INSCRITE A BORD DE L'AVION

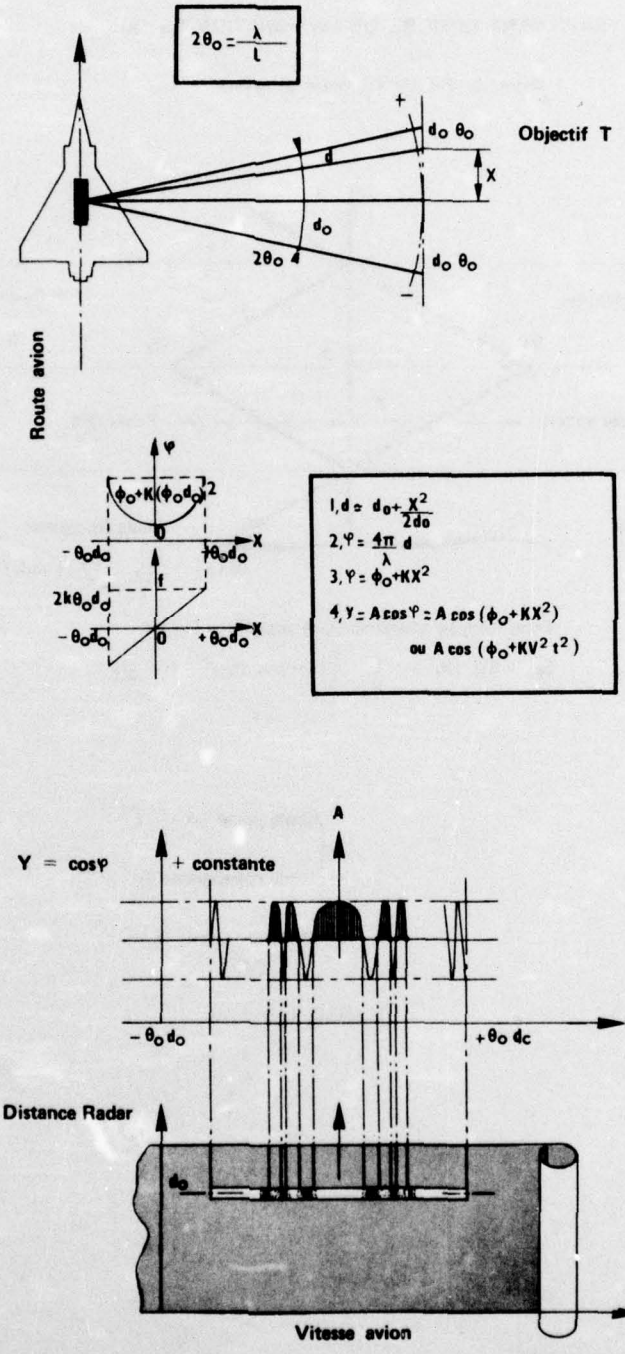

PLANCHE 5

TRAITEMENT OPTIQUE DE LA FONCTION S_R (X)

Point de vue de l'optique géométrique

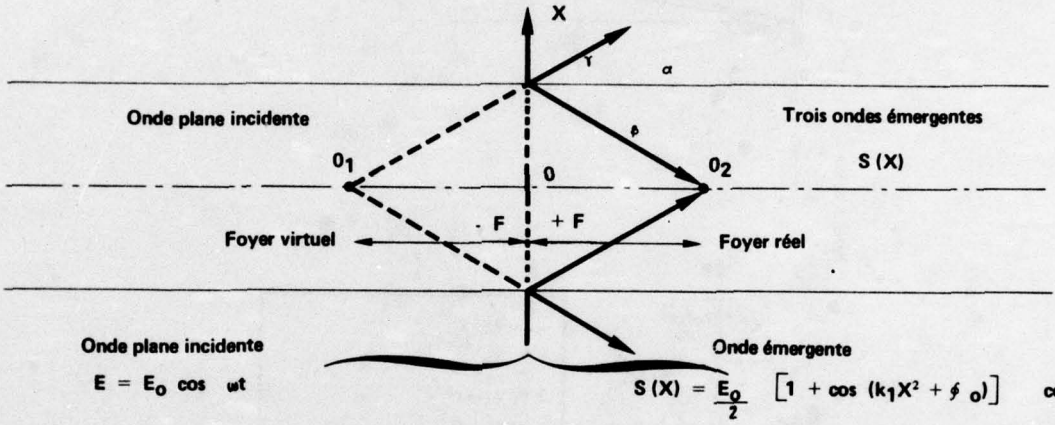

Echo Doppler inscrit en transparence sur le film

$$S_0 + S_R(X) = \frac{1}{2} \left[1 + \cos (k_1 X^2 + \phi_0)\right]$$

Distance focale : $F = \mu^2 \frac{\lambda}{\lambda_L} \frac{d_0}{2}$

$$S(X) \begin{cases} \text{Onde plane } \alpha : & \frac{E_0}{2} \cos \omega t \\ \text{Onde convergente } \beta : & \frac{E_0}{4} \cos (\omega t + KX^2 + \Phi_0) \\ \text{Onde divergente } \gamma : & \frac{E_0}{4} \cos (\omega t - KX^2 - \Phi_0) \end{cases}$$

PLANCHE 6

SIGNAL COMPRIME S_{RC} APRES TRAITEMENT OPTIQUE

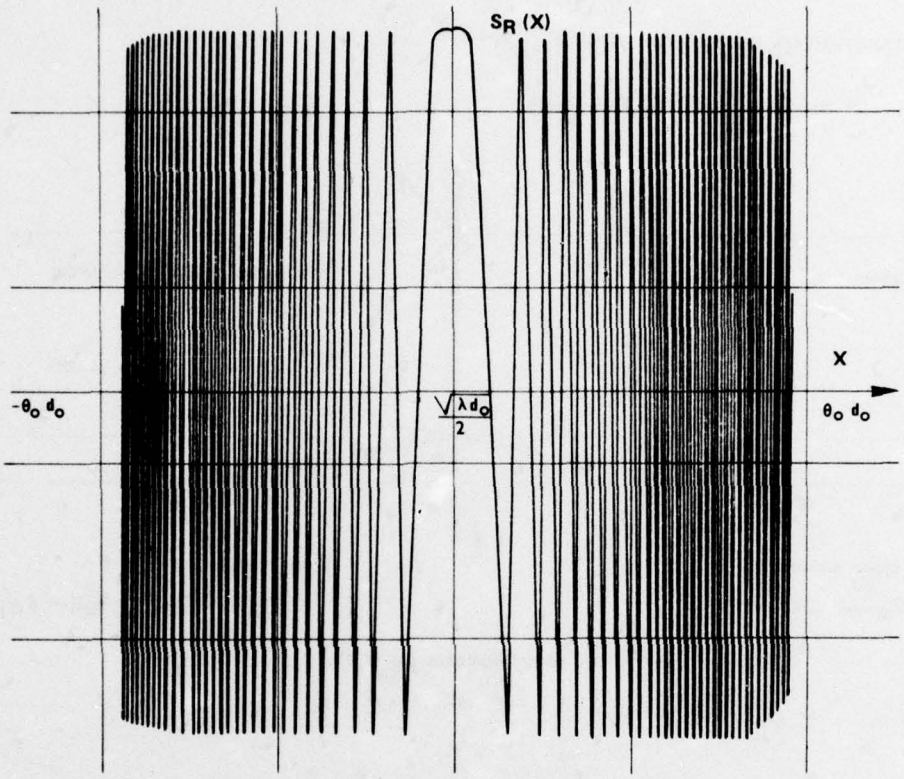

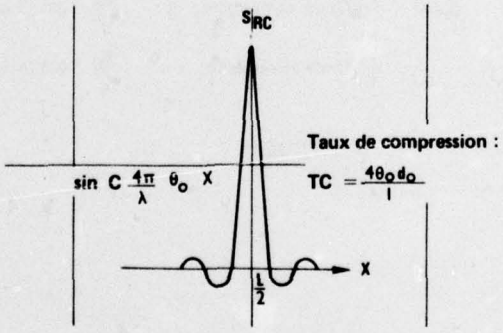

PLANCHE 7

-TRAITEMENT DE LA FONCTION $S_R(X)$

-INTRODUCTION D'UNE PORTEUSE

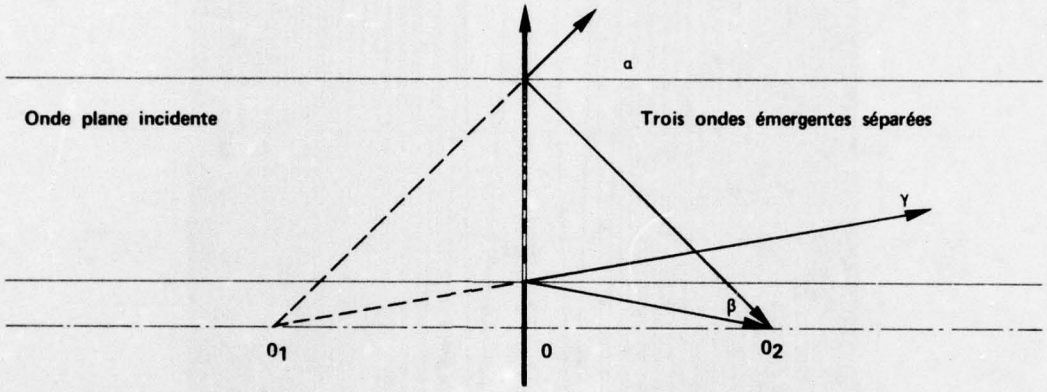

Onde plane incidente

$E = E_o \cos \omega t$

Onde émergente

$\frac{E_o}{2}\left[1 + \cos (k_1 X^2 + k_2 X + \phi_0)\right] \cos \omega t$

Echo Doppler inscrit en transparence sur le film

$$S_o + S_R(X) = \frac{1}{2}\left[1 + \cos (k_1 X^2 + k_2 X + \phi_0)\right]$$

Distance focale $F = \mu^2 \frac{\lambda}{\lambda_L} \frac{d_o}{2}$

$$S(X) \begin{cases} \text{Onde plane } \alpha & : \frac{E_o}{2} \cos \omega t \\ \text{Onde convergente } \beta & : \frac{E_o}{4} \cos (\omega t + k_1 X^2 + k_2 X + \phi_0) \\ \text{Onde divergente } \gamma & : \frac{E_o}{4} \cos (\omega t - k_1 X^2 - k_2 X - \phi_0) \end{cases}$$

PLANCHE 8

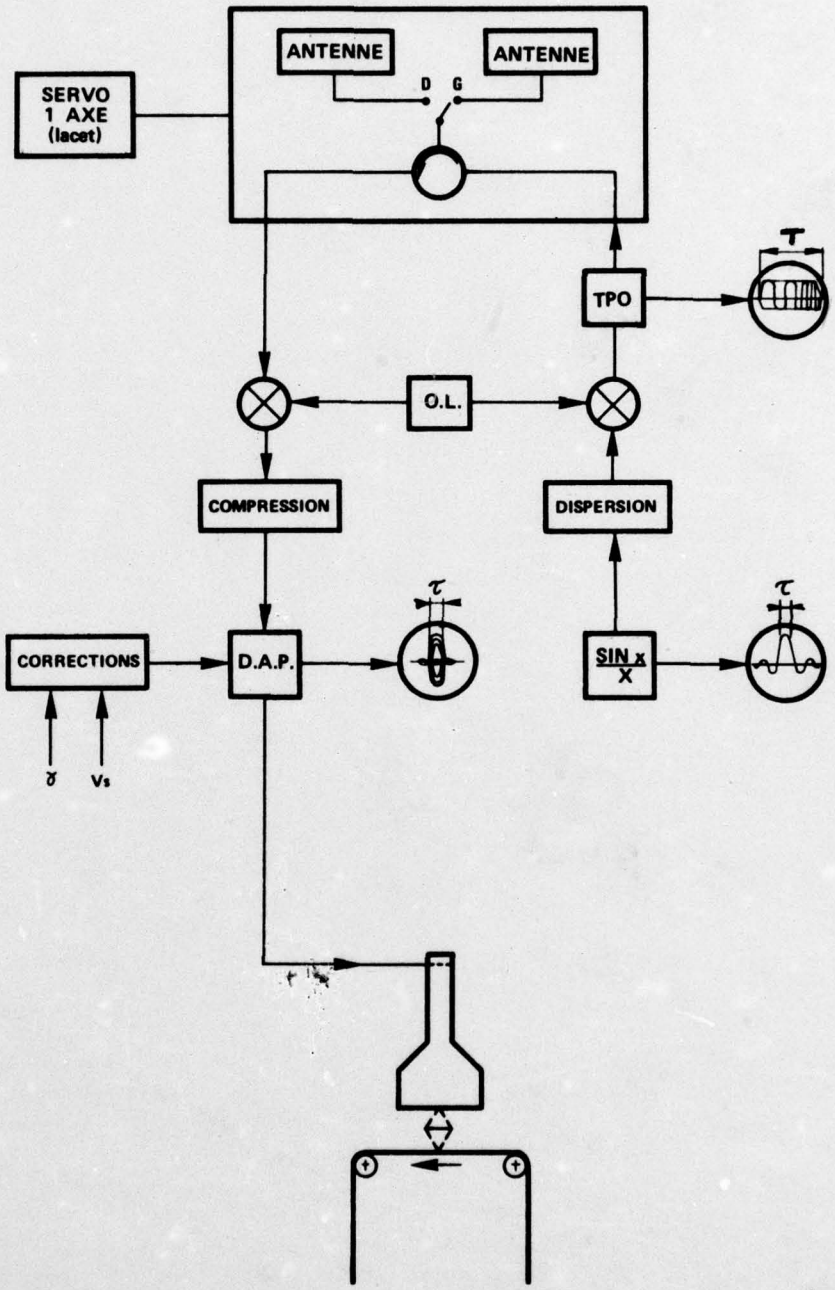
ANTENNE
ANTENNE
D
G
SERVO
1 AXE
(lacet)
T
TPO
O.L.
COMPRESSION
DISPERSION
τ
τ
CORRECTIONS
D.A.P.
SIN x
X
γ
Vs

PLANCHE 9

RADAR TRACK EXTRACTION SYSTEMS

A L C Quigley
J E Holmes
R J Tunnicliffe

The authors are with:

Admiralty Surface Weapons Establishment
Portsdown, Cosham
Portsmouth, England

SUMMARY

This paper describes the main constituents of a largely automatic radar track-while-scan system. It is shown to contain a plot extractor, clutter map, stationary plot filter and automatic tracking software. The system is designed to operate in high false alarm conditions without formation of false tracks.

The clutter map is used to select the optimum video for processes by the plot extractor, which is of fairly conventional design using cell-averaging CFAR and single level quantisation. The plot extractor output has the majority of land clutter removed by the stationary plot filter and remaining plots are used in the formation and updating of tracks.

The track updating algorithms are based on adaptive Kalman filters with various arithmetic simplifications for efficient computer processing. The automatic track initiation adapts to suit observed local false alarm conditions in order to hold false track generation at an acceptable level.

1. INTRODUCTION

1.1 Modern radar data handling systems are required to provide accurate tracks on all air targets within the surveyed space. The data processing system has to examine the radar data in order to identify returns from genuine targets as early as possible whilst rejecting all false responses. In the past, all of the data processing was manual, being carried out using P.P.Is, men and grease pencils. However, this had limitations due to operator fatigue, easy operator saturation and problems where fast response is required. As a consequence there has been a widespread interest in automating the track extraction function. There have been no major problems in benign (ie clutter free) environments, but these systems have foundered in conditions of clutter or interference, due to the generation of false tracks and the resulting system saturation.

1.2 The obvious solution to the clutter problem is to use moving target indication (MTI), but this introduces a processing loss where it is used unnecessarily, and some operating conditions can obviate its use altogether. As a result, it is appropriate to use a clutter sensing device to switch in the MTI only where it is needed. The resulting optimised video is then fed into a plot extractor whose function is to identify those groups of returns having the characteristics of target returns (Fig 1). The plot extractor uses a more or less conventional cell-averaging constant false alarm rate (CFAR) processor followed by integration of single level quantised video. Although more sophisticated processors are available, none of them offer ideal performance, and the subsequent processing has to be tolerant of this non-ideal behaviour. As a result, simplicity is opted for.

1.3 The data from the plot extractor is fed to a stationary plot filter, whose function, as the name suggests, is to remove returns from stationary sources - that is, land clutter. Such a filter is necessary since it is an efficient way of removing the bulk of radar detections and thus prevents the rest of the processing chain from being saturated. Any plots which are not cancelled by the stationary plot filter are fed on to the autotracking software. Any plots which are not recognised as belonging to known tracks are available for the formation of new tracks and are also used to create new entries in the stationary plot filter. This arrangement introduces the need for feedback from tracking to stationary plot filtering, but it represents the best way of preventing the filter from cancelling returns from tracks which slow down (eg helicopters) or from tracks which are always moving relatively slowly (eg ships).

The tracking subsystem itself breaks down into several stages - plot to track association, track updating, and track initiation.

1.4 Plot to track association is the process of comparing the incoming plots with known tracks and deciding on the correct pairings. Once a pairing is made, the appropriate track can be updated, using the new plot information to refine the track estimates of position and velocity. The track updating process has to smooth out the effects of measurement inaccuracies whilst at the same time having a good response to manoeuvres. Various tracking algorithms were studied, principally variations of the Kalman filter and $\alpha\beta$ filter. For the particular application, an $\alpha\beta$ filter was used although with certain other types or mixes of radars, a Kalman filter would have been more appropriate.

1.5 Any plots which remain after the above processes are treated as possible new tracks. Such plots are used to form tentative tracks for which the probability of track validity is continually computed, the tracks eventually being either confirmed as genuine or erased as false on the basis of the computed probability of validity. The probability is computed as a function of its previous value for that track and the local detection and track environment. In this way, tracks which are formed in clear areas are confirmed quickly whereas tracks formed in confused areas are confirmed slowly - if at all. In this way any imperfections in the earlier constant false alarm processing are allowed for by a process which attempts to maintain a constant false alarm rate at the track level.

1.6 The main constituents of the data processing system are discussed in more detail in the following sections of this paper.

At this point it must be made clear that it does not normally pay to try to optimise any one of the processes in isolation. For example, a superb track updating process is of limited value if it is overloaded by handling rubbish from a poor plot-to-track association or track initiation algorithm. Similarly, since no radar false alarm control is ever going to be perfect, processes such as those described are clearly necessary. The fact that they have to be implemented gives some clues as to how much it is worth spending on the radar false alarm control.

2. PLOT EXTRACTION

2.1 The first radar data processing step shown on Fig 1 is plot extraction. The plot extractor analyses the optimised stream of radar video and identifies those groups of returns having target-like characteristics. In doing this the plot extractor is required to reject all other returns, namely noise, clutter and interference. The main elements are shown in Fig 2.

2.2 Given the presence of the environment map with its action of switching the MTI in over cluttered regions, one might expect the plot extractor to be extremely simple. This would appear to follow from the dual action of the environment map's sensing of clutter conditions for:

(a) switching the MTI in over clutter, and

(b) controlling the plot extractor threshold as an area MTI function when (a) is not permitted.

However, in a real world there are inevitably residues from clutter and interference, and any false alarms arising from these residues could cause saturation of the data processing system. In such conditions, genuine returns are lost in a sea of spuria and may therefore be missed. Thus a balance has to be struck between missing detections and suffering false alarms. This introduces the requirement for a constant False Alarm Rate (CFAR) processor as the first element of the plot extractor. Various CFAR processor designs are available (eg Gregers Hansen, V, 1973 and Trunk, G V, 1974). None of the devices available is perfect and for the reasons indicated in the introduction, the simplest CFAR (the background averager) was selected. Fig 3 shows the principles of the background averager. It works by taking samples of the background (in range) with respect to any radar cell and subtracts this from the current video signal. In this way, one in effect has a threshold which floats on top of the observed background thereby holding a reasonably constant false alarm rate against changes in noise level or clutter. As mentioned earlier, this device is imperfect in that it will not hold a constant false alarm rate under all conditions. However, no other CFAR is perfect and thus some later processing is required to allow for this in any case, meaning that simplicity is appropriate here.

2.3 Somewhat similar remarks can be applied to the processing following the CFAR. All plot extractors do some form of video integration, matched to the characteristics of the radar beam. This can vary from a beam shape recognition technique, a two-pole filter whose characteristic output matches beam shape (Cantrell, B H, 1973) to the well known m/n detector (Swerling, P, 1952). Since beam shape recognition has problems with fluctuating targets and because of the insensitivity of single level quantised systems (such as m/n) to spiky interference, an m/n detector was originally selected.

2.4 The m/n detector was selected in preference to other single level quantised detectors because of a requirement to store one beamwidth of video 'hits' in order to investigate detection for fast targets, ie where there is significant motion during the beam dwell time. In a development system, the intention is to use a staircase integration of the form described by Marcoz and Galati, 1972. Analysis shows this technique to be slightly more efficient than m/n (both in performance and hardware), whilst retaining the insensitivity of single level quantisation to spikes and corrupted beam shapes. Fig 4 shows a possible transition diagram for such a detector, optimised for a radar having 8 pulses/beamwidth.

3. TRACK UPDATING

3.1 The track updating algorithm is needed to smooth the incoming plot data in order to give accurate, reliable estimates of track position, speed and heading. The smoothing process has traditionally been based upon the well known $\alpha\beta$ equations (Fig 5). Typically, the equations are applied independently in the co-ordinates used. When straight tracks are considered, α and β can be controlled to give least squares smoothing (Marks, B L, 1961 and Simpson, H R, 1962) using the following equations:

$$\alpha = \frac{2(2n-1)}{n(n+1)} \quad , \quad \beta = \frac{6}{n(n+1)} \quad , \text{ n being the plot number.}$$

This is satisfactory for straight tracks, but since smoothing gets heavier with time (α and β get smaller), manoeuvre response deteriorates with time. Hence some modifications are needed to give adequate manoeuvre following characteristics. Various manoeuvre handling methods may be developed and it is convenient to derive these from adaptation of a Kalman filter.

The Kalman filter equations may be summarised in words as follows:

find forecast position and velocity of track;
find its uncertainty;
use uncertainty of forecast and measurement to calculate filter gain;
find smoothed position and velocity;
find uncertainty in smoothed position and velocity.

It is notable that the $\alpha\beta$ equations represent a degenerate Kalman filter. Indeed, the sequence of gains (ie values of α and β) from the least squares $\alpha\beta$ filter are identical to those from a Kalman filter for constant accuracy and constant data rate with tracking in a single co-ordinate (Quigley, A L C, 1971, 1972,

1975). The Kalman filter has advantages in that it is general, ie it does not assume constant accuracy, data rate etc and it allows for the kind of measurement to vary (eg a conventional and a doppler radar both providing measurements to a track). However, this generality of the Kalman filter comes at a price - it has a high computer load compared with the αβ filter. Thus the generality of the Kalman filter makes it a useful tool for developing the manoeuvre response mechanism, this being followed by a study of ways of reducing the computer burden.

3.2 Adapting a Kalman Filter

Perhaps the most straightforward way of producing a Kalman filter for tracking is to assume that targets basically travel in straight lines but are subject to random accelerations which slowly die away. This approach has been followed by Singer, 1970. Although this filter sets out to fairly accurately represent the real situation, it tends to offer insufficient smoothing when used with conventional surveillance radars.

An alternative is to assume that targets undergo random accelerations, but that these accelerations are normally minimal. As far as the filter is concerned, the effect of these manoeuvres is to degrade the accuracy of track forecasts. Since the accuracy of forecasts is used by the filter to control filter gain, it is seen that control of the term which describes the effects of manoeuvre errors will in turn cause the filter to adapt its response. In particular, the filter gain may be shown to be of the form:

$$\text{gain} = \frac{\text{uncertainty of forecast}}{\text{uncertainty of forecast} + \text{uncertainty of measurement}}$$

If the forecast uncertainty is increased (to allow for a manoeuvre), the filter gain is driven towards unity, ie α and β rise towards 1, thereby relaxing the damping and improving manoeuvre response. One way of operating the filter is to continually monitor the track quality in terms of observed error between measured and forecast positions, and use this to control the manoeuvre error term in such a way as to maximise the observed quality. A simplification to this is to assume zero manoeuvre and continually monitor the tracking error, declaring the track to have turned when the error is significant. Whilst the track is deemed to be turning, the manoeuvre error term is applied, meaning that damping is relaxed in a controlled way, and damping is applied as heavily as justifiable in the absence of manoeuvres.

In tests, there was no significant difference between the results of the three methods. It has to be stressed, however, that this was for surveillance radars - the result might not be the same for high data rate tracker radars. The next stage in development is then to find a suitable adaptation of the algorithm for efficient implementation in a computer. The standard approach is based upon the reduced Kalman filter, in which all unnecessary terms and calculations are eliminated. This can be tricky in terms of selecting the appropriate co-ordinate system to use and requires careful programming to avoid some computational problems.

3.3 Approximation by αβ Filter

An alternative is to modify the αβ equations to have the same effect (Quigley, A L C, and Holmes, J E, 1975).

It can be shown (Quigley, A L C, 1971) that the variance of forecast position for a track which has received n-1 measurements and is just about to receive the n-th measurement is given by σ_f^2:

$\sigma_f^2 = \frac{2(2n-1)}{(n-1)(n-2)}r$, r being measurement variance.

Consideration of the Kalman filter (Quigley, A L C, 1971) shows that:

$\alpha = \frac{\sigma_f^2}{\sigma_f^2 + r}$, and that position variance just after inclusion of the n-th measurement is given by αr.

Thus for a track of constant data rate and constant measurement accuracy, the position variance lies between:

$\frac{2(2n-1)}{n(n+1)}r$ and $\frac{2(2n-1)}{(n-1)(n-2)}r$

The variation of track variance with time is shown on Fig 6.

In terms of the discussion on adapting a Kalman filter, let the variance associated with manoeuvre errors be 'q'. Thus, in the absence of manoeuvre:

$\sigma_f^2 = \frac{2(2n-1)}{(n-1)(n-2)}r$, but where manoeuvres are detected,

$\sigma_f^2 = \frac{2(2n-1)}{(n-1)(n-2)}r + q$

Since $\alpha = \frac{\sigma_f^2}{\sigma_f^2 + r}$, and since σ_f^2 is increased on detection of manoeuvre, it is clear that α is increased when manoeuvres are detected.

Given that the forecast variance is a function of n, r and q, it is possible to modify n in such a way that the new value gives the same value for σ_f^2 without the use of q. If this modified value of n is called m:

$$\text{Let } F = \frac{2(2n-1)}{(n-1)(n-2)}r + q$$

$$\text{and } F = \frac{2(2m-1)}{(m-1)(m-2)}r$$

Thus, although the track is based on n measurements, the effect of the manoeuvre is that the track accuracy has degraded to that for a track based on only m measurements. Hence the value of m is used to overwrite n (Fig 6).

The foregoing assumed that the manoeuvre had been detected, which is based upon observing unexpectedly large error between measured and forecast track position. The error observed on each track update can be smoothed by a simple equation, and the result compared with a threshold value selected to give an appropriate false response rate. The derivation of the final algorithm is straightforward though tedious (Quigley, A L C, and Holmes, J E, 1975) and the result is shown in Figs 7, 8 and 9.

3.4 Choice of Co-ordinate System

The foregoing has so far not mentioned the optimum co-ordinate system to use. Clearly, the manoeuvre detector must use radar (ie polar) co-ordinates. Also, it is clear that a typical surveillance radar will have a manoeuvre response (in terms of control of n) which is dominated by this polar nature. This suggests that tracking should be in polars with separate values of n for range and azimuth. However, this representation is incorrect for straight tracks. On the other hand, the above response is difficult to apply in a fixed or track orientated Cartesian system. Note that the polar nature of radar measurement errors is generally far more significant than track orientated manoeuvre capabilities, particularly against military targets as seen by 2-D radars. The way out of this dilemma is to use sensor orientated Cartesian co-ordinates. In this way, two n counts are run, one for along sight and one for cross sight, corresponding to range and bearing respectively. The co-ordinate system is shown in Figs 10 and 11.

3.5 Maximum Value of n

The maximum value to allow n to take is shown (Quigley, A L C, and Holmes, J E, 1975) to be calculable on the same basis as manoeuvre response, but using a value of q related to roughness of flight. The analysis yields:

$$n_{max} = 2\tfrac{1}{2} + \tfrac{1}{2}\sqrt{1 + \frac{16}{q}}$$

3.6 Handling Missed Looks (Fades)

By analogy with the manoeuvre handling, it is possible to compute the effect on n when observations are missed. This is shown graphically in Fig 12. Since the nature of the resulting algorithm is fairly complex, the end result is best tabulated as in Fig 13. The table in this figure must be used with care. If the 'old value of n' relates to the m-th observation, which was actually a missed look, the 'effect on n' shows what to add to m for use in the selection of α and β for the (m+1)th observation. For example, consider Fig 12. The 7th observation was missed (m=7). At the 8th look, the value of n to use is, from the table, 7-1 = 6. Thus the value of n to use when the 8th measurement is made is 6. Thus the track will have actually received 7 measurements (on looks 1-6 and 8), but the tracking proceeds as if only 6 had been received.

Further applications of the same theory may be used to handle variations in measurement accuracy, but it is felt that under these conditions a reduced Kalman filter may be a better solution.

3.7 Plot to Track Association

The process of correlating new radar detections with existing tracks can be seen to consist of two main steps. The first step is to produce a list of all possible plot and track pairings together with the probability of correctness of each pairing (Quigley, A L C, 1971, 1972). This is then followed by a selection of the best overall set of associations (Magowan, S, 1965), a process called ambiguity resolution. The detailed formulae involved in the calculations are quite complex and are as such unattractive for use in a real time system.

One technique for load reduction is to minimise the number of unnecessary attempts at association. To do this, a prefilter such as the stationary plot filter is useful (see Section 5). The residual detections are then checked for association with known system tracks, using association gates which make no allowance for manoeuvre - which means that gates are small enough to make ambiguity resolution unnecessary. Plots which are still left unassociated are tested against any remaining tracks, this time allowing for manoeuvres. Because of the relatively large size of this association gate, ambiguity resolution might be required, but this would only normally happen with manoeuvering tracks which are near each other. The expressions used for calculating association probability are also simplified, the extreme being to reduce them to the formulae used in track manoeuvre detection.

3.8 Track Seduction

One final point regarding manoeuvre gate sizes is worth mention. Clearly, such a gate has terms in t^4. If the local false alarm rate is high and if there is a series of fades, the gate can expand to such a size that it is practically certain that spuria will be detected in the gate. Under these conditions, track seduction is likely. One solution is to reduce the association gate to such a size that the probability of track seduction is held to an acceptable level.

The probability of track seduction can be shown to be:

$$P_S = (1 - P_D)\{1 - (1 - P_{FA})^N\}$$

where N = no of cells in association gate
P_{FA} = false alarm probability in gate
P_D = track detection probability
P_s = probability of track seduction

If P_s is too high, the area of the association gate, A, can be reduced by δA to give a modified P_s':

$$P_s' = (1-P_D)\ \{1-(1-P_{FA})^{\frac{N\ (A-\delta A)}{A}}\}$$

The operation of this control is linked to the automatic track initiation logic (next section) in that it depends upon the monitoring of the local detection environment.

4. TRACK INITIATION

4.1 Requirements of the Initiation Process

In operational systems excellence in the plot-to-track association and track updating processes may be of no significance if the system is saturated with spurious tracks or if the formation of tracks on threat targets is not timely. Saturation can be avoided by manual track initiation methods but at the expense of a fast system response particularly when each man deals with more than just a few tracks. Thus the requirement of a good auto-initiation process is to achieve an optimum balance between its ability to speedily initiate tracks and its generation of false tracks. Since measurement conditions can vary significantly with position and time the optimum scheme must be adaptive. Without the ability to adapt its parameters the initiation process cannot remain optimum under all conditions or even those of a single, fast track.

4.2 Description of Existing Methods

On successive radar scans the plots which remain after failing to associate with existing tracks can be used to form new tracks. Two such plots from different scans will be used to form a tentative track. This track is then confirmed as genuine or is deleted as further plots do or do not associate with it.

The transition matrix approach uses a matrix definition of the possible paths between the various states in which a tentative track may exist (a Markov process, as illustrated in Fig 4). Starting from an initial state the track may progress to the final state (track confirmation) or return to the initial state (Driessen, H B and Hunt, E W Le M, 1971).

This scheme is non-adaptive due to the defined paths within the transition matrix and there exists no obvious method of synthesising the optimum matrix for a given set of conditions.

An alternative approach is to use a consistency counter scheme. Target detections cause increments to be added to the track consistency while non-detections cause decrements to be removed from it (Turner, R D and Marder, S, 1972). When the counter reaches an upper or lower limit the track is confirmed or deleted as appropriate. Whilst this type of scheme generally uses fixed parameters and is thereby non-adaptive a variation of the scheme to be outlined here can be implemented as such a counter scheme but with adaptive step sizes.

4.3 The Proposed Method

The proposed method is based on probability theory using Bayes theorem for manipulation of conditional probability terms. The conditional probability of validity of each tentative track is determined from the observed measurement sequence and the observed local detection environment for each track. By using the a priori value for the ratio of valid and invalid track probabilities and the probabilities of successful measurements on such tracks the a posteriori value for the ratio of valid and invalid track probabilities can be found. The rule to be used is based on Bayes theorem (Fig 14) and is derived from it in a simple manner (Fig 15). The a posteriori value after one scan is used as the a priori value for the next scan. The measurement attempt made on that scan is then used to update the a priori value to give a new a posteriori value.

If the measurement on the j-th scan has been made and is to be used to update data from the i-th scan (where $j = i+1$) and $P\{VT|M\}$ after scan i is denoted by P_i then:

$$\frac{P_j}{1-P_j} = \frac{P_i}{1-P_i} \cdot \left.\frac{P\{M|VT\}}{P\{M|\overline{VT}\}}\right|_{\text{scan } j}$$

This relation is obtained from our single scan updating rule and from the knowledge that a track is either valid or invalid only; hence $P\{VT\} + P\{\overline{VT}\} = P\{VT|M\} + P\{\overline{VT}|M\} = 1$.

By the simple expedient of taking logarithms the variable step consistency counter scheme can be derived:

$$R_j = R_i + \alpha_j$$

$$\text{or } R_j = R_i - \beta_j$$

where $R_i = \log[P_i/(1-P_i)]$

and $\alpha_i = \log\left[P\{M|VT\}/P\{M|\overline{VT}\}\big|_{\text{scan } i}\right]$

$\beta_i = \log\left[P\{\overline{M}|\overline{VT}\}/P\{\overline{M}|VT\}\big|_{\text{scan } i}\right]$

The increment α is used in the case of a successful measurement and β is the decrement for an unsuccessful measurement.

Prior to track formation or updating attempts occurring in any given area some value for the likely probability of validity of any track formed from target detections within that area can be postulated. Such factors as false target detection rate, true target detection rate, expectancy of target(s) based on data from other sensors or flight plan information, stationary plot filter efficiency or rate of leakage of false target detections to the track formation logic can all influence the a priori value of valid track probability

Change of track status to a confirmed level or deletion occurs if R_j reaches suitable upper or lower limits based on the acceptable false alarm rate for the track promotion logic or the likely deletion of a true track respectively. If the probability of track validity is required to reach say 0.999 for track promotion then the upper limit to be used for R_j is about 3 (using base 10 logarithms). Similarly, if the lower limit of probability used for track deletion is 0.001 then the lower limit for R_j is about -3. The symmetry of this scheme is illustrated in Fig 16. The false alarm rates thus set are constant false alarm rates and enable the logic to operate under any conditions with known and acceptable performance.

4.4 Illustration of the Advantages of the Proposed Method

As an illustration of the advantages of the adaptive logic a simulation has been made comparing this logic with a simple logic requiring four detections on four consecutive target scans. The logics have comparable false alarm rates at a clutter density of about 0.2 hits/km^2. The target is closing radially at about Mach 3 against a background of uniformly distributed clutter. The graph of Fig 17 illustrates the behaviour of the range at which a 50% probability of track confirmation exists. It shows the clearly advantageous gain in track confirmation range for the adaptive logic. The fixed parameter logic (4/4) is unable to adapt to the changing detection and clutter conditions with the consequence of only a small change in the track confirmation range over the clutter density range concerned. The real change that is taking place is in the logic's false alarm rate which becomes unnecessarily low at low clutter densities. The penalty of this is non-optimum performance.

5. STATIONARY PLOT FILTERING

5.1 One of the most common sources of false alarm from the plot extractor is land clutter. In an automated data processing system such returns may be damaging in two ways:-

(a) the number of such detections may be large, leading to computer overload;

(b) spurious tracks may be formed, thus reducing confidence in the system's track extraction capability.

The stationary plot filter is used to eliminate the majority of such false detections.

5.2 The basic principles of the stationary plot filter are exceedingly simple. Data on all tracks which appear to be stationary (ie correlate from scan to scan) are stored in the filter and each incoming plot is compared with this data. If the new detection falls within a defined capture area around one of the filter entries, the plot is deemed to be clutter and is cancelled. If, however, there is no correlation, the plot is passed on to the tracking process for comparison with known system tracks. If there is an association the appropriate track is updated. In the absence of an association it is concluded that:

(a) the plot is from a moving object not yet being tracked;

(b) the plot is a detection from a new piece of clutter;

(c) the plot is otherwise spurious.

The system action is to create a new entry in the stationary plot filter (SPF). If the detection is from a stationary object, the tentative moving track will die due to lack of supporting data, which is being removed in the SPF by the newly created entry. Periodically, the SPF contents are examined and entries which have not been updated recently are removed.

5.3 The parameters which control the removal of old entries, ie the effective memory length, merit consideration in more detail. The memory is controlled by a consistency counter, which is incremented by γ every time the filter entry is updated and decremented by δ (usually one) each time no association is made. When a new entry is created, the counter is set to an initial value, usually equal to γ. The maximum value of the counter (M) limits the time an entry which is not being updated can remain in the filter, as entries are cancelled when the counter reaches zero.

Clearly, clutter points with high detection probabilities are likely to have entries in the SPF and are therefore likely to be cancelled, ie the probability of observing them at the SPF output is low. Equally, clutter points with low detection probabilities are not likely to have SPF entries, but by virtue of their low detection probabilities are unlikely to be seen at the input and hence also at the output of the SPF. From the foregoing, it is expected that there will be some value of the detection probability for which there exists a maximum value of probability of presence at the output of the SPF. Fig 18 shows a set of curves which relate the detection probability at the input and output of the SPF for various parameter settings. Note that the expected maximum is clearly visible and that it is a function of the memory parameters. It is also clear that the output detection probability can never exceed the input detection probability.

In the case where the input to the SPF consists solely of detections from land clutter, the longer the memory length, the greater the rejection efficiency of the process. However, if other forms of clutter (or interference) are considered, the situation is somewhat different. Each spurious entry in the filter has associated with it a capture area, which effectively blanks out part of the radar cover, as seen by the tracking process. The SPF relies for its viability on inter-clutter visibility and so the number of spurious entries in the filter store needs to be minimised in order to maximise the area where detections of moving tracks can be made. The values of the parameter γ and to some extent the maximum value of the counter (M)

require to be a compromise between cancellation of real returns with low values of detection probability and limitation of the time which spurious entries remain in the filter memory.

5.4 The other SPF parameter which needs to be considered is the size of the capture area around each filter entry. This area would normally need to be several times the radar measurement standard deviation (to allow for radar measurement errors), but is likely to be less than the radar resolution capability (Quigley, A L C, 1973). The size of the capture area clearly dictates the minimum speed that a target requires to evade capture by the filter and hence allow automatic initiation to occur. The capture area, therefore, requires to be a compromise between filter efficiency and a reasonable escape velocity.

Using minimum escape speeds of up to a few hundred knots, this system allows automatic initiation on fast tracks, where it is most needed, whilst allowing manual initiation on slower moving tracks. This is achieved simply by removing the appropriate filter entry, which ensures that subsequent detections are output to the tracking process.

5.5 Experimental measurements have been obtained from an area of land clutter, using two radars with pulse lengths of 2 μsec and 50 nsec respectively. The optimum (standard) value for each of the parameters was determined empirically and each was then varied in turn while keeping the others constant. The smoothing factor relates to the constant value of α in the position only tracking filter used to update the positions of the stationary plots. The standard values used are tabulated in Fig 19.

The results are summarised in Figs 20-25, where the capture areas are shown in terms of range bins and beamwidths. It can be seen that the results obtained are similar for both the radars and that there is an optimum size of captive area around 8 range bins by 1.5 beamwidths, which gives a filter rejection efficiency in excess of 95%. In the case of the shorter pulse length radar, this represents a minimum escape speed for radial tracks of 32 knots and for the longer pulse length of 320 knots. Increasing the memory parameters (ie gamma and the initial and maximum values of the consistency counter) over the standard values shown in Fig 19 appears to have little effect on either the efficiency or the total number of stationary plots held in the store. The value of the smoothing factor (α) also has little effect, the optimum value being approximately 0.5.

It should be emphasised that this data was obtained from a land-based site, and the process has yet to be validated for shipborne use, where the characteristics of the observed land clutter may well be different.

6. CONCLUSIONS

This paper has described an automatic track extraction system which recognises the realities of typical radar operating conditions (clutter, interference), meaning that the track extraction has to operate in varying false alarm rate conditions. In order to accommodate these variations, several stages of false alarm control are introduced, culminating in false alarm control at the track level by means of adaptive track initiation logic.

The existence of these stages makes it clear that none of the system elements may necessarily be optimised in isolation - for example, the fact that no plot extractor CFAR is going to be perfect gives rise to the need to allow for the imperfections in the subsequent processes, meaning that there must be an optimum CFAR to aim for, given the existence of the other processes. It follows from the above that any new major radar development must include the data processing as part of the radar. This is needed to avoid mismatching the quality of the system elements which could lead to either a shortfall in system performance or the wasting of resources in striving for performance in system elements where it is not really needed.

REFERENCES

CANTRELL, B H and TRUNK, G V, 1973, "Angular Accuracy of a Scanning Radar Employing a Two-Pole Filter", IEE Trans AES-9 Vol 5, September 1973.

DRIESSEN, H B and HUNT E W Le M, 1971, "An Analytic Evaluation of Track Initiation Logics", SHAPE Tech Memo STC TM 303.

GREGERS HANSEN, V, 1973, "Constant False Alarm Rate Processing in Search Radars", Conference on Radar, Present and Future, IEE Conference Publication No 105.

JAZWINSKI, A H, 1969, "Adaptive Filtering", Automatica Vol 5 pp475-485.

MAGOWAN, S, 1965, "A Method of Plot to Track Correlation", RRE Memo 2153.

MARCOZ, F and GALATI, G, 1972, "A Suboptimal Detection Technique: The Accumulator Detector", Alta Frequenza, Feb 1972.

MARKS, B L, 1961, "Adjustment Rules for Automatic Tracking", RAE Tech Note Math 79.

QUIGLEY, A L C, 1971, "A Theory for Simple Associations During Target Tracking", ASWE TR-71-11.

QUIGLEY, A L C, 1971, "The Estimation of Forecasting Errors for Least Squares αβ Trackers", ASWE TR-71-21.

QUIGLEY, A L C, 1972, "Tracking Study: An Introduction to the Use of Kalman Filters", ASWE TR-72-14.

QUIGLEY, A L C, 1972, "A Theory for Complex Associations", ASWE TR-72-13.

QUIGLEY, A L C, 1973, "Tracking and Associated Problems", Conference on Radar, Present and Future, IEE Conference Publication No 105.

QUIGLEY, A L C and HOLMES, J E, 1975, "The Development of Algorithms for the Formation and Updating of Tracks", ASWE Working Paper WP-XBC-7512.

SIMPSON, H R, 1962, "A Method of Processing Radar Plot Data to Obtain Position, Velocity and Turn Information", RRE Memo 1924.

SINGER, R A, 1970, "Estimating Optimal Tracking Performance for Manned Manoeuvering Targets", IEEE Trans AES-6 Vol 4, July 1970.

SWERLING, P, 1952, "The Double Threshold Method of Detection" Rand Comp Report RM-1008.

TRUNK, G V, CANTRELL, B H and QUEEN, F D, 1974, "Modified Generalized Sign Test Processor for 2-D Radar", IEEE Trans AES-10 Vol 5, September 1974.

TURNER, R D and MARDER, S, 1972, "The Track Establishment Process in a Mixed False Alarm Rate Environment", Institute for Defense Analysis Paper F-728.

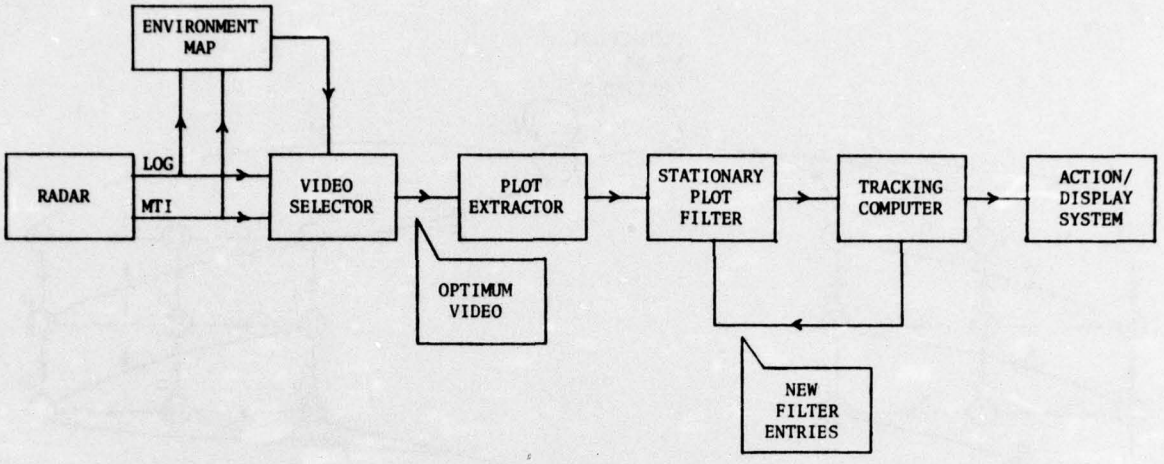

Fig.1 Overall processing arrangement

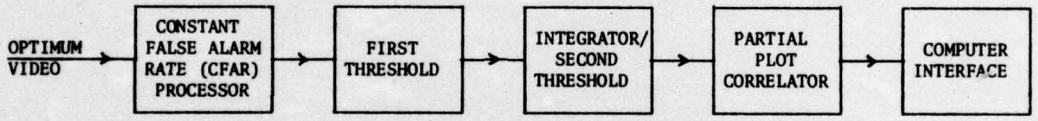

Fig.2 Main elements of plot extractor

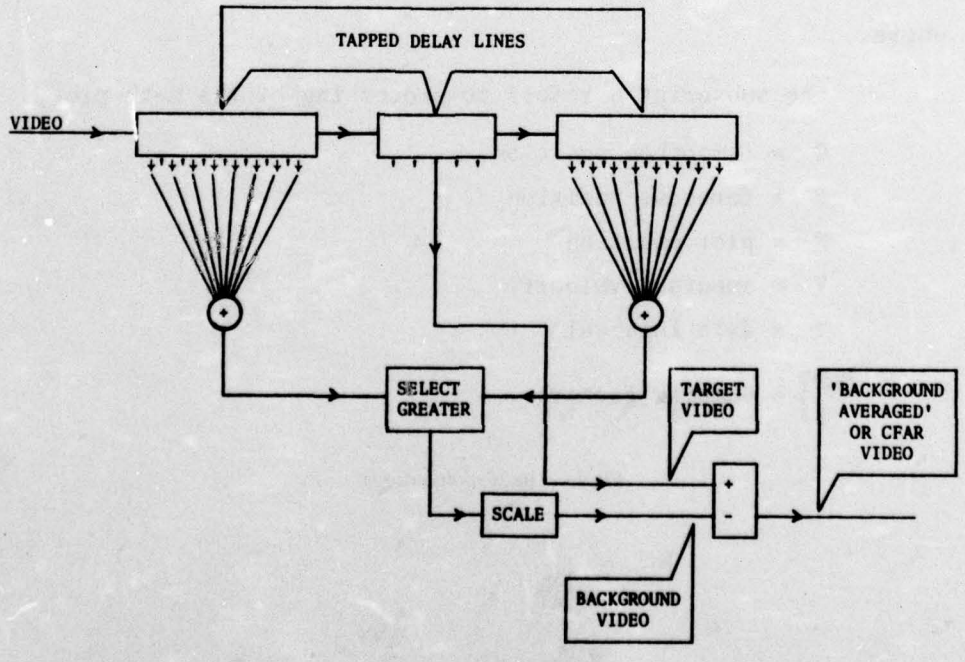

Fig.3 CFAR processor principles

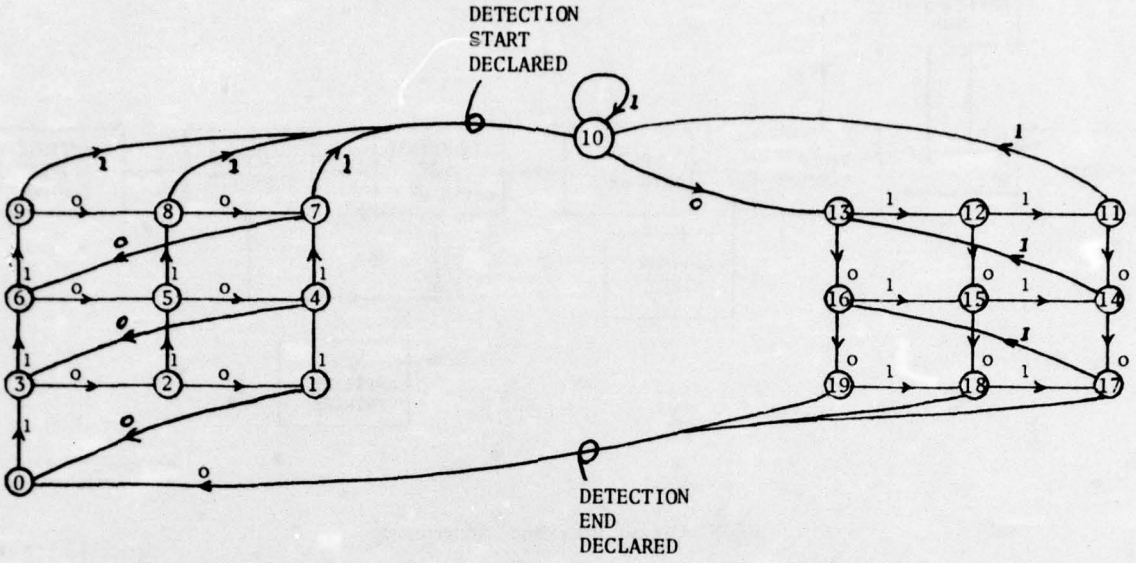

Fig.4 Transition diagram for optimum staircase integrator, 8 pulses/beamwidth

$$G_n = F_n + \alpha(P_n - F_n)$$

$$V_n = V_{n-1} + \frac{\beta}{T}(P_n - F_n)$$

$$F_{n+1} = G_n + V_n \cdot T$$

where,

the subscript n refers to processing of the n-th plot,

G = smoothed position

F = forecast position

P = plot position

V = smoothed velocity

T = data interval

$\left.\begin{matrix}\alpha \\ \beta\end{matrix}\right\}$ = damping factors

Fig.5 The α–β equations

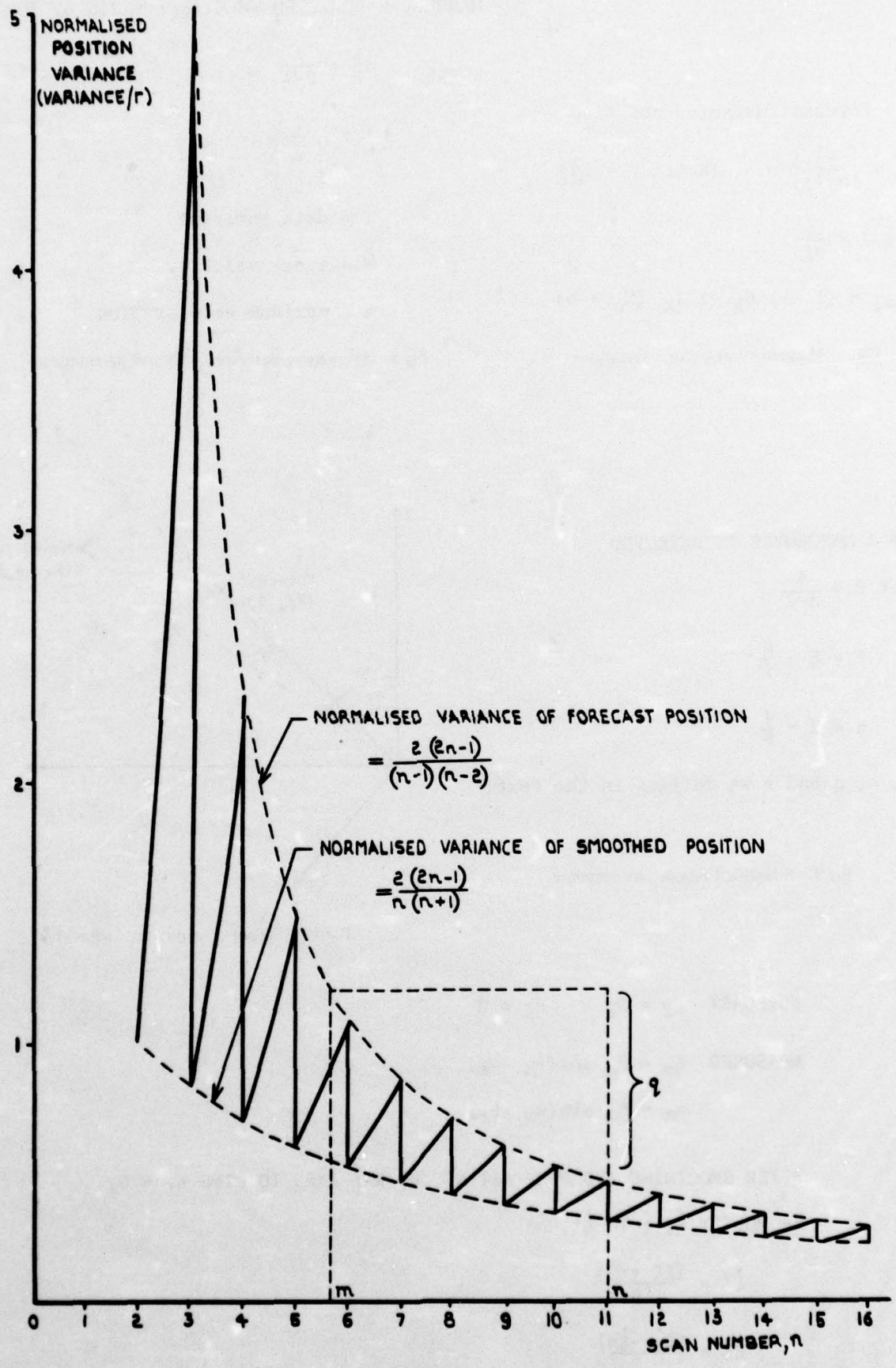

Fig.6 Manoeuvre processing

δ = forecast-measured position

$\sigma_\delta \simeq \left(\frac{n+\frac{1}{2}}{n-1\frac{1}{2}}\right)\sigma_M$ (Note: $r = \sigma_M^2$)

Let $J = \frac{\delta}{\sigma_\delta}$

$E_{K+1} = (1-\lambda)\, E_K + \lambda\, J_K \quad (E_o = o)$

Fig.7 Manoeuvre detector: integrator

MANOEUVRE DETECTED WHEN $|E_k| > 2.5$ or $3 \times \sigma_E$,

WHERE $\sigma_E^2 = \frac{\lambda}{2-\lambda}$

$\lambda \simeq \frac{T}{\frac{V}{a} + \frac{T}{2}}$

T = data interval

V = track velocity

a = maximum acceleration

Fig.8 Manoeuvre detector: test and parameters

IF A MANOEUVRE IS DETECTED

Let $E = \frac{4}{n-2}$

$F = E + \frac{q}{r}$

$m = 2 + \frac{4}{F}$

m, n, q and r as defined in the text.

Fig.9 Simplified manoeuvre response

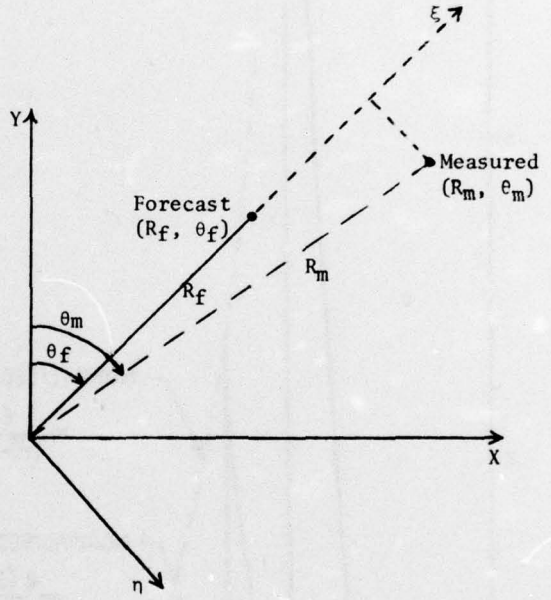

Fig.10 Sensor co-ordinates: geometry

FORECAST $\xi_f = R_f \qquad \eta_f = 0$

MEASURED $\xi_m = R_m \cos(\theta_m - \theta_f)$

$\eta_m = R_m \sin(\theta_m - \theta_f)$

AFTER SMOOTHING AND FORECASTING, ROTATE AXES TO GIVE $\eta_f = 0$,

ie MODIFY $\dot{\xi}$, $\dot{\eta}$ TO $\dot{\xi}'$, $\dot{\eta}'$

$\dot{\xi}' = \frac{(\xi\dot{\xi} + \eta\dot{\eta})}{R}$

$\dot{\eta}' = \frac{(\xi\dot{\eta} - \dot{\xi}\eta)}{R}$

Fig.11 Sensor co-ordinates: algebra

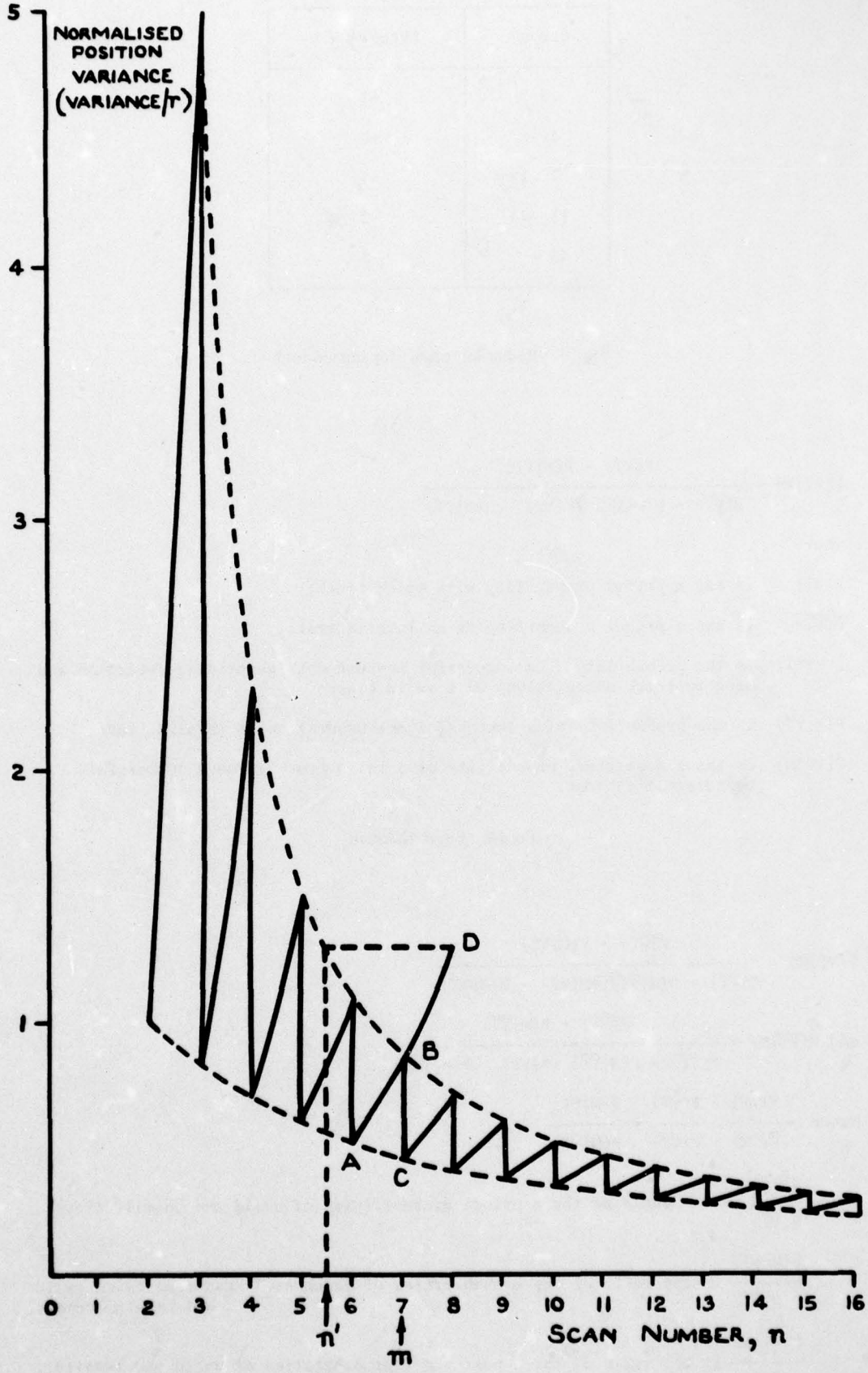

Fig.12 Missed look processing

OLD n	EFFECT ON n
3	+1
4 -6	+0
7 -12	-1
13 -44	-2
45 +	-3

Fig.13 Reduction of n for missed look

$$P\{VT|M\} = \frac{P\{VT\} \cdot P\{M|VT\}}{P\{\overline{VT}\} \cdot P\{M|\overline{VT}\} + P\{VT\} \cdot P\{M|VT\}}$$

where,

$P\{VT\}$ is the a priori probability of a valid track;

$P\{\overline{VT}\}$ is the a priori probability of an invalid track;

$P\{M|VT\}$ is the probability of a successful measurement (comprising detection and plot-to-track association) on a valid track;

$P\{M|\overline{VT}\}$ is the probability of a successful measurement on an invalid track;

$P\{VT|M\}$ is the a posteriori probability of a valid track given a successful measurement attempt.

Fig.14 Bayes theorem

$$P\{VT|M\} = \frac{P\{VT\} \cdot P\{M|VT\}}{P\{\overline{VT}\} \cdot P\{M|\overline{VT}\} + P\{VT\} \cdot P\{M|VT\}}$$

$$\text{and } P\{\overline{VT}|M\} = \frac{P\{\overline{VT}\} \cdot P\{M|\overline{VT}\}}{P\{\overline{VT}\} \cdot P\{M|\overline{VT}\} + P\{VT\} \cdot P\{M|VT\}}$$

$$\text{hence } \frac{P\{VT|M\}}{P\{\overline{VT}|M\}} = \frac{P\{VT\}}{P\{\overline{VT}\}} \cdot \frac{P\{M|VT\}}{P\{M|\overline{VT}\}}$$

where $\frac{P\{VT\}}{P\{\overline{VT}\}}$ is the ratio of the a priori probabilities of valid and invalid tracks;

$\frac{P\{M|VT\}}{P\{M|\overline{VT}\}}$ is the ratio of the probabilities of successful measurements on valid and invalid tracks;

$\frac{P\{VT|M\}}{P\{\overline{VT}|M\}}$ is the ratio of the a posteriori probabilities of valid and invalid tracks.

Fig.15 Single scan updating rule for track validity

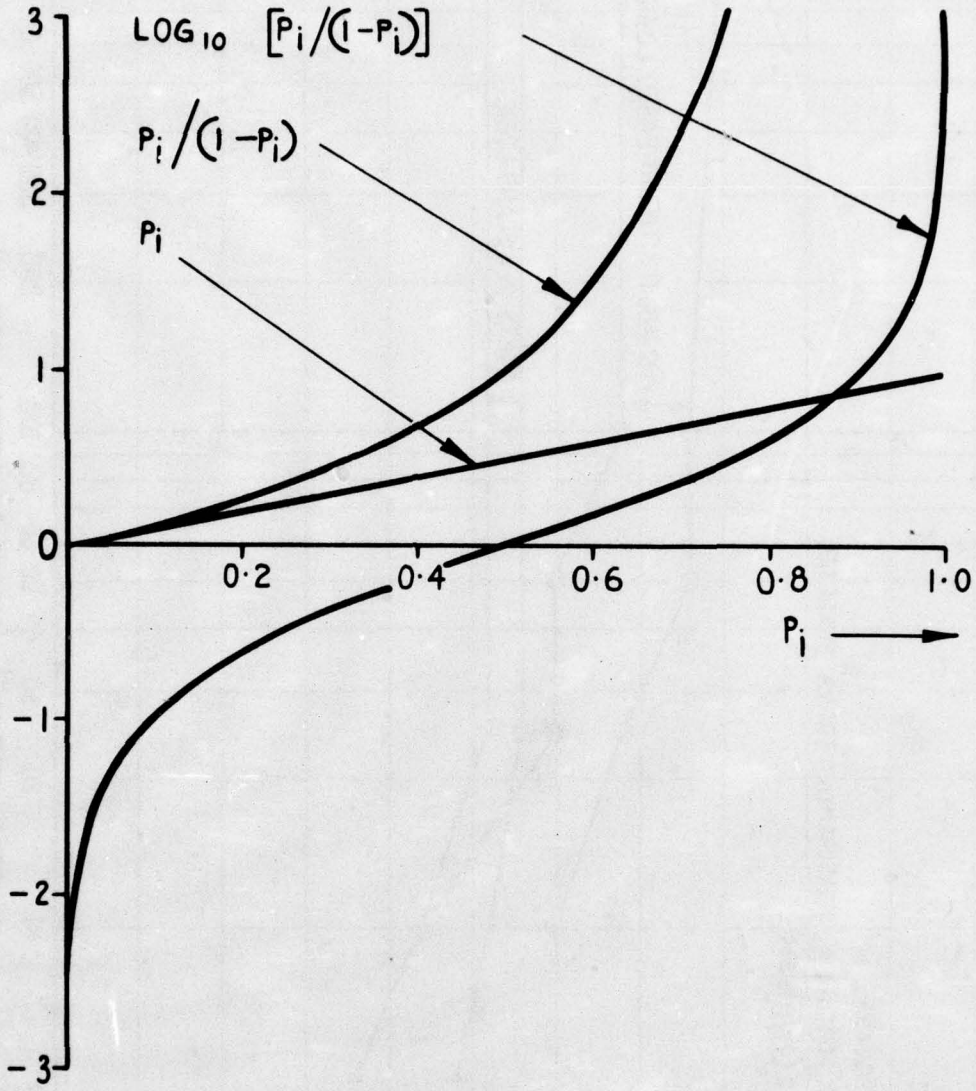

Fig.16 Graphed various functions of P_i

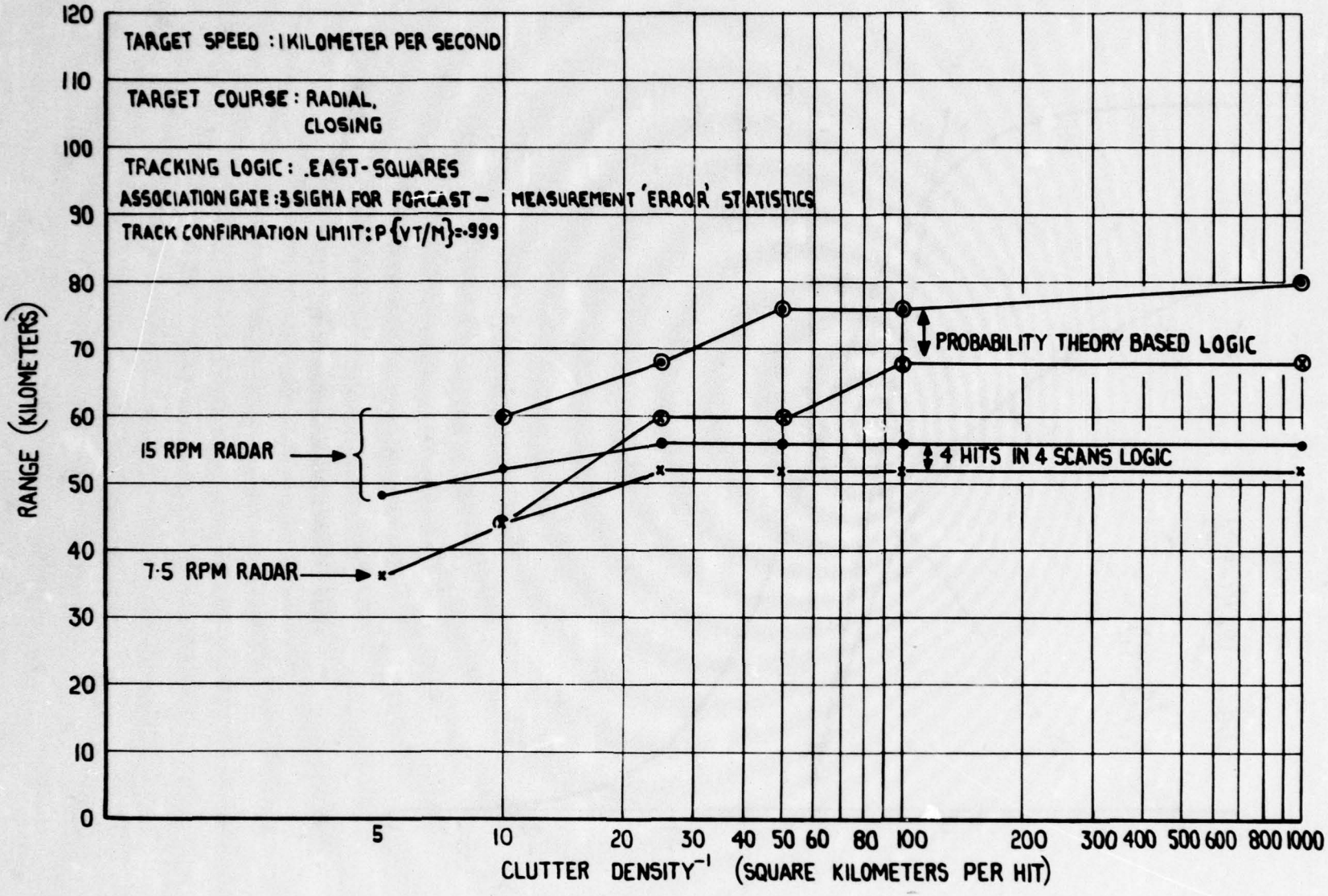

Fig.17 Graph of range for 50% (± 10%). Cumulative probability of initiation vs clutter density^{-1}

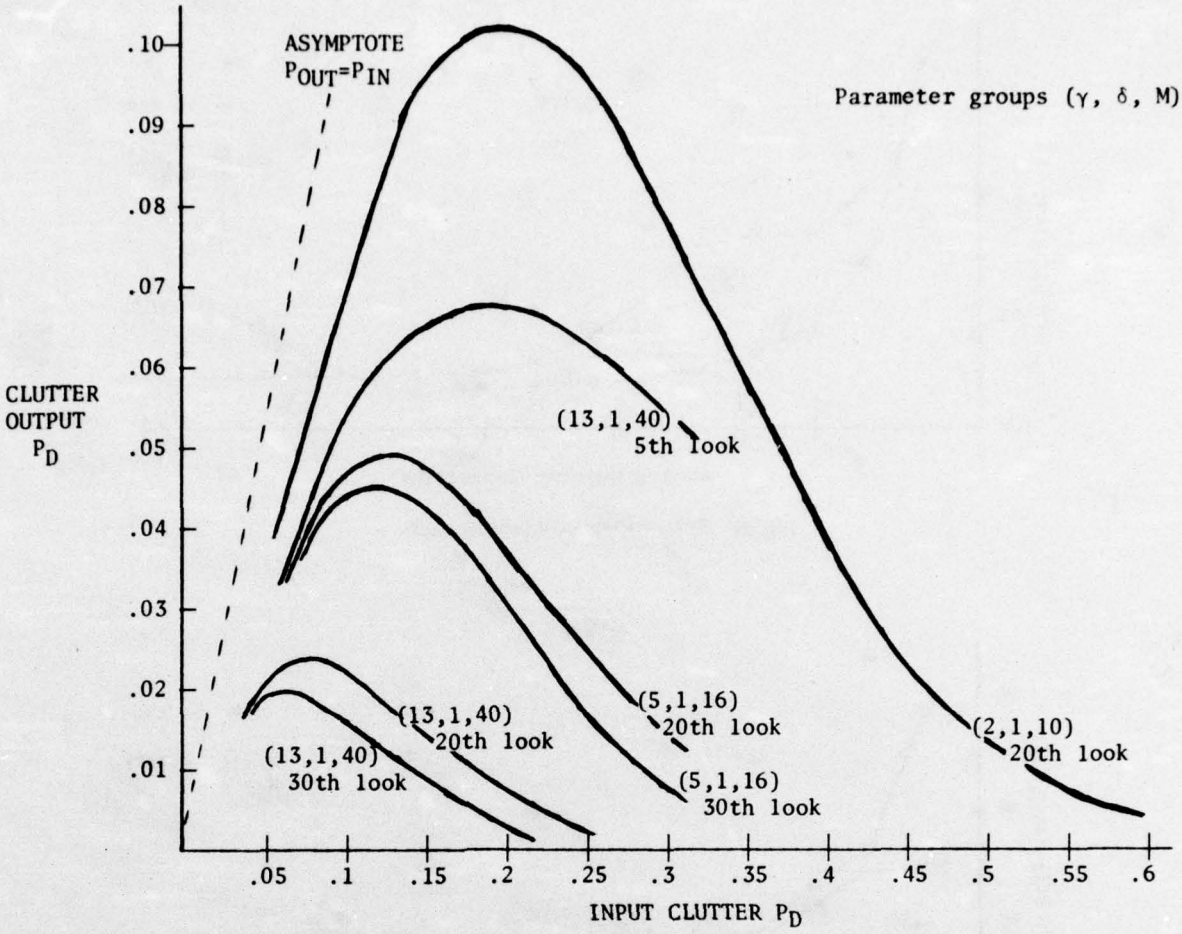

Fig.18 Stationary plot filter: output P_D vs input P_D

PARAMETER	STANDARD VALUE
RANGE CAPTURE	6 RANGE BINS
BEARING CAPTURE	1.5 BEAMWIDTHS
COUNTER INCREMENT (γ)	5
COUNTER DECREMENT (δ)	1
COUNTER INITIAL VALUE	5
COUNTER MAXIMUM VALUE	15
SMOOTHING FACTOR (α)	0.3

Fig.19 Table of standard values of SPF parameters

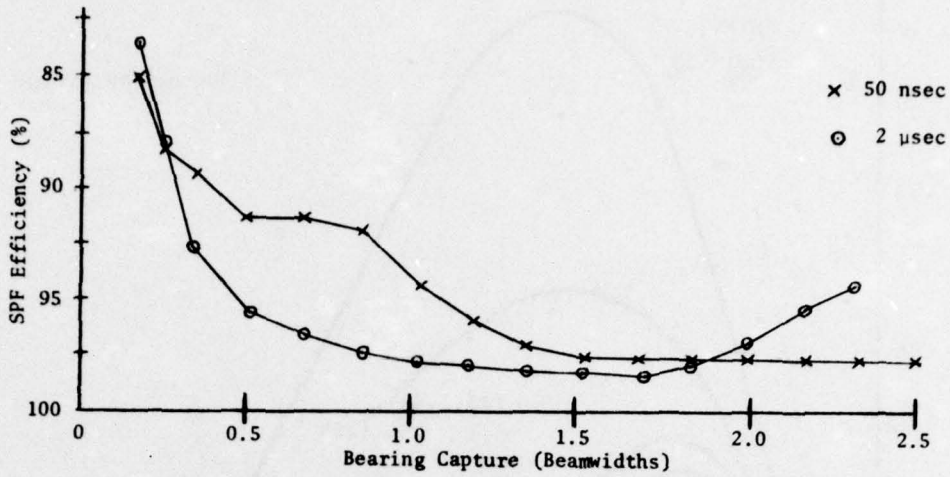

Fig.20 SPF efficiency vs bearing capture

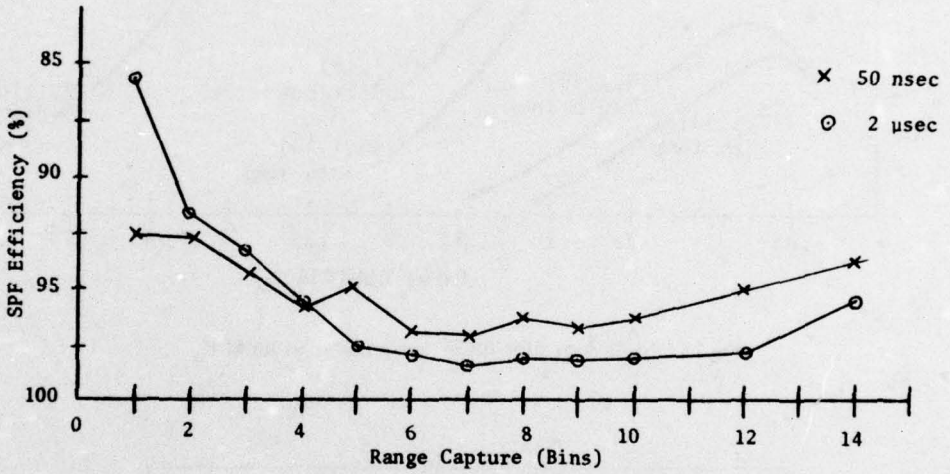

Fig.21 SPF efficiency vs range capture

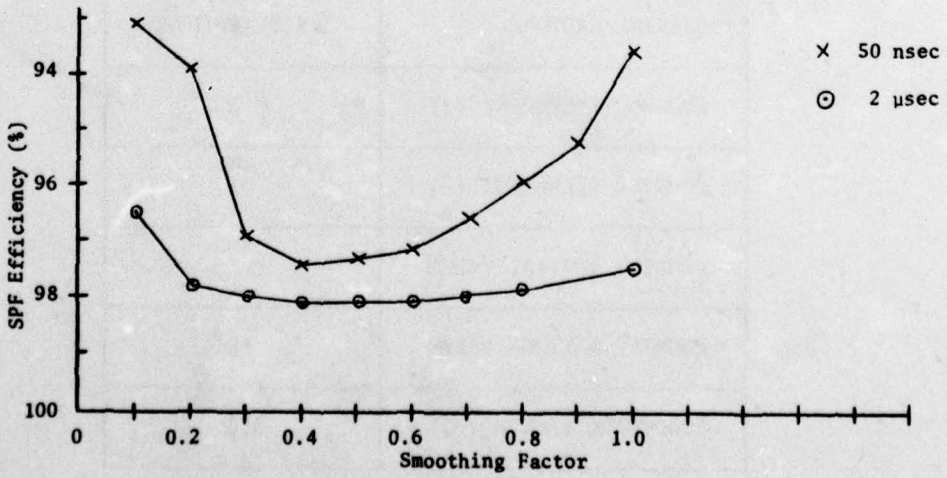

Fig.22 SPF efficiency vs smoothing factor

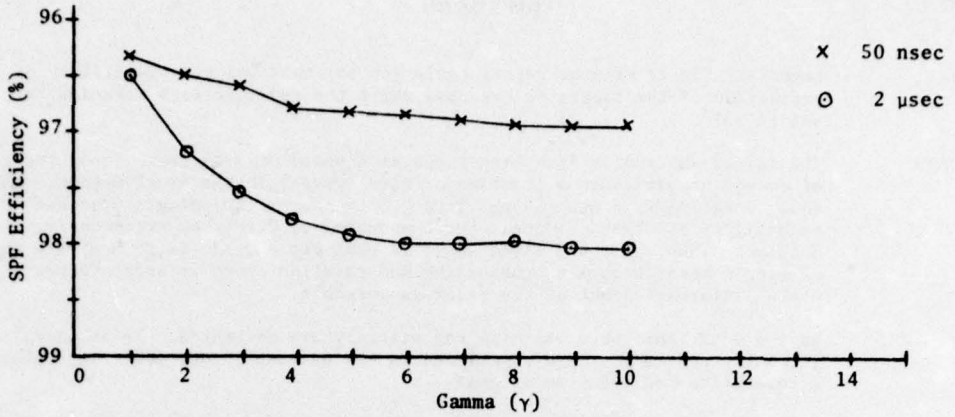

Fig.23 SPF efficiency vs gamma

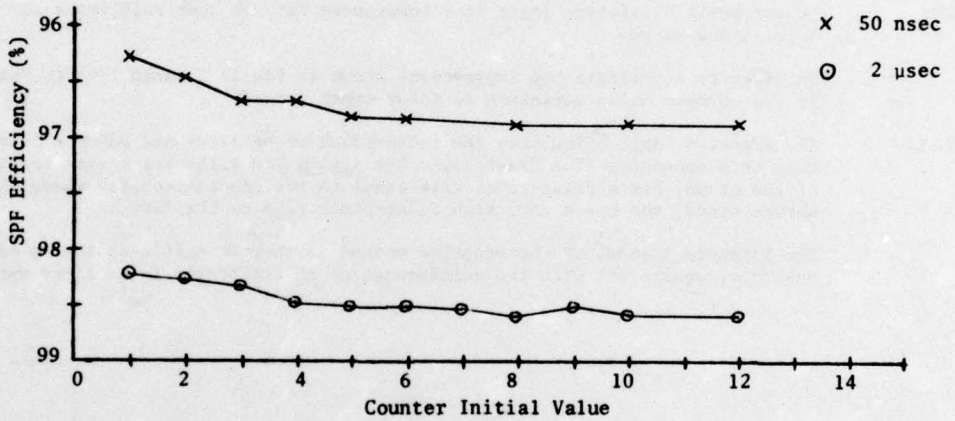

Fig.24 SPF efficiency vs counter initial value

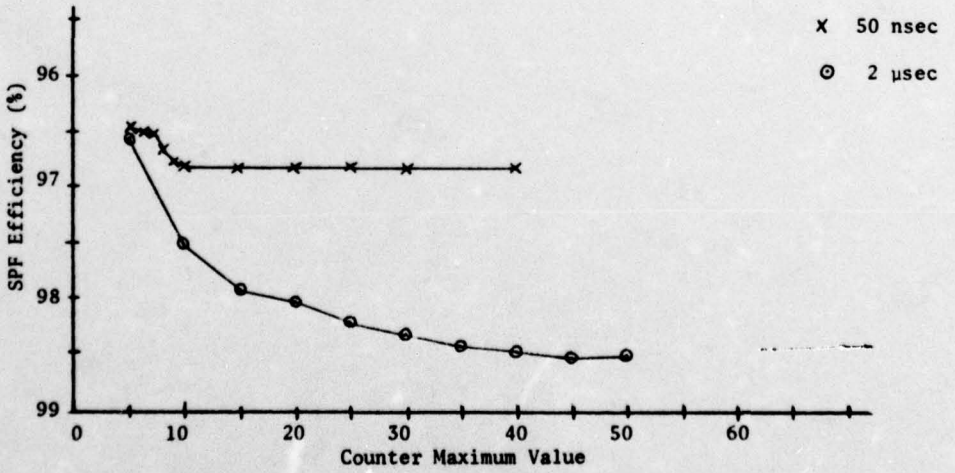

Fig.25 SPF efficiency vs counter maximum value

DISCUSSION

A J KAMPSTRA: Regarding Fig 17 of your paper, could you say what was the probability of plot extraction of the target in the case where the radar antenna rotation rate was set at 15?

A L C QUIGLEY: The target was run in from long range at a speed of 1 Km/sec. Thus, the probability of detection varied as a function of time (range) in the usual manner. When the radar rotation rate was changed from 7.5 to 15 rpm, the single scan detection probability is always reduced, but the number of detection attempts is, of course, doubled. Thus, what the slide shows is that one should aim to maximise the product of single-scan detection probability and rotation speed in order to get as much useful information out of the radar as possible.

R BAUERLE: In α-β equations, only position and velocity are estimated. Is it useful to estimate, and do you have experience in the estimation of, position, velocity and acceleration for α-β-γ equations?

A L C QUIGLEY: Yes. The α-β-γ equations have been looked at, particularly where polar coordinates are used. However, for the use of the acceleration term to be of value, the vehicle being tracked must hold a constant acceleration for a relatively large number of scans. This is an unrealistic assumption for surveillance type radars, although it could be useful for searchlight type trackers.

D F HAMMERS: Was not the 4/4 track initiation criterion rather harsh (or lossy) from the standpoint of comparative analysis, with your adaptive scheme?

A L C QUIGLEY: Yes.

H B DRIESSEN: An automatic initiation logic is a compromise between fast initiation and small false-track rates.

In order to appreciate the improvement shown in Fig 17 I would like to know: "What is the corresponding variation in false-track rates?"

A L C QUIGLEY: The adaptive logic calculates the false-track probability and adjusts itself to keep this constant. The fixed logic has a very low false-track rate on the right of the graph, has a false-track rate equal to the adaptive system where the two curves cross, and has a very high false-track rate to the left.

The intended feature of the adaptive method is that it initiates tracks as fast as possible, consistent with the maintenance of an acceptable false alarm rate.

PLOT EXTRACTOR AND DATA PROCESSING EQUIPMENT FOR A MOBILE HIGH RESOLUTION 3D PENCIL-BEAM RADAR

Dr.-Ing. Heinz Ebert
AEG-TELEFUNKEN
Radar Department
D-79 Ulm
Postbox 1730

SUMMARY

The principle of sequential 3D scanning of the airspace by means of a pencil-beam antenna pattern, for reasons of complexity, is particularly suited for a highly mobile 3D air surveillance radar of high resolution. Advanced radar concepts of this type are using antennas with simultaneous electronic and mechanical beam scanning. For plot extraction, a procedure specially tailored to pencil-beam-scanning and having the following basic features is used: 1) signal amplitude evaluation, 2) target detection within the elevation scan (sliding window), 3) center azimuth determination by means of an associative processor. For further processing of extracted plots (height value calculation, automatic tracking, display control, data remoting) a freely programmable process computer particularly suited for radar data processing is used. The software applied for this purpose is of a modular structure; program control is accomplished along the task management principle. An engineering model of the system described by way of an example is under evaluation.

1. INTRODUCTION

Highly mobile 3D Radar Systems are being increasingly implemented by many Armed Forces, mainly for the performance of operational functions of the following types:

a) air surveillance and simultaneous height-finding;
b) battlefield observation;
c) simultaneous sea and air surveillance in the offshore area;
d) acquisition radar for high ranges and heights.

For these applications, 3D Radars can be used both as autonomously operating systems with automatic data transmission, e.g. to weapon systems, and as sub-systems or "radar sensors" of higher echelon command and control systems. In both instances, radar information must be handled by machines, i.e. by EDP means. In this connection, one of the objectives to be accomplished is the indication of radar information on computer-controlled displays, in a "synthetic" fashion, i.e. using symbols supplemented by alphanumeric characters. The evaluation of radar signals by means of computers is subject to their "digitalization" by special systems, the "radar plot extractors". The function of such plot extractors, however, largely exceeds a mere analog/digital conversion, actually including a genuine radar plot detection, i.e. the performance by machines of a function so far excercised by man on the radar display. In addition, this provides the possibility of transmitting radar pictures via narrow-band links, e.g. telephone channels. A desirable feature for synthetic radar information display and for further EDP evaluation of radar information is automatic tracking, i.e. detection by machines of the direction and speed of radar target movements. This capability is based on the plot messages furnished continuously by the plot extractor originating from the successive revolutions of the radar antenna. The variety of the functions indicated explains why highly mobile 3D Radar Systems require considerable additional devices in the form of special data handling equipment. The following paragraphs will mainly describe this special equipment.

2. HIGHLY MOBILE 3D ACQUISITION RADAR WITH PENCIL-BEAM ANTENNA PATTERN

2.1. General

The basic data processing problems in connection with a mobile 3D Radar will be discussed mainly on the basis of a system already realized.

This 3D Radar consists of two separate functional units, the Sensor and the Evaluation Equipment (Fig. 1). The Sensor includes the radar equipment proper, comprising antenna, transmitter, receiver and signal processor. The Evaluation Equipment essentially comprises all data handling equipment such as primary radar and IFF plot extractors, computer, data output to narrow-band network and the operating positions including analog and digital displays. Each unit is transported by a 10-ton truck and will be ready for operation within 30 minutes.

2.2. Sensor

Details of the Sensor will be covered only to the extent required for comprehension of the data processing problems described later on: the space is scanned by a phased-array antenna having a pencil-beam pattern (Fig. 2). While the antenna is rotating mechanically in azimuth, the antenna beam scans electronically in elevation. The movement in azimuth during one elevation scan corresponds to a maximum value of one half-power beamwidth. To optimize system cycle time, the elevation beamwidth, angular velocity and the pulse repetition frequency vary as a function of the slant range.

To eliminate interference, the radar resolution cell, by narrow beaming and phase-coded pulse compression, has been minimized.

Furthermore, a switchable single/double cancellation step-scan MTI system is used. The transmitter is of the coherent type. The block diagram (Fig. 3) shows the Sensor units. At the output of the Sensor, the following video signals are available:

a) Normal or MTI video
b) Dicke Fix video
c) IFF video.

These signals, together with trigger signals and information on antenna positioning, constitute the input signals to the Evaluation Equipment.

2.3. Evaluation Equipment

The block diagram Fig. 4 shows the main units of the evaluation equipment: the heart of the evaluation equipment is a primary radar (PR) plot extractor tailored to the 3D radar method described above. The IFF information obtained through an IFF detector is correlated in the Correlator with the PR plots.

Special attention is drawn to the fact that, other than in a 2D radar, a plot extractor is always indispensable in a 3D radar whenever the height information is to be evaluated in an optimum manner. This means, for instance, that in an advanced 3D radar concept the height value of <u>all</u> targets (i.e. not only of selected targets) is determined automatically.

In accordance with the present state of the art, the processes of automatic target detection in a radar of high range resolution can only be performed in hardware devices specially designed for the particular application, whereas all functions of further processing of extracted plots can be performed in EDP systems using freely programmable process computers. The main tasks performed by a process computer (Fig. 4) in the Evaluation Equipment are: computation of the height of the plots and of the ground range based on the slant range and the elevation angle, filtering of the plots for pre-set operational criteria, digital display control and data output to a narrow-band network.

Due to the easier adaptability of software system compared to purely hardware-oriented systems, it is possible to make allowance for particular wishes of the various users (army, air force, navy), e.g. special data transmission formats and procedures, automatic tracking etc.

The EDP system concept provides for interaction of an operator in the plot handling process by means of a rolling ball and the command keyboard (Fig. 4). The processing operation can be observed by means of a multi-colour display (cf. Section 5) and an alphanumeric display.

Availability of an efficient and flexible EDP system forming part of the radar system is in keeping with the modern trend of decentralizing EDP functions in military (and civil) systems. This means that subsequent operations centrals can be efficiently relieved of such EDP operations which can also be assigned to the radar equipment. In the event of a failure of the operations central, the radar system can continue to operate as a self-contained unit.

3. PLOT EXTRACTION PROBLEMS AND TECHNIQUE IN CONNECTION WITH A 3D PENCIL-BEAM RADAR

3.1. General

The technique applied for a 3D plot extractor is closely linked with the 3D radar method used, in particular with the radar antenna scanning pattern. One may distinguish mainly between parallel scanning (multibeam or stacked-beam method) and sequential scanning using a pencil beam. As plot extraction for the multibeam method is sufficient-

ly known, and further as a multibeam 3D radar can hardly be designed as a highly mobile system due to its great complexity and high weight (cf. 2.1), this paper is confined to plot extraction for pencil-beam radars.

As stated in 2.2 above, such advanced radar concepts operate along the principle of electronic elevation beam scanning and mechanical antenna rotation in azimuth. One may distinguish between two basic concepts:

a) The time interval of successive radar sweeps in elevation is such that the antenna patterns are touching each other at the 3 dB points; the same applies for azimuth.
b) There exists an overlap of the antenna patterns in elevation (possibly also in azimuth), so that, for instance, four radar sweeps come within the 3 dB elevation beamwidth.

In the event of a) above, (automatic) target detection must be performed on the basis of a single hit, as only <u>one</u> target reply will be available within the 3 dB beamwidth. In the event of b) above, target detection will occur in the usual manner by integration over several hits. The advantage of a) is the considerable gain in time in 3D all-around scanning, the draw-backs being higher transmitter power with the radar range remaining the same, and the considerably lower height-finding accuracy (cf. 3.2.3).

3.2. Target Detection Method

3.2.1. Amplitude Quantization

Other than with 2D radars, with 3D radars very few hits (in the extreme case only one) are available only within the 3 dB beamwidth. As for the purpose of height-finding, the elevation angle of a target must be determined as accurately as ever possible (in certain cases the azimuth value, too), it is absolutely necessary for 3D extractors to evaluate the signal amplitude. When sequential scanning is applied using the pencil-beam method, it will be necessary to store the signal amplitude values in a buffer. This involves the necessity of digitization of the signals, a 4-bit quantization being normally sufficient (= 15 amplitude increments).

Investigations on the detection behaviour of a sliding window integrator using multiple bit quantized amplitudes show that there exists an optimum ratio between quantization increment width and noise r.m.s. value. This means that in the event of this ration amounting to between 0.5 and 0.7, the necessary S/N value at the input will be reduced to a minimum for a preset probability of detection. Thus, as the noise r.m.s. value rises, the quantization increment width would have to be increased, too. For reasons of optimum target detection, therefore, a non-linear amplitude quantizer, i.e. a quantizer providing for increasing quantization increment width as the input amplitude rises, can be recommended [1]. This, however, will increase the complexity of the algorithm for azimuth computation (cf. 3.2.4.).

3.2.2. Single Hit Evaluation

The process of target detection on a single hit basis is illustrated in Fig. 5. The echoes originating from a radar sweep of a designated elevation value are stored in a memory following their quantization, (e.g. 4-bit quantization). The memory address used is the current elevation angle value J and the current number I of the elscan (elevation scan). If the echo signal of a designated radar resolution cell - which, in our example, is stored in location E - is to be finally evaluated, then the echo results from the directly adjacent resolution cells (elevation values J-1 and J-1, elscans Nos. I-1 , I and I-1) are also used.

If defined amplitude patterns are present, a coherent plot can be detected, and a pertinent elevation and azimuth angle value is computed based on the amplitude values. This action depicted for a single range increment only is performed for each range increment during the current radar sweep. Neglecting the random amplitude distortion, the maximum elevation or azimuth errors amount to $\pm 1/2$ of the antenna elevation or azimuth half-power beamwidth.

3.2.3. Multiple Hit Evaluation (Sliding Window Detector)

Although 3D Radars using single hit evaluation have been realized, a design permitting multiple hit evaluation is to be preferred. The system discussed here which has been realized in practice, within the elevation half-power beamwidth, provides to the evaluation equipment the target echoes originating from four radar sweeps. In this instance, the sliding window principle can be used for integration of the 4-bit quantized echo signals; in contrast with the usual 2D extractors, however, the sliding window here is slid in the direction of the elevation scan, i.e. vertically downward. This process is shown in Fig. 6. Whenever a 6-bit target detection threshold is exceeded, start-of-target is declared, and the respective elevation angle value is read. Similarly end-of-target is declared when the amplitude drops below the threshold. From these values the elevation angle value of the target center is determined. In the event of undistorted amplitudes, the accuracy amounts to $\pm 1/2$ elevation increment (i.e. angular spacing between two radar sweeps), which means that it is four times higher than the accuracy attained in single hit evaluation.

The development engineer, as in the case of 2D extractors, here, too, is interested in the relationship between probability of target detection W_D, false alarm probability

W_{fa}, S/N ratio at the extractor input, as well as the (normalized) threshold voltage V_s of the target detection threshold (for an explanation of these terms, please refer to [2]). Normally, the values for W_D, W_{fa} and S/N are given, and the required threshold voltage V_s must be computed. The detection process applied here corresponds to an "incoherent" integration which is described in sufficient detail in the well-known book "Radar Design Principles" by Nathanson [3]. A collection of curves making allowance for the well-known Swerling fluctuation models is contained in [4].

The Attachment gives a short outline of the mathematical relationships.

As it is imperative in clutter and jamming areas to avoid any flooding of the extractor with false targets, a clutter detector is coupled to the detection threshold to raise the latter as a function of the clutter background. The function of the clutter detector must be regarded as an ultimate safety measure against an unintentionally high clutter rate; it is desirable to efficiently eliminate clutter by radar or signal processor measures. In order to obtain information on the clutter background, the amplitude mean value is measured in a defined area around the sliding window. The measurement of the mean value can be performed more easily than, for instance, that of the r.m.s. value. It is justifiable on the assumption of Rayleigh-distributed clutter, as there exists a linear relationship between mean and r.m.s. value. Association of a threshold value with a measured value occurs through a read-only memory.

3.2.4. Target Azimuth Center Determination

As a strong target may be detected several times, i.e. during two or three successive elscans, target azimuth center determination creates problems of a particular nature. It is necessary, in a special extractor sub-assembly, to combine the target data from the respective elscans to a single plot and to compute a resulting azimuth value. To this effect, the mean value of the signal amplitudes contained in the sliding window is continuously determined. The maximum of this mean value between start-of-target and end-of-target is stored and used as a basic value for azimuth center determination. Evaluation then proceeds as follows: for each newly detected target a process is started by which a match having the same range and elevation values is searched for in the stored data of the previous elscan. In view of the inaccuracy of target position detection, directly adjacent increments must also be included in the search process. In addition, due to the small resolution cell, the search process must be accomplished within a very short period of time. For this purpose, a so-called "associative" processor [5] is particularly suited, the elevation and range values being used as search criteria in the associative (= content-addressable) memory. The capacity of the associative memory is adapted to the expected number of plots per two elscans; for the present instance, the number of plots has been assumed to amount to 160. From the difference of the stored amplitude mean values of the matches found, the resulting azimuth value is derived. Any possible third corresponding plot of a target determined in this manner during the immediately following elscan will be suppressed.

3.2.5. Data Reduction

By the plot extraction process, the high radar resolution resulting from the pulse compression method is to be fully exploited in the interest of minimizing clutter signals detection. This means that the size of the range increment in the extractor must be adapted to the sub-pulse length, or that the integration process must occur at a corresponding speed. This requirement has been met in the example under discussion. As, however, the high resolution is employed for reasons of clutter signal reduction only, (adaption of radar resolution cell to target dimensions), while a less high resolution would be sufficient for this radar application, the plots from several range increments, in a data reduction unit, are combined to a resulting plot. Again, the mean amplitude is used as a selection criterion; the plot having the highest amplitude value in the so-called "coarse range increment", i.e. the resulting range increment after data reduction, is passed on, the remaining ones being suppressed. In this manner, an adaption of the data flow to the speed of normal process computer input channels is simultaneously accomplished.

3.2.6. PR/IFF Correlation

Normally, an IFF equipment is also coupled to a 3D acquisition radar, as it is usually employed with a 2D radar. This requires availability of an IFF plot extractor to enable IFF target replies to be also automatically detected and processed. The extracted PR and IFF target replies, to the extent possible, are combined to common target replies, i.e. the attempt is made to correlate them. In view of the necessary high speed of the respective search processes, it is again expedient to use an associative processor.

3.3. PR/IFF Plot Extractor Block Diagram

Fig. 7 shows the block diagram of an extractor resulting from the above considerations and developed for the radar described herein:

The video signals output by the sensor are quantized in 15 increments (= 4 bits) in the "hit processor" unit; in view of the subsequent azimuth center determination, linear increments have been adopted. As a constant video level must be available for quanti-

zation, video amplification is controlled in a preceding control amplifier in accordance with the signal of an integrator using a slow feedback loop. This integrator records the instance whenever the threshold is exceeded by the video signal compared to a threshold value in a window at the end of the radar coverage area. The integral value is held constant throughout the gain control process.

This unit is followed by the sliding window detector coupled to a clutter detector, and the target elevation center determination unit. The basic function of these three units is identical to that in a normal 2D extractor, the difference being, as stated earlier, that the sliding window is moved vertically during the elevation scan, and that the signal amplitude is evaluated. The following units, viz. "target azimuth center" and "data reduction", however, are specific to the pencil-beam 3D plot extractor; their function has been explained in detail in 3.2.4. and 3.2.5. above, respectively. Then, in the "PR/IFF correlation" unit, the PR and IFF information is combined; correlation is performed neglecting the PR height information. Then the plots are transferred to the EDP system (process computer) of the evaluation equipment.

3.4. Extraction of Sea Targets

As the tasks of the 3D Radar System described include off-shore control, the question of automatic extraction of sea targets must be solved in addition to aircraft target extraction.
In this connection, two basic problems arise:

1) Frequently, sea targets are rather sizeable, which means that they cannot be considered point-type targets as can aircraft targets.

2) The sea clutter caused by the waves, within the sweep period of an antenna beam, provides highly correlated return echoes of a target-type nature.

Target detection carried out by an operator, and to a still higher extent target detection performed by machines, is thus rendered difficult or even impossible.

The problem of additional sea target extraction may be solved by the following variations of or supplements to the basic versions of the sensor and the evaluation equipment:

1) For sea target extraction, the lowermost beam position within each elevation scan is used (cf. Fig. 2).

2) The antenna beam remains in the lowermost position for a longer period than it does in the basic version, so that at least 12 radar sweeps will come within the 3 dB beamwidth.

3) For decorrelation of sea clutter, pulse-to-pulse frequency agility is applied.

4) Target center determination in azimuth direction, i.e. correlation of plots from the same target originating from several elscans is extended to observation of more than two successive elscans. Plots from a maximum of 15 successive elscans can be utilized for target azimuth center determination.

5) As the extension of a ship target in range direction may also considerably exceed the range resolution, an additional range center determination will be required. In this case, too, center determination is accomplished based on the principle of the beam-splitting method, i.e. the mean value is computed based on the measured values for start-of-target and end-of-target criteria.

Fig. 8 shows the principle of the measures enumerated for additional sea target extraction. These functions are included in the extractor by means of a retrofittable "marine supplement".

4. FURTHER PROCESSING OF EXTRACTED PLOTS IN THE PROCESS COMPUTER SYSTEM

4.1. General

In an earlier 2D plot extractor project, a freely programmable computer has been successfully applied for plot processing purposes [6]. The 15 plot extractors used in the FRG for civil air traffic control include one dual-computer system TR86 each (operation and standby). In the application discussed here, however, the process computer performs functions which largely exceed the tasks of a plot extractor: it is possible, for instance, to extend plot processing by automatic target tracking; furthermore, it is possible, as required, to extend the evaluation equipment to a mini operations central. Realization of the particular functions in the form of software provides the evaluation system with a high flexibility and permits to meet the individual requirements of various users (army, navy, air force). The software is broken down into a basic software used for all system versions, and supplements which are established to meet the specific requirements of the respective users. The basic system functions which are covered by the basic software include the tasks of further plot processing, such as computation of the height value, conversion of target coordinates from rho/theta into X/Y coordinates, etc., preparation of information for narrow-band transmission, as well as system monitoring using a computer-controlled display. This includes also the ope-

$$P_{D_4}(2/4) = 1 - S_4(2/4) \qquad (4\text{-}2)$$

rator's action on data evaluation, by inputting data filtering criteria for height values, geographical sectors, etc. The supplements include, for instance, target tracking, sea target evaluation or extension to a mini operations central.

The structure and organization of EDP systems for the functions described above is similar to the structure and organization of typical process data handling systems. A coarse break-down results in the following three main components: 1) Process hardware, 2) operating software or operating system, respectively, 3) application software. The typical functions of these components can be explained by means of a trivial comparison: During a flight, the aircraft accomplishes the function of the "hardware", the pilots and stewardesses constitute the "operating system" applicable for all passengers, while the passengers themselves, each of whom has a special goal linked with his travel, constitute the "application software". In the following paragraphs, the typical functions of these three components of the process computer system for 3D radar data processing are discussed.

4.2. Structure and Organization of the Process Computer System

4.2.1. Hardware

Fig. 9 is a block diagram of the main components of the process computer system used in the radar system: the heart is a UNIVAC process computer of the latest generation meeting military environmental requirements. The memory can be extended to a maximum of 64 K words (word length = 16 bits); for the present task, 32 K words will be sufficient. The program is loaded once only through a magnetic tape cassette which also meets the military requirements. The complete program established in a computer center is written onto this cassette (cf. 4.4.).

For system operation by the operator, a command keyboard connected to the display, and a rolling ball unit are available. A separate alphanumeric display indicates any additional information desired or acknowledges command inputs. Another keyboard and a small printer are used for computer operation and monitoring. All operating functions must be designed in such a manner that the operators need not have any special computer or software knowledge. An automatic test system continuously monitors the system functions and locates the failed unit in the event of any malfunctions.

The computer used is particularly suited for radar data processing tasks. This can be seen from the following characteristics:

- High instruction repertory (over 100) including single-bit instructions which are very desirable for radar data evaluation;
- high-speed I/O channels with direct memory access and separate instruction repertory;
- Hardware "Cordic" arithmetic unit for the computation of trigonometric functions, coordinate transformation, vector computations etc. within a period of as little as 12 µs. This accelerates rho/theta - X/Y coordinate transformation of target data and special target tracking computations (cf. 4.3.) by more than one order of magnitude.
- A total of 64 hardware general-purpose registers; by high-speed register-register operations, the program flow can thus be considerably accelerated;
- Simplification and reduction of the program interrupt process by application of general-purpose registers which can be broken down into four program levels.

The characteristics enumerated above show the increased performance of advanced process computers compared with previous computer generation. In view of the technological progress of semiconductor technique, this improved performance is also coupled with a considerable reduction in volume. This results in the fact that today highly mobile radar systems can be provided with a data processing capacity which is by no means inferior to that of fixed systems.

4.2.2. Application Software and Operating System

In section 4.1., the difference between application software and operating system has been briefly explained. Application programs automate processes; they reflect the process actions. Programming of a process computer, therefore, means in particular, the generation of application programs in accordance with the process task requirements. It is of particular importance to break down the overall process into individual, self-contained partial processes or modules. In doing so, the goal shall be to obtain program modules, having but a single, exactly defined input and output. Upon an exact definition of the input and output interfaces as to data structure, data format etc., the individual program modules can be generated, tested and subsequently assembled to the overall program. This form of program organization thus adds both to the lucidity of the overall program and the better organization of the workflow for program generation.

Whenever a certain program module becomes effective, i.e. whenever the computer processes data based on the instructions from this program, this program becomes a "task". This means that a task is the active application of a program. The start of a certain task, its possible interruption, its completion and the making available of all necessary input data is a special process within a computer. This process also includes control of peripherals, or the transport of programs, files and data. The operating system is the program by which these processes are automated, i.e. it is a program for automation of the computing process. During the computing process, the process computer continuously alternates between the application status during which application programs are pro-

cessed, and the organization status during which the operating system is effective.

The operating system program performing real-time activation and monitoring of the various application tasks, based on an exactly defined time and organization schedule, is called scheduler program. The organization of application task control through a scheduler with exactly defined time relationships and priorities described here may also be called "task management". Its advantage over other organization structures is that it is possible at any time to obtain an exact picture of the status and the flow of the processing process. It is, for instance, possible to avoid that the computer gets stuck in a particular program due to any unforeseen input data configurations. In addition, the task management procedure provides an unsurpassed flexibility for the program test, as well as in the event of any subsequent extensions or changes, by bypassing, eliminating or replacing individual tasks in a simple manner without affecting the remaining programs.

The only disadvantage of modular program organization in connection with task management might prove to be the fact that, as a result of the input and output buffers of the modules, the overall storage requirement is somewhat increased and additional times are required for scheduling. Its advantages as described above, however, are of such a high value that it must be preferred to all other organizational structures for real-time radar data processing.

Although the producers of process computers today mostly also provide a real-time operating system, it has time and again proved necessary to establish a special operating system for such specific-to-task applications as radar data processing, the reasons for this being, above all, the peripheral conditions whose nature differs from those applicable for usual process control systems, and the absolute requirement of optimum process control flow with respect to time. This is why a special operating system has been prepared for the described process computer system for 3D radar data processing.

4.3. Special Tasks of Further 3D Radar Plot Processing

Fig. 10 shows the main program modules used in the process computer portion of the evaluation equipment of the 3D Radar described here. The basic programming version, extended by an automatic tracking of aircraft and marine targets, is shown; the function of an independent operations central is not contemplated. The typical processing functions in a 3D radar data evaluation system, as shown in the diagram, are as follows:

1) Data Transfer from Plot Extractor
   This program ensures real-time transfer of data blocks from the extractor and prepares the information thus transferred for the follow-on-processes.
2) Calculation of Height Value
   As the radar measures the target slant range, the height and the ground range of each target must be computed based on the slant range and the elevation angle data.
3) Data Filtering/Insertion of Maps
   Depending on the operator's inputs, the plots, prior to being passed on, can be filtered for criteria such as appertaining to a designated height layer, a designated geographical area or clutter area, or other defined criteria. By insertion of map and position information, areas subject to filtering processes can be identified.
4) Rho-theta/X-Y Coordinate Transformation
   This program, by means of the CORDIC arithmetic unit, transforms all target information into X-Y coordinate data (cf. 4.2.1.).
5) Command Input and Processing
   These programs process the commands input through the operator's keyboard and cause the commands to influence the evaluation process.
6) Target Tracking
   This program provides the possibility of simultaneously and automatically tracking a total of 100 targets. These targets may be aircraft or marine targets or both. Tracking is initiated manually by the operator, as an automatic initiation might involve a high calculation effort, and inadmissibly high clutter rates might result in a computer overflow. The targets are automatically sorted into "fast" aircraft targets and "slow" sea targets; the position of a slow target is output once only per 10 antenna revolutions. The initial tracking gate is a circle; for target tracking proper, however, tracking gates formed by circle segments are used, making allowance for radar measuring errors and any possible maneuvers of the target being tracked. For computation of the tracking gates and the prediction position of the targets, the advantage of a high-speed hardware CORDIC arithmetic unit can be fully utilized: computation of the trigonometric or vector functions is ten times faster than program-controlled calculation by computers without this device. Non-availability of the high-speed CORDIC arithmetic unit would, in the present instance, result in the necessity of utilizing considerably simpler tracking gate types detrimental to the tracking efficiency.

   In Plot-track correlation, the height of the target is taken into account. Failure of target detection over several antenna revolutions can be bypassed, the number of bypasses being an adjustable parameter. For "smoothing" of the target prediction position, the well-known alpha-beta method is employed.
7) Data Output to Display
   This program controls the output of data to the evaluation equipment display for

synthetic presentation of the situation (cf. 5). As the display has a picture updating memory of its own, it may be omitted in the computer.

8) Output to Alphanumeric Display
The alphanumeric display is an auxiliary means for the operator: input instructions can be acknowledged, and additionally requested target information (e.g. speed in the event of tracking) can be indicated.

9) Data Output to Data Link
This program organizes data output to the respective users; normally, the extracted radar information is transmitted through one or more telephone-channel-type links to remote operations centrals.

Programm-controlled plot processing is arranged in such a manner that a maximum of 1000 plots per antenna revolution can be input to the computer. As a result of filtering processes for various criteria, plot selection by the operator etc., 300 plots out of the total of 1000 are assumed to be supplied to the input of the target tracking logic; based on these 300 plots, the tracking logic will be able to simultaneously detect a maximum of 100 target movements. It must be particularly mentioned that both the target tracking processes and all other extractor-specific processing tasks can be jointly performed in a single computer. Normally, these two work packages requiring a great deal of real-time operations can be handled in separate computers only. The reason for this fact is the combination of the computer features described above, the following of which must be particularly emphasized: a) efficient interrupt system, b) program flow acceleration by high-speed register-register operations, c) hardware CORDIC arithmetic unit.

4.4. Computer Center for Program Generation

The user of radar systems with freely programmable EDP systems is not so familiar with the fact that, in addition to the operationally employed EDP system, a computer center is required where all programs are generated based on optimum working aspects, and where subsequently, during the operating lifetime of the system, these programs can be maintained, i.e. improved or adapted to new requirements. For an economical handling of programs, extended peripheral devices such as high-speed printer, tape devices and/or disc memories are required. Furthermore, the main memory of the computer should have a higher capacity than that of the operational system in order to permit test programs etc. to be applied. Fig. 11 shows the equipment of the computer center set up for the generation of programs for the 3D radar described.

5. DISPLAY PRESENTATION

In presenting 3D radar information on a display, the basic problem of presenting the third dimension, i.e. the height information, exists. In the present application, the requirement is limited to association of the plots with one height layer out of a total of five. This is why a defined symbol shows that a target appertains to a defined height layer, which means that five different synthetic display symbols are available in accordance with the five height layers. (Fig. 12). To each target, up to three history symbols can be assigned, their position permitting to extract the direction of motion and the speed (Fig. 12).

As in the synthetic situation display the targets, based on the preceding computer evaluation, are presented with their correct ground range data, whereas the radar measures the slant range, it is not possible to directly superimpose raw video and synthetic information. For this reason, separate displays are used for these two types of information, i.e. a 16-inch monitor display for raw radar and extractor signals, and a 23-inch three-colour display for the computer-processed information. (For extractor control - without computer processing - the raw video at the input and the plots fed to the computer can be directly superimposed). To improve visibility, it is thus possible to assign a colour to the symbols, e.g. green to friendly targets, red to unknown or hostile targets, yellow to background information such as radar site, map symbols, rolling ball symbol etc.

Fig. 12 shows a selection of the most important target symbols. Based on a picture updating frequency of 40 Hz, the display capacity of the colour display amounts to 1000 targets without history positions, or 250 targets including three history positions and additional information.

6. CONCLUSION

The problems of plot extraction and plot processing in connection with 3D radar systems have been discussed based on an evaluation system designed for a highly mobile pencil-beam radar. Early in 1976, evaluation of an engineering model completed after several years of development affort has been started; manufacture of a prototype is under way. On the occasion of the conference in June 1976, it will be possible to show display photos and to give a report on initial evaluation results.

Fig. 13 shows a photo of the Sensor vehicle of the 3D radar with its shelter and with the antenna folded down.

7. ANNEX TO 3.2.3.

According to [3], equations (3-1) and (3-4), the probability of false alarm W_{fa}, the normalized threshold voltage V_s and the number M of pulses integrated are related as follows:

$$1 - W_{fa} = \int_0^{V_s} \frac{V^{M-1} \cdot e^{-V}}{(M-1)!} \, dV \qquad (1)$$

where

$$V = \sum_0^M v \qquad (1a)$$

v is the normalized detector output voltage (normalization to the root mean square noise).

In accordance with the given value for W_{fa}, the extractor's target detection threshold must be adjusted to the V_s value resulting from Eq. (1). The probability of target detection W_D, then, in accordance with [3], Eq. 3-5, can be calculated for the "Marcum" case (i.e. without considering any fluctuations) from the following relationship:

$$W_D(x, V_s) = e^{-Mx} \sum_{k=0}^{\infty} \frac{(Mx)^k}{k!} \sum_{j=0}^{M-1+k} \frac{e^{-V_s} \cdot V_s^j}{j!} \qquad (2)$$

where x = S/N = signal-to-noise ratio at the extractor input. With a constant false alarm rate W_{fa} and a correspondingly adjusted threshold voltage V_s, the probability of detection W_d is but a function of the S/N ratio (M is given by the number of radar sweeps or number of target echoes within the 3 dB antenna beamwidth).

If target fluctuations (Swerling cases 1 through 4) are to be taken into account, it is preferable to use the extensive collection of curves contained in [4].

BIBLIOGRAPHY

[1] Hansen, Optimization and Performance of Multilevel Quantization in Automatic Detectors, IEEE Transact. Aerospace Vol. AES-10, No.2, March 1974

Hansen, Weak-Signal Optimization of Multilevel Quantization and Corresponding Detection Performance, NTZ 1969, Heft 2

[2] Ebert, Automatische Erkennung von Flugzielen durch digitale Radarzielextraktion, Wissensch. Ber. AEG-TELEFUNKEN 42 (1969) 1, S. 39-48

[3] Nathanson, Radar Design Principles, McGraw-Hill, New York 1969

[4] Meyer, Mayer, Radar Target Detection, Academic Press, New York/London 1973

[5] Ebert, Radarsignal-Auswertung unter Verwendung frei programmierbarer EDV-Systeme mit paralleler Verarbeitungsstruktur (Assoziativ-Prozessoren), Wissensch. Ber. AEG-TELEFUNKEN 45 (1972) 4, S. 166-173

[6] Ebert, Siegenthaler, Digital Radar Plot Extraktor - A System Module of an Automatic Air Traffic Control System, AGARD Conf. Proc. 66 on Advanced Radar Systems 1970 (Istanbul 1970)

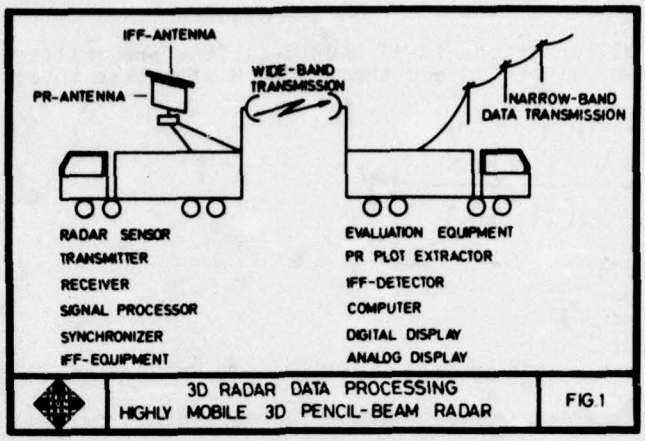

3D RADAR DATA PROCESSING
HIGHLY MOBILE 3D PENCIL-BEAM RADAR
FIG.1

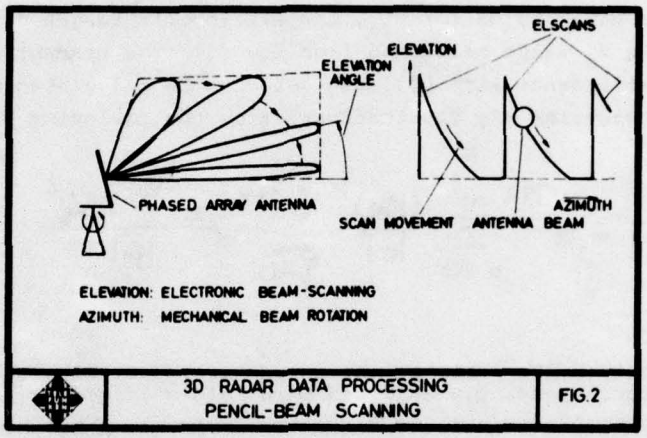

3D RADAR DATA PROCESSING
PENCIL-BEAM SCANNING
FIG.2

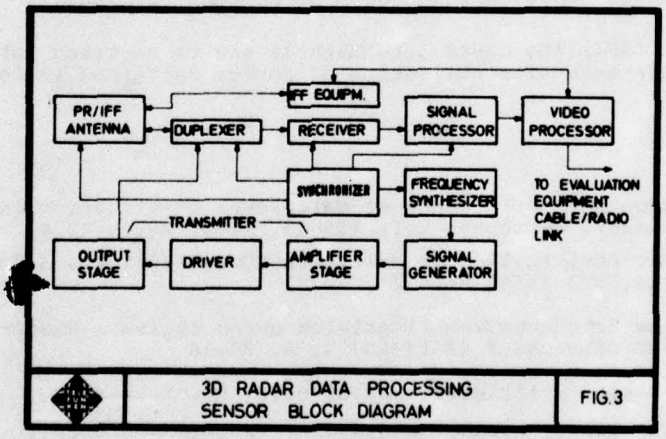

3D RADAR DATA PROCESSING
SENSOR BLOCK DIAGRAM
FIG.3

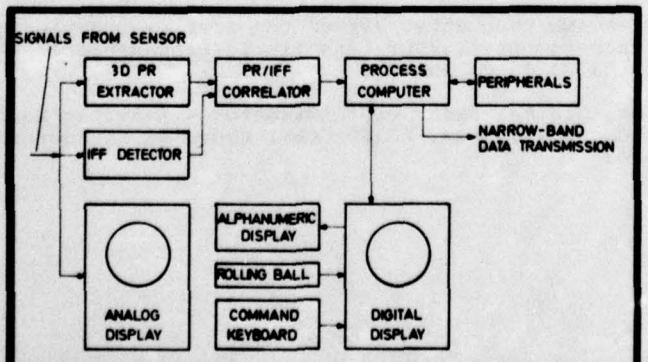

3D RADAR DATA PROCESSING
EVALUATION EQUIPMENT BLOCK DIAGRAM
FIG.4

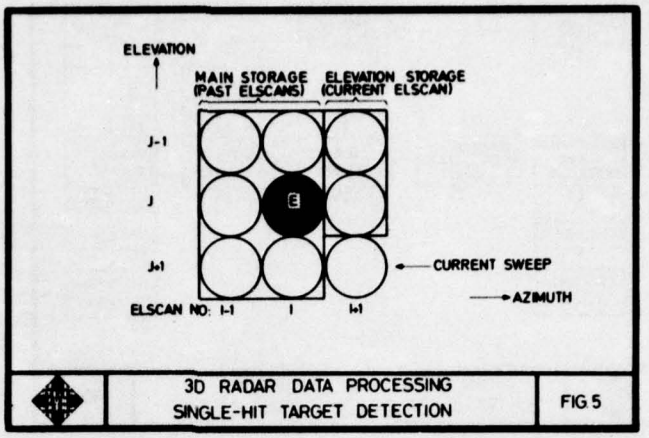

3D RADAR DATA PROCESSING
SINGLE-HIT TARGET DETECTION
FIG 5

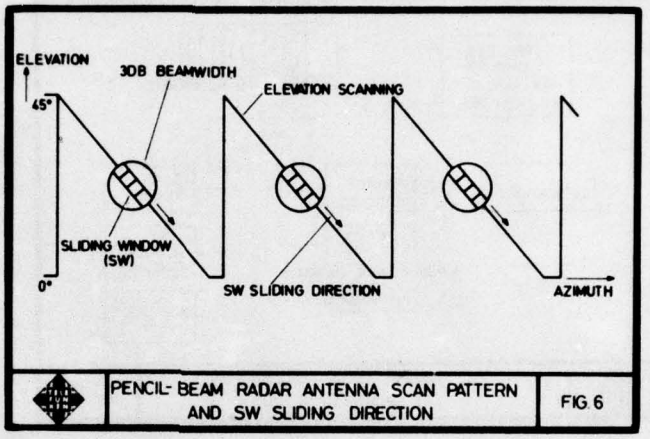

PENCIL-BEAM RADAR ANTENNA SCAN PATTERN
AND SW SLIDING DIRECTION
FIG 6

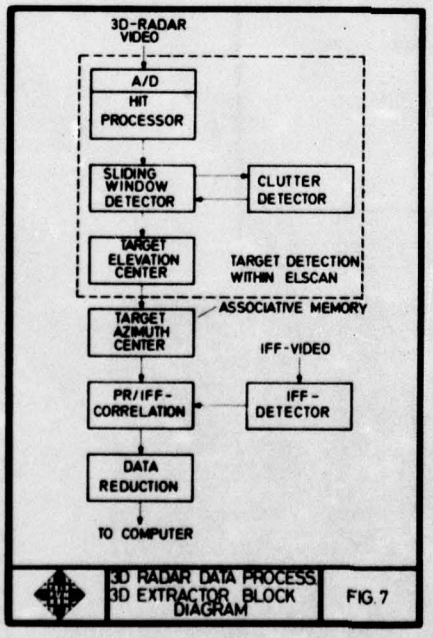

3D RADAR DATA PROCESS.
3D EXTRACTOR BLOCK DIAGRAM
FIG 7

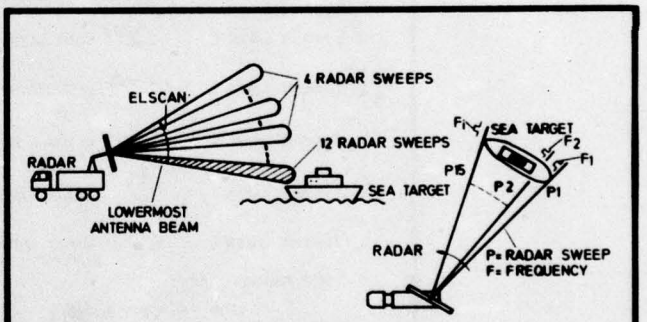

3D RADAR DATA PROCESSING
PRINCIPLE OF ADDITIONAL SEA TARGET EXTRACTION
FIG 8

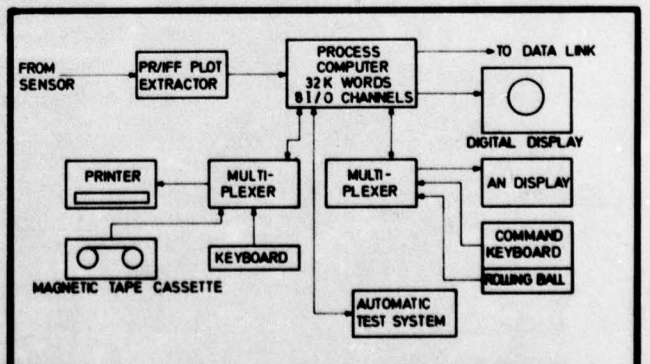

3D RADAR DATA PROCESSING
PROCESS COMPUTER • PERIPHERALS
FIG 9

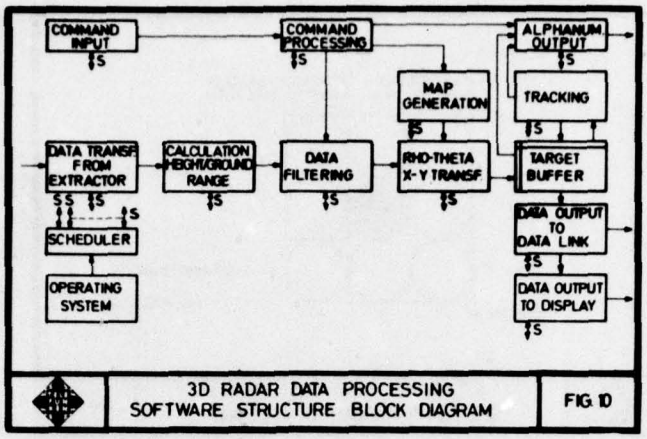

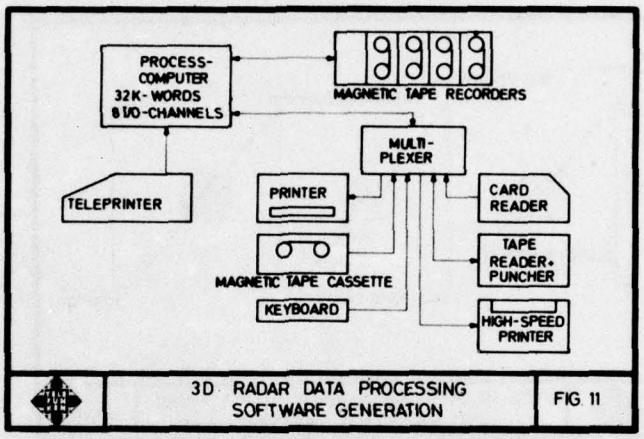

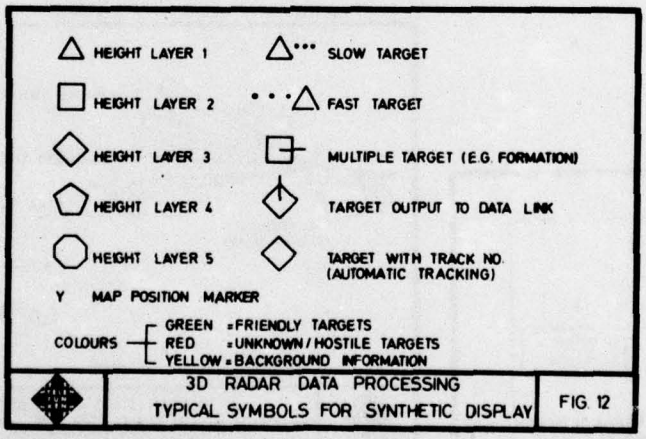

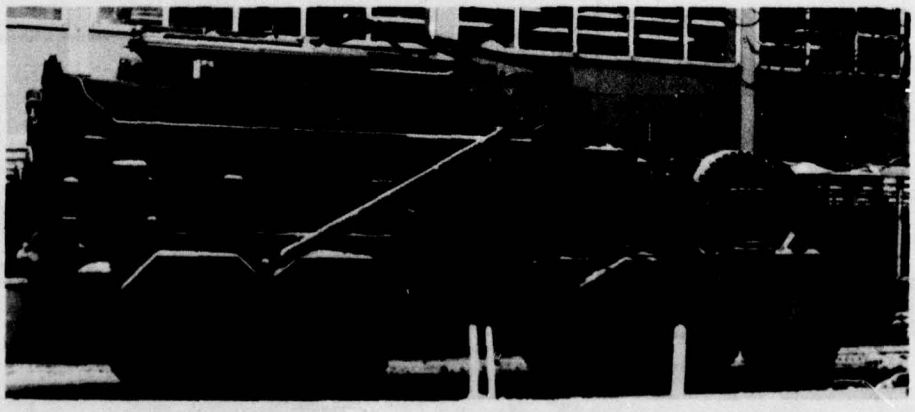

Fig.13 Sensor vehicle of the 3D radar with its shelter and with the antenna folded down

DISCUSSION

A L C QUIGLEY: My question concerns the clutter detector:

a) does it work in range, azimuth or both?

b) does it control the first threshold or the second?

H EBERT: In the clutter detector the amplitude mean values of some adjacent range bins ahead of and behind the sliding window 'in process' are determined. The result is used to adjust the target detection threshold in order to maintain a constant false alarm rate. As the sliding window is moved in accordance with the elevation scan, ie vertically downward, the clutter detector works in range and elevation. The integrator used is of the 'incoherent' type which means that the signal amplitude is processed for target detection. Therefore only one threshold is needed which is in fact the target detection threshold (and can thus be compared with the second threshold of the binary integrator normally used in conventional plot extractors).

R BAUERLE: You are tracking the targets and plot them with symbols. How do you separate unknown targets without IFF?

H EBERT: The radar is able to separate unknown targets according to its range, elevation and azimuth resolution capabilities. The range resolution, for instance, is determined by the use of pulse compression, which gives a far better range resolution than is needed for operational use of the system. Therefore, as indicated in the paper, a 'data reduction unit' is used to combine the information from several range cells.

C E MUEHE: On Fig 20-7 it says "Tracking is initiated manually by the operator, as an automatic initiation might involve a high calculation effort, and inadmissably high clutter rates might result in computer overflow". What clutter causes possible overflow? Do you get any complaints from remote users of the data due to the filtering of tracks caused by the manual initiation of tracks?

H EBERT: My intent was to emphasise that, under all circumstances, a flooding of the extractor (and the computer) with false targets should be avoided. The best way to do this is to use a highly effective signal processor in the radar, so that the clutter detector need not work, ie the target detection threshold remains unchanged. The clutter detector should have a 'watch dog' function only.

The use of manual track initiation rather than automatic initiation can be better understood from the operational purpose of the system. In most cases, the 3-D radar will be used as a sensor system for higher echelon command and control systems and automatic tracking will then not be used. In order to extend the system to the possible function of a mini-operation centre, tracking should be available without the need for adding a second computer, so both plot and track processing has to be done in this case in the same computer. In order to avoid uncontrolled overflow, the most suitable way was to omit automatic track initiation.

E FLAD: Does the tracking logic automatically detect targets flying in formation?

H EBERT: No. The operator acquires data on formation flights from other sources, and he inputs these manually to the computer, which displays a special symbol for such flights.

TECHNIQUES FOR AUTOMATIC TARGET DETECTION IN SCANNING 3-D RADAR

D.E.Hammers
ITT Gilfillan
7821 Orion Avenue
Van Nuys, CA 91405

SUMMARY

Rigorous methods are presented here for characterizing and analyzing sliding gate, Automatic Target Detection functions for 3-D scanning radars. Established detection techniques do not accurately apply to this problem since they do not account for correlation properties associated with the sliding action of the gate in relation to the azimuth-elevation hit pattern. A typical approach might be to consider Monte Carlo computer simulation to iteratively derive the best Automatic Target Detection function. However, this method can incur excessive computer time and manhours if the model has not been initially derived in consideration of correlation properties of the sliding gate. Here, through a stochastic difference equations approach, it is shown that the desired detection function is a Markov process and, as such, it can be systematically derived relative to maximizing target sensitivity relative to false alarm requirements. As a result, overall radar performance and implementation costs can be quickly assessed, leaving the investigation of scan modulation losses and target location accuracy to the more extensive resources required by the process of simulation. Performance curves and design methodology are generated for some particular examples for various target models.

1. INTRODUCTION

During the past decade, digital processing techniques have heavily impacted radar systems design [Hammers, D. E., 1974]. One of the most important areas of application has been that of Automatic Target Detection (also called Automatic Plot Extraction).

1.1. The Scanning 3-D Automatic Target Detection Problem.

The automatic detection process, in most general terms, consists of integration and thresholding of envelope detected returns to automatically declare the presence or absence of a target. The implementation from a digital sense can either be an accumulation of full amplitude A/D converted video followed by a threshold (Figure 1) or a single level, binary, thresholded video followed by a binary integrator with a second threshold (Figure 2). In some cases, partially limited video may be used to reduce signal losses [Hansen, V.G., 1974]. Here we treat the hard limited detection approach (in particular, the sliding binary detector) because it has been found to save hardware when considering the complex scan patterns found in scanning 3-D radar systems.

The binary integration or second threshold process commonly applied is the process of coincidence detection, which follows from the early work of Harrington [Harrington, J. V., 1955] and Schwartz [Schwartz, M., 1956]. This type of detection process is commonly called m out of n detection after the concept of Bernoulli trials (m successes out of n trials) and is treated in some detail in several modern radar texts [Meyer, D. P.]. When applying this process as a "sliding window" detector (for example in a 2-D radar), it can be shown to be equivalent to the commonly used "Sequential Observer" Detector [Skolnik, M. I., 1970]. In the latter, an accumulated count is increased by a constant on a thresholded hit and decreased by a constant on a miss. But the sliding m/n process is more readily implemented for a 3-D scan pattern since the "Sequential Observer" would tend to collapse or smooth pattern returns whereas the m/n correlator processes the pattern relative to its spatial distribution. The problem is further complicated in a 3-D search radar since, instead of a symmetric pattern, quite often a complicated *nonsymmetric azimuth-elevation scan pattern must be sequentially tested.*

A major difficulty exists with the scanning or sliding 3-D m/n process. It cannot be exactly analyzed by the method of Bernoulli Trials mentioned in modern radar texts since each trial is not statistically independent from the previous trial. In fact, there does not appear to be any current unified approach for designing this type of automatic detection process for 3-D scanning radar. For example, the accepted method for determining the optimum threshold and correlation criteria ($m_{opt} = 1.5\sqrt{n}$) applies more to the fixed dwell m/n process rather than the sliding gate. Also the sliding process will tend to be less "lossy" relative to ideal integration than the fixed dwell since it will not be subject to tar-

get straddle losses in the azimuth-elevation planes. It is intended then, in the following sections, to present methods for selecting and analyzing the sliding m/n process in relation to automatically detecting both non-fluctuating and fluctuating targets in a 3-D radar system.

A system analysis methodology is presented which is based on characterizing the sliding m/n detector as a Markov process in terms of stochastic difference equations. These equations in effect model the detection process as a stochastic operator which is used to accomplish systems performance analyses. Several examples are presented to illustrate the derived methods.

1.2. Formatting the Problem in Terms of a 3-D Beam Scan.

The 3-D scan which intercepts the target consists of an interlaced raster of points (corresponding to beam centers) sweeping in both the azimuth and elevation planes (see Figure 3). We can assume frequency agility in one plane or the other but for now this will not be an important issue. The target is considered to be a point source in that its elevation, azimuth and range dimensions are much less than the spacial extents of the 3 dB azimuth-elevation beamwidths, (θ_A, θ_E) and the transmitted pulsewidth (PW). The problem is to sequentially detect and correlate each new return with the appropriate number of returns already received in order to declare the presence or absence of a target. The appropriate number of returns (N_H) corresponds to the average number of returns within a boundary defined by θ_A and θ_E. Referencing to the 3 dB beamwidths is typical for radar sensitivity performance; however, we will be more specific and assume a beamshape loss of 3.2 dB relative to all returns within 1.1 θ_A x 1.1 θ_E [Blake, L. V., 1969]. Thus our analysis will be independent of scan modulation. As shown later, scan modulation can be accounted for more exactly by simulation.

The sliding coincidence gate should simultaneously correlate a number of returns less than or equal to N_H depending upon the criteria selected. The matched coincidence process is one which simultaneously correlates N_H returns every time a new return is received. We will call this a Matched Correlation (MC) Detector. Each positioning of the gate depends upon the sequential format of the azimuth-elevation scan. For purposes of example we will always assume that the beams are sequentially transmitted along an elevation plane and then the scan is stepped in azimuth and another elevation scan is completed. In this manner the MC Detector sequentially correlates the returns as shown in Figure 4. A Leading-Edge Correlation (LEC) Detector can be implemented when less than N_H returns are simultaneously correlated (see Figure 5). While the LEC Detector is less sensitive than the MC Detector, it is easier to implement since less memory is required. Basically, it becomes a multi-level correlator as opposed to the single level "matched" correlator. The performance equations developed in the following sections will be applied to both types.

2. STOCHASTIC DIFFERENCE EQUATION FORMULATION OF THE SLIDING COINCIDENCE DETECTOR

The analytical methods to be applied here depend on describing the action of the sliding correlator by difference equations. It will be shown that the equations consist of higher order differences of random variables, and therefore can be classified as stochastic difference equations. From this description we will be able to show that the sliding coincidence detector is a Markov-k process [Papoulis, A., 1965] (k being the highest order difference). As such, the method of characteristic equations (similar to that applied by Feller to the Gamblers Ruin problem [Feller, W., 1950] will be used to derive important performance measures for automatic detection. In the following a rather simple scan pattern is considered as the input signal space to develop the equations for a Matched Correlator. This will be extended to a more complex pattern where the equations for a Leading Edge Correlator will be discussed. Note that while specific patterns are used for both cases, the principles are general and can be applied to different conditions.

2.1. Matched Correlation Detector.

Consider the scan pattern shown in Figure 6 where it can be shown that N_H equals 4 hits on the average within the beamwidth criteria. The Matched Correlator implies that $N_H = n$, so, as the scan progresses (in this case up elevation scan A), an m/4 test must be made for each new beam position $A_1, A_2, A_3 \ldots$. Now define the following probabilities:

$p \triangleq$ Probability of a single return crossing the threshold

$q \triangleq 1 - p$

$S_N(m/N_H) \triangleq$ Probability that the gate will <u>not</u> have gone true on or before the Nth trial. That is, m successes will not occur within any contiguous four hits.

Sequential detection logic can be mechanized in relation to detecting the target as elevation scan A develops (see Figure 6). Letting

$G_N(m/n) =$ m/n conditions met in detection gate at the Nth trial (threshold crossings)

$+$ = logical "or"

then
$$G_N(1/4) = B_N + B_{N-1} + B_{N-2} + A_{N-1} + A_{N-2} \quad (2\text{-}1)$$

$$G_N(2/4) = B_N(B_{N-1} + A_{N-1} + A_{A-2}) + B_{N-1}(A_{N-1} + A_{N-2}) + A_{N-1}(B_{N-2} + A_{N-2}) + A_{N-2}\,B_{N-2} \quad (2\text{-}2)$$

$$G_N(3/4) = (A_{N-1} + A_{N-2})(B_N B_{N-1} + B_{N-1} B_{N-2}) + A_{N-1} A_{N-2}(B_N + B_{N-1} + B_{N-2}) \quad (2\text{-}3)$$

$$G_N(4/4) = B_{N-1} A_{N-1} A_{N-2}(B_N + B_{N-2}) \quad (2\text{-}4)$$

From the above logic, truth tables can be formulated to illustrate the Markov properties of the detection gate (see Table 1). The desired stochastic difference equations for S_N are written as linear combinations of the non-redundant a priori conditions, viz

$$S_N(1/4) = qS_{N-1} \quad (2\text{-}5)$$

$$S_N(2/4) = q\,S_{N-1} + pq^3\,S_{N-4} \quad (2\text{-}6)$$

$$S_N(3/4) = q\,S_{N-1} + pq\,S_{N-2} + q^2p^2\,S_{N-4} - q^3p^3\,S_{N-6} \quad (2\text{-}7)$$

$$S_N(4/4) = q\,S_{N-1} + qp\,S_{N-2} + qp^2\,S_{N-3} + qp^3\,S_{N-4} \quad (2\text{-}8)$$

Notice the negative coefficient associated with the S_{N-6} term for the 3/4 detector. This was necessary to negate an extra event added to the S_N probability space by the qpS_{N-2} term. Similar equations can be derived for larger values of N_H; however, the non-redundant conditions become more difficult to derive. The equations for m/5 are given in Appendix B.

2.2. Leading Edge Correlation Detector.

A hit analysis of the sample scan pattern shown in Figure 7 reveals that an N_H of about 16 hits exist. These hits can be correlated over at least 3 beams in the elevation plane and 8 separate elevation scans in the azimuth plane, thus requiring 16 delay elements to save all the hit data for a Matched Correlation Detector. Instead we apply a 2-dimensional Leading Edge Detector with $m_e/3 \times m_a/4$ requiring only about 1/2 the total delay elements. Sequential detection logic for this approach results as follows:

Define:

$A_{N_e} \triangleq$ successful threshold crossing in elevation scan A, beam position N_e

$A_{N_a} \triangleq$ successful meeting of the elevation gate criteria at azimuth position N_a

$G_{N_a} \triangleq$ successful meeting of the azimuth gate criteria at azimuth position N_a

"+" $\triangleq$ logic "or"

Then for a particular criteria, $m_e/n_e \times m_a/n_a = 2/3 \times 2/4$, we have,

$$A_{N_a}(2/3) = A_{N_e-1}(A_{N_e} + A_{N_e-2}) \quad (2\text{-}9)$$

$$B_{N_a}(2/3) = B_{N_e-1}(B_{N_e} + B_{N_e-2}) \quad (2\text{-}10)$$

$$C_{N_a}(2/3) = C_{N_e-1}(C_{N_e}+C_{N_e-2}) \tag{2-11}$$

$$D_{N_a}(2/3) = D_{N_e-1}(D_{N_e}+D_{N_e-2}) \tag{2-12}$$

and

$$G_{N_a}(2/4) = A_{N_a}(B_{N_a}+C_{N_a}) + B_{N_a}(C_{N_a}+D_{N_a}) + D_{N_a}(B_{N_a}+C_{N_a}) \tag{2-13}$$

Similar equations can be written for different values of $m_e/n_e \times m_a/n_a$.

To develop the Markov analysis for the Leading Edge Correlator, separate difference equations are derived for the elevation and azimuth planes. Following the model established in Figure 7 and the above logic, we apply Equations (2-5) through (2-8) for the azimuth plane. Further, it is clear that the following equations can be applied along the elevation plane.

$$S_{N_e}(1/3) = q\,S_{N_e-1} \tag{2-14}$$

$$S_{N_e}(2/3) = q\,S_{N_e-1} + pq^2\,S_{N_e-3} \tag{2-15}$$

$$S_{N_e}(3/3) = q\,S_{N_e-1} + qp\,S_{N_e-2} + qp^2 S_{N_e-3} \tag{2-16}$$

3. PROBABILITY OF FALSE ALARM

The Probability of False Alarm (P_F) will be defined in a manner similar to that discussed in Meyer and Mayer [Meyer, D. P., 1973] where they refer to Kaplan's and McFall's P_F as the inverse of the average time between false target indications. In that sense, our P_F will be the ratio of the average time that the sliding correlation is true to the sum of the average times it is false and true. Here we consider the input to the gate to be binary thresholded white Gaussian noise which is uncorrelated pulse-to-pulse. Correlated noise (distributed clutter) could also be treated by the stochastic difference equation approach but it is quite complicated and a subject for further work. Wirth [Wirth, W., 1968] presents some simulation results for the one-dimensional sliding window in correlated noise.

Let D_1 be the average number of trials (number of azimuth-elevation beam positions at a particular range bin) that the correlation gate stays true and D_0 be average number of trials the gate stays false, then from the discussion above it follows that

$$P_F = \frac{D_1}{D_1 + D_0} \tag{3-1}$$

Defining p_f as the single crossing Probability of False Alarm where [Marcum, J. I., 1948]

$$p_f = e^{-Y_b} \tag{3-2}$$

and $Y_b = \frac{d}{2\sigma_o}$, d = threshold, σ_o = RMS noise level.

Normally $p_f << 1$ so that $D_0 >> D_1$ and for small values of n, $D_1 \approx 1$ thus we can write

$$P_F = \frac{1}{D_0} \tag{3-3}$$

Now note from the definition of S_N that

$1 - S_N \doteq$ Probability that gate goes true sometime between trials 1 and N

Also let T_N be the probability that the gate goes true exactly at the Nth trial, then

$$1 - S_N = T_1 + T_2 + T_3 + \ldots + T_N \tag{3-4a}$$

and $$1 - S_{N-1} = T_1 + T_2 + T_3 + \ldots + T_{N-1} \quad (3\text{-}4b)$$

or $$T_N = (S_{N-1} - S_N) \quad (3\text{-}5)$$

Now since $p_f << 1$ we can reasonably assume that an all zero initial state exists when the gate is off, so that the average number of trials existing from the gate's initial state to the trial it first turns on can be determined from:

$$D_0 = \sum_{N=1}^{\infty} N T_N \quad (3\text{-}6)$$

Equation 3-6 above is solved by computing the first moment from the characteristic function (or in this case polynomial), f(x), of T_N. Letting

$$f(x) = E(x^N) = \sum_{N=0}^{\infty} x^N T_N \quad (3\text{-}7)$$

it follows that

$$D_0 = f'(x)\Big|_{x=1} \quad (3\text{-}8)$$

In Appendix A the method of solving for D_0 is illustrated when m/n is 3/4. In a similar fashion we can solve D_0 for ther m/n conditions as shown in Table 2 for all nontrivial cases of m/2, up to m/5. P_F is then computed for the Matched Correlation Detector by applying Equation (3-3) directly. P_F for the Leading Edge Detector is found by applying Equation (3-3) first on the elevation criteria m_e/n_e and then using this result on the azimuth criteria m_a/n_a as shown below.

Let P_{F_e} ≙ probability of False Alarm function out of elevation gate

P_{F_a} ≙ probability of False Alarm function out of azimuth gate

then

$$P_F = P_{F_a}(P_{F_e}(p_f)) \quad (3\text{-}9)$$

where

$$P_{F_a} = \frac{1}{D_0(m_a/n_a)}$$

$$P_{F_e} = \frac{1}{D_0(m_e/n_e)}$$

4. PROBABILITY OF DETECTION

Since we are not considering the effects of scan modulation the Probability of Detection will be dependent on the threshold determined from P_F analysis above, N_H, the target model (input single pulse snr) and the sliding gate correlation function defined by the previous stochastic difference equations. In general, it follows from the definition of S_N that for N hits on the target

$$P_{D_N}(m/n) = 1\text{-}S_N(m/n) \quad (4\text{-}1)$$

4.1. Matched Correlation Signal Detection.

For the MC Detector, we seek to determine P_{D_N} relative to the instant the N_H^{th} beam is sampled by the sliding matched gate, i.e., $P_{D_N}(m/n \rightarrow N_H)$. For example, considering m/n = 2/4, we have from Equations (2-6) and (4-1) that

computation of the height value, conversion of target coordinates from rho/theta into X/Y coordinates, etc., preparation of information for narrow-band transmission, as well as system monitoring using a computer-controlled display. This includes also the ope-

$$P_{D_4}(2/4) = 1-S_4(2/4) \tag{4-2}$$

Under the above assumptions, and since $p_f << 1$, the gate can be assumed loaded with all zeroes prior to sampling the N_H target returns. Letting p_d be the Probability of a single beam threshold crossing when signal is present, $P_{D_4}(2/4)$ is determined as follows:

$$S_0 = 1 \tag{4-3a}$$

$$S_1 = 1 \tag{4-3b}$$

$$S_2 = 1-p_d^2 \tag{4-3c}$$

$$S_3 = q_d^2 (1+2p_d) \tag{4-3d}$$

so that

$$P_{D_4}(2/4) = 6p_d^2 - 8p_d^3 + 3p_d^4 \tag{4-4}$$

Note: This equation is identical to the 2/4 fixed window Bernoulli trials result. So when $N = N_H$ for the MC Detector, fixed window analysis holds only for detection. False alarm analysis still follows the previous section.

Additional equations for other m/n conditions are given in Table 3. For a non-fluctuating (Marcum) target it is well-known [Marcum, J. I., 1948] that

$$P_d = \int_{Y_b}^{\infty} Q(x, y)\, d_y \tag{4-5}$$

where $Q(\cdot)$ = Marcum Q function

x = single pulse snr

Thus the x corresponding to the required P_{D_N} is solved, for the 2/4 case for example, by applying (4-4) and (4-5). For a fluctuating target, that is, Swerling Case 1 [Swerling, P., 1954], the average value of P_{D_N} has to be computed relative to the target snr probability density function. Let $p(x, \bar{x})$ be this density function with $\bar{x}$ the average value of x, then it follows for the Case 1 target that

$$P_{D_N} = \int_0^{\infty} p(x, \bar{x})\, P_{D_N}(x)\, dx \tag{4-6}$$

where $P_{D_N}(x)$ is the probability of the sliding gate being true and for a square law detector

$$p(x, \bar{x}) = \frac{1}{\bar{x}}\, e^{-x/\bar{x}} \quad (x \geq 0) \tag{4-6a}$$

and for the example of m/n = (2/4),

$$P_{D_4}(x) = 6\left(\int_{Y_b}^{\infty} Q(x, y)\, dy\right)^2 - 8\left(\int_{Y_b}^{\infty} Q(x, y)\, dy\right)^3 + 3\left(\int_{Y_b}^{\infty} Q(x, y)\, dy\right)^4 \tag{4-6b}$$

If all N_H returns can be made statistically independent (e.g., completely decorrelating the target with frequency agility) then it follows [Swerling, P., 1954] that

$$P_d = e^{-\frac{Y_b}{1+\bar{x}}} \tag{4-7}$$

and $\bar{x}$ is solved by successive applications of (4-4) and (4-7). Partial decorrelation by frequency scanning results in a more complicated set of equations and will not be presented here. Needless to say it is bounded by the results obtained from (4-6) and (4-7). Specific results for this case can be obtained by simulation as discussed in a later example.

4.2. Leading Edge Correlation Signal Detection.

For the LEC Detector we seek to determine P_{D_N} relative to the instant the $N_H{}^{th}$ beam is sampled by the combination of sliding elevation and azimuth gates. Here it is assumed that both n_e and n_a are less than N_H. Further, for sake of example, we assume the elevation criteria is matched to the average number of hits within the elevation beamwidth criteria; whereas, the azimuth criteria is somewhat less than the azimuth beamwidth criteria such that

$$n_a < P \tag{4-8}$$

where P represents the number of elevation scans eclipsed along the azimuth plane. Figure 8 illustrates for $(n_e, n_a) = (3, 4)$. Letting (m_e, m_a) be (2, 2) then the full detection criteria over N_H hits become

$$m_e/n_e \, X \, m_a/n_a \, X \, P = 2/3 \, X \, 2/4 \, X \, P \tag{4-9}$$

The LEC Detector model is determined from the simultaneous solution of Equations (2-15) and (2-6) where $N \rightarrow P$ in the latter. Then depending on the statistical target model (4-5), (4-6) or (4-7) are applied to find the required single pulse snr.

5. EXAMPLES

The following section attempts to illustrate the method of analyzing the sliding 3-D detector by simple example. Extensive performance curves could be generated in relation to increasing the number of hits. However, it was felt that this should be left to the analyst depending on his particular scan program and beam shapes.

5.1. Matched Correlation Detector.

The object here will be to generate a set of pertinent performance curves for the MC Detector for the particular case of $N_H = 4$ hits. Applying the equations of Table 2 for n = 4, the (P_F, p_f) curves of Figure 9 can be developed. The Probability of Detection versus snr is investigated for various values of P_F by computing the threshold Y_b from the corresponding values of p_f from these curves. Then the equations of Table 3 are applied for m/n = 2/4, 3/4 and 4/4 and the snr target model is included from Equations 4-5, 4-6 or 4-7. A set of resulting target sensitivity curves are shown in Figure 10 for $p_f = 10^{-2}$. Note that if a P_F of about 10^{-6} was desired, the 3/4 criteria is best. On the other hand we see that added sensitivity may be obtained by using the 2/4 detector but another set of curves would have to be generated for $p_f = 10^{-3}$. Another important point to note is the severe penalty paid in relation to the target fluctuation model. Notice that the "harder" sliding m/n criteria (i.e., closer m approaches n) causes high snr penalities. In particular notice that the Case II target is more "lossy" than the Case I target for m = n. This is due to the fact that it is more difficult for all the returns of a pulse-to-pulse fluctuating model to cross the threshold than for all pulses of group fluctuation. This, of course, is just the opposite of the ideal summing results and would also be true for the fixed coincidence detector. Finally, if the sliding MC Detector is compared to ideal video integration of 4 pulses, about 1-1.2 dB loss is apparent (see Figure 10 for the 2/4 NF case). This is about .5 dB less than the fixed coincidence detector since extra patterns are sensed by the overlapping action of the sliding gate.

5.2. Leading Edge Correlation Detector

The object here will be to generate a set of pertinent performance curves for a 3-D scan in which about 24 hits occur within $1.1\,\theta_E \times 1.1\,\theta_A$ such that about 3 hits on the average occur along each elevation scan. This type problem is illustrated back in Figure 8 where an LEC Detector is suggested for $(n_e, n_a, P) = (3, 4, 8)$. The (P_F, p_f) analyses can be investigated by substituting the appropriate equations of Table 2 into Equation 3-9. Comparing the performance of two criteria, i.e.,

$$m_e/n_e \, X \, m_a/n_a = \left\{(2/3 \, X \, 2/4), \; (3/3 \, X \, 2/4)\right\} \tag{5-1}$$

we have,

$$P_F^{-1} = \frac{2 - Q_{F_e}{}^3}{P_{F_e}(1 - Q_{F_e}{}^3)} \tag{5-2}$$

where

$$P_{F_e}^{-1}(2/3) = \frac{2 - q_f^2}{p_f(1 - q_f^2)}, \quad P_{F_e}(3/3) = \frac{p_f^3}{1 + p_f + p_f^2} \tag{5-3}$$

and $$Q_{F_e} = 1 - P_{F_e} \tag{5-4}$$

$$q_f = 1 - p_f \tag{5-5}$$

Plotting (P_{F_e}, p_f) as in Figure 9, it can be shown for $P_F = 10^{-6}$ that $p_f = 2 \times 10^{-2}$ and $p_f = 10^{-1}$ for m_e/n_e of 2/3 and 3/3 respectively. Target sensitivity is investigated by comparing the two criteria for P = 8, or when

$$m_e/n_e \text{ X } m_a/n_a \text{ X } P = \left\{(2/3 \text{ X } 2/4 \text{ X } 8), \quad (3/3 \text{ X } 2/4 \text{ X } 8)\right\} \tag{5-6}$$

we have

$$P_{D_e}(2/3) = 3p_d^2 - 2p_d^3 \tag{5-7}$$

$$P_{D_e}(3/3) = p_d^3 \tag{5-8}$$

and upon solving (2-6) and (4-1) for N = 8 it follows that

$$P_{D_8}(2/4) = 1 - Q_{D_e}^5(1 + 5P_{D_e} - 3P_{D_e}^2 - 3P_{D_e}^3) \tag{5-9}$$

with $$P_{D_e} = 1 - Q_{D_e} \tag{5-10}$$

Establishing a single equation relating P_{D_8} to p_d by substituting (5-7) and (5-8) into (5-9) is tedious. Instead we plot all three equations on a single input-output probability graph as shown in Figure 11 and graphically solve for the final (P_{D_8}, p_d) curves. Target sensitivity curves can then be generated from these results and Equations (4-5), (4-6) and (4-7) as shown in Figure 12. Notice that we did not "harden" the detection criteria enough here to cause the Case III target to exhibit better performance than the Case II as in the MC example. This LEC Detector loses about 2.5-3 dB over ideal integration of 24 pulses at $P_F = 10^{-6}$ for the non-fluctuating target (see Figure 12). Similar losses can be determined for the fluctuating target models. Recall from the previous example that the MC Detector losses were not of this magnitude for 4 pulses but the cost to build a 24 MC Detector would be prohibitive.

6. CONCLUSION

A method for designing and analyzing an automatic target detection function for a scanning 3-D radar has been presented. We purposely avoided computer simulation methods since the goal was to develop the theory necessary to derive a detection model that would be applied at the beginning of simulation analysis. For example, a simulation to investigate false alarm performance can be very costly and, at best, is still usually an approximation. In Section 3 a method for deriving a closed form expression for the Probability of False Alarm was developed, so the foregoing activity is not needed.

Since binary, scanning 3-D Automatic Detection is a non-linear process, several aspects of it have to be addressed by simulation. Signal-to-noise ratio losses due to antenna scan modulation fall into this category; however, as pointed out in Section 1, a 3.2 dB loss usually associated with Gaussian Beams (1.6 dB in each angle plane) [Blake, L. V., 1969] can be taken without the use of simulation. This issue of angle accuracy for target location is heavily dependent on beam shape and as a result, Monte Carlo analysis seems to be the best means for investigation. It can be shown by simulation [Landreth, J. H., 1976] that the method of Edge Point Estimation provides very good angle accuracy when applied to the sliding binary detector. The issue of partially correlated returns due to frequency or spatial decorrelation within the 3-D hit pattern results in extremely complicated P_D equations for [illegible] binary [illegible] would only seem worthwhile to generate exact equations for those patterns in which N_c is [illegible] order 4). Thus simulation analysis would also be very

APPENDIX A

DERIVATION OF GATE DURATION FOR 3/4 SLIDING CORRELATION DETECTOR

The Probability of the 3/4 sliding detector not being true by the N^{th} trial is described by the following stochastic difference equation

$$S_N - q\,S_{N-1} - pq\,S_{N-2} - q^2p^2S_{N-4} + q^3p^3S_{N-6} = 0 \qquad \text{(A1)}$$

subject to the initial conditions,

$$S_0 = 1 \qquad \text{(A1-1)}$$

$$S_1 = 1 \qquad \text{(A1-2)}$$

$$S_2 = 1 \qquad \text{(A1-3)}$$

$$S_3 = 1 - p^3 \qquad \text{(A1-4)}$$

$$S_4 = q^2(1 + 2p + 3p^2) \qquad \text{(A1-5)}$$

$$S_5 = q^3(1 + 2p + 3p^2) + q^2(p + 2p^2) \qquad \text{(A1-6)}$$

Defining the characteristic function f(x) as

$$f(x) = \sum_{N=0}^{\infty} S_N x^N \qquad \text{(A2)}$$

the following equations can be formed:

$$f(x) = \sum_{N=0}^{5} S_N x^N + \sum_{N=6}^{\infty} S_N x^N \qquad \text{(A3)}$$

$$-qxf(x) = -q \sum_{N=1}^{5} S_{N-1}x^N - q \sum_{N=6}^{\infty} S_{N-1}x^N \qquad \text{(A4)}$$

$$-qpx^2f(x) = -qp \sum_{N=2}^{5} S_{N-2}x^N - qp \sum_{N=6}^{\infty} S_{N-2}x^N \qquad \text{(A5)}$$

$$-q^2p^2x^4f(x) = -q^2p^2 \sum_{N=4}^{5} S_{N-4}x^N - q^2p^2 \sum_{N=6}^{\infty} S_{N-4}x^N \qquad \text{(A6)}$$

$$q^3p^3x^6f(x) = q^3p^3 \sum_{N=6}^{\infty} S_{N-6}x^N \qquad \text{(A7)}$$

Summing (A3) through (A7) and from (A1) it follows after some manipulation that

$$f(x)\,[1 - qx - qpx^2 - q^2p^2x^4 + q^3p^3x^6] =$$

$$S_0 + (S_1 - qS_0)x + (S_2 - qS_1 - qpS_0)x^2$$

$$+ (S_3 - qS_2 - qpS_1)x^3 + (S_4 - qS_3 - qpS_2 - q^2p^2S_0)x^4$$

$$+ (S_5 - qS_4 - qpS_3 - q^2p^2S_1)x^5 \qquad \text{(A8)}$$

Applying the initial conditions (A1-1) to (A1-6), f(x) becomes

$$f(x) = \frac{1 + px + p^2x^2 + p^2qx^3 - qp^3x^4 - q^2p^3x^5}{1 - qx - q\,px^2 - q^2p^2x^4 + q^3p^3x^6} \qquad (A9)$$

But from equation (3-8) the expected Duration, D_0, that the sliding gate is not true is determined as

$$D_0 = f'(x)\Big|_{x=1} \qquad (A10)$$

so that finally we have

$$D_0 = \frac{1 + p + p^2 + p^2q - qp^3(1+q)}{p^2(1 - q^2 + pq^3)} \qquad (A11)$$

APPENDIX B

STOCHASTIC DIFFERENCE EQUATIONS FOR m/5 GATE

$p \doteq$ Probability of a threshold crossing on any hit.

$q \doteq 1 - P$

$S_N(m/5) \doteq$ Probability that the gate will not have gone true on or before the N^{th} trial. When m successes out of 5 attempts define the sliding gate.

$$S_N(1/5) = q\,S_{N-1} \qquad (B1)$$

$$S_N(2/5) = q\,S_{N-1} + pq^4S_{N-5} \qquad (B2)$$

$$S_N(3/5) = q\,S_{N-1} + pq^2S_{N-3} + 2p^2q^3S_{N-5} - p^3q^5S_{N-8} - p^4q^6S_{N-10} \qquad (B3)$$

$$S_N(4/5) = q\,S_{N-1} + pqS_{N-2} + p^2q^2S_{N-4} + 2p^3q^2S_{N-5} - p^4q^3S_{N-7} - p^6q^4S_{N-10} \qquad (B4)$$

$$S_N(5/5) = q\,S_{N-1} + qpS_{N-2} + qp^2S_{N-3} + pq^3S_{N-4} + qp^4S_{N-5} \qquad (B5)$$

ACHNOWLEDGEMENT

The author would like to acknowledge John Bailey and Dick Kaltenbach for their contributions and suggestions for applying the difference equation approach to the sliding gate detection problem.

REFERENCES

Blake, L. V., "A Guide to Basic Pulse-Radar Maximum-Range Calculation - Part 1," Naval Research Laboratory Report 6930, Washington, D. C., Dec. 1969, p. 71.

Feller, W., Probability Theory and its applications, Vol. 1, Wiley, New York, London, 1950, p. 302.

Hammers, D. E., "On Digital Signal Processing in Radar Systems," Conference Record, Eighth Asilomar Conference on Circuits, Systems, and Computers, Dec. 1974, p. 429-439.

Hansen, V. G., "Optimization and Performance of Multi-Level Quantization in Automatic Detectors," IEEE AES, March 1974.

Harrington, J. V., "An Analysis of the Detection of Repeated Signals in Noise by Binary Integration," IRE Trans., Vol. IT-1, p. 1-9, March 1955.

Landreth, J. H., "Simulation of Radar Tracking of a Scintillating Glinting Aircraft Target in a Multipath Environment," To be presented at the 1976 AGARD Symposium, The Hague, Netherlands, June 1976.

Marcum, J. I., "A Statistical Theory of Target Detection by Pulsed Radar, Mathematical Appendix," ASTIA Document No. AD101882, 1 July 1948.

Meyer, D. P., H. A. Mayer, Radar Target Detection, Academic Press, New York and London, p. 19, p. 79.

Papoulis, A., Probability, Random Variables and Stochastic Processes, McGraw-Hill, 1965, p. 536.

Schwartz, M., "A Coincidence Procedure for Signal Detection," IRE Trans., Vol. IT-2, No. 4, p. 135-139, Dec. 1956.

Skolnik, M. I., Radar Handbook, McGraw-Hill, 1970, p. 38-24.

Swerling, P., "Probability of Detection of Fluctuating Targets," Rand Research Memo - 1217, March 1954.

Wirth, Wulf-Dieter, "Das statistische Verholten des Wanderfenster-Detektors bei korreliertem Rauschen," Information from the Research Institute for Electronics and Mathematics, Wirthhoven, NTZ, 1968 Heft 5, p. 255.

TABLE 1

Non-Redundant Markov Conditions for the Matched m/4 Detector

m/n	NON-REDUNDANT A PRIORI CONDITIONS CONTRIBUTING TO NOT TRUE STATE ON OR BEFORE TRIAL N							PROBABILITY OF NON-REDUNDANT GATE NOT GOING TRUE ON OR BEFORE TRIAL N
	N-6	N-5	N-4	N-3	N-2	N-1	N	
1/4	x*	x	x	x	x	x	0	$q\,S_{N-1}$
2/4	x	x	x	x	x	x	0	$q\,S_{N-1}$
	x	x	x	0	0	0	1	$p\,q^3\,S_{N-4}$
3/4	x	x	x	x	x	x	0	$q\,S_{N-1}$
	x	x	x	x	x	0	1	$qp\,S_{N-2}$
	x	x	x	0	0	1	1	$q^2p^2\,S_{N-4}$
	x	0	0	1	1	0	1	$-q^3p^3\,S_{N-6}$
4/4	x	x	x	x	x	x	0	$q\,S_{N-1}$
	x	x	x	x	x	0	1	$qp\,S_{N-2}$
	x	x	x	x	0	1	1	$qp^2\,S_{N-3}$
	x	x	x	0	1	1	1	$qp^3\,S_{N-4}$

TP161 - 7

*"x" IMPLIES THAT EITHER A 1 OR 0 IS PRESENT

TABLE 2

Solutions for D_0 for m/n Conditions

GATE CRITERIA		D_0
n	m	
2	2	$\frac{1+p}{p^2}$
3	2	$\frac{2-q^2}{p(1-q^2)}$
3	3	$\frac{1+p+p^2}{p^3}$
4	2	$\frac{2-q^3}{p(1-q^3)}$
4	3	$\frac{1+p+p^2(1+q^3)}{p^2(1-q^2+pq^3)}$
4	4	$\frac{1+p+p^2+p^3}{p^4}$
5	2	$\frac{2-q^4}{p(1-q^4)}$
5	3*	$\frac{Q_0(3/5)}{p^2(1+q-2q^3+pq^5+p^2q^6)}$
5	4*	$\frac{Q_0(4/5)}{p^3(1+q-2q^2+pq^3+p^3q^4)}$
5	5	$\frac{1+p+p^2+p^3+p^4}{p^5}$

TP161 - 9

*Q_0 (m/5) = COMBINATION OF PROBABILITIES THAT m/5 GATE WILL NOT BE TRUE BEFORE THE 10TH TRIAL

TABLE 3

Matched Correlation Detector, $N = N_H$

GATE CRITERIA		$P_{D_N}(m/n = N_H)$
n	m	
2	2	p^2
3	2	$3p^2 - 2p^3$
3	3	p^3
4	2	$6p^2 - 8p^3 + 3p^4$
4	3	$4p^3 - 3p^4$
4	4	p^4

TP161 - 10

$p = p_d$ = SINGLE HIT PROBABILITY OF DETECTION

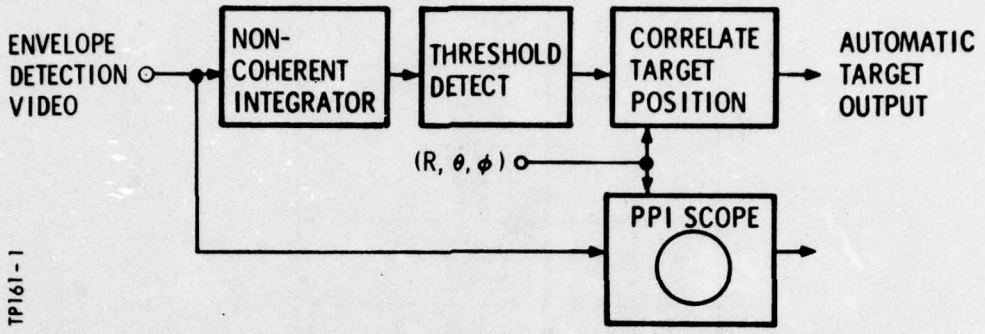

Fig.1 Full amplitude ATD process

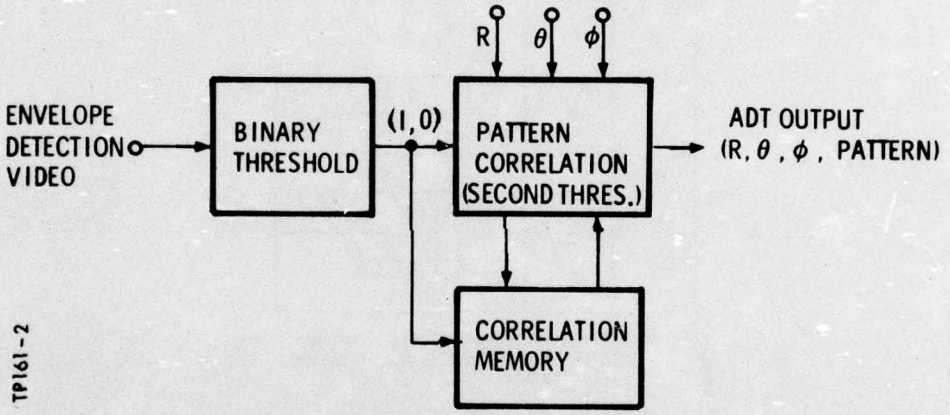

Fig.2 Binary ATD process

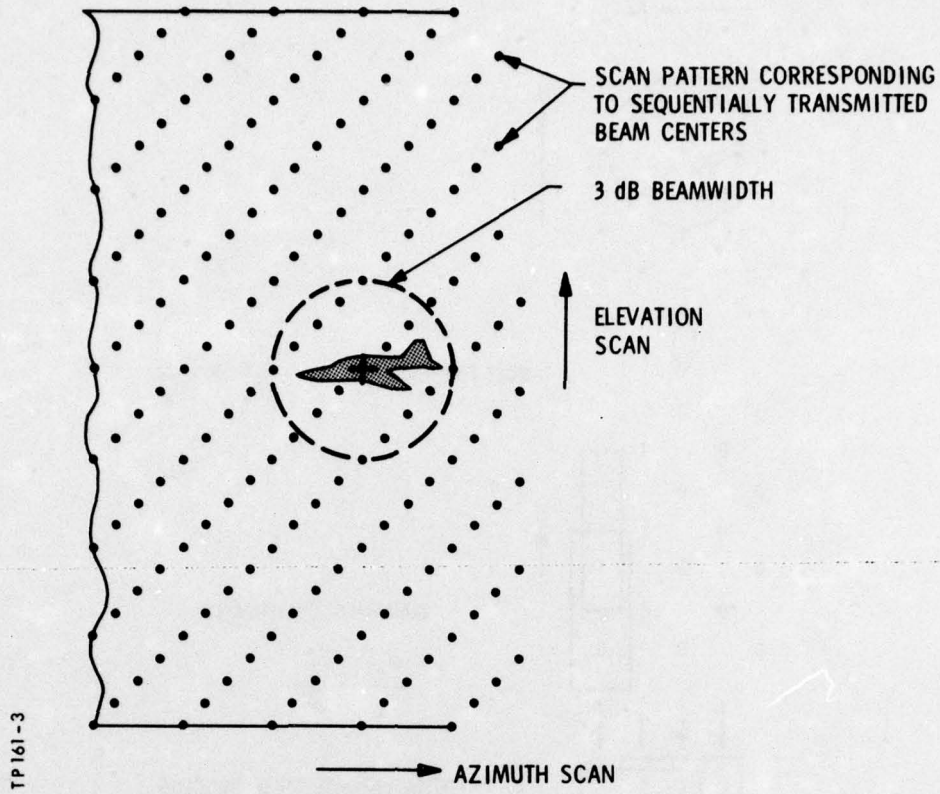

Fig.3 Typical 3-D search scan

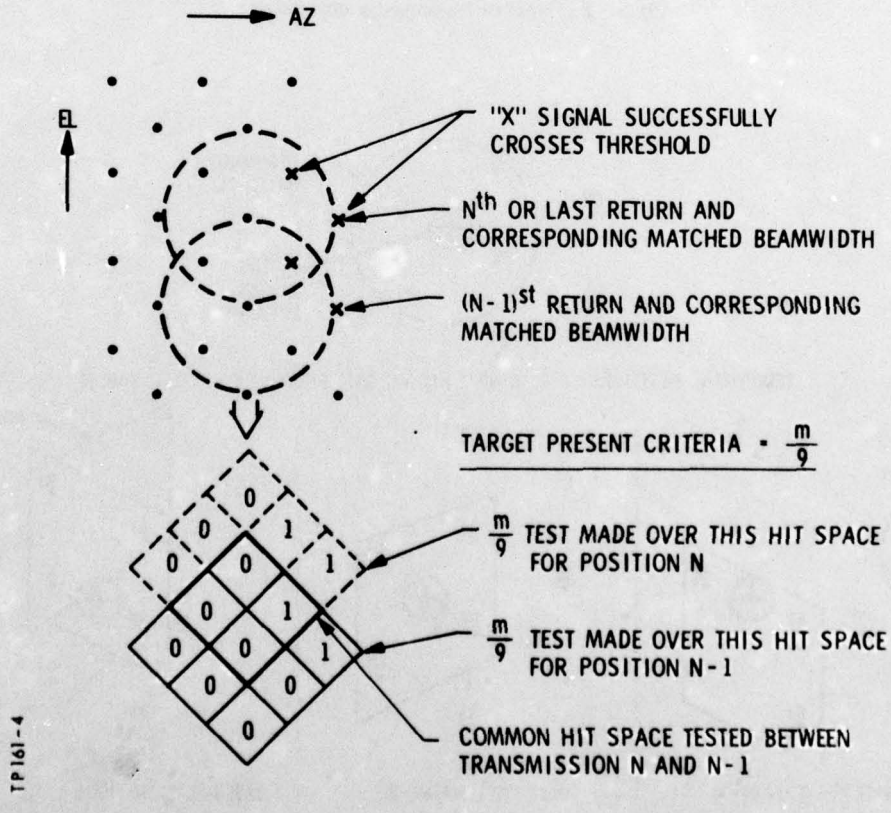

Fig.4 Example of fully matched correlator

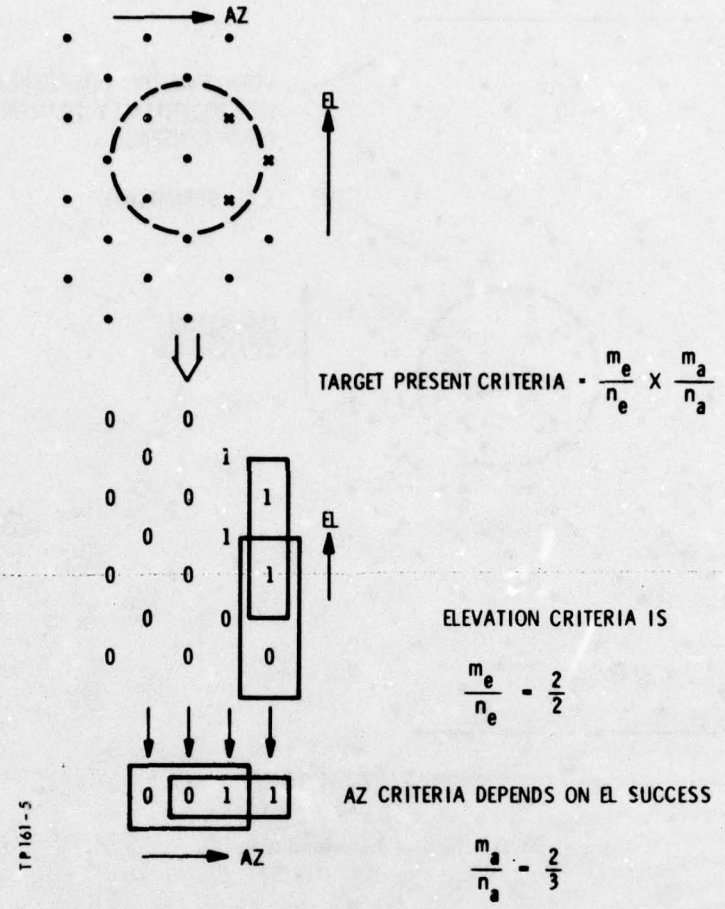

Fig.5 Example of leading edge correlator

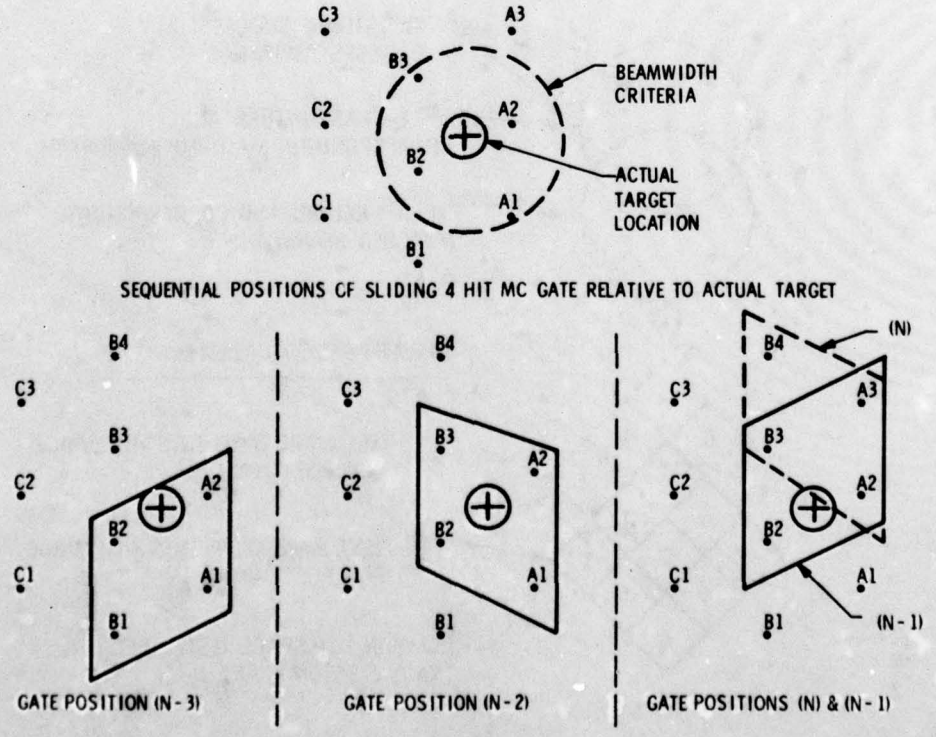

Fig.6 Four hit example of MC detector

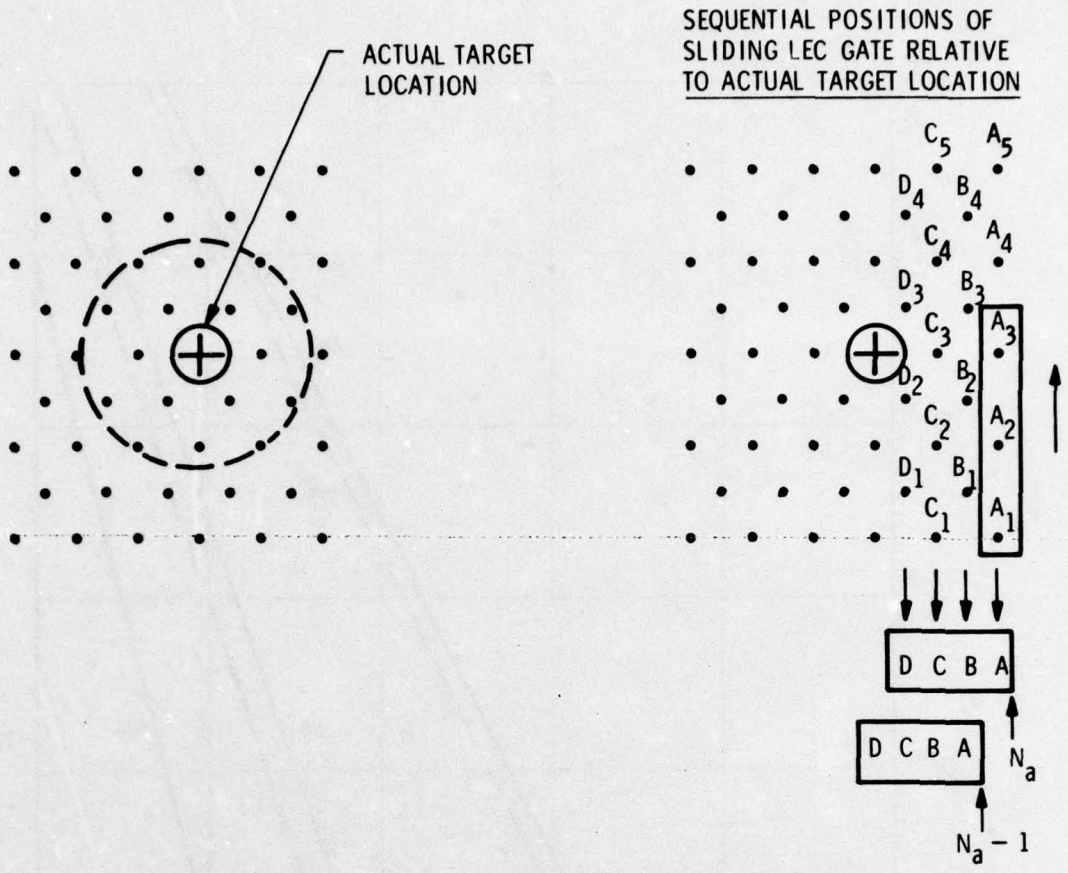

Fig.7 Sixteen hit example of LEC detector

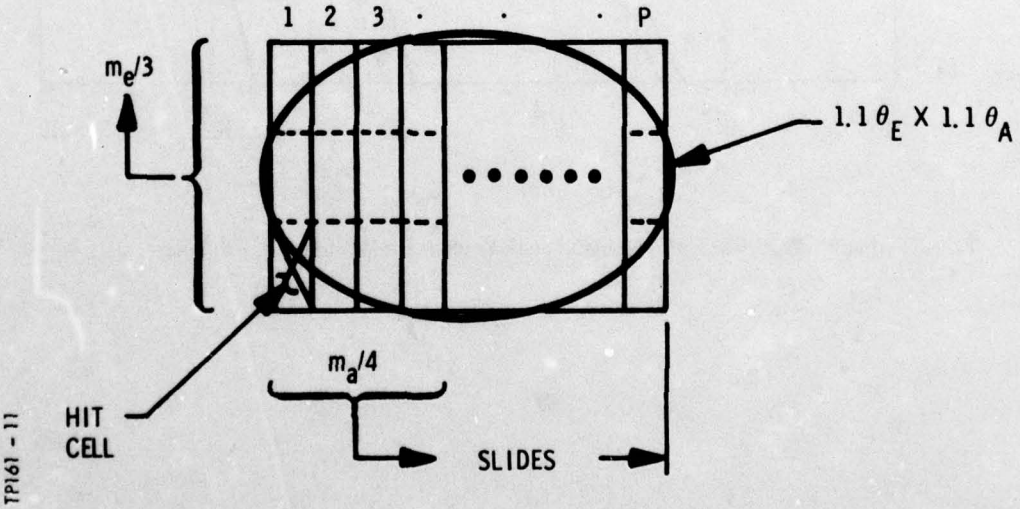

Fig.8 Leading edge correlation ($m_e/3 \times m_a/4 \times P$)

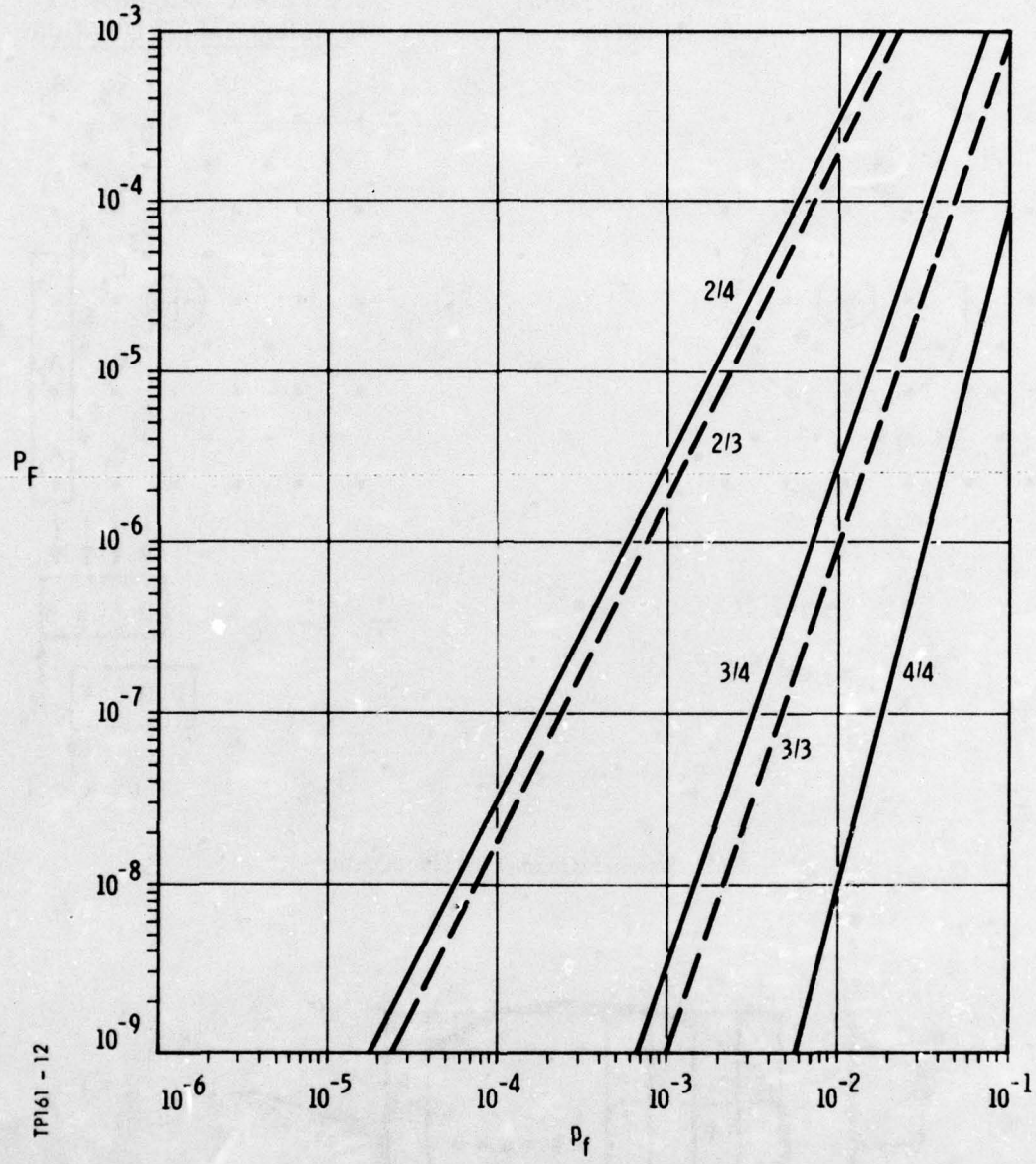

Fig.9 Probability of false alarm analysis chart for MC and LEC examples

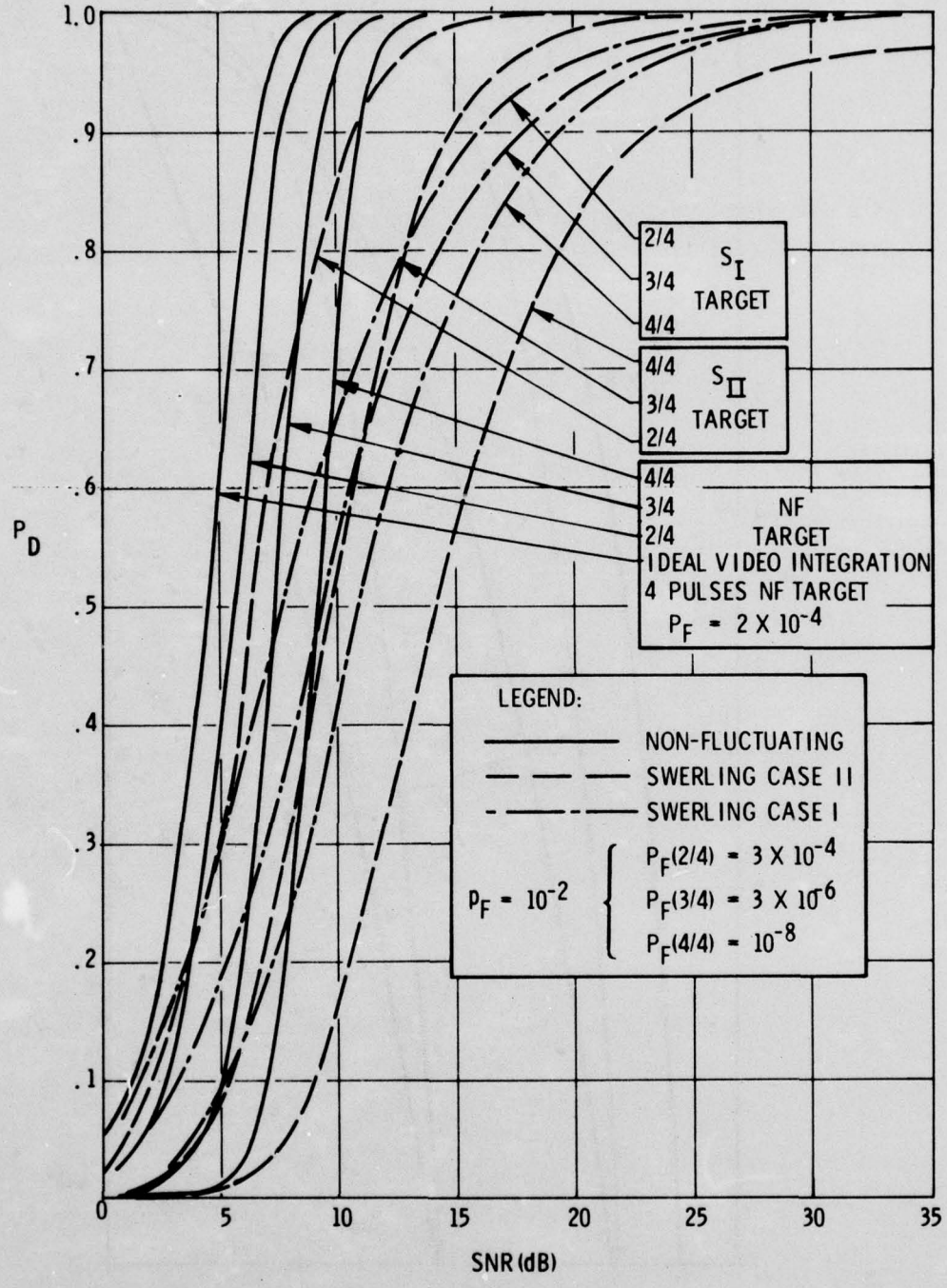

Fig.10 Probability cf detection vs snr for m/4 matched correlation detector

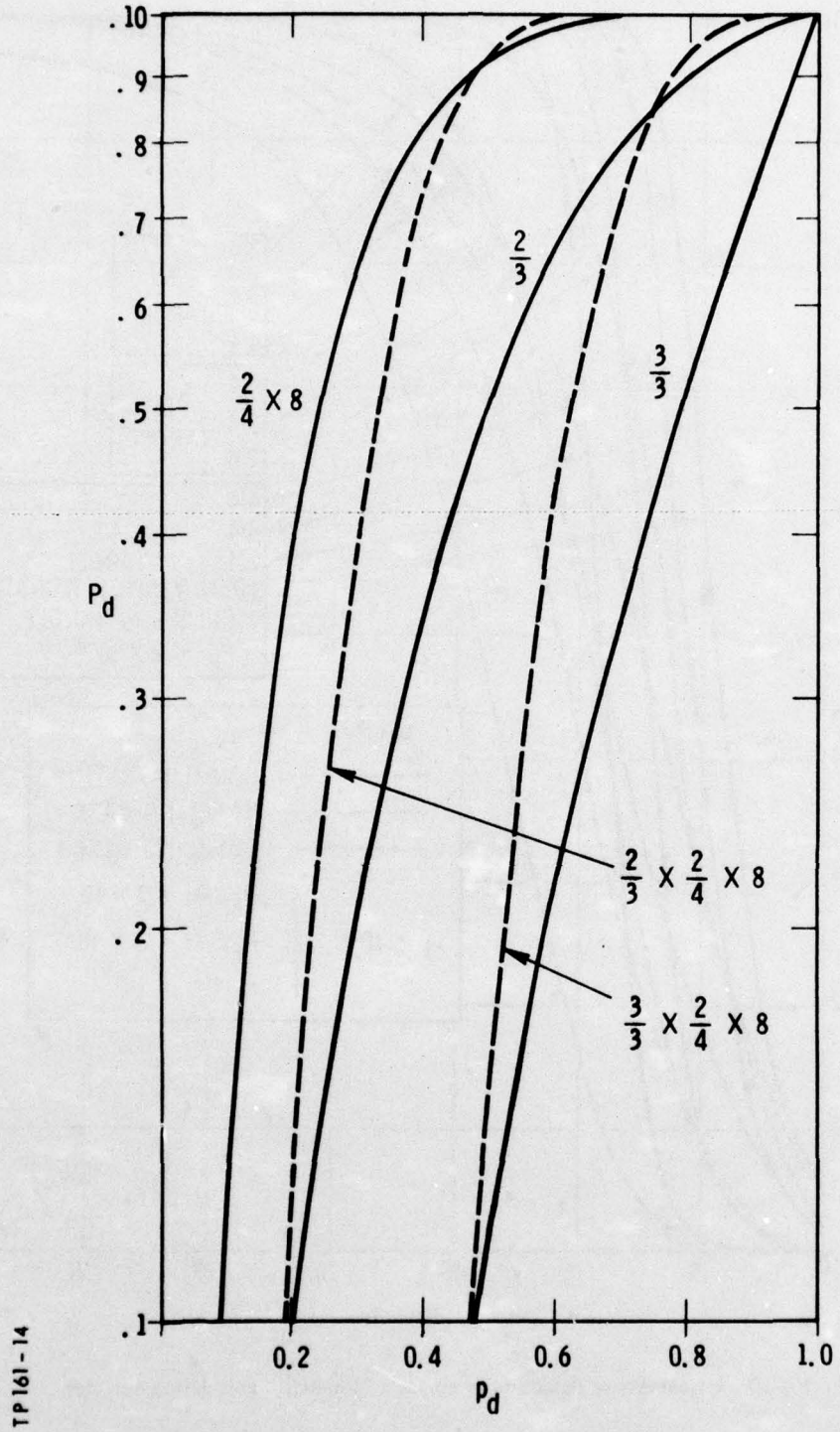

Fig.11 Input-output P_D curves for simultaneous solution of LEC detector

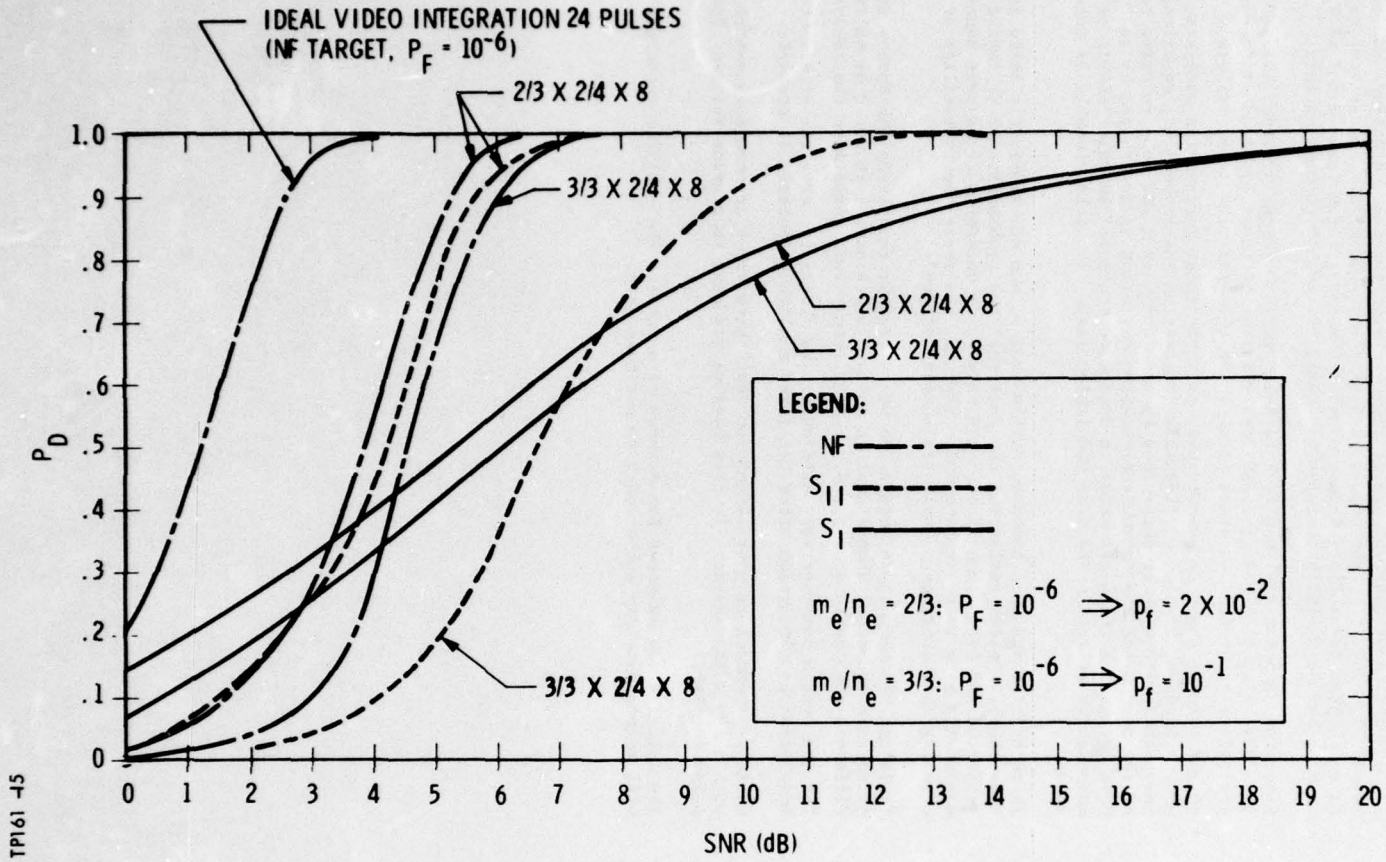

Fig.12 Leading edge correlator sensitivity plots

DISCUSSION

H FANCY: Do you make an allowance in your analysis for range quantisation effects, and does it make the analysis more difficult?

D F HAMMERS: I presume you mean range straddling effects. We allow for this by introducing a loss factor into the signal-to-noise figures.

K MILNE: The assumption of constant probability of first threshold crossings suggests that, for small M out of N, the results are slightly pessimistic, since some hits will have a higher probability than average. Conversely, for large M out of N, the results may be slightly optimistic. Could the author comment on this?

D F HAMMERS: Since the detector analysed is a hard-limited non-linear process, its performance is always characterised by a SNR loss relative to ideal amplitude integration. The analysis presented gives exact results for this relative to N_h uniformly weighted pulses between the 3 dB beamwidths. As with linear integration analysis, inclusion of amplitude modulation considerably complicates the probability equations. Thus we leave this effect to be determined by simulation as a SNR loss relative to the nose of the beam after the optimum correlation criterion is determined by analysis. I have not made a trade-off study to determine the possible relationship between correlation criterion and scan modulation loss. It would probably be interesting to do so.

A L C QUIGLEY: In methods of analysis based on Markov chains, one can explicitly build in the beam shape, thereby reflecting the fact that the probability of threshold crossing varies as the beam scans through the target. I understand from your paper that you assume the beam to be rectangular - that is, you treat the probability of a threshold crossing as a constant. Could you comment please?

D F HAMMERS: Including the beam shape modulation would greatly complicate the Markov stochastic difference equations when signal is present since each term would be multiplied by different combinations of P_i, P_{i-1}, P_{i-2}, etc. This would make the analysis problem for the system designer very difficult. We choose to leave the effect of beam modulation to simulation after the fixed amplitude analysis is complete.

G A VAN DER SPEK: Could you comment on your assumption that there are 4 or more beam centre positions within the 3 dB contour? Is this because you want to prevent the need for a mono-pulse facility?

D F HAMMERS: The number 4 was selected for purpose of example. The analysis technique presented will accommodate any number of hits per beamwidth.

AD-A040 144 ADVISORY GROUP FOR AEROSPACE RESEARCH AND DEVELOPMENT--ETC F/G 17/9
NEW DEVICES, TECHNIQUES AND SYSTEMS IN RADAR.(U)
FEB 77

UNCLASSIFIED AGARD-CP-197 NL

4 OF 7
AD
A040144

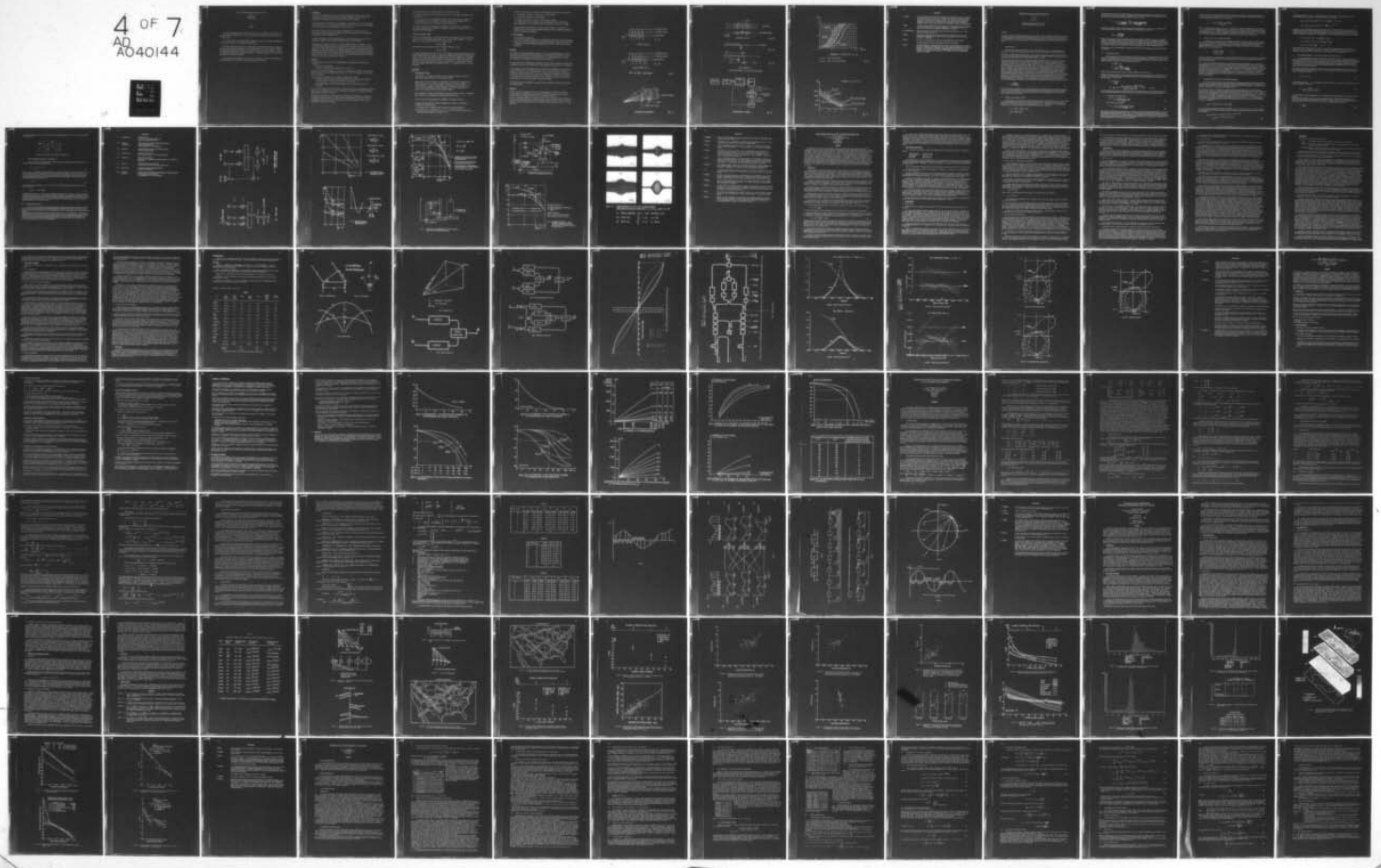

TESTS NON-PARAMETRIQUES APPLIQUES AU RADAR

R.Carre
Thomson-CSF
Malakoff, France

RESUME

Les tests "non paramétriques" peuvent être utilisés dans le traitement de la vidéo radar. Ils sont particulièrement utiles pour les radars qui ne peuvent pas séparer les cibles du Clutter par filtrage Doppler.

Le traitement basé sur ce principe permet d'obtenir une fausse alarme constante indépendante de la puissance du Clutter et de la forme de sa distribution.

Un exemple d'application est décrit. La vidéo radar est échantillonnée et codée en numérique. Les valeurs sont conservées en mémoire sur 4 récurrences successives. Le test consiste à comparer les signaux sélectionnés dans une fenêtre glissante. Cette façon de procéder ressemble au travail d'un opérateur qui exploite un indicateur panoramique : il compare tout signal fort à son entourage pour décider qu'une cible est présente.

Les performances sont comparées à celles des tests classiques, on montre que l'indépendance aux caractéristiques du bruit est acquise sans perte importante d'information.

1 - INTRODUCTION

Les tests "non paramétriques" permettent d'obtenir des détections à fausse alarme constante quelle que soit la distribution du bruit ou du Clutter superposé aux signaux utiles. Les performances de la détection restant voisines de celles du filtre adapté.

Ces tests peuvent être utilisés dans le traitement de la vidéo radar. Ils sont particulièrement intéressants lorsqu'il n'est pas possible de séparer les cibles du Clutter par filtrage Doppler, c'est par exemple le cas des cibles marines et du Clutter de mer.

Pour obtenir une bonne efficacité des tests non paramétriques, il est nécessaire que les échantillons de Clutter ne soient pas corrélés. On obtient la décorrélation en faisant varier la fréquence du radar à chaque émission.

Les études théoriques des tests non paramétriques et de leurs applications au radar ont été effectuées au CETHEDEC. Les résultats ont été publiés dans la revue CETHEDEC.

Une maquette de traitement vidéo a été réalisée par THOMSON-CSF sous contrat DRME. Les essais ont été effectués sur signaux simulés et sur signaux réels enregistrés à bord d'un avion muni d'un radar de surveillance de la mer. Les résultats sont satisfaisants, la vidéo est parfaitement normalisée, la qualité des images sur un indicateur panoramique est fortement améliorée ce qui réduit beaucoup la fatigue de l'opérateur assurant ainsi de meilleures performances de détection. On peut aussi envisager à l'avenir des dispositifs de détection automatique dans des conditions difficiles telles que la présence de Clutter de mer.

2 - PRINCIPES

Il existe plusieurs sortes de tests "non paramétriques" qui peuvent être classés en deux catégories :

- les tests à un échantillon
- les tests à deux échantillons appelés aussi tests de rang.

Dans les tests à un seul échantillon, on se base sur la connaissance a priori de la distribution du signal pour décider de sa présence dans le bruit ou le Clutter (par exemple : test de signe, test de la médiane).

Dans les tests à deux échantillons, on compare deux séquences de signaux :

- une première séquence dite "échantillon litigieux" formée des mesures pour lesquelles on doit décider de la présence ou de l'absence du signal utile,
- une seconde séquence dite "échantillon témoin" qui est formée de mesures de bruit ou de Clutter.

Les tests à deux échantillons ont été choisis à cause de leurs meilleures performances en détection radar. Le test de rang qui a servi de base au traitement a été étudié à l'origine par WILCOXON. Son principe est rappelé à la figure 1.

Les signaux des deux séquences sont comparés sur une même échelle d'amplitude. Le rang pris sur cette échelle constitue la nouvelle valeur attribuée à chaque signal. La décision est obtenue en comparant la somme des rangs à un seuil fixe dont la valeur est réglée en fonction de la probabilité de fausse alarme tolérable.

L'analyse théorique de ce test permet d'énoncer les propriétés suivantes :

1) Le résultat ne dépend pas de la puissance du bruit. Le test agit comme un contrôle de gain automatique

2) La distribution du bruit est normalisée. Quelle que soit la distribution, la comparaison d'une séquence de bruit de l'échantillon litigieux à une séquence de même bruit de l'échantillon témoin fournit des valeurs des rangs équiprobables.

Afin d'obtenir de meilleures performances en présence de bruit thermique, il est possible d'utiliser une expansion avant d'effectuer la sommation des rangs. Ceci ne modifie pas les propriétés énoncées précédemment.

Contrôle de la fausse alarme

Avec un test non paramétrique, la probabilité de fausse alarme minimale que l'on peut contrôler est bornée. Cette borne dépend du rang maximal n que l'on peut obtenir (exemple : n = 10 à la figure 1). Pour un bruit non corrélé, on la relation suivante :

$$PFA\ min = \left(\frac{1}{n}\right)^n$$

Avec un test à un seul échantillon (signe ou test de la médiane) on aurait :

$$PFA\ min = \left(\frac{1}{2}\right)^n$$

Ceci montre l'avantage des tests de rang sur les tests simples à un seul échantillon. Pour obtenir la même probabilité de fausse alarme, la longueur de la séquence témoin peut être beaucoup plus réduite, ce qui conduit à une fenêtre de mesure de Clutter de petite dimension qui s'accommode bien mieux de la non stationnarité du Clutter. En fait, pour obtenir de bonnes performances de détection, la fausse alarme contrôlée doit être bien supérieure à la valeur limite. On pourra voir sur les mesures effectuées sur la maquette qu'avec n = 15 on peut obtenir PFA = 10^{-5} sans difficulté.

3 - REALISATION

3.1. Test appliqué au radar

Pour réaliser le traitement de la vidéo d'un radar à antenne tournante, le test est appliqué aux signaux recueillis dans une fenêtre glissante.

Comme on peut le voir à la figure 2, cette fenêtre est très étroite en distance et elle s'étend en azimut sur une portion du faisceau d'antenne. Sa forme est adaptée à la non stationnarité du Clutter. La distribution varie rapidement avec la distance, par contre, elle varie lentement entre deux récurrences successives (à même distance) à cause de la corrélation spatiale due au faisceau d'antenne.

Dans la maquette, la vidéo est échantillonnée à intervalles de $\tau/2$ (τ: durée de l'impulsion émise). Elle est mise en mémoire sur quatre récurrences successives.

Le test de rang est réalisé comme il est indiqué sur les figures 3a, 3b, 3c.

Le signal vidéo qui apparaît au temps correspondant à la distance D est comparé à l'ensemble des signaux suivants :

1) aux signaux reçus à la même distance D aux quatre récurrences précédentes

2) aux signaux reçus au voisinage de D (D + d et D - D) à la récurrence actuelle et aux quatre récurrences passées (d correspond à 1,5 τ).

Pour noter le signal reçu à la distance D, les amplitudes sont divisées en deux classes :

A : les amplitudes inférieures au plus grand des signaux témoins

B : les amplitudes supérieures à ce même signal.

Si le signal reçu est dans la classe A, il est noté par son rang,
si le signal reçu est dans la classe B, son rang est multiplié par un coefficient K (dans la maquette K = 2). Ce traitement réalise l'expansion des rangs de façon simple.

On peut remarquer que la logique du test qui consiste à comparer le signal reçu à la distance D avec les signaux voisins ressemble beaucoup au travail qu'effectue un opérateur radar sur un indicateur panoramique.

3.2. Bloc-diagramme

Il est représenté à la figure 4.
A la suite du traitement, on dispose d'une vidéo échantillonnée codée en valeurs numériques. On peut l'utiliser après décodage sur un indicateur panoramique. On peut aussi faire suivre ce traitement par une post-intégration numérique pour réaliser un dispositif de détection automatique.

4 - RESULTATS

Pour évaluer les pertes d'information introduites par le test non paramétrique, les résultats des mesures ont été comparés à ceux que donnerait un test paramétrique de référence. Le bruit était gaussien et stationnaire (conditions optimales pour le test paramétrique). Le signal utile fluctuait d'une récurrence à la suivante en loi de RAYLEIGH.

Les performances du test paramétrique de référence ont été calculées en supposant une régulation automatique du niveau de bruit réalisée dans la même fenêtre glissante que celle de la maquette.

Les performances du test non paramétrique ont été déterminées au CETHEDEC pour des probabilités de fausse alarme de 10^{-3} en simulation numérique. Elles ont été vérifiées sur la maquette et mesurées pour des probabilités de 10^{-4} et 10^{-5}. La figure 5 donne la probabilité de détection en fonction du rapport signal sur bruit pour une post-intégration réalisée sur 30 récurrences. Sur la figure 6, on donne le rapport signal sur bruit nécessaire pour obtenir une probabilité de détection de 0,5 en fonction du nombre N d'échos post-intégrés.

Les résultats des mesures effectuées sur signaux réels ont confirmé ceux obtenus en laboratoire sur signaux simulés.

5 - CONCLUSION

L'étude a montré que l'application des tests "non paramétriques" au radar pouvait apporter des améliorations considérables dans son exploitation principalement lorsque le radar doit travailler dans des conditions difficiles dues à la présence du Clutter.
La perte d'information résultant de l'application de ces tests est du même ordre de grandeur que celle des dispositifs habituels de régulation de fausse alarme, cependant la régulation obtenue en présence de bruits non gaussiens et non stationnaires est bien supérieure à celle ces anciens dispositifs.

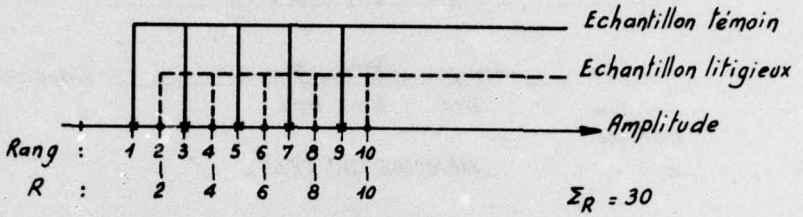

Absence de signal

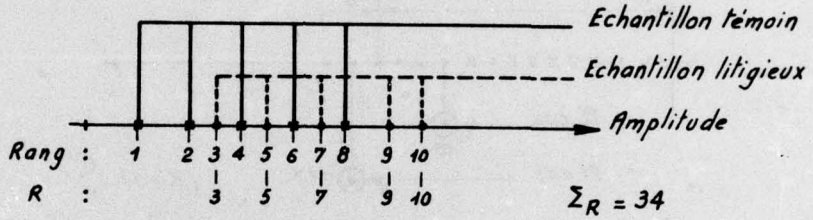

Signal faible et bruit

- TEST DE RANG - (WILCOXON) -

Fig. 1

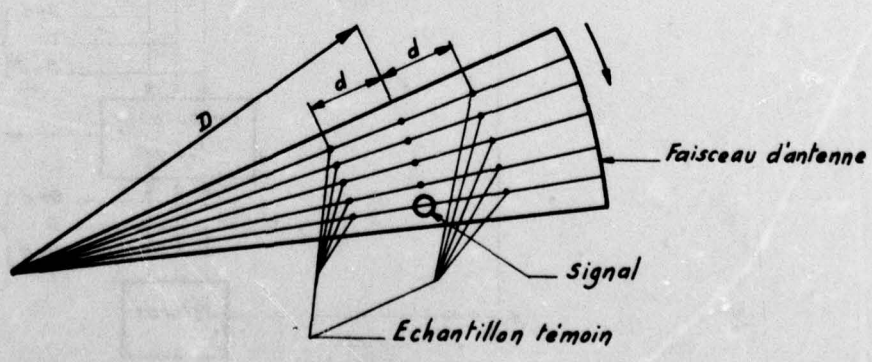

- FENETRE GLISSANTE -

Fig. 2

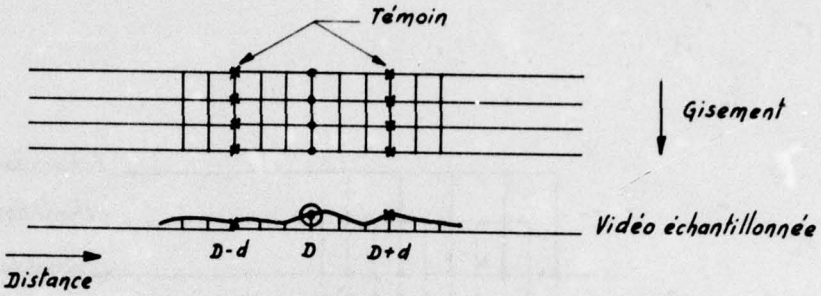

- MEMOIRE DU TEST -

Fig. 3a

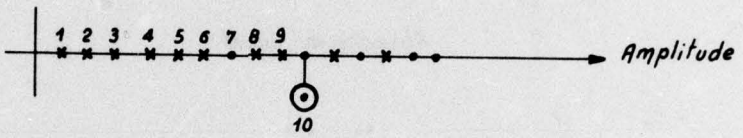

Fig. 3b

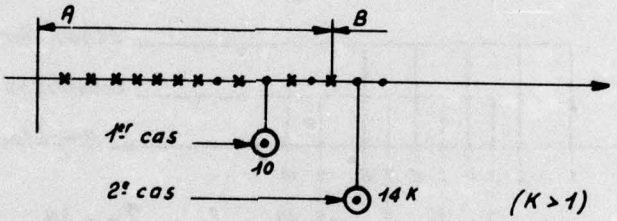

Fig. 3c

- TEST MODIFIÉ -

pour exploitation sur indicateur panoramique

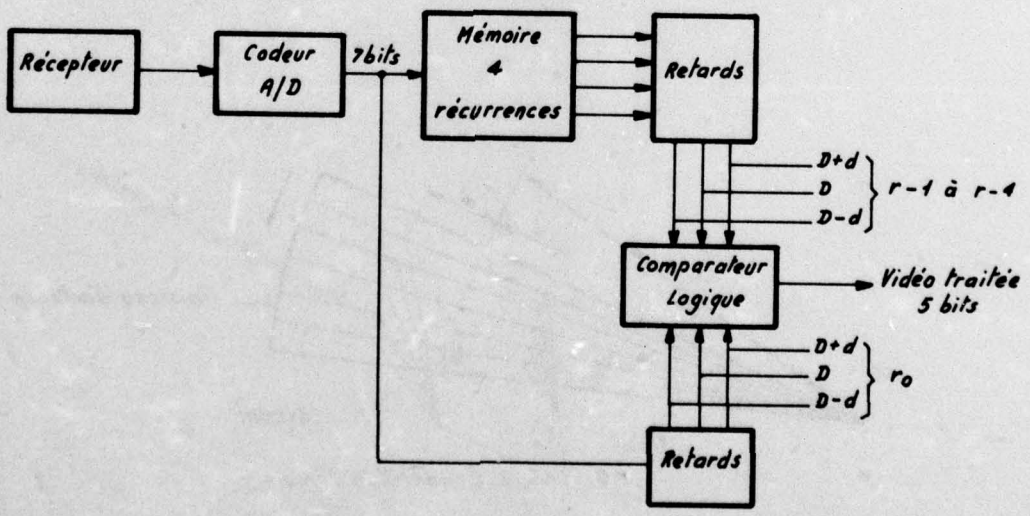

- TRAITEMENT VIDEO -

Fig. 4

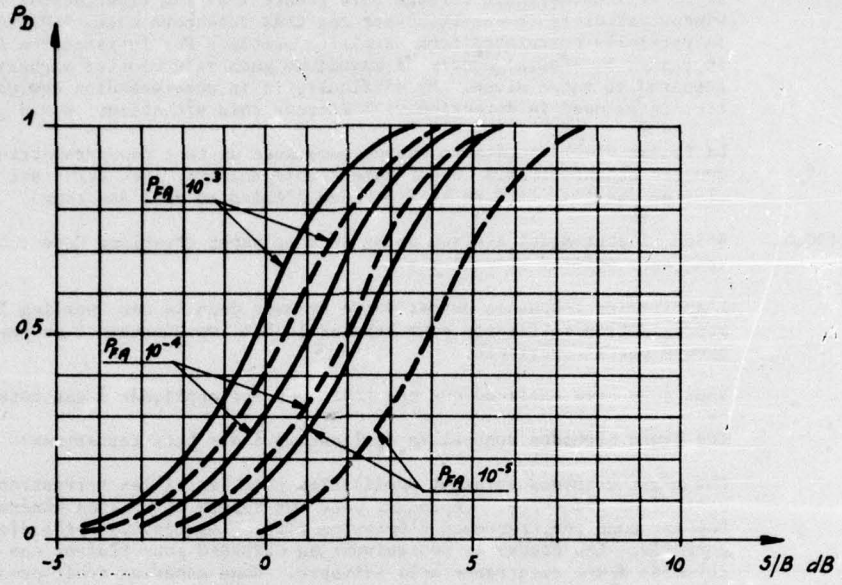

PROBABILITE DE DETECTION (N = 30)

——— Test paramétrique

– – – – Test non paramétrique

Fig. 5

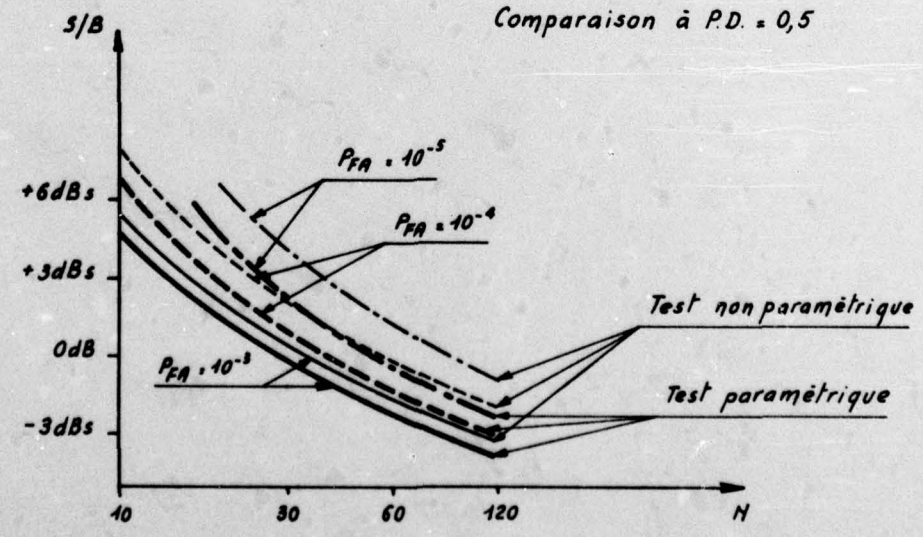

Fig. 6

DISCUSSION

C E MUEHE: It is well established through both theoretical and experimental work that sliding-window detectors (m out of n) are not CFAR detectors when the interfering signal is partially correlated from sample to sample. For instance the false alarm rate increases by several orders of magnitude when rain clutter signals are present compared to noise alone. My difficulty is in understanding how non-parametric techniques used in detection will improve this situation. Would you please comment?

R CARRE: La fausse alarme constante est obtenue avec un test non-paramétrique à la condition que les échantillons de bruit soient indépendants. Cet effet est obtenu sur le clutter par l'agilité de la fréquence d'émission de l'émetteur.

B C KAYSERILIOGLU: Which clutter model are you using in your paper (Swerling Case I or II) to use frequency agility effectively?

R CARRE: L'agilité de fréquence permet de se trouver dans le cas Swerling II avec une approximation suffisante pour assurer le bon fonctionnement du test ce qui est prouvé par l'expérience.

Y BRAULT: Vous nous avez expliqué que ces tests ont été appliqués à des buts marins.

Ces mêmes méthodes sont-elles applicables à des buts terrestres?

R CARRE: Ces mêmes méthodes seraient applicables pour les cibles terrestres avec un radar à agilité de fréquence. Cependant pour ces radars on utilise généralement du filtrage Doppler donc une fréquence d'émission fixe. Les résidus après éjections restent corrèlés. Les études se poursuivent au CETHEDEC pour traiter ces cas de bruit corrèlés d'une recurrence à la suivante. Nous espérons avoir prochainement des solutions à proposer.

PROBLEMS OF ADAPTIVE SIDELOBE SUPPRESSION

G. Ries

K. Krücker

Forschungsinstitut für Hochfrequenzphysik
D 5307 Wachtberg-Werthhoven, Germany

SUMMARY

In this paper we present some investigations dealing with decorrelation effects in a suboptimal spatial filter for adaptive interference suppression. Degradation caused by decorrelation is partly determined by the antenna configuration, partly by mismatch between the receiving channels. Additional degradation caused by the target signal and by correlator offset errors in the adaptive control loops are discussed, too. Finally the paper gives some results of a special experimental system.

1. INTRODUCTION

This paper deals with particular problems in adaptive spatial filtering for coherent sidelobe suppression. The advantages of this technique for radar applications in ECM environments are evident and should only be mentioned.

Vector-matrix notation is used throughout this paper. Column vectors are represented by underlined lower case letters, for example $\underline{d}$. The asterisk $\underline{d}^*$ is used to denote conjugate transposition. Matrices are denoted by underlined upper case letters, e.g. $\underline{Q}$. Expected values are denoted by overlined letters, e.g. $\overline{\underline{n}\,\underline{n}^*}$.

Starting with the problem of detection of target signals in spatially distributed interferences, some optimality criteria, for example the maximum signal to noise ratio S/N or the likelihood ratio test, lead to an optimum linear array configuration according to Fig. 1. Target and gaussian noise signals s and n of each array element, given by the complex signal vector $\underline{x}$, are multiplied by the complex weighting vector $\underline{k}_{opt}$. Compared with a conventionally steered array with a weighting vector equal to the target signal vector $\underline{s}$, the target signal vector has to be transformed by $\underline{Q}_{opt}^{-1}$ with $\underline{Q}_{opt} = \overline{\underline{n}\,\underline{n}^*}$, the hermitian noise covariance matrix. From this weighting an array pattern results with a main beam in target direction and minima for angles of interference. For broad-band signals the optimum weighting vector is a function of frequency but for narrow-band conditions all weighting elements may be approximated by frequency independent factors without severe degradation in noise suppression. Further reduction of the complexity of this configuration, especially in the matrix conversion process, results in a configuration as shown in Fig. 2, the sidelobe canceller /1/. Assuming a very small S/N at the isotropic auxiliar-array elements compared to the small S/N at the high gain main antenna, steering of the auxiliar array is neglected. For radar applications this assumption gives no severe degradation of the noise suppression. The weighting vector is determined for minimum noise at the output, which results in a processing gain or cancellation ratio g, defined as the ratio of output noise without and with auxiliary array.

$$g = \frac{\overline{n_0 n_0^*}}{\overline{|n_0 - \underline{k}^* \underline{n}|^2}} \tag{1}$$

In the following sections degradations of the processing gain caused by the suboptimality of the configuration according to Fig. 1 as well as by component errors are discussed. Convergence problems of the adaptively controlled weighting vector are not considered. Finally this paper gives a description of an existing experimental system with an auxiliar array of 6 elements and its performance.

2. EFFECTS OF THE TARGET SIGNAL

As mentioned in the introduction the contribution of the target signal $\underline{s}$ in the auxiliar array to the output signal and from this the steering of the auxiliar array may be neglected as far as the number of the quasi isotropic auxiliar elements N is small compared to the directivity of the main antenna. Further, the effect of $\underline{s}$ on the processing gain according to eq. (1) has to be considered. The weighting vector $\underline{k}$ from Fig. 2 is given by:

$$\begin{aligned} \underline{k} &= (\underline{Q} + \overline{\underline{s}\,\underline{s}^*})^{-1} (\overline{\underline{n}\,n_0^*} + \overline{\underline{s}\,s_0^*}) \\ &\approx \underline{Q}^{-1} (\overline{\underline{n}\,n_0^*} + \overline{\underline{s}\,s_0^*}) \end{aligned} \tag{2}$$

The approximation proves to be reasonable because of the much lower S/N in the auxiliar array compared to the main antenna S/N. The second term of $\underline{k}$ leads to a degradation of the processing gain g_o achievable without signal. From eq. (1) results for a configuration with only one auxiliar element, i.e. N = 1:

$$g = \frac{g_o}{1 + g_o\left(\frac{|\overline{ss_o^*}|^2}{\overline{nn^*}\,\overline{n_o n_o^*}} + 2\,Re\left\{\frac{\overline{nn_o^*} - \overline{n^* n_o}}{\overline{nn^*}\,\overline{n_o n_o^*}}\,\overline{ss_o^*}\right\}\right)} \tag{3}$$

According to this equation, effects of target signal have to be considered only for very large g_o. For targets in $\Theta = 0$ direction with complete correlation of s and s_o the maximum achievable gain is limited to:

$$g_{max} = \frac{\overline{nn^*}}{\overline{ss^*}}\,\frac{\overline{n_o n_o^*}}{\overline{s_o s_o^*}} \tag{4}$$

Because of low average S/N over long integration periods the resulting g_{max} is sufficient. Low g_{max} for interference directions corresponding to minima of the main antenna pattern with high S/N of the main antenna are not significant. Low g_{max} may be problematic for short effective integration time constants, that means approximately equal to the pulse width of the target signal, when the higher pulse S/N has to be considered. But under these conditions additional effects are caused by the short-time correlation between interference and target signal, which was neglected in eq. (2).

The maximum output S/N of the suboptimal configuration according to Fig. 2 is limited by g_{max} to N/S in the auxiliar array element.

3. BANDWIDTH EFFECTS

The processing gain g may be derived from eq. (1) with the $\underline{k}$ from Fig. 2 for negligible signal effects. From this, the achievable g depends primarily on the correlation of the interference signals n_ν in the auxiliar array /2/. Starting with an n_ν given by only one quasi monofrequent interference with $\overline{n_\nu n_\nu^*} = \overline{nn^*}$ equal for all auxiliar elements ν and additional receiver noise power j in each channel, $\underline{Q}$ and g come out to:

$$\underline{Q} = \overline{\underline{n}\underline{n}^*} + j\,\underline{I}$$

$$g = \frac{\overline{n_o n_o^*}}{\overline{n_o n_o^*} - \overline{n_o n^*}\,\frac{\overline{nn^*}N}{j + \overline{nn^*}N}} \tag{5}$$

Because of the uncorrelated receiver noise, g is limited, compared to $g \to \infty$ for $j \to 0$.

Additional gain reduction results from the signal bandwidth, which deforms the dyadic $\underline{Q} = \underline{n}\underline{n}^*$ to the Toeplitz matrix $\underline{Q} = \overline{\underline{n}\underline{n}^*}$. No simple expression for the inverted $\underline{Q}$ and from this for g can be derived except for an auxiliar array with only one element, i.e. N = 1 with:

$$g = \frac{1}{1 - \left|\frac{r_1}{q_{00}}\right|^2}$$

$$\text{with: } \frac{r_1}{q_{00}} = R_{01} = \frac{\int_{-\infty}^{\infty} S(f)\,|H(f)|^2\, e^{i\pi \frac{d}{\lambda/2} \sin\theta \frac{f}{f_o}}\, df}{\int_{-\infty}^{\infty} S(f)\,|H(f)|^2\, df} \qquad j \to 0 \tag{6}$$

From this g depends on the pre-processing filter function H (f) and the power spectrum S (f) of the interference process as well as on the element distance d and Θ, the direction of the interference. For white noise spectrum results:

1. rectangular filter of bandwidth B

$$g = \frac{1}{1 - \mathrm{sinc}^2\left(\frac{\pi}{2}\,\frac{B}{f_o}\,\frac{d}{\lambda/2}\sin\theta\right)} \tag{7}$$

2. sinc-filter of 3 dB bandwidth B

$$g = \frac{1}{1 - \left(1 - 0.35\,\frac{\pi}{2}\,\frac{B}{f_o}\,\frac{d}{\lambda/2}\sin\theta\right)^2} \tag{8}$$

Approximations of these equations reasonable for $g \geq 10$ dB shows Fig. 3 where the bandwidth of both filters is optimized for a rectangular pulsed target signal of pulse length 1/1.37 B. According to this figure high processing gain g may be obtained by filter functions with strong sideband attenuation. The resulting pattern of the antenna configuration has a deep minimum for the center frequency only, and from this interference suppression for far-off side bands, for example in the spectrum according to filter function 2 proves to be insufficient.

The processing gain may be increased by pattern minimums of higher order. These are a result of additional degrees of freedom when the number of discrete interference directions is less than the number N of elements in the auxiliar array. For only one interference direction and N = 2 g is given by:

$$g = \frac{1}{1 - \frac{|R_{01}|^2 + |R_{02}|^2 - 2 R_{01} R_{02}^* R_{12}}{1 - |R_{12}|^2}} \tag{9}$$

Results for a rectangular filter function and $d_2 = 2d_1 = 2d$ shows Fig. 3, again as an approximation for $g \geq 10$ dB and $j \to 0$. Because of the broadened pattern minimum g increases with the forth power of decreasing bandwidth compared to the second power for N = 1. High processing gain may be realized only neglecting receiver noise. On the other side it should be mentioned that the large time constant in the transition from the small g according to N = 1 to g according to N = 2, which is caused by one vanishing eigenvalue in the covariance matrix, proves to be problematic.

4. EFFECTS OF THE MAIN ANTENNA PATTERN

The degradation of the processing gain by bandwidth as discussed in the previous section is caused by frequency dependent phase angles at the interference signals of all antenna elements. An additional degradation results from the frequency dependent amplitude of the interference signal in the high-gain main antenna, given by its frequency dependent sidelobe pattern. For a main antenna of dimenskon D in direction of the auxiliar array, the pattern in the sidelobe region may be approximated by:

$$A = \frac{\sin\left(\pi \frac{D}{\lambda_0} \sin\theta \frac{f}{f_0}\right)}{\left(\pi \frac{D}{\lambda_0} \sin\theta \frac{f}{f_0}\right)^l} \qquad l \geq 1/2 \tag{10}$$

This pattern amplitude has to be considered as a frequency dependent weighting function for the spectrum of the interference signal in the main antenna. For the quasi isotropic elements of the auxiliar array the corresponding weighting function is constant within the bandwidth.

With A taken into consideration processing gain for a configuration with one auxiliar element, i.e. N = 1 may be computed according to eq. (6). Fig. 4 shows some results for only one interference direction, rectangular filter functions, and negligible receiver noise. For large distances d between the main antenna phase centre and the auxiliar element, compared to the main antenna dimension D, the phase effects as discussed in the previous section dominate, and amplitude effects of the main antenna pattern A may be neglected. The influence of A is also negligible for small d/D as far as the interference direction coincides with a sidelobe peak in A, i.e. $D/\lambda_0 \cdot \sin\Theta = 1.5, 2.5, 3.5\ldots$ Severe gain degradations are observed for all other interference directions with A variations over the bandwidth. Unter these conditions no considerable increase of g may be obtained for $d \leq D/2$, that means when the auxiliar element is within the main-antenna aperture.

5. DECORRELATION EFFECTS DUE TO RECEIVER MISMATCH

As already mentioned, influences which decorrelate the interference process on the way from the noise source to the weighting filter $\underline{k}$ degrade the processing gain of the canceller. Besides the effects discussed in the previous sections, mismatch in the receiver channels has to be considered. It should be mentioned that the optimum array processor Fig. 1 is sensitive to decorrelation in the same way as the sidelobe canceller.

We concentrate our attention in this chapter on amplitude response mismatch between main and auxiliary channels, deriving an upper limit for the cancellation ratio due to decorrelation in the channels of the receiver front-end. To derive an expression for the processing gain in the presence of decorrelating prefilters, the quadratic form $\underline{r}^* \underline{Q}^{-1} \underline{r}$ which results in eq. (1) for the optimum $\underline{k}$ according to Fig. 2, has to be evaluated. The crosscorrelations $r_\nu^*(o) = \overline{x_0(t) x_\nu^*(t)}$ and $q_{\nu\mu}(o) = \overline{x_\nu(t)\, x_\mu^*(t)}$ are components of the correlation vector $\underline{r}^*$ and the covariance matrix $\underline{Q}$. x_0, x_ν, x_μ can be regarded as new signal processes after convolving the original element signals $x'_{0,\nu,\mu}(t)$ with the impulse response of the corresponding decorrelating prefilter. With transfer functions $H_\nu(\omega)$, $H_\mu(\omega)$, the crosscorrelation of x_ν and x_μ is given by /3/:

$$q_{\nu\mu}(0) = \int_\omega S_{\nu\mu}(\omega)\, H_\nu(\omega)\, H_\mu^*(\omega)\, \frac{d\omega}{2\pi} \tag{11}$$

$S_{\nu\mu}(\omega)$ is the cross-spectral density of the input processes $x'_\nu(t)$, $x'_\mu(t)$. With $x'_\nu(t) = x'(t - (\nu-1)\sigma)$, where σ is the propagation delay of the process between two adjacent elements for a given interference direction Θ, we get by Fourier-transform:

$$\begin{aligned} S_{\nu\mu}(\omega) &= \int q_{x'}[\alpha - (\nu-\mu)\sigma]\, e^{-i\omega\alpha}\, d\alpha\; e^{-i\omega_0(\nu-\mu)\sigma} \\ &= S_{x'}(\omega)\, e^{-i\omega(\nu-\mu)\sigma}\, e^{-i\omega_0(\nu-\mu)\sigma} \end{aligned} \tag{12}$$

with the power spectrum $S_{x'}(\omega)$ of $x'(t)$. From eq. (11) and eq. (12) we get the general form of the resulting correlation of two processes which are transformed by different transfer functions.

$$q_{\nu\mu}(0) = \int_{\omega} S_{x'}(\omega)\, H_{\nu}(\omega)\, H_{\mu}^{*}(\omega)\, e^{-i\omega(\nu-\mu)d} \frac{d\omega}{2\pi}\, e^{-i\omega_0(\nu-\mu)d}$$

$$r_{\nu}^{*}(0) = \int_{\omega} S_{x'}(\omega)\, H_{m}(\omega)\, H_{\nu}^{*}(\omega)\, e^{i\omega\nu d} \frac{d\omega}{2\pi}\, e^{i\omega_0\nu d} \qquad (13)$$

We apply eq. (13) in two examples, thus giving an impression of the required tracking tolerances. For simplicity the interference process is described by a bandlimited white noise process, $S_{x'}(\omega) = \text{const.}$, and the phase responses of all prefilter transfer functions are assumed to be linear and equal. Fig. 5 illustrates the cancellation ratio g as a function of relative bandwidth×array dimension for a linear decreasing and a cosine ripple amplitude response of the main channel.

a) $H_0 = H_m(\omega) = \left(H_{m0} + a - 2a\frac{|\omega|}{\Delta w/2}\right) rect\frac{\omega}{\Delta w}$

b) $H_0 = H_m(\omega) = \left(H_{m0} + a\cos 2\pi n\frac{\omega}{\Delta w/2}\right) rect\frac{\omega}{\Delta w}$

$H_{\nu} = H_a(\omega) = H_{a0}\, rect\frac{\omega}{\Delta w}$ for $\nu = 1 \ldots N$

The corresponding formulas for g when $d = 0$ ($\Theta = 0$) - i.e. no additional bandwidth effects due to the antenna configuration - with g independent from the number of elements N, are given in Fig. 5, too. It is important to note that the processing gain is limited to 25-30 dB due to a mismatch of about 0.5 dB im amplitude response.

6. OFFSET-ERROR PROBLEM OF LOW PASS CORRELATOR CONTROL LOOPS

In changing interference environment the optimum filter weighting $\underline{k}^* = \underline{r}^*\,\underline{Q}^{-1}$ should be controlled in an adaptive way to guarantee optimum performance. Updating and matrix inversion methods or Gradient-following techniques could be applied. A well known solution is given by adaptive control loops which realize the Steepest-Descent algorithm in a continuous manner. /1/, /4/, /5/. Fig. 6 shows the principle network for adoptively controlled filter weights. A lot of literature (see reference list in /6/) has been published dealing with the performance of the control loops with regard to dynamic and convergence problems.

We consider in this chapter the influence of an additive correlator error (correlator offset or drift) for a low pass version of the canceller system. Adding an offset vector $\underline{\varepsilon}^* = \underline{c}^*\underline{\Delta}$ to the outputs of the correlator multipliers (see Fig. 6) results in a modified filter weighting:

$$\underline{k}^* = (\underline{r} + \underline{\varepsilon})^*\,\underline{Q}^{-1} \qquad (14)$$

with amplitude vector $\underline{c}^* = (c_1 \ldots c_N)$ and diagonal matrix of the phase error $\underline{\Delta} = \text{diag}\,(e^{-i\vartheta_\nu})$. With $\underline{k}^*$ from eq. (14) we get the cancellation ratio eq. (1):

$$g = \frac{\overline{|n_0|^2}}{\overline{|n_0|^2} - \underline{r}^*\underline{Q}^{-1}\underline{r} + \underline{\varepsilon}^*\underline{Q}^{-1}\underline{\varepsilon}} \qquad (15)$$

Eq. (15) shows that for an unavoidable offset error $\underline{\varepsilon}^*$ a severe reduction in processing gain occurs when $\underline{Q}$ becomes singular.
A simplified analysis of offset error influence for a single element canceller, neglecting bandwidth effects, $\Theta = 0$, gives a lower bound estimate for offset requirements. $\underline{\varepsilon}^*\underline{Q}^{-1}\underline{\varepsilon}$ reduces to c_1^2/P_j, with the interference power P_j at the correlator input. From eq. (15) we get with $\overline{|n_0|^2} = \underline{r}^*\,\underline{Q}^{-1}\,\underline{r}$, neglecting isotropic system noise:

$$g = \frac{1}{c_1^2/P_j^2} \qquad (16)$$

The following table shows that for a given P_j the offset requirements become very critical, even for a relatively modest cancellation ratio.

P_j/dBm	g/dB	
	20	30
- 10	o.o1 mV	3.2 μV
0	o.1 mV	32 μV

Table 1) Tolerable offset error for a given cancellation ratio.

7. SINGLE-SIDEBAND MODULATION WEIGHTING

In order to avoid correlator offset problems it seems reasonable to use IF-Bandpass correlator loops, /7/ with a bandpass version of the optimum weighting vector

$$\underline{k}^* = \underline{r}^* \, \underline{Q}^{-1} \, e^{-i\omega_1 t} \tag{17}$$

with $\omega_1 \geq \Delta w$, the interference process bandwidth, to prevent spectrum fold-over. However, the IF-loops are more critical with regard to control loop stability than the low-pass version /8/. Instability is caused by time delay in the loop network and by the higher-order filters, necessary to attenuate the unused sidebands. In practical cases, the loop gain and therefore the processing gain is stability-limited. Instability caused by additional filters can be avoided by considering the weighting process (see Fig. 6)

$$z = \underline{k}^* \underline{x} \tag{18}$$

carried out by the analytic signals $\underline{k} = \underline{w} + i\,\hat{\underline{w}}$ and $\underline{x} = \underline{b} + i\,\hat{\underline{b}}$ ($\hat{w}$, $\hat{b}$ are Hilbert-transformed processes). The real part of z is given by

$$Re\{z\} = \underline{w}^* \underline{b} + \hat{\underline{w}}^* \hat{\underline{b}} \tag{19}$$

The operation described by eq. (19) cancels the unused frequency components and is realized by two Hilbert-transformers and multipliers per array element. This procedure introduced here for the purpose of simultaneous weighting and filtering is known as Single Sideband Modulation and eliminates the need of additional sideband filters. Compared to the in-phase and quadrature channel low pass correlator, the number of correlators is reduced by a factor of two. Fig. 7 shows the discussed modification of the IF-canceller system.

8. EXPERIMENTAL RESULTS

In order to study some fundamental properties and problems of adaptive spatial filtering, an experimental system with an auxiliar array of 6 elements and loops implementing the results of chapter 7 has been built (see Fig.7). Fig. 8 shows some theoretical and experimental values of processing gain as a function of $B/f_o \; d/\lambda_o/2 \sin\Theta$ for a single interference direction.

Decorrelation effects limit the cancellation ratio to a value of about 28 dB. For a relative bandwidth > 5%, bandwidth effects predominate. Increased gain, using additional spatial samples (N = 2) can be recognized. A qualitative impression of the benefits of the canceller system is given by the pictures of Fig. 9. Two target signals with a bandwidth ratio of about 4 are immersed in the main channel interference. With processing gain corresponding to the bandwidth of the process, target signals appear in a reduced noise background.

REFERENCES

/1/ Applebaum S.P. — "Adaptive Arrays" Syracuse University Research Corporation Report No. SPL 769 June 30, 1964

/2/ Ries G., Söntgerath W. — "Untersuchungen an analogen Regelschleifenschaltungen für adaptive Antennengruppen" Forschungsbericht 2-74, FHP Werthhoven

/3/ Papoulis A. — "Probability Random Variables and Stochastic Processes" McGraw-Hill Book Company

/4/ Widrow B. et al. — "Adaptive Antenna Systems" Proc. IEEE Vol. 55 No. 12 Dec. 1967 p. 2143-2159

/5/ Brennan L.E. — "Theory of Adaptive Radar" IEEE Transact. on Aerospace and Electronic Systems, Vol. AES-9 No.2 March 1973

/6/ Rees F.L. — "Adaptive Beam Forming and Filtering" TSC Course, Oct. 1973, Silver Spring, Maryland, USA

/7) Howells P.W. — "Intermediate Frequency Sidelobe Canceller" US Patent No. 3,202,990

/8/ Krücker K., Bock H.W. — "Theoretische und experimentelle Untersuchungen zur Signalverarbeitung in einem adaptiven räumlichen Filter" Forschungsbericht Nr. 3-74, FHP Werthhoven

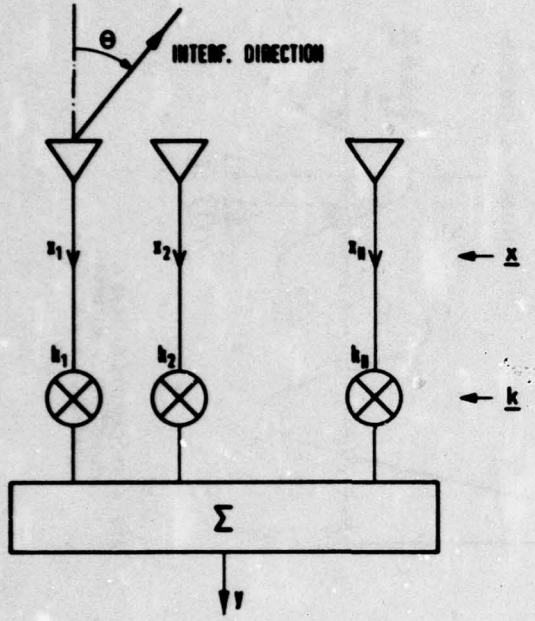

$$\underline{x}(\omega) = \begin{pmatrix} x_1 \\ \vdots \\ x_n \end{pmatrix} = \underline{s} + \underline{n}$$

$$\underline{k}_{opt}(\omega) = \begin{pmatrix} k_1 \\ \vdots \\ k_n \end{pmatrix} = \underline{Q}_{opt}^{-1}\ \underline{s}\ ;\ \underline{Q}_{opt}(\omega) = \overline{\underline{n}\,\underline{n}^*}$$

$$y(\omega) = \underline{k}_{opt}^*\ \underline{x}$$

FIG. 1 OPTIMAL ARRAY

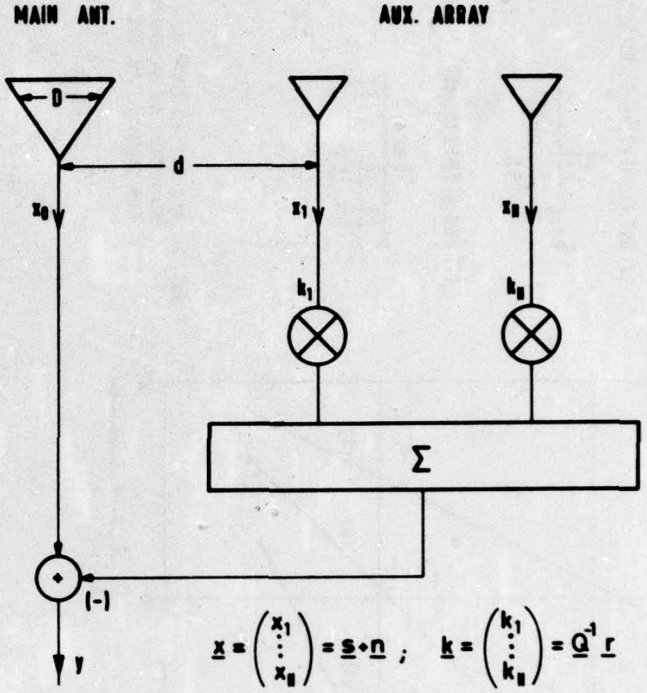

$$\underline{x} = \begin{pmatrix} x_1 \\ \vdots \\ x_n \end{pmatrix} = \underline{s} + \underline{n}\ ;\quad \underline{k} = \begin{pmatrix} k_1 \\ \vdots \\ k_n \end{pmatrix} = \underline{Q}^{-1}\,\underline{r}$$

$$\underline{Q} = \overline{\underline{n}\,\underline{n}^*};\quad \underline{r} = \overline{\underline{n}\,n_0^*}$$

$$y = x_0 - \underline{k}^*\,\underline{x}$$

FIG. 2 SUBOPTIMAL CONFIGURATION WITH A HIGH-GAIN MAIN ANTENNA

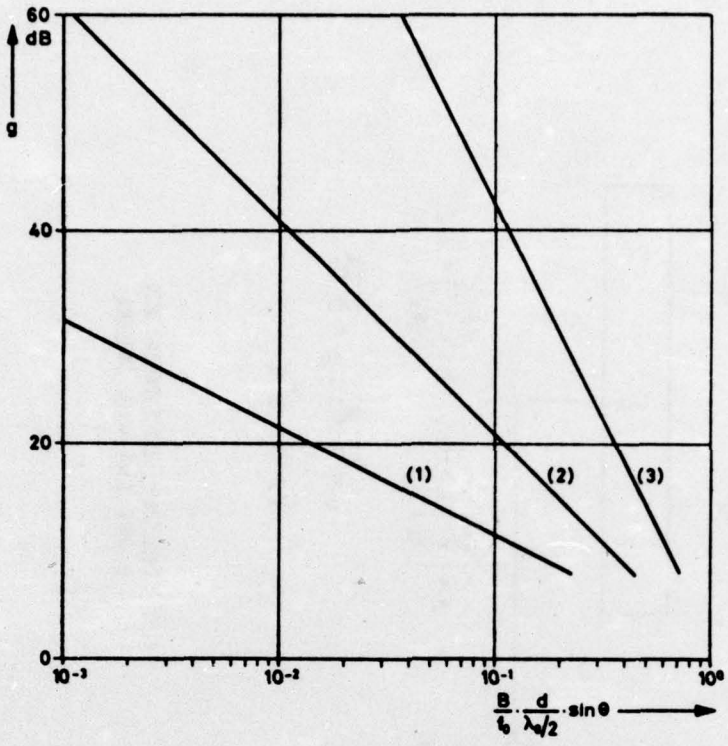

(1) ONE ELEMENT, sinc - FILTER

$$g = \frac{1,43}{\frac{0,66\,B}{f_0} \cdot \frac{d}{\lambda_0/2} \sin\Theta}$$

(2) ONE ELEMENT, rect. - FILTER

$$g = \frac{1,21}{\left(\frac{B}{f_0} \cdot \frac{d}{\lambda_0/2} \sin\Theta\right)^2}$$

(3) TWO ELEMENTS, rect. - FILTER

$$g = \frac{1,84}{\left(\frac{B}{f_0} \cdot \frac{d}{\lambda_0/2} \sin\Theta\right)^4}$$

FIG. 3 PROCESSING GAIN AS A FUNCTION OF BANDWIDTH FOR DIFFERENT FILTERS

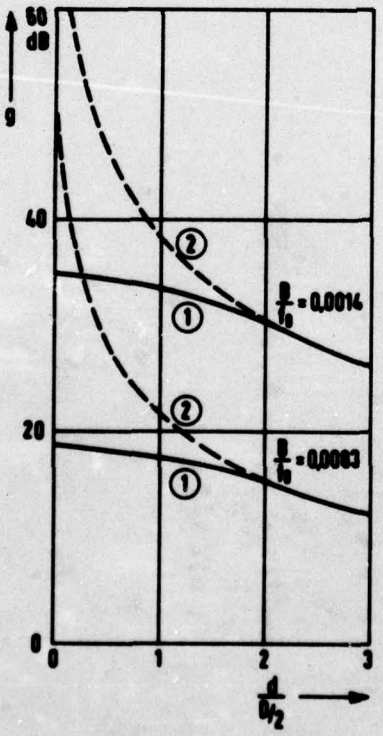

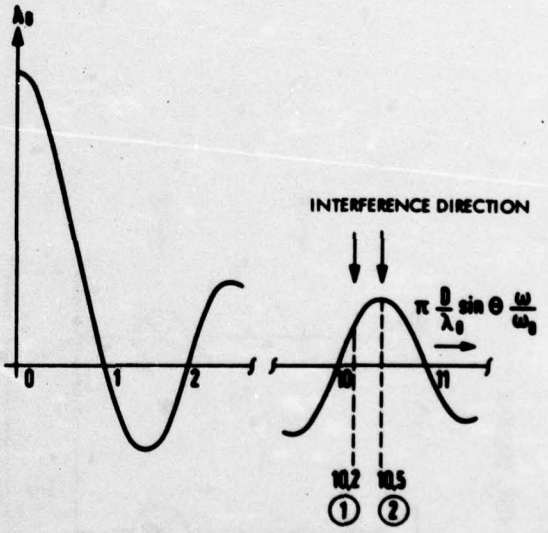

FIG. 4 PROCESSING GAIN AS A FUNCTION OF AUXILIAR ELEMENT DISTANCE

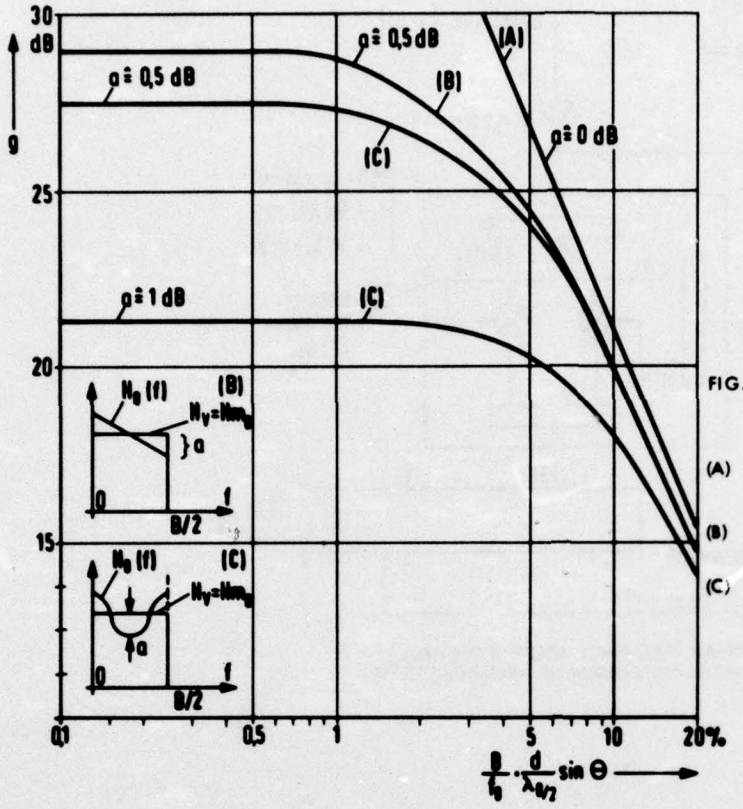

for $\Theta = 0$, $a' = a/Hm_0$, $N \geq 1$

(B) $g = 1 + \frac{3}{a'^2}$

(C) $g = \frac{2}{a'^2}$

FIG.5 DECORRELATION INFLUENCE OF DIFFERENT PREFILTER TRANSFER FUNCTIONS ON THE CANCELLATION RATIO.

(A) MAIN AND AUXILIAR CHANNEL TRANSFER FUNCTIONS ARE EQUAL.(RECT f/B)

(B) LINEAR DISTORTIONS; LINEAR DECREASING AMPLITUDE RESPONSE OF THE MAIN CHANNEL.

(C) LINEAR DISTORTION; COSINE RIPPLE.

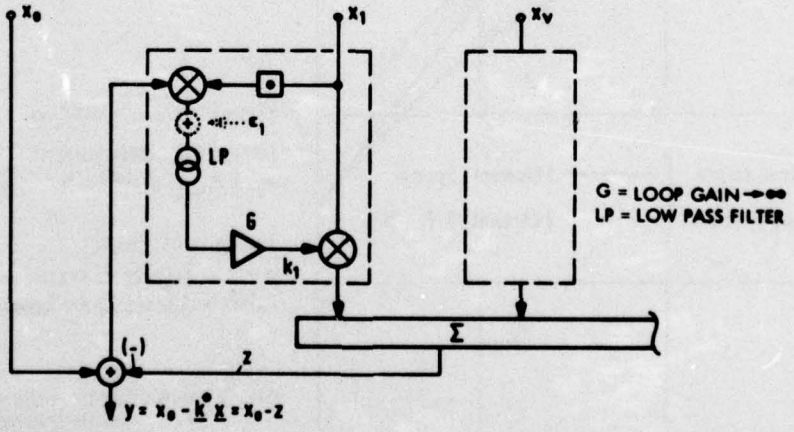

FIG. 6 REALISATION OF THE FILTERVECTOR $\underline{k}^* = \underline{r}^* \underline{Q}^{-1}$ BY ADAPTIVE CONTROL LOOPS (APPLEBAUM / BRENNAN)

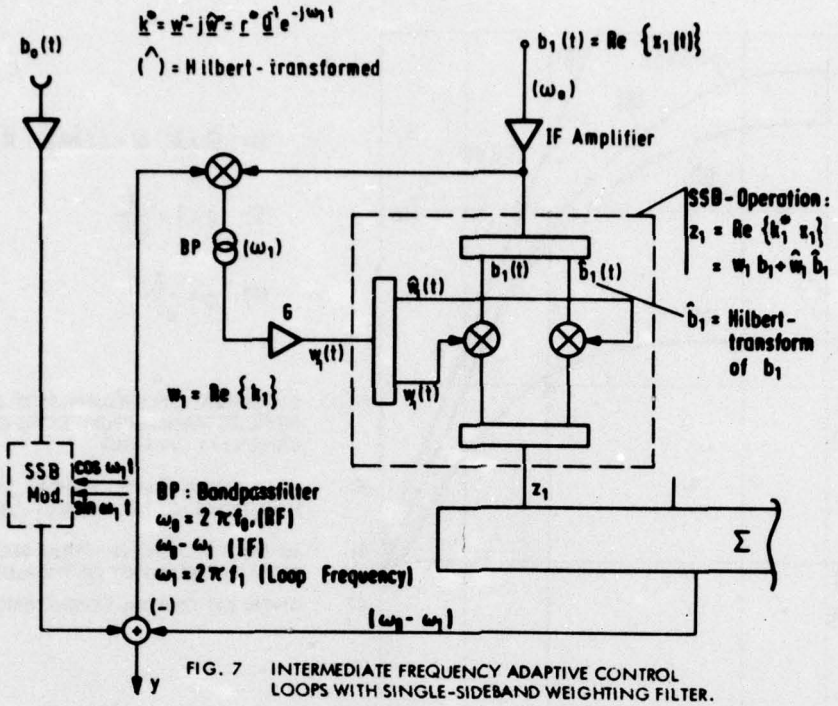

FIG. 7 INTERMEDIATE FREQUENCY ADAPTIVE CONTROL LOOPS WITH SINGLE-SIDEBAND WEIGHTING FILTER.

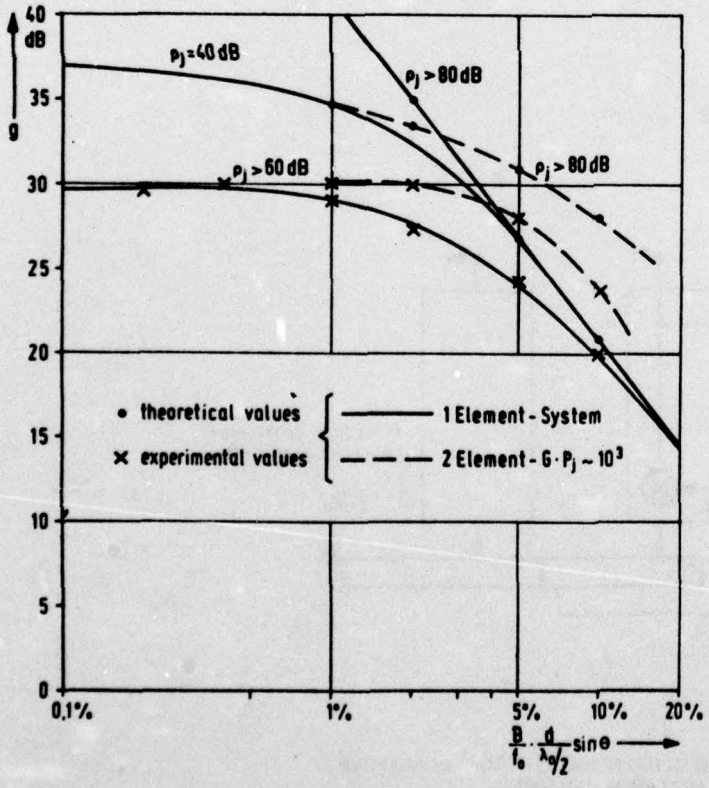

EXPERIMENTAL CONDITIONS:

PREFILTER TRANSFER FUNCTION: APPROXIMATELY RECT $\frac{\omega-\omega_0}{\Delta W} \cdot e^{-j(\omega-\omega_0)t_0}$

SINGLE NOISE SOURCE;

$\rho_j = \frac{P_j}{P_n}$ = JAMMER TO SYSTEM NOISE POWER RATIO, MEASURED AT AN ARRAY ELEMENT.

FIG. 8 INTERFERENCE SUPPRESSION g/dB AS A FUNCTION OF BANDWIDTH B, ELEMENT DISTANCE d AND JAMMER LOCATION Θ FOR A ONE AND TWO ELEMENT IF CANCELLER WITH SSB WEIGHTING.

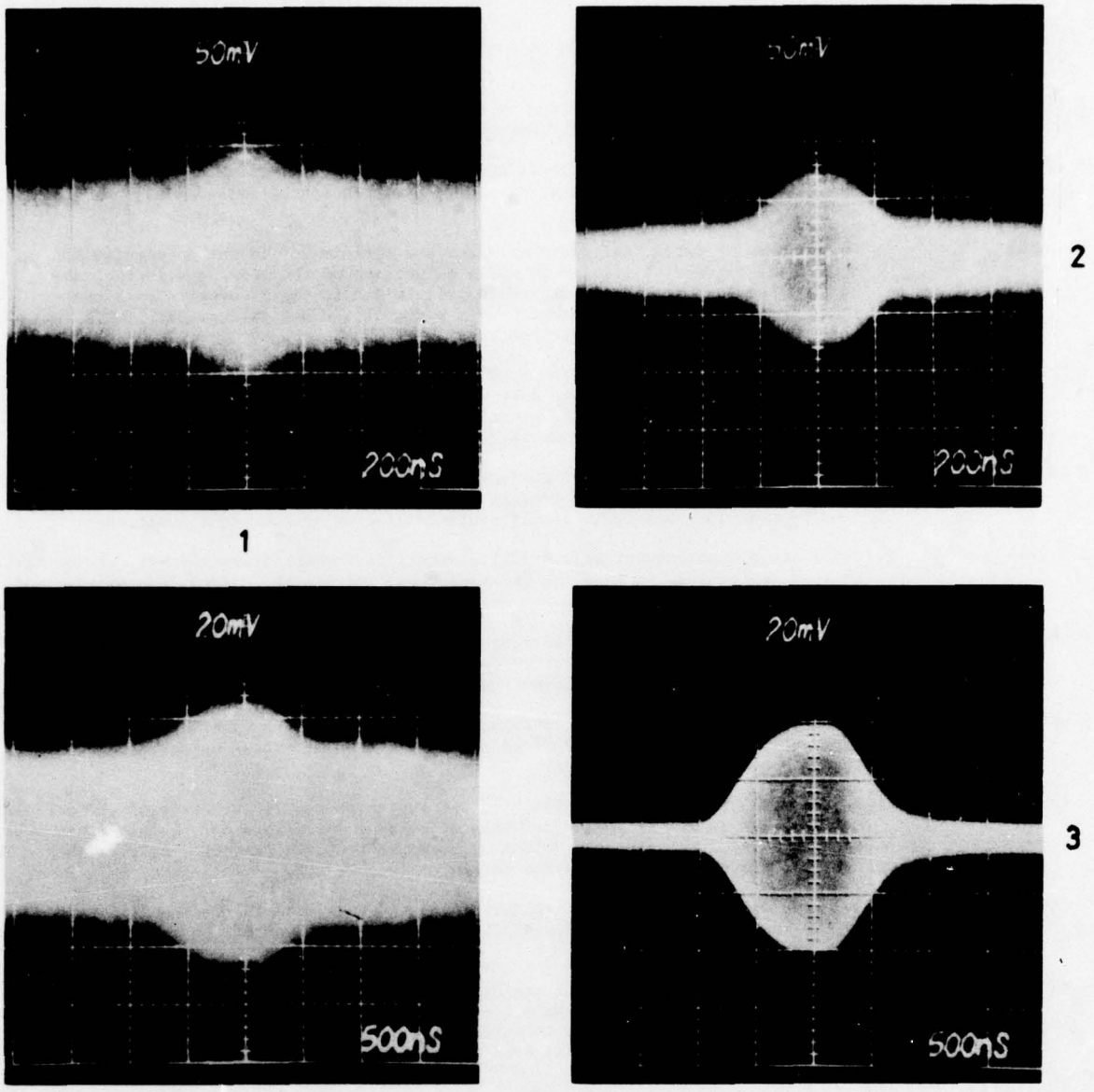

FIG. 9 IMPROVEMENT IN S/N BY A ONE ELEMENT SIDELOBE CANCELER SYSTEM WITH $d = 10\ \lambda_o/2$ AND $\Theta = 90°$.

(1) MAIN CHANNEL S/N = - 3 dB (WITHOUT SLC)

(2) WITH SLC: $\frac{B}{f_o} = 0.04$, g ~ 8 dB

(3) WITH SLC: $\frac{B}{f_o} = 0.01$, g ~ 20 dB

DISCUSSION

J FREEDMAN: Would you please indicate the results obtained for the case of m independent noise sources and n loops where $m \leq n$?

K KRUCKER: As long as $m = n - 1$, processing is similar to that discussed here for $m = 1$, $n = 2$ depending on the spatial distribution of the interferences.

R VOLES: Have you estimated the additional number of degrees of freedom taken by a source which is amplitude modulated at a rate faster than can be followed by the adaptive loops?

K KRUCKER: No, because we think that, in that case, the performance is not a function of additional degrees of freedom but only a function of the time behaviour of the control loops. When the interference pulse width is small compared with the canceller learning time constant, performance of the SLC is degraded. This statement is confirmed by our experiments.

K MILNE: Is there an optimum spacing for auxiliary antennas? Wide spacings are required to obtain closely-spaced nulls to deal with jamming sources with small angular separations but, on the other hand, close element spacing is desirable to achieve broadband operation. Is the optimum perhaps a random distribution of spacings?

K KRUCKER: We considered several element positions, especially different distances between main and auxiliary elements. The results are highly dependent on the interference conditions. In general, it is difficult to give an optimum configuration.

J S YU: Could you please comment on why your elements in the auxiliary channel are not fixed in their spacing to improve the processing gain within the narrow band of your main channel?

K KRUCKER: In order to get sufficient interference suppression it is necessary to have a small product of bandwidth x propagation delay. Even with narrow radar bandwidth, the distance between auxiliary elements and main antenna phase centre has to be small.

P BRADSELL: Would you please explain the advantage of the system using upper and lower sideband separation to prevent spectrum folding, over a simpler system using real and imaginary components of the signal?

K KRUCKER: A prime problem of an analog baseband SLC system is the offset error of the correlator multiplier. In the IF system only one sideband is processed and the other one must be suppressed. Foldover is avoided by a properly chosen frequency relationship. The advantage is that no offset error occurs.

G GALATI: Have you done any analytical evaluations of SLC with more than one auxiliary antenna and/or more than one interference? Have you taken account of the internal (white) noise?

K KRUCKER: As seen from Fig 3, analytical evaluations of a two-element system have been performed. Further analytical evaluations under narrow-band conditions have been done for a six-element SLC with up to three interference directions. In this case, uncorrelated (system) noise has been taken into account.

PHASE COMPARISON MONOPULSE APPLIED TO SECONDARY SURVEILLANCE RADAR

Brian A Wyndham
Royal Signals and Radar Establishment
St Andrews Road
Malvern
Worcestershire
United Kingdom

SUMMARY

Developments in future civilian Secondary Surveillance Radar (SSR) Systems are being aimed at increasing the amount as well as the integrity of information exchanged between the ground station and the interrogated aircraft, whilst reducing the actual interrogation rate to the minimum necessary for reliable performance. The ultimate reduction would be to a single interrogation made only in the expected direction of an aircraft. Such extreme measures would reduce the overall interference problem and hence improve message reliability, but would make it necessary to adopt some technique for azimuth measurement other than the sliding window plot extractor usually used. The simplest solution to this problem is the use of monopulse designed to yield off-axis measurements of the azimuth of transponder signals, and the incorporation of such a system has been specified in both the British Selective Address (ADSEL) and the American Discrete Address Beacon System (DABS) proposals (Bowes R C et al 1975). Its use also for standard SSR is under consideration as an alternative to sliding window techniques, and the experimental work at RSRE has been conducted with existing signal formats. After a brief discussion this paper reports on the results of the initial phase of the experiments aimed at comparing the performance of alternative processes.

1 INTRODUCTION

Current methods of identifying target azimuth in SSR systems rely on sliding window plots which in effect bracket the skirts of the rotating aerial's directivity pattern as it is sampled by consecutive signals elicited from each aircraft transponder. If everything were perfect the azimuth corresponding to the point at which the signals are at boresight could be identified by taking the mean of the azimuths at which signals of equal amplitude appear on either side of centre. With a finite sampling rate set by the Pulse Repetition Frequency (PRF) signal equality cannot be guaranteed and the accuracy is limited to the azimuth interval between consecutive replies.

In practice, each interrogation is not always followed by a response, due either to fading or capture of a transponder by another interrogator. The result of this is that there is no clearly defined threshold where one can place each bracketing azimuth, and a variety of rules have been established to give a measure of confidence to the identity of the leading and trailing edges.

As the aerial scans a transponder, about 20 or so replies are obtained according to aerial rotation speed, PRF and beamwidth, and all of these signals must be processed to produce a reliable result. All the information regarding the true azimuth is however available in each signal irrespective of its apparent position in the beam and monopulse techniques offer one solution to the problem of acquiring it.

Monopulse radar is too well documented to justify an elaborate description of its operation but it should be emphasised that most of the literature relates to closed-loop tracking systems in which the aerial alignment is adjusted to keep the target signals on boresight and boresight parameters are of more importance than the precise characteristics to the beam edges.

In this paper we will be concerned only with phase comparison monopulse for which two aerials are placed side by side and so aligned as to give coincident beams. The aerials outputs will be of equal magnitude but their phases will depend on the direction of the signal source, Fig 1a, b.

To find the indicated direction θi, the electrical length of the delay ϕ must be measured and

$$\theta i = \sin^{-1}\left(\frac{\phi}{2\pi d\lambda}\right) \qquad (1)$$

in which the distance $d\lambda$ is the separation of the phase centres of the two aerials in wavelengths.

The vector diagram Fig 1b shows that there are two obvious ways of measuring the angle ϕ. By placing a phase detector between the aerial outputs Vl, Vr the angle may be measured directly, or alternatively, by obtaining the vector sum and difference to produce Vs and Vd, it is evident that since

$$\phi = 2\tan^{-1}\left[\frac{|Vd|}{|Vs|} \cdot \sin\psi\right] \qquad (2)$$

one may compare the ratio of the two amplitudes and noting their relative phase. The measurement of the amplitudes $|Vs|$ and $|Vd|$ only yields the magnitude of the angle and a further observation must be made to detect its sense. This can be done by introducing a quadrature phase shift between Vs and Vd and noting if they are in or out of phase. With the direct phase angle measurement on Vl and Vr, both sense and magnitude result from a single process.

A point worth noting is that a simple phase comparison monopulse such as described suffers from ambiguities in the declared value of ϕ making it possible to indicate a signal as being within the overall beamwidth when in fact it may be outside. One way of overcoming this problem is to make a second measurement in quadrature with the first.

A number of alternative arrangements have been described from time to time but in this paper we will be concerned only with the two basic processes already referred to and the configuration adopted at RSRE for our initial studies.

As to which of the two basic phase measuring processes is the best is largely determined by the magnitude of the errors to be expected within each process. Assuming that fixed system errors can be balanced out one needs to identify the sources of variable errors which can arise from changes in signal strength and position within the beam as well as those that may result from changes in equipment operating conditions. In the simplest concepts it could be stated that phase errors are more important than amplitude errors in those parts of the circuit directly related to each beam and conversely for circuits where the phase has been translated to amplitude as in the sum and difference process. However this is far too naive an assumption for an adequate basis to find if any significant differences occur between the processes.

2. THE NATURE OF SSR SIGNALS

It is relevant at this point to specify the signals which an SSR monopulse receiver is required to handle.

Centre Frequency	1.09 GHz ± 3 MHz
Pulse length	0.45 ± 0.1 μS
Rise Time	0.05 to 0.1 μS
Fall Time	0.05 to 0.2 μS

Each signal contains a group of pulses from 2 to 14 in number of which the first and last, designated bracket or framing pulses, are always present with a spacing of 20.3 μS. The pulses between these indicate aircraft identity if responding to a Mode A interrogation, or altitude if to Mode C, and sometimes do not occur at all.

There are some points worth emphasising which distinguish SSR signals from those of a primary radar.

(1) The ground station transmitter (interrogation) frequency is 1.03 GHz and far removed from the received signal frequency.

(2) ICAO recommendations are that the receiver bandwidth should be adequate to faithfully reproduce the transponder pulses to a rise time of 0.1 μS. Whereas a primary radar receiver would normally have a matched bandwidth to maximise detectability, this is not a particular problem in a beacon system.

(3) The received signals are not under the control of the ground station and can lie anywhere within a ± 3 MHz range. Any individual transponder is reasonably stable but may be subject to incidental frequency modulation. RSRE observations have supported those made elsewhere that transponder carrier frequencies are distributed in an approximately Gaussian manner over the full 6 MHz allowed with a few outside this range. The implication of this is that in spite of the requirements noted above, the receiver bandwidth must be wider than that which would be used in a primary radar, and signal to noise ratio must suffer. It is recommended within ICAO standards that a signal of at least -85 dbm be available from a transponder at 200 miles, but it is usual for received signals to be well above this magnitude.

(4) The expected dynamic range of the received signals is less than those of a primary radar. This follows from the inverse square law applicable to beacon systems whose transponders radiate a relatively constant output. From 200 miles down to 3 miles a range of 36 dbs is expected from transponders in direct view of the interrogator. Civil aircraft transponder aerials are mounted below the fuselage and turning or banking may screen the aerial from view causing fades and missed replies.

Multipath interference likewise causes signal variations and it cannot therefore be assumed that all signals lie within a relatively narrow dynamic range, although most of them do.

3 SYSTEM ERRORS

3.1 Aerial Errors

Because the aerial is common to any process we will note briefly some of the errors which it may introduce.

The aerial system adopted by RSRE was manufactured by Cossor Electronics Ltd and is a modification for phase comparison monopulse of their standard aerial used with the SSR 700 Interrogator Receiver. It is a 49 element Dolph-Chebyshev array so combined to provide Sum, Difference and Control patterns. The main sum beam is also part of the transmitter system and has a beam width of 2^{o} and a gain of 24 dbs with 24 db sidelobes. The difference pattern has a central notch at least 30 db below the peak. The control pattern is a transmitter function only and does not concern the operation of the receivers except that it could be available as part of the receiver sidelobe suppression system if desired. The basic receiver patterns are depicted in Fig 2 together with the individual left and right hand beams for comparison. These latter will have approximately twice the width and half the gain of the sum pattern.

The vertical coverage is 45^{o} and the electrical errors that arise within this range are kept to within limits equivalent to 3.5' of azimuth error at boresight, but at the edges the effective beamwidth is modified.

It will be appreciated that elevation of the signal source would introduce an error in the indicated angle simply as a result of the geometry of the system. A signal source at a high elevation but at the same slant range as one closer to the ground would have a ground range which is less, and the azimuths would differ. This difference would not be revealed by the monopulse measurement but a correction could be made if the height of the aircraft were known from the Mode C replies. Fig. 3.

One aspect of phase error could arise through the use of an aerial with a tapered distribution. It may be assumed that the phase centre of the sum beam is at the physical centre of the array and does not move as the signal source swings away from boresight. However, if one considers the two half aerials then it is relevant to recognise that the spacing of their individual phase centres determines the phase difference of their signals. For a uniformly distributed aperture the separate phase centres are at the centre of each half and $d\lambda$ is half the total array width for all signals. A tapered array brings the phase centres closer together but for signals arriving from directions away from boresight, one finds that the effective phase centre spacing becomes even less. It has been found that for the aerial in question the corresponding phase error resulting from this cause is about 1^{o} at the 3 db beam edge but increases rapidly to 11^{o} at twice the beamwidth. This corresponds to a point about 12 dbs down the sum directivity pattern, in a region near to where the Interrogator Sidelobe Suppression system (ISLS) becomes operative.

The ISLS permits interrogations in a region about boresight where the transmitter sum/interrogator pattern has at least 9 dbs more gain than the control pattern and for the RSRE aerial this is within about $\pm 2^{o}$ of boresight. If one aims only to make measurements within the 3 db beamwidth of $\pm 1^{o}$ then the phase error arising from phase centre mobility is insignificant, but it is conceptually possible to widen the effective beamwidth by making measurements outside these limits, so making use of valid transponder replies which would otherwise be rejected. In practice the operational calibration of the system would of course take account of any departures from the ideal.

3.2 Direct Phase or Interferometric Measurement

In this arrangement the relative phase of the two aerial input signals is measured directly, usually after coherent frequency conversion, and amplification. Fig 4. The need for limiting amplifiers preceding the phase detector is governed by the choice of circuit for the latter and most of these are also amplitude sensitive. The limiters must match in their phase characteristics over the entire dynamic range of input signals expected, in the order of 70 dbs. For the commonly used IF of 60 MHz, phase departures of 5^{o} are a typical maximum and about 2^{o} between matched limiters with equal inputs and such characteristics should be maintained over the full working bandwidth.

An initial phase shift of 90^{o} is needed to avoid an ambiguity around boresight, but the use of two phase detectors in quadrature allow unambiguous measurements up to the full beamwidth of each aerial. Note however that these are twice the width of the equivalent sum beam.

The 5^{o} phase error measured on practical limiters corresponds to a proportional error of about 4' of indicated azimuth, remaining almost constant over the beamwidth. This assumes a phase centre spacing of 12 wavelengths appropriate to the RSRE aerial.

Limiting amplifiers have been found to have an output level variation of $\pm$ 0.5 db over a 70 db dynamic range. Assuming that the two amplifiers tracked in amplitude it will be seen that a phase detector may emphasise the distortion. A phase detector may be represented as a multiplier and the output, after low pass filtering, is

$$V_{out} \propto V_1 V_2 \cos\phi$$

where V_1 and V_2 are the inputs from the limiters. For equal inputs this reduces to

$$V_{out} \propto V^2 \cos\phi.$$

In the absence of any knowledge of the true magnitudes of the input signals, one must assume that V_{out} varies only with ϕ.

For a $\pm$ 0.5 db variation the resulting error in the indicated azimuth rises from 0 at boresight to 21' at the 1^{o} beam edge. A quadrature phase detector would help to reduce this overall error to about half. It is evident therefore that simple multiplicative phase detectors are not entirely suitable for this application unless the limiter output variation can be reduced to a more acceptable figure over the full 6 MHz bandwidth needed, but at RSRE such phase detectors are being used.

The addition of swept gain preceding the limiters may help to reduce amplitude induced errors for non-fading signals but this cannot be completely satisfactory.

3.3 Sum and Difference Measurement

The two aerial outputs are vectorially added to yield sum and difference signals. After frequency conversion and amplification their ratio is derived and this process is most conveniently performed by the use of logarithmic receivers, Fig 5. The limiting amplifiers shown in parallel with the main amplifiers belong to the direction sensing circuit implemented by phase detection between the sum and difference channels. With a fixed 90^{o} in circuit these will be either in phase or antiphase. Because of the need to accommodate a wide dynamic range of input signal the main amplifiers would be of the successive detection type. Their video performance in terms of stability, matching and closeness to a logarithmic transfer function must be impeccable since it is on these factors that the accuracy of the measurement depends. RSRE amplifiers track within 0.1 db over most of the dynamic range, and their departure from an ideal characteristic is no worse than $\pm$ 0.4 db, corresponding to an azimuth error of 2.1' at the beam edge.

It is inherent in the design of logarithmic receivers that the IF chain is a wide range limiter in its own right and hence it is not necessary for separate limiters to be used for the sense detection circuit.

Some work has been done in recent years to advance the techniques for producing a true IF logarithmic amplifier. Such amplifiers produce an IF output whose peak excursions are compressed by the transfer function whilst preserving the phase of the input signal. However, it has been the experience at RSRE,

when receiver designs were being formulated, that the phase performance of these amplifiers was degraded.

Since magnitude and sense can be separated, one has the ability to process the values in different ways. For a succession of readings subject to uncertainties one can either sum the values algebraically or else one may sum their moduli and apply a majority decision as to their sense. Supposing that the ratio V_d / V_s is subject to only small error, whilst the relative phase error is such as to indicate a measurable excess on one side of boresight compared to the other. The mean of these measurements taken algebraically would be nearer to boresight than the magnitude would indicate. Averaging their moduli and taking the majority of the sense indication produces an indicated azimuth closer to the true position.

4. IMPLEMENTATION

From the aforesaid it will be deduced that there are advantages and otherwise of both processes and although intuitively one expects both systems to be equivalent, much depends on how good the component parts can be kept within specified limits and there seems to be no overwhelming reason for choosing one against the other. At RSRE, it was decided to test the comparative performance of the two systems simultaneously whilst maintaining a measure of flexibility to incorporate modifications as needs arise.

4.1 RF/IF Circuitry

The basic arrangement takes the sum and difference outputs from the aerial hybrid and after frequency conversion and amplification, the signals are split into the logarithmic amplifiers and also combined into a 90° hybrid followed by the limiting amplifiers, Fig 6. This latter hybrid effectively reconstitutes the left and right hand beams, but with a 90° phase shift between them, if the original sum and difference signals are brought into phase previously.

The sum and difference signals alone give ambiguous results about boresight and the phase measurement made on the reconstituted beams can be used to determine the sense of direction. This arrangement is not identical to that discussed earlier in which sense was derived from the phase angle between the sum and difference signals, and it can be expected that because the noise in the reconstituted channels is uncorrelated with that in the sum and difference channels, the system is subject to larger errors from that cause. On the other hand, the ambiguity in the phase channel at the beam edges is resolved by the sum and difference measurement since within the beam limits the sum signal is larger than the difference signal and vice versa outside these bounds. It would be possible to cover up to twice the 3 db beamwidth without ambiguity, but for various reasons it is not thought practicable to extend the observable range of angles as far as this and in the experimental system only the nominal beamwidth is covered.

The effect of phase distortion in the sum and difference circuit preceding the reconstituting hybrid is shown in Fig 7. The plots show the computed response of a phase detector with varying degrees of phase shift and it is seen that for shifts of up to about 20° the output error is quite small. An interesting plot occurs with 40° shift for which an almost linear output is available over most of the angular range. Although no advantage has been taken of this at present it is conceivable that in some applications it could be exploited.

Fig 8 shows the complete receiver as it is currently constructed. The sum channel input feeds to a diplexer which comprises two 90° hybrids coupled by differential delay cables. The directional filter so formed allows the transmitter to be isolated from the receiver input whilst providing a low loss path from aerial to receiver. An advantage of this arrangement is that an aerial mismatch does not reflect to the receiver. The difference circuit is equalised to the same delay.

The RF filters that follow are principally to reject signals from other navigational aids, notably DME, which operate near the SSR frequencies. A somewhat unexpected difficulty arose at Malvern because the local TV station radiates three programmes, at frequencies below 850 MHz, so as to cause interference near the 60 MHz IF, and these filters eliminated this problem.

The filters have a 3 pole Chebyshev response with 0.1 db ripple over 15 MHz. A comb line configuration is used in order to bring the stop band to 3 GHz at which frequency a co-mounted primary radar operates. The combs are $\lambda/12$ long and allow a compact construction. The Chebyshev response was chosen because the phase response over the central 6 MHz is more linear than an equivalent Butterworth filter, but a more practical reason is that they appear to be less prone to misalignment through thermal expansion.

Protection limiters precede the mixers which are a commercial balanced Schottky design, fed with a local oscillator which was somewhat unique at the time of installation in that it uses a SAW line at a fundamental of 1.03 GHz and was designed and constructed by the Applied Physics Group at RSRE. A hybrid splitter is used to feed the local oscillator to the mixers and this brings the IF signals in phase, (Lewis M F, 1974).

The head amplifiers are tuned to an overall bandwidth of 10 MHz and use low noise dual gate FETs producing a gain of 41 dbs including the mixers, with an RF noise figure of 7.5 dbs.

The entire RF head with head amplifiers is mounted in a heated box adjacent to the aerial.

The 60 MHz IF signals feed to the main amplifiers via 20 m of low loss cable. The lines first divide through 90° hybrids to the logarithmic amplifiers for sum and difference measurement and the other ports are then cross coupled in a further 90° hybrid to reconstitute the separate beams. Limiting amplifiers then follow to the phase detector and optionally a further pair of logarithmic amplifiers can be worked in parallel for monitoring purposes. Ideally, the signals at the input to the limiters would be equal but interference may not only cause phase distortion but amplitude variations. An inequality indication from the monitor lowers the degree of confidence in the measurement. Unfortunately, the converse is not also true and equality does not necessarily indicate a high degree of integrity.

The outputs from the logarithmic amplifiers and the phase detector feed through 75 ohm cable and coaxial sliprings to the video processing unit.

4.2 Video Processing

So far we have been concerned only with the actual measurement of the off-boresight angle without consideration of signal detectability or validity.

Each expected signal will contain a group of two or more pulses of nearly equal amplitude and this fact enables the process to include a method of recognising wanted signals from extraneous ones. The question does present itself as to whether monopulse measurements be made on all the pulses in the group or only on one, or some of them. If the group contains pulses occupying predetermined positions as is the case for SSR Mode A replies, the receiver need only examine those particular places in order to make any measurement, but in general the content between the bracket pulses is flexible. This is particularly the case for Mode C replies and even more so for the longer messages proposed for ADSEL/DABS. It must be accepted that if multipulse processing is adopted, the data must be stored until the last bracket pulse appears in its correct relationship to the first and if it does not then the data must be rejected as invalid.

There are several options as to the means by which multipulse measurements can be implemented. Among these are those in which the received signals are integrated as a group before quantisation and conversion to equivalent angles, and those in which each is converted first. With sum and difference processing, the logarithmic amplifier outputs may be integrated before or after subtraction to derive the log (ratio), an arrangement which is dependent on the number of pulses in the group and must therefore be adaptive. It is to be noted that the integration of logarithmic receiver outputs is not entirely meaningful if all the pulses are not of about equal amplitude. If a low level interference pulse occurs within the group, the system may not recognise it as false but its effect on the measurement would be out of all proportion to its magnitude.

With direct phase angle measurement, integration could only be performed after the phase detector, but again some adaptivity is needed to take account of the number of pulses integrated.

The only satisfactory method of multipulse measurement is to process each pulse independently but this does call for faster circuitry if quantisation is to be performed as each pulse appears. One way of overcoming this requirement would be to take advantage of the newer CCD devices, but in operational equipment this could prevent observations of signal groups occurring closely in range. In the RSRE experimental receiver, only the last bracket pulse is measured, thus reducing all signals to a worst case situation for it is to be expected that multipulse measurements must be of a higher integrity.

The fact that sum and difference channels are available for angle measurement also provides a means of receiver sidelobe suppression (RSLS). As already stated, ISLS elicits replies over about twice the sum channel 3 db beamwidth whereas the crossover between sum and difference beams occurs at the beamwidth limits of about 3 dbs. Although RSLS causes loss of information it also reduces the amount of interference. In practice, as is the case for the RSRE aerial, the difference pattern has other crossover points in the nearer sidelobe region but outside the ISLS range, and non-coherent interference (fruit) is then able to penetrate the monopulse measurement system. The incorporation of an extra channel in the control pattern would prevent this trouble but at the extra cost of a complete amplifier and diplexer.

A problem which frequently presents itself in pulse sampling systems relates to the timing accuracy of the sampling pulse in relation to the pulse being sampled, when the former is derived from the latter. Since the timing is usually derived by relating the signal pulse to a fixed threshold set near peak noise level, the finite rise time of the pulse causes variations in the timing of the crossover as the signal level varies. At RSRE, this is also followed by an adaptive threshold which automatically sets itself to a level 3 dbs below the peak pulse amplitude and is therefore capable of defining the width of each received pulse. Sampling is arranged to take place over the plateau of the signal and short pulse rejection circuits are incorporated. A further threshold comes into operation at about -6 dbs and this is held for 24 μS so as to allow only those signals of similar amplitude to the first to appear at the output whilst low level interference occurring within the group is rejected. Bracket pair detection is then performed on the available signals to envalidate recognised SSR replies. Higher level interference within a group would be accepted as part of the coding since no form of code correlation is used but the second bracket pulse would still terminate the message. To take account of the fact that most SSR reply pulses droop in amplitude towards the end of a group, a similar droop is permitted in the second threshold. The code pulses between the bracket pair are used to activate a numeric display showing identity and height positioned alongside a standard PPI display which presents only signals from validated replies.

Quantisation of signal amplitude is performed on the output of an integrator gated during the plateau period of the second bracket pulse. This helps to smooth out the effect of noise and ripples. As is well known, the pulse shape resulting from a passage through a logarithmic amplifier has a fast rise time but a slower linear decay. Integration over the whole pulse length would result in an output which is not directly related to amplitude since the effective pulse length varies also.

Aerial bearing is encoded to a resolution of 2.6' and provision is available to lock the interrogation rate to the shaft encoder so as to eliminate uncertainties derived from this. Digitised data of off-boresight angle, aerial azimuth and range are punched onto paper tape and the various operations of processing are performed by an ICL1907F computer.

5. INTERFERENCE

Interference in SSR can take several forms:

FRUIT: Non-coherent signals from transponders replying to other interrogators.

GARBLING: The effect of random or synchronous signals from transponders at similar ranges, causing overlapped code groups.

MULTIPATH: Coherent signals arriving via a secondary path and either interfering with the direct signals or causing the appearance of false targets.

Signals may also be observed from DME, which covers the same part of the spectrum. Although some frequencies are reserved as a protection for SSR the possibility of images being received still remains.

Since the interference difficulty in SSR is already well documented, we need only be concerned here with the effect it will have on the monopulse measurements.

Fruit interference arises because of the multiplicity of interrogators at present deployed within operational range of each other. The eventual implementation of ADSEL/DABS will reduce the number of interrogators and by virtue of the considerable decrease in the interrogation rate from each, the fruit problem will be largely overcome. There must be a transitional period when both systems operate and standard SSR will remain for some time to come.

Fruit signals arriving in the main beam are accepted as genuine unless they can be recognised by their lack of coherence or by their code content. In the sidelobe region fruit can be rejected by RSLS, but since this process is conducted at video level the possibility of both main or sidelobe fruit being present simultaneously with a genuine signal cannot be ignored. So far as monopulse is concerned a measurement of the off-boresight angle will be made on the resultant of the interfering signals. In general one may expect that since the fruit will not have identical code content or coherence with the intended signal, measurements on each pulse in the group will result in different indicated angles. It cannot be assumed that sidelobe fruit is necessarily of small relative amplitude, because a transponder appearing in a sidelobe at close range may produce a larger signal at the aerial terminals than a more distant mainlobe transponder. The 24 db sidelobe level of the RSRE aerial corresponds to a range ratio of 16:1 for equal signals in main and sidelobes, and it is therefore to be expected that large sidelobe interference levels are common. Because of the incoherence from pulse to pulse within a code group which fruit interference may have, especially as the carrier frequency offset could be as large as 6 MHz, multipulse monopulse measurements may be processed to yield better estimates of off-boresight angle although with larger variance, or if interference is detected the reading may be deleted altogether.

Synchronous garbling has a similar effect on the measurement as fruit with the exception that whereas fruit is transitary and not likely to affect all replies obtained within a beamwidth, overlapping of replies from aircraft at similar ranges will occur for a much longer period and extending to several minutes for aircraft on parallel tracks. It is seen that observations of aircraft in holding patterns can create particular difficulties.

ADSEL/DABS with their ability to selectively interrogate aircraft would eliminate this problem, excepting the possibility of the occasional falsely generated reply.

Multipath creates a more serious problem because the interfering signals are coherent with the desired signal and have long correlation times. Because of the limited acceptance angle of the main beam, the path length difference between direct and multipath signals is generally less than 20 feet or so and separation of the signals by their time of arrival cannot be performed. Sidelobe multipath may have much longer delay times. A flat earth might be expected to cause no error in an azimuth measurement since the indirect path lies immediately below the direct path. This does assume however that the overall signal to noise ratio has not been affected and it will be seen that for low signal to noise, the mean value of $\sin \psi$ in (2) can only be reduced from its ideal value of unity as a result of introducing a uniform phase distribution and the indicated angle will be biased towards boresight. The presence of a strong multipath signal in antiphase with the direct wave will result in a lower signal to noise ratio and a bias towards boresight can be expected.

The effect of multipath arriving from a different direction from the direct signal is governed not only by the separation of their respective azimuths but by the signal to interference ratio. If this is greater than about 20 dbs the resulting errors are of the order of 0.1 beamwidths or less corresponding to 12' for the RSRE aerial. It has been shown that the type of process used can affect the overall performance in the presence of interference (Cooper D C and Wyndham B A, 1973). Using a statistical model in which the interferer is uncorrelated with the desired signal, the maximum error obtained by the 'worst' system is about twice that of the 'best', but no rigid rules are established as to which system remains the best under all possible conditions. In the paper referred to, it was shown that the direct phase measuring system gave smaller maximum errors than its competitors, including amplitude monopulse processes, over a wide range of signal to interference ratios. It is to be expected that most multiplath signals will have a measure of coherence with the desired signal and it has been shown that the largest errors occur for the antiphase condition. (McAulay R J, 1973).

In general, it may be stated that whereas fruit interference effects may be largely reduced by multipulse processing, multipath interference will not be amenable to this treatment and one is left mainly with systems which indicate the presence of multiple signals so that the degree of confidence is lowered.

As the elevation angle increases, the azimuth multipath error increases also to a maximum followed by a decline, as determined by surface conductivity, permittivity and the roughness of the ground. It is clear therefore that aerials with a sharp bottom edge cut-off would be advantageous and for future systems

such aerials will be installed but in existing SSR the wide vertical fan beam has the unfortunate ability to cover large areas of local ground. Fuller treatment of the interference problem have been published elsewhere and in particular, work at the Lincoln Laboratories has been directed to SSR. (Kulke B, Rubinger B, Haroules G G, 1971 and McAuley R J, McGarty T P, 1973).

6. EXPERIMENTAL PROGRAMME

Observations have been made of transponders located on the ground at known positions and of aircraft in flight.

6.1 Fixed Transponders

Although ground based transponders have some merit in that they can afford an accurate reference for determining biases in the monopulse results, they also suffer from the practical difficulty of deployment at reasonable ranges within line of sight without the added problem of multipath. A particular site available to RSRE appeared to be ideal before measurements were made, being at an elevation of 0.6^{o} at 16 Km, but a serious multipath effect amounting to about $\pm 0.75^{o}$ was noted. This latter error was found using different equipment at a slightly different position to the radar reported on in this paper, but the experience did produce some caution in choosing sites for future experiements.

6.2 Results of Fixed Transponder Measurements

Several sites were chosen and a number of aerial sweeps were made for each position. Each sweep records 28 possible replies for both direct phase and sum and difference processes, and programmes have been written to make available a number of output presentations. Figs 9a, 9b show both sum and difference and the phase detector responses for about 200 independent plots each at two sites.

Fig 9a shows the outputs from a site relatively clear of multipath. The sum and difference curve is from the quantised output of the log differencing circuit whilst the phase curve is the quantised output from the phase detector. Fig 9b shows the effect of multipath causing a decrease in the difference/sum ratio.

The same results are replotted in Figs 10a, 10b after conversion to indicated azimuth. The sum and difference plots have been offset upwards by 5' and the phase plots displaced downwards by 5' so as to avoid confusion with each other. The scales are in minutes from true north.

The multipath effect of Fig 9b is shown in Fig 10b in which the sum and difference plots not only show a step in the indicated azimuth about boresight but a progressive error as the aerial rotates. As Fig 9b shows, there is a much reduced boresight notch depth which is interpreted by the calibration characteristic as a larger off-boresight angle than would otherwise occur. At the beam edges where the largest angles are expected, the indicated azimuth is approximately correct, but as boresight is approached, the error increases until the sense indication causes a switch about the boresight position. The phase process results appear to be more acceptable in that the errors are larger at the beam edges but are correct closer to boresight. In spite of this, the two processes yield a statistically similar bias error of about -5' whilst the rms error over the beamwidth is found to be about 2.5 times larger for the sum and difference process.

The plots of Figs 10a and 10b are included in Table 1 which summarises the results from a number of different sites at distances up to 30 Km. The true azimuths were derived from National Grid references. Interrogations were exclusively with Mode D and consequently the transponder was not captured by interrogations from operational SSR sites within range. For this reason sliding window comparisons are not too meaningful since the conditions are not representative of a true-life situation. It is to be expected that results for sliding window plots with no missed replies will not be dissimilar to the monopulse results but it is emphasised that the latter are obtained on a single reply basis only.

The table shows the indicated azimuth for Phase and Sum Difference (S & D) processes, based on 7 consecutive aerial sweeps for each site and up to 28 replies in each. The standard deviations (σ) for both processes are about 3' and it must be remembered that one source of uncertainty lies in the limited resolution of the aerial shaft encoder, namely $\pm$ 1.3'.

An experiment has been made, but not detailed here, in which the interrogator PRF is locked to the least significant bit of the shaft encoder in order to eliminate encoder error, and this has been successful.

The bias errors average to less than 2' for all processes and it is pointed out that the true azimuths for two of the sites are not known accurately.

It is evident from Figs 10 that the overall errors for the phase monopulse is worse nearer the beam edges than closer to boresight. This is due mainly to an incomplete knowledge of the calibration characteristic. Phase distortion in the sum and difference circuits preceding the combining hybrids was assumed to be zero but if a correction is applied in accordance with Fig 7, a more consistent result would be obtained across the beam. Further, the phase detector output for near beam edge responses may occasionally equal or exceed the assumed maximum value normally obtained for true beam edge signals. These must be assigned the beam edge value and the indicated azimuth will then diverge rapidly.

6.3 Airborne Transponders

Observations on aircraft offer opportunities for continuous measurements under real-life conditions. Indeed, there may be a problem in acquiring too much data, but the main difficulty lies in the fact that an uncooperative aircraft cannot be assigned a true position at each point in its track. The best that can normally be done is to compute a best fit curve through a succession of measured points by any of the well known track smoothing techniques and noting the departures made. This routine would not reveal any

bias in the measurement which can only be found if one knows true position. For this reason, RSRE have made observations mainly on a cooperative aircraft. Before elaborating on these results it is worth considering the options.

To establish the true position of an aircraft at long ranges it is usually necessary to rely on the aircraft's own navigational equipment for a fix and to transmit the information to the remote observer. That this procedure is inadequate for continuous track following is self evident. A special channel of communication would need to be opened although it is conceivable that the downlink message formats of the ADSEL/DABS proposals would allow such a channel to be incorporated within the observing system. Alternatively the position data may be recorded on board and made available at some later time. Either way there must be some degree of cooperation on the part of the aircraft operator and it is therefore not possible to extend such arrangements to include any aircraft observable to the ground station. On-board recording also presents the necessity for accurate simultaneous time recording which would need to be made from Standard Time transmissions or local atomic clocks which have been previously synchronised.

It must be accepted that with the exception of specially equipped aircraft, the integrity of on-board navigational data is open to scepticism and it is not likely that any position can be relied on to be better than about 0.5 mile. To be independent of on-board sensors, observations would need to be made from ground based radars which are themselves subject to the same kind of errors as the system under test. At RSRE a co-mounted primary radar is available but for the reason given was not used as a reference standard.

One possibility which is being investigated uses the SSR system itself but in collaboration with specially deployed slave interrogators. The latter would comprise a standard interrogator/receiver coupled so as to cause a second interrogation after receipt of a signal from an aircraft transponder. If the slave is deployed close to the side of an air corridor with a fixed vertical fan beam positioned across the path of aircraft in the corridor, then slave interrogations only occur whilst an aircraft is within its beam. A remote interrogator will initiate a response from the transponder which in turn causes itself to be re-interrogated after a delay determined by its range from the slave and a fixed delay to clear the transponder's dead time. The remote observer will then see a reply from the initial interrogation followed by a further response only whilst the aircraft is in the relatively closely defined region of the slave beam. It is conceivable that by the incorporation of a monopulse detector in the slave and modulating the delay of alternate slave interrogations with the angle information so obtained, the position of an aircraft within the slave beam can be more localised. Although this scheme is suggested mainly as a temporary calibration device, the possibility of its deployment as a permanent performance monitor available to any SSR interrogator might be worth further consideration.

6.4 Results of Aircraft Measurements

It was stated earlier that RSRE measurements were made on a cooperative aircraft, namely a Comet 4B fitted with accurately calibrated recording navigational equipment. Data is obtained from multistation DME, an Inertial Navigator and other standard equipment, and is referenced to Rugby Standard Time transmissions. Positional data is recorded on magnetic tape and track plots can be reproduced at leisure.

At the time the recordings were made that are presented in this paper, no time reference was available at RSRE and consequently we can only relate track positions from the navigational data to those obtained by SSR monopulse measurements without correlating the time.

Fig 11 shows a series of plots obtained from monopulse measurements for a succession of orbits of 5 miles diameter, 70 miles south of the interrogator. The centre of each circle is the mean of the range and azimuth values obtained for each sweep of the aerial translated to map positions. The radius of the circle is equal to the standard deviation of the azimuth measurements. Plots are shown of the positions obtained for both monopulse processes and sliding window, and for reference, Fig 11 shows the track as recorded by the aircraft's inertial navigator which was known to have developed a bias error of 2.5 Km during the course of several hours flying.

It will be seen that the standard deviations for most of the plots are less than 0.1 mile. The largest deviations arise from single fruit signals in each sweep fortuitously occurring at the same range and not therefore rejected. The error over the ground must obviously increase with range and translating these observations to 200 miles we could expect ground errors of about 0.5 mile not taking account of propagation effects. The sliding window plots shown for comparison must be viewed with caution. Mode D interrogations were made for these plots as for the static results, excepting that the aircraft transponder was open for Mode A so that capture by that mode was possible, but not by Mode C. Consequently, errors from missed plots will be smaller than for operational systems. Further departures from normal practice arise because detections are based on a sum > difference threshold and also, by virtue of the nature of the pulse definition circuitry with its own threshold operation, the effect of interference on the sliding window estimates will be different. Whereas monopulse measurements maybe made on 28 replies separately, sliding window estimates require all valid replies obtained in each sweep and it is not possible to present standard deviations for this process.

7. CONCLUSIONS

The number of measurements made under a wide range of conditions has so far been small, but results presented here show that off-boresight monopulse is capable of yielding plots of a high integrity, even on the basis of single pulse measurements. Multipulse processing combined with interference detection would no doubt improve the reliability further, as would a more detailed knowledge of the system calibration. Experiments are continuing and the problem of establishing bias error on aircraft plots is being investigated in more detail.

ACKNOWLEDGEMENTS

Thanks are due to colleagues at the Royal Aircraft Establishment, Farnborough for their assistance in providing flight data presented in this paper. The work is supported by the Civil Aviation Authority.

REFERENCES

BOWES, R. C., STEVENS, M. C., DROUILHET, P. R., WEISS, H. G., 1975, "ADSEL/DABS - A Selective Address Secondary Surveillance Radar", AGARD 20th Guidance and Control Panel Symposium, Plans for Developments in ATC Systems, Boston.

KULKE, B., RUBINGER, B., HAROULES, G. G., December 1971, "Monopulse Azimuth Measurement in the ATC Radar Beacon System", Transportation Systems Centre Technical Report DOT-TSC-FAA-72-6.

LEWIS, DR. M. F., May 1974, "SAW Devices and Applications", No. 6. Ultrasonics, P115-123.

McAULAY, R. J., 1973, "The Effect of Interference on Monopulse Performance", Lincoln Laboratory Technical Note 1973-30.

McAULAY, R. J., McGARTY, T. P., 1973, "An Optimum Interference Detector for DABS Monopulse Data Editing", Lincoln Laboratory Technical Note 1973-48.

TABLE 1

Site	True Azimuth (mins)	Phase Bias (mins)	Phase σ	S & D Bias (mins)	S & D σ	Sliding Window Bias (mins)	Sliding Window σ
Bartlow House	8927.6	-5.9	1.64	-5.6	1.38	-7	1.31
Birdlip 1	9223.8*	8.9	1.73	10.4	3.28	9.46	2.63
Birdlip 2	9219.6	0.6	1.44	2.6	2.49	-1.52	3.08
F C Gate	10650.5	3.3	1.85	1.9	2.34	-0.19	1.6
High House	2442.7	-1.0	2.9	+0.9	3.89	0.52	1.31
Hewell Grange	2539.6	-4.5	2.78	-2.9	1.51	-4.54	0.92
Crumpfield	2842.4	-3.0	1.66	-1.7	3.23	-3.18	2.44
Lippets' Farm	20930.1	4.6	2.79	5.3	7.53	1.99	1.73
Lickey C P	1961.1*	10.3	4.43	13.2	3.06	11.8	1.31
Cobley Hill	2315.7	-4.9	2.1	-5.3	1.89	-6.65	1.64
Windmill	2420.1	-5.2	2.07	-4.4	1.58	-4.26	1.3
Adams' Hill	1296.3	3.7	2.1	6.0	1.32	5.52	1.48
Clent Hills	1402.5	4.2	1.6	3.7	1.96	3.28	1.44
	mean bias	-0.74		0.45		-1.46	
	overall rms error		2.37		3.16		1.81

*Position not certain. Bias errors not included in the total.

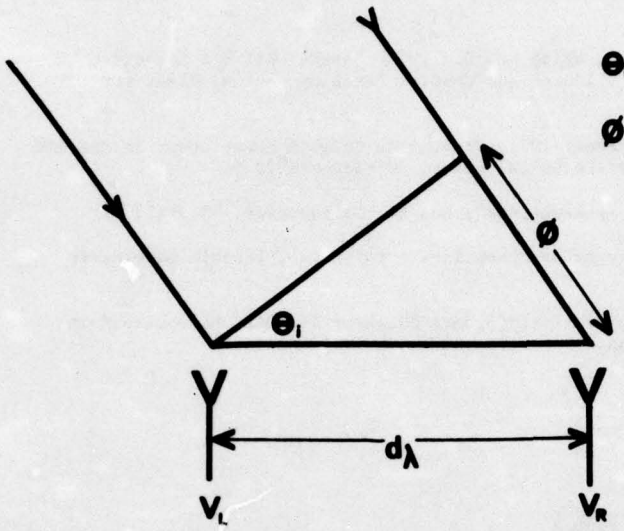

Fig.1(a) System geometry

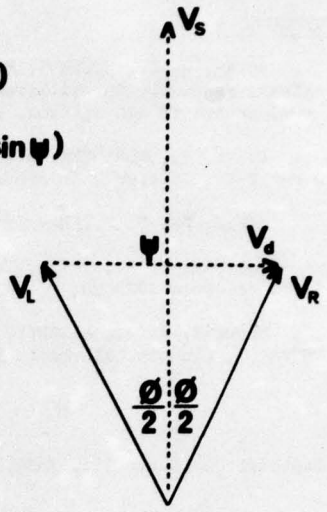

Fig.1(b) Vector diagram

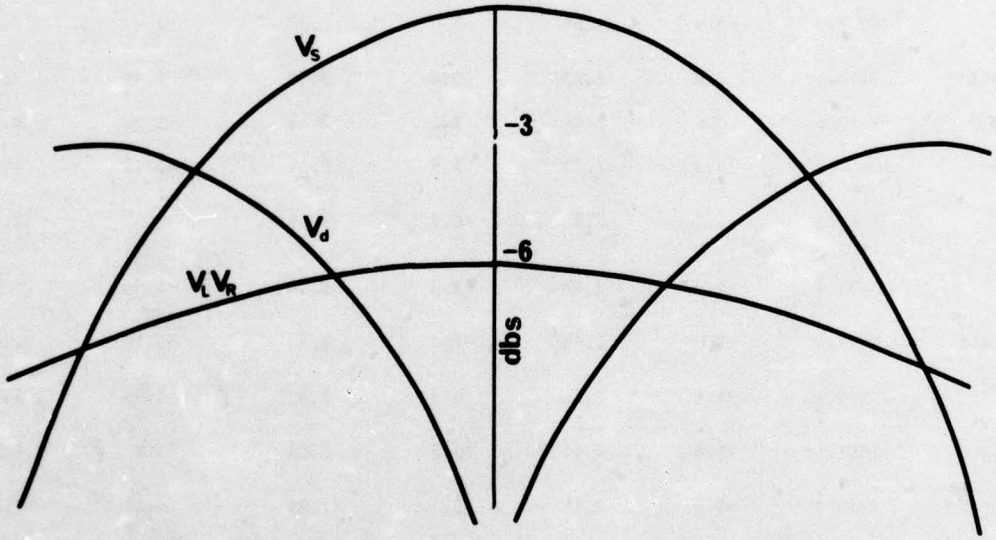

Fig.2 Aerial patterns

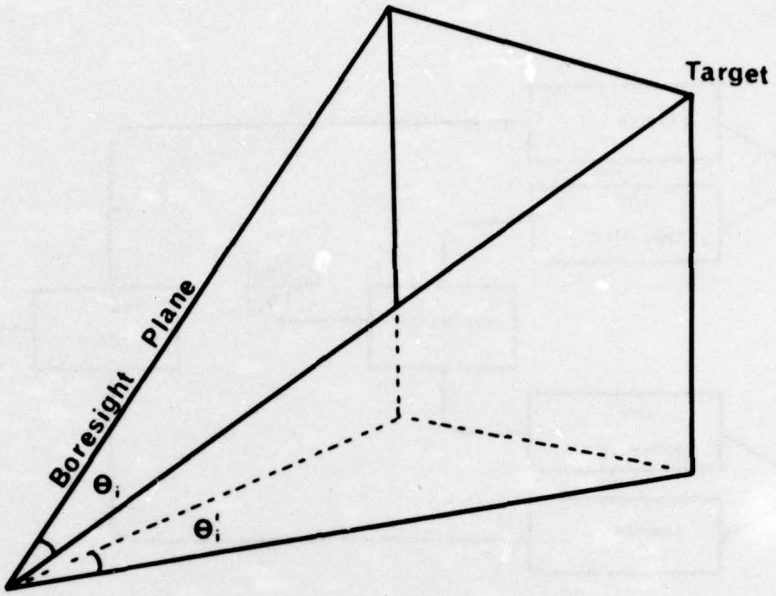

θ_i Indicated Azimuth

θ_i' True Azimuth

$\theta_i' > \theta_i$

Fig.3 Elevation error

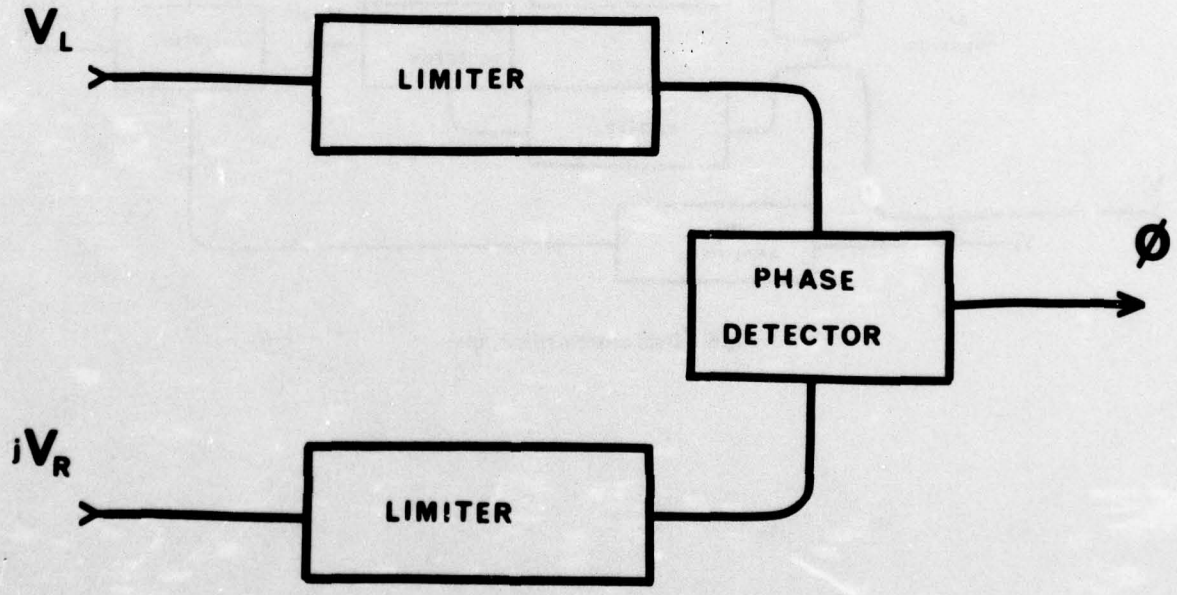

Fig.4 Basic interferometer

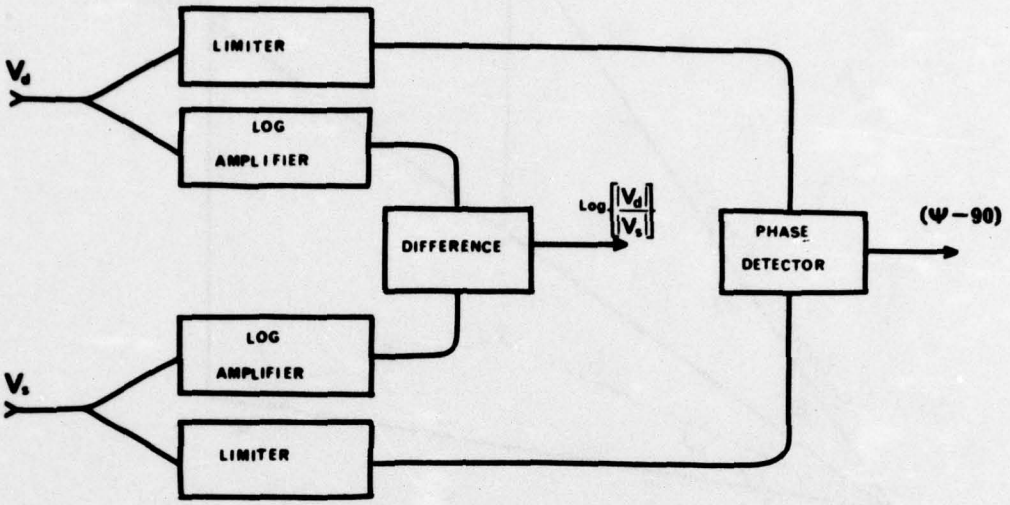

Fig.5 Basic sum and difference process

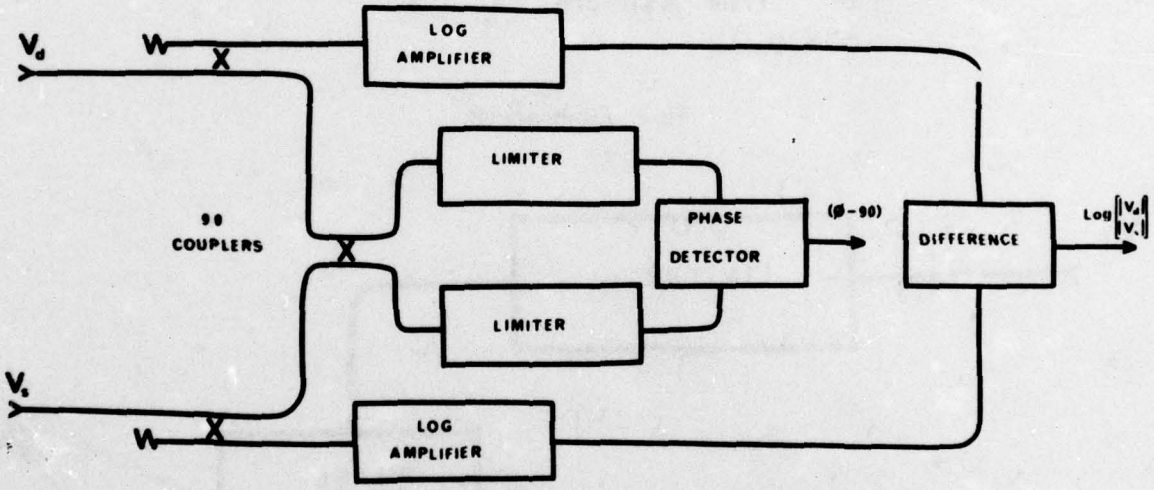

Fig.6 Dual process monopulse

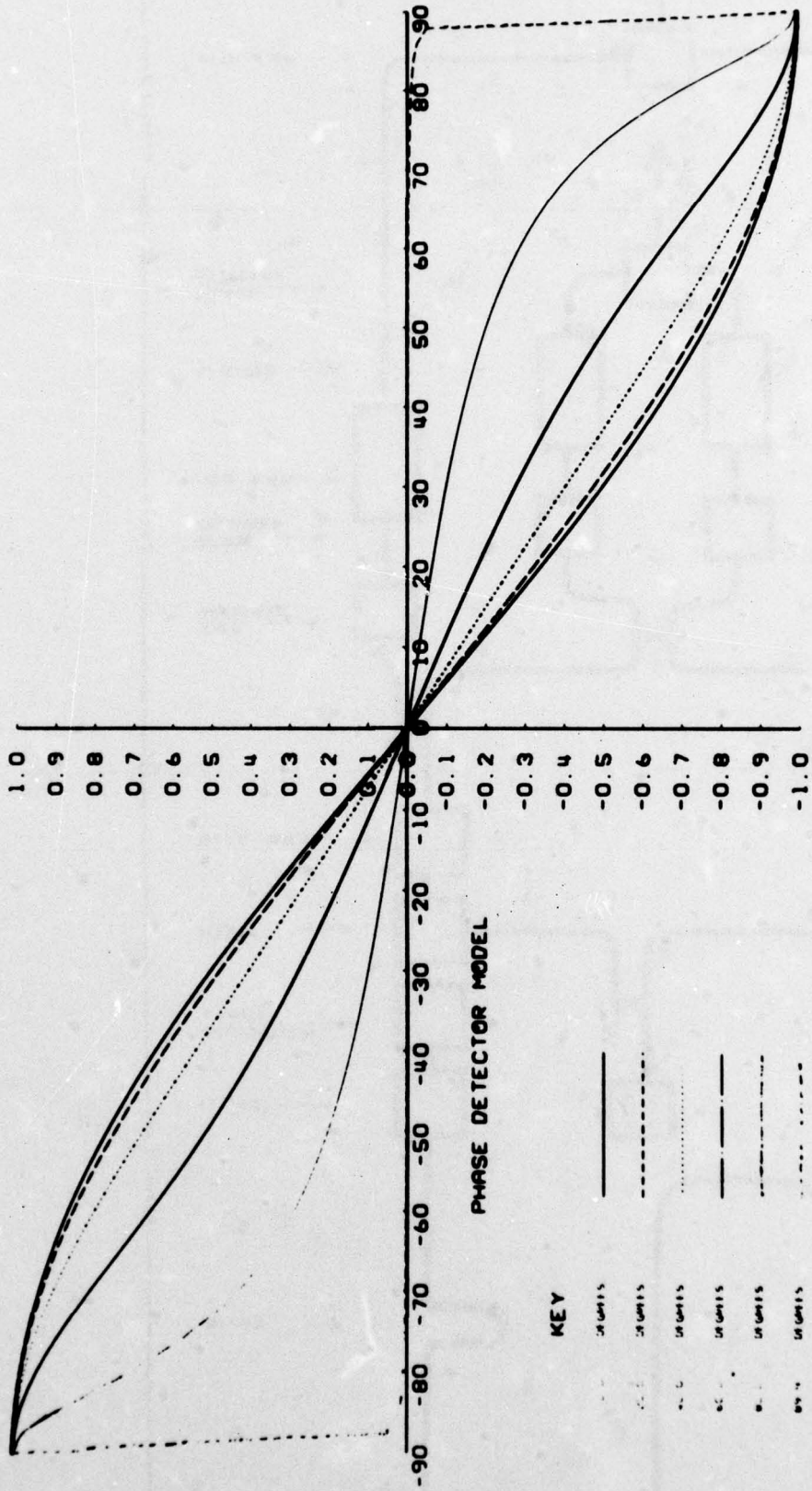

Fig.7 Effect of sum and difference phase shift on reconstituted beam phase

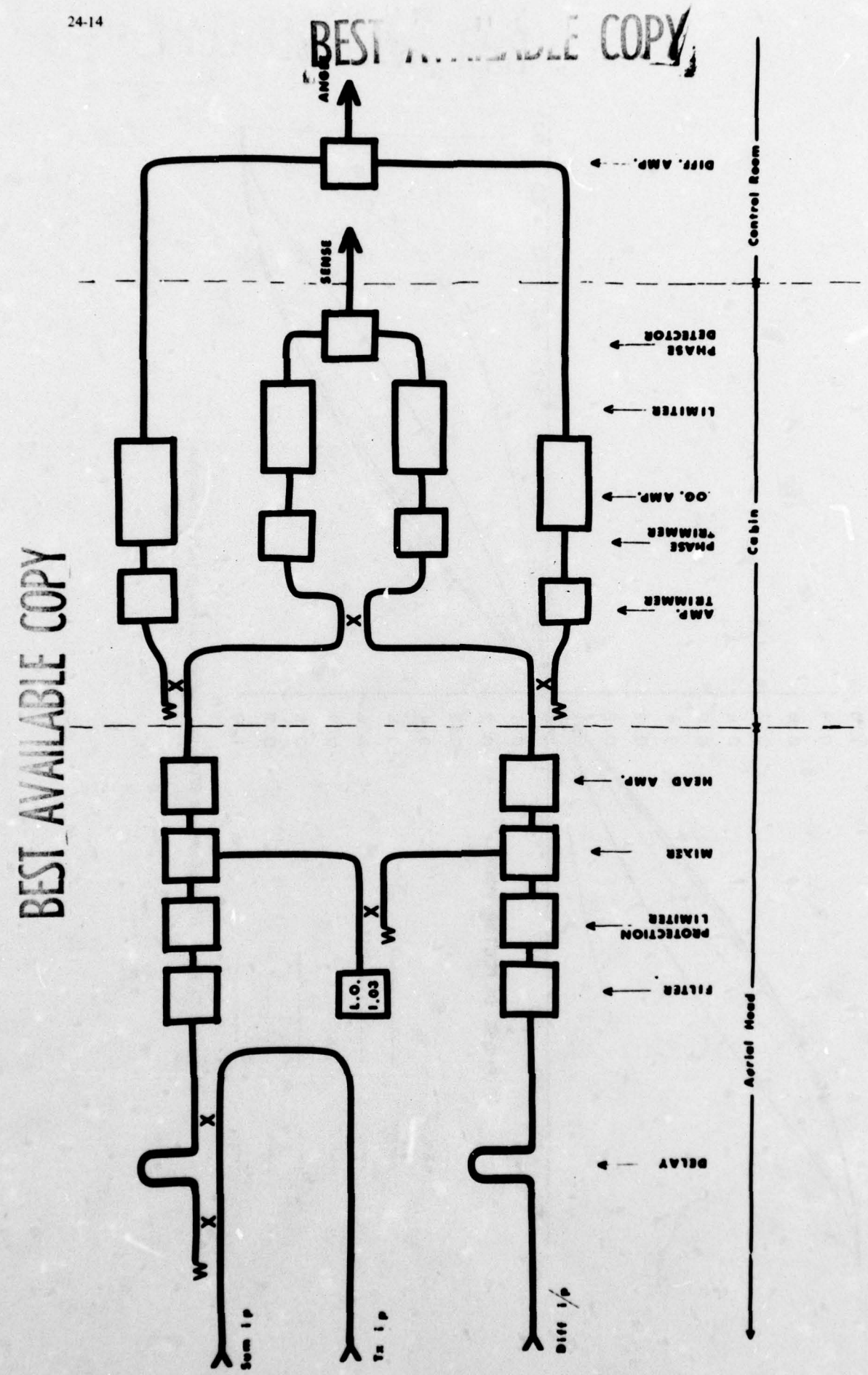

Fig.8 Dual process receiver

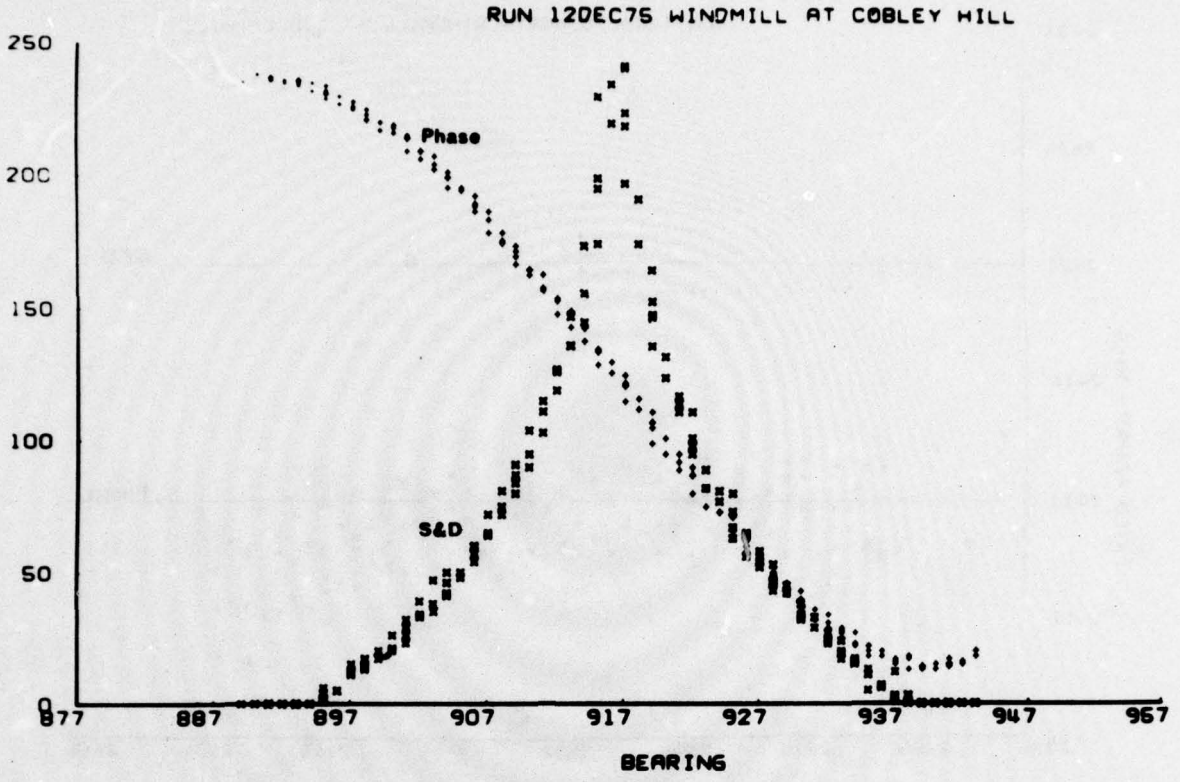

Fig.9(a) Receiver outputs (uncorrupted)

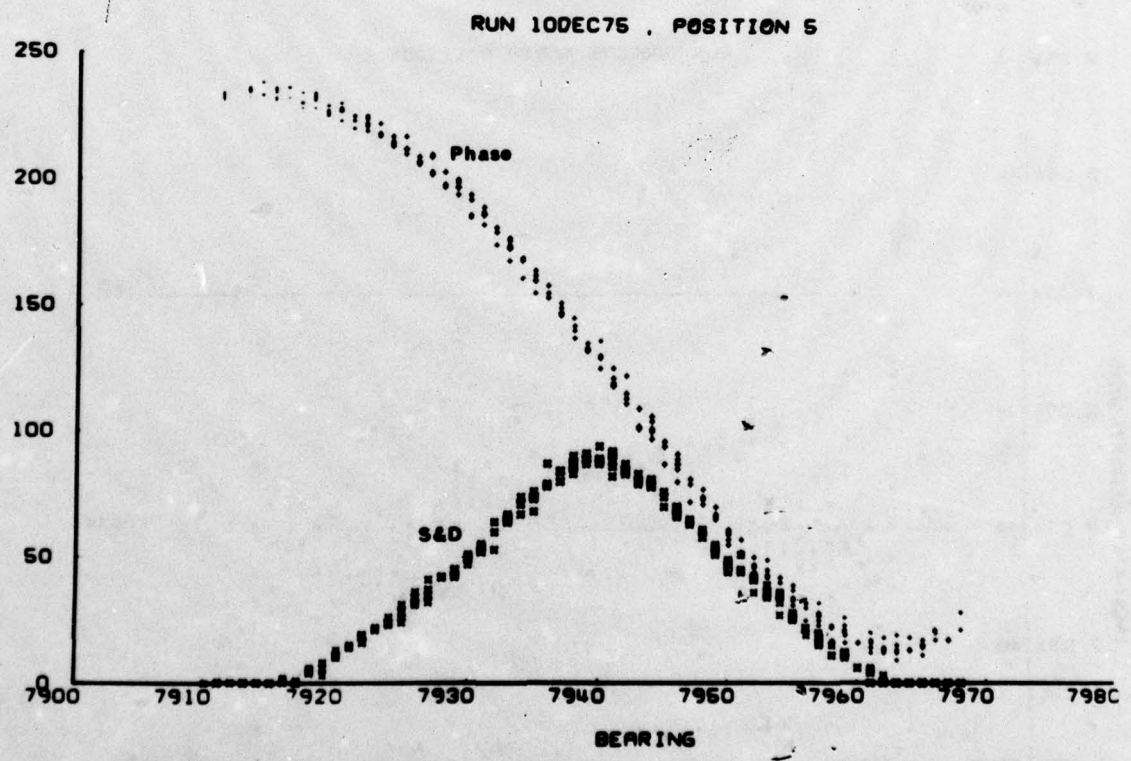

Fig.9(b) Receiver outputs (corrupted)

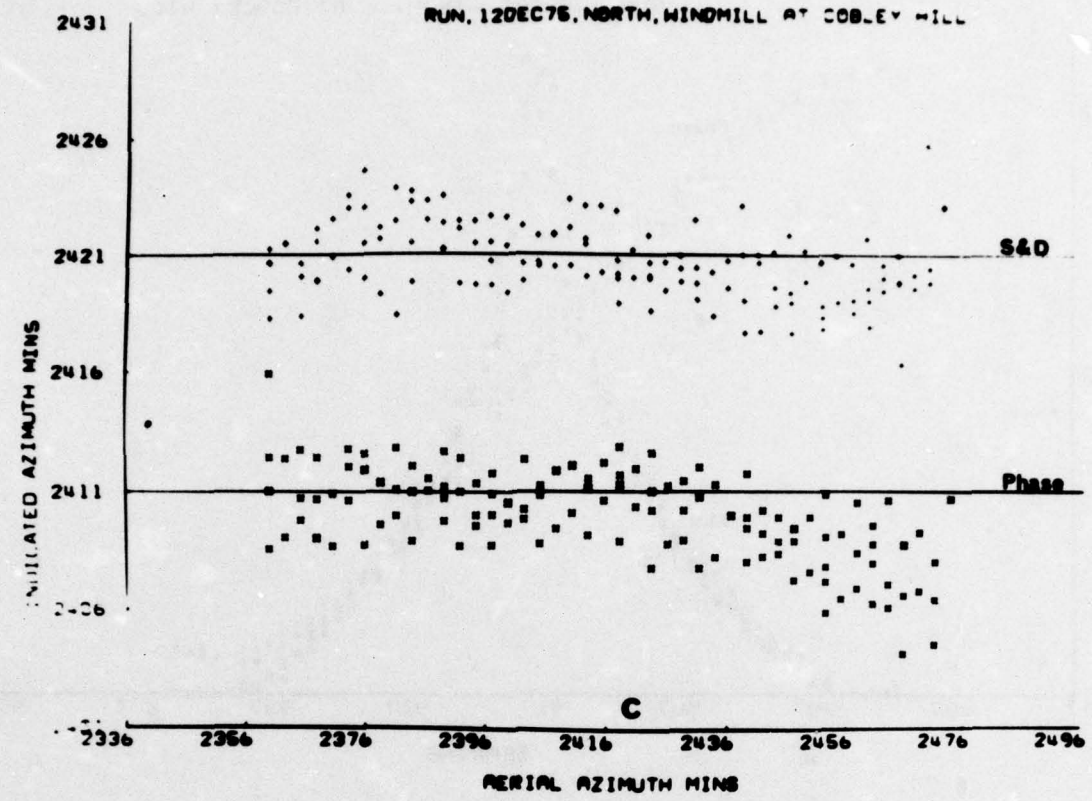

Fig.10(a) Indicated versus aerial azimuth

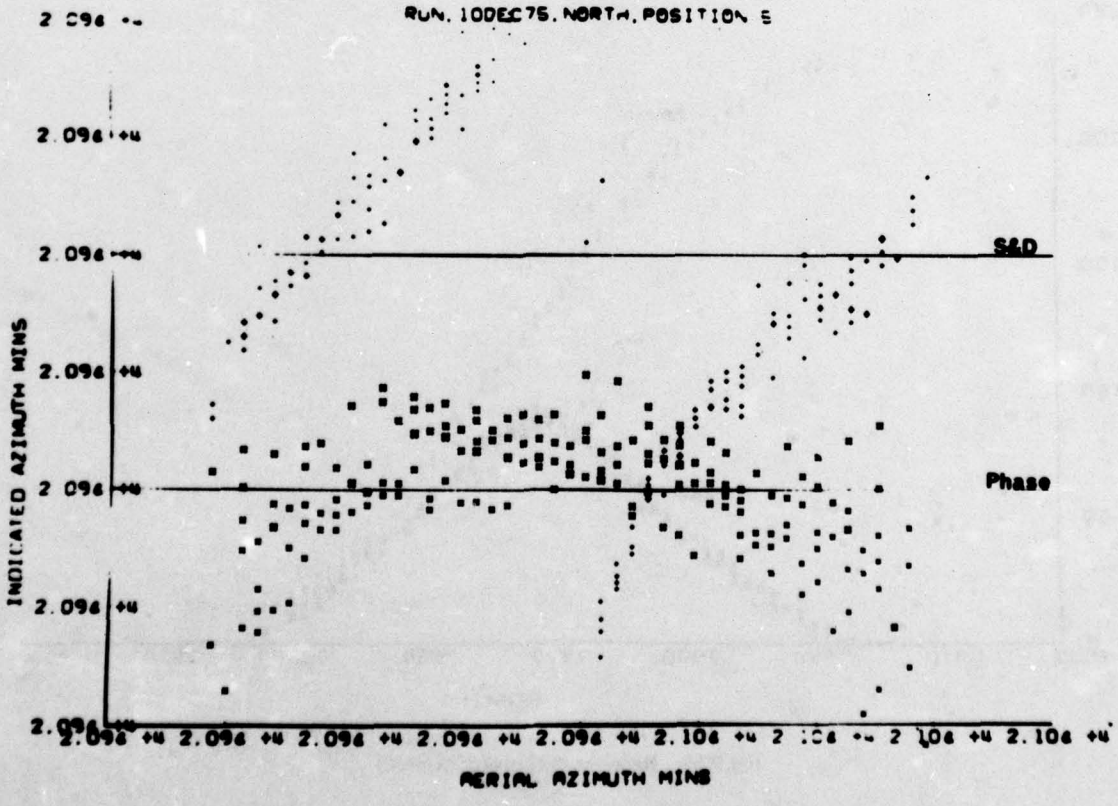

Fig.10(b) Indicated versus aerial azimuth

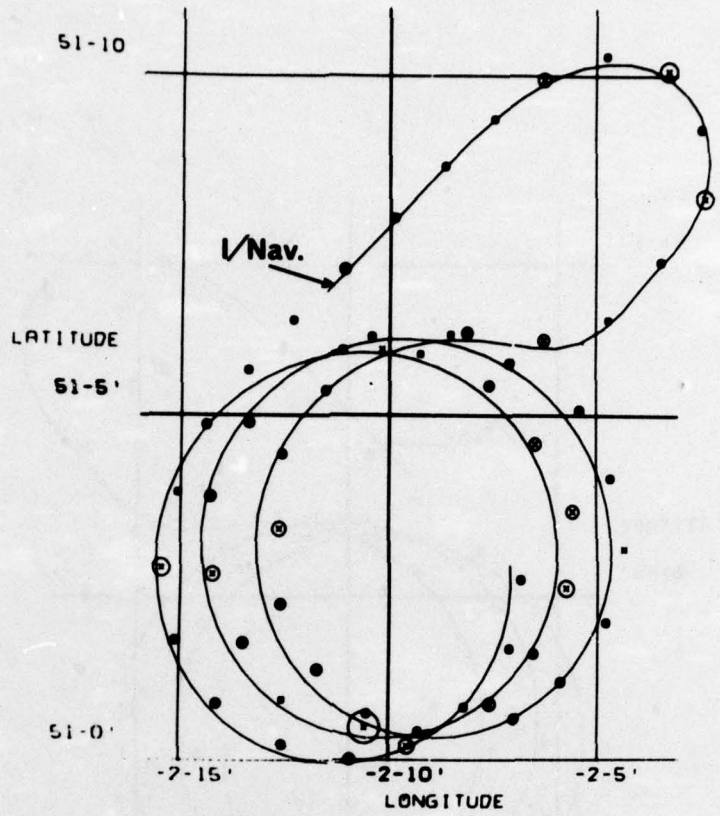

Fig.11(a) Phase monopulse plots

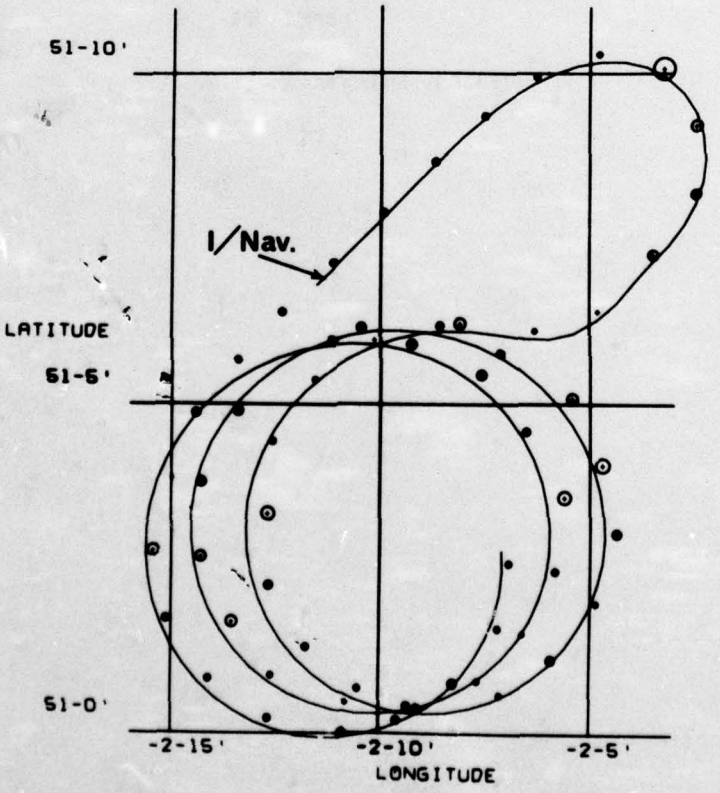

Fig.11(b) Sum and difference monopulse plots

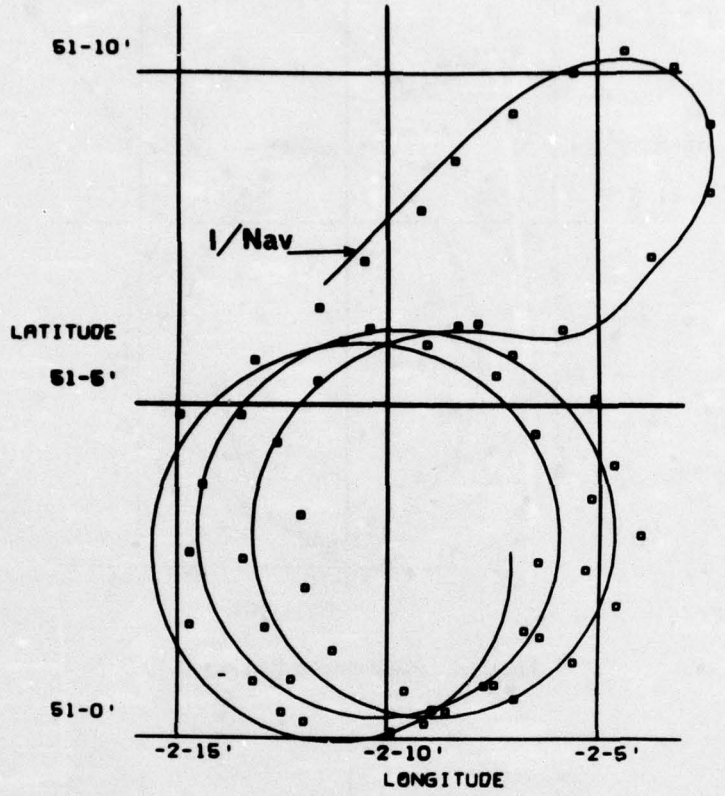

Fig.11(c) Sliding window plots

DISCUSSION

P C J HILL: Using two antenna arrays there are three degrees of freedom (two amplitude and one relative phase) for determining individual signals from a multipath environment; this is insufficient to properly direct a wanted signal (amplitude and phase) in the presence of a reflected signal. Have you considered the use of an additional element thus providing five degrees of freedom, which is sufficient to resolve the two signal contributions?

B A WYNDHAM: I am, of course, aware of the advantages of extra elements to improve direction-finding accuracy in a multipath environment, and reports of such systems have been published. However, I should point out that our own experiment is being made with an aerial which is a modification of an existing widely used design and no provision for extra elements, or re-distribution of existing elements, would have been possible.

L MILOSEVIC: Je vais faire plutôt un commentaire que poser la question. La technique monopulse dans le SSR devient nécessaire avec une interrogation sélective, avec une interrogation/réponse par passage du lobe.

Cette interrogation sélective est envisagée pour éviter le "garbling" c'est à dire le brouillage des réponses par leur chevauchement.

Ce chevauchement résulte des réponses des aréonefs dont la séparation est inférieure à la longueur du message de réponse soit 20,3 m/s ou $\pm$ 3,5 km.

Ce chevauchement dépend donc de la configuration du vol et non pas de la cadence d'interrogations.

Il en résulte que sa durée peut être très longue. Elle entraine cependant essentiellement la perte d'information, l'identité ou l'altitude suivant le mode d'interrogation sans toutefois empêcher la détection de la présence des avions, grâce a la séparation des impulsions d'encadrement (frame pulses) d'où néanmoins-une difficulté de la poursuite des cibles et la recherche d'une solution pour éliminer le garbling.

Une solution est celle d'interrogation sélective utilisée dans le système ADSEL/DABS.

Une autre solution peut être trouvée dans le SSR en modifiant essentiellement la procédure des réponses.

A la place des réponses régulières à chaque interrogation reçue à bord on peut envisager des réponses suivant une loi aléatoire 1 fois sur 2, ou 1 fois sur 3 ou sur 4 suivant le cas.

Le nombre d'interrogations peut être augmenté-le nombre de réponses étant réduit-pour avoir le nombre de réponses suffisant pour assurer la poursuite des aéronefs satisfaisant de même que le défruitage des réponsés.

Nous avons simulé le procédé et les résultats obtenus sont satisfaisants.

Nous avons présenté ce procédé dans une réunion d'Eurocais et dans une journée d'études du SEE en 1975. Nous fournirons des résultats plus detaillés au Congres des Instituts Internationals de Navigation à Cambridge (USA) en Août prochain.

B A WYNDHAM: I thank M Milosevic for his comment but I do not think there is time to elaborate on comparisons of his proposal with ADSEL/DABS. However, my paper referred to the application of monopulse in SSR and it seems to me that the procedure of randomly, and deliberately, suppressing responses has the same effect as over-interrogation and reinforces the case for monopulse.

IDENTIFICATION IFF DANS LES ZONES A FORTE CONCENTRATION D' INTERROGATEURS

F.X. PRUVOT - S E C R E
214, rue du Faubourg Saint Martin
75010 - PARIS - FRANCE

SOMMAIRE

Le système IFF ou le Radar secondaire de surveillance (SSR) est utilisé depuis plusieurs dizaines d'années et ses inconvénients sont assez bien connus. Les diverses études effectuées ont permis de définir précisément les limitations du système. Mais, généralement, ces études ont été conduites en s'attachant à l'évolution du trafic, c'est-à-dire à l'augmentation du nombre d'aéronefs . L'examen des limitations du système dans le cas particulier des zones à forte concentration d'interrogateurs montre que la réduction du taux de réponses due aux blocages du répondeur est la principale perturbation . Les situations pour lesquelles la densité de fruits est très importante peuvent provoquer également une réduction du taux de décodage . Enfin, lorsque les fréquences d'interrogation sont les mêmes, les fruits reçus ne seront plus asynchrones et l'on verra apparaître des réponses fantômes .

Pour remédier à ces divers inconvénients les procédés de traitement traditionnels peuvent être différents et si les caractéristiques de l'ensemble d'interrogation sont définies à partir des caractéristiques globales du systéme c'est-à-dire principalement, le nombre d'unités déployées, l'ordonnancement de ce déploiement et le mode de surveillance adopté, on pourra alors espérer obtenir des performances satisfaisantes:

I.- GENERALITES

Les principales limitations des performances du SSR, manque de réponses, fruits et garbling, se retrouvent bien sûr dans la présente étude, mais avec des influences très différentes .

En effet, un répondeur situé dans la zone d'action de plusieurs interrogateurs peut être sollicité par les lobes principaux et par les lobes secondaires des antennes de ces interrogateurs. Le récepteur du répondeur se trouve bloqué pendant des temps non négligeables et l'accumulation de ces derniers provoque une diminution très sensible du taux de réponse .

D'autre part lorsque les fréquences d'interrogation sont les mêmes et compte tenu de la très grande stabilité des oscillateurs modernes, les " fruits " reçus ne seront plus asynchrones et l'on verra apparaître des réponses fantômes.

Enfin un avion peut passer totalement inaperçu d'un interrogateur si son signal d'interrogation est précédé par celui d'un interrogateur voisin, d'un intervalle inférieur au temps mort du répondeur concerné.

L'étude théorique des diverses configurations de zone à forte concentration d'interrogateurs, a permis d'évaluer approximativement l'importance des perturbations affectant un réseau de surveillance donné .

Pour cela nous avons examiné successivement :

- le taux de réponse du répondeur
- les fruits
- le traitement élémentaire des réponses .

2.- LE TAUX DE REPONSE

Un répondeur n'envoie pas de réponse lorsque :

a) le niveau de l'interrogation n'est pas suffisant pour franchir le récepteur du répondeur, soit par éloignement, soit par manque de couverture de l'antenne, soit par désensibilisation du récepteur.

b) le récepteur est bloqué

soit par une interrogation en provenance d'un lobe principal et provoquant une réponse (100 µs)

soit par une interrogation en provenance d'un lobe secondaire et ne donnant pas lieu à une réponse (30 µs)

Le manque de réponse dû à l'insuffisance du niveau de l'interrogation n'a pas été examiné puisque cela découle de l'étude de mise en oeuvre de l'interrogateur. Par contre la désensibilisation du répondeur sera examinée après l'étude des variations du taux de réponse due au blocage du répondeur .

2.1.- Blocages dus aux réponses

Ces blocages nous conduisent à examiner les conditions dans lesquelles un transpondeur peut être sollicité par n interrogateurs et donc la probabilité d'être éclairé simultanément par k interrogateurs .

Si α représente l'ouverture en degré d'angle du lobe principal :

On a : $PK = \frac{n!}{k!(n-k)!} \cdot (\frac{\alpha}{360})^k \cdot (1 - \frac{\alpha}{360})^{n-k}$

PK est la probabilité d'avoir k stations qui interrogent la cible à un instant donné.

On suppose, dans cette relation, que :

- tous les interrogateurs sont répartis d'une façon homogène
- n est le nombre d'interrogateurs qui sont susceptibles d'atteindre l'avion
- les n stations ont les mêmes caractéristiques (PRF , largeur de lobe et vitesse de rotation)

En prenant comme fréquence d'interrogation 450 hertz, on peut calculer la probabilité de réponse en fonction de k, en tenant compte de ce qu'une interrogation peut arriver pendant la période de blocage du répondeur qui ici a été estimée à un maximum de 100 µs (Figure 1) .

Connaissant pour chaque valeur de n la fonction de répartition du nombre de recouvrement on peut tracer la médiane en fonction du nombre d'interrogateurs , c'est-à-dire le taux de réponse ayant 50 % de chance d'être atteint .

Pour donner une représentation du taux de réponse minimum , on a tracé en pointillé le dernier décile et le dernier centile, c'est-à-dire que dans 10 ou 1 % des cas le taux de réponse pourra descendre en dessous des valeurs indiquées par les courbes en pointillé de la figure 2.

Influence de la désensibilisation

On sait que la valeur maximum du nombre de réponses émises par le répondeur est généralement située aux alentours de 1200 réponses par seconde et qu'au-delà, la désensibilisation aura pour effet de ne prendre en compte que les interrogations les plus proches .

Ceci nous amène à constater que le taux de réponse peut être considéré de deux façons :

- d'une part lorsque le nombre de réponses est inférieur à 1200 réponses , le taux de réponse varie de 100 à 88 %
- d'autre part lorsque le nombre d'interrogations est supérieur à 1200 , le taux de réponse est de 0 ou 88 % .

En effet la baisse de sensibilité sera telle que les interrogations les plus lointaines ne seront pas détectées et par conséquent ne donneront pas lieu à réponses .

Toutefois la baisse de sensibilité du transpondeur ne s'effectue pas d'une manière instantanée et l'on peut remarquer que lorsque le recouvrement de plusieurs lobes se réalise rapidement la densité de réponses pendant une courte période peut aller bien au-delà de 1200/ s et le taux de réponse peut être alors inférieur à 88 % . (voir figure 1) .

2.2.- Blocages dus aux interrogations sur lobes secondaires

Pour étudier cette configuration nous avons fait l'hypothèse que les lobes secondaires émis étaient assimilables à un rayonnement omnidirectionnel . Cette valeur peut être calculée en fonction de la portée du lobe principal et du rayonnement moyen des lobes secondaires.

On sait par ailleurs que le répondeur n'envoie pas de réponse lorsqu'il détecte une interrogation par les lobes secondaires et qu'il bloque le décodage pendant un temps de 30 microsecondes environ. Si le taux de blocage atteint 5000 par seconde le répondeur doit être muni d'un dispositif du type à réduction de sensibilité afin de limiter le taux de blocages à un maximum de 10000par seconde .

On peut donc calculer le taux de réponse du répondeur lorsqu'il est bloqué par des interrogations dues aux lobes secondaires, en focntion du nombre de blocages, c'est-à-dire du nombre de recouvrements de lobes en prenant comme fréquence d'interrogations 450 Hertz , et en tenant compte du fait qu'une interrogation peut arriver pendant une période de blocage . (Voir Figure 3) .

Pour mettre en évidence la variation du taux de réponse en fonction de la densité des interrogateurs nous avons tracé ce taux en fonction du nombre d'interrogateurs pour différentes valeurs de k : $k = n$, $k = n/10$ et $k = n/100$ correspondant à une concentration plus ou moins forte des interrogateurs - Voir Figure 4 en pointillé .

Ces courbes ne tiennent pas compte de l'incidence sur le lobe principal de la baisse de sensibilité du récepteur lorsque le taux d'interrogation sur lobes secondaires atteint ou dépasse 10000 par seconde.

Cette baisse de sensibilité aura pour effet de supprimer les réponses des interrogations les plus lointaines et sera donc fonction de l'implantation des interrogateurs , de leur densité et de leur nombre .

Les courbes en traits pleins de la figure 4 découlent des courbes en pointillé , corrigées en fonction du taux de réponse dû aux blocages provoqués par l'émission d'une réponse (Figure 2). Elles expriment donc le taux de réponse global en fonction de tous les types de blocages.

3.- LES REPONSES ASYNCHRONES OU FRUITS

L'étude du nombre de fruits est faite ici dans le but de donner un aperçu de l'évolution des fruits en fonction du nombre d'interrogateurs. Pour constater l'influence des fruits sur le traitement des réponses on a été amené à examiner non pas le nombre de fruits par tour d'antenne, mais plutôt la densité de fruits dans un lobe d'antenne .Cela nous conduit à calculer la probabilité du nombre de " sources de fruits " situées dans le lobe de l'antenne pendant son passage sur la cible choisie.

Les différentes hypothèses faites sont les suivantes :

- Utilisation de l' ISLS et du RSLS
- Les stations interrogatrices ont les mêmes paramètres (PRF, vitesse de rotation, puissance d'interrogation , largeur de lobe)
- Il n'a pas été tenu compte de la diminution de sensibilité du répondeur .

Les paramètres utilisés pour les calculs sont les suivants :

- Nombre moyen d'avions dans le lobe d'antenne

$$Ma = \frac{A\,\alpha}{360}$$

A = nombre d'avions sous la couverture de la station considérée
α = ouverture du lobe principal de l'antenne en degré d'angle

- La position des avions étant supposée équiprobable en azimut , le nombre d'avions dans le lobe d'antenne est donné par une loi de Poisson de moyenne Ma .

PnA = probabilité de trouver n avions dans le lobe d'antenne

- Nombre moyen de stations éclairant un avion :

$$ms = \frac{S\,\alpha}{360}$$

S = nombre de stations pouvant atteindre l'avion .

Le nombre de stations éclairant un avion est donné par une loi de Poisson de moyenne ms.

A partir de ces deux lois de probabilité on peut calculer celle du nombre de " sources de fruits "

- Nombre de " sources de fruits " en fonction du nombre Ai d'avions dans le lobe .

Ce nombre est donné par une loi de Poisson de moyenne ms . Ai .

PNnSF = Probabilité de N sources de fruits lorsqu'il y a n avions dans le lobe .

La fonction de probabilité du nombre de " sources de fruits " est alors :

$$PNSF = \sum_{n=1}^{\infty} PnA.PNnSF$$

La Figure 5 donne la médiane du nombre de fruits pour les valeurs suivantes des paramètres :

ma = 0,5 ; 1 ; 2 , 4,8 et 16
et = 3,6° , 6° , 12°

Sur la figure 5 nous avons représenté pour chaque valeur de ma et pour les trois valeurs de le nombre A d'avions correspondants .

L'examen de cette figure nous permet de constater que le nombre moyen des fruits est proportionnel au nombre d'interrogateurs ou au nombre de répondeurs et que par ailleurs ce nombre est proportionnel au carré de l'ouverture de l'antenne.

En figure 6 est représentée la répartition des sources de fruits en fonction du nombre d'interrogateurs pour le paramètre m = 8

Les courbes de la figure 6 donnent , en fonction du nombre d'interrogateurs le premier centile , décile et quartile , la médiane , le dernier quartile , décile et centile , c'est-à-dire les valeurs ayant respectivement une probabilité d'être atteintes de 99 %, 90%, 75% 50 % , 25 % 10% et 1% .

4.- FREQUENCES D' INTERROGATION

Il est assez fréquent de constater que de nombreux interrogateurs possèdent la même fréquence d'interrogation . De plus l'utilisation de quartz de référence pour la chronométrie de base des stations entraîne une amélioration considérable sur la précision et la stabilité de cette fréquence d'interrogation. Malheureusement cette amélioration s'accompagne de quelques inconvénients .

Dabord les réponses émises par un répondeur, à partir d'interrogations en provenance d'autres interrogateurs , deviennent synchrones et donneront lieu à des réponses " fantômes " .

Puis, la probabilité de non réponse totale augmente, car il suffit que l'interrogation utile arrive dans les 100 microsecondes suivant une interrogation parasite, pour que cette réponse soit totalement inhibée.

Pour pallier à ces défauts, il faut donc que ces fruits synchrones soient rendus asynchrones. Pour ce faire on peut envisager d'affecter à chaque interrogateur une fréquence d'interrogation différente calculée de telle sorte que les différentes périodes d'interrogation soient décalées entre elles d'environ 100 microsecondes .

Cette solution peut être valable lorsque les interrogateurs sont fixes et que leur nombre est relativement faible.

Lorsque les stations interrogatrices sont mobiles et que leur nombre est grand, il devient difficile, peu pratique et quelquefois impossible, de mettre en place un tel programme . Aussi doit-on, dans ce cas, envisager d'autres solutions.

La technique combinée de la vobulation de la fréquence d'interrogation et du défruiteur résoud assez bien ce problème .

Le vobulateur sert d'ailleurs de remède à trois maux :

- transformation des fruits en réponses asynchrones
- diminution du risque de non réponse totale notamment dû aux blocages des interrogations sur lobes secondaires des autres interrogateurs.
- élimination des réponses fantômes provenant d'avions lointains interrogés par la récurrence précédente.

Les caractéristiques principales du vobulateur sont le nombre de paliers et la longueur de chaque palier. Il serait évidemment souhaitable d'avoir le plus grand nombre possible de paliers, mais, la valeur de la PRF limite souvent ce nombre à quelques unités etdecefait limite dans certains cas les avantages que l'on pourrait en attendre .

D'autre part il ne faut pas oublier que cette vobulation doit être aléatoire pour chaque interrogateur de manière à se rapprocher le plus possible du caractère aléatoire du fruit.

Pour mettre en évidence les inconvénients de ce procédé, nous avons tracé pour un nombre de paliers de 6.8 . 12 et 16 , la probabilité d'atteindre les critères 2/3 et 5/8 . Ces critères , définis par le synchronisme de 2 ou 5 réponses parmi 3 ou 8 successives, sont en réalité ceux qui sont retenus par le défruiteur ; si toutefois les exigences opérationnelles imposent un tel traitement .

L'examen de la Figure 7 nous indique le danger d'utiliser un critère de corrélation trop faible même avec une vobulation à 16 paliers .

Par contre avec un critère de 5/8 les courbes de la Figure 8 montrent une amélioration notable et l'on peut constater, par exemple, que le critère ne sera atteint que dans 10 % des cas avec 8 paliers et 18 réponses dans le plot .

5.- TRAITEMENT DES REPONSES

Les perturbations mentionnées ci avant vont provoquer des dégradations sur le traitement des réponses et selon l'utilisation opérationnelle, traitement manuel ou automatique, les principes jusqu'alors traditionnels devront être modifiés . On peut donc examiner quelles sont les principales incidences qui risquent de modifier les principes du traitement .

Il y a tout d'abord le taux de réponse qui, de part sa faible valeur possible écarte l'utilisation de l'entrelacement des modes . En effet le taux de réponse du répondeur sera encore diminué par l'utilisation du défruiteur et de l'éventuel vobulateur, et le nombre de réponses susceptibles d'être exploitées risque d'être trop faible même si l'on utilise l'entrelacement sur deux modes .

Puis, lorsque la densité de fruits devient trop grande, les circuits de traitement peuvent être saturés et donc provoquer une diminution du taux de décodage .

Pour illustrer ces derniers points nous avons mesuré quelques paramètres sur les deux parties du traitement les plus importantes .

a) L'extraction de la présence d'un code et le degarbling pouvant être perturbés par la présence de fruits, nous avons relevé sur des équipements de performances différentes le taux de décodage en fonction de la densité de fruits dans laquelle baigne la réponse ; le taux de décodage est défini par le rapport du nombre d'accord passif (comparaison du code incident avec un code préaffiché) et du nombre de réponses reçues.

On remarque sur la Figure 9 que les fruits peuvent affecter assez largement le taux de décodage, selon le matériel utilisé. En effet avec un taux de 10000 fruits par seconde, le taux de décodage peut passer de 55 à 82 % .

Les résultats exprimés sur la figure 9 ont été relevés en l'absence de défruiteur et le taux de décodage indiqué est celui obtenu sur une récurrence.

b) Les résultats du tableau de la figure 10 expriment la probabilité d'obtenir au moins un accord passif en fonction du taux de réponse . Ces mesures ont été réalisées dans les conditions suivantes :

- Nombre d'interrogations reçues par le répondeur : 16
- Critère de corrélation du défruiteur : 5/8
- Nombre de fruits perturbateurs : 0

Les résultats donnés par les Figures 9 et 10 nous laissent espérer que, malgré une grande densité d'interrogateurs, on peut, moyennant quelques précautions, obtenir un taux de décodage donc une identification assez satisfaisante .

Lors de la définition d'un systéme à grande densité d'interrogateurs on devra donc s'attacher plus particulièrement aux caractéristiques suivantes :

- Ouverture du lobe principal . Elle devra être la plus petite possible tout en restant compatible avec la vitesse de rotation de l'aérien, la fréquence d'interrogation et le nombre de coups au but espéré .
- Ouverture des lobes secondaires . Elle devra être le plus faible possible pour éviter une diminution du taux de réponses.
- Interrogation - à utiliser seulement en cas de besoin et si possible par secteur.
- Portée - à limiter en fonction des besoins opérationnels
- Sensibilité du récepteur de l'interrogateur - Il serait souhaitable qu'elle soit limitée en fonction de la portée .

6.- CONCLUSION

On vient de voir que l'accroissement du nombre d'interrogateurs dans une aire donnée peut provoquer une diminution du nombre de réponses recueillies dans des proportions parfois considérables. Dans le cas des systémes IFF d'identification il semble que les caractéristiques de l'ensemble d'interrogation doivent être définies à partir des caractéristiques globales du système , c'est-à-dire principalement, le nombre d'unités déployées, l'ordonnancement de ce déploiement et le mode de surveillance adopté. On pourra alors envisager d'obtenir des performances satisfaisantes .

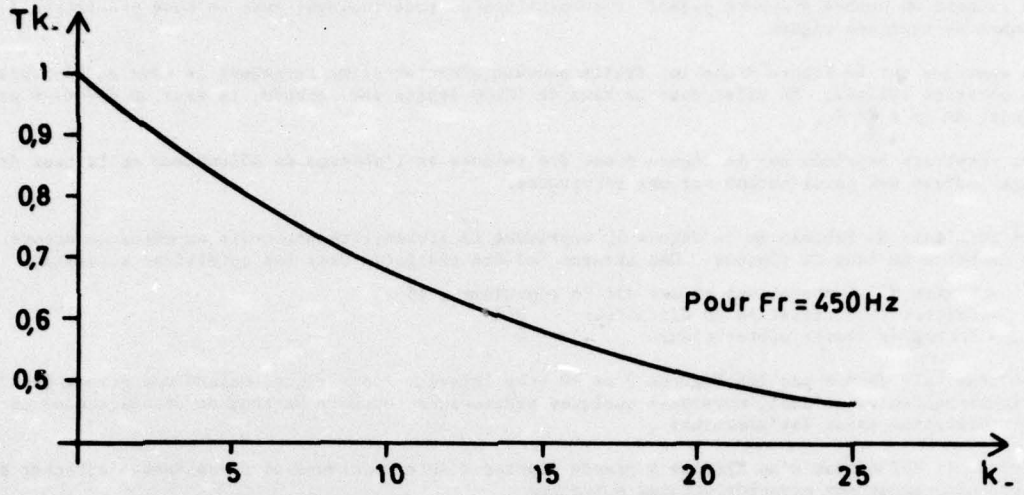

FIG. 1 = TAUX DE REPONSE _Tk_ EN FONCTION DU NOMBRE _k_ DE RECOUVREMENT DE LOBES PRINCIPAUX.

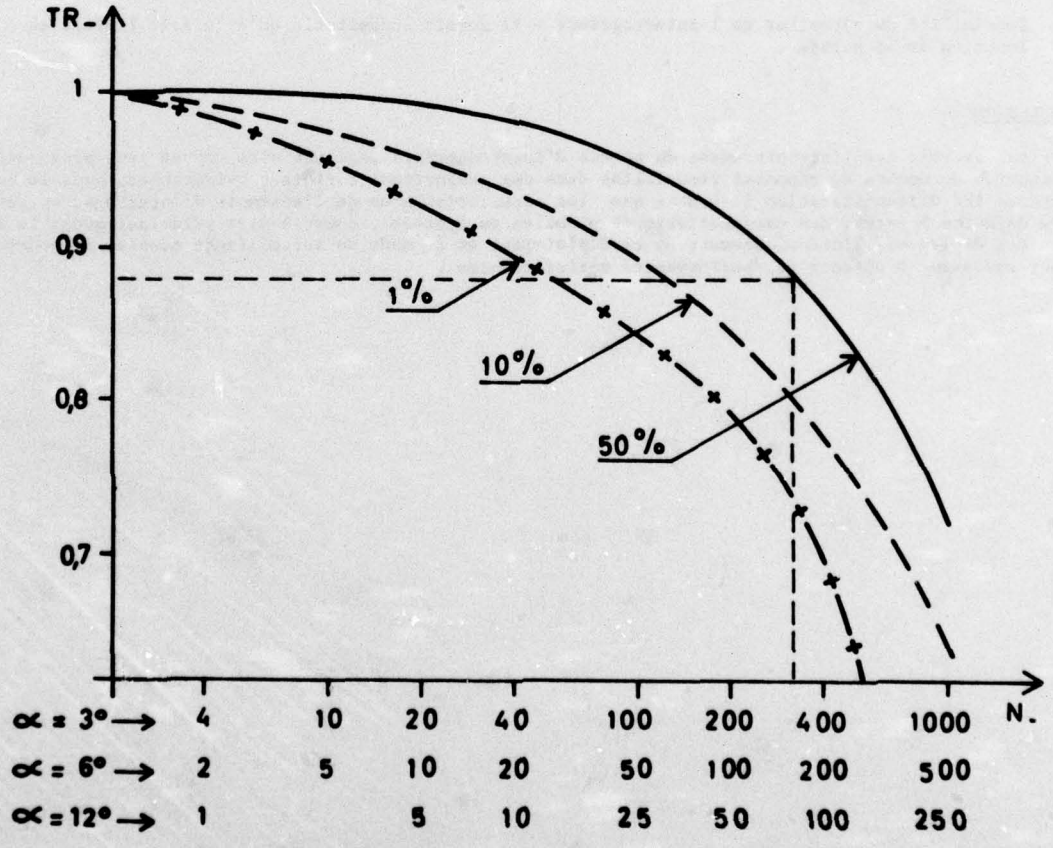

FIG. 2 = TAUX DE REPONSE _TR_ EN FONCTION DES NOMBRES D'INTERROGATEURS _N_.

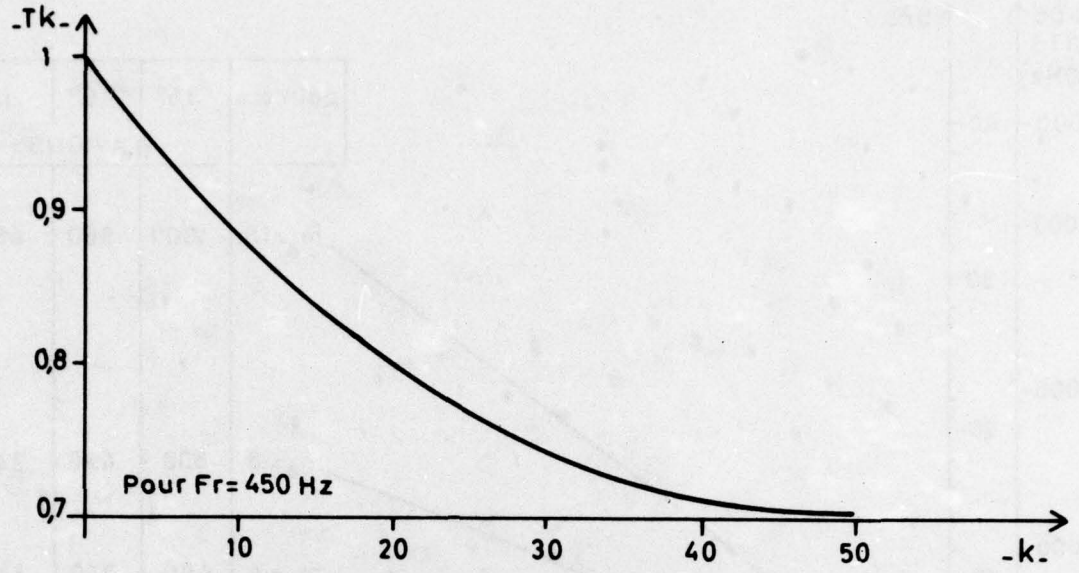

FIG.3 : TAUX DE REPONSE -Tk- EN FONCTION DU NOMBRE -k- DE RECOUVREMENT DE LOBES SECONDAIRES.

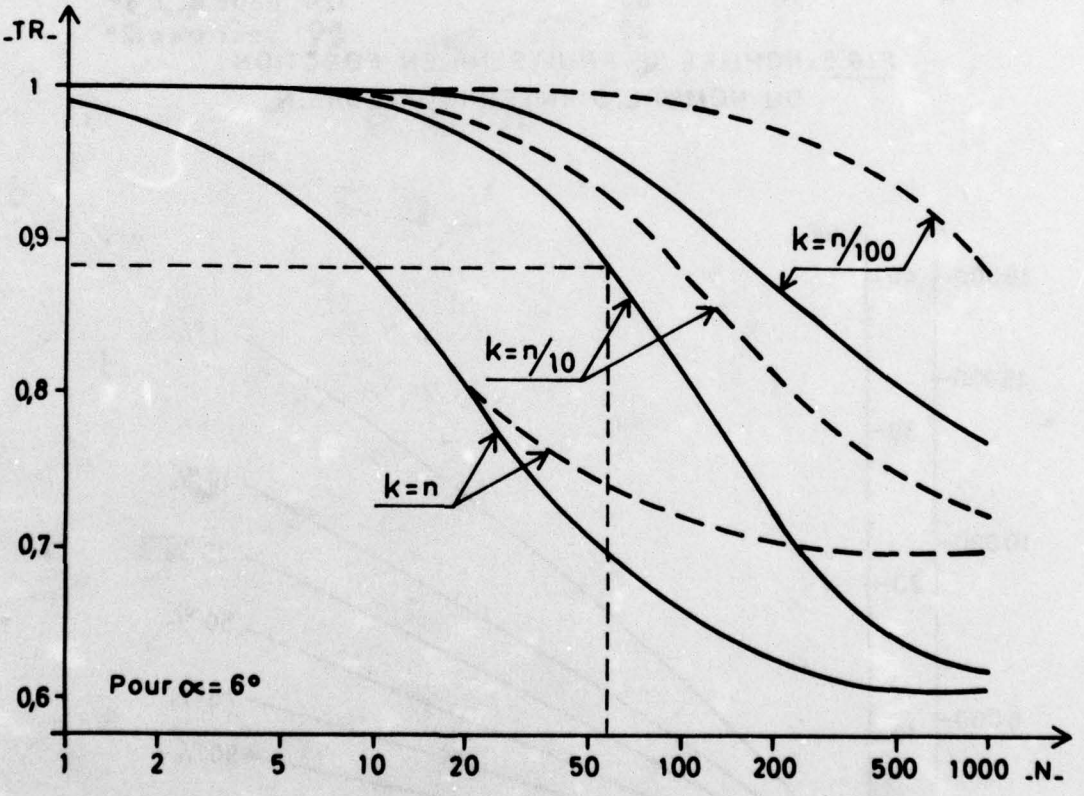

FIG.4 : TAUX DE REPONSE -TR- EN FONCTION DU NOMBRE D'INTERROGATEURS -N- PERTURBATEURS.

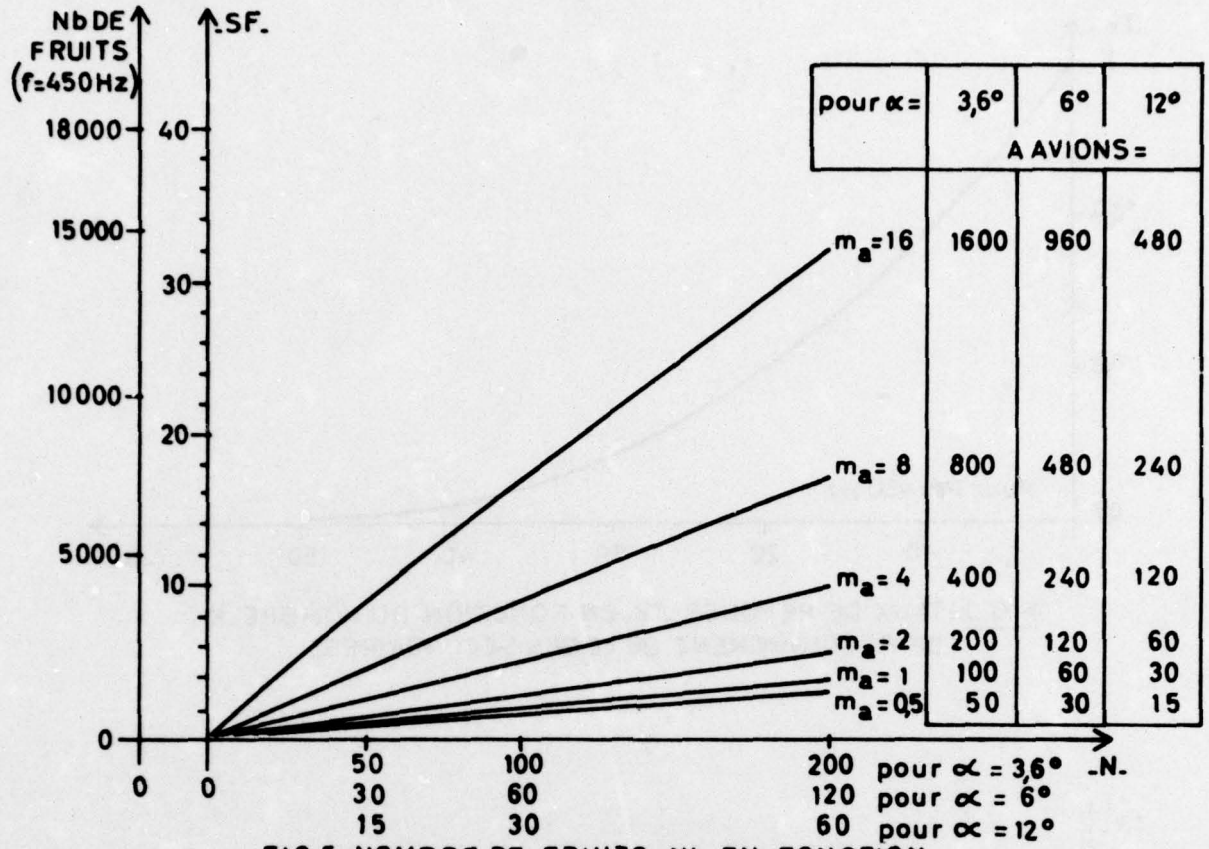

pour α =	3,6°	6°	12°
	A AVIONS =		
m_a=16	1600	960	480
m_a= 8	800	480	240
m_a= 4	400	240	120
m_a= 2	200	120	60
m_a= 1	100	60	30
m_a=0,5	50	30	15

FIG.5 : NOMBRE DE FRUITS _Nb_ EN FONCTION DU NOMBRE D'INTERROGATEURS _N_

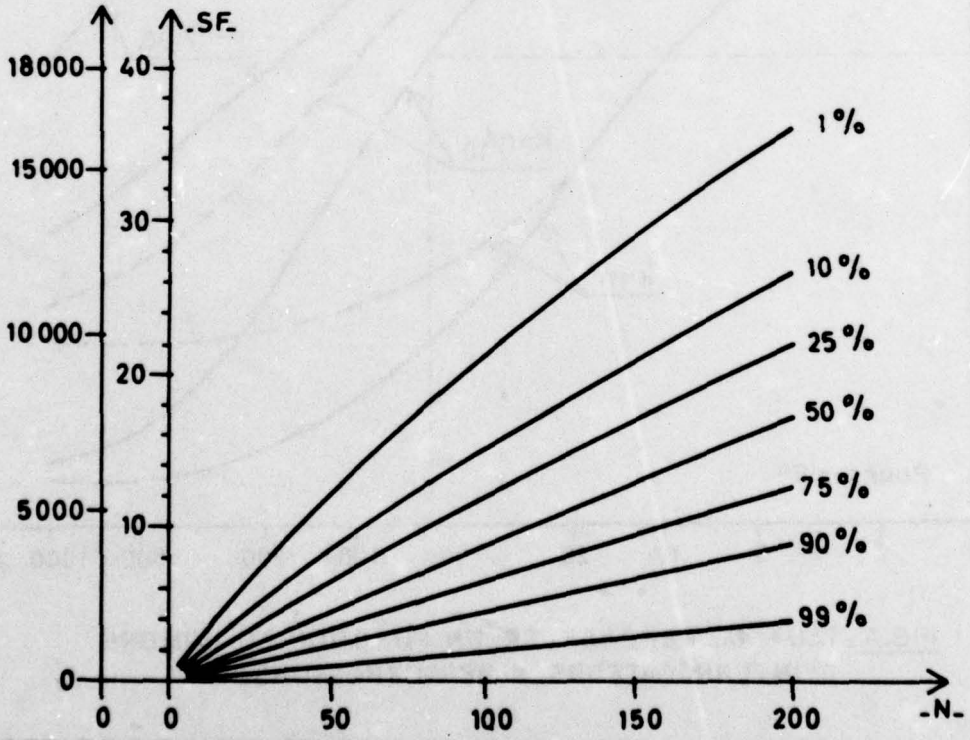

FIG.6 : REPARTITION DES SOURCES DE FRUITS _SF_ EN FONCTION DU NOMBRE D'INTERROGATEURS _N_ POUR m_a = 8.

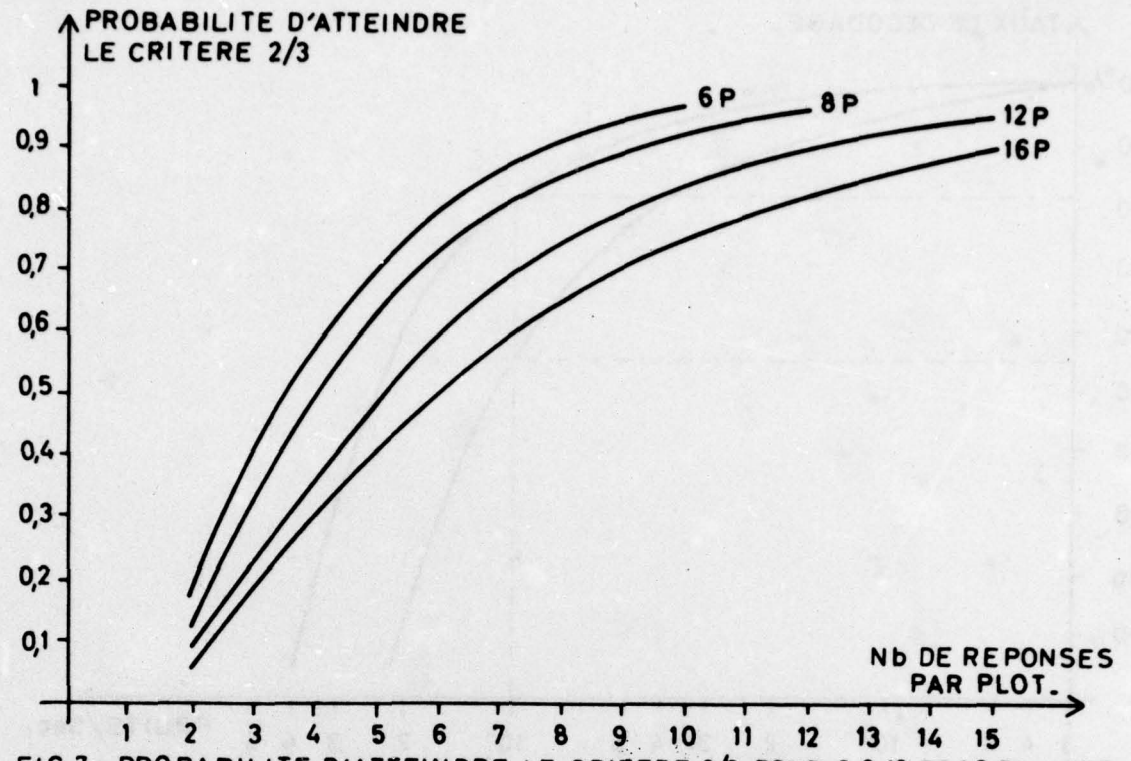

FIG.7 = PROBABILITE D'ATTEINDRE LE CRITERE 2/3 POUR 6,8,12 ET 16 PALIERS. EN FONCTION DU NOMBRE DE REPONSES PAR PLOT.

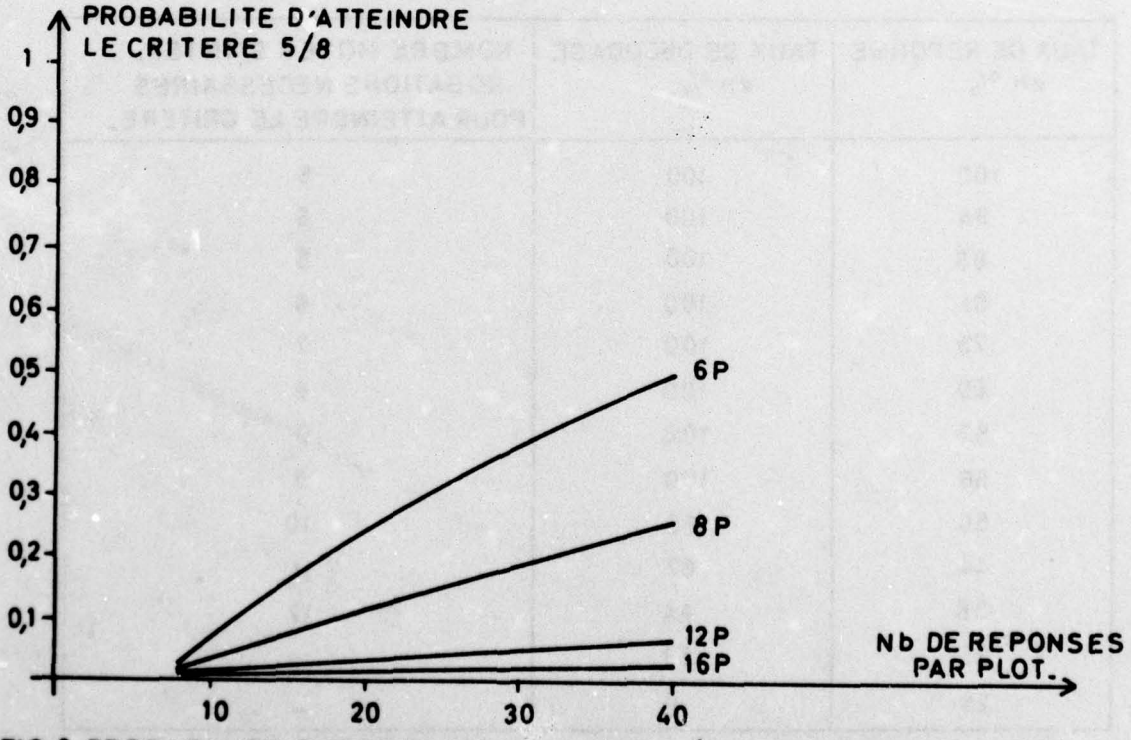

FIG.8 PROBABILITE D'ATTEINDRE LE CRITERE 5/8 POUR 6,8,12 ET 16 PALIERS EN FONCTION DU NOMBRE DE REPONSES PAR PLOT.

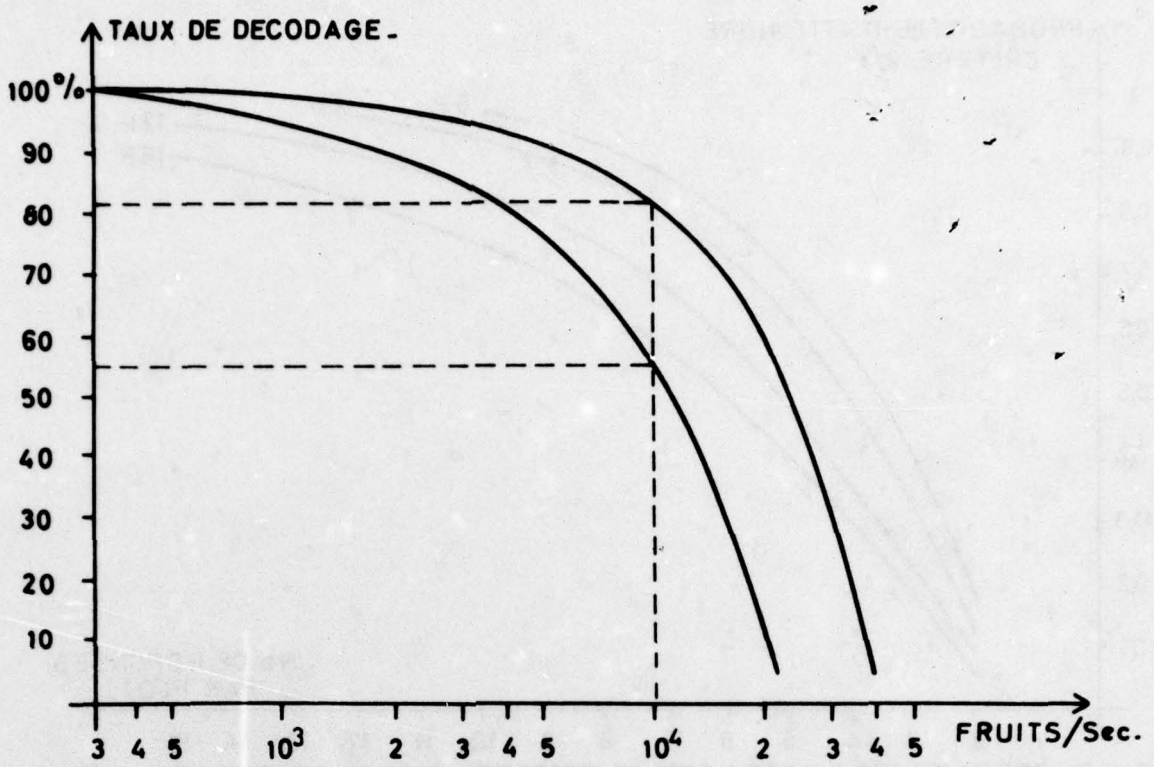

FIG.9 = TAUX DE DECODAGE EN FONCTION DE LA DENSITE DE FRUITS.
(DEFRUITEUR HORS SERVICE)

TAUX DE REPONSE en %	TAUX DE DECODAGE en %	NOMBRE MOYEN D'INTER. -ROGATIONS NECESSAIRES POUR ATTEINDRE LE CRITERE.
100	100	5
94	100	6
88	100	6
81	100	6
75	100	7
69	100	8
63	100	9
56	100	9
50	88	10
44	67	11
38	44	12
31	23	12
25	0	–

FIG.10 = TAUX DE DECODAGE, CORRÉLÉ 5/8, EN FONCTION DU TAUX DE REPONSE.

THE CASCADE REALISATION OF M.T.I. FILTERS WITH STAGGERED P.R.F. AND TIME VARIABLE WEIGHTS

H.W. Thomas and T.M. Abram
Electrical Engineering Department
University of Manchester
Dover Street
Manchester
M13 9PL
England

SUMMARY

Non-uniform sampling is used in conjunction with time varying coefficients in M.T.I. filters to extend the first blind speed of the system, without degradation of the stopband. A z-transform matrix notation is introduced which leads to a concise representation of cascaded time varying filter sections. It is shown that the cascade realisation has certain advantages in terms of sensitivity to arithmetic wordlength and a step-by-step design procedure for such filters is described. The design of each section is based on the determination of coefficients to locate zeros in the z-plane for optimum rejection of the clutter spectrum. This approach has the advantage that the coefficients of the cascade form are computed directly without the need for factorisation of the transfer function of the direct form.

1. INTRODUCTION

The use of non-uniform sampling, or staggered p.r.f., in moving target indication radars is well known, and serves to extend the first "blind speed" of the system. However, unless time varying coefficients are used in the M.T.I. filter the stopband attenuation, and hence the clutter rejection of the system, is degraded (Skolnik, M.I. 1970; Thomas, H.W., 1974).

The implementation of a digital filter as a series of cascaded sections has been shown to have the advantage over the direct form of reduced sensitivity to coefficient errors (Gold, B. 1969; Oppenheim, A.V., 1975), both for recursive and non-recursive filters with constant coefficients. However, the cascade form of time varying filters involves additional complications both in analysis and design. Individual sections are no longer described by a single z-transform expression, but have a different transfer function for each point in the stagger cycle. Consequently the overall transfer function due to the cascading of several sections cannot be obtained by simple multiplication of polynomials in z and the factorisation of, for example, a 6th order filter into three 2nd order sections is not straightforward.

However, a matrix notation for cascaded sections has been developed using z-transform methods (Thomas H.W.; 1972) which leads to a straightforward design procedure based on the placing of zeros to achieve optimum clutter rejection. An important advantage of this approach is that a particular zero is associated with each section, so that clutter is progressively diminished through the filter, and, consequently, the storage requirements may be reduced. In addition coefficient errors in later sections are less important, allowing economies to be made in coefficient wordlength.

2. THE MATRIX NOTATION FOR TIME VARYING FILTERS.

In the z-transform analysis of sampled data systems z^{-1} may be considered as a delay operator, corresponding to a delay of one intersample interval. If the period between samples is T then $z = e^{sT}$ and so it is apparent that such a notation cannot be used to describe a filter where the sampling rate is not constant. However, the sequence of non-uniform sample intervals is generally designed as integral multiples of some common factor δT, (Skolnik, M.I., 1970; Thomas, H.W., 1976) e.g. $3\delta T$, $4\delta T$, $5\delta T$, which is readily described by an alternative z notation. If a new z is defined as $z = e^{s\delta T}$ then any delay $m\delta T$ can be represented in the z-transform by z^{-m}. Thus a signal r(t), sampled non-uniformly at intervals $3\delta T$, $4\delta T$, $5\delta T$ as in Fig. (1) would lead to a sequence

$$R(\delta T) = r(0) + r(3\delta T), r(7\delta T), r(12\delta T), r(15\delta T), r(19\delta T) \ldots\ldots\ldots$$

which is represented by the z transform

$$R(z) = r(0) + r(3\delta T)z^{-3} + r(7\delta T)z^{-7} + r(12\delta T)z^{-12} + r(15\delta T)z^{-15} + r(19\delta T)z^{-19} + \ldots.$$

Similarly since the output of a digital filter is formed by weighting previous input samples, its transfer function can be expressed in the same form. For example a 2nd order filter with uniform sampling might have a transfer function

$$a_o + a_1 z^{-1} + a_2 z^{-2}$$

whereas, for a non-uniformly sampled filter, the transfer function is dependent on the sample instant at which the output is formed. For the same second order filter with sample periods $3\delta T$, $4\delta T$, $5\delta T$, the transfer functions will be

$$a_0 + a_1 z^{-3} + a_2 z^{-8} \quad \text{following sample period of } 3\delta T,$$

$$a_0 + a_1 z^{-4} + a_2 z^{-7} \quad \text{following sample period of } 4\delta T,$$

$$a_0 + a_1 z^{-5} + a_2 z^{-9} \quad \text{following sample period of } 5\delta T.$$

In a uniformly sampled filter the resultant transfer function of two or more cascaded sections is obtained by multiplication of the transfer functions of the individual sections, e.g.

$$(1 - z^{-1})^2 = (1 - 2z^{-1} + z^{-2}).$$

However, for non-uniform sampling, the product of several sections' transfer functions does not represent the correct overall transfer function, e.g. in $(1 - z^{-3})(1 - z^{-3}) = (1 + -2z^{-3} + z^{-6})$ the z^{-6} term does not correspond to two sample delays in a nonuniform sequence of $3\delta T, 4\delta T, 5\delta T$.

However, using an analysis based on that of Thomas and Lutte (Thomas H. W., 1972) a non-uniform sample sequence may be 'decomposed' into a number of uniform sample sequences which leads to a more convenient transfer function expressed in matrix form. Using this approach, the overall transfer function of a filter may be obtained by multiplication of the matrices of individual sections.

Referring to Fig. 2, the complete sequence 2(a) may be decomposed into the uniform sequences $R_1(m\delta T)$, $R_2(m\delta T)$, $R_3(m\delta T)$. Similarly the output sequence shown in 2(e) is decomposed into $C_1(m\delta T)$, $C_2(m\delta T)$, $C_3(m\delta T)$. Each $C_p(m\delta T)$ consists of weighted contributions from each $R_i(m\delta T)$ as indicated by coefficients $g_{p,i}$, so that, using z-transform notation

$$C_p(z) = \sum_{i=1}^{n} R_i(z) \cdot g_{p,i}(z) \quad \ldots\ldots(1)$$

The weighting functions $g_{p,i}$ are obtained from the filter transfer function at sample instant p by selecting those terms of the transfer function which delay each $R_i(z)$ to the appropriate $C_p(z)$. For example, consider a 3rd order filter with sample periods $3\delta T$, $4\delta T$, $5\delta T$, i.e. the transfer functions are:-

$$a_0 + a_1 z^{-3} + a_2 z^{-8} + a_3 z^{-12}$$
$$a_0 + a_1 z^{-4} + a_2 z^{-7} + a_3 z^{-12}$$
$$a_0 + a_1 z^{-5} + a_2 z^{-9} + a_3 z^{-12}$$

By inspection of Fig. 2 we have

$$C_1(z) = R_1(z)\left\{a_0 + a_3 z^{-12}\right\} + R_2(z).\left\{a_2 z^{-8}\right\} + R_3(z).\left\{a_1 z^{-3}\right\}$$
$$C_2(z) = R_1(z)\left\{a_1 z^{-4}\right\} + R_2(z)\left\{a_0 + a_3 z^{-12}\right\} + R_3(z).\left\{a_2 z^{-7}\right\}$$
$$C_3(z) = R_1(z)\left\{a_2 z^{-9}\right\} + R_2(z)\left\{a_1 z^{-5}\right\} + R_3(z)\left\{a_0 + a_3 z^{-12}\right\}$$

This may conveniently be written in matrix form as

$$\begin{bmatrix} C_1 \\ C_2 \\ C_3 \end{bmatrix} = \begin{bmatrix} g_{11} & g_{12} & g_{13} \\ g_{21} & g_{22} & g_{23} \\ g_{31} & g_{32} & g_{33} \end{bmatrix} \begin{bmatrix} R_1 \\ R_2 \\ R_3 \end{bmatrix}$$

i.e. $\underline{C} = \underline{G} \cdot \underline{R}$ $\ldots\ldots(2)$

An important consequence of this notation is that the output vector $\underline{C}$ is in the same form as the input vector $\underline{R}$, so that the output vector of one section of a filter may be considered as the input vector to the next, as shown in Fig. 3.

It is readily apparent that

$$\underline{C}_3 = \underline{G}_3 \cdot \underline{G}_2 \cdot \underline{G}_1 \cdot \underline{R} \quad \ldots\ldots(3)$$

and hence the overall transfer function is $\underline{G}_3 \cdot \underline{G}_2 \cdot \underline{G}_1$. It is significant that matrix multiplication is non-commutative, indicating that the order of sections to implement a particular filter characteristic is unique.

Further, each row of every $\underline{G}$ matrix relates to the input and output sequences at a particular point in the stagger cycle, and involves only the coefficients of the filter sections corresponding to that instant. Thus the effect of time varying coefficients is readily included by determing row p of each G matrix from the coefficients implemented in each section at sample instant p. As an example, the cascaded transfer function of two 2nd order sections

$$\begin{matrix} a_{10} + a_{11}z^{-3} + a_{12}z^{-8} \\ a_{20} + a_{21}z^{-4} + a_{22}z^{-7} \\ a_{30} + a_{31}z^{-5} + a_{32}z^{-9} \end{matrix} \quad ; \quad \begin{matrix} b_{10} + b_{11}z^{-3} + b_{12}z^{-8} \\ b_{20} + b_{21}z^{-4} + b_{22}z^{-7} \\ b_{30} + b_{31}z^{-5} + b_{32}z^{-9} \end{matrix}$$

is given by $\underline{G}_2 . \underline{G}_1$

$$\begin{bmatrix} b_{10} & b_{12}z^{-8} & b_{11}z^{-3} \\ b_{21}z^{-4} & b_{20} & b_{22}z^{-7} \\ b_{32}z^{-9} & b_{31}z^{-5} & b_{30} \end{bmatrix} \cdot \begin{bmatrix} a_{10} & a_{12}z^{-8} & a_{11}z^{-3} \\ a_{21}z^{-4} & a_{20} & a_{22}z^{-7} \\ a_{32}z^{-9} & a_{31}z^{-5} & a_{30} \end{bmatrix}$$

3. DESIGN OF FILTER COEFFICIENTS.

The technique proposed for the design of filter weights is a development of that of Thomas et al (Thomas H. W., 1974) where the coefficients are calculated to implement zeros at certain location in the z-plane. A zero placed on the unit circle in the z plane at $z = e^{j\omega\delta T}$, corresponds to a null in the frequency response at ω. Furthermore, in the frequency domain the response is periodic with period $\omega = 2\pi/\delta T$, which corresponds to traversing the unit circle in the z plane once. Consequently there is a direct correspondence between the location of zeros and the frequency response of the filter. The effect of placing a zero at any point is easily interpreted in terms of its effect on the performance of the filter. Uniformly sampled filters contain a number of zeros equal to the order of the filter and the stopband may be defined by locating these zeros on the unit circle around the point z= 1. In the case of non-uniform sampling, however, the total number of zeros is greater than the filter order but only a limited number are controllable by choice of coefficients (Thomas, H. W., 1974). As an example consider a 2nd order filter with sample periods $3\delta T$, $4\delta T$, $5\delta T$, which has transfer function $a_{10} + a_{11}z^{-3} + a_{12}z^{-8}$ at sample instant 1. Although it represents only a second order filter this polynomial contains 8 zeros only two of which can be controlled by choice of a_{10}, a_{11}, a_{12}. If these two zeros are placed in the stopband the remaining six zeros will lie away from the unit circle and determine the passband characteristics. It has been observed (Thomas, H. W. 1974) that the effect of these additional zeros on the passband is determined mainly by the stagger sequence, and is largely independent of the coefficient choice. Thus the controllable zeros should be placed to define the stopband and their location can be specified to optimise the rejection of a given clutter spectrum. For clutter which falls predominantly within the stopband the optimum zero positions are not greatly influenced by the passband response, so that the same zero locations may be used for filters with a range of uniform or non-uniform sample sequences. Coefficients are thus readily computed without the necessity for lengthy optimisation for each different stagger cycle.

3.1. Design Procedure.

The output of a time varying M. T. I. filter is normally averaged over all instants of the stagger cycle and is defined by Thomas and Lutte (Thomas H. W., 1972) as

$$\left| G(\omega) \right|^2 = \sum_{p=1}^{n} \left| C'p \left(e^{j\omega\delta T} \right) \right|^2$$

where $|C'p\ (e^{j\omega\delta T})|$ represents the magnitude of the output of the filter at sample instant p in response to a sinusoidal input $e^{j\omega t}$. It is shown in Appendix (1).

$$\underline{C}' = \begin{bmatrix} C'_1(e^{j\omega\delta T}) \\ C'_2(e^{j\omega\delta T}) \\ \vdots \\ C'_n(e^{j\omega\delta T}) \end{bmatrix} = \underline{G}\ (e^{j\omega\delta T}) \cdot \begin{bmatrix} 1 \\ 1 \\ \vdots \\ 1 \end{bmatrix} = \underline{G} \cdot \underline{I} \quad \ldots\ldots\ldots\ldots (4)$$

The value of $|C'p(e^{j\omega\delta T})|^2 = C'p(e^{j\omega\delta T}).\ C'p\ (e^{-j\omega\delta T})$ for a filter with real coefficients and is determined by the position of the zeros of C'p(z). $Cp'(z^{-1})$. The zeros of the complete M. T. I. filter are those of $|G'(z)|^2$, where

$$\left| G'(z) \right|^2 = \sum_{p=1}^{n} C'p(z).\ C'p(z^{-1})$$

If each C'p (z). $C'p(z^{-1})$ contains a zero on the unit circle at $z = e^{j\omega\delta T}$) then $|G'(z)|^2$ will also contain that zero and a null occurs in the frequency response at ω. Furthermore, a sufficient condition for a zero in $Cp'(z)\ Cp'(z^{-1})$ is that C'p(z) contains that zero. Thus the computation of time varying coefficients to place a zero in the complete transfer function of the filter is achieved by ensuring that the transfer function at each sample instant contains that zero.

If a zero at $z = r . e^{j\omega\delta T}$ is present in each Cp' (z), then

$$\underline{C}'\ (r . e^{j\omega\delta T}) = \underline{0} = \underline{G}(r . e^{j\omega\delta T}).\ \underline{I} \quad \ldots\ldots\ldots\ldots\ldots\ldots (5)$$

where $\underline{0} = \begin{bmatrix} 0 \\ 0 \\ 0 \\ \vdots \\ 0 \end{bmatrix} \Big\} n$

and this defines the elements of $\underline{G}$, and hence the filter coefficients.

For example, a 3rd order filter with sample instants $3\delta T$, $4\delta T$, $5\delta T$, has a $\underline{G}$ matrix.

$$\begin{bmatrix} a_{10} + a_{13}z^{-12} & a_{12}z^{-8} & a_{11}z^{-3} \\ a_{21}z^{-4} & a_{20} + a_{23}z^{-12} & a_{22}z^{-7} \\ a_{31}z^{-5} & a_{32}z^{-9} & a_{30} + a_{33}z^{-12} \end{bmatrix}$$

By making the substitution $z = e^{j\omega\delta T}$ and multiplying by $\underline{I}$ three equations defining the coefficients at the three sample instants are obtained.

$$0 = a_{10} + a_{11}e^{-3j\omega\delta T} + a_{12}e^{-8j\omega\delta T} + a_{13}e^{-12j\omega\delta T}$$

$$0 = a_{20} + a_{21}e^{-4j\omega\delta T} + a_{22}e^{-7j\omega\delta T} + a_{23}e^{-12j\omega\delta T}$$

$$0 = a_{30} + a_{31}e^{-5j\omega\delta T} + a_{32}e^{-9j\omega\delta T} + a_{33}e^{-12j\omega\delta T}$$

This is equivalent to the substitution of $z = e^{j\omega\delta T}$ in the filter transfer functions at each sample instant.

In order to determine all filter coefficients it is necessary to specify a number of zero positions equal to the order of the filter, together with arbitary coefficients $a_{p,0}$. For real coefficients zeros must occur in conjugate pairs, or lie on the real axis. Thus the values of coefficients to place zeros on the unit circle at $z = e^{\pm j\phi}$, and $z = 1$ are specified by the three matrix equations.

$$\underline{0} = \underline{G}\,(e^{j\phi}) \cdot \underline{I}$$
$$\underline{0} = \underline{G}\,(e^{-j\phi}) \cdot \underline{I}$$
$$\underline{0} = \underline{G}\,(1) \cdot \underline{I}$$

These equations are solved to yield the required a_{pi}. Applied to the design of a filter implemented in the direct form this procedure is little different from the method of Thomas et al (Thomas, H. W., 1974) and can be used for the synthesis of filters of any order or stagger length. However, where it is desired to implenent the filter in cascade form an extension of the above procedure can be used to determine directly a matrix representing the transfer function of each section. It has been noted in section 2 of this paper that a filter composed of a number of cascaded units has an overall transfer function

$$\underline{G} = \underline{G}_m \cdot \underline{G}_{m-1} \cdots\cdots \underline{G}_i \cdots\cdots \underline{G}_1$$

and each $\underline{G}_i$ can be used to implement a number of zeros. Having calculated $\underline{G}_1$ as described above, a further section $\underline{G}_2$ may be computed by solution of the equations

$$\underline{0} = \underline{G}_2\,(e^{j\phi}) \cdot \underline{G}_1\,(e^{j\phi}) \cdot \underline{I}$$

for

$$\phi = \pm\theta_1, \pm\theta_2 \cdots\cdots\cdots\cdots$$

Since $\underline{G}_1$ is known only m equations are required to solve for the coefficients of an mth order section $\underline{G}_2$. In general, having determined the coefficients for the preceding s sections the coefficients of the $(s + 1)$ section are found from

$$\underline{0} = \underline{G}_{(s+1)}(e^{j\phi}) \cdot \underline{G}_s(e^{j\phi}) \cdot \underline{G}_{(s-1)}(e^{j\phi}) \cdots\cdots\cdots\cdots \underline{G}_1(e^{j\phi}) \cdot \underline{I}$$
$$\phi = \pm\theta_1, \pm\theta_2 \cdots\cdots$$

The matrix multiplications and solution of simultaneous equations can be performed with the aid of short computer routines and at little cost in computing time, and a suitable routine for the design of a filter section is listed in Appendix (2). Note that the iterative nature of the process eliminates the factorisation of the direct transfer function into its component sections

$$\underline{G} = \underline{G}_{(s+1)} \cdot \underline{G}_s \cdots\cdots\cdots\cdots\cdots\cdots\cdots\cdots \underline{G}_1$$

which requires the solution of polynomials and may not be possible analytically.

A modification of this procedure is required for the placing of multiple zeros. For example, if it is desired to follow a section $\underline{G}_1$, containing a zero at $z = e^{j\theta}$, by another section including a zero at the same position the design equation is

$$\underline{0} = \underline{G}_2(e^{j\phi}). \quad \underline{G}_1(e^{j\phi}). \quad \underline{I}, \quad \phi = \pm\theta \qquad \ldots\ldots(6)$$

However, the term $\underline{G}_1(e^{j\phi})$. $\underline{I}$ represents the output of section (1), which by virtue of the zero at $z = e^{j\theta}$, is identically zero, resulting in the identity

$$\underline{0} = \underline{G}_2(e^{j\theta}). \quad \underline{0} \quad \text{for equation (6)}$$

This difficulty may be overcome by differentiating $\underline{G}_2(z)$. $\underline{G}_1(z)$ and solving the equation

$$\underline{0} = \frac{d}{dz}\left\{ \underline{G}_2(z) \cdot \underline{G}_1(z) \right\} \cdot \underline{I} \qquad z = e^{j\phi}, \ \phi = \pm\theta$$

analagous to the method of the reference (Thomas, H. W., 1974)

It is important that although the $G_i(z)$ of any particular section except the 1st does not, in isolation, contain the required zeros, each one, in conjunction with the preceding sections, is responsible for the implementation of those zeros for which it was designed. In order to ensure that these zeros are, in fact, realised, the sections must be cascaded in the correct order.

In practice it is convenient to use a single canceller as the first section of any filter which, in this position, has coefficients of 1, -1, independent of non-uniform sampling. This has the effect of removing clutter at $\omega = 0$ and is not subject to coefficient errors, leading to further advantages as described in the next section.

4. ADVANTAGES OF THE CASCADE FORM

The decision of whether to implement a filter in direct form or cascade form must be based on their relative merits in terms of performance and economy. The cascade form has potential advantages both in terms of sample storage and arithmetic wordlength. These are discussed below.

4.1. Sample Storage.

The input signal to an M.T.I. filter consists of two components; the signal due to a target, which is to be extracted and that due to clutter, which the filter should attenuate as much as possible. As the signal progresses through a cascade filter the clutter residue will be reduced at each stage, while the component due to the target remains almost constant. Thus the dynamic range of the total signal will be reduced and consequently fewer bits are required for its representation. This process may be illustrated by considering, for example, a 7th order filter realised in 4 sections; a single canceller followed by three 2nd order sections. The stagger sequence is 13, 15, 14, 16 and for a first blind speed of 1000 knots the clutter considered has gaussian power spectrum with σ = 3.2 knots and a clutter/target ratio of 40 dB. The coefficients are normalised for a maximum voltage gain of unity, and for an input wordlength of 14 bits the signal levels are as follows:-

Section	Zeros of Section	Input		Output	
		Volts	Bits	Volts	Bits
1	$\omega\delta T = \pm 0.0$	1.0	14	0.203	12
2	$\omega\delta T = \pm 0.0044$	0.203	12	0.0218	9
3	$\omega\delta T = \pm 0.0257$	0.0218	9	0.0104	8
4	$\omega\delta T = \pm 0.0713$	0.0104	8	0.0100	8

For a direct filter as shown in Fig. (4a) storage of 7 x 14 = 98 bits is required, while the cascade form Fig. (4b) requires storage of only 71 bits. The extent of the saving is determined by the expected clutter spectrum, and the target clutter ratio.

Alternatively wordlength could be increased, without increasing cost, giving improved performance with reference to quantisation error effects.

4.2. Coefficient wordlength.

Variations in performance of equivalent digital filter configurations arise, in general, from inaccuracies in implementation inherent in the use of finite wordlength arithmetic (Oppenheim A.V., 1975) Such errors are introduced by the process of quantisation of both the signal and the filter coefficients. It is shown below that time varying filters realised in cascade form are less sensitive to the rounding errors of coefficients than those realised in the direct form.

The design procedure outlined above is based on the location of stopband zeros, and one method

of assessing filter accuracy is on the basis of the positional accuracy of these zeros in the z-plane. The effect of small zero movements away from their ideal locations is readily interpreted from a visual inspection of the zero diagram.

The plot of zeros in the z-plane, as proposed in (Thomas H. W., 1974) is concerned with the complete M. T. I. transfer function, i.e. averaged over all sample instants in the stagger cycle; so that

$$\left| G'(z) \right|^2 = \sum_{p=1}^{n} \left| C'p\,(z) \right|^2$$

However, the location of zeros for the individual C'p(z) also yields information as to the filter characteristics, since all stopband zeros are realised in each C'p(z) which describes the transfer function of the filter at the sample instant p. Thus any movement of these zeros is reflected in the filter output.

If each C'p (z) is considered in factored form

$$C'p\,(z) = \prod_{i=1}^{m} (z - z_i)$$

then the filter output in response to a sinusoidal input may be represented as the product of the vector distances from $z = e^{j\omega\delta T}$ to each of the zeros, as shown in Fig. 5. Consequently, any movement of zeros away from the unit circle will degrade the clutter rejection at that point. Further, if optimum zero positions exist, then any movement along the unit circle will also lead to a sub-optimal performance. Accordingly the movement of zero placements provides a good indication of changes in clutter rejection due to coefficient errors.

The displacement of poles and zeros in the z-plane in response to coefficient errors has been the subject of considerable study since the advent of digital computation (Kaiser, J. F., 1965, Mitra, S. K., 1974; Maley, C. E., 1962; Herman O, 1970) and methods of predicting pole and zero displacement have been developed. Mitra and Sherwood (Mitra S. K, 1974) show that for small coefficient errors, β_i, in a polynomial

$$B(z) = \sum_{i=0}^{m} b_i z_i$$

the resulting displacement Δz_k in the position of a zero z_k is given by

$$\Delta z_k = -\rho_k \sum_{i=0}^{m} \beta_i (z_k)^i \qquad \ldots\ldots (7)$$

where $\rho_k = \left. \frac{(z - z_k)}{B(z)} \right|_{z = z_k}$ $\qquad \ldots\ldots (8)$

A polynomial C'p(z) of the form $1 + \sum_{i=1}^{m} b_i z^{-i}$ factorises to $\prod_{i=1}^{m} (1 - z_i z^{-i})$

and hence

$$\Delta z_k = -\rho_k \left(\sum_{i=1}^{m} \beta_i (z_k)^{-i} \right), \quad \rho_k = \left. \frac{1 - z_k z^{-1}}{B(z)} \right|_{z = z_k}$$

Now, since $C'p\,(z) = \prod_{i=1}^{m} (1 - z_i z^{-1})$,

$$|\rho_k| = \frac{1}{\prod_{\substack{i=1 \\ i \neq k}}^{m} |z_k - z_i|}$$

This may be interpreted as the reciprocal of the product of the moduli of the distances between z_k and all other filter zeros. Thus, if C'p(z) contains other zeros close to z_k then ρ_k becomes large. The C'p(z) of non-uniformly sampled M. T. I. filters are characterised by a cluster of closely spaced zeros on the unit circle around z = 1, forming the stopband, and a number of more widely spaced zeros away from the unit circle, distributed, typically, in the manner shown in Fig. (5). Consequently an M. T. I. filter with more than one stop band zero can be expected to have a large "sensitivity factor" ρ. The zero movements Δz_k are determined from equation (7) by ρ_k and $\sum_{i=1}^{m} \beta_i (z_k)^{-i})$, . For rounding errors (β_i) of the same magnitude, this latter term may vary considerably between direct and cascade realisations.

A filter with the same ideal zero locations can be realised in cascade form, with each pair of zeros implemented in a 2nd order section following one or more previous sections. The preceding part of the filter is represented by a matrix $\underline{G}_1$, and the transfer function of this initial section at sample instant p is

$$C'p\,(z) = a_{po} + a_{p1} z^{-r_{p,1}} + a_{p2} z^{-r_{p,2}} + \ldots\ldots + a_{m-2} z^{-r_{p,m-2}}$$

where $r_{p,i}$ represents the appropriate index for a delay of i samples previous to instant p.

Let the section for which zero displacements are to be calculated have coefficients b_{pi}, with errors β_{pi}. This transfer function at instant p is given by :-

$$C'p(z) = b_{p0} + \beta_{p0} + (b_{p1} + \beta_{p1})z^{-r_{p,1}} + (b_{p2} + \beta_{p2})z^{-r_{p,2}}$$

$$= (b_{p0} + b_{p1}z^{-r_{p,1}} + b_{p2}z^{-r_{p,2}}) + (\beta_{p0} + \beta_{p1}z^{-r_{p,1}} + \beta_{p2}z^{-r_{p,2}})$$

and the complete transfer function matrix for this section may be written as

$$\underline{G}_{2(\text{complete})} = \underline{G}_2 + \underline{Y}_2 \quad \ldots\ldots\ldots\ldots\ldots\ldots\ldots\ldots\ldots\ldots\ldots\ldots (9)$$

where $\underline{Y}_2$ is a matrix derived from the error terms $\beta_{pi}z^{-r_{p,i}}$, only and $\underline{G}_2$ represents the exact transfer function matrix.

The overall transfer function of all sections is found as

$$\underline{C}' = (\underline{G}_2 + \underline{Y}_2)\ \underline{G}_1.\underline{I}$$

$$= \underline{G}_2\underline{G}_1\ \underline{I} + \underline{Y}_2\underline{G}_1 \cdot \underline{I}$$

$\underline{G}_2.\underline{G}_1.\underline{I}$ leads to an overall ideal transfer function identical to the direct form, so that ρ_k is the same in both cases.

$\underline{Y}_2\underline{G}_1 \cdot \underline{I}$ is due to the error terms and its row p is given by

$$\beta_{p0}\left\{a_{p0} + a_{p1}z^{-r_{p,1}} + \ldots\ldots\ldots\ldots\ldots\ a_{p(m-2)}z^{-r_{p,(m-2)}}\right\}$$

$$+ \beta_{p,1}z^{-r_{p,1}}\left\{(a_{(p-1),0} + a_{(p-1),1}z^{-r_{(p-1),1}} + \ldots\ldots\ldots a_{(p-1),(m-2)}z^{-r_{(p-1),(m-2)}}\right\}$$

$$+ \beta_{p,2}z^{-r_{p,2}}\left\{a_{(p-2),0} + a_{(p-2),1}z^{-r_{(p-2),1}} + \ldots\ldots\ldots\ldots a_{(p-2),(m-2)}z^{-r_{(p-2),(m-2)}}\right\}$$

This must be compared with the summation of error terms $\sum_{i=1}^{m} \beta_{p,i}z^{-i}$ for the direct form.

The expressions in parenthesis are the transfer functions of the preceding section, and each one contains the stopband zeros implemented so far. Thus for a z_k close to one of the preceding zeros these terms evaluated at $z = z_k$ will in general, be small and the effect of the rounding errors $\beta_{p,i}$ will be diminished.

As an example consider a single canceller followed by a second order section with zeros at $\omega\delta T = \pm 0.01$. For the direct form, with 6 bit rounding,

$$\sum_{i=0}^{3} \beta_i z^{-i} = 0.00192 - j0.000486$$

The corresponding summation for the cascade form is given by evaluating (10):-

$$\beta_0\ (1 - z^{-3}) = \beta_0\ (0.0004 + j\ 0.02996)$$

$$+ \beta_1 z^{-3}\ (1 - z^{-5}) = +\beta_1 z^{-3}\ (0.0012 + j\ 0.04998)$$

$$+ \beta_2 z^{-8}(1 - z^{-4}) = +\beta_2 z^{-8}\ (0.0008 + j\ 0.03999)$$

$$= -\ 0.0000318 + j\ 0.000218$$

so that the magnitude of the overall effect of the errors is decreased. The result is that the predicted displacement for 6 bit rounding in this case is approximately 9 times greater for the direct filter than the cascade relisation. The ratio of sensitivities of direct and cascade forms are necessarily dependent on the appropriate β_i, which, for a large number of filters, are usually assumed to be uniformly distributed between $\pm \frac{E_o}{2}$ and statistically independent with respect to each other (Knowles, J. B. 1968). On this basis the expected modulus of the $\sum_{p=0}^{m} \beta_i z^{-i}$ for the direct form is

$$\left[(m + 1)\ \frac{E_o^{\ 2}}{12}\right]^{\frac{1}{2}}$$

whereas for the cascade form this becomes

$$\left[\frac{E_o^{\ 2}}{12}\right]^{\frac{1}{2}} \cdot \left[\sum_{q=p}^{p-2} \left| a_{q0} + a_{qi}z_k^{-r_{p1}} + \ldots\ldots\ a_{q(m-2)}z_k^{-r_{p(m-2)}} \right|^2\right]^{\frac{1}{2}}$$

which is diminished by virtue of the zeros contained in

$$a_{p,0} + a_{p,1}z^{-r_{p,1}} + \ldots\ldots\ldots a_{p,(m-2)}z^{-r_{p,(m-2)}}$$

It is apparent from this approach that, in general, the sensitivity of zero positions to coefficient errors is increased by the proximity of other zeros but that this increase is reduced considerably if the zeros are realised in separate sections. There is also some interaction between the position of subsequent zeros and the errors in a previous section, but a full treatment of the subject is not within the scope of this paper.

5. PRACTICAL IMPLICATIONS.

Despite the restriction of the above analysis to small errors the investigation of practical examples of filters indicates that the conclusions drawn from the case of small errors can be extended to filters with larger coefficient errors. Indeed the advantages obtained through the cascade realisation become more noticeable for filters with larger rounding errors.

Table (1) shows the clutter attenuation due to 3rd, 4th, 5th and 7th order filters with rounded coefficients. These figures were obtained by adding 500 sets of "simulated" rounding errors, with appropriate probability density functions to the ideal coefficients and averaging the results. The clutter attenuation figure is a direct measure of the "improvement factor" (Skolnik M.I., 1970) since the coefficient errors have little effect on the passband. Table (1) shows that in every case the cascade form results in better clutter attenuation than does the direct form.

Other significant points arise from these results. Notice that as the wordlength is decreased the higher order direct filters deteriorate rapidly. The sensitivity of the 4th order cascade filter, composed of two 2nd order sections, emphasises the desirability of a single canceller as the first stage of any filter, as in the 3rd, 5th and 7th order cases. A single canceller with its zero at $z = 1$ has a transfer function $(1 - z^{-1})$ which is independent of the stagger sequence chosen. This may be realised exactly without coefficient multiplications, and consequently the zero is placed without error. Furthermore, by virtue of the cascade nature of the filter the following zeros are rendered less sensitive to any errors in the coefficients of later sections.

Table (2) shows that by taking full advantage of the "step-by-step" nature of the design process the advantages of the cascade form can be enhanced further. Here later sections of the filter are designed to follow the rounded coefficients of preceding sections rather than their ideal values, and greater accuracy of zero positioning is obtained. However, care is necessary in certain cases. For example an attempt to duplicate the position of a zero using rounded coefficients for the previous sections will lead to equations based solely on the rounding errors and will only result in a single zero at the required location being realised by the combination of both sections. Consequently multiple zeros must be placed by the solution of the derivative of the simultaneous equations as described in Section (3.1).

The major disadvantage of the cascade form is its requirement for greater hardware complexity. For example, a 6th order direct filter requires 7 coefficient multipliers, but if realised in three 2nd order sections a total of nine is necessary. Also, since multiplier outputs are subject to rounding or truncation additional noise sources are introduced by the cascade form. However, the hardware cost is reduced if the section weights are normalised such that the modulus of the largest coefficient in each section is unity. Since unity coefficients do not require multipliers, as such, the multiplier count is then identical for both forms. Alternatively some of the benefits of the sectional approach are achieved by the insertion of a single canceller before the remainder of the filter, which may then be realised in a single larger section. This reduces the sensitivity of zero displacement at the cost of little additional hardware.

With reference to the problem of multiplier roundoff noise, Table (3) shows revised figures for Table (1), including the effect of these noise sources. Equal signal and coefficient wordlength have been used, and it is seen that although higher order filters suffer more severely the cascade form is still superior. Once again, however, the use of a high order filter does not necessarily result in improved performance, and if maximum economy is to be achieved care should be exercised in the choice of optimum filter order and arithmetic wordlength.

6. CONCLUSIONS.

It has been shown that the cascade form has certain advantages over the direct implementation of M.T.I. filters in terms of accuracy of response. Since errors in frequency response are closely related to arithmetic precision it follows that an improvement in performance could be offset by a reduction in wordlength and hence in hardware cost. The reduction of cost is always an important design factor but equally significant is that hardware simplicity may permit increased speed and extend the areas of application.

The advantages of the cascade form must be balanced against the requirement for an increased number of arithmetic units, albeit with fewer bits each, but even this may not be necessary for certain forms of coefficient scaling. If care is excercised in the choice of units to be cascaded then additional hardware can be minimised.

Current design methods for time varying filters (Jacomini, O.J, 1972 ; Prinsen, P.J.A. 1973) have been restricted to the direct form and the conversion of such a design to separate sections is not straightforward. Consequently, an alternative design procedure based on the placement of zeros in the z-plane

has been developed. This approach has the advantage that each pair of zeros may be implemented by a single section in a step by step manner. The calculation of the coefficients of each section requires only the solution of a set of simultaneous equations, and is readily performed by a digital computer. Using analysis suitable for the case of small rounding errors and zero displacements, it has been shown that the cascade form of M.T.I. filters is, in general, superior to the direct form. Finally, a number of examples have been used to illustrate that the same conclusions apply to filters with larger rounding errors.

7. REFERENCES.

GOLD, B., RADER, C.M., 1969, "Digital Processing of Signals", McGraw-Hill.

HERRMAN, O, SCHUSSLER, W., 1970 "On the Accuracy Problem in the Design of Non-Recursive Digital Filters".., Arch. Elek. Ubertragung. Vol. 24, pp. 525 - 526.

JACOMINI, O.J., 1972, "Weighting Factor and Transmission Time Optimisation in Video M.T.I. Radar", I.E.E.E. Trans. Vol. AES 8. No. 4.

KAISER, J.F., 1965, " Some Practical Considerations in the Realization of Linear Digital Filters". Proc. 3rd Annu. Allerton Conf. Circuit System Theory, pp. 621 - 633.

KNOWLES, J.B., OLCAYTO, E.M. 1968, "Coefficient Accuracy and Digital Filter Response", I.E.E.E. Trans. Vol. CT15. No. 1.

MALEY, C.E., 1962, "The Effect of Parameters on the Roots of an Equation System", Computer Journal, Vol. 4, pp 62 - 63.

MITRA, S.K., SHERWOOD, R.J., 1974, "Estimation of Pole Zero Displacements of a Digital Filter Due to Coefficient Quantization", I.E.E.E. Transactions, Vol. CAS 21, No. 1.

OPPENHEIM, A.V., SCHAFER, R.W., 1975, "Digital Signal Processing", Prentice Hall

PRINSEN, P.J.A., 1973, " Elimination of Blind Velocities of M.T.I. Radar by Modulating the Interpulse Period", I.E.E.E. Trans. Vol. AES9 No. 5.

SKOLNIK, M.I., 1970, "Radar Handbook" McGraw Hill.

THOMAS, H.W., LUTTE, N.P., 1972 "Z-Transform Analysis of Non-Uniformly Sampled Digital Filters", Proceedings I.E.E. Vol. 119. No. 11.

THOMAS, H.W., LUTTE, N.P., JELFS, M.W., 1974, "Design of M.T.I. Filters with Staggered P.R.F. : A Pole Zero Approach", Proceeding I.E.E. Vol. 121. No. 12

THOMAS, H.W., ABRAM, T.M., 1976, "Stagger Period Selection for Moving Target Radars", Proceedings I.E.E. Vol. 123, No. 3.

8. APPENDIX 1.

Consider the steady state response of a filter represented by the matrix G to a sinusoidal input $e^{j\omega t}$.

$$\underline{C} = \underline{G} \cdot \underline{R}$$

The filter has intersample periods $\tau_1 \delta T$, $\tau_2 \delta T$, ... $\tau_n \delta T$ and $\sum_{i=1}^{n} \tau_i = T'$ as illustrated in Fig. 6 for a 4 period sequence.

τ_i and T' are integers.

Each R_p of the input vector $\underline{R} = \begin{bmatrix} R_1 \\ R_2 \\ R_n \end{bmatrix}$ is found by taking the advanced z-transform with sample period $T'\delta T$ of the sinusoid and delaying this to place it correctly, relative to the other $R_i(z)$.

$$\text{Thus } R_1(z) = \frac{e^{j\omega \tau_1 \delta T} \; z^{-\tau_1}}{1 - e^{j\omega T' \delta T} z^{-T'}}$$

$$\text{in general } R_p(z) = \frac{e^{j\omega \delta T \cdot \sum_{i=1}^{p} \tau_i} \; z^{-\sum_{i=1}^{p} \tau_i}}{1 - e^{j\omega T' \delta T} z^{-T'}}$$

$$\therefore \quad \underline{R} = \begin{bmatrix} e^{j\omega\delta T.\tau_1} & z^{-\tau_1} \\ \vdots & \vdots \\ e^{j\omega\delta T \sum_{i=1}^{p} \tau_i} & z^{-\sum_{i=1}^{p} \tau_i} \\ \vdots & \vdots \end{bmatrix} \cdot \frac{z^{j\omega T'\delta T}}{z^{T'} - e^{j\omega T'\delta T}}$$

Define $\underline{R}'$ as the above matrix.

The output sequences $C^*_p(mT'\delta T + \sum_{i=1,}^{p} \tau_i \delta T)$ are obtained by use of the inverse z-transform on the C(z) matrix.

$$\therefore \quad \underline{C}^* = \frac{1}{2\pi j} \oint \frac{z^{T'}}{z^{T'} - e^{j\omega T'\delta T}} \left\{ z^{mT'-1} \left[z^{\tau_1} \ldots . z^{\sum_{i=1}^{p} \tau_i} \ldots . \right] \right\} \underline{G} \cdot \underline{R}' \, dz$$

The steady state response is found by evaluating the inversion integral of the forcing function only, which leads to

$$\underline{C}''(mT'\delta T) = e^{j\omega T'\delta T} \left[z^{j\omega \tau_1 \delta T} \ldots\ldots\ldots e^{j\omega\delta T \sum \tau_i} \ldots . \right] \underline{G}(e^{j\omega\delta T}).\underline{R}'(e^{j\omega\delta T})$$

$$\underline{R}'(e^{j\omega\delta T}) = \left[\begin{matrix} 1 \\ 1 \\ \vdots \\ 1 \end{matrix} \right]_n = \underline{I}$$

so that each $C_p''(mT'\delta T)$ consists of a sinusoidal envelope $e^{j\omega T'\delta T}$, with a phase term due to the row vector $[e^{j\omega\tau_1\delta T} \ldots\ldots]$ The magnitude of the envelope is determined by $\underline{G}(e^{j\omega\delta T})$. $\underline{I}$, leading to the statement of section 3.1 that

$$\underline{C}'(e^{j\omega\delta T}) = \underline{G}(e^{j\omega\delta T}) \cdot \underline{I}$$

where $C'(e^{j\omega\delta T})$ describes the magnitude of the sinusoidal output evelope for each sample instant of the stagger cycle.

9. APPENDIX 2.

```
      SUBROUTINE DESIGN ( G,ORDER, TAU,N, R,W )
C
C     THIS ROUTINE FORMS AND SOLVES THE EQUATIONS NECESSARY TO PLACE A
C     ZERO OR PAIR OF COMPLEX CONJUGATE ZEROS IN A FIRST OR SECOND ORDER
C     FILTER SECTION.  THE ROUTINE IS ENTERED WITH THE INPUT VECTOR (R)
C     EVALUATED AT W ( IN RADIANS) - THE FREQUENCY AT WHICH THE ZEROS ARE
C     TO BE PLACED. THE TIME VARYING COEFFICIENT SET (G) IS NORMALISED
C     SO THAT G(P,P) IS SET EQUAL TO 1.0
      REAL G(10,10),AP(3)
      INTEGER TAU(10),ROW,COLUMN,ORDER
      COMPLEX R(10),J,EQU(3),LHS(2),RHS
      DATA J / (0.0,1.0) /
C     SOLVE THE EQUATION SET FOR EACH STAGGER TIME I.E. EACH ROW OF A.
      DO 1 ROW = 1 , N
C     FORM THE EQUATION SET
      T=0.0
      DO 2 COLUMN = 1 , 3
      INDEX = MODULO( N, ROW-COLUMN ) + 1
      EQU(COLUMN) = R(INDEX) * CEXP( J*W*T )
2     T = T + FLOAT( TAU(INDEX) )
C     NOW REARRANGE THE EQUATIONS INTO STANDARD FORM FOR SOLUTION
      RHS    = -EQU(1)
      LHS(1) =  EQU(2)
      LHS(2) =  EQU(3)
      CALL SOLVE( LHS,RHS,ORDER )
      AP(1) = 1.0
      AP(2) = REAL ( RHS )
      AP(3) = AIMAG( RHS )
C     COPY THE SOLUTION VECTOR INTO THE CORRECT ELEMENTS OF G.
      DO 3 COLUMN = 1 , 3
      INDEX = MODULO( N, ROW-COLUMN ) + 1
3     G(ROW,INDEX ) = AP(COLUMN)
1     CONTINUE
      RETURN
      END
```

INTEGER FUNCTION MODULO (N,I) returns the number I modulo N (i.e. in range 0 N-1). SUBROUTINE SOLVE (LHS, RHS, ORDER) solves complex 1st or 2nd order equations in the form LHS* X=RHS The value of X(1) is returned in the real part of RHS, X(2) in the imaginary part.

A complete program for the design of a general filter is available from the authors.

TABLE 1

No. of bits.	3rd		4th		5th		7th	
	Dir.	Cas.	Dir.	Cas.	Dir.	Cas.	Dir.	Cas.
10	37.40	37.50	44.46	45.04	49.92	55.88	49.30	68.96
8	36.15	37.48	39.30	43.19	39.53	55.21	37.35	64.02
7	33.73	37.41	34.66	40.09	33.41	53.83	31.41	59.15
6	29.67	37.12	28.66	35.75	27.57	50.63	25.38	53.40
5	24.37	36.21	22.93	30.24	21.57	45.88	19.46	47.60
4	18.45	33.92	16.92	24.06	15.50	40.37	13.67	41.36
3	12.87	29.82	11.10	18.31	10.18	34.24	8.34	35.73
2	7.57	24.47	6.12	12.07	5.25	28.30	3.90	29.28

TABLE 2

No. of bits	4th	5th	7th
10	45.10	55.90	69.21
8	43.64	55.43	65.17
7	40.71	54.55	59.70
6	35.47	51.62	54.85
5	29.62	46.54	50.31
4	25.65	41.61	45.11
3	22.95	35.08	40.84
2	16.68	31.42	33.21

TABLE 3

No. of bits	3rd		4th		5th		7th	
	Dir.	Cas.	Dir.	Cas.	Dir.	Cas.	Dir.	Cas.
10	37.37	37.48	44.23	44.87	48,75	54.09	47.76	57.84
8	35.73	37.07	38.06	41.58	38.61	50.81	35.72	46.06
7	32.71	35.99	32.91	37.18	31.68	40.53	27.65	34.09
6	28.03	33.24	26.91	31.81	25.82	34.61	23.79	34.04
5	22.41	28.66	21.06	25.96	19.80	28.61	17.87	28.02
4	16.50	23.10	15.09	19.82	13.75	22.58	12.02	21.97
3	10.80	17.24	9.17	13.89	8.31	16.56	6.60	15.96
2	5.25	11.34	4.11	7.89	3.40	10.60	2.18	9.89

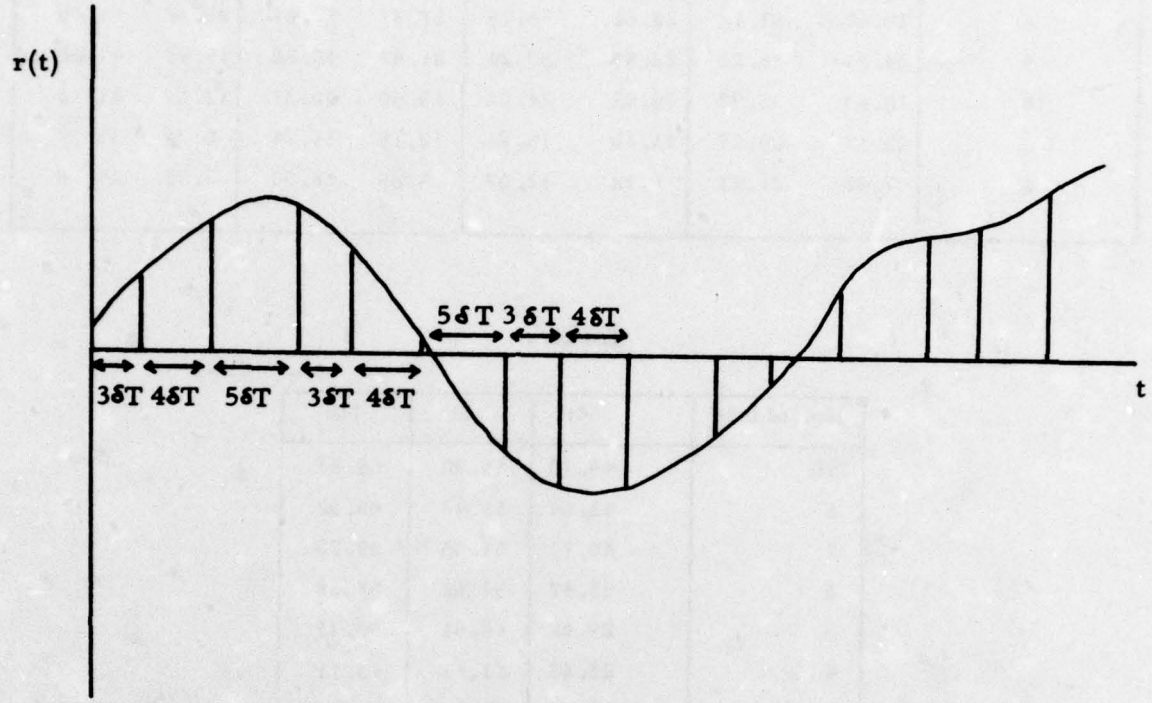

Figure 1

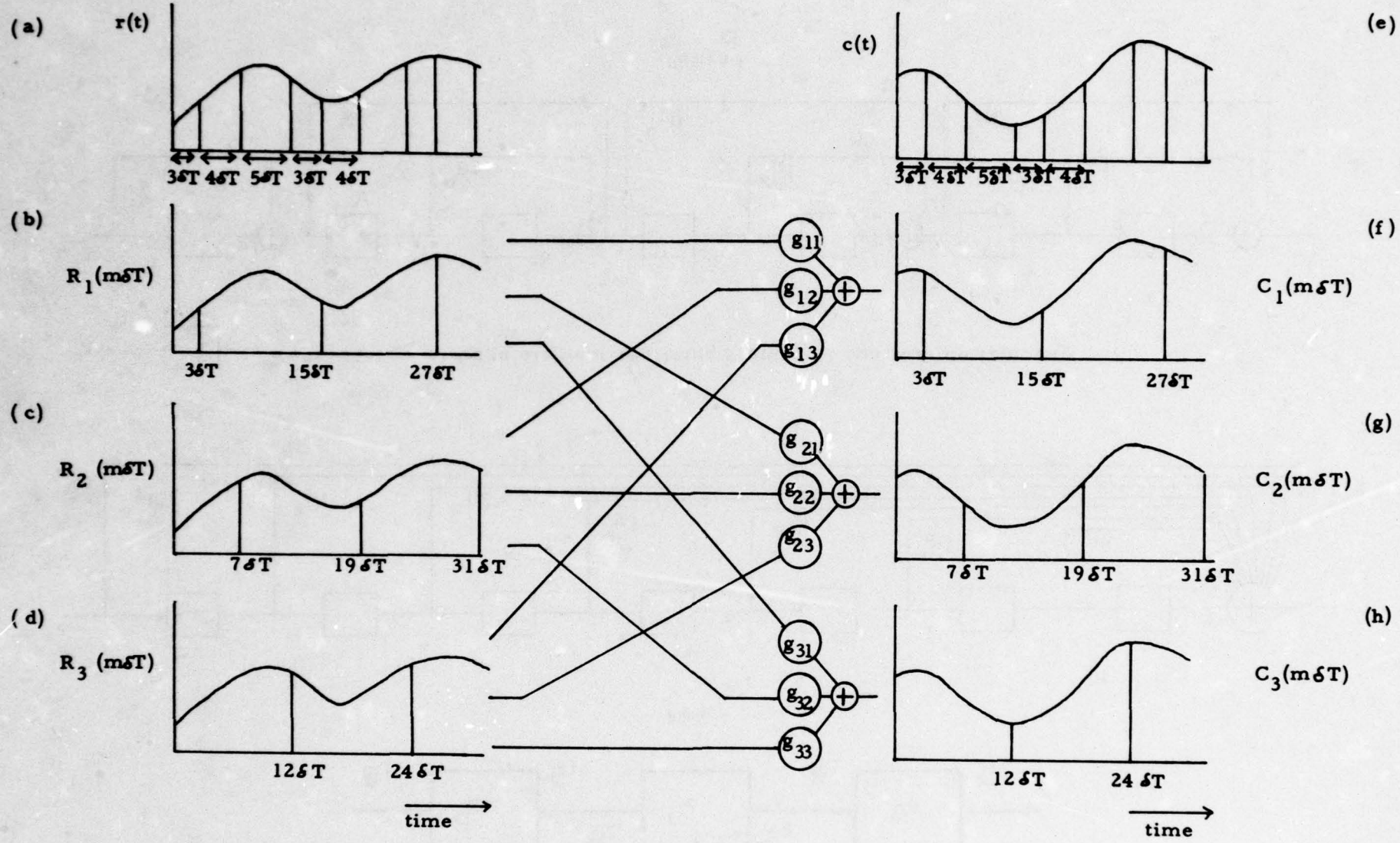
(a)
r(t)
3δT 4δT 5δT 3δT 4δT
(b)
R1(mδT)
3δT
15δT
27δT
(c)
R2 (mδT)
7δT
19δT
31δT
(d)
R3 (mδT)
12δT
24δT
time
g11
g12
g13
g21
g22
g23
g31
g32
g33
(e)
c(t)
3δT 4δT 5δT 3δT 4δT
(f)
C1(mδT)
3δT
15δT
27δT
(g)
C2(mδT)
7δT
19δT
31δT
(h)
C3(mδT)
12δT
24δT
time

Figure 2

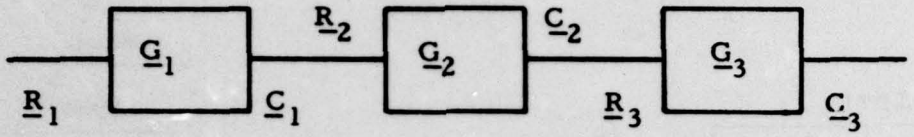

Figure 3

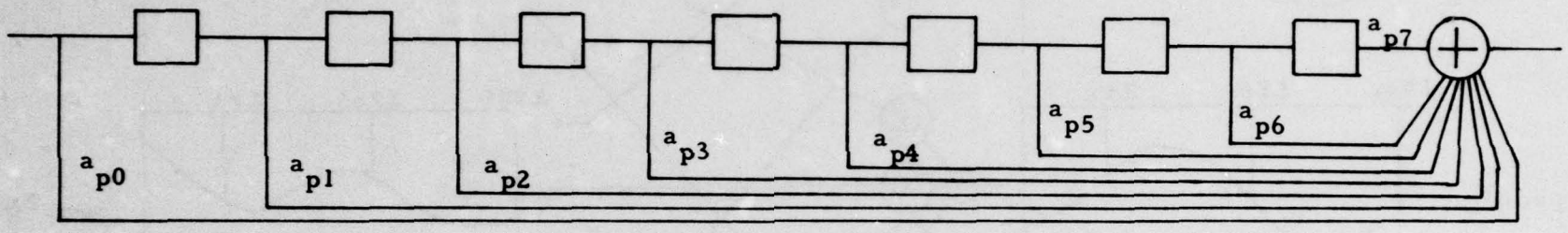

Represents a storage element realising a delay of one sample interval

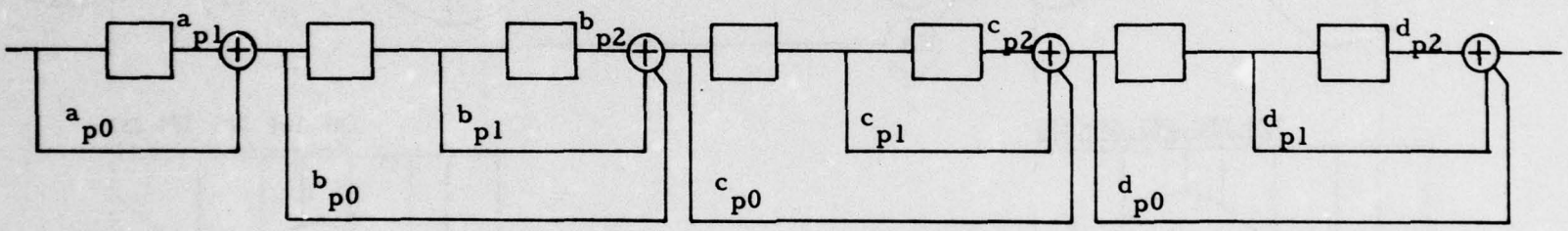

Figure 4

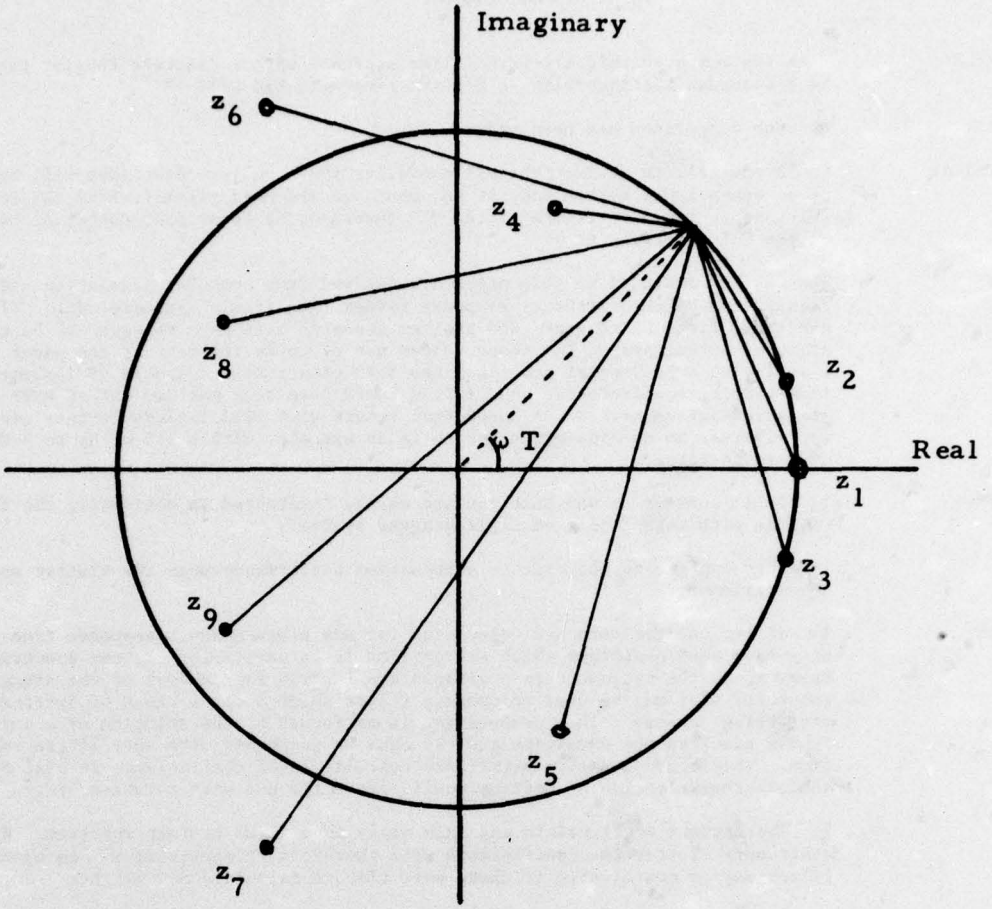

Figure 5

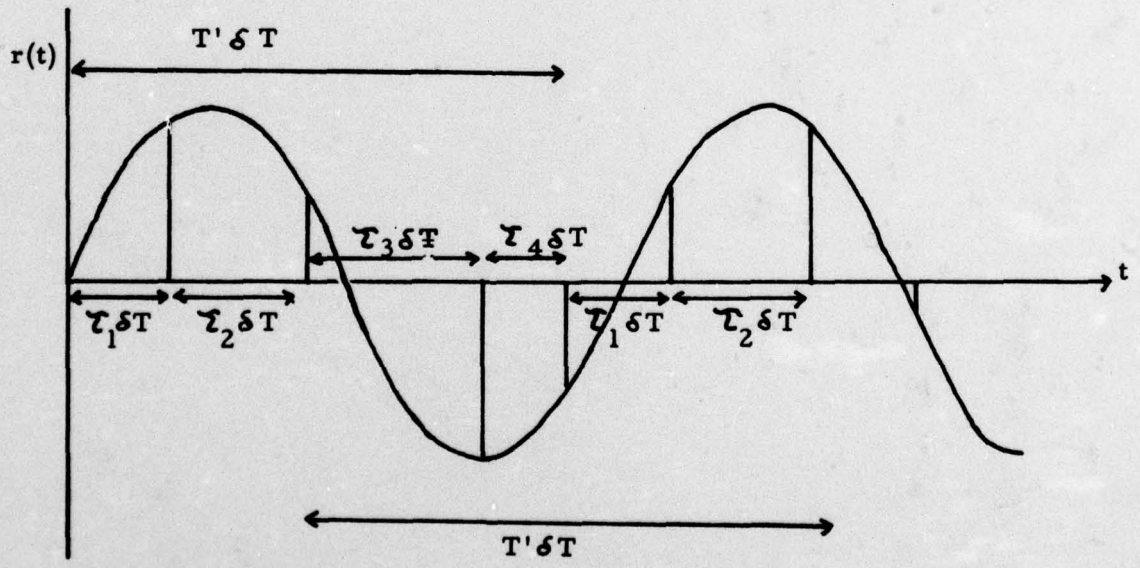

Figure 6

DISCUSSION

D F HAMMERS: Have you compared this all-zero filter approach with a discrete Fourier transform, ie 8 cascaded sections with an 8-point time-weighted DFT?

T M ABRAM: No such comparison has been made.

A J KAMPSTRA: Could you tell me whether the MTI canceller you have just described will become part of an operational system and, if so, what are the main parameters of the radar relevant to the performance of the MTI (wavelength, beamwidth, number of hits, range of the MTI interval, etc)?

T M ABRAM: The results included in this paper are derived from computer simulation and calculation of the frequency response rather than from a hardware unit. Clutter spectrum, first blind speed and stagger sequence have been selected to be representative of a real system and these values are given in the text of the paper. However, a real-time experimental processor has been constructed, capable of implementing time-varying coefficients, and limited tests have been carried out at RSRE on a staggered-prf radar. It is hoped that future work will include further use of this canceller as an on-line processor to radar signals, with a prf of up to 4 KHz and 1000 range gates.

K KRUCKER: 1) Is it correct to say that you are mainly interested in optimising the filter weights with regard to a variable-stagger system?

2) What happens to the clutter attenuation performance when the clutter spectrum is non-stationary?

T M ABRAM: 1) Filter coefficients are calculated for any given stagger sequence from a set of stop-band zero positions which are optimum for a particular clutter spectrum. However, as the optimum zero positions are largely independent of the stagger sequence, they may be used to compute filter weights for a range of different staggering schemes. This computation is performed by the solution of a set of linear simultaneous equations and may thus be performed with very little computer time. This could possibly permit the calculation of coefficients in real time to achieve the selection of optimum coefficients for use with a random prf.

2) The optimum coefficients can only apply to a fixed clutter spectrum. With non-stationary clutter the coefficients will therefore be non-optimum. An adaptive filter may be conveivable if there were time to calculate new weights.

POOR-RESOLUTION SATELLITE OBSERVATIONS OF RADAR RETURN FROM NORTH AMERICA, BRAZIL, AND THE OCEANS*

Richard K. Moore
University of Kansas Remote Sensing Laboratory
2291 Irving Hill Drive -- Campus West
Lawrence, Kansas 66045, USA

Arun Sobti
Motorola, Inc.
Schaumburg, Illinois 60172

James D. Young
General Dynamics
Fort Worth, Texas 76101

ABSTRACT

The 13.9 GHz radar scatterometer on Skylab produced statistics of radar returns from thousands of points in North America and Brazil, as well as from the oceans. The resolution cell of the system varied from about 11 km in diameter at vertical incidence to 20 by 30 km at 50° incidence. Although these cells are larger than the preprocessing cells to be expected from spacecraft synthetic-aperture radars, they are at least as comparable with such cells as are the observation cells when aircraft radars are used. The statistics presented are therefore of considerable interest to designers of spaceborne radar systems, for they set preprocessing sensitivities and dynamic ranges required.

Results are presented both in terms of composite statistics for North America, Brazil, and the oceans, and in terms of statistics for particular classes of terrain. Both vertical and horizontal polarization data are presented for the land, and cross-polarized measurements are presented as well for the sea. Correlations are indicated for the returns at different angles and polarizations.

1. INTRODUCTION

The Skylab spacecraft was launched in May of 1973. Among the instruments carried on the spacecraft was a radiometer/scatterometer operating at 13.9 GHz. This flexible instrument was used to obtain measurements of both emission and backscatter from both land and sea, with most of the land experiments conducted over North America and the ocean experiments in the North Atlantic and North Pacific Oceans. Some experiments were conducted in other areas and a few results from Brazil are included in this paper.

The observations over the ocean were intended to demonstrate the capability of the scatterometer as a wind-measuring instrument; and, indeed, they did demonstrate that the scatterometer on a spacecraft provides a good anemometer. The measurements over the land were intended both to gather design data for future spacecraft radars and to establish whether a coarse-resolution sensor could be used to determine different things about the characteristics of the land. Reasonable correlation was obtained with soil moisture in certain controlled experiments reported elsewhere [Eagleman et al., 1975] but these will not be discussed here. The general conclusion, however, is that in a complex environment such as most of those observed in North America the coarse resolution sensor cannot be used adequately to establish the category of land use, although certain gross statements can be made about the difference between heavily vegetated and barren areas.

Comparisons were made with theory of various types, but the general conclusion is that the average response can best be described in terms of either an exponential variation with angle of incidence or a pair of such exponentials.

2. THE SKYLAB EXPERIMENT

The radiometer/scatterometer on Skylab operated at a frequency of 13.9 GHz. The instrument used an interrupted-continuous-wave transmitter and a receiver that was applied to both radiometer and scatterometer experiments. For the radiometer, the receiver had a bandwidth of 200 MHz; and for the scatterometer, the bandwidth was restricted to 75 kHz or thereabouts, depending on the Doppler bandwidth expected at different angles of incidence. The antenna was a one-meter parabolic dish with a multiply-polarized feed. The footprint on the ground for this antenna was a circle 11 kilometers in diameter directly beneath the spacecraft and it became an ellipse about 16 by 25 kilometers at the maximum angle of incidence of around 50°.

The antenna was scanned mechanically in one of four different modes illustrated in Figures 1, 2, 3 and 4. Figure 1 shows the in-track non-contiguous (ITNC) mode. This was designed to obtain a set of measurements at intervals of approximately 100 kilometers and was used primarily over the ocean. For each point on the surface, it was possible to determine the scattering coefficient in each of four polarizations: vertical transmit, vertical receive (VV); horizontal transmit, horizontal receive (HH); vertical transmit, horizontal receive (VH); and horizontal transmit, vertical receive (HV). In addition, measurements were made of both the vertically and horizontally polarized radiometer signals. These measurements were made at nominal pointing angles from the spacecraft of 0, 15, 30, 40, and 48 degrees from the vertical. Because of the wide spacing of the footprints, this mode was seldom used over the land.

Figure 2 illustrates the cross-track non-contiguous (CTNC) mode. The same measurements were made as in the ITNC mode, but the antenna was scanned to the side of the spacecraft to the same angles used in ITNC. In the ITNC mode, each point on the ground was observed at each of the angles, but in the CTNC mode, only a single angle could be observed for each point on the ground.

* This work was supported by NASA Johnson Space Center under Contract NAS 9-13331.

Figure 3 illustrates the cross-track contiguous (CTC) mode. In this mode, the antenna was scanned approximately 11° either side of a central point obtaining about 12 cells of measurement for each scan. The central point could be either straight down or pointed ahead or to the side at angles of 15 and 30 degrees. The 30°-ahead pointing angle was used extensively over North America and Brazil.

The fourth mode was the in-track contiguous (ITC) mode and was designed to obtain a measurement about every 25 kilometers at each of the angles described for the ITNC mode. Because the measurements were closer together, there was less time to integrate the signals and to observe different polarizations. Consequently, both the CTC and ITC modes were restricted to one or two polarizations so that multiple polarization comparisons were not possible with them. The ITC mode was intended to obtain scattering coefficient as a function of angle over land where the 25-kilometer footprint spacing was more appropriate.

Coverage during the summer occupancies (SL 2 and 3) over North America was obtained in the areas shown in Figures 5 and 6. Coverage in Brazil during these missions was repeated over many ground tracks, but only three were used in our analysis and they are not shown here. Oceanic coverage was wide-spread, but no maps for this type of coverage are shown.

During the winter mission (SL 4), the coverage over North America was much less extensive; but over the oceans it was more extensive than during the summer. In September of 1973 a failure of the antenna scan mechanism occurred. This was repaired by the astronauts early in the SL 4 mission, but the repair did not permit scanning in the along-track direction. Consequently, both ITC and ITNC modes were prohibited during the winter and the CTC mode could only be used with the central angle straight down or to the side. Because of this, most of the measurements over North America during the winter were performed in the CTC modes centered about the nadir which meant that the angles of incidence were small.

3. OCEAN OBSERVATIONS

3.1 Composite Measurements

The radar returns from the ocean are extremely variable and indeed, studying this variation was the prime purpose of the oceanic experiments. Nevertheless, for design purposes composite information on the oceanic measurements is of value. Figure 7 shows the average response from the ocean during the summer mission for vertical polarization and for the cross-polarized measurements involving horizontal transmission and vertical reception. The angular-variation curves are quite steep. The scattering coefficient near vertical is close to the saturation level of the instrument. Both the mean and the upper and lower decile values are indicated on the graph; however, at vertical incidence the upper decile shown is the saturation level of the instrument so that the upper decile probably is actually somewhat higher and indeed, the mean is also probably higher. Note that the average scattering coefficient for vertical polarization amounts to a value in the vicinity of -20 dB at 46° for vertical polarization. For the cross-polarized response, the curve is not so steep and starts at a value below 0 dB. At vertical incidence, the mean is some 15 dB below that for the vertical polarization, but at 46° it is only 10 dB below vertical polarization.

Figure 8 shows the same type of curve for horizontal polarization. The difference in the vertical incidence value from that for vertical polarization is an experimental fluctuation; at vertical the two polarizations should be about the same. However, the horizontally polarized curve is steeper than that for vertical polarization; the 46° value is about 4 dB below that for vertical polarization. The relatively wide spread of the upper and lower decile values is associated with the significant differences in the scattering coefficient as a function of wind speed, which of course was quite variable. Curves of this nature are not presented here for the winter mission except in Section 5 dealing with models. However, it should be noted that the ocean backscatter curves were not as steep during the winter as during the summer. This is primarily because the seas are calmer during the summer than during the winter so that scattering from large angles of incidence is less in the summer than in the winter.

3.2 Wind Response

Measurements of the wind response of the scattering coefficient utilized information about the surface winds based on "objective analysis". This objective analysis technique was applied by oceanographers at the City University of New York, Institute of Marine Sciences. It uses reports from ships scattered throughout the ocean. Some of these ships send their reports by radio to meteorological centers and others send in the wind information by mail for climatological purposes. Both kinds of observations were used in determining the wind fields. Nevertheless, in many cases the ships were located in the wrong places to obtain measurements suitable for comparison with the scattering coefficients so considerable extrapolation goes in to the analysis. Furthermore, ship reports are of variable quality. Some ships read anemometers at known heights every six hours. Others, however, report winds simply by the mariner's visual observation of the sea conditions. Thus, the "surface truth" is far from "true". A study was made of the value of the surface wind information by comparing the objective analysis values at the weather ships operated for aeronautical purposes in the North Atlantic. The objective analysis was used to calculate the wind at the weather ship without use of the observation from the weather ship. The difference between the wind so calculated and that reported by the weather ship, which presumably has a high quality observation, was then analyzed. Figure 9 shows one sample of the kind of observations found in this experiment for the speed of the wind. Clearly, the variance of the data is large indeed. Similar plots could be shown for the direction of the wind. The mean deviation in direction between the weather ship report and the objective analysis at the weather ship location was found to be 38°!

With this background, one can observe the relationship between the velocity and the scattering coefficient and not be too surprised at a considerable spread in the observations. Figures 10, 11, 12 and 13 are examples of the wind observed as function of the scattering coefficient. Of course, the scattering coefficient was observed with each polarization at five different angles, but Figures 10, 11 and 12 illustrate what was found at the approximately 50° angle of incidence during the summer mission. Figure 10 shows the vertically polarized result, Figure 11 the horizontally polarized result, and Figure 12 the cross-polarized result for this angle of incidence. Similar plots were prepared for the winter mission. Figure 13 is presented to show the kind of non-response observed near vertical. Clearly, the scattering coefficient

is not very sensitive to the wind speed at vertical. It is even less sensitive at 15° angle of incidence (not shown).

Regression lines were determined for the wind versus scattering coefficient data and from these regression lines, values of the scattering coefficient were used to estimate the surface winds. Thus, plots could be made of the radar estimate of the surface wind in comparison with the "objective analysis" estimate. An example of such a plot is shown in Figure 14. This clearly indicates the value of the radar scattering measurement for anemometry but the spread of the data points also shows the difficulty of making such measurements using the uncertain values of the wind obtained from ship reports. Most of the scatter in the data can be explained by the variations in the ship reports as indicated in the study exemplified by Figure 9.

The exponents relating the scattering coefficient to the wind speed can be characterized as in Figure 15. It is interesting to note that these exponents are even higher than those reported previously by Claassen et al [1972]. These exponents are much higher than those reported by Daley [1973]. Nevertheless, the results are somewhat consistent with those reported from aircraft measurements by Claassen et al, and are quite consistent with more recent observations using an aircraft radiometer/scatterometer developed for NASA Langley Research Center [Jones, L. J., et al, 1975].

4. LAND OBSERVATIONS

4.1 Composite Observations

A major purpose of the land experiment was to determine design data for use in future spacecraft radar systems. The data are also valuable in a design of aircraft radar systems, but less so than for spacecraft radar. The problem is that the very large footprint of the Skylab instrument averages over a region much larger than would be feasible with an aircraft instrument. Consequently, the variability of the Skylab observations is much less than would be observed where the instrument looks at a smaller area on the ground. The observations, however, are useful for example, in considering the design of a spacecraft synthetic-aperture radar even though the illuminated area for the synthetic-aperture radar would be smaller. Synthetic-aperture radar would have a relatively long antenna and consequently a narrower beamwidth and in the other direction its illumination would be over a much smaller distance because of the finer range resolution. Nevertheless, this area is large enough for the synthetic aperture so that the averaging should be somewhat similar to that observed on the Skylab information and the data reported here should be valuable for design of spacecraft synthetic-aperture radars.

Figure 16 shows the composite observations made over North America during the summer mission for vertical polarization. A similar figure could be presented for horizontal polarization, but is not presented here. This figure should be compared with Figures 7 and 8 for the oceans. Over the land, the scattering coefficient near vertical is in the neighborhood of 0 dB but it only falls off to about -11 dB for the maximum angle. In the case of the oceans, the scattering coefficient for vertical polarization at the maximum angle was around -20 dB and for horizontal polarization about 4 dB lower. Over land, the vertical and horizontal polarizations are almost the same. The variability, as indicated by the spread between the upper and lower decile values, is quite small except in the immediate vicinity of the vertical. Thus, one can expect that these average values are quite representative of the expected returns for a spacecraft radar system in which the illuminated area is large. Obviously, the variability would be greater if the illuminated area were smaller so that variations between different kinds of terrain would become more important. However, mean values should be about the same, even with a much smaller illuminated area.

No attempt has been made here to present similar curves for the winter mission because most of the observations were made quite close to vertical. The indications, however, are that the scattering coefficient curves are somewhat steeper in the winter than in the summer. No doubt this is true because of the lack of vegetation in the winter, since the scattering from vegetation is high at all angles of incidence.

An attempt was made to segregate the different returns from land having different categories of use, as forest, agriculture, grazing (range), etc. Figure 17 illustrates this. The relatively small distinction between all the land categories is quite apparent. Nearly all of them have about the same kind of scattering coefficient as a function of angle. When smaller areas are delineated by a radar carried on an aircraft or on the ground, the differences between different kinds of vegetation and soil preparation (for agriculture) are very apparent. With this large footprint, however, these differences are all averaged out.

4.2 Histograms of Return From the Land

To illustrate the variability observed in more detail than possible by showing just the upper and lower deciles, a study was made in which histograms were plotted of the return at different angles of incidence for different polarizations over North America and South America. In fact, similar histograms were prepared for different land use categories, but they are not shown here. Figure 18 shows the variability in the 1 to 2° range over North America using the nominal vertical polarization (in this range of angle, vertical and horizontal polarization are essentially the same). Here the spread of the values is considerable and, in fact, some very strong returns are shown. Probably these came from quite flat areas such as lakes, and playas. Figure 19 shows similar results for the range of 32 to 36°. Not only is the difference in average levels apparent, but the variation is much less than in the 1 to 2° range of angles. Figure 20 shows the same kind of thing over South America. The South American area covered was in the Brazilian Amazon region, although part of it was forest and part was grassland. Nevertheless, the spread of the values is much less in Brazil than it is in North America. This is not surprising, however, because the terrain in Brazil is much more homogeneous than the North American terrain.

4.3 Attempts at Classification By Land Use or Vegetation

Numerous attempts were made at classification by land use or vegetation using a number of pattern recognition algorithms. In Brazil, the method was reasonably successful, as indicated in Figure 21. Here, the land use categories were homogeneous over large areas so that little averaging of observations from different kinds of land cover took place. Hence, the categorization was reasonably good. Figure 22 shows the best of the classification results over North America. The large errors present are clear although classification shows some promise. Here, as in the case of the ocean, the "surface truth" may be as much at fault as variations in the radar data themselves. No attempt was made to actually visit the areas involved. Rather, the land use categorizations were obtained from existing maps and occasionally from Landsat photography. Since the maps may be inaccurate either because of inadequate data or because they are old, much variation is expected. However, if the data from the maps were all useful, one would expect a better classification accuracy than indicated in Figure 22.

Another method for observing the ground can be based on the use of CTC mode to produce a "quasi" image. Figure 23 is an example of such an image obtained over an area in Brazil. Here, major variations are clearly delineated and the correspondence between the variations and the image and those on the map is as good as can be expected, considering the fact that the map itself is probably considerably in error. Such pseudo images over the United States were not very successful for determining differences that could be discerned on the map. However, in some cases where information was available about the soil moisture, a clear correlation could be observed between soil moisture and the variations on the image [Ulaby, F. T., L. F. Dellwig, T. Schmugge, 1975]. Other measurements and analyses involving soil moisture also have indicated that a reasonable correlation exists between the radar backscatter and the soil moisture [Eagleman, 1974].

5. COMPARISON WITH THEORETICAL MODELS

5.1 Background

The theory of radar backscatter has been the subject of hundreds of papers. However, most of these papers depend upon assumptions about the roughness of the surface that are probably unrealistic except over the ocean and they might even be unrealistic over the ocean in some cases. Some of the models are based upon geometric optics. For these models, a Gaussian angular variation of the scattering coefficient, at least near vertical, results. Most modern theories assume that well away from the vertical neither the geometric optics nor the straight-forward physical optics model is applicable, but rather, a model based upon the small pertubation theory must be used. This method works well over the ocean, but probably is not valid over the land. Since insufficient data are available on the surface roughness of land to apply to the small pertubation model, a comparison was not possible.

However, observations of the moon and the planets generally assume a physical optics model in which the correlation coefficient may be approximated by an exponential. The resulting expression for the scattering coefficient is

$$\sigma^\circ \propto (\cos^4 \theta + K \sin^2 \theta)^{-3/2}$$

Comparisons were made between the various models and the mean values observed for the ocean and the land. The worst fit of the models for both oceanic and land cases was with the geometric optics formulation. The physical optics formulation using the exponential correlation function gave a somewhat better fit, but the best results in every case were obtained using a straight exponential angular variation of the scattering coefficient. None of the theories predicts that this should be the case, but the correlation with the observations averaged over these large areas is quite evident.

5.2 Comparison of Theory and Experiment

Figure 24 is a comparison of the summer observations over the ocean with the exponential model. Clearly, the regression fit of the exponential is quite good over the entire angular range, at least with the points as far apart as they are for this measurement. It is interesting to note that the e-folding angle for all polarizations is in the neighborhood of 6°, although it is somewhat smaller for horizontal polarization because of the steeper curve and somewhat larger for cross polarization. Figure 25 shows similar results over the land for the summer mission. Here, no single model can fit all of the data. Best correlation for the angles of 15° and above is obtained with a straight exponential with an e-folding angle of 34.6°. The Gaussian result based upon geometric optics is not nearly so good a fit, although, for the small number of data points observed, the correlation is high for it also. The formula based upon the exponential correlation function gives results that are considerably better than the Gaussian, but not as good as the exponential. The Lambert's law model gives $\cos^2 \theta$ as the variation, and the correlation with this model is much poorer. Near vertical, a different exponential must be used. Similar comparisons not shown on the graph for the near-vertical region show that the exponential is a better fit in the small angle region than any of the theoretically justified models just as it is in the larger angles. The similarity of the near vertical e-folding value for land with the one that fits throughout the angular range for the ocean is interesting.

The situation during the winter mission (SL 4) is somewhat different, but here too, the exponential gives the best fit. Figure 26 shows the results over land for vertical polarization. The need for the two different angles is clearly demonstrated; however, a word of caution should be inserted since the data for the larger angles included only desert, whereas numerous categories were included within the smaller angular range. Also of interest here is the smaller e-folding value for angles near vertical during the winter than that observed during the summer. This steeper decay in the winter is almost certainly caused by the relative absence of vegetation for the winter measurements. Similar plots were made for the other polarizations, but are not presented here.

Figure 27 illustrates the winter measurements for vertical polarization over the ocean. In this case,

unlike the summer measurements, a single exponential does not seem to fit the data very well. However, the variation for angles well away from the vertical is much less steep in the winter than in the summer and it is somewhat less steep near the vertical. This can no doubt be explained by the fact that many of the observations made in the winter were made in the stormy seas of the North Atlantic, whereas during the summer the wind only exceeded 15 meter per second in a few special cases of tropical storms or hurricanes. Thus, the summer observations are heavily weighted toward relatively calm seas and the winter observations toward relatively rough seas. Apparently, for calm seas, a single exponential from 0° to 45° is adequate, but for rough seas this is not the case as shown in Figure 27.

A comparison was made of the results from various attempts to fit the data with exponential for the summer and winter missions. This result is shown in Table 1. Certain values were not calculated in the summer because of a lack of data and the larger angles (15 - 39°) during the winter were primarily based on scattering coefficients observed from desert. The smaller e-folding angles for the winter over land are apparent as discussed above. Over the ocean, the reverse applies. One should look at the values for 30 to 50°, for instance, for vertical and horizontal polarization where the e-folding angles are less over the ocean than over the land in the summer, whereas during the winter the oceanic e-folding values are larger indicating, as mentioned above, the effect of the stormier seas. In the case of cross polarization, the absolue values for the winter measurement are grossly in error. The cause of the error is known and is associated with a part of the antenna failure problem. The error size, however, is not known. Thus, although the e-folding values may be appropriate for the cross-polarized case in winter, the absolute magnitudes are in error. No cross polarization results are presented for the land because the cross polarization measurements were possible only using the non-contiguous modes and these were primarily operated over the oceans.

6. CONCLUSIONS

Observations from Skylab provide useful design information both for radars operating in space and for aircraft radars. In the case of spacecraft radars, the large area averaged by the Skylab measurement should not be a problem. For aircraft radars, however, the variations to be expected about the mean values reported for the Skylab measurements will be much greater than those observed in Skylab operation.

The scattering-coefficient-versus-angle relations appeared to be best described in terms of exponentials. Except for the summer oceanic data, two different exponential expressions are required; one for the angle close to the nadir, and the other for the angles further out. The strong correlation between these expressions and the observed radar returns indicates that these exponential expressions may be used in design without fear of significant error, although there might be some question about their value for detailed analysis of different kinds of terrain.

The Skylab data indicated without question the value of the radar scatterometer as an anemometer. The scattering coefficient is proportional to wind speed raised to an exponent in the neighborhood of 2 for VV and HH and near 3 for HV and VH. The exponent varies as function of angle of incidence and polarization. This exponent applies for angles of 30° from nadir and beyond, but there is little wind sensitivity close to vertical. These results are reported in more detail in a series of reports issued by The University of Kansas Center for Research, Inc., Remote Sensing Laboratory, and we hope to present several papers detailing the different classes of observation in the near future.

7. ACKNOWLEDGEMENT

The authors acknowledge with thanks support from NASA Johnson Space Center under contract NAS 9-13331 and NAS 9-13642 and from the University of Kansas Computation Center. Special thanks are due Dr. W. J. Pierson, Jr., and Dr. V. J. Cardone of University Institute of Oceanography, City University of New York and their staff, coinvestigators with us on the oceanographic part of this research.

REFERENCES

Claassen, J. P., H. S. Fung, R. K. Moore, W. J. Pierson, Jr., (1972), "Radar Sea Return and the Radscat Satellite Anemometer," presented at IEEE International Ocean '72 Conference, Newport, Rhode Island, September 1972.

Daley, J. C. (1973), "Wind Dependence of Radar Sea Return," Journal of Geophysical Research, Vol. 78, No. 33, pp. 7823-7833.

Eagleman, J. R. (1974), "Moisture Detection From Skylab," Proceedings of the 9th International Symposium on Remote Sensing, Environmental Research Institute, Ann Arbor, Michigan, 1974, pp. 701-705.

Eagleman, J. R., E. C. Pogge, R. K. Moore, et al. (1975), "Detection of Soil Moisture and Snow Characteristics From Skylab," Final Report No. 239-23, Atmospheric Science Laboratory, The University of Kansas Center for Research, Inc., Lawrence, Kansas 66045, October 1975. Supported by EREP No. 540-A2, NASA Contract NAS 9-13273.

Jones, L. J., W. L. Grantham, L. C. Schroeder, J. W. Johnson , C. T. Swift and J. L. Mitchell (1975), "Microwave Scattering from the Ocean Surface," to be published in IEEE Transactions on Microwave Theory and Technique.

Ulaby, F. T.,L. F. Dellwig, T. Schmugge (1975), "Satellite Microwave Observations of the Utah Great Salt Lake Desert," RSL Technical Report 243-6, Remote Sensing Laboratory, University of Kansas Center for Research, Inc., Lawrence, Kansas, August 1975. Supported by NASA Contract NAS 9-13331.

Table 1.

Regression Analysis of SL 4 Composite S-193 Data Compared with SL 2/3 Data.

Area	Polarization	Angular Range of Fit	SL4 Function of Theta	SL2/3 Function of Theta
Land	VV	$1^\circ - 13^\circ$	$1.51\, e^{-\theta^\circ/4.67^\circ}$	$1.67\, e^{-\theta / 5.60^\circ}$
Land	HH	$1^\circ - 13^\circ$	$2.38\, e^{-\theta/6.49^\circ}$	Not calculated
Land	VV + HH	$1^\circ - 13^\circ$	$1.84\, e^{-\theta/5.28^\circ}$	Not calculated
Land	VV	$15^\circ - 39^\circ$	$0.38\, e^{-\theta/19.04^\circ}$	$0.36\, e^{-\theta/29.6^\circ}$
Land	HH	$15^\circ - 39^\circ$	$0.83\, e^{-\theta/10.94^\circ}$	Not calculated
Ocean	VV	$0^\circ - 50^\circ$	$5.59\, e^{-\theta/8.42^\circ}$	$15.6\, e^{-\theta/6.13^\circ}$
Ocean	HH	$0^\circ - 50^\circ$	$4.75\, e^{-\theta/8.04^\circ}$	$21.9\, e^{-\theta/5.35^\circ}$
Ocean	VV	$0^\circ - 50^\circ$	$7.41\, e^{-\theta/7.37^\circ}$	$15.6\, e^{-\theta/6.13^\circ}$
Ocean	VV	$30^\circ - 50^\circ$	$0.39\, e^{-\theta/18.1^\circ}$	$15.6\, e^{-\theta/6.13^\circ}$
Ocean	HH	$0^\circ - 15^\circ$	$4.75\, e^{-\theta/8.04^\circ}$	$21.9\, e^{-\theta/ 5.35^\circ}$
Ocean	HH	$30^\circ - 50^\circ$	$0.29\, e^{-\theta/17.8^\circ}$	$21.9\, e^{-\theta/5.35^\circ}$
Ocean	VH	$0^\circ - 15^\circ$	$11.0 * e^{-\theta/7.57^\circ}$	$0.32\, e^{-\theta/5.35^\circ}$
Ocean	VH	$30^\circ - 50^\circ$	$0.25 * e^{-\theta/39.8^\circ}$	$0.32\, e^{-\theta/5.35^\circ}$

* Absolute values of VH σ° for SL4 are uncorrected and therefore too large.

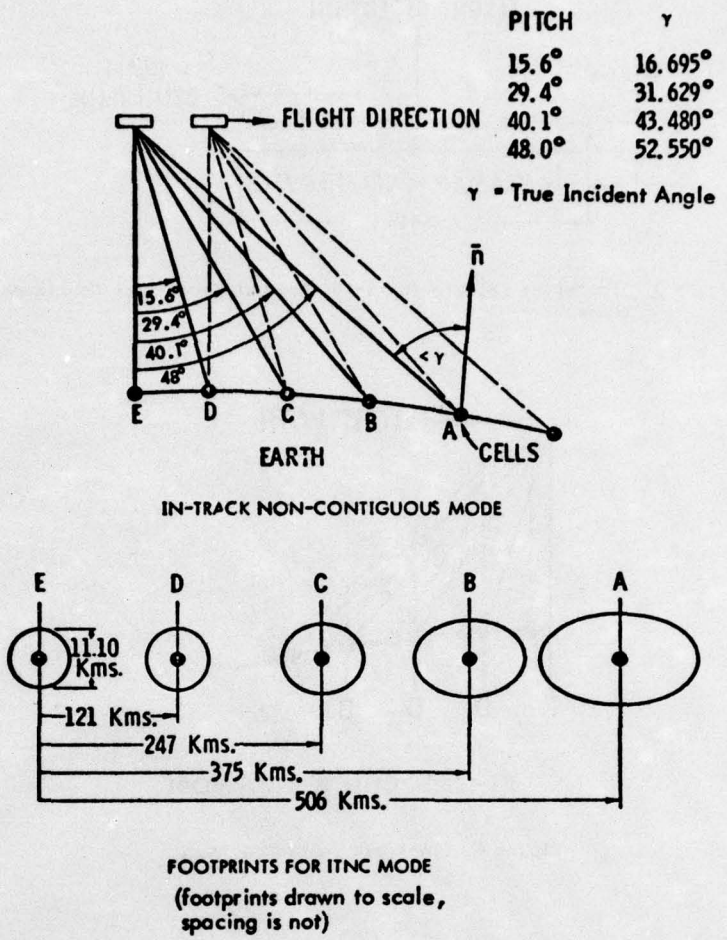

Figure 1. Geometry of S-193 Radscat In-Track Non-Contiguous Mode (From Sobti, 1973).

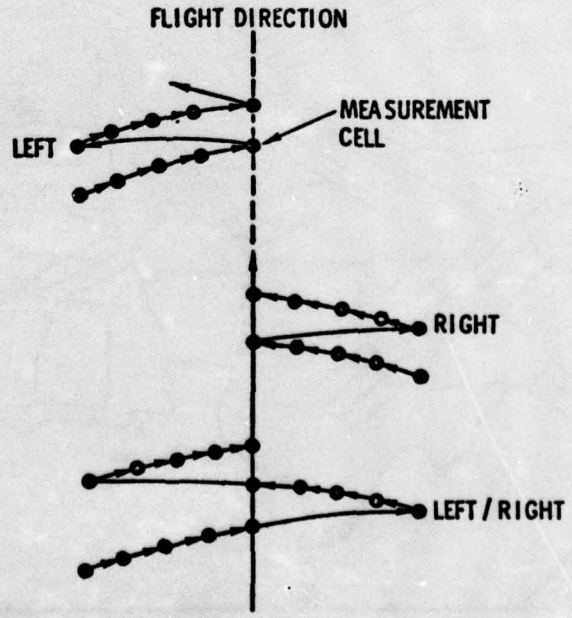

Figure 2. Footprint Pattern for S-193 Radscat Cross-Track Non-Contiguous Mode (From Sobti, 1973).

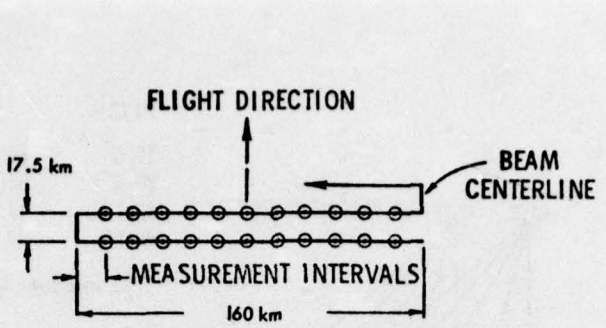

Figure 3. Footprint Pattern for S-193 Radscat Cross-rack Contiguous Mode.

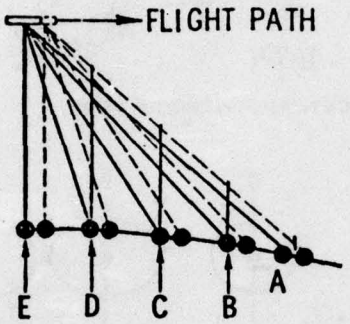

IN-TRACK CONTIGUOUS MODE

Figure 4. In-Track Contiguous Mode.

CROSS-TRACK CONTIGUOUS

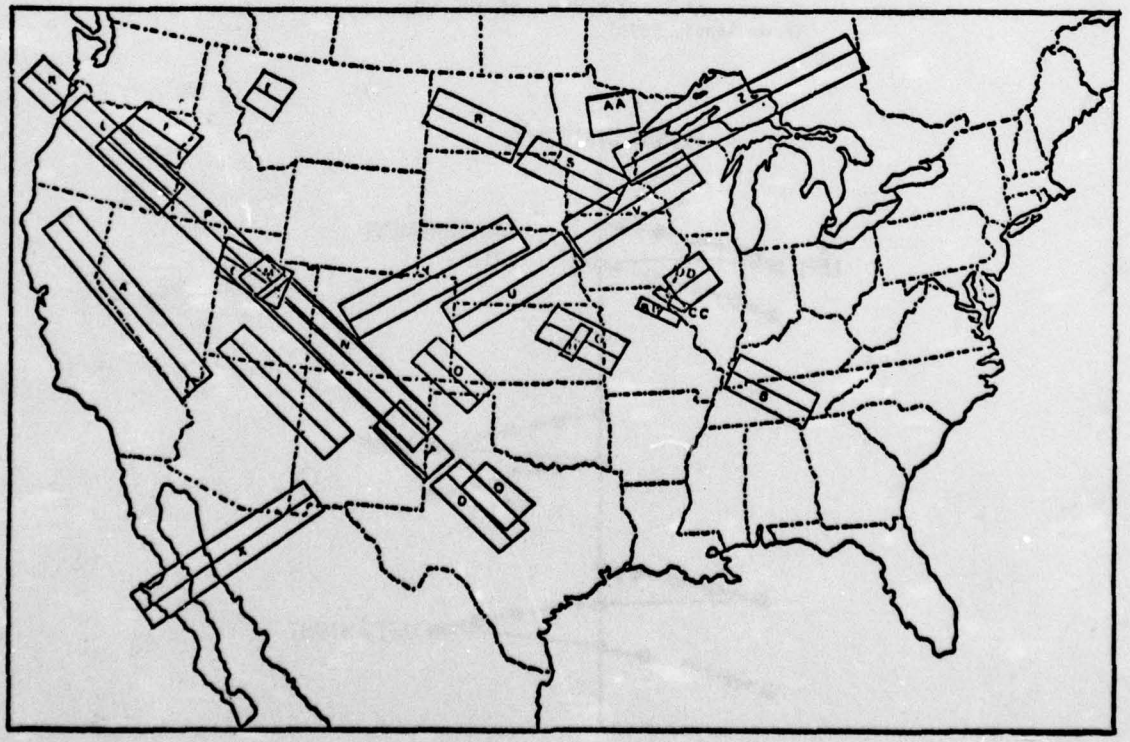

Figure 5. Cross-Track Contiguous Data Takes Over U.S.A. During SL 2 and SL 3 Missions considered in Designing Data Catalogue.

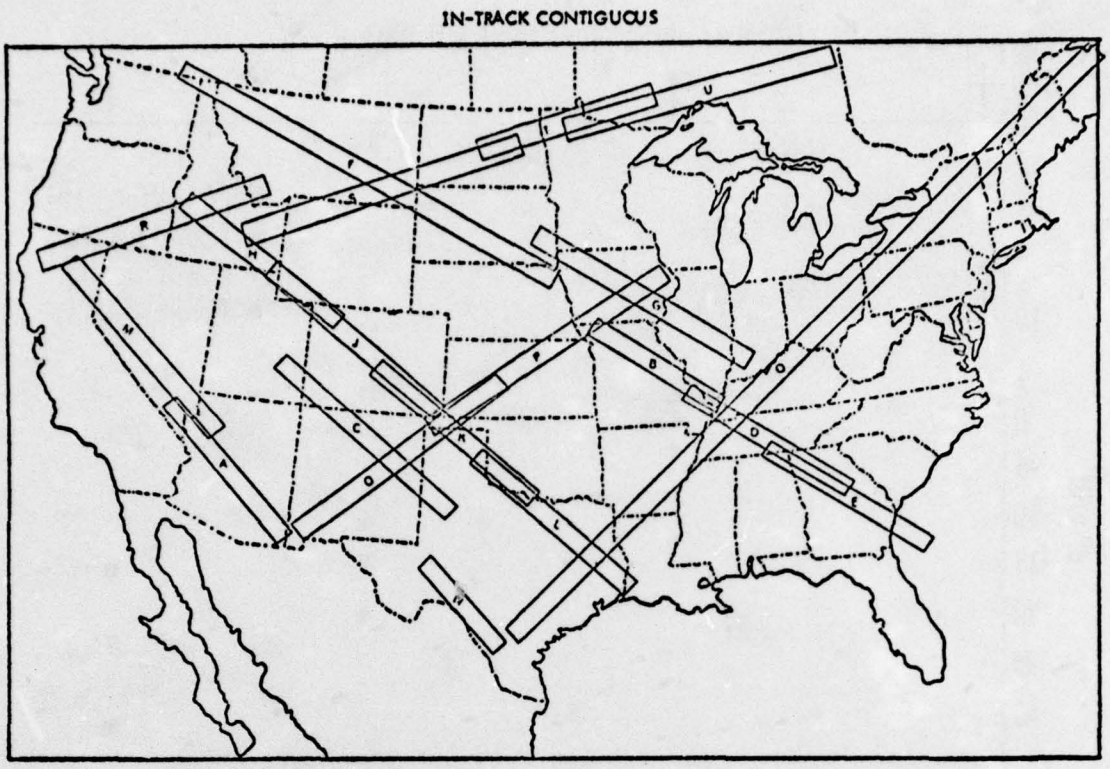

Figure 6. In-Track Contiguous Data Segments Over U.S.A. During SL 2 and SL 3 Missions considered in Design of Data Catalogue.

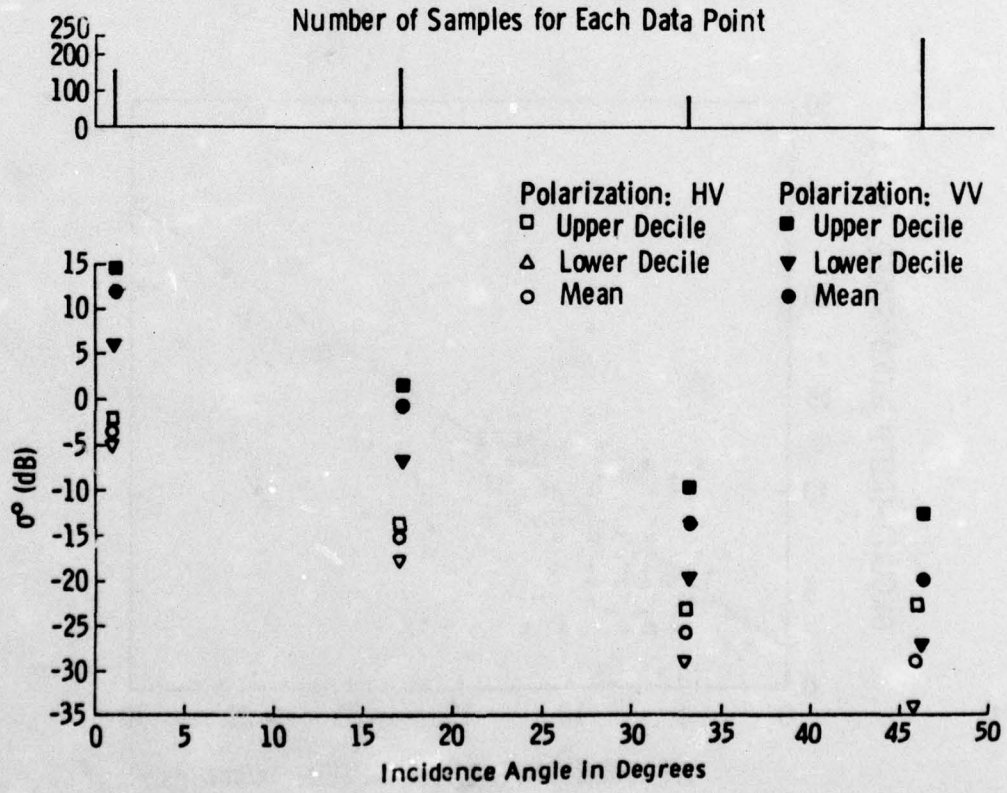

Figure 7. Summary of angular scatterometric response over ocean surfaces for VV and HV polarizations from S-193 scatterometer operations during SL 2 - SL 3.

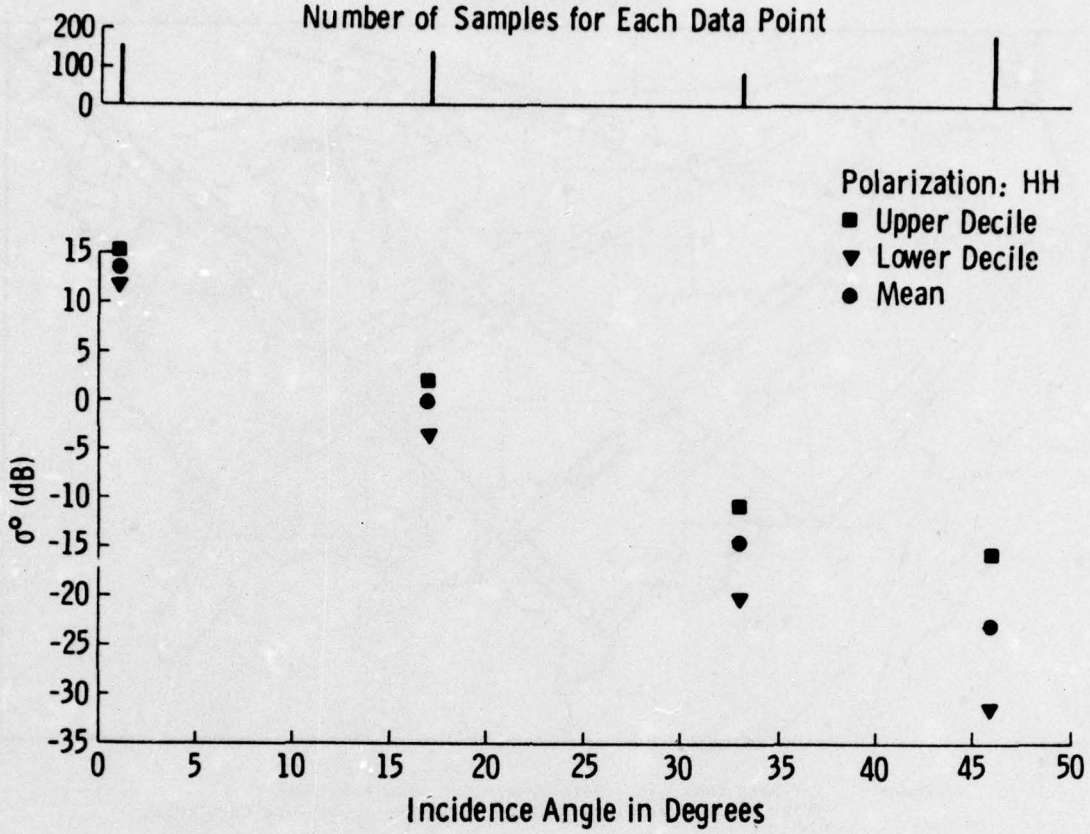

Figure 8. Summary of angular scatterometric response over ocean surfaces for HH polarization from SL 2 - SL 3 data.

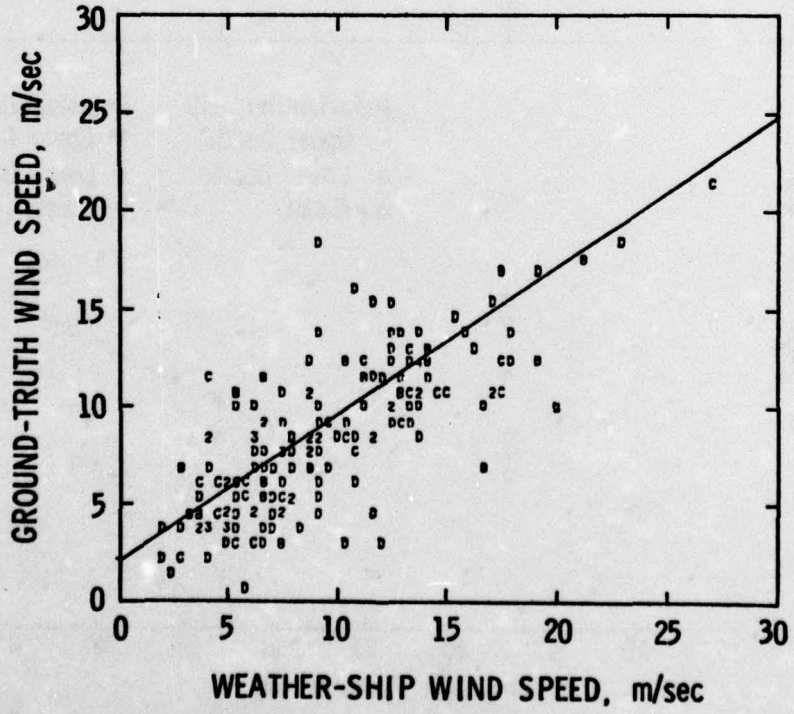

Figure 9. Scattergram of withheld weather ship wind speed (adjusted for air/sea temperature and anemometer height) versus ground-truth wind speed for categories 2, 3, and 4.

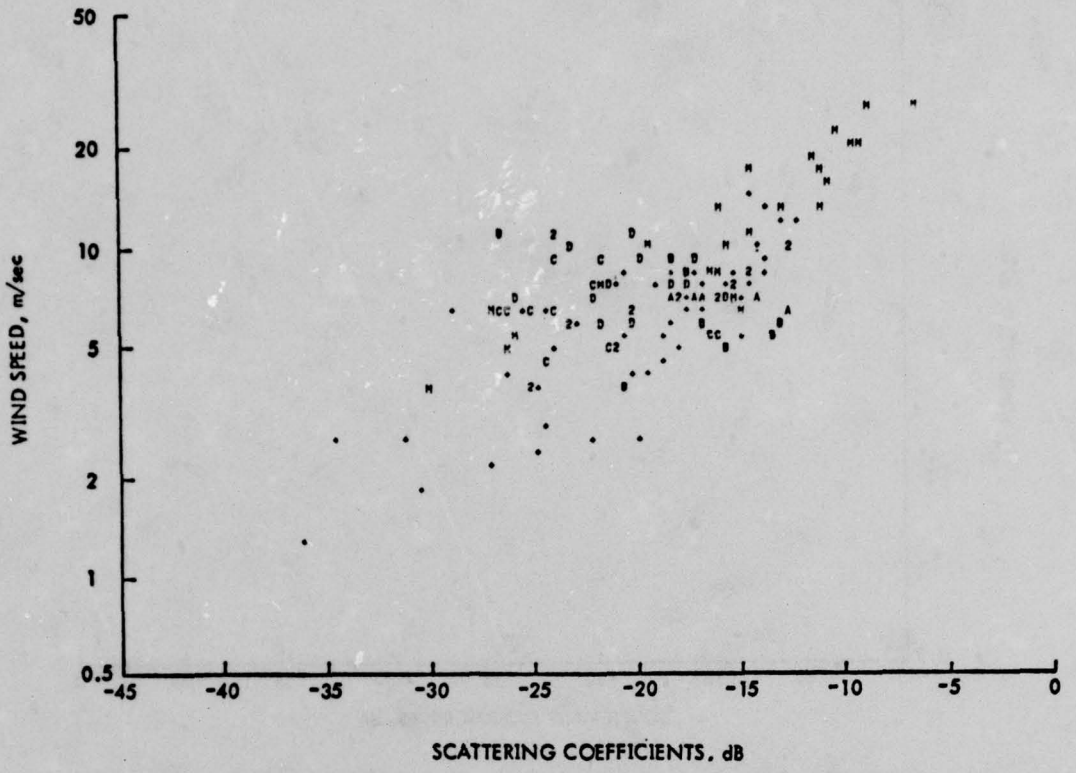

Figure 10. Scattergram of ground truth wind speed versus σ°_{VV} at 50° incident angle using logarithmic scales. The scattering coefficients are adjusted to upwind. SL 2 and 3 data.

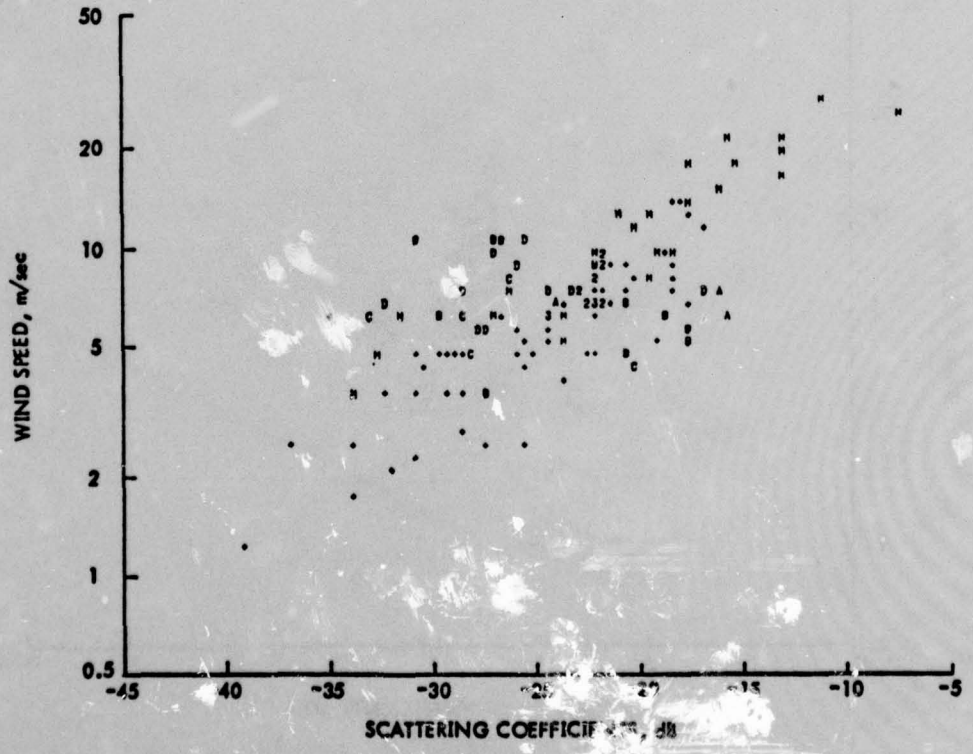

Figure 11. Scattergram of ground truth wind speed versus σ°_{HH} at 50° incident angle using logarithmic scales. The scattering coefficients are adjusted to upwind. SL 2 and 3 data.

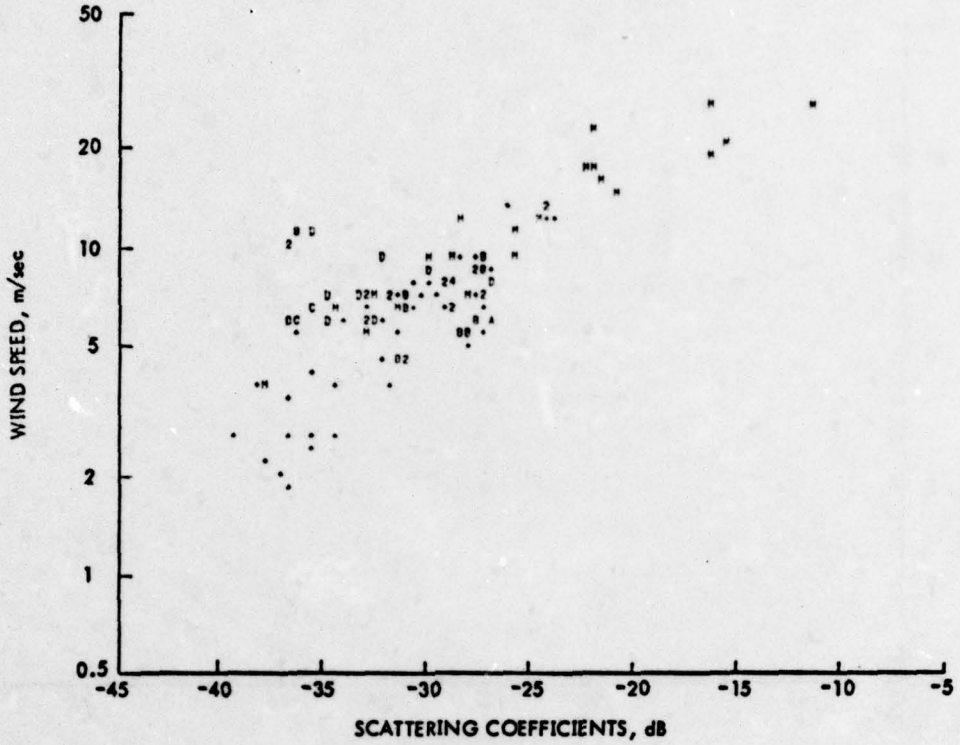

Figure 12. Scattergram of ground truth wind speed versus σ°_{VH} at 50° incident angle using logarithmic scales. The scattering coefficients are adjusted to upwind. SL 2 and 3 data.

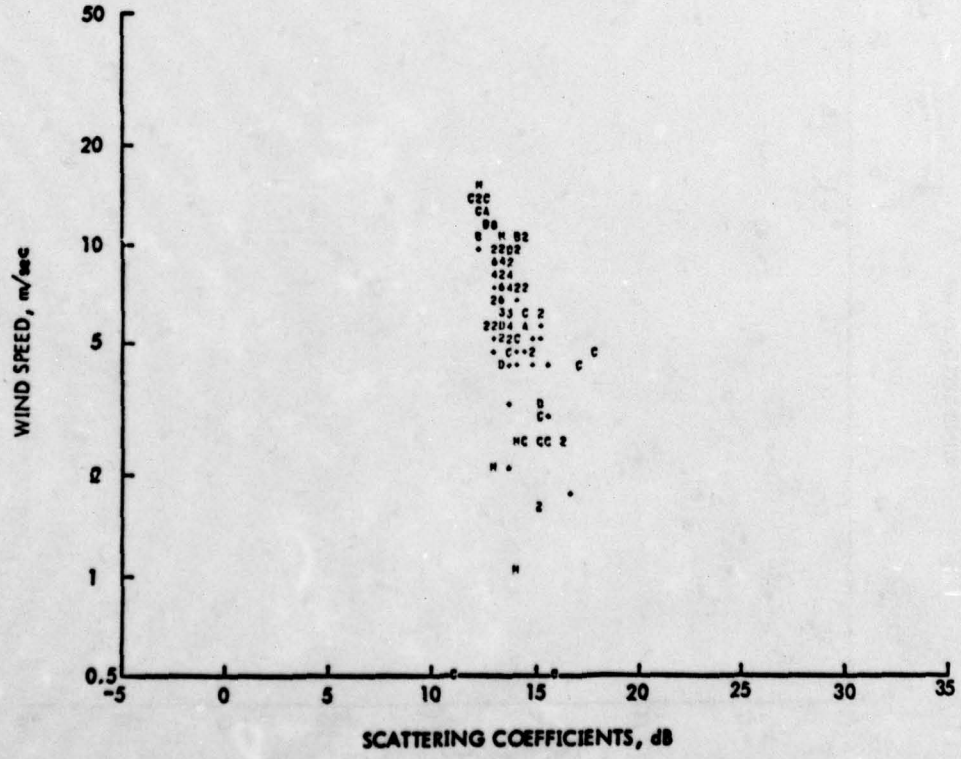

Figure 13. Scattergram of ground truth wind speed versus σ°_{VV} at 1° incident angle using logarithmic scales. SL 2 and 3 data.

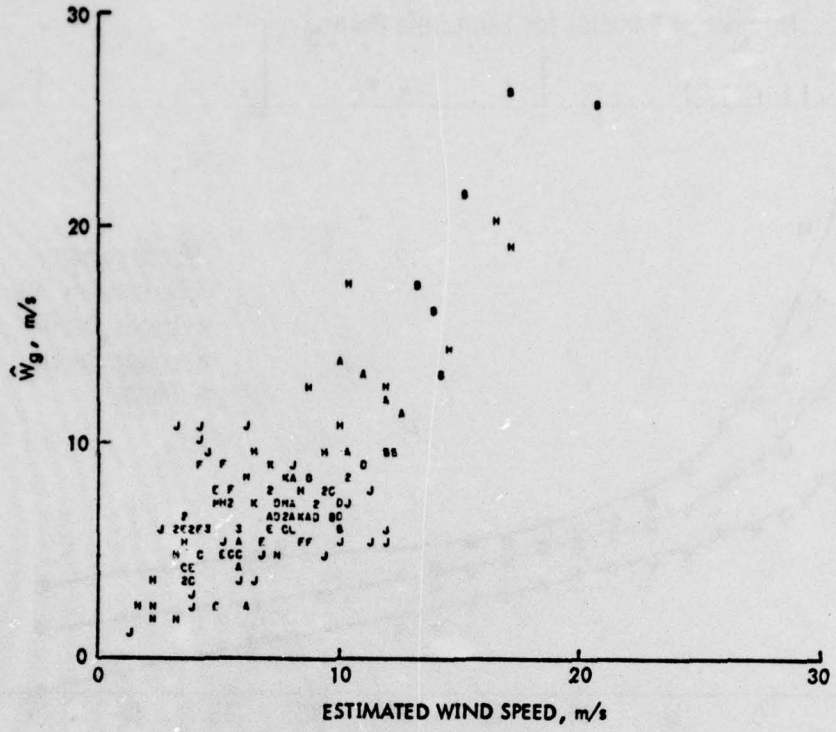

Figure 14. Scattergram of ground truth wind speed, $\hat{W}_g$, versus wind speed estimated from σ°_{VV} at 50° incident angle using linear scales. Wind speed estimates from σ° were determined from nonlinear regression estimates of a_0 and a_1 in the model $W_g = a_0 \sigma^{\circ\, a_1} + \varepsilon$ where σ° is numeric (not in dB) and is adjusted to upwind. SL 2 and 3 data.

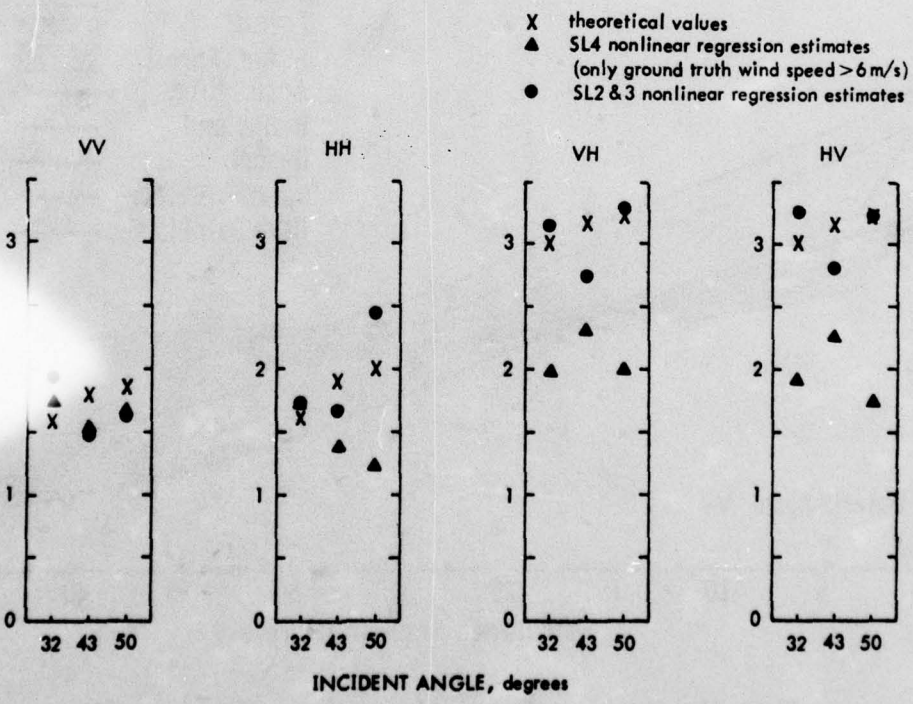

Figure 15. Theoretical values and nonlinear regression estimates of the exponent, α, in the model $\sigma^\circ = U^\alpha$, when U is wind speed and σ° is measured in the upwind direction.

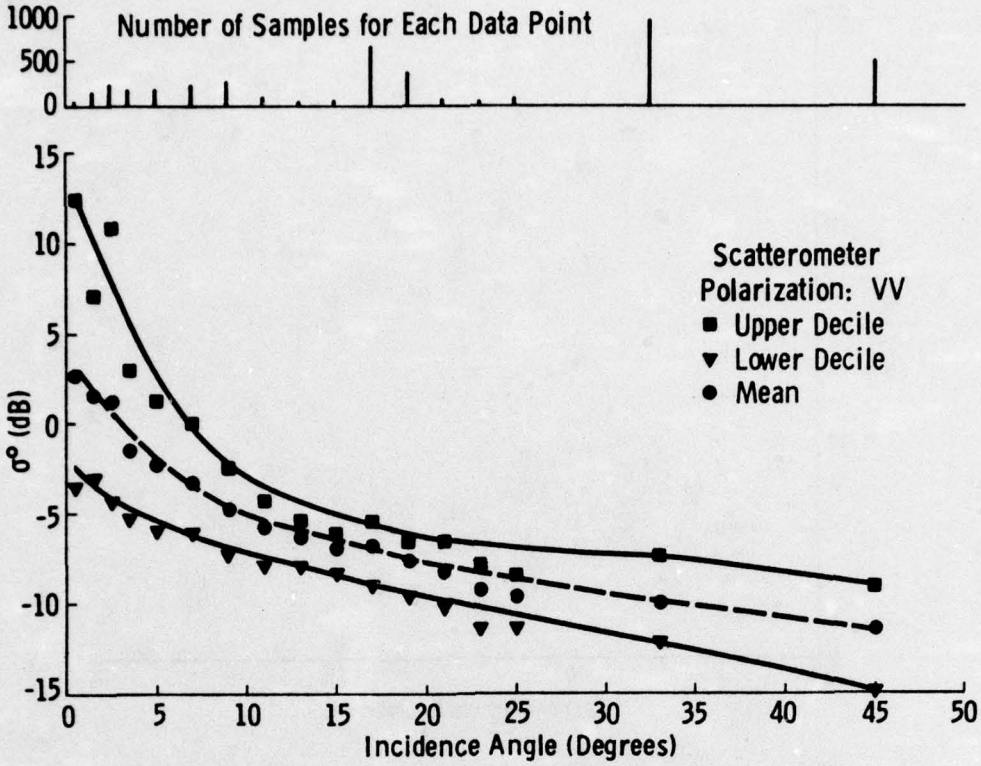

Figure 16. Summary of angular scatterometer response for VV polarization from S-193 scatterometer operations during SL 2 - SL 3.

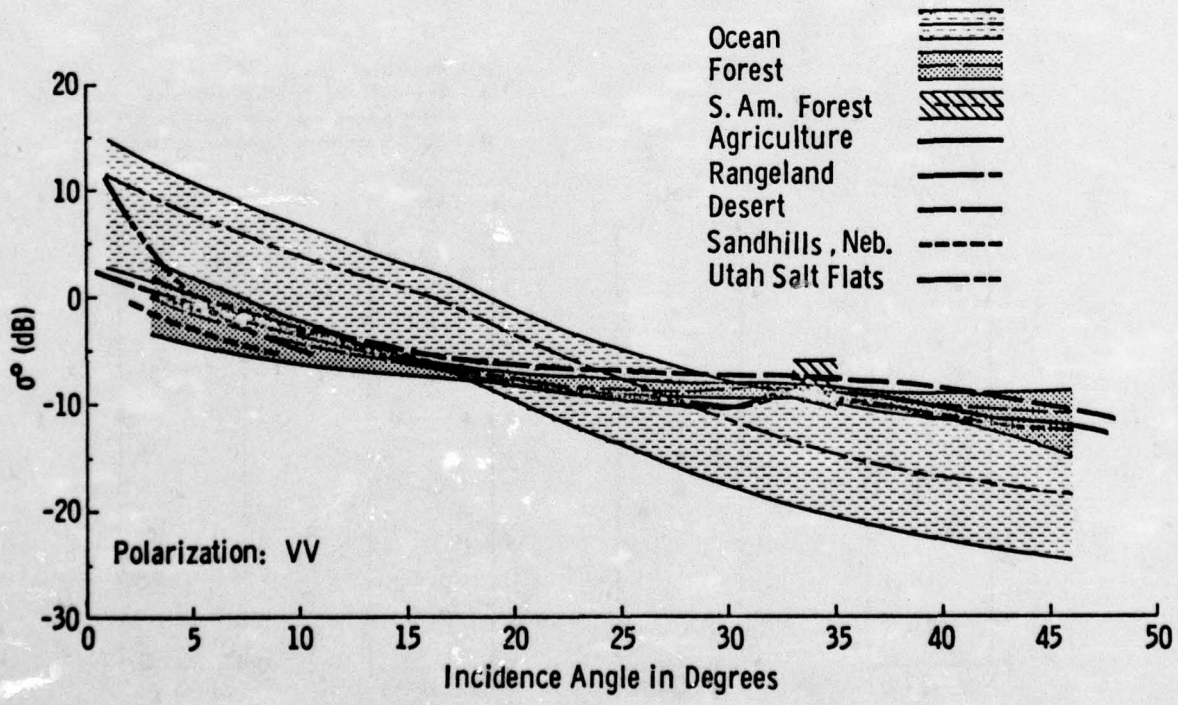

Figure 17. Comparison of angular backscatter response from various categories. Ranges, where shown, are between upper and lower deciles, not standard deviation.

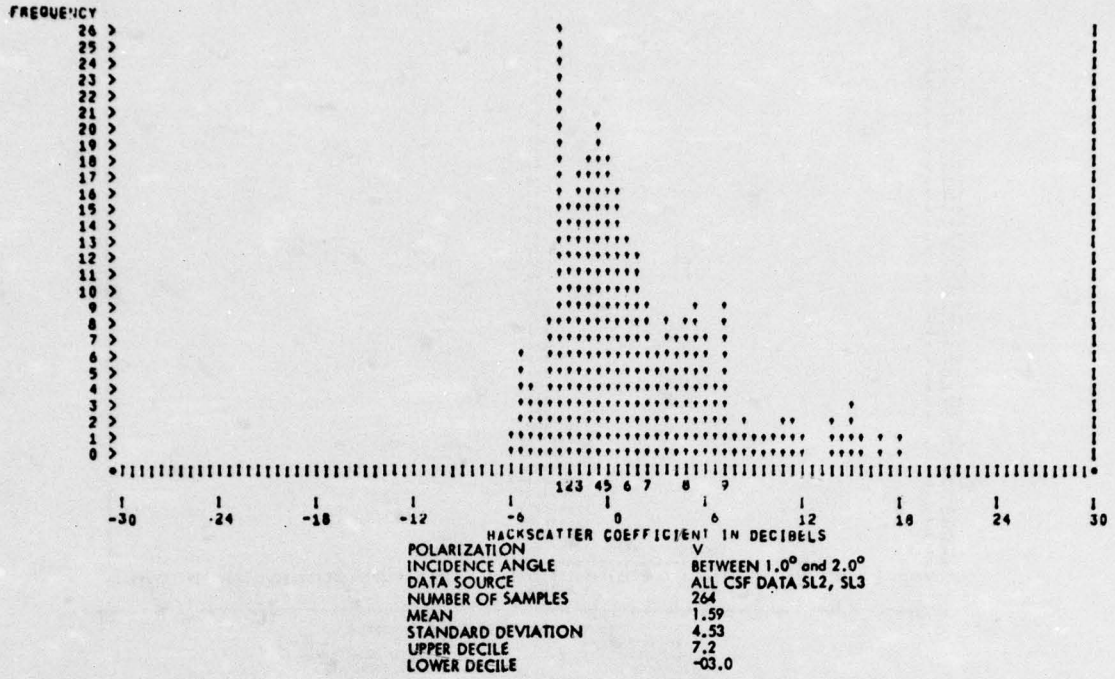

POLARIZATION	V
INCIDENCE ANGLE	BETWEEN 1.0° and 2.0°
DATA SOURCE	ALL CSF DATA SL2, SL3
NUMBER OF SAMPLES	264
MEAN	1.59
STANDARD DEVIATION	4.53
UPPER DECILE	7.2
LOWER DECILE	-03.0

Figure 18. Histogram of the scatterometer backscatter coefficient, between 1.0° and 2.0°, V Polarization, North America.

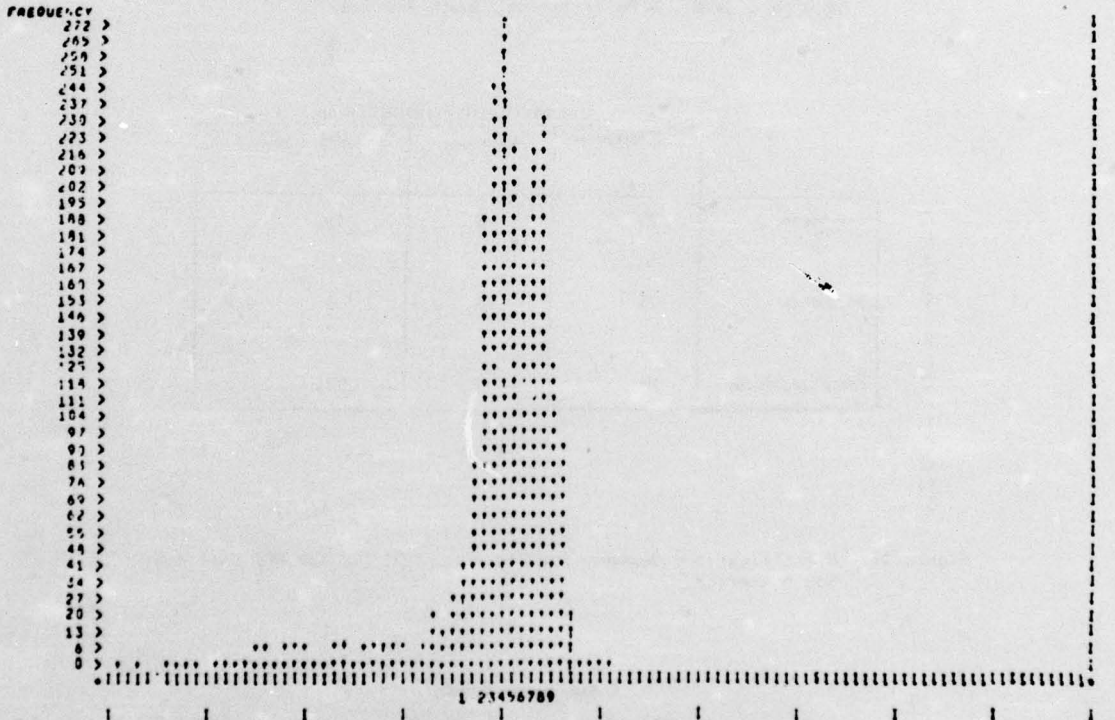

POLARIZATION	V
INCIDENCE ANGLE	BETWEEN 32 AND 34°
DATA SOURCE	ALL CSF DATA SL2, SL3
NUMBER OF SAMPLES	2161
MEAN	-9.86
STANDARD DEVIATION	2.97
UPPER DECILE	-7.5
LOWER DECILE	-12.0

Figure 19. Histogram of the scatterometer backscatter coefficient, between 32° and 36°, V Polarization, North America.

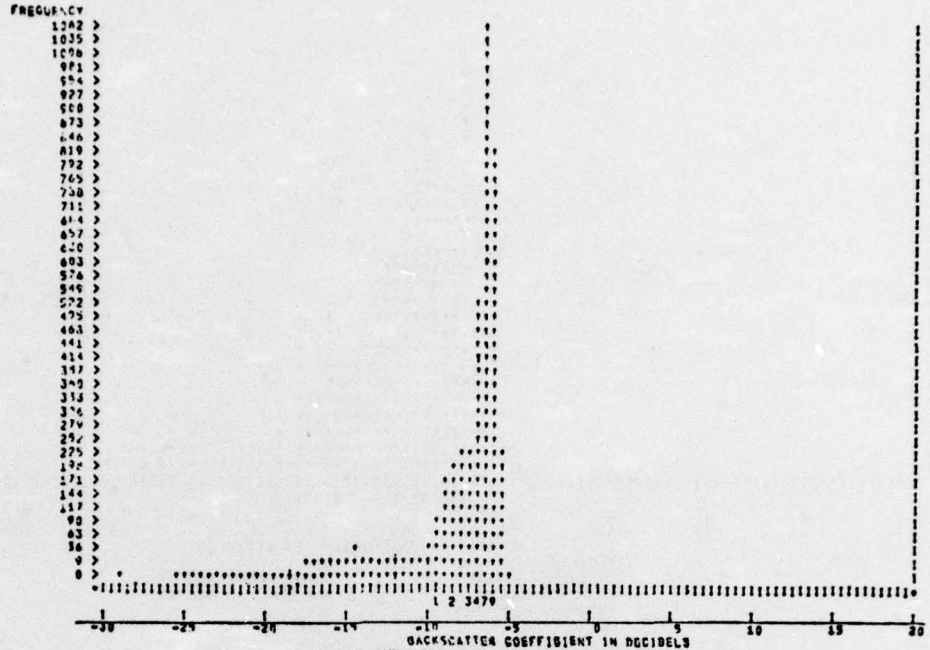

Figure 20. Histogram of the Scatterometer Backscatter Coefficient, between 32.0° and 34.0°, V Polarization, South America.

CLASSIFICATIONS	Groups (Underlying Distributions) Evergreen	Savannah	Semi-Deciduous
Evergreen	25	5	16
Savannah	5	45	0
Semi-Deciduous	10	0	27

Figure 21. Classifications summary for CTC Pitch 29° (VV and HH) data over South America.

Classification Results

(Groups Underlying Distributions)

	Agric.	Forest	Range
Agric.	2	41	31
Forest	0	31	14
Range	0	6	29

Figure 22. Classification summary using ITC (VV) backscatter data at 42°, 33°, 17° from North American targets.

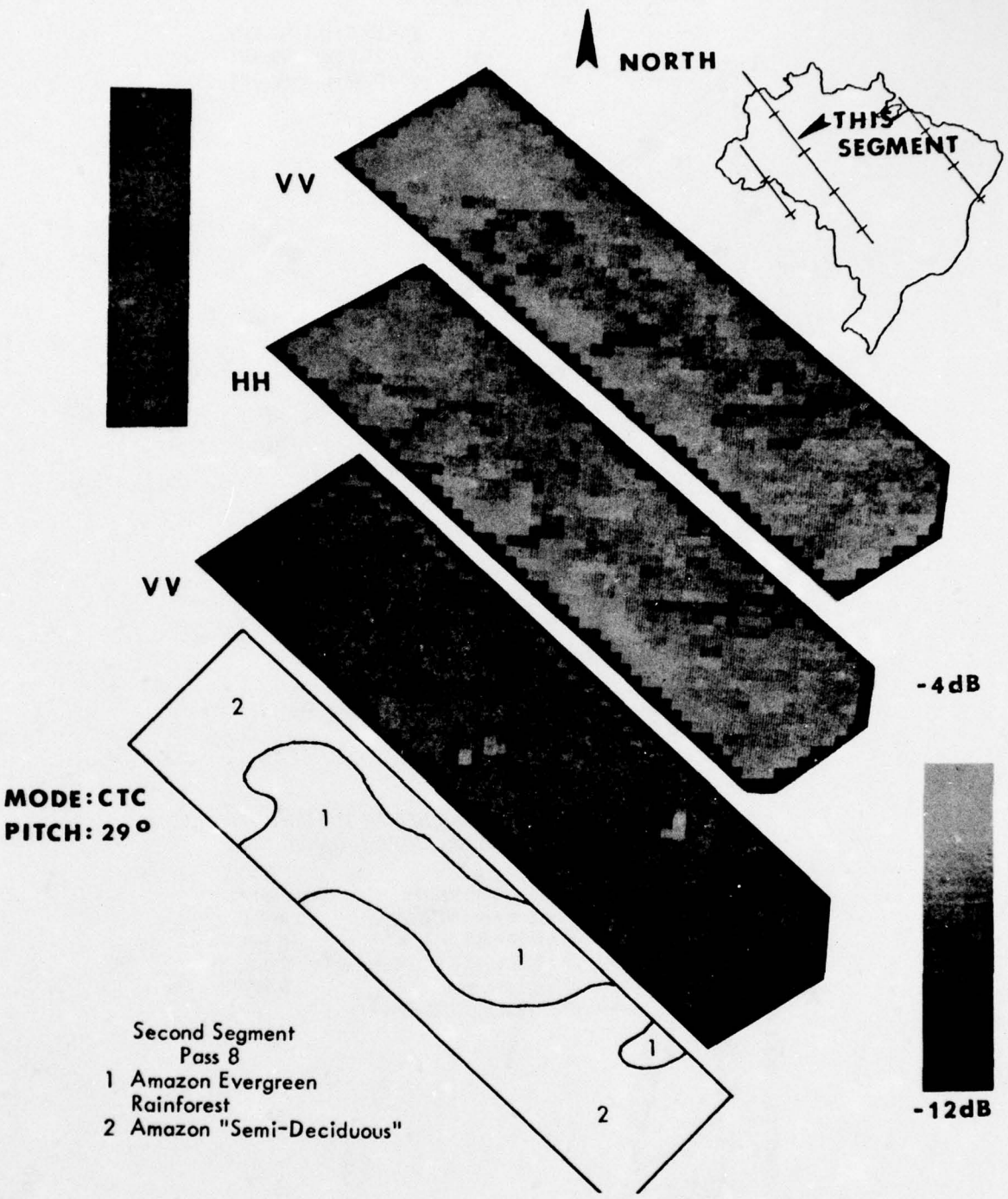

Figure 23. Pseudo-Images Produced from Backscatter Response with Cross-Track Contiguous, Pitch 29° Mode of S-193 Operation on Day 162, Bass 8, SL 2 Over Brazil.

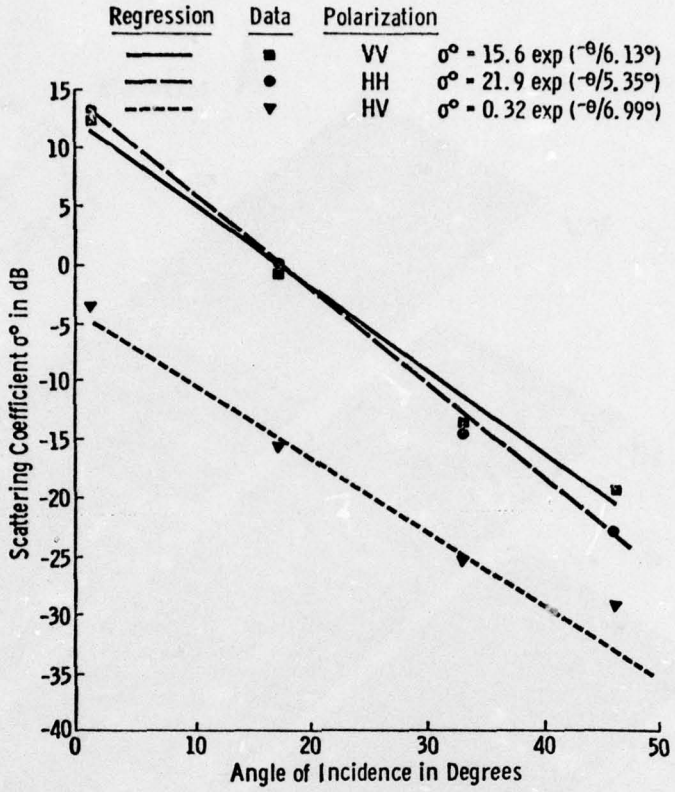

Figure 24. Comparison of Mean Oceanic Response with Exponentials - 13.9 GHz Skylab Data.

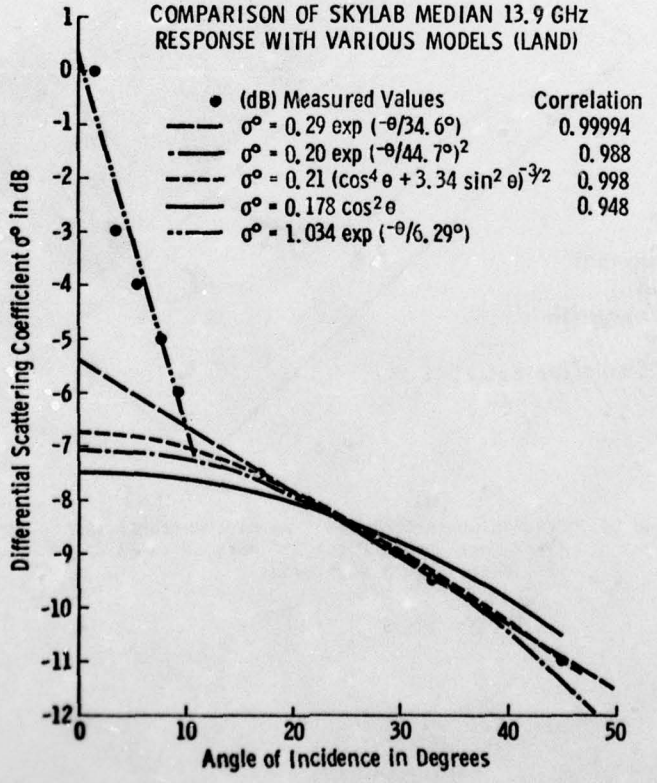

Figure 25. Comparison of Skylab Median 13.9 GHz Response with Various Models (Land).

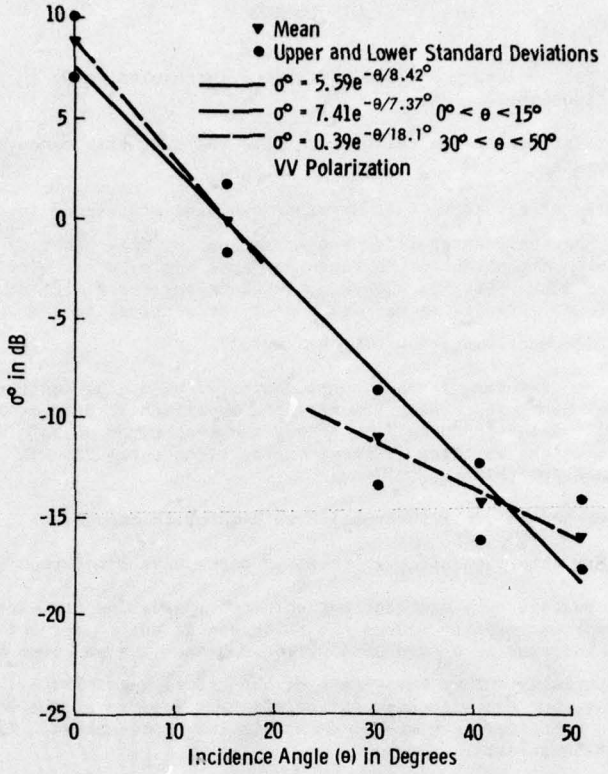

Figure 26. Composite Scattering Coefficient of Ocean From SL 4 S-193 Scatterometer - Vertical Polarization.

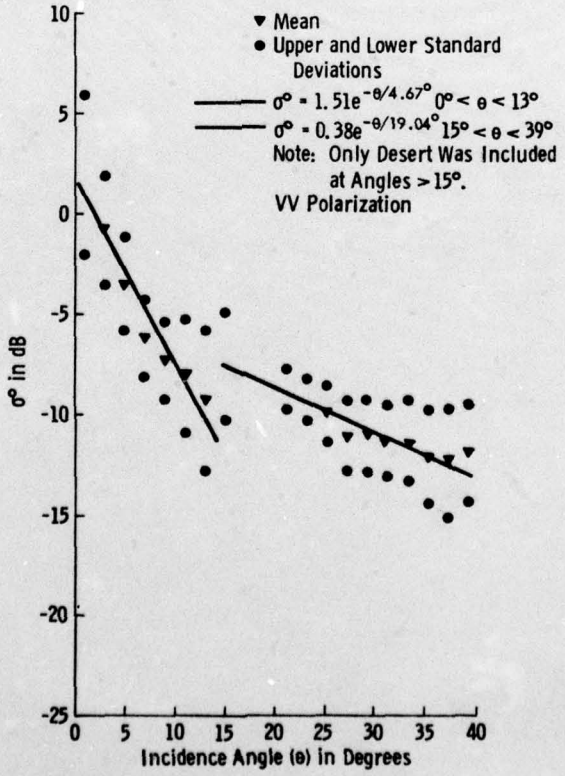

Figure 27. Composite Scattering Coefficient of Land From SL 4 S-193 Scatterometer - VV Polarization.

DISCUSSION

K MILNE: What is the reason for the difference in results at 0° incidence for V/V and H/H polarisations?

R K MOORE: Minor differences in calibration plus the fact that measurements occurred 10 Km or more apart.

R VOLES: In view of the known 6 dB up-wind/down-wind difference in σ_o, have you considered reducing the scatter in your observations by only plotting the average of pairs of measurements taken at the same incidence angle but looking in opposite directions in azimuth - this means working in the along-track mode of course? Also, although you found very little variation of σ_o at vertical incidence with wind speed, did you find much variation with sea swell?

R K MOORE: 1) The measurements shown were converted to upwind equivalent from original values using theory that best fits aircraft experimental data of Jones, et al (NASA Langley Research Center). However the mean error of 38° in wind direction casts doubt on the validity of these "corrections"; the fit with uncorrected data is almost as good for this reason.

2) We had no swell information with which to compare.

B JACKSON: Was any data obtained over snow, in particular coniferous forest?

R K MOORE: Yes, but not very much and not very conclusive due to infrequent observation. An attempt was made to deduce the thickness of snow cover but this was inconclusive. Some increase in σ_o was noted with increase in snow cover but it was suspected to be partially due to the effect of the underlying terrain. Data were obtained over forest, but not with snow on the ground. Because of the large footprint, "forest" areas contained open spaces except in the Amazon basin. Details are contained in our NASA reports.

CHARACTERISTICS OF CLUTTER AND TARGETS AT X- AND Ku-BAND

H. Sittrop
PHYSICS LABORATORY TNO
The Hague
Netherlands

SUMMARY

CLUTTER CHARACTERISTICS

The radar backscatter of the sea per unit area, σ_o, and the rms clutter velocity spread are described versus grazing angle and wind velocity by an experimental model. A thorough comparison is made with measurements and calculations which are considered in literature as significant. The obtained results justify the assumption that the model can be used in the so-called near grazing and in the plateau region. The two scatter mechanism of Bragg resonant capillary waves and small facets overlaying the shorter gravity waves is discussed. Characteristic ratios of σ_o are presented versus windvelocity.

TARGET CHARACTERISTICS

A multipath Radar Cross Section (RCS) approximation is given in a closed form and numerically, for a variety of target models and clusters. Optimum signal to clutter ratios are discussed for the detection of buoys by shipping-traffic. Characteristics of arbitrarily chosen target clusters are simulated and typical discrepancies between clutter and target scintillations are demonstrated.

The influence of precession, nutation and rotation on the radar backscatter, due to irregularities of a body of revolution, is shown. Results of dynamic, in flight, measurements and simulations based on static measurements are included. Clutter and target model application may contribute in finding an optimum combination of relevant and environmental parameters.

I CLUTTER CHARACTERISTICS

1. INTRODUCTION

Since world war II many investigators have studied characteristics of sea reflections. In 1957 Katzin introduced the multipath interference effect of scattering by facets, superimposed on the large scale wave pattern. Definitions of slightly rough surfaces and very rough surfaces opened the way for rigorous mathematical treatment of scattering based on the fundamental work of Rice, S.O. (1951). In his new model for sea-clutter Wright used a surface roughness whose length is Bragg resonant and whose height is determined from the range spectrum proposed by Phillips. The effect of tilting the scattering surface by the wave structure is included; the influence of screening and spray not.

It became apparent that the backscatter of the sea is predominantly determined by a mixture of wind generated capillary waves which are Bragg resonant according to the relation $\Lambda\cos\varphi = n\lambda/2$ and small facets overlaying the shorter gravity waves. (Λ = water wavelength, λ = radar wavelength and φ is grazing incidence angle). The interactions of these waves with the swell are giving not only an extra displacement in the vertical and horizontal plane, but also a tilting of facets. The influence of screening and spray effects become important at small grazing angles and high windvelocities. They may have a significant impact on the backscatter characteristics at different radar frequency bands. Facets, influenced in size by the wind, are modulated in aspect by the shorter gravity waves. Application of shorter pulse lengths can resolve the periods of these waves, thus causing a slow modulation of the horizontally polarized backscatter. The probability distribution of the backscattered signal depends on the clutter cell size. A large cell results in a Rayleigh distribution, a small cell in a log-normal distribution. Range and pulse length,therefore, are of significance. Long has developed similar ideas on a two-scatter theory of sea echo.

The purpose of this paper is not to develop a new theory, but to propose an experimental model based on the results of 4 series of experiments, performed at X- and Ku-band. In most cases a rather good fit is shown with results in the near grazing and plateau region reported by other investigators. The model can be simply applied for the determination of signal/clutter ratios and various other significant ratios of σ_o and clutter spectrum bandwidth.

2. THE EMPIRICAL SEA CLUTTER MODEL

Based on 4 independent series of measurements an experimental model of sea-clutter has been developed for the North Atlantic environment. The model describes the average radar backscatter per unit area, σ_o, and the rms clutter velocity spread versus grazing angle and wind velocity. Parameters, incorporated in the model, relate to the dependency of radar wavelength, pulse length, polarization and observation angle with respect to wind direction.

An essential requirement to develop such a model is to allocate the prevailing wind directions and velocities to the actual measured clutter area, incorporating coastal effects. This labelling of the data and the measurements have been described by Sittrop, H, 1974 [7].

2.1 The average Radar Cross Section per unit area, σ_o.

The following expression can be derived for the average RCS per unit area, σ_o, (Sittrop H, 1974 [7]).

$$\sigma_o = \alpha + \beta \log \frac{\varphi}{\varphi_o} + [\delta \log \frac{\varphi}{\varphi_o} + \gamma] \log \frac{W_v}{W_o} \quad dB \qquad (1)$$

Reference values are: φ_o = ref. grazing angle in degrees,
W_o = ref. windvelocity in knots
$\alpha_o = \sigma_o$ at (σ_o, W_o).

The parameters β and δ are correction factors, γ is the σ_o slope versus windvelocity, W_v, as valid for φ_o. This slope appears to be an interesting variable depending on radar frequency, wind direction with respect to observation angle and polarization. The model has been developed at X- and Ku-band, for pulse length τ = 0,5 µsec. Parameter values to apply the model are given in tabel 1. An attempt is made for extrapolation to shorter pulse length τ = 0.12 µsec (see for details section 4).

The measurements on which the model is based have been performed in the so-called near grazing angle region. The model is rigorously tested with results of measurement and calculation of various other investigators, which have been recognized in literature as significant. For this purpose, reference is made to the recently published volume on Radar Reflectivity of land and sea (Long, Maurice, W. [3]) and to Nathansons book on Radar design principles [6]. It is hereby assumed that the most significant data and calculations on sea-clutter are accumulated in these two volumes.

σ_o dB

FREQ. BAND	λcm WAVE LENGTH	WIND - DIRECTION	POL.	φ_o	Wo Kts	α dB	β dB	γ dB	σ dB	SPREAD dB MAX.	SPREAD dB MEAN.
X	3.2	UPWIND	HOR.	0.5	10	-50	+12.6	+.34	-13.2	±1	≤±0.5
X	3.2	CROSSWND	HOR.	0.5	10	-53	+6.5	+.34	0	+4 −2	≤±1
X	3.2	UPWIND	VERT.	0.5	10	-49	+.17	+.30	-12.4	+3.5 −2	≤±1
X	3.2	CROSSWND	VERT.	0.5	10	-58	+.19	+.50	-33	+3.5	≤±1.5
Ku	1.85	UPWIND	HOR.	0.5	10	-46	+13.6	+.26	-10	+2.5 −1.5	≤±1
Ku	1.85	CROSSWND	HOR.	0.5	10	-48	+.13	+.21	-6.6	±2	≤±1
Ku	1.85	UPWIND	VERT.	0.5	10	-46	+.17	+.22	-9	±2	≤±0.5
Ku	1.85	CROSSWND	VERT.	0.5	10	-47	+.13	+.22	-8.4	+2 −1.5	≤±1

Table 1. Model parameter values of σ_o, at τ = 0.5 µsec.

2.2 Discussions on the scattering mechanisms of sea-clutter

Guinard en Daley have shown (1970 [2]) that the Wright model presents a comparable trend for the results of measurements of σ^oVV. Significant deviations have been observed for σ^oHH at incidence angles below 30°. The explanation for the lack of agreement between σ^oHH and the limiting values at the smaller grazing angles may be found by considering the cross section of a composite surface. Wright (1968 [10]), Valenzuela (1968 [9]) and Long (1974 [4]), (1975 [3]) have introduced the effect of a combination of capillary waves and tilting of the scattering surfaces on the slopes of the swells and shorter gravity waves. The effects of the tilting of these facets would be expected to produce significantly larger variations in the horizontally polarized cross section than in the vertically polarized cross section.
Independent of Longs approach, the author of this paper has investigated the influence of pulse length on the facet mechanism (Sittrop, H, 1975 [8]). A similar approach has been followed by analysing the relative power for the low and high frequency spectra. The influence of shorter pulse lengths on the resolution of the periodic effect of shorter gravity waves is investigated. Details will be shown in section 4.
In summary we can say that the influence of the facet mechanism on the cross section at horizontal polarization is quite significant, in particular at shorter pulse lengths.

The slightly rough surfaces, i.e. one whose height variations are small compared with the incident wavelength and whose slopes are small compared with unity, are of dominant importance for the cross section at vertical polarization. In the small perturbation theory these surfaces are related to the radar wavelenght by the Bragg scattering condition that the radar return of adjacent crests adds in phase. For small angles in the near grazing angle region, these scattering surfaces are in the order of $\lambda/2$ and, for the radar wavelengths as considered here, they are in order of 1.6 and 0.9 cm. These wavelengths are in the capillary region. An impression of capillary waves superimposed on sea waves is given in fig. 1.
For angles in the plateau region and even more in the near vertical incidence region Bragg resonant surfaces have longer wavelengths. At 80° incidence angle they are respectively 9.2 cm and 5.4 cm, for X- resp. Ku-band. Particulary in this region saturation effects can be significantly different from those in the near grazing angle region. The increase of cross section with windvelocity, therefore, is expected to be quite different in these observation regions, in particular at Ku-band.
Differences in the increase of cross section with windvelocity observed at Ku-band by Moore (1970 [5]) and the author of this paper (1975 [8]) can be explained partly by this mechanism. Another assumption which can be made is that in the near grazing angle region, in particular at incidence angle in the order of 1° or below, the effects of attenuation by spray may have an important impact at Ku-band. This effect, obviously, will be increased at higher windvelocities and consequently, the increase of cross section with windspeed will be reduced. While on one hand this effect will diminish the increase of cross section with windspeed at near grazing incidence, on the other hand the increase of water wavelengths to satisfy the Bragg resonance criterium will require higher windspeeds in the near vertical incidence region. In this latter region the attenuation by spray is negligeable, due to the short passage. The troughs of the shorter gravity and swell waves can be observed clearly, while they are screened at grazing incidence angles in the order of 1°.

Both observations, however, clearly show no saturation effect. The model described in this paper indicates for the windvelocity region of 40-70 kts an increase of cross section of resp. 4 dB and 2 dB at

incidence angles of 10^o and 45^o. Between 20 and 40 kts the increase is respectively 5 dB and 2.5 dB. Referring to the work described by Claassen (1972 [1]) no saturation effect in the plateau region is expected due to capillary waves.

2.3 The experimental model and results obtained by other investigators

In this section we will make an effort to compare the model with results which may be considered as significant and have been published in literature. These comparisons are made for upwind observations at X-band.

2.3.1 Comparisons with Wrights new model for sea-clutter

The increase of σ_o with incidence angle, presented on a linear scale, changes rather abruptly when these angles are entering the so-called plateau region. Results in literature are often presented in such a way.
Plotting of σ_o versus incidence angle φ on a log-log scale shows in general a linear relationship. Rearranging Wrights calculations of σ_oVV and Guinards measurements results in fig. 2. In this figure, the median values given by NRL are transformed to average RCS. Longs assumptions on the differences between average and median values, as described in section 6.2 of [3], have been applied. We will now examine step by step the correlations and discrepancies between results obtained by NRL and the author of this paper.
The following is observed.
- Wrights model calculations predict a logarithmic relationship of σ_o vs φ. Three regions are indicated
- the near grazing angle and plateau region, $5^o<\varphi<45^o$
- the near vertical incidence angle region, $45^o<\varphi<80^o$
- and the lower part of the near grazing incidence angle region $\varphi<5^o$

For this latter part Wright did not make calculations, but assumed a φ^4 relationship, based on the interference mechanism. As a result of these assumptions the σ_o vs log φ curve makes a rather abrupt change in slope, as shown in fig. 2.1 (Fig. 2.1, 2.2, 2.3 and 2.4^o are comprised in fig. 2).
In this incidence angle area of observation, such effects have not been observed by the author of this paper. Let us now examine in more detail results of calculations and measurements. The upper boundary of results of measurements performed by Guinard and Daley (1970 [2]) is given in fig. 2.2. The measurements are made down to about 4^o. Measurements and calculations then coincide, while for all other incidence angles a bias varying from 2-4 dB is observed. These differences decrease for smaller incidence angles and appear at about 4^o. No reason seems to be on hand that the scattering mechanism in this observation region changes significantly. Therefore an abrupt change in σ_o vs log φ slope can not readily be explained. In order to obtain more specific information of σ_o in this grazing angle region, relevant results of other investigators have been accumulated and are used for comparison. In particular, results at incidence angles below 4^o are then of importance.

In fig. 2.3 measurements performed by MacDonald (1957) Wiltse et al (1957), Bishop (1970), Guinard (1970) and Nathanson [6] are collected.
In order to complete the picture, in fig. 2.4 a series of curves is given, computed with the experimental model presented in this paper.
Collation of the above mentioned information may lead to the following remarks.
- Results obtained by Bishop, Guinard (up to 15 kts), Nathanson (for $\varphi<1^o$), MacDonald and the author of this paper are in good to reasonable agreement.
- Wiltses results show an increase of cross section, varying from 3-6 dB, between reported windspeeds of 16 to 26 kts.
- Guinards measurements show hardly any increase and sometimes even a decrease for reported windspeeds between 10-15 kts and 47 kts. In particular the decrease is in contradiction with the results of the other investigators who reported an increase.

Nathansons data will be discussed in the next section.

2.3.2 Comparison with data collated by Nathanson

Nathansons data are reported for sea states. Capillary waves disappear quickly with decreasing wind. Significant wave heights representative for a certain sea state may be maintained. Because σ_oVV is mainly determined by Bragg resonant capillary waves the radar return will diminish in the latter case and σ_oVV will indicate too low values, as the sea state may be quoted to be unchanged.
Nathansons data are given as an average of upwind, crosswind and downwind. Comparisons with upwind results, as done in this case, may lead to discrepancies. It is therefore essential to examine the impact of incidence angle and windspeed on the average cross section for these directions of observation. For this purpose we apply the model proposed by the author of this paper. This model indicates a significant increase of the upwind/crosswind ratio of σ_oVV for larger incidence angles and windspeed. In this area we therefore may expect discrepancies with the upwind observations. In fig. 3 a general survey is given of the upwind/crosswind ratio of σ_o, obtained at X- and Ku-band. The observed increase of ratio leads to a decrease of average values of upwind-crosswind and downwind observations, when compared with upwind results. Data collated by Nathanson show a similar trend for larger incidence angles and windspeeds combined with the effects of sea-state labelling, as mentioned earlier in this section. Deviations with results obtained by the author of this paper may be explained. In fig. 2.3 and 2.4 it is shown that Nathansons data are gradually decreasing with respect to the model curve, at increasing incidence angle.
We now compare values obtained for σ_oHH. Upwind/crosswind ratios computed with the model show large values for increasing incidence angles at low windvelocities. Consequently the average values of upwind crosswind and downwind decrease at lower windvelocities when compared with upwind. In fig. 4 it is shown that Nathansons data are gradually decreasing with respect to the model curve at increasing incidence angle and for low windvelocities. At windspeeds of about 30 kts the upwind/crosswind ratio does not vary with incidence angle; it varies less than $\pm$ 1 dB between 25 and 35 kts. Nathansons data and the model curve are than in reasonable to good agreement. The agreement is better at smaller incidence angles, which confirms the results of fig. 3.
The model calculations are presented in fig. 4 and in fig. 5 als fully drawn or dashed curves.

2.3.3 Comparison with data collated by other investigators

In the previous section we have presented σ_oVV respectively σ_oHH versus incidence angle, with the windspeed as a parameter. In this section we will also give σ_oVV, respectively σ_oHH versus windvelocity, with the angle of incidence as a parameter. Results of various investigators are compared with the model curve. They are shown in fig. 5 and 5.1, fig. 6.1 and 6.2, fig. 7.1 and 7.2 and fig. 8.1 and 8.2.

In fig. 5 Schooleys and Guinards (up to 15 kts) data do remarkably well fit in the model predictions. Deviations between the model calculations and Guinards measurements at 47 kts are clearly demonstrated in fig. 5.1. However a remarkable good model fit is obtained with Bishops results at an incidence angle $\varphi = 1$, both for σ_oHH and for σ_oVV. Guinards measurements then correspond to a model curve of $W_v = 20$ kts. Model calculations are represented by fully drawn or dashed lines.

The information, accumulated at an incidence angle of $\varphi = 1^o$, is given in fig. 6.1-2. A reasonable to remarkable good agreement with the model is obtained with results obtained by Nathanson, Bishop and Schooley.

In fig. 7.1-2 results are compared at an incidence angle $\varphi = 10^o$. Grants and Yaplee's data, copied from Long's book [3], are not clearly specified concerning the direction of observation. In case they are also an average of upwind, crosswind and downwind values, the discrepancies with the model can be explained in a similar manner, as those concerning Nathansons data.
Deviations between the model curve and NRL data are observed for high windvelocities and to some extend for very low windvelocities at vertical polarization.

In fig. 8.1-2 results are given for an incidence angle $\varphi = 30^o$. Guinards and Delays Bermuda results for σ_oHH are in good agreement with the model. The other results obtained by NRL are about 3 dB below the model curve. An explanation cannot readily be given.

In conclusion we may say that results obtained with the model proposed in this paper are in reasonable to good agreement with data and calculations presented in literature by various other investigators. However, the impact of direction of observation on the radar return is of great significance and has to be taken into account. Observed discrepancies can then be explained. We therefore may assume that the model can be applied in the near grazing angle and in the plateau region.
The comparisons have been made at X-band and for pulselength τ, which vary between 0.25 µsec. and 0.50 µsec. This is done because literature provides only these kind of results in sufficient quantity. Ku-band information is only available to a very limited extend in these observation regions and consequently cannot be used as a basis for comparison.

3. CHARACTERISTICS OF σ_o

For decisions in system design it is of practical significance to be informed of typical characteristics of clutter return at specific freq. bands, polarization and pulselengths. In the previous sections it has been shown that σ_o values can be computed versus incidence angle, windvelocity, polarization and angle of observation. The determination of an optimum combination of these parameters requires the possibility of comparison in order to make the right decision. The presented model makes this possible in a simple way. In the next sections we will discuss some examples.

3.1 The increase of σ_o with windvelocity at X- and Ku-band

The increase of σ_o with windvelocity is dependent on incidence angle. In the near grazing angle region this increase is larger at X-band than at Ku-band. The smaller the angle, the larger the increase. In the plateau region ($\varphi > 10^o$), the increase is about the same.
These effects are shown in fig. 9. They can be explained by influences of screening and spray at low grazing angles. Increase of wind causes spray. As is well known, X-band frequencies are less sensitive for attenuation by precipitation than Ku-band frequencies. Consequently at very low grazing angles and in particular at crosswind observations this spray effect, which is more dense at crosswind, can have a serious impact on the σ_o characteristics at Ku-band. This impact is more severe at vertical polarization due to the fact that the radar return is then predominantly determined by Bragg resonant capillary waves.

3.2 Ratios of σ_o for X- and Ku-band

Bragg resonant capillary waves are more easily excited at Ku-band than at X-band. Inversely they die away more rapidly. Therefore X/Ku-band ratios of σ_o expressed in dB's are negative at low windvelocities. The Ku-band return is then larger. For increasing wind X- and Ku-band return become comparable at small incidence angles. As explained in the previous section, spray effects then have a significant impact on the radar return. In the plateau region these effects do not occur. The increase of water wavelength to satisfy the Bragg resonance criterion will require higher windspeeds, in particular in the near vertical incidence angle region. Consequently the Ku-band return is larger in these latter two cases. A survey of these characteristics is given in fig. 10.

3.3 Upwind/crosswind ratios of σ_o

In general it is assumed that these ratios expressed in dB's are always positive, in other words upwind is always larger than crosswind return. The model shows the contrary. Depending on polarization and incidence angle inverse effects are observed as shown in fig. 3. In particular, effects at vertical polarization are interesting. Because σ_oVV is mainly determined by capillary waves, crosswind observations at very small grazing angles show a larger crosswind than upwind return.

3.4 Polarization ratios of σ_o

The two scatter mechanism of capillary waves and facets plays a dominant role when considering polarization effects. The tilting of facets by the interaction of swell and wind driven shorter gravity waves is important for the direction of backscatter at horizontal polarization. Because these facets are overlaying the wave structure, σ_oHH at larger incidence angles gradually decreases for upwind observations. The main direction of backscatter then does not correspond with the angle of incidence. For crosswind observation the facet tilt dependence due to the above mentioned interaction effects can become quite complicated. It proves to result in a different response for σ_oHH and σ_oVV. Because the facets in the waves now contribute to the backscatter, σ_oHH increases at very small incidence angles. The increase of σ_oHH in the plateau region may be explained by the possibility that for large windspeeds the facet slope is not so steep as for upwind observations. In general σ_oVV larger than σ_oHH. For very small grazing angles σ_oVV becomes smaller than σ_oHH; up and crosswind show an inverse effect. Results of model calculations are given in fig. 11.

4. THE DEPENDENCE OF THE CLUTTER RETURN ON PULSELENGTH

Results discussed in the previous sections are representative for τ = 0.5 µsec, as far as the model is concerned. The shorter gravity waves cannot be resolved individually with these pulselengths. The two scatter mechanism therefore cannot clearly be separated from each other and a noiselike signal is observed. The probability distribution of the clutter signal obeys a Rayleigh law, provided that the gate in which the signal is detected has a much smaller width than the pulselength.

4.1 The influence of shorter pulse lengths

A shorter pulselength opens the possibility of resolving the shorter gravity and obviously the swell waves. The facet mechanism will now play a dominant role in the total scattering at horizontal polarization. A slow modulation due to this facet scattering will be superimposed on the capillary scattering. Long [4] has observed a similar effect. Depending on the observation time, a rather large excursion of magnitude of radar return is observed; the clutter looks targetlike. In literature this is often qualified as non-Rayleigh sea-clutter, which is log-normally distributed. In fact the observation time, over which the distribution is made, is of great significance in determining the type of distribution. Due to the fact that vertical polarization is much less influenced by the facet scatter mechanism, the slow modulation by the shorter gravity waves is not observed. In short, the character of σ_oVV is hardly influenced by pulselength.
Measurements made at a pulse length τ = 0.12 µsec result only in a bias cross section for σ_oVV. Bias incorporation in the model results in a good fit with the measurements. At horizontal polarization model calculations indicate an upper boundary of σ_oHH. Results are shown in fig. 12. Bias values to adapt the model to pulselength τ = 0.12 µsec are given in table 2. It must be emphasized that the Ku-band values are only given on a preliminary and indicative basis. Not enough measurements are available to accept these values as final. Due to the different trend they show, we thought it interesting to mention them. However, for the time being, these values have to be thoroughly verified. More information is available in the X-band, though not in such quantities as for pulselength τ = 0.5 µsec.

The existence of a slow modulation effect will be demonstrated in the next section.

FREQ.	OBSERVATION ANGLE	POL.	$\sigma^o_{HH}-\sigma^o_{VV}$ dB	α' dB
K_u-BAND	UPWIND	VERT.	-48	-2
	UPWIND	HOR.	-49	-3
	CROSSWIND	VERT.	-47	0
	CROSSWIND	HOR.	-48	0
X-BAND	UPWIND	VERT.	-48	+1
	UPWIND	HOR.	-47,5	+2,5
	CROSSWIND	VERT.	-55	+3
	CROSSWIND	HOR.	-56	+3

Table 2. Corrections of the parameter α for τ = 0.12 µsec.

5. THE SPECTRUM BANDWIDTH MODEL

Based on measurements an expression has been derived for the spectrum bandwidth [7]. Rewriting this expression results in

$$f_{0.5} = f_0 \cdot 10^{\frac{\beta \log \frac{\varphi}{\varphi_o} + (\delta \log \frac{\varphi}{\varphi_o} + \gamma) \log \frac{W_v}{W_o}}{10}} \quad \text{Hz}$$

Constants and variables allocated to this expression are given in table 3. As can be expected, the rms velocity spread is larger for Ku-band than for X-band. Details are given in [7]. An interesting aspect is the allocation of a slow modulation effect in the scattering mechanism by spectrum analysis. These effects have been described independently by Long [4] and the author of this paper [8]. For this purpose we examine the scintillation spectrum of the reflected signal.

3dB SPECTRUM BANDWIDTH												
FREQ BAND / λ cm WAVE LENGTH		WIND-DIRECTION	POL.	f_o Hz	φ_o Degr	W_o Kts	β dB	δ dB	γ dB	SPREAD dB MAX	SPREAD dB MEAN
X	3.2	UPWIND	HOR.	60	0.5	10	0	-17	+7	±1	≤±0.2
X	3.2	CROSSWIND	HOR.	32	0.5	10	+2.6	-9.6	+15	±2	≤±0.5
X	3.2	UPWIND	VERT.	63	0.5	10	0	-7.4	+8	±1	≤±0.3
X	3.2	CROSSWIND	VERT.	50	0.5	10	-2.2	-1.6	+9.2	+1.5	≤±0.5
Ku	1.85	UPWIND	HOR.	130	0.5	10	-3	+3.6	+3.4	<±0.2	
Ku	1.85	CROSSWIND	HOR.	160	0.5	10	-3	+3.3	+2	<±0.2	
Ku	1.85	UPWIND	VERT.	125	0.5	10	-4.1	+6	+4	<±0.5	
Ku	1.85	CROSSWIND	VERT.	150	0.5	10	-5.4	+7	+3.4	<±0.2	

Table 3. Model parameter values for the spectrum bandwidth at τ = 0.5 µsec.

5.1 The scintillation spectrum

The fluctuations around the mean can be described with the scintillation spectrum of the reflected signal. The spectrum is calculated by Fast Fourier Transform (FFT). A 10 bit A/D conversion is used, the number of samples corresponds to N = 1024 and the frequency resolution is 1.46 Hz. The spectrum ordinate is normalized in such a way, that 0 dB is the variance of the signal, corresponding to the total energy contents of fluctuations.

5.1.1 The low frequency part of the spectrum up to f_o = 10 Hz and examples of the spectrum in excess of 1 Hz

The fluctuation behaviour around the mean appears to be significantly different for τ=0.12µsec. compared with τ = 0.5 µsec. For horizontal polarization, a low frequency spectrum is superimposed on the characteristic clutter spectra. This effect is increased for crosswind observation and is more pronounced at larger incidence agles. It can be hardly noticed at vertical polarization. In fig. 13.1 and fig. 13.2 two examples are given for horizontal polarization and in fig. 14 one example for vertical polarization. They are typical for these phenomena. Only the low frequency part of the spectrum is shown, up to f = 20 Hz. The very low frequency component of 0.1 Hz <f< 0.2 Hz, which is observed both for horizontal and vertical polarization, represents the larger sea structure, the swell.
Apart from this swell effect the low frequency part of the spectrum is flat for vertical polarization. This is not the case for horizontal polarization, indicating that a relatively significant part of the energy contents of the fluctuating signal is contained in the lower frequency part of the spectrum. This suggests that the clutter return behaves more targetlike. An estimation is made of the power contents of the fluctuating signal, after extraction of the mean. The analysis is made for frequencies up to 10 Hz and is relative to the total power contents of the fluctuating signal. The results are given in table 4. This table shows that the relative low frequency contents of the fluctuating signal can be as high as 40% of the variance. For frequencies in excess of 10 Hz the spectrum shows to be similar for horizontal and vertical polarization at all measured grazing and observation angles. Typical samples of the scintillation spectra in excess of 1 Hz are given in fig. 15 and fig. 16 for respectively X-band and Ku-band.

POLARIZATION FREQ. BAND	OBSERVATION ANGLE	GRAZING ANGLE	RELATIVE POWER %
HH/X-BAND	CROSSWIND	6→2	40→15
HH/X-BAND	UPWIND	8→1	28→14
VV/X-BAND	UPWIND	8→2	15→11
HH/X-BAND	UPWIND	4	19
HH/X-BAND	CROSSWIND	4	30
VV/X-BAND	CROSSWIND	4	14
HH/K_u-BAND	CROSSWIND	4→1	22→13
VV/K_u-BAND	CROSSWIND	4→1	13→7
HH/K_u-BAND	DOWNWIND	4→2	29→18

Table 4. Relative power contents of slow modulation effects

5.1.2 The spectrum bandwidth

As mentioned earlier in this paper, relatively few measurements at short pulselength have been made by the author of this paper. Available data at X-band show a larger increase at crosswind than at upwind. Comparisons made between results at τ = 0.5 µsec and τ = 0.12 µsec are demonstated in fig. 17 and fig. 18.

II TARGET CHARACTERISTICS

1. THE INFLUENCE OF THE EARTH ON THE RCS

A radar operated in the presence of the earth does not even remotely correspond to operation in free space. Three major influences have an important effect on the propagation of e.m. waves.
- Due to reflection of the earth, interference effects are caused
- Due to shadowing effects of the earth, diffraction phenomena occur
- Due to the inhomogeneity of the earth, refraction effects are produced

in this paper we will consider the so-called multipath effects, producing interference patterns and their increasing or reducing the radar return under specific conditions of observation.
Small angles of incidence are the main objective, although no restrictions are made for larger angles of incidence.
The above mentioned phenomena have been extensively treated by Kerr [1]. He has grouped all these factors into a single quantity called the pattern propagation factor $F \equiv \left|\frac{E}{E_o}\right|$ (1)
in which:
E_o = The electric field under free space conditions at a given point, with the transmitting antenna directed towards that point.

E = The electric field to be investigated at the same point.

For a given orientation of transmitting antenna F is a scalar function of position.

The generalised form of the radar equation is: $P_r = \frac{P_t G^2 \lambda^2}{(4\pi)^3 R^4} \cdot \sigma_o \cdot F^4$, where σ_o is the RCS in free space. (2)

Departing from these basic concepts we will develop a simple model to describe target characteristics in the presence of the earth. In relation with the first part of this paper we will consider targets in a sea environment.

1.1 Assumptions of the scattering mechanism

Rather crude assumptions are made for the scattering mechanism of the target. An individual target structure is considered to be composed of a linear array of point scatterers distributed vertically above the water surface. The contribution of each scattering center is assumed to be independent of the adjacent scatterers. The magnitude of the reflections is determined by the free space RCS of the target. The water surface can be considered to be perfectly smooth or rough. Two methods are used. An approximation of the total backscattered field strength, the coherent integration method, and approximation of the total backscattered power, the incoherent integration method. A solution is given in closed form and numerically.

1.2 The multipath RCS approximation

For this purpose we assume a radar target configuration which is given in fig.1.
Following Kerr [1] we may write the following expression for the field strength, incident on the target:

$$E = E_r + E_d = E_o \left[f(\theta_1) + \rho f(\theta_2)\, e^{-i(\beta + k\Delta R)} \right] \tag{3}$$

$$|E| = |E_o|\, F = |E_o| \sqrt{f^2(\theta_1) + \rho^2 f^2(\theta_2) + 2\rho f(\theta_1) f(\theta_2) \cos\alpha,} \tag{4}$$

$$\text{as } F = \left| f(\theta_1) + \rho f(\theta_2) e^{-i\alpha} \right| \tag{5}$$

$$\text{and } \alpha = \beta + k\Delta R \approx \beta + \frac{4\pi z_1 z}{\lambda R} \tag{6}$$

The path length differences, ΔR, in the farfield zone are obtained by expanding each path length by the binomial theorem and substracting. We than denote

$$R = \frac{2z_1 z}{r} \left(1 - \frac{z_1^2 + z^2}{2r^2} + \frac{3z_1^4 + 10 z_1^2 z^2 + 3z^4}{8r^4} - \ldots\ldots \right) \tag{7}$$

We assume a complex reflection coefficient

$$F \equiv \rho e^{-i\beta} \qquad \begin{array}{l} 0<\rho<1 \\ \rho = \rho_o \rho_s \\ \beta \approx \pi \quad \text{(in most cases)} \end{array} \tag{8}$$

ρ_o is the rms specular scattering coefficient
ρ_s is the magnitude of the reflection coefficient

The assumption that $r >> z_1 >> z$ implies that all angles involved are depression angles if the maximum of the antenna beam is directed above the target. Further assumptions are that $\Psi_1 = \Psi_2 = \varphi$ = incidence angle. In case of a wide beam in the vertical plane, which is slightly depressed to obtain an optimum illumination of the target, $f(\theta_2)$, $f(\Psi_1)$ and $f(\Psi_2)$ approximate unity, otherwise the antenne pattern and position functions can be taken into account giving rise to a reduced reflection magnitude.
The field strength at the radar due to one scattering center at the target can then be written as:

$$\Delta E = \frac{|E_o| F^2}{2\delta} \cdot \Delta\delta$$

or, because $|E_o| \propto \sqrt{\sigma_o}$:

$$\Delta E \propto \frac{\sqrt{\sigma_o}}{2\delta} \cdot \Delta\delta \cdot \left(1 + \rho^2 - 2\rho\cos \frac{4\pi z_1 z}{\lambda r} \right) \tag{9}$$

We will now substitute the target by an array of N discrete scattering centers, distributed over a length 2δ. They contribute independently to the total back scattered field strength at the radar.

$$N = 1 + \frac{2\delta}{\Delta\delta} \tag{10}$$

A continous target description is obtained in the limit situation whereby $\Delta\delta \to 0$. In that case

$$dE \propto \frac{\sqrt{\sigma_o}}{2\delta} \left(1 + \rho^2 - 2\rho\cos \frac{4\pi z_1 z}{\lambda r} \right) dz \tag{11}$$

1.2.1 The coherent integration method

Assuming a smooth reflecting surface, the reflected field strength (E_s) at the radar can be written as

$$|E_s| = \int_{h-\delta}^{h+\delta} dE \propto \frac{\sqrt{\sigma_o}}{2\delta} \int_{h-\delta}^{h+\delta} (1+\rho^2 - 2\rho\cos\frac{4\pi z_1 z}{\lambda r}) \, dz$$

which given: $|E_s| \propto \sqrt{\sigma_o} \, (1 + \rho^2 - 2\rho\cos 4\pi\varphi q . \frac{\sin 4\pi\varphi p}{4\pi\varphi p})$, where:

$\varphi \approx \operatorname{tg} \varphi = \frac{z_1}{r}$, φ is incidence angle

$p = \frac{\delta}{\lambda}$ and $q = \frac{h}{\lambda}$, z_1 and h are radar - resp. target height, 2δ is target length

Due to propagation effects over the earth, the power at the radar receiver is now proportional to $|E_s|^2$ and the multipath RCS approximation can be written as

$$\sigma_a = \sigma_o \, [1 + \rho^2 - 2\rho\cos 4\pi\varphi q . \frac{\sin 4\pi\varphi p}{4\pi\varphi p} \,]^2 \qquad (12)$$

also called the apparent RCS.

1.2.2 The incoherent integration method

In case the target and reflecting surface are rough and of random nature, the phase of the signal scattered by each reflecting center may lie between zero and 360 , with all values being equally likely, when reflected on a fixed point on the water surface. The apparent cross section is then taken as the sum of the cross sections of the scattering centers

$$\sigma_a = \sum_{i=1}^{N} \sigma_i . \qquad (13)$$

We then apply the incoherent integration method.
The pattern propagation factor is then

$$F^4 = (1 + \rho^2 - 2\rho \cos \frac{4\pi z_1 z}{\lambda r})^2 \qquad (14)$$

The power reflected by each scattering center is then proportional to:

$$\frac{\sigma_o}{2\delta} (1 + \rho^2 - 2\rho \cos \frac{4\pi z_1 z}{\lambda r})^2 \, dz \qquad (15)$$

and the back scattered power at the radar can be written as

$$P_r \propto \int_{h-\delta}^{h+\delta} \frac{\sigma_o}{2\delta} (1 + \rho^2 - 2\rho \cos \frac{4\pi z_1 z}{\lambda r})^2 \, dz$$

from which results that

$$\sigma_a = \sigma_o \, [(1+\rho^2) + \rho^2 - 4\rho(1+\rho^2)\cos 4\pi\varphi q . \frac{\sin 4\pi\varphi p}{4\pi\varphi p} +$$

$$+ 2\rho^2 \cos 8\pi\varphi q \, \frac{\sin 8\pi\varphi p}{8\pi\varphi p} \,]$$

1.2.3 The numerical integration method

The coherent and incoherent integration method are applied for the far field region, for which the binomial theorem expansion of path length differences ΔR is valid.
Laboratory conducted experiments however usually have to take place at short range. In particular at very small grazing incidence angles a significant error in path length difference occurs. The binomial expansion is not valid any more and a solution in closed form is not possible.
A numerical integration method then has to be applied. Deviations between short range, small angle measurements and those performed in the far field can thus be explained. Path length differences for each scattering center are then computed for each of them, taken into account their respective phases.
The length of the direct ray path is $\sqrt{r^2 + (z_1 - z)^2}$. (17)

The length of the reflected ray path is $\sqrt{r^2 + (Z_1+Z)^2}$. (18)
The total incident and reflected field strength of one scattering center is proportional to:

$$A_1 e^{-i\alpha_1} + A_2.\rho\, e^{-i\alpha_2} + A_3.\, \rho^2\, e^{-i\alpha_3} \tag{19}$$

and for N_k discrete scattering centers of the k^{th} target:

$$\sum_{j=1}^{N_k} \{(A_1)_{kj}\, e^{-i(\alpha_1)_{kj}} + (A_2)_{kj}.\, 2\rho.e^{-i(\alpha_2)_{kj}} + (A_3).\rho^2.\, e^{-i(\alpha_3)_{kj}}\} \tag{20}$$

As $(A_1)_{kj} = (A_2)_{kj} = (A_3)_{kj} = \frac{\sqrt{\sigma_{ok}}}{N_k}$, we can then write:

$$\sigma_{a_k} = \frac{\sigma_{o_k}}{N_k^2} \left[\sum_{j=1}^{N_k} e^{-i(\alpha_1)_{kj}} \{1 + 2\rho.\, e^{-i(\alpha_2-\alpha_1)_{kj}} + \rho^2.\, e^{-i(\alpha_3-\alpha_1)_{kj}}\}\right]^2 \tag{21}$$

or

$$\sigma_{a_k} = \frac{\sigma_{o_k}}{N_k^2} \left[\sum_{j=1}^{N_k} e^{-i(\alpha_1)_{kj}} \{1+\rho.\, e^{-i(\alpha_2-\alpha_1)_{kj}}\}^2\right]^2 \tag{22}$$

as

$$\alpha_3 - \alpha_1 = 2(\alpha_2-\alpha_1) = 2\{\sqrt{r^2 + (z_1+z)^2} - \sqrt{r^2 + (z_1-z)^2}\} \tag{23}$$

Additional advantages of the numerical integration method are the following:
- Tilting of the array of scatterers can be easily taken into account. The relevant path lengths for each scattering center can be adapted to the tilt by inserting the correction Δr on the ground range, as is shown in fig. 2.

$$\Delta r = z \tan \theta \tag{24}$$

- A combination of coherent and incoherent integration can be performed relatively easy.
- Almost any target configuration can be covered within the restrictions imposed by the application of scattering centers.

A disadvantage may be the relatively long computing time required, compared with the solution in a closed form. An optimum may be obtained by a combination of the two methods for complicated target structures.
A numerical integration program has been developed and tested at the Physics Laboratory TNO.

2. THE APPARENT RCS OF VARIOUS TARGETS

This section considers targets with smooth, almost ideal, surface contours and practical configurations. The first type of target is applied to verify the validity of the multipath RCS approximation model, the latter to test the applicability on real targets.

2.1 Smooth surface targets

The measurements to verify the model has been performed in a laboratory conducted measuring facility.
The targets are mounted on a turntable which can be adjusted in height by moving an underwaterplatform, while the radar is installed on a tower lift platform which can be adjusted vertical up to 15 m above the waverlevel.
An external calibration method is adopted, using a calibrated flat plate in a free space configuration.
An accuracy is obtained to within 1 dB.
The measurement set-up is symbolized in fig. 3.

2.1.1 The cylinder

The basic target configurations are shown in fig. 1. Results of measurements and calculations are given in fig. 4.

Degrading interference effects at vertical polarization and increasing incidence angles are demonstrated in fig. 5. These effects do not occur at horizontal polarization, as shown in fig. 6.
In both cases the cylinders are respectively 0.1 m and 0.5 m above the water surface. The radar frequency is X-band and the water surface is considered smooth.

2.1.2 The cylindrical "belt"

Results of measurement and calculations are given in fig. 7.1-3. The difference between the far field and short range approximation is shown in respectively fig. 8 and fig. 9. In these latter two cases the radar is in the Ku-band and the target configuration is as shown in fig. 7.3.

Results of measurement and calculations shown in these sections are in good agreement. This implies That the assumptions to substitute the target by an array of discrete scattering centers can be applied. The cylinder and cylindrical belt can be applied in most cases for a variety of target configurations which are situated above the water surface.
Due to practical considerations of measurement in the laboratory measuring facility, only targets situated relatively close to the water surface have been investigated.
Other examples of application of the cylindrical belt model are target configurations such as the ellipsoid, the diabolo, the sphere, the cone sphere, the cylinder sphere and all kinds of double curved surfaces. "Belt" height determination is essential. A physical interpretation of cross section, which can be derived from the equivalent body under consideration, relates it to the flat plate area A_p which would provide an equal return signal. In our case, the belt height corresponds to the maximum vertical length of A_p. A criterion to match the energy balance of the radar return of plat plate and body is to take that part on the body which lies within a distance of $\lambda/4\pi$ of the wavefront when it just touches the front of the body. This is in general as ellips. In case the Z-axis is perpendicular to the water surface, the belt height is $\delta \equiv z = \sqrt{\frac{b\lambda}{2\pi}}$.
In case the X-axis is perpendicular to the water surface, the belt height is $\delta \equiv x = \frac{a}{b}\sqrt{\frac{\lambda b}{2\pi}}$.
For the direction of observation and in free space, the return of the flat plate area A_p is: $\sigma = \frac{4\pi A_p^2}{\lambda^2}$.
With $A_p = \pi \frac{a}{b}\sqrt{(\frac{\lambda b}{2\pi})^2} = \frac{a\lambda}{2}$ follows: $\sigma = \pi a^2$, which satisfies the energy balance.

2.2 Practical configurations

The implementation of the derived models on practical configurations requires dominating scattering areas, which can be isolated from the remainder of the target.
In fig. 11 an example is given of a buoy. The cylindrical belt dominates slots, ridges and rivets distributed over the target surface. The measurements are in reasonable to good agreement with the multipath RCS approximation, which satisfies the requirements to find optimum detection criteria.

2.3 The target cluster

In general the target cluster of M targets can be considered as an incoherent summation of the M individual targets, according to the relation

$$\sigma = \sum_{k=1}^{M} \sigma_k \tag{30}$$

in which

$$\sigma_k = \sigma_{o_k} \left[1 + \rho^2 - 2\rho\cos 4\pi\varphi q_k \cdot \frac{\sin 4\pi\varphi p_k}{4\pi\varphi p_k}\right]^2 \tag{31}$$

Mutual interaction effects are then considered to produce a phase retardation which lies between zero and 360^o, with all values being equally likely. Screening and persistent coupling effects are not considered. An example is given of an arbitrarily chosen target cluster, consisting of M targets. The configuration of target distribution is given in fig. 12, in which the first 4 targets have to be taken. The RCS in free space is given in table 1. For k = 2 two values are chosen, respectively 3 and 30 m^2.

Table 1.

k	1	2(1)	2(2)	3	4	5	6	7	8	9	10	11	12	13	14	15
σ_{o_k} m^2	10	3	30	2	6	5	7	9	8	11	13	4	3	7	9	11

Results of computation at X-band are given in fig. 13. The radar altitude is 100 ft. The maximum target cluster height is assumed to be 1.40 m. The second target (k=2) has been given a value of 3 m^2.

When we assume that the individual targets are consisting of randomly distributed scattering centers, we can rewrite expression (16) and denote now.

$$\sigma_k = \sigma_{o_k} \left[(1+\rho^2)^2 + 2\rho^2 - 4\rho(1+\rho^2)\cos 4\pi\varphi q_k \cdot \frac{\sin 4\pi\varphi p_k}{4\pi\varphi p_k} + 2\rho^2 \cos 8\pi\varphi q \, \frac{\sin 8\pi\varphi p_k}{8\pi\varphi p_k}\right] \tag{32}$$

For expression (25) we can now write

$$\sum_{n=1}^{N} \left[W_{M,n} \int_{h_n}^{h_{n+1}} (1+\rho^2 - 2\rho\cos\frac{4\pi z_1 z}{\lambda r})^2 \, dz\right] \tag{33}$$

$W_{M,n}$ is the weighting function for M targets at level h_n. It implies that for the M targets, the contribution of scattering centers to the total reflected power may be added per level.
For the k^{th} target, the contribution is proportional to:

$$\frac{\sigma_{o_k}}{2\delta_k}, \text{ where } 2\delta_k = \text{length of the } k^{th} \text{ target.} \tag{34}$$

in which σ_{o_k} and $2\delta_k$ are the free space RCS respectively the targetlength.

An example is given for an arbitrarily chosen target cluster, consisting of respectively 4 and 15 individual targets, distributed at various height levels. Projected on one reference plane, the cluster can be represented by an ensemble of scattering centers for which N is the total height.
The configuration of target distribution is given in fig. 12. The weighting function W_{kh} for M = 4, resp. M = 15, is shown in fig. 14.1 and 15. The arbitrarily chosen target RCS's are given in table 1. The multipath RCS approximation σ_a for M = 4 is given in fig. 16. The radar altitude is 100 ft. Computations are made at X-band. Comparisons with fig. 13 show that almost identical results are obtained. Some minor discrepancies can be observed for short ranges below 0.4 nm. This implies that for practical purposes the incoherent approximation method can be applied. The application of weighting functions can contribute to a better understanding of the multipath RCS behaviour. An example is given in fig. 14.2; an increase of σ_{o_2}, results in a significantly different weighting function.

3. TARGETS AND CLUTTER

The implementation of results, discussed in the previous sections, may contribute to the search in finding an optimum use of radar. For this purpose, we will apply the derived models for targets and clutter to investigate signal/clutter ratios.

3.1 The relation between radar frequency band, target height, radar height and environment in order to obtain an optimum signal/clutter ratio

It is generally known that the clutter return per unit area reduces at smaller incidence angles. Consequently an optimum signal/clutter ratio can be obtained in an area of observation where small incidence angles correspond with maximum apparent RCS's of targets to be detected.

A typical example, often met in practice, is the detection of small buoys by ship traffic. The radar antennas are usually located close to the water surface and the buoys are floating on the water.

Optimum signal/clutter ratios can be derived with the aid of the presented target and clutter models.

A buoy is represented by a cylindrical belt of 0.2 m height. In fig. 17 and 18 coherent model calculations of such a belt are shown. The apparent RCS in dB's relative to free space is plotted versus target height. The angle of incidence is a parameter and varies from 0.1^o to 0.8^o, as these angles are considered to be of importance. The calculations, performed with the numerical integration method, are made for X- and Ku-band at horizontal- and vertical polarization.

In fig. 19 the angle of incidence is plotted versus distance between radar and target. The radar platform height H is a parameter.

Depending on the range, at which we want to distinguish the buoy from the sea clutter environment, we can now search for an optimum combination of radar-, target height and radar frequency band for specific weather conditions.

We will demonstrate an example in 3.1.1 and 3.1.2.

3.1.1 Short range requirements

At ranges between 1 and 3 nm, the angle of incidence varies between 0.3^o and 0.1^o respectively. Referring to fig. 17, 18, 19, resp. fig. 10, 11 of part I, the optimum combination is: Radar height at 33 ft, target height 1 m, radar frequency Ku-band and for upwind observations, polarization vertical.
This can be explained as follows:

Radar height : a larger height implies larger incidence angles and consequently more destructive interference

Target height : at Ku-band, constructive interference effects result in a 4-11 dB increase relative to free space RCS for incidence angles of $0.1^o < \varphi < 0.3^o$.

Ku-band : because, for the considered incidence angles:
1) The constructive interference effects result in a larger increase of free space RCS than at X-band.
2) X- and Ku-band sea clutter return are about the same. At higher windvelocities the Ku-band clutter is less than the X-band clutter.
3) The free space RCS at Ku-band is about 3 dB larger than at X-band for the cylindrical configuration ($\sigma \propto \lambda^{-1}$).
4) The ratio of RCS at Ku- X-band varies between 6 and 9 dB, Ku-band being larger.

Vertical polarization : For upwind observation the clutter return is 2-3 dB smaller than at horizontal polarization.

In summary, the above mentioned combinations result in a signal/clutter ratio which can be 8-12 dB larger at Ku-band than at X-band for the considered situation. An application at rivermouths or harbours seems to be feasible.

3.1.2 Long range requirements

A similar procedure as for the short range can be adopted. For the same incidence angle region of $0.1 < \varphi < 0.3^o$ identical results are obtained at Ku-band for situations as indicated in fig. 19.

In summary, we can say that an optimum combination of radar- and observation parameters can be predicted. Obviously, the target does not need to be limited to a cylindrical structure. Any target cluster can be approximated, taking into account the imposed restrictions.

AD-A040 144 ADVISORY GROUP FOR AEROSPACE RESEARCH AND DEVELOPMENT--ETC F/G 17/9
NEW DEVICES, TECHNIQUES AND SYSTEMS IN RADAR.(U)
FEB 77

UNCLASSIFIED AGARD-CP-197 NL

5 OF 7
AD
AD040144

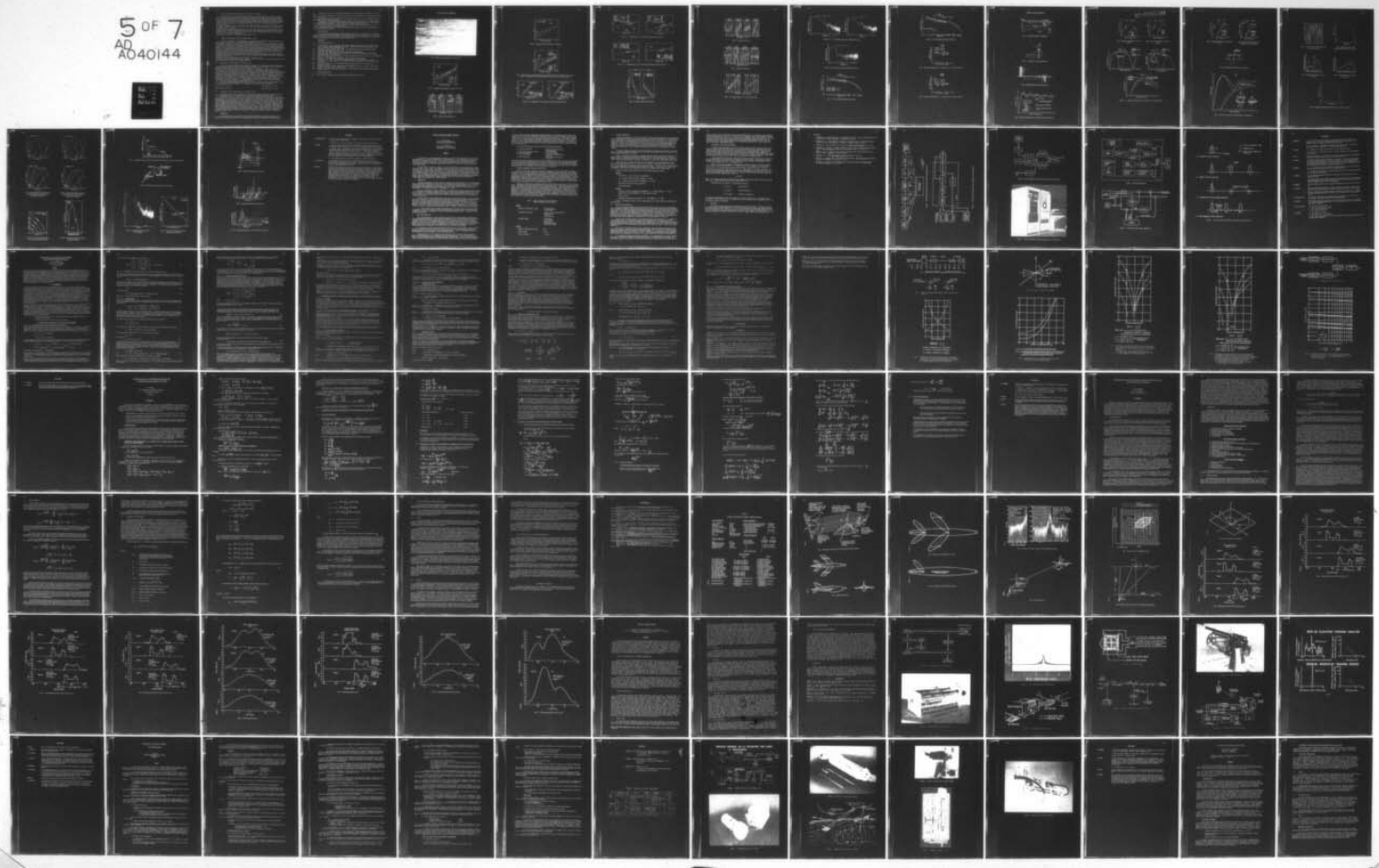

3.2 Typical discrepancies between clutter and target scintillations

Detailed analysis of clutter spectra has shown that the spectrum bandwidth is twice the median value of clutter spectrum. Based on the information, contained in the clutter spectrum model, we can now derive a histogram of median values of clutter spectrum estimates. The median value of cumulative spectrum is weighted with the mean variance and a histogram is made of these weighted values; such a typical histogram is made of sea clutter at X-band and horizontal polarization. The number of spectrum estimates is 675. They are representative for grazing angles between 0.3^{o} and 2^{o} at windvelocities which vary between 5 and 35 kts.
The results are shown in fig. 20.1. For a buoy floating on the water a similar type of histogram is made. The number of spectrum estimates in this case is 50, each containing 512 datapoints. A typical spectrum is incorporated in fig. 20.2.
Target and clutter spectrum demonstrate significant differences. Accepting a false alarm probability, one configuration can basicly be distinguished from the other by declaring a target present, when the median spectrum estimate is below a specified frequency. From fig. 20 a frequency of 30 Hz with a false alarm probability of less than 1% is suggested.
This situation is feasible in practice and symbolized in fig. 2.1.

4. TARGET SCINTILLATIONS OF A BODY OF REVOLUTION IN FLIGHT

A ballistic projectile in flight performs a typical pattern of movements, generally known as precession, nutation and rotation. These movements are symbolized in fig. 22.
These movements generate a complex aspect variation between the axis of symmetry of the projectile and the radar observer. Irregularities on the body of revolution, combined with the variation of aspect, introduce a pattern of scintillations of reflected amplitude. These are typical for the kind of movement. Spectrum analysis of measured target scintillations, caused by a body of revolution in flight, show resonance effects. This occurs at frequencies which correspond to the frequency and the higher harmonics of rotation, nutation and under some conditions of observation also precession. Complicated ballistic theories describe the decrease of frequency of rotation during the flight. Spectrum analysis of target scintillations indicate a comparable rate of decrease with those as predicted by these theories.
Specific discontinuities, on the target body or in the nose section, can emphasize the earlier mentioned resonance effects. Thus the frequency of rotation and its decrease during flight can be better analysed and determined to within 1 Hz.
A typical scintillation spectrum of a body in flight is shown in fig. 23.
The measured and calculated decrease of the frequency of rotation is given in fig. 24; the calculations have been made by ballistic experts of the Netherlands Army.

4.1 Simulations of target aspects of a body in flight

To a limited extend target aspect variations with respect to the radar observer are simulated for a specific flight trajectory. These calculations have been made by Ir. B. Poelsema, formerly at the Physics Laboratory TNO. Only the basic principles of his approach are given here.
The origin of the coordinate system is the focal point for our simulation procedure (see fig. 25).
The target axis is symbolized by a unit vector. The observer looks along the negative X-axis into the origin. The direction of horizontal polarization is along the positive Y-axis, of vertical polarization along the positive Z-axis. The aspect angle of the target is symbolised by α, the target elevation by θ and the target aspect without precession and nutation by α_o. Precession of the target is simulated by revolution of the unit vector along the contour of a cone, with a half cone-angle $\tau_p = 2.4^{o}$. Superimposed on this precession is the nutation. This is simulated by revolution of the unit vector along the contour of a nutation cone with a half cone-angle $\tau_n = 1^{o}$. The frequency of precession and nutation are assumed to be respectively 5 Hz and 20 Hz. On top of all these movements is the rotation, with a rotation frequency $f_{rot} = 150$ Hz. All these movements are symbolized in fig. 25.
The above mentioned assumptions have resulted in the simulation of a complicated mathematical relationship between the various parameters. In a general form they can be written as follows:

$$\alpha_p = f_1 (\alpha_o, \tau_p, \omega_p, \beta_o) \qquad \beta_p = f_2 (\beta_o, \tau_p, \omega_o, \alpha_o)$$

$$\alpha_{p+n} = g_1 (\alpha_p, \tau_n, \omega_n, \beta_p) \qquad \beta_{p+n} = g_2 (\beta_p, \tau_n, \omega_n, \alpha_p)$$

4.2 Simulation of scintillation spectra of a body in flight

The derivation of a continuous range of in flight target aspect variations, with respect to the observer, served as a basis for the simulation of scintillation spectra of the radar return.
The magnitude of target reflections is measured staticly at discrete target positions, which are determined by φ, θ, α and β. Relevant results of these static measurements are now related to the simulated target aspects, taking into account the rate of aspect variation with respect to the observer. Thus scintillation spectra are simulated for a certain observation time during the in flight trajectory. The procedure of simulations has been developed by B. Poelsema and H. Gravesteijn of the Physics Laboratory TNO. Typical examples of the effect of rotation are shown in fig. 26. These scintillations are dominating those caused by precession and nutation. An analysis in time intervals of 1 sec. is presented in the figure. The target response, relative to an arbitrarily chosen reference level, is plotted against a linear frequency scale. The effect of higher harmonics, including aliasing, is demonstrated clearly. Scintillations caused by precession and nutation are also simulated for observation of a target from the rear. The analysis is made for target aspects of $180^{o} \pm 4^{o}$, in steps of 1^{o}. Depending on aspect a maximum is obtained and shown in fig. 27.

CONCLUSIONS

An experimental sea clutter model has been developed that shows a reasonable to good fit with measurement and calculations that have been recognized in literature. Discrepancies can be explained.

Characteristic ratios of σ_o and spectrum bandwidth can be calculated with the model in a simple way.

The two scatter mechanism of sea clutter and its polarization dependency is demonstrated for pulse length of 0.12 μsec.

Multipath RCS approximation methods are developed and tested for a variety of targets. Methods to approximate target clusters are suggested.

Characteristic differences between specific target and clutter scintillation are demonstrated.

Implementation of target and clutter models can result in a proper combination of radar, observation and environmental parameters in order to obtain an optimum signal/clutter ratio.

Typical scintillations of a body of revolution, in flight, can be related to specific types of movements such as rotation, nutation and precession.

The decrease of frequency of rotation can be determined by spectrum analysis of measurements, recorded on a pulse to pulse basis.

Acknowledgements

The author wishes to acknowledge stimulating discussions with his co-worker, Mr. H. Gravesteijn, who also developed and tested the computer programs which have been used in this paper. Mr. L. v. Wijk took care of all the illustrations presented in this paper. Both co-workers are a member of the team which performed the measurements on clutter and target characteristics.

REFERENCES

1. Clutter characteristics

[1] Claassen, John, P., H.S. Fung, Richard K. Moore, Willard, J. Pierson, Sept. 1972, "Radar return and the Radscat satellite anemometer", 1972, IEEE, International conference engineering in the ocean environment, Newport, Rhode Island.

[2] Guinard, N.W., and J.C. Daley, April 1970, "An experimental study of a sea clutter model", Proceedings of the IEEE, vol. 58, no. 4.

[3] Long, M.W., 1975 "Radar reflectivity of land and sea", Lexington Books.

[4] Long, M.W., Sept. 1974, "On a two scatter theory of sea-echo", IEEE Transactions on antennas and propagation", Vol. AP-22, no. 5.

[5] Moore, R.K., 1970, "Worldwide Oceanic wind and wave predictions using a satellite radar radiometer", Journal of hydromautics, vol. 5, no. 2.

[6] Nathanson, F.E., "Radar design principles, 1969, Mc.Graw-Hill Book company.

[7] Sittrop, H., Sept. 1974, "X- and Ku-band radar backscatter characteristics of sea clutter". Proceedings of the URSI, commission II, Microwave scattering and emission from the earth , Berne Switserland.

[8] Sittrop, H., April 1975, "X- and Ku-band backscatter characteristics of sea clutter, Part II, report PHL 1975-09.

[9] Valenzuela, G.R., Nov. 1968, "Scattering of electromagnetic waves from a tilted slightly rough surface", Radio Science, vol. 3 (new series).

[10] Wright, J.W., 1968, "A new model for sea clutter, IEEE Transactions on antennas and propagation, vol. AP-16, no. 2.

2. Target characteristics

[1] Kerr, Donald W, "Propagation of short radio waves, Rad.Lab.series, MIT-13.

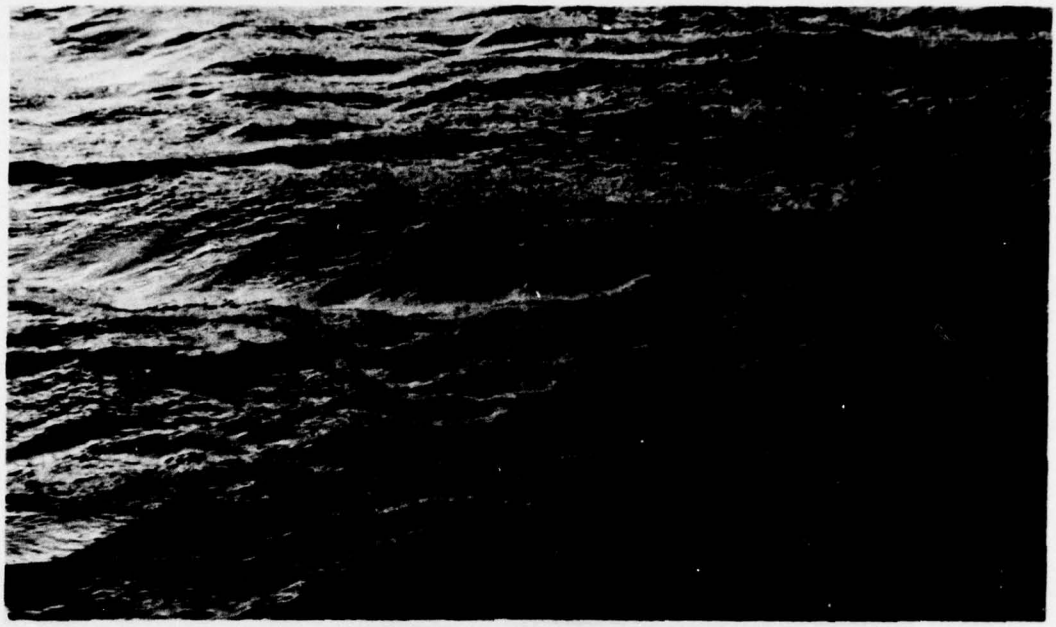

Fig.1 Capillary waves superimposed on water waves

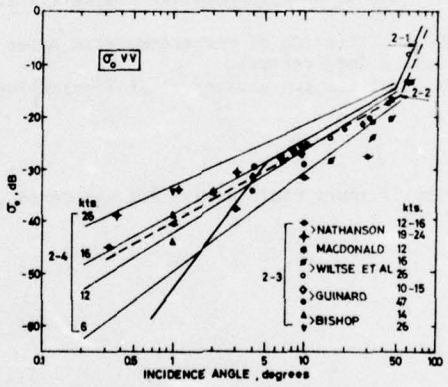

Fig.2 Comparisons with Wrights new model of sea clutter

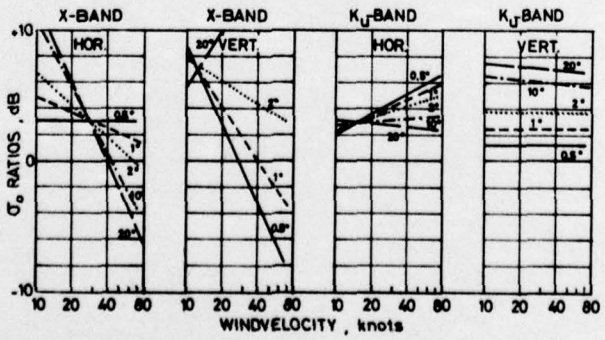

Fig.3 Upwind/crosswind ratios of σ_0

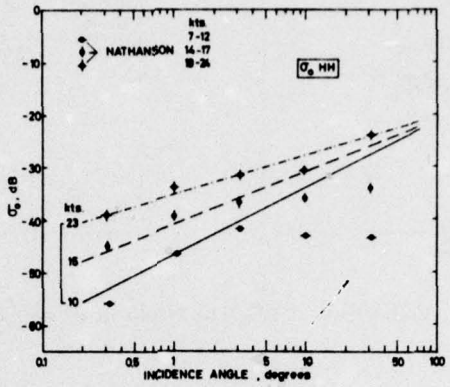

Fig.4 Comparisons with data collected by Nathanson

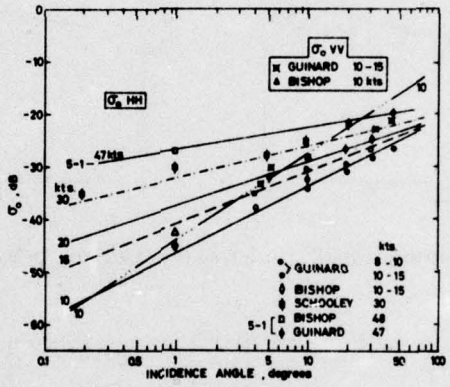

Fig.5 Comparisons with results of measurement obtained by Schooley and Guinard (up to 15 kts)
Fig.5.1 Comparisons with results obtained by Guinard at 47 kts and Bishop at 48 kts

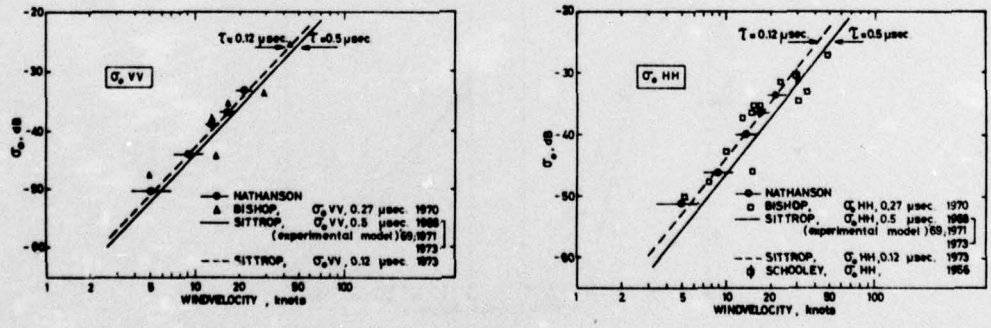

Fig.6 (1–2) Comparison at 1°, with results of Nathanson, Bishop, Schooley

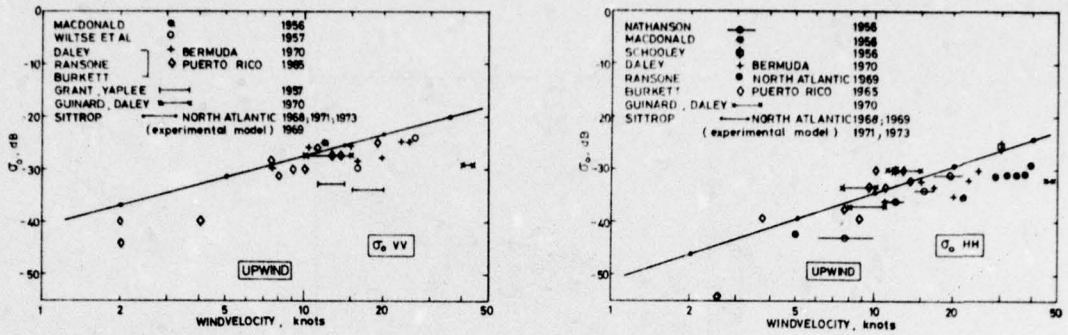

Fig.7 (1–2) Comparison at 10°, with results of Grant-Yaplee and NRL

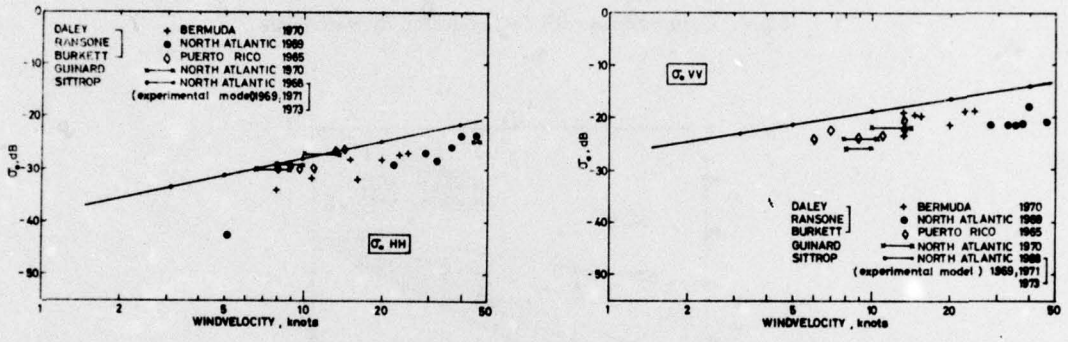

Fig.8 (1–2) Comparison at 30°, with results of Guinard, Daley, Ransone, Burkett

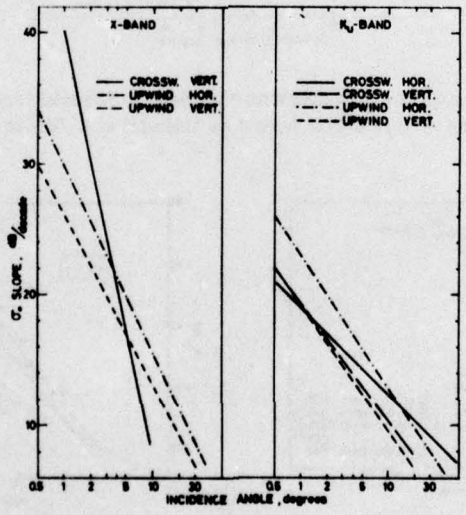

Fig.9 σ_0 slope in dB's vs incidence angle

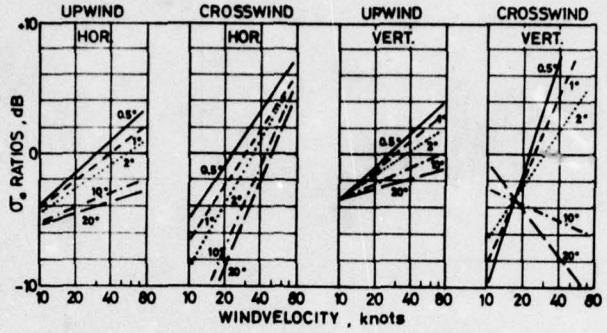

Fig.10 X/Ku-band ratios of σ_o

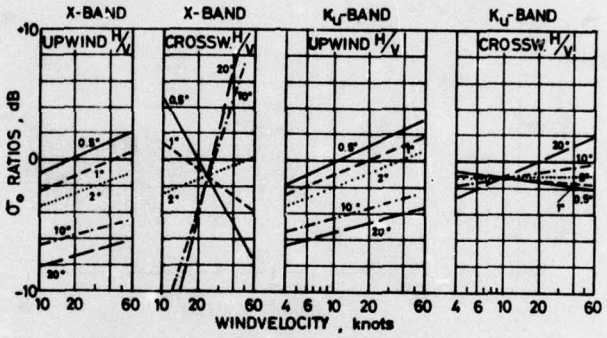

Fig.11 Polarization ratios of σ_o

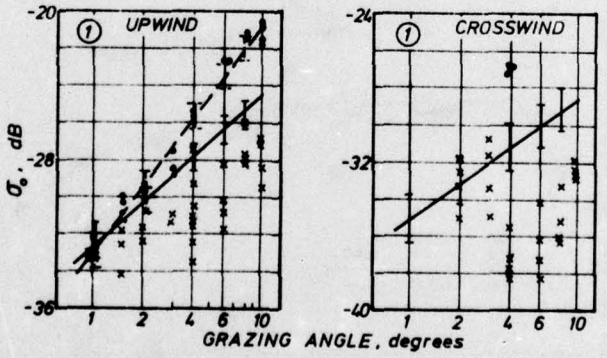

Fig.12 σ_o vs grazing angle at $\tau = 0.12\,\mu$sec and X-band

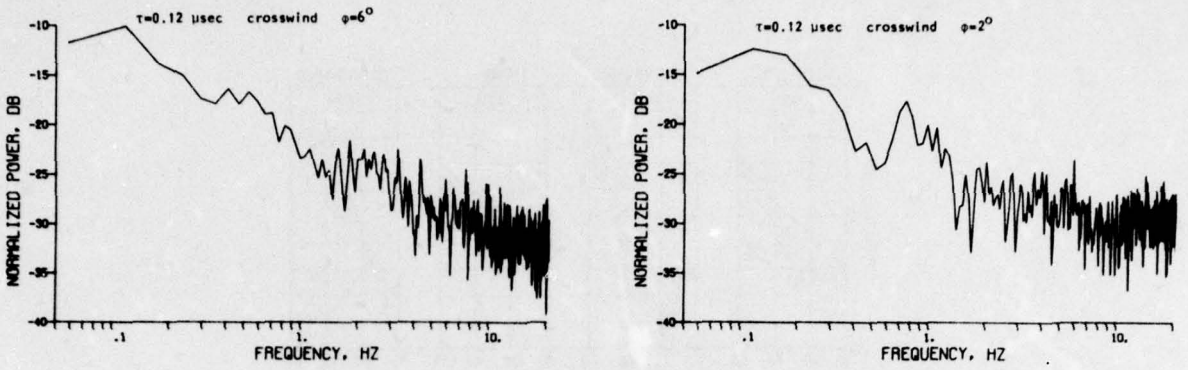

Fig.13 (1–2) Low frequency spectrum at X-band and hor. pol.

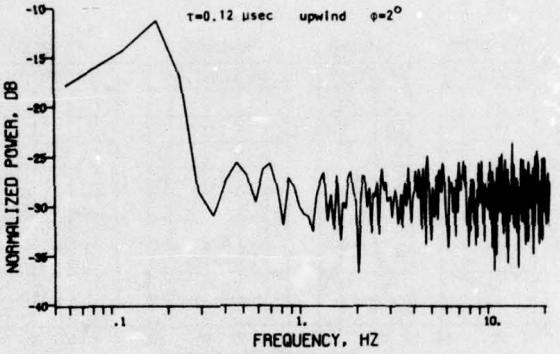

Fig.14 Low frequency spectrum at X-band and vert. pol.

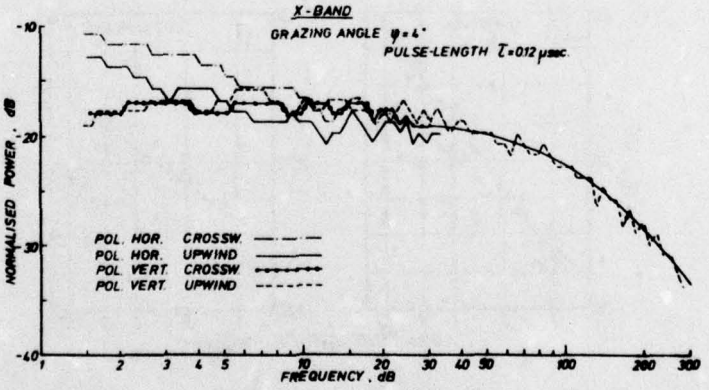

Fig.15 Typical scintillation spectrum at X-band

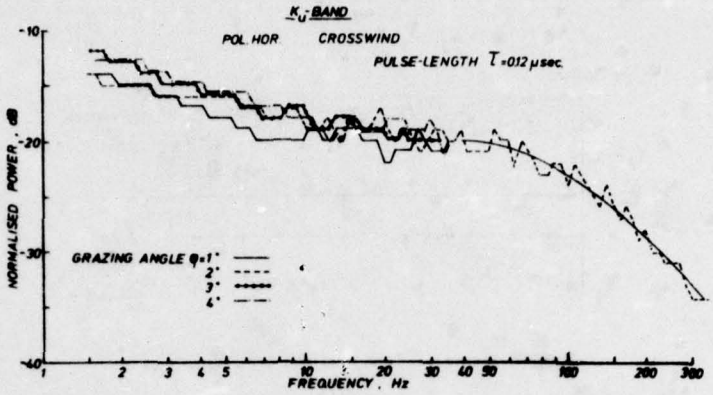

Fig.16 Typical scintillation spectrum at Ku-band

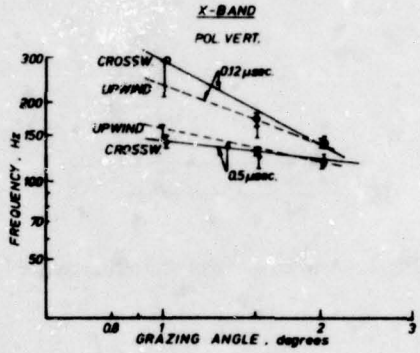

Fig.17 Spectrum bandwidth at $\tau = 0.5$ μsec and $\tau = 0.12$ μsec. Pol = vert

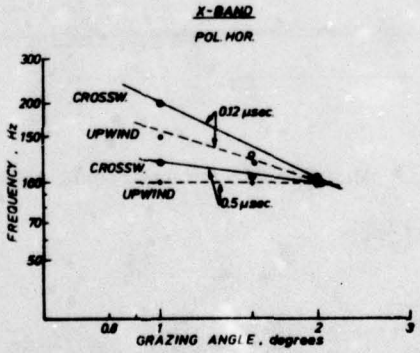

Fig.18 Spectrum bandwidth at $\tau = 0.5$ μsec and $\tau = 0.12$ μsec. Pol = hor.

TARGET CHARACTERISTICS

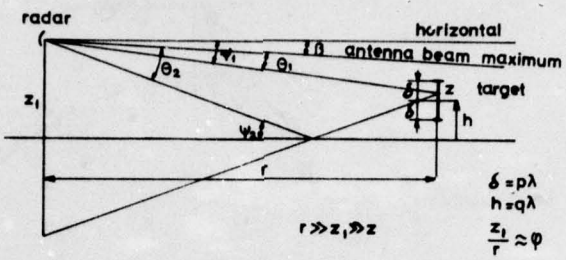

Fig.1 Schematic radar target configuration

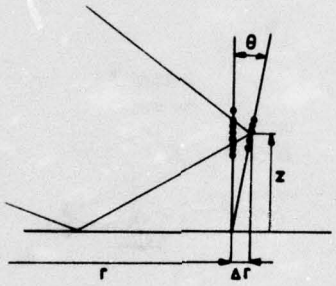

Fig.2 A tilted array of scattering centers

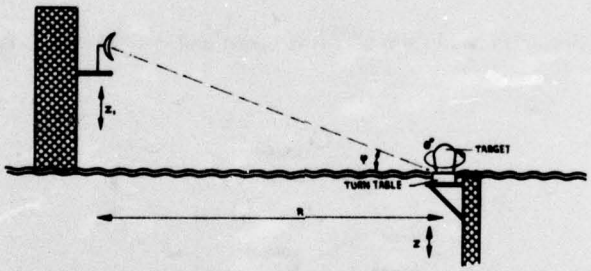

Fig.3 Multipath RCS measuring configuration

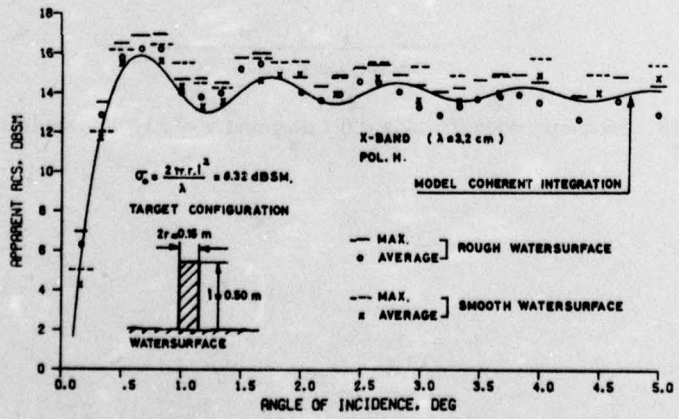

Fig.4 Results of measurement and calculation on a metal cylinder

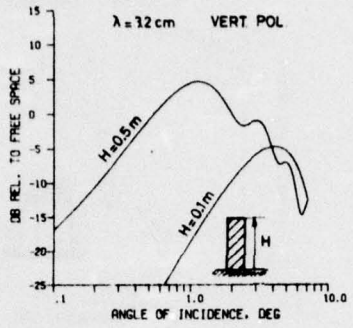

Fig.5 Results of calculation on a metal cylinder

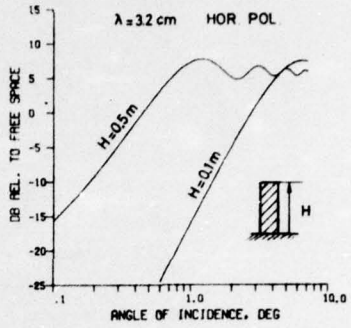

Fig.6 Results of calculation on a metal cylinder

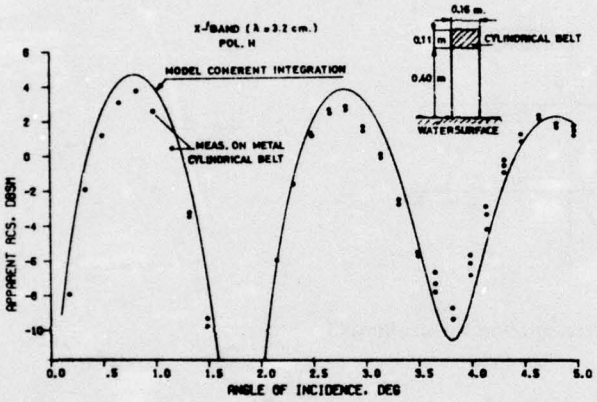

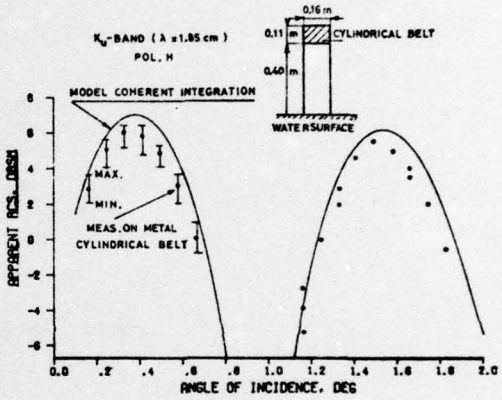

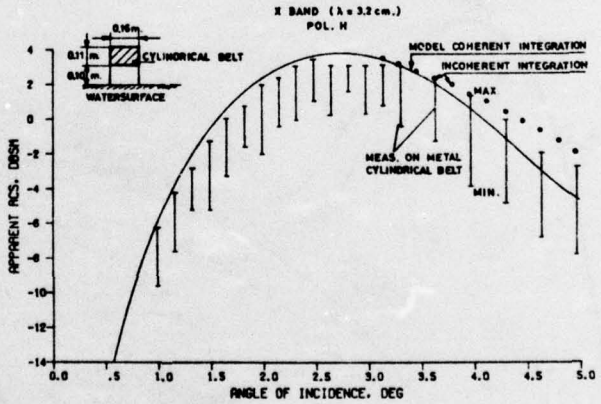

Fig.7 (1–3) Results of measurement and calculation on a cylindrical belt

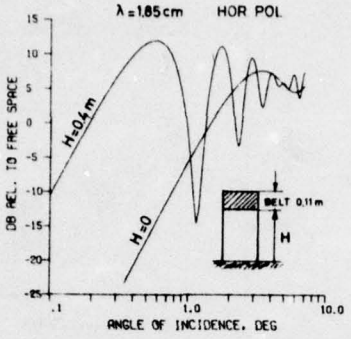

Fig.8 Farfield calculations on a cylindrical belt

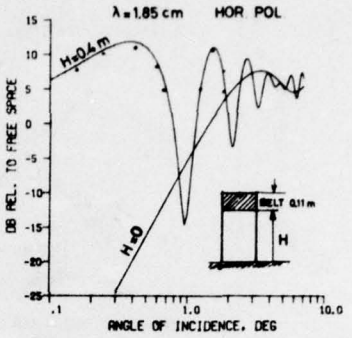

Fig.9 Short range measurement and calculation on a cylindrical belt

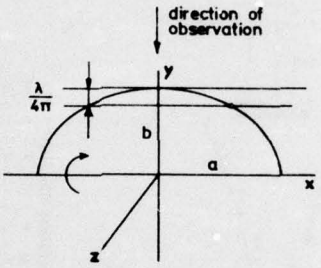

Fig.10 Belt height determination for an ellipsoid

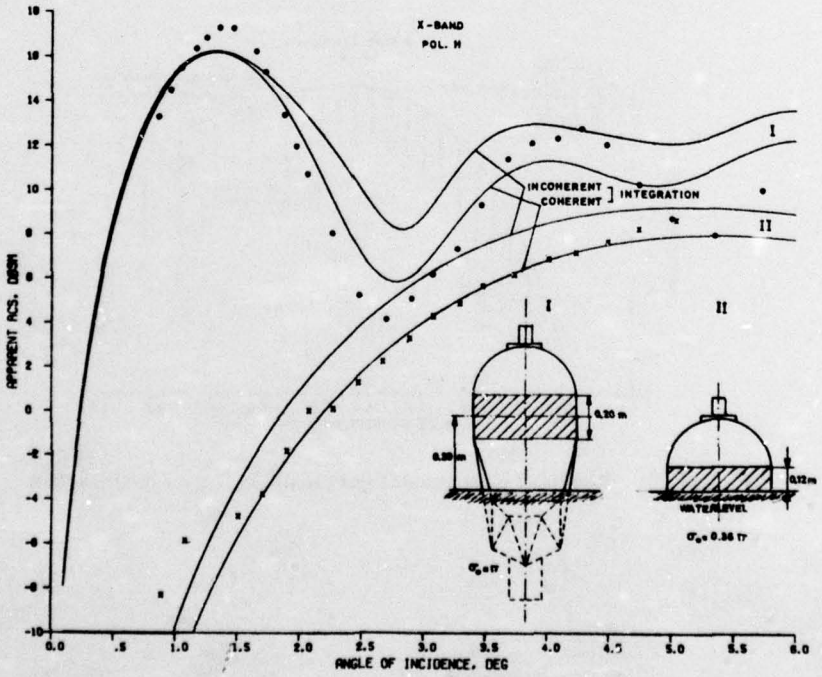

Fig.11 Results of measurement and calculation on a floating buoy

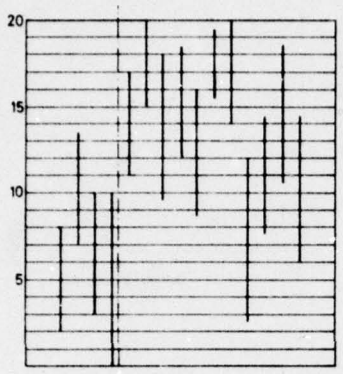

Fig.12 Arbitrarily chosen targets projected on a reference plane

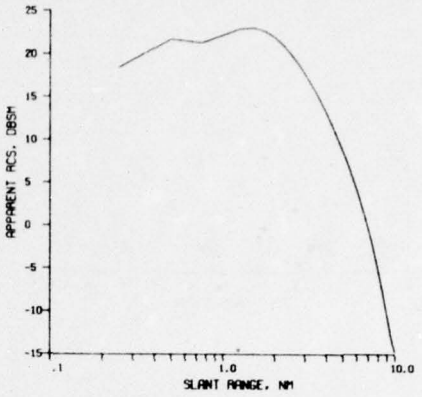

Fig.13 Multipath (voltage) RCS approximation for a cluster of 4 targets

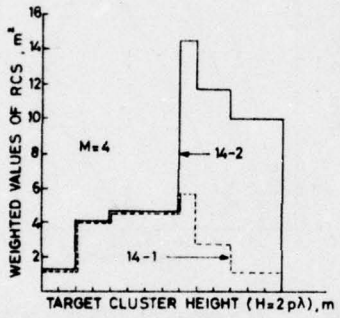

Fig.14 Weighting function for a cluster of 4 targets

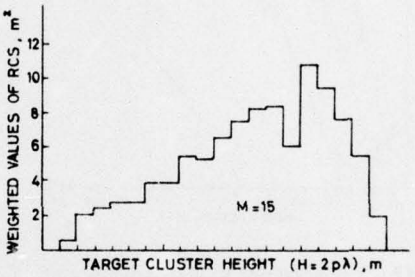

Fig.15 Weighting function for a cluster of 15 targets

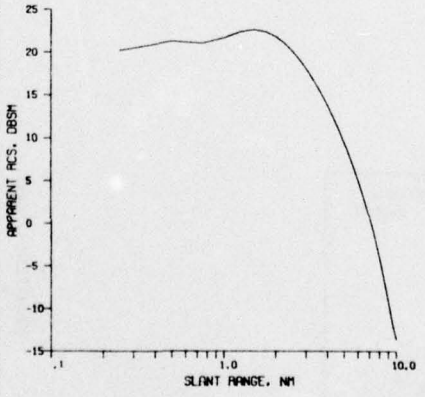

Fig.16 Multipath (power) RCS approximation for a cluster of 4 targets

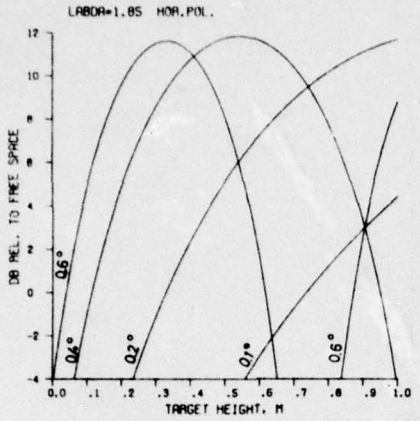

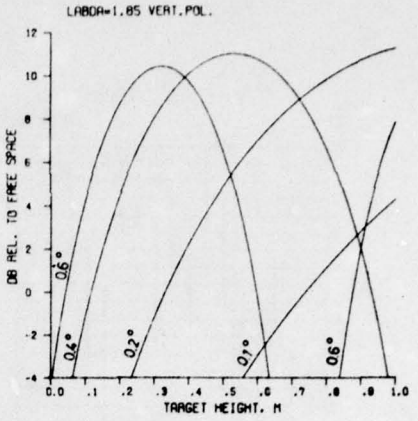

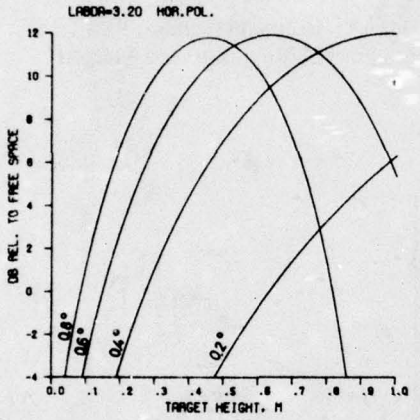

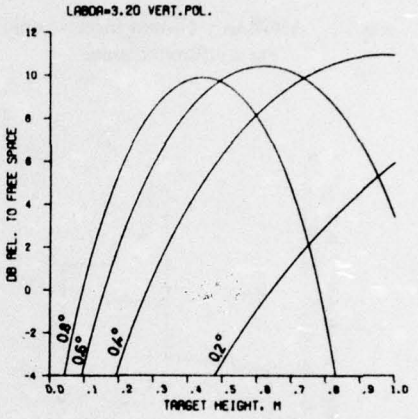

Fig.17 The apparent RCS of a buoy vs its height above water, with the angle of incidence as a parameter

Fig.18 The apparent RCS of a buoy vs its height above water, with the angle of incidence as a parameter

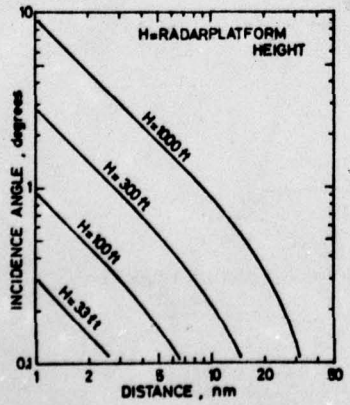

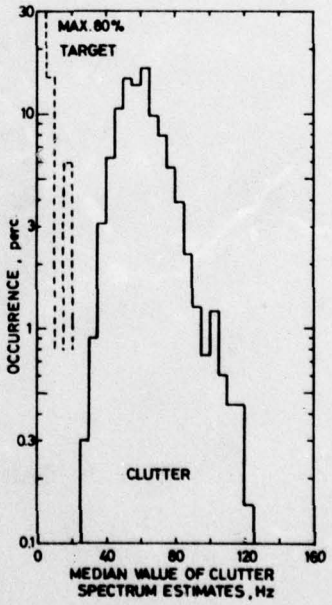

Fig.19 The incidence angle vs distance, with the radar height as parameter

Fig.20 Typical target (buoy) and clutter spectrum estimates

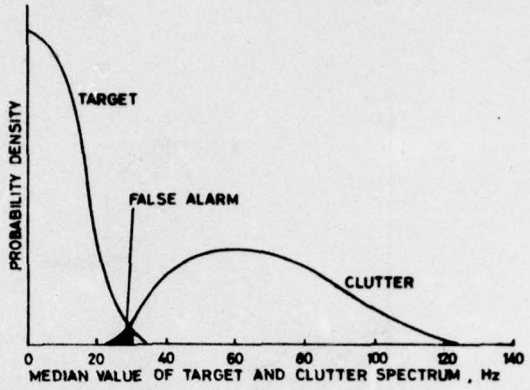

Fig.21 Probability density functions of median values of target and clutter spectrum estimates

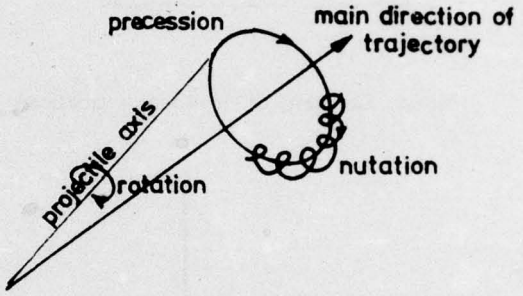

Fig.22 Precession, nutation and rotation of a projectile

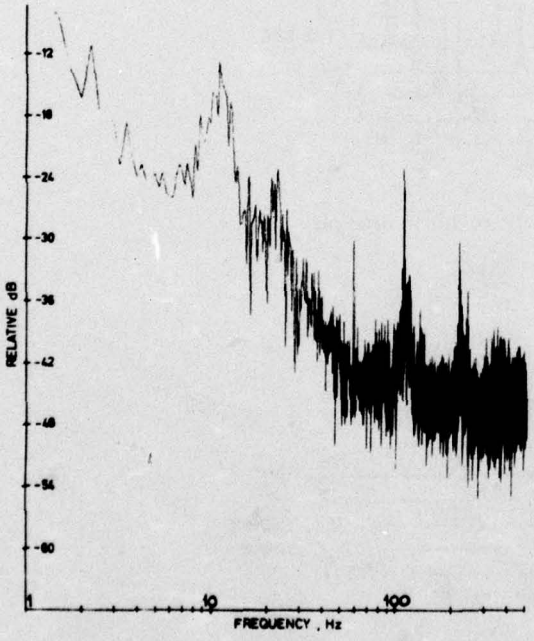

Fig.23 Typical scintillation spectrum of body in flight

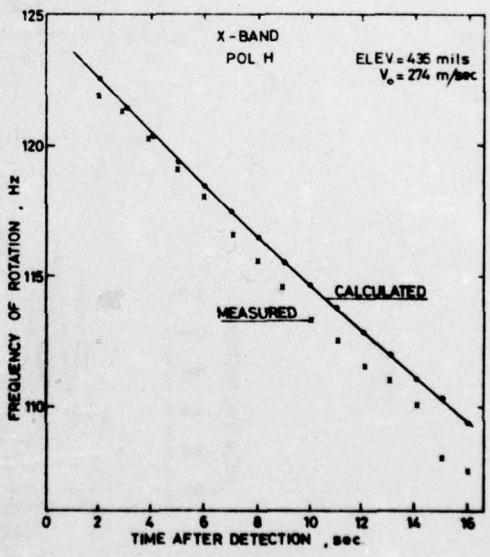

Fig.24 Measured and calculated decrease of the frequency of rotation

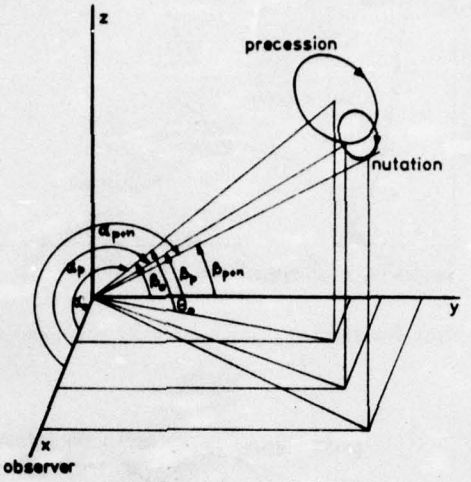

Fig.25 Geometry of target aspect variations

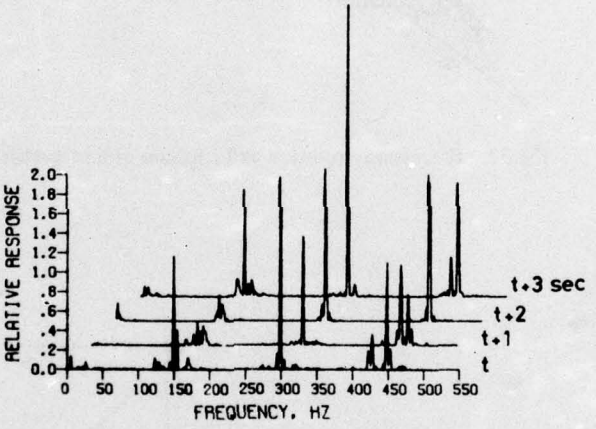

Fig.26 Simulated scintillations, due to rotation

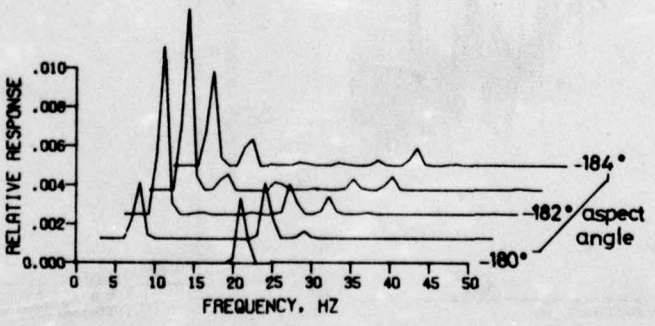

Fig.27 Simulated scintillations, due to precession and nutation

DISCUSSION

B C KAYSERILIOGLU: 1) Why do you use wind speed as a parameter to define the σ_o of the sea? Could you equally well use sea state?

2) What is the σ_o of the sea clutter at K_u band with circular polarisation?

H SITTROP: 1) Bragg-resonant capillary waves are generated or increased almost instantly by an increase in wind and hence also the σ_o. The definition of sea state is coupled to a certain 'fetch' and 'duration' and does not necessarily give a good description of capillary waves. Conversely a sudden decrease of wind reduces the amount of capillary waves significantly and hence also the σ_o. The sea state however may remain the same for some time or reduce much more slowly. Therefore the use of sea state as a variable is inadequate and outdated; it is an inheritance of the time when facet-scattering was recognised as the only scattering mechanism.

2) Unfortunately we have no information available at these polarisations.

A L C QUIGLEY: I am interested in the possibility of eliminating sea clutter returns from a tracker radar by stationary plot filtering. To do this I need sea clutter spectral data which was gathered using a patch which moves with the sea. Do you know if data has ever been gathered in this way?

H SITTROP: NRL has collected sea clutter data from a flying platform. However I doubt whether they have done that with the purpose you have in mind. However, I believe that you can extract the information you need from the short-pulse results I presented in my paper. Returns at vertical polarisation are insensitive to the movement of shorter gravity waves which are driven by the wind. The clutter then depends merely on capillary waves. Hence, application of vertical polarisation will result in a stationary spectral return, which will depend only on windspeed. Obviously a sudden wind gust will introduce discontinuity effects at the wind front. I recommend you to have a close look at Figs 13, 14, 15 and 16 of my paper, including the relevant sections on shorter pulse lengths.

A REAL-TIME RADAR ENVIRONMENT SIMULATION

G. E. Pollon
Malibu Research Associates
Santa Monica, California, USA

J. F. Walker
Technology Service Corporation
Santa Monica, California, USA

SUMMARY

A new approach to radar development and testing using real-time signal simulation has recently been developed and successfully demonstrated in the development of a major phased-array radar system--the AN/TPQ-37 Artillery Location Radar. This concept is the use of a real-time Radar Environment Simulation System (RESS) to serve as a test bed for the development and test of the host radar. The RESS generates target and clutter environment signal returns for insertion into the radar front-end video signal stream.

The main feature of the RESS concept is its direct application of realistic target and clutter models to radar testing. Complex environmental models are used in an off-line general purpose computer to generate signal control tapes, which are used in an on-line, real-time signal simulation unit. The on-line system is interactive with the radar, i.e., it generates signal modulations due to beam scanning and transmitted waveform in real time on cue from the radar transmission. Target characteristics which are reflected in the RESS output signals include detailed prescribed trajectories and RCS fluctuation models. Over 100 independent targets can be generated thus simulating a highly complex test environment. Clutter properties include spectral shapes, amplitude fluctuation, and spacial non-homogenities. Clutter types include ground, rain, and false targets.

1. INTRODUCTION

The Radar Environment Simulator System was developed under the sponsorship of the Program Manager - MALOR, and the CSTA Laboratory, U.S. Army Electronics Command, Fort Monmouth, New Jersey, at Technology Service Corporation, Santa Monica, California. To date, the RESS has been intensively used in the development of three computer-controlled phased-array radars; most notably the highly successful U.S. Army AN/TPQ-37 Artillery Location Radar. (HARRISON, W. J., 1975)

Figure 1 illustrates the authors' estimate of an example of the typical accumulated hours of RESS use in these radar developments, extending over a period of approximately eighteen months from the time of first completion of a portion of the signal processor to live field testing of the radar set. Also shown in Figure 1 are continued expected uses of the RESS through operator training and comprehensive performance evaluation.

The RESS real-time simulation has proven itself to be a highly valuable tool in radar processing development and testing. It was enthusiastically accepted by both the radar-hardware contractors, who used it as a continual debugging and test tool, and by the U.S. Army Program Manager who used it as a test bed to accurately monitor hardware and software development progress. The system test results obtained with the RESS proved to be highly correlated with the live field test results. The RESS was employed in parallel with the live field testing to further explore problem areas as they arose and to serve as a test bed for evaluating the performance impact of changes as they were made to the systems.

It is hard to place a dollar savings on the above uses of the real-time simulation, but surely it amounts to a significant percentage of the radar development and testing costs. The RESS has been credited with savings of a minimum of six months in the radar development time in at least two of the above mentioned cases.

2. REAL-TIME SIMULATION

The real-time generation of radar signals for use with actual radar processing represents the final stage in the application of radar simulation technology to its ultimate objective, the testing of the radar hardware and its associated system. The pacing considerations in this type of simulation, compared to one which is fully computer implemented, are the speed requirements of the on-line signal generation and the interactive nature of the radar with the state of the environment. The relationships between the critical off-line and on-line components of the simulation are essentially dictated by these considerations as they apply to the object radar and its operating environment.

It is important to realize that the practical feasibility of a real-time radar signal simulation is based on the nature of the received radar signal which, for all practical purposes, consists of delayed and Doppler shifted replicas of the transmitted waveform. The entire information content of the environment exists as modulations of the transmitted waveform.

The applications of a well conceived, real-time radar signal simulation extend through all phases of the development, test, and operational use of the object radar. Such a simulation can be used as a test bed for radar data processing development and debugging, as a tool for testing and evaluating a completed prototype system, for operator training, and for exercising the radar as an element

in a total system, all being accomplished without the benefit of live operating time on targets and clutter. Such a simulation is useable for the superposition of terrain and weather clutter on true target signals, and for simulating targets under actual clutter conditions. A real-time environment simulation is able to produce test conditions that include the entire target and clutter environment behavior; thus, a single simulated test signal injected into the front of the radar will properly exercise all radar signal processing functions, including MTI, CFAR, and detection, and all data processing functions including discrimination, tracking, data handling, and display. Operator functions can also be exercised.

The real-time simulation involves five distinct processing operations:

a)	Data Base Generation	- done off-line with general-purpose computer
b)	Bulk Data Storage and Transfer	- via magnetic tape
c)	On-Line Processing	- with a minicomputer
d)	Signal Generation	- with special-purpose digital hardware
e)	Real-Time Output	- D/A conversion and analog processing

The realism and ultimate credibility of the simulation depends most heavily on the data base generation since this is where the target trajectories, RCS data, and fluctuation, and the clutter spectral and spacial characteristics are established. The cost of the simulation, on the other hand, is dominated by the real-time signal generation and output functions since these must be accomplished with special-purpose hardware, in any reasonable case of target and clutter density.

3. THE RADAR ENVIRONMENT SIMULATOR SYSTEM (RESS)

Figure 3 shows a block diagram and Figure 4 a photograph of the real-time Radar Environment Simulator System. The signal generator is comprised of separate target generation and clutter generation units. Table 1 provides the performance characteristics of the RESS. The target scenario, which can last up to one hour depending upon its complexity, is contained on the magnetic tape. An on-line minicomputer is used in the RESS to provide a high degree of operator on-line controllability. Through teletype entered commands during initialization, the operator selects ground and rain clutter spatial distributions, spectral shape, bandwidth, and velocity offset from several models that have been pre-stored on tape. The simulation target scenario can be configured on-line as desired from those target flights which have been provided in the pre-generated scenario.

To date over 10,000 hours of simulation operating time have been accumulated with five different radars. The characteristics of these radars cover a wide range, but all radars are serviced by similar on-line simulation units having different off-line generated data bases. The radars include mechanical, phase, and frequency one-dimension scan, and phase-phase and phase-frequency two-dimensional scan antenna types. The beamwidths, sectors, PRF's, and bandwidths of these radars vary by over an order of magnitude. Virtually all radar bands are represented. Signal processing types include digital pulse compression, digital MTI cancelers, and Doppler filter banks. Power levels vary by over an order of magnitude. Both monopulse and sequential lobing tracking are represented. The radars also employ computer processing and control and are highly interactive with the environment, performing search, track, discrimination, and other data processing functions.

Table 1. Typical Characteristics of Real-Time Radar Environment Simulator System

TARGETS	
Number of Simultaneous Targets	30 High-speed plus 100 Slow-speed
Parameter Quantization	.12 Milliradian azimuth/elevation 15 Meters range .40 dB RCS .90 m/s Velocity
Parameter Range	± 60° azimuth ± 30° elevation 270 km range ± 1000 m/s velocity 48 dB dynamic range
CLUTTER	
Number of Range Gates per Beam	128
Dynamic Range	54 dB
Spurious Signals	< -54 dB

4. DATA-BASE GENERATION

The data-base generation is the basic simulation process by which descriptions of the target and clutter environment are provided to the on-line processing. The data-base generation is based on models for the target and clutter environment and the known characteristics of the radar. It is desirable to spend as much effort in preparing the data base as possible in order to ease the burden of real-time computation. However, this preparation of the data is limited by a lack of a priori knowledge of the sequence of events in the interactive radar. In addition, the amount of off-line data preparation is practically limited by the data volume and transfer speed problem between the off-line and on-line portions of the simulation. This limitation can be particularly severe in the generation of clutter signals.

The central feature of being able to use a GP computer to construct the data base is the potential to use realistic models and actual data for target and clutter representation, and the ability to perform a complex manipulation of these.

Figure 5 shows the block diagram of the general-purpose computer tape data-base generation. The target scenario is combined with a trajectory generator and radar cross-section data (or fluctuation model) to obtain discrete time update points for each target in radar coordinates--range, azimuth, elevation, range rate, and amplitude. The latter is computed as a function of instantaneous aspect angle.

The clutter data--for ground and rain--which are generated for the taped data base include spatial models and spectral models. The former is put on tape as a backscatter coefficient σ_o map which has non-homogeneities, shadowing, and terrain type included. The latter is put on tape as samples of a random process having the desired spectral shape (see 6, below). These samples are obtained by performing an Inverse Fast Fourier Transform on samples of the desired model spectral shape.

Examples of models which have been used in the data-base generation include:

Targets:

Live RCS data - table look-up and transformation

Chi - Squared fluctuation models (SWERLING, P., 1965)

Log - Normal fluctuation models (HEIDBREDER, G. R., 1967)

Modified point mass ballistic trajectories

Linear trajectories

Clutter:

Log-Normal Spatial non-homogeneity (GREENSTEIN, L. J., 1969; FISHBEIN, W. S., 1967)

Gaussian and f-cubed (FISHBEIN, W. S. 1967) spectral shapes

Velocity offset

Radar angel characteristics (POLLON, G. E., 1972; KONRAD, J. G., 1968)

Finally, as indicated in Figure 5, basic radar data such as antenna patterns are stored on the data-base tape.

5. TARGET SIGNAL GENERATION

The target generator computes the real-time coherent target pulses based on the instantaneous radar transmisson parameters--beam position and waveform--and the current target descriptor parameters--range, azimuth, elevation, range-rate, and amplitude--as provided by the tape inputs and modified by the preprocessor. The interactivity between the real-time simulation and the radar takes place in the signal generator, as this is the prime component that is responsive to the instantaneous radar transmission. The structure and speed of the entire simulation is based largely on the parameters of the interface between the simulation and the radar, since they determine both the amount of off-line computation that can be performed and the complexity and speed on the on-line signal generator operations.

Figure 6 shows the block diagram of the interactive target signal computation. It operates on a pulse-by-pulse basis. The operations involved are the computation of the antenna beam pattern--including monopulse patterns--and the computation of the target phase. The former depends on the antenna beam pointing angle and the latter on the current radar frequency and time of pulse transmission (PRF). These are combined with the instantaneous target amplitude to produce the target in-phase and quadrature components.

In all cases of practical interest with a pulsed radar, the signal generator response to the transmitted waveform is considered to be a delayed and Doppler shifted replica of the transmitted waveform applied to each point in the target and clutter environment. It is assumed that the instantaneous waveform bandwidth is not sufficiently wide to result in either spatial beamshape or Doppler smearing. Either case can be accommodated in principle, but it greatly complicates the simulation implementation.

It is convenient to separate the signal generation into the computation of the initial amplitude and phase of a pulse and the production of the pulse waveform. The former operation represents the environment response to an ideal or infinitesimally narrow pulse transmission while the latter applies

the finite resolution and coding properties of the transmitted pulse. The interactive signal generator operation takes place on a time scale corresponding to the interpulse period and beam dwell time while the pulse waveform formation occurs on a time scale that corresponds to the signal bandwidth. The latter operation, including pulse coding (if any) takes place in the output waveform generator, which also provides the precise timing and superposition of the individual target outputs. Finally, the real-time digital data is D/A converted, filtered, and inserted into the radar video signal stream or converted to the radar intermediate frequency.

6. DISTRIBUTED CLUTTER SIGNAL GENERATION

The clutter signal generation is similarly interactive with the radar beam position and transmissions. Pseudo-independent range samples of the clutter random process are generated at the radar signal-bandwidth rate, in each transmission interpulse period. At each range gate, successive pulse returns have the Doppler spectrum of the clutter process, but the magnitude of the clutter return varies with range, azimuth (and elevation), according to the input clutter spatial distribution. Ground and rain clutter Doppler spectra are superimposed. In the RESS, 128 (pseudo-) independent range samples are generated, which may be replicated to cover any portion of the interpulse period.

In the generation of the clutter, signal spectral purity is highly important if the simulation is to be used on an MTI radar featuring a high degree of clutter rejection. This presents a central problem in the simulation in which the basic clutter random process samples are generated off-line, since the instantaneous radar PRF is not a priori known.

Figure 7 illustrates the sequence of signal spectra that are involved. The original desired clutter signal, having an RMS bandwidth σ_c, is sampled in the off-line generator at an equivalent real-time rate of f_o and these samples are stored on the tape, having the spectrum in Figure 7b. In the on-line clutter generator these samples are used to produce samples at the radar PRF, by means of interpolation between the two nearest stored time samples corresponding to the radar pulse time. The spectrum after interpolation is shown in Figure 7c. Finally, Figure 7d shows the clutter spectrum as seen by the radar after resampling at the PRF. If

$$f_o \neq k \text{ PRF}$$

where k is an integer, then the interpolation residue appears as a spurious clutter signal to the radar which falls at some undesired spectral point between the PRF lines.

The magnitude of this residue r is approximately given by:

$$r = (\sigma_c/f_o)^2 \qquad \text{sample and hold}$$

$$r = 3\,(\sigma_c/f_o)^4 \qquad \text{linear interpolation}$$

$$r = 15\,(\sigma_c/f_o)^6 \qquad \text{quadratic interpolation}$$

for a Gaussian-shaped spectrum and in the absence of a clutter velocity shift. In the RESS, linear interpolation is used with a typical f_o = 2000 Hz so that for an example clutter RMS bandwidth of 50 Hz the residue is down by -59 decibels.

7. CONCLUSION

This paper has described the Radar Environment Simulation System (RESS). The RESS is a device which marries the environment generation realism of a large-scale general-purpose off-line data processor with the interactive on-line flexibility of a real-time minicomputer-controlled signal generation unit. The utility of the RESS during the development of several U.S. radar systems has been discussed. Finally, the major components of the RESS, including some of the basic design problems, have been described.

8. REFERENCES

1. FISHBEIN, W.S., W. Graveline, and O. E. Rittenbach, March 1967, "Clutter Attenuation Analysis," USAECOM Technical Report ECOM-2808, Fort Monmouth, New Jersey.

2. GREENSTEIN, L. J., A. Brindley and R. Carlson, 15 September 1969, "A Comprehensive Ground Clutter Model for Airborne Radars," ITT Research Institute, Chicago, Illinois.

3. HARRISON, W.J., May-June 1975, "Zero-In and Zap," National Defense Magazine, pp. 473-476.

4. HEIDBREDER, G. R. and R. L. Mitchell, "Detection Probabilities for Log-Normally Distributed Signals," IEEE Transactions on Aerospace and Electronic Systems, Vol. AES-3, No. 1.

5. KONRAD, J. G., J. J. Hicks, and E. B. Dobson, 19 January 1968, "Radar Characteristics of Birds in Flight," Science, Vol. 159, pp. 274-280.

6. NATHANSON, F. E., 1969, Radar Design Principles, McGraw-Hill, New York.

7. POLLON, G. E., November 1972, "Distribution of Radar Angels," IEEE Transactions on Aerospace and Electronic Systems, Vol. AES-8, pp. 721-727.

8. SWERLING, P., July 1965, "More on Detection of Fluctuating Targets," IEEE Transactions on Information Theory, Vol. IT-11, No. 3.

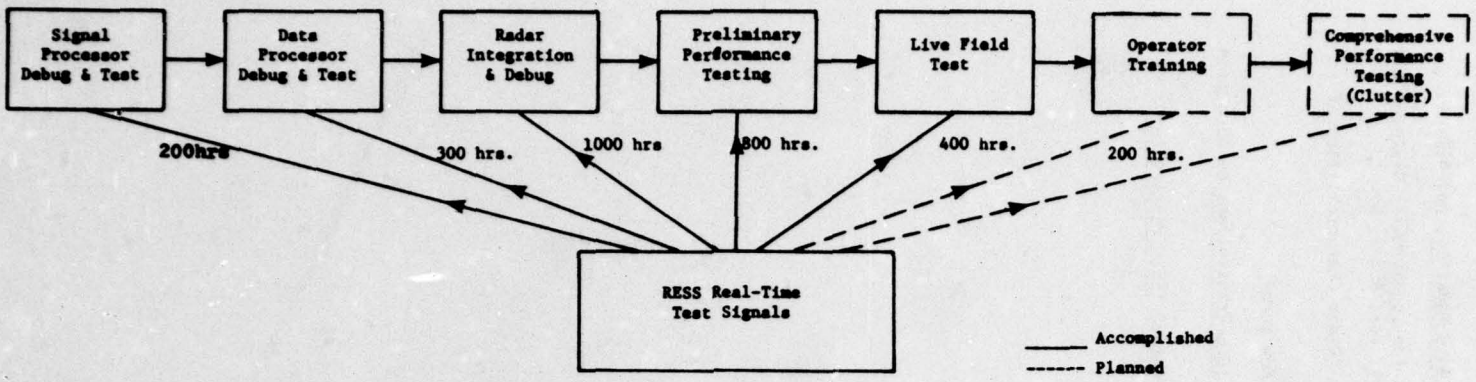

Figure 1. RESS Real-Time Simulation Use in Radar Development Cycle

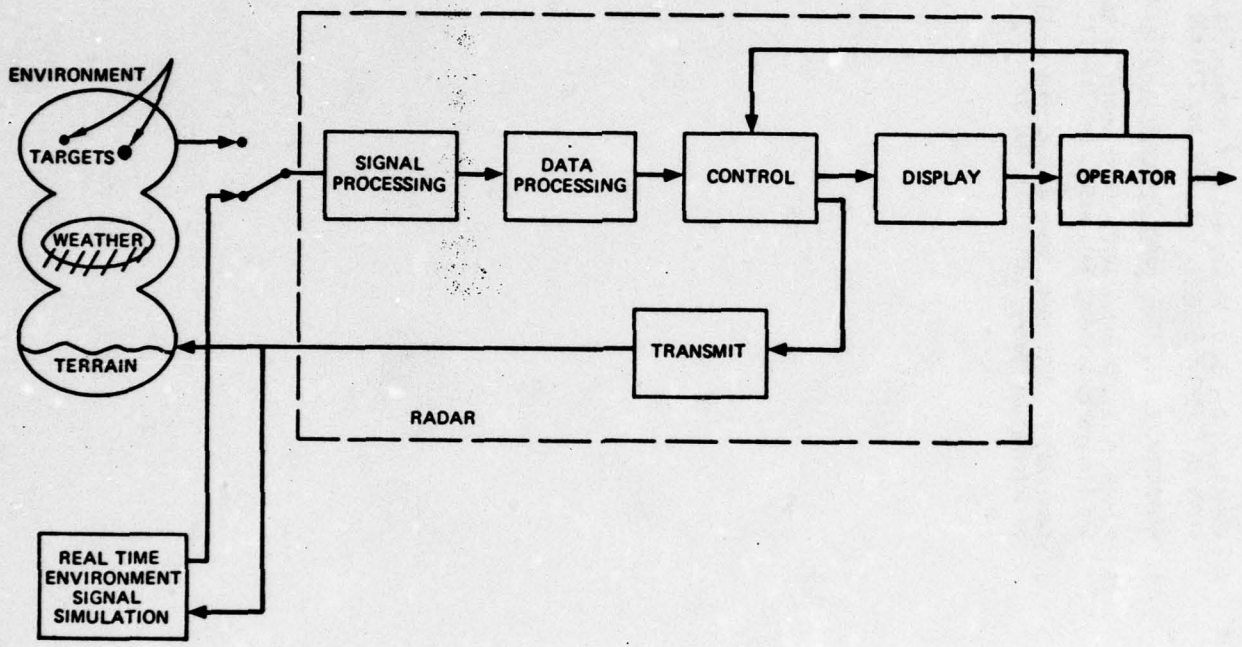

Figure 2. Real-Time Environment Signal Simulation for System Test

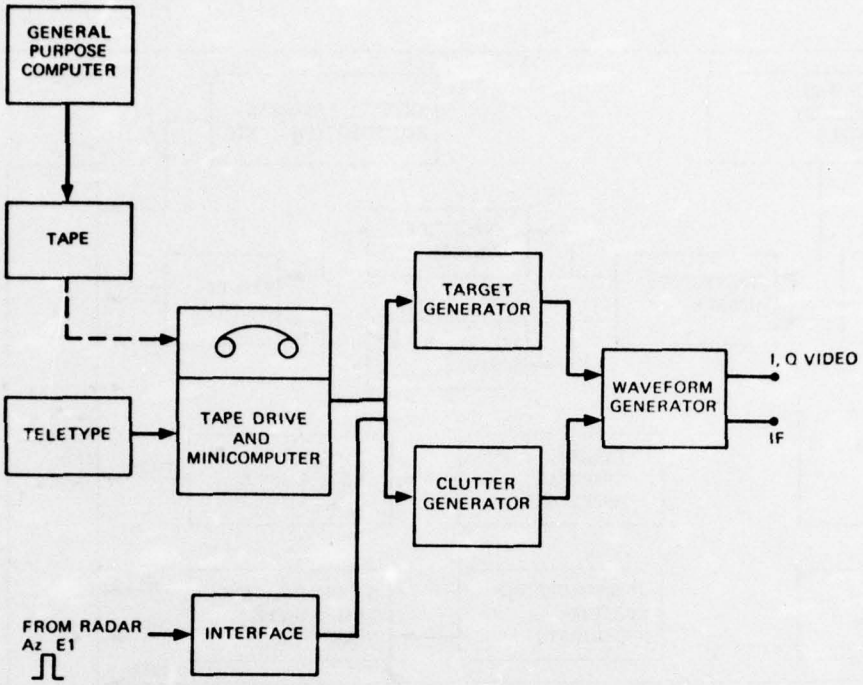

Figure 3. Block Diagram of RESS Real-Time Radar Signal Simulation

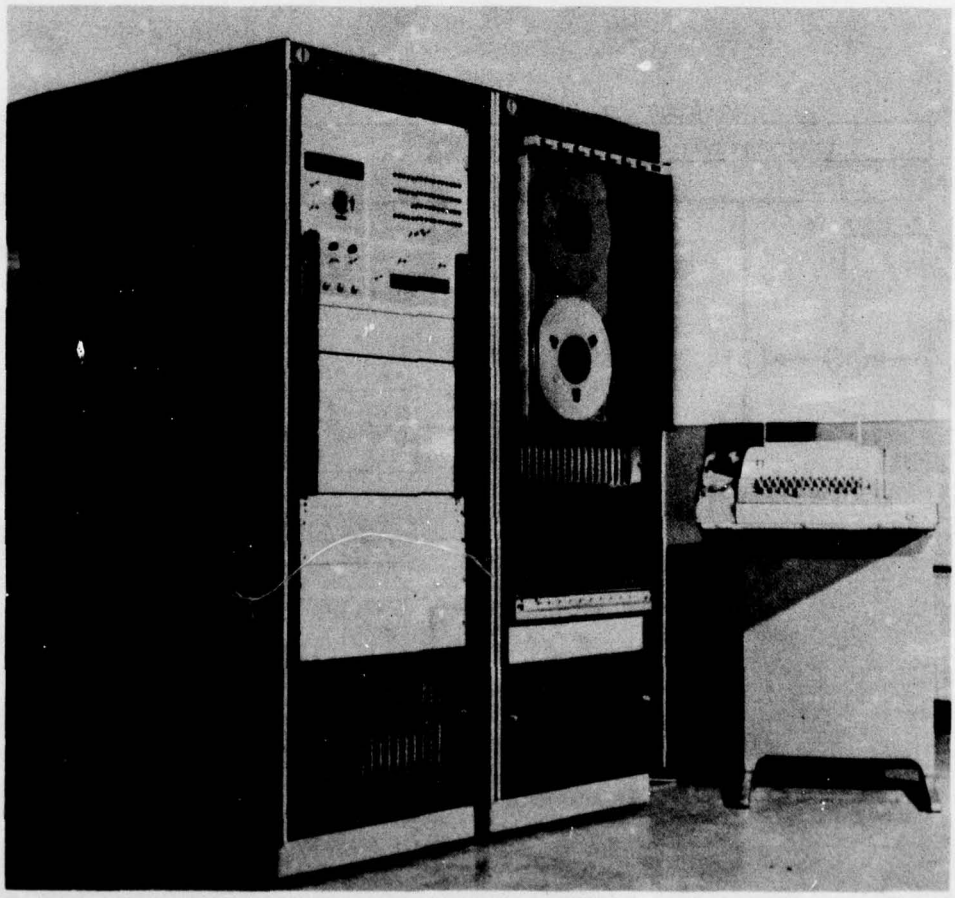

Figure 4. Radar Environment Simulation System (On-Line Components)

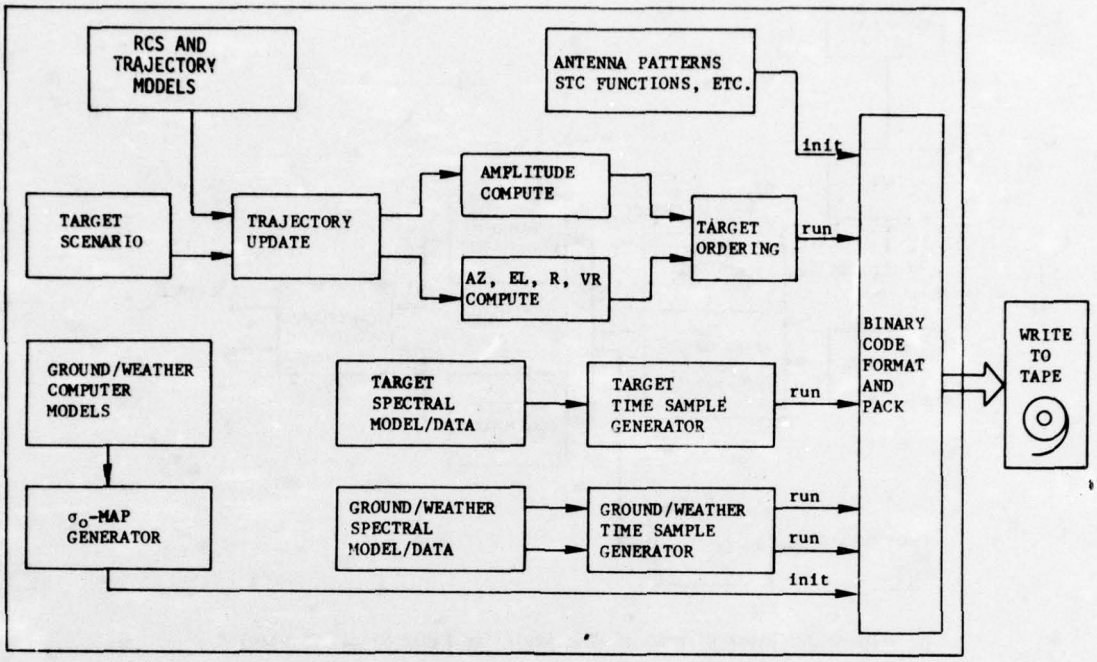

Figure 5. Data Base Generation

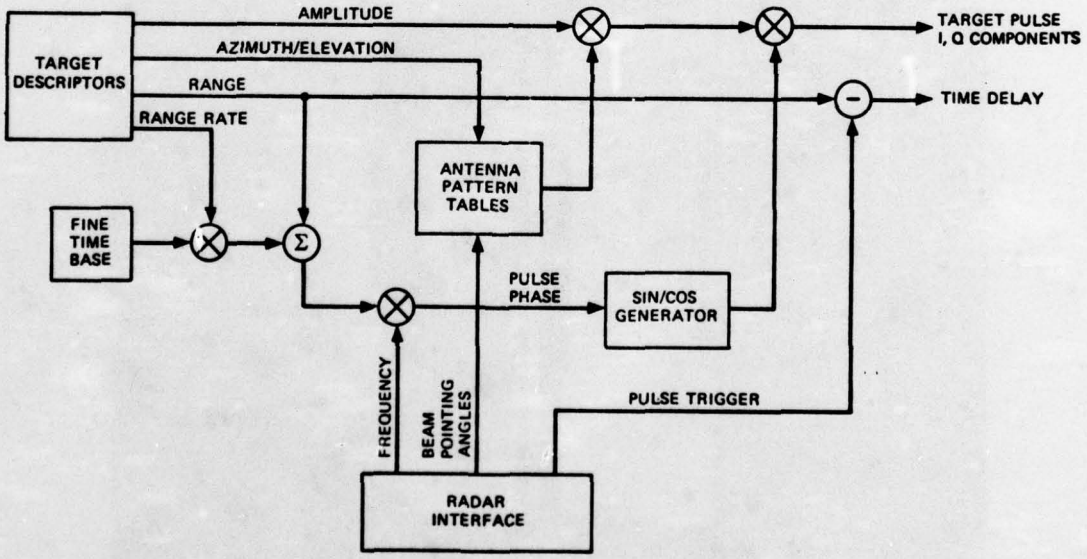

Figure 6. Interactive Target Signal Computation

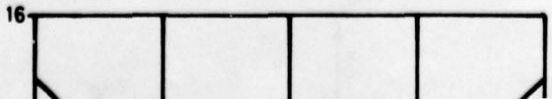

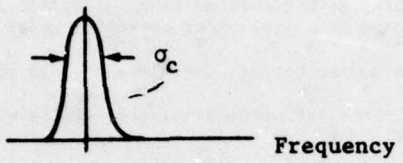

σ_c = clutter bandwidth - RMS

f_o = sampling rate

PRF = radar pulse repetition frequency

a) Original Clutter Spectrum

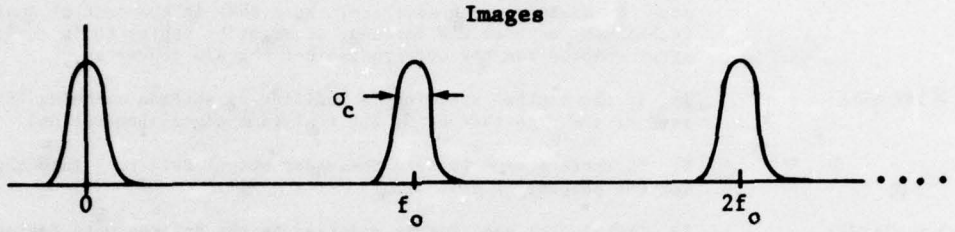

b) Sampled Clutter Spectrum

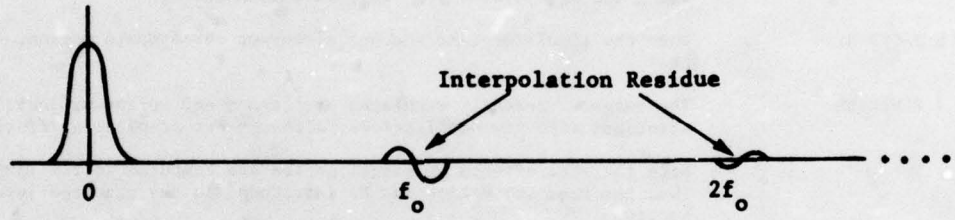

c) Interpolated Clutter Sample Spectrum

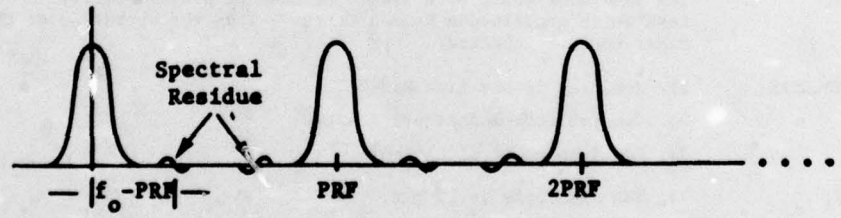

d) PRF Resampled Clutter Spectrum

Figure 7. Clutter Spectrum with Sampling Interpolation and Resampling

DISCUSSION

A J KAMPSTRA: 1) Can you indicate the limitations on target density, ie when one wants to simulate a raid of closely spaced aircraft? What is the maximum number of skin-echoes the RESS can produce at the same azimuth position?

2) Is it possible to superimpose a simulated radar signal (target aircraft) on a background of clutter obtained in a live radar operation mode?

J F WALKER: 1) A maximum of 40 targets may be output at a given azimuth position.

2) In practice all combinations are used; simulated targets with real background and vice versa.

G GALATI: An important feature of modern radars is the use of coded waveforms in transmission. How does the simulator take account of the radar waveform?

J F WALKER: The simulator performs signal generation in two steps. First the signal response to an ideal radar is computed. The result is passed to a pulse coder which generates the desired coded waveform. Note that in the case of analog compression techniques, such as SAW devices, it might be easier to inject the simulator signals after compression has occurred, after the A/D converter.

P BRADSELL: 1) If the clutter spectrum is modified by antenna scanning, is this dealt with as part of the data base or in the real-time signal generation?

2) Is there a need to feed the radar output data back into the simulation facility for the purpose of assessment?

J F WALKER: 1) The clutter spectrum is modified by the antenna scan during the real-time signal generation.

2) Since the output of location data occurs at slow data rate, it is quite easy to compare printout of locations from the radar to the actual locations used in generating the simulator tape. This is done manually.

B JACKSON: Does the simulator take account of target aerodynamic motion, eg yaw oscillations etc?

J F WALKER: The targets presently simulated are cannon and mortar projectiles. These are not simulated with yaw oscillations, although out-of-plane drift effects are included.

Note that the effects of target motion are computed in the large scale GP computer. Thus the required motion may be introduced to the required level of detail quite easily.

B C KAYSERILIOGLU: It could be a good idea to have Kalman filtering simulation in your simulator to check Kalman filter operation itself during tracking mode.

J F WALKER: The simulator would more likely be used to provide realistic data to a radar under test which contained a Kalman filter. Thus the operation of the filter within the radar could be checked.

G A VAN DER SPEK: 1) How fine is the time base?

2) Can you accommodate prf stagger?

3) Can jamming be simulated?

J F WALKER: 1) The time base is 10 MHz.

2) PRF stagger can be accommodated.

3) Any type of point target (ie a deception jammer) or distributed target (ie chaff, barrage) can be simulated.

RECONSIDERATION OF THE TARGET DETECTION CRITERION BASED ON ADAPTIVE ANTENNA POLARIZATIONS

A.J. Poelman
SHAPE TECHNICAL CENTRE
P.O. Box 174 - The Hague
The Netherlands

SUMMARY

This paper reconsiders the target detection problem taking into account the polarization state of the target backscattered and interference fields, and deals with radar object backscattering in terms of its scattering matrix. As the polarization state of an electromagnetic wave is a carrier of information, its employment may result in an improved target detection capability of the radar system both in natural and man-made interference environments. The study is concerned with adaptive suppression of unwanted signals by means of proper matching of the antenna polarizations at transmit and receive, and with consequent improvement in average target signal power to average unwanted signal power ratio at the input of the detection receiver. As the adaptive schemes require significant digital processing, it is advisable to study the applicability in particular in those areas, where a limited number of radar cells need to be treated simultaneously, e.g. in tracking radars.

1. INTRODUCTION

In most radar systems the target is usually regarded as a point source of return scattering and the backscattered wave at receive is processed by first converting to a scalar quantity. This scalar approach limits the information content which inherently is contained in the target return signal to cross-section and doppler-shift. The fact that the backscattered wave is depolarized due to the extension of the target is not exploited since the polarization vector is lost in the process. Most of nowadays operational radar systems employ circular polarization for rain clutter suppression. This is the only example of the utilization of the depolarization effect for improving the average wanted signal power to average unwanted signal power ratio at the input to the receiver. This improvement is based on the experience that unlike aircraft targets, the specular reflections for a rain cloud far dominate the non-specular reflections. Nevertheless at receive the backscattered waves are still converted to scalar quantities. A consequence of this approach is an observed loss of 3 to 6 dB in target detectability in rain clutter free sectors, since practice shows that for aircraft targets the specular reflections are of the same order as the non-specular reflections.

The vector approach on the other hand takes into account the polarization state of the transmitted wave and backscattered wave. It deals with target reflection in terms of its scattering matrix, which may be considered as a generalization of the radar cross-section type of observable. The motivation for studying the vector approach in target detection is, that improvements are expected in target detection performance in a clutter and interference environment. This would result from maximum suppression of the unwanted signals by means of proper adaptation of the antenna polarizations at transmit and receive. As a matter of fact any polarization vector state of a plane e.m. wave can be decomposed into two arbitrary orthogonal polarization vectors. Drawing full benefit of the vector approach for unwanted signal suppression requires two special features of the radar sensor:

- a transmission mode, such that orthogonally-polarized electro-magnetic pulses can alternately be radiated;
- orthogonally-polarized receive antennas and channels.

2. MATHEMATICAL DESCRIPTION OF POLARIZED WAVES AND ANTENNAS

2.1 General expressions for polarized waves and antennas

The mathematical description presented in this section is not new (HUYNEN, J.R., 1970), but is is necessary to go back to the basic theory in order to have a better grasp of the problem. In a cartesian right-handed x-y-z coordinate system, a time harmonic elliptically-polarized plane wave can be described by a complex electric field vector (E) which decomposes into the electric field components, E_y and E_x as follows

$$\underline{E} = \begin{bmatrix} E_y \\ E_x \end{bmatrix} = \begin{bmatrix} |E_y| \exp(j\delta_y) \\ |E_x| \exp(j\delta_x) \end{bmatrix} \qquad (1)$$

The same expression may be used to characterize the transmit antenna ($\underline{h}_T$) and the orthogonally-polarized receive antennas ($\underline{h}_R$ and $\underline{h}_{R_\perp}$). Normalized representations with the absolute phase discounted are:

$$\underline{h}_T = \begin{bmatrix} \cos(\varepsilon_T) \\ \sin(\varepsilon_T)\exp(j\delta_T) \end{bmatrix}, \underline{h}_R = \begin{bmatrix} \cos(\varepsilon_R) \\ \sin(\varepsilon_R)\exp(j\delta_R) \end{bmatrix}, \underline{h}_{R_\perp} = \begin{bmatrix} \sin(\varepsilon_R)\exp(-j\delta_R) \\ -\cos(\varepsilon_R) \end{bmatrix} \qquad (2)$$

with $\underline{h}_T \cdot \underline{h}_T^* = \underline{h}_R \cdot \underline{h}_R^* = \underline{h}_{R_\perp} \cdot \underline{h}_{R_\perp}^* = 1$, and $\underline{h}_R \cdot \underline{h}_{R_\perp}^* = 0$.

Here δ ($-180^\circ < \delta \leq 180^\circ$) represents the phase difference between the x and y (vertically- and horizontally-polarized) field components and ε ($0^\circ \leq \varepsilon \leq 90^\circ$) defines the ratio of the amplitudes of these components. If $-180^\circ < \delta \leq 0^\circ$, the sense of elliptical polarization is left-handed and if $0^\circ < \delta \leq 180^\circ$ it is called right-handed.

When one is only interested in amplitudes or powers the absolute phase is not a relevant parameter. A convenient representation then of an elliptically polarized plane electromagnetic wave and transmit and receive antennas is the "Stokes vector". The Stokes vector of an electromagnetic plane wave is related

to the electric field components (1) as follows:

$$h(\underline{E}) = \begin{bmatrix} h_0 \\ h_1 \\ h_2 \\ h_3 \end{bmatrix} = \begin{bmatrix} |E_y|^2 + |E_x|^2 \\ 2I_m\,(E_y^{*}E_x) \\ |E_y|^2 - |E_x|^2 \\ 2R_e(E_y^{*}E_x) \end{bmatrix} = (h_0,h_1,h_2,h_3) \qquad (3)$$

where $h_0 = [h_1^2+h_2^2+h_3^2]^{\frac{1}{2}}$ is the total power per unit area contained in the wave.

Furthermore, the expression for the power received (P), upon transmission between two antennas, $\underline{h}_1$ and $\underline{h}_2$, is of importance. Using the notation f for the Stokes parameters of antenna $\underline{h}_1$ and g for antenna $\underline{h}_2$, we have

$$P(\underline{h}_1,\underline{h}_2) = \tfrac{1}{2}\,(f_0g_0+f_1g_1+f_2g_2-f_3g_3), \qquad (4)$$

where the minus sign is due to a transformation of coordinates of antennas $\underline{h}_1$ and $\underline{h}_2$ facing each other, instead of being aligned in the same (z) direction. We shall henceforth include this minus sign in f_3 or g_3. Further the relation corresponding to $\underline{E}.\underline{E}_{\perp}^{*} = 0$ and $\underline{h}.\underline{h}_{\perp}^{*} = 0$ for orthogonally polarized waves and antennas in terms of Stokes vectors is given by,

$$g.g_{\perp} = 0 \qquad (5a)$$

or in other words,

$$\text{if } g = (g_0,g_1,g_2,g_3) \text{ then } g_{\perp} = G_{\perp}(g_0,-g_1,-g_2,-g_3), \qquad (5b)$$

where $G_{\perp}$ is a real quantity that can have any value.

2.2 Fixed objects

In the x-y-z reference frame adopted , the backscattered properties of a fixed, non time-varying radar object are completely described by its scattering matrix (T). When the law of reciprocity holds T can be written as

$$T = \begin{bmatrix} t_{yy} & t_{yx} \\ t_{yx} & t_{xx} \end{bmatrix} = \begin{bmatrix} a_{yy}\exp(j\alpha_{yy}) & a_{yx}\exp(j\alpha_{yx}) \\ a_{yx}\exp(j\alpha_{yx}) & a_{xx}\exp(j\alpha_{xx}) \end{bmatrix} \qquad (6)$$

the matrix elements being a function of radar wavelength , object orientation angle and aspect angle. Here the matrix T is defined in terms of horizontal (y) and vertical (x) polarization. It follows from (6) that ignoring the absolute phase, T is determined by five parameters, viz. three amplitude factors and two phase factors. Once T is known, the backscattered return from the object is known for any combination of polarized antennas $\underline{h}_T$ and $\underline{h}_R$.

The complex electric field vector of the backscattered wave ($\underline{E}_s$) is given by,

$$\underline{E}_s = \begin{bmatrix} E_y \\ E_x \end{bmatrix}_s = T\underline{h}_T, \qquad (7)$$

and the received voltages at the antenna terminals of $\underline{h}_R$ and $\underline{h}_{R_{\perp}}$ are determined by respectively

$$v_R = \underline{E}_s.\underline{h}_R = T\underline{h}_T.\underline{h}_R, \text{ and } v_{R_{\perp}} = \underline{E}_s.\underline{h}_{R_{\perp}} = T\underline{h}_T.\underline{h}_{R_{\perp}} \qquad (8)$$

In case $\underline{h}_T=\underline{h}_R=\underline{h}$, it follows from (8) that $\underline{h}$ may be chosen such that

$$T\underline{h} = c\underline{h}_{\perp}^{*} \qquad (9)$$

and consequently

$$v_R = 0 \text{ and } v_{R_{\perp}} = c|\underline{h}_{\perp}|^2 \qquad (10)$$

It has been proved that (9) results in two solutions for $\underline{h}$, which are called the characteristic "null-polarizations" of the radar object. It follows from (6), (7), and (8), that the matrix T can be completely determined by the measurements of $|v_R|$, $|v_{R_{\perp}}|$, and $v_R v_{R_{\perp}}^{*}$ with horizontally- and vertically-polarized receiving channels (thus absolute phase of T excluded), for horizontally- and vertically-polarized object illuminations (HUYNEN, J.R., 1965). Further the total backscattered power and the received powers are given by,

$$P_s = \underline{E}_s.\underline{E}_s^{*} = (T\underline{h}_T).(T\underline{h}_T)^{*},$$

$$\text{and} \quad P_R = |v_R|^2 = (T\underline{h}_T.\underline{h}_R)(T\underline{h}_T.\underline{h}_R)^{*},\ P_{R_{\perp}} = |v_{R_{\perp}}|^2 = (T\underline{h}_T.\underline{h}_{R_{\perp}})(T\underline{h}_T.\underline{h}_{R_{\perp}})^{*} \qquad (11)$$

Alternatively one can formulate expressions for P_R and $P_{R_{\perp}}$ as follows

$$P_R = M\,f(\underline{h}_T).g(\underline{h}_R) = h(\underline{E}_s).g(\underline{h}_R),\ P_{R_{\perp}} = M\,f(\underline{h}_T).g_{\perp}(\underline{h}_{R_{\perp}}) = h(\underline{E}_s).g_{\perp}(\underline{h}_{R_{\perp}}), \qquad (12)$$

where f, g, and h are Stokes vectors, as defined in (3), and M is the so-called Stokes reflection matrix of the object.

The factor one-half, see (4) is included in M. The object is now represented by the 4 x 4 Stokes reflection matrix M instead of the 2 x 2 matrix T. M will be written in the following form

$$M = \begin{bmatrix} (A_0+B_0) & F & C & H \\ F & (-A_0+B_0) & G & D \\ C & G & (A_0+B) & E \\ H & D & E & (A_0-B) \end{bmatrix} \tag{13}$$

for a given radar frequency, object orientation angle and aspect angle. It is noted that ignoring the absolute phase of T, there is a one-to-one correspondence between the matrix T and matrix M representations of fixed radar objects ((11) and (12)). Consequently the nine parameters of M in (13) can not be independent; these nine parameters are uniquely determined by the five parameters of T.

2.3 Time varying objects and fields

When the radar object is time-varying, a time-varying elliptically-polarized backscattered wave is observed with complex electric field components $E_x(t)$ and $E_y(t)$. In this paper the time variations of the backscattered wave or interference wave are attributed to random processes in which the absolute phases of the components $E_y(t)$ and $E_y(t)$ are uniformly distributed and independent of the moduli; consequently $\langle E_x(t)\rangle$ and $\langle E_y(t)\rangle$ are zero (the angular brackets represent time averages). It is then customary to define a time-varying partially-polarized plane wave in terms of the coherency matrix or the average Stokes vector of the complex field components $E_x(t)$ and $E_y(t)$, which both are second-moment characterizations. In this paper the average Stokes vector representation will be used. It follows (3),

$$h\{\langle \underline{E}(t)\rangle\} = \begin{bmatrix} h_0 \\ h_1 \\ h_2 \\ h_3 \end{bmatrix} = \begin{bmatrix} \langle|E_y|^2\rangle + \langle|E_x|^2\rangle \\ 2\,\langle \mathrm{Im}(E_y^* E_x)\rangle \\ \langle|E_y|^2\rangle - \langle|E_x|^2\rangle \\ 2\,\langle \mathrm{Re}(E_y^* E_x)\rangle \end{bmatrix} \tag{14}$$

where

$$h_0^2 \geq h_1^2 + h_2^2 + h_3^2.$$

Here the equal sign holds when the wave is completely polarized, and the wave is completely unpolarized or randomly polarized if $h_1 = h_2 = h_3 = 0$.

A decomposition theorem states, that any partially polarized wave may be regarded as the sum of a completely polarized wave and a completely unpolarized wave, which are mutually independent; this representation is unique. (BORN, M., and WOLF, E., 1965). In terms of average Stokes vectors (14)

$$h\{\langle \underline{E}(t)\rangle\} = (\bar{h}_0, h_1, h_2, h_3) + (h_0 - \bar{h}_0, 0, 0, 0) \tag{15}$$

where $\bar{h}_0 = (h_1^2+h_2^2+h_3^2)^{\frac{1}{2}}$ is the power contained in the completely polarized portion and $(h_0-\bar{h}_0)$ the power in the completely unpolarized portion. The ratio of the power contained in the completely polarized portion to the total average power is called "DEGREE OF POLARIZATION", p, of the wave (BORN, M., and WOLF, E., 1965)

$$p = \frac{\bar{h}_0}{h_0} = \frac{(h_1^2+h_2^2+h_3^2)^{\frac{1}{2}}}{h_0}, \quad 0 \leq p \leq 1. \tag{16}$$

It follows from (4) and (5), that the normalized receive antenna polarization producing a minimum average response, $\langle P_R\rangle_{min}$, to the incoming field (15), is given by

$$g(\underline{h}_R) = \{1, g_1, g_2, g_3\} = \{1, -h_1/\bar{h}_0, -h_2/\bar{h}_0, -h_3/\bar{h}_0\}, \tag{17}$$

and the normalized orthogonal receive antenna polarization then yields $\langle P_{R\perp}\rangle_{max}$.
In terms of h_o and p,

$$\langle P_R\rangle_{min} = \tfrac{1}{2}h\{\langle \underline{E}(t)\rangle\}.g(\underline{h}_R) = \tfrac{1}{2}h_o(1-p); \langle P_R\rangle_{max} = \tfrac{1}{2}h\{\langle \underline{E}(t)\rangle\}.g_\perp(\underline{h}_{R_\perp}) = \tfrac{1}{2}h_o(1+p) \tag{18}$$

The parameter p plays an important role in the suppression of unwanted signals through adaptation of the antenna polarizations.

In case of radar scattering from moving objects, time-averaged measured powers are used to characterize its reflective properties. The average power is obtained from (12):

$$\langle P_R\rangle = \langle M\rangle f(\underline{h}_T).g(\underline{h}_R), \text{ and } \langle P_{R_\perp}\rangle = \langle M\rangle f(\underline{h}_T).g_\perp(\underline{h}_{R_\perp}), \tag{19}$$

where the averaging is applied to all matrix elements of the Stokes reflection matrix (13).
It is noted that the degree of polarization of the backscattered wave $\langle M\rangle f(\underline{h}_T)$ depends on the antenna polarization at transmit (POELMAN, A.J.,1975/2). The average Stokes reflection matrix, $R=\langle M\rangle$ now is determined by 9 independent parameters, while as we have seen before, the scattering matrix of a fixed object is determined by 5 parameters (absolute phase excluded). Consequently, the class of averaged time-varying objects is larger than of that of fixed objects. It has been proved, that the average return from a time-varying object $R=\langle M\rangle$ may be decomposed into a component due to an average fixed object

M and a component N, which arises from changes from the average fixed object and thus will have a noisy behaviour.

In analogy with (9) and (10), $\underline{h}_T=\underline{h}_R=\underline{h}$ in (19) may be chosen such, that $\langle P_R\rangle = \langle P_R\rangle_{min}$. Also here there exists in general two solutions for $\underline{h}$ (POELMAN, A.J., and van der VOORT, J.P., 1972), which might be called the object "average minimum polarizations".

The elements of R=<M> of a radar object can be estimated , by means of alternate transmission of N orthogonally-polarized pulses (e.g. horizontal and vertical polarization) and reception of the returns in orthogonally-polarized channels. The 9 estimates (6)

$$\langle|t_{yy}|^2\rangle,\langle|t_{xx}|^2\rangle,\langle|t_{yx}|^2\rangle,\langle t_{yy}t^*_{xx}\rangle,\langle t_{yy}t^*_{yx}\rangle,\langle t_{xx}t^*_{yx}\rangle,$$

then determine R=<M>.

Equation (19) may be worked out for different cases of radar transmission and reception. Of particular interest is transmission of circularly-polarized (CP) waves and separate right-circular (RC) and left-circular (LC) reception. It follows for the average received powers,

$$\langle P_R\ (RC\text{-}RC)\rangle = 2(B_0+F),\ \langle P_R\ (LC\text{-}LC)\rangle = 2(B_0-F), \tag{20}$$

$$\langle P_{R_\perp}(RC\text{-}LC)\rangle = \langle P_{R_\perp}(LC\text{-}RC)\rangle = 2A_0,\ \text{where } A_o,\ B_o, \text{ and F represent averaged quantities.}$$

For objects which are symmetric on the average, F = 0. In that case same-sensed CP antennas measure B_0, which we associate with total average power of the irregular depolarizing components of the object scattering, while opposite-sensed CP antennas measure A_0, which we associate with regular non-depolarized scattering (HUYNEN, J.R., 1970). The parameters A_0, B_0, and F are orientation independent!

Therefore it is concluded that the RC and LC polarizations are the logical antenna polarizations to be used for the estimation of object Stokes reflection matrices, since then immediately information is obtained concerning the regular and irregular scattering properties of the object.

3. SUPPRESSION OF NATURAL AND MAN-MADE INTERFERENCE BY MEANS OF ADAPTIVE ANTENNA POLARIZATIONS

3.1 General

The method presented in this section is grounded on adaptive suppression of the completely polarized portion of the interference field. Consequently the degree of polarization p (16) of this field determines the suppression factor achievable. However, if the antenna polarization was adapted for optimum suppression of unwanted signals alone, this may also result in a reduced target signal strength. As the objective is the improvement of the average wanted signal power to average unwanted signal power ratio (as compared to the linear polarization case), large suppression factors may not necessary lead to considerable improvement factors.

In case of active noise interference the average Stokes vector of the interference field must be estimated. It is necessary in this case to sample over a window of M range rings.

In case of clutter, the suppression method requires estimation by measurement of the average Stokes reflection matrix (SRM) (13) of the clutter cells. Therefore, the radar system radiates alternately right-sensed and left-sensed circularly-polarized waves (RC and LC) and receives the signals with orthogonally-polarized (RC-LC) channels.

Distinction can be made between extended clutter with very different polarization properties of the different cells (e.g. ground clutter) and extended clutter, where the different cells exhibit nearly identical average SRMs at least in range and thus have a high degree of "polarization correlation" (e.g. sea clutter, weather clutter, and chaff clutter). In the latter case, it is obvious to use a window of M range rings in order to estimate the average SRM.

Since there appear to be no measured polarization dependent target and clutter models, the limitations of the adaptive suppression method will be examined with the aid of simple radar object models.

3.2 Noise interference suppression

A promising suppression method follows from observing (15) through (18) and consists of proper adaptation of $g(\underline{h}_R)$ after having estimated $h\{\langle E(t)\rangle\}$.

Principle of operation.

Step 1 - Continuous measurement in a (running) window of the interference signals in RC and LC receiver channels, $v_{1_{ij}}$ and $v_{2_{ij}}$ such that

$$\underline{v}_{ij} = v_{1_{ij}}\,\underline{h}_{RC} + v_{2_{ij}}\,\underline{h}_{LC}\ ,\qquad \begin{matrix} i = \text{range cell number} \\ j = \text{sweep number}\end{matrix}$$

- Calculation of instantaneous Stokes vectors, $h_{ij}\ (\underline{v}_{ij}) = (h_0,h_1,h_2,h_3)_{ij}$, see (3).

Step 2 - Estimation of average Stokes vector of the interference field in the window (14) and decomposition (15) into a completely unpolarized field and a completely polarized field

$$H = \{H_0-\bar{H}_0,0,0,0\} + \{\bar{H}_0,H_1,H_2,H_3\}$$

Step 3 - Decomposition of H into orthogonal Stokes vectors, see (5) and (17),

$$H = H_1+H_2 = \tfrac{1}{2}(H_0-\bar{H}_0)\{1,-H_1/\bar{H}_0,-H_2/\bar{H}_0,-H_3/\bar{H}_0\}+\tfrac{1}{2}(H_0+\bar{H}_0)\{1,H_1/\bar{H}_0,H_2/\bar{H}_0,H_3/\bar{H}_0\}$$

where now $(-H_1/\bar{H}_0,-H_2/\bar{H}_0,-H_3/\bar{H}_0)$ determines the required adaptive antenna polarization $\underline{h}_R$ (3), so that (18)

$$\langle P_R \rangle = \langle P_R \rangle_{min} = \tfrac{1}{2}(H-\bar{H}_0)$$

Step 4 - Processing of the measured data of each range ring in the window separately through the established polarization filter, such that $\underline{v}_{ij}$ will be transformed to a new set of polarization vectors.

$$\underline{v}_{ij} = \bar{v}_{1_{ij}} \underline{h}_R + \bar{v}_{2_{ij}} \underline{h}_{R_\perp}, \text{ where } \bar{v}_{1_{ij}} = \underline{v}_{ij}.\underline{h}_R^* \text{ and } \bar{v}_{2_{ij}} = \underline{v}_{ij}.\underline{h}_{R_\perp}^*$$

Step 5 - Processing of $\bar{v}_{1_{ij}}$ for target detection.

The limit of the suppression capability is determined by the degree of polarization p of the interference field. As an example it follows from (18):

$$p = 0.75(0.90); \text{ maximum suppression } \langle P_R \rangle_{min}/\langle P_R \rangle_{max} = 8.5 \text{ dB } (12.8 \text{ dB}).$$

Taking into account that there may be a loss in target signal strength as compared with horizontal polarization in the order to 3 to 6 dB, it is concluded that such an adaptive suppression scheme is only meaningful in case of nearly, say at least, 75% fixed-polarization noise interference.

3.3 Clutter interference suppression

3.3.1 Inhomogeneous clutter

When the average SRMs of the clutter cells are completely different, like often is the case with ground clutter, the suppression method consists of the estimation of the average SRM of each clutter cell individually (repeated measurements) and consequent estimation of polarization filters, for average minimum clutter signal power reception. If the clutter backscattering characteristics are only slowly varying with time, near optimum suppression can be expected by adaptation of $\underline{h}_T = \underline{h}_R$.

Principle of operation. Adaption of $\underline{h}_R = \underline{h}_T$.

Step 1 - Continuous measurement (repeated observations) of the received signals from each clutter cell in RC and LC channels, such that

$$\underline{v}_i(RC) = v_{1_i}(RC\text{-}RC)\,\underline{h}_{RC} + v_{2_i}(RC\text{-}LC)\,\underline{h}_{LC} \text{ and } \underline{v}_i(LC) = v_{1_i}(LC\text{-}RC)\,\underline{h}_{RC} + v_{2_i}(LC\text{-}LC)\,\underline{h}_{LC},$$

- Calculation of the instantaneous SRM, M_i, see (13)

Step 2 - Estimation of the average SRM, $R = \langle M_i \rangle$ of each clutter cell and determination of the antenna polarizations $\underline{h}_T = \underline{h}_R = \underline{h}$, such that the average received power (19)

$$Rf(\underline{h}_T).g(\underline{h}_R) \text{ is a minimum}$$

Step 3 - Processing of the instantaneous measured data of each cell, transformed into the scattering matrix T_i or the SRM(M_i) with the established antenna polarizations $f(\underline{h}_T=\underline{h})$ and $g(\underline{h}_R=\underline{h})$:

$$\bar{v}_i = T_i\,\underline{h}_T.\underline{h}_R \text{ or } P_{R_i} = M_i f(\underline{h}_T).g(\underline{h}_R)$$

Step 4 - Processing of $\bar{v}_i$ or P_{R_i} of each cell for target detection.

Figure 1 presents the simple fixed radar object models considered in this study. In Fig. 2 graphs are presented, showing the suppression of the returns from simple fixed target models (relative to horizontal polarization, HP) when the antenna polarizations $\underline{h}_T=\underline{h}_R=\underline{h}$ are adapted such that the returns from the fixed background model are fully suppressed.

The graphs indicate that the greater the difference in regularity of target and background the larger is the improvement factor. The influence of the relative orientation of target and background becomes more significant as they both behave more irregular.

3.3.2 Homogeneous clutter

When the extended clutter exhibits nearly identical average SRMs (homogeneous clutter), e.g. in range, like sea-, weather-, and chaff-clutter, a window can be used for the estimation of $R = \langle M \rangle$. Further the same principle of operation can be applied as outlined in 3.3.1, which the exception that now the measured range ring data transformed into the SM(T) or the SRM (M) will be processed with the established antenna polarizations $f(\underline{h}_T=\underline{h})$ and $g(\underline{h}_R=\underline{h})$.

In case of homogeneous time-varying clutter, the optimum suppression method results from separate adaptation of the antenna polarizations at transmit and receive; $f(\underline{h}_T)$ to be adapted for average minimum power in the completely unpolarized portion of the backscattered field and $g(\underline{h}_R)$ to be adapted for average minimum signal power reception (POELMAN, A.J., 1975/2).

Principle of operation. Adaptation of $\underline{h}_R \neq \underline{h}_T$.

Step 1 - As in sub-section 3.3.1.

Step 2 - Estimation of the average SRM, $R = \langle M_{ij} \rangle$ in the window.

- Determination of the antenna polarization $f(\underline{h}_T)$ such that $H_0-\bar{H}_0$ in

$$Rf(\underline{h}_T) = \{H_0-\bar{H}_0,0,0,0\} + \{\bar{H}_0,H_1,H_2,H_3\}$$

see (15) and (19), is a minimum

- Determination of $g(\underline{h}_R)$ such that $Rf(\underline{h}_T).g(\underline{h}_R)$ is a minimum

Step 3 - Processing of the measured data of each range ring in the window, transformed into the $SM(T_{ij})$ or $SRM(M_{ij})$, separately with the established antenna polarizations $f(\underline{h}_T)$ and $g(\underline{h}_R)$

$$\bar{v}_{ij} = T_{ij}\, \underline{h}_T \cdot \underline{h}_R \text{ or } P_{R_{ij}} = M_{ij}\, f(\underline{h}_T).g(\underline{h}_R)$$

Step 4 - Processing of $\bar{v}_{ij}$ or $P_{R_{ij}}$ for target detection.

In order to obtain an indication of the effectiveness of the suppression method in case of time-varying clutter, a normalized polarization dependent statistical model of a random dipole cloud (POELMAN, A.J. and van der VOORT, J.R., 1972) has been studied. This model assumes that the space angle describing the probability space of dipole axis direction (uniformly distributed), is identical for all dipoles and is determined by $0 \leq \psi < \pi$ and $\theta_0 \leq \theta \leq \pi - \theta_0$ (Fig. 3). The polar angle θ_0 is the dipole cloud parameter.

Figure 4 presents graphs, of the dipole cloud signal power suppression relative to horizontal polarization. It clearly shows that independent adaptation of $f(\underline{h}_T)$ and $g(\underline{h}_R)$ results in maximum suppression.

The graphs in Figs. 5 and 6 show the improvement in average target signal power to average dipole cloud signal power ratio relative to horizontal polarization, obtainable with adaptive antenna polarizations $\underline{h}_T = \underline{h}_R$ and $\underline{h}_T \neq \underline{h}_R$. There again the simple target models of Fig. 1 are considered; (i) fixed horizontally oriented and (ii) with the orientation uniformly distributed over an angle of $\pm 30^o$ to the horizontal. The results indicate that the more the background tends to exhibit a fixed object behaviour (increasing θ_0, see Fig. 3) and the greater the average background and the average or fixed target differ in degree of regularity, the larger the improvement factor. In the latter case adaptation of $\underline{h}_T \neq \underline{h}_R$ is most promising, however, when the average background and the average or fixed target exhibit regularity of the same degree adaptation of $\underline{h}_T = \underline{h}_R$ will be more successful.

3.4 Conclusions

Adaptive polarization in a radar system permits to obtain marked improvements in average wanted signal power to average unwanted signal power ratio in the individual radar cells, as shown by the examples. The less the background SRM elements vary with time relative to the data rate, i.e. the more the background tends to exhibit a fixed object behaviour, the larger the improvement factors will be. One procedure is to adapt the antenna transmit and receive polarizations identically ($\underline{h}_T = \underline{h}_R$), which yields promising results when average background and average target behave regular to the same extend. The alternative procedure is to adapt the antenna transmit and receive polarizations independently ($\underline{h}_R \neq \underline{h}_R$), which will be successful if average background and average target show an entirely different degree of regularity.

As the adaptive schemes require significant digital processing, one should concentrate on the applicability in those areas, where a limited number of radar cells need to be treated simultaneously, e.g. in tracking radars.

4. THE DETECTION STRATEGY IN CLEAR AND QUIET SECTORS

4.1 Target model and detection scheme

Dual polarized (RC-LC) antennas for transmission and reception are considered, where the transmission mode is characterized by the alternative radiation of RC and LC pulses. It is further assumed that narrow-band additive Gaussian (thermal) noise of equal average power (σ^2) is present in the orthogonally-polarized (RC and LC) receiving channels, with the noise variates mutually independent.

The existing statistical target models, like the well-known Swerling models (SWERLING, P., 1960), do not explicitly account for the dependence on polarization. It seems that such improved statistical target models are not available. In this paper a simple statistical target model is considered which assumes that due to the interaction of the illuminated wave and the radar target, the backscattered wave will be depolarized. The backscattered wave will consist of a component due to the "average effective target" and a "target-noise" component due to changes from the average effective target,

$$T(t) = a(t)\, T_0 + T_{noise}(t)$$

Here we assume that the average effective target is a horizontally oriented cylinder, whilst the noise component is due to scattering from a sphere and an oriented di-plane,

$$T(t) = a(t) \underbrace{\begin{bmatrix} 1 & 0 \\ 0 & \lambda \end{bmatrix}}_{T_0} + b(t) \underbrace{\begin{bmatrix} 1 & 0 \\ 0 & 1 \end{bmatrix}}_{T_{N_1}} + c(t) \underbrace{\begin{bmatrix} 0 & 1 \\ 1 & 0 \end{bmatrix}}_{T_{N_2}}$$

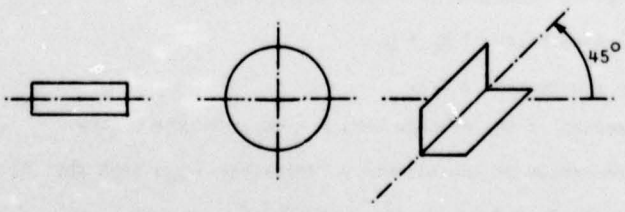

cylinder sphere di-plane

where a, b, c are independent zero mean Gaussian random variables with for the noise component the additional condition

$$\overline{|b|^2} = \overline{|c|^2} = \sigma_N^2$$

This model may be considered as an extension of Swerling model I/II (target scintillation), where $T_{noise}(t)$ is applicable for circular polarizations; b(t) T_{N_1} generates a random orthogonally-polarized and c(t) T_{N_2} a random parallel-polarized component.

With normalized antenna polarizations, the average received powers, based on (8), (11), (12), and (19), will be

$$\bar{P}_{R_{\parallel}} = \bar{P}_{R_{\parallel}}(RC\text{-}RC) = \bar{P}_{R_{\parallel}}(LC\text{-}LC) = \tfrac{1}{4}(1-\lambda)^2\,\overline{|a|^2} + \overline{|c|^2} = \sigma_{e_{\parallel}}^2 + \sigma_N^2 = \sigma_{R_{\parallel}}^2$$

and

$$\bar{P}_{R_{\perp}} = \bar{P}_{R_{\perp}}(RC\text{-}LC) = \bar{P}_{R_{\perp}}(LC\text{-}RC) = \tfrac{1}{4}(1+\lambda)^2\,\overline{|a|^2} + \overline{|b|^2} = \sigma_{e_{\perp}}^2 + \sigma_N^2 = \sigma_{R_{\perp}}^2$$

The correlation factor between the received signals in both channels is expressed by

$$\rho = \frac{\overline{v_{R_{\parallel}} \cdot v_{R_{\perp}}^*}}{(\bar{P}_{R_{\parallel}} \cdot \bar{P}_{R_{\perp}})^{\frac{1}{2}}} = \frac{\sigma_{e_{\parallel}} \cdot \sigma_{e_{\perp}}}{\sigma_{R_{\parallel}} \cdot \sigma_{R_{\perp}}} = \frac{\sigma_{e_{\parallel}} \cdot \sigma_{e_{\perp}}}{\{(\sigma_{e_{\parallel}}^2 + \sigma_N^2)(\sigma_{e_{\perp}}^2 + \sigma_N^2)\}^{\frac{1}{2}}}$$

The signal received in each channel consists of an incoherent pulse train (N pulses) of constant amplitude. Furthermore the coherency between the simultaneously received signals in the channels is not utilized.

The detection scheme being analyzed applies square-law detection after matched filtering in each channel, integration and a threshold after linear addition of videos (Fig. 7). It represents the optimum incoherent detection scheme for low average signal power to average noise power ratios, when the average received powers in both channels are identical (DIFRANCO, J.V., and RUBIN, W.L., 1968). Weighting is not applied, as in general the ratio of average received powers in the channels is a priori unknown.

Two extreme cases will be treated:

Case I-i: Channel signals $v_{R_{\parallel}}$ and $v_{R_{\perp}}$ completely uncorrelated;

$\rho = 0$ and consequently $\sigma_{R_{\parallel}}^2 = \sigma_{R_{\perp}}^2 = \sigma_N^2$.

Case I-c: Channel signals $v_{R_{\parallel}}$ and $v_{R_{\perp}}$ completely correlated:

$\rho = 1$ and consequently $\sigma_{R_{\parallel}}^2 = \sigma_{e_{\parallel}}^2$ and $\sigma_{R_{\perp}}^2 = \sigma_{e_{\perp}}^2$

Study parameter is: $F = \sigma_{e_{\perp}}^2 / \sigma_{e_{\parallel}}^2 = (1+\lambda)^2/(1-\lambda)^2$

4.2 Derivation of formulas for probability of false alarm and probability of detection

If N denotes the number of noise variates integrated per channel, and Y_B denotes the threshold level normalized with respect to the average channel noise power, the probability of false alarm P_{fa} is given by (MARCUM, J.I., 1960),

$$P_{fa} = 1 - I\{Y_B/\sqrt{2N},\ 2N-1\}$$

where I is Pearson's form for the incomplete gamma function (ABRAMOWITZ, M., and STEGUN, I.A., 1964). The Y_B values as functions of P_{fa} and N have been tabulated (PACHARES, J., 1958).

The probability of detection P_d is determined by (MARCUM, J.I., 1960).

$$P_d = 1 - \int_0^{Y_B} f_z(z)\,dz, \qquad (21)$$

where z is the normalized signal obtained after integration and video addition, and $f_z(z)$ is the probability density function.

The formulas for P_d, in a format suitable for computation have been derived by extending the procedures given by Swerling (SWERLING, P., 1960; POELMAN, A.J., 1975/1).

Case I-i The characteristic function of the probability density function of the signal z is (Eq. III.3, SWERLING, P., 1960, p.283)

$$\bar{C}_z(p) = \bar{C}_{y_{\parallel}}(p) \cdot \bar{C}_{y_{\perp}}(p) = (p+1)^{-(2N-2)}\{1+p(1+N\bar{x})\}^{-2} = \alpha^{m_2}(p+1)^{-m_1}(p+\alpha)^{-m_2},\ m_1+m_2 = 2N \qquad (22)$$

where $\bar{x} = \bar{x}_{\parallel} = \bar{x}_{\perp}$ is the average signal power to average noise power ratio in the two channels (σ_N^2/σ^2).

Case I-c The unweighted characteristic function of the probability density fuction of the signal z is (Eq. III.1, SWERLING, P., 1960, p.283)

$$C_z(p) = C_{y_{\parallel}}(p).\ C_{y_{\perp}}(p) = (p+1)^{-2N} \exp\{-N\bar{x}_{\parallel}(1+F)\frac{p}{p+1}\}$$

It follows for the weighted characteristic function (Eqs. I.1 and III.2, SWERLING, P., 1960, p.274 and p.283)

$$\bar{C}_z(p) = (p+1)^{-(2N-1)}\left[1 + p\{1+ N\bar{x}_{\parallel}(1+F)\}\right]^{-1} = \alpha^{m_2}(p+1)^{-m_1}(p+\alpha)^{-m_2},\ m_1+m_2 = 2N \qquad (23)$$

where $\bar{x}_{\parallel}$ is the average signal power to average noise power ratio in the parallel channel ($\sigma^2_{e_{\parallel}}/\sigma^2$) and F is the study parameter ($F=\sigma^2_{e_{\perp}}/\sigma^2_{e_{\parallel}} = \bar{x}_{\perp}/\bar{x}_{\parallel}$).

The probability density function $f_z(z)$, which is the inverse Laplace transform of (22) and (23) (pair 581.1, CAMPBELL, G.A., and FOSTER, R.M., 1954, p.64), is inserted in (21) to give

$$P_d = 1-(\alpha)^{-m_1} \sum_{k=0}^{\infty}\left[\left\{\begin{matrix} m_1+k-1 \\ k \end{matrix}\right\} \left(\frac{\alpha-1}{\alpha}\right)^k I\left\{\frac{\alpha Y_B}{\sqrt{2N+k}},\ 2N+k-1\right\}\right]$$

where I is Pearson's form of the incomplete gamma function and $\left\{\begin{matrix} m_1+k-1 \\ k \end{matrix}\right\} = \frac{(m_1+k-1)!}{k!(m_1-1)!}$.

4.3 Presentation of results and conclusions

In a single channel receiving system the detectability factor D_s, is defined as the ratio of average target signal power to average noise power required at the detector input for given values of P_{fa}, P_d, and N (BLAKE, L.V., 1961). For the dual-channel receiving system considered here, this definition of D_s has been adopted for the "parallel channel" at the video addition unit, with parameters P_{fa}, P_d, N and F.

To make the results more meaningful, the detection performance of the dual-channel receiving system may be expressed in terms of a "figure of merit" (ΔD_s). This is defined as the gain in the D_s of the dual-channel receiving system relative to the D_s of the single-channel receiving system with horizontally polarized (HP) transmission and reception. The D_s values for the single-channel system and parameter values considered can be determined by using the relevant formulas of P_d (SWERLING, P., 1960).

However, as in case I-c, the average cross-sections for circular-polarization (CP) and horizontal-polarization (HP) are not identical. Therefore the detection performance will be expressed in terms of "efficiency, E". The efficiency (E) of the dual-channel detection receiver operating in the CP mode is defined as the reduction in transmitter peak power relative to the single-channel detection receiver operating in the HP mode, for the same P_{fa}, P_d, N and pulse width.

Curves showing the variation of E versus N up to N≈20 are presented for the extreme cases I-i and I-c in Fig. 8, with values of λ between 0 and 1, $P_{fa}=10^{-6}$ and P_d values of 0.5 and 0.8.

Extreme cases have been considered i.e. incoherent pulse trains of which the amplitudes are mutually uncorrelated or completely correlated. In practice the amplitudes of both pulse trains will be partially correlated. Another observation is that the target model in case I-c is unfavourable for CP, in that then HP is the maximum polarization.

Therefore it is concluded that the performance of the dual-channel detection receiver, operating in the RC-LC transmission mode for adaptive clutter suppression, in clutter free sectors (where simple linear video addition is applied) will be virtually the same as that of the single-channel detection receiver operating in the HP mode.

ACKNOWLEDGEMENT

The author wishes to thank Dr. J.R. Huynen for his stimulating comments and Mr. R.C. Reyman for his assistance in preparing the computer programs.

REFERENCES

ABRAMOWITZ, M., and STEGUN, I.A., 1964, "Handbook of Mathematical Functions", p. 262, Dover Publ.: New York.

BLAKE, L.V., 1961, "Recent advances in radar range calculation technique", IRE Trans. Military Electronics, Vol. MIL-5, pp. 154-164.

BORN, M., and WOLF, E., 1965, "Principles of Optics", section 10.8, third edition, Pergamon Press, New York.

CAMPBELL, G.A., and FOSTER, R.M., 1954, "Fourier Integrals for Practical Applications", Van Nostrand, Princeton, N.J.

DIFRANCO, J.V., and RUBIN, W.L., 1968, "Radar Detection", section 11.2, Prentice Hall, Englewood Cliffs, N.J.

HUYNEN, J.R., 1965, "Measurement of the target scattering matrix", Proc. of the IEEE, Vol. 53, pp. 936-946.

HUYNEN, J.R., 1970, "Phenomenological Theory of Radar Targets", Dissertation Delft University, Dec. 1970.

MARCUM, J.I., 1960, "A statistical theory of target detection by pulsed radar", IRE Trans. Information Theory, Vol. IT-6, Mathematical Appendix, pp. 145-169, (Special Monograph Issue).

PACHARES, J., 1953, "A table of bias levels useful in radar detection problems", IRE Trans. Information Theory, Vol. IT-4, pp. 38-45.

POELMAN, A.J., and Van der VOORT, J.P., 1972, "The polarization dependence of received backscattered power from a random dipole cloud", Technical Memorandum TM-276, SHAPE Technical Centre, The Hague, The Netherlands, (NATO Unclassified).

POELMAN, A.J., 1975, "On using orthogonally polarized non-coherent receiving channels to detect target echoes in Gaussian noise", IEEE Trans. Aerospace and Electronic Systems, Vol. AES-11, pp. 660-663.

POELMAN, A.J., 1975, "Cross correlation of orthogonally-polarized components of an electro-magnetic field backscattered by a complex radar object", paper forwarded to the AES Transaction of the IEEE for acceptance consideration.

SWERLING, P., 1960, "Probability of detection for fluctuating targets", IRE Trans. Information Theory, Vol. IT-6, pp. 269-308, (Special Monograph Issue).

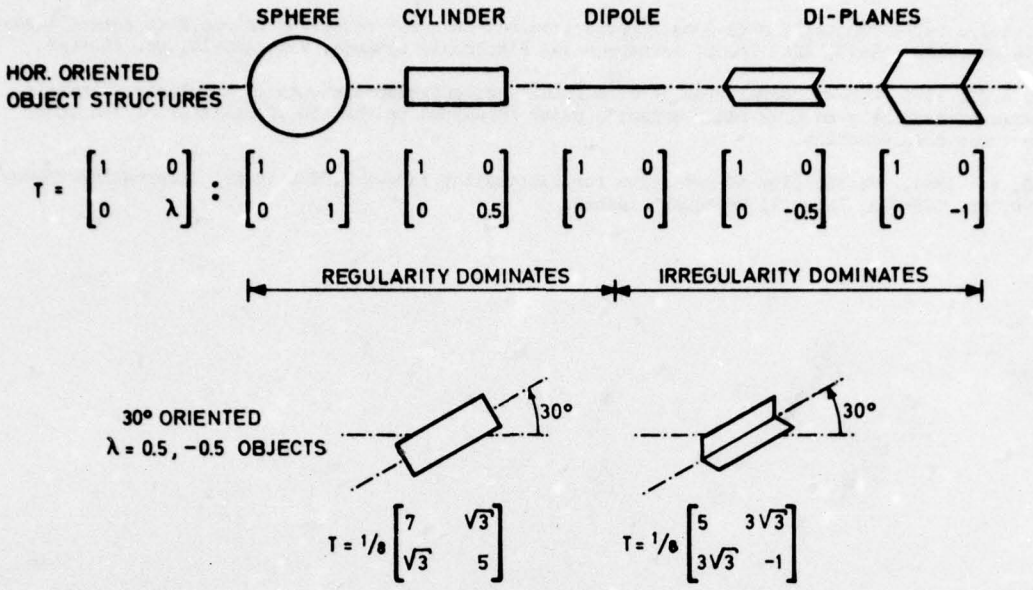

Fig. 1 Simple fixed target and background models (absolute phase ignored).

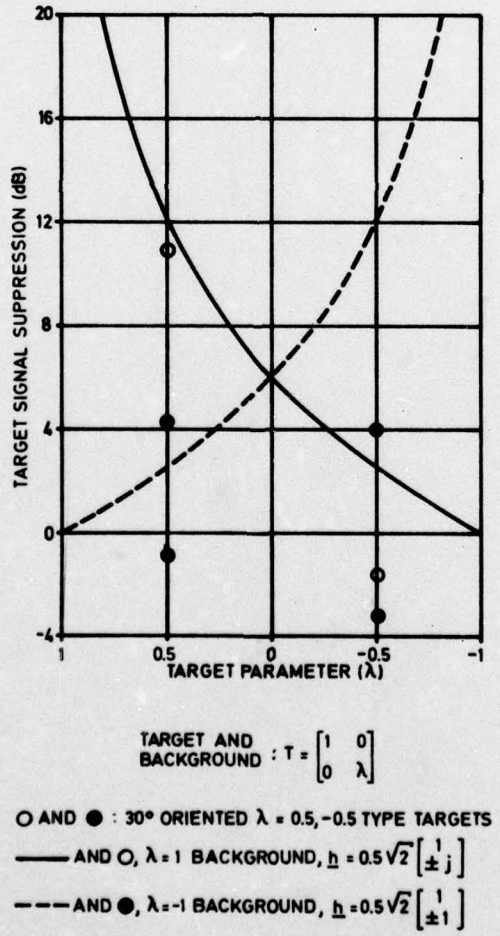

Fig. 2 Suppression of the returns from simple fixed horizontally oriented and ± 30° oriented targets relative to horizontal polarization, when the antenna polarization $\underline{h}_T = \underline{h}_R$ is adapted for complete suppression of the fixed background.

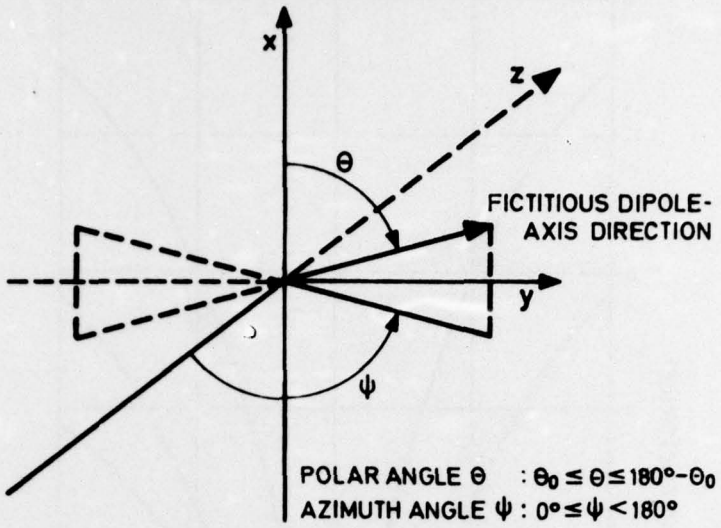

Fig. 3 The dipole in its coordinate frame.

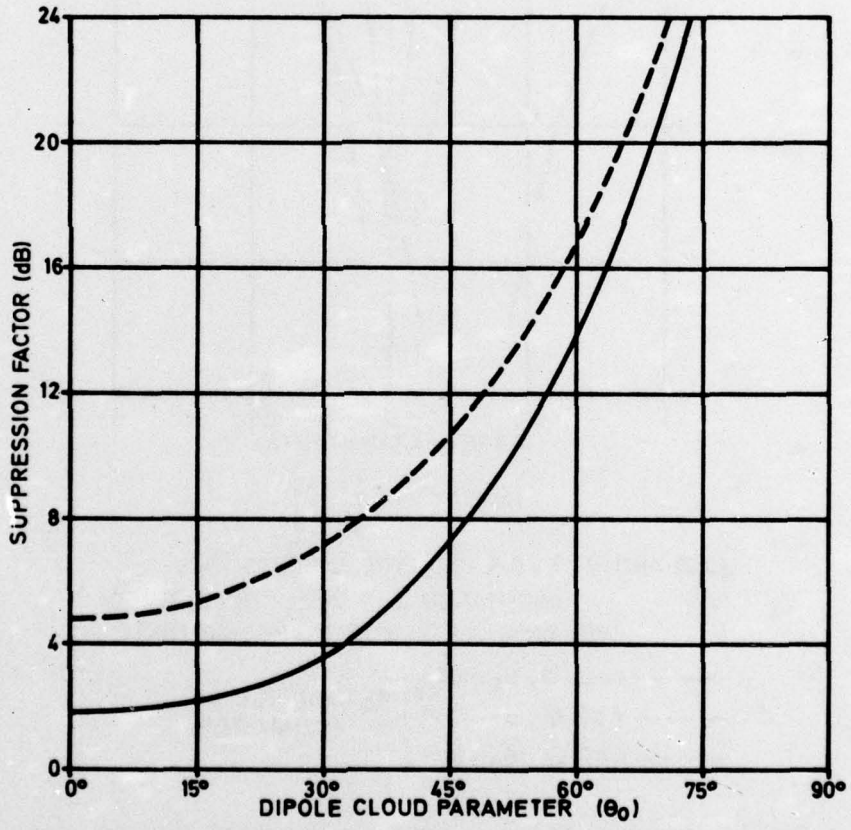

Fig. 4 Optimum dipole cloud signal power suppression relative to horizontal polarization: $\underline{h}_T = \underline{h}_R$ and $\underline{h}_T \neq \underline{h}_R$.

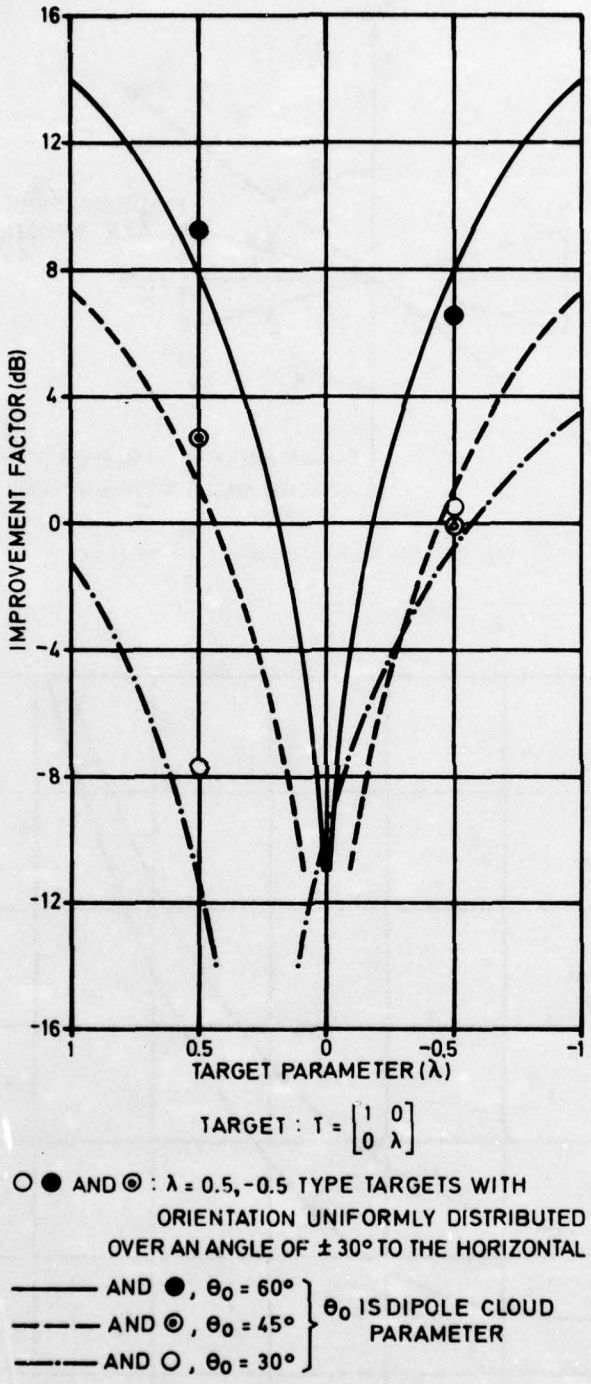

Fig. 5 Improvement in average target signal power to average dipole cloud signal power ratio relative to horizontal polarization; $\underline{h}_T = \underline{h}_R$ adapted for minimum average dipole cloud signal power reception.
(i) horizontally oriented simple fixed targets and
(ii) simple targets with orientation uniformly distributed over an angle of $\pm$ 30° to the horizontal.

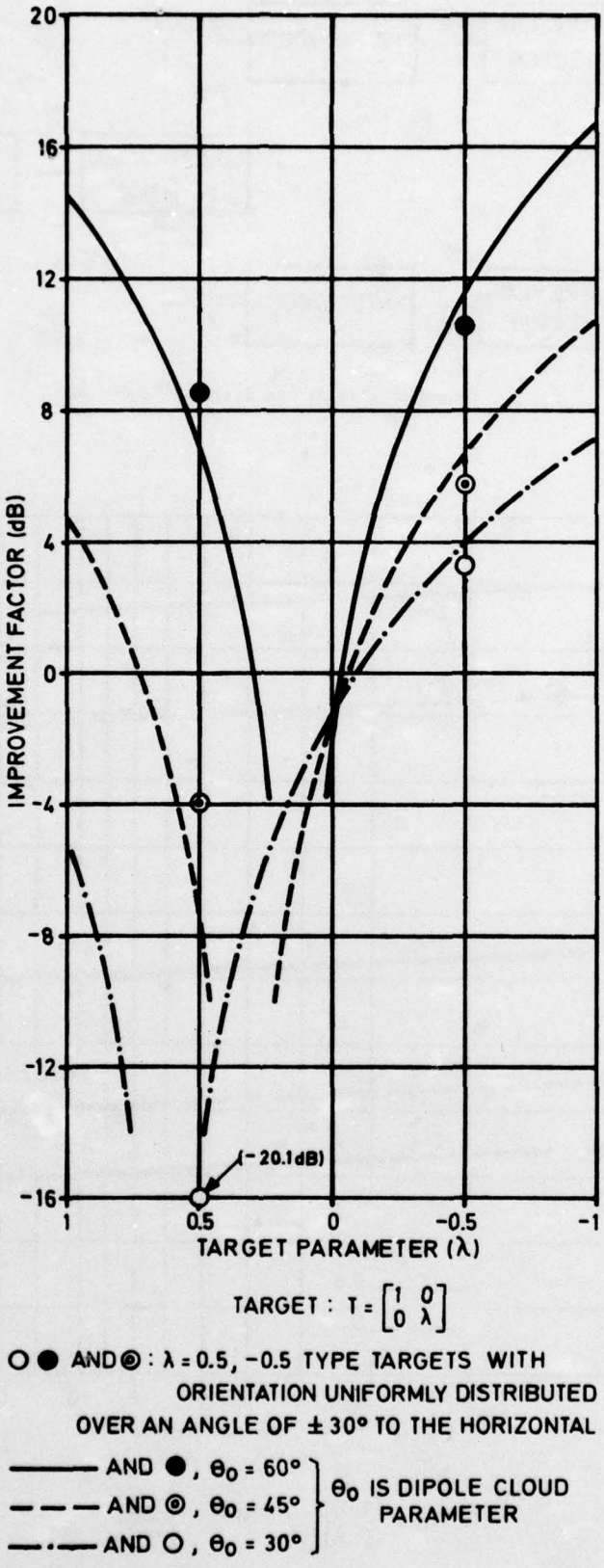

Fig. 6 Improvement in average target signal power to average dipole cloud signal power ratio relative to horizontal polarization; $\underline{h}_T$ adapted for minimum average power in the completely unpolarized portion of the dipole cloud backscattered field and $\underline{h}_R$ adapted for minimum average dipole cloud signal power reception.
(i) horizontally oriented simple fixed targets and
(ii) simple targets with orientation uniformly distributed over an angle of $\pm$ 30° to the horizontal.

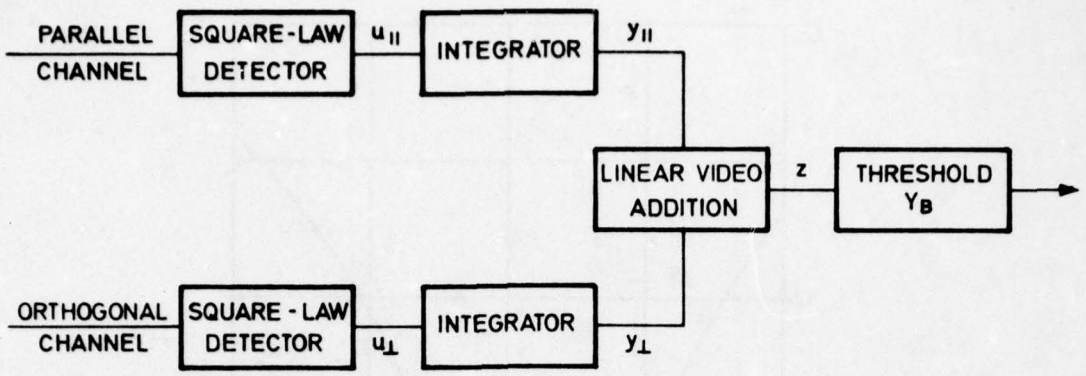

Fig. 7 Blockdiagram of the detection receiver.

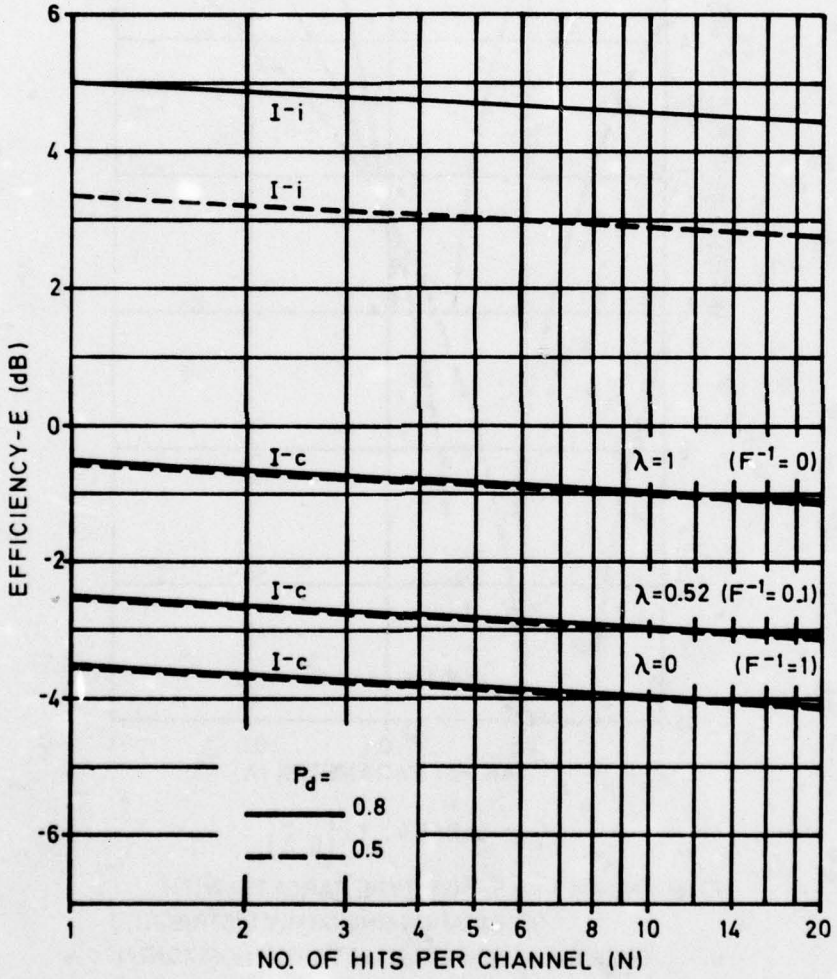

$$T_0 = \begin{bmatrix} 1 & 0 \\ 0 & \lambda \end{bmatrix} \qquad F^{-1} = \left[\frac{1-\lambda}{1+\lambda}\right]^2$$

Fig. 8 Efficiency versus N for the dual-channel system operating in the RC-LC mode, relative to the single-channel system operating in the HP mode ($P_{fa}=10^{-6}$; non-coherent integration; slow scintillating target).

DISCUSSION

A J DUNLOP: Have you considered using polarisation agility for target classification?

A J POELMAN: This paper has been devoted to only one aspect of the use of controllable polarisation. In the near future we shall certainly consider the applicability of target classification schemes based on polarisation characteristics.

METHODE DE CALCUL NUMERIQUE DE PROBABILITE DE DETECTION DE SIGNAUX FLUCTUANTS

P. BLONDY
ELECTRONIQUE MARCEL DASSAULT
92214 SAINT CLOUD
FRANCE

SOMMAIRE

Dans les cas de fluctuations intermédiaires aux cas I et II de SWERLING, c'est à dire de corrélation partielle de la cible, on montre que la fonction caractéristique de la sortie de l'intégrateur parfait après détection quadratique s'exprime simplement en fonction des valeurs propres de la matrice de covariance des échantillons de la voie en phase (ou en quadrature) du signal utile. Trois méthodes de calcul de la probabilité de détection sont examinées :

- approximation par la série de Gram Charlier, elle s'avère peu commode et peu précise.
- inversion de la fonction caractéristique par Transformée de Fourier Discrète ; elle est toujours utilisable et donne de bons résultats.
- inversion de la fonction caractéristique par le calcul des résidus ; elle est extrèmement précise quand elle converge, mais s'accommode mal des grands nombres d'échantillons et des valeurs propres multiples d'ordre élevé.

1. INTRODUCTION

L'évaluation des performances de radars modernes utilisant certaines techniques de décorrélation d'écho de cible nécessite une méthode d'évaluation de la probabilité de détection dans des cas de décorrélation partielle intermédiaire entre les cas I et II de Swerling. Dans ces cas de fluctuation, on peut exprimer facilement la fonction caractéristique de la sortie de l'intégrateur parfait alimenté par un détecteur quadratique en fonction des valeurs propres de la matrice de covariance des échantillons de la voie en phase (ou en quadrature) du signal utile. A partir de ce résulat, différentes méthodes numériques permettant d'accèder à la probabilité de dépassement d'un seuil sont étudiées, mettant en évidence leurs avantages et leurs limitations.

2. FONCTION CARACTERISTIQUE DE LA SORTIE DE L'INTEGRATEUR PARFAIT APRES DETECTION QUADRATIQUE

Plaçons nous dans l'hypothèse des signaux à bande étroite, où chaque échantillon d'information se compose d'un échantillon de la voie en phase

$$x_{Ij} = s_{Ij} + b_{Ij}$$

et d'un échantillon de la voie en quadrature

$$x_{Qj} = s_{Qj} + b_{Qj}$$

s et b étant les contributions du signal d'une part et du bruit d'autre part.

Ajoutons les hypothèses d'indépendance statistique du signal et du bruit et d'indépendance statistique des voies en phase et en quadrature. Les x, s et b sont des variables aléatoires gaussiènnes, centrées et on a pour tout i et j

$$E\{s_{Ii} \cdot s_{Qj}\} = 0$$

$$E\{b_{Ii} \cdot b_{Qj}\} = 0$$

$$E\{s_{Ii} \cdot b_{Ij}\} = E\{s_{Qi} \cdot b_{Qj}\} = E\{s_{Ii} \cdot b_{Qj}\} = E\{s_{Qi} \cdot b_{Ij}\} = 0$$

$$E\{b_{Ii} \cdot b_{Ij}\} = E\{b_{Qi} \cdot b_{Qj}\} = 0 \quad \text{pour } i \neq j$$

Notons les vecteurs colonnes de taille N

$$S_I = \{s_{Ii}\} \quad S_Q = \{s_{Qi}\} \quad B_I = \{b_{Ii}\} \quad B_Q = \{b_{Qi}\}$$
$$X_I = \{x_{Ii}\} \quad X_Q = \{x_{Qi}\}$$

Notons C la matrice de covariance des échantillons d'une voie $\{x_{Ii}\}$ ou $\{x_{Qi}\}$

$$C = E\{X_I . X_I^T\} = E\{X_Q . X_Q^T\}$$

Le détecteur quadratique suivi de l'intégrateur parfait effectue l'opération

$$z = \sum_{i=1}^{N} x_{Ii}^2 + x_{Qi}^2 = X_I^T . X_I + X_Q^T . X_Q$$

z constitue l'échantillon de sortie sur lequel est effectué la décision ; on peut chercher sa fonction caractéristique.

C est une matrice de covariance. Elle est donc positive semi définie et il existe une transformation unitaire $U^T CU$ qui la diagonalise

$$U^T CU = [\lambda]$$

U est une matrice unitaire
$[\lambda]$ est la matrice diagonale des valeurs propres réelles positives ou nulles de C.

Formons les vecteurs Y_I et Y_Q $\quad Y_I = \{y_{Ii}\} \quad Y_Q = \{y_{Qi}\}$

$$Y_I = U^T X_I \quad Y_Q = U^T X_Q$$

Cherchons leur matrice de covariance $E\{Y_I . Y_I^T\} = E\{U^T X_I . X_I^T U\} = E\{U^T C U\} = [\lambda]$

et de même pour $E\{Y_Q . Y_Q^T\}$

Les y_{Ii} et y_{Qi} sont donc des variables aléatoires gaussiennes, centrées, indépendantes et de variance λ_i et λ_j

Exprimons z en fonction des y :

$$z = X_I^T X_I + X_Q^T X_Q = Y_I^T U^T U Y_I + Y_Q^T U^T U Y_Q$$
$$z = \sum_{i=1}^{N} y_{Ii}^2 + y_{Qi}^2$$

z est donc la somme des carrés de 2N variables aléatoires gaussiennes indépendantes, de variances égales aux valeurs propres λi de C

Sa fonction caractéristique s'écrit donc :

$$\Phi_z(u) = \prod_{i=1}^{N} \frac{1}{1 - 2ju\lambda_i}$$

Application aux cas I et II de Swerling et intermédiaire

Posons $E\{b_{Ii}^2\} = E\{b_{Qi}^2\} = 1/2$

et notons $\bar{X}$ le rapport signal bruit, R la matrice de corrélation des échantillons d'une voie du signal.

Il vient $C = \frac{1}{2}(I + \bar{X}R)$ et si μ est valeur propre de R, alors $\lambda = \frac{1}{2}(1 + \bar{X}\mu)$ est valeur propre de C.

Dans le cas I, tous les éléments de R valent 1 et ses valeurs propres sont 0 d'ordre N-1 et N d'ordre 1.

Les valeurs propres de C sont donc $\frac{1}{2}$ d'ordre N-1 et $\frac{1 + N\bar{X}}{2}$ d'ordre 1

La fonction caractéristique de z s'écrit alors :

$$\Phi_z(u) = \frac{1}{(1 - ju)^{N-1} . [1 - (1 + N\bar{X})ju]}$$

Dans le cas II, R est diagonale de valeur propre 1 d'ordre N et Φ_z s'écrit :

$$\Phi_z(u) = \frac{1}{[1 - (1 + \bar{X})ju]^N}$$

Remarquons que la localisation des valeurs propres de C sur la ligne réelle suggère une méthode de juger de la "proximité" d'un cas de décorrélation du cas I ou II ; la proximité du cas I se traduit par une migration de N-1 valeurs propres vers la valeur 2 et la Nième vers la valeur $(1 + N\overline{X}/2)$ tandis que la proximité du cas II se traduit par une concentration des valeurs propres autour de la valeur $(1+\overline{X}/2)$

Application au cas I affecté d'une modulation d'amplitude du signal utile

Plaçons nous dans le cas I où les échantillons de signal sont parfaitement corrélés mais où le signal subit une modulation d'amplitude revenant à une pondération des échantillons a_{ji} et b_{qi} par un coefficient αi Soit X le rapport signal bruit correspondant à la valeur unité de αi.

C s'écrit alors :

$$C = \frac{1}{2}\left\{1 + \overline{X}\begin{pmatrix}\alpha_1^2 & \alpha_1\alpha_2 & \alpha_1\alpha_N \\ \alpha_1\alpha_2 & & \\ \alpha_1\alpha_N & & \alpha_N^2\end{pmatrix}\right\}$$

et a pour valeurs propres 1/2 d'ordre N-1 et : $\frac{1}{2}\left(1 + \overline{X}\sum_{i=1}^{N}\alpha_i^2\right)$

Ce sont celles qu'aurait donné, dans le cas I un rapport signal/bruit $\overline{X}_{oq} = \frac{\sum_1^N \alpha_i^2}{N}\overline{X}$, moyenne du rapport signal/bruit des échantillons.

3. METHODES DE CALCUL NUMERIQUE DE LA PROBABILITE DE DETECTION

3.1. La série d'Edgeworth

On montre que si la statistique de l'échantillon z ne diffère pas trop de celle de Gauss, on peut exprimer la probabilité de dépassement d'un seuil Y_B par une série :

$$P_d = \frac{C_0}{2}\operatorname{erfc}\frac{Y_B - m}{\sigma} + \frac{1}{\sqrt{2\pi}}e^{-\frac{(Y_B-m)^2}{2\sigma^2}}\sum_{i=1}^{\infty} C_i\, He_{i-1}\left(\frac{Y_B-m}{\sigma}\right)$$

m et σ étant la moyenne et l'écart type de l'échantillon de sortie, Hei le polynôme d'Hermite d'ordre i et les Ci des coefficients s'exprimant en fonction des cumulants de la distribution de z. On montre que C1 = C2 = 0 et qu'afin d'obtenir des contributions du même ordre, il faut regrouper les termes de la série dans un certain ordre. La série regroupée par ordre de magnitude décroissante s'appelle série d'Edgeworth, et les termes à prendre dans l'ordre sont : i=0, puis i=3, puis i=4 et 6, puis i=5, 7, 9, etc...

On trouve dans la littérature l'expression des Ci en fonction des cumulants

$$C_3 = -\frac{1}{3!}\frac{\chi_3}{\chi_2^{3/2}}$$
$$C_4 = \frac{1}{4!}\frac{\chi_4}{\chi_2^2}$$
$$C_5 = -\frac{1}{5!}\frac{\chi_5}{\chi_2^{5/2}}$$
$$C_6 = \frac{1}{6!\chi_2^3}\left(\chi_6 + 10\chi_3^2\right)$$
$$C_7 = -\frac{1}{7!\chi_2^{7/2}}\left(\chi_7 + 35\chi_4\chi_3\right)$$
$$C_9 = -\frac{1}{9!\chi_2^{9/2}}\left(\chi_9 + 84\chi_6\chi_3 + 125\chi_5\chi_4 + 280\chi_3^3\right)$$

Pour exprimer les cumulants en fonction des valeurs propres de la matrice de covariance, on développe l'expression de la seconde fonction caractéristique en puissance de ju.

$$\Psi_B(u) = \operatorname{Log}\Phi_B(u) = \sum_{i=1}^{N}\operatorname{Log}\frac{1}{(1-2ju\lambda_i)} = \sum_{r=1}^{\infty}(r-1)!\,2^r\sum_{i=1}^{N}\lambda_i^r\,\frac{(ju)^r}{r!}$$

On en tire le cumulant d'ordre r :

$$\chi_r = (r-1)!\,2^r\sum_{i=1}^{N}\lambda_i^r$$

Remarquons que $\sum_{i=1}^{N}\lambda_i$ est la trace Tr de la rième puissance de la matrice de covariance. En reportant ceci dans l'expression des coefficients Ci, on trouve :

$$C_3 = -\frac{1}{3}\frac{T_3}{T_2^{3/2}}$$
$$C_4 = \frac{1}{4}\frac{T_4}{T_2^2}$$
$$C_5 = -\frac{1}{5}\frac{T_5}{T_2^{5/2}}$$

$$C_6 = \frac{1}{T_2^3}\left(\frac{T_6}{6} + \frac{T_3^2}{18}\right)$$

$$C_7 = -\frac{1}{T_2^{7/2}}\left(\frac{T_7}{7} + \frac{T_4 T_3}{12}\right)$$

$$C_9 = -\frac{1}{T_2^{9/2}}\left(\frac{T_9}{9} + \frac{T_6 T_3}{18} + \frac{T_5 T_4}{20} + \frac{T_3^3}{162}\right)$$

On voit que le calcul des Ci ne requière pas l'extraction des valeurs propres, mais simplement le calcul de la trace des puissances successives de la matrice de covariance.

Un programme de calcul a été écrit pour traduire ces relations et tester la méthode sur certains cas particuliers connus.

Résultats pour un χ^2_{20} (N = 10), Y_B = 25

- Coefficients de Gram Charlier

Co = 1
C3 = 0,105
C4 = 0,025 C6 = 0;007
C5 = 0,006 C7 = 0,003 C9 = 0,001

- Probabilités élémentaires			Sommes partielles
Po = 0,215			0,215
P3 = -0,012			0,203
P4 = -0,014	P6 = 0,015		0,204
P5 = -0, 001	P7 = -0,07	P9 = -0,014	0,197
- Résultat exact			0,201

Conclusion

On voit que le meilleur résultat est obtenu pour la somme partielle Po + P3 et que poursuivre la sommation jusqu'à un rang plus élevé dégrade la précision.

La méthode de Gram Charlier paraît donc inadéquate et l'expérience démontre qu'elle l'est d'autant plus que le cas est plus proche du cas I et que le seuil est placé dans la queue de la distribution.

3.2. Inversion de la fonction caractéristique par Transformée de Fourier Discrète

Connaissant la fonction caractéristique, on peut imaginer de l'inverser par Transformée de Fourier Discrète en utilisant un algorithme de F.F.T.
En discrétisant l'intégrale de Fourier, on trouve :

$$P(z) \sim \frac{\Delta}{2\pi} \sum_{-\infty}^{+\infty} \Phi_z(k\Delta)\, e^{-jzk\Delta}$$

En remarquant que : $\Phi_z(u) = \Phi_z^*(-u)$

$$P(z) \sim \frac{\Delta}{2\pi}\left(2\,\mathrm{Re} \sum_{i=0}^{\infty} \Phi_z(k\Delta)\, e^{-jzk\Delta} - 1\right)$$

Prenons K échantillons de la fonction caractéristique de 0 à (K-1)Δ.
L'algorithme de F.F.T. fait apparaître K quantités

$$g_l = \sum_{i=0}^{K-1} \Phi_z(k\Delta)\, e^{-j\frac{2\pi}{K}kl} \qquad 0 \leq l \leq K-1$$

On peut donc approcher la densité P(z) aux points :

$$z = l\frac{2\pi}{K\Delta} \qquad 0 \leq l \leq K-1 \text{ par}$$

$$P\left(l\frac{2\pi}{K\Delta}\right) = \frac{\Delta}{2\pi}\left(2\,\mathrm{Re}(g_l) - 1\right)$$

En fait, dans l'algorithme de FFT, seuls $\frac{K}{2}$ points sont significatifs ; si donc on s'intéresse à un domaine $[0, z_0]$ de variation de z pour p(z), il convient de prendre $\frac{\pi}{\Delta} = z_0$, soit $\Delta = \frac{\pi}{z_0}$ et on accède à $\frac{K}{2}$ échantillons de p(z) espacés de $2z_0/K$

Dans notre cas particulier, nous nous interessons à un domaine de variation de z centré sur la moyenne m et d'étendue $\pm$ 6 fois l'écart type σ.
Il suffit de décaler p(z) vers la gauche de $m-6\sigma$ en multipliant $\Phi_z(u)$ par $\exp(-j(m-6\sigma)u)$ puis de l'échantillonner avec un pas $\Delta = \pi/12\sigma$
Le nombre de points à prendre dépend de la finesse de l'échantillonnage recherché pour p(z).

m et σ sont calculés à partir des valeurs propres par $m = 2\sum_{i=1}^{N} \lambda_i$ $\quad \sigma = 2\sqrt{\sum_{i=1}^{N} \lambda_i^2}$

La méthode a été programmée sur ordinateur avec un échantillonnage de 2048 points sur $\Phi_z(u)$. On obtient donc 1024 points de la densité aux abscisses $z = m-6\sigma+\ell \cdot \frac{12\sigma}{1024}$ $0 \le \ell \le 1023$
On en tire la cumulative par simple sommation des échantillons et la probabilité de dépassement d'un seuil par extrapolation linéaire entre deux échantillons et complémentation à 1.

Elle a été testée sur des distributions du type X^2 à 2N degrés de liberté, N variant de 1 à 100. Avec le nombre de points de 2048, les résultats obtenus sont très satisfaisants. Dans le cas du X^2_2, ou la densité présente une discontinuité à l'origine, la précision obtenue est de quelques unités de la troisième décimale ; elle s'améliore à mesure que la distribution étudiée s'approche de Gauss. Avec un échantillonnage plus serré il est possible d'améliorer la précision, mais ce gain n'est que linéaire en fonction du nombre de points.
Enfin, un des avantages de la méthode est de donner d'un coup la cumulative, autorisant le calcul de la probabilité de détection pour différents seuils (mais pour une seule valeur du rapport signal/bruit)

3.3. Inversion de la fonction caractéristique par le calcul des résidus

3.3.1. Expression ananlytique de la probabilité de détection en fonction des résidus

La cumulative de la distribution s'exprime en fonction de la fonction caractéristique par l'expression :

$$F(z) - F(0) = \frac{1}{2\pi} \int_{-\infty}^{+\infty} \Phi_z(u) \frac{1 - e^{-juz}}{ju} du$$

Soit Y_B le seuil pour lequel on veut calculer la probabilité de détection.

Alors :

$$P_d = 1 - F(Y_B) = 1 - \left(F(Y_B) - F(0)\right) - F(0)$$

$$= 1 - \frac{1}{2\pi} \int_{-\infty}^{+\infty} \Phi_z(u) \frac{1 - e^{-juY_B}}{ju} du \quad - F(0)$$

$$= 1 - F(0) - \frac{1}{2\pi} \int_{-\infty}^{+\infty} \frac{\Phi_z u}{ju} du + \frac{1}{2\pi} \int_{-\infty}^{+\infty} \frac{\Phi_z(u)\, e^{-juY_B}}{ju} du$$

La première intégrale s'écrit :

$$\int_{-\infty}^{+\infty} \frac{\Phi_z u}{ju} du = \int_{-\infty}^{+\infty} \frac{1}{ju} \int_{-\infty}^{+\infty} e^{juz} p(z)\, dz$$

En permutant les ordres d'intégration :

$$= \int_{-\infty}^{+\infty} p(z) \left\{ \int_{-\infty}^{+\infty} \frac{e^{juz}}{ju} du \right\} dz$$

mais $\int_{-\infty}^{+\infty} \frac{e^{juz}}{ju} = \pi\, \mathrm{sgn}(z)$

d'où :

$$\int_{-\infty}^{+\infty} \frac{\Phi_z u}{ju} du = \pi \int_{-\infty}^{+\infty} p(z)\, \mathrm{sgn}(z)\, dz$$

$$= -\pi \int_{-\infty}^{0} p(z)\, dz + \pi \int_{0}^{\infty} p(z)\, dz = \pi\left(1 - 2F(0)\right)$$

En reportant dans l'expression de Pd.

$$P_d = \frac{1}{2} + \frac{1}{2\pi}\int_{-\infty}^{+\infty} \frac{\Phi_z(ju)}{ju} e^{-juY_B}\, du$$

Au paragraphe 2, on montre que :

$$\Phi_z(u) = \prod_{i=1}^{N} \frac{1}{(1-2ju\lambda_i)}$$

la fonction $\frac{\Phi_z(u)}{ju}$ présente donc un pôle à u = 0

et un certain nombre de pôles de la forme $\frac{1}{2j\lambda_i}$
situés dans le demi plan inférieur du plan complexe

Pour calculer $\int_{-\infty}^{+\infty} \frac{\Phi(u)}{ju} e^{-juY_B} du$ on peut donc calculer

l'intégrale complexe le long du contour C représenté à la figure ci-après :

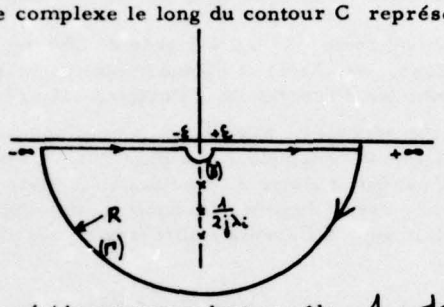

$$\int_C \frac{\Phi_z(u)}{ju} e^{-juY_B} du = -2\pi j \sum_i R_i$$

Ri étant le résidu correspondant au pôle $\frac{1}{2j\lambda_i}$ de $\frac{\Phi_z(u)}{ju} e^{-juY_B}$

Mais : $\int_C = \int_{-\infty}^{-\varepsilon} + \int_{(\gamma)} + \int_{\varepsilon}^{+\infty} + \int_{(\Gamma)}$

$\int_\gamma \to \pi$ lorsque $\varepsilon \to 0$ et $\int_\Gamma \to 0$ lorsque $R \to \infty$

donc $\int_{-\infty}^{+\infty} \frac{\Phi_z(u)}{ju} e^{-juY_B} du = -\pi - 2\pi j \sum_i R_i$

En reportant dans l'expression Pd, on trouve donc :

$$P_d = -j \sum_i R_i$$

Ri étant le résidu de $\frac{\Phi_z(u) e^{-juY_B}}{ju}$ au pôle $\frac{1}{2j\lambda_i}$

La probabilité de détectiop s'exprime donc très simplement en fonction des résidus de la fonction

$$\frac{\Phi(u) e^{-juY_B}}{ju}$$

3.3.2. Calcul des résidus

Cas d'une valeur propre simple de la matrice de covariance

Soit λi une valeur propre simple de la matrice de covariance.
Il lui correspond donc un pôle simple de $\frac{\Phi_z(u) e^{-juY_B}}{ju}$

Le résidu correspondant vaut donc :

$$R_i = \frac{u - \frac{1}{2j\lambda_i}}{\prod_{k=1}^{N} (1 - 2ju\lambda_k)} \frac{1}{ju} e^{-juY_B} \Bigg|_{u = \frac{1}{2j\lambda_i}}$$

$$= -\frac{1}{2j\lambda_i} \frac{1}{\prod_{k=1,\, k\neq i}^{N} 1 - 2ju\lambda_k} \frac{1}{ju} e^{-juY_B} \Bigg|_{u = \frac{1}{2j\lambda_i}}$$

$$= j \prod_{\substack{k=1 \\ k\neq i}}^{N} \frac{1}{1 - \lambda_k/\lambda_i} e^{-\frac{Y_B}{2\lambda_i}}$$

Cas d'une valeur propre multiple de la matrice de covariance

Soient λ_1 λ_2 ... λ_p les valeurs propres d'ordre
α_1 α_2 ... α_p de la matrice de covariance.

Il leur correspond les pôles :

$\frac{1}{2j\lambda_1}$) $\frac{1}{2j\lambda_2}$ ... $\frac{1}{2j\lambda_p}$ d'ordre

α_1 α_2 ... α_p de la fonction caractéristique : $\phi_z(u) = \prod_{k=1}^{p} \frac{1}{(1-2ju\lambda_k)^{\alpha_k}}$

Soit R_i le résidu au pôle $\frac{1}{2j\lambda_i}$ d'ordre α_i

Appelons $g_i(u)$ la fonction définie par

$$g_i(u) = \left(u - \frac{1}{2j\lambda_i}\right)^{\alpha_i} \frac{\phi_z(u)\, e^{-juY_B}}{ju}$$

$$= \left(-\frac{1}{2j\lambda_i}\right)^{\alpha_i} \left(\prod_{\substack{k=1 \\ k\neq i}}^{p} \frac{1}{(1-2ju\lambda_k)^{\alpha_k}} \right) \frac{e^{-juY_B}}{ju}$$

Le résidu R_i est donné par l'expression :

$$R_i = \frac{1}{(\alpha_i - 1)!}\, g_i^{(\alpha_i - 1)}\left(\frac{1}{2j\lambda_i}\right)$$

Pour calculer R_i il faut donc calculer :

$$g_i^{(\alpha_i - 1)}\left(\frac{1}{2j\lambda_i}\right)$$

Le calcul de l'expression littérale de $g_i^{(\alpha_i - 1)}(u)$ étant trop complexe, il est possible d'utiliser une méthode récurrente permettant de calculer sur ordinateur les dérivées de gi et de 1/gi par le biais des dérivées logarithmiques de la manière suivante :

Calcul des dérivées logarithmiques :

$$\mathrm{Log}(g_i(u)) = -juY_B - \mathrm{Log}(ju) + \alpha_i \mathrm{Log}\left(\frac{1}{2j\lambda_i}\right) - \sum_{\substack{k=1 \\ k\neq i}}^{p} \mathrm{Log}(1-2ju\lambda_k)$$

$$\frac{d}{du}\mathrm{Log}(g_i(u)) = -jY_B - \frac{1}{u} + \sum_{\substack{k=1 \\ k\neq i}}^{p} \alpha_k \frac{2j\lambda_k}{1-2ju\lambda_k}$$

$$\frac{d^2}{du^2}\mathrm{Log}(g_i(u)) = \frac{1}{u^2} + \sum_{\substack{k=1 \\ k\neq i}}^{p} \alpha_k \left(\frac{2j\lambda_k}{1-2ju\lambda_k}\right)^2$$

$$\frac{1}{(m-1)!}\frac{d^m}{du^m}\mathrm{Log}(g_i(u)) = (-1)^m \frac{1}{u^m} + \sum_{\substack{k=1 \\ k\neq i}}^{p} \alpha_k \left(\frac{2j\lambda_k}{1-2ju\lambda_k}\right)^m$$

et pour $u = \frac{1}{2j\lambda_i}$ les valeurs de ces dérivées logarithmiques sont :

$$\frac{d}{du} \operatorname{Log} g_i \Big|_{u=\frac{1}{2j\lambda_i}} = -j\gamma_B - 2j\lambda_i + \sum_{\substack{k=1 \\ k\neq i}}^{P} \alpha_k \frac{2j\lambda_k}{1-\frac{\lambda_k}{\lambda_i}}$$

$$\frac{d^2}{du^2} \operatorname{Log} g_i \Big|_{u=\frac{1}{2j\lambda_i}} = (2j\lambda_i)^2 + \sum_{\substack{k=1 \\ k\neq i}}^{P} \alpha_k \left(\frac{2j\lambda_k}{1-\frac{\lambda_k}{\lambda_i}}\right)^2$$

$$\frac{1}{(m-1)!} \frac{d^m}{du^m} \operatorname{Log} g_i \Big|_{u=\frac{1}{2j\lambda_i}} = (-1)^m (2j\lambda_i)^m + \sum_{\substack{k=1 \\ k\neq i}}^{P} \alpha_k \left(\frac{2j\lambda_k}{1-\frac{\lambda_k}{\lambda_i}}\right)^m$$

Toutes ces valeurs des dérivées logarithmiques de $g_i(u)$ pour la valeur $\frac{1}{2j\lambda_i}$ peuvent être calculées facilement sur ordinateur.

Calcul des dérivées en fonction des dérivées logarithmiques :

$$\frac{d}{du} \operatorname{Log} g = \frac{dg}{du} \cdot \frac{1}{g} = g^{(1)} \frac{1}{g}$$

$$\frac{d^m}{du^m} \operatorname{Log} g = \frac{d^{m-1}}{du^{m-1}} \frac{dg}{du} = \frac{d^{m-1}}{du^{m-1}} g^{(1)} \cdot \frac{1}{g}$$

$$= \frac{1}{g} g^{(m)} + (m-1) \left(\frac{1}{g}\right)^{(1)} g^{(m-1)} + \cdots + C_{m-1}^{i} \left(\frac{1}{g}\right)^{(i)} g^{(m-i)} + \cdots + \left(\frac{1}{g}\right)^{(m-1)} g^{(1)}$$

$$\frac{d^m}{du^m} \operatorname{Log} 1/g = g \left(\frac{1}{g}\right)^m + (m-1) g^{(1)} \left(\frac{1}{g}\right)^{(m-1)} + \cdots + C_{m-1}^{i} g^{(i)} \left(\frac{1}{g}\right)^{(m-i)} + \cdots + g^{(m-1)} \left(\frac{1}{g}\right)^{(1)}$$

Ces expressions permettent de tirer g^m et $\left(\frac{1}{g}\right)^m$ en fonction de $\frac{d^m \operatorname{Log} g}{du^m}$ et des dérivées de g et $\frac{1}{g}$ jusqu'à l'ordre $m-1$

$$g^{(m)} = g \left\{ \frac{d^m}{du^m} \operatorname{Log} g - (m-1) \left(\frac{1}{g}\right)^{(1)} g^{(m-1)} - \cdots - C_{m-1}^{(i)} \left(\frac{1}{g}\right)^{(i)} g^{(m-i)} - \cdots - \left(\frac{1}{g}\right)^{(m-1)} g^{(1)} \right\}$$

$$\left(\frac{1}{g}\right)^m = \frac{1}{g} \left\{ - \frac{d^m}{du^m} \operatorname{Log} g - (m-1) g^{(1)} \left(\frac{1}{g}\right)^{m-1} - \cdots - C_{m-1}^{i} g^{(i)} \left(\frac{1}{g}\right)^{(m-i)} - \cdots - g^{(m-1)} \left(\frac{1}{g}\right)^{(1)} \right\}$$

En fait, il est plus simple de calculer :

$$\frac{g^m}{(m-1)!} \quad \frac{\left(\frac{1}{g}\right)^m}{(m-1)!}$$

$$\frac{g^{(m)}}{(m-1)!} = g \left\{ \frac{\frac{d^m}{du^m} \operatorname{Log} g}{(m-1)!} - \sum_{i=1}^{m-1} \frac{1}{i} \frac{(1/g)^{(i)}}{(i-1)!} \cdot \frac{g^{(m-i)}}{(m-i-1)!} \right\}$$

$$\frac{(1/g)^{(m)}}{(m-1)!} = \frac{1}{g} \left\{ - \frac{\frac{d^m}{du^m} \operatorname{Log} g}{(m-1)!} - \sum_{i=1}^{m-1} \frac{1}{i} \frac{g^{(i)}}{(i-1)!} \cdot \frac{(1/g)^{(m-i)}}{(m-i-1)!} \right\}$$

d'où la méthode récurrente pour calculer :

$$g^{(\alpha_i - 1)} \left(\frac{1}{2j\lambda_i}\right)$$

1) Calcul des valeurs des dérivées logarithmiques successives de g et $1/g$ pour $u = \frac{1}{2j\lambda_i}$

jusqu'à l'ordre $\alpha_i - 1$

2) Calcul "en échelle" de : $\frac{g^{(m)}}{(m-1)!}$ et $\frac{(1/g)^m}{(m-1)!}$

pour $u = \frac{1}{2\delta\lambda_i}$ par les formules précédentes jusq'à l'ordre $\alpha_i - 1$ d'où le calcul du résidu.

3.3.3. Résulats d'exploitation

Un programme de calcul sur ordinateur a été écrit pour mettre en oeuvre cette méthode sur des distributions du type χ^2 a 2N degrés de liberté. Les calculs étaient effectués en double précision. La comparaison avec les résultats tabulés a mis en évidence :

- que pour des valeurs de N relativement faibles ($N < 15$) la précision est remarquable et atteint quelques unités de la sixième décimale.

- que pour des valeurs de N plus grandes les résultats deviennent rapidement inutilisables.

Afin d'expliquer cette constation, les intermédiaires de calcul permettant d'aboutir au résidu ont été examinés avec attention.

Il apparaît alors qu'un certain nombre de grandeurs interviennent à des puissances égales au nombre des valeurs propres. Dans ces conditions, les calculs mettent en jeu des nombres soit rapidement énormes, soit tout petits, qui font perdre toute précision sur les calculs effectués.

La méthode du calcul de la probabilité de détection par la méthode des résidus ne doit donc être utilisée qu'avec de grandes précautions et pour des valeurs de N faibles.

En règle générale, la précision qu'elle permet d'atteindre quand elle converge est superflue il est donc préférable d'utiliser la méthode par F.F.T.

DISCUSSION

D F HAMMERS: I know of two treatments of similar problems in US literature, ie computing P_o for partially correlated targets:

1) Kanter, I, - computing P_o for fluctuating target at MTI output; EASCON, 1974.

2) Another paper on P_o frequency decorrelation of S_I targets. I cannot remember the title etc but I will be glad to mail a copy to Mr Blondy.

Note: both 1) and 2) use the residue method.

P BLONDY: I thank Mr Hammers for these interesting references which I will be glad to read.

G GALATI: Has the possibility of using a Monte Carlo simulation to provide the same results on detection probability been considered and if so what were the results and comparisons?

P BLONDY: Of course the Monte Carlo method could be used to obtain detection probability. However, to obtain the same level of accuracy (if needed) a large number of runs would be necessary, which would be costly in computer time. In this respect, the method of inversing the characteristic function using the FFT is very interesting since it delivers the entire cumulative at once, providing knowledge of detection probability for all thresholds (but for one signal-to-noise ratio). Lastly, I believe that, when analytical methods are available, they should be preferred to Monte Carlo methods, since they quite generally provide a better understanding of the phenomena.

SIMULATION OF A RADAR TRACKING A GLINTING AIRCRAFT TARGET IN A MULTIPATH ENVIRONMENT

Jay H. Landreth
ITT Gilfillan
7821 Orion Avenue
Van Nuys, California 91406

SUMMARY

Models of a radar, the target and the terrain are developed for the Fresnel field range so that a radar designer can optimize a radar when tracking is required at short ranges near the ground. Those features of the radar that effect target information or the processing of it are part of the radar model. The target is assumed to be an ensemble of simple shaped scatterers while the roughness of the terrain is represented by a statistically rough surface and a slightly rough surface. A coherent time summation of the signals received from the direct and indirect signal paths are formed into a range facsimile of the real signal. A two channel coherent receiver and processor were emulated to process the data. An application of the model has been developed into a computer simulation in which a pencil beam radar employs three dimensional tracking.

1. INTRODUCTION

The ability of a high resolution radar to track a target is limited by the effects of the environment and the characteristics of the target. This paper describes a quantitative approach into the target-induced effects of glint and scintillation, and the environmental effects of multipath propagation.

Ideally a tracking radar should provide a tracking accuracy at any range that is dependent only upon the characteristics of the radar: beamwidth, power, pulsewidth, thermal noise, etc. This idealized tracking accuracy is almost never attained in the deployment of the radar. If a pulse of electromagnetic energy impinges upon a typical target, the reflected wavefront is nonspherical: its amplitude and phase are a function of the aspect angles. In the case of radar, the typical wavelengths (3 to 30 cm) are relatively short compared with the size of target, hence the tilt of wavefront is rapidly changing due to target motion.

The typical radar target can be described as a collection of phase centers which reflect the radar energy. To get the total reflected energy the independent reflections are vectorially summed for a particular instant of time. A short time later a new summation must be computed because the relative range to each scattering center will be different due to a change in the position or attitude of the target. If we map out the point in space where the vector sum is a maximum, we find that this point rarely appears at the center of gravity for the target or any other fixed reference on the target. This point of maximum return is non-stationary, hence the target appears to have some intrinsic moving virtual radar image and this property is usually referred to as glint. A similar effect is produced by a phenomena known as multipath propagation. When a ground radar must track a low-angle target, a number of multipath bounce propagation paths are consistent with the timing of a range gated radar, hence there are a number of virtual radar images associated with the multipath phenomena. The simultaneous occurrence of glint and multipath propagation will produce a radar signal that is difficult to track in any coordinate system due to the apparent motion of the radar cross section centroid.

In the application of early studies of glint, Delano [Delano R. H., 1953], Dunn et al [Dunn, J. H., 1959], Muchmore [Muchmore, R. B., 1960], and Lindsay [Lindsay, J. E., 1968], it was difficult to quantify all the problems that occurred in a tracking radar. The basic statistical properties of glint rest with the scattering properties of the target and its motion. With the event of large scale digital simulations it is now feasible to model the target and simulate its motions. Graf and Nagle, [Graf, E. R., 1972], developed a four point model to represent an aircraft scattering complex. Each point is assigned a pair of sinusoidal functions that control the amplitude and phase of the reflected signal. The normal to the glint phase front is computed and compared with the line of sight from the radar.

Wright [Wright, J. W., 1972], developed an approach where the target consists of an ensemble of ellipsoids. The target elevation and azimuth errors and phase are computed from a vector summation of the target scattering elements. His thesis includes a summary of the important investigations that have contributed to our knowledge of glint phenomena.

Early studies of multipath propagation also suffered the deficiency of quantification when the approach was applied to a real radar system [Evans, G.D., 1966 and Barton, D.K., 1969]. Graf and Nagle [Graf, E.R., 1974] employed the basic ellipsoidal model of Wright to investigate and quantify the effects of multipath propagation. The reflective properties and surface roughness of the ground were accounted for by combining the investigations of Rice [Rice, S. O., 1951] and Ruck et al [Ruck, G. T., 1970].

These previously described approaches of large scale simulations to the problems of glint and multipath have serious limitations which can influence their results. First, no combined effort was made to allow for a simultaneous investigation of glint and multipath. Second, the complete target and antenna were assumed to be in the fair field. Third, it was assumed that the entire target was always in one angular and range resolution cell. Fourth, there was no attempt to apply the results of the simulations to an actual system tracking an aircraft in three dimensions (azimuth, elevation, and range). The objective of this research has been to combine the work of Wright and Graf and Nagle and to remove all but one of these limitations; the entire target is assumed to be in one range resolution cell. When an actual radar simulation is used in combination with a glint and multipath simulation, it becomes difficult to separate the errors caused by imperfect signal and data processing and those caused by the glint and multipath. The characteristics of the observing radar (transmitted pulse shape, pulsewidth, receiver on-time, antenna and intermediate frequency transfer functions, resolution cell size, wave-length, polarization, and tracking algorithms) have a decided effect on any effort to minimize tracking errors. This particular investigation does not presuppose any rigid set of assumptions associated with the actual radar except in the case of range resolution cell. Rather, it is a general purpose program which allows a radar designer to form the multipath and target modeling with a set of target and ground characteristics around a particular radar. There has not been made any approximation to the target and multipath modeling due to the radar's inability to process the data except for the aforementioned exception.

2. APPROACH

The primary purpose of this investigation was to provide a design tool for the development of a short range approach radar. A quantitative analytic approach was required, one which allowed a designer to analyze the problems of a ground radar tracking a target when the antenna was in the Fresnel range of target and the target was in the Fresnel range of the antenna. Futhermore, the problem was complicated by multipath propagation. The radar was assumed to be tracking the target in three dimensions (range, azimuth and elevation), where the information would be mutually coupled in all dimensions. It was necessary to obtain the effects of the design characteristics intrinsically associated with the radar as well as those inherently associated with the target and the multipath ground reflection properties. To be specific, the characteristics are enumerated as the following:

Target Characteristics Considered

- Course and Fine structure signature modeling
- Monostatic and bistatic RCS
- Specular point phase reference
- Phase and gain of the illumination
- Far Field and Fresnel Field Effects
- Target Motion

Radar Characteristics Considered

- Pulsewidth and transmitted wave form
- Receiver listening time and its time relationship with the transmitted pulse
- Angular resolution cell size
- Intermediate frequency filtering
- Method of antenna scanning: phase and frequency
- Antenna gain and phase contours for far field and Fresnel field
- Polarization
- Antenna scanning geometry
- Measurement algorithms for angle and range
- Tracking algorithms and the design coordinate space
- Range gating algorithm

Ground Properties Considered

- Reflection coefficient
- Polarization
- Surface roughness
- Illuminated area
- Phase and gain of the illumination

It is appropriate that we now discuss in detail each aforementioned characteristics. A complete pictorial of the radar, the target, and the environment is provided in Figure 1.

2.1. Target Modeling.

The target model, which is an extension of the work by Wright [Wright, J. W., 1972], assumes that a target in the Fresnel field can be divided into M different scattering elements located at fixed points in the target coordinate system. Each scatterer is considered to be a simple shape in the far field for which the geometric optics radar cross section (RCS) equation has been previously developed.

For example a BQM-34A drone aircraft (Figure 2) can be modeled with an ensemble of eight ellipsoids sized to the major aircraft components (fuselage, wings, horizontal stabilizer, etc.). The engine intake and exhaust require two additional spherical shapes. More accurate engine modeling is possible with cylinders, cavities, etc. The model is appropriate in the high frequency region where the source of the scattering can be considered to originate from a specular point or a discontinuity. In the high frequency region the RCS can be approximated by geometrical optics. For an ellipsoid, Ruck [Ruck, G. T., 1970] gives this cross-section in the bistatic case as

$$\sigma = \frac{4\pi a^2 b^2 c^2}{[a^2 (\sin\theta \cos\phi + \sin\theta' \cos\phi')^2 + b^2 (\sin\theta \sin\phi + \sin\theta' \sin\phi')^2 + c^2 (\cos\theta + \cos\theta')^2]^2} \quad (1)$$

and in the monostatic case as

$$\sigma = \frac{\pi a^2 b^2 c^2}{[a^2 \sin^2\theta \cos^2\phi + b^2 \sin^2\theta \sin^2\phi + c^2 \cos^2\theta]^2} \quad (2)$$

$$\phi = \phi' \qquad \theta = \theta'$$

where a, b and c are the axes of the ellipsoid, and where θ and ϕ are incident angles, and θ' and ϕ' are reflected angles. Both monostatic and bistatic specular cross-sections are calculated to support direct and indirect propagation.

Figures 3 and 4 depict a model for a BQM-34A. It can be seen that reflections arising from discontinuities (wing-fuselage junction, vertical stabilizer fuselage junction, etc.,) are generated by synthetic specular points. To allow for further adjustments in the individual elemental cross sections and shadowing, a series of modulation and shadowing functions that are aspect angle dependent are benerated.

A test program was developed for target modeling so that a calculated far field synthetic monostatic and bistatic RCS for a particular model could be compared with measured data. This program allows one to make minor adjustments in sizing and placement of the individual simple shapes. Figure 5 compares synthetic and measured monostatic RCS data at C-band for a BQM-34A drone aircraft for aspect angles 0 through 90 degrees with 0 degree roll and pitch angles. The mean of the synthetic data around 20 degrees aspect is about 2 dB higher than measured data with a 4 dB difference from 40 to 70 degrees. No attempt was made to minimize the differences for all aspect angles because the region of interest was 0-10 degrees where the two means are very close. There are many fluctuation extents of both sets of data that do not match up but it is obvious that fine structure variational rates are reasonably close. This type of comparison offers a point of departure only, as the modeling, in the simulation develops the target as a set of coherent scatterers which is being eclipsed by a pulse of energy where each of the simple shapes is treated separately.

The problem geometry, depicted in Figure 6, shows an aircraft on final approach with a ground radar placed to one side of the runway. A primary reference frame is formed at the intersection of the glideslope and the runway. Secondary reference frames are set up at the aircraft center of gravity and at the base of the antenna. Euler transformations are used to transform coordinates from one system to another; thus a rolling, pitching and yawing aircraft with an arbitrary flight path may be tracked by an electronically scanned antenna tilted and rotated to an arbitrary angle. The simulation allows for six degrees of freedom in target motion so that the location of each scatterer can be updated between each pulse of radar energy.

The primary phase reference is the direct path monostatic specular point on each of the simple shapes. For multipath propagation computations the bistatic, radar-ground-target-radar specular points are computed. To maintain phase coherency the aircraft position is updated between each transmitted pulse with a new computation of all specular points.

Since one of the assumptions was that the target was in the Fresnel field of the antenna, a simple antenna gain amplitude contour independent of range is not acceptable. The illumination gain and phase as a function of frequency and range are computed from amplitude and phase measurements of each antenna slot. It is assumed that the rays approaching/leaving any particular target scatterer are parallel but the collective assumption that all rays approaching the target ensemble are parallel was not an assumption. When the projected angular dimension of a scatterer subtends more than a 3 dB change in the illumination amplitude, computation of the equivalent electric field to be applied to each scatterer requires an integration of the elemental gain and phase over the projected area on a plane perpendicular to the line-of-sight. Figure 7 gives an example of the approach where the scatterer is assumed to be an ellipsoid and the projected area is assumed to approximate an ellipse. An ellipsoid projects into the (μ, ν) plane with its major axis oriented at an angle α away from the horizontal reference frame of the antenna. The projected area is divided into equal squares between μ min and μ max which delineates the horizontal extent of the area. An equivalent electric field intensity ($E(\mu, \nu)$) is computed by an integration of the incremental illumination amplitude and phase plane.

2.2 Radar Modeling.

The transmitter emulation consists of an identification of the shape for the transmitted pulse and the particular set of points in space to be sequentially scanned. A rectangular pulse and the scan shown in Figure 8 were used to obtain the results to be described later. For the direct path propagation a weighted transmitted pulse is convolved with the target response to form the steady-state in-phase and quadrature signals represented in Equations (3) and (4):

$$E_{REAL} = \frac{\lambda_{ij}\sqrt{Pt}}{(4\pi)^{3/2}} \sum_{n=1}^{N} \frac{En(\mu,\nu)^2 \sqrt{S_n}}{R_n^2} \cos\left(\frac{4\pi}{\lambda_{ij}} R_n + \pi\right) \tag{3}$$

$$E_{IMAG} = \frac{\lambda_{ij}\sqrt{Pt}}{(4\pi)^{3/2}} \sum_{n=1}^{N} \frac{E_n(\mu,\nu)^2 \sqrt{S_n}}{R_n^2} \sin\left(\frac{4\pi}{\lambda_{ij}} R_n + \pi\right) \tag{4}$$

where P_t is the transmitted peak power, R_n is the range; $E_n(\mu, \nu)$ is the equivalent electric field intensity; λ_{ij} is the wavelength, associated with i, j scan numbers shown in Figure 8; S_n is the monostatic radar cross section for one part of the target ensemble at a wavelength λ_{ij}, and N is the number scatterers.

Provision has been made so that a different transmitted wavelength may be used for each sequentially scanned point. This option allows for an investigation of frequency correlation effects. In the results to be described later, azimuth scanning was based on phase and elevation on frequency.

In the case of multipath propagation the pulse is convolved with the target and the ground specular points by an application of Equations (5) and (6):

$$E_{REAL} = \frac{\lambda_{ij}\sqrt{P_t}}{(4\pi)^2} \sum_{m=1}^{M} \frac{E_m(\mu,\nu)\sqrt{\sigma_m}}{R_{1m}R_{2m}} \sum_{n=1}^{N} \frac{E_n(\mu,\nu)\sqrt{S_n}}{R_{3n}} \cos\left(\frac{2\pi}{\lambda_{ij}}(R_{1m} + R_{2m} + R_{3m}) + 2\pi\right) \tag{5}$$

$$E_{IMAG} = \frac{\lambda_{ij}\sqrt{P_t}}{(4\pi)^2} \sum_{m=1}^{M} \frac{E_m(\mu,\nu)\sqrt{\sigma_m}}{R_{1m}R_{2m}} \sum_{n=1}^{N} \frac{E_n(\mu,\nu)\sqrt{S_n}}{R_{3n}} \sin\left(\frac{2\pi}{\lambda_{ij}}(R_{1m} + R_{2m} + R_{3m}) + 2\pi\right) \tag{6}$$

where $E_m(\mu, \nu)$ is the electric field intensity illuminating the ground, $E_n(\mu, \nu)$ in the electric field intensity illuminating the target; S_n is bistatic target radar cross section; σ_m is the bistatic ground radar cross section; R_{1m}, R_{2m}, and R_{3m} are the bistatic specular point ranges from the antenna to the ground to the target and back to the antenna respectively, and M is the number of elements of ground reflectors. Equations (3) through (6) are readily derived from the radar range equation [Skolnik, M.I., 1962].

Before the aforementioned summations are computed the signals from all sources are sorted out on the basis of ascending range. These equations represent the steady state computation where the entire target is illuminated. During the period of partial illumination, when the pulse is eclipsing the target at the front or rear, a partial sum is formed in the aforementioned equations. It can be seen that the granularity of the time response is based upon the spacial location of the reflective surfaces.

A coherent receiver emulation performs a vector sum of the receiver noise (Gaussian amplitude and uniform phase) and signals received coincidentally from the ground and the target in two gates centered on a calculated predicted position. In most cases the granularity in range is beyond the capability of the radar due to the time response of the intermediate frequency filter, hence a low pass equivalent filter of the IF filter has been implemented.

In this application envelope detection was performed by an amplitude integration of two range gates. Coincidence detection and edge point algorithms (as described by Hammers [Hammers, D. E., 1976] were used to detect the presence of a target and determine its elevation and azimuth. The range was calculated by use of the integrated sums and a calibration table as an adjustment to the latest pre-

dicted range. This table is built up from a priori information; i.e., the shape of the transmitted pulse and the transfer function of the IF filter. The ability to compute meaningful range information is considered to be unique to this simulation in that a close reasonable range facsimile of the return signal is computed for each transmitted pulse. This is considered essential in the development of tracking algorithms when the desired signal is corrupted with multipath returns.

Even though a particular type of receiver and transmitter were simulated, the target and ground modeling are limited only by the restriction that the pulselength must be longer than the target. Monopulse systems would only require a change to the antenna and receiver modeling.

2.3. Multipath Ground Modeling.

The terrain scatter model is an extension of the work done by Graf and Nagle [Graf, E. R., 1974], who applied the theories of Rice [Rice, S. O., 1951] and Ruck [Ruck, G. T., 1970]. For most radar frequencies the wavelength is short enough so as to require two types of surfaces to be represented. The first is referred to as a very rough surface with a RMS height variation (h) in the terrain greater than a wavelength ($\frac{2\pi}{\lambda} \cdot h > 1$). At this end of the roughness scale the scattered field is usually considered incoherent and dominated by specular reflections. The second type of surface referred to as a slightly rough surface ($\frac{2\pi}{\lambda} \cdot h < 1$). Here the scattered field is considered generally more coherent and is dominated by diffuse reflections. Ruck typifies the composite surface reflection as a sum of both types of terrain scattering. Phase information is of a random nature but the scattered power can be computed as well as the time of signal return for a particular illuminated ground patch. The total illuminated area is defined as that amount of surface that would be subtended in azimuth by the mainlobe were it to spotlight the terrain with a range extend defined by the range gate of the radar receiver. For purposes of the simulation, the surface was further divided into equal range and azimuth sectors determined by the range and azimuth resolution of the radar.

From Ruck [Ruck, G. T., 1970] the terrain scattering equation for a slightly rough surface is

$$\gamma_{pq} = \frac{4}{\pi} k_o^4 h^2 \cos^2\theta_i \cos^2\theta_s \left|\alpha_{pq}\right|^2 I \qquad (7)$$

where:

γ_{pq} = Average incoherent scattering cross section per unit surface area where p and q represent the polarization states of the scattered and incident E-fields, respectively.

k_o = Wave number

h = RMS height variation of the surface roughness

θ_i = Angle between incident line-of-sight and the terrain

θ_s = Angle between reflected wave and the terrain

ϕ_s = Angle between the plane of the incident wave and the reflected wave. (See Figure 10.)

α_{pq} = Polarization dependent variable

$I = 2\pi \int_o^\infty r\rho(r) J_o\left(k_o \sqrt{\xi_x^2 + \xi_y^2}\, r\right) dr$

r = Surface height separation between two points.

$\rho(r)$ = Surface-height correlation coefficient

$J_o(x)$ = Cylindrical Bessel function of order zero

$\xi_x = \sin\theta_i - \sin\theta_s \cos\phi_s$

$\xi_y = \sin\theta_s \cdot \sin\phi_s$

$\xi_z = -\cos\theta_i - \cos\theta_s$

If we assume a Gaussian correlation coefficient model, then

$$I = \pi \ell^2 \exp\left[\frac{-k_o^2 \ell^2 (\xi_x^2 + \xi_y^2)}{4}\right]$$

where ℓ is surface correlation length.

When $R_{11} = -1$ and $R_\perp = 1$, then

$$\alpha_{vv} = \frac{\text{Sin}\theta i \ \text{Sin}\ \theta_s - \text{Cos}\phi_s}{\text{Cos}\theta_i \quad \text{Cos}\ \theta_s}$$

$$\alpha_{hv} = \frac{\text{Sin}\phi_s}{\text{Cos}\theta_i}$$

$$\alpha_{hh} = -\text{Cos}\,\phi_s$$

$$\alpha_{vh} = \frac{-\text{Sin}\phi_s}{\text{Cos}\theta_s}$$

where the left subscript refers to the polarization of the scattered wave while the right subscript refers to the polarization of the incident wave. The equations for α_{pg} in the general case, where $R_{11} \neq -1$ and $R_\perp \neq 1$, are developed in Ruck [Ruck, G. T., 1970]. The scattering matrix for circular polarization is then:

$$\alpha_{LR} = \frac{\alpha_{hh} + \alpha_{vv} + i\ (\alpha_{hv} - \alpha_{vh})}{2}$$

$$\alpha_{RR} = \frac{\alpha_{hh} - \alpha_{vv} + i\,(\alpha_{hv} - \alpha_{vh})}{2}$$

$$\alpha_{RL} = \frac{\alpha_{hh} + \alpha_{vv} - i^2\,(\alpha_{hv} - \alpha_{vh})}{2}$$

$$\alpha_{LL} = \frac{\alpha_{hh} - \alpha_{vv} - i\,(\alpha_{hv} + \alpha_{vh})}{2}$$

From Ruck [Ruck, G. T., 1970] the terrain scattering equation for a very rough surface is

$$\gamma_{pq} = \left| B_{pq} \right|^2 J \qquad (8)$$

where

B_{pq} = Polarization dependent variable

$$J = \frac{4\pi}{\xi_z^2} \ P\left(-\frac{\xi_x}{\xi_z}, -\frac{\xi_y}{\xi_z}\right)$$

If the Gaussian surface-height probability density function is assumed

$$J = \frac{4}{S^2 \xi_z^2} \ \exp\left[-\frac{1}{S_2}\left(\frac{\xi_x^2 + \xi_y^2}{\xi_z^2}\right)\right]$$

where $S^2 = 4h^2/\ell^2$

For linear polarization states the scattering matrix is

$$R_{vv} = \frac{A_2 A_3 R_{11} + \text{Sin}\theta_i \ \text{Sin}\theta_s \ \text{Sin}^2\phi_s \ R_\perp}{A_1 A_4}$$

$$B_{vh} = \sin\phi_s \frac{-\sin\theta_i A_3 R_{11} + \sin\theta_s A_2 R_\perp}{A_1 A_4}$$

$$B_{hv} = \sin\phi_s \frac{\sin\theta_s A_2 R_{11} - \sin\theta_i A_3 R_\perp}{A_1 A_4}$$

$$B_{hh} = \frac{-\sin\theta_i \sin\theta_s - \sin^2\phi R_{11} - A_2 A_3 R_\perp}{A_1 A_4}$$

where

$$A_1 = 1 + \sin\theta_i \sin\theta_s \cos\phi_s - \cos\theta_i \cos\theta_s$$

$$A_2 = \cos\theta_i \sin\theta_s + \sin\theta_i \cos\theta_s \cos\phi_s$$

$$A_3 = \sin\theta_i \cos\theta_s + \cos\theta_i \sin\theta_s \cos\phi_s$$

$$A_4 = \cos\theta_i + \cos\theta_s$$

The β_{pq} scattering matrix for circular polarization is the same as that given for α_{pq}.

It should be observed that when vertical or horizontal polarization states are used the cross-polarized scattering was assumed to be negligible, whereas for circular polarization it is assumed that the reflected energy is evenly divided between the incident polarization state and the cross polarized product. This phenomenon is considered to occur at the surface reflection points as well as the target. Equations (7) and (8) are used to compute the average bistatic scattering cross section per unit area and the location of the reflection point is considered to be at the center of each subdivision of the illuminated area. For each incremental terrain radar cross-section (σ_m) used in Equations (5) and (6), the sum of the rough and slightly rough scattering is computed.

The properties of the terrain are described by the mean square surface height variation (h^2), the correlation length (ℓ), and the Fresnel reflection coefficients (R_{11}, $R_\perp$) as defined by Equations (9) and (10). If the incident and reflected components of the E-field are in the plane incidence, then

$$R_{11}(\theta_i) = \frac{\epsilon_r \cos\theta_i - \sqrt{\epsilon_r \mu_r - \sin^2\theta_i}}{\epsilon_r \cos\theta_i + \sqrt{\epsilon_r \mu_r - \sin^2\theta_i}} \tag{9}$$

where θ_i is angle of incidence as depicted in Figure 9, ϵ_r is the relative permitivity, and μ_r is the relative permeability. When the incident and reflected components of the E-field are normal to the plane of incidence, then

$$R_\perp(\theta_i) = \frac{\mu_r \cos\theta_i - \sqrt{\epsilon_r \mu_r - \sin^2\theta_i}}{\mu_r \cos\theta_i + \sqrt{\epsilon_r \mu_r - \sin^2\theta_i}} \tag{10}$$

For Equations (7) and (8), it was assumed that $R_{11} = -1$ and $R_\perp = 1$ which implies that the surface is a perfect conductor. In most cases the surface roughness has a more pronounced effect on multipath reflections than the reflective properties of the terrain.

3. AN APPLICATION OF THE SIMULATION

All of the aforementioned modeling was developed into a computer program. The results to be presented represent a very small fraction of the potential capability of this simulation, but they do indicate that accurate short range tracking is feasible.

Table 1 lists the important input parameters for the radar and the geometry and the target. In Case I we assume the target has no roll, pitch, or yaw rate and is on glideslope with negligible multipath effects. For Case II we assume that the target is performing the indicated maneuvers and that the main beam of the antenna is grazing the terrain.

3.1. Case I.

For Case I the range, elevation and azimuth profiles for two consecutive frames 0.5 seconds apart are depicted in Figures 10 through 14. Figure 8 shows the geometry of the scan points on the range profiles in respect to the target and the terrain, whereas the elevation azimuth profiles scan all the applicable points which are depicted below the plots.

The primary purpose of generating range profiles was to be able to compute the energy in a set of consecutive range bins, as indicated on each range versus signal volts graph, because the accuracy of range tracking is based on computing the distribution of this energy. For this purpose we do not have to produce an exact replica of the signal; rather, a close reasonable distribution of the energy is desired. In all cases the granularity of the synthetic raw data is much greater than the receiver intermediate frequency filter can resolve. This fact, which can be observed by contrasting the raw data with the filtered data, is a consequence always observed for a narrow band system where the bandwidth of the IF approximates the reciprocal of the pulsewidth. It also should be noted that receiver noise has been added to the signal as well as that portion of the range gate where there is no signal present.

A high degree frame-to-frame and scan point-to-scan point correlation for the azimuth range profiles can be observed with a lesser degree observed for the same comparison in the elevation range profiles. For Case I the aircraft is approaching the radar in a fixed straight and level 10^{o} noise high attitude where the azimuth and elevation rate of change are very close (0.8 mills per second). A noticeable difference in correlation is observed when the top and bottom elevation range profiles are compared with the correlation of the right and left azimuth range profiles for the same frame. The reason for these results lies in the fact that the target is considerably more symmetric in azimuth than in elevation and this is accentuated by the geometry of the scenario.

The quantification of the glint phenomenon can be readily observed in the elevation profiles, and to a lesser degree in the azimuth profiles, where both spacial and time glint are evident. If one were to boresight track this target, considerable error would result. In the case of edge point tracking algorithm [Hammers, D. E., 1976], we assume the signal-to-noise ratio is high enough so that the target edges can be measured and centroided accurately while neglecting the larger signal amplitudes associated with target center tracking.

The quality of angle track is dependent on the slope of angle profiles near some threshold value where a large, well-behaved slope of the signal amplitude versus scan angle is important. If the slopes of the angle profiles are well-behaved with the event of time and the energy in the range gate is about evenly distributed, RMS tracking errors less than 0.5 mils in angle and 3 meters in range have been obtained at ranges between 10,000 meters and 300 meters. If the azimuth and/or elevation profile slopes flatten or the symmetry changes with time, considerable degradation in tracking accuracy can be experienced.

3.2. Case II.

Case II is identical to Case I except for the aircraft dynamics listed in Table 1 and the fact that the multipath energy is not neglected. The dynamics are typical normal movements of an aircraft where the pilot or autopilot is maintaining a course in a slightly turbulent environment. The starting attitude is the same for Case I and Case II. In Frame 5 the aircraft is 11.69 degrees nose high in respect to the horizon, 0.85 degrees to the right of the heading in Case I, and the left wing is rolled up 3.39 degrees.

The unfiltered range profiles are depicted in Figure 15 for the azimuth scan point -73 and elevation scan point 110. A comparison of the same azimuth scan point in Cases I and II from Frame 1 indicates a high degree of correlation. The multipath energy shows little effect because the azimuth scan positions are far enough from the surface of the terrain so that only the lower antenna sidelobes illuminate the ground. A comparison of the same azimuth scan point for Cases I and II for Frame 5 show a marked difference due to the little changes in aircraft attitude. It is clear that range profiles can quantify time glint in the range dimension and provide a tool for range tracking evaluation.

Figure 15 also depicts the unfiltered elevation range profiles for scan point 110. In this instance the ground illumination is the result of the mainlobe at a point 5.5 dB (one way power) down from center gain. In most cases the normal bistatic cross section for each scatterer is about double the monostatic

cross section and, in this case, the grazing angle is less than 1 degree. As a result, multipath energy is comparable to the direct path energy. Considerable time glint is evident when Frame 1 is compared with Frame 5 but the significant observation is the amount of multipath energy in the rear end of the range gate in Frame 1. This phenomenon could seriously degrade range tracking.

The azimuth and elevation cross range profiles are portrayed in Figures 16 and 17. A comparison of the azimuth profiles of Cases I and II show marked difference for very little change in aircraft attitude; hence, considerable time glint is evident in the azimuth plane. Even more noticeable is the st iking difference between Case I Frame I elevation profile and Case II Frame 1. Multipath energy has double the signal amplitude in the lower arm. When the elevation profile of Case II Frame 1 is compared with Case II Frame 5 it is evident that multipath problems have accentuated the problems of glint to make boresight tracking in the elevation plane extremely difficult. Of significant importance is the inversion of the curve slope in the bottom portion of the scan for Frame 5.

It is obvious that the general application of edge point tracking in all directions is not the panacea to the problem of tracking in a multipath environment. One might try top edge tracking for the elevation plane but, at this time, a grading of the various approaches to elevation tracking is not available. For the present there are no quantitative measurements for tracking accuracy in the case of multipath. The maneuvering aircraft has not shown any noticeable degradation of edge point tracking accuracies as listed in Case I.

4. CONCLUSIONS AND FUTURE CONSIDERATIONS

With the event of high resolution tracking radars, demands for short range tracking near the terrain has developed. The complexity of problem has retarded the proper evolution of an adequate solution to the problems of glint and multipath. This paper has shown the development of a tractable quantitative approach, whereby the radar designer can design his radar to meet the problem. With this simulation in hand he can try out special waveforms, frequency, polarization and spacial agility, special adaptive processing, and adaptive tracking algorithms.

Although the primary purpose of this investigation was not to develop target statistics, they are an inherent dividend. In the future the author hopes to develop some statistical modeling for fluctuating targets when the radar employs polarization and/or frequency agility. Pulse-to-pulse and frame-to-frame correlation information is readily available from the program also.

Future development is required into the intrinsic nature of glint. Some portion of the glint statistics might be separable from the nature of the target while the remaining portion changes measurably from one aircraft to another. Also, further investigation is needed to develop the correlation of glint statistics with the aircraft dynamics. Later this year, dynamic measurements will be available for correlation of the simulation model.

Other applications include the investigation of special waveforms and processing techniques for target recognition and identification radars. For this purpose it should be possible to develop the frequency spectra for target by improvement of the target modeling.

At this time there is work going on to remove the only major limitation of this investigation. Transient impulse response functions for the simple shapes are being used to develop short pulse response functions [Moffatt, D.L., 1967]. Upon a replacement of the geometric optics radar cross section equations with these time response equations, the assumption that the radar pulse must be longer than the target can be dropped. This approach is being used to develop a simulation of an airport surveillance radar.

ACKNOWLEDGEMENTS

The author is indebted to Dr. D. E. Hammers, who critiqued the paper and provided some insight essential to the model development. For the most part the meticulous job of programming went to Mr. K. M. Wegner to whom the author is most grateful.

REFERENCES

Barton, D. K. and H. R. Ward, Handbook of Radar Measurement, Prentice-Hall, Inc., New Jersey, 1969.

Delano, R. H., "A Theory of Target Glint or Angular Scintillation in Radar Tracking," Proc. of the IRE, Vol 41, 1778-84, Dec. 1953.

Dunn, J. H., D. D. Howard, and A. M. King, "Phenomena of Scintillation Noise in Radar Tracking Systems," Proc. of the IRE, Vol 47, No. 5, 855-63, May 1959.

Evans, G. C., "Influence of Ground Reflections on Radar Target Accuracy," Proc. of the IEEE, Vol 113, No. 8, pp. 1281-1286, August 1966.

Graf, E. R. and H. T. Nagle, "Frequency Agility and Radar Pointing Errors due to Multipath," Interim Technical Report, (DAAH01-71-C-103) Army Missile Command, Auburn Univ. Alabama, Oct. 1, 1974.

Graf, E. R and H. T. Nagle, "Frequency Diversity and Signal Processing to Reduce Glint Pointing Errors," Technical Report, No. 1 (DA-AH01-71-C1303), Army Missile Command, Auburn Univ. Alabama, June 30, 1972.

Hammers, D. E., Techniques for Automatic Target Detection in Scanning 3-D Radar, to be presented at the 1976 AGARD Symposium, The Hague, Netherlands, June 1976.

Lindsay, J. E., "Angular Glint and Moving, Rotating, Complex Radar Target," IEEE Trans. on Aerospace and Electronic Systems, Vol AES-4, No. 2, 162-73, March 1968.

Moffatt, D. L., Interpretation and Application of Transient and Impulse Response Approximations in Electromagnetic Scattering Problems, Thesis Ohio State University, 1967.

Muchmore, R. B., "Aircraft Scintillation Spectra," IRE Trans. Antenna and Propagation, Vol AP-8, 201, 1960.

Rice, S. O., "Reflection of Electromagnetic Waves from Slightly Rough Surfaces," Symposium on the Theory of Electromagentic Waves, New York University, 1959, Interscience, pp. 351-378, 1951.

Ruck, G. T., et al, Radar Cross Section Handbook, Plenum Press, New York, 1970.

Skolnik, M. I., Radar Systems, McGraw-Hill, New York, 1962.

Wright, J. W., "On the Statistical Modeling of Radar Targets," Thesis Univ. of Illinois, Illinois, 1972.

TABLE 1

Important Input Parameters Applied to Simulation Programs

RADAR PARAMETERS	
CENTER FREQUENCY	9100 MHz
BANDWIDTH	4 MHz
TRANSMITTER POWER	120 KW
LOSES - RF & PROCESSING	5.65 dB
PULSEWIDTH	37.5 METERS
RECEIVER GATEWIDTH	45 METERS
NOISE TEMPERATURE	30.71 dB
PRF	4000 PULSES/SECOND
DATA RATE	10 FRAMES/SECOND

ANTENNA PARAMETERS:	
GAIN	39 dB
BEAMWIDTH AZIMUTH	1.1^0 MAX.
BEAMWIDTH ELEVATION	0.7^0 MAX.
SIDELOBE MAXIMUM	- 18 dB
ANTENNA HEIGHT	2.4 METERS

TERRAIN PARAMETERS:	
ROUGH SURFACE RMS HEIGHT VARIATION	0.05 METERS
ROUGH SURFACE CORRELATION LENGTH	0.5 METERS
SLIGHTLY ROUGH SURFACE RMS HEIGHT VARIATION	0.0025 METERS
SLIGHTLY ROUGH SURFACE CORRELATION LENGTH	0.025 METERS
REFLECTION COEFFICIENTS	$R_1 = 1$, $R_{11} = -1$

SCENARIO PARAMETERS:	CASE I	CASE II
INITIAL RANGE	2200 METERS	2200 METERS
INITIAL ALTITUDE	30 METERS	30 METERS
INITIAL VELOCITIES		
V_x	- 60 METERS PER SECOND	
V_y	- 5 METERS PER SECOND	
V_z	0	
INITIAL ACCELERATIONS	0	

TARGET DYNAMICS	CASE I	CASE II
PITCH RATE OF CHANGE	0	1.5 RADIANS/SECOND
PITCH MEAN ATTITUDE	$+10^0$ ABOVE THE HORIZON	$+10^0$ ABOVE THE HORIZON
PITCH MAXIMUM ATTITUDE	$+10^0$ ABOVE THE HORIZON	13^0 ABOVE THE HORIZON
PITCH MINIMUM ATTITUDE	$+10^0$ ABOVE THE HORIZON	7^0 ABOVE THE HORIZON
ROLL RATE OF CHANGE	0	1.5 RADIANS/SECOND
ROLL MEAN ATTITUDE	0^0 RESPECT TO THE HORIZON	0^0 RESPECT TO THE HORIZON
ROLL MAXIMUM ATTITUDE	0^0 RESPECT TO THE HORIZON	$+6^0$ RESPECT TO THE HORIZON
ROLL MINIMUM ATTITUDE	0^0 RESPECT TO THE HORIZON	-6^0 RESPECT TO HORIZON
YAW RATE OF CHANGE	0	1.5 RADIANS/SECOND
YAW MEAN HEADING	ON RUNWAY HEADING	ON RUNWAY HEADING
YAW MAXIMUM HEADING	ON RUNWAY HEADING	$+1.5^0$ FROM RUNWAY HEADING
YAW MINIMUM HEADING	ON RUNWAY HEADING	-1.5^0 FROM RUNWAY HEADING
GLIDESLOPE DEVIATION RATE	0	1.5 RADIANS/SECOND
MEAN DEVIATION	AIRCRAFT CENTER OF GRAVITY ON GLIDESLOPE	AIRCRAFT CENTER OF GRAVITY ON GLIDESLOPE
MAXIMUM DEVIATION	AIRCRAFT CENTER OF GRAVITY ON GLIDESLOPE	+2.44 METERS IN y AND/OR z COORDINATES
MINIMUM DEVIATION	AIRCRAFT CENTER OF GRAVITY ON GLIDESLOPE	-2.44 METERS IN y AND/OR z COORDINATES

TP162-9

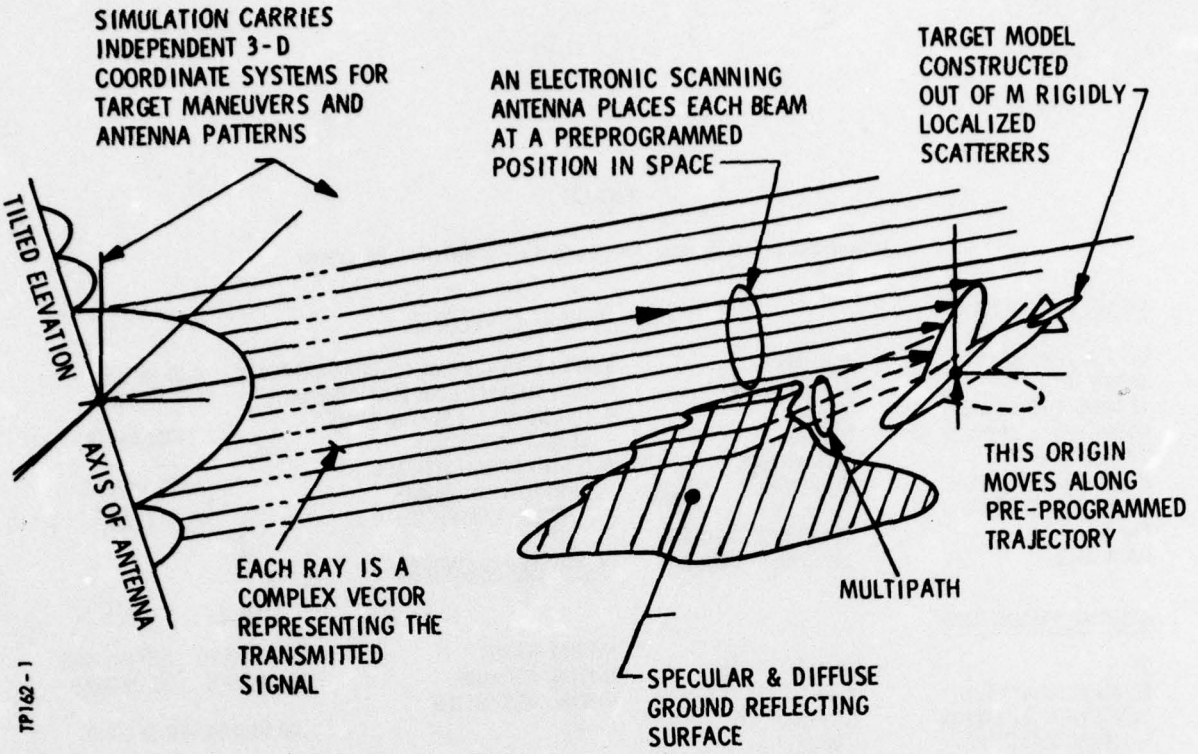

Fig.1 Single plane transmission for distributed target model simulation

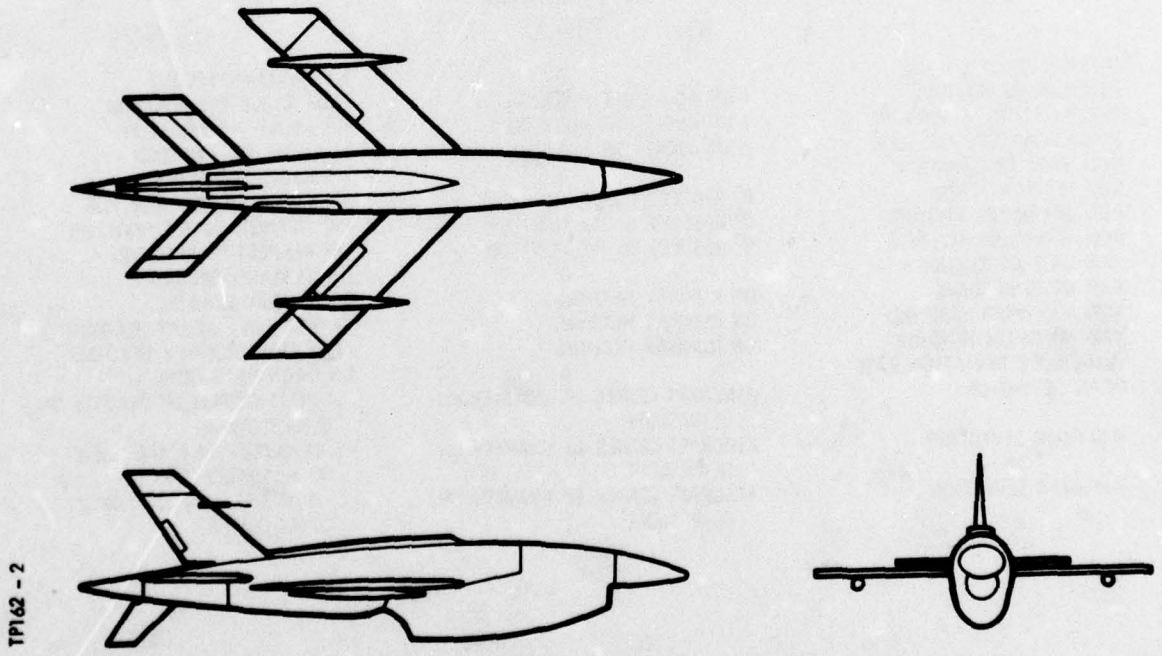

Fig.2 BQM-34A target drone

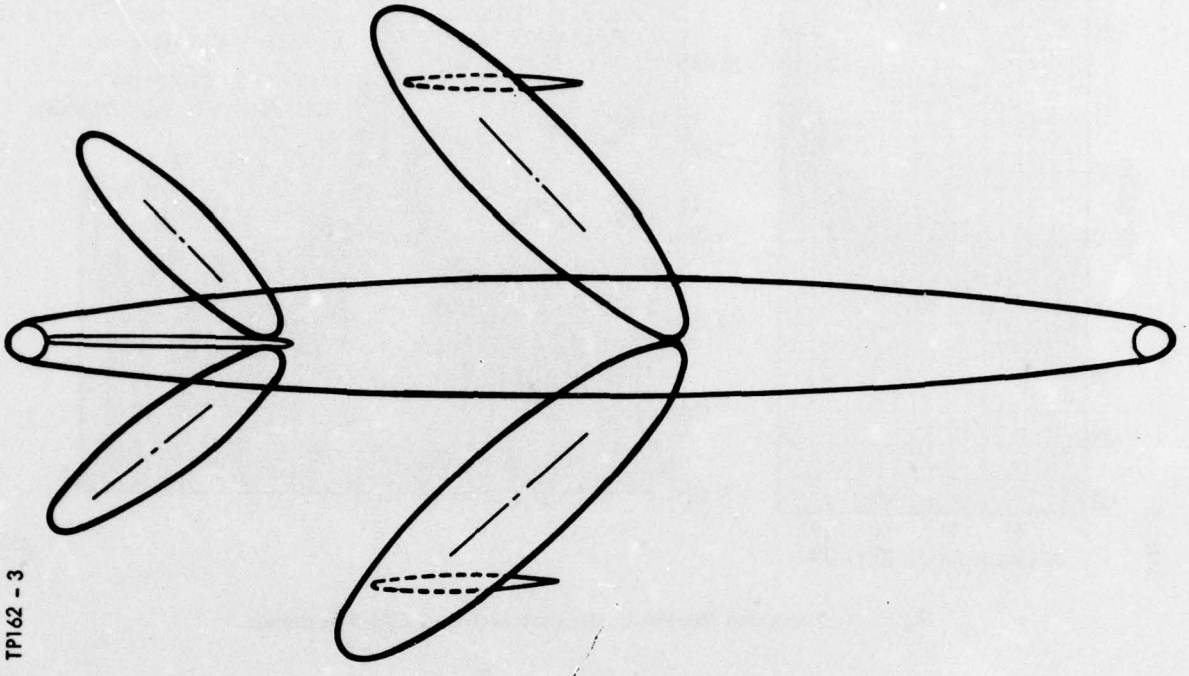

TP162 - 3

Fig.3 Ellipsoidal model of BQM-34A, top view

TP162 - 4

Fig.4 Ellipsoidal model of BQM-34A, side view

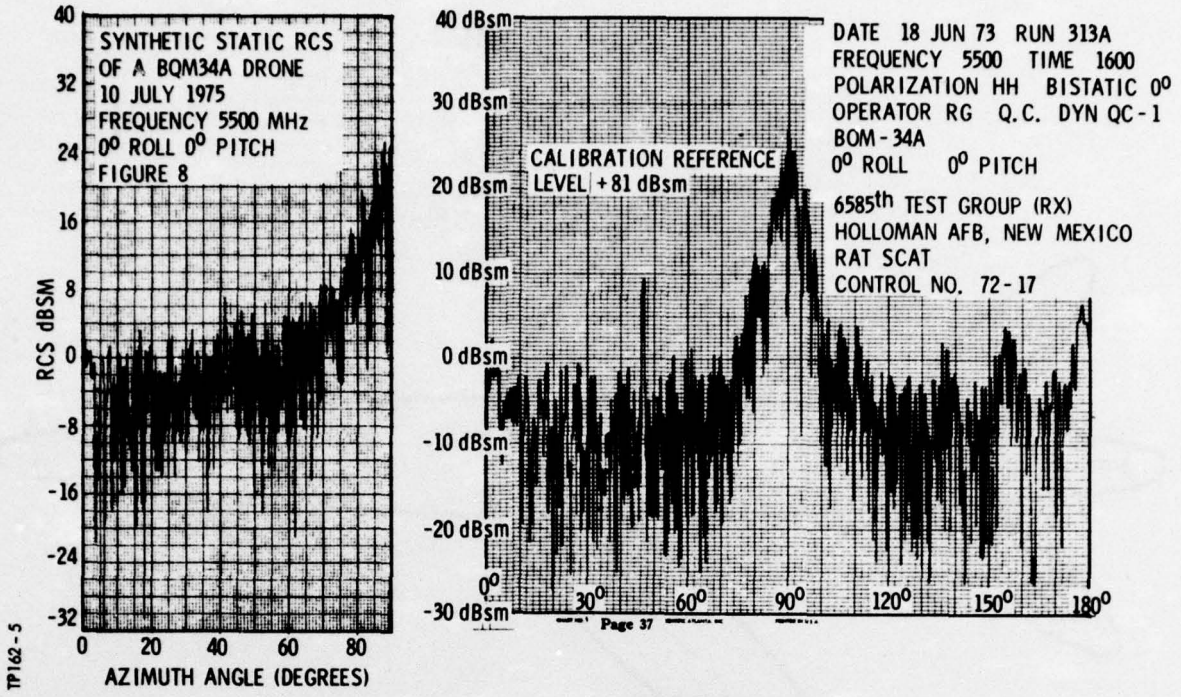

Fig.5 Synthetic and measured radar cross sections (BQM-34A drone)

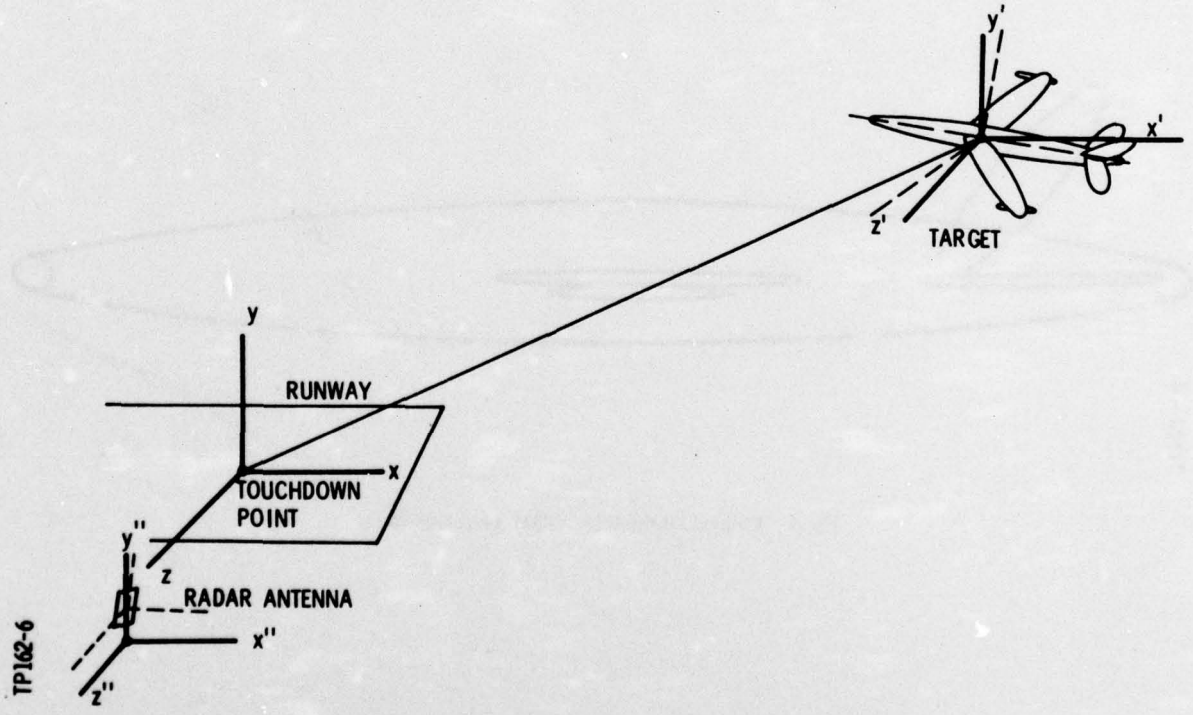

Fig.6 Problem geometry

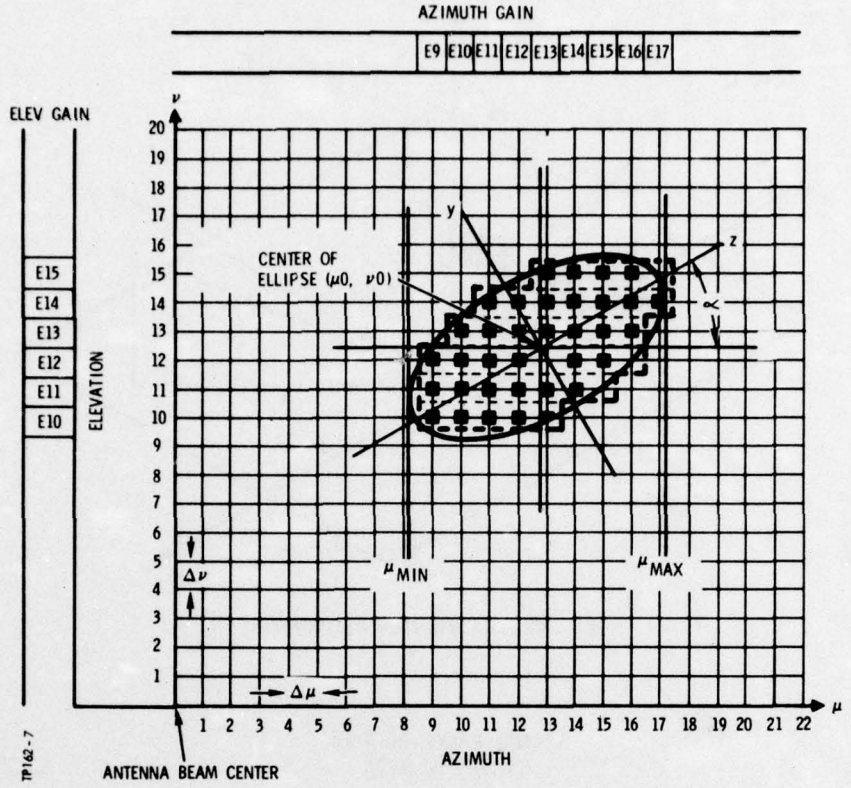

Fig.7 Projected area of an ellipsoidal scatterer

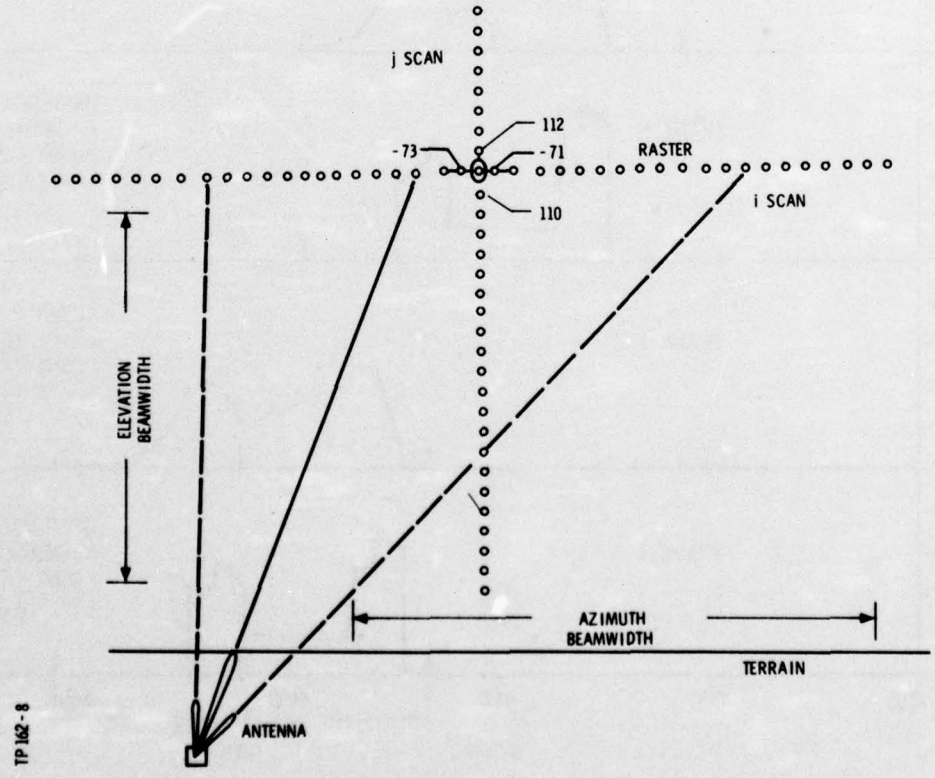

Fig.8 Radar azimuth scan time slice (2200 M range, 30 M altitude)

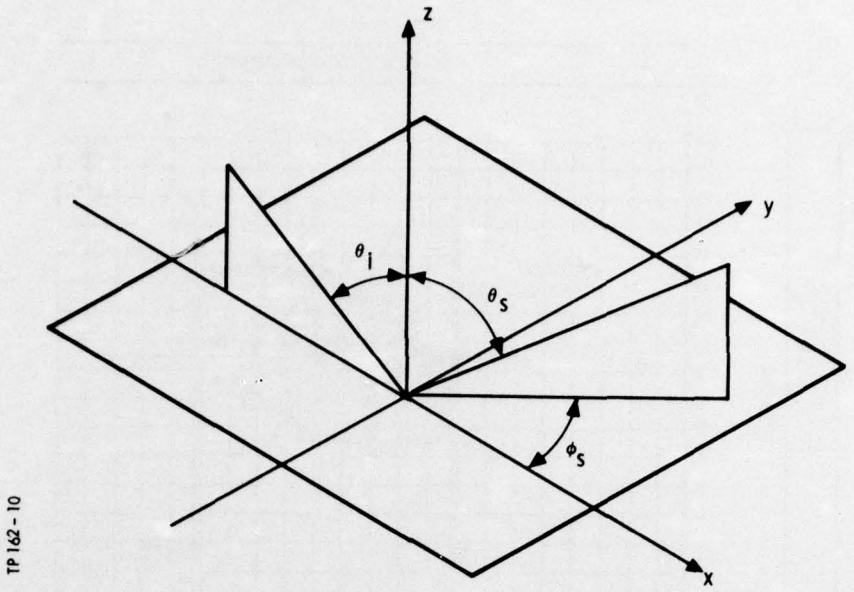

Fig.9 Ground-reflection coordinates

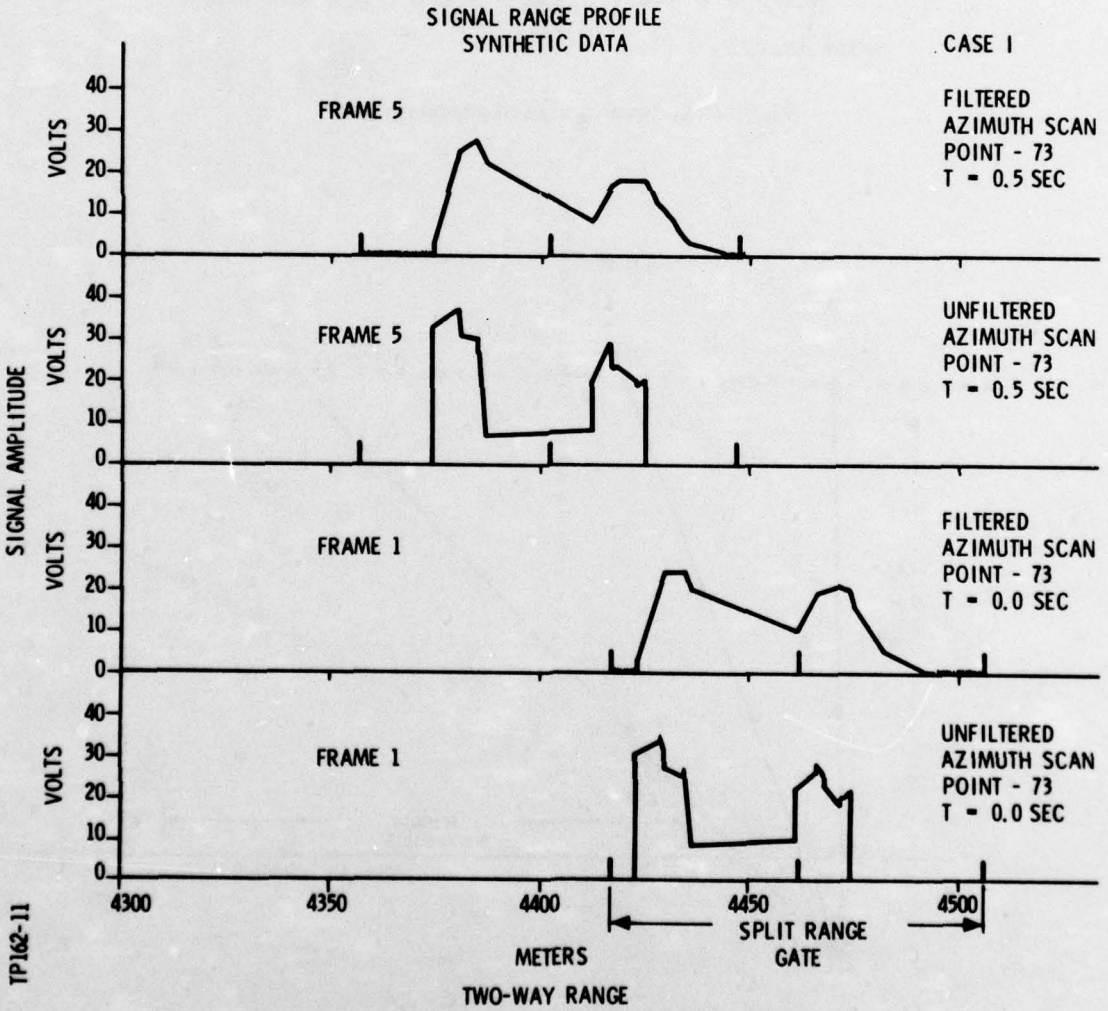

Fig.10 Signal range profile for the left azimuth, Case I

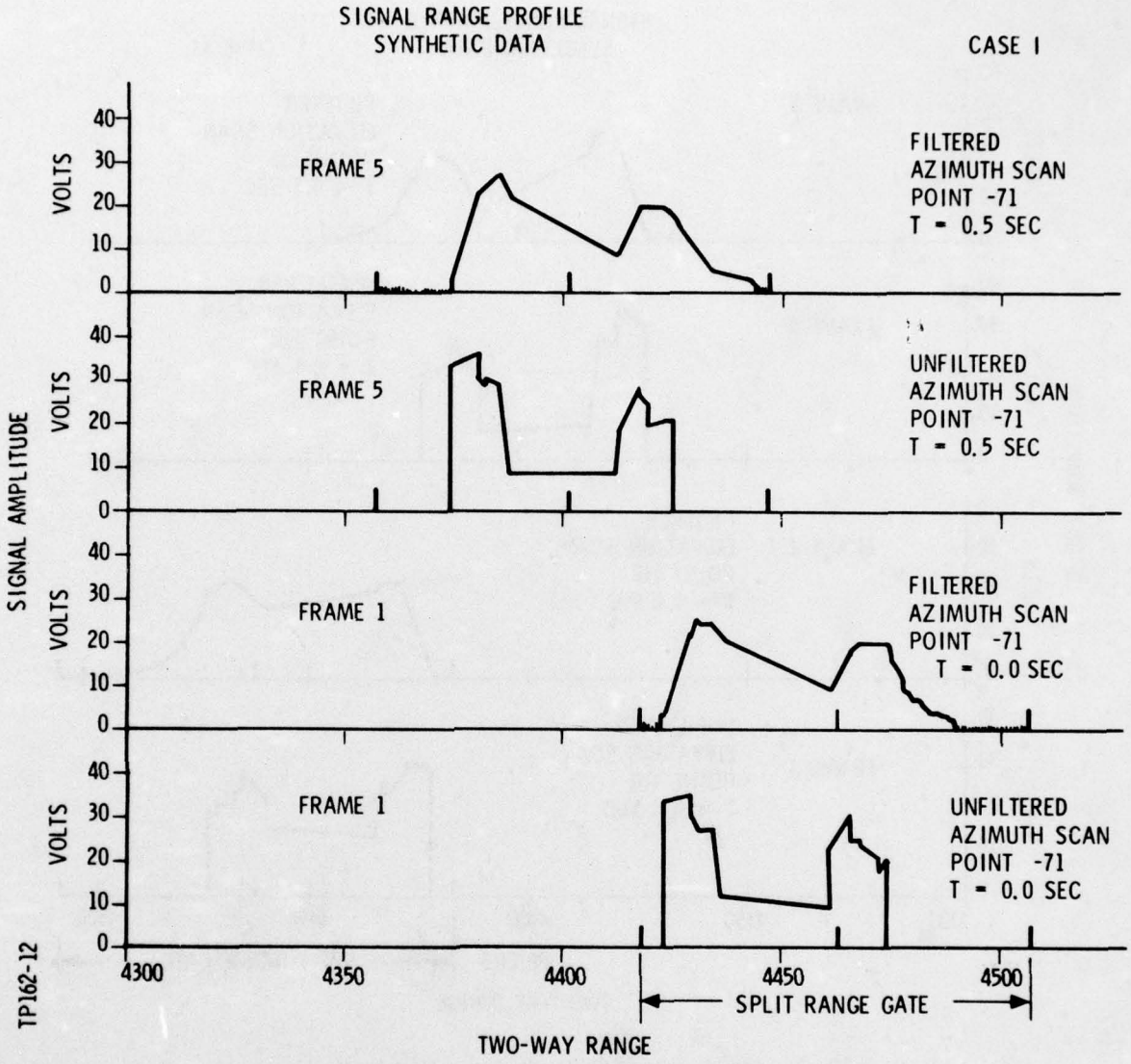

Fig.11 Signal range profile for the right azimuth, Case I

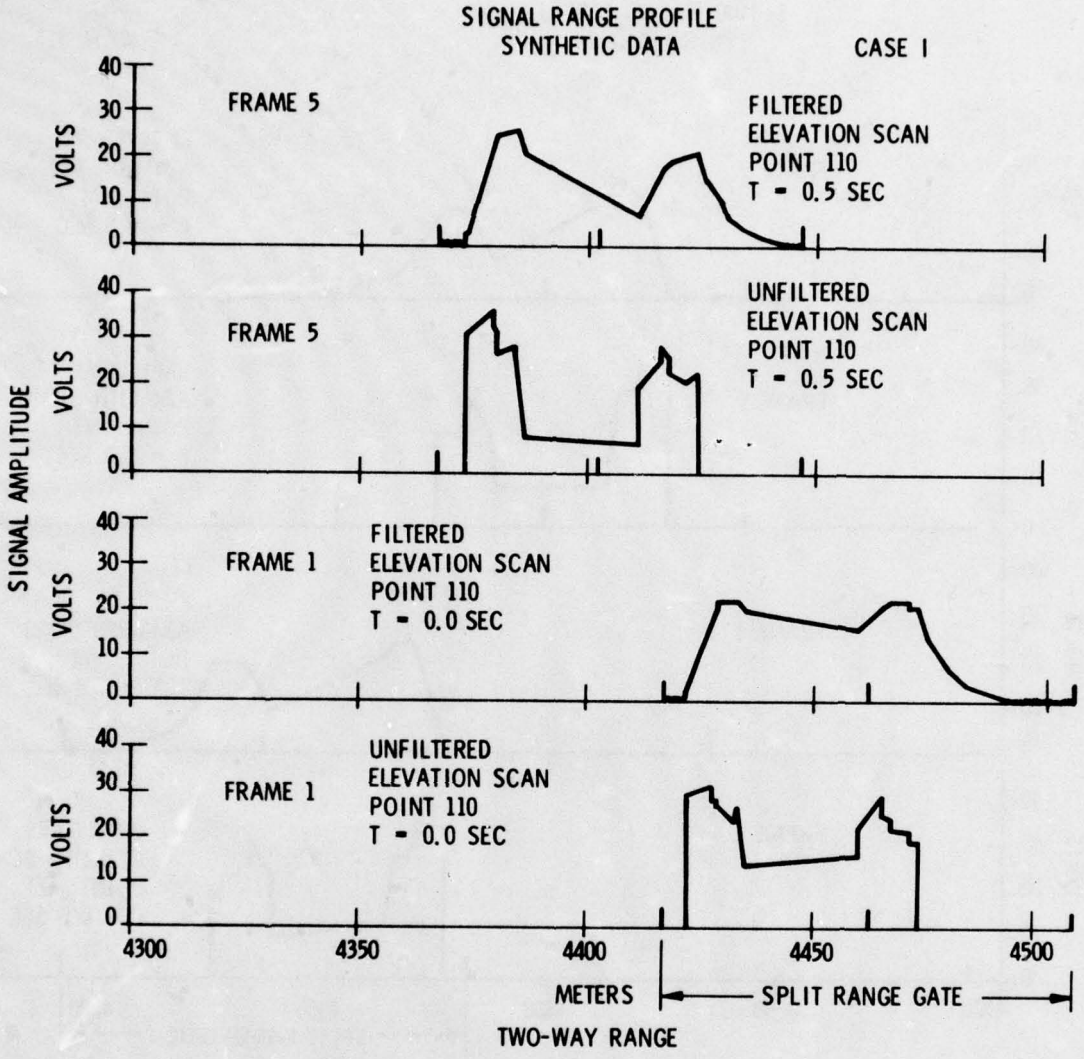

Fig.12 Signal range profile for the lower elevation, Case I

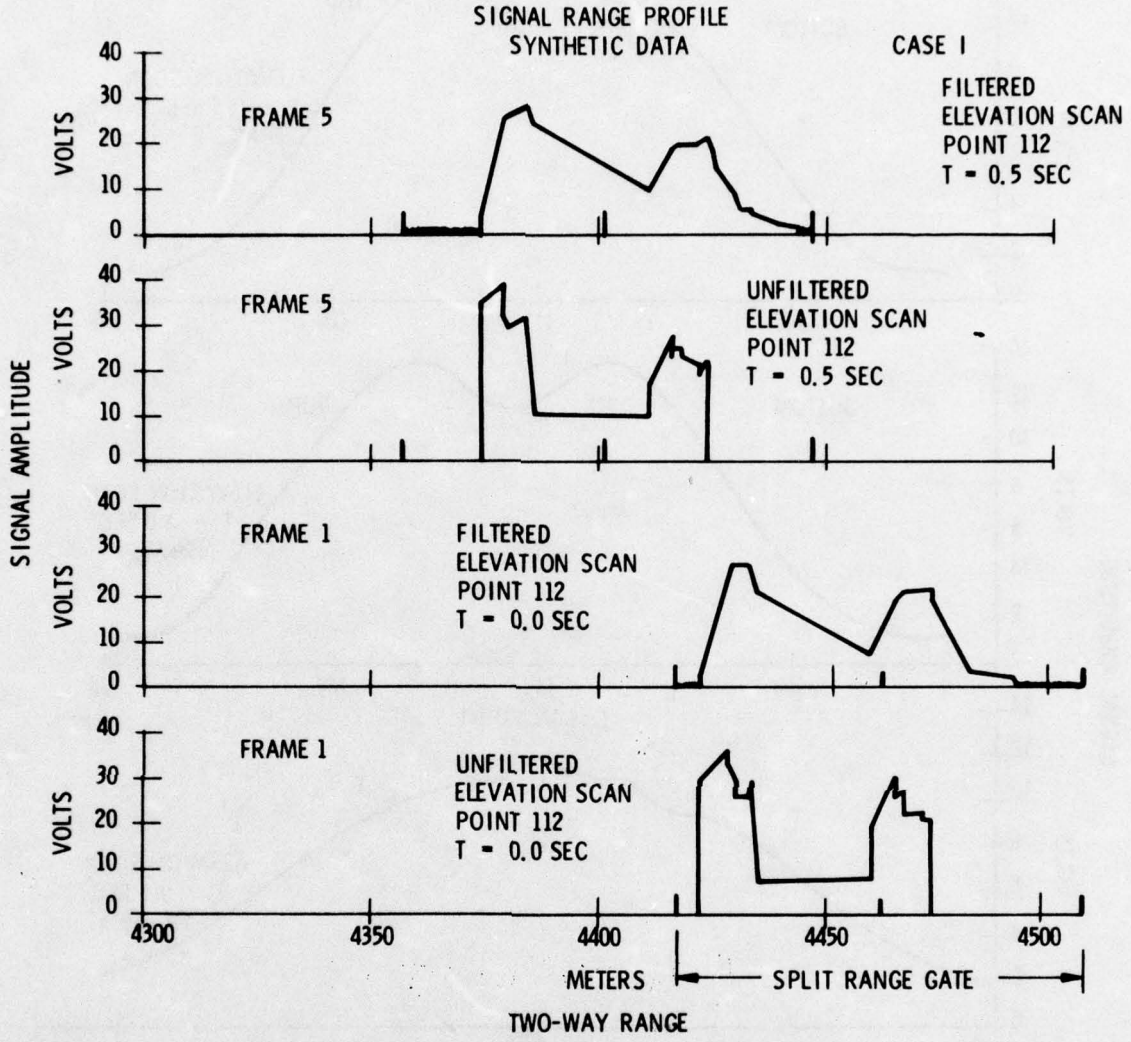

Fig.13 Signal range profile for the upper elevation, Case I

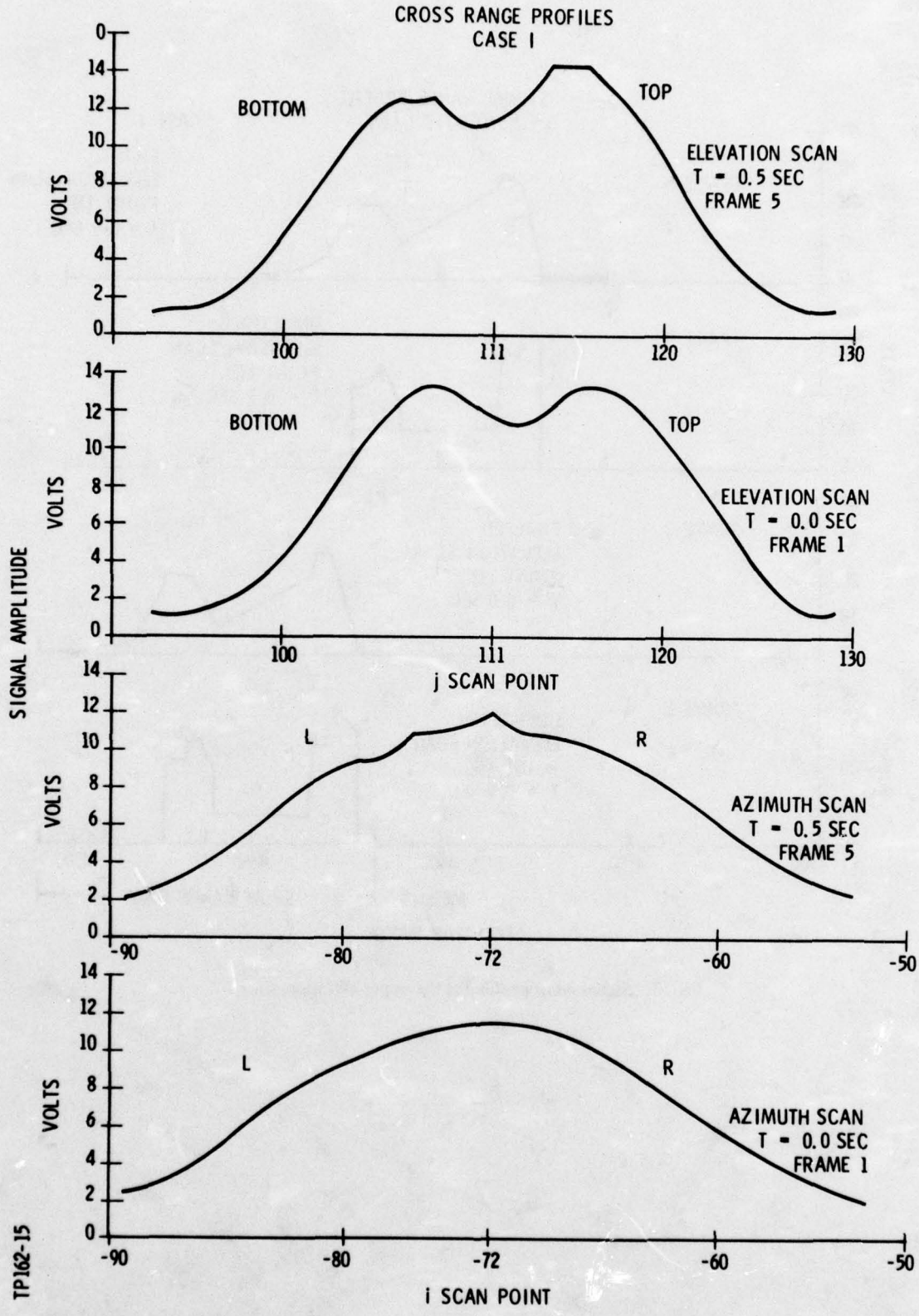

Fig.14 Cross range profiles, Case I

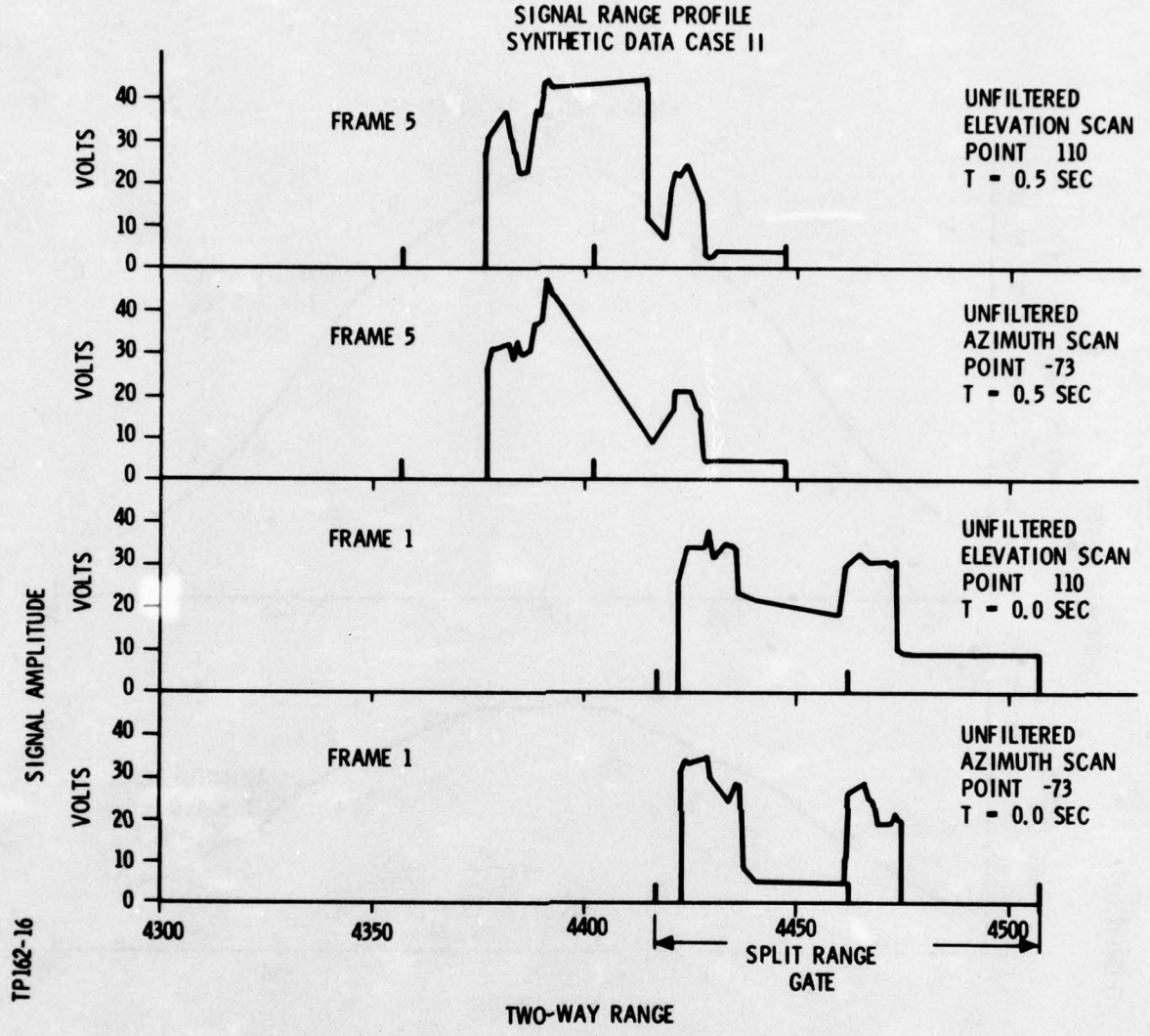

Fig. 15 Signal range profiles, Case II

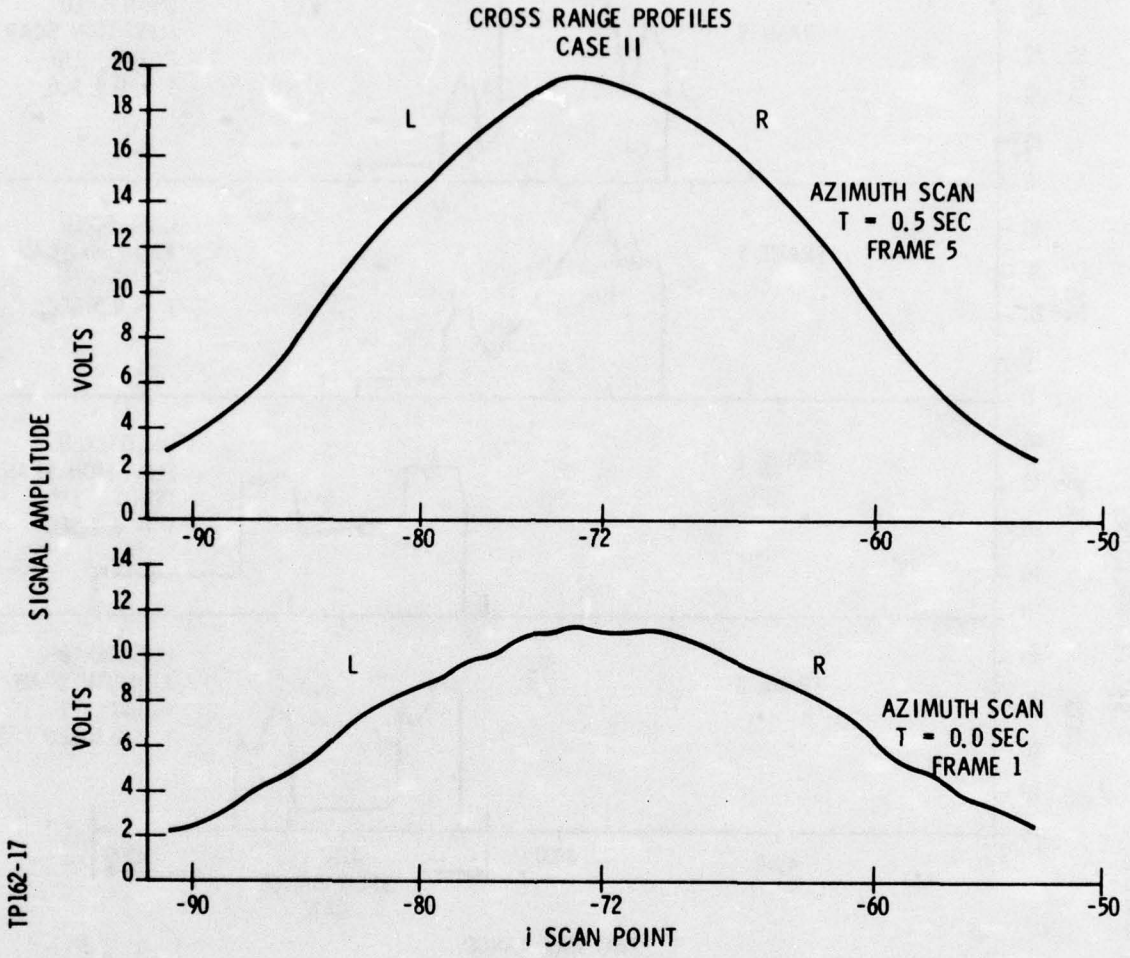

Fig.16 Cross range profiles for azimuth, Case II

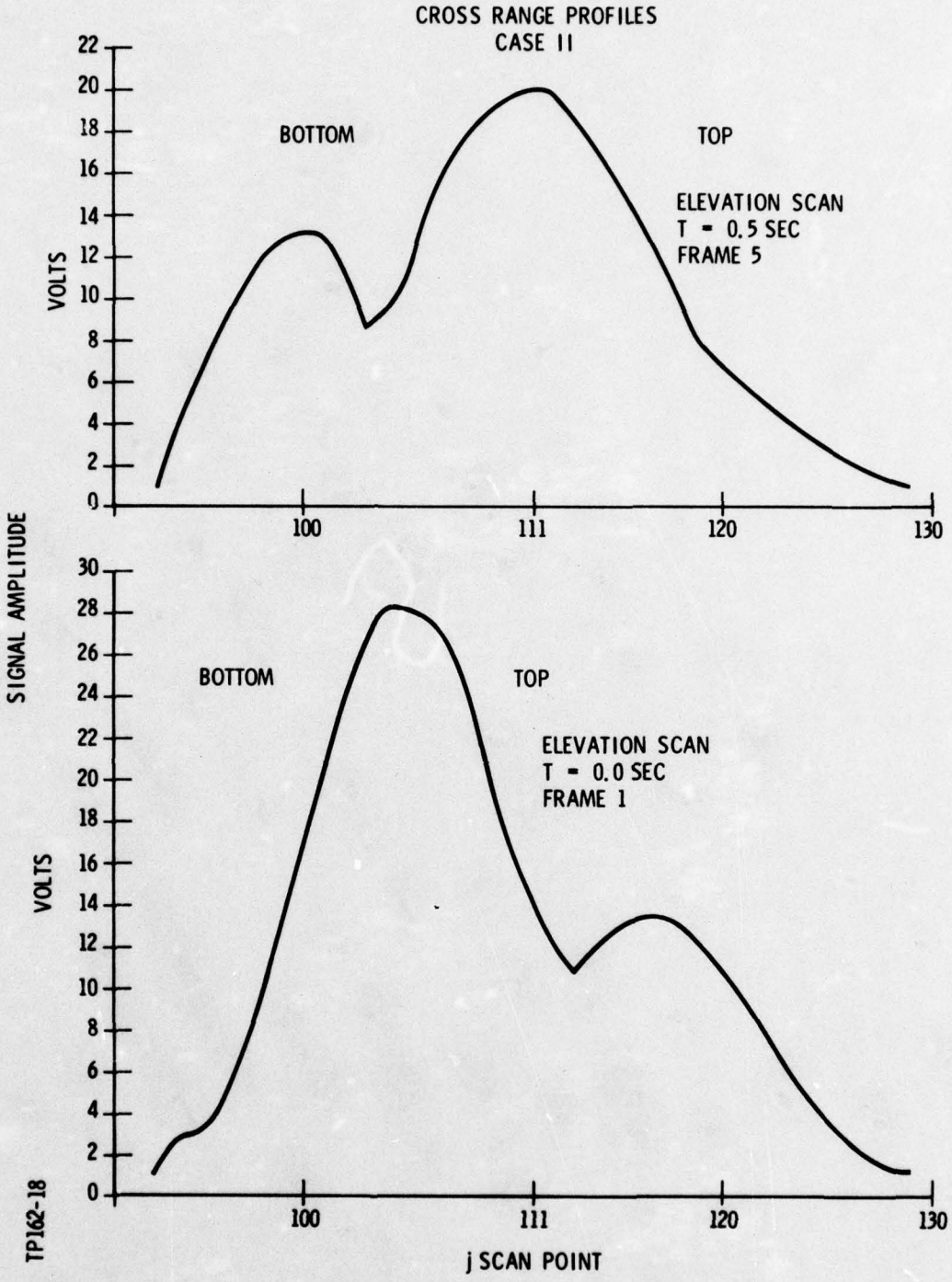

Fig. 17 Cross range profiles for elevation, Case II

COHERENT INFRARED RADAR*

Robert H. Kingston and Leo J. Sullivan
Lincoln Laboratory, Massachusetts Institute of Technology
Lexington, Massachusetts, U. S. A.

SUMMARY

Infrared radar operating in the coherent mode has many similarities to standard microwave radar although the much shorter wavelength and the use of lasers results in several major differences in system design. In this paper, we describe a coherent radar system operating at a wavelength of 10.6 micrometers or approximately 0.01 mm, using an ultra-stable CO_2 laser oscillator and one kilowatt amplifier. Although limited to clear weather conditions, the high Doppler sensitivity, 2 kHz/cm/sec, and narrow beamwidth, 10 microradians result in extremely precise velocity and angle measurements. The critical components of the system are reviewed as well as the special properties and techniques peculiar to this wavelength region. The overall system is described as well as recent experiments utilizing the retroreflector-equipped GEOS-C satellite.

1. RADAR CONSIDERATIONS AT INFRARED WAVELENGTHS

The extremely short wavelength of the infrared radar results in two significant phenomena not applicable to microwave systems. First, the short wavelength results in an extremely narrow beamwidth, (λ/D), for reasonable-sized transmit-receive apertures in a coherent system. As an example, at a wavelength of 10 micrometers, the one meter aperture used in the present system results in a beamwidth of 10 microradians or 2 arc-sec. This beamwidth is comparable with typical angle-of-arrival fluctuations due to atmospheric turbulence, (GILMARTIN, T. J. and HOLTZ, J. Z., 1974) and effectively places an upper limit on usable aperture size. At the same time, using such a large aperture for optimum sensitivity, the target tracking must be extremely precise and capable of tracking out the angular fluctuations associated with the atmosphere. These fluctuations fortunately occur at rates less than 10 Hz and as will be discussed later, can be compensated for in a well-designed system.

The second important consideration in an infrared coherent system is the high ratio of Doppler shift to target velocity. In the 10 micrometer case this ratio is 2 kHz frequency shift per cm/sec. As a result, especially for satellites, the Doppler shift is many orders of magnitude greater than the matched spectral bandwidth for typical radar pulse widths. In our satellite observations, the Doppler shift may be as high as 1000 MHz for low elevation angles while the pulse width, from 1 to 4 milliseconds corresponds to a matched bandwidth of the order of 1 kHz or less. Thus, the radar system must have provision for searching or designating in frequency as well as angle, in order to obtain optimum signal-to-noise performance in the receiver.

2. SYSTEM DESCRIPTION

A simplified schematic of the radar system is shown in Fig. 1, where the wavy lines indicate the optical path and the solid lines, electrical signal flow. Although the Doppler shifts on all moving targets yield an adequate frequency offset in the heterodyne detector, a frequency-shifted local oscillator, offset by 10 MHz, is used to allow observation of stationary calibration targets. Many of the components shown are described in more detail below and are similar in many respects to those in a microwave radar system. One exception is the so-called "aberration" corrector, which is a computer-controlled mirror that corrects for the finite transit time to and from the target. The aberration effect was first studied in classical astronomy and is associated with the physical motion of the target during the time of flight of the light wave from target to telescope. In the case of satellite observations the transmit beam must lead the target by this aberration angle and the receive must lag by the same angle. The angle in each case is given by the ratio of the transverse target velocity to the velocity of light. In our system the corrector mirror must displace the received beam by twice this angle with respect to the transmitter boresight angle. For a satellite in low-altitide orbit, with velocity of 8 km/sec, this angle is 50 microradians at closest approach, or five beamwidths. The correction is thus essential for satisfactory system operation.

2.1. Oscillators

For the ultimate in Doppler precision the short-term stability of the master and local oscillators in the radar system should be at least the inverse of the pulse width, and in the limit of pulse-to-pulse coherent Doppler measurements should be less than the

*This work was sponsored by the Advanced Research Projects Agency of the Department of Defense.

frequency spread introduced by atmospheric fluctuations. For pulses up to 4 milliseconds, this yields a requirement of 250 Hz stability, while current estimates of atmospheric phase fluctuations yield a lower limit of the order of 10 Hz. The oscillators used in our system are of the design shown in Fig. 2, a sealed-off low-pressure CO_2 laser with 5 watts, single-frequency, single spatial mode output (FREED, C., 1968). Measurements in a quiet laboratory environment yield short term stability for this type of laser of the order of 10 Hz, as shown in Fig. 3, which displays the beat frequency spectrum between two independent lasers operating with no external tuning control. In actual system use, we have observed frequency stability of approximately 1 kHz over the same observation time, currently limited by the vibrational and acoustical environment at the radar facility. This stability is adequate for millisecond pulse operation, and improved isolation should yield the ultimate stability of 10 Hz. In the system shown in Fig. 1, the local oscillator is slaved to the master oscillator using a piezo-electric driven tuning mirror. The frequency stability of this locked loop is of the order of 2 Hz, so that the actual frequency resolution of the system is limited by random frequency fluctuations of the master oscillator over the round-trip time to and from the target, of the order of 10 milliseconds.

2.2 Isolator

To reduce the effects of backscattered radiation, especially from vibrating objects in the beam path, an isolator is used to maintain the stability of the master oscillator. Figure 4 is a schematic diagram of such a device using Faraday rotation of free electrons in the semiconductor, indium antimonide (DENNIS, J. H., 1967). A practical device can handle beam powers of 10 watts and yields a reverse isolation of 20 to 25 db, limited in the case shown by the rejection of the Brewster angle polarizers.

2.3 Duplexer

In contrast to microwave systems, there is no simple gas-discharge device which can adequately protect the heterodyne detector from the transmitted beam power. As a result, the present most effective system is a rotating disk, synchronized with the radar pulse repetition frequency. During transmission of the pulse an opening in the disk allows the beam to propagate to the pointing mount, while during the reception period, a highly reflective surface on the disk reflects the beam onto the receiver optics. Fortunately the repetition frequency, from 50 to 200 Hz, is low enough so that the angular velocity (several thousand rpm) is not a serious mechanical design problem. Since the beam is focussed to a spotsize of a millimeter the switching action is also rapid in comparison with the pulse repetition interval. A typical disk is 50 cm in diameter and contains four equally spaced curved slots, each 22.5° in extent, corresponding to a 25% duty cycle for the transmit mode.

2.4. Amplifier

The master oscillator used in the radar system is a longer version of the unit shown in Fig. 2 and delivers approximately 10 watts to the amplifier after passage through the isolator and a second set of slots in the duplexer. This latter switching of the oscillator input is necessary to prevent the transmitter output from illuminating the duplexer disk during the receive mode. The amplifier is a low-pressure longitudinal discharge CO_2 system with a maximum output power of 1 kW when driven with 10 watts input (MILES, P. A. and LOTUS, J. W., 1968). The actual output power can be varied by adjusting the gas mix, (carbon dioxide, helium and nitrogen) flowing in the system.

2.5. Detection System

The detection system utilizes the coherent heterodyne mode (TEICH, M. C., 1968) and as shown in Fig. 5, four separate detector elements provide both signal amplitude and monopulse error signals for tracking. The target return beam is shown distorted to indicate the effects of the atmosphere on the focussed received signal wave. The mercury cadmium-telluride detector (SPEARS, D. L., 1976) operates at liquid nitrogen temperature and has a frequency response more than adequate to cover the required Doppler range. In addition the size of the four element device, 0.3 mm diameter, and the thin structure result in excellent isolation, greater than 30 dB, between individual elements even at frequencies greater than 1 GHz. The sensitivity of 10^{-19} watts/Hz is within a factor of 5 of ideal, $P = h\nu B$, the limitation being an approximately 50% quantum efficiency and the added noise from the broadband preamplifier following each detector element. Figure 6 shows the frequency conversion scheme used in each detector channel and indicates the technique for cancelling out the Doppler shift before final signal processing. The frequency synthesizer may be computer-directed using Doppler information from a microwave radar, or alternatively, frequency discrimination in the final i.f. stage may be used for closed-loop frequency track. In any event, the final output is processed in a filter bank with 1 kHz resolution for real-time observation and also recorded for later data analysis.

2.6. Pointing Mount

As shown in Fig. 7, the final transmit-receive aperture is a one meter steerable mirror which expands the beam from an initial diameter of 15 cm to the final full aperture size. The 15 cm beam is obtained by recollimating the output beam from the duplexer and is then transmitted by means of folding mirrors through the center of the azimuth platform, horizontally and vertically to the elevation axis, and thence to the secondary by means of a folding mirror in front of the primary. The vertical-horizontal folding

mirror on the elevation axis has a separate servo pointing system for fine tracking and narrow angle beam scanning.

3. GEOS-III TRACKING EXPERIMENTS

As an example of the capability of this system, tracking experiments have been carried out using the GEOS-III satellite as a target. This satellite is equipped with a corner cube retroreflector having an effective radar cross-section at 10 micrometers of approximately 10^3 square meters. The tracking technique is shown schematically in Fig. 8, and uses input information obtained from an adjacent microwave radar which supplies medium-precision range, angle, and range rate data. This input data is smoothed in a Kalman filter and is used to direct the main pointing mount, while the monopulse error signal from the infrared radar drives the vernier pointing mirror after appropriate filtering. Initial angle biases between the microwave and infrared systems are removed by TV observation of the satellite with the visible optics shown on the top of the mount. Figure 9 shows the results of a 20-second track of the satellite, while at a range of approximately 1000 km. The upper graphs are the total residual errors from a smooth orbit fit obtained by summing the angular position of the vernier mirror and the monopulse error angle output. They thus represent the fluctuation of the smoothed angle inputs from the microwave radar combined with angle-of-arrival jitter associated with atmospheric turbulence. The lower graphs show only the monopulse error, indicating a track of the apparent position of the satellite with a standard deviation of 1 microradian. It may be seen that the vernier mirror loop has tracked out a majority of those errors having frequencies up to 2 Hz, with the remaining higher frequency errors similar in magnitude to the non-tracked case. The 2Hz limit to the tracking correction is consistent with the measured servo response of the vernier mirror.

4. CONCLUSION

Further experiments are planned to demonstrate the extremely precise metric capability of the radar system. These include precision angle as well as Doppler measurements on targets such as the GEOS-III satellite. In addition, upon demonstration of frequency stability of 10 Hz or less, the behavior of the atmosphere will be measureable in terms of the phase fluctuation as well as the angle-of-arrival effects. We are indebted to all our colleagues in the infrared radar group for the results reported and in particular to R. Teoste for the monopulse tracking experimental data.

REFERENCES

DENNIS, J. H., 1967, "A 10.6-Micron Four-Port Circulator Using Free Carrier Rotation in InSb." IEEE J. Quant. Electron. QE-3, p. 4.6

FREED, C., 1968, "Design and Short-Term Stability of Single-Frequency CO_2 Lasers," IEEE J. Quant. Electron. QE-4, p. 404.

GILMARTIN, T. J. and HOLTZ, J. Z., 1974, "Focused Beam and Atmospheric Coherence Measurements at 10.6 μm and 0.63 μm," Appl. Optics, 13, p. 1906.

MILES, P. A. and LOTUS, J. W., 1968, "High-Power CO_2 Laser Radar Transmission," J. Quant. Electron. QE-4, P. 811.

SPEARS, D. L., 1976, "Planar HgCdTe Quadrantal Heterodyne Arrays with GHz Response at 10.6 μm," to be published in Infrared Physics.

TEICH, M. C., 1968, "Infrared Heterodyne Detection," Proc. IEEE 56, p. 37.

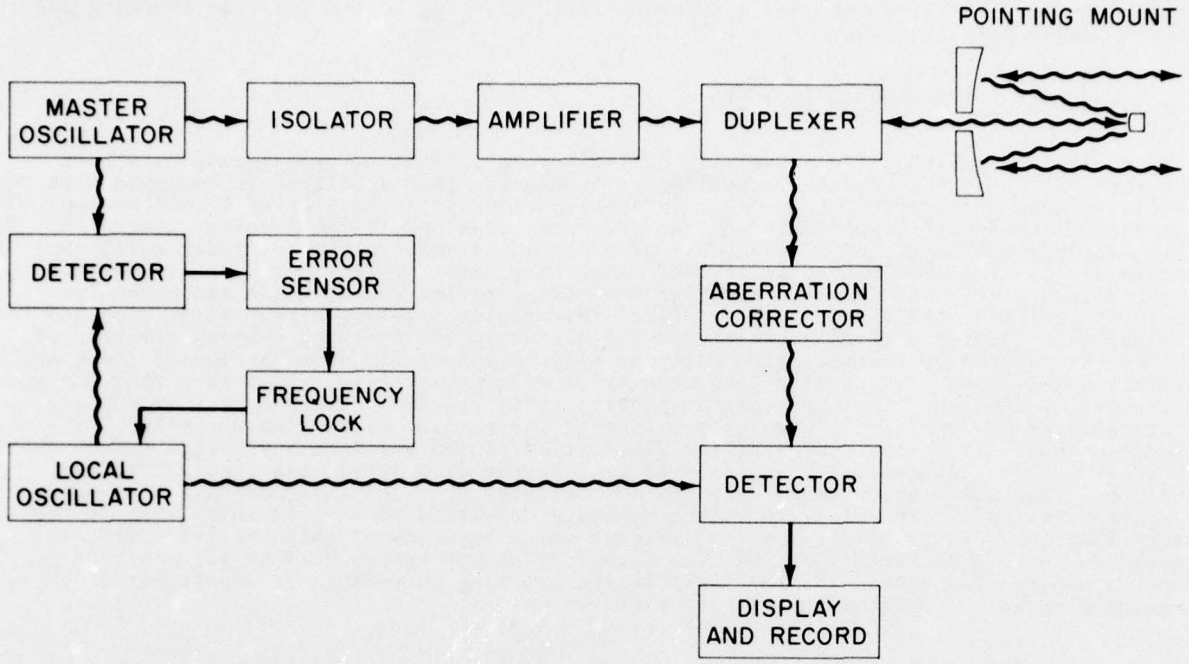

Figure 1. Infrared Radar System Design

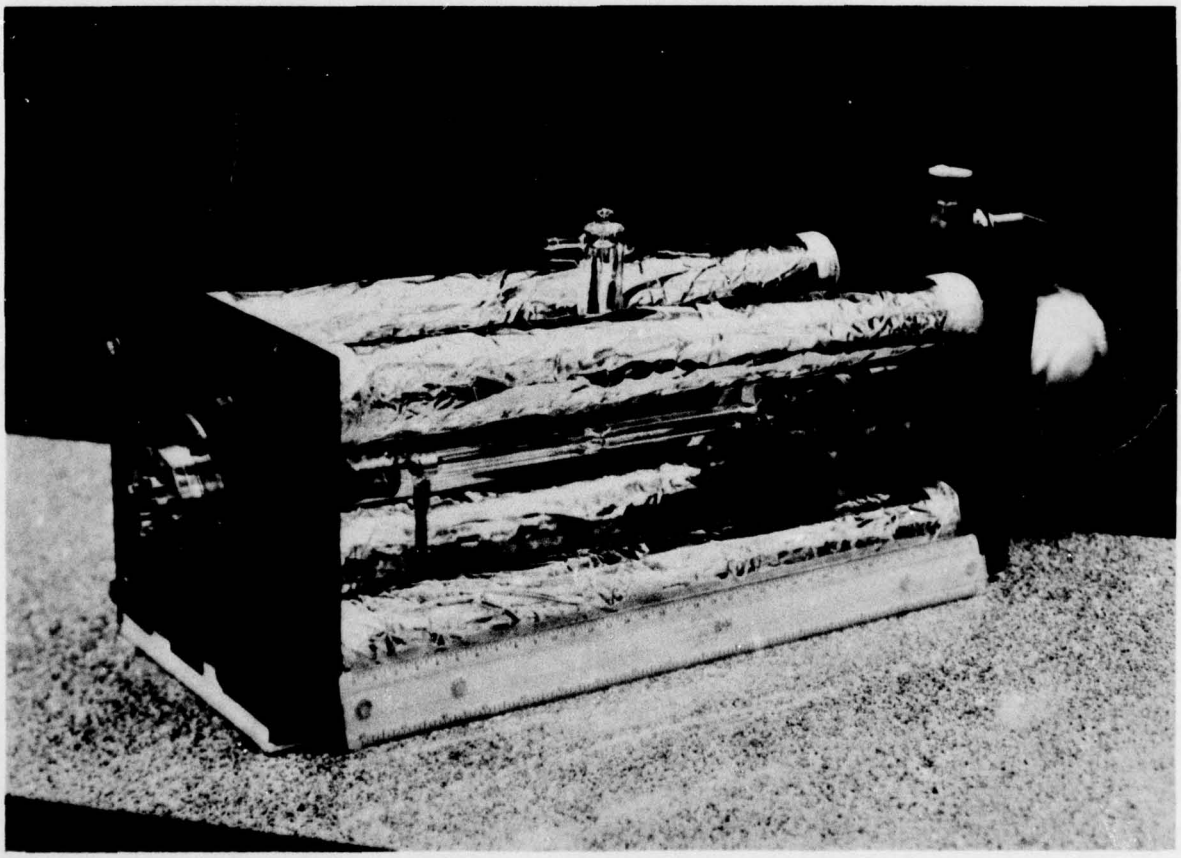

Figure 2. Stable CO_2 Laser Oscillator

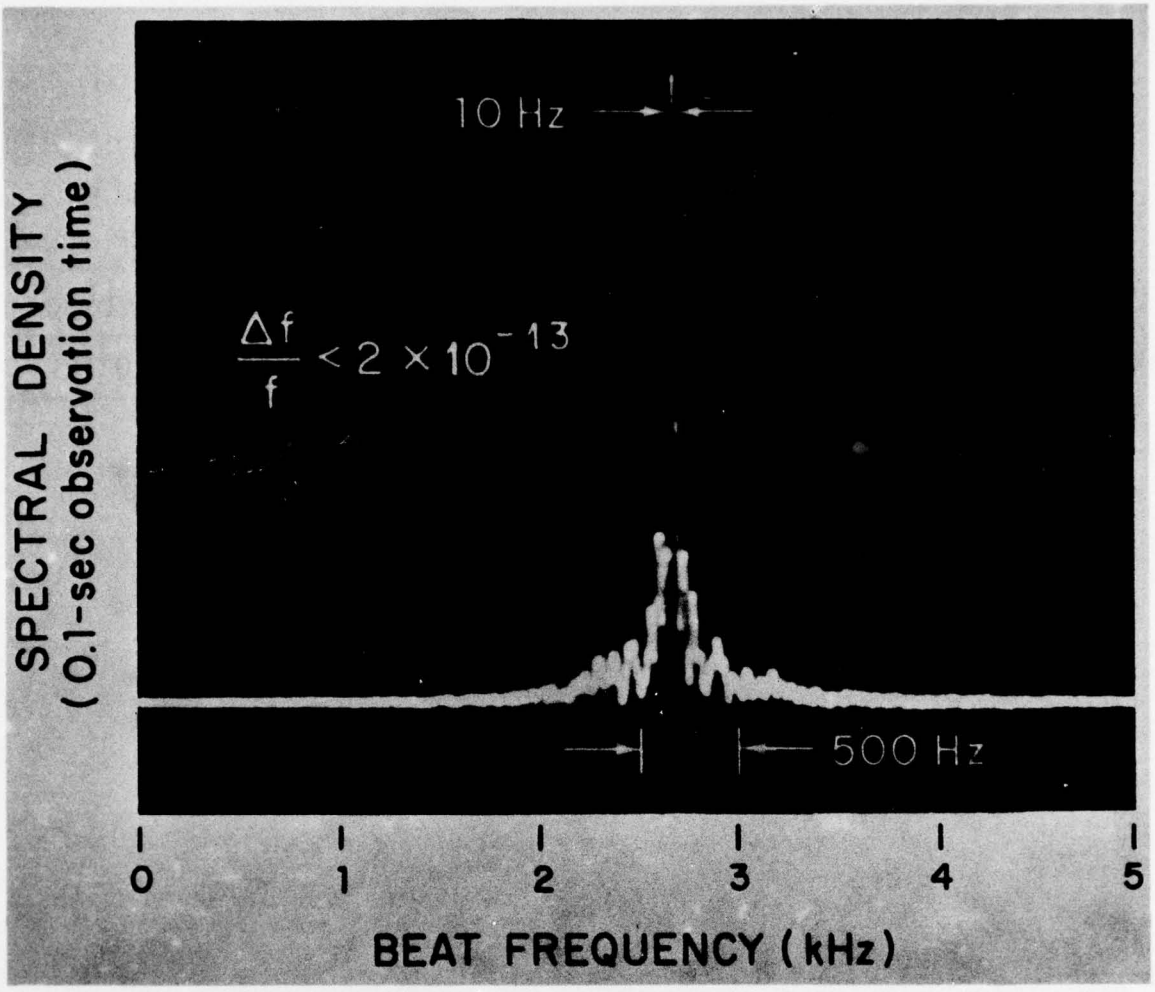

Figure 3. Short Term Stability Measurement

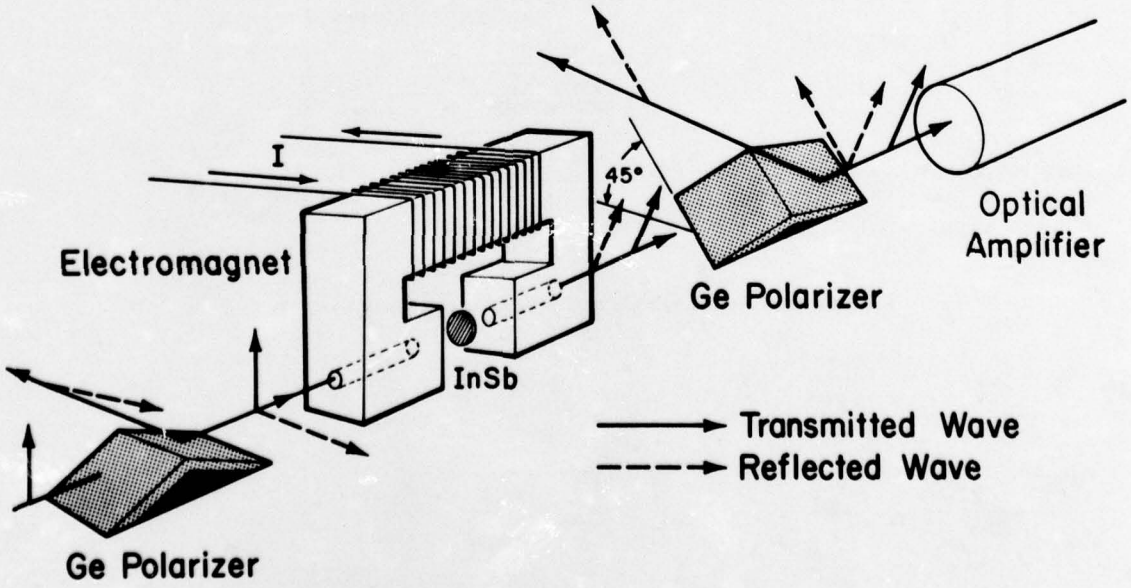

Figure 4. Faraday Rotation Isolator

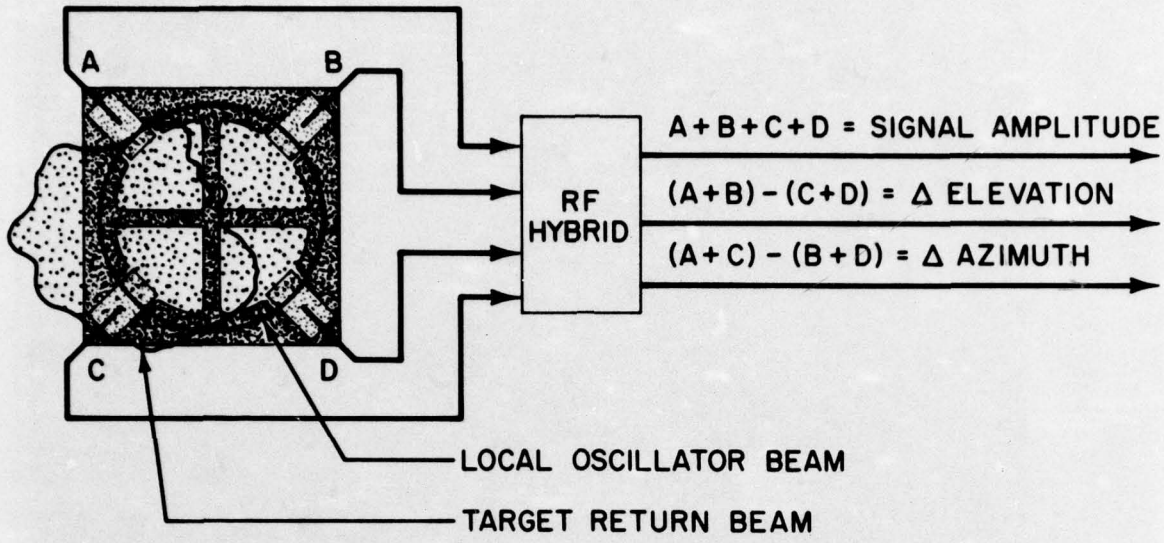

Figure 5. Detector Array

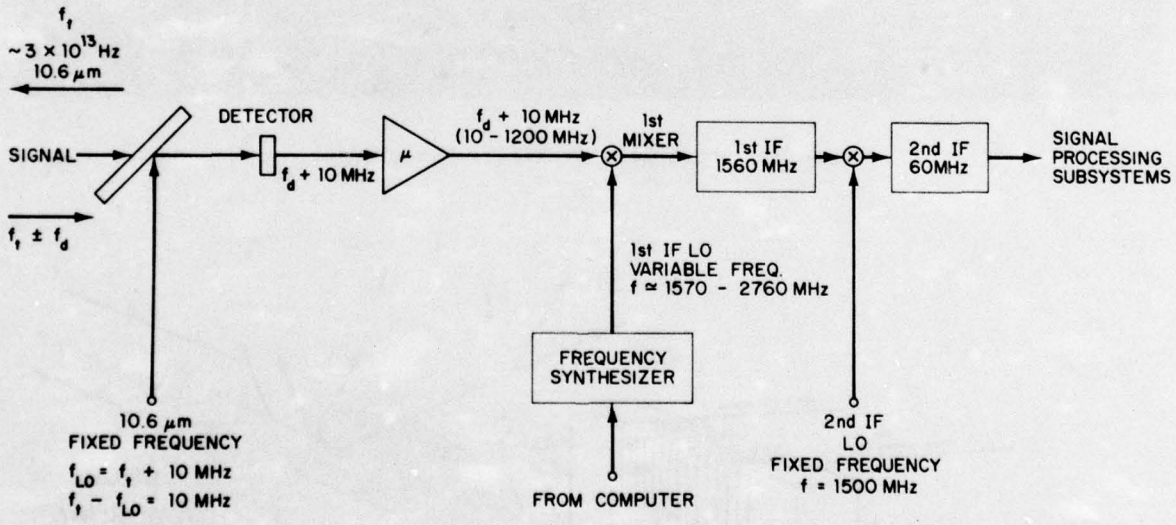

Figure 6. Detector Frequency Conversion System

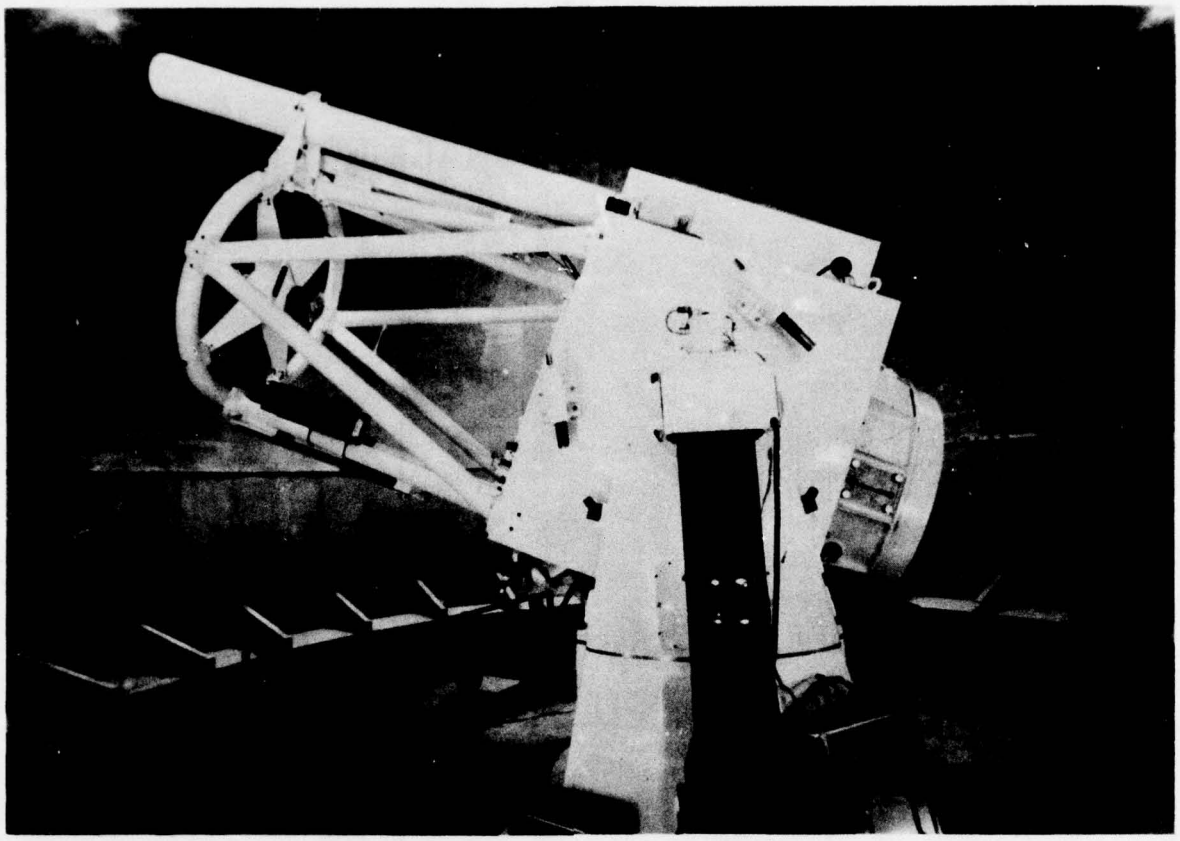

Figure 7. Pointing Mount

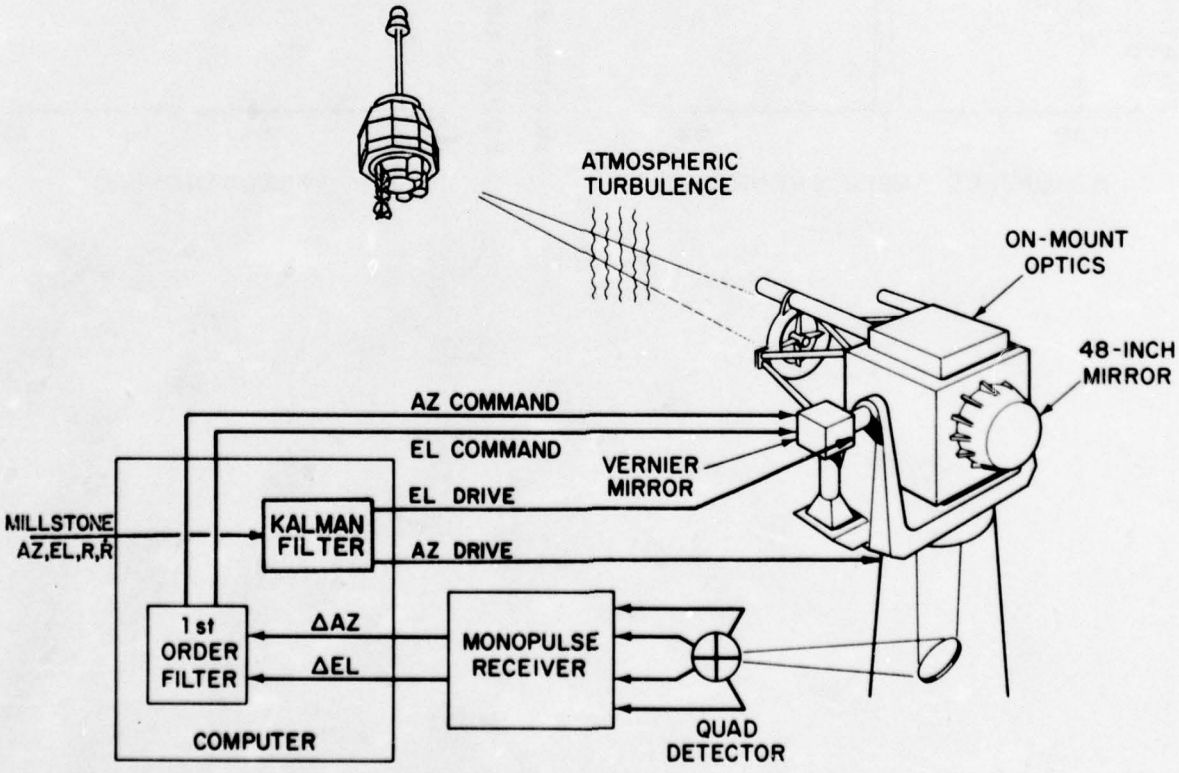

Figure 8. Satellite Tracking Experiment

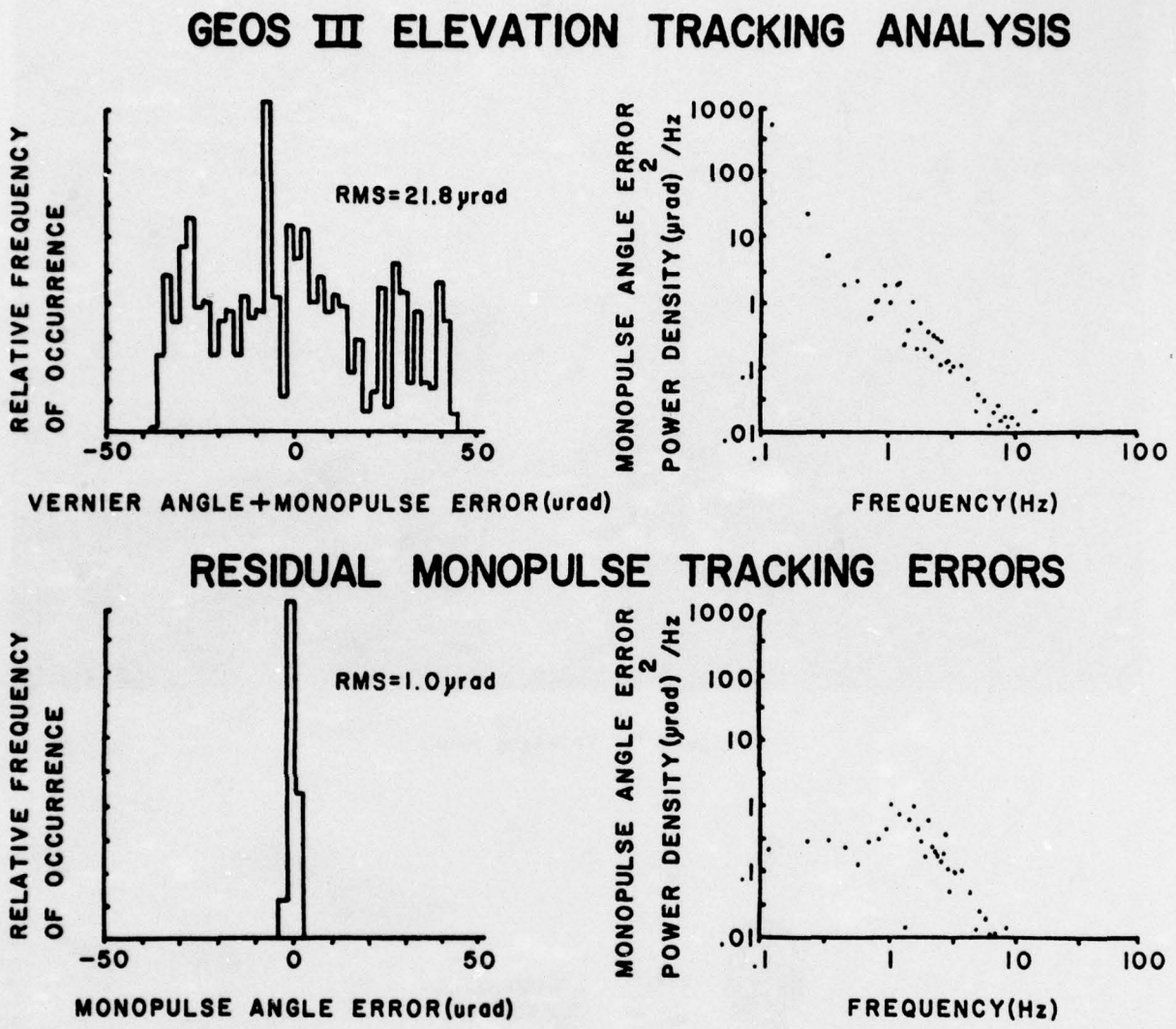
GEOS III ELEVATION TRACKING ANALYSIS
RELATIVE FREQUENCY OF OCCURRENCE
RMS=21.8 μrad
-50
0
50
VERNIER ANGLE + MONOPULSE ERROR (urad)
MONOPULSE ANGLE ERROR² POWER DENSITY (μrad)²/Hz
1000
100
10
1
.1
.01
.1
1
10
100
FREQUENCY (Hz)
RESIDUAL MONOPULSE TRACKING ERRORS
RELATIVE FREQUENCY OF OCCURRENCE
RMS=1.0 μrad
-50
0
50
MONOPULSE ANGLE ERROR (urad)
MONOPULSE ANGLE ERROR² POWER DENSITY (μrad)²/Hz
1000
100
10
1
.1
.01
.1
1
10
100
FREQUENCY (Hz)

Figure 9

DISCUSSION

J M COOK: What is the lifetime of the sealed-off CO_2 laser oscillator?

L J SULLIVAN: For the oscillator, about 1½ months. The amplifier is a continuous flow system and has a much longer life.

A L C QUIGLEY: What is the range measurement accuracy as observed at the input and output of the Kalman filter? One would expect the filter to give a great improvement by virtue of its full coupling and the high accuracy of angle and doppler measurement.

L J SULLIVAN: Due to the wide pulse width (1 to 4 milliseconds) the accuracy in range is very approximately 1 to 2 kilometres. The range accuracy at the output of the Kalman filter can approach a few metres as the radar tracks over an increasing segment of the orbit within the angular coverage of the radar due to the integrated effect of the high resolution doppler data.

W KOETHMANN: Can you give an indication of the system losses (transmitter, telescope, receiving diode)?

L J SULLIVAN: The transmitting losses due to the optical path are very approximately 1 dB. The loss in the receiving path is, perhaps, 2 dB. The stated detector sensitivity of 10^{-19} watts per Hz in terms of minimum detectable power per unit frequency interval already takes into account the fact that the detector performance is approximately 1/5 the theoretical value given by $P_{min} = h\nu B$.

Y BRAULT: Pouvez vous nous indiquer l'attenuation en function de l'humidite?

L J SULLIVAN: The atmospheric attenuation is due to molecular absorption in CO_2 and H_2O vapour. While the CO_2 attenuation is essentially constant, that due to H_2O vapour is dependent on the humidity and temperature and can be as much as approximately 1.5 dB/Km one way for high humidity levels.

APPLICATIONS DU LASER DANS LE DOMAINE

DES TECHNIQUES RADAR

P. TREVOUX
COMPAGNIE INDUSTRIELLE DES LASERS
91460 MARCOUSSIS
FRANCE

RESUME

Le laser donne la possibilité d'étendre les techniques RADAR vers des longueurs d'onde beaucoup plus courtes, du spectre visible ou infra-rouge. Il permet d'obtenir de grandes directivités à l'émission et à la réception avec un encombrement et un poids beaucoup plus faibles.

Le laser est actuellement couramment utilisé dans les télémètres. Il est en cours d'expérimentation plus ou moins avancée dans d'autres applications telles que la détection d'obstacles et l'anti-collision, la surveillance et la reconnaissance du terrain, la détection de la turbulence en ciel clair.

Nous décrivons plus particulièrement les possibilités du laser pour les applications suivantes :

- le guidage sur cible désignée par laser
- la trajectographie d'aéronefs avec poursuite automatique
- la détection et la poursuite de cibles basses dans le cadre d'une défense anti-aérienne.

I - INTRODUCTION

L'apparition du laser comme source d'ondes électromagnétiques cohérentes offre de nouvelles possibilités techniques, en particulier dans le domaine des applications radar.

Rappelons très brièvement ce qu'est le laser

Le laser est une source de rayonnement électromagnétique cohérent, dont la longueur d'onde s'étend de l'ultraviolet à l'infra rouge, en passant par le visible.

Certains milieux actifs, convenablement excités, peuvent devenir amplificateurs par un mécanisme d'émission stimulée. Ce milieu, placé dans une cavité résonnante à faibles pertes, devient le siège d'une oscillation qui peut être couplée vers le milieu extérieur sous forme d'un faisceau parallèle et monochromatique.

Les lasers diffèrent par :

- le milieu actif ou amplificateur, qui peut être un gaz, un solide (cristal ou verre) ou un liquide,
- le mode d'excitation du milieu actif qui peut être :
  - une décharge électrique dans les gaz
  - une illumination intense par une lumière incohérente que le milieu absorbe
  - un courant électrique dans un semi-conducteur.

Les lasers peuvent fournir une émission continue ou impulsionnelle suivant les applications envisagées.

Le tableau I donne quelques exemples des lasers les plus courants.

Quelles sont les propriétés pratiques les plus importantes des lasers pour le domaine d'applications qui nous intéresse ?

Par rapport aux radars classiques, ils se caractérisent par une longueur d'onde de l'ordre de 10^5 fois plus courte. Cette onde électromagnétique de faible longueur d'onde permet d'obtenir une très grande directivité du faisceau émis. A dimensions d'aériens égales, la directivité serait de l'ordre de 10^5 fois plus grande que celle des radars microondes. Il est donc possible d'avoir de grandes directivités à l'émission et à la réception avec un matériel d'encombrement et de poids beaucoup plus faibles. /

Cette grande directivité permet :

- de sélectionner des cibles de faibles dimensions, de définir avec précision un objectif, une direction,
- de s'affranchir des échos parasites dus à l'environnement de la cible ou du sol lorsque celle-ci est à très basse altitude.

La réception peut se faire avec une grande sensibilité. Par contre, la portée des lasers est très sensible aux conditions de transmission atmosphérique et se trouve limitée à la portée optique. Mais dans beaucoup de cas, la cible est sélectionnée par visée optique et le laser suffit alors pour atteindre une portée au moins égale à la limite de visibilité.

II - GENERALITES

Le laser peut être utilisé, comme un radar, pour émettre et recevoir l'information lumineuse qui, au retour, est modulée par les obstacles rencontrés, permettant ainsi de les détecter, d'en mesurer certaines caractéristiques et les poursuivre.

II.1 - L'application la plus répandue actuellement du laser est le télémètre, dont le principe est celui du radar : la mesure de distance d'une cible s'effectue en déterminant le temps t mis par l'impulsion laser très brève (15 à 30 nanosecondes) pour aller se réfléchir sur l'obstacle et revenir. La figure 1 représente le schéma de principe d'un tel télémètre. La figure 2 représente un télémètre aéroporté fabriqué actuellement en série par CILAS. Il s'agit d'un laser à verre dopé au néodyme (figure 3) et dont les performances sont les suivantes :

Energie par impulsion	100 millijoules
Puissance crête	4 Mégawatts
Divergence de sortie du système optique	0,7 milliradian
Intervalle minimal entre impulsions	1 seconde
Nombre d'impulsions par minute	12
Gamme de température	- 40° à + 70°C

La portée de ces télémètres, fonction des conditions atmosphériques, peut atteindre 20 km par très bonne visibilité.

Dans le même ordre d'idées, le laser permet en instrumentation aéroportée de réaliser des altimètres.

II.2 - D'autres applications, en cours d'expérimentation peuvent être citées brièvement :

- La finesse du pinceau laser peut être utilisée pour la détection d'obstacles, l'anti-collision et le suivi de terrain, en particulier pour les vols à basse altitude. Dans ce domaine, l'efficacité des lasers s'est révélée supérieure à celle des radars micro-ondes ou millimétriques.

- Il peut également servir à détecter des turbulences risquant de provoquer des contraintes dangereuses pour les structures des avions. Dans ce cas, le laser mesure la vitesse des particules dans la zone de turbulence.

Pour ces deux premiers groupes d'applications, les lasers utilisés sont les lasers à YAG ou à CO_2.

- Le pinceau laser balayant le terrain et la lumière réfléchie étant modulée par le sol, permet de reconstituer une image de celui-ci et d'effectuer de la surveillance et de la reconnaissance. De grands pouvoirs de résolution peuvent être obtenus (1cm) avec des optiques de faible ouverture (10 cm).

Dans ce domaine, ce sont les lasers à gaz Hélium-Néon qui ont d'abord été utilisés ainsi que les lasers à semiconducteurs qui doivent encore progresser.

II.3 - Nous décrirons ci-dessous plus en détails les applications suivantes du laser qui relèvent toutes de la poursuite optique.

Le faisceau laser a été utilisé dans des systèmes de guidage aussi bien dans des applications civiles que militaires. Deux principes peuvent être retenus :

- le guidage sur faisceau laser, qui sert de référence pour le récepteur du système à guider,

- le guidage sur cible illuminée : dans ce domaine, nous décrirons les applications suivantes
  - . le guidage d'engins sur cibles désignées par laser
  - . la trajectographie d'aéronefs ou d'engins
  - . les applications dans le cadre de la défense anti-aérienne

III - DESIGNATION D'OBJECTIFS ET GUIDAGE

On peut schématiser le fonctionnement de la façon suivante :

- un observateur (hélicoptère, avion, fantassin) équipé d'un émetteur laser dirige le faisceau par visée optique sur la cible choisie

- l'objectif ainsi désigné est détecté et situé par rapport à un système de référence. L'information ainsi obtenue peut servir à visualiser le point désigné et à réaliser le guidage d'une bombe ou d'un missile sur la cible.

Le même laser peut donner une information de télémétrie pour déclencher le tir à la distance correcte de la cible.

Ces principes sont appliqués par exemple dans le système représenté sur la figure 4.

La cible est choisie et désignée par l'opérateur à une caméra de télévision qui est associée à un système double de poursuite (par corrélation et par contraste) : le pointage du faisceau laser sur la cible sera maintenu automatiquement, sans intervention du pilote, quelles que soient les évolutions de l'avion.

Ce système, monté dans une nacelle adaptable à de nombreux types d'appareils, est employé en liaison avec un autodirecteur équipant divers types d'engins (missiles, roquettes, bombes). Grâce à certains perfectionnements, le guidage peut se poursuivre lorsque l'avion effectue son virage de dégagement pour échapper à la défense ennemie.

Ces dispositifs sont couramment équipés de lasers à YAG dopé au néodyme, dont la longueur d'onde d'émission 1,06 µm est discrète. Ces lasers ont une puissance crête élevée (jusqu'à 10 MW), une faible divergence (de l'ordre de quelques dizièmes de milliradian après afocal) et une cadence de répétition pouvant atteindre aisément 20 Hz. La cadence de l'émission peut être codée, par exemple par l'intermédiaire de la commande électronique du déclenchement électro-optique du laser.

Dans certains équipements, le laser est associé à un système infra-rouge qui visualise le paysage pour l'opérateur et lui permet de sélectionner la cible.

IV - TRAJECTOGRAPHIE PAR LASER

Dans d'autres cas, le laser permet à des fins de mesure de relever les éléments de la trajectoire d'une cible que l'on poursuit. Il s'agit alors d'une cible amie (aéronef ou engin) que l'on peut équiper préalablement avec des rétro-réflecteurs.

Les moyens utilisés précédemment faisaient appel :

- soit à l'optique avec cinéthéodolites qui demande des temps de dépouillement beaucoup trop long,

- soit à des systèmes radar qui restituent les trajectoires en temps réel mais sont perturbés par des effets de "site bas" lorsque la cible est au voisinage du sol.

Le laser permet de réunir les conditions de rapidité de traitement et de grande précision, même au voisinage immédiat du sol, jusqu'au point d'atterrissage.

Les applications possibles sont très nombreuses : qualification de systèmes d'atterrissage, des aéronefs, vérification des trajectoires en vols d'essais ou d'entrainement, relevé de précision de systèmes d'armes ; qualification des champs de tirs, de leurs autres équipements de trajectographie, des dispositifs de sécurité et de contrôle.

La trajectographie comporte 3 fonctions principales :

- l'acquisition de la cible,
- la poursuite de la cible,
- l'élaboration de la trajectoire, soit en temps réel, soit en temps différé...

La position de la cible est exprimée par rapport à un trièdre de coordonnées lié à des installations existantes. Les mesures brutes doivent donc être traduites en coordonnées cartésiennes, lissées et un changement d'axes permet de les référer au système d'axes choisi.

Pour l'acquisition, le laser dont le champ est trop étroit, a besoin de moyens complémentaires, comme :

- la visée optique par un opérateur,
- une caméra de télévision,
- l'orientation à partir de coordonnées de la cible fournies par un dispositif de repérage (en général un radar)
- le balayage systématique d'un domaine de l'espace où la cible doit se présenter.

La poursuite de la cible est assurée au moyen d'un goniomètre ou d'un écartomètre monté sur un support orientable en site et en gisement. Ce support est piloté par l'écartomètre.

L'élaboration de la trajectoire nécessite l'enregistrement des mesures faites au cours de la poursuite en fonction du temps. Le rapprochement des mesures d'écartométrie, de télémétrie et du support permet, après les corrections nécessaires, de restituer la trajectoire. Ces traitements sont effectués en général par un calculateur.

Pour éviter les dangers d'une exposition au faisceau laser, des moyens de sécurité sont prévus pour une utilisation avec des aéronefs pilotés ou dans une zone où le personnel peut séjourner. Ce sont :

- L'atténuation de la puissance laser en fonction de la distance du système à l'aéronef.
- La définition d'un volume de sécurité en dehors duquel l'émission laser est arrêtée.

Dans les systèmes à structure monostatique, on effectue généralement les mesures d'écartométrie (site et gisement) et de télémétrie, les informations de vélocimétrie se déduisant des premières.

Pour l'écartométrie, on peut procéder :

- soit par analyse du champ à l'émission, en défléchissant le faisceau laser, dont la direction est repérée lorsqu'un écho est reçu,
- soit par analyse du champ de réception. Plusieurs types de détecteurs peuvent alors être utilisés :
  - . des photodétecteurs à quatre quadrants,
  - . des mosaïques de photodétecteurs qui permettent d'obtenir une écartométrie linéaire dans tout le champ,
  - . des photodétecteurs à balayage électronique, analogues à des tubes de prise de vue de télévision et qui fournissent également une écartométrie linéaire dans tout le champ.

Le système de TRAjectographie D'Atterrissage STRADA est prévu pour les essais des systèmes d'atterrissages automatiques de catégorie III, et inclut donc les atterrissages entièrement automatiques

Ce système est capable de restituer en temps réel les positions et vitesses précises d'un point particulier d'un avion (équipé de rétro-réflecteurs) en phase d'approche et d'atterrissage y compris l'impact et le roulement sur la piste .

La station est constituée d'un radar laser ou LIDAR placé au sommet d'un bâtiment, d'équipements de traitement des informations et de visualisation, d'un pupitre rassemblant les moyens de commande et de contrôle, placés dans la salle d'opérations du bâtiment.

Le LIDAR comprend une tourelle de poursuite (figure 5) supportant un émetteur laser à impulsions (figure 6) et un ensemble de réception. L'orientation de l'axe de visée du laser est caractérisée par les angles de site (S) et d'azimut (G) mesurés sous forme digitale par des codeurs de haute précision, montés sur la tourelle.

L'énergie lumineuse réfléchie par la cible vers l'ensemble de réception est distribuée :

- vers un dispositif de mesure de distance D (télémètre)
- vers un dispositif d'écartométrie mesurant les écarts angulaires en site ΔS et en azimut ΔG séparant l'axe de visée de la direction émetteur laser - cible. Ces dernières informations permettent la commande des servomécanismes de la tourelle et la poursuite automatique de l'avion.

Les mesures angulaires S, G, $\dot{S}$, $\dot{G}$ et la distance D sont transmises à grande cadence à un calculateur qui assure en temps réel le calcul de la trajectoire et l'édition de la position et de la vitesse du point de référence de l'avion.

Le LIDAR comprend une tête laser YAG (figure 7) dont l'élément actif est un cristal de Grenat d'Yttrium et Aluminium, pompé par une lampe à arc continu au Krypton de 2 KW. Il émet à 1,06 µm sous forme d'impulsions déclenchées par un système mécanique à prismes tournants, à la cadence de répétition de 3 200 Hz.

Deux baies standard situées à proximité contiennent les circuits d'alimentation et de commande, et les dispositifs de stabilisation thermique du liquide de refroidissement du laser.

Les performances sont les suivantes :

Puissance crête	5 KW
Largeur d'impulsion	80 ns
Divergence du faisceau après afocal	10 mrd

La portée du système est supérieure à 7000 m pour une absorption atmosphérique de 1 db/km (brume légère). Les mesures primaires effectuées par le LIDAR ont un écart type σ = 0,2 mètre en distance et $\sigma = 10^{-4}$ rd en site et azimut.

La maitrise d'oeuvre de ce système a été assurée par le Service des Equipements de Champs de Tir (SECT). Le LIDAR et la tourelle ont été réalisés par la Société THOMSON-CSF, l'émetteur laser et le télémètre ont été sous traités aux Laboratoires de Marcoussis, Centre de Recherches de la C.G.E. Le système est exploité depuis deux ans par le C.E.V. de Brétigny, où il rend de très grands services. Il a servi à l'homologation de nombreux avions, en particulier le Mercure, l'Airbus et Concorde.

V - POURSUITE DANS LE CADRE D'UNE DEFENSE ANTI-AERIENNE

Cette poursuite consiste à :

- acquérir un engin dans son environnement,
- déterminer sa position et sa vitesse afin de guider une arme anti-aérienne.

Ce matériel doit donc permettre de grandes portées d'acquisition sur des cibles non coopératives.

Dans ce domaine, le laser apporte les avantages suivants :

- acquisition avec un grand pouvoir de discrimination
- poursuite à site très bas
- possibilité de fonctionnement dans un environnement de contre mesures électromagnétiques.

Les principes utilisés pour l'écartométrie, la télémétrie et la vélocimétrie sont les mêmes que pour la trajectographie.

Pour ce type de matériel on peut utiliser :

- des lasers YAG à impulsions
- des lasers CO_2 continus que l'on peut moduler en fréquence, avec détection hétérodyne.

Les lasers ont une excellente capacité de résolution en distance et en angle. Mais étant donné leur faible champ élémentaire d'analyse nécessité par l'obtention de portées élevées, les systèmes à laser ne peuvent acquérir une cible que dans un volume restreint de l'espace.

Pour analyser un volume suffisant, tout en conservant la faible divergence du faisceau et par conséquent une bonne portée, on peut prévoir un système de balayage avec une définition satisfaisante. La cadence de répétition du laser est alors de l'ordre de 1 à 3 KHz, comme pour les systèmes de trajectographie.

Le LIDAR est couplé avec un système de conduite de tir.

A site bas, les systèmes de poursuite par radar sont mis en difficulté, principalement par des phénomènes de parasitage introduit par les échos fixes et de propagation polyangle (notamment au dessus de la mer) perturbant la poursuite en site.

Dans le domaine de la poursuite à site bas, les systèmes à laser peuvent donc apporter leur concours à la défense :

- soit en complétant le radar dont la poursuite en site est perturbée par des réflexions polyangles,
- en se substituant à lui au-dessous d'un site de 10 mrd.

VI - CONCLUSIONS

Depuis quelques années, le laser a fait la preuve des nouvelles possibilités qu'il apporte dans le domaine des techniques radar grâce à :

- ses caractéristiques de très grande directivité,
- son faible encombrement,
- sa facilité de mise en oeuvre.

La robustesse et la fiabilité de ces matériels croissent progressivement.

Les directions dans lesquelles il faut poursuivre l'effort sont :

- la moindre sensibilité de la portée aux conditions de transmission atmosphérique,
- l'amélioration du rendement du laser,
- l'augmentation de puissance du laser.

Sur ces points, le laser à CO_2 est bien placé pour permettre des progrès et son utilisation devrait se développer largement.

D'autre part, l'effort doit être poursuivi pour surmonter les limitations de performances liées non pas à des principes théoriques mais à des problèmes technologiques se présentant sur certains composants du laser : c'est le cas pour les matériaux optiques ou les couches diélectriques dont la résistance à des densités de puissance toujours plus élevées du faisceau laser est nécessaire. L'augmentation des sensibilités des détecteurs à température ambiante, l'amélioration des systèmes de refroidissement et des systèmes de déclenchement de l'impulsion laser sont également des directions dans lesquelles les efforts doivent être poursuivis.

D'une manière générale, toutes les améliorations qui peuvent réduire la masse, les dimensions, le coût et la puissance consommée sont souhaitables.

Ces efforts permettront le développement de toutes les applications potentielles du laser dans le domaine des techniques radar.

REFERENCES

1 - COUDERC G. 1972 "Description du Système de Détection et de Poursuite de l'Equipement STRADA" Conférence à la Journée d'Etude de la S.E.E.

2 - COUDERCG., de NORAY, MAILLET H., MOREAU R. 1974 "Trajectographie - Poursuite" AGARDOGRAPHIE n° 195 Chapitre 8

3 - MARVILLET J.P., JOUZEAU J.L. 1972 "Le système de Trajectographie d'Atterrissage STRADA" L'Aéronautique et l'Astronautique.

TABLEAU I : Tableau des principaux lasers actuels

TYPE	MILIEU AMPLIFICATEUR	ION ACTIF	EXCITATION	LONGUEUR D'ONDE	MODE DE FONCTIONNEMENT	PUISSANCE
LASERS SOLIDES	CRISTAUX : Rubis	Cr^{3+}	Lumineuse par lampe flash	0,6943 µm	Impulsionnel	100 MW
	YAG	Nd^{3+}	Lumineuse par lampe flash	1,06 µm	Impulsionnel 10 - 20 Hz	7 MW
			Lampe à arc	1,06 µm	Impulsionnel 1000-5000 Hz continu	100 Watts
	VERRES	Nd^{3+}	Lampe flash	1,06 µm	Impulsionnel 1 Hz	10 MW
SEMICONDUCTEUR	As Ga		Courant électrique	0,85 µm	Impulsionnel 1 Hz - 1 KHz	1 W - 10 KW
A GAZ	He - Ne	Ne	Décharge électrique	0,6328 µm	Continu	1 mW - 50 mW
	Ar	A^+	Décharge électrique	0,4880 µm 0,5145 µm	Continu	1 W - 10 W
	CO_2		Décharge électrique	10,6 µm	Continu	1 W - 1 KW
COLORANTS	Rhodamine 6 G		Lumineuse (lampe flash)	0,56 à 0,66 µm	Impulsionnel	1 MW

PRINCIPE GENERAL DE LA TELEMETRIE PAR LASER A IMPULSIONS

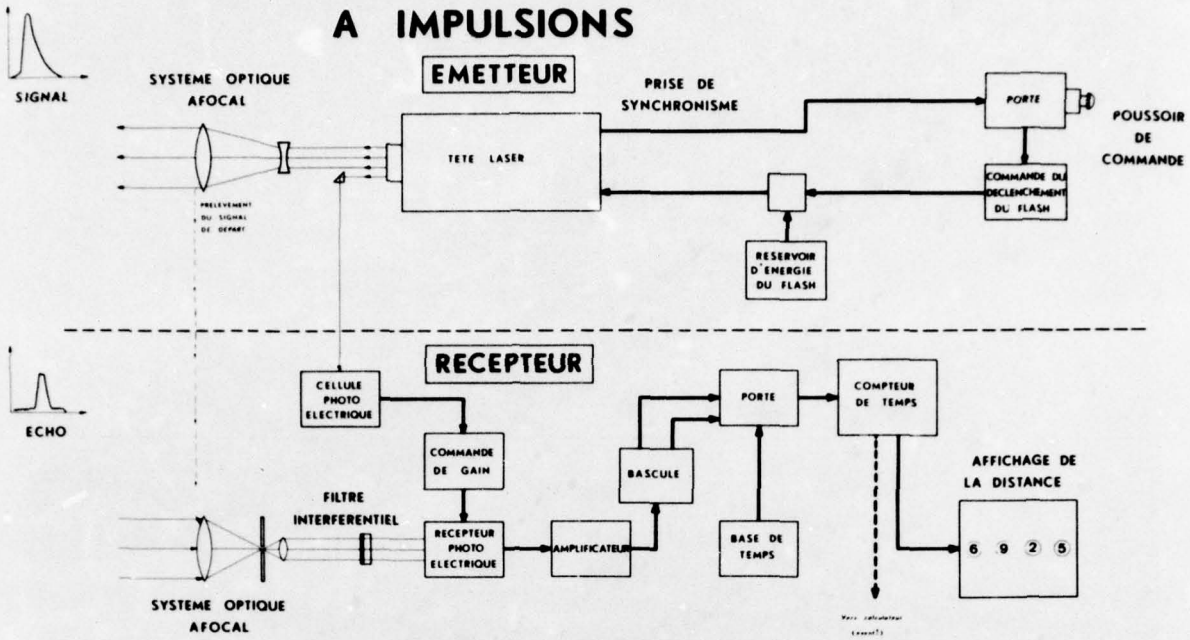

FIGURE 1 : Schéma de principe d'un télémètre laser

FIGURE 2 : Télémètre aéroporté à laser verre

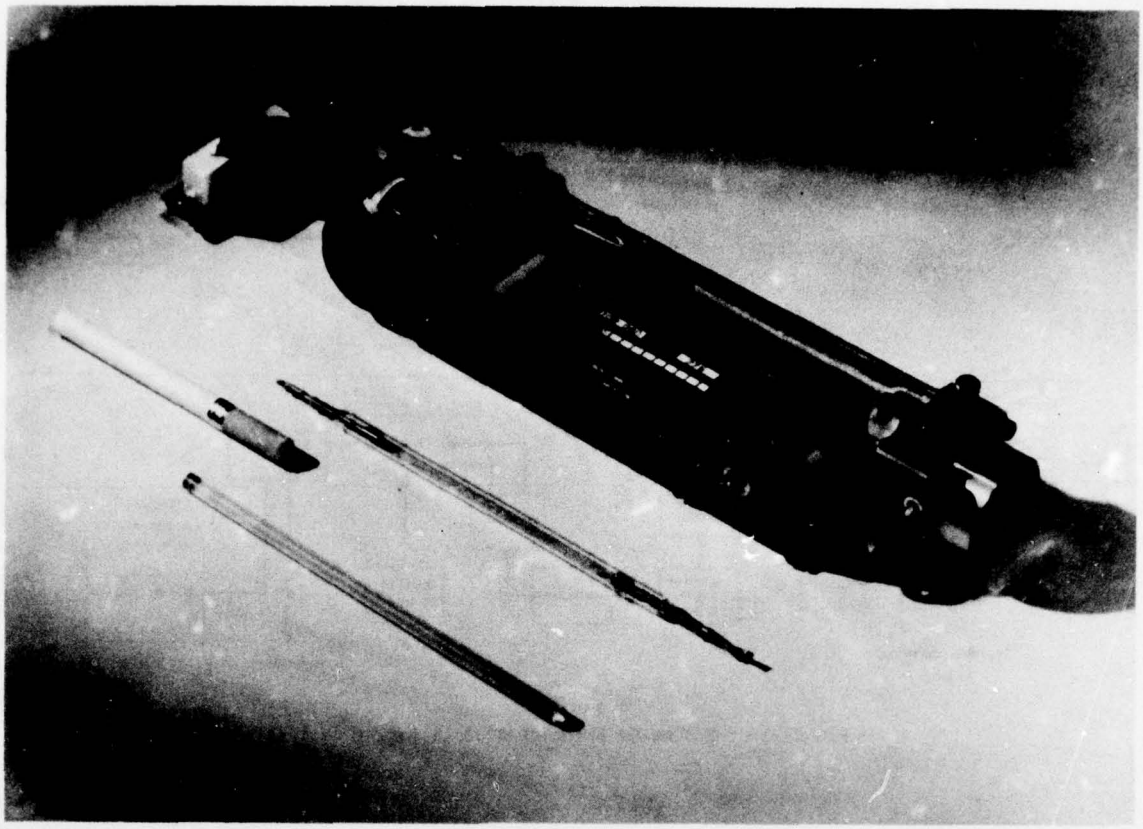

FIGURE 3 : Tête laser à verre dopé au Néodyme

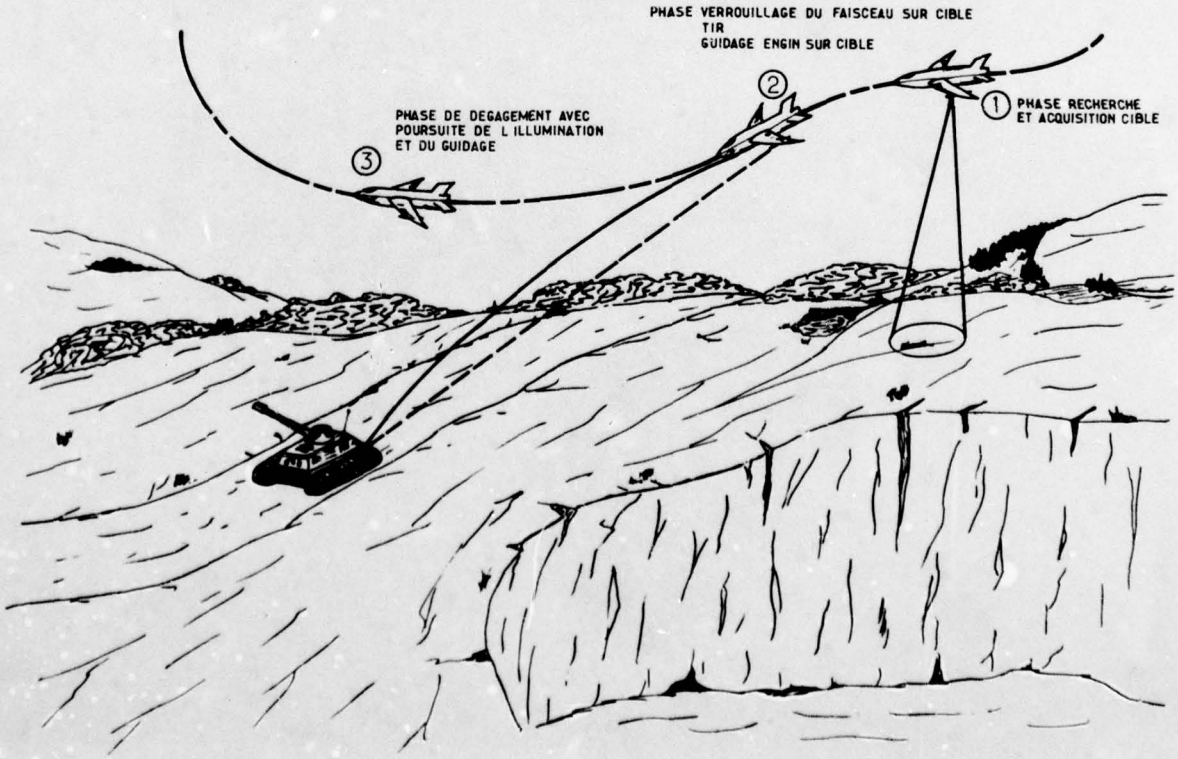

FIGURE 4 : Guidage sur objectif désigné par laser

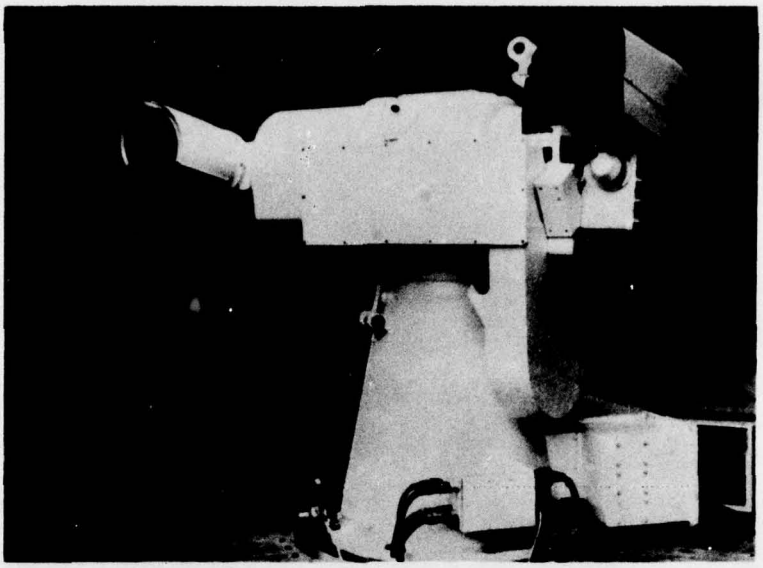

FIGURE 5 : Tourelle de poursuite du système STRADA

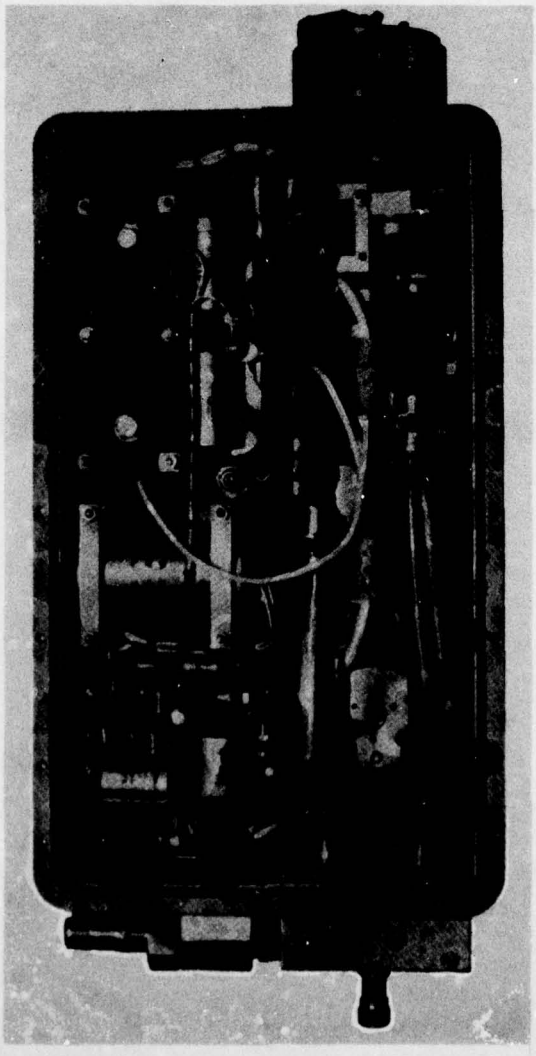

FIGURE 6 : Boitier de l'émetteur STRADA

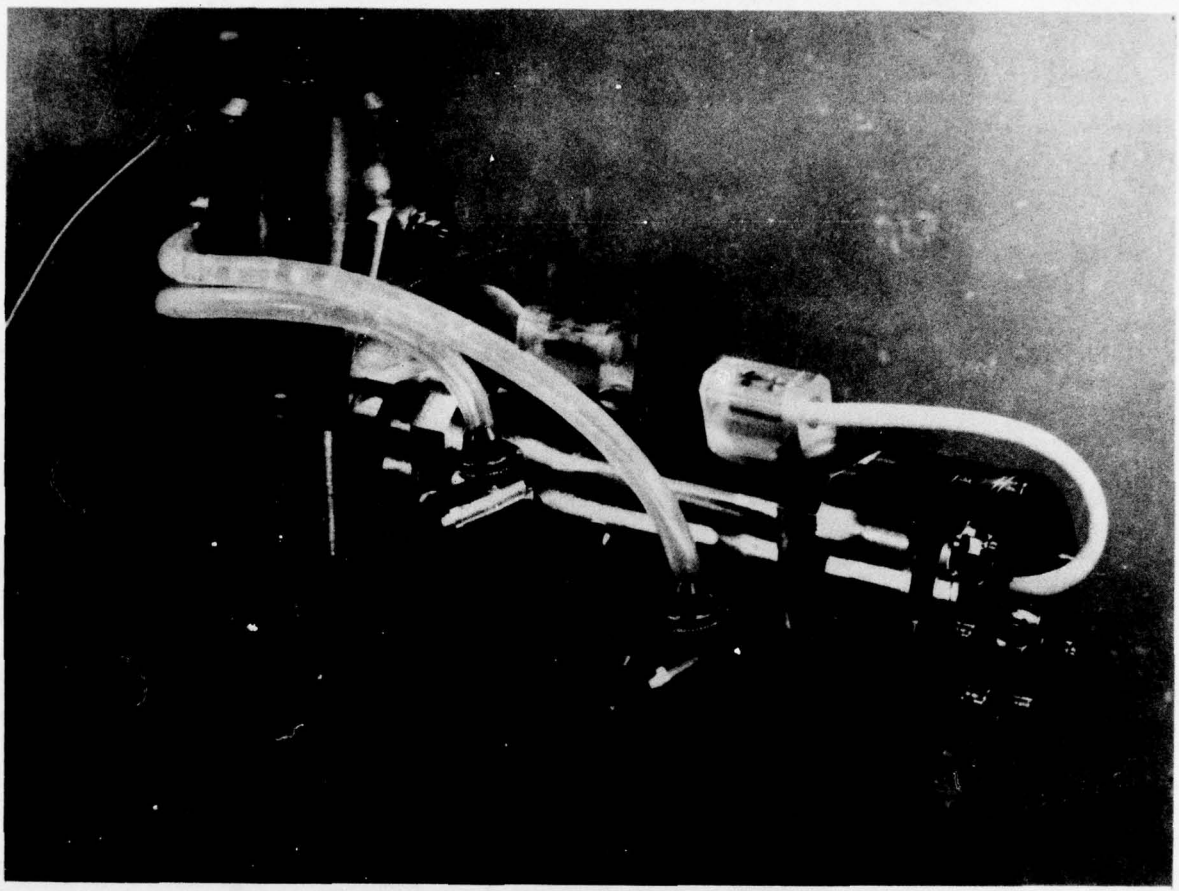

FIGURE 7 : Tête laser de l'émetteur STRADA

DISCUSSION

J FREEDMAN: 1) Has your organisation performed any measurements of backscatter characteristics at any of the wavelengths of micron radars discussed by you?

2) Have you given thought to the problem of making far-field measurements (range greater than D^2/λ) on a model range?

P TREVOUX: 1) Nous n'avons pas fait de mesures systématiques sur la retrodiffusion. Les calculs de portée, bien verifiés dans la pratique, sont couramment faits pour des albédos de 0,1. Quant à la rétrodiffusion parasite par l'atmosphère, il suffit pratiquement de prévoir une distance convenable d'aveuglement du récepteur (300 mètres environ pour les télemètres) pour s'en protéger dans les conditions d'utilisation.

2) Ces mesures n'ont pas été faites.

Y BRAULT: Dans le domaine des turbulences en ciel clair, avez-vous des résultats comparés de cette technique avec celle basée sur les contrastes thermiques dans les bandes IR?

P TREVOUX: Trois méthodes ont été utilisées pour la détection des turbulences en ciel clair: par radar, détection des variations d'indice, en IR par contraste thermique, en optique visible, par mesure des vitesses des particules dans la zone de turbulence. Les méthodes de mesure sont différentes. La corrélation entre les zones réelles et les zones détectées n'est pas toujours clairement établie. Il est donc difficile de faire une comparaison de ces systèmes, si ce n'est pour le poids qui est inferieur pour les systèmes optiques.

MILLIMETER WAVE MONOPULSE TRACK RADAR

Dr. Lester H. Kosowsky
Kenneth L. Koester
Robert S. Graziano

Norden Division of United Technologies Corporation
Norwalk, Connecticut 06856
U.S.A

SUMMARY

A high accuracy millimeter wave monopulse radar has been developed for use in high resolution tracking applications. The system utilizes a real aperture millimeter wave antenna transmitting a medium power noncoherent narrow pulse.

An analysis of attenuation and backscatter in adverse weather conditions indicates that against a 10 square meter target, a range of 10 km may be obtained in clear air and 4.8 km in 4 mm/hr or rain. A description of the system configuration is given together with currently available experimental data. Accuracies of better than 1.0 mr have been achieved.

1. INTRODUCTION

The utilization of millimeter wavelengths for high resolution, high accuracy applications is becoming increasingly significant as components and technology develop rapidly. For a given size aperture, there are advantages to the use of millimeter wave radiation namely, high resolution and ECM immunity. As a consequence, a millimeter monopulse radar is an attractive sensor for short range, adverse weather tracking applications such as terminal guidance and fire control.

Because adverse weather plays a significant role in determining the performance limits of any millimeter radar, a careful examination and measurement of the absorption and backscatter from fog, rain, and snow has been made. It has been shown, both theoretically and experimentally that fog and snow produce little effect on system performance, whereas rain contributes significant absorption and backscatter and must be carefully considered in system design. The effects of weather and clutter on system performance have been examined in detail. Curves depicting detection range are presented for a variety of weather conditions.

The tracking of complex targets requires knowledge of the glint characteristics of the target as well as the clutter in which it is immersed. Because of the complexity in analytically deriving the glint statistics of targets and clutter, an experimental program was undertaken to develop a four lobe amplitude monopulse track radar which could be utilized to obtain experimental data and to provide a "brassboard" configuration for use in demonstration tracking systems.

The millimeter track radar which has been configured, operates at 70 GHz, utilizes an 18 inch antenna, and has a static tracking accuracy of less than one milliradian. The system transmits a 100 nanosecond, 10 kW pulse at a PRF of 4 KHz, utilizing a pulsed magnetron source. The receiver achieves a 10 dB noise figure with Schottky Barrier mixer crystals. Experimental tracking data are presented for isolated targets and targets in clutter.

2. THE TRACK PROBLEM

Many tracking problems require accurate tracking of a relatively small target in close proximity to a large competitive clutter area. This is particularly true in the case of tracking low flying aircraft and missiles from a ground location. As shown in Figure 1, we shall consider cases in which the aircraft is located 30 meters above a clutter area at ranges out to 10 kilometers. The solution to this difficult tracking problem has proceeded classically along a number of different paths, namely:

Clutter suppression by statistical data processing, e.g. MTI

Coherent techniques e.g. pulse compression, synthetic aperture, doppler discrimination

Spatial discrimination e.g. narrow beamwidths

Of the techniques enumerated, the direct generation of narrow beamwidths by multiwavelength apertures provides the simplest most direct method of resolving small targets in the presence of clutter. In order to utilize reasonable size antennas, the designer is forced to high frequencies of operation where propagation becomes a significant parameter in limiting system performance.

3. PROPAGATION FACTORS IN THE MILLIMETER REGION (60-100 GHz)

The design of millimeter wave systems is extremely sensitive to propagation losses in the atmosphere. Although a detailed analysis of the factors involved in producing energy loss is beyond the scope of the present paper, several of the most significant propagation characteristics are summarized below.

3.1 Clear Air Attenuation

The attenuation of millimeter wave energy in clear air has been the subject of intensive investigation by a number of researchers (VanVleck, J.H., 1964, Rosenblum, E.S., 1961, Straiton, A.W. and C.W. Tolbert, 1960, and Koester, K.L., Sept 1971) and has been confirmed by careful measurement (Tolbert, C.W. and A.W. Straiton, 1957, and Hogg, D.C., 1968). A summary of available data is given by Rosenblum, and is shown in Figure 2. Examination of the M-band region, 60-100 GHz, shows that the clear air attenuation varies from a peak of 15 dB/km at the oxygen line at 60 GHz, to a minimum of 0.39 dB/km at the "window" at 94 GHz. It should be noted that the propagation loss is strongly dependent on the amount of oxygen in the atmosphere and thus varies considerably as a function of altitude and path length through the atmosphere.

3.2 Rain

In addition to the energy loss resulting from atmospheric gases, the performance of a radar operating in rain is degraded by the absorption and scattering of the energy by the rain drops. The propagation of millimeter waves in rain has been investigated in depth (Koester, K.L., Sept 1972, and Wilcox, F.P. and R.S. Graziano, 1974). The attenuation as a function of rain rate is shown in Figure 3 for 70 and 94 GHz. It can be seen that for a moderate rainfall rate of 4 millimeters per hour, the attenuation is 2.3 dB/km at 70 GHz and 2.8 dB/km at 94 GHz (Wilcox, F.P. and R.S. Graziano, 1974).

Accompanying the absorption loss in rain is the microwave energy reflected by the rain drops which contributes additional noise to the system. The backscatter coefficients for rain have been measured (Richard, V.W. and J.E. Kammerer, 1974), and are shown in Figure 4. The use of circularly polarized antennas results in a 15 dB reduction of rain backscatter at 70 GHz and 94 GHz as shown by Richard.

3.3 Fog and Clouds

Of great significance to the performance of a track radar is its ability to follow aircraft and missiles through cloud cover and fog. The attenuation coefficient for millimeter wave propagation of fog has been investigated in detail (Koester, K.L., March 1971, Koester, K.L. and L.H. Kosowsky, Nov 1970, and Koester, K.L. and L.H. Kosowsky, Sept 1970) and has been shown to be linearity dependent on the liquid water content of the fog. In addition, there is a significant dependence of attenuation on the temperature of the fog. The attenuation is shown in Figure 5 as a function of liquid water content. The attenuation coefficient for a liquid water content of 0.1 g/m^3 is 0.35 dB/km at 70 GHz and 0.47 dB/km at 94 GHz at 0°C.

The backscatter coefficient of fog in the millimeter band is more than two orders of magnitude smaller than that of rain and has a negligible effect on radar system performance (Koester, K.L., March 1971).

3.4 Snow

In cold climates, the presence of snow severely influences optical detection of targets. The attenuation in snow as a function of snowfall rate (Skolnik, M.I., 1962) is shown in Figure 6 for frequencies of 70 and 94 GHz. In a moderate snow (accumulation rate of 30 millimeters per hour) the attenuation is 0.62 dB/km at 70 GHz and 1.95 dB/km at 94 GHz. Experiments conducted by Norden at 70 GHz indicate that the backscatter from very heavy snow is negligible.

4. FREQUENCY SELECTION

The theoretical analysis and experimental work performed by Norden has demonstrated that millimeter radar systems will provide adequate adverse weather performance.

During the course of Norden's internally funded programs, a careful comparison was made of cost and availability of components at both 70 and 94 GHz. Greater availability and lower cost of components led to the choice of 70 GHz as a representative frequency for experimental work in the millimeter band. The work at 70 GHz is compatible with 94 GHz requirements permitting design anywhere within the band.

AD-A040 144 ADVISORY GROUP FOR AEROSPACE RESEARCH AND DEVELOPMENT--ETC F/G 17/9
NEW DEVICES, TECHNIQUES AND SYSTEMS IN RADAR.(U)
FEB 77

UNCLASSIFIED AGARD-CP-197 NL

6 OF 7
AD
AD40144

5. MONOPULSE CONCEPTS

Monopulse, as defined by Rhodes, "....is a concept of precision direction finding of a pulsed source of radiation. The direction of the pulsed source is determined by comparing the signals received on two or more antenna patterns simultaenously." (Rhodes, D.R., 1959). The two basic types of systems which are commonly used, phase or amplitude, are shown in Figure 7. The type of system derives from the antenna configuration since phase information received in a phase monopulse can be readily converted to amplitude information and vice versa.

In either case, by forming the sum and difference, the information on target location is contained in the relative amplitudes of the two signals.

In the system discussed in this paper, an amplitude monopulse system is used as the antenna sensor in which four squinted beams are produced from a single aperture to yield an azimuth difference pattern, an elevation difference pattern, and a common sum pattern.

Figure 8 shows the feed/comparator for a single coordinate amplitude monopulse antenna. In this configuration, the sum pattern is used for transmission, while on reception, both the sum and difference patterns are obtained. The sum signal provides target intensity information as well as range to the target. The difference signal is processed together with the sum signal to yield the error signal.

Of significance to the designer is the sensitivity of the error signals and the discrimination of scatterers in the vicinity of the target. Both of these conditions are optimized with narrow highly directional antenna beams (Skolnik, M.I., 1962). Thus, the smaller the beamwidth of the antenna, the larger the error slope and the better the tracking accuracy.

Since, for a given aperture, the beamwidth decreases directly with the wavelength, the sensitivity of a monopulse antenna operating at 70 GHz can be expected to be seven times greater than a comparable aperture operating at 10 GHz.

6. PERFORMANCE PREDICTIONS

A block diagram of the monopulse system currently being evaluated at Norden is shown in Figure 9. As indicated, the system consists of the following major subsystems: transmitter/modulator, microwave package, antenna, receiver, data processing unit, gimbal and servo electronics unit. (A description of each subsystem is contained in the following sections.) Parameters of the radar are summarized in Table 1.

Table 1. Millimeter Monopulse Track Radar Parameters

TRANSMITTER		
Frequency	70 GHz	
Peak Power	10 kW	
Pulse Width	100 ns	
Pulse Repetition Rate	4 kHz	
ANTENNA		
Type	Parabola	Cassegrain
Sum Beamwidth (Pencil)	0.66°	0.67°
Gain	47.2 dB	45.5 dB
Sidelobes	-18 dB	-25 dB (Lower)
Null Depth	32 dB	35 dB
Polarization	Linear	Circular
RECEIVER		
Type	Linear, Lin/Log	
IF Frequency	60 MHz	
Bandwidth	20 MHz	
Noise Figure	10 dB	

The range performance of the tracking radar can be determined using the radar range equation. The single pulse signal to noise ratio is given by

$$(S/N)_{SP} = \frac{P_T G^2 \lambda^2 \sigma_T}{(4\pi)^3 \, KTB \, \overline{NF} \, R^4 \, L_S L_A} \tag{1}$$

where

P_T is the peak transmit power

G is the peak antenna gain

λ is the transmit wavelength

σ_T is the target cross section

K is Boltzmann's constant

T is the absolute temperature of the receiver

B is the receiver bandwidth

$\overline{NF}$ is the system noise figure

R is the range to the target

L_S is the system loss

L_A is the atmospheric loss

Using the radar parameters in Table 1, system performance against a 10 square meter target was calculated using Equation 1. The single pulse signal to noise ratio is shown in Figure 10 as a function of range for clear air and 100 meter visibility fog.

For the noise only case, the single pulse signal to noise required to obtain a 90% probability of detection can be determined using the curves presented by Rubin and DiFranco (Rubin, W.L. and J.V. DiFranco, 1964). Assuming a 10^{-6} probability of false alarm, a Swerling 1 target, and the integration of 100 pulses, the $(S/N)_{SP}$ required for a 90% Pd is approximately 6 dB. Thus for the clear air and fog cases radar range in excess of 10 km is achieved.

During rainfall, rain backscatter must be considered to determine the system performance. The rain backscatter introduces a clutter return which is proportional to the rain clutter cross section given by

$$\sigma_\omega = V \, \sigma_r \tag{2}$$

where V is the volume of the radar pulse packet and σ_r is the normalized rain backscatter cross section.

The volume of the pulse packet for a pencil beam antenna pattern is approximately

$$V = \left(\frac{\pi}{4}\right) (R\theta)^2 \, \Delta R \tag{3}$$

where

R is the radar range

θ is the antenna half power beamwidth

ΔR is the length of the pulse packet

Using the normalized rain backscatter cross section measured by Richard, the rain clutter cross section was determined as a function of range using Equations (2) and (3), (Richard, V.W. and J.E. Kammerer, 1974). The results are summarized in Table 2. A 15 dB reduction in rain backscatter through the use of circular polarization has been assumed.

Table 2. Rain Clutter Cross Section

Range (KM)	Rainfall Rate (mm/hr)	Rain Cross Section (σ_ω)* (m^2)
1	1	.005
	4	.01
5	1	.125
	4	.27
10	1	.54
	4	1.08

*A 15 dB reduction in σ_ω due to the use of circular polarization has been assumed.

To determine system performance during rainfall, the integration gain must be evaluated by first examining the decorrelation time of rain. The standard deviation of the rain clutter frequency spectrum is due primarily to wind turbulence. If we assume a fluctuating wind speed (Ws) of 1 m/sec, then the standard deviation of the rain clutter spectrum is given by

$$\sigma_c = \frac{2\ Ws}{\lambda} = 465\ Hz$$

The number of independent clutter samples is approximately

$$N_I = \frac{2.5\ \sigma_c\ N}{f_r}$$

where

f_r is the radar PRF

N is the number of radar pulses

For the 100 pulse case,

$$N_I = 29\ pulses$$

Thus the effective number of pulses integrated for signal to rain clutter improvement is 29.

As the target observation time increases to

$$\sigma_c > .4\ f_r$$

then

$$N = N_I$$

may be employed. At the radar range of interest, the signal to clutter plus noise ratio is limited by thermal noise. Thus, the signal to clutter plus noise required for a 90% Probability of detection remains approximately 6 dB. At shorter ranges, where the rain backscatter limits system performance, the effective number of radar pulses must be determined. As shown in Figure 10, the radar range for a 90% Probability of detection for 1 mm/hr and 4 mm/hr of rain is 9.3 km and 4.8 km respectively. A summary of the system range performance predictions is contained in Table 3.

Table 3. System Range Performance Predictions

Environment	Attenuation (dB/km)	Backscatter (m^2/m^3)	Target Detection Range (km)
Clear Air	.4	-	>10 km
Fog (100m Visibility)	.7	-	10.0
Light Rain (1mm/hr)	.8	1×10^{-4}	9.3
Moderate Rain (4mm/hr)	2.7	2×10^{-4}	4.8

Target Cross Section = 10 square meters

Target Model = Swerling Case 1

Probability of detection = 90%

Probability of false alarm = 10^{-6}

7. SYSTEM DESCRIPTION

The Norden experimental millimeter track radar is shown in Figure 11. A description of each of the major subsystems follows.

7.1 Transmitter/Modulator

The transmitter/modulator employs a conventional line-type thyratron modulator with a solid state driver to produce the grid trigger and a pulse-to-pulse regulator to reduce output power amplitude variations due to fluctuating input voltage. The magnetron, which operates at 70 GHz, provides 10 kW peak power at an 0.0004 duty ratio. The nominal transmitted pulse width is 100 nanoseconds. A ferrite isolator prevents magnetron pulling due to load VSWR. A pressurization unit provides 31 psia of dry air pressure to prevent arcing in the waveguide and pulse transformer housing.

7.2 Antenna

Two monopulse antennas are available for use with the system. The antenna used in the experiments described in this paper is an 18-inch parabola with an f/D ratio of 0.67. The microwave comparator and four-horn feed are constructed as an integral unit to minimize precomparator phase shift. A manual polarization selection capability allows the choice of either vertical or horizontal polarization depending on antenna orientation.

Sum channel gain at the comparator is 47.2 dB. The radiation pattern is a pencil beam with a 3 dB beamwidth of 0.66 degree and first sidelobe levels of -18 dB with respect to the sum peak. The null depth of the difference pattern is -32 dB. The four lobe antenna was designed for use between 69 and 71 GHz and meets its performance specifications over this region.

A Cassegrain monopulse antenna was also developed for use with the system. The 18-inch plastic reflector provides a sum channel gain of 45.5 dB and a 3-dB beamwidth of 0.67 degrees. The lower sidelobe level is -25 dB with respect to the sum peak. The null depth of the difference pattern exceeds 35 dB. The isolation between sum and difference ports exceeds 30 dB.

The microwave comparator and four-horn feed were constructed as an integral unit to minimize pre-comparator phase shift. The antenna provides circularly polarized energy (axial ratio < 1.2 dB) to minimize rain clutter signals.

7.3 Microwave

The microwave package incorporates specially designed waveguide assemblies to minimize insertion loss. The sum channel loss is 2.8 dB while losses for the difference channels are less than 1.0 dB each. The duplexing function is accomplished in a ferrite circulator which provides more than 22 dB isolation.

Translation to IF is accomplished by mixer/preamplifier assemblies using Schottky Barrier diodes in a balanced mixer configuration. The units provide 25 dB minimum gain (RF to IF) with a noise figure of 10 dB and a 20 MHz bandwidth centered at 60 MHz, resulting in a receiver sensitivity of -87 dBm. The sensitive Schottky crystals are protected by a switchable ferrite attenuator inserted before the mixer in each channel.

An IMPATT diode oscillator is used as the system local oscillator. A voltage-controlled current source drives the IMPATT which, used in conjunction with an AFC module, maintains the IF within 1 MHz of the center frequency.

7.4 Receiver

Because of the attenuation in the atmosphere, significant variations in signal return can be expected as a function of target range. Thus for amplitude monopulse systems, in which AGC is an important design consideration, it becomes advantageous to convert to angle processing circuitry to minimize the effects of the large dynamic range.

Amplitude monopulse information contained in the IF signals is converted to phase information by the Monopulse IF (MIF) Processor and phase detected to determine the angle-off-boresight in each difference channel. The sum channel signal is split with one output acting as a reference for the phase detector and the other output processed through a log amplifier for information and display purposes. The overall receiver dynamic range is 68 dB.

The angle-error output voltages of the MIF Processor are a function of the phase difference between the sum and difference channel signals and range from zero volts for the on-boresight condition to a maximum value of about 45 mV. The polarity or sense of the error signal depends on the location of the target with respect to the antenna boresight axis. For targets above or to the left of the axis, the sense is positive. For targets below or to the right of the axis, the sense is negative.

Of particular interest is the slope of the angle-error curve, especially in the linear region around boresight, since it is this signal that will ultimately provide the control signals for the servo system. For the millimeter track radar, the slope (or scale factor) at the output of the MIF Processor is 10 mV/mr in the linear region. Scaling amplifiers with variable gains are provided for interface with the processing circuitry.

7.5 Data Processing Unit (DPU)

The data processing unit provides the essential circuitry needed to process the received signals. In addition, the system timing trigger of 4 KHz and all synchronization signals are developed in the unit. The MIF and AFC modules are also contained in the DPU.

The pulsed sum video, azimuth and elevation error signals are received from the MIF and processed.

The sum video generates a position-correcting servo loop for range tracking a single range-gated target. A range swath of 4 nautical miles is searched in a period of 1 second.

Clutter rejection logic is also incorporated in the DPU. The logic, which uses pulsewidth discrimination, allows lock to be broken if the range gate locks onto broad-based clutter. As soon as lock is broken the range gate continues searching for a hard target at a closer range.

Range and range rate readouts are also provided in the system.

7.6 Pedestal

The Antenna/Receiver is mounted on a pedestal which allows tracking the azimuth and elevation. The transmitter/modulator and data processing unit are mounted in the base of the pedestal. Rotary joints are utilized to send energy to the antenna/receiver.

The antenna can track a target over a ± 45 azimuth sector and -5° to +30° in elevation.

8. PRELIMINARY EXPERIMENTAL RESULTS

8.1 Target Acquisition

To demonstrate the acquisition and track capability of the millimeter track radar, the system was integrated with a helmet-mounted optical sight. The sight, provided by General Electric, Burlington, Vermont, is used for rapid acquisition of a potential target and hand-off to the track radar. The helmet sight, operator and track radar are shown in Figure 12.

The helmet sight is comprised of a reticle sight mounted on a standard flight helmet and an electromechanical linkage from the helmet to the common mount of the radar antenna. The reticle sight has a birefringent optical element that creates a pattern of concentric circles. Once the operator aligns the sight to the target, the radar antenna will follow his head motion.

As the operator moves the helmet sight to maintain the target in the sight, the slaved beam is maintained on the target. The automatic range acquisition is engaged and the radar locks onto the target.

When this condition is met the radar system takes over the angle track function and drives the antenna in azimuth and elevation. If the radar should lose range lock, the antenna will automatically track the helmet providing a back-up safety feature.

8.2 Tracking Tests

All tests of the monopulse radar have thus far been conducted as the Norden facility in Norwalk, Connecticut, USA. The radar was placed in a tower facility which is 18.3 meters above ground level. A view from the laboratory is shown in Figure 13.

A corner reflector, shown in Figure 14, is mounted on a pole 17.7 meters in height, at a range of 487.7 meters from the tower. Clutter, at the base of the support pole, is 36 milliradians below the reflector.

Figure 15 shows an A-scope presentation of radar returns as a function of range. Examination of the figure indicates that when the radar is tracking the reflector, the clutter returns in the vicinity of the pole are well below the minimum detectable signal. Since the pole subtends about 36 milliradians at this range, it can be seen that targets can readily be tracked to within 2° of the clutter. The ground clutter shown in the figure is 365.8 meters behind the corner reflector.

Initial observations indicate that no measurable wander occurs, even during windy conditions. This phenomena will be investigated in detail in comprehensive glint studies to be conducted during Calendar 1976.

A series of dynamic tracking experiments were conducted using a Bell 47G helicopter. Figure 13 shows the helicopter flying in the vicinity of the Norden test facility.

The target aircraft was acquired using the helmet sight and tracked. Results of the tests were being evaluated at the time this paper was prepared.

9. CONCLUSIONS

A high accuracy millimeter wave monopulse radar has been developed for use in low angle tracking applications. Predictions of system performance indicate that adverse weather performance permits system operation in dense fog and rainfall rates of 4 mm/hr. Tracking tests are in progress using a corner reflector and helicopter.

Application of the millimeter track radar to aircraft and missiles for weapon delivery and terminal guidance is being investigated.

10. ACKNOWLEDGEMENT

The authors wish to acknowledge the assistance of John Carulli who was responsible for the assembly and test of the brassboard radar and to John Fitzgerald, Tom Ikeda and Albert Sokolowski for their assistance in the development of the radar system.

11. REFERENCES

Hogg, D.C., January 1968, "Millimeter Wave Communication through the Atmosphere," Science, pp. 39-46

Koester, K.L. and L.H. Kosowksy, November 1970, "Attenuation of Millimeter Waves in Fog," presented at the Fourteenth Radar Meteorology Conference

Koester, K.L., March 1971, "Propagation of 70 GHz Energy through Rain and Fog," Norden Technical Report 4302 R 0001, Rev. A

Koester, K.L. and L.H. Kosowsky, September 1971, "Millimeter Wave Propagation in Fog," presented at the IEEE International Antennas and Propagation Symposium

Koester, K.L., September 1971, "Clear Air Propagation in the 4 mm Band," Norden Technical Report 4337 R 0009

Koester, K.L., September 1972, "Millimeter Wave Propagation," Norden Technical Report 4392 R 0005

Richard, V.W. and J.E. Kammerer, 1974, "Millimeter Wave Rain Backscatter Measurements," presented at NELC Millimeter Waves Techniques Conference

Rhodes, Donald R., 1959, Introduction to Monopulse, McGraw-Hill, New York

Rosenblum, E.S., March 1961, "Atmospheric Absorption of 10 to 400 KMCPS Radiation," Microwave Journal, pp. 91-96

Rubin, W.L. and J.V. DiFranco, April 1964, "Radar Detection," Electro Technology, pp. 61-90

Skolnik, Merrill I., 1962, Introduction to Radar Systems, McGraw-Hill, New York pp. 164-197

Straiton, A.W. and C.W. Tolbert, May 1960, "Anomalies in the Absorption of Radio Waves by Atmospheric Gases," Proceedings of the IRE, Vol. 48, pp 898-903

Tolbert, C.W. and A.W. Straiton, April 1957, "Experimental Measurement of the Absorption of Millimeter Radio Waves over Extended Ranges," IRE Transactions on Antennas and Propagation, pp 239-241

Van Vleck, J.H., 1964, "Theory of Absorption by Uncondensed Gases" in D.E. Kerr (ed.), Propagation of Short Radio Waves, pp. 646-664, Boston Technical Publishers, Massachusetts

Wilcox, F.P. and R.S. Graziano, March 1974 "Millimeter Wave Weather Performance Projections," presented at the NELC Millimeter Waves Techniques Conferences

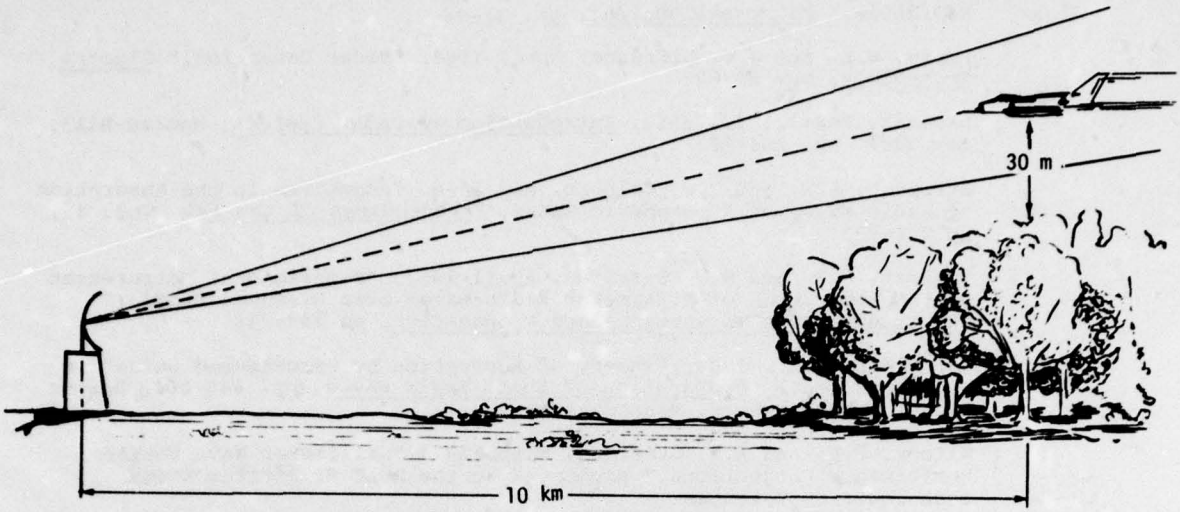

Figure 1. Low Angle Track Scenario

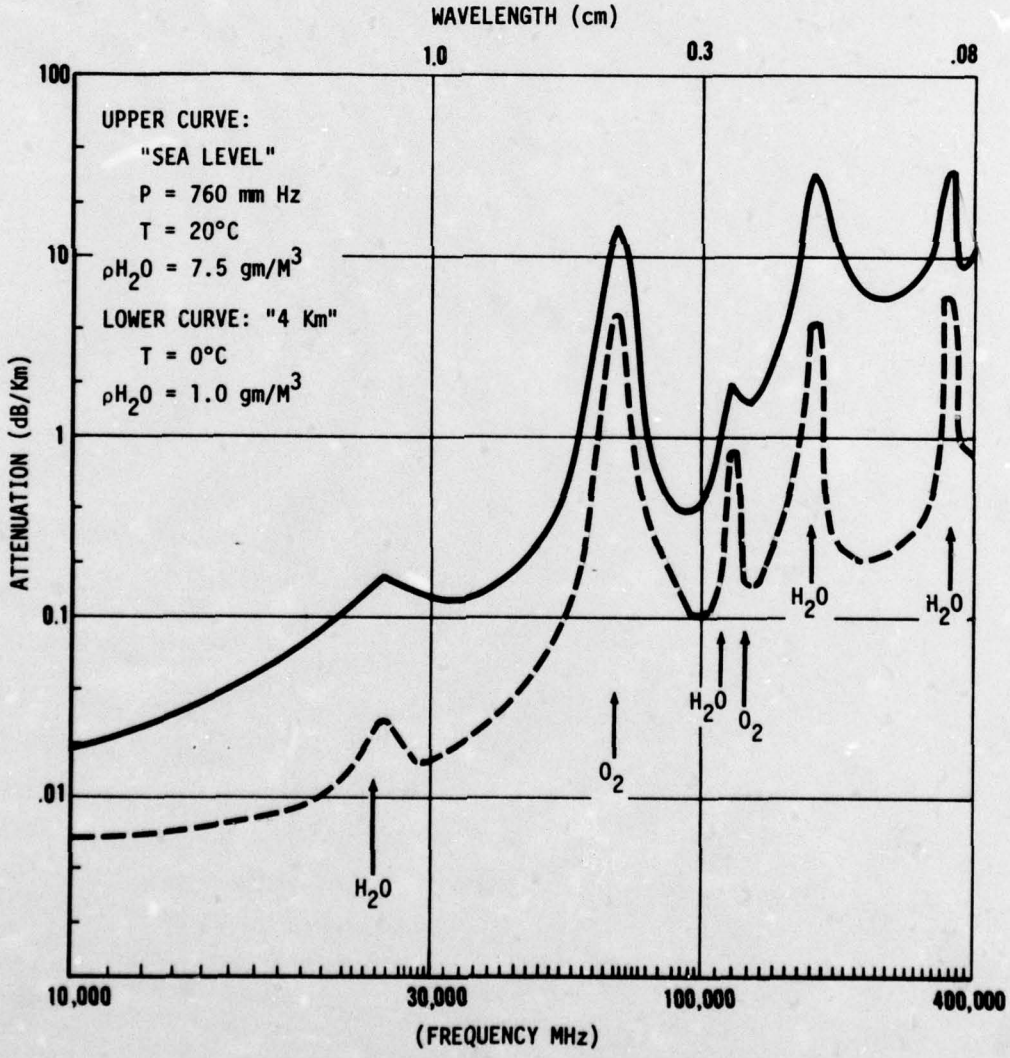

Figure 2. One-Way Attenuation for Horizontal Propagation in Clear Air (E.S. Rosenblum 1961)

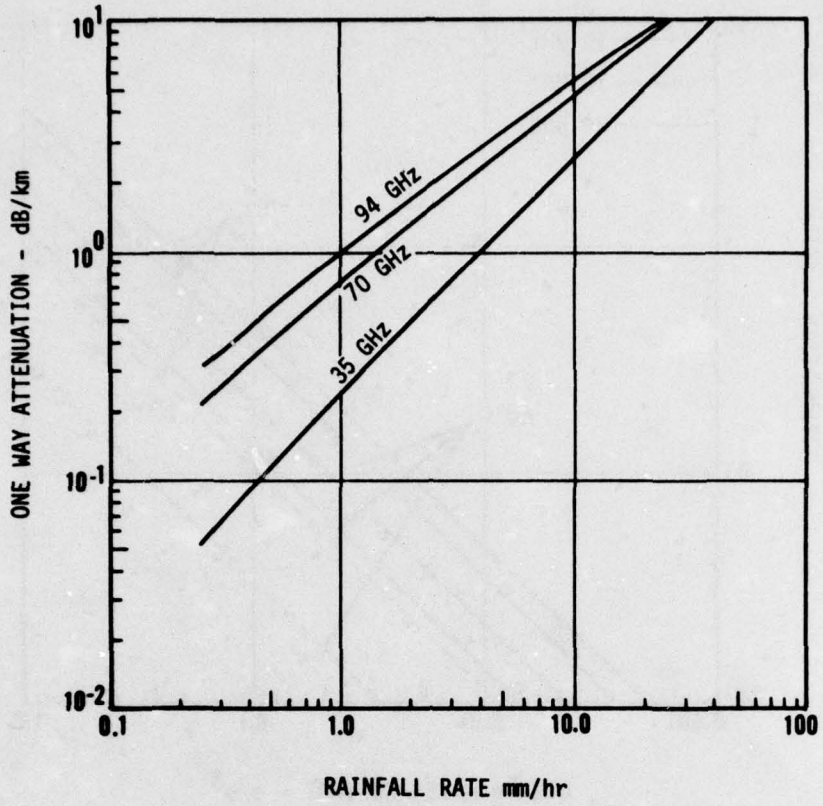

Figure 3. One-Way Attenuation in Rain

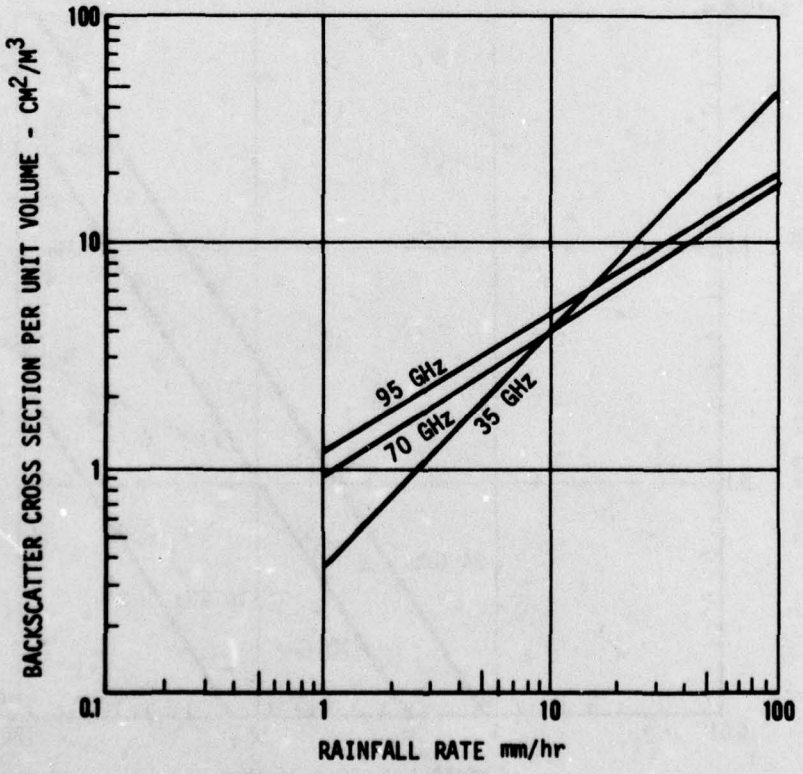

Figure 4. Measured Backscatter Cross Section of Rain (V.W. Richard and J.E. Kammerer - March 1974)

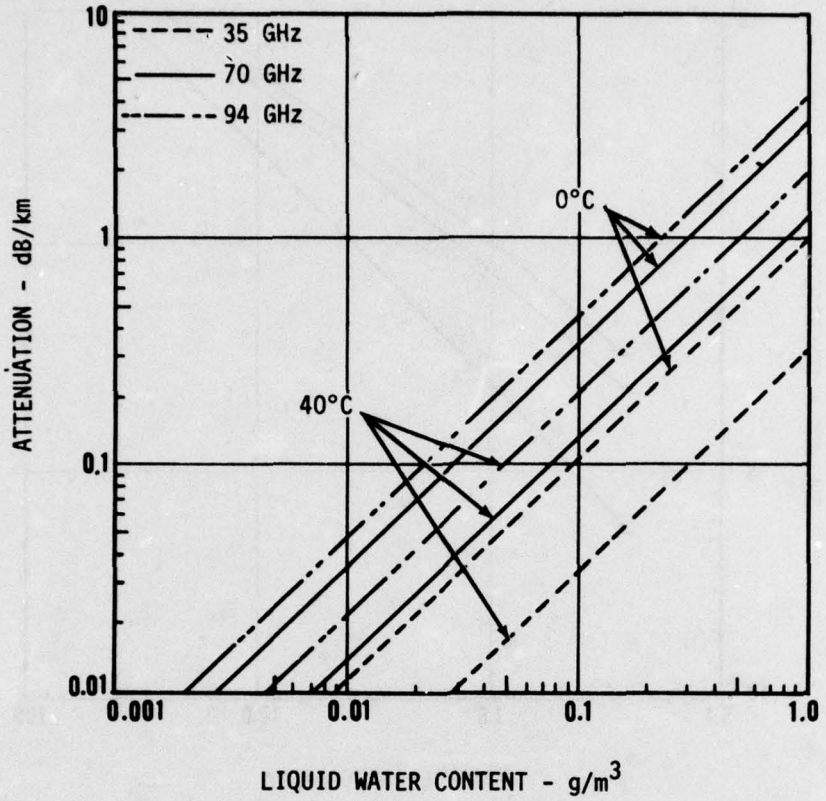

Figure 5. One-Way Attenuation in Fog

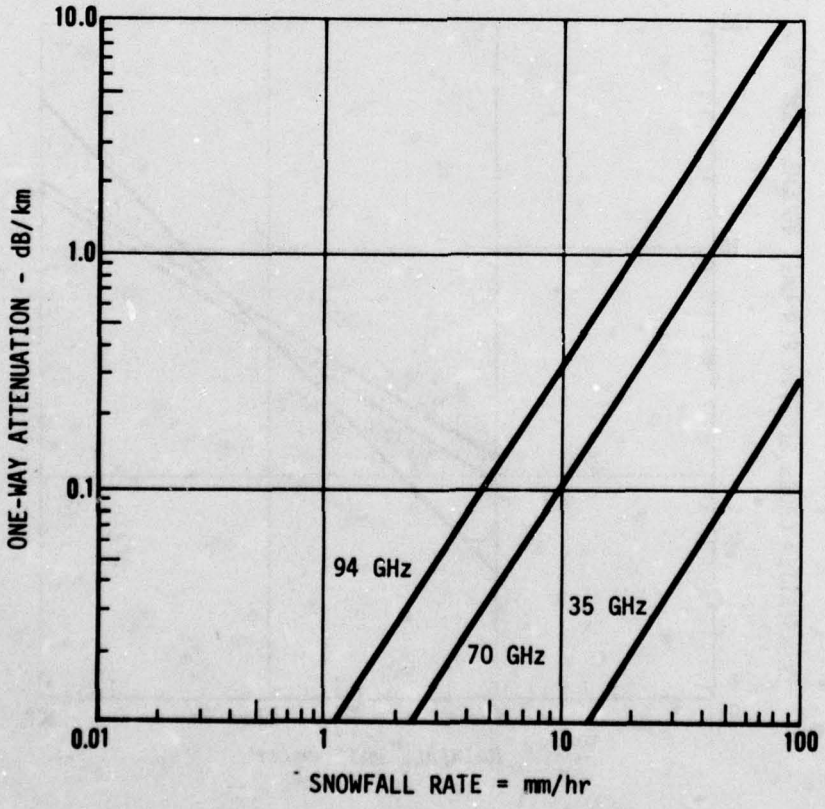

Figure 6. One-Way Attenuation in Snow

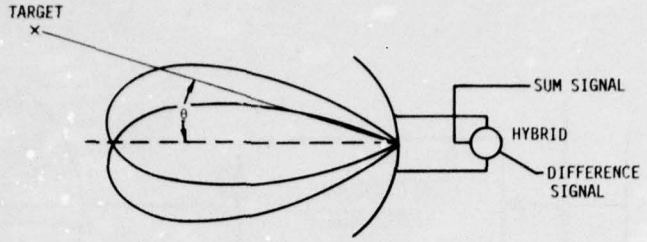

A) AMPLITUDE MONOPULSE

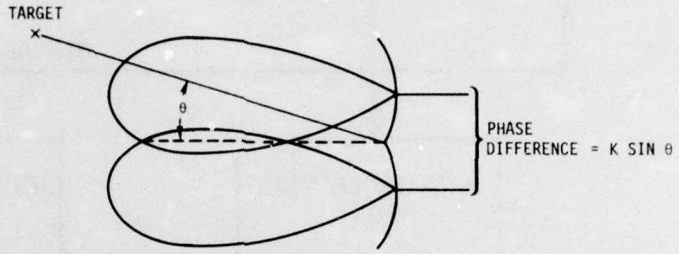

B) PHASE MONOPULSE

Figure 7. Monopulse Antenna Configuration

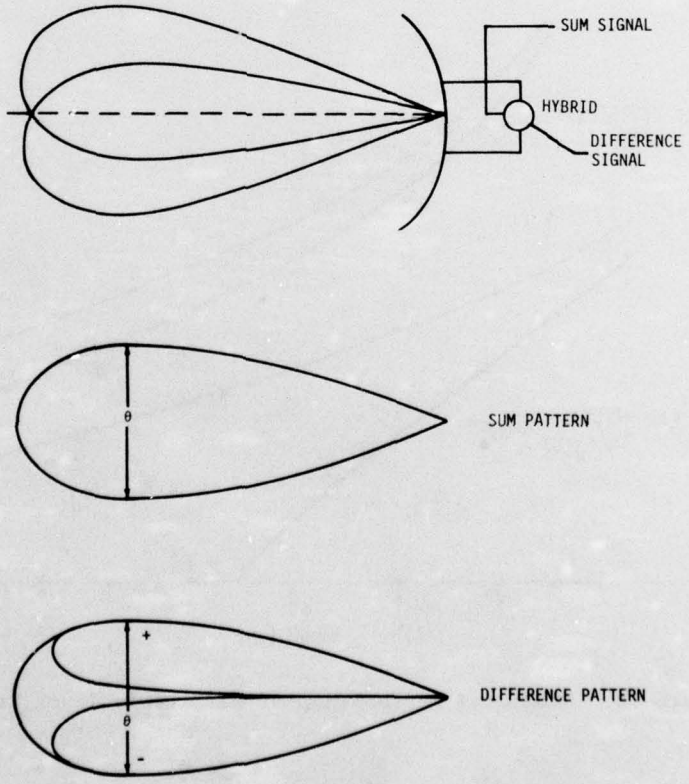

Figure 8. Single Coordinate Amplitude Monopulse Antenna Configuration

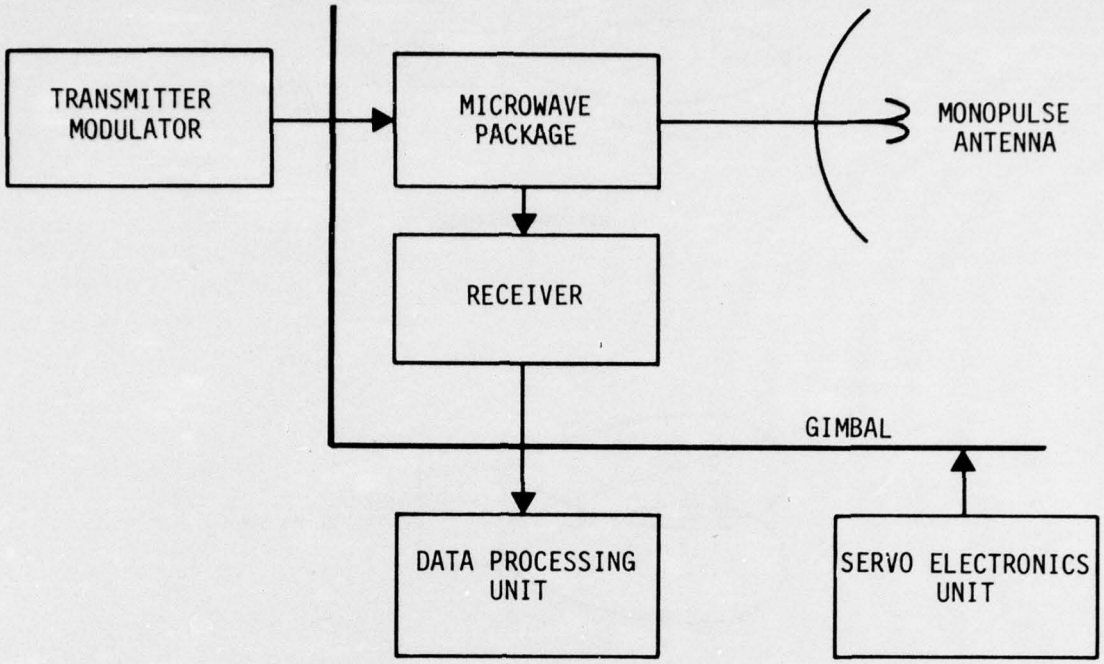

Figure 9. Block Diagram of Millimeter Monopulse Track Radar

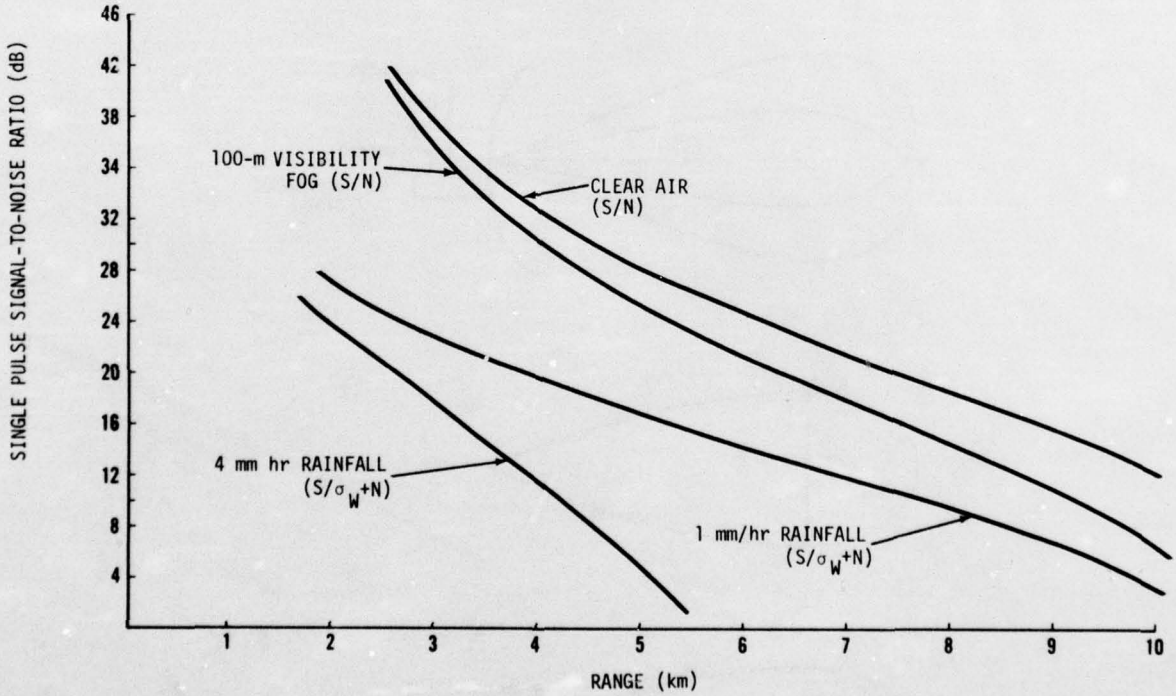

Figure 10. Predicted Performance of Millimeter Track Radar

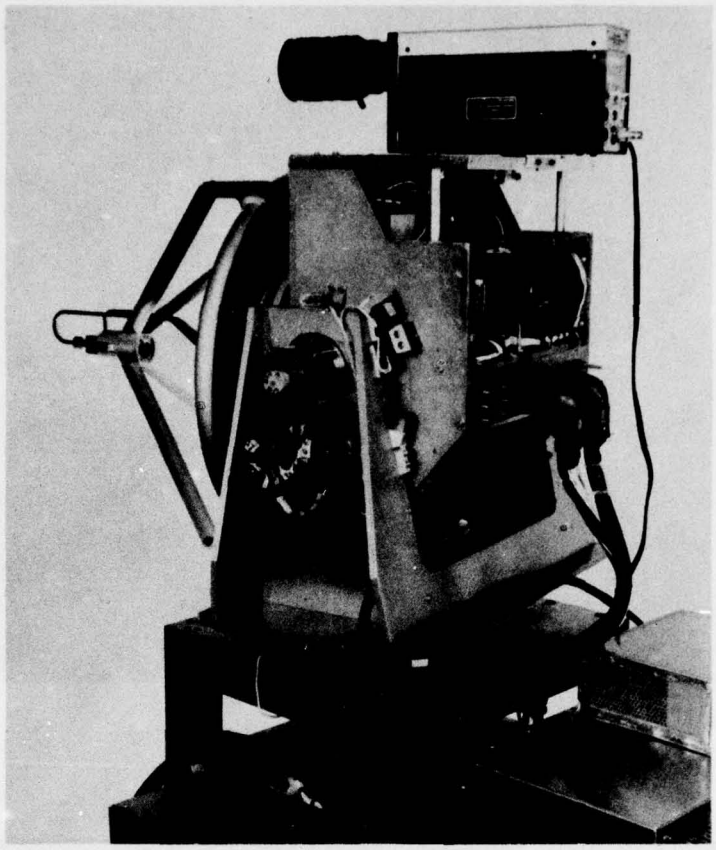

Figure 11. Norden Experimental Millimeter Track Radar

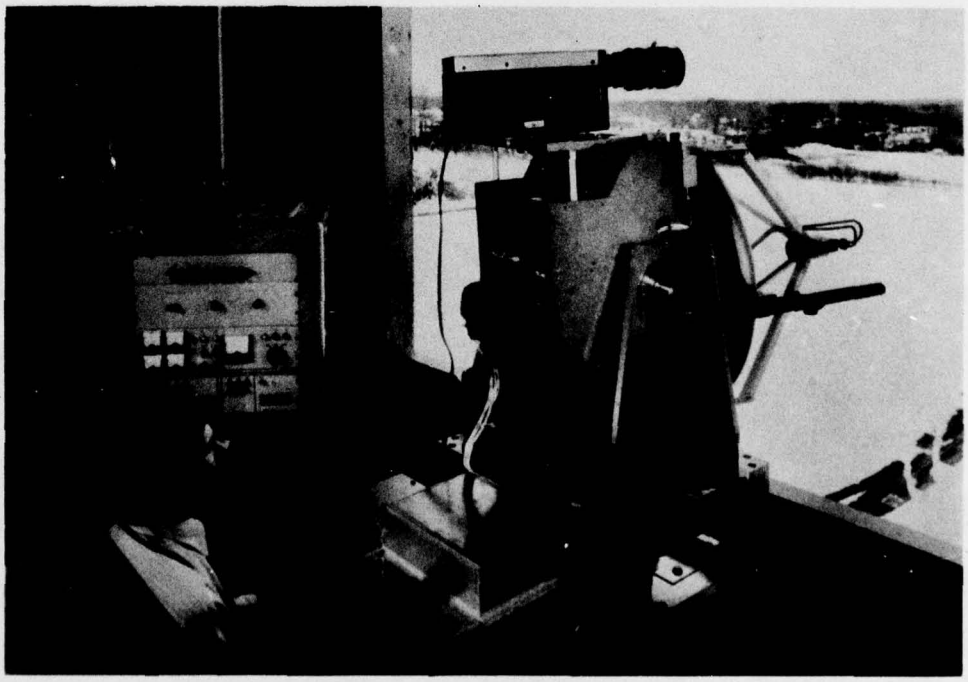

Figure 12. Norden Millimeter Track Radar with Operator and Helmet Sight

Figure 13. View from Tower Facility

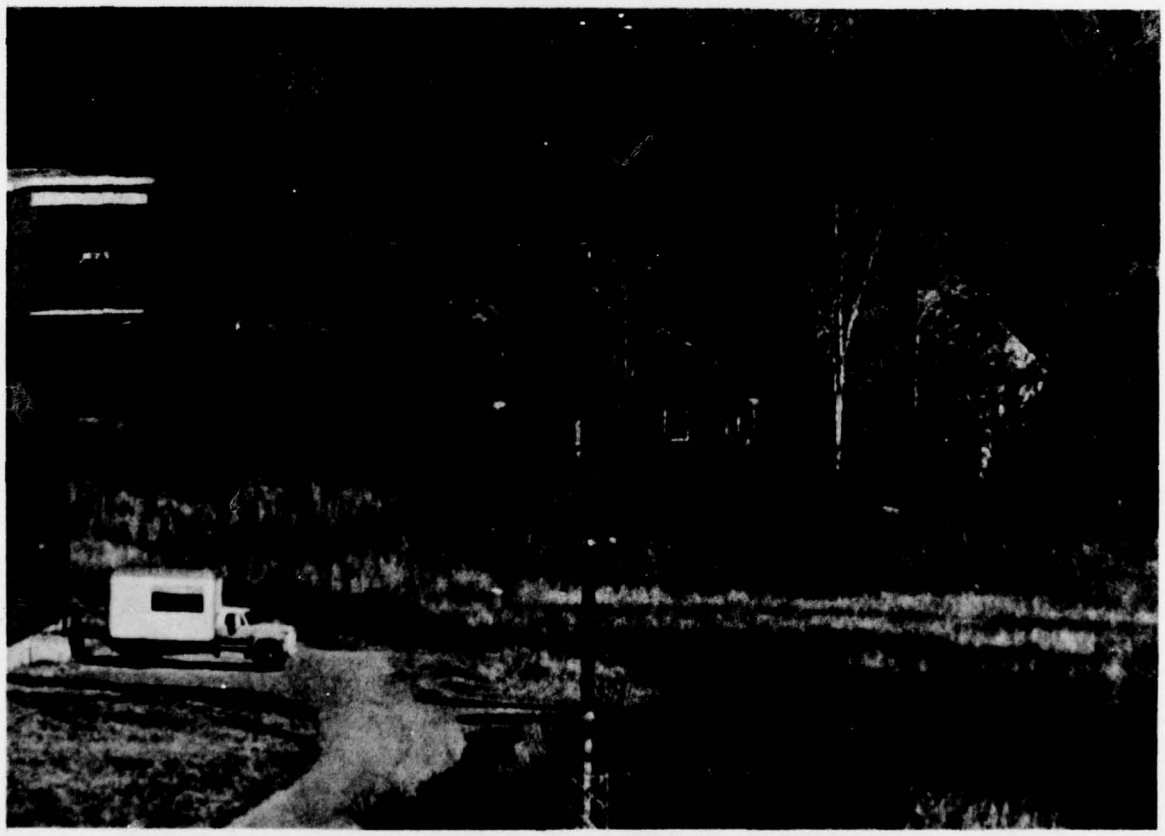

Figure 14. Corner Reflector Target

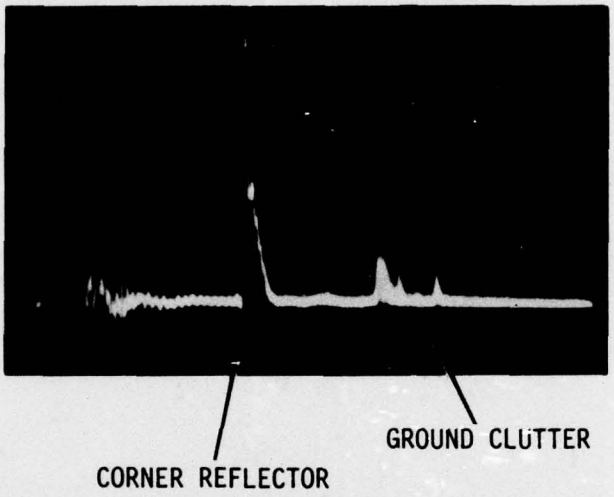

Figure 15. A-Scope Display of Sum Channel Video

DISCUSSION

H SITTROP: Have you made any very low-angle tracker experiments over water, in particular to investigate the "Beckmann Spizzichino" specular reflection coefficient over water? If not, are you planning to do so?

L H KOSOWSKY: No tracking experiments have been made over water and none is presently planned unless sponsorship is obtained. The monopulse radar would be capable of making such measurements.

J SNIEDER: Has attention been given to the attenuation due to rain where the drop size distribution has been taken into account? This distribution gives a better relationship to attenuation than does total rainfall.

L H KOSOWSKY: We have not taken into account the drop size distributions of raindrops in computing the attenuation coefficients, and we have not considered multiple scattering in the rain volume. Various drop size distributions in different parts of the world would also affect the calculations. The published curves appear to be valid in the US.

J FREEDMAN: 1) Does the gain of 15 dB in backscatter attenuation, using circular polarisation on rain, depend upon theoretical or experimental work?

2) How dependent is the result on the sphericity of the raindrops?

L H KOSOWSKY: 1) The 15 dB reduction in rain backscatter was measured at 70 GHz using a circularly polarised 18 inch antenna.

2) The dependence of polarisation sensitivity on raindrop deformation has been studied by Oguchi in Japan. Our results indicate that 15 dB improvement can be achieved at 4 mm/hr of rain, but I do not know of data at higher rain fall rates.

THE ELRA PHASED-ARRAY RADAR WITH AUTOMATIC PHASE ADJUSTMENT IN PRACTICE

G. Hüschelrath and W. Sander
Forschungsinstitut für Funk und Mathematik
5307 Wachtberg-Werthhoven
Federal Republic of Germany

SUMMARY

The Electronic Steerable Radar (ELRA) project of the Forschungsinstitut für Funk und Mathematik (FFM) embodies an experimental phased array radar with multiple beam and multifunction capability. It is a versatile tool for proving modern signal and data processing techniques. This paper gives a short description of the whole system, presently implemented parts, and first experimental results.

1. INTRODUCTION

The ELRA system includes two separated phased arrays with 500 transmitter and 1300 receiver modules in the S-band, as shown in Fig.1. The antenna elements - printed dipoles - are randomly distributed on tilted, planar, circular apertures and form thinned arrays. The scan volume is 120° in azimuth and 90° in elevation, the beamwidth of the pencil beam about 1.5° and the maximum range about 200 km. The current stage with 100 transmitter and 200 receiver modules covers a range of about 30 km but can yet demonstrate the most functional properties of the final system. Some peculiarities of ELRA are

- the real-time automated focussing and monitoring system (APFC),
- the phase computing unit,
- the beam forming matrix,
- the generation of up to six independently steerable beams (time multiplex operation),
- coherent (MTI-filter, doppler filter bank) and incoherent (sequential detector) signal processing units,
- the radar control and data transfer by a TR 86 process computer,
- the central computer with a satellite computer for display tasks.

2. SYSTEM DESCRIPTION

2.1. Transmitting Antenna

The main problem of designing the transmitter is the right choice of the power dividing network, type of amplifier and phase shifter. Besides the technical data and specifications special attentions must be focussed on the search for an economic solution.

If the radar system implies a good monitoring part to detect and locate faulty elements, the most practical and economic solution will be corporate feed with active modules as shown in Fig. 2 [1]. This system of low power amplifiers and dividers can be designed optimally for nearly every number of radiating elements. This makes it attractive for a step by step completion of the antenna.

The relatively low power level in the system allows much cheaper and less problematic components. For instance, the power dividers are etched in usual microstrip technique and the interconnections are made by normal coaxial lines.

As the phase shifters are placed ahead of the output amplifiers, they are designed to handle 100 W peak power at a duty cycle of 3 %. The 3 bit switching is done by PIN-diodes with a switching time of < 250 ns. There are no severe specifications concerning the transmission losses as long as the attenuation between two amplifier stages does not exceed the power gain of the amplifiers. Therefore 3 dB losses for the phase shifters are acceptable. As a phase correcting loop is involved in the system, no specifications concerning the transmission phase values must be demanded.

After calculating the cost efficiency of the transmitter including MTBF, price and technical data of different types of amplifiers and considering some basic demands:

500 W peak power min
10 dB power gain
20 % RF efficiency

as well as the need of a phase coherent amplification, disc seal triodes were chosen. These tubes reach a peak power of 1 kW at a duty cycle of 3 % and a power gain of 10 dB.

Fig. 3 shows the construction of an amplification unit. In contrast to a conventional construction the heat-sink has been removed into the inner conductor of the anode resonator in order to avoid undesired oszillations while scanning the antenna. The cooling is done by forced air. The RF input and output couplings are inductive, each tunable by a variable capacitor. These capacitors proved to be very useful to reduce the mechanical specifications of the amplifiers and to compensate the tolerances of the tubes.

Fig. 4 shows the assembled rackmounts within the transmitter cabin. Each rackmount contains five output amplifiers, one pre-amplifier, the five phase shifters, the power divider (see also Fig. 2), the modulator and the safety equipment.

2.2. Receiving Antenna

The receiving antenna consists of many identical modules which contain the following elements:

- a printed folded-dipole,
- a single-balanced mixer with Schottky-barrier diodes,
- a low noise IF-preamplifier,
- an IF-amplifier with a SAW-filter for matching rectangular 10 µs transmit pulses,
- the 3 bit phase shifter located in the synchronous detector reference branch consisting of a tapped delay line and an analog switch,
- an universal digital phase shift control which allows a rapid change of the phase shift between up to six predetermined values,
- a synchronous detector which delivers the in-phase and quadrature components of the signal in the video band.

The noise figure of the receiver is about 6 to 7 dB. It could be reduced by a low-noise transistor preamplifier, which nowadays is realizable in the S-band at reasonable costs.

The arrangement of the phase shifting device at a point where the signal-to-noise ratio is insignificant and the ability of rapidly changing the bandwidth and the phase shift allows the lossless generation of up to six independently steerable beams by a time-multiplex method.

Like the transmitter modules the receiver modules have no hardware means for equalizing the phases of all channels. This task is fulfilled by the APFC unit. Phase differences are cancelled out by software procedures while calculating the phase shifting commands. So the requirements on phase tolerances and stability are reduced.

The elements of the receiver channels are distributed partly close to the aperture, partly in racks. This arrangement is accommodating the research tasks. An operational system however should use a complete module in a separate case for each receiving channel. By use of modern technologies a reduction of size is possible. This is shown in Fig. 5 where the first mixer with IF-amplifier from our own laboratory production is compared with new industrial ones. The circuits were developed, tested and partly produced in the FFM. The next expansion to 600 receiving channels will use elements from industrial production.

2.3. The Beam Forming Matrix

Summing operational amplifiers combine the in-phase like the quadrature components of 16 channels with equal weights to form subarray sum beams. A secondary set of amplifiers sums up these subarray signals with different complex weights and generates a cluster of beams with various shapes and directions within the subarray beam, e.g. a sum beam, difference beams for azimuth and elevation, or squinted sum beams. These beams are mutually fixed and only simultaneously steerable by the phase shifter settings. They are mainly used to give more information about target parameters (precise angular coordinates, multipath or multiple targets detection).

2.4. Signal Processing

Presently the following signal processors are used:

- a threshold detector for the detection of targets in areas without clutter,
- a monopulse processor giving estimates of the angular coordinates in areas without clutter,
- a doppler filter bank (31 filters) [3] for the pulse series integration and for detection of targets in areas with clutter.

In the future these devices will be replaced by the following more sophisticated processors:

- An incoherent sequential detector for multiple range elements [4] which uses the signals of five independent beams to detect targets in areas without clutter. This detector has been completed and will be involved soon.
- A hard wired digital processor is being developed which has to accomplish all tasks connected with coherent signal processing:

a) Target search in clutter
(digital matched filter at doppler frequency zero for clutter suppression cascaded with a doppler filter bank).

b) Position finding
(the monopulse processing requires about 13 dB S/N. Therefore, the difference signals of detected targets have to pass a clutter filter and a doppler filter bank) [6].

c) Variable number of transmitted pulses
(for coherent sequential detection, sequential estimation of the target velocity and adaptation of the integration to the S/N required (or monopulse)).

d) Staggered and equally spaced pulses
(this requires flexibility with respect to the coefficients of the clutter filter and the doppler filter bank).

e) Adaptive suppression of weather clutter
(by means of a frequency-dependent threshold control).

2.5. Radar and Antenna Control

A general purpose computer controls the ELRA radar tasks including 6-beam multiplex data processing, the data transfer to and from the central computer implemented for tracking and system control, and a variety of special units for antenna control and signal processing. The installations required for multiplexing enable simultaneous searching in up to five directions and position finding for one target in a further direction or position finding of up to six targets in different directions and ranges [5].

Fig. 6 shows the data flow in successive intervals. At the beginning of each period the radar gets the control information for up to six radar tasks. Subsequently, the set of phase values for each antenna element is calculated in a phase computing unit by realizing the formula

$$\varphi = u \cdot x(i) + v \cdot y(i) + \varphi(i)$$

with

u, v = beam direction cosines

$x(i), y(i)$ = position of the dipoles in the array

$\varphi(i)$ = correction phase values measured by the automatic phase correction unit (APFC).

This special unit calculates the phase data for all antenna elements for six directions from the coordinates of the beam directions. During the following interval the real radar handling takes place. Up to six pulses are sent to different directions in an order according to the beam number. Then signals from the different directions are received in parallel or serial operation. The succession of the receiving intervals may differ from the beam number. At the beginning of the next interval the gathered radar results are available.

2.6. The Automatic Phase Correction Unit

The Automatic Phase and Failure Control (APFC) unit has been designed to measure the phase errors of each channel and to detect and locate faulty elements within the antenna system, controlled by the process computer. Measured phase values are transfered to the phase computing unit, while the error data are handled in the TR 86 process computer in order to locate the defect element by combining the results of several measuring loops (see Fig. 1). The APFC-unit measures the electrical field strength in front of each array antenna by a horn antenna. These horn antennas are located outside the normal scan directions in the near-field zone. In the case of the transmitter array the horn is connected to a receiver channel while in case of the receiver measurement the horn is radiating at the transmit frequency (see Fig. 1).

The principal way of monitoring the elements is explained by Fig. 7. This Figure shows the input of the APFC-unit for the example of a five-element array. The field vectors $\underline{A}_n$ are summed up to the sum vector $\underline{A}$. Changing the phase values of channel 1 (5) will give a circle centered around the sum $\underline{A}_{S1}$ ($\underline{A}_{S5}$) of the remaining unchanged channels. The diameter and the position of this circle indicate the output magnitude and phase value of that channel. This means that at a fixed scan direction only one channel has to change its phase value cyclically. The eight possible points (3 bit phase shifters) must be measured by the APFC-unit. From these data one can easily calculate the current magnitude and phase value of that channel. Checking also the correct sequence and location of the measured data on the circle leads to a binary failure word that will indicate channel malfunctions, if present.

Using this kind of measuring loop the ELRA system is able to compensate static and slowly dynamic phase errors during normal radar operation. As the scan direction is of no importance for the measurements the only limitation is, that the loop needs eight radar intervals for minimum scanned into the same direction. Although the channels are tested serially it is possible to detect a severe break down in less than 100 ms. The detection time of a single failed element depends on the number of channels. In a 1000 element array it will be 16 s maximum. This graduated detection time, depending upon the importance of the error due to system availability, is another advantage of the ELRA-system. The good redundancy of the antenna system (graceful degradation) allows to insert only few and relatively cheap stand-by equipment to guarantee the continuous operation of the radar.

As the horn antennas are located in the nearfield zone of the arrays the measured phase values have to be corrected. Otherwise the array is focussed on the point of the horn antenna and not on the far field. As focussing on the horn is only interesting for a pattern measuring mode, the correcting phase values which result from the different path lengths between

the single elements and the horn must be measured once for a given horn position and added to the measured phase values.

3. EXPERIMENTAL RESULTS

First results of the ELRA system can be demonstrated by the roughly measured antenna patterns and the radar responses of the normal radar mode. The antenna patterns were measured using the horn antennas of the APFC-unit in the near field. The array-antennas were focussed on the horn position and scanned. Fig. 8 and Fig. 9 show the results for the receiving (200 elements) and transmitting (100 elements) array.

To explain the automatic focussing mode, the receiver antenna pattern had been focussed in steps of 40 channels and scanned in between to demonstrate the actual pattern. Fig. 10 shows the growing of the beam.

As the antenna patterns in the above stated form are measured and focussed in the near field zone, one would have to check the pattern in the far field region in order to see whether the near to far field transformation is correct or not. This far field antenna pattern was measured scanning the antenna over an isolated fixed target (Fig. 11). This method is just a test and cannot replace an exact pattern measurement which will be done in the next future.

The A-scope picture of a fixed target (Fig. 12) was taken over several seconds to demonstrate the excellent short-time stability of the antenna system - important for a coherent signal processing.

The first results in the radar mode were the mapping of the nearby clutter area (Fig. 13). The hilly country site is crossed by the river-Rhine-valley. The farest echoes came from up to 30 km. The first 5 km were suppressed.

Fig. 14 shows the same area with clutter suppression by a doppler filter bank. The main echoes are caused by a helicopter. Following the target in a combined track- and search-mode leads to a PPI similar track evaluation response.

4. CONCLUSIONS

The measurement data have verified the analytically predicted performance of the ELRA conception. Besides the normal properties of phased array radars the insertion of the APFC unit into the system proved to be very useful. The reduction of component specifications combined with the ability to correct phase errors and to detect and locate faulty elements is a promising way to decrease costs and the problems of maintenance.

The present state of the system gives a fundamental functional confirmation of the system conception. Future tasks will be the increase of the number of modules to aim lower sidelobes and higher range, the installation of versatile signal processors, and the gradual application of the hardware-prepared multifunction capability by software means.

ACKNOWLEDGEMENTS

The authors wish to acknowledge the constructive suggestions of several colleagues. We are especially indebted to Dr. W.D. Wirth as the project leader, Dr. E. Hanle who is responsible for the radar control (TR 86), and Dr. R. Klemm for his contribution concerning the signal processing units planned within the ELRA phased array radar.

REFERENCES

[1] Hüschelrath, G. — A Special Design of System and Components Enables a More Economic Phased Array Antenna. Proc. of the 4th European Microwave Conference, Montreux, 1974, pp. 263-267.

[2] Sander, W. — Mehrkeulenbildung mit elektronisch gesteuerten Antennen. Symposium über Radartechnik, 13 to 15 November 1974, Munich.

[3] Wirth, W.D. — Detection of Doppler Shifted Radar Signals with Clutter Rejection. AGARD Conference Proceedings 66 "Advanced Radar Systems", Paper 30.

[4] Wirth, W.D. — Fast and Efficient Target Search with Phased Array Radars. IEEE International Radar Conference, 22 to 23 April 1975, Arlington.

[5] Hanle, E. — Control of a Phased Array Radar for Position Finding of Targets. IEEE International Radar Conference, 22 to 23 April 1975, Arlington.

[6] Sander, W. — Off-Boresight Angle Estimation with a Phase Comparison Monopulse System. AGARD Conference on Antennas for Avionics, 26 to 30 November 1973, Munich.

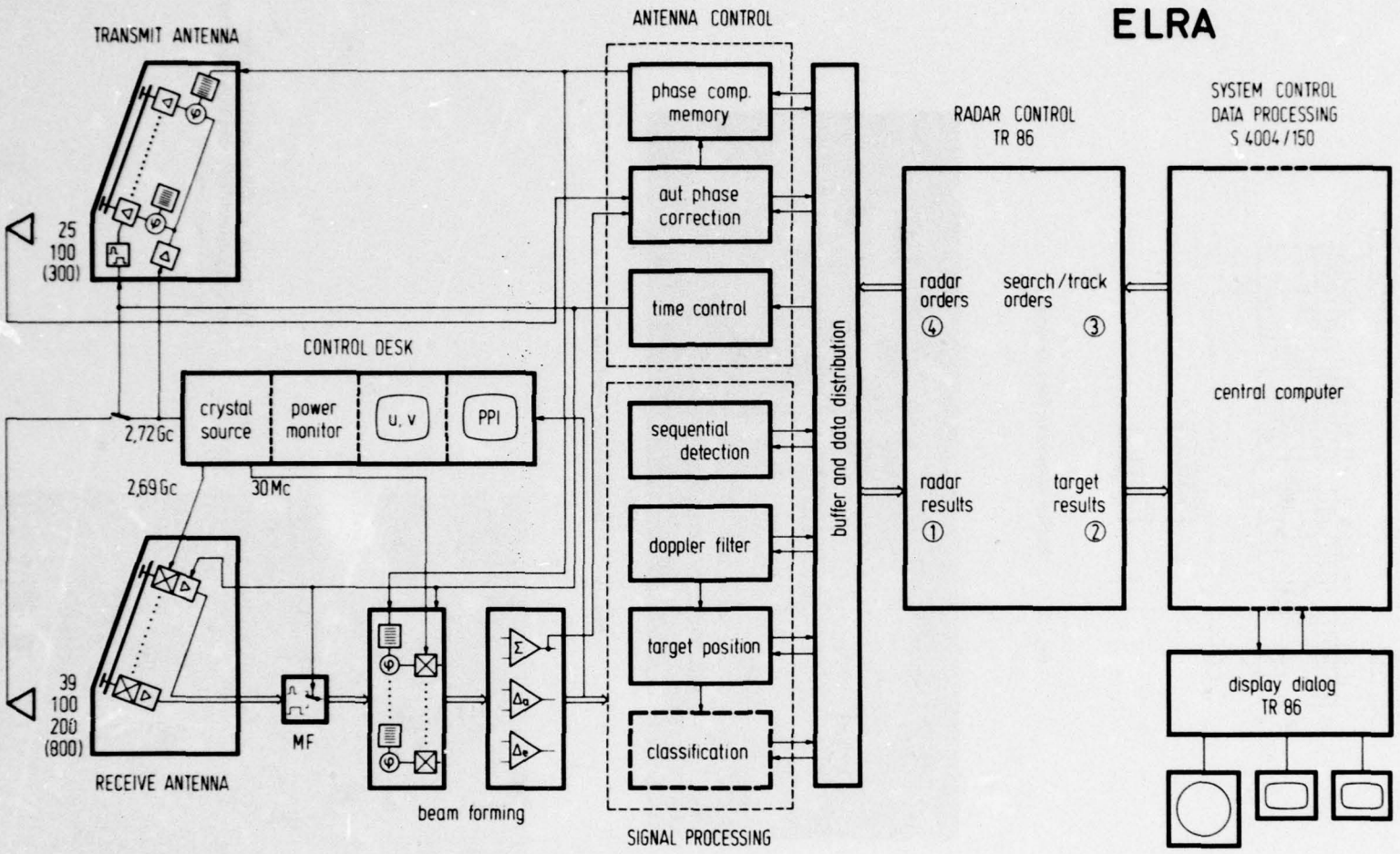

Fig. 1 **Block diagram of the ELRA system.**

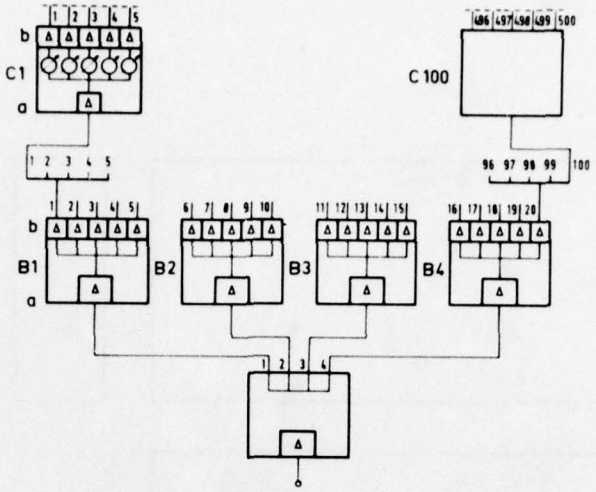

Fig. 2 Active corporate feed network.

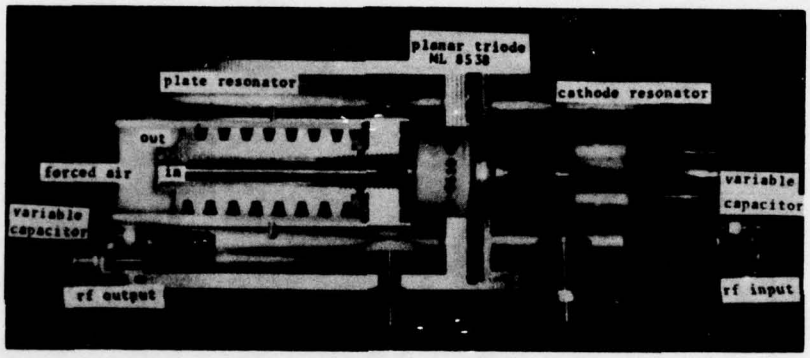

Fig. 3 Triode power amplifier.

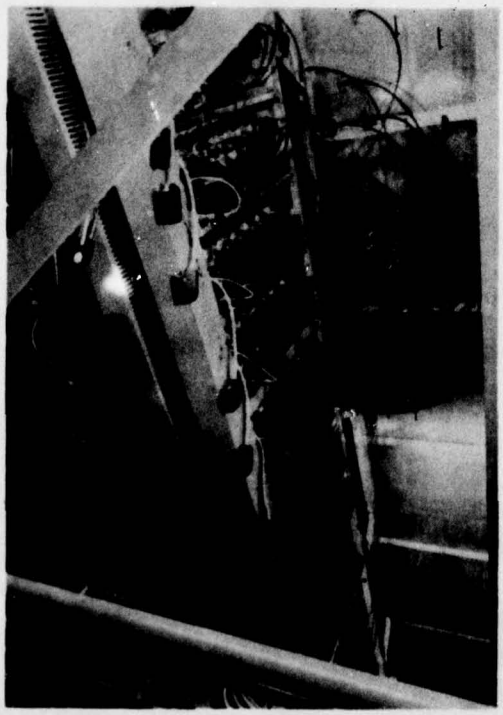

Fig. 4 Inside view of the transmitter array showing assembled racks connected to the space tapered aperture.

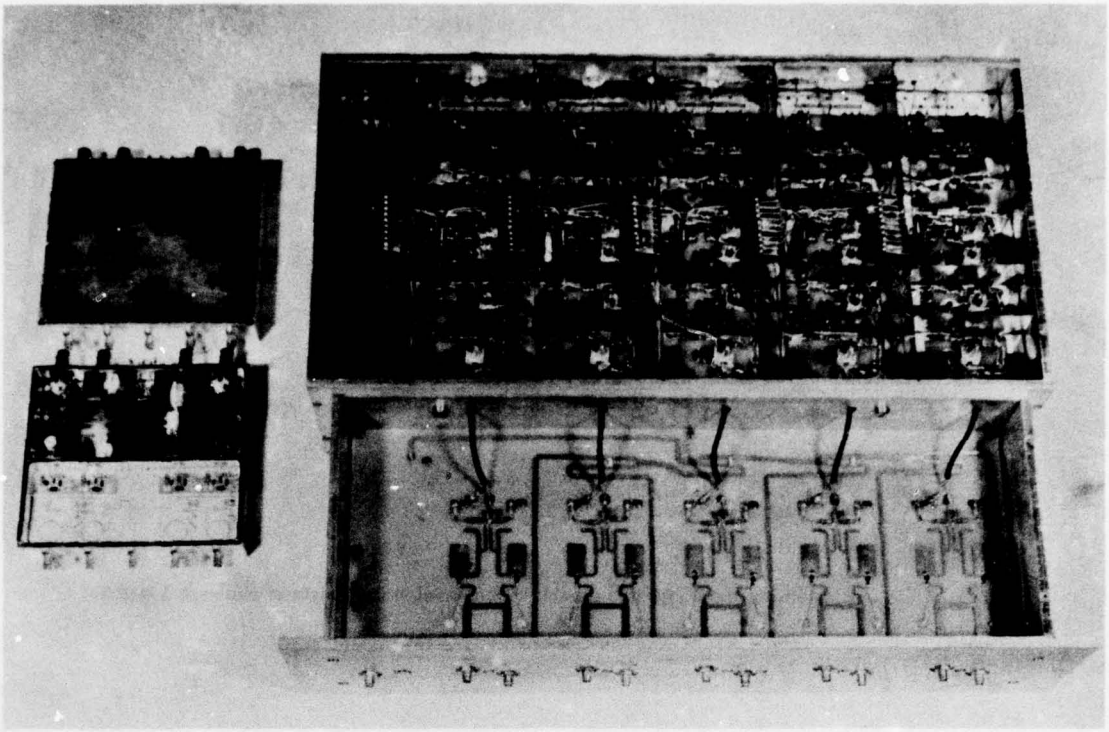

Fig. 5 Equivalent receiver modules from laboratory (right, 10 channels) and industrial production (4 channels, manufactured by AEG-Telefunken).

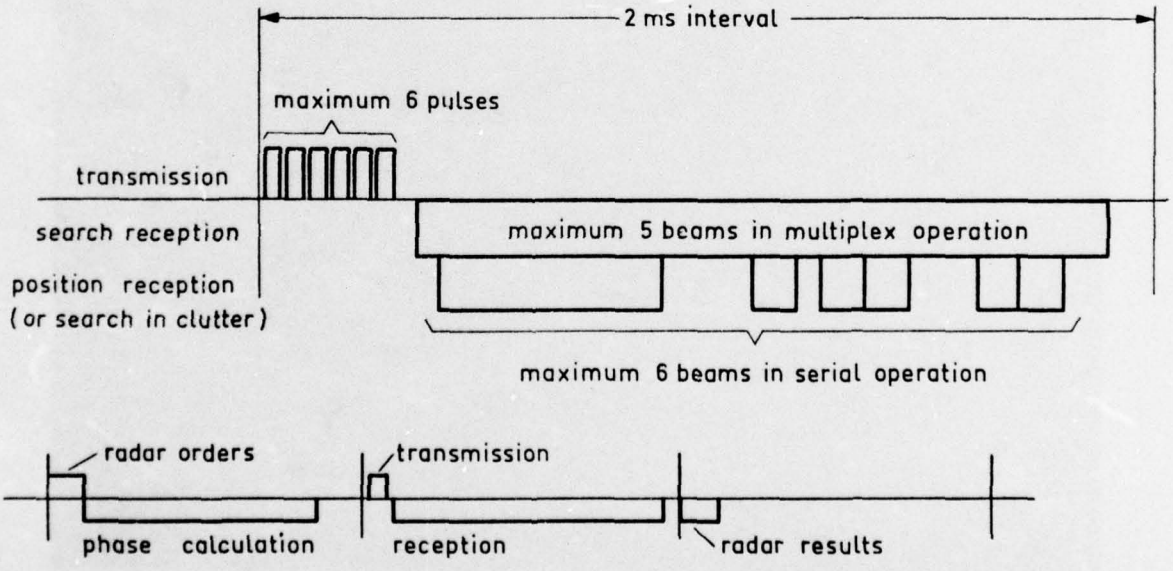

Fig. 6 Multiplex interval operation for 6 beams.

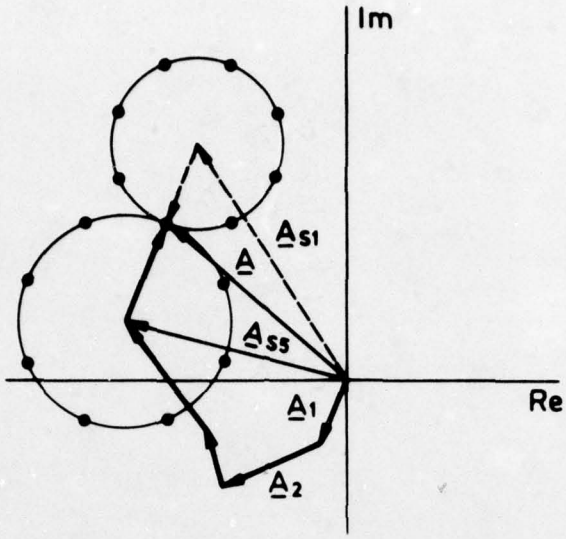

Fig. 7 Schematic of the horn response during the serial measurement of channels 1 and 5.

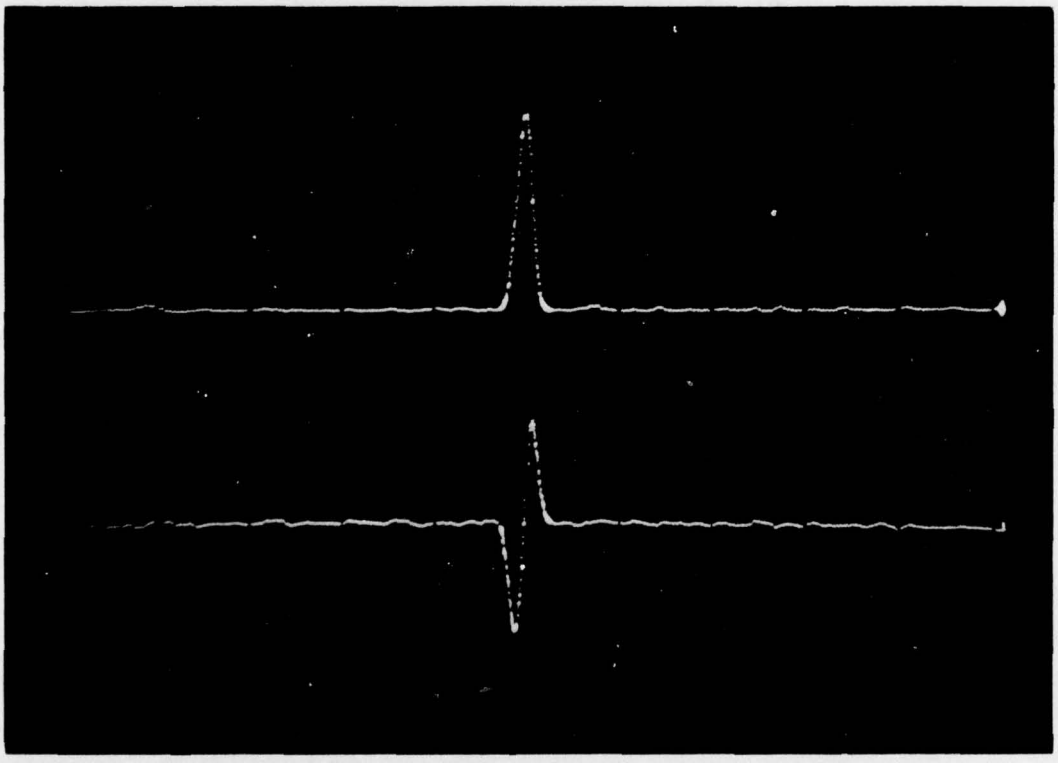

Fig. 8 Receiver antenna patterns focussed into the near field: sum beam power pattern and product of sum and difference pattern (sum beamwidth: 2°).

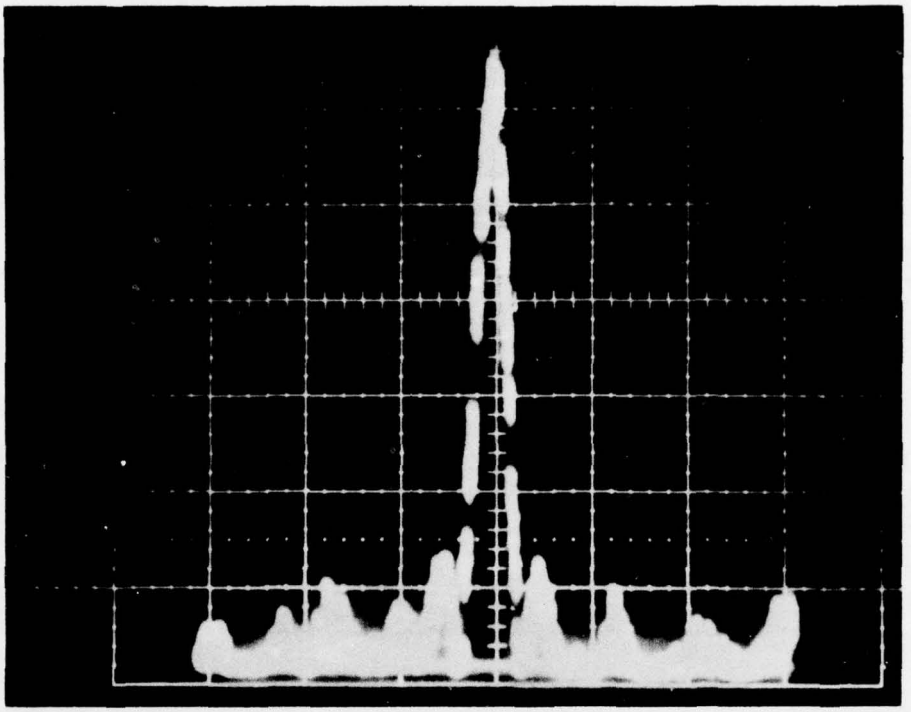

Fig. 9 Transmitter one-way antenna pattern focussed into the near field (beamwidth 3.5°).

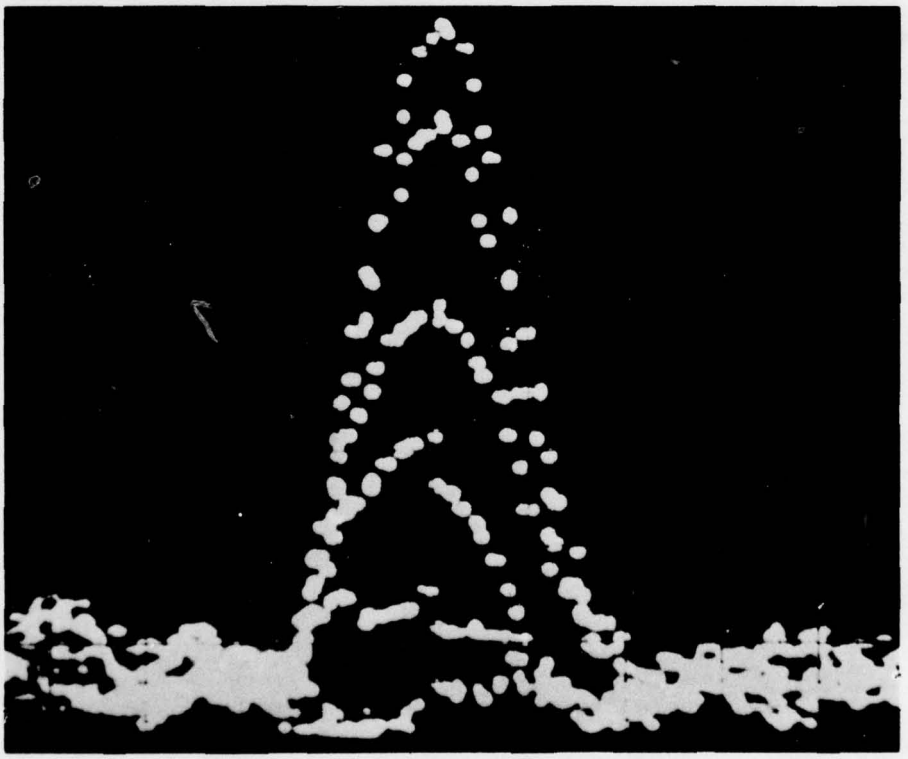

Fig. 10 Near field receiver antenna pattern, unfocussed and focussed in steps of 40 channels.

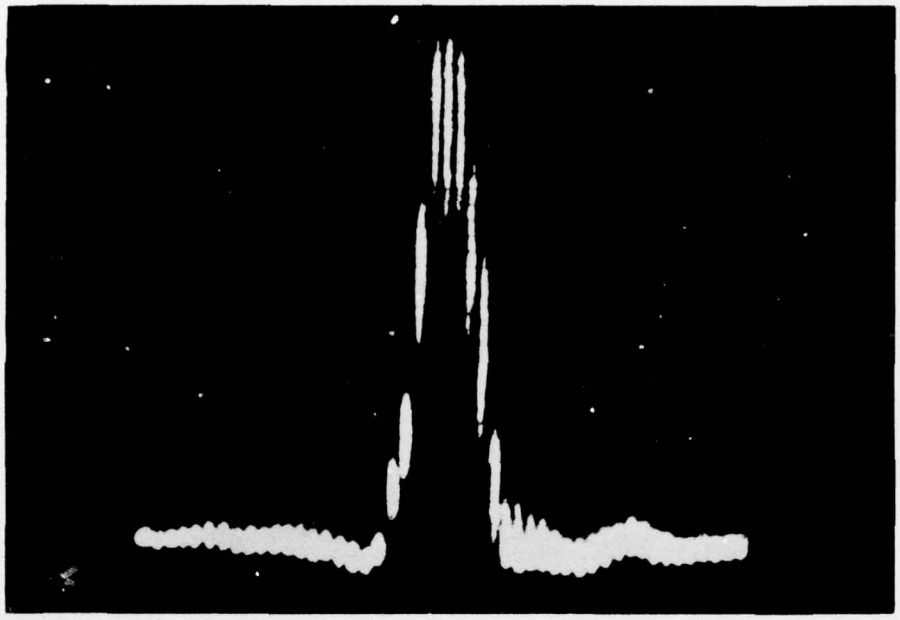

Fig. 11 Antenna pattern measured by the reflections of an isolated target to prove the near to far field transformation.

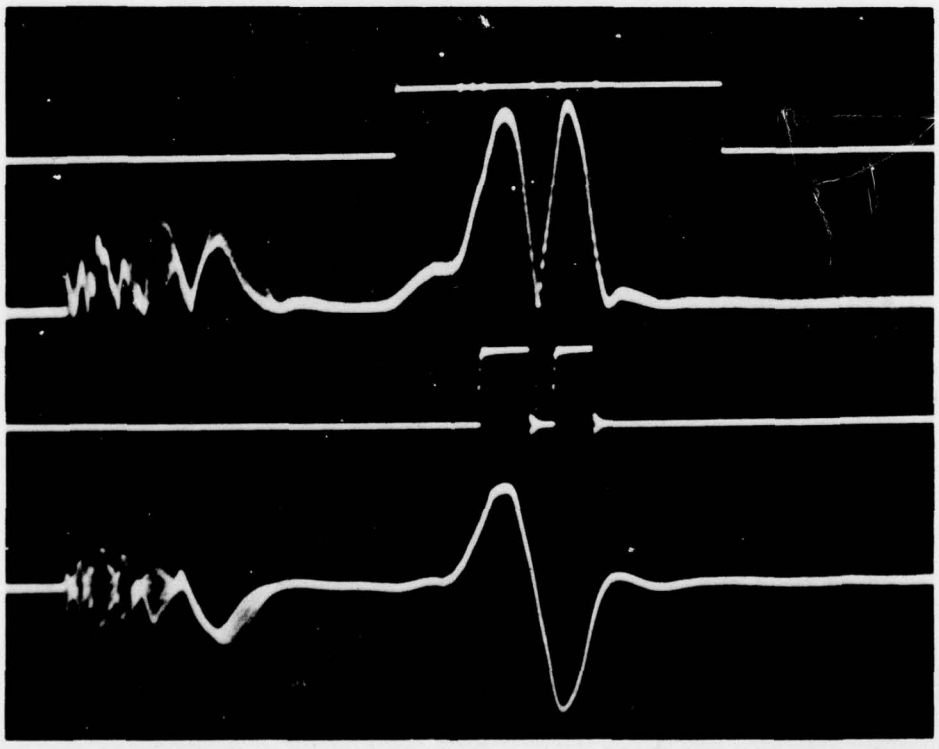

Fig. 12 A-scope representation of the range gate, threshold detector output, amplitude, and in-phase components of the received signal.

Fig. 13 Clutter area with range marker at 5 and 10 km (scan angle: $\pm 50^{\circ}$).

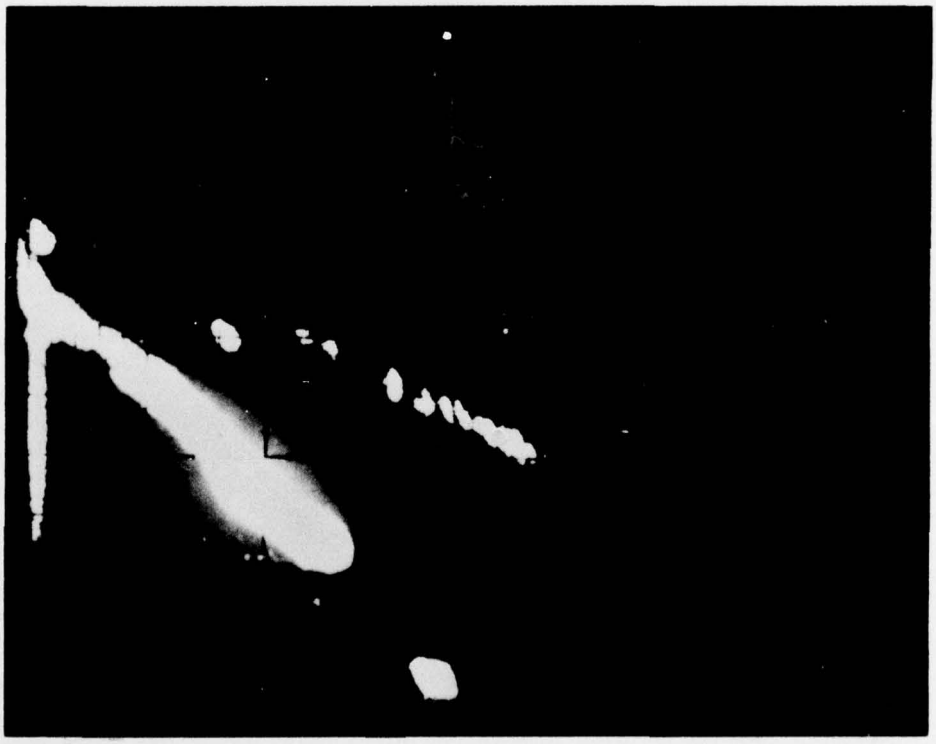

Fig. 14 Same area as in Fig. 13 with clutter suppression and track of an helicopter.

WIDEBAND RADAR IMAGING AND SIGNAL PROCESSING ARRAY

Jiunn S. Yu and David T. Bailey
BDM Corporation/Albuquerque Operations
2600 Yale Blvd., S.E.
Albuquerque, New Mexico 87106
U.S.A.

SUMMARY

Wideband coherent radar is capable of high-resolution target imaging. Similar to synthetic aperture radars used in terrain mapping, the analytical formulation of "space-object" scattering and imaging are developed in the first part of this paper. Three targets are selected to obtain their backscattering fields in computer simulation. Complex signal and spectral densities are then used to perform the image-synthesis procedure based on the Woodward method. Numerical examples are given to demonstrate resolution capability and image enhancement. The second part of this paper describes the dispersive radiation field of LP (Log-Periodic) antennas, and develops the LP signal processing models based on the fractional bandwidth of radiating elements. Elemental transfer functions of narrow-band signals are developed to synthesize the overall broadband-filter function for performing pulse compression. Compression gains for signal-energy density are derived using the LP-phase model. Potential performance of combining the image synthesis and LP-signal processing are briefly discussed in terms of signal resolutions, frequency agility, and waveform diversity.

1. INTRODUCTION

Wideband coherent radar technology has provided the capability of detecting targets with high resolution (Rihaczek, 1969). One practical example is the synthetic aperture radars (Harger, 1970) for mapping terrains and rotating targets. This paper applies the principle similar to that of synthetic aperture radars to synthesize the scattering intensity of certain targets that may orbit or rotate in space. Emphasis is placed on the analytical procedures of formulating the synthesis method (Woodward, 1946) that can yield a cross-range resolution of arbitrarily small increments and a slant-range resolution inversely proportional to the radar bandwidth.

A better slant-range resolution requires a wider radar bandwidth which can take the form of a coherent short-pulse system (McCoy and Yu, 1970). Practical limitations in high-field breakdown at antenna terminals (as well as transmission lines) have led to the concept and technique (Cook and Bernfield, 1967) of transmitting dispersed pulses of moderate amplitude and long duration to avoid breakdowns and to assure a sufficient energy for target detection. Target-scattered pulses are compressed by radar receivers to produce high-resolution short pulses with high energy densities. In addition to using the radar receiver for pulse compression, this paper considers the concept of pulse compression (VanEtten, 1972) using the dispersive properties (Pulfer, 1961) of log-periodic antennas (DuHamel and Isbell, 1957; Rumsey, 1966). Special emphasis is placed on the analytical model that is useful in describing the LP antenna radiation characteristics and pulse compression capabilities. For an LP antenna with N elements, the potential pulse-compression gain of N^2 is derived.

The first part (section 2) of this paper covers the formulation of image-synthesis algorithms and the numerical examples of entire analytical procedures. Measurements and modeling of LP antennas for both one-way (transmit only) and two-way (transmit and receive) pulser compressions are discussed in section 3. The significance and potential applications of these results to future radar surveillance and radar adaptivity to its environment will then be discussed in the concluding section (section 4).

2. WIDEBAND RADAR IMAGE SYNTHESIS

This section will consider the analytical formulation of target scattering and the synthesis procedures for constructing target images. Three targets are selected for both analysis and synthesis.

In the analysis area, the CW scattered fields are treated by using only electric fields. The scattered magnetic fields or the orthogonally polarized scattering can be treated in a similar manner. In order to construct the wideband target scattering, the scattered pulses are assumed to have been compressed and coherently detected. The pulse compression is needed because practical radars do transmit dispersed pulses to avoid high-field breakdowns. The coherent detection means simply that both amplitude and phase of the scattered signals are preserved during the detection process.

After formulating the coherent pulse through pulse compression, the synthesis procedure will be formulated in both time domain and frequency domain. The time-domain synthesis appears to be more direct, because the coherent detector output is most commonly in the form of short pulses. On the other hand, the frequency domain synthesis utilizing a complex spectral distribution can also be implemented. The two procedures in time and frequency domain synthesis are analytically identical, although one may be preferred over the other for practical implementation.

Synthesized target images for the three chosen examples will be discussed in terms of resolution capability and weak scattering-center enhancement. The realizable resolution capability in comparison with that of the well-known synthetic aperture radars is covered at the end of this section.

DISCUSSION

G RINGENBACH: 1) Quel est le nombre maximal de cibles que votre système peut traiter par seconds en mode recherche?

2) Quel est le coût par voie d'émission?

G HUSCHELRATH: 1) Approximately one hundred.

2) Approximately one thousand marks per channel for both transmitter and receiver.

A J DUNLOP: How often do you find it necessary to update the phase correction?

G HUSCHELRATH: Precise measurements on this subject are a task for the near future. Nevertheless, from experience I can say that changes to the correction seem unnecessary for periods of some hours.

E FLAD: How long was the flight time of the helicopter in the last slide?

G HUSCHELRATH: Approximately five minutes.

2.1 Compressed Short-Pulse Waveform

Assuming that a point-target scattered pulse has been compressed and coherently detected by a radar receiver, a Hamming-weighted spectrum (Cook and Bernfield, 1967) can be represented as shown in figure 1. The center frequency is designated as f_o for the "carrier" frequency. The pulse repetition frequency is designated f_r. A summary of the spectral distribution and the signal waveform is given in table 1. The cutoff bandwidth is $2f_c$ in the frequency domain; and the "cutoff" duration is $2/f_c$ in the time domain. All the time-domain sidelobes are approximately -43 dB or lower.

TABLE 1. "COMPRESSED" WAVEFORM OF A POINTSOURCE BACKSCATTERING

Spectral Distribution With Hamming Weighting:

$$S(f_o + nf_r) = f_r \left[0.54 + 0.46 \cos(n\pi f_r / f_c) \right] \quad \text{for } |nf_r| < f_c. \qquad \text{(Eq.1)}$$

$n = 0, \pm 1, \pm 2, \pm 3, \text{ --- } \pm N.$

$2Nf_r = 2f_c$ is the cutoff bandwidth

(f_o, f_r) are the pulse ("carrier," repetition) frequencies.

Pulse Train with Repetition Frequency f_r:

$$s(t) = f_r \left[0.54 \left\{ \frac{\sin(2N-1)\pi f_r t}{\sin \pi f_r t} + \cos 2N\pi f_r t \right\} \right.$$

$$+ \frac{0.46}{2} \left\{ \frac{\sin(2N-1)\pi f_r (t + 1/2f_c)}{\sin \pi f_r (t + 1/2f_c)} + \cos 2N\pi f_r (t + 1/2f_c) \right\}$$

$$\left. + \frac{0.46}{2} \left\{ \frac{\sin(2N-1)\pi f_r (t-1/2f_c)}{\sin \pi f_r (t-1/2f_c)} + \cos 2N\pi f_r (t-1/2f_c) \right\} \right] \exp(j2\pi f_o t) \qquad \text{(Eq. 2)}$$

$2/f_c$ is the "cutoff" pulse duration.

2.2 Target-Plane Scattering

Scattered signals are to be formulated for three targets as shown in figures 2, 3, and 4. They are selected for the purpose of developing necessary data sets to perform image synthesis. A three-point target of different scattering intensities is selected at the coordinates shown in figure 2. The yz plane is designated as the target plane and the y'z' plane is designated as the image plane. The angle formed between z axis and z' axis is defined as the aspect angle for the radar.

A circular conducting cylinder is the second target shown in figure 3. It is the simplest among all the axially symmetric targets and has a simple solution (Ufimtsev, 1958) that has been found to agree well with measured data.

A fairly complex target, shown in figure 4, is selected as the third target. The wedge angles are designated for the convenience of applying the circular-wedge solution developed by Ufimtsev.

In order to apply the circular-wedge scattering solution, figure 5 is given to illustrate the coordinate systems that are used in table 2. The computation for all the discrete spectra defined in equation 1 are made by using equation 3.

TABLE 2. BACKSCATTERED E-FIELDS FROM WEDGES OF AXIALLY SYMMETRIC TARGETS

First-Order Scattered Field From All Illuminated Wedges:

$$E(f_o + nf_r,\gamma) = S(f_o + nf_r) \cdot R^{-1}\exp(-jk_nR) \sum_{m=1}^{M} \frac{-jdm}{4} \left[(-1)^{m+1} J_1(k_n d_m \sin\gamma)\right] \cdot$$

$$\cdot \frac{\sin\pi/p_m}{p_m} \left[\frac{1}{\cos\pi/p_m - 1} - \frac{1}{\cos\pi/p_m - \cos 2\phi_m/p_m}\right] \exp(-j2k_n z_m \cos\gamma). \qquad \text{(Eq. 3)}$$

R is the radial distance from radar to target.

$k_n = 2\pi/\lambda_n = 2\pi(f_o + nf_r)/c$, where c is the speed of light.

(d_m, z_m) are the (diameter, z-coordinate) of the m^{th} wedge.

(J_1, J_2) are the Bessel functions of the (first, second) orders.

p_m = (Exterior Angle of the m^{th} Wedge)/π.

ϕ_m is the incidence angle referred to a surface of the m^{th} wedge.

γ is the (common) incidence angle referred to the z-axis of target plane.

The illuminating field is assumed unity.

By use of the equations shown in tables 1 and 2, the frequency domain target scattering for all the selected targets can be computed at different aspect angles and for different spectral components. The results of these complex spectral densities are then used to formulate the time-domain pulses.

2.3 Coherent Short Pulses

For point targets, the formula in equation 2 can be used directly with the relative time delays and relative intensities that are assigned. As for general targets, equations 4 and 5 in table 3 can be used to construct short pulses.

TABLE 3. TARGET-PLANE SCATTERED PULSES FOR NUMERICAL COMPUTATIONS

Scattered E-field at Discrete Spectra and Aspect Angles:

$$E_{np} = E(f_o + nf_r, \gamma + p\delta); \text{ where } n = 0, \pm1, \pm2, \pm3 \text{ --- } \pm N, \text{ and}$$

$$p = 0, \pm1, \pm2, \pm3 \text{ --- } \pm P. \qquad \text{(Eq. 4)}$$

Target Scattered Pulse Train in Time Domain:

$$e(t,\gamma+p\delta) = \sum_{-N}^{N} E_{np}\exp(j2\pi(f_o + nf_r)t). \qquad \text{(Eq. 5)}$$

The short pulses obtained for the three-point target are shown in figure 6 where points #1 and #3 are coincident in time because they are at the same slant range (figure 2). Although they are unresolvable in the time domain, they can be distinctly resolved by performing the image synthesis procedure to be discussed later in this section.

The complex target of figure 4 has been used to produce the time-domain pulses in figures 7 through 9. The wedge numbers are indicated to pulses where individual wedges are not resolvable in time domain. The pulses plotted in figures 8 and 9 are normalized by the same amplitude as that used in figure 7. Therefore, the sidelobes are not as numerous, nor do they disappear entirely. The resolution capability of the compressed pulses can be observed in figure 9 where wedges 3 and 4 are distinguished from wedges 1 and 2. These two sets of wedges are separated only by 40 centimeters, as can be seen in figure 4.

All the time domain pauses are produced with amplitude plots alone. However, the phase informations of these pulses are preserved in computer simulation for image synthesis purpose.

2.4 Image-Plane Scattering Intensity

All the formulations considered above belong to the target scattering analysis. This subsection will start the first step in the formulation of target synthesis procedure. The objective of performing target image synthesis is to obtain the target scattering intensity of an unknown target. Let the unknown target scattering intensity be designated as G in table 4. The contribution of target scattering to different spectral components can be formulated as shown in equation 6, where the phase centers of different scattering points are referred to the center of the image plane.

TABLE 4. IMAGE-PLANE-SCATTERED SPECTRAL DENSITY

Complex Sepctra Scattered in the Image Plane:

$$E(nf_r, p\delta) = S(f_o + nf_r)\int_{-Y'/2}^{Y'/2}\int_{-Z'/2}^{Z'/2} G(y', z')\exp(-j4\pi(f_o + nf_r)\cdot(y'\cos p\delta - z'\sin p\delta)/c) \cdot dy'dz'. \qquad \text{(Eq. 6)}$$

$G(y', z')$ is the assigned real function of target scattering intensity.

Approximation under Small Aspect Angle Extent:

$$E(nf_r, p\delta) \simeq S(f_o + nf_r)\int_{-Y'/2}^{Y'/2}\int_{-Z'/2}^{Z'/2} G'(y', z')\exp(-j4\pi(nf_r y' - p\delta f_o z')/c)dy'dz'. \qquad \text{(Eq. 7)}$$

$$G'(y', z') = G(y', z')\exp(-j4\pi(f_o y' - p\delta nf_r z')/c). \qquad \text{(Eq. 8)}$$

$|p\delta| \ll 1.$

Another weighting factor $f_o/(f_o + nf_r)$ can be used by assuming the scattering behaves like a planar strip, although this is not generally true.

In the process of collecting the backscattering from different aspect angles, the overall angular extent has been limited to 5° or less as shown in figures 6 through 9. With this small approximation, equation 6 can be written as shown in equation 7. The new target-scattering intensity, G' is now a complex function that includes the relative phase shifts among all the scattering points in the image plane. This complex scattering intensity function is defined in equation 8. The Hamming weighting has been included in all these formulations. However, the amplitude of target scattering itself is frequency-dependent. Therefore, if the scattering of a long axially symmetric target is approximated as conducting strip scattering (Yu and Rudduck, 1967), another frequency weighting function given in table 4 can be used to reduce the time-sidelobe degradation due to the frequency-dependent scattering.

The corresponding time-domain description for the coherent detector output can be formulated by the equations in table 5. The integrand of equation 9 can be simplified by making use of the definition in equation 10. By choosing a sequence of time intervals which corresponds to the peak value of the time function of equation 10, the peak value of Nf_r can be substituted into equation 9 and integrated. The integrated result in equation 11 means that the coherent detector output is sampled in the time sequence indicated.

TABLE 5. IMAGE-PLANE-SCATTERED PULSES AFTER COHERENT DETECTION

Pulse Train at Various Aspect Angles:

$$e(t,p\delta) = \sum_{-N}^{N} E(nf_r, p\delta) \exp(j2\pi nf_r t)$$

$$= \int_{-Y'/2}^{Y'/2} \int_{-Z'/2}^{Z'/2} G'(y', z') s(t-2y'/c) \exp(j4\pi p\delta f_o z'/c)\, dy'dz'. \qquad \text{(Eq. 9)}$$

$$s(t-2y'/c) = \sum_{-N}^{N} f_r(0.54 + 0.46 \cos(n\pi f_r/f_c)) \exp(j2\pi nf_r(t-2y'/c)). \qquad \text{(Eq. 10)}$$

Approximation at $t = q2\Delta y'/c = qY'/Qc$:

$$e(qY'/QC, p\delta) = Y'Nf_r \int_{-Z'/2}^{Z'/2} G'(q\Delta y', z') \exp(j4\pi p\delta f_o z'/c)\, dz'. \qquad \text{(Eq. 11)}$$

The index q may be equal to n such that $\Delta y' = Y'/2N$.

The results arrived at in equations 7 and 11 are the desired relationships between the unknown scattering intensity function and the measurable functions at the coherent detector output. These two equations complete the first step in both frequency-domain and time-domain synthesis procedures. The next subsection is to obtain the unknown scattering intensity.

2.5 Synthesis Methods in Frequency and Time Domains

Since the target-scattering intensity function is unknown but with finite scattering energy, the function can be represented by a Fourier series with undetermined coefficients. This is done in equations 12 and 13 of table 6. The undetermined coefficients A_{qs} and B_{qs} are designated separately because the former belongs to the frequency-domain data and the latter belongs to the time-domain data.

TABLE 6. SCATTERING DENSITY SYNTHESIS IN THE FREQUENCY AND TIME DOMAINS

Image-Plane Scattering Density With Undetermined Coefficients:

$$G'(y', z') = \sum_{q}\sum_{s} A_{qs} \exp(j2\pi qy'/Y' + j2\pi sz'/Z'). \qquad \text{(Eq. 12)}$$

$$G'(q\Delta y', z') = \sum_{q}\sum_{s} B_{qs} \exp(j2\pi sz'/Z'). \qquad \text{(Eq. 13)}$$

Integrated Results of $E(nf_r, p\delta)$ and $e(qy'/Qc, p\delta)$:

$$E(nf_r, p\delta) = Y'Z' S(f_o + nf_r) \sum_{q}\sum_{s} A_{qs} \frac{\sin \pi(q-2nf_r Y'/c)}{\pi(q-2nf_r Y'/c)} \frac{\sin \pi(s+2np\delta f_o Z'/c)}{\pi(s+2np\delta f_o Z'/c)} \qquad \text{(Eq. 14)}$$

$$e(qY'/Qc, p\delta) = Y'Z'Nf_r \sum_{s} B_{qs} \frac{\sin \pi(s+2p\delta f_o Z'/c)}{\pi(s+2p\delta f_o Z'/c)}. \qquad \text{(Eq. 15)}$$

Coefficients Determined from Frequency and Time Domain Data:

$$A_{qs} = E(nf_r = qc/2Y', p\delta = -sc/2f_o Z')/Y'Z'S(f_o+nf_r). \qquad \text{(Eq. 16)}$$

$$B_{qs} = e(t = qY'/Nc, p\delta = -sc/2f_o Z')/Y'Z'Nf_r. \qquad \text{(Eq. 17)}$$

In order to solve for the unknown coefficients, the Fourier series representations in equations 12 and 13 can be substituted into equations 7 and 11. Integrated results are shown in equations 14 and 15 where samplings can be taken at the discrete sequence of values. By performing the sampling at the indicated discrete points, the undetermined coefficients are obtained as shown in equations 16 and 17. The results of these two sets of unknown coefficients can now be substituted back into equations 12 and 13 to obtain the solution for the originally unknown target-scattering intensity.

The sequence of operations involved in table 6 is indeed an approximation to obtain the target-scattering intensity function by first assuming that they are representable by Fourier series of unknown coefficients. The unknown coefficients are then solved through sampling theorem applied to the measurable functions at the coherent receiver outputs. Substitution of these coefficients in equations 12 and 13 gives rise to the desired image-intensity functions. Some examples follow.

2.6 Target Image Example

The synthesized images for the three examples are shown in figures 10 through 14. The three-point target image is shown in figure 10 with 10 levels of shading that corresponds to a 40 dB dynamic range. Each sampled square corresponds to 0.3m x 0.3m. This figure indicates that the three-point target with different intensities appears with different sizes corresponding to the point scatters. This is due to the limited shading scale of the automated computer plotting.

Figure 11 indicates the synthesized image for the circular conducting cylinder. The image around the 0-degree aspect angle indicates nonuniform rows of intensities. The estimated mean-intensity line is nearly coincident with the cylinder end. The image around the 5-degree aspect angles is also shown here to indicate the concept of scattering centers. At both edges of the cylinder, the scattering becomes weak compared to the specular scattering that is not received by the radar receiver around this aspect angle. The weak scattering centers would require intensification if the image of the cylinder is to be enhanced to resemble the geometrical appearance of the target.

The fairly complex target has been synthesized around the three aspect angles as indicated in figure 12. The maximum diameter of this target is 1 meter. This synthesized result indicates that the shape of this target is difficult to determine if no additional image enhancement is performed to identify the weak scattering centers.

In order to produce the image that can resemble more closely the geometrical shape of the target, small scattering centers need to be enhanced. One example is given in figure 13, where the enhanced small scatters are superimposed onto the image in figure 12. Moreover, by knowing that the target is axially symmetric, the synthesized and enhanced data are mirror-reflected onto the other half of the aspect angles. The result is a composite of the fairly complex target whose maximum diameter is 1 meter.

To illustrate what would be the effect of increasing the target size with the same radar resolution capability, figure 14 is produced for the same complex-target shape with all the linear dimensions increased to twice the target originally selected. It can be seen that the resolution capability of a radar has now become adequate, in that the geometrical shape can be more easily determined. Nevertheless, the conical surface joining wedges (1,2) and wedges (3,4) does not appear in the image. This is because the specular return from this surface has a singularity inherent in the first-order diffraction used in the analysis (Yu and Williams, 1975). During the synthesis procedure, any encounter of singularities is automatically excluded from synthesis. The existence of singularities may be undesirable in other target shapes. In order to eliminate this type of singularity from the analysis, a more elaborate analysis formulation (Ryan and Peters, 1970) may be used.

The above examples serve to complete the procedure by which the target image is obtained by synthesizing the target-scattered results obtained analytically. The resolution capability of the chosen waveform is in agreement with its inherent resolution limit. It may be appropriate to comment that the synthesis is performed by noise-free numerical simulation. Therefore, it will be necessary in the future to introduce certain types of noise, both deterministic and random, into the backscattered results in order to more realistically simulate the actual performance capabilities and limitations.

2.7 Target Image Summary

The algorithms and numerical examples for the analysis and synthesis of a 3-point target and two axially symmetric targets have been developed. This section started with the assumption that the pulse compression and coherent detection have been peformed by a radar receiver. The coherently compressed pulse is ideal in that no noise is present and the spectra distribution is Hamming weighted with less than -43 dB sidelobes. The scattered components from the targets are obtained by the first-order diffraction only, and certain regions where singularities exist are excluded from the synthesis procedure.

The backscatter data used in the synthesis procedure were started with the assignment of a real function for the image-plan scattering intensities. The relative phases due to image-plane coordinates are then incorporated to obtain the complex intensity functions for which the synthesis procedure is used to solve.

The synthesis method used is essentially that of Woodward, reported in 1946. In summary, table 7 serves to review some of the important functions treated so far. Both time-domain and frequency-domain synthesis procedures have been considered. The two procedures are analytically identical, although there are numerical discrepancies due to truncations and imprecisions. The effects are too small to be noticeable in the synthesized images. Both time-domain and frequency-domain images are found to be almost identical (Yu and Williams, 1975). Also, the images synthesized by the use of electrical-field scattering are almost identical to those obtained through the magnetic-field backscattering. Although the backscattering patterns are different for the two polarizations, the synthesized results are extremely difficult to distinguish for targets that are very large in terms of wavelengths.

TABLE 7. SUMMARY OF FUNCTIONS AND DESCRIPTIONS

FUNCTIONS	DESCRIPTIONS
$S(f_o + nf_r)$	Discrete Spectra Hamming-Weighted for short-pulse radars or pulse-compression radars with (f_o, f_r) = (carrier, repetition) frequencies.
$s(t)$	Time-Domain Pulses corresponding to $S(f_o + nf_r)$.
$E(f_o + nf_r, \gamma)$	Target-Scattered Electric Fields perpendicular to the plane of incidence (for analyzing the scattering of axially symmetric targets, the aspect angle γ is referred to the target axis).
E_{np}	Scattered Electric Field of discrete (frequency, aspect angle) = $(f_o + nf_r, \gamma + p\delta)$ where δ is a small increment of aspect angle and (n, p) are designated indices.
$e(t, \gamma + p\delta)$	Time-Domain Pulses of E_{np} at an aspect angle = $\gamma + p\delta$.
$E(nf_r, p\delta)$	Complex Spectra frequency-shifted from carrier to dc and aspect-angle shifted from the target plane to the image plane.
$e(t, p\delta)$	Time-Domain Pulses corresponding to $E(nf_r, p\delta)$.
$e(q\gamma'/Qc, p\delta)$	Sampled set of $e(t, p\delta)$ at 2Q points with the index q.
$G(y', z')$	Assigned Real Electric-Field Intensity scattered from a unit area in the image-plane (It is an unknown function to be obtained by the image-synthesis procedures).
$G'(y', z')$	Complex Intensity of the image-plane ($y'z'$- plane) scattering as the product of $G(y', z')$ and relative phase factors.
$G'(q\gamma'/Qc, p\delta)$	Sampled set of $G'(y', z')$ at 2Q points with the index q.
(A_{qs}, B_{qs})	Fourier Coefficients solved by the image synthesis procedures in the (frequency, time) domain to construct the target images (or scattering intensity functions).

The basic concept of the synthesis procedure is based on the ambiguity criteria given in table 8. For a given maximum target slant size Z', the coherent processing rate (the pulse repetition frequency) should not exceed c/2Z'. The pulse repetition frequency is chosen strictly from an analytical point of view. In practice, the rate is dependent on the range of the target. In the area of avoiding the cross-range ambiguity, the coherent processing interval in the aspect angle should also be limited to less than (c/f)2Y' where Y' is the maximum cross-range size of the target to be imaged.

TABLE 8. SUMMARY OF PARAMETERS AND INDICES

To Avoid the Slant-Range and Cross-Range Ambiguities:

$$f_r < c/2Z' \quad \text{and} \quad \delta < (c/f)/2Y'. \qquad \text{(Eq. 18)}$$

$(f_o, f_r) = (5667, 16.667)$ MHz.

(f, f_r, c) are the (highest frequency, repetition frequency, speed of light).

(Z', Y') are the maximum (length or depth, width) of the image plane.

δ is the incremental aspect angle separating two neighboring backscatterings.

Nominal (Half-Power Pulse Width) Slant-Range Resolution:

$$z'\text{-Resolution} > \frac{1.3c}{4Nf_r} \quad (\approx 40 \text{ cm for } N = 16 \text{ and } f_r = 15.625 \text{ MHz used}) \qquad \text{(Eq. 19)}$$

The Hamming-Weighted Cutoff Bandwidth is $2Nf_r$.

Maximum Cross-Range Sampling Interval:

$$\Delta y' < (c/f)/4Q\delta \quad (\approx 0.3\text{m for } Q = 16 \text{ and } \delta = 0.156^\circ \text{ used}) \qquad \text{(Eq. 20)}$$

Synthesized image is sampled with $(\Delta y', \Delta z') = (0.3\text{m}, 0.3\text{m})$.
The upper limits of all indices are set N=Q=P=S=16.

The image-plan sampling after the completion of the synthesis procedure is chosen to be 0.3m x 0.3m. This is adequate in terms of the slant-range and cross-range resolution capabilities inherent in the synthesis procedure chosen. Although the synthesis performed here is similar to that of synthetic aperture radars used in ground mapping, the simulation algorithms are different in three respects. First, no doppler frequencies are used here to provide a cross-range resolution. Second, the cross-range resolution is independent of antenna size and can be as small as desired. Third, the targets are entirely in the far zone and no quadratic phase terms are used.

The complete algorithms developed for both analysis and synthesis can be used for simulating the wideband radar imaging performance. The Hamming weighting is chosen to approximate the practical limitations in the dynamic range of most radars. Nevertheless, there are radars that can be designed to perform with a dynamic range larger than 40 dB. Therefore, it may become necessary to adapt another type of weighting that can reduce sidelobe levels to less than 50, or even 60 dB.

A more realistic simulation of radar performance is to introduce simulated noise and to incorporate the capabilities of thresholding and filtering to allow the enhancement of weak scattering centers. The thresholding and digital filtering can perhaps be considered as future improvements for synthesizing unique images for all targets with both strong specular returns and weak scattering centers.

3. SIGNAL PROCESSING ANTENNA ARRAY

LP antennas have a broadband capability with dispersive characteristics. If treated as a filter function, it can disperse a coherent short pause used as the driving source. It can also perform pulse compression if the driving source is conjugate-matched to the phase function of the LP antenna.

This section will first describe measurements made on the radiation field of LP antennas. The results are then digitized to analyze the dispersive characteristics of which the LP phase functions are established for analytical modeling.

The measurement of the dispersive characteristics of six antennas has led to the conclusion that they have uniform fractional bandwidths centered around their radiation elements. The dispersive characteristics are then modeled to simulate the capability of performing pulse compressions when the conjugate-matched sources are made available.

The last part of this section will consider the formulation and the numerical results of radiation-field compression. Because of the concern with the danger of high-field breakdown, special emphasis is placed on the analysis of near-field compression phenomena.

3.1 Radiated Dispersive Pulse

An instrumentation block diagram is shown in figure 15 for the radiation-field measurement of antenna ASN-117AA. The source used to drive the antenna is an approximation to an impulse generator. The "impulse" is used to drive the antenna and the radiated pulse is measured by a short stub sensor. The radiated waveform is recorded by the sampling oscilloscope.

Prior to the dispersive pulse measurement, a test on the sensor probe is performed using the measurement configuration of figure 16. The radiating antenna in this particular arrangement is a long-wire monopole which is known to radiate nearly the duplicate of the driving source if the wire and the ground plane is indefinitely long. In the bottom half of the same figure, both the pulser waveform and the waveform received by the short stub monopulse are shown for comparison. Because of the practical limitations in the cable sizes, the received pulse is only approximately the same as the pulser waveform. This short stub receiver probe is used to measure the dispersive antenna under consideration.

Making use of the dispersive antenna as a radiator, the dispersive waveform received by the short-stub probe is shown in figure 17. The total dispersion time is approximately 15 ns. The pulser waveform, also shown in figure 17, is estimated to have about 1.5 ns duration. Therefore, the antenna under test has dispersed the driving waveform by a factor of about 10.

The results of the driving pulse and the dispersed-radiation pulse are digitized to perform spectral analysis. The digitized dispersive waveform is shown at the top of figure 18. The complex spectrum of this dispersed pulse has been divided by the spectrum of the driving pulse to obtain the transfer function with amplitude and phase as plotted in figure 18. The spectrum variation from 0.4 GHz to 4 GHz is about 9 dB which might have been contributed by the probe sensitivity. The more important aspect of the transfer function is the phase angle that has a clear log-periodicity from .2 to 1 GHz. On both sides of this bandwidth, the LP phase characteristics do not exist. The nonperiodicity below 0.2 GHz is outside of the lower limit of specified operating bandwidth. The nonperiodicity above 1 GHz is probably contributed by the weak spectral strength in the driving pulse waveform and the practical imprecision associated with antenna fabrication. For the purpose of analytical modeling, the LP phase from 0.2 to 1.0 GHz will be assumed to extend over the entire specified operating bandwidth (0.4 to 4.0 GHz) of ASN-117AA.

3.2 LP Dipole Array Characterization

In addition to the measured antenna ASN-117AA, other antenna measurements from RADC (Rome Air Development Center) have also been analyzed. A summary of the antennas which were analyzed during the program is listed in table 9. The data in the last two columns are analyzed results under ideal LP conditions over the specified bandwidths. Similarly, the potential values of N are evaluated by equation 23 to represent the possible number of active regions. These analyzed data will be discussed in section 3.3 The remaining data of the table are the manufacturer's specifications.

TABLE 9. SOME SPECIFICATIONS AND RESULTS FOR THE ANTENNAS ANALYZED.
(ALL ANTENNAS ARE BY AEL (AMERICAN ELECTRONIC LABORATORIES, INC.))

MODEL BY AEL	ANTENNA TYPE	BANDWIDTH (GHz)	POLARIZATION (POTENTIAL N)	CW GAIN (dB)	DIMENSIONS TRANVERSE (cm)	DIMENSIONS AXIAL (cm)	$\frac{1}{\ell n(1+\delta)}$	δ
ASN-1232A	CAVITY-BACKED SPIRAL	0.2 - 4.0	CIRCULAR (50)	6	46	27	17.1	0.06
ASN-117AA	CAVITY-BACKED SPIRAL	0.4 - 4.0	CIRCULAR (19)	6	30	15	8.77	0.12
ASN-116A	CAVITY-BACKED SPIRAL	1.0 - 10.0	CIRCULAR (20)	6	16	8	8.95	0.118
APX-254A	CROSSED PLANAR LOG-PERIODIC	0.4 - 4.0	LINEAR (35)	7	41	58	15.5	0.069
APN-995B	COPLANAR LOG-PERIODIC	0.03 - 1.1	LINEAR (47)	6	503	263	13.4	0.079
APN-502A	PYRAMIDAL LOG-PERIODIC	0.2 - 3.0	LINEAR (14)	11	97	79	5.6	0.195

Allowing that the transfer-function amplitude of an LP antenna can be compensated to a desired distribution by adjusting a transmitter output, a special emphasis on phase-angle characterization is made for the purpose of signal processing. Analysis of measured results for all antennas has indicated that the phase angles are nearly log periodic over large portions of their operating bandwidths. Figure 19 is a summary of the phase-angle functions that are measured to have constant slopes along the operating frequencies in log scale.

3.3 Analytical Model of LP Filter Function

The overall phase functions of LP antennas and the phase functions of decomposed active regions are summarized in table 10. Equation 21 is obtained under the assumption that within the entire operating bandwidth, the phase function is ideally log-periodic. The parameter δ is associated with the fractional bandwidth which is constant for all active regions. Frequency assignments in each active region and the total number of active regions are given in equations 22 and 23, respectively. The separation between two neighboring regions is by a phase angle π.

The extremely broad bandwidth of a log periodic antenna has been analytically represented as a filter function. However, there is an inherent difficulty in defining the signal processing procedures regarding signal group velocity and instantaneous frequency. The approach in this paper is to decompose the entire transfer function of an LP filter into N active elements that are consistent with the narrow-band signal characteristics. The elemental bandwidths of decomposed filter functions may be defined in two ways. If the spectral sampling is made by using a Hamming-weighted function that extends to the neighboring elements, the "cutoff" bandwidth would be $2\delta f_{no}$ and the effective bandwidth is about δf_{no}. If, on the other hand, the spectral sampling is made with a rectangular pulse without extending to the neighboring elements, the cutoff bandwidth and the effective bandwidth are equal and are designated also as $2\delta f_{no}$ with the understanding that the δ will be one-half the δ used in Hamming-weighted sampling. This latter case is the definition used in equation 24.

TABLE 10. ELEMENTAL FREQUENCIES AND ACTIVE REGIONS ASSIGNED TO LOG-PERIODIC ANTENNAS

Spectral Phase Function of LP Antennas:

$$\theta(f) = a + b\ell n(f), \text{ where } \theta(f_h) = o \text{ and } \theta(f_\ell) = -(N+1)\pi;$$

$$= \frac{\pi}{\ell n(1+\delta)}\ \ell n(f/f_h)\ , \text{ where } f_h/f_\ell = (1+\delta)^{N+1}. \qquad \text{(Eq. 21)}$$

The total number of active regions is N, and the phase slope along $\ell n(f)$ is $b = \pi/\ell n(1+\delta)$.

(f_ℓ, f_h) = (lowest, highest) "cutoff" frequencies of the bandwidth.

The parameter δ is associated with the fractional (percentage) bandwidth.

Equal Fractional Bandwidth of All Active Regions (n = 1,2,3,...N):

$$f_{nh} = (1+\delta)f_{no}, \text{ and } f_{n\ell} = (1-\delta)\ f_{no}, \text{ where } f_{no} \text{ is the } n^{th} \text{ center frequency.} \qquad \text{(Eq. 22)}$$

$$N = \ell n(f_h/f_e)\Big/\ell n(1+\delta) - 1 = \ell n(f_h/f_{No})\Big/\ell n(1+\delta). \qquad \text{(Eq. 23)}$$

Elemental Phase Function of the n^{th} Active Region:

$$\theta_n(f) = \frac{\pi}{\ell n(1+\delta)}\left[\ell n(f_{no}/f_h) + (f/f_{no} - 1) + \text{----}\right]$$

$$\approx -n\pi + \frac{(f-f_{no})\pi}{f_{no}\,\ell n(1+\delta)} = -n\pi + (f - f_{no})\pi/f_{no}\delta, \text{ for } \delta << 1 \qquad \text{(Eq. 24)}$$

The elemental bandwidth is equal to $2\delta f_{no}$ for uniform spectral density.

The decompositions of the entire transfer function into N segments of narrow-band filter functions are summarized in table 11. The composite filter function can now be expressed in equations 27 and 28 as a discrete set of filters with distinct instantaneous frequencies and with distinct group velocities. The frequency-domain characterizations in equations 25 and 27 are made with the assumption that the spectra density is uniform. The corresponding time-domain characterizations in equations 26 and 28 are the results of this assumption.

TABLE 11. BROADBAND TRANSFER FUNCTION BY NARROW-BAND ANALYSIS AND SYNTHESIS

Active Regions With Small Fractional Bandwidth and Constant Amplitudes:

$$\theta_n(f) \approx -(n+1/\delta)\pi + f\pi/f_{no}\delta, \quad (1-\delta)\, f_{no} < f < (1+\delta)f_{no} \qquad \text{(Eq. 25)}$$

$$S_n(t) \int_{(1-\delta)f_{no}}^{(1+\delta)f_{no}} \exp(-j\theta_n(f) + j2\pi ft)\, df = 2f_{no}\delta \frac{\sin(2\pi f_{no}\delta t - \pi)}{(2\pi f_{no}\delta t - \pi)} \exp(j2\pi f_{no} t + n\pi) \qquad \text{(Eq. 26)}$$

Frequency and Time-Domain Characterization of LP Antennas With Uniform Spectrum:

$$S(f) \approx \sum_{n=1}^{N} \exp(-j\theta_n(f)) = \exp(+j\pi/\delta) + \sum_{n=1}^{N} \exp(+jn\pi - j\pi f/f_{no}\delta) \qquad \text{(Eq. 27)}$$

$$s(t) \approx 2\delta \sum_{n=1}^{N} f_{no} \frac{\sin(2\pi f_{no}\delta t - \pi)}{(2\pi f_{no}\delta t - \pi)} \exp(j2\pi f_{no} t + n\pi) \qquad \text{(Eq. 28)}$$

Elemental group-delay time is $\theta'(f)/2\pi = 1/2f_{no}\delta$

3.4 Numerically Simulated LP Dispersion

Table 12 summarizes the analytical simulation of an LP filter function. The bandwidth starts from 0.156 to 2.0 GHz. The spectra weighting function is chosen as the square root of the Hamming-weighted function to approximate more closely the actually measured distributions. The distribution in each active region is also assumed as the square root of the Hamming-weighted function. The phase functions for the entire filter as well as the elemental filter are maintained to be log periodic in equations 29 and 30. Both amplitude and phase of equation 29 are plotted in figure 20 using linear frequency scale. The amplitudes at the cutoff frequencies are about -10 dB. A total of 13 π-phase variations is seen to result from the choice of 13 active regions.

Figure 21 is the result of a composite impulse response summarized in equation 31. This dispersed pulse is the sum of all the contributions from 13 pulses defined in equation 32. Examples for the pulses contributed by the 1st, 6th, and 10th active regions are given in figures 22 and 23. The value of δ for this example is 0.2 to simulate the antenna APN-502A in table 9. The dispersed duration in figure 21 agrees well (Wiggins and Yu, 1974) with that measured for APN-502A.

3.5 Two-Way (Transmit and Receive) Compression Gain

In order to use the dispersive properties of LP antennas to perform pulse compression, the driving source is required to have reversed dispersion in the time-domain characterization. In the frequency domain, the driving source function needs to be a complex conjugate of the LP filter function. Assuming an LP antenna is to be used for this compression during transmit and receive, the equations in table 13 can be used to simulate its performance.

An LP antenna can be treated as a reciprocal filter (i.e., the lower frequency signals are exponentially delayed during both transmit and receive). A conjugate-matched transmitter phase function will be required to have twice the LP phase function with negative sign. With this transmitter phase function, uniform and exponential spectral densities are shown in equations 33 and 34.

Assuming that the LP fileter has a flat spectrum in its impulse response and that a point target is used to backscatter its radiated pulse back to the antenna, the compessed spectrum after transmit and receive can be normalized as equations 35 and 36. The compressed pulses in the time domain are simply superposition of all elemental pulses whose peaks have been made coincident in time. Equations 37 and 38 give the peak values as products of the first elemental peak value and other LP filter parameters. The energy-density compression gains (G_1, G_2) are finally obtained for the assumed (uniform spectrum, exponential spectrum) transmitter waveforms. As has been discussed earlier, it is noted that the parameter δ is defined for Hamming-weighted spectral function with ($2f_{no}\delta$, $f_n\delta$) as the cutoff, "effective") bandwidths in the nth active region. The cutoff bandwidth of a rectangular spectral function has also been designated $2f_{no}\delta$. Since the cutoff bandwidth in this case is identical to the effective bandwidth, the value of δ should be reduced to one-half of that used in Hamming-weighted sampling function.

TABLE 12. NUMERICAL EXAMPLE APPROXIMATING THE MEASURED ANTENNA (ASN-117AA)

REGION	f_{no}	f_{nh}	$f_{n\ell}$
1	1.667E+09	2.000E+09	1.389E+09
2	1.389E+09	1.667E+09	1.157E+09
3	1.157E+09	1.389E+09	9.645E+08
4	9.645E+08	1.157E+09	8.038E+08
5	8.038E+08	9.645E+08	6.698E+08
6	6.698E+08	8.038E+08	5.582E+08
7	5.582E+08	6.698E+08	4.651E+08
8	4.651E+08	5.582E+08	3.876E+08
9	3.876E+08	4.651E+08	3.230E+08
10	3.230E+08	3.876E+08	2.692E+08
11	2.692E+08	3.230E+08	2.243E+08
12	2.243E+08	2.692E+08	1.869E+08
13	1.869E+08	2.243E+08	1.558E+08

Normalized Spectrum of Log-Periodic Filter Function:

$$S(f) \approx \left[0.54 + 0.46\cos\frac{\pi(f-f_o)}{f_h-f_e}\right]^{1/2} \exp\left(\frac{j\pi\ell n(f/f_n)}{\ell n(1+\delta)}\right) \quad \text{(Eq. 29)}$$

Complex Spectra in Active (Elemental) Regions:

$$S_n(f) \approx S(f_{no}) \left[0.54 + 0.46\cos\frac{\pi(f - f_{no})}{f_{nh} - f_{no}}\right]^{1/2} \cdot \exp(-j\pi f/f_{no}\delta). \quad \text{(Eq. 30)}$$

$$f_o = (f_h + f_e)/2 = 1.073 \text{ GHz}.$$

Composite Impulse Response:

$$s(t) = \sum_{n-1}^{13} s_n(t). \quad \text{(Eq. 31)}$$

$$s_n(t) = \int_{f_{no}(1-\delta)}^{f_{no}(1+\delta)} S_n(f)\exp(j2\pi ft)df \quad \text{(Eq. 32)}$$

TABLE 13. TWO-WAY (TRANSMIT AND RECEIVE) COMPRESSION GAIN OF LP ANTENNAS

Transmit Waveforms With Twice the Reversed LP Dispersion:

$$S_1(f) = \exp(j2\pi/\delta) \sum_{n=1}^{N} \exp(j2n\pi - j2\pi f/f_{no}\delta), \text{ and} \quad \text{(Eq. 33)}$$

$$S_2(f) = \exp(j2\pi/\delta) \sum_{n=1}^{N} (1+\delta)^{n-1} \exp(j2n\pi - j2\pi f/f_{no}\delta), \; f_{n\ell} < f < f_{nh}. \quad \text{(Eq. 34)}$$

Group-advance time is $1/\delta f_{no} \approx (1+\delta)^{n+1}/\delta f_{10}$.

Received Waveforms Using LP Antennas as Conjugate-Matched Filters:

$$C_1(f) = S_1(f)S_1^*(f) = \sum_{n=1}^{N} U(f-f_{no}) \quad \text{(Eq. 35)}$$

$$C_2(f) = S_2(f)S_1^*(f) = \sum_{n=1}^{N} (1+\delta)^{n+1} U(f-f_{no}) \quad \text{(Eq. 36)}$$

$U(f-f_{no}) = 1$ for $|f-f_{no}| < \delta f_{no}$ and is zero otherwise. (Eq. 37)

$$\text{Max } c_1(t) = c_1(0) = \sum_{n=1}^{N} 2\delta f_{no} = 2\delta f_{10} \sum_{n=1}^{N} \frac{1}{(1+\delta)^{n-1}} = 2\delta f_{10}\left(\frac{1+\delta}{\delta}\right)\left[1 - \frac{1}{(1+\delta)^N}\right] \quad \text{(Eq. 38)}$$

$$\text{Max } c_2(t) = c_2(0) = 2\delta \sum_{n=1}^{N} f_{no}(1+\delta)^{n-1} = 2\delta f_{10} N \quad \text{(Eq. 39)}$$

$2\delta f_{10}$ is the peak amplitude of the first-region pulse.

Peak Compression Gains Over the First-Region's Peak Energy Density:

$$G_1 \approx \left((1+\delta)/\delta\right)^2 \text{ for N very large.} \quad \text{(Eq. 40)}$$

$$G_2 = N^2. \quad \text{(Eq. 41)}$$

As an example of two-way pulse compression, the compressed pulse using an estimated spectrum from actually measured results is shown in the solid curve of figure 24. In contrast, if the compressed spectra were Hamming-weighted, the compressed pulse would be that shown in dashed curve having a pulse duration of equal to two complete cycles of the center frequency.

3.6 Radiated Field (One-Way) Compression

One of the problems associated with radiation field compression (VanEtten, 1972) is to determine the near-field structure and to assess the possibility of high-field induced air breakdown. Studies have been conducted for LP dipole arrays by assuming two types of compression. One is the longitudinal-delay compression approximating coplanar-type LP antennas and the other is the transversal-delay compression approximating cavity-backed spirals. Some numerical results will be given before a conclusion is drawn on the issue of high-field air breakdown.

Practical LP antennas are known to radiate predominantly in dipole modes. However, small higher-order modes do exist in all LP antennas, and these are significant in the near-field structure because their amplitudes increase more rapidly toward the radiation point. Figure 25 shows that the "resonant-dipole" near-field using the dipole mode above does "diverge" more gracefully than that including also the octopole and quadrupole modes (Yu and Peters, 1970). For all field points farther than 0.25 wavelength, the ratio of the two curves is at most 1.3. Therefore, it is concluded that near-field computations for LP dipole antennas can be made using the dipole modes above so long as the field point is maintained outside of the apparent antenna "volume."

Two types of radiation-field compression are modeled using the geometries shown in figure 26. The longitudinal-delay compression is assumed to have all the phase angle of active regions coincident in space in order to establish an upper bound on the near-field intensity. Equations 42 and 43 are used to compute this type of radiation compression as shown in figure 27. It is noted that the near-field structures are produced under the assumption that the radiated field is perfectly compressed at a range of 100 m.

Transversal-delayed near-field compressions are computed by equation 44 and the results are shown in figure 28. One can observe the interesting differences between the two compressions by referring to figure 29. The highest frequency used is 10.2 GHz corresponding to a wavelength of the highest frequency. The compressed pulses have their effective pulse durations equal to 0.2 ns or longer. According to figure 28 and the tabulated maximum allowable field strength (Wiggins and Yu, 1974) it is concluded that both types of field compression will not induce air breakdown at ranges larger than 1.5 cm for the parameters shown in table 14. For the longitudinal-delayed near-field compression at ranges less than 1.5 cm, the peak field will rapidly reach the maximum allowable value of 15 MV/m and may induce air breakdown.

The ultimate pulse compression of an LP antenna is shown on the top of figure 30. Further compression in angular extent is possible by forming an array of LP-dipole arrays. Regardless of what type of LP arrays are used, grating suppression in the higher-frequency regions would have to be accomplished to produce the space-time compressed pulse shown in the bottom of figure 30. The space-time pulse compression may be useful, among others in future deep-space, low-data-rate communications.

TABLE 14. RADIATED (ONE-WAY) PULSE COMPRESSION WITH HAMMING WEIGHTING

Radiated Fields Approximated for Longitudinal-Delay Pulse Compression:

$$E(r,f) \approx \frac{120\, I_o}{r_o}\left[0.54 + 0.46\cos\frac{\pi(f-f_o)}{f_h-f_o}\right]\left[1 - 0.5(2\pi fr/c)^{-2} - j(2\pi fr/c)^{-1}\right]. \qquad \text{(Eq. 42)}$$

I_o is the peak dipole-current density at the center frequency.

$$E(r,f,r_o) = \left[E(r,f)\right] \Big/ \left[E(r_o,f) / |E(r_o,f)|\right]. \qquad \text{(Eq. 43)}$$

All phase centers of LP elements are assumed coincident in space.

$E(r_o,f)$ is the compressed field at r_o in the far zone of LP.

$(I_o, r_o, f_\ell, f_o\ f_h) = (10^{-8}$ Amp/Hz, 100 m, (0.2, 5.2, 10.2) GHz) are used.

The peak current with 2 GHz bandwidth would be 20 amperes.

Radiated Fields by Transversal-Delay Pulse Compression:

$$E(r,r_n,f,r_o) = \sum_{n=1}^{N} E(r_n, f_{no}, r_o)\left[0.54 + 0.46\cos\frac{\pi(f-f_{no})}{f_{nh}-f_{no}}\right]\cos\theta_n,\ f_{n\ell} < f < f_{nh} \qquad \text{(Eq. 44)}$$

Phase centers are spatially displaced to approximate cavity-backed LP antennas.

3.7 Signal-Processing Array Summary

An analytical model of the LP antenna has been formulated through characterizations of radiated dispersive pulses. Decomposition of the broadband LP filter function has been performed to identify the narrow-band active regions for the purpose of defining signal group delays and instantaneous frequencies. Synthesis of these active regions permit straightforward signal processing that is essential in the under standing of pulse dispersion and compression. Energy-density compression gains have been established for two types of spectral distributions required of the transmitter waveform for conjugate-matching. These gains are capable of reaching the 40 dB range if the number of active regions can be designed to be 100 or more. The same gain could also be reached by designing an LP with effective fractional bandwidth around 0.034 or 3.4. Table 15 gives a summary of the functions discussed on signal procesing antennas.

TABLE 15. SUMMARY OF FUNCTIONS AND DESCRIPTIONS FOR LP ANTENNAS

FUNCTIONS	DESCRIPTIONS
$\Theta(f)$, $\Theta_n(f)$	(Continuous, Elemental) Log-Periodic Phase Functions of Antenna.
$(f_{no}, 2\delta)$	Elemental (Carrier Frequency, Fractional Bandwidth).
$\pi/\ell n(1+\delta)$	Phase Slope of $\Theta(f)$ in the $\ell n(f)$ domain.
$2\delta f_{no}$	Elemental Bandwidth or Pulse Peak of the n^{th} element with unity spectrum.
$1/2\delta f_{no}$	Elemental Group-Delay Time of the n^{th} element in transfer function.
$-(\delta f_{no})^{-1}$	Group-Advance Time required of the transmitter-dispersed pulse for performing two-way (transmit and receive) pulse compression by conjugate-matched filtering.
$G_1 \approx \left(\frac{1+\delta}{\delta}\right)^2$	Energy-Density Compression Gain (over the 1^{st} group density) by using LP antenna as the two-way conjugate-matched filter, if the reversed twice-dispersed pulse is of a uniform spectrum.
$G_2 \approx N^2$	Energy-Density Compression Gain, if the dispersed pulse has a spectrum of $(1+\delta)^{n-1}$ with N = the total log-periodic elements.
$E(r, f, r_o)$	Approximate Longitudinal-Delay Compressed Electric Field radiated by a coplanar LP dipole antennas driven by a conjugate-matched source.
$E(r, r_n, f, r_o)$	Approximate Transverse-Delay Compressed Electric Field radiated by a cavity-backed spriral and detected by a linearly-polarized probe.

Radiation-field compressions has been analyzed with emphasis on the near-field structures. Based on the available data of power-handling capabilities, the LP antennas analyzed here are not expected to induce high-field breakdown before the antennas reach voltage breakdowns on the antenna structures. Space-time compression appears to have potential for incorporation into certain radar systems with extremely high radiated-power densities.

4. CONCLUSION

The synthesis procedure indicates that the image cross-range resolution can be made arbitrarily small. However, the sampling theorem indicates that a one-half wavelength interval should contain all the information in the scattering density function. Therefore, the resolution limit of the developed synthesis procedure is considered to be one-half wavelength of the radar center frequency. Further improvement in image resolution is in the slant-range resolution.

The pulse compression antennas have the capability of being extremely broadband. Assuming the coherently compressed pulse has an ideal Hamming-weighted spectrum, the nominal slant-range resolution can be one wavelength of the radar center frequency. Therefore, the ultimate resolution capability of radar imaging is estimated to be one squared wavelength. This capability appears to be attractive for imaging deep-space targets such as geosynchronous satellites or planets.

Should broadband LP antenna arrays be used for radar pulse compression, the selection of fractional bandwidth depends entirely on the transmitter which may be a parallel of transmitter banks whose availability can be automated through computer selection. This means that within the extremely broad bandwidth, the agility of operating frequencies can be programmed with relative ease. The attendant signal processing can also be automated through the use of narrow-band active region designations. Compression gains can be systematically estimated through the algorithms developed here. One area that requires further study is the spectral weighting after pulse compression. This study will provide insight into the time sidelobe levels required to avoid overshadowing of weak scattering centers.

A diversified radar tarnsmitter waveform is made possible by using predetermined active regions and coded sequencing through narrow-band signal management and blocked-bnad transmitters operated in parallel. Information regarding the sequenced active regions may be stored in computers for every transmitted pulse group, and the conjugate-matched pulse-compression filter banks would be ready to process target-returned signals.

Potential advantages and limitations of a better radar signal resolution, frequency agility, and waveform diversity require more quantitative studies based on the deterministic algorithms developed here with the introduction of both deterministic and random noise into the space-time domain.

REFERENCES

Cook, C. E. and M. Bernfield, 1967, Radar Signals, Academic Press, New York.

Du Hamel, R. H. and D. E. Isbell, 1957, "Broadband Logarithmically Periodic Antenna Structures," IRE National Convention Record, pt. 1, pp. 119-128.

Harger, R. O., 1970, Synthetic Aperture Radar Systems: Theory and Design, Academic Press, New York.

McCoy, D. R. and J. S. Yu, August 1970, "Short Pulse Theory and Verification Program," Rome Air Development Center, Rome, N. Y., Tech. Rep. RADC-TR-70-133.

Pulfer, J. K. , March 1961, "Dispersive Properties of Broadband Antennas," Proc. IRE (correspondence), Vol. 49, p. 644.

Rihaczek, A. W., 1969, Principles of High-Resolution Radar, McGraw-Hill Book Company.

Rumsey, V. H., 1966, Frequency Independent Antennas, Academic Press, New York.

Ryan, C. E. Jr. and L. Peters, Jr., May 1969, "Evaluation of Edge-Diffracted Fields Including Equivalent Currents for the Caustic Regions," IEEE Trans. of Antenna and Propagation, Vol. AP-17, pp. 292-299, (corrections on p. 275, March, 1970).

Utimtsev, P. Ya., 1958, "Approximate Calculation of the Diffraction of Plane Electromagnetic Waves by Certain Metal Objects, II: The Diffraction by a Disk and by a Finite Cylinder," Sov. Phys. - Tech. Phys., Vol. 28, pp. 535-548.

VanEtten, P., September 1972, "Temporal-Spatial Compression Antennas," RADC-TR-73-179 Technical Report, Rome Air Development Center, Griffiss Air Force Base, New York.

Wiggins, C. M. and J. S. Yu, 1974, "Radiation Field Compression by Dispersive Broadband Antennas," RADC-TR-74-104.

Woodward, P. M., 1946, "A Method of Calculating the Field Over a Plane Aperture Required to Produce a Given Polar Pattern," J. Inst. Elec. Engrs., Part IIa, p. 1554.

Yu, J. S. and J. W. Williams, 1975, "Space Object Scattering Density Synthesis," RADC-TR-75-55, Volume I.

Yu, J. S. and L. Peters Jr., June 1970, "Measurement of Constitutive Parameters Using the Mie Solution of a Scattering Sphere," Proceedings of the IEEE, Vol. 58, No. 6, pp. 876-885.

Yu, J. S., and R. C. Rudduck, September 1967, "On Higher-Order Diffraction Concepts Applied to a Conducting Strip," IEEE Trans. on Antennas and Propagation, Vol. AP-15, pp. 662-668.

ACKNOWLEDGEMENT

This paper includes work performed under RADC (Rome Air Development Center) Contracts No. F30602-73-C-0343 and No. F30602-73-C-0110, and the BDM Advanced Research Program. The contractual effort was monitored by Mr. D. L. Tauroney (RADC) who is one of the original proponents in wideband target imaging, and by Mr. P. VanEtten (RADC) who kindly provided his measured data for most of the LP antennas analyzed here. Dr. J. W. Williams (BDM) implemented the computer programs for most of the target-imaging algorithms. The dispersed waveforms of ASN-117AA antenna were measured at BDM under the supervision of Mr. C. M. Wiggins who has also derived the BT (Bandwidth-Time) products as functions of geometric parameters (Wiggins and Yu, 1974) by considering LP antennas as slow-wave structures.

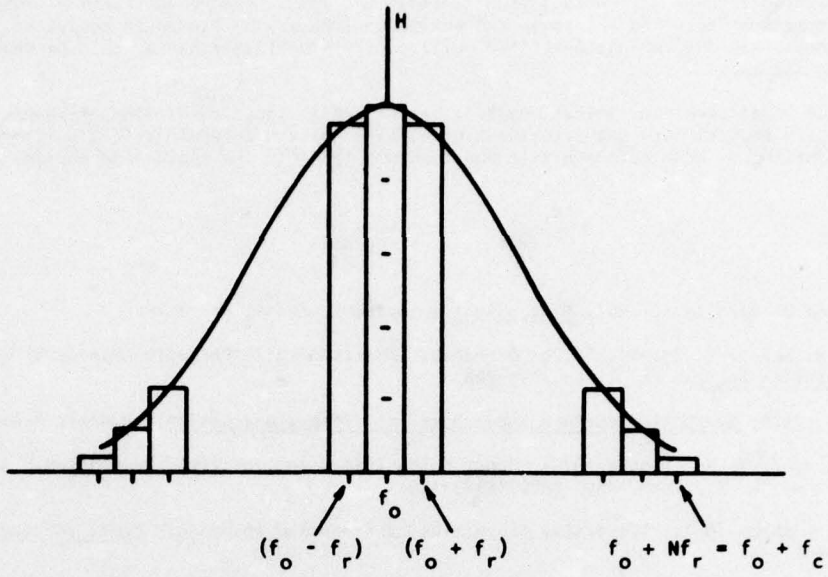

Fig.1 Discrete spectral density H(f) centered at the carrier frequency f_o of periodic pulses with repetition frequency f_r

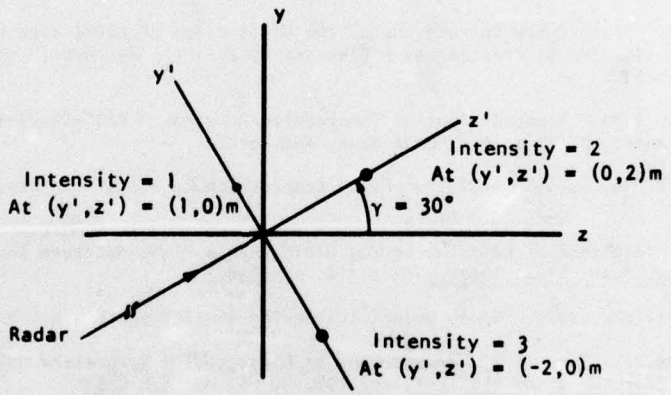

Fig.2 The target plane (yz plane) and the image plane (y'z' plane) with 30° aspect angle for a three-point target

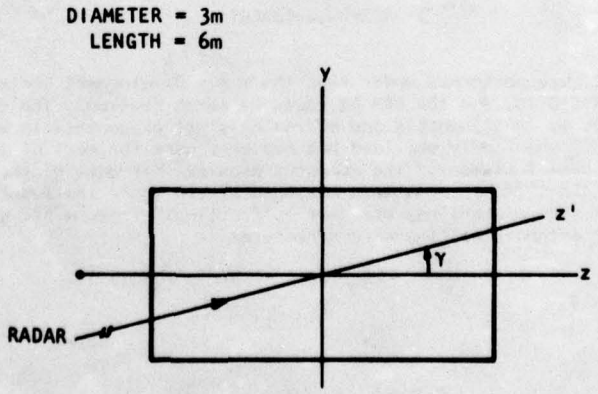

Fig.3 A circular-cylinder's target plane (yz plane) and image plane rotated with aspect angle γ

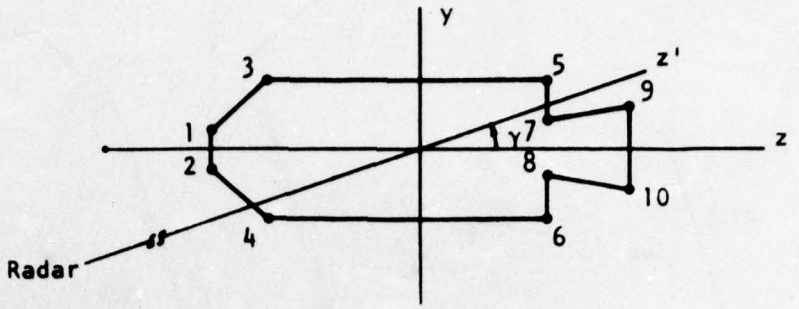

WEDGE #	y(m)	z(m)
(1, 2)	(0.15, -0.15)	-1.50
(3, 4)	(0.50, -0.50)	-1.10
(5, 6)	(0.50, -0.50)	0.90
(7, 8)	(0.20, -0.20)	0.90
(9, 10)	(0.30, -0.30)	1.50

Fig.4 A complex target with the maximum length 3 m and maximum diameter 1 m

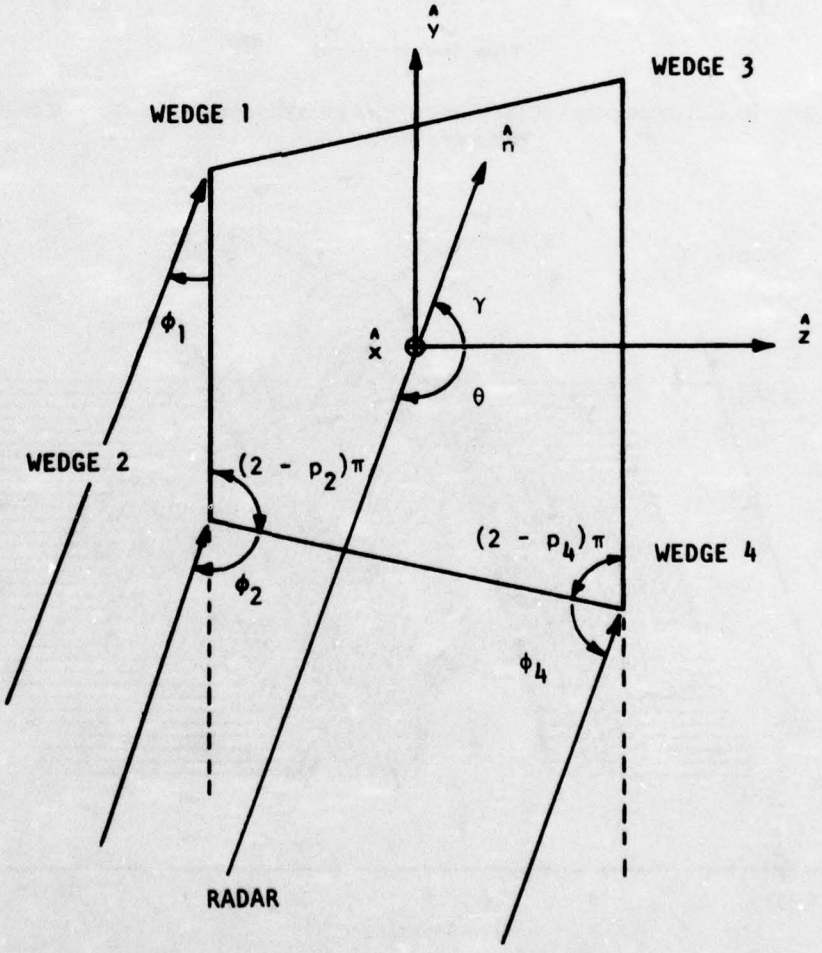

Fig.5 An example of axially symmetric target consisting of two circular wedges

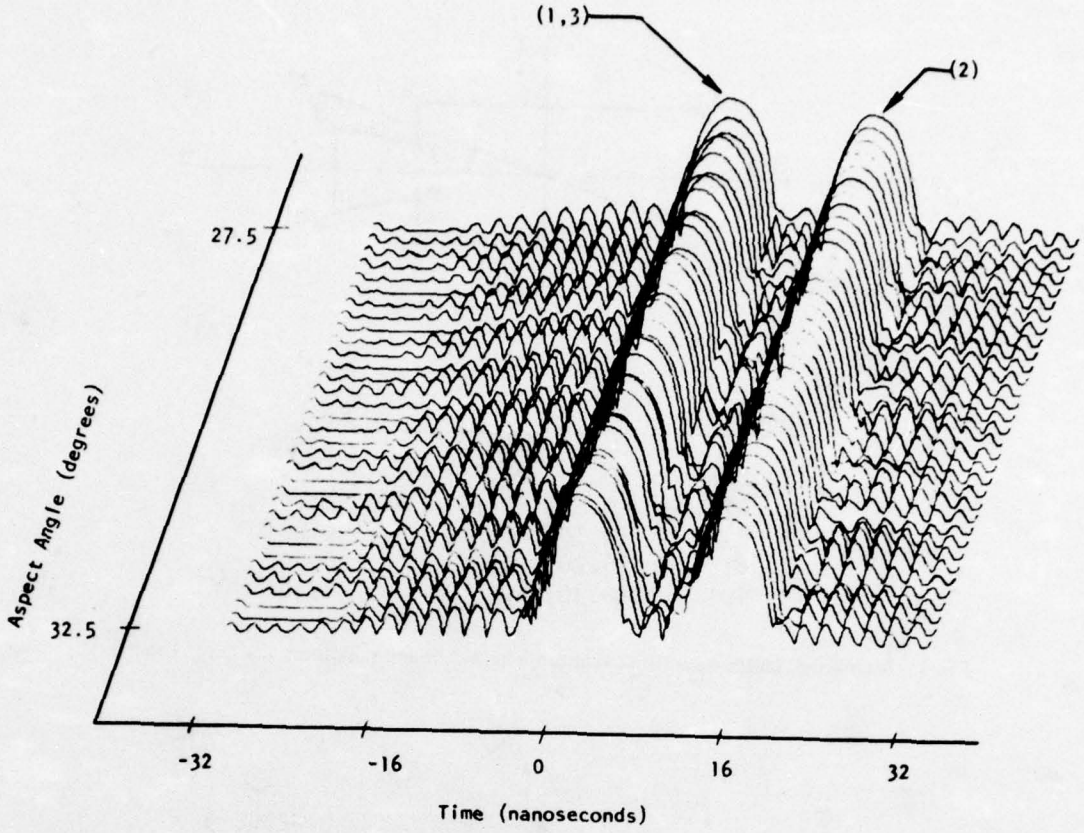

Fig.6 Backscattered pulses of the three-point target with aspect angles centered at 30° (dynamic range 60 db)

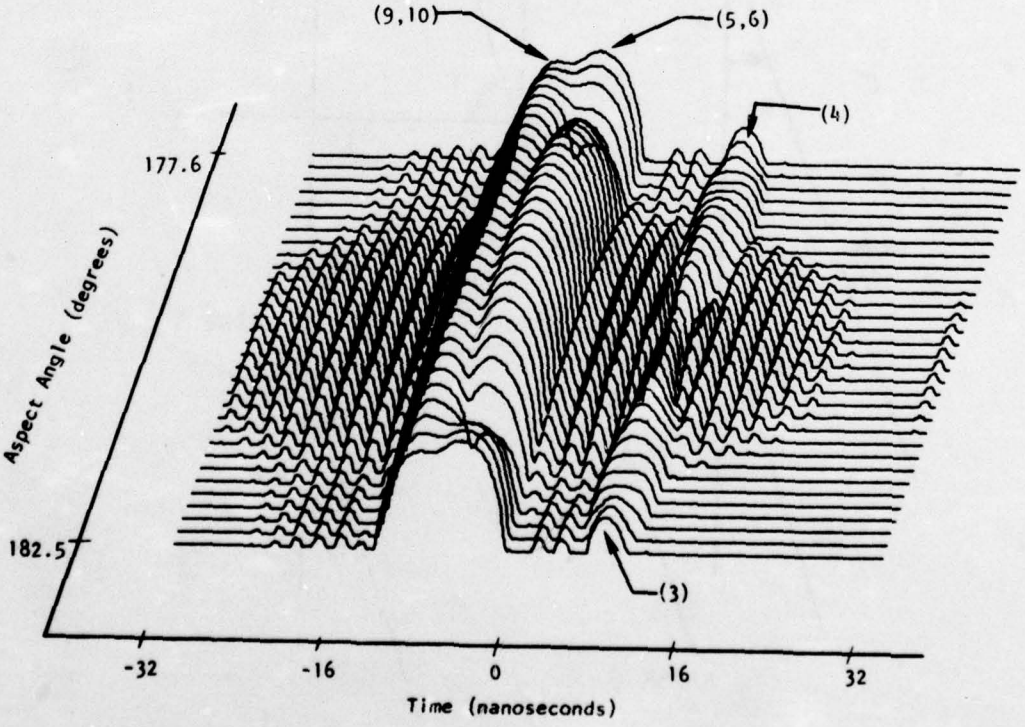

Fig.7 Backscattered pulses of the complex target with aspect angles centered at 180° (dynamic range 60 dB)

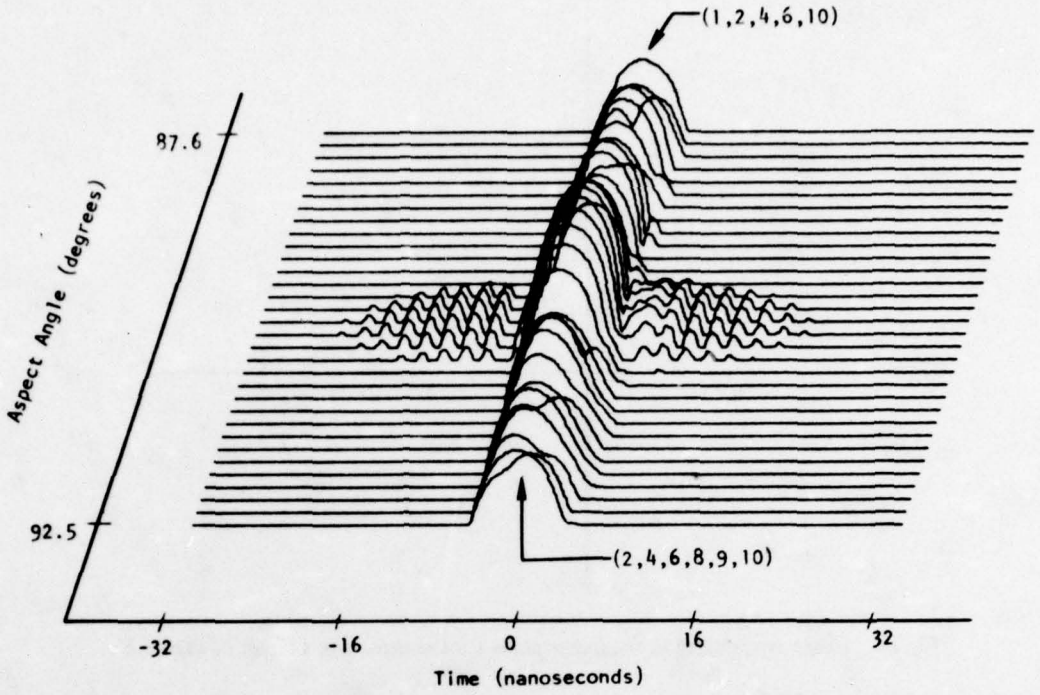

Fig.8 Backscattered pulses of the complex target with aspect angles centered at 90°

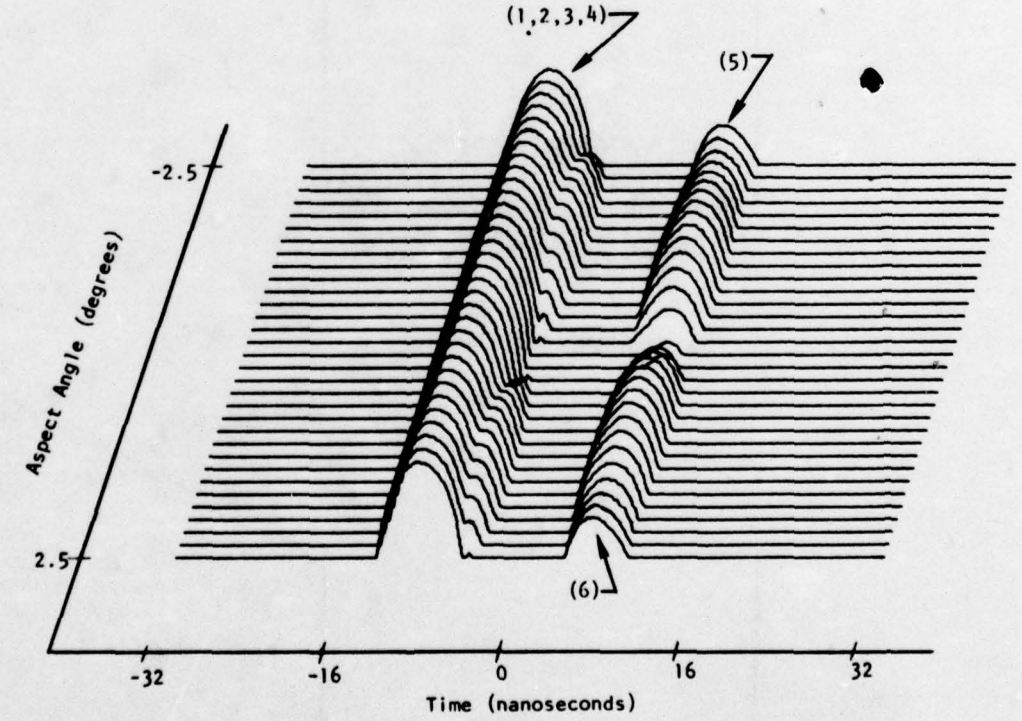

Fig.9 Backscattered pulses of the complex target with aspect angles centered at 0°

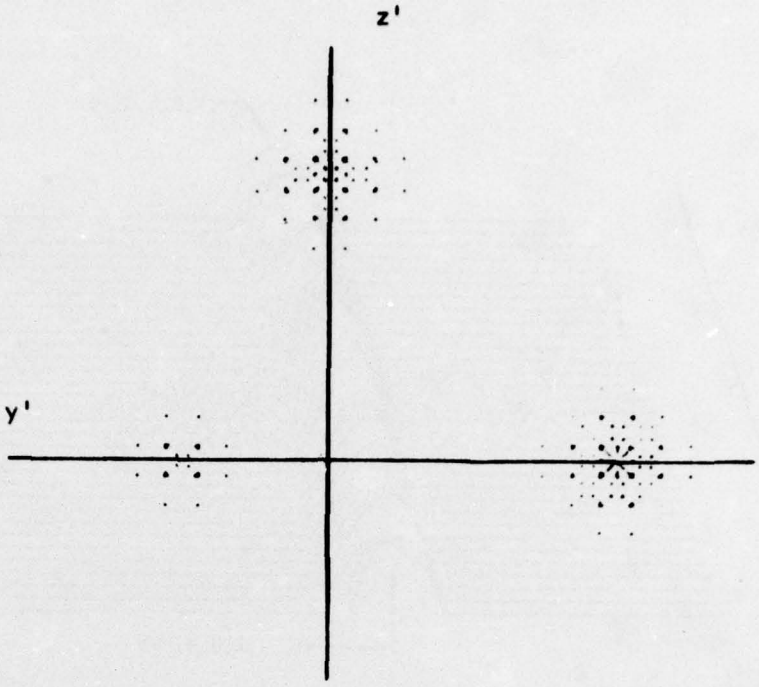

Fig.10 Image synthesized in the image plane for the three-point target of Figure 2

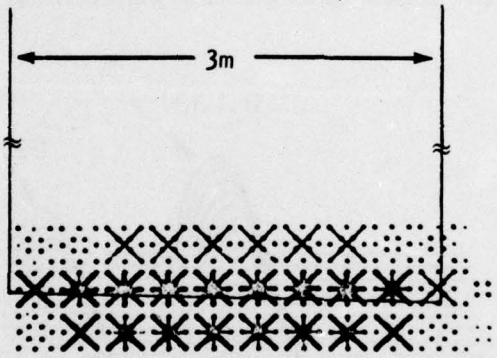

(a) Aspect angles centered at 0°

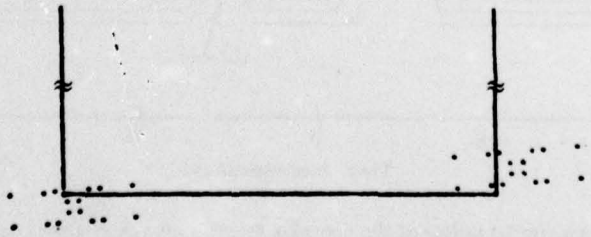

(b) Aspect angles centered at 5°

Fig.11 Images synthesized around two aspect angles for the circular-cylinder target

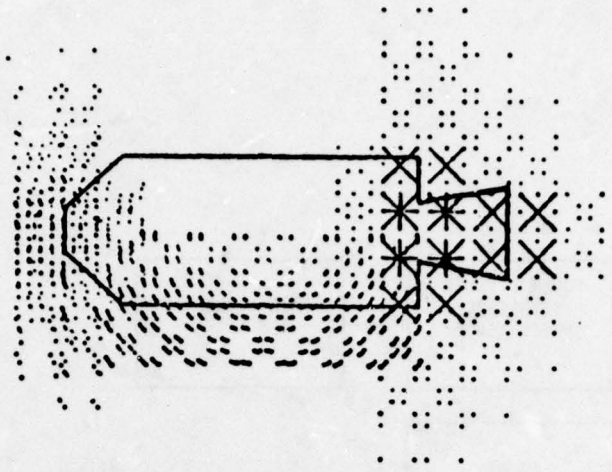

Fig.12 Composite image of the complex target (superposition of those synthesized around aspect angles 0°, 90°, and 180°)

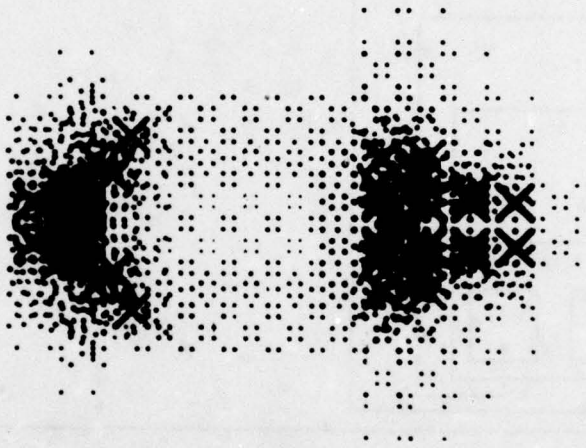

Fig.13 Composite image of the complex target with weak-scatterer enhancements and mirror-reflection superposition

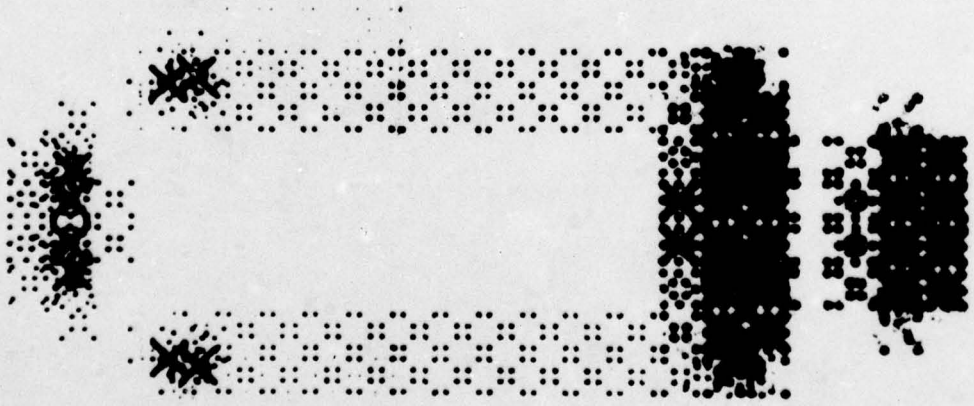

Fig.14 Composite image of the complex target with all linear dimensions doubled

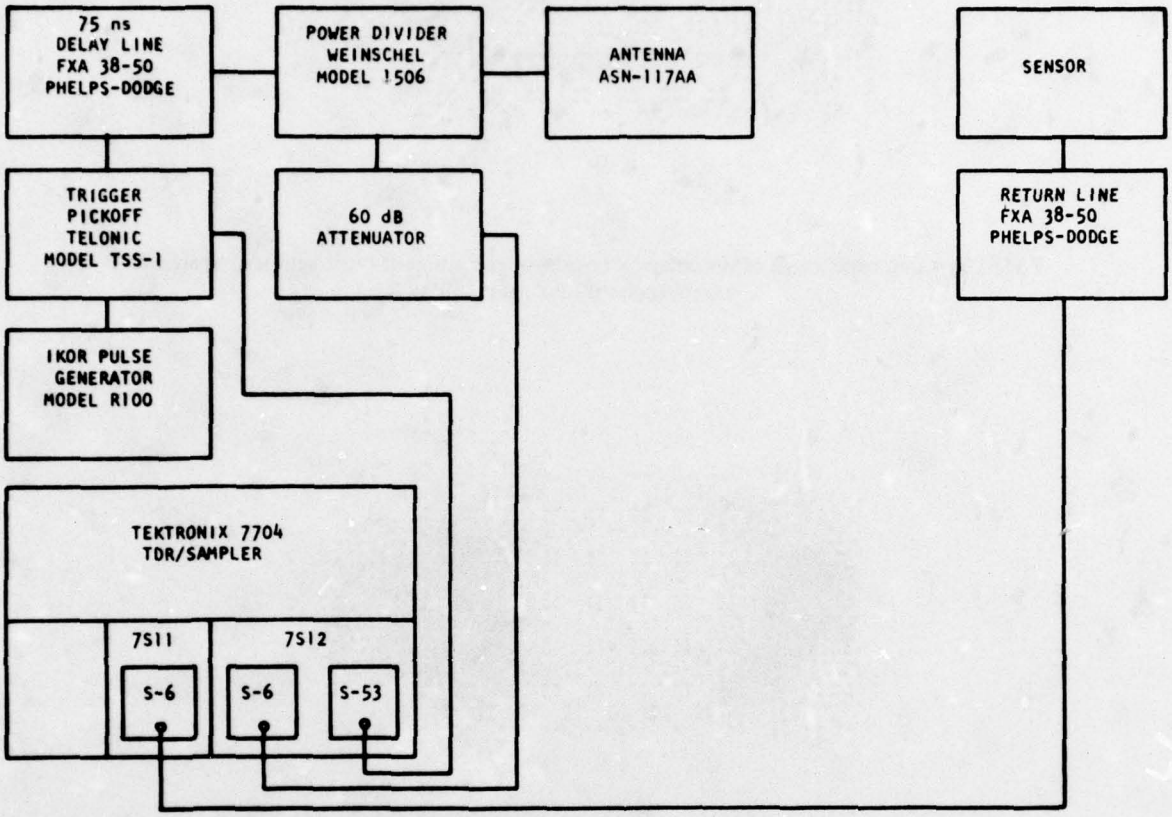

Fig. 15 Instrumentation for the dispersed pulse measurements at BDM/Albuquerque

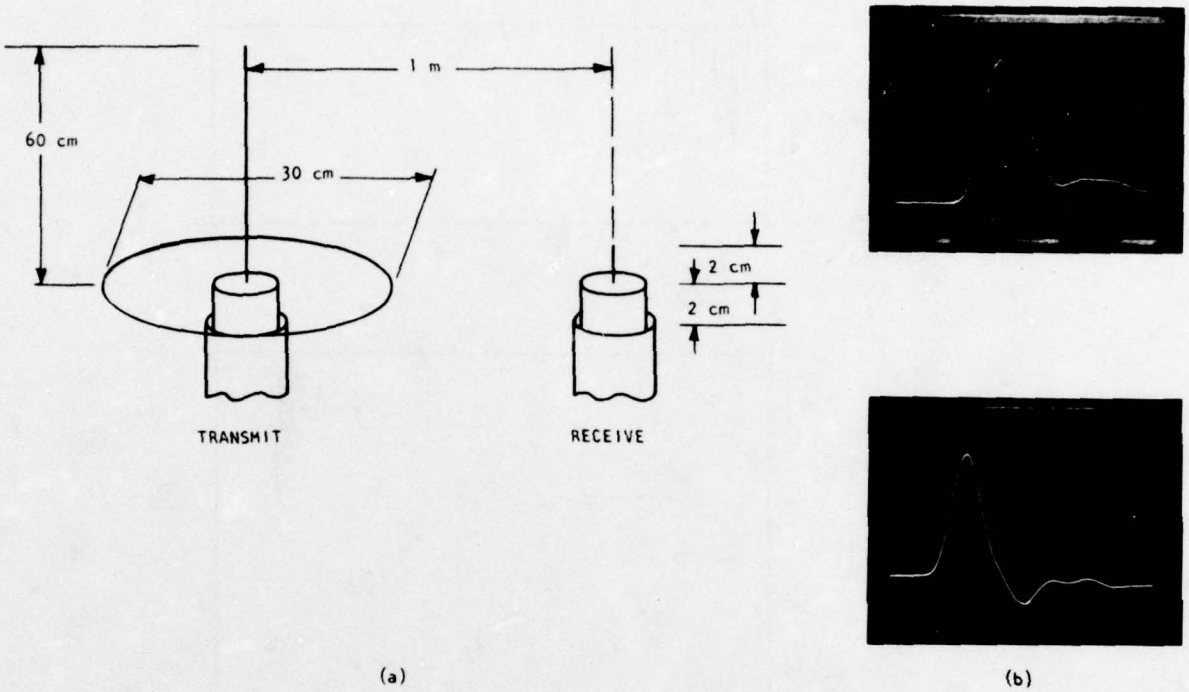

Fig. 16 Long-wire monopulse transmit and short-stub receive measurements. (a) Transmit-receive arrangement, (b) Pulser waveform, and (c) Received waveform. (Coaxial cable with ID = 02 cm, OD = 0.7 cm and plastic jacket. Photos are in 200 ps and 100 mV per division)

Fig. 17 Dispersed pulse (lower trace) and pulser waveform (upper trace) using transmitting antenna (ASN-117AA of American Electronic Laboratories, Inc.) and receiving stub

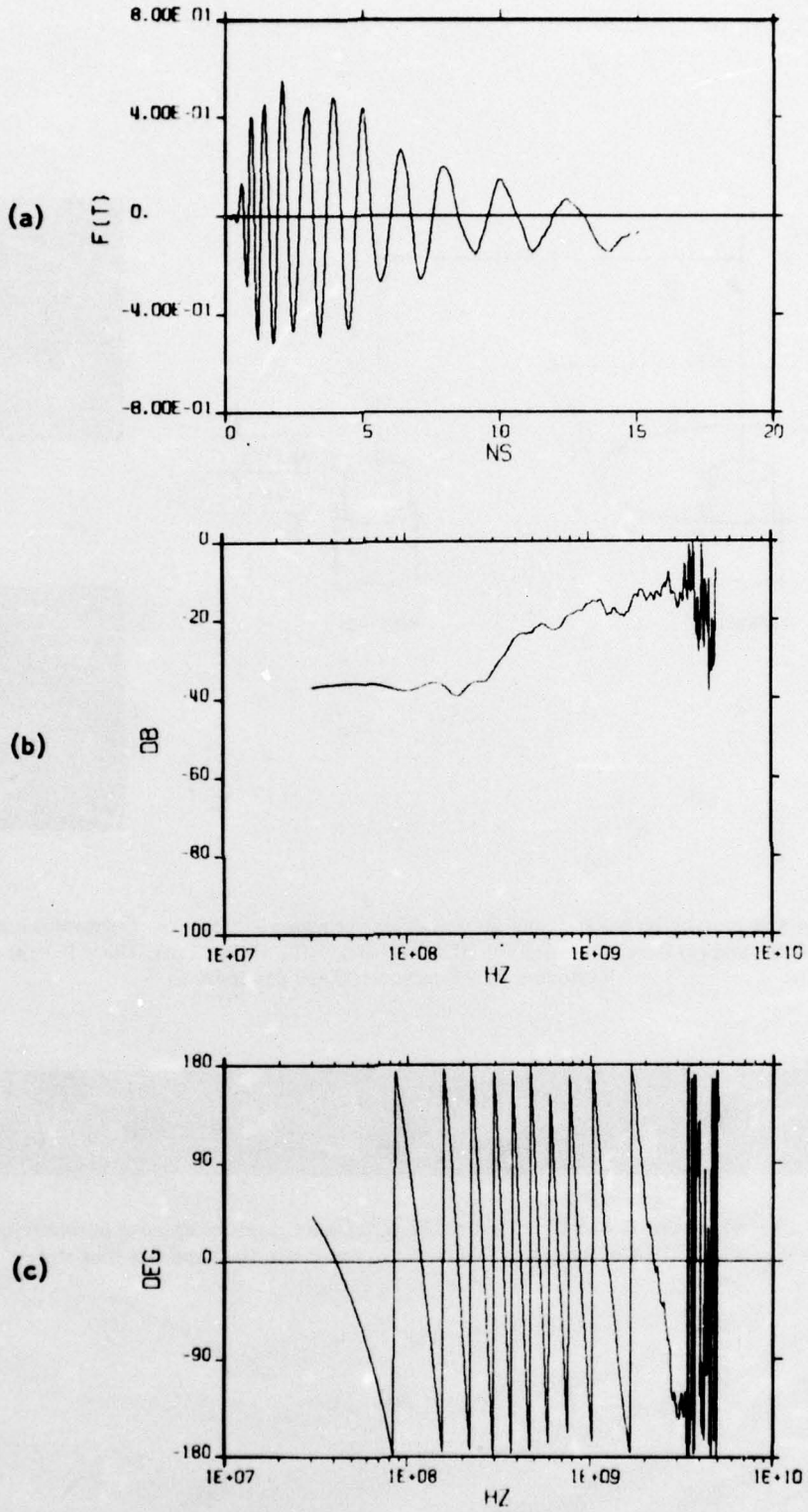

Fig.18 Analyzed results of cavity-backed spiral ASN-117AA. (a) Digital dispersed pulse; (b) Transfer function amplitude; (c) Transfer function phase

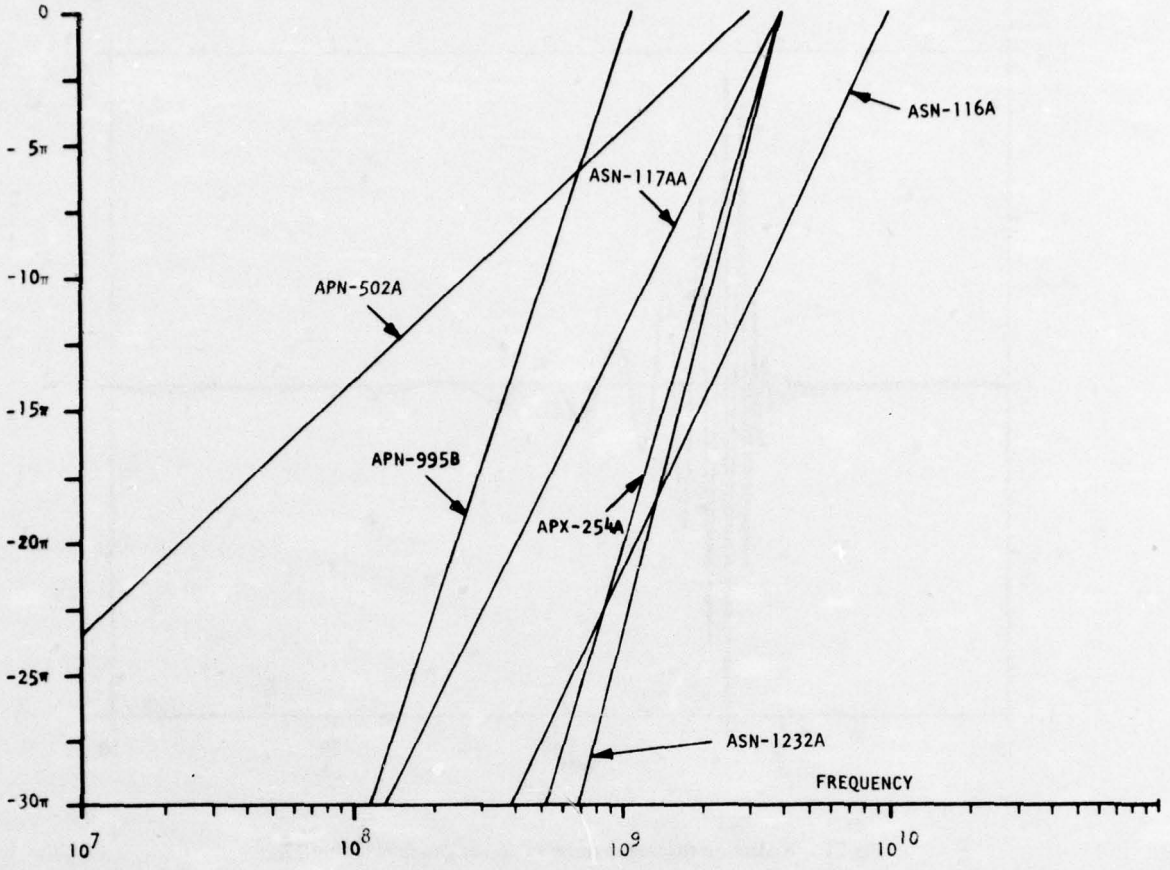

Fig. 19 Phase angles obtained from measured log-periodic portions and extended to the entire "Operating" bands

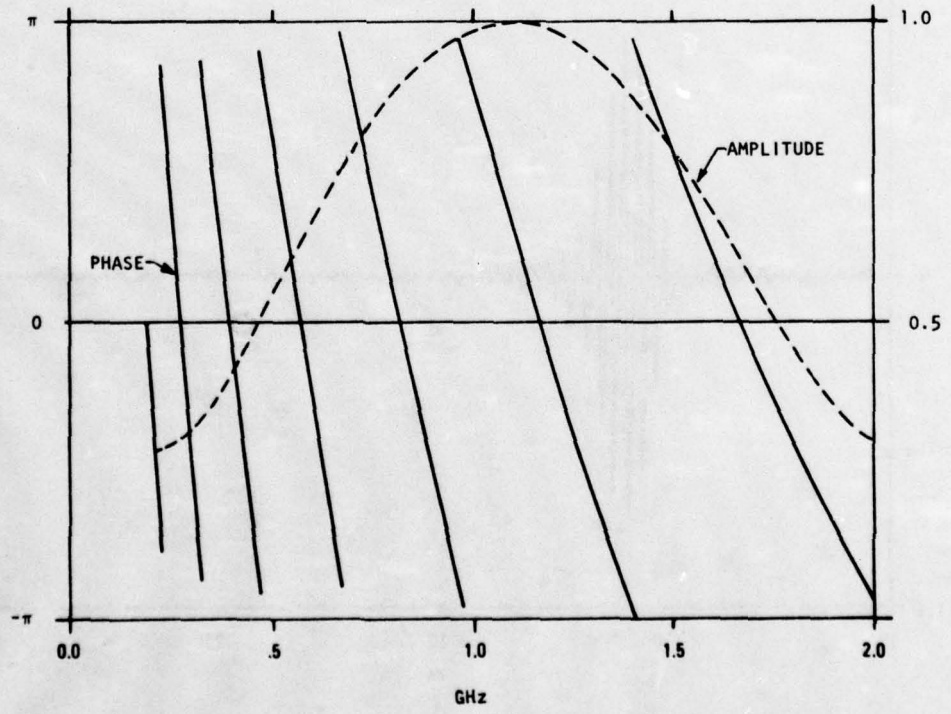

Fig. 20 Amplitude and phase distributions of the example in Table 12

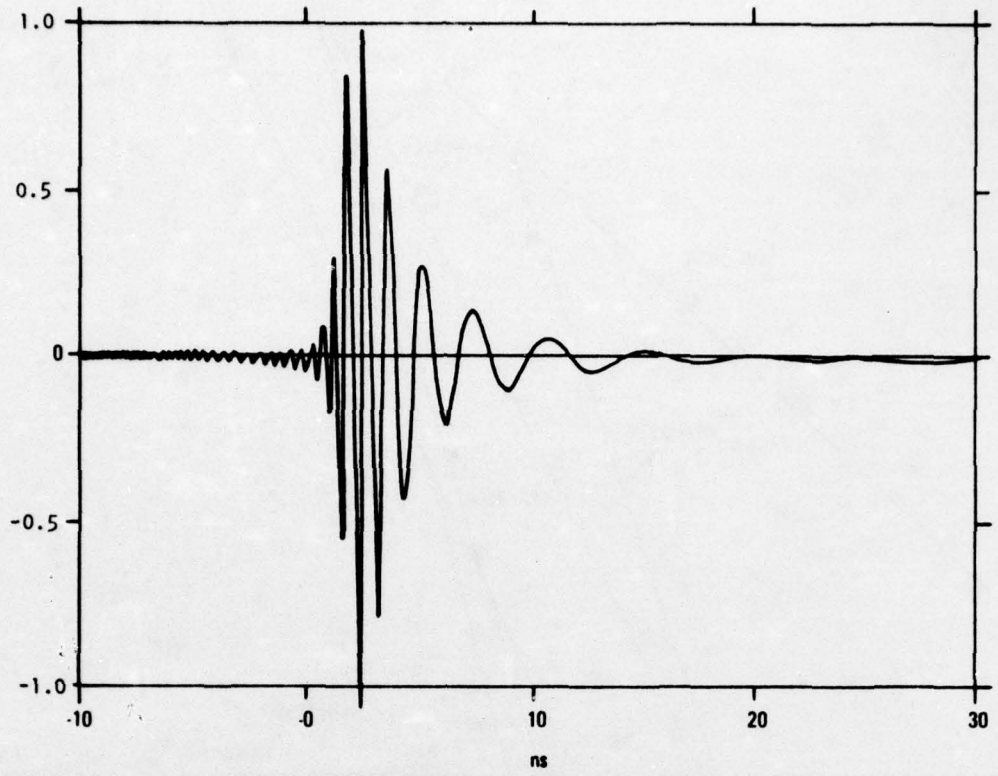

Fig.21 Radiation dispersed pulse of the example in Table 12

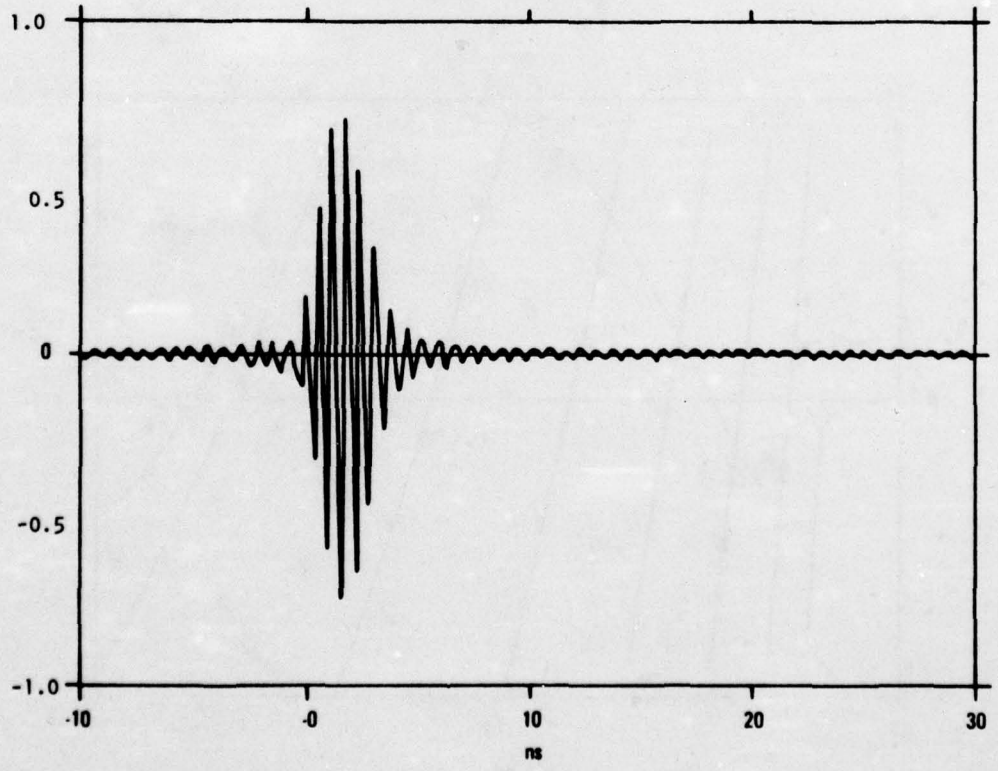

Fig.22 Radiated pulse of the first region defined in Table 12

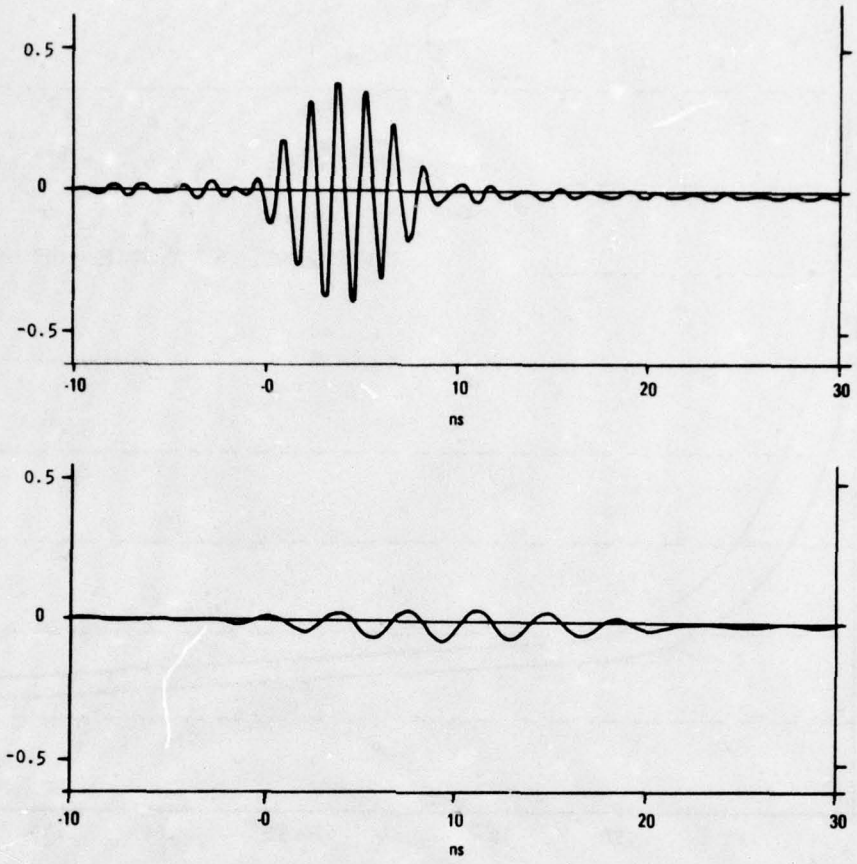

Fig.23 Radiated pulse of the sixth and eleventh regions

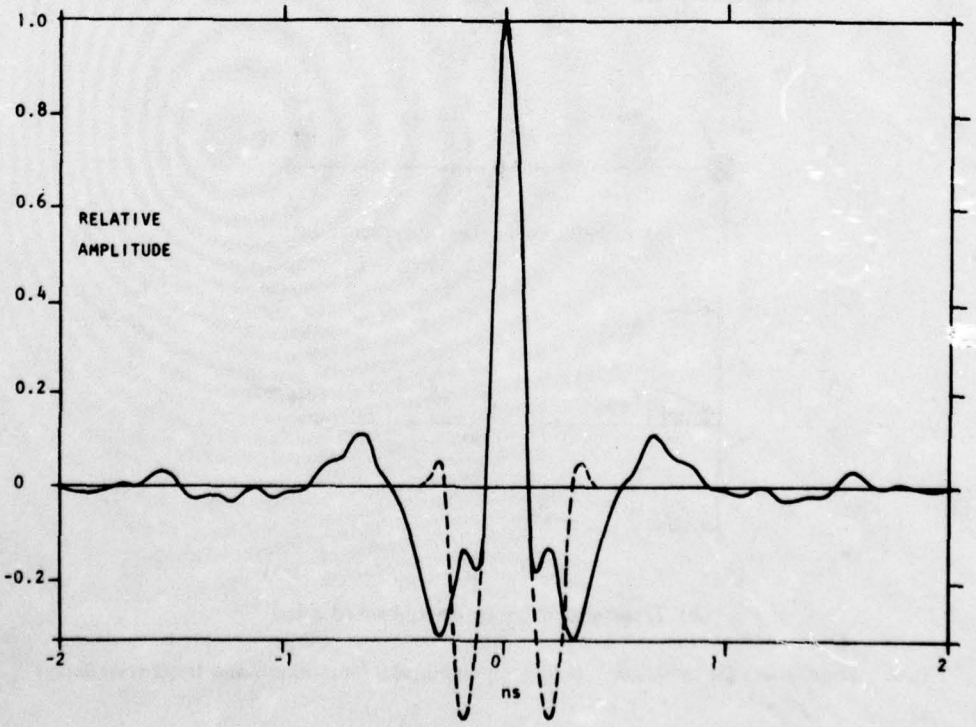

Fig.24 Compressed pulses of an estimated spectral distribution of an actual antenna (solid) and an ideal Hamming-Weight spectral distribution (dashed) from 0.5 to 6.5 GHz

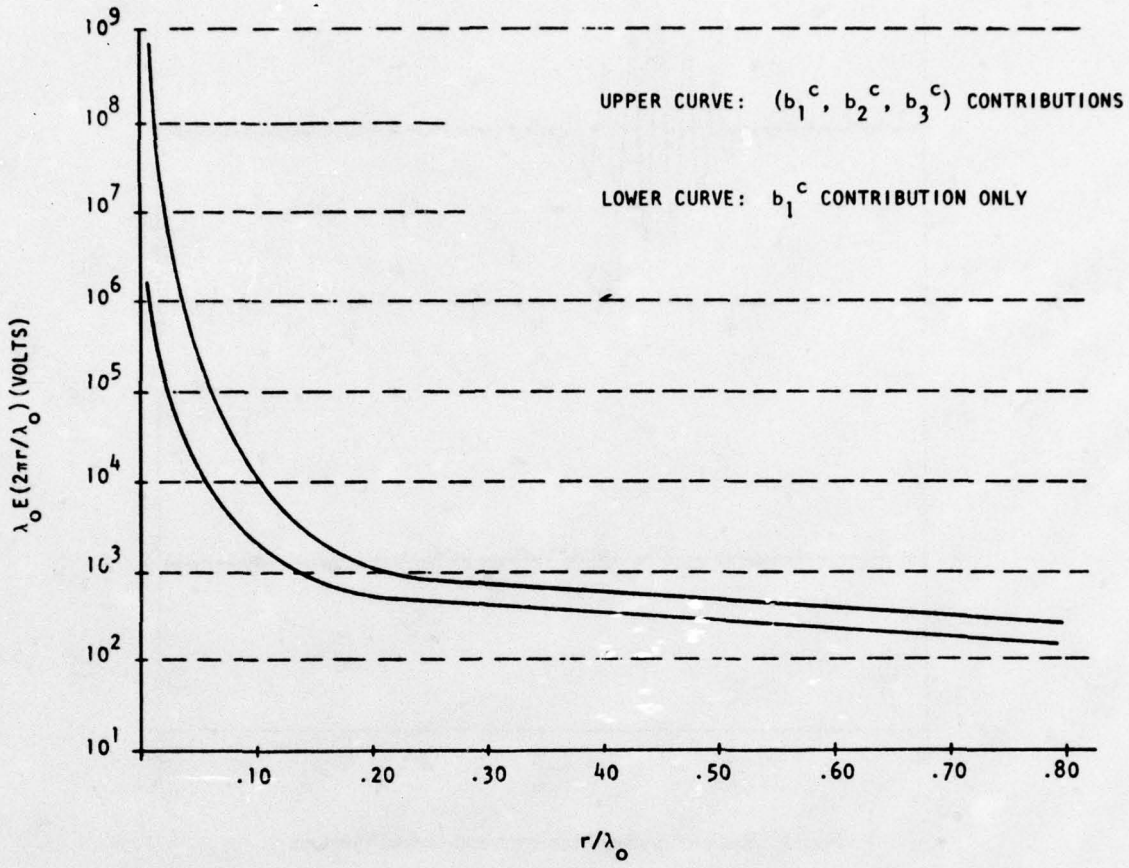

Fig.25 Spectral amplitudes of near fields by including the resonant dipole ($b_1 c$) and the associated (quadrupole, octupole) = $b_2 c$, $b_3 c$) modes of a radiating sphere

(a) Longitudinal delay by coplanar LP

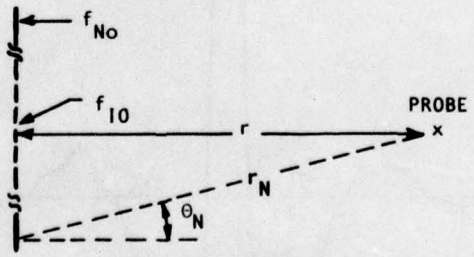

(b) Transversal delay by cavity-backed spiral

Fig.26 Coordinates for radiation – field compressions by longitudinal and transversal delays

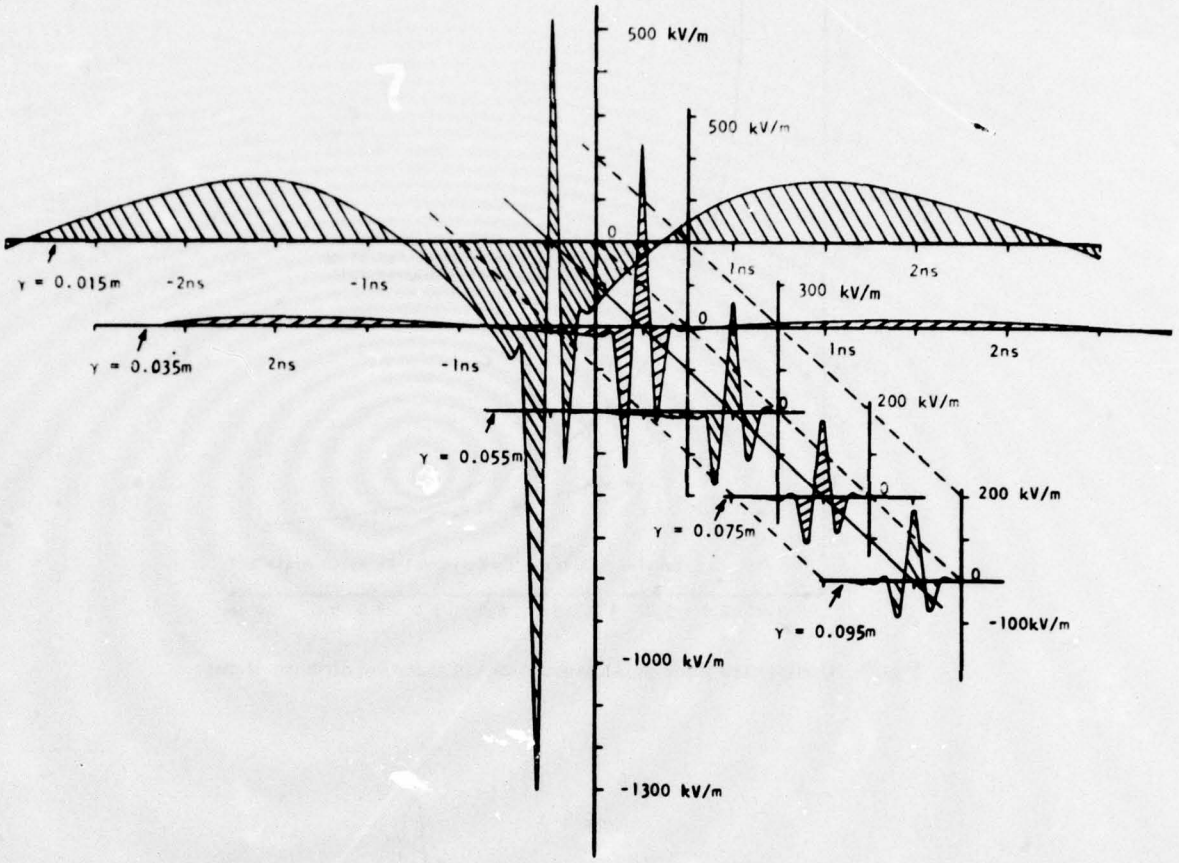

Fig.27 Near-field pulse compression for an antenna (see Table 14) with longitudinal time delay

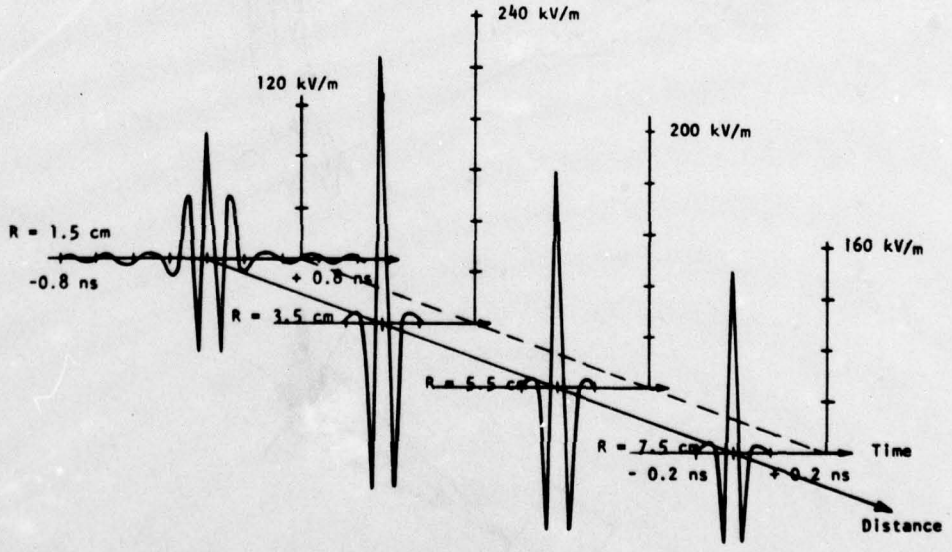

Fig.28 Near-field pulse compression for an antenna (see Table 14) with transverse time delay

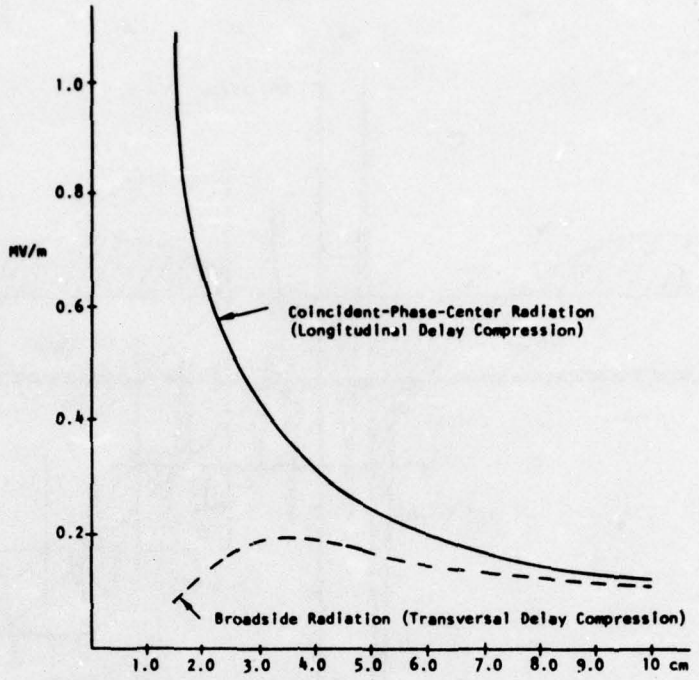

Fig.29 Compressed pulse peaks as functions of radiation distance r(cm)

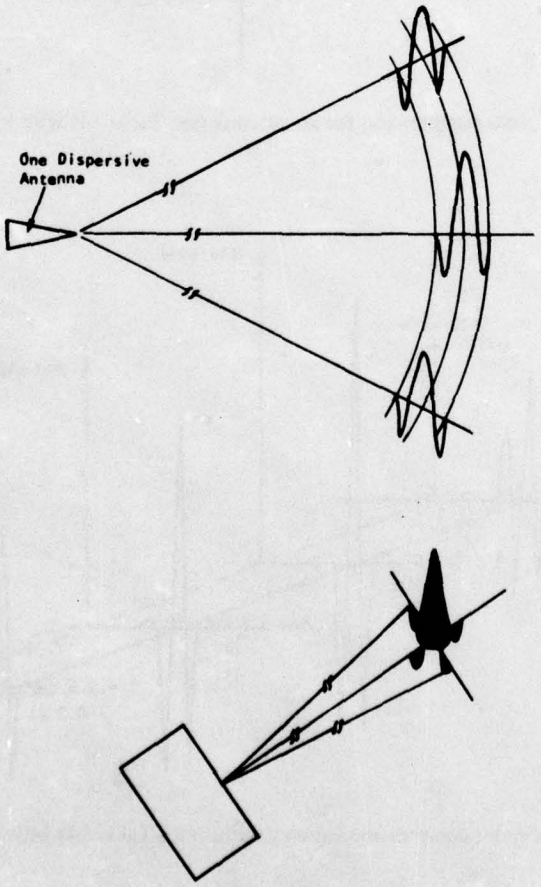

Fig.30 Possible radiation pulses of a single and "arrayed" antennas driven by conjugate-matched pulses

DISCUSSION

J LANDRETH: 1) Did you consider the work of Dr Moffat of Ohio State University, on transient waveforms for simple shapes, in the development of a simulator to attain the time-domain response of a complex object?

2) What problems do you envisage in the synthesis of the time domain response when the antenna is in the Fresnel field of the target?

J S YU: 1) I am aware of this work, but we did not use our responses to perform image synthesis. However, the time-domain data of the present technique have been used for synthesis and produce the same result.

2) Our study did not have the near-field problem because the targets are well in the far zone. If a target is in the Fresnel zone the quadratic phases would have to be compensated, or focussed, in order to obtain a well-focussed coherent image.

MULTIBEAM MONOPULSE ARRAY ANTENNA WITH INDEPENDENT ELEVATION BEAM SCANNING

B. Palumbo, A. Cucci
Selenia S.p.A.
Antenna Dept., Techn. Div.
Rome, Italy

SUMMARY

A multiple beam, monopulse type array antenna is presented. The antenna solution has been chosen after a trade-off study and experimental verification of the achievable performances.
The antenna beams are independently scanned in elevation and independent optimization of the sum and difference illumination distribution for high performance monopulse operation is provided. Use is made of an RF matrix comprising a center fed dual series-feed network for each beam. Diode and ferrite phase shifters perform the scanning of the beams, each in its angular sector of the coverage elevation angle. A set of stacked linear arrays of radiating elements, each fed by a power dividing network, in a planar array configuration, is utilized for the azimuthal beam forming.
The antenna operating principles are outlined, and the chosen solution and the design criteria are presented. Some realization techniques of the various components are described and the main characteristics of the antenna system are summarized, after a presentation of some significant experimental results.

1. INTRODUCTION

The antenna described in this paper has been developed for use in a long range, multiple beam, 3D phased array radar for air surveillance. The study, design and development of the antenna system is part of a program contracted to Selenia by the Italian Defense Administration. The acceptance test of the antenna prototype is scheduled by the end of 1976. The antenna system consists of a planar array fed by a multiple beam forming matrix and it has been designed for air transportation. Mobile versions, with short time deployment capability, can be derived. The antenna is mechanically scanned over 360° in azimuth at 6 r.p.m. Multiple beam scanning in elevation up to 30° is provided by ferrite and diode phase shifters. Elevation angle data are obtained by processing the received signals from the individual independent contiguous beams in the sum and difference modes.
Frequency agility capability is provided and the beams can be independently scanned, each in its own elevation coverage sector. The low sidelobe level, characteristic of the planar array configuration, is an effective characteristic to minimize the effects of noise jamming. Besides, the sidelobe structure and its frequency dependence in the operating band permits an additional antijamming capability, by means of an automatic selection of the minimum jamming disturbance frequency of operation.

The mechanical structure of the antenna is extremely compact and extensive use is made of special fabrication techniques, suitable for large scale repeatable production of parts, like dip-brazing of waveguide components and precision photoetching of RF circuitry and radiating elements. The antenna is protected by a radio frequency transparent, plane cover with honeycomb structure for maximum stiffness and minimum weight. No pressurization is necessary to satisfy the required power handling capability, neither special cooling nor heating systems are requested.

2. ANTENNA SOLUTION TRADE-OFFS

In order to perform volumetric (3D) search, various antenna system configurations can be envisaged. Adaptability to system requirements, minimization of sidelobe levels, angular coverage, broad frequency band capability are relevant characteristics.

Full mechanical scanning or full electronically scanning antenna systems have been excluded respectively for system requirements and cost and complexity of the solution. Combined mechanical and electronically scanning antenna system have therefore been considered. Mechanical azimuthal scanning is performed by continuous antenna rotation. Electronic scanning in elevation could be obtained by making use of frequency or phase scanning techniques. ECCM and transmitter considerations have favoured a phase scanning antenna system with multiple beams independently scanned. Use of elevation monopulse technique associated to each beam allows accurate elevation angle measurements.
Multiple beams from a common aperture can be obtained from an optically fed system (as in the case of multiple primary feeds in the focal region of reflector systems or lenses), or from a matrix fed array of elements. Optical feeding systems consisting of simple reflector fed by a cluster of adjacent feeds have inherent poor scanning capability, since

the beam shape is deteriorated quite rapidly at only a few beamwidths of beam squint from broadside. Use of lens systems would imply a mechanically cumbersome solution with some problems to obtain different antenna beamwidths at different elevation angular ranges as required by system considerations.
Matrix fed linear arrays appear a more attractive solution to form multiple beams in the elevation plane. The required azimuth beamwidth can be obtained from a single curvature optical system, as cylindrical reflector or lenses, or by means of stacked azimuthal beam forming networks. The latter solution has been preferred, due to its compactness and better possibilities of controlling the illumination distribution and therefore the azimuthal beam characteristics.

3. DEFINITION OF THE CONFIGURATION OF THE ELEVATION BEAM FORMING NETWORK

In order to obtain the proper phase and amplitude distribution of the illumination over the elevation aperture, various feeding systems can be envisaged, that fall into the following principal classes: parallel feed (with the corporate feed as special case), series feed and combination of parallel and series feed [1]. Series feed networks present some advantages in the present case, since a more compact configuration and monopulse mode operation are obtained. In a series feed, for the elevation beam forming network, the power is progressively coupled from a main feed line to the elements of the vertical array. The array is of the travelling-wave type and the power beyond the last element is absorbed by a matched load. Since monopulse operation is required, center feeding can provide sum and difference beams.
A simple hybrid junction at the center of the network could generate the two required separate excitations along the array, but this network doesn't allow any degree of freedom for the independent control of the sum and difference excitations. Therefore high performances in terms of beam shape, sidelobe level, gain for both sum and difference beams are not possible with this scheme. Compromise solutions can be found for the aperture illumination distribution by making use of constrained optimization techniques [2] and of suitable illumination functions [3], but some of the required antenna characteristics must be sacrificed. A different type of solution makes use of hybrid junctions, each feeding a pair of elements of the array, symmetrically disposed with respect to the center. The isolated sum and difference ports of the hybrid are separately combined in two power dividing networks, where proper weighting coefficients make independent the sum and difference illumination distribution [4] . A different class of series-feed network that provides complete independent control of the sum and difference modes makes use of two transmission lines feeding two sets of directional couplers connected by equal length lines [5], [6]. In the hypothesis of passive, reciprocal and lossless network, the orthogonality condition holds, if the two excitation input ports, relative to the sum and difference beams, are decoupled. In the more general case, all the theoretical limitations on the formation of more than one beam in a linear array must be considered [7] .
The physical symmetry of the network, that is required for monopulse operation with beam pointing not dependent on the frequency, is obtained by means of a center-fed technique. The sum mode is excited by the power coupled through one set only of directional couplers, while the difference mode illumination distribution is obtained by the superposition of the power coupled from both the feeding transmission lines. The technique of the center feeding has the additional advantage that the maximum differential phase delay between the outputs is half that of an end fed series network; then the phase compensating transmission line lenghts, to be inserted for broad instantaneous bandwidth at the outputs, are shorter. With the addition of the above compensating line lenghts, the operating bandwidth is essentially limited only by the bandwidth of the couplers and of the hybrid dividers for the sum and difference modes. An analysis has been carried out to evaluate the possibility of using short length fixed phase shifters instead of transmission line lengths for equalizing the electrical path from the input to the various outputs: the results of the analysis and of an optimization program have not been encouraging, so that the use of phase shifters has been disregarded, also in view of possible instantaneous bandwidth problems. A schematic of the dual series feeding network is shown in fig. 1.

Some considerations are made now about the multiple beam formation techniques. Multiple independent beams relative to mutually coherent signals can be formed by a lossless passive antenna, if the individual beams are orthogonal. The definition of orthogonality relative to the beam forming network in terms of decoupling between the ports, can be transferred to the concept of orthogonality of the beams in terms of convolution cross-product.

The above indicated condition is met with sufficient approximation, if the individual beams are angularly spaced by a sufficient amount in terms of beamwidths, and the conditions of low loss matrix and high directivity of the coupling devices are satisfied.

A multiple beam forming network, that appears attractive for this case, where the number of beams is much less than the number of output ports, is the Blass type array matrix [8] [1]. A block diagram of this configuration is shown in fig. 2, where the principle

of the dual series feeding network is extended to many pairs of sum and difference beams. The intrinsic broad band capabilities of the individual networks are valid for the whole matrix.

Another advantage of the Blass type beam forming matrix is that the number N of output ports of the matrix must not be necessarily the same for all the beams, but can be less, if the feeding transmission lines relative to the given beams are coupled only to a part (M × N) of the lines connected with the outputs.
This gives an additional freedom in the choice of the beamwidth relative to each beam.

The Blass type forming matrix presents however a major limitation, related to the series feeding networks. The efficiency of the latter depends on the maximum realizable coupling value in the directional couplers, as it is shown in two particular cases in Fig.3.

On the other hand, the disturbance on each individual beam forming networks due to the other networks interposed before the output lines increases as the maximum coupling in the directional coupler increases. This is evidenced in fig. 4, where the required amplitude distribution at the input of a "passing" beam forming network is shown together with that to be realized at the input, with a maximum coupling of 10 dB.

The evident difference between the two distributions indicates a low efficiency of the network. Since the maximum coupling, for a given amplitude illumination distribution, decreases with the array length and therefore with the number of output ports, it can be stated that acceptable efficiency figures from a Blass type, multiple beam forming matrix can be achieved only above a certain number of output ports.
This condition is not met in our case and an appreciable loss of efficiency has been calculated for the beams formed by the networks preceeding one nearest the to the output lines.

A different configuration has been then devised for forming multiple beams. The chosen solution is highly dependent on the technique used to feed from one transmitter all the beam forming networks, as it is shown in fig. 5. The transmitted pulse duration is divided in a number of time slots, corresponding to the number of beams, in which the operating frequency belongs to sub-bands of the whole frequency band of the radar system.
By making use of a frequency multiplexing device, the transmitted signal is fed to the various beams, each operating in a given portion of the entire frequency band. Within the above sub-bands, each beam is operated in a frequency agility mode. The multiplexing technique is utilized in reception also for the difference beams.

A common RF reception front end handles together the signals from the various beams and after frequency conversion, the signals coming from different angle sectors are separated on the basis of the frequency. With the above described multiplexing technique, a new configuration has been defined in order to obtain multiple beams in elevation. A block diagram is shown in fig. 6, and with reference to it, one can see that the outputs of the various dual series feeding networks are paralleled by means of frequency multiplexers, each feeding one of the stacked azimuthal beam forming networks.

Since the various vertical beams are frequency multiplexed, no angular separation constraint exists with the above described configuration. The scanning programs for each beam can therefore be individually optimized on the basis of system requirements and of the jamming environment.

4. ANTENNA OPERATING PRINCIPLES

As has been already indicated in the solution trade-off analysis, the three elevation beams are generated from a single trasmitter. If during the transmitter pulse time, the frequency is step changed to three different values belonging to adjacent sub-bands of the whole operating frequency band, the multiplexer sequentially feeds the beam forming networks connected to its outputs. Since the transmitter pulse is code modulated, the elementary pulses of the burst relative to each frequency are interlaced, so that an effective simultaneous transmission of the three beams takes place in the transmitter pulse duration.

In reception the signals relative to the three beams, and therefore belonging to different adjacent frequency bands, are combined together by the same triplexer utilized in transmission. An identical triplexer combines the received signals at the difference ports of the beam forming networks. The signals are then separated and individually processed in the receiver, by utilizing the frequency as identifying parameter. The antenna multiple beam forming principle is indicated qualitatively in fig. 7. The (coded) transmitter pulse is shown with the interlaced pulse bursts, belonging each to one of the adjacent sub-bands. The signals at the relative triplexer outputs are then shown, together with an indicative diagram of the triplexer response in the frequency domain at the three outputs. The corresponding outputs of the three beam forming networks are then combined together by means of triplexers, conceptually similar to those utilized for the

transmitter signal multiplexing, as has been schematically indicated in fig. 6. Since the above mentioned triplexers are identical, the illumination distribution at their outputs is the same as that realized at the corresponding outputs of the beam forming network. The scanning of the individual beams is obtained by means of proper phase shifters at the outputs of the relative beam forming network. The scanning is performed by introducing a linearly varying progressive phase shift. As has already been indicated no constraint exists about the individual beam position and separation, since they are frequency separated. The scanning program can therefore be different for each angular sector, depending on the targets and jammers situation.

The elevation angular sector to be covered (0° to 30°) is divided into three angular regions, each relative to one of the three independent beams (see fig. 8). The first sector extends from the horizontal plane up to 3° and is covered by two positions of the first beam, with an angular separation equal to the beam width. Also the second sector, extending from 3° to 6°, is covered by two positions of the second beam, with the same performance , relative to the first beam. The third elevation sector, from 6° to 30°, is covered by eight positions of the third beam with a -3 dB width of 3°. Also in this case, as for the first and second beam, the crossover level of the adjacent positions of the beam is -3 dB nominally. The mechanical boresight of the antenna is at 5.25° above the horizontal plane and corresponds to the direction of the peak of the second beam at the higher position.

Since the two lower beams assume only two positions, use of a two phase conditions circuit is sufficient for the scanning of each of the two beams. The circuit is shown in fig. 9 and consists of a -3 dB hybrid with outputs at 90° of phase difference. Two diodes, shunt mounted with respect to transmission lines terminated by a short circuit at the outputs of the hybrid, determine , with the state of their polarization, two different insertion phase values, corresponding to the two beam positions. The length of the transmission lines beyond the diodes is a linear function along the vertical aperture and therefore it is not the same for all the phase shifters.
The third beam is scanned by means of a set of ferrite phase shifters on the outputs of the third beam forming network. The ferrite phase shifters are of reciprocal dual mode type, basing their operation on the Faraday effect. The driving technique utilizes a pulse current of variable length to set the working point of the ferrite phase shifter. Since independent sets of phase control devices are utilized for each beam forming network, their performance can be individually optimized on their own operating frequency band.

The accurate height measurement is performed by processing the signals received on each pair of sum and difference beams, that are simultaneously scanned by the same phase control devices.

5. DESCRIPTION OF THE SOLUTION AND DESIGN CRITERIA

The main parts of the antenna assembly in the final configuration are the RF multiple beam forming and scanning network, the set of stacked azimuthal power dividing networks and the radiating elements. An outline of the entire antenna system is shown in fig. 10. The T-shaped cross-section structure shows the two main separated functions of the antenna: the tail of the T is devoted to the elevation multiple beam forming, whilst the wings correspond to the planar array, that performs the azimuthal beam shaping.

The elevation multiple beam forming matrix comprises three similar networks. Each of them is formed by two parallel, centre fed, waveguides terminated at both ends, feeding a number of transverse waveguide lines. These are slot coupled to the two parallel feeding waveguides through cross guide directional couplers. The waveguides of the three networks are of reduced height , in order to obtain high coupling values, that are necessary for high efficiency. The practical limitation on coupling values for cross-guide couplers is in bandwidth and isolation characteristics, that begin to deteriorate for values above -10 ÷ -9 dB. The optimization of the network efficiency, under the constraint of the maximum allowable coupling value, for a given illumination distribution, is performed in such a way to minimize the power dissipated on the end loads. Programs have been developped (PRE-L1 and PRE-L2), that perform a constrained optimization according to the above principles for the coupling values to be realized both in the front transversal line (sum) and in the second line, in combination with the above for the difference mode. This non linear programming problem is solved with the procedure indicated in [6] and the optimum coupling parameters can be found. Ideal directional couplers are assumed, i.e. no power is coupled at the isolated arm. The optimization is performed at the center frequency of each band of operation. The sum amplitude function is a Tayler type distribution [9] and the difference illumination belongs to a class of antisymmetric functions generating, from the linear array, difference patterns with characteristics of sidelobe level, sidelobe decay law, beamwidth and slope at the boresight, that represent the best compromise.

It is well known that a Fourier transform relationship holds between a line source distribution $f(x)$, $|x| \leq 1$, and its far field radiation pattern $F(u)$, where $u = 2\pi/\lambda \sin\Theta$ (Note that λ is the operating wavelength and Θ the field angle, measured from the normal to the aperture). It can be seen [6] [10], that an optimum line distribution $f(x)$, that is physically realizable over an aperture of finite size L, is obtained by differentiating a sum pattern $F_\Sigma(u)$, in the form of a λ function of the first kind, and then Fourier antitrasforming it. The difference pattern $F_\Delta(u)$ is therefore given by the following expression:

$$F_\Delta(u) = d F_\Sigma(u)/du = d \Lambda_{p,b}(u)/du = \left(\Gamma(p+1)\, 2^p u/(\sqrt{u^2-b^2})^{p+1}\right) J_{p+1}(\sqrt{u^2-b^2}) \qquad (1)$$

where $\Gamma(p+1) = p\Gamma(p)$ is the Gamma or factorial function, J_{p+1} is the Bessel function of the first kind of order p+1, and p and b are the controlling parameters to be chosen for the best compromise solution. From the difference pattern of equation (1), by antitransforming it, the distribution function $F_\Delta(x)$ for the difference mode is expressed, apart from normalizing constants, by the equation (11) in [6]. In the present case values of p= .5 and b= 4 have been chosen. From the required illumination distributions for the sum and difference modes and a maximum coupling value of 10 dB, the coupling values from both the transverse lines are found. They are shown in the diagrams of fig. 11, together with the amplitude illumination distributions at the outputs of the beam forming network, relative to the first beam.

A more general analysis and synthesis program (3DIANA) has been developed for multiple transverse lines (and therefore multiple beam forming) networks in cascade. Actual phase and amplitude coupling of the directional couplers and the electrical lengths of all the connecting lines as functions of the frequency are taken into account. The transmission characteristics of the cross-guide coupler have been carefully measured and phase compensating sections, in form of properly spaced pairs of irises, are inserted between the transverse lines in the waveguide interconnecting sections. The irises are of inductive or capacitive nature according to the sign of the compensating phase shift. The design of the distribution of the reactances of the successive pairs of irises is such that good matching conditions and required insertion phase over the operating frequency band is obtained.

An additional electrical length compensation has been provided at the outputs of the beam forming network with the purpose of equalizing the path lengths from the input to each of the outputs. This compensation is required in order to have frequency independence of the phase distribution along the outputs, and with the center feeding technique the length of the compensating lines increases from the center to the end of the network. Besides, the lengths are linearly corrected for the first and the third beam forming networks in order to have the proper linearly varying phase distribution for the first position of the two above beams. The operation of the phase shifters then changes the slope of this linear distribution of the phase over the aperture for the beam scanning. The necessity of the line lengths to equalize the electrical paths to the outputs comes also from the transient behaviour of the network, particularly relevant for the very narrow elementary pulses of the coded transmitted waveform.

The design criteria of the frequency triplexers are to minimize the in-band insertion loss for a given sub-bands allocation. Insertion phase equalization is another important parameter that has been specified over the operating temperature range and for the temperature gradients occurring in different parts of the feeding networks.

The outputs of the stacked triplexers are connected to the azimuthal beam forming networks. These each consist of a power dividing device, that realizes an equiphase power distribution according to a prescribed illumination over the horizontal aperture. The power division is performed by means of equal and unequal by-two dividers with equiphase outputs. The corporate feed type configuration permits a broad band of operation, accurate control of the phase and amplitude distribution and the possibility of using different types of transmission lines for the power division. In fact a trade-off study for the definition of the configuration of the azimuthal beam forming network has been performed, by taking into account the electrical characteristics, as insertion loss and phase/amplitude accuracy, and mechanical parameters, as complexity, weight and fabrication problems, and cost aspects.

The final solution consists of a by-eight power divider formed by two-way dividers in cascade, realized by means of a triplate technique, with connecting lines in waveguide. The eight waveguide, outputs each feed a by-eight power divider in triplate. This consists of two-way Wilkinson type, unequal amplitude, power dividers, in cascade, realized on the same board. The unbalanced outputs of each final 8-way power divider feed directly the radiating elements, in form of printed dipoles, photoetched on the faces of the triplate board. The transformation from the unbalanced output of the power divider to the balanced input to the dipole is obtained by means of a suitable type of

balun. For the choice of the structure of the dipole, as radiating element, many possibilities are offered, that are compatible with the triplate 8-ways power divider:

a) Slot fed dipole (with different techniques for the slot excitation).

b) Bifilar line fed dipole, with one arm excited by the extension of the center conductor, and the other arm, on the opposite side of the board by a line extending from one of the ground planes of the triplate feeding line.

The second solution has been preferred for many electrical and fabrication advantages. It permits minimum loss at the transforming section from unbalanced to balanced transmission line and minimum radiated energy from the feeding line in the nominal polarization. One minor disadvantage is that the polarization is not exactly horizontal, since the two arms of the dipole are on two opposite sides of the etched laminate.
The measured angle between the polarization plane and the plane of the circuit board is 2.5°, corresponding to a cross-polarized component of the field 27 dB below the nominal polarization, with the same illumination distribution over the aperture. Then the gain loss is negligible and no significant departure from the sidelobe structure in the nominal polarization is to be expected.

The impedance at the input of the dipole feeding line has been optimized for a good matching to the output impedance of the triplate power divider, with a VSWR less than 1,15:1 over the operating bandwidth. The effect of the mutual coupling has been evaluated by measuring the radiation pattern of a dipole in an environment of other sorrounding elements, terminated in matched loads. This is the well known "realizable radiation patter", that has been evaluated by making use of an array of 5x5 radiating elements, with the central one excited and the others terminated in matched loads.

The azimuthal array and beam forming network have been analyzed in terms of uniformity of transmission phase and transmission loss, in order to evaluate the effects on the antenna impedance, gain, sidelobe level and structure. The latter characteristic is particularly relevant in the present case, where automatic frequency selection, for improving the antijamming capability, requires a frequency sensitive, multilobed pattern out of the main lobe region. In order to evaluate the transmission phase errors, a program has been utilized for the computation of the radiation pattern of the array, in presence of random errors, due to manufacturing tolerances, measurement errors, material variations of the various components of the beam forming network.

The assumed insertion phase error is principally determined by the different reflection coefficients of the various components of the feeding network in cascade. In fact, the required amplitude distribution at its outputs is obtained by means of power dividers with unequal amplitudes at the two ports and then the paths from the input to each of the outputs of the beam forming network are not identical. Mismatches that are normally concentrated in a discrete number of points of the transmission paths, as dividers bends, transitions, impedance discontinuities, have therefore to be kept minimum, to guarantee minimum phase error over the entire operating frequency band.

The front cover is of honeycomb structure, with skins formed by fibreglass cloth, epoxy resin impregnated and a dielectric core, with low RF losses. The skin thickness and separation have been determined, in order to minimize the reflections over the operating frequency band and the required range of angles of incidence.

6. DESCRIPTION OF THE COMPONENTS AND DEVELOPMENT TESTS.

In order to evaluate the performances of a multiple beam antenna, a feasibility breadboard has been designed and tested. It is shown in fig. 12, mounted on a positioner during the electrical tests. It consists of the central part of the complete array and the beam forming matrix has been realized in form of three dual series center-fed networks in cascade. The three vertical beams are obviously wider than those of the complete antenna, but are spaced angularly, in terms of their beamwidths, as in the final configuration. The agreement between the theoretical and experimental phase and amplitude distributions, relative to each beam, at the output of the multiple beam forming matrix, has been extremely good. No elevation scanning control device was provided in this feasibility breadboard. The stacked azimuthal beam forming networks have been realized by a first power division with semirigid air-dielectric cables as transmission lines, followed by a successive power division in microstrip, on the same board where the printed dipoles are realized. The two sides of two boards, with power dividers, baluns and printed dipoles are shown in fig. 13.

Some components of the final antenna system are presented in the following figures. Fig. 14 and 15 show the triplate power dividing network and the new type of printed dipole in the breadboard configuration. An internal view of the power divider with the dipoles in the final configuration is shown in fig. 16, that is relative to one of the modules of the azimuthal beam forming network.

One of the three beam forming networks is presented in fig. 17 during the adjustment and test phase. Some parts of the network are shown in fig. 18, before the dip-brazing operation. The basic device of the entire system, that is the cross-guide directional coupler, is shown more than once in the above figure. As an indication of the experimental data from the coupler, utilized for the network design, the direct and coupled arms insertion phase is shown in fig. 19, in terms of the coupling value. Finally, calculated elevation sum and difference patterns of the first beam, by taking into account the effects of random errors in the illumination distribution, are shown in figs 20 and 21.

The photograph of fig. 22 shows a mechanical mock-up of the complete antenna system in one of the operating configurations.

7. CONCLUSIONS.

The presented antenna appears a suitable solution to the requirements of a 3D, frequency agile, radar system with a wide elevation angular coverage. The monopulse capability gives a high height evaluation accuracy and the independent beam scanning performance is suited to a choice of the beam position control program that best fits the target and jamming environment.
The operating frequency band (of the order of about 13% at S-band) is appreciably wide and the near and far sidelobe structure enjoys the advantages of the absence of any blockage, typical of planar arrays. The mechanical solution is very compact and able to be air transportable in a deployed configuration. The choice of ferrite and diode phase shifters for the beam scanning resulted in a better matching of the requirements of each individual beam. The extensive use of dip-brazing and photoetching techniques has permitted characteristics of reproducibility and good accuracy in the fabrication of the various components of the antenna.

Acknowledgement

The authors wish to thank their collegues in the development laboratory, and especially those in the antennas section, and they are also indebted to the staff of the technical design service and of the missile and radar division. The results presented in this paper would not have been possible without the work they have performed.

References

1 R. C. Hansen: "Microwave scanning antennas", Vol. III - Array Systems, Ch. 1 and 3, Academic Press, 1966

2 S. M. Sanzgiri, J. K. Butler, R. C. Voges: "Optimum Aperture Monopulse Excitations", IEEE Trans. Antennas Propagat., Vol. AP-20, No 3, May 1972

3 E. J. Powers: "Utilization of the Lambda Functions in the Analysis and Synthesis of Monopulse Antenna Difference Patterns".
IEEE Trans. Antennas Propagat., Vol. AP-15, No 6, Nov. 1967

4 N. S. Wang, R. Tang, E. E. Barber: "A Multielement High Power Monopulse Feed with Low Sidelobe and High Aperture Efficiency"
IEEE Trans. Antennas Propagat., Vol. AP-22, No 3, May 1974

5 A. R. Lopez: "Monopulse Networks for Series Feeding an Array Antenna"
IEEE Trans. Antennas Propagat, Vol. AP-16, No 4, July 1968

6 W. R. Jones, E.C. DuFort: "On the Design of Optimum Dual-Series Feed"
IEEE Trans. Microwave Theory Tech., Vol. MTT-19, No 5, May 1971

7 J. L. Allen: "A theoretical Limitation on the Formation of Multiple Beams in Linear Formation of Multiple Beams in Linear Arrays"
IRE Trans. Antennas Propagat., Vol. AP-9, No 4 , July 1961

8 J. Blass: "Multidirectional Antenna - A New Approach to Stacked Beams"
1960 IRE National Conv. Rec, pt 1, pp 48-50

9 T. T. Taylor: "Design of line-source antennas for narrow beamwidth and low sidelobes"
IRE Trans. Antennas and Propagation, Vol. AP-3; pag. 16-28, Jen.65.

10 J. F. Ramsay: "Lambda Functions describe Antenna/Diffraction Patterns" Antenna Design Supplement - Microwaves, June 1967 pp 69-104

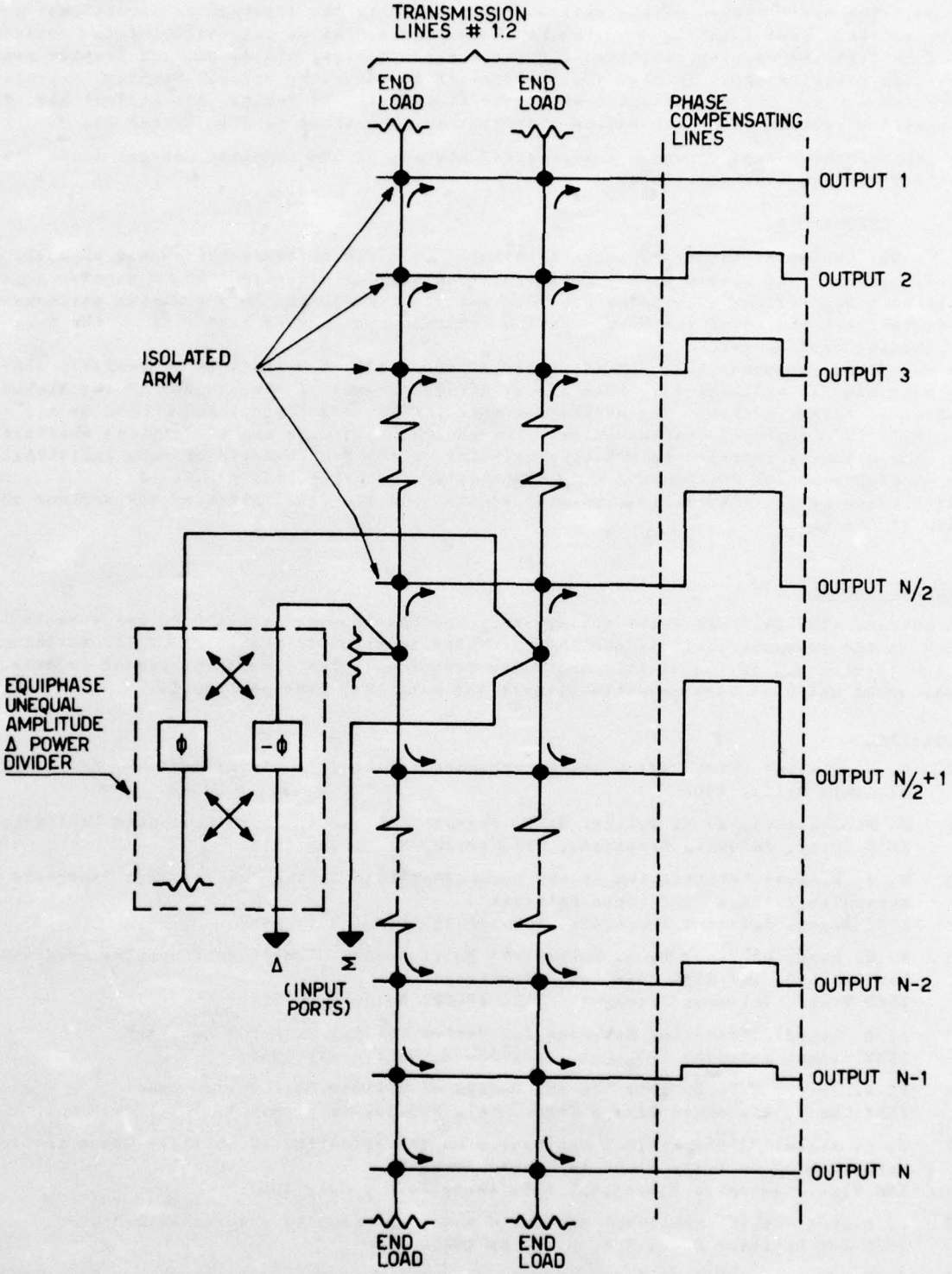

Fig.1 Dual series sum and difference feeding network

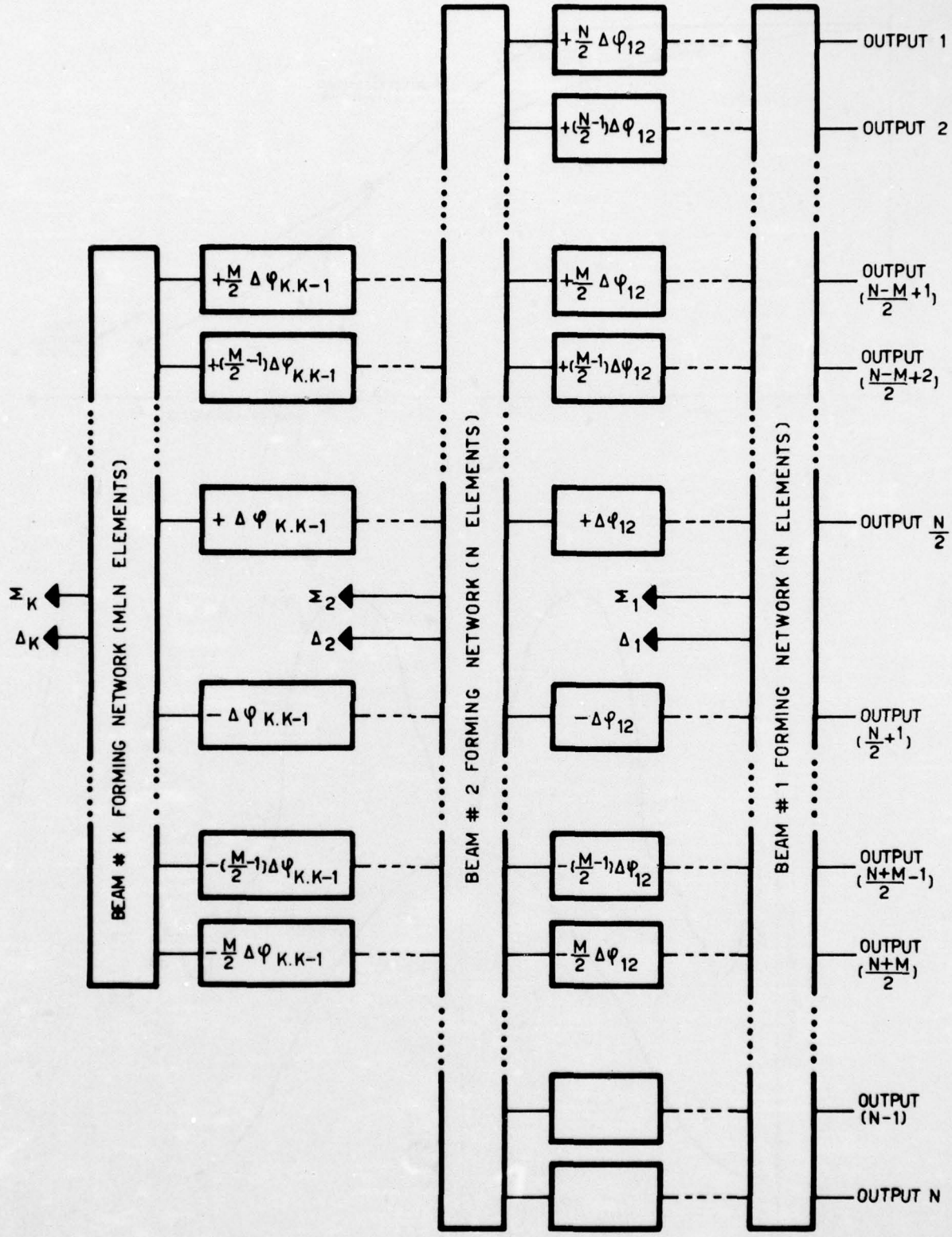

Fig.2 Multiple beam forming matrix utilizing dual series feeding networks in cascade

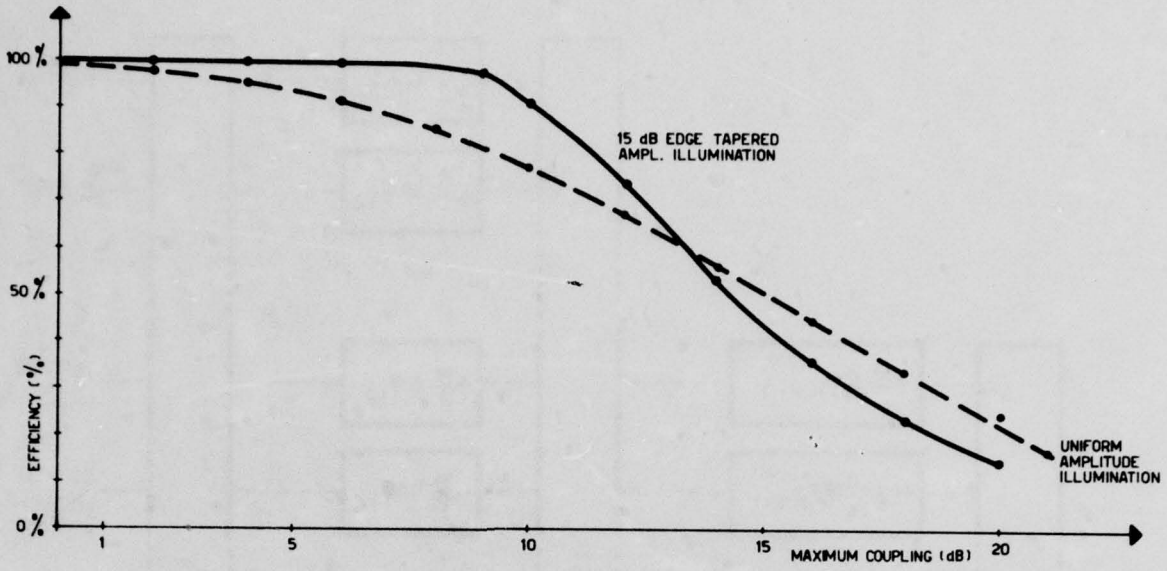

Figure 3

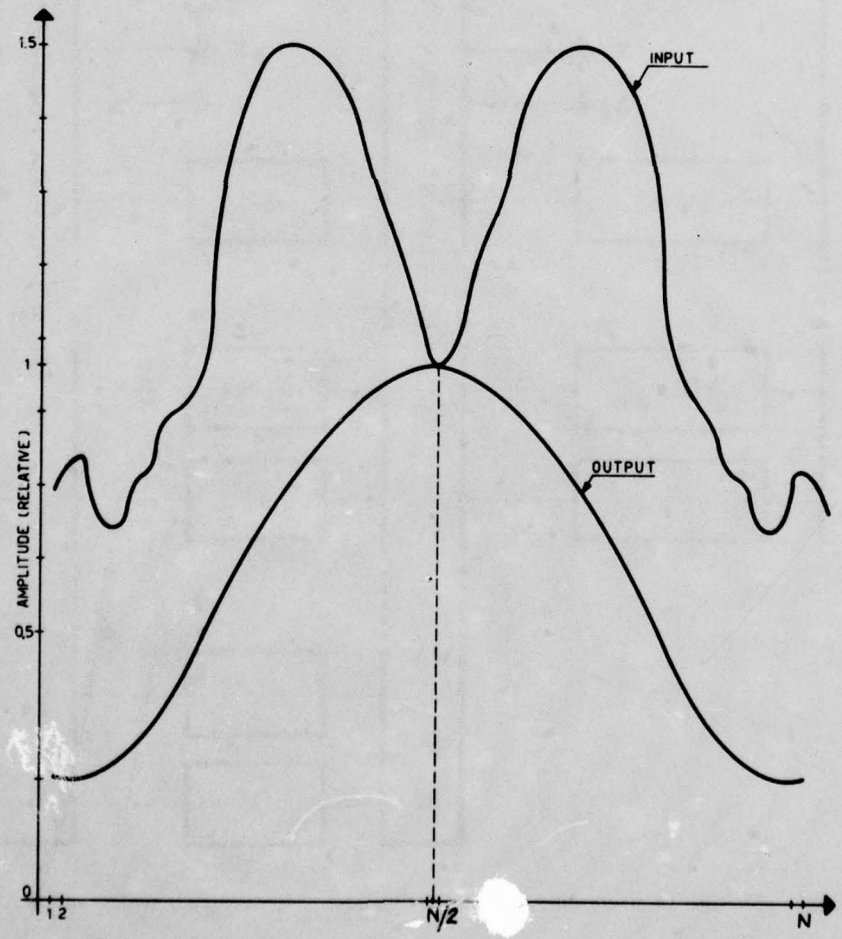

Fig.4 Amplitude (field) illumination distribution at the input and at the output of a dual series feeding network

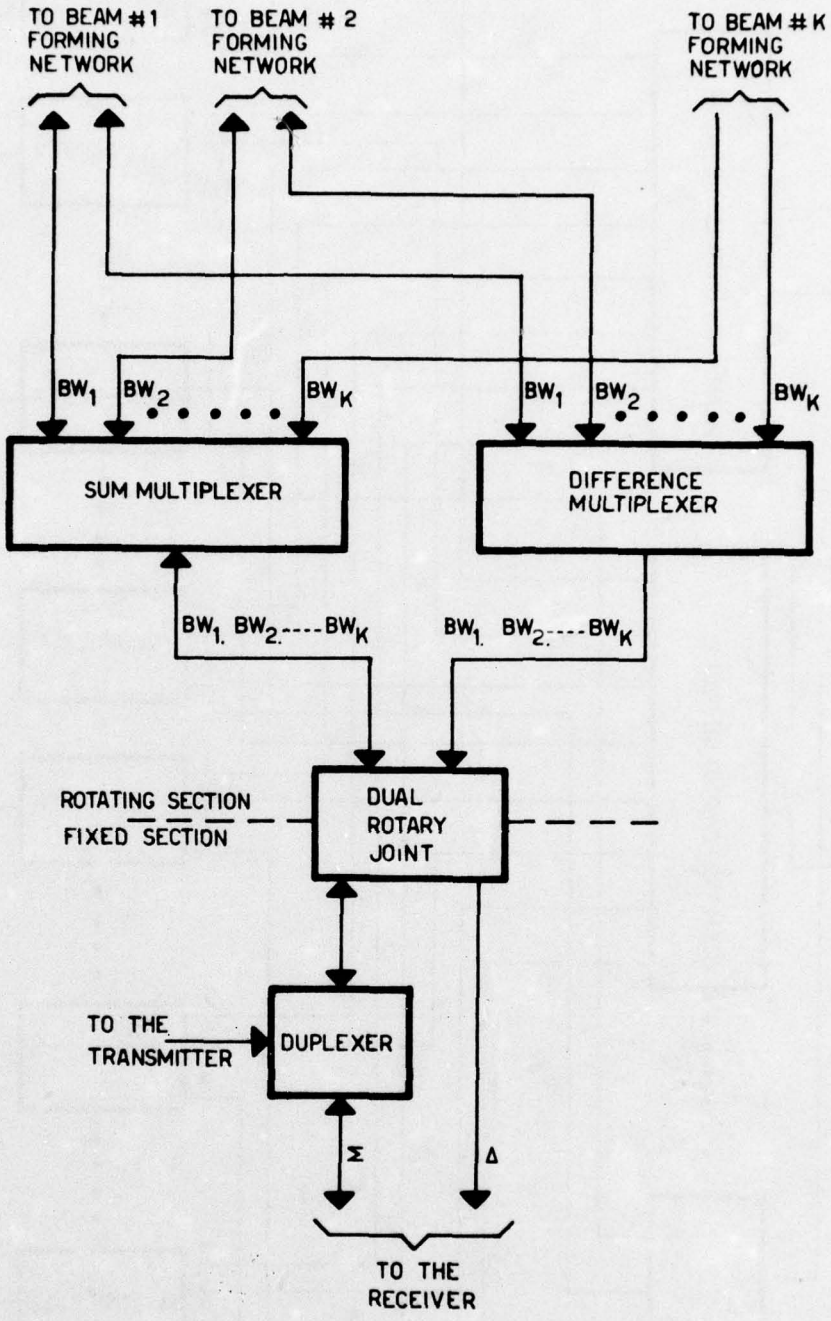

Fig.5 Block diagram showing the technique for multiplexing the signals relative to the individual beams

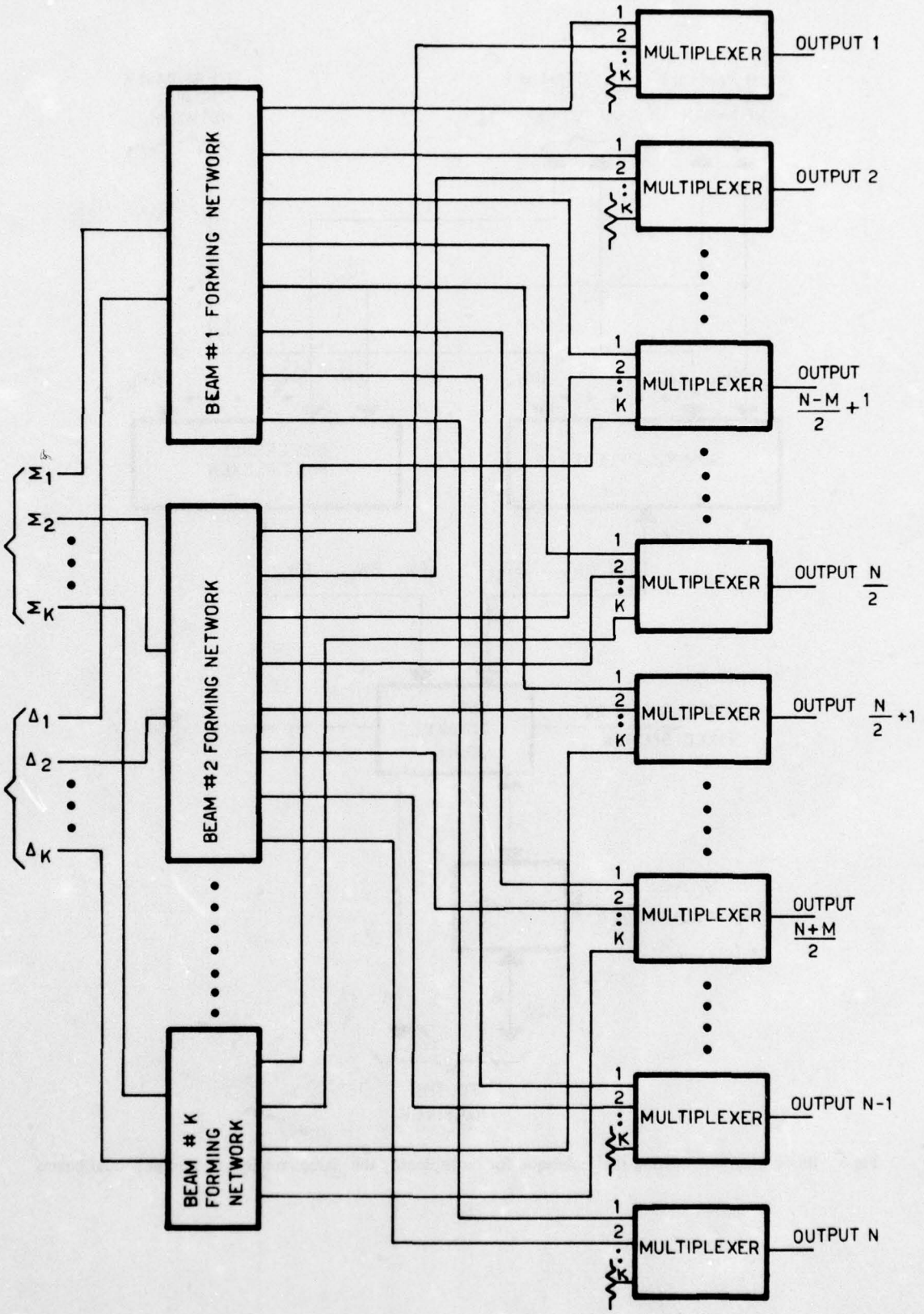

Fig.6 Multiple beam forming matrix with individual beam forming network in parallel configuration

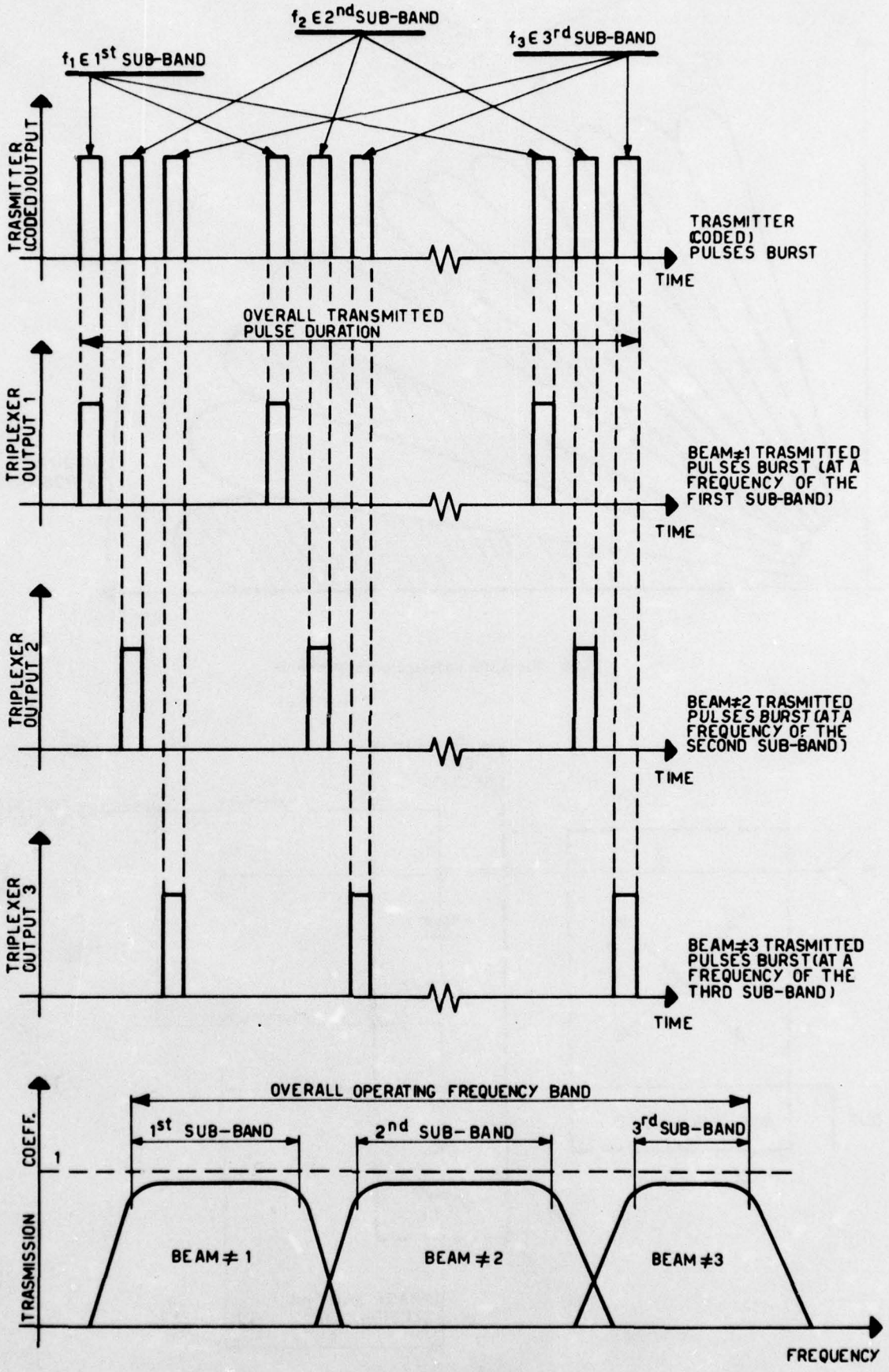

Fig.7 Beam multiplexing principle

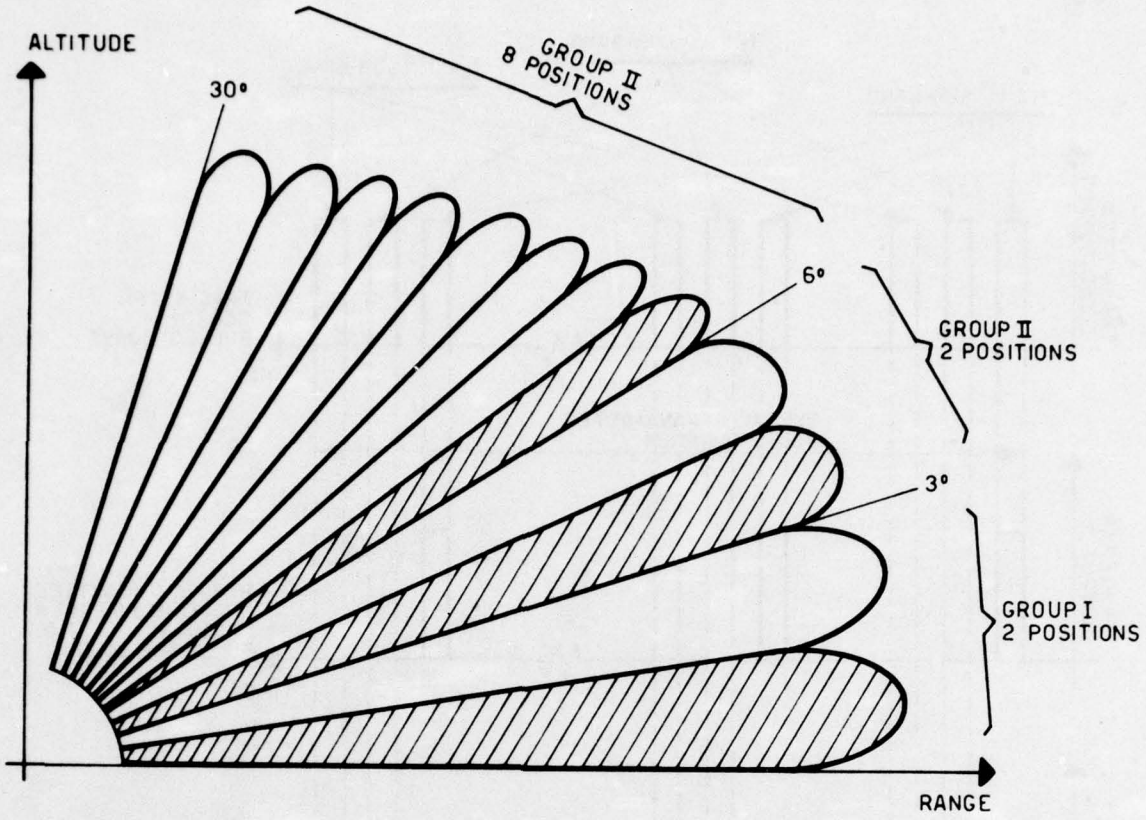

Fig.8 Elevation coverage beam positions

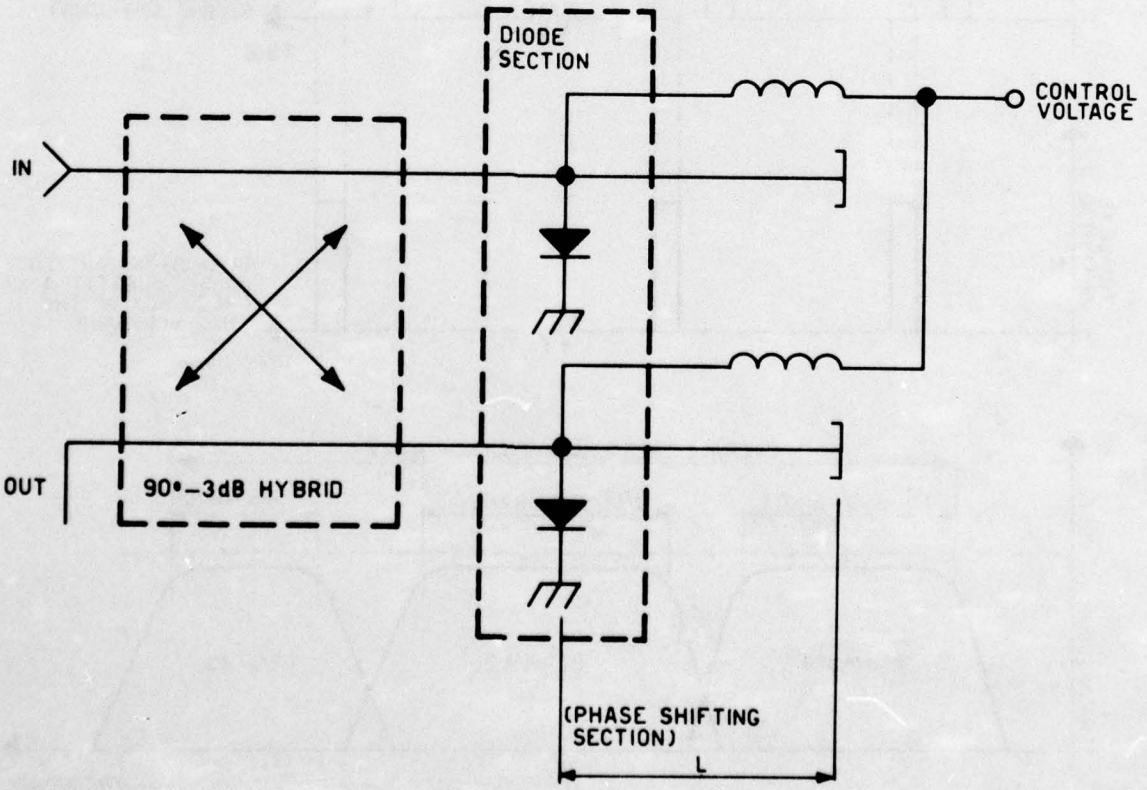

Fig.9 Diode phase shifter schematic

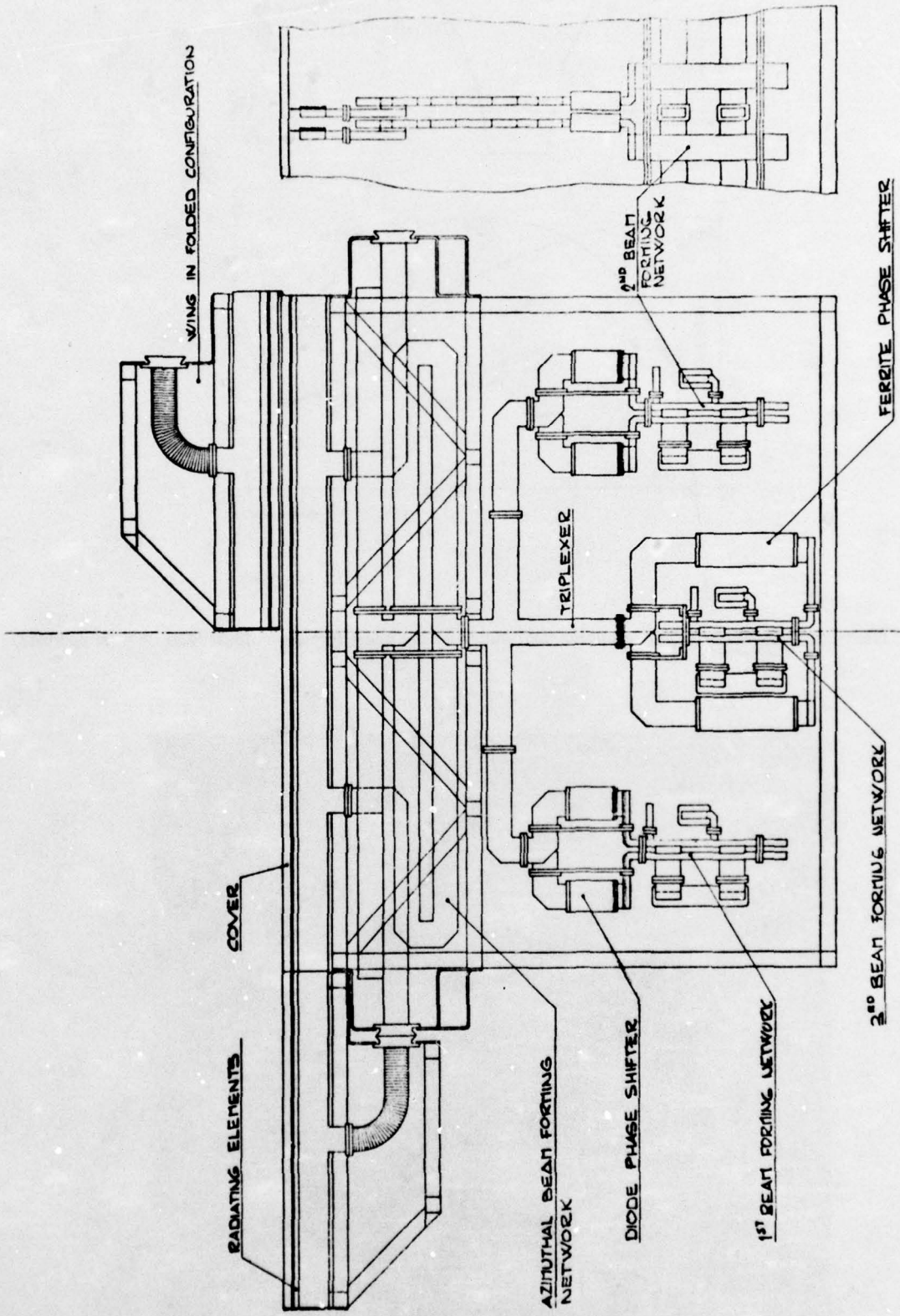

Fig.10 Antenna outline

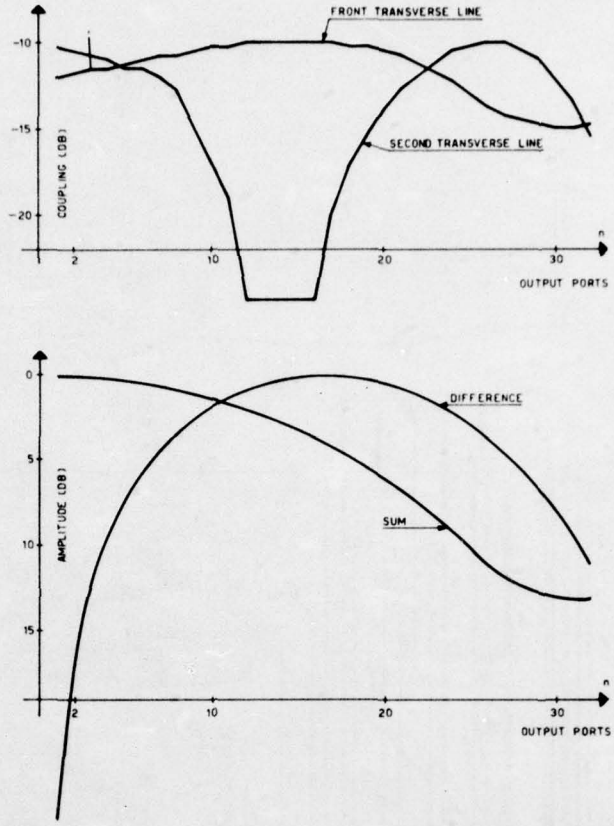

Fig.11 Transverse lines coupling and amplitude distribution at the beam forming outputs (half of total aperture)

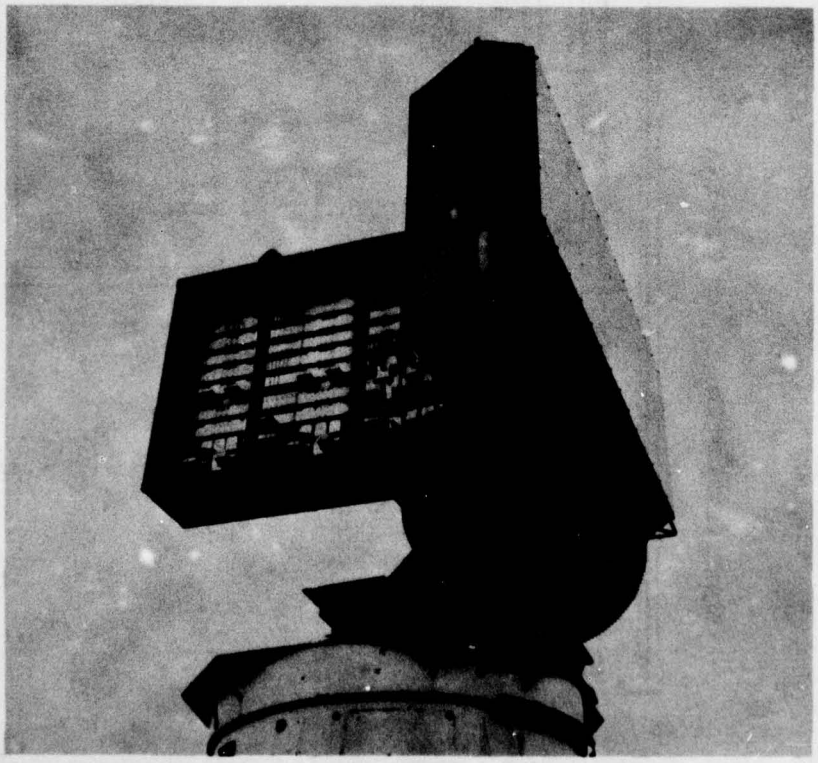

Fig.12 Feasibility breadboard

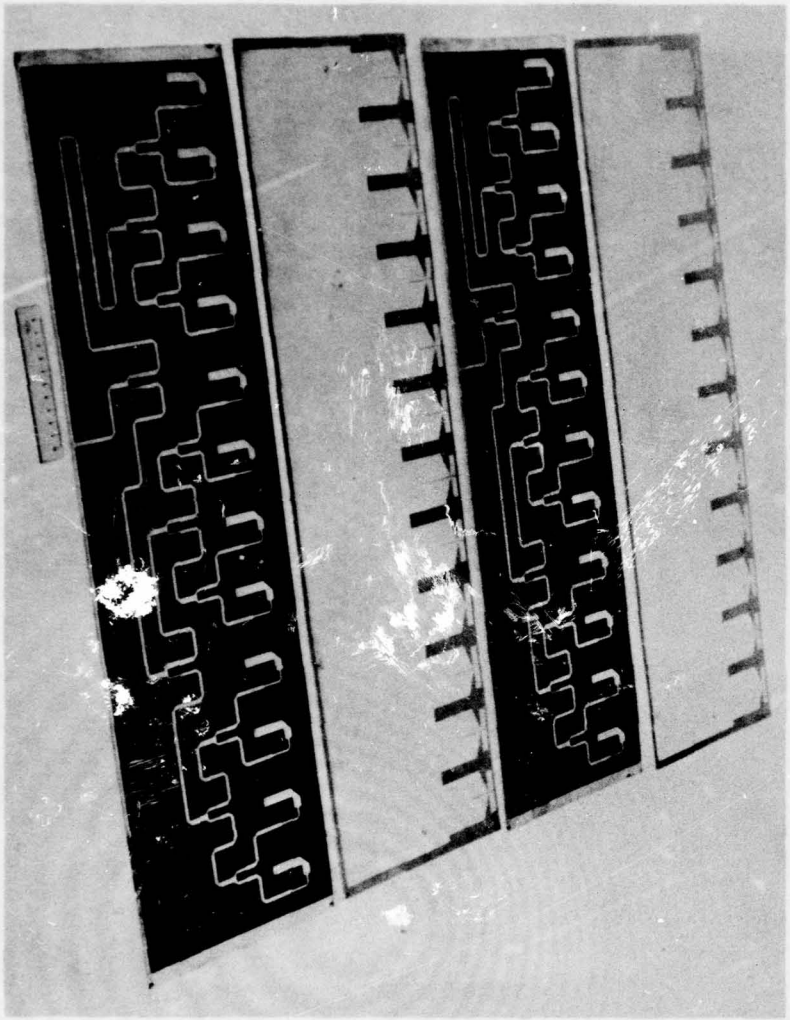

Fig.13 Microstrip power divider, baluns and printed dipoles of the feasibility breadboard

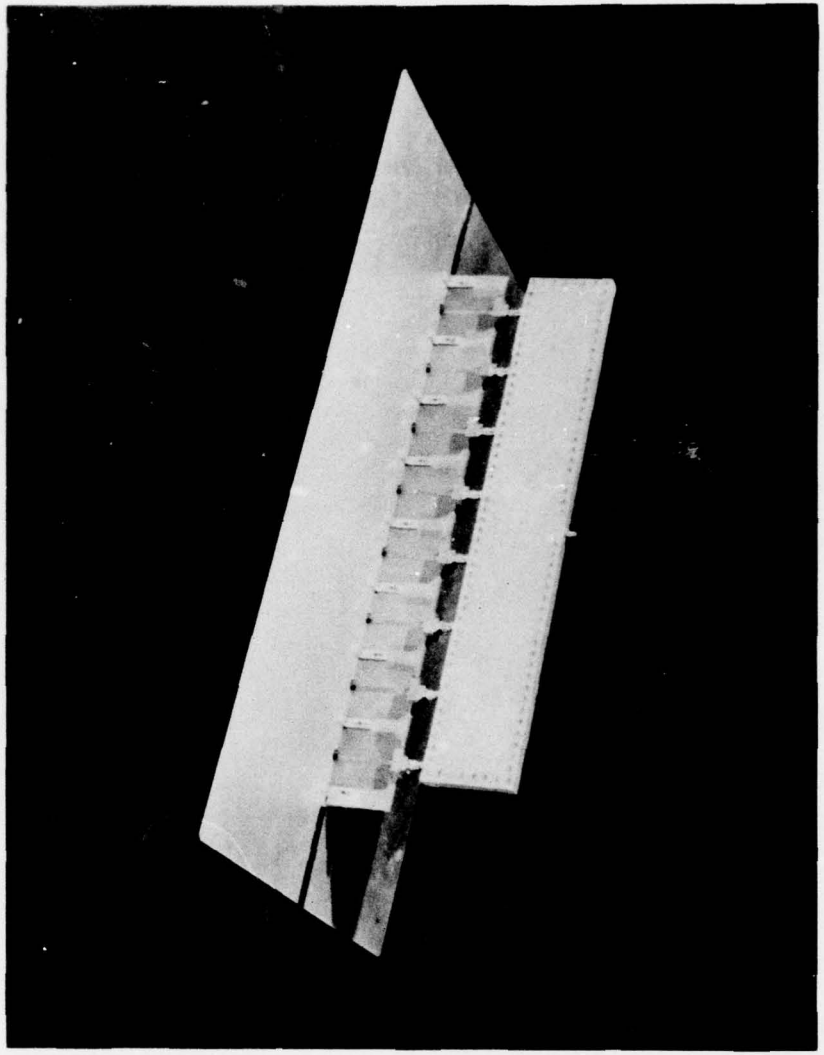

Fig.14 Triplate power dividing network

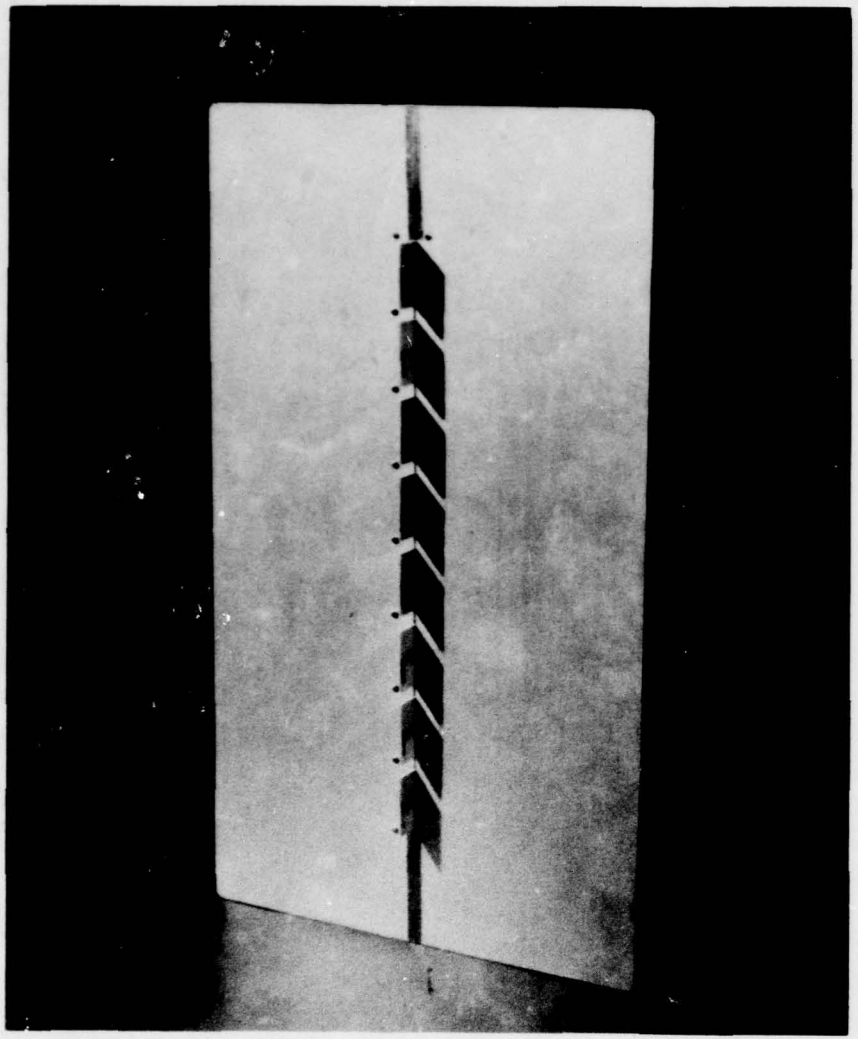

Fig.15 Array of 8 radiating elements in form of printed dipoles with ground plane

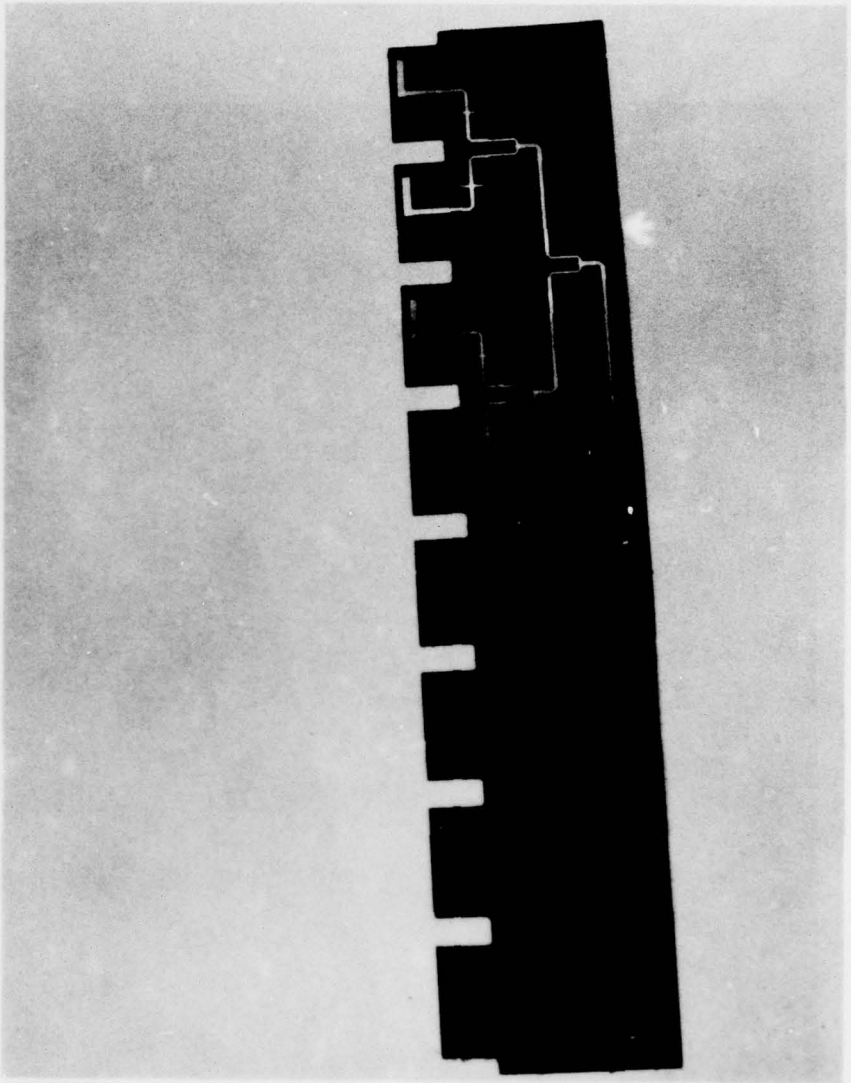

Fig.16 Internal view of the power dividing network, baluns and dipoles of one module of the azimuthal beam forming network

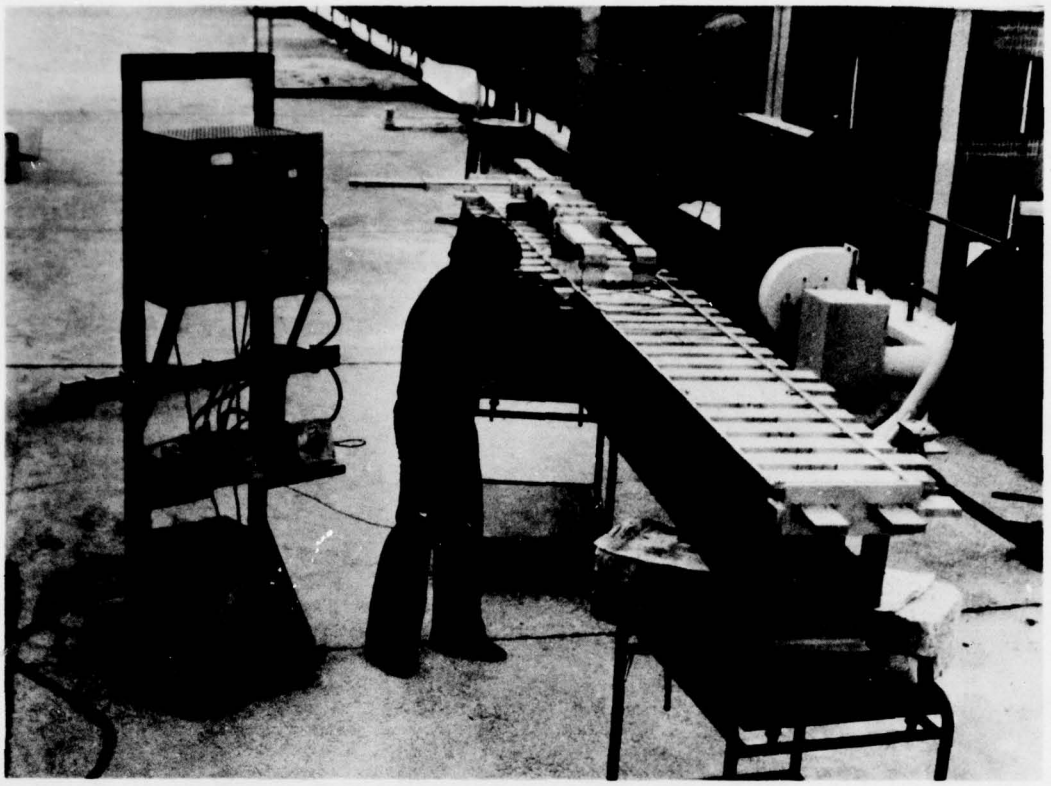

Fig.17 1st beam forming network during the tests

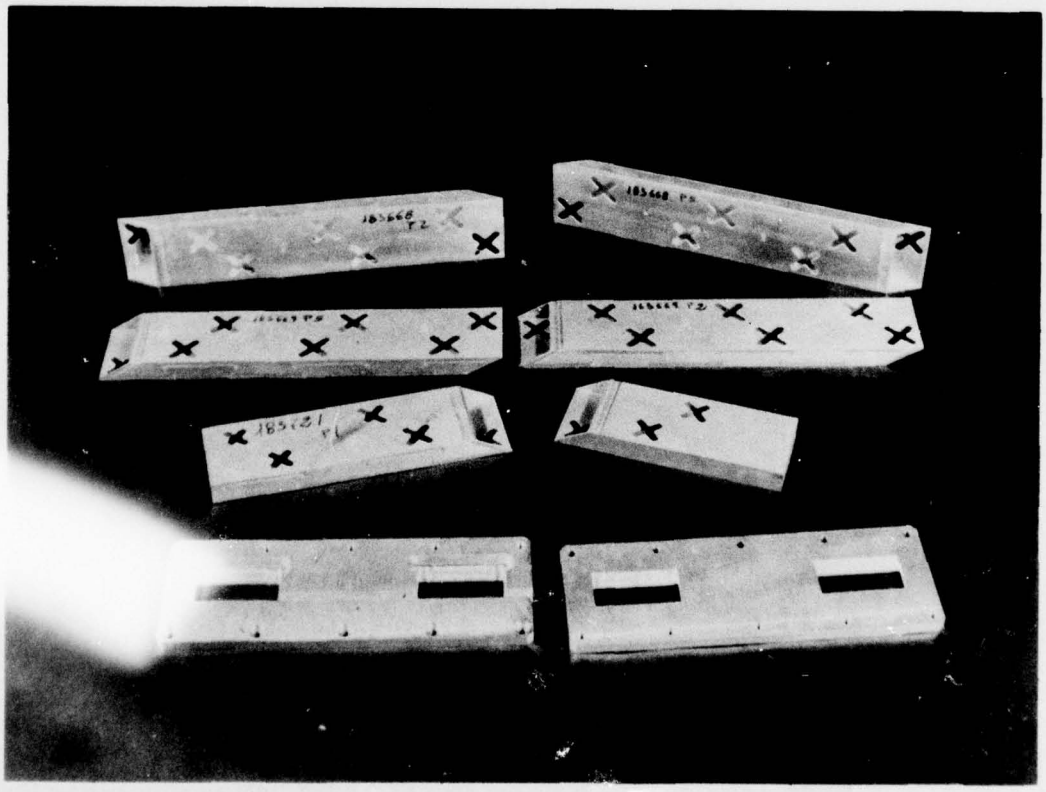

Fig.18 Machined parts of the beam forming network before assembling

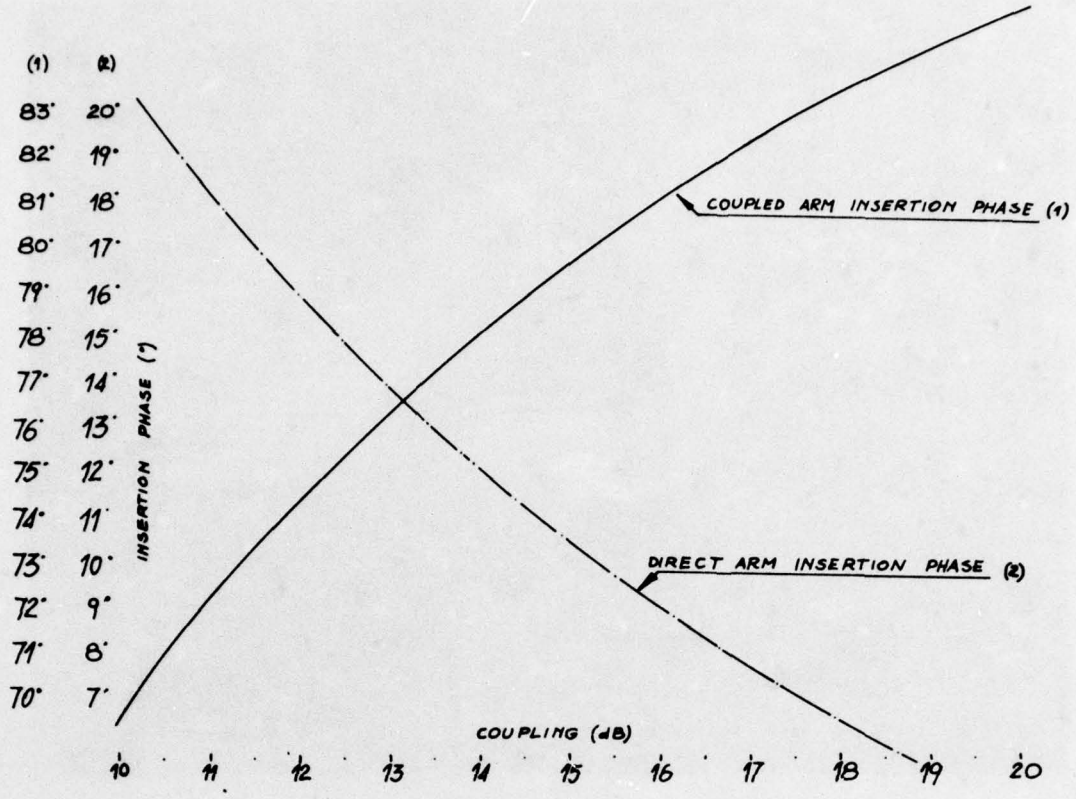

Fig.19 Directional coupler insertion phase

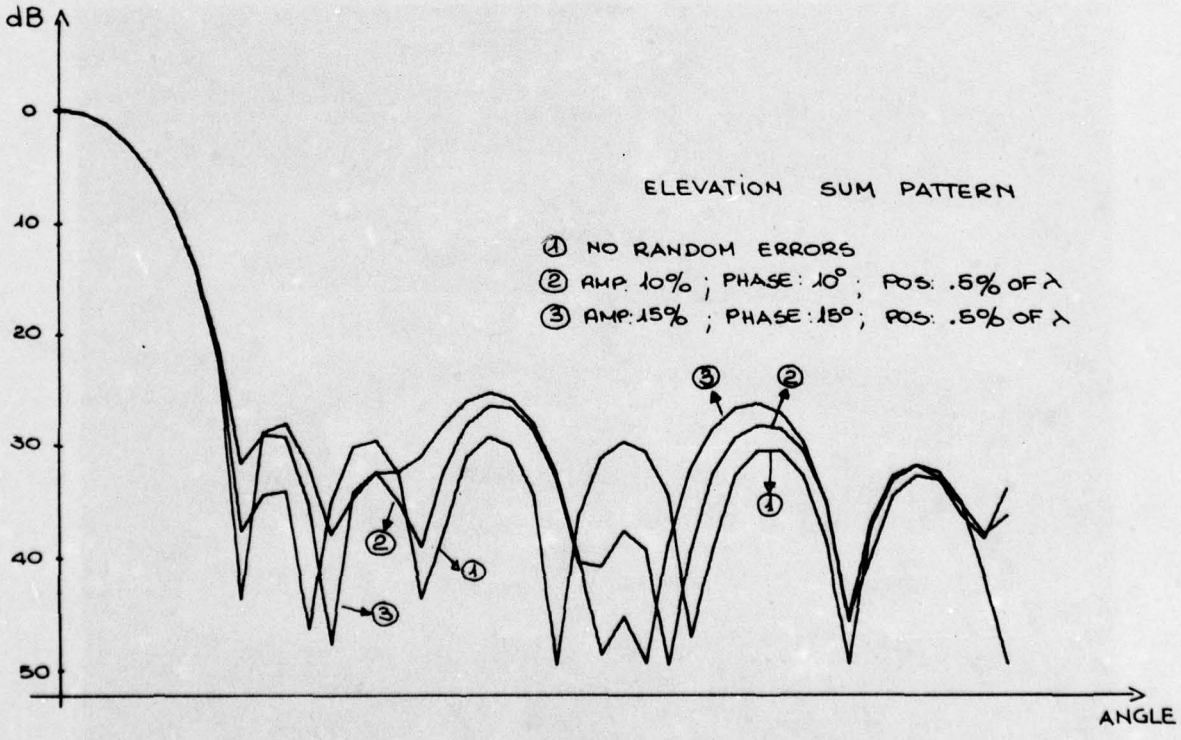

Fig.20 Calculated effect of random errors on radiation pattern

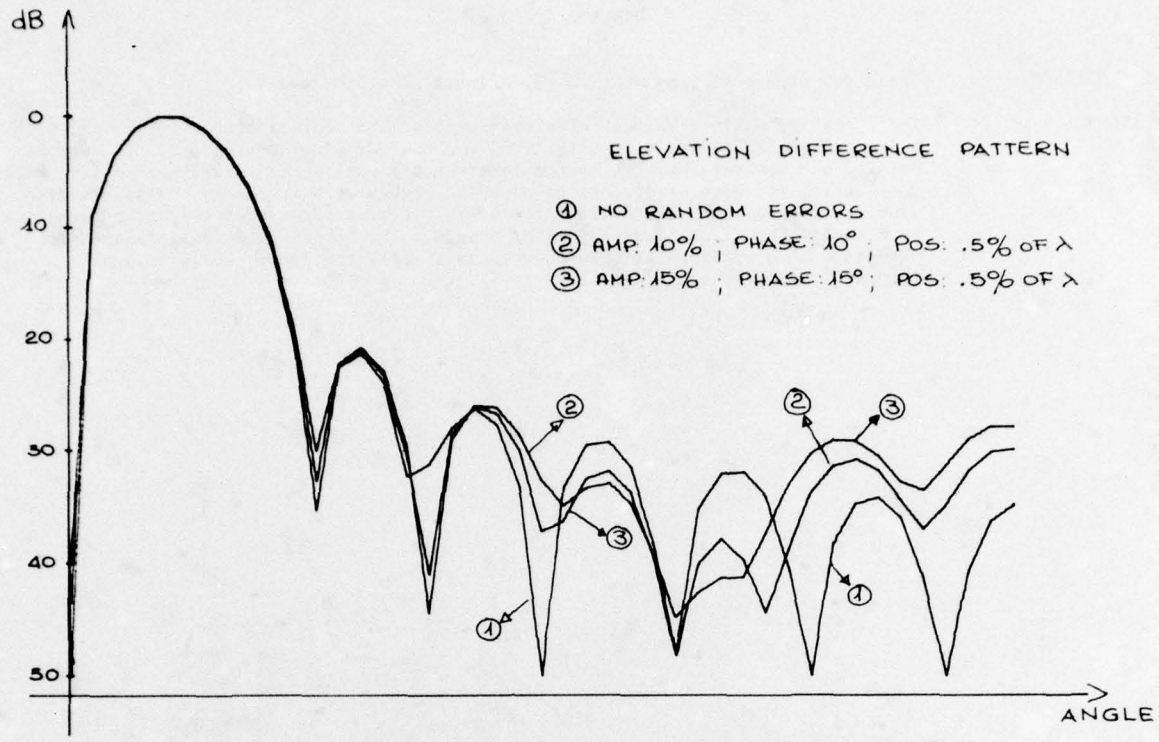

Fig.21 Calculated effect of random errors on radiation pattern

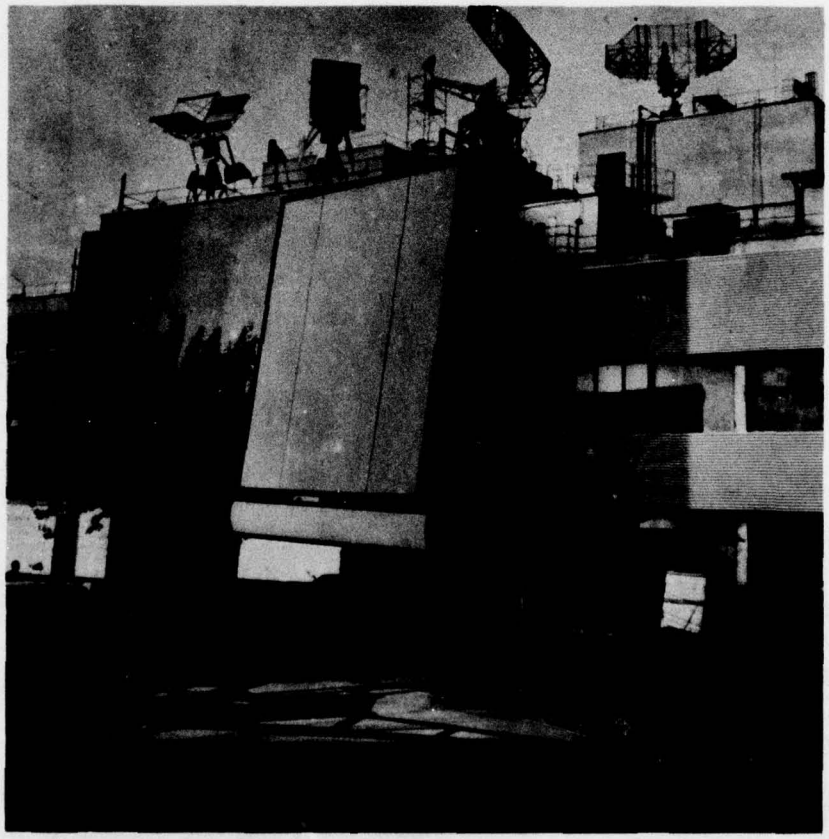

Fig.22 Antenna mock-up in one of the operational configuration

DISCUSSION

A L C QUIGLEY: Could you please tell me what is the azimuth sidelobe level?

B PALUMBO: The specified maximum azimuth sidelobe level of the near sidelobes is -23 dB, with a prescribed law of decay of this level for the far sidelobe regions. It must be pointed out however that the system requirements call for a sidelobe structure with deep nulls, the angular directions of which change with frequency. This requirement is essential for the utilisation of an automatic frequency selection technique to minimise the signal from a jamming source. The chosen solution (planar array) permits such a sidelobe structure, whereas a reflector system would give a 'plateau' type structure.

SECONDARY RADAR FOR AIRFIELD GROUND MOVEMENT MONITORING

H. N. Griffiths
Royal Signals and Radar Establishment
St. Andrews Road
Great Malvern
Worcestershire
WR14 3PS
United Kingdom

SUMMARY

Secondary radar is used for the in-flight identification of aircraft. An extension of the secondary radar technique is suggested for the identification and location of aircraft taxying on the airfield surface. This has sufficient positional accuracy for use alone or for the labelling of a high definition primary radar display of airfield ground movements.

The results of trials on an airfield site are discussed and experiments to determine the effects of ground reflections and aircraft self screening are described with polar diagrams of selected aircraft. Accurate position finding using trilateration is discussed.

1. INTRODUCTION

High definition primary radar sensors for ground movement monitoring of aircraft have been installed at some large airports to assist the ground movement controller at night or in poor visibility. In order to label the display the proposed system would utilise existing secondary radar transponders fitted to aircraft hence avoiding the need for any aircraft modifications which can be costly and difficult to implement.

Interrogation techniques for use on the airfield surface have been devised to minimise the garbling problem of overlapping replies which occurs with normal SSR. As shown in figure 1, the reply code is long (20.75 μsec) so replies from transponders up to 3 Km apart may overlap and garble. Transponders only reply to a correctly spaced pair of pulses (known as P_1 and P_3) which are normally sent from one transmitter at fixed spacing, 8 μsec for a mode 3/A identity reply.

By sending the pulses separately from 2 spaced transmitters narrow lanes of interrogation can be formed.

2. AREA INTERROGATION

For area interrogation the two pulses P_1 and P_3 are radiated separately from 2 antennas at opposite ends of the airfield (figure 2). The relative timing of the two pulses is controlled so that a P_1/P_3 pulse pair of 8 μsec spacing occurs somewhere between the two transmitters. Because of the transponder acceptance tolerance to P_1/P_3 spacing, a hyperbolic lane of response is formed: as explained in Appendix 3 the width of this lane is typically 150 metres for a good commercial transponder but can increase to 300 metres for the worst case transponder permitted by the ICAO specification. By stepping the P_1/P_3 timing, the position of the interrogation lane can be repeatedly swept between the two transmitting sites.

As shown in figure 3 the addition of a directional scanning antenna at one transmitting site reduces the area of interrogation to the area of overlap of the beam with the hyperbolic lane. A complete scan of a sector is performed by a combination of rapid lane sweeping (range scan) with rotation of the antenna beam (azimuth scan).

3. GROUND MOVEMENT TRIAL SITE

The technique of area interrogation has been proven on the trial site on Pershore airfield (figure 4). A scanning antenna at the P_1 site with a beamwidth of approximately 9° covers a 90° sector bounded to the north by a line of 3 metal hangars and to the south by the airfield perimeter track on which there are 3 round concrete dispersal pads for aircraft. All 3 runways cross the site. The main features of the site are indicated on the CRT graticule with the real time display of transponder replies.

The early display showed each correctly decoded reply received by the scanning antenna as a dot on the screen (figure 5). The timebase was stepped in range in synchronism with the 15 metre increments of the interrogation lane so that a sequence of replies from one transponder appeared as a line of dots in range. Similarly all the replies across the scanning beamwidth were displayed so that a complete set of replies formed a rhombus with the transponder at its 'centre of gravity'. This experimental display had the merit of simplicity but presented plot extraction problems as well as demanding a high number of replies from each transponder to obtain sufficient positional accuracy.

Improved positional accuracy and a simplified display have now been achieved by bilateration.

4. BILATERATION

Two receivers sited at the ends of the baseline are used to obtain accurate rangefinding on transponder replies by measuring the difference of arrival times of the leading edge of the first framing pulse (F_1) between both sites. The timing information from the remote site is sent back to the main site as a single pulse on 1030 MHz. A counter, clocked at 10 MHz is started by the direct framing pulse and stopped by the remote framing pulse. The output of the counter converted to analogue form provides the X deflection (Range) for the CRT display (figure 6). Decoders are used for the validation of the identity of each

plot. Typical bilateration displays are shown in figures 7, 8 and 9. A group of returns from a transponder appears as single 'paint' similar to a normal PPI picture. Ranging accuracy of the experimental system is high, better than 15m on baseline. Figure 7 shows a beamwidth of replies from a transponder sited on a concrete dispersal pad (lower centre). Figure 8 shows replies from a transponder alongside No 1 hangar (top left). Figure 9 shows direct replies from a transponder near No 2 hangar (top centre) with a reflection (upper top centre) caused by a reflecting interrogation and reply path via the metal sides of No 1 hangar.

Since the high positional accuracy of bilateration has been demonstrated it is reasonable to assume that trilateration (position finding using 3 receiving sites) will provide the necessary position finding accuracy on transponder replies.

5. AIRCRAFT POLAR DIAGRAMS

The feasibility of ground movement monitoring of transponder equipped aircraft depends on the ability of the system to interrogate transponders whose antennas are mounted on the underside of the aircraft fuselage. The aircraft transponder antenna can be screened at certain angles by parts of the aircraft such as undercarriage, engines etc. To measure the extent of screening, polar diagrams have been plotted for various aircraft using the method and apparatus described in Appendix 1.

The results for 4 aircraft types are summarised below:

(i) Meteor

Picture - figure 10
Polar diagram - figure 14

An obsolete fighter aircraft with lower transponder antenna mounted on the underside of the tail boom, 1.76 metres above the ground. Good coverage over 280° the transponder antenna screened for approximately 40° either side of the nose by the undercarriage legs and the engine nacelles. The minima are approximately 15 dB down on the unscreened signal power.

(ii) Hastings

Picture - figure 11
Polar diagram - figure 15

An obsolete 4 engined military aircraft with tail wheel undercarriage. A transponder antenna was positioned for the experiment in the expected worst case lower antenna position, between the main wheels of the undercarriage with the antenna only directly visible 70° either side of the nose. The depths of the signal minima vary from 15 to 25 dB down on the direct signal power.

(iii) Varsity

Picture - figure 12
Polar diagram - figure 16

A twin engined propeller driven military training aircraft with tricycle undercarriage. The lower transponder antenna is mounted beneath the fuselage towards the tail at a height of 1.07 metres. The antenna is screened by the undercarriage (0° nose, 30° main legs) and also by the fuselage up to 15° either side of the nose. The signal minima are approximately 15 dB down on the direct signal power.

(iv) Concorde

Picture - figure 13
Polar diagram - figure 17

The most modern of the aircraft measured. The transponder antennas are mounted beneath the fuselage in front of the nosewheel leg at a height of 4 metres.

6. CONCLUSIONS

Ground movement identification of aircraft using their SSR transponders is feasible. High positional accuracy is possible using trilateration. The screening effects of aircraft structure are not as dominant as originally thought, especially with modern civil aircraft. The propagation trials indicate that there is no optimum antenna height for the ground interrogators. The best overall coverage at ranges greater than 250m occurs with a high antenna (16 metre height). Closer than 250m a lower antenna is a better choice, but the coverage beyond 250m is markedly inferior (worse than 12 dB down on 16 metre antenna).

7. ACKNOWLEDGEMENTS

The author is grateful to the Civil Aviation Authority for funding the work on airfield ground movement monitoring. The assistance of the British Aircraft Corporation and the Department of Trade and Industry during the Concorde polar diagram measurements is also gratefully acknowledged.

Normal Secondary Radar Interrogation (Mode 3/A)

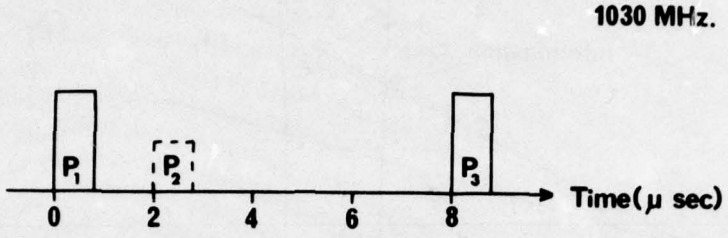

Identity Reply

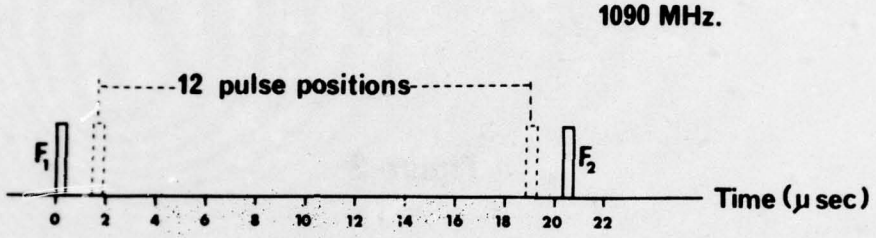

Figure 1

Use of 2 Transmitters to generate Lane of Interrogation

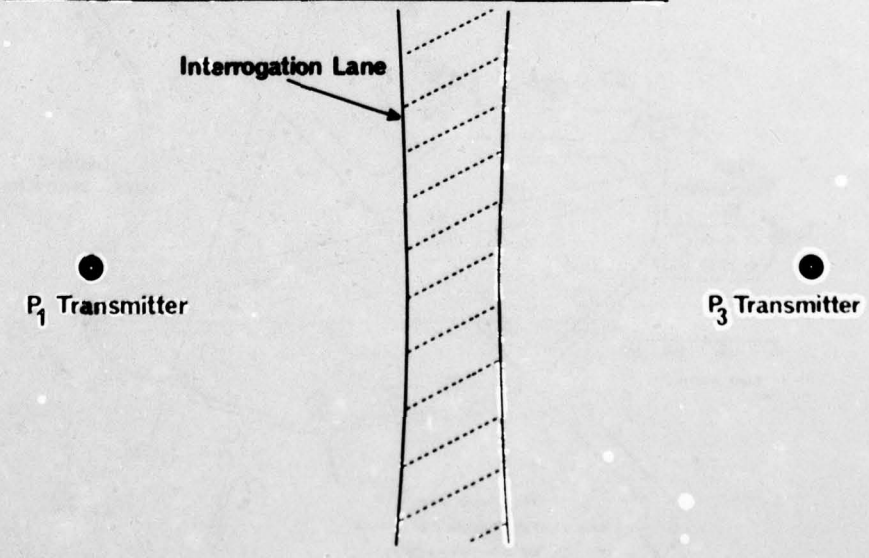

Figure 2

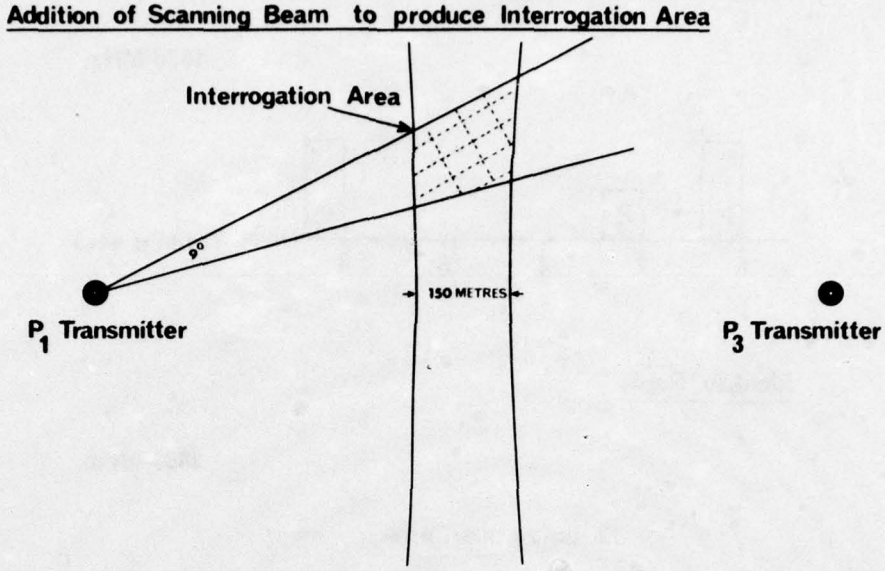

Figure 3

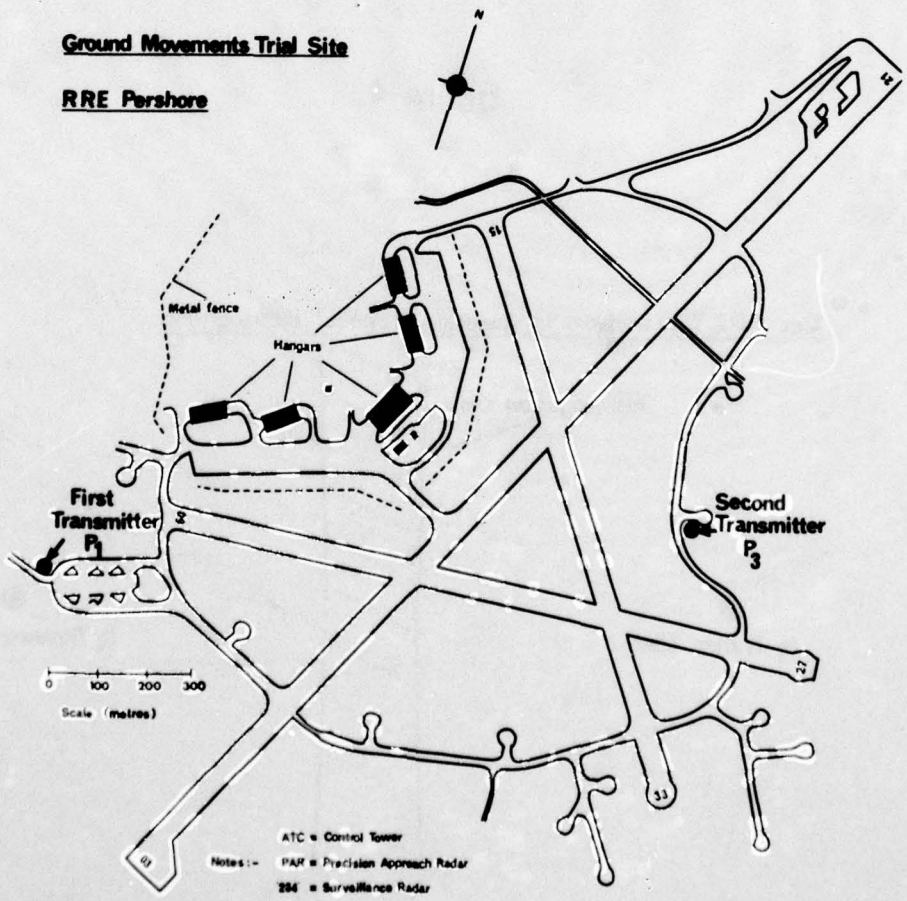

Figure 4

Experimental Display

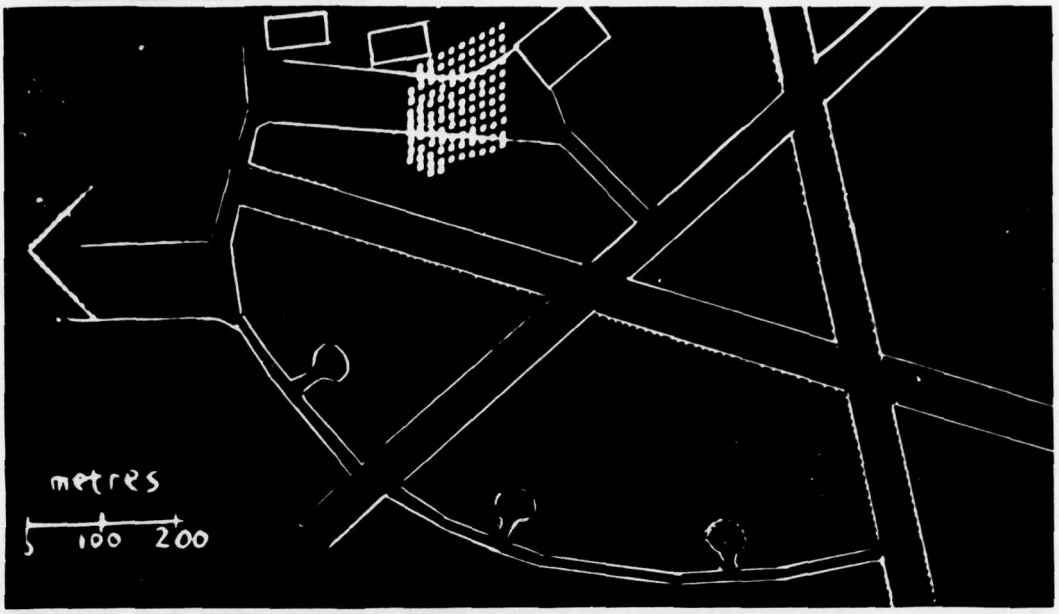

Figure 5

Trial Equipment

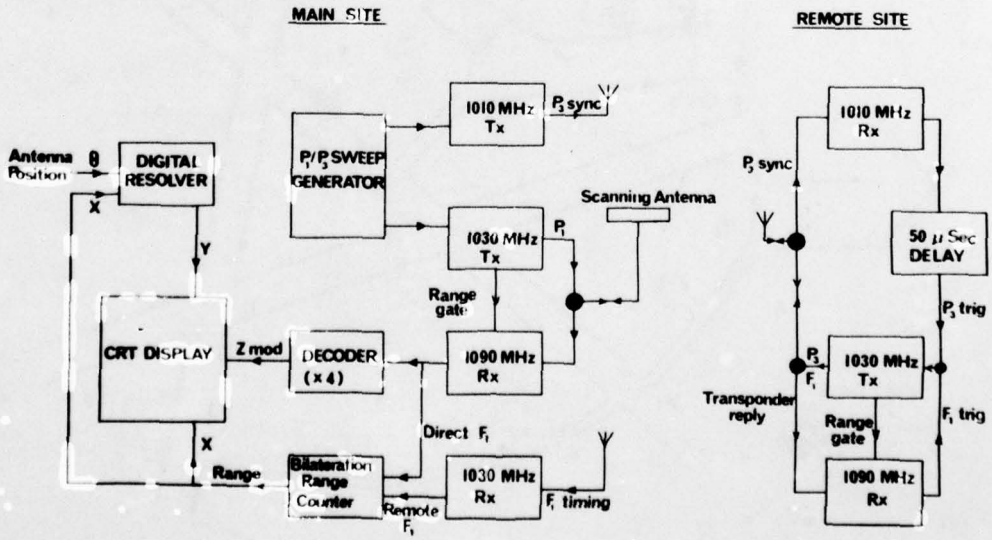

Figure 6

Bilateration Display(1)

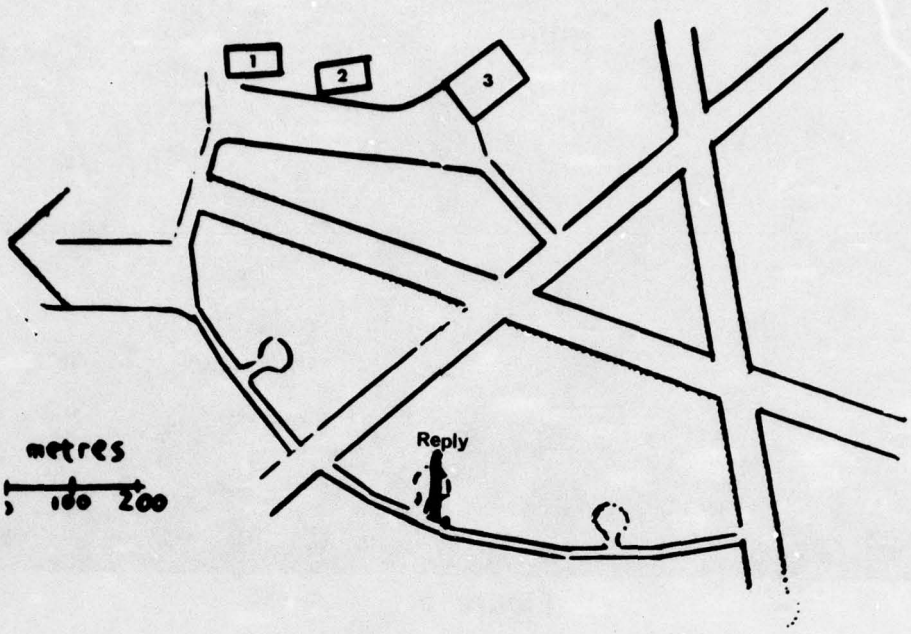

Figure 7

Bilateration Display(2)

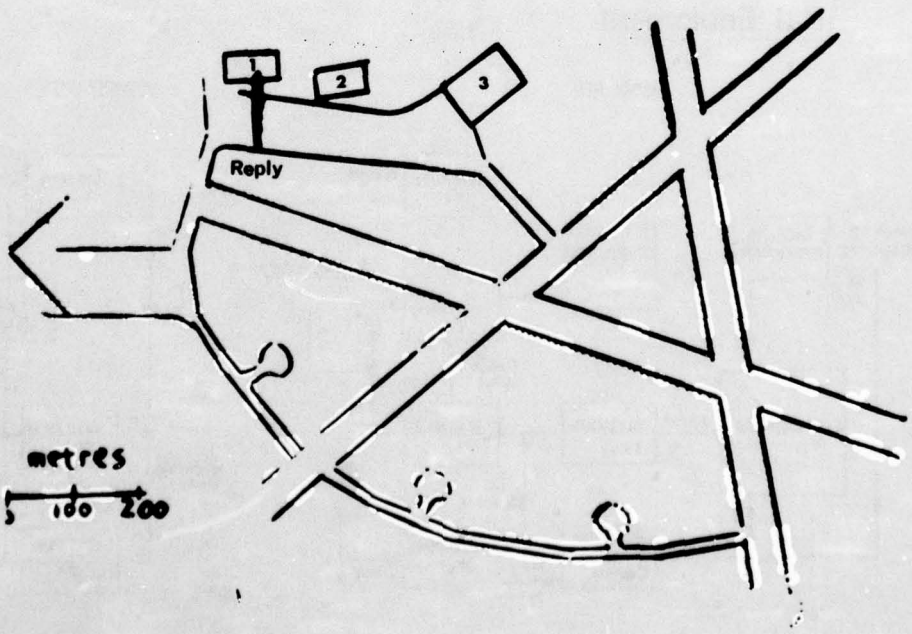

Figure 8

Bilateration Display (3)

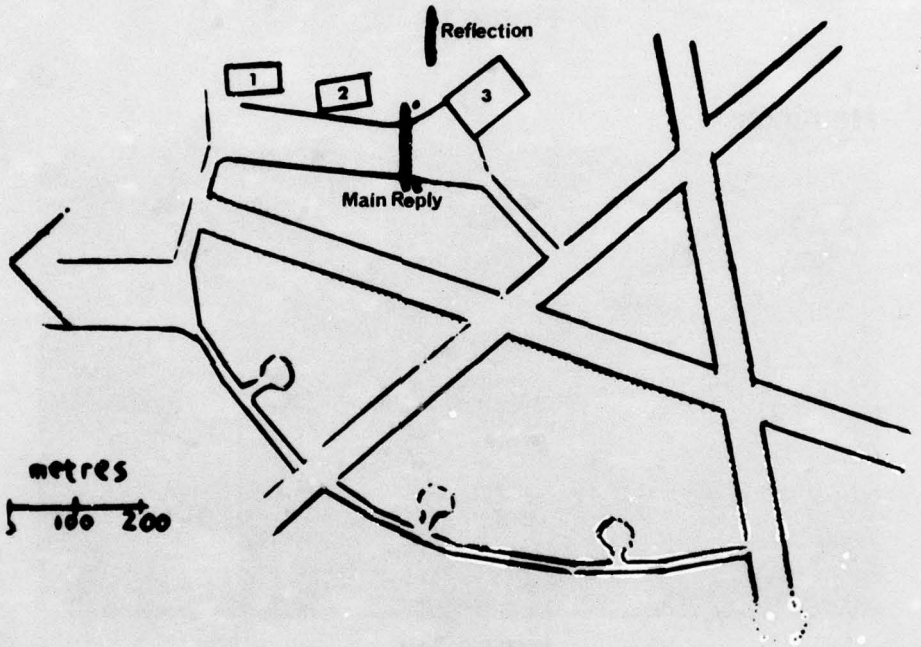

Figure 9

Meteor

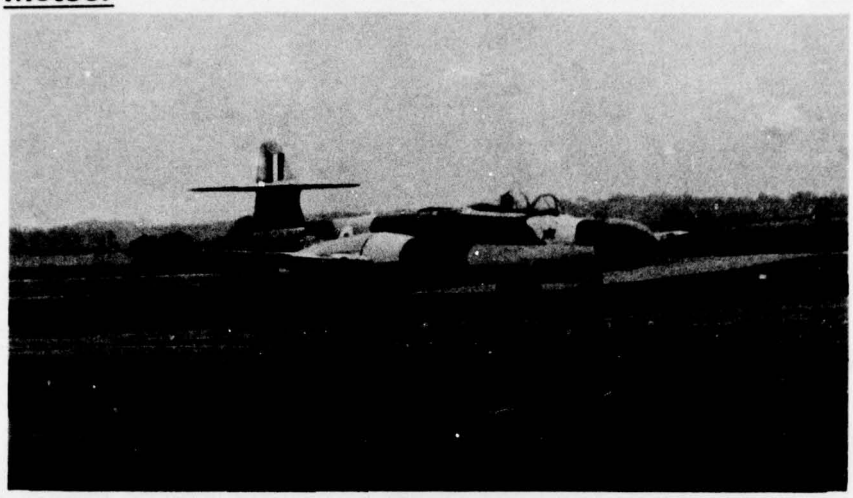

Figure 10

Hastings

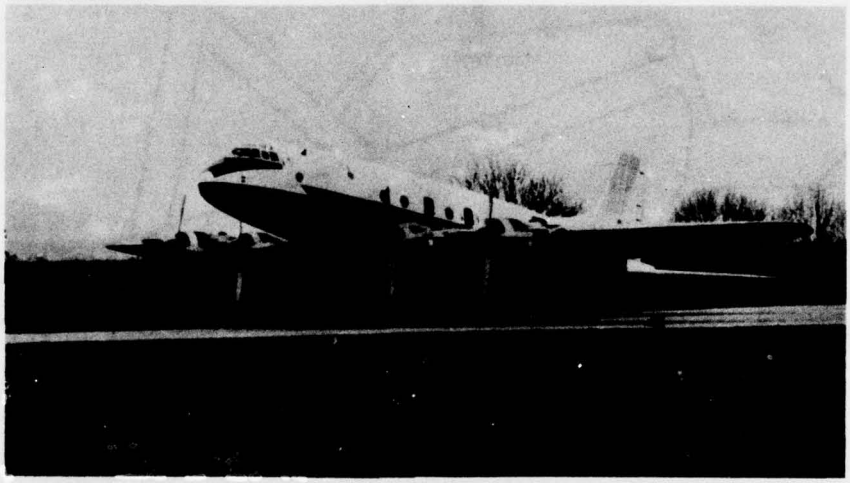

Figure 11

Varsity

Figure 12

Concorde

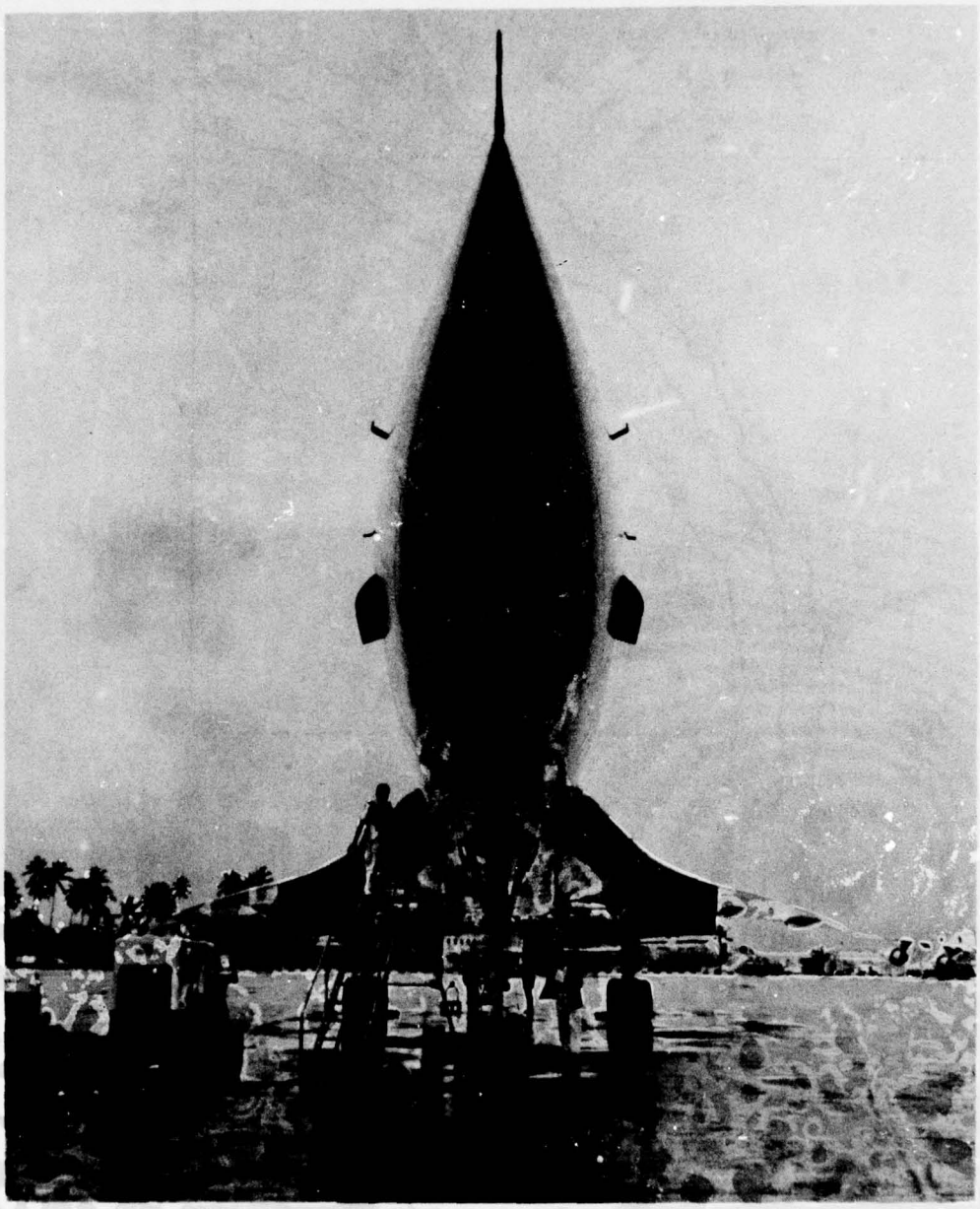

Figure 13

By courtesy of British Aircraft Corporation, Filton, Bristol.

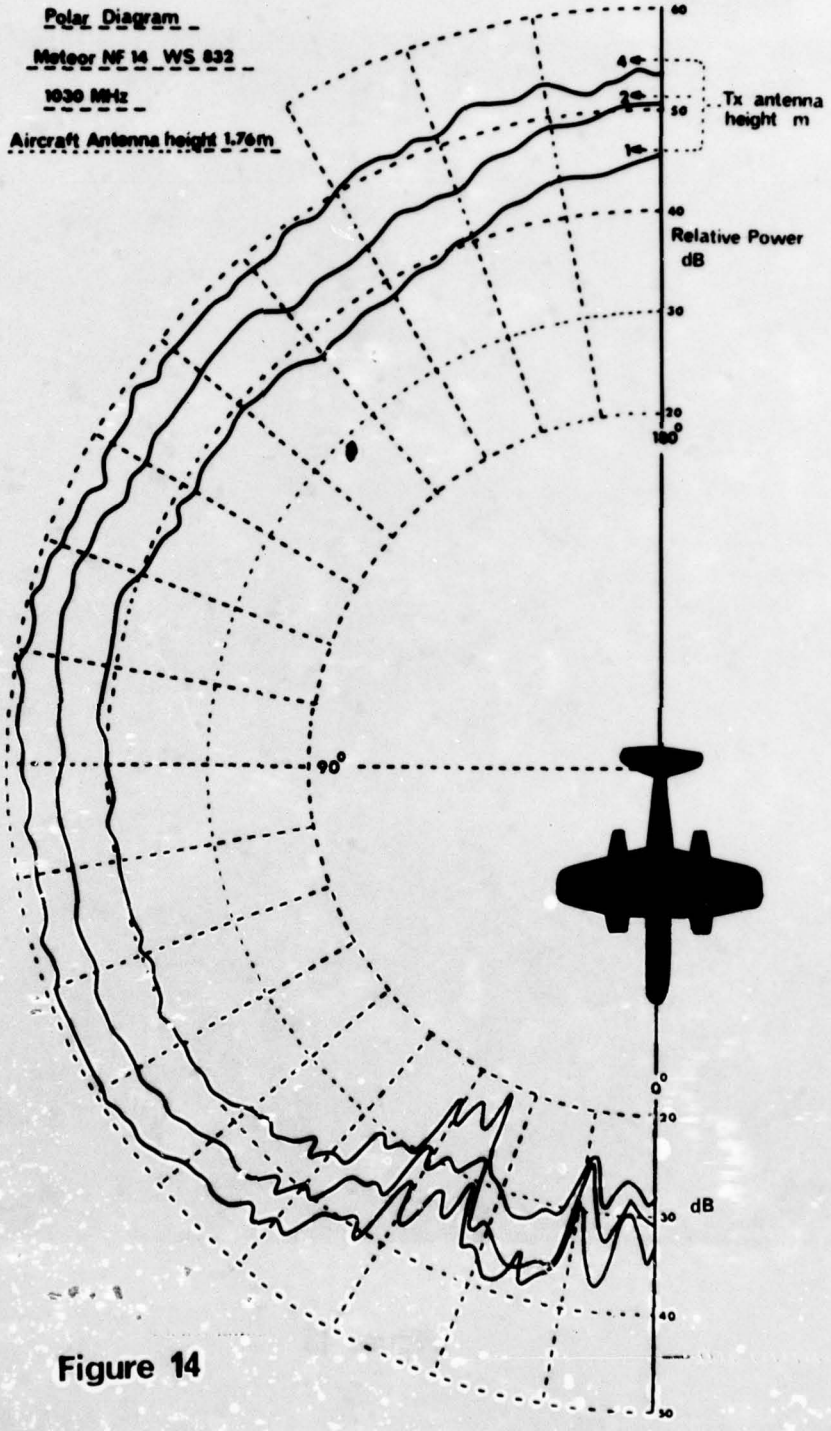
Polar Diagram
Meteor NF 14 WS 832
1030 MHz
Aircraft Antenna height 1.76m
Tx antenna height m
Relative Power dB
dB
90°
180°
0°

Figure 14

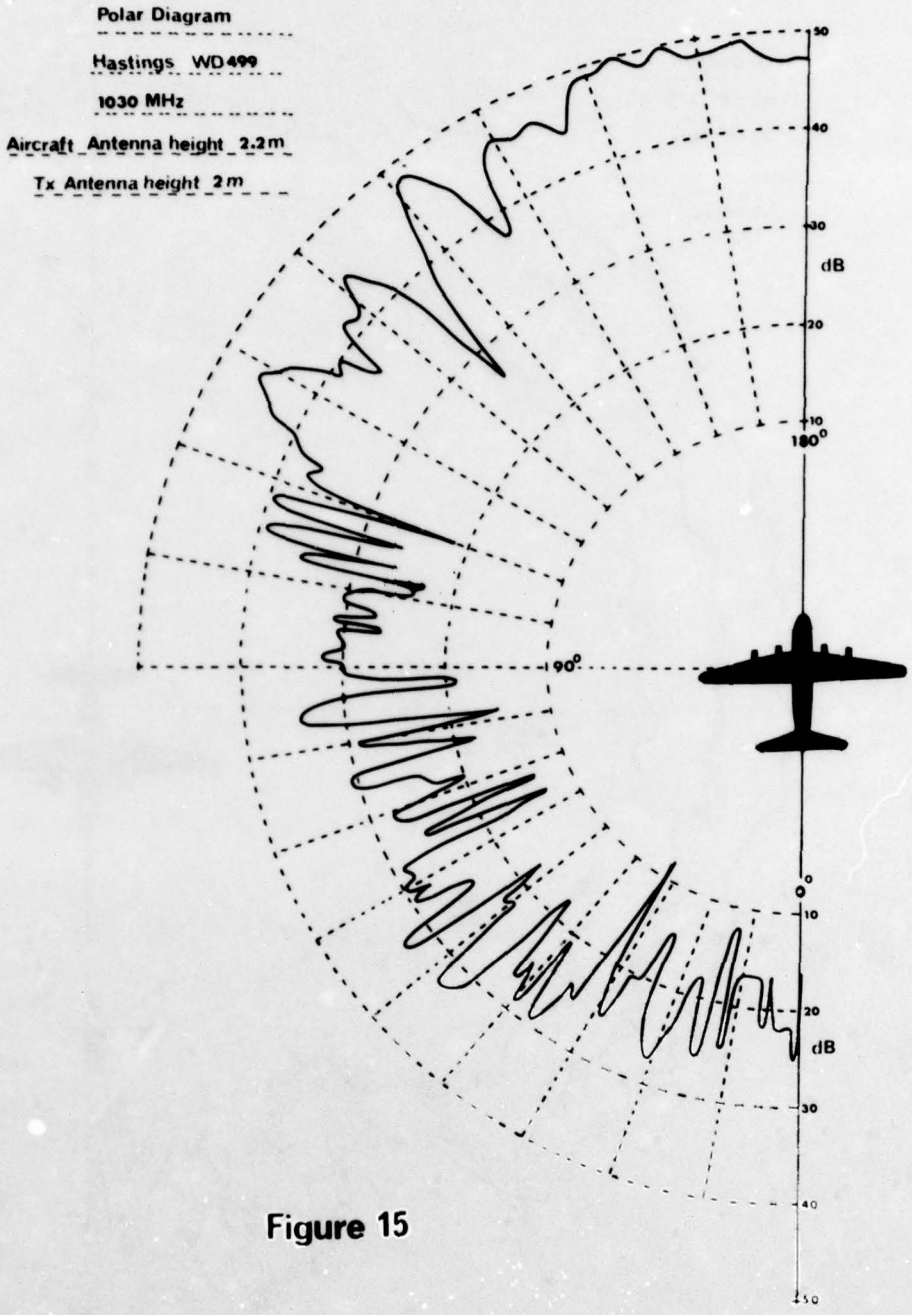
Polar Diagram
Hastings WD499
1030 MHz
Aircraft Antenna height 2.2m
Tx Antenna height 2m
50
40
30
dB
20
10
180°
90°
0°
10
20
dB
30
40
50

Figure 15

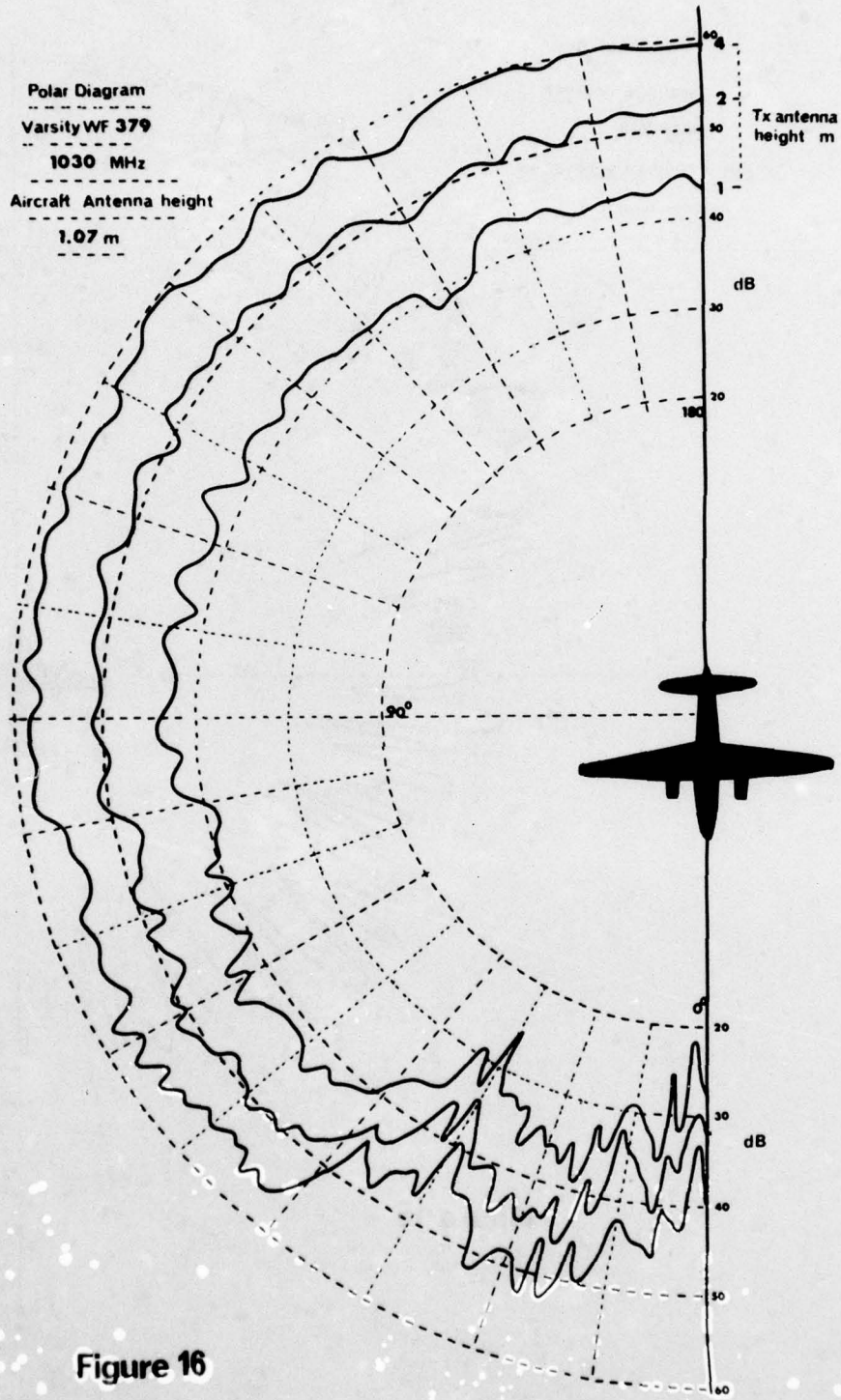
Polar Diagram
Varsity WF 379
1030 MHz
Aircraft Antenna height
1.07 m
Tx antenna height m
4
2
1
dB
90°
0°
dB

Figure 16

Interrogator for Polar Diagram measurement

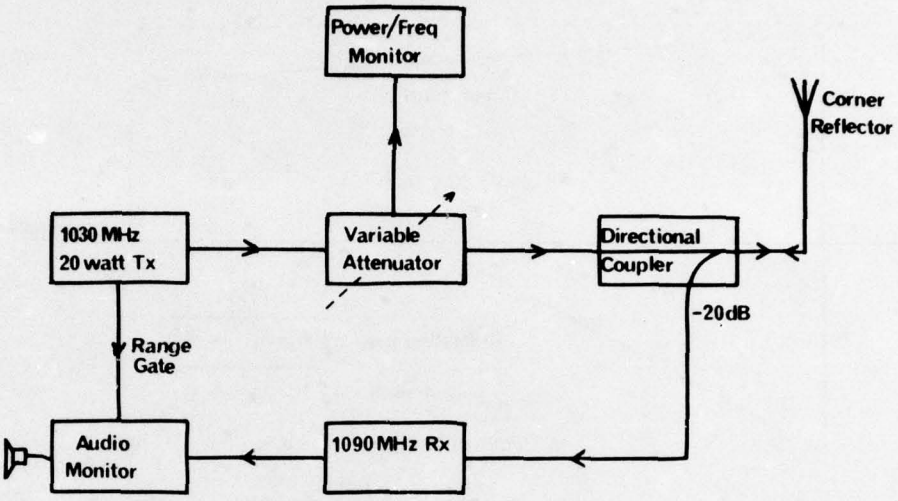

Figure 18

Measurement Trolley

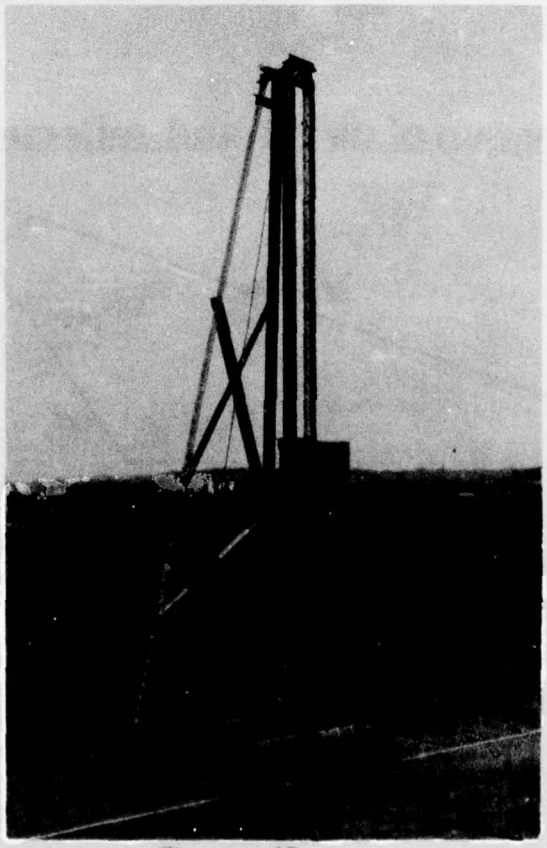

Figure 19

Geometry of direct and reflecting paths

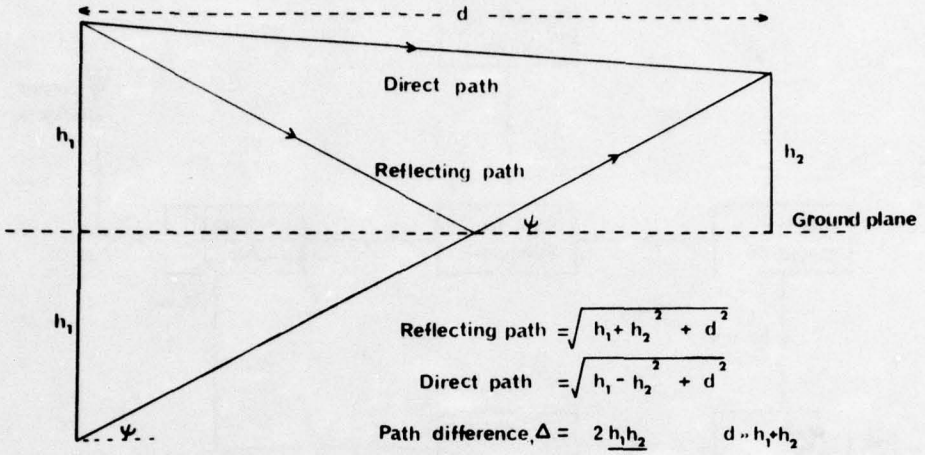

Reflecting path $= \sqrt{h_1 + h_2^2 + d^2}$

Direct path $= \sqrt{h_1 - h_2^2 + d^2}$

Path difference, $\Delta = \frac{2 h_1 h_2}{d}$ $\quad d \gg h_1 + h_2$

Grazing angle $\psi = \tan^{-1} \frac{h_1 + h_2}{d}$

Figure 20

Vector diagram of direct and reflected signals

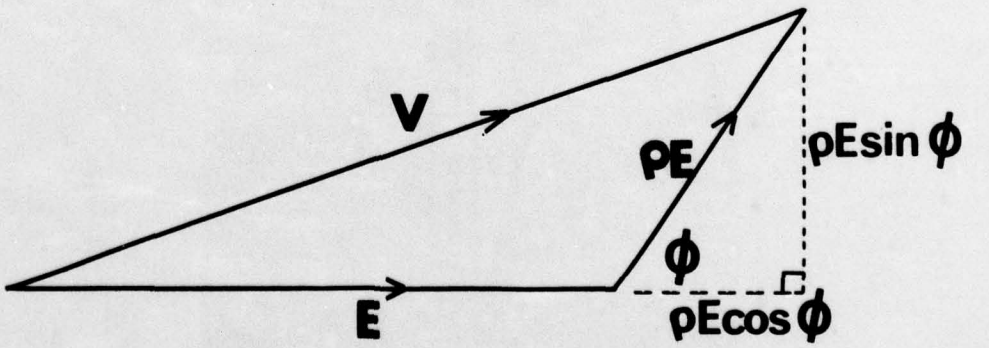

E = Direct

ρE = Reflected

V = Resultant

Figure 21

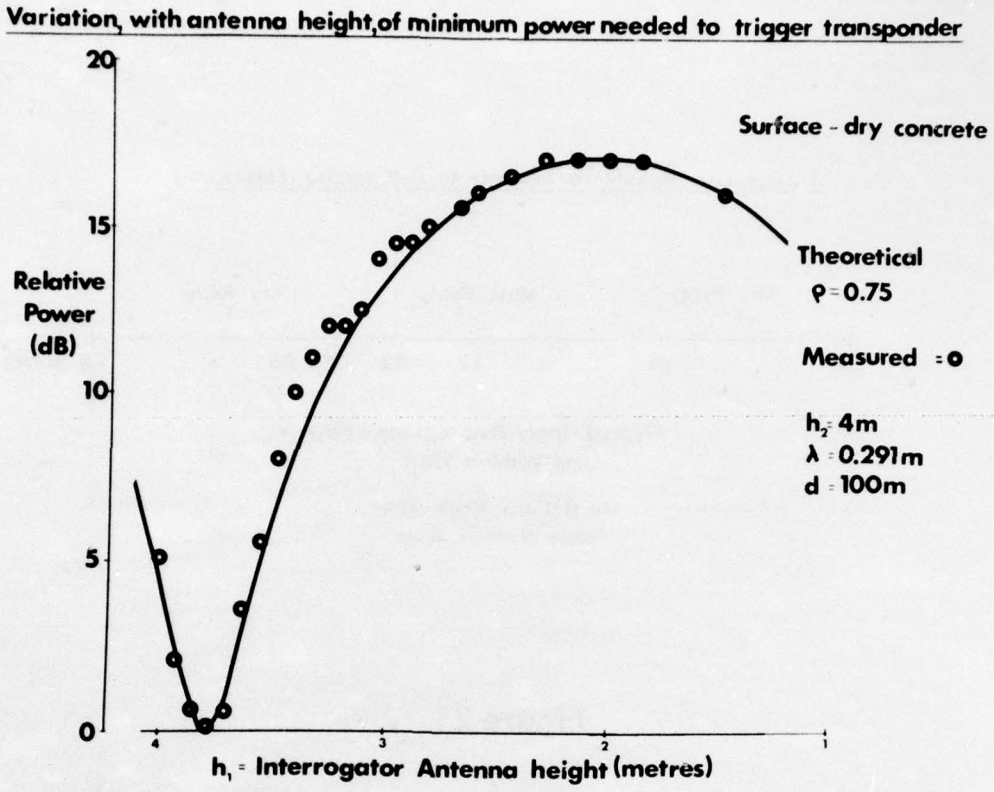

Figure 22

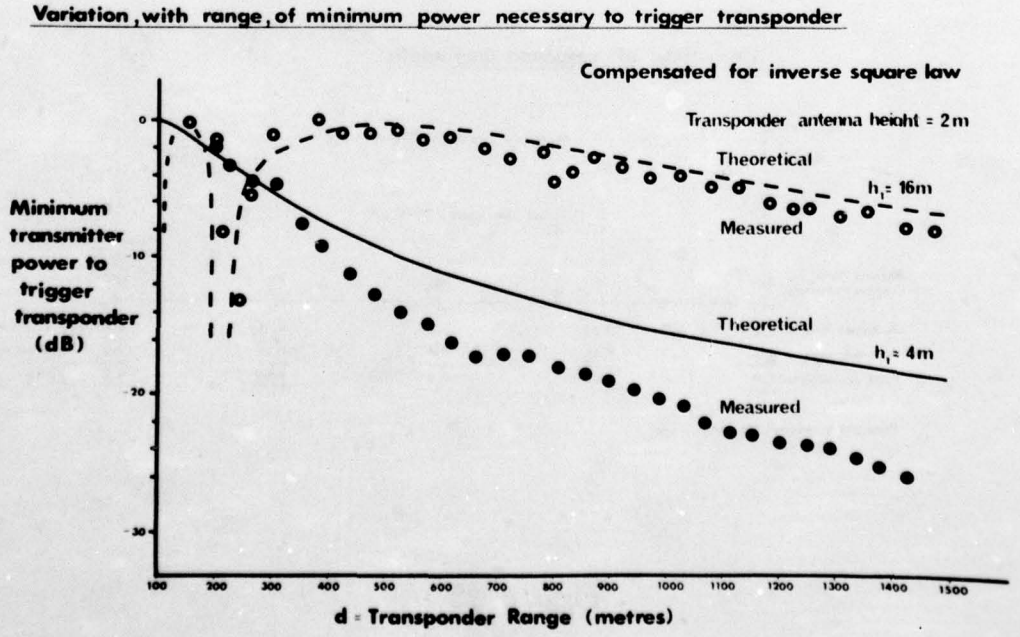

Figure 23

AD-A040 144 ADVISORY GROUP FOR AEROSPACE RESEARCH AND DEVELOPMENT--ETC F/G 17/9
NEW DEVICES, TECHNIQUES AND SYSTEMS IN RADAR.(U)
FEB 77

UNCLASSIFIED AGARD-CP-197 NL

7 OF 7
AD
A040144

END

DATE
FILMED
6-77

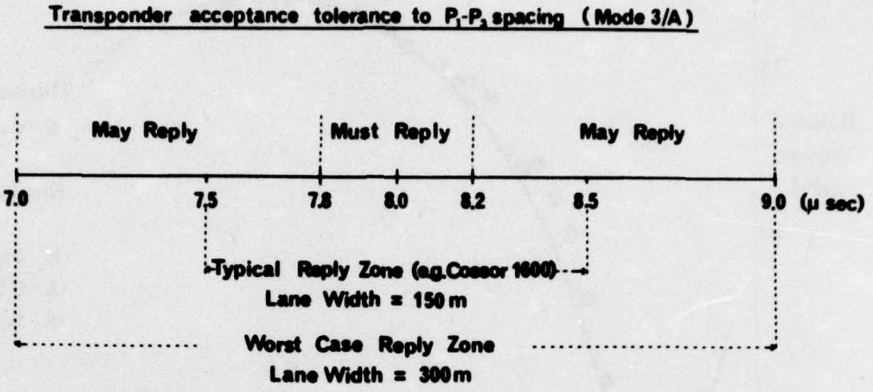

Figure 24

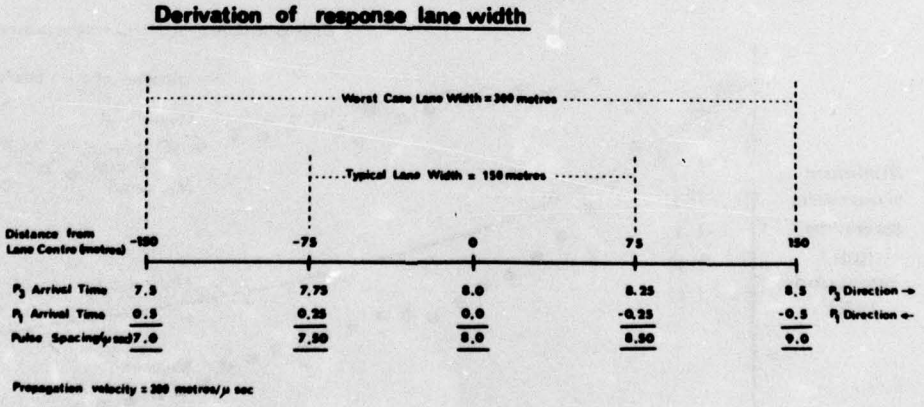

Figure 25

APPENDIX 1

THE MEASUREMENT OF POLAR DIAGRAMS OF TRANSPONDER EQUIPPED AIRCRAFT

The aircraft is positioned at the centre of a 100 metre radius circle. A mobile secondary radar interrogator is moved around the circle in 1 degree steps. At each position the transmitter power is adjusted with a variable attenuator until the transponder just triggers. Antenna heights of 1, 2 and 4 metres are normally used.

Figure 18 shows a block diagram of a mobile interrogator. The 1030 MHz transmitter has a peak power of 20 watts and a PRF of 250 Hz. All normal SSR modes can be selected, and transmitter power output and frequency are monitored. The variable attentuator has a range of insertion loss from 6 dB to 120 dB. Antenna height is adjustable from 0.5 metres to 4 metres. Transponder replies on 1090 MHz are range gated and used to trigger an audio monitor.

The interrogator trolley is shown in figure 19. A corner reflector antenna, set at 2 metres can slide vertically for adjustment. The base of the trolley supports the interrogator, battery pack and monitoring equipment. Polar diagrams measured with this equipment are given in figures 14, 15, 16 and 17 and are discussed in the text in section 5.

APPENDIX 2

THE EFFECT OF GROUND REFLECTION ON PROPAGATION BETWEEN 2 ANTENNAS

Since, at L band, the airfield surface may be assumed to be a smooth reflecting surface at low grazing angles it is possible to estimate the effects of the ground reflection using simple image theory:

Figure 20 shows the geometry of the direct and reflecting paths between two antennas heights h_1 and h_2 above a reflecting ground plane, spaced by a distance d

By simple geometry

$$\text{Direct path} = \sqrt{d^2 + (h_1 - h_2)^2}$$

$$\text{Reflecting path} = \sqrt{d^2 + (h_1 + h_2)^2}$$

$$\text{Path difference, } \Delta, = \sqrt{d^2 + (h_1 + h_2)^2} - \sqrt{d^2 + (h_1 - h_2)^2}$$

$$\Delta = \frac{2h_1h_2}{d} \quad \text{providing } d \gg h_2 + h_1 \tag{1}$$

For vertical polarisation, the phase shift ϕ between reflected and direct signals $= \pi + \frac{2\pi\Delta x}{\lambda}$

(fixed term π comes from 180° phase shift of reflected signal at low grazing angles ($<10^\circ$ at L band))

$$\text{Hence } \phi = \pi\left[1 + \frac{4h_1h_2}{\lambda d}\right] \tag{2}$$

Figure 21 shows the vector relationship between the direct and reflected signals:

$$V^2 = E^2 (1 + \varrho \cos\phi)^2 + E^2 \varrho^2 \sin^2\phi$$

$$= E^2 (1 + \varrho^2 + 2\varrho \cos\phi)$$

$$= E^2 \left(1 + \varrho^2 + 2\varrho \cos\pi\left[1 + \frac{4h_1h_2}{\lambda d}\right]\right) \tag{3}$$

When direct and reflected signals are in phase

$$V_{max} = E(1 + \varrho)$$

When direct and reflected signals are in antiphase

$$V_{min} = E(1 - \varrho)$$

$$\text{Hence } \frac{\text{Power max}}{\text{Power min}} = \frac{V_{max}^2}{V_{min}^2} = \left(\frac{1+\varrho}{1-\varrho}\right)^2$$

$$\left[P_{max} - P_{min}\right]_{dB} = 20 \log \left(\frac{1+\varrho}{1-\varrho}\right) \tag{4}$$

Hence by varying the interrogator antenna height (h_1) and measuring the maximum and minimum powers needed to trigger a transponder distant d with aerial height h_2 it is possible to obtain an estimate of the average reflection coefficient (assumed constant over the range of grazing angles used).

The results of such an experiment are given in figure 22. The 1030 MHz interrogator antenna height h_1 was slowly reduced from 4 metres to 1 metre and measurements were made of the minimum interrogator power needed to trigger a transponder with its antenna height h_2 fixed at 4 metres and with 100 metres spacing between the antennas. The measured points can be compared with the theoretical curve (plotted from equation 3) for reflection coefficient $\varrho = 0.75$.

$$\text{The grazing angle } \psi = \tan^{-1}\left[\frac{h_1 + h_2}{d}\right] \tag{5}$$

Hence for signal minimum $\psi = 4.6^\circ$
maximum $\psi = 3.4^\circ$.

At much shallower grazing angles it may be assumed that $\varrho \rightarrow 1$ ($d \geqslant 100$m, $h_2 = 2$m, $h_1 \leqslant 16$m, $\lambda = 0.291$m).

Using this assumption figure 23 shows theoretical and measured interrogation powers needed to trigger a transponder at range d metres. Inverse square law propagation is assumed and the actual powers used are therefore range corrected.

It is seen that the 16 metre antenna gives much better coverage at long range ($\geqslant$250 metres), whereas the 4 metre antenna gives optimum coverage closer than 250 metres where the nulls of the 16 metre antenna pattern occur.

The rate of decline of signal power for the 4 metre antenna height is higher than theoretically predicted. This is because the site is not in fact, flat but slightly dome shaped which means that the effective antenna heights are reduced at range.

APPENDIX 3

THE EFFECTS OF TRANSPONDER P_1/P_3 ACCEPTANCE TOLERANCE ON LANE WIDTH

ICAO specification limits exist which define the P_1/P_3 acceptance tolerance for aircraft transponders. These are:

Transponder must reply if P_1/P_3 spacing is within Normal Mode $\pm$ 0.2 μsec.

Transponder may reply if P_1/P_3 spacing is within Normal Mode $\pm$ 1.0 μsec.

Transponder must not reply if P_1/P_3 spacing is outside Normal Mode $\pm$ 1.0 μsec.

Figure 24 shows these limits for a mode 3/A interrogation and indicates that a typical commercial transponder such as the Cossor 1500 will respond only over the range 7.5 to 8.5 μsec.

Figure 25 shows the effect of transponder P_1/P_3 tolerance limits on lane width for both a typical and a worst case transponder. For the typical transponder the lane width is 150 metres and for the worst case transponder the lane width is 300 metres.

DISCUSSION

Y BRAULT: Avez vous l'intention d'utiliser a système pour le guidage des avions en Cat 3 sur le pistes?

H N GRIFFITHS: Ground movement identification would be exceptionally useful in category 3 conditions, but would also be valuable in congested traffic conditions.

P BRADSELL: Has there been any sign of malfunction, during the trials, caused by local SSR interrogators operating in the normal surveillance mode?

H N GRIFFITHS: On the trial site at Pershore, little interference was experienced since the nearest interrogator is more than 20 miles away. At Heathrow, on the other hand, interrogations and sidelobe suppression from the local secondary radar make it essential that the ground movement interrogations be synchronised with the 500 microsecond dead time of the local airfield SSR.

RADAR WIND MEASUREMENT SYSTEM

G. Rosenberg
Norwegian Defence Research Establishment
P O Box 25 - N-2007 Kjeller
Norway

SUMMARY

An all solid state low power X-band radar for wind profile determination in the lower atmosphere is described. Measurements of wind velocity and direction are made by tracking a balloon-borne corner-reflector.

Angle tracking is performed manually with the aid of the angle error signal which is presented on a liquid crystal display.

A Gunn oscillator/Impatt amplifier combination gives a 1 - 2 W output which is biphase modulated using Barker and modified Barker codes. A maximum range of 10 km is achieved using four range zones with pulse lengths from 0.28 to 47 μs. A correlation receiver with double IF is used, the active demodulation being performed in the second mixer. Video integration is performed digitally by a microcomputer which also guides target acquisition and range tracking.

The microcomputer samples range, angle and angle error information and calculates wind speed and direction, which is presented in height zones according to NATO-standard format.

1. INTRODUCTION

This paper presents an all solid state X-band radar for wind profile determination in the lower atmosphere. The radar is being developed as part of a meteorological observation and data processing system for the Norwegian field artillery.

A number of different techniques have been employed for wind profile determination. However, only radio frequency based systems have the necessary all-weather capability when range requirements exceed 1 km. Furthermore, in order to minimize total costs a radar system with a passive device for wind tracing, such as a balloon-borne corner-reflector, is the most appropriate solution. Military systems of this kind include the AMET-system in the United Kingdom and the French SIROCCO.

Basic field artillery requirements for a meteorological observation system are determined by two factors:

- The scale and frequency of variations in the meteorological fields.
- The deployment pattern, engagement distances and mobility requirements in tactical field artillery operations.

A careful analysis based on these factors gave the initial terms of reference which defined a short range (10 km) system suited for small unit operations. This implies a limited physical size and a minimum personnel requirement. Technologically this favours an all solid state system which is advantageous from a ruggedness and reliability point of view, and offers an improvement against detection by enemy search receivers as compared to a conventional radar.

In order to confine costs, however, only fairly well established technology has been utilized, and although some interesting features have been included it is the system as a whole which represents something new.

2. GENERAL SYSTEM DESCRIPTION

To keep within the framework outlined in the introduction an X-band manually operated conical-scan tracking radar has been designed. The main specifications are given in Table 1.

Antenna	:	diameter	:	75 cm
		3 dB beamwidth	:	2.8°
		gain	:	34 dB
		conical scan rate	:	83 Hz
Transmitter	:	frequency	:	9.575 GHz
		peak power	:	1-2 W
		pulse widths	:	0.28, 4, 25 and 47 μs
		prf	:	6000 pps
Receiver	:	noise factor	:	7 dB
		1st IF	:	140 MHz
		2nd IF	:	10.7 MHz
Range tracker	:	maximum range	:	10 km
		minimum range	:	200 m
		acquisition gate	:	300 m
Estimated radar performance	:	angle accuracy (rms)	:	< 0.4°
		range accuracy (rms)	:	< 10 m
Estimated system performance	:	zone wind speed accuracy, σ_v	:	$\begin{cases} < 0.5 \text{ m/s}, & v < 5 \text{ m/s} \\ < 0.1 \cdot v, & v > 5 \text{ m/s} \end{cases}$
		zone wind direction accuracy, σ_θ	:	< 3°

Table 1 Spesifications

Two extra features are being added as options.

- Option 1 is automatic tracking with manual or semi-automatic target acquisition.
- Option 2 is a 1 m diameter monopulse antenna with a time-multiplexed single channel receiver.

Although performance is improved with the addition of these options cost and size limitations prevent them from being part of the standard system.

The overall system can be described with reference to Table 1 and Figure 1 and 2.

The antenna is a 75 cm diameter parabolic reflector with Cassegrain optics. A tilted subreflector rotating with 5000 rpm gives the conical scan movement. A cabinet immediately behind the main reflector contains the transmitter, receiver and signal-processor. The elevation over azimuth suspension is dynamically damped for smooth operation.

Angle tracking is performed manually. In the initial search or acquisition mode the operator is aided by a ring sight and in the track mode by using the conical scan error signal which is presented in a 15×15 cm^2 liquid crystal display. Target acquisition in range and range tracking is performed automatically by a microcomputer.

The microcomputer executes a number of signal processing, data processing and control functions and plays a central part in the system. This gives a very desirable flexibility in the development process and facilitates the implementation of special customer options at a later stage.

The microcomputer guides and controls communication with the operator through the control panel and the display. It also runs automatic hardware and software test programs and has available a simulation program for operator training. During measurements it does the necessary sampling of information, smoothing and numerical calculations in order to provide a standard weather message according to STANAG 4082 to a height of at least 2 km. This message can be linearly extrapolated to a height of 10 km.

In order to attain the desired 10 km maximum range with a low power transmitter and a 70 m^2 average target radar cross section a step-wise range dependent pulse compression system with active detection has been introduced. Four range zones are used, the corresponding binary codes and code lengths are shown in Table 2.

Zone no	Range (m)	Code	Length ($\Delta\tau$ = 0.28 μs)
I	100-800	Single pulse	1
II	700-4400	Barker	13
III	4300-7900	Barker×Barker	7×13
IV	7800-10000	Barker×Barker	13×13

Table 2 Range zones with corresponding codes and code lengths

Disregarding processing loss the relative signal to noise ratios are shown in Figure 3. With a 6000 pps p.r.f. the maximum duty cycle is 0.28 in zone IV. In order to provide a more graceful degradation under adverse conditions a higher p.r.f. may be introduced for the nearer range zones.

2.1. Transmitter

Figure 4 shows a block diagram of the transmitter. The 140 MHz IF-signal is converted to 9.575 GHz in an upper sideband varactor upconverter driven by a 9.435 GHz Gunn oscillator. The signal at 9.575 GHz is amplified in a two stage Impatt amplifier before passing the T/R-switch.

The IF part consists of a crystal controlled 140 MHz oscillator, a biphase modulator and an amplifier with two built-in switches giving 55 dB isolation each. The oscillator is also used as basis for generation of the second local oscillator signal in the receiver. Adequate phase and amplitude linearity in the upconverter and Impatt amplifier makes modulation possible at IF with a negligible contribution to the processing loss. The two switches in addition to the T/R-switch provide the necessary isolation between transmitter and receiver. By placing both the modulation and most of the isolation in the IF-part the functions can be realized with relatively simple and inexpensive components and losses are less important than in the SHF-part.

The pump source is a 0.5 W free running Gunn oscillator. In a copper waveguide structure it has a 0.3 MHz/°C temperature drift in the range from -40°C to +60°C. The Gunn oscillator is isolated from the rest of the system to prevent frequency pulling when the system switches from transmit to receive. This is necessary because the oscillator also acts as first local oscillator in the receiver. Requiring less than 1 dB loss in the compressed pulse the change in frequency f_d between the transmitted signal and the reference signal is limited by

$$f_d \, T \leq 0.25$$

where T is the transmitted pulselength. For $T = 50$ µs this becomes

$$f_d \leq 5 \text{ kHz}$$

This also includes the FM-noise contribution which, however, is negligible.

The bandstop-filter prevents spurious frequencies, primarily the second harmonic, from the upconverter from entering the rest of the system while the bandpass-filter after the circulator selects the upper sideband.

The Impatt amplifier is made as a two-stage circulator coupled coaxial structure. Double drift HP-5082-0610 and 0611 Si diodes are used with maximum oscillator powers of 1.4 W and 2.3 W respectively. This gives a $\Delta T_j = 200°C$ temperature rise at the junction which limits the ambient temperature to 50°C in order to comply with a maximum junction temperature of 250°C. Reducing ΔT_j to 150°C reduces the maximum oscillator powers correspondingly to 1.1 W and 1.6 W.

With the given drive level it is possible with the HP-5082-0611 to achieve a 10 dB gain in one stage with a 0.5 dB gain variation from -40°C to +60°C at a fixed frequency. In order to achieve a 2 W output, however, two stages are necessary and the HP5082-0610 is used in the first stage.

2.2. Receiver

A block diagram of the receiver is shown in Figure 5a.

It is an active receiver designed as a double superheterodyne system with a first IF at 140 MHz and a second IF at 10.7 MHz. This gives several advantages:

- The Gunn oscillator temperature stability requirement is reduced and filters simplified.
- Since the phase of the received signal is unknown the otherwise necessary in-phase and quadrature channels are avoided.

With an IF at 10.7 MHz the basic pulsewidth $\Delta\tau$ is chosen according to

$$3/\Delta\tau = 10.7 \text{ MHz}$$

which gives a null in the Barker code frequency spectra at 10.7 MHz. From this $\Delta\tau = 0.28$ µs and the range resolution $\Delta R = 42$ m. Together with the antenna characteristics this now defines the clutter performance. The three main clutter problems are due to

- rainclutter, time sidelobe contributions
- landclutter, short range main lobe contributions
- landclutter, sidelobe contributions.

The system is designed to stand 4 mm/hour uniform gain which in Norway corresponds to a fallout probability of less than 0.1%. Using Nathansons [1] value for the reflectivity, $\eta = 6.3 \cdot 10^{-7}$ m^2/m^3, it can be shown by integrating the clutter contribution in accordance with the ambiguity function, that the worst case at maximum range gives a signal to clutter ratio > 10 dB.

In the acquisition phase the elevation angle is low and the main beam touches the ground. Assuming a backscattering coefficient $\sigma_o = 0.01$ m^2/m^2 as cited in Nathanson for Swedish countryside the worst signal to clutter ratio in zone I becomes ≈ 6 dB. This is rather marginal considering normal fluctuations in target and clutter cross sections and is the reason for using visually aided acquisition.

The importance of sidelobe clutter has been estimated from Nathansons high clutter data which are approximated with a log-log-distribution and from the antenna E and H-plane diagrams which are extrapolated to cover intermediate values. Using a balloon rate of ascent = 5 m/s and limiting the measurement to heights < 2000 m the probability of obtaining a signal to clutter ratio < 1 has been calculated for different wind velocities. For high velocities, ≈ 30 m/s, the probability approaches 0.15 which is marginal for proper operation but acceptable when compared with the probability of occurrence for such conditions.

Referring to Figure 5a and 5b the receiver mode of operation is described by showing how an rf-pulse modulated with the code A (+-) is handled.

The SHF-signal B passes the T/R-switch before it reaches the first mixer and is converted down to 140 MHz. The main amplifier includes a computer controlled AGC-function. Since the bandwidth is limited the signal C has finite rise and fall-times.

The second LO-signal at 129.3 MHz is derived from the 140 MHz and 10.7 MHz oscillators and passed through a switch which is open only when the arrival of a target return signal C is expected. The oscillator signal D is biphase modulated with the code A giving the reference signal E which is mixed with the signal C in the second mixer. This mixing converts the signal to second IF and removes the phasemodulation. The resulting rf-pulse F goes through a filter matched to the original pulse length. Thus in principle four filters with corresponding envelope detectors are necessary, but only around 1 dB is lost in zone III by using the zone IV filter for both zones. The video pulse H is now sampled at its peak value. This completes the pulse compression. After A/D conversion the signal is fed to the microcomputer for further processing.

The signal is also lowpass filtered and fed to a phase sensitive detector together with the two 90° out of phase subreflector encoder signals. This gives the error signals in azimuth and elevation which are fed to the computer. The signals are retransmitted to the radar display and also used to correct the angle information.

2.3. Signal Processor and Display

The signal processor can be described with reference to Figure 6. It consists of a microcomputer and a radar/computer interface. The computer is based on a fast, (clock frequency > 3 MHz) and powerful 16 bit microprosessor, MIPROC, using a 4 K program memory and a 2 K data memory.

The control logic administers all data transport between radar and computer. Basicly it consists of an 8 bit programmable sequencer and a family of clocks all deduced from a fundamental frequency of 21.4 MHz. The sequencer cycle time is equal to the basic pulse width 0.28 μs. It may be considered as a simple computer which performs only two instructions, execute and conditional jump, and runs independently after being initiated by MIPROC. Thus by doing the necessary code selection and switching the sequencer keeps the radar in formal operation, transmitting and receiving pulses. The main computer is essential, however, in interpreting the received signals.

Two different modes are used. In the search or acquisition mode angle search is done visually while an automatic search in range is made within a window determined from crude initial values of release position and ground wind data. A modified distribution free detection algorithm has been implemented.

When the search routine accepts a target the operator is informed and he has to decide when to switch to the track mode. In the track mode the target range is known and the target motion is estimated using a split gate tracking technique with a 7 m step length. By using every second pulse in the early-gate and the intermediate pulses in the late-gate quasi-simultaneous ranging is achieved. This is important when considering target fluctuations.

Angle error information is presented in a 15×15 matrix liquid crystal display which gives a 3×3° field of view equivalent to 0.2° resolution. The display utilizes the dynamical scattering principle which gives a 20:1 contrast. By switching to a twisted nematic design an even better daylight performance can be achieved with a 80:1 contrast.

In the track mode range, elevation, azimuth, and the angle errors are sampled every second and transferred to the data processing routine. Together with information about temperature, pressure, and various other parameters this is the basis for calculating a NATO standard weather message complying with STANAG 4082.

As mentioned in the general description the availability of a computer also makes possible some extra features:

- An automatic hardware and software test program which checks key functions and informs the operator.

- A tracking simulator which enables an operator to track fictitious balloons launched by the computer and have his tracking performance evaluated.

3. CONCLUSION

An all solid state low power tracking radar has been designed for a limited range, wind measurement system. By introducing a microcomputer based signal processor a flexible custom-oriented system has been achieved. A careful choice of technology has given a rugged system in compliance with military requirements.

The standard system presupposes manually assisted target acquisition and tracking and gives an estimated zone wind accuracy which except for small wind speeds is limited by turbulence only. This contribution, however, cannot be removed.

3.1. References

NATHANSON, F.E., 1969, "Radar Design Principles", McGraw Hill

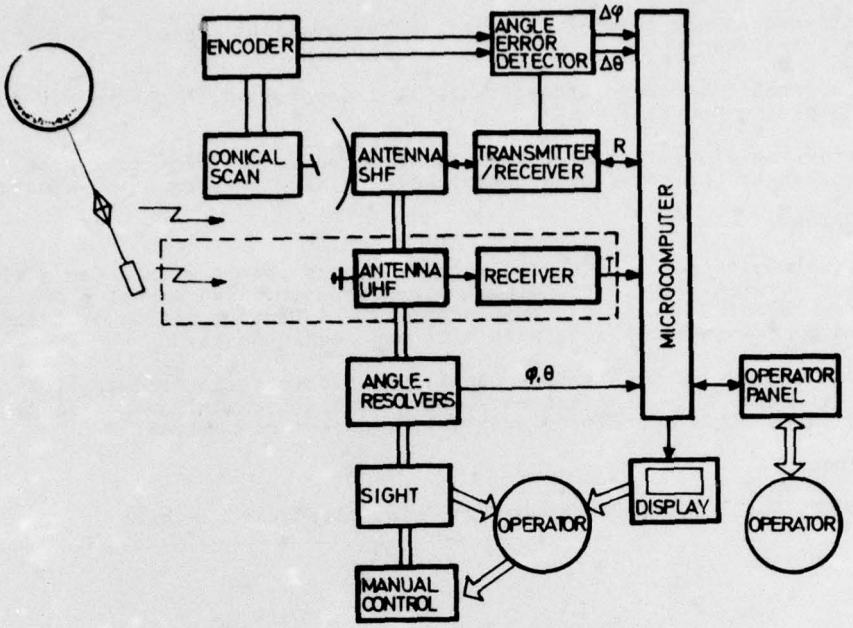

Fig.1 System configuration

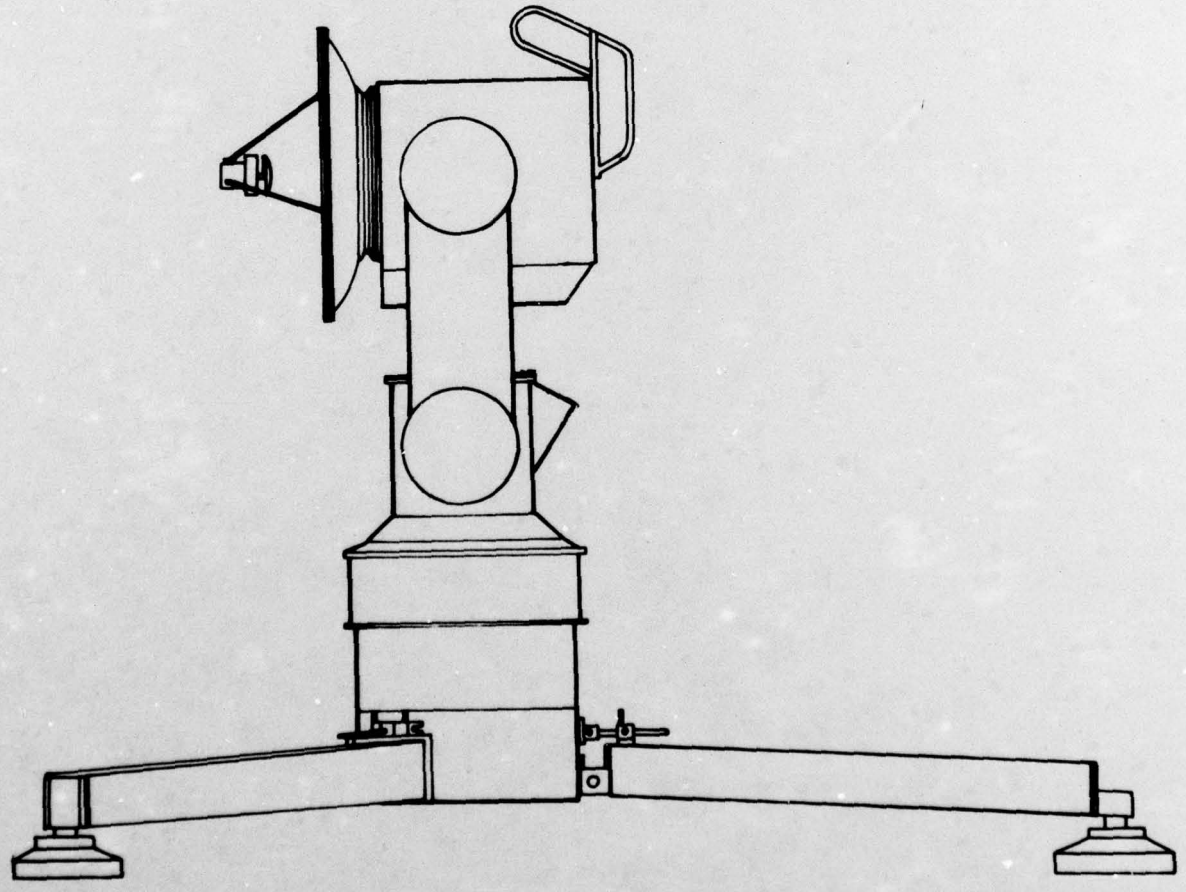

Fig.2 Physical appearance

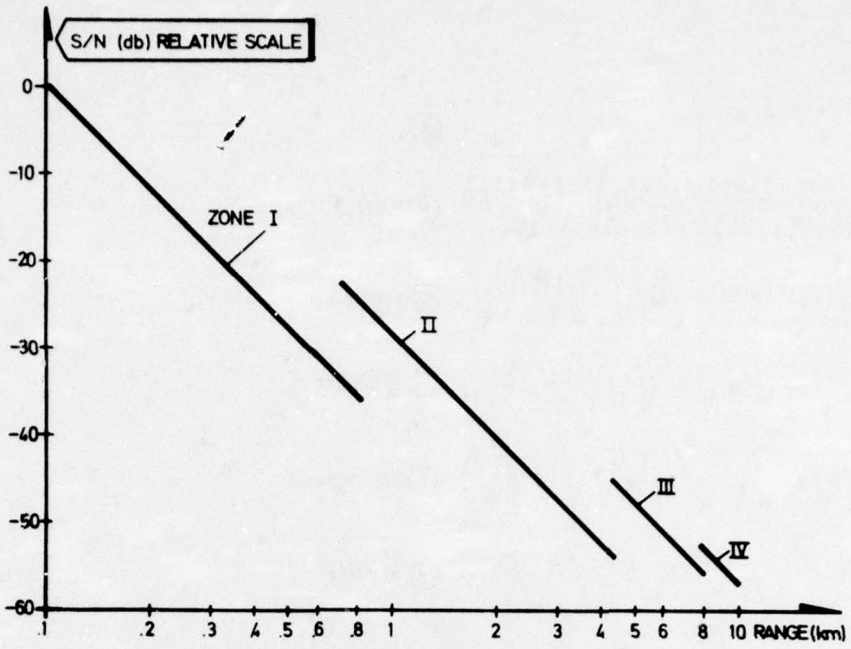

Fig.3 Signal to noise ratios versus range

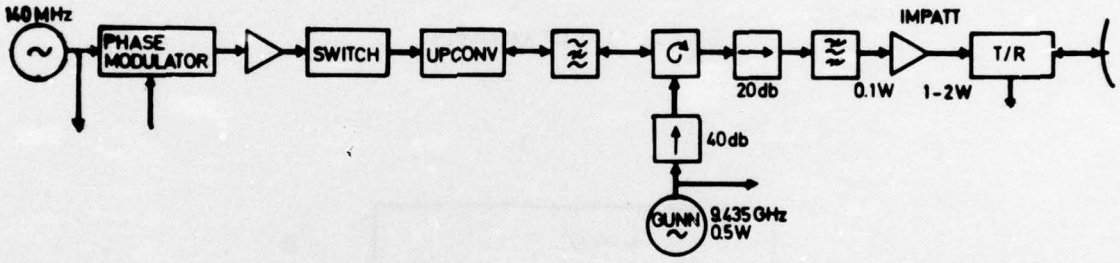

Fig.4 Transmitter

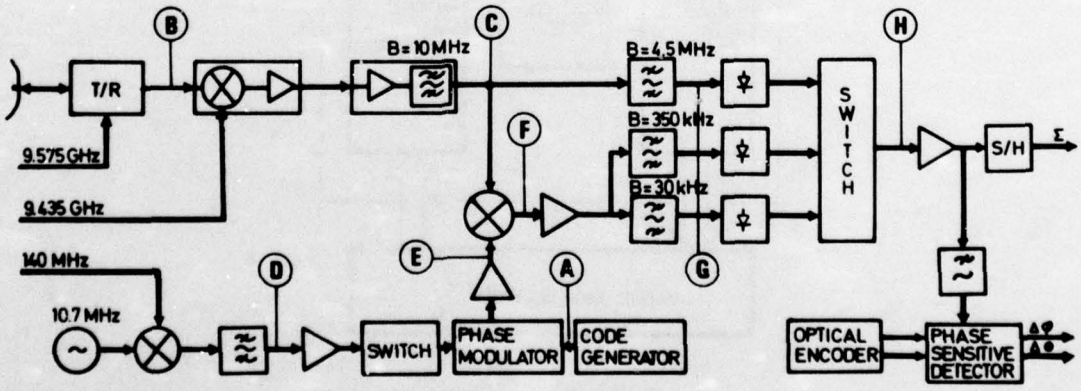

Fig.5(a) Receiver

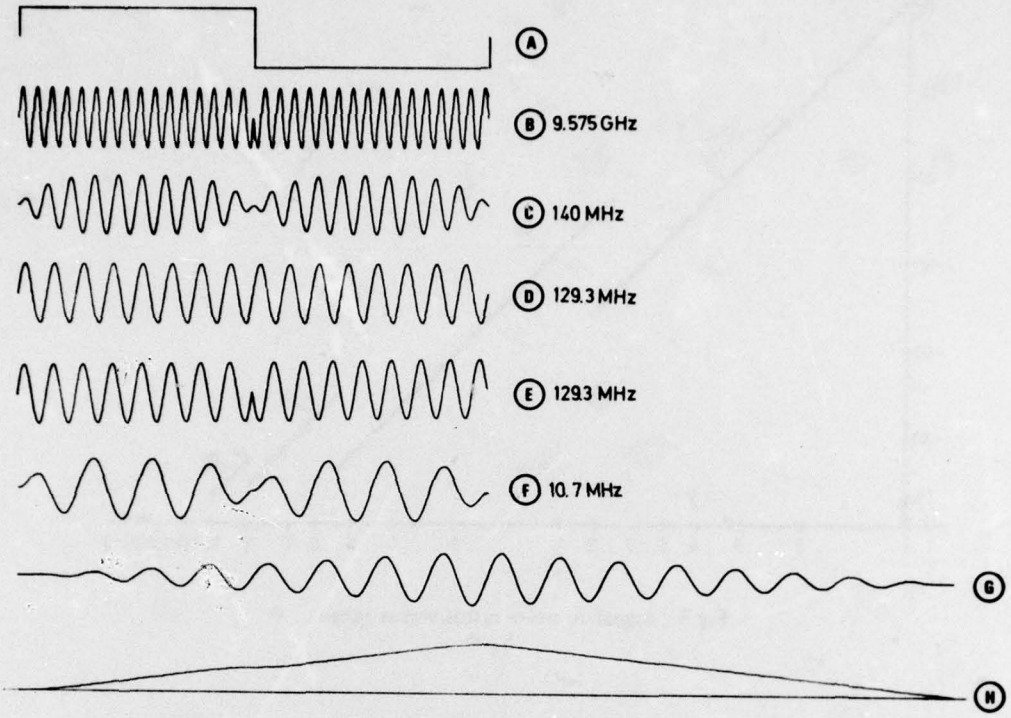

Fig.5(b) Typical waveforms

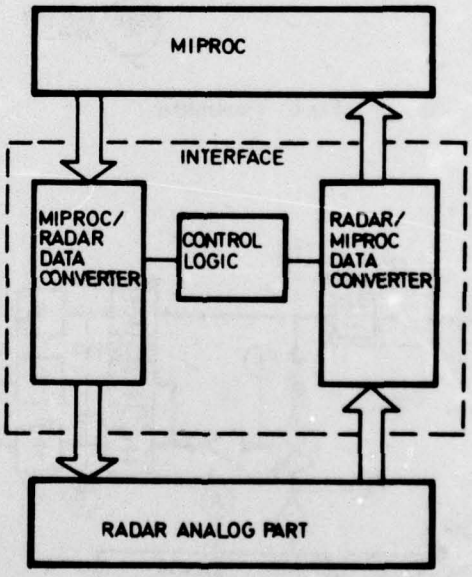

Fig.6 Signal processor

DISCUSSION

J F WALKER: Can you tell us more about the microprocessor?

G ROSENBERG: The MIPROC, developed originally by NDRE, is now being manufactured by the Norwegian company Aksjeselskapel Mikroelektronik, Horten, Norway; and by Plessey in the UK. Two versions are available, one PC board-DIP version and a more compact hybrid integrated version.

J D MAINES: Would you like to comment on your choice of bi-phase coding rather than, for example, linear FM?

G ROSENBERG: We found bi-phase coding to be a more flexible solution for a tracking radar and an advantage in the development stage.

G COLLOT: You have revealed that you are able to produce a NATO standard weather message, but the system is voluntarily limited to 10 Km in slant range. Why have the Norwegian forces developed this system with such a limited range?

G ROSENBERG: Although the minimum height is 2 Km, normal heights will be > 5 Km which is sufficient for the trajectory heights reached by light and medium field artillery. Furthermore, from these heights, sufficiently good extrapolations can be made to fill in the missing lines in the weather message.

REPORT DOCUMENTATION PAGE			
1. Recipient's Reference	2. Originator's Reference AGARD-CP-197	3. Further Reference ISBN 92-835-0185-3	4. Security Classification of Document UNCLASSIFIED

5. Originator	Advisory Group for Aerospace Research and Development North Atlantic Treaty Organization 7 rue Ancelle, 92200 Neuilly sur Seine, France
6. Title	NEW DEVICES, TECHNIQUES AND SYSTEMS IN RADAR
7. Presented at	the Avionics Panel Symposium held in The Hague, Netherlands, 14–17 June1976.

8. Author(s) Various	9. Date February 1977
10. Author's Address Various	11. Pages 606

12. Distribution Statement	This document is distributed in accordance with AGARD policies and regulations, which are outlined on the Outside Back Covers of all AGARD publications

13. Keywords/Descriptors

Meetings	Digital techniques	Radar equipment
Radar	Clutter	
Systems engineering	Electronic countermeasures	

14. Abstract

This publication comprises the proceedings of a Symposium on New Devices, Techniques and Systems in Radar held in The Hague, Netherlands in June 1976 by the Avionics Panel of AGARD.

The objective was to review the influence on radar systems of new devices and techniques, improvements in fundamental knowledge and better methods of performance prediction.

The papers and discussion are grouped under the following headings; Devices and Modules; Radar Techniques; Targets, Clutter and Propagation; Simulation and Detection Theory; and New Systems and Concepts.

The technologies of antennas and displays were not emphasised as these topics had been covered by AGARD Symposia in 1972 and 1975 respectively.

DISCUSSION

J F WALKER: Can you tell us more about the microprocessor?

G ROSENBERG: The MIPROC, developed originally by NDRE, is now being manufactured by the Norwegian company Aksjeselskapel Mikroelektronik, Horten, Norway; and by Plessey in the UK. Two versions are available, one PC board-DIP version and a more compact hybrid integrated version.

J D MAINES: Would you like to comment on your choice of bi-phase coding rather than, for example, linear FM?

G ROSENBERG: We found bi-phase coding to be a more flexible solution for a tracking radar and an advantage in the development stage.

G COLLOT: You have revealed that you are able to produce a NATO standard weather message, but the system is voluntarily limited to 10 Km in slant range. Why have the Norwegian forces developed this system with such a limited range?

G ROSENBERG: Although the minimum height is 2 Km, normal heights will be > 5 Km which is sufficient for the trajectory heights reached by light and medium field artillery. Furthermore, from these heights, sufficiently good extrapolations can be made to fill in the missing lines in the weather message.

AGARD Conference Proceedings No.197 Advisory Group for Aerospace Research and Development, NATO NEW DEVICES, TECHNIQUES AND SYSTEMS IN RADAR Published February 1977 606 pages This publication comprises the proceedings of a Symposium on New Devices, Techniques and Systems in Radar held in The Hague, Netherlands in June 1976 by the Avionics Panel of AGARD. The objective was to review the influence on radar systems of new devices and techniques, improvements in fundamental knowledge and better methods of performance prediction. P.T.O.	AGARD-CP-197 Meetings Radar Systems engineering Digital techniques Clutter Electronic countermeasures Radar equipment	AGARD Conference Proceedings No.197 Advisory Group for Aerospace Research and Development, NATO NEW DEVICES, TECHNIQUES AND SYSTEMS IN RADAR Published February 1977 606 pages This publication comprises the proceedings of a Symposium on New Devices, Techniques and Systems in Radar held in The Hague, Netherlands in June 1976 by the Avionics Panel of AGARD. The objective was to review the influence on radar systems of new devices and techniques, improvements in fundamental knowledge and better methods of performance prediction. P.T.O.	AGARD-CP-197 Meetings Radar Systems engineering Digital techniques Clutter Electronic countermeasures Radar equipment
AGARD Conference Proceedings No.197 Advisory Group for Aerospace Research and Development, NATO NEW DEVICES, TECHNIQUES AND SYSTEMS IN RADAR Published February 1977 606 pages This publication comprises the proceedings of a Symposium on New Devices, Techniques and Systems in Radar held in The Hague, Netherlands in June 1976 by the Avionics Panel of AGARD. The objective was to review the influence on radar systems of new devices and techniques, improvements in fundamental knowledge and better methods of performance prediction. P.T.O.	AGARD-CP-197 Meetings Radar Systems engineering Digital techniques Clutter Electronic countermeasures Radar equipment	AGARD Conference Proceedings No.197 Advisory Group for Aerospace Research and Development, NATO NEW DEVICES, TECHNIQUES AND SYSTEMS IN RADAR Published February 1977 606 pages This publication comprises the proceedings of a Symposium on New Devices, Techniques and Systems in Radar held in The Hague, Netherlands in June 1976 by the Avionics Panel of AGARD. The objective was to review the influence on radar systems of new devices and techniques, improvements in fundamental knowledge and better methods of performance prediction. P.T.O.	AGARD-CP-197 Meetings Radar Systems engineering Digital techniques Clutter Electronic countermeasures Radar equipment

The papers and discussion are grouped under the following headings; Devices and Modules; Radar Techniques; Targets, Clutter and Propagation; Simulation and Detection Theory; and New Systems and Concepts.

The technologies of antennas and displays were not emphasised as these topics had been covered by AGARD Symposia in 1972 and 1975 respectively.

ISBN 92-835-0185-3

The papers and discussion are grouped under the following headings; Devices and Modules; Radar Techniques; Targets, Clutter and Propagation; Simulation and Detection Theory; and New Systems and Concepts.

The technologies of antennas and displays were not emphasised as these topics had been covered by AGARD Symposia in 1972 and 1975 respectively.

ISBN 92-835-0185-3

The papers and discussion are grouped under the following headings; Devices and Modules; Radar Techniques; Targets, Clutter and Propagation; Simulation and Detection Theory; and New Systems and Concepts.

The technologies of antennas and displays were not emphasised as these topics had been covered by AGARD Symposia in 1972 and 1975 respectively.

ISBN 92-835-0185-3

The papers and discussion are grouped under the following headings; Devices and Modules; Radar Techniques; Targets, Clutter and Propagation; Simulation and Detection Theory; and New Systems and Concepts.

The technologies of antennas and displays were not emphasised as these topics had been covered by AGARD Symposia in 1972 and 1975 respectively.

ISBN 92-835-0185-3